

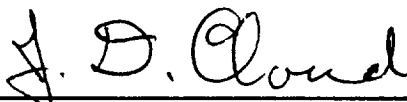
This work was performed for the Jet Propulsion Laboratory,  
California Institute of Technology, sponsored by the  
National Aeronautics and Space Administration under  
Contract NAS7-100.

Surveyor Spacecraft System

**SURVEYOR II FLIGHT PERFORMANCE  
FINAL REPORT**

JPL Contract 950056/January 1967

SSD 68189-2R



---

J. D. CLOUD  
Manager  
System Engineering and Analysis Laboratory



---

T. B. VAN HORNE  
Manager  
Analysis Department



---

R. H. LEUSCHNER  
Head  
Post Flight Analysis Section

**HUGHES**

HUGHES AIRCRAFT COMPANY  
SPACE SYSTEMS DIVISION

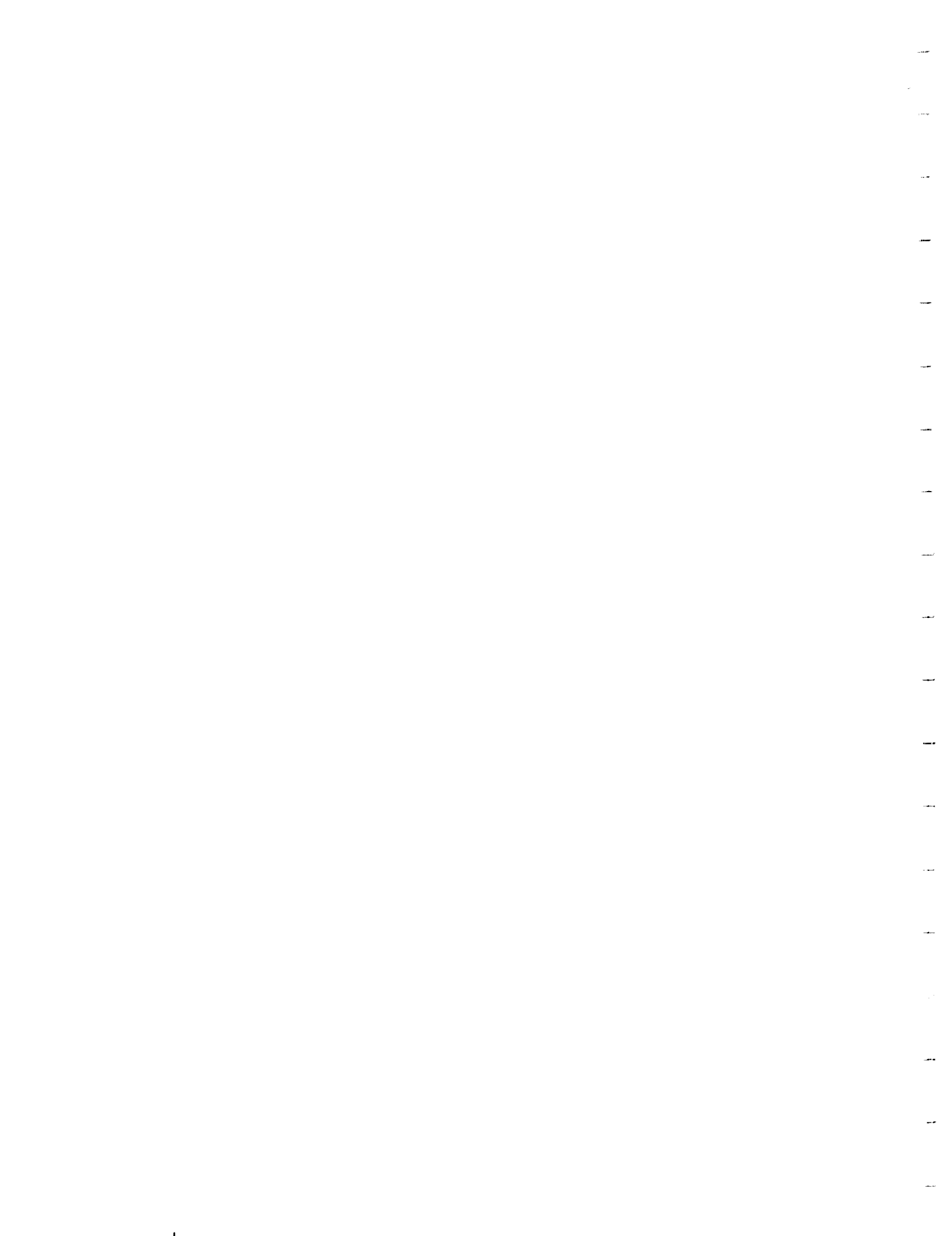


CONTENTS

	Page
1.0 SCOPE AND PURPOSE	1-1
2.0 DESCRIPTION OF SURVEYOR SYSTEM	
2.1 Surveyor II Mission Objectives	2-1
2.2 Surveyor II Flight Configuration	2-2
2.3 Reference	2-2
3.0 SYSTEM SUMMARY	
3.1 Summary of Significant Anomalies	3-1
3.2 System Performance Parameters	3-3
3.3 Conclusions and Recommendations	3-3
4.0 SYSTEM PERFORMANCE ANALYSIS	
4.1 SYSTEM PERFORMANCE ANALYSIS	
4.1.1 General Mission Summary	4.1-1
4.1.2 Trajectory Analysis	4.1-1
4.1.3 Summary of Deviations From EPD-180	4.1-7
4.1.4 Spacecraft Events Summary and Command Log	4.1-14
4.2 PRELAUNCH COUNTDOWN	4.2-1
4.3 LAUNCH, INJECTION, AND SEPARATION	
4.3.1 Launch Trajectory Profile	4.3-1
4.3.2 Spacecraft Performance	4.3-1
4.3.3 Evaluation of Vibration Data for AC-7/SC-2 Boost Environment	4.3-4
4.4 DSIF ACQUISITION	
4.4.1 Acquisition Predictions	4.4-1
4.4.2 Spacecraft Performance	4.4-1
4.5 COAST PHASE I (INCLUDING CANOPUS ACQUISITION)	4.5-1
4.6 MIDCOURSE CORRECTION	
4.6.1 Midcourse Maneuver Analysis	4.6-1
4.6.2 Spacecraft Performance	4.6-11

4.7	DYNAMIC ANALYSIS OF SC-2 MIDCOURSE PHASE	
4.7.1	Introduction	4.7-1
4.7.2	Conclusion	4.7-4
4.7.3	Computer Simulation	4.7-5
4.7.4	Computer Simulation Input	4.7-8
4.7.5	Simulation of Sun Sensor Data	4.7-12
4.7.6	Simulation of Automatic Gain Control Data	4.7-16
4.7.7	Simulation of Gyro Crossover Profile	4.7-27
4.7.8	Simulation of Initial Gyro Response	4.7-28
4.7.9	Midcourse Thrust Duration	4.7-41
4.7.10	Moment of Inertia Uncertainty	4.7-45
4.7.11	Closed-Loop Analog Simulation Results	4.7-47
4.7.12	References	4.7-51
4.8	POSTMIDCOURSE SEQUENCES	
4.8.1	Operational Discussion	4.8-1
4.8.2	Analysis of Spacecraft Rotational Motion	4.8-3
4.8.3	Summary	4.8-15
4.8.4	References	4.8-17
4.9	RELIABILITY ANALYSIS	
4.9.1	Performance	4.9-1
4.9.2	Performance Versus Predictions	4.9-1
4.9.3	Future Reliability Predictions	4.9-5
4.9.4	Reference	4.9-5
5.0	PERFORMANCE ANALYSIS	
5.1	THERMAL CONTROL SUBSYSTEM	
5.1.1	Introduction	5.1-1
5.1.2	Anomalies and Failure Support Data	5.1-3
5.1.3	Summary and Conclusions	5.1-46
5.1.4	Analysis Discussion	5.1-54
5.1.5	Reference	5.1-62
5.1.6	Acknowledgements	5.1-63
5.2	ELECTRICAL POWER SUBSYSTEM	
5.2.1	Introduction	5.2-1
5.2.2	Anomaly Description	5.2-1
5.2.3	Summary and Conclusions	5.2-4
5.2.4	Analysis	5.2-4
5.2.5	References	5.2-30
5.2.6	Acknowledgements	5.2-30
5.3	RF DATA LINK SUBSYSTEM	
5.3.1	Introduction	5.3-1
5.3.2	Anomaly Description	5.3-13
5.3.3	Summary and Conclusions	5.3-22
5.3.4	Subsystem Performance Analysis	5.3-27
5.3.5	References	5.3-64
5.3.6	Acknowledgements	5.3-64

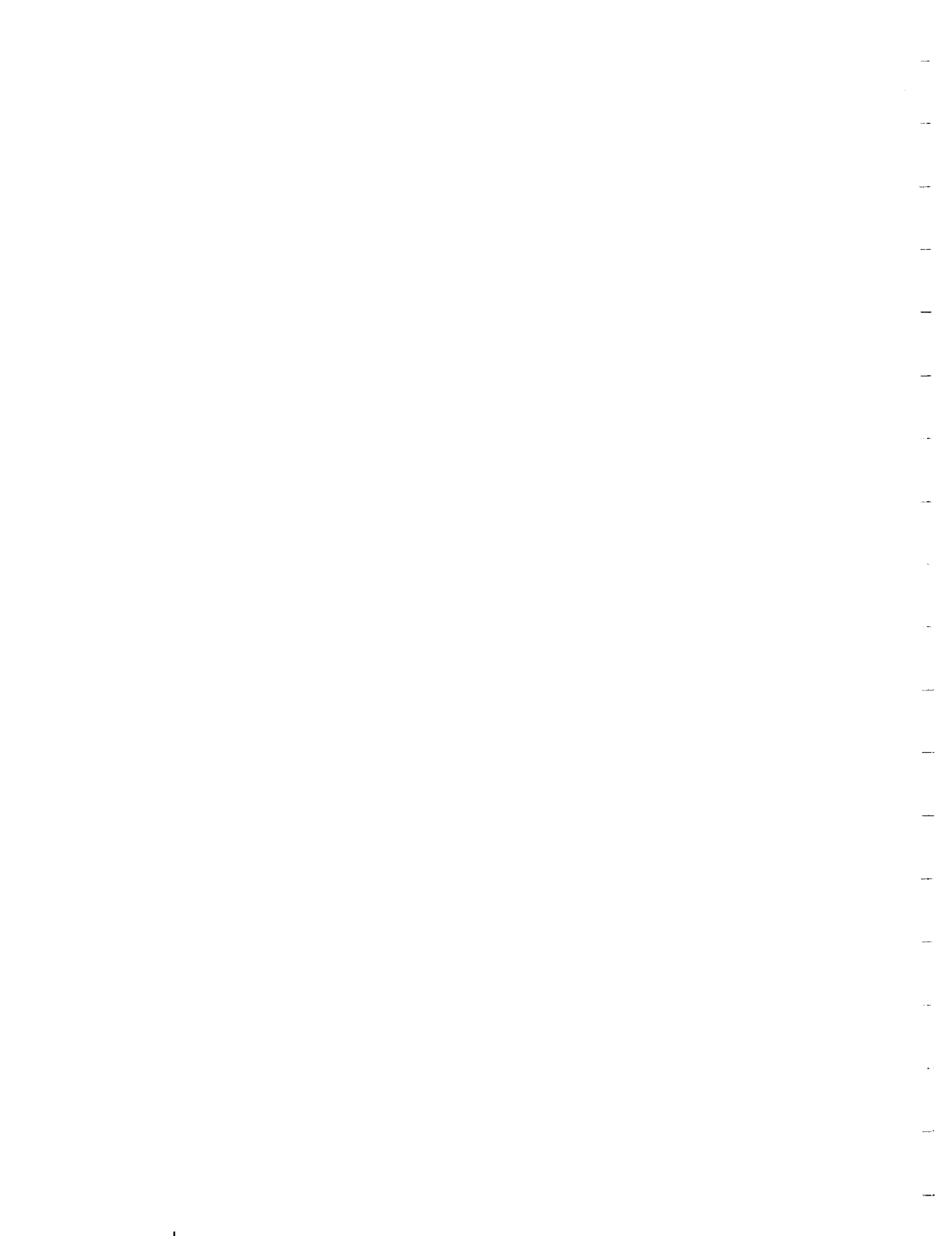
5.4	SIGNAL PROCESSING	
5.4.1	Introduction	5.4-1
5.4.2	Anomalies	5.4-1
5.4.3	Summary and Recommendations	5.4-3
5.4.4	Signal Processing Analysis	5.4.4
5.4.5	Reference	5.4-20
5.4.6	Acknowledgements	5.4-20
5.5	FLIGHT CONTROL	
5.5.1	Introduction	5.5-1
5.5.2	Anomaly Description	5.5-7
5.5.3	Summary and Conclusions	5.5-7
5.5.4	Performance Analysis	5.5-13
5.5.5	References	5.5-167
5.5.6	Acknowledgements	5.5-169
5.6	VERNIER PROPULSION SUBSYSTEM	
5.6.1	Introduction	5.6-1
5.6.2	Anomaly Description	5.6-7
5.6.3	Summary and Conclusions	5.6-11
5.6.4	Subsystem Performance Analysis	5.6-12
5.6.5	References	5.6-26
5.6.6	Acknowledgements	5.6-26
5.7	MECHANISMS SUBSYSTEM	
5.7.1	Introduction	5.7-1
5.7.2	Anomaly Description	5.7-1
5.7.3	Summary and Conclusions	5.7-2
5.7.4	Detailed Analysis	5.7-4
5.7.5	Reference	5.7-11
5.7.6	Acknowledgement	5.7-11



## 1.0 SCOPE AND PURPOSE

At 12:32 GMT (05:32 PDT) on 20 September 1966, the second Surveyor spacecraft (SC-2) was launched from Cape Kennedy. Throughout the early stages of the flight, the overall performance of the spacecraft was excellent, with DSIF acquisition and Canopus acquisition and verification being successfully accomplished. However, during the midcourse velocity correction sequence, vernier engine 3 did not respond properly, resulting in spacecraft tumbling. Subsequent attempts to correct this condition failed. Communication with the spacecraft was lost approximately 45 hours after launch when the main retro engine was fired to obtain additional engineering data.

The basic purpose of this report is to document the actual performance of this second spacecraft throughout the mission, compare its performance with that predicted by the spacecraft design, and recommend any changes or modifications that should be made in the spacecraft design or prediction models. The report is based on both real-time and postmission data analysis. Special attention will be given to the anomaly that caused mission failure, although this report in no way attempts to present the complete logic leading to the final conclusions regarding the cause of that anomaly. This latter task falls rightfully within the jurisdiction of the Failure Review Board.





## 2.0 DESCRIPTION OF SURVEYOR SYSTEM

The Surveyor spacecraft is designed and built by the Hughes Aircraft Company under the direction of the California Institute of Technology Jet Propulsion Laboratory for the National Aeronautics and Space Administration. It has been conceived and designed to effect a transit from earth to the moon, perform a soft landing, and transmit to earth basic scientific and engineering data relative to the moon's environment and characteristics. A brief but complete description of the Surveyor mission objectives and vehicle design is given in the Surveyor I Final Performance Report (Reference 1). Thus only principal variations between the first and second Surveyor missions and designs will be discussed in this section.

### 2.1 SURVEYOR II MISSION OBJECTIVES

The basic objectives of the Surveyor spacecraft system, as defined in Reference 2, were as follows:

- 1) Primary objectives
  - a) Accomplish a soft landing on the moon at a site east of the Surveyor I landing point.
  - b) Demonstrate spacecraft capability to soft land on the moon with an oblique approach angle not greater than approximately 25 degrees.
  - c) Obtain postlanding television pictures and touchdown dynamics, radar reflectivity, and thermal data of the lunar surface.
- 2) Secondary objective: Demonstrate capability of DSS-61 and 72 to support future Surveyor missions.

The secondary objective was subject to resolution of conflicts between Surveyor and Lunar Orbiter for the use of DSN facilities and support. In the event these conflicts could not be resolved, the secondary objective would have been dropped.

## 2.2 SURVEYOR II FLIGHT CONFIGURATION

For a summary description of the major Surveyor functions and design mechanization, see the Surveyor I Final Performance Report (Reference 1). All major differences in the SC-2 configuration compared with that of the first spacecraft are discussed in detail in Table 2-1. A complete listing of SC-2 control items, separated by subsystem or function, is given in Table 2-2.

## 2.3 REFERENCE

- 1) "Surveyor I Flight Performance Final Report," Hughes Aircraft Company, SSD 68189R, October 1966.

TABLE 2-1. SC-2 MAJOR CONFIGURATION DIFFERENCES WITH SC-1

Item	Description															
1) Boost regulator overload trip circuit	In SC-1, the overload trip circuit in the boost regulator had to be disabled because it would trip with a 2-millisecond transient. The SC-2 boost regulator has an overload trip circuit that does not trip unless the transient is 20 to 30-milliseconds.															
2) a) Filter chokes on input to ESP and AESP b) Filter on A/D converter 2 nulling amplifier in CSP	Both of these design improvements eliminate the large variations in temperature readouts on telemetry which were present on SC-1.															
3) Telemetry of flight control return signal	In SC-2 the flight control return signal is telemetered so that varying harness voltage drops can be corrected to provide more accurate data on flight control telemetry signals.															
4) A/SPP pin pullers	A/SPP pin puller modules were redesigned to simplify installation at AFETR.															
5) A/SPP drive motor	All SC-2 drive motors on the A/SPP have roller detents instead of ball detents used in all but the SC-1 roll axis. This is a design improvement.															
6) Omnidirectional antenna latch and release mechanism	SC-2 release mechanisms for omnidirectional antennas A and B have been redesigned to prevent the deployment problem that occurred in the SC-1 flight. The clevis opening has been broadened, and a kickout spring has been added.															
7) Command assignments	SC-2 engineering mechanisms auxiliary had been modified to combine functions of two commands so that two command channels would be made available for fuel and oxidizer dump. It has since been determined that fuel and oxidizer dump are not necessary, but the engineering mechanisms auxiliary change had already been accomplished.															
	<table border="1"> <thead> <tr> <th data-bbox="824 877 865 894">SC-1</th> <th data-bbox="967 884 1057 900">Command</th> <th data-bbox="1182 884 1222 900">SC-2</th> </tr> </thead> <tbody> <tr> <td data-bbox="761 911 938 930">Roll actuator unlock</td> <td data-bbox="987 911 1027 930">0605</td> <td data-bbox="1081 911 1263 947">Roll actuator unlock and pressurize VPS</td> </tr> <tr> <td data-bbox="761 963 902 982">Pressurize VPS</td> <td data-bbox="987 963 1027 982">0607</td> <td data-bbox="1081 963 1122 982">Spare</td> </tr> <tr> <td data-bbox="761 999 930 1018">Unlock roll-(lunar)</td> <td data-bbox="987 999 1027 1018">0633</td> <td data-bbox="1081 999 1263 1035">Unlock elevation and roll (lunar)</td> </tr> <tr> <td data-bbox="761 1052 902 1071">Unlock elevation</td> <td data-bbox="987 1052 1027 1071">0634</td> <td data-bbox="1081 1052 1122 1071">Spare</td> </tr> </tbody> </table>	SC-1	Command	SC-2	Roll actuator unlock	0605	Roll actuator unlock and pressurize VPS	Pressurize VPS	0607	Spare	Unlock roll-(lunar)	0633	Unlock elevation and roll (lunar)	Unlock elevation	0634	Spare
SC-1	Command	SC-2														
Roll actuator unlock	0605	Roll actuator unlock and pressurize VPS														
Pressurize VPS	0607	Spare														
Unlock roll-(lunar)	0633	Unlock elevation and roll (lunar)														
Unlock elevation	0634	Spare														
8) Boost regulator flight control regulator filter	SC-2 boost regulator has a new filter on the flight control regulator to eliminate oscillations that would sometimes occur, causing an overload on the shunt regulator. SC-1 did not have this filter, but apparently did not need it.															
9) Vx and Vy gain in flight control sensor group	Vx and Vy radar attitude loop gains have been reduced in SC-2 to eliminate a potential instability problem at velocities greater than 535 fps.															
10) Solder splash in ESP and AESP	All SC-2 units have had the Kit 10 modification performed to eliminate the solder splash problem (except the spare central command decoder).															
11) RADVS sidelobe rejection logic	Two resistors in the SC-2 signal data converter were removed in order to lower the point at which the sidelobe signals are rejected from 28 to 25 db.															
12) Canopus sun reference filter change	SC-1 had a Canopus sun filter with a reduction of 50 percent (filter factor of 1.5) to compensate for any possible fogging of Canopus sensor window, in accordance with recent measurements of Canopus brightness at Tucson.															
	SC-2 has a filter factor of 1.2. This has been reduced from 1.5 to 1.2 because the fogging problem did not materialize at the Canopus sensor temperature of 79°F for the SC-1 flight.															
13) Canopus window	The O-rings on the Canopus window were changed for SC-2 in an effort to prevent possible fogging of the Canopus filter.															
14) A/SPP pulse duration	Battery charge regulator was changed to reduce A/SPP stepping current pulse duration from 65 to 40 milliseconds. This change reduced the power dissipation in the battery charge regulator and in the A/SPP drive motors.															
15) Quick disconnects	Q3 and Q4 were replaced on SC-2 by changing valves CV3 and CV4.															
16) Auxiliary battery cover paint pattern	The paint pattern of the auxiliary battery container was changed to increase the temperature of this unit, which became too low during Coast Mode II for SC-1.															

TABLE 2-2. SPACECRAFT UNIT CONFIGURATION AT LAUNCH

Subsystem or Classification; Control Item Description	Control Item Part Number	Serial Number
<u>Telecommunications</u>		
Transmitter A	263220-4	15
Transmitter B	263220-4	11
Command receiver and transponder A	231900-3	15
Command receiver and transponder B	231900-3	16
Omnidirectional antenna A	232400	12
Omnidirectional antenna B	232400	21
RF single pole double throw switch	283983	13
RF transfer switch	283984	15
Low pass filter A	233466	1
Low pass filter B	233466	2
Amplifier, telemetry Buffer A	290780	13
Amplifier, telemetry Buffer B	290780	14
Planar array antenna	232300	15
<u>Signal Processing</u>		
Central command decoder	232000-5	3
Central signal processor	232200-8	2
Engineering signal processor	233350-7	1
Auxiliary engineering signal processor	264900-3	3
Signal processing auxiliary	232540-1	1
Low data rate auxiliary	264875-2	2
Television auxiliary	232106-5	11

Table 2.2 (continued)

Subsystem or Classification Control Item Description	Control Item Part Number	Serial Number
<u>Electrical Power</u>		
Battery charge regulator	274100-4	12
Boost regulator	274200-12	14
Solar panel	237760-3	2
Main battery	237900	63
Auxiliary battery	237921-1	64
Auxiliary battery control unit	273000-2	16
Auxiliary battery compartment	263730	5
Main power switch	254112	5
Boost regulator unregulated bus filter	290080	12
Boost regulator unregulated bus choke	290390	12
<u>Fixed Wire-Wound Meter Shunt Resistors</u>		
Battery current	988645-2	778002
RADVS current	988647-1	1
Unregulated output current	988645-3	778007
<u>Flight Control</u>		
Flight control sensor group	235000-9	1
Canopus sensor	235300-2 (Part of 235000-9)	11
Secondary sun sensor	235450-1	2
Attitude jet 1	235700-2	1
Attitude jet 2	235700-3	4
Attitude jet 3	235700-3	6
Attitude jet gas supply	235600-2	4
Roll actuator	235900-3	7

Table 2-2 (continued)

Subsystem or Classification; Control Item Description	Control Item Part Number	Serial Number
<u>Radars</u>		
Altitude marking radar	283827-1	13
RADVS signal data converter	232908-2	AM-7 (9)
RADVS klystron power supply modulator	232909	AM-3 (5)
RADVS altimeter/velocity sensor antenna	232910	AM-4 (6)
RADVS velocity sensor antenna	232911-1	AM-3 (5)
RADVS waveguide assembly	232912	AM-3 (5)
<u>Television</u>		
Approach television camera	284302-1	13
Survey television camera	284312-3	11
Photometric chart on omnidirectional antenna B	231051	12
Photometric chart on landing gear 2	230992	12
<u>Propulsion</u>		
Fuel tank 1	287000-3	1
Fuel tank 2	287001-3	4
Fuel tank 3	287000-3	2
Oxidizer tank 1	287002-3	1
Oxidizer tank 2	287004-3	3
Oxidizer tank 3	287003-3	1
Thrust chamber assembly 1	285063-1	542
Thrust chamber assembly 2	285063-2	546

Table 2-2 (continued)

Subsystem or Classification; Control Item Description	Control Item Part Number	Serial Number
Thrust chamber assembly 3	285063-3	544
Helium tank and valve assembly	262789-2	4
Retro rocket engine	238612	A21-27
<u>Thermal Control</u>		
Thermal switches, compartment A	238810	15, 22, 23, 44
	238810-1	8
	238810-3	11, 12, 29
	238810-4	1
Thermal switches, compartment B	238811	7, 16, 17, 18, 19, 20
Thermal shell assembly Compartment A	286459	1
Compartment B	286460	1
Thermal control and heater assembly	232210-1	15
	232210-2	18
Thermal tray assembly Compartment A	264334-1	3
Compartment B	276935	6
Thermostat, heater, and temperature sensing assemblies: legs 1, 2, and 3		
<u>Thermal Resistors</u> <u>Compartment A</u>		
Tray top	988653-2	6538
Lower Support	988653-2	155
Insulation	988653-2	6542

Table 2-2 (continued)

Subsystem or Classification; Control Item Description	Control Item Part Number	Serial Number
Canister	988653-2	6276
Thermal switch 2	988653-2	180
Thermal switch 5, inner contact ring	988654-10	1954
Thermal switch 5, outside	988653-2	176
Thermal switch 8	988653-2	6349
<u>Thermal Resistors, Compartment B</u>		
Thermal switch 1	988653-2	6380
Thermal switch 5	988653-2	6379
Lower spaceframe 1	988653-2	171
Lower spaceframe 2	988653-2	167
Tray top	988653-2	6271
Lower support	988653-2	6386
Canister	988653-2	6269
Thermal switch 4, inner face radiator	988653-2	6368
Thermal switch 4, inner contact ring	988650-2	6150
<u>Thermal Resistors, Spaceframe</u>		
Upper spaceframe 1	988654-2	113
Upper spaceframe 2	988654-2	116
Leg 2 upper web	988653-2	117
Retro attach 1	988653-2	196
Retro attach 2	988653-2	163
Retro attach 3	988653-2	164
Harness tunnel	988657-1	106
Crushable block	988653-2	217
Auxiliary battery compartment	988653-2	6414



Table 2-2 (continued)

Subsystem or Classification; Control Item Description	Control Item Part Number	Serial Number
<u>Mechanisms and Instrumentation</u>		
Spaceframe subassembly	264178-1	1
Landing gear 1	261278	4
Footpad leg 1 subassembly	(263947)	-
Landing gear 2	261279	3
Footpad leg 2 subassembly	(263947)	-
Landing gear 3	261280	4
Footpad leg 3 subassembly	(263947)	-
Shock absorber, leg 1	264300-1	9
Shock absorber, leg 2	264300-1	10
Shock absorber, leg 3	264300-1	11
Leg position potentiometer 1	988684-1	989062
Leg position potentiometer 2	988684-1	989920
Leg position potentiometer 3	988684-1	989919
Omnidirectional antenna A mechanism	287300-1	2
Omnidirectional antenna B mechanism	273880-1	1
Cartridge actuated pin pullers, mechanical		
Omnidirectional antenna A	236390-5	140
Omnidirectional antenna B	236390-5	142
Antenna and solar panel positioner	287580	1

Table 2-2 (continued)

Subsystem or Classification; Control Item Description	Control Item Part Number	Serial Number
Cartridge actuated pin puller - A/SPP subassemblies		
Roll latch	293184-2	1
Roll latch	293184-3	2
Elevation	293184-1	2
Solar panel	293184-5	2
Solar panel	293184-4	2
Solar panel	287490-9	141
Retro rocket release mechanisms, legs 1, 2, and 3	230069-1	28, 29, 30
Separation sensing and arming devices, legs 1, 2, and 3	293400	1, 9, 7
Cartridge actuated pin pullers, legs 1, 2, and 3	236390-7	141, 144, 147
Cartridge actuated pin puller, roll actuator	236390-7	143
Engineering mechanism auxiliary	263500-6	12
EMA board 4	273341 (Part of 263500-6)	F-4
Strain gage amplifier assembly, leg 3	238930	5
Accelerometer 1, leg 1	239002-1	17
Accelerometer 2, leg 2	239002-2	18
Accelerometer 3, leg 3	239002-3	19
Accelerometer 4, flight control sensor group	239002-4	20
Accelerometer 5 A/SPP mast	239002-5	21

Table 2-2 (continued)

Subsystem or Classification; Control Item Description	Control Item Part Number	Serial Number
Accelerometer 6, velocity sensor antenna (RADVS)	239002-6	22
Accelerometer 7, compartment A	239002-7	23
Accelerometer 8, compartment B	239002-8	16
Accelerometer amplifier	239011	3
<u>Cables and Harnesses</u>		
Wiring harnesses		
A/SPP	286417	1
Compartment A	286207	4
Compartment B	286242	4
Retro rocket engine	286390	2
TV camera	276979	5
Auxiliary battery	264100	3
Basic bus 1	3025357	1
Basic bus 2	286398	2
Battery cell voltage	3025155	2
RF cable assemblies		
Planar array	276828-1	4
	261714	4
Transmitter A	276266-2	5
	261713	10
	261711	10
Omnidirectional antenna A	261719	9
	261720	8
Transfer switch	261712-1	10
	261712	11
Planar array	261714	4
	261719-2	9

Table 2-2 (continued)

Subsystem or Classification; Control Item Description	Control Item Part Number	Serial Number
Transmitter B	276266-1	2
	261711-1	5
Omnidirectional antenna B	261720-1	8
	261719-1	17
	261721-1	9
Accelerometer coaxial cables		
		16
		17
		18
		19
		20
		21
		22
23		

## 3.0 SYSTEM SUMMARY

### 3.1 SUMMARY OF SIGNIFICANT ANOMALIES

The anomalies that occurred during Mission B are summarized in Table 3-1. For this report, an anomaly is defined as an unexpected occurrence that might be indicative of a spacecraft trouble or failure. The anomalies are discussed in detail in the sections noted in this table.

Eight spacecraft anomalies were designated for the flight of SC-2. The first six of these, as outlined in Table 3-1, would not have prevented the completion of a successful mission. The failure of vernier engine 3 to ignite resulted in an unsuccessful completion of the mission. The last anomaly, in which a late shutdown was probably indicated for vernier engine 1 during engine firing 27, could have resulted in loss of spacecraft control.

TABLE 3-1. SPACECRAFT ANOMALIES

Number	TIME		Anomaly	Cause	Effect On Mission	TFR Number	Disposition of TFR
	GMT, day:hr:min	From Launch					
1	263:12:37	0H 5M	Two accelerometer channels (IRIG channels 14 and 17) CY 52 0 and CY 53 0 did not function properly (see subsection 4.3.3).	Unknown	Associated boost vibration data was not obtained.	18251, 18252	Closed 17 November 1966. Refer to IDC 2294. 6/21 for additional information.
2	263:12:43	0H 11M	At approximately the time of the landing leg extension (35 seconds prior to spacecraft/Canopus separation), flight control changed from rate to inertial mode (see subsection 5.2.2.1). Vernier line 2 heater was full on early in coast mode I (see subsection 5.1.2.1).	Transients produced on legs down and/or separation lines caused incorrect triggering of programmer latches.	None. Flight control automatically returned to rate mode at separation (normal operation).	18247	Closed 5 October 1966. Refer to ECA 111775 for corrective action in effect.
3	263:15:27	3H	Vernier line 2 heater was full on early in coast mode I (see subsection 5.1.2.1).	Epoxy contamination resulting in increased emittance	Would have decreased battery charge at landing by 3 or 4 amp-hr.	18253	Closed 22 December 1966. Refer to ECAs 113133, 113096 for corrective action in effect.
4	263:18:38	6H 6M	During Canopus star map, star lock signal was not obtained when Canopus was in field of view (see subsection 5.5.2.2).	Effective gain of star sensor was great enough to place star signal outside upper lockon gate.	None. Acquired Canopus by manual lockon command.	18250	Closed 8 December 1966. Refer to IDC 2223/2570 for corrective action in effect.
5	263:19:15	6H 43M	Receiver B AGC telemetry indicated that signal level was 18 db below predicted value during star verification maneuver. Downlink (DSS receiver AGC) agreed with predicted values (see subsection 5.3.2). Helium transducer pressure indicated a sudden 720-psi zero offset after pressurization command (see subsection 5.6.2.1).	Probably a loss in gain in either the A6 or A8 modules.	Associated telemetry channel recalibrated during flight. Positive command margin was still available at lunar distance.	18249	Closed 22 December 1966. Refer to IDC 2294. 2/55 for corrective action in effect.
6	264:04:53	16H 21M	Helium transducer pressure indicated a sudden 720-psi zero offset after pressurization command (see subsection 5.6.2.1).	Shock loading of transducer during squib actuation.	None. A limited amount of zero shift had been expected. In the future, this will not be considered an anomaly.	18254	Closed 18 November 1966. Corrective action in effect.
7	264:05:00	16H 28M	Vernier engine 3 did not respond to vernier ignition command. All subsequent attempts to obtain normal engine 3 thrusting were unsuccessful. For various discussions, see subsections 5.1.2.4, 5.1.2.4, 5.2.4.5, 5.5.2.3, and 5.6.2.3.	Specific cause of failure to be determined by Failure Review Board.	Unbalanced thrust caused spacecraft rotation which could not be nullified by cold gas jet system.	18248	Open
8	265:03:47	39H 15M	Late shutoff of vernier engine 1 during burn 27 (see subsection 5.5.2.4)	Unknown. Probably a valve problem.	Possibility of losing control of spacecraft if all engines do not shutdown simultaneously.		

## 3.2 SYSTEM PERFORMANCE PARAMETERS

Performance parameters that could be determined through post-mission analysis of spacecraft telemetry data are given in tables near the beginning of each subsystem part of Section 5. The major or significant system performance parameters are summarized in Table 3-2. Required or predicted values for these parameters are included in this summary for comparison purposes.

## 3.3 CONCLUSIONS AND RECOMMENDATIONS

### 3.3.1 Conclusions

Prior to the scheduled midcourse correction, the SC-2 flight was uneventful. All spacecraft subsystems performed as designed except for a few almost trivial instances (Table 3.1, number 1-6). At midcourse, the spacecraft tumbled when only two of the three vernier engines ignited. After repeated nonstandard procedures could not regain control of the spacecraft, ignition of the retro engine (while still 18 hours away from the lunar surface) caused loss of spacecraft contact. The cause of the catastrophic failure of vernier engine 3 is under continuing investigation.

### 3.3.2 Recommendations

Table 3-3 is a summary of the status of Surveyor I recommendations. Additional operational and procedural recommendations as a result of the Surveyor II flight are made in each subsection of Section 5. The SC-2 recommendations are summarized in Table 3-4.

TABLE 3-2. SUMMARY OF SYSTEM PERFORMANCE PARAMETERS

Parameter	Required	Source	Predicted	Source	Actual	Subsection Reference
<u>Overall</u>						
1) Injected weight					2207.83 pounds	
2) Mission payload weight					63.64 pounds	
3) Dry landed weight					631.82 pounds	
<u>Launch to injection</u>						
1) Launch time	Between 263:11:46 and 12:32 GMT				263:12:41:54	
2) Spacecraft angular rates during boost	<3.0 deg/sec	224510E			1.386 deg/sec (pitch) 0.534 deg/sec (yaw)	5.5.4.2
3) Spacecraft angular rates at separation	<3.0 deg/sec	224510E			0.113 deg/sec (pitch)	5.5.3.1
4) Time to null separation rates	<50 seconds	224510E			4 seconds	5.5.4.2
<u>Separation to acquisition</u>						
1) Solar panel deployment time			624 seconds 620 seconds	STV 2R STV retest	612 seconds	5.8.4.3
2) Sun acquisition time	<18 minutes	224510E			174.3 seconds	5.5.3.1
3) Required maneuvers to acquire sun						
Roll					71.0 degrees	5.5.3.1
Yaw					15.9 degrees	5.5.3.1
4) Time of first DSS visibility: Delta time to:			263:12:55:00		263:12:54:55	5.3.4.2
One-way lock	<12 minutes	224510E			12 seconds	5.3.4.2
Two-way lock	<30 minutes	224510E			10 minutes and 3 seconds	5.3.4.2
Transmission of first command	<18 minutes	224510E			21 minutes and 38 seconds	5.3.4.2
5) Time of initiation of Canopus acquisition	2 hours prior to midcourse	224510E	Launch + 6H	EDP 180	264:18:37:34 (L + 6H+M35S)	5.5.4.4
6) Time required to acquire Canopus	<38 minutes	224510E			32 minutes and 9 seconds	5.5.4.4
7) Roll angle from beginning of third revolution to Canopus			<360 degrees		249.0 degrees	5.5.3.1 5.5.4.4
8) Total roll angle from beginning of maneuver to Canopus lockon			<1080 degrees		960.2 degrees	5.5.4.4
<u>Coast Phase</u>						
1) Attitude orientation						
Mean error from sun line	<0.2 degree	224510E			-0.07 (pitch) -0.1 (yaw)	5.5.3.1 5.5.3.1
Mean error from Canopus	<0.2 degree	224510E			-0.06 (roll)	5.5.3.1
2) Limit cycle-optical mode						
Roll-average amplitude	<0.6 degree	224510E	0.44		0.441 degree	5.5.3.1
Pitch-average amplitude	<0.6 degree	224510E	0.44		0.459 degree	5.5.3.1
Yaw-average amplitude	<0.6 degree	224510E	0.44		0.479 degree	5.5.3.1
Average period (time between gas jet pulses)		224510E	80 sec/pulse		64 sec/pulse	5.5.3.1
3) Gyro drift						
Roll	<1 deg/hr	224510E			0.78 deg/hr	5.5.3.1
Pitch	<1 deg/hr	224510E			0.24 deg/hr	5.5.3.1
Yaw	<1 deg/hr	224510E			1.04 deg/hr	5.5.3.1
4) Mean solar panel output	89 ± 5 watts	224510E			88 watts	5.2.4.2
5) Mean OCR output					70 watts	5.2.4.2
<u>Midcourse Correction</u>						
1) Pre-midcourse maneuver angles						
Roll					75.372 degrees	5.5.3.1
Yaw					110.841 degrees	5.5.3.1
2) Pointing accuracy	<0.7 degree error	224510E			0.39 degree (pitch) 0.04 degree (yaw)	5.5.3.1
3) Midcourse engine burn time					3.89 seconds	5.5.4.8
<u>Postmidcourse</u>						
<u>Tumble rate</u>						
Initial midcourse					448 deg/sec	5.5.2
After 14.5 minutes with gas jet damping					106 deg/sec	5.5.2



TABLE 3-3. STATUS OF SURVEYOR I RECOMMENDATIONS

Paragraph and Itemization Numbers in SSD68189R	Recommendation (See reference for details)	Status
4. 2. 2. 1	1) Redesign omnidirectional antenna extend mechanism.	Change accomplished on SC-2.
	2A) Revise calibration methods for spacecraft receiver AGC signals.	Special calibration procedure to be followed during STV for SC-4 and following spacecraft.
	2B) Include AGC in every commutator mode.	Included in all modes except 3 for SC-5 and following spacecraft.
	3) Change Canopus sensor gain calibration. Change dependent on whether fogging is expected.	Since potential fogging existed for SC-2, gain was changed to 1.2 Canopus.
	4) Revise paint pattern on auxiliary battery.	Paint changed on SC-2.
4. 2. 2. 2	1) Gyro speed measurement improvement or deletion during test.	Gyro speed signal processing channels were improved for SC-2.
	2) Change in postlanding TV picture mirror scanning techniques.	Not applicable to SC-2; still desired for SC-3 and subsequent spacecraft.
	3) Additional DSIF station reports on phase jitter and AGC levels.	Data will be supplied at request of SPAC.
4. 2. 2. 3	1) SFOF digitized tapes should be used instead of DSIF tapes whenever possible.	SFOF digitized tapes being used.
	2) Reduction in number of 66-hour transit phase averaged plots.	66-hour plots not being made for telemetry signals for which these plots are not useful.
	3) Copies of real-time SFOF teletype data and bulk printer data made available for postmission analysis.	Teletype data have been made available. Bulk printer data have not been available and are still desired.
	4A) Closer coordination and exchange of reduced data between Hughes and JPL to avoid excessive duplication of efforts.	Improvements have been made and will continue in the future.
	4B) Publish Quick Look reports on SPAC and FPAC activities. Eliminate postmission analysis Quick Look Report.	SPAC and FPAC reports are being published. Earlier publication of reports is desirable.
	5) Eliminate frame-by-frame corrections for current differential amplifier calibrations.	Since current amplifier gain was not so stable on SC-2 as it was on SC-1, frame-by-frame corrections were still required.
	6A) Eliminate automatic unbalance current corrections for telemetry channels having a capacitive output impedance.	Corrections have been eliminated.
	6B) Additional unbalance current correction dependent on commutator switch used for telemetry signal.	Additional correction not yet provided.
	7A) Proper placement of "end of file" marks when digitizing raw telemetry tapes.	Greater care has been taken in proper placement of these marks.
	7B) Proper discriminator adjustment to avoid "bit slip" when digitizing raw telemetry tapes.	"Bit slip" is still a problem.
	8) Modify reformatter program to eliminate addition of fictitious time tags when time coding on a digitized tape is noisy.	This program feature will be eliminated for SC-3 postmission data processing.
	9A) More timely transmittal of all DSIF telecommunication parameters to postmission analysis personnel.	Time of transmittal has been improved.
	9B) Make available data on DSIF subcarrier oscillators (frequency, when used, etc.).	Data not available and are still desired.
	9C) TV data be made available in a more timely manner to fully evaluate survey camera performance.	Not applicable to SC-2. Still desired for future missions.
4. 2. 3	1) Continue use of a "high sun" solar intensity of 112 percent of one solar constant (an Eppley radiometer reading of 105 percent).	Plans for future STV tests assume the same test chamber solar intensities used on SC-1 and SC-2.
	2) Investigate battery parameters to permit a more accurate model of the state of charge.	Model accuracy is being improved as more data become available.
	3) FAT vibration levels should be reduced to more nearly approximate the actual Centaur vibration environment.	FAT vibration levels have been reduced for SC-2 and subsequent spacecraft.
	4A) Change reliability model to allow for lessened boost vibration effects.	Model is being improved as more data become available.
	4B) Change reliability model to allow for nonstandard procedures.	Allowance for nonstandard procedures not yet included in model.
	5) Revise A/SPP thermal prediction model.	Revised model has been developed based on SC-1 performance data.
	6) Revise survey TV thermal model for prediction of postlanded thermal performance.	Model has been revised based on SC-1 performance data.

TABLE 3-4. SUMMARY OF SURVEYOR II RECOMMENDATIONS

Number	Section	Recommendations
<u>Spacecraft Design Change Recommendations</u>		
1	5.1	Increase thermal dissipation capability of vernier engine 2 line heater. Change has already been accomplished (see Table 3-1, disposition of TFR 18253).
2	5.3	Place temperature transducers on transmitter and receiver modules that contain the respective VCXOs. This would enable correlation between frequencies and telemetered temperature data in order to check prelaunch frequency reports and to update DSIF tracking predictions.
3	5.5	Mechanize on-board calibration for flight control variables.
4	5.5	Mechanize on-board clock to standardize mission time base.
5	5.5	Provide a number of continuous analog data channels (e.g., FM/FM).
6	5.5	Measure thrust chamber pressure (all legs).
7	5.5	Measure shutoff valve (propellant) inlet pressure (all legs) for oxidizer and fuel.
8	5.5	Measure thrust command in terms of coil currents rather than coil voltage drops.
9	5.5	Sample vernier engine strain gages (all legs) at as high a rate as possible in all modes if these gages remain primary measure of engine response.
10	5.5	Synchronize magnitude register start of countdown with telemetry word time.
11	5.5	Install a lower transmissibility filter in the Canopus sensor sun channel to set effective gain in vicinity of 1/10. This change has been accomplished (see Table 3-1, disposition of TFR 18247).
12	5.6	Make vernier line temperatures available during thrusting.
13	5.6	Make thrust chamber assembly (engine) temperatures available during thrusting.
14	5.6	A fuel pressure (pressure tap in fuel line) measurement should be added to the vernier engine subsystem.
<u>Operational Recommendations</u>		
1	5.3	Improved recovery of DSIF station data for use in postmission analyses. Need calibration data to translate oscillograph deflections back to physical parameters in absolute engineering units.
2	5.5	(SFOF) - Add NASA time code (36 bit) to all SFOF data. Slow and fast codes should be provided for selection keyed to recorder paper speed.
3	5.5	(SFOF) - Record SPAC signals (voltages) with wideband FM on magnetic tape with time code.
4	5.5	(SFOF) - Provide dub copies of all necessary magnetic tapes (digital or analog) to Hughes.
5	5.5	(SFOF) - Provide copies of all SPAC brush recordings to Hughes.
6	5.5	(SFOF) - Add a sufficient number of brush recorders to SPAC so that 90 to 100 percent of quick-look analysis requiring continuously recorded data can be performed independent of digital data processing.
7	5.5	(SFOF) - Provide an electrical interlocked event marker on all brush recorders.
8	5.5	(SFOF) - Provide 1-second marking pens on all brush recorders.
9	5.5	(SFOF) - Standardize brush recorder paper speeds (1 and 5 mm/sec are recommended).
10	5.5	(SPAC) - Assign responsibility for early termination of midcourse velocity correction to one person in flight control area who would communicate his decision directly to the SPAC bus chief.
11	5.5	(SPAC) - In case early termination of the midcourse velocity correction is required, prearrangements for necessary termination command should be made, to be activated immediately upon verbal request of bus chief or his designee, without question.
<u>Postmission Data Processing Recommendations</u>		
1	5.5	Graphic presentation of data is recommended as primary mode of data presentation. Backup with tables for use in interpreting details and checking questionable digital word structure.
2	5.5	Point plots are preferred for detailed analysis. Staircase plots are adequate for majority of analyses.
3	5.5	Time base should be selectable and standardized for like events.
4	5.5	Plot scales and limits should be selected as a function of data (sample rate, curve slope), and should not be "floating". Raw BCD values should be plotted, unless otherwise specified. Data values in both BCD and engineering units are required on tabulations.
5	5.5	Fortran data tape output from reformatter program is recommended.
6	5.5	Develop methods for producing wideband FM tapes of flight control variables.
7	5.5	Expedite acquisition of DSIF data (telemetry on magnetic tapes). Assume DSIF is primary source of data with fillin supplied from the real-time (SFOF) data.
8	5.4	Process of decommutating DSIF telemetry tapes should be changed to retrieve all possible data.
<u>Test and Performance Prediction Model Recommendations</u>		
1	5.1	Prohibit the attachment of wire harnesses with high emittance surfaces to lines during solar thermal vacuum tests.
2	5.1	Perform black light inspection on unit level at Hughes after epoxy application (but before curing). Remove excess epoxy that would contaminate the lines.
3	5.1	Perform final black light inspection on spacecraft before shipping to AFETR.
4	5.3	For receiver AGC, a system calibration should be made during solar thermal vacuum tests. Also, all applicable prelaunch tests run at AFETR should check for AGC changes. This would aid in postmission analyses and may flag impending receiver failures.
5	5.5	Investigate gas jet double pulsing phenomenon (SC-1 and SC-2).
6	5.6	Establish more stringent acceptance criteria during solar thermal vacuum tests for line heaters. The criteria should detect lines operating in a marginal thermal environment.

## 4.0 SYSTEM PERFORMANCE ANALYSIS

### 4.1 INTRODUCTION

#### 4.1.1 GENERAL MISSION SUMMARY

At 05:32 PDT on 20 September 1966, the second Surveyor spacecraft (SC-2) was launched from Cape Kennedy. Through the early stages of the flight, overall spacecraft performance was excellent, with DSIF acquisition and Canopus acquisition and verification being successfully accomplished. However, approximately 16 hours and 28 minutes after launch, when the command to ignite the three vernier engines was sent to the spacecraft as part of the standard midcourse velocity correction sequence, vernier engine 3 did not respond properly. The thrust provided by vernier engines 1 and 2 resulted in spacecraft spin at approximately 1.22 rps. An initial attempt to halt the spinning, with the cold gas jets being controlled by the flight control subsystem operating in the rate mode, was terminated when it required approximately 60 percent of the available gas supply to reduce the spin rate to approximately 0.97 rps, thereby indicating that the available gas supply would not be sufficient to stop the spacecraft rotation. Because the spacecraft was spinning about an axis such that the sun was not in the upper hemisphere of the vehicle, the solar panel was not illuminated, and the main and auxiliary batteries were the only spacecraft power sources from this point in the mission. Thirty-nine subsequent attempts to obtain normal firing of vernier engine 3 were unsuccessful and resulted in the spacecraft rotational rate being increased to a maximum of 2.43 rps. With the available power decreasing steadily, it was decided to fire the main retro engine at L + 45H0M. Communication with the spacecraft was lost approximately 30 seconds following retro engine ignition.

#### 4.1.2 TRAJECTORY ANALYSIS

The earth track traced by Surveyor II is shown in Figure 4.1-1. Specific events, such as sun and Canopus acquisition, attempted midcourse maneuver, and rise and set times for the DSIF stations, are also shown. Figures 4.1-2, 4.1-3, and 4.1-4 show the trajectory path on the stereographic projection of DSS-51, -11, and -42. In Table 4.1-1, premidcourse injection and terminal conditions have been tabulated. These results were obtained several days after the mission and are considered final.

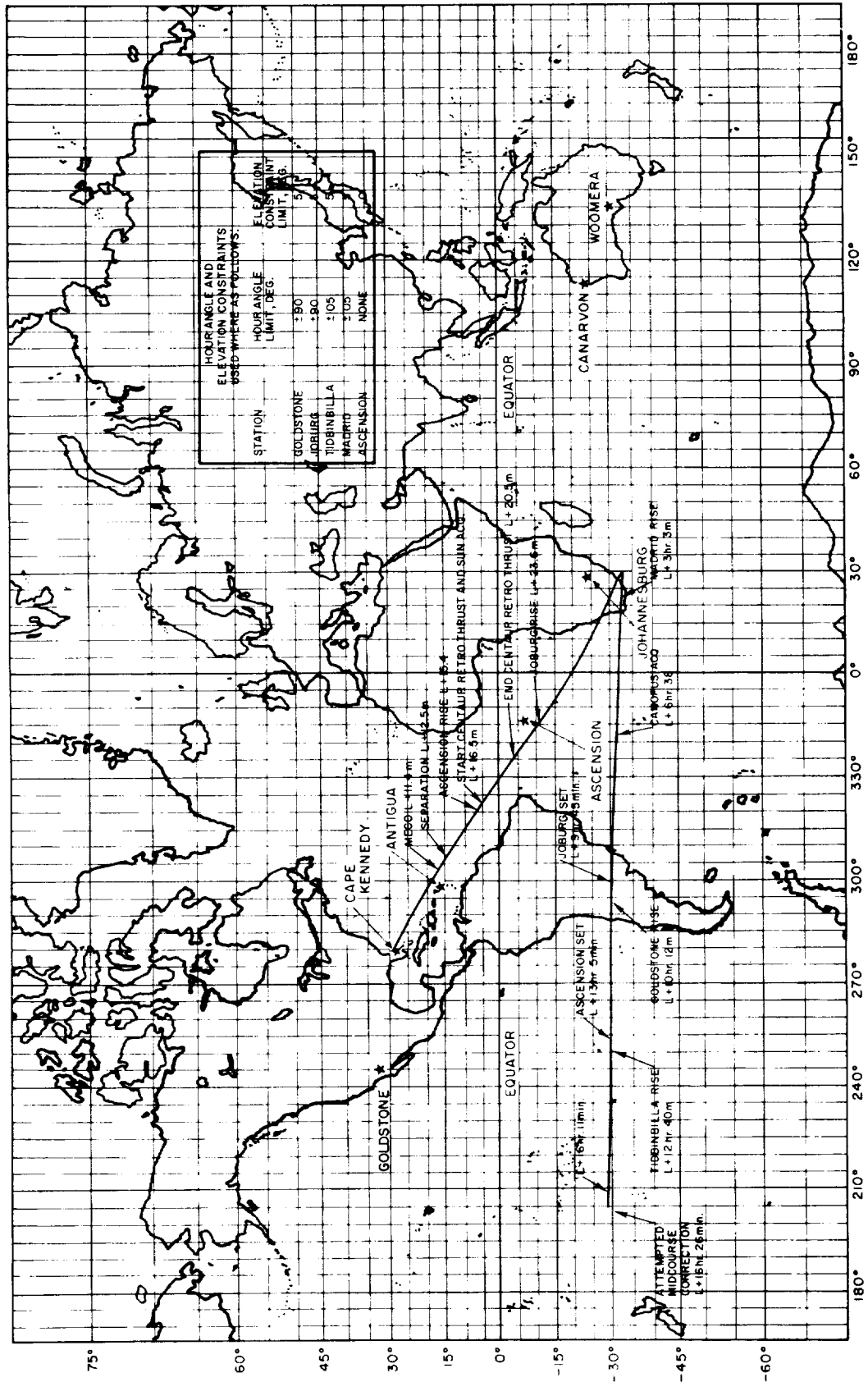


Figure 4.1-1. Surveyor II Earth Track

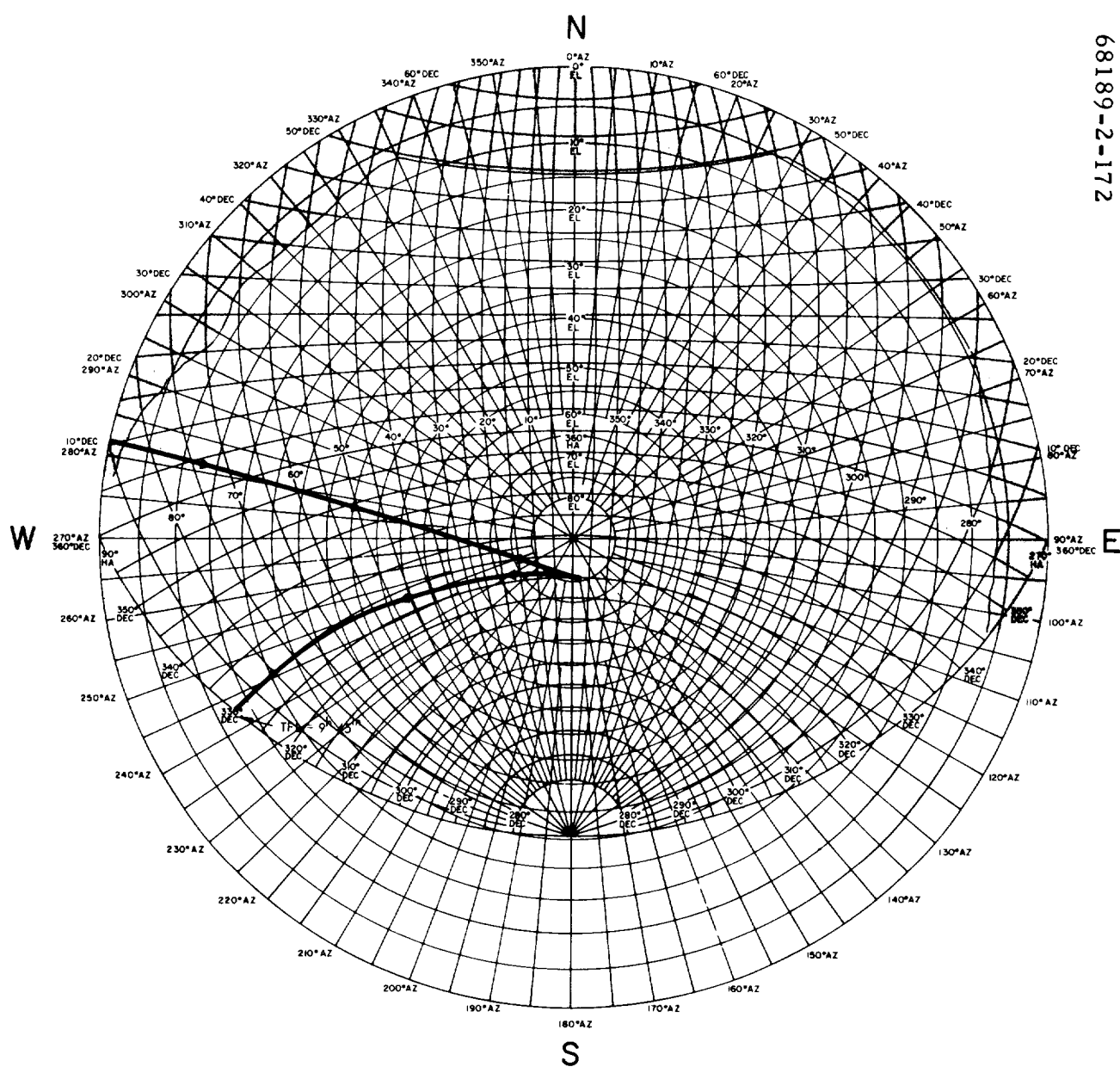


Figure 4.1-2. AZ-EL and HA-DEC Coordinates Stereographic Projection, DSS 51, Johannesburg

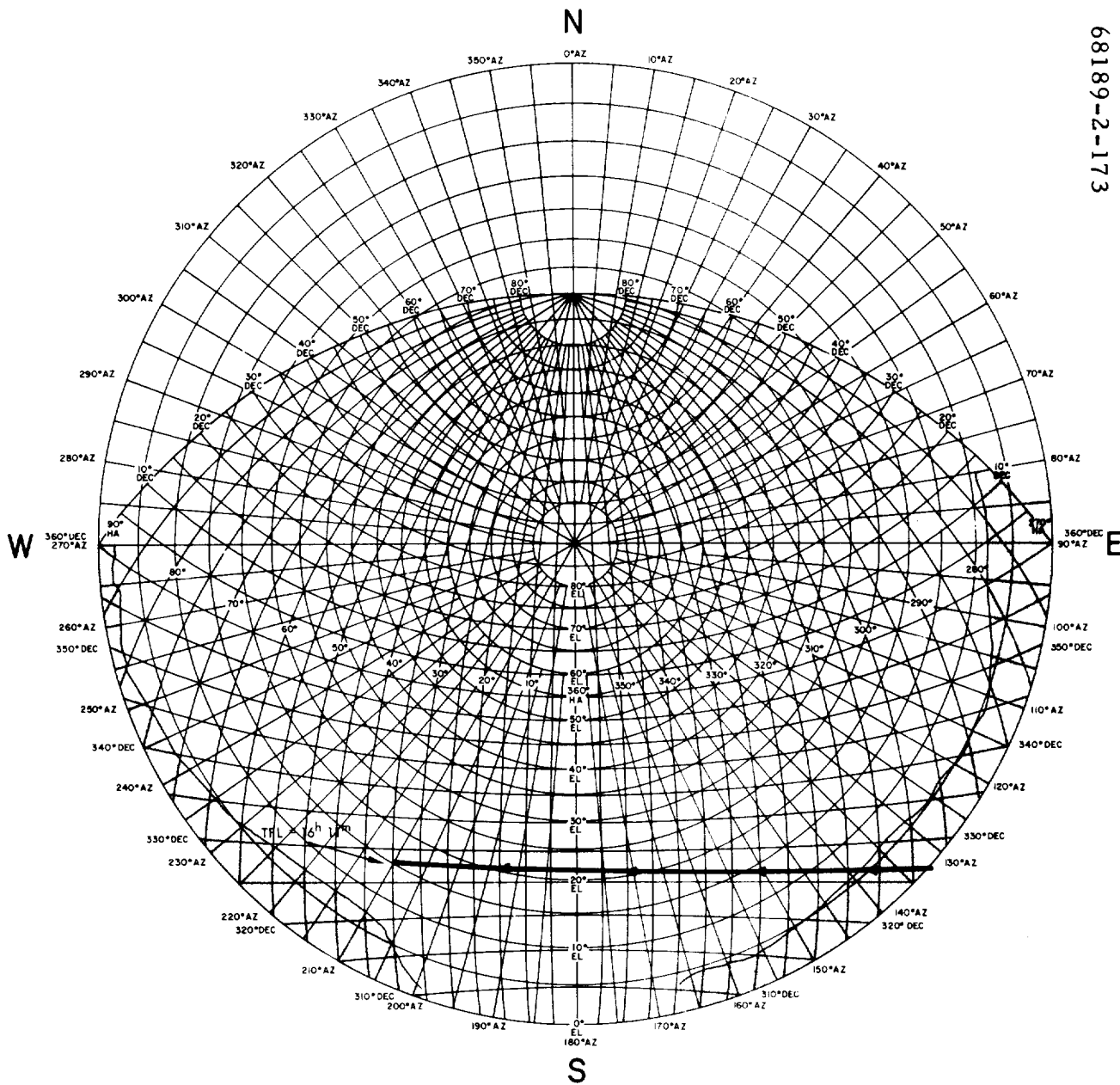


Figure 4.1-3. AZ-EL and HA-DEC Coordinates, Stereographic Projection, DSS 11, Goldstone (Pioneer)

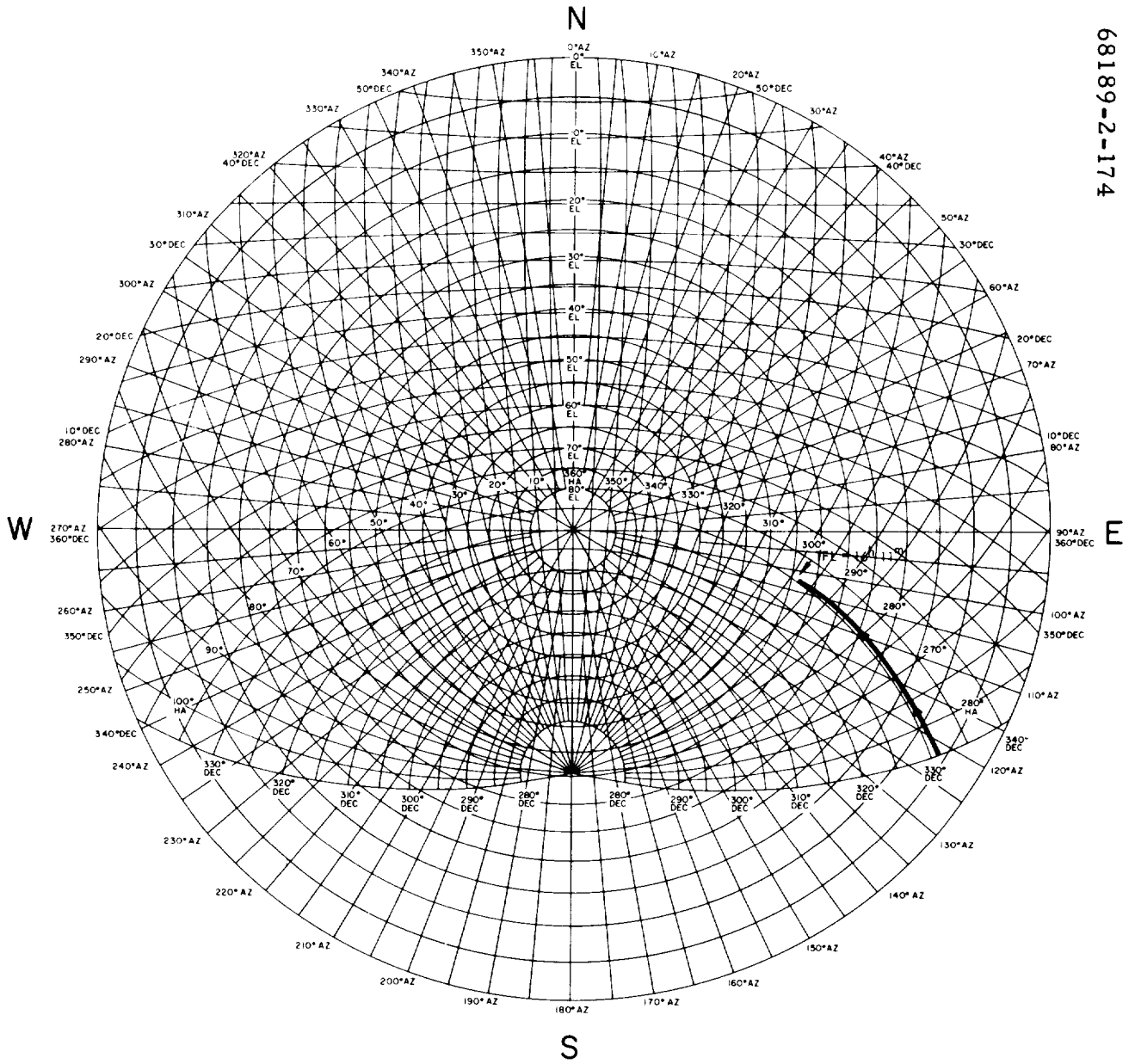


Figure 4.1-4. AZ-EL and HA-DEC Coordinates, Stereographic Projection, DSS 42, Canberra

TABLE 4.1-1. PREMIDCOURSE INJECTION AND TERMINAL CONDITIONS

Coordinate System	Premidcourse Injection Conditions, 20 September 1966, 12:43:13.670 GMT					
Inertial Cartesian	X = -4360.9041 kilometers	Y = 4616.8513 kilometers	Z = 1896.4001 kilometers	DX = -8.7282187 km/sec	DY = -4.5253066 km/sec	DZ = -4.7559824 km/sec
Inertial spherical	RAD = 6627.9056 kilometers	DEC = 16.626021 degrees	RA = 133.36699 degrees	VI = 10.921519 km/sec	PTI = 6.4654237 degrees	AZI = 119.42063 degrees
Earth-fixed spherical	RAD = 6627.9056 kilometers	LAT = 16.626021 degrees	LON = 303.60264 degrees	VE = 10.523257 km/sec	PTE = 6.7112166 degrees	AZE = 120.66787 degrees
Orbital elements	C3 = -1.0001392 km <sup>2</sup> /sec <sup>2</sup>	ECC = 0.98358240	INC = 33.423575 degrees	TA = 13.039233 degrees	LAN = 340.26840 degrees	APF = 135.66564 degrees
Coordinate System	Premidcourse Encounter Conditions, 23 September 1966, 03:19:54.426 GMT					
Selenocentric	RAD = 1738.5 kilometers	LAT = -0.051930781 degree	LON = 354.70985 degrees	VP = 2.6614642 km/sec	PTP = -69.779146 degrees	AZP = 90.222833 degrees
Miss parameter earth equator	BTQ = 1321.7977 kilometers	BRQ = -1793.8803 kilometers	B = 1333.9151 kilometers			
Miss parameter moon equator	BTT = 1333.9064 kilometers	BRT = 5.1242575 kilometers	B = 1333.9162 kilometers			



The predicted premidcourse view periods for the three committed tracking stations are shown in Table 4.1-2. The rise and set criteria are included under the column marked "Event." This table shows that Tidbinbilla, Australia, did not see the spacecraft until late in the flight. Some trajectories yield a small view period for this station during the first Johannesburg pass. The time periods during which each tracking station received data from and controlled the spacecraft are also shown in this table.

Figures 4.1-5 and 4.1-6 are plots of probe geocentric radius and velocity as a function of time from launch. Figure 4.1-7 shows the earth-probe-moon, sun-probe-moon, and earth-probe-sun angles versus time from launch. Figure 4.1-8 shows the cone and clock angles as a function of time. The coordinate system is defined on the figure. In the normal cruise mode, the spacecraft -Z axis is aligned to the sun and the -X axis to the projection of Canopus.

Figure 4.1-9 illustrates the Centaur and Surveyor trajectories. The projection of earth trajectory is plotted on the earth's equatorial plane. The best estimate of the Centaur injection conditions was obtained from AFETR. Although considered poor ( $1\sigma$  velocity error = 13 m/sec), these conditions are the best available. They were mapped out to 5 hours, and the Centaur/Surveyor separation distance was calculated to be 680 kilometers. A mission design constraint states that the separation distance must be 335 kilometers by at least 5 hours after injection to eliminate possible Centaur interference during Canopus acquisition. Therefore, using this "poor" set of Centaur injection conditions, the constraint is well satisfied.

#### 4.1.3 SUMMARY OF DEVIATIONS FROM EPD-180

Significant changes in procedure from the prepared standard mission sequence documented in Engineering Planning Document EPD-180, revision S/MB, were as follows:

- 1) L + 45M: did not send cruise mode on command because star intensity signal indicated that an object was in the Canopus sensor field of view.
- 2) L + 4H33M: when transferring from DSS-51 to DSS-72, decreased bit rate to 137.5 bits/sec due to lower gain antenna at DSS-72.
- 3) L + 6H6M: unscheduled use of manual lockon to acquire Canopus was necessary instead of automatic star acquisition mode.
- 4) L + 9H46M: reduced bit rate to 17.2 bits/sec when DSS-51 lost visibility of spacecraft and had to transfer to DSS-72.
- 5) L + 13H6M: did an "in-flight" calibration of receiver B automatic gain control.

TABLE 4.1-2. DSIF PREDICTED VIEW AND CONTROL PERIODS

Station	Predictions		Mission Performance		Station Transfer and Control Summary	
	Event, degrees	GMT, day:hr:min:sec.	Event	GMT, day:hr:min:sec	Station	Two-way Lock Begins, day:hr:min:sec
DSS-72 (Ascension)	0 rise	263:12:47:53	Acquisition	263:12:48:50	DSS-51	263:13:04:58
DSS-51 (Johannesburg)	5 rise	263:12:55:39	Acquisition	263:12:57:10	DSS-72	263:16:53:38
DSS-51	90 HA set	263:22:17:04	Transfer to DSS-72	263:22:01:40	DSS-51	263:17:45:01
DSS-11 (Goldstone)	5 rise	263:22:43:40	Acquisition	263:22:52	DSS-72	263:22:01:40
DSS-72	0 set	264:01:37:21	Transfer to DSS-11 (Data continues until...?)	263:22:52	DSS-11	263:23:05:00
DSS-42 (Tidbinbilla)	5 rise	264:01:47:01	Good data	264:02:30 approximately	DSS-42	264:05:51:00
DSS-11	5 set	264:06:11:33	Loss of signal	264:05:58		
DSS-51			Acquisition	264:11:10	D55-51	264:15:00:00
DSS-61 (Madrid)			Three-way lock (16 minutes)	264:16:36		
DSS-61			Start three-way lock	264:20:39	DSS-61	264:22:05:00
DSS-61			Loss of signal	264:22:56		
DSS-11			Acquisition	264:23:XX	DSS-11	264:23:11:44
DSS-42			Acquisition	265:XX:XX	DSS-42	265:06:05:00
DSS-42			Loss of signal	265:09:30:00		

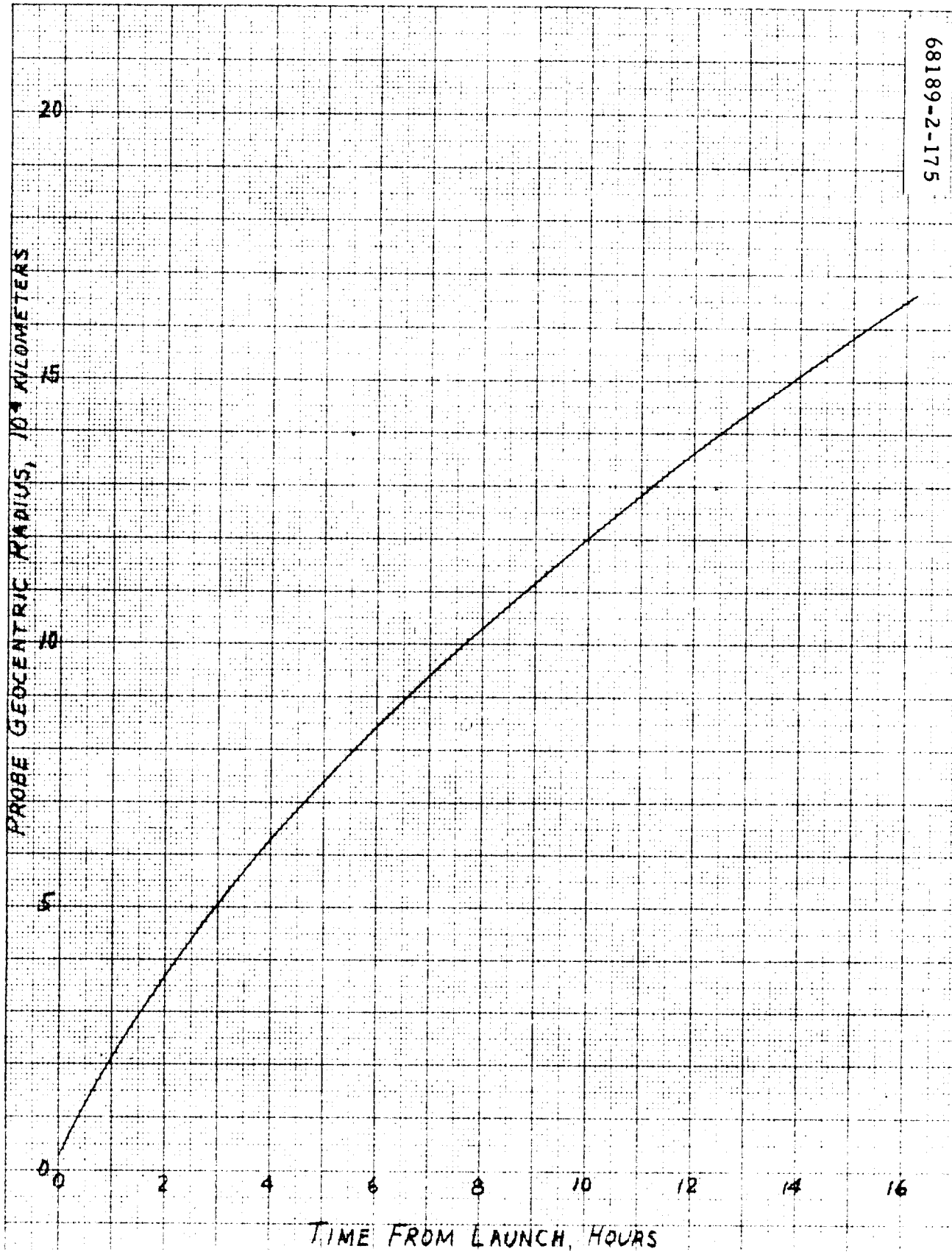


Figure 4.1-5. Probe Geocentric Radius Versus Time From Launch

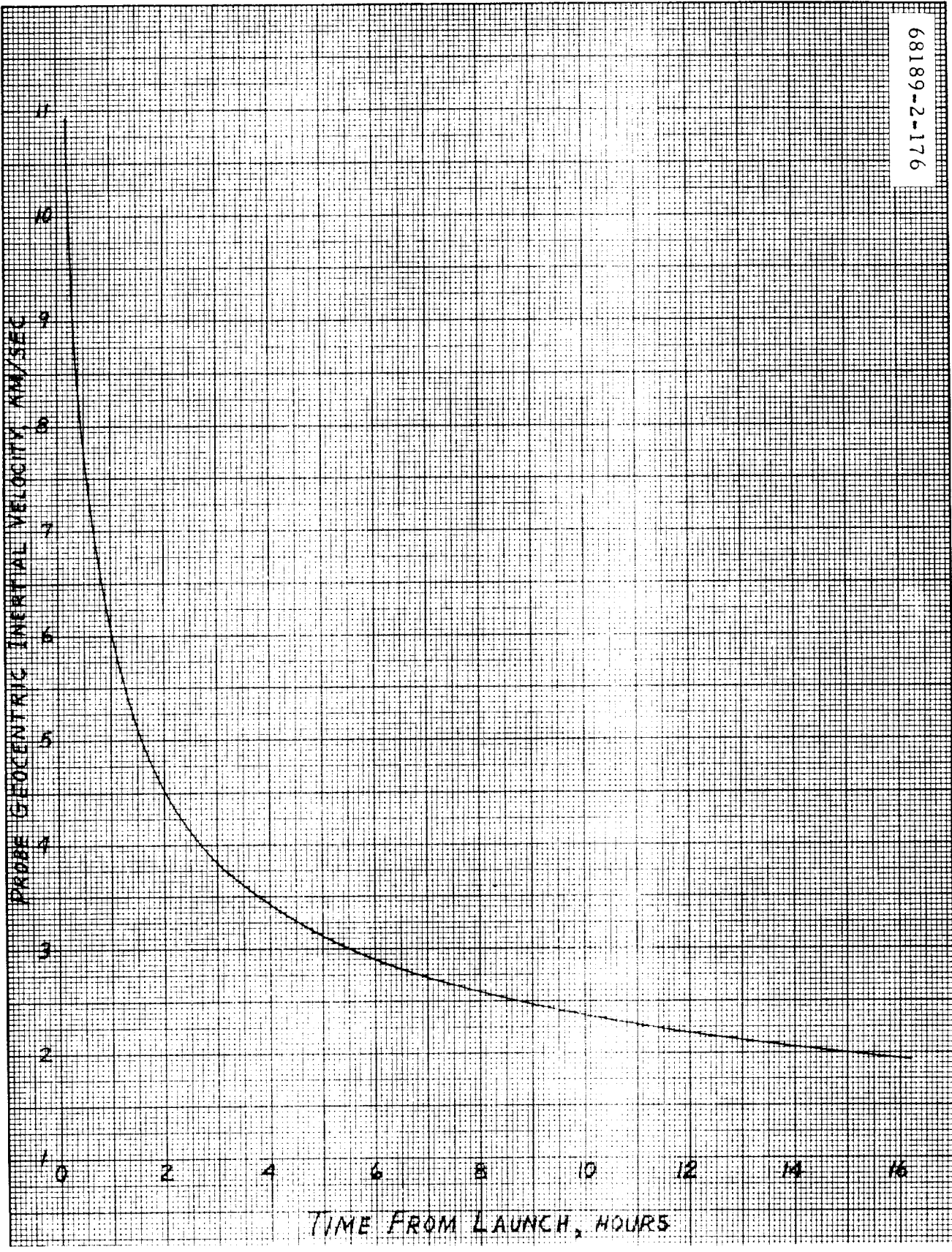


Figure 4.1-6. Probe Geocentric Inertial Velocity Versus Time From Launch

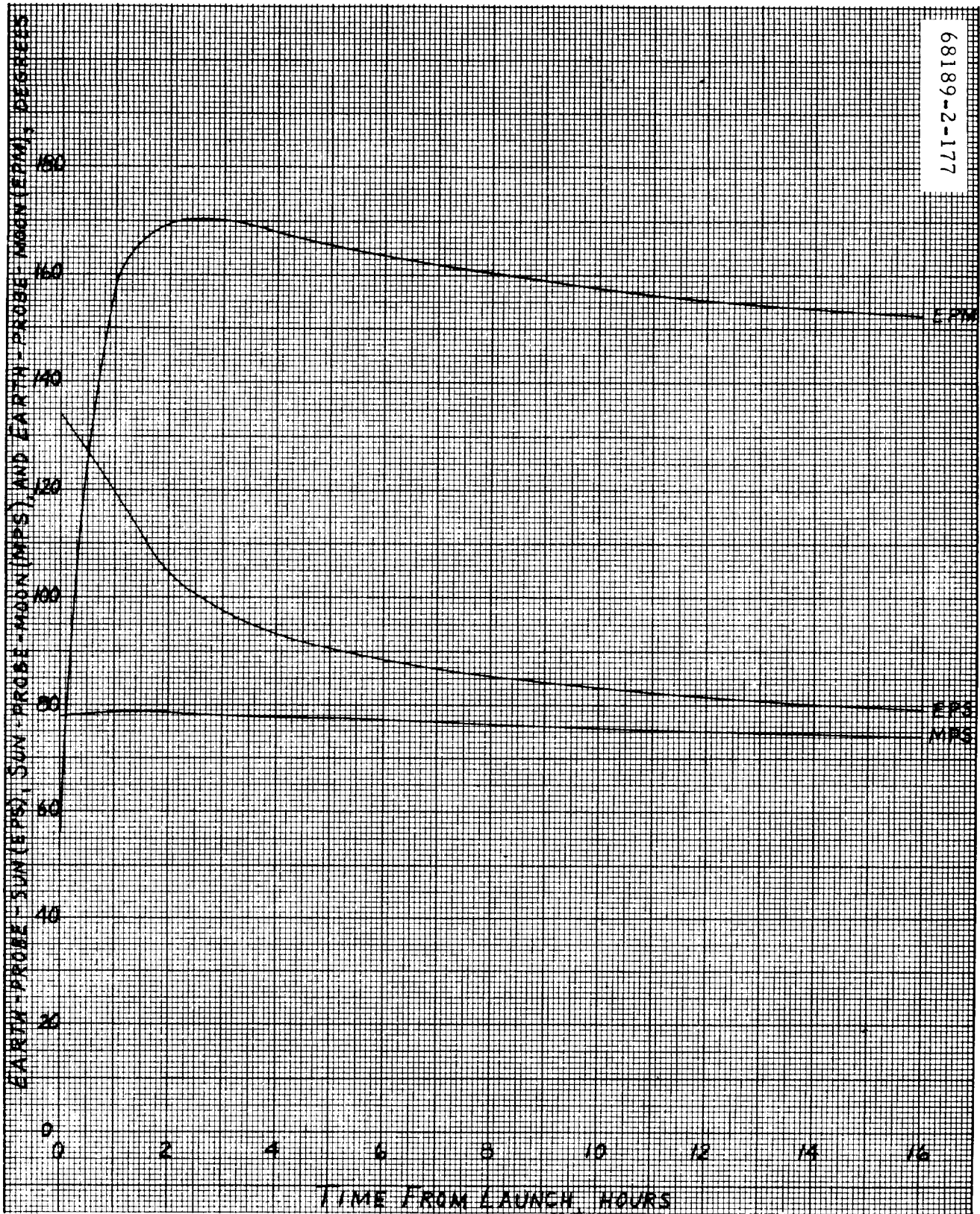


Figure 4.1-7. Earth-Probe-Sun, Sun-Probe-Moon, and Earth-Probe-Moon Angles Versus Time From Launch

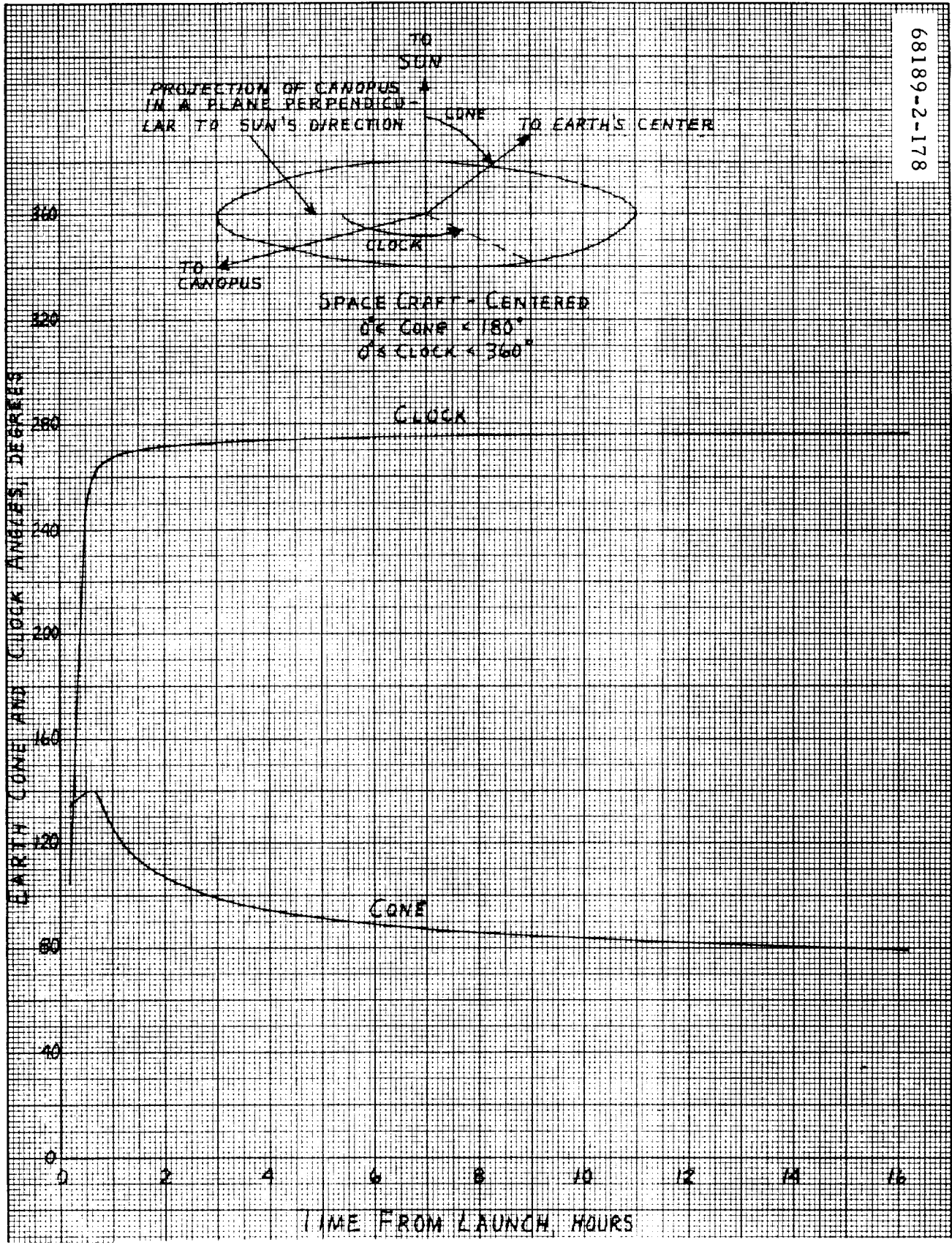


Figure 4.1-8. Earth Cone and Clock Angles Versus Time From Launch

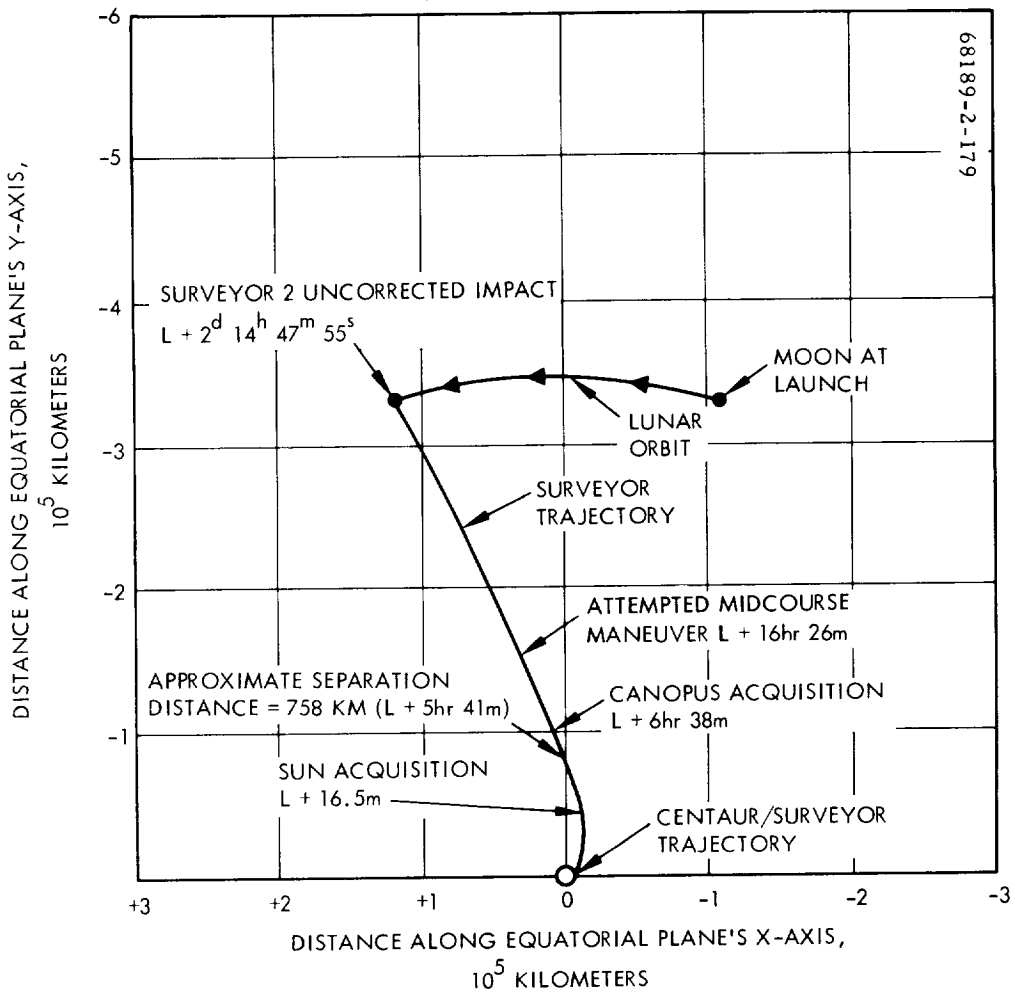


Figure 4.1-9. Surveyor and Centaur Trajectory in Earth's Equatorial Plane

There were no other significant deviations until midcourse thrust correction was initiated, after which point Mission B consisted of all non-standard sequences. Some of the most important sequences of the postmid-course period are given in Table 4.1-3. A complete list of all vernier engine firings, with supplementary data on the spacecraft spin rate, is found in Table 4.1-4. Finally, all periods when flight control power was turned off (never occurs in a standard flight) are given in Table 4.1-5.

#### 4.1.4 SPACECRAFT EVENTS SUMMARY AND COMMAND LOG

In the preceding subsection, data concerning nonstandard events was presented, much of which will be required (especially the vernier burn summary) to follow the analyses that are presented in the remainder of the report. In the tables that follow, all other data of general interest will be given. Table 4.1-6 lists major spacecraft events, although detailed event logs will also be found in most of the subsystem analysis sections. Tables 4.1-7 and 4.1-8 give listings of all transmitter high power and thrust power intervals. Finally, the complete postlaunch command sequence, compiled from DSS digital command tapes (and thus accurate only within a 1-second interval), will be found in Table 4.1-9. A complete mode and bit rate summary has not been given here, since this will be found in the RF data link discussion (Section 5.3), combined with a configuration log of that subsystem.



TABLE 4.1-3. SUMMARY OF POSTMIDCOURSE DEVIATIONS  
FROM EPD-180

Mission Time	Decision/Output	Reason
L + 18H56M L + 19H18M	Two additional 2-second firings were commanded.	To attempt to clear vernier engine 3 problem.
L + 26H12M	A sequence was initiated in which flight control coast phase power was turned off periodically. Power on for approximately 40 minutes and off for approximately 90 minutes.	To conserve energy.
L + 31H12M L + 35H2M L + 36H28M L + 37H29M L + 38H45M L + 39H45M	Pulsed fire the engines five times with a 0.2-second period for firing and a 5-minute interval between firings.	To attempt to clear vernier engine 3 problem.
L + 38H13M L + 38H19M	Commanded deployment of planar array upward from its launch position.	To illuminate solar panel for following reasons: 1) to get more energy for the spacecraft, and 2) to illuminate secondary sun sensor cells to help in establishing spacecraft orientation.
L + 41H11M	Commanded retro sequence mode on and emergency retro eject.	To achieve a higher thrust level with less rise-time by placing flight control subsystem in the postretro eject mode.
L + 42H22M	By ground command, unlock solar panel squib was blown.	In an attempt to step solar panel in another effort to illuminate secondary sun sensor cells.
L + 43H13M	Pulse firing engines five times (0.2 second for each firing) with 1 minute between firings, followed by a 20-second firing in the post-retro eject mode.	To attempt to clear vernier engine 3 problem.
L + 44H41M	Initiated helium dumping sequence.	To obtain a calibration curve of pressure decay as function of time in order to determine whether zero-shift had occurred in helium pressure telemetry signal.
L + 44H48M	Flight control thrust phase power and RADVS were turned on.	To determine if battery was capable of supplying power under terminal descent heavy load conditions.
L + 44H59M	RADVS was turned off in accordance with the direction of the SFOD.	Bus voltage had dropped from 19.4 to 17.3 volts, with a load of 47 amperes on the battery.
L + 45H2M	Emergency AMR signal was sent to the spacecraft to initiate the retro engine firing sequence.	To fire main retro engine in normal descent mode.

TABLE 4. 1-4. VERNIER ENGINE IGNITION SUMMARY

Burn Number	Ignition Time, day:hr:min:sec	Burn Time, seconds	Station	Telemetry Mode	Bit Rate, bits/sec	Transmitter and Power Mode	Tumbling Rate, rpm		
1	264:05:00:02	9.825	DSS-11	1	4400	B-Hi	50		
2	264:07:28:25	1.975	DSS-42	1	1100	B-Hi			
3	264:07:50:03	1.975	DSS-42	1	1100	B-Hi			
4	264:19:44:59	0.225	DSS-51	1	137	B-Lo	58		
5	264:20:07:05	0.225	DSS-51	1	137	B-Lo			
6	264:20:35:20	0.225	DSS-51	1	137	B-Lo			
7	264:20:55:06	0.225	DSS-51	1	137	B-Lo			
8	264:21:15:12	0.225	DSS-51	1	137	B-Lo			
9	264:23:33:23	1.975	DSS-11	1	1100	B-Hi			
10	265:01:00:34	0.225	DSS-11	1/5	137	B-Lo		60	
11	265:01:05:42	0.225	DSS-11	1/5	137	B-Lo			
12	265:01:09:23	0.225	DSS-11	1/5	137	B-Lo			
13	265:01:14:41	0.225	DSS-11	1/5	137	B-Lo			
14	265:01:19:46	0.225	DSS-11	1/5	137	B-Lo			
15	265:01:28:11	1.975	DSS-11	1/5	1100	B-Hi			
16	265:02:01:19	0.225	DSS-11	1/5	137	B-Lo	70.5		
17	265:02:08:11	0.225	DSS-11	1/5	137	B-Lo			
18	265:02:13:34	0.225	DSS-11	1/5	137	B-Lo			
19	265:02:19:37	0.225	DSS-11	1/5	137	B-Lo			
20	265:02:26:06	0.225	DSS-11	1/5	137	B-Lo			
21	265:02:39:14	1.975	DSS-11	1/5	1100	B-Hi			
22	265:03:17:24	0.225	DSS-11	1/5	137	B-Lo			75
23	265:03:23:53	0.225	DSS-11	1/5	137	B-Lo			
24	265:03:29:07	0.225	DSS-11	1/5	137	B-Lo			
25	265:03:34:33	0.225	DSS-11	1/5	137	B-Lo			
26	265:03:39:07	0.225	DSS-11	1/5	137	B-Lo			
27	265:03:47:56	1.975	DSS-11	1/5	1100	B-Hi			
28	265:04:17:31	0.225	DSS-11	1/5	137	B-Lo	80		
29	265:04:23:53	0.225	DSS-11	1/5	137	B-Lo			
30	265:04:29:51	0.225	DSS-11	1/5	137	B-Lo			
31	265:04:35:34	0.225	DSS-11	1/5	137	B-Lo			
32	265:04:41:20	0.225	DSS-11	1/5	137	B-Lo			
33	265:04:56:12	1.975	DSS-11	1/5	1100	B-Hi			
34	265:05:43:19	2.5*	DSS-11	6	1100	B-Hi		85.6	
35	265:07:45:00	0.225	DSS-42	1	1100	B-Hi			
36	265:07:46:12	0.225	DSS-42	1	1100	B-Hi			
37	265:07:47:15	0.225	DSS-42	1	1100	B-Hi			
38	265:07:48:18	0.225	DSS-42	1	1100	B-Hi			
39	265:07:49:25	0.225	DSS-42	1/5	1100	B-Hi			
40	265:08:05:12	21.5*	DSS-42	6	1100	B-Hi			
41	265:09:31:59	-	DSS-42	5/2	1100	B-Hi	128		

\*High thrust.

TABLE 4.1-5. FLIGHT CONTROL POWER OFF PERIODS

Mission Time Off, hr:min	Time Off, GMT, day:hr:min:sec	Time On, GMT, hr:min:sec	Total Off Time, hr:min:sec
21:48	264:10:19:43	12:05:57	1:46:14
25:15	13:47:16	15:09:24	1:22:08
28:55	17:26:48	17:51:50	0:25:02
38:11	265:02:43:07	03:15:49	0:32:42
39:20	03:51:34	04:15:55	0:24:21
40:27	04:59:16	05:30:18	0:31:02
41:17	05:48:51	07:34:49	1:45:58
43:38	08:10:28	09:13:00	1:02:32

TABLE 4.1-6. MAJOR SPACECRAFT EVENTS

Time, GMT, day:hr:min:sec	Mission Time, hr:min:sec	Event
263:12:31:59.8	00:00:00	Liftoff (Note: this report will use 12:32:00 for simplicity)
12:34:56	00:02:56	Insulation panel jettison
12:43:51	00:11:51	Extend legs command, Centaur
12:44:01	00:12:01	Extend omni command, Centaur
12:44:21	00:12:21	Transmitter high power command, Centaur
12:44:26	00:12:26	Separation signal (M-9)
12:44:34	00:12:34	Solar panel unlock and step
12:45:18	00:13:18	Start of sun acquisition roll
12:48:13	00:16:13	Primary sun sensor lockon
12:50:34	00:18:34	Solar axis lock; begin roll axis step
12:54:46	00:22:46	Roll axis lock
18:37:34	06:05:34	Start of roll for star map
19:09:38	06:37:38	End of roll (cruise mode on)
19:11:57	06:39:57	Manual Canopus acquisition
19:26:24	06:54:24	Begin gyro drift check
21:35:22	09:03:22	Complete gyro drift check
21:39:23	09:07:23	Reacquire Canopus
264:01:38	13:06	Special receiver test (AGC calibration)
03:07:43	14:35:43	Gyro speed check
04:44:00	16:12:00	Premidcourse sun and roll maneuver
04:48:05	16:16:05	Premidcourse yaw maneuver
04:53:38	16:21:38	Pressurize helium, unlock roll actuator
05:00:02	16:28:02	Midcourse velocity correction
05:03:48	16:31:48	Rate mode on
05:14:29	16:42:29	Inhibit gas jets
11:41:09	23:09:09	Auxiliary battery mode selected
265:02:44:58	38:12:58	Unsuccessful attempt to step polar axis
06:54:33	42:22:33	Solar panel unlocked; slips 20 degrees
09:13:16	44:41:16	Helium dumped
09:19:57	44:47:57	RADVS turnon
09:22:16	44:50:16	Begin power mode switching
09:30:09	44:58:09	RADVS off
09:30:33	44:58:33	Enable gas jet amplifiers
09:32:19	45:00:19	Telemetry mode 2 on for terminal descent
09:34:17	45:02:17	Emergency AMR command
09:34:27.2	45:02:27	Vernier engine ignition
09:34:28.6	45:02:29	Retro engine ignition
09:35:00	45:03:00	Loss of data and spacecraft control

TABLE 4.1-7. TRANSMITTER B HIGH POWER ON PERIODS

Mission Time On, hr:min	Time On, GMT, day:hr:min:sec	Time Off, GMT, hr:min:sec	Delta Time, min:sec	Event
00:12	263:12:44:21	13:16:33	32:12	For initial acquisition
05:59	263:18:30:46	19:22:05	51:19	Star map
16:05	264:04:36:43	05:23:02	46:19	Midcourse
18:47	264:07:19:16	07:34:47	15:31	Burn 2
19:13	264:07:46:36	07:58:16	11:40	Burn 3
26:59	264:15:30:57	15:48:51	17:54	
34:48	264:23:20:02	23:43:31	23:29	Burn 9
36:52	265:01:24:02	01:30:24	06:22	Burn 15
38:02	265:02:34:07	02:42:21	08:14	Burn 21
39:12	265:03:43:52	03:50:06	06:14	Burn 27
40:21	265:04:52:46	04:58:19	05:33	Burn 33
41:01	265:05:32:59	05:47:01	14:02	Burn 34
42:01	265:06:32:45	06:59:12	26:27	Solar panel stepping
43:10	265:07:41:49	07:51:17	09:28	Burns 35 through 39
43:29	265:08:00:52	08:09:19	08:27	Burn 40
44:40	265:09:11:50	(09:35)	23:10	Retro fire

TABLE 4.1-8. THRUST PHASE POWER ON PERIODS

Mission Time On, hr:min	Time On, GMT, day:hr:min:sec	Time Off, GMT, hr:min:sec	Delta Time, min:sec	Event
16:22	264:04:54:20	05:00:41	6:21	Midcourse
18:53	07:25:02	07:28:33	3:31	Burn 2
19:17	07:49:06	07:50:18	1:12	3
31:11	19:43:34	19:46:01	2:27	4
31:24	20:05:47	20:07:41	1:54	5
32:02	20:33:43	20:35:58	2:15	6
32:21	20:53:23	20:55:37	2:14	7
32:40	21:12:04	21:15:38	3:34	8
35:01	23:32:35	23:33:40	1:05	9
36:28	265:01:00:06	01:00:47	0:41	10
36:33	01:05:24	01:05:53	0:29	11
36:37	01:09:05	01:09:32	0:27	12
36:42	01:14:24	01:14:50	0:26	13
36:47	01:19:31	01:19:56	0:25	14
36:55	01:27:30	01:28:27	0:57	15
37:29	02:00:45	02:01:32	0:47	16
37:35	02:07:29	02:08:19	0:50	17
37:41	02:13:14	02:13:42	0:28	18
37:47	02:19:21	02:19:44	0:23	19
37:54	02:25:47	02:26:13	0:26	20
38:07	02:38:48	02:39:27	0:39	21
38:45	03:17:06	03:17:36	0:30	22
38:51	03:23:27	03:24:01	0:34	23
38:57	03:28:55	03:29:16	0:21	24
39:02	03:34:24	03:34:42	0:18	25
39:07	03:38:53	03:39:14	0:21	26
39:15	03:47:35	03:48:06	0:31	27
39:45	04:17:11	04:17:40	0:29	28
39:52	04:23:38	04:24:00	0:22	29
39:58	04:29:36	04:30:00	0:24	30
40:03	04:35:18	04:35:41	0:23	31
40:09	04:41:04	04:41:26	0:22	32
40:23	04:55:26	04:56:21	0:55	33
41:10	05:41:34	05:43:47	2:13	34
43:13	07:44:36	07:49:31	4:55	35 - 39
43:33	08:04:31	08:05:45	1:14	40
44:47	09:19:06	(09:35)	15:54	RADVS and retro fire

TABLE 4.1-9. COMMAND SEQUENCE

GMT, hr:min:sec	Command	Function	GMT, hr:min:sec	Command	Function
Day 263 - DSS-51			Day 263 - DSS-11		
13:16:33	0107	XMTR Hi Pwr off	19:22:13	0110	Xmtr Fil Pwr Off
17:07	0110	XMTR Fil Pwr off	22:14	0130	Xfer Sw B Lo Pwr
17:08	0130	XFER Sw B Lo Pwr	26:24	0700	Inertial Mode on
18:45	0623	Accel. Amps 1-4 off	21:35:22	0704	Cruise Mode
18:46	0316	Solar Panel Deploy Logic off	39:23	0716	Manual Lock on
18:46	0522	Prop Strain Gage Pwr off	47:54	0505	17.2 bits/sec
18:47	0512	Aux Accel Amp 5-8 off	50:06	0204	Coast $\phi$ Clock Rate
18:47	0516	T. D. Strain Gage Pwr off	50:31	0220	7.35 kc SCO off
20:16 to 20:21	0402(10)	Step Solar Panel minus	50:53	0501	560 cps SCO on
20:21 to 20:23	0401(5)	Step Solar Panel plus	Day 264 - DSS-11		
21:44 to 21:49	0405(10)	Step Roll Axis plus	23:11:54	0502	560 cps SCO off
21:49 to 21:51	0406(5)	Step Roll Axis minus	12:02	0216	7.35 kc SCO on
26:19	0510	AESP off	12:10	0205	1100 bits/sec
26:29	0226	Mode 1 on	40:31	0510	AESP off
29:26	0237	Lo Mod Index SCO off	40:40	0231	Mode 4 on
29:26	0216	7.35 kc SCO on	44:45	0227	Mode 2 on
29:27	0205	1100 bits/sec	47:46	0232	ESP off
32:51	0231	Mode 4 on	47:53	0506	Mode 5 on
34:50	0227	Mode 2 on	Day 264 - DSS-11		
37:37	0230	Mode 3 on	02:54:44	0510	AESP off
39:24	0232	ESP off	54:51	0231	Mode 4 on
39:31	0506	Mode 5 on	59:37	0510	AESP off
41:19	0126	Xfer Sw A Lo Pwr	59:44	0231	Mode 4 on
16:38:38	0504	137.5 bits/sec	03:02:28	0227	Mode 2 on
38:56	0204	Coast $\phi$ Clock Rates	04:08	0226	Mode 1 on
39:13	0220	7.35 kc SCO off	05:41	0232	ESP off
39:29	0500	960 cps SCO on	05:49	0506	Mode 5 on
18:01:26	0502	960 cps SCO off	07:42	0220	7.35 kc SCO off
01:34	0216	7.35 kc SCO on	07:43	0221	Gyro Speed Sig Pwr on
01:45	0205	1100 bits/sec	09:05	0222	Next Gyro
09:31	0510	AESP off	10:06	0222	Next Gyro
09:41	0231	Mode 4 on	10:31	0222	Next Gyro
13:25	0227	Mode 2 on	13:07	0223	Gyro Speed Sig Pwr off
20:15	0226	Mode 1 on	13:18	0216	7.35 kc SCO on
24:35	0232	ESP off	04:14:00	0510	AESP off
24:43	0506	Mode 5 on	14:08	0231	Mode 4 on
28:59	0105	Xmtr B Fil Pwr on	15:51	0227	Mode 2 on
30:46	0127	Xfer Sw B Hi Pwr	18:10	0226	Mode 1 on
30:46	0106	Xmtr Hi Volt on	34:55	0105	Xmtr B Fil Pwr on
33:01	0124	Xpndr Pwr off	36:43	0127	Xfer Sw B Hi Pwr
34:19	0704	Cruise Mode on	36:44	0106	Xmtr B Hi Volt on
34:19	0715	Man Delay Mode on	37:36	0220	7.35 kc SCO off
34:20	0710	Pos Angle Maneuver	37:45	0217	33 kc SCO on
37:34	0714	Sun + Roll	37:53	0206	4400 bits/sec
54:45	0120	Omni A	40:58	0710	Pos Angle Maneuver
19:06:37	0121	Omni B	41:16	3617	Interlock
09:38	0704	Cruise Mode on	41:16	M1331	Magnitude (377 counts) (75.4°)
11:57	0716	Manual Lock on	44:00	0714	Sun and roll
14:21	0123	Xpndr B Pwr on	47:15	3617	Interlock
22:05	0107	Xmtr Hi Voltage off	47:16	M2111	Magnitude (553 counts) (110.6°)
			48:05	0713	+ Yaw
			52:22	0521	Prop Strain Gage Pwr on

Table 4.1-9 (continued)

GMT, hr:min:sec	Command	Function	GMT, hr:min:sec	Command	Function
04:52:22	0700	Inertial Mode on	07:29:53	0220	7.35 kc SCO off
52:35	0720	Reset Group IV	30:04	0215	3.9 kc SCO on
53:37	3617	Interlock	30:15	0204	Coast & Clock Rates
53:38	0605	Unlock R. Act., Pressurize He	30:22	0503	550 bits/sec
54:20	0727	FC Thrust & Pwr on	30:37	0232	ESP off
54:47	3617	Interlock	30:47	0506	Mode 5 on
54:48	M0605	Magnitude (197 counts) (9.85 Sec)	34:04	0504	137.5 bits/sec
05:00:01	3617	Interlock	34:15	0220	7.35 & 3.9 kc SCOs off
00:02	0721	M/C Correction	34:27	0500	960 cps SCO on
00:13	0735	M/C Terminate	34:47	0107	Xmtr Hi Volt off
00:14	0735	M/C Terminate	35:05	0130	Xfer Sw B Lo Pwr
00:41	0737	Thrust & Pwr off	35:25	0110	Xmtr Fil Pwr off
00:42	0737	Thrust & Pwr off	44:40	0105	Xmtr B Fil Pwr on
00:53	0522	Prop Strain Gage Pwr off	46:27	0127	Xfer Sw B Hi Pwr
00:54	0512	Aux Accel Amp 5-8 off	46:36	0103	Xmtr Hi Volt on
00:54	0516	T. D. Strain Gage Pwr off	47:10	0502	960 cps SCO off
00:55	0205	1100 bits/sec	47:19	0216	7.35 kc SCO on
03:48	0701	Rate Mode on	47:31	0205	1100 bits/sec
14:29	0707	Inhibit Gas Jet Amps	47:47	0510	AESP off
19:23	0503	550 bits/sec	47:58	0226	Mode 1
20:21	0204	Coast & Clock Rates	48:11	0521	Prop Strain Gage Pwr on
20:31	0220	33 kc SCO off	48:35	3617	Interlock
20:38	0215	3.9 kc SCO on	48:36	M0110	Magnitude (40 counts) (2.0 Sec)
23:02	0107	Xmtr B Hi Pwr off	49:06	0727	FC Thrust & Pwr on
23:12	0110	Xmtr Fil Pwr off	50:03	3617	Interlock
23:17	0130	Xfer Sw B Lo Pwr	50:03	0721	M/C Correction (3)
29:20	0504	137 bits/sec	50:06	0735(2)	Terminate M/C
29:36	0220	3.9 kc SCO off	50:18	0737(2)	Thrust & Pwr off
29:51	0500	960 cps SCO on	50:18	0220	7.35 kc SCO off
31:46	0227	Mode 2 on	51:00	0215	3.9 kc SCO on
48:43	0232	ESP off	51:12	0204	Coast & Clock Rates
48:50	0506	Mode 5 on	51:22	0503	550 bits/sec
Day 264 - DSS-42			51:37	0232	ESP off
07:16:36	0105	Xmtr B Fil Pwr on	52:52	0232	ESP off
18:28	0127	Xfer Sw B Hi Pwr	53:02	0506	Mode 5
19:16	0103	Xmtr Hi Volt on	57:40	0504	137.5 bits/sec
21:08	0502	960 cps SCO off	57:54	0220	3.9 SCO off
21:23	0216	7.35 kc SCO on	58:04	0500	960 cps SCO on
22:06	0205	1100 bits/sec	58:16	0107	Xmtr Hi Volt off
22:20	0510	AESP off	58:23	0130	Xfer Sw B Lo Pwr
22:31	0226	Mode 1 on	58:38	0110	Xmtr Fil Pwr off
22:46	0521	Prop Strain Gage Pwr on	58:55	0522	Prop Strain Gage Pwr off
23:10	3617	Interlock	10:19:43	3617	Interlock
23:11	M0110	Magnitude (40 counts) (2.0 Sec)	19:43	0311	FC Pwr off
25:02	0727	FC Thrust & Pwr on	21:05	0510	AESP off
26:28	3617	Interlock	21:14	0231	Mode 4 on
26:31	0735	Terminate M/C	29:58	0227	Mode 2 on
28:24	3617	Interlock	38:23	0232	ESP off
28:25	0721	M/C Correction (2)	38:31	0506	Mode 5 on
28:28	0735(2)	Terminate M/C	11:41:09	0317	Aux Batt Mode on
28:33	0737(2)	Thrust & Pwr off	41:34	0510	AESP off



Table 4.1-9 (continued)

GMT, hr:min;sec	Command	Function	GMT, hr:min;sec	Command	Function
11:41:44	0231	Mode 4	20:02:12	0226	Mode 1 on
52:14	0227	Mode 2	02:49	0521	Prop Str Gage Pwr on
12:04:28	0232	ESP off	03:50	3617	Interlock
04:36	0506	Mode 5	03:50	M0005	Magnitude (5 counts) (0.25 Sec)
05:57	0300	FC Pwr on	05:47	0727	FC Thrust $\phi$ Pwr on
12:12	0120	Omni A	07:04	3617	Interlock
15:00	0121	Omni B	07:05	0721	M/C Correction (5)
13:22:14	0510	AESP off	07:06	0735(2)	Terminate M/C
22:26	0231	Mode 4	07:41	0737(2)	FC Thrust $\phi$ Pwr off
37:08	0227	Mode 2	09:42	0232	ESP off
41:25	0232	ESP off	09:50	0506	Mode 5 on
41:33	0506	Mode 5	27:47	0510	AESP off
47:15	3617	Interlock	28:32	0226	Mode 1 on
47:16	0311	FC Pwr off	29:34	0521	Prop Str Gage Pwr on
Day 264 - DSS-51			32:41	3617	Interlock
15:09:24	0300	FC Pwr on	32:42	M0005	Magnitude (5 counts) (0.25 Sec)
16:30	0510	AESP off	33:43	0727	FC Thrust $\phi$ Pwr on
16:44	0226	Mode 1 on	35:20	3617	Interlock
28:56	0105	Xmtr B Fil Pwr on	35:20	0721	M/C Correction (6)
30:48	0127	Xfer B Sw Hi Pwr	35:21	0735(4)	Terminate M/C
30:57	0106	Xmtr Hi Volt on	35:58	0737(2)	FC Thrust $\phi$ Pwr off
36:03	0502	960 cps SCO off	37:21	0232	ESP off
36:15	0216	7.35 kc SCO on	37:28	0506	Mode 5 on
36:34	0205	1100 bits/sec	46:09	0510	AESP off
47:33	0504	137.5 bits/sec	46:24	0226	Mode 1 on
48:02	0204	Coast $\phi$ Clock Rates	47:28	0521	Prop Str Gage Pwr on
48:18	0220	7.35 kc SCO off	48:37	3617	Interlock
48:34	0500	960 cps SCO on	48:38	M0005	0.225 Sec.
48:51	0107	Xmtr Hi Volt off	52:09	3617	Interlock
49:31	0110	Xmtr Fil Pwr off	52:09	M0005	Magnitude (5 counts) (0.25 Sec)
49:38	0130	Xfer Sw B Lo Pwr	53:23	0727	F/C Thrust $\phi$ Pwr on
50:23	0232	ESP off	55:06	3617	Interlock
50:39	0506	Mode 5 on	55:06	0721	M/C Correction (7)
17:26:47	0000		55:07	0735(3)	Terminate M/C
26:48	0311	All FC Pwr off	55:37	0737(2)	FC Thrust $\phi$ Pwr off
28:07	3617	Interlock	56:18	0232	ESP off
28:08	0311	All FC Pwr off	56:27	0506	Mode 5 on
51:50	0300	FC Pwr on	21:10:41	0510	AESP off
19:34:35	0510	AESP off	10:51	0226	Mode 1 on
35:18	0226	Mode 1 on	11:16	0521	Prop Str Gage Pwr on
36:01	0521	Prop Str Gage Pwr on	11:40	3617	Interlock
37:58	3617	Interlock	11:40	M0005	Magnitude (5 counts) (0.25 Sec)
37:59	M0005	Magnitude (5 counts) (0.25 Sec)	12:04	0727	FC Thrust $\phi$ Pwr on
43:34	0727	FC Thrust $\phi$ Pwr on	15:11	3617	Interlock
44:58	3617	Interlock	15:12	0721	M/C Correction (8)
44:59	0721	M/C Correction (4)	15:12	0735(3)	Terminate M/C
45:00	0735(3)	Terminate M/C	15:38	0737(2)	FC Thrust $\phi$ Pwr off
46:01	0737(2)	FC Thrust $\phi$ Pwr off	16:43	0232	ESP off
49:30	0232	ESP off	16:53	0506	Mode 5 on
50:06	0506	Mode 5 on	27:44	0320	Enable Batt Xfer Logic
20:01:43	0510	AESP off			

Table 4.1-9 (continued)

GMT, hr:min:sec	Command	Function	GMT, hr:min:sec	Command	Function
Day 264 - DSS-61					
22:42:23	0522	Prop Str Gage Pwr off	01:00:49	0737	Thrust $\phi$ Pwr Off
42:37	0516	Str Gage Pwr off	00:54	0522	Prop Strain Gage Pwr Off
42:50	0512	Aux Accel Amp 5-8 off	00:59	0512	Aux Accel Amp 5-8 Off
Day 264 - DSS-11			01:05	0516	T. D. Strain Gage Pwr Off
23:18:16	0105	Xntr B Fil Pwr on	01:12	0232	ESP Off
19:58	0127	Xfr Sw B Hi Pwr	01:20	0506	Mode 5 On
20:02	0103	Xntr Hi Volt on	04:38	0510	AESP Off
22:17	0502	960 cps SCO off	04:43	0226	Mode 1 On
22:26	0217	35 ke SCO on	04:49	0521	Prop Strain Gage Pwr On
22:35	0206	4400 bits/sec	05:00	3617	Interlock
23:35	0510	AESP off	05:00	M0005	Magnitude (5 counts) (0.25 Sec)
23:47	0226	Mode 1 on	05:24	0727	FC Thrust $\phi$ Pwr On
23:59	0521	Prop Strain Gage Pwr on	05:42	3617	Interlock
24:42	3617	Interlock	05:42	0721	M/C Correction (11)
24:42	M0110	Magnitude (40 counts) (2.0 Sec)	05:45	0735(2)	Terminate M/C
28:08	0205	1100 bits/sec	05:53	0737(2)	Thrust $\phi$ Pwr Off
29:38	0220	33 ke SCO off	06:00	0522	Prop Strain Gage Pwr Off
29:49	0216	7.35 ke SCO on	06:06	0512	Aux Accel Amp 5-8 Off
32:35	0727	FC Thrust $\phi$ Pwr on	06:10	0516	T. D. Strain Gage Pwr Off
33:22	3617	Interlock	06:16	0232	ESP off
33:23	0721	M/C Correction (9)	06:22	0506	Mode 5 On
33:27	0735(2)	Terminate M/C	08:23	0510	AESP Off
33:40	0737(2)	Thrust $\phi$ Pwr off	08:28	0226	Mode 1 On
33:52	0512	Aux Accel Amp 5-8 off	08:34	0521	Prop Strain Gage Pwr On
33:53	0516	T. D. Strain Gage Pwr off	08:46	3617	Interlock
33:53	0205	1100 bits/sec	08:47	M0005	Magnitude (5 counts) (0.25 Sec)
34:24	0232	ESP off	09:05	0727	FC Thrust $\phi$ Pwr On
34:33	0506	Mode 5 on	09:23	3617	Interlock
38:46	0510	AESP off	09:23	0721	M/C Correction (12)
38:51	0231	Mode 4 on	09:25	0735(2)	Terminate M/C
40:17	0232	ESP off	09:32	0737(2)	Thrust $\phi$ Pwr Off
40:22	0506	Mode 5 on	09:39	0522	Prop Strain Gage Pwr Off
40:42	0504	137.5 bits/sec	09:44	0512	Aux Accel Amp 5-8 Off
40:51	0220	7.35 ke SCO off	09:49	0516	T. D. Strain Gage Pwr Off
40:58	0500	960 cps SCO on	09:54	0232	ESP Off
42:40	0204	Coast $\phi$ Clock Rates	10:02	0506	Mode 5 On
43:31	0107	Xntr Hi Volt Off	13:43	0510	AESP Off
43:35	0130	Xfr Sw B Lo Pwr	13:49	0226	Mode 1 On
43:40	0110	Xntr Fil Pwr Off	13:55	0521	Prop Strain Gage Pwr On
Day 265 - DSS-11			14:03	3617	Interlock
00:59:21	0510	AESP Off	14:04	M0005	Magnitude (5 counts) (0.25 Sec)
59:27	0226	Mode 1 On	14:24	0727	FC Thrust $\phi$ Pwr On
59:36	0521	Prop Strain Gage Pwr On	14:41	3617	Interlock
59:46	3617	Interlock	14:41	0721	M/C Correction (13)
59:46	M0005	Magnitude (5 counts) (0.25 Sec)	14:43	0735(3)	Terminate M/C
01:00:06	0727	FC Thrust $\phi$ Pwr On	14:50	0737(2)	Thrust $\phi$ Pwr Off
00:33	3617	Interlock	14:56	0522	Prop Strain Gage Pwr Off
00:34	0721	M/C Correction (10)	15:02	0512	Aux Accel Amp 5-8 Off
00:37	0735	Terminate M/C	15:06	0516	T. D. Strain Gage Pwr Off
00:37	0735	Terminate M/C	15:11	0232	ESP Off
00:38	0735	Terminate M/C			
00:47	0737	Thrust $\phi$ Pwr Off			

Table 4.1-9 (continued)

GMT, hr:min:sec	Command	Function	GMT, hr:min:sec	Command	Function
01:15:17	0506	Mode 5 On	01:59:59	0226	Mode 1 On
18:21	0510	AESP Off	02:00:09	0521	Prop Strain Gage Pwr On
18:26	0226	Mode 1 On	00:35	3617	Interlock
18:33	0521	Prop Strain Gage Pwr On	00:36	M0005	Magnitude (5 counts) (0.25 Sec)
18:41	3617	Interlock	00:45	0727	FC Thrust $\phi$ Pwr On
18:42	M0005	Magnitude (5 counts) (0.25 Sec)	01:19	3617	Interlock
19:31	0727	FC Thrust $\phi$ Pwr On	01:19	0721	M/C Correction (16)
19:45	3617	Interlock	01:21	0735(3)	Terminate M/C
19:46	0721	M/C Correction (14)	01:32	0737(2)	Thrust $\phi$ Pwr Off
19:48	0735(3)	Terminate M/C	01:43	0522	Prop Strain Gage Pwr Off
19:56	0737(2)	Thrust $\phi$ Pwr Off	01:49	0512	Aux Accel Amp 5-8 Off
20:03	0522	Prop Strain Gage Pwr Off	01:53	0516	T. D. Strain Gage Pwr Off
20:08	0512	Aux Accel Amp 5-8 Off	01:58	0232	ESP Off
20:13	0516	T. D. Strain Gage Pwr Off	02:06	0506	Mode 5 On
20:20	0232	ESP Off	06:53	0510	AESP Off
20:25	0506	Mode 5 On	07:00	0226	Mode 1 On
21:36	0105	Xmtr B Fil Pwr On	07:11	0521	Prop Strain Gage Pwr On
23:52	0127	Xfr Sw B Hi Pwr	07:22	3617	Interlock
24:02	0103	Xmtr Hi Volt On	07:22	M0005	Magnitude (5 counts) (0.25 Sec)
24:22	0502	960 cps SCO Off	07:29	0727	FC Thrust $\phi$ Pwr On
24:47	0216	7.35 kc SCO On	08:11	3617	Interlock
25:06	0205	1100 bits/sec	08:11	0721	M/C Correction (17)
25:37	0510	AESP Off	08:13	0735(3)	Terminate M/C
25:53	0226	Mode 1 On	08:19	0737(2)	Thrust $\phi$ Pwr Off
26:23	0521	Prop Strain Gage Pwr On	08:26	0522	Prop Strain Gage Pwr Off
27:06	3617	Interlock	08:31	0512	Aux Accel Amp 5-8 Off
27:07	M0110	Magnitude (40 counts) (2.0 Sec)	08:35	0516	T. D. Strain Gage Pwr Off
27:30	0727	FC Thrust $\phi$ Pwr On	08:40	0232	ESP Off
28:11	3617	Interlock	08:47	0506	Mode 5 On
28:11	0721	M/C Correction (15)	12:38	0510	AESP Off
28:16	0735(4)	Terminate M/C	12:47	0226	Mode 1 On
28:27	0737(2)	Thrust $\phi$ Pwr Off	12:54	0521	Prop Strain Gage Pwr On
28:37	0522	Prop Strain Gage Pwr Off	13:09	3617	Interlock
28:37	0512	Aux Accel Amp 5-8 Off	13:09	M0005	Magnitude (5 counts) (0.25 Sec)
28:38	0516	T. D. Strain Gage Pwr Off	13:14	0727	FC Thrust $\phi$ Pwr On
28:38	0205	1100 bits/sec	13:33	3617	Interlock
29:09	0232	ESP Off	13:34	0721	M/C Correction (18)
29:15	0506	Mode 5 On	13:35	0735(2)	Terminate M/C
29:38	0504	137 bits/sec	13:42	0737(2)	Thrust $\phi$ Pwr Off
29:46	0204	Coast $\phi$ Clock Rates	13:48	0522	Prop Strain Gage Pwr Off
29:53	0220	7.35 kc SCO Off	13:52	0512	Aux Accel Amp 5-8 Off
30:05	0500	960 cps SCO On	13:56	0516	T. D. Strain Gage Pwr Off
30:24	0107	Xmtr Hi Volt Off	14:01	0232	ESP Off
30:28	0130	Xfr Sw B Lo Pwr	14:08	0506	Mode 5 On
30:31	0110	Xmtr Fil Pwr Off	18:34	0510	AESP Off
39:53	0510	AESP Off	18:41	0226	Mode 1 On
40:09	0231	Mode 4 On	18:47	0521	Prop Strain Gage Pwr On
44:36	0232	ESP Off	18:59	3617	Interlock
44:48	0506	Mode 5 On	18:59	M0005	Magnitude (5 counts) (0.25 Sec)
59:51	0510	AESP Off	19:21	0727	FC Thrust $\phi$ Pwr On

Table 4.1-9 (continued)

GMT, hr:min:sec	Command	Function	GMT, hr:min:sec	Command	Function
02:19:36	3617	Interlock	02:42:21	0107	Xntr Hi Volt Off
19:37	0721	M/C Correction (19)	42:29	0130	Xfr Sw Lo Pwr
19:38	0735(3)	Terminate M/C	42:34	0110	Xntr Fil Pwr Off
19:44	0737(2)	Thrust $\phi$ Pwr Off	43:06	3617	Interlock
19:53	0522	PropStrainGage Pwr Off	43:07	0311	FC Power Off
19:57	0512	Aux Accel Amp 5-8 Off	44:58		
20:02	0516	T.D. StrainGage Pwr Off	to	0403	Step Polar Axis Plus
20:07	0232	ESP Off	52:12	(240)	
20:15	0506	Mode 5 On	03:12:40	0510	AESP Off
24:27	0510	AESP Off	12:47	0226	Mode 1 On
24:35	0226	Mode 1 On	12:56	0521	PropStrainGage Pwr On
24:41	0521	Prop Strain Gage Pwr On	13:06	3617	Interlock
24:54	3617	Interlock	13:06	M0005	Magnitude (5 counts) (0.25 Sec)
24:55	M0005	Magnitude (5 counts) (0.25 Sec)	15:48	3617	Interlock
25:47	0727	FC Thrust $\phi$ Pwr On	15:49	0300	FC Power On
26:06	3617	Interlock	16:44	3617	Interlock
26:06	0721	M/C Correction (20)	16:45	M0005	Magnitude (5 counts) (0.25 Sec)
26:08	0735(3)	Terminate M/C	17:06	0727	FC Thrust $\phi$ Power On
26:13	0737(2)	Thrust $\phi$ Pwr Off	17:24	3617	Interlock
26:21	0522	PropStrainGagePwr Off	17:24	0721	M/C Correction (22)
26:24	0512	Aux Accel Amp 5-8 Off	17:28	0735(2)	Terminate M/C
26:28	0516	T.D. StrainGage Pwr Off	17:36	0737(2)	Thrust $\phi$ Pwr Off
26:35	0232	ESP Off	17:41	0522	PropStrainGage Pwr On
26:43	0506	Mode 5 On	17:46	0512	Aux Accel Amp 5-8 Off
32:02	0105	Xntr B Fil Pwr On	17:49	0516	T.D. StrainGage Pwr Off
34:00	0127	Xfr Sw B Hi Pwr	17:56	0232	ESP Off
34:07	0103	Xntr Hi Volt On	18:03	0506	Mode 5 On
35:36	0502	960 cps SCO Off	22:39	0510	AESP Off
35:47	0216	7.35 kc SCO On	22:46	0226	Mode 1 On
35:54	0205	1100 bits/sec	22:55	0521	PropStrainGage Pwr On
36:22	0510	AESP Off	23:09	3617	Interlock
36:33	0226	Mode 1 On	23:09	M0005	Magnitude (5 counts) (0.25 Sec)
36:53	0521	PropStrainGage Pwr On	23:27	0727	FC Thrust $\phi$ Pwr On
37:18	3617	Interlock	23:53	3617	Interlock
37:19	M0110	Magnitude (40 counts) (2.0 Sec)	23:53	0721	M/C Correction (23)
38:48	0727	FC Thrust $\phi$ Pwr On	23:58	0735(3)	Terminate M/C
39:14	3617	Interlock	24:01	0737(2)	Thrust $\phi$ Pwr Off
39:14	0721	M/C Correction (21)	24:09	0522	PropStrainGage Pwr Off
39:17	0735(2)	Terminate M/C	24:14	0512	Aux Accel Amp 5-8 Off
39:27	0737(2)	Thrust $\phi$ Pwr Off	24:17	0516	T.D. StrainGage Pwr Off
39:35	0522	PropStrainGage Pwr Off	24:23	0232	ESP Off
39:35	0512	Aux Accel Amp 5-8 Off	24:30	0506	Mode 5 On
39:36	0516	T.D. StrainGage Pwr Off	28:06	0510	AESP Off
39:36	0205	1100 bits/sec	28:11	0226	Mode 1 On
40:08	0232	ESP Off	28:16	0521	PropStrainGage Pwr On
40:16	0506	Mode 5 On	28:25	3617	Interlock
41:16	0504	137 bits/sec	28:26	M0005	Magnitude (5 counts) (0.25 Sec)
41:24	0204	Coast $\phi$ Clock Rates	28:55	0727	FC Thrust $\phi$ Pwr On
41:35	0220	7.35 kc SCO Off	29:07	3617	Interlock
41:45	0500	960 cps SCO On	29:07	0721	M/C Correction (24)
			29:09	0735(2)	Terminate M/C
			29:16	0737(2)	Thrust $\phi$ Pwr Off
			29:22	0522	PropStrainGage Pwr Off

Table 4.1-9 (continued)

GMT, hr:min:sec	Command	Function	GMT, hr:min:sec	Command	Function
03:29:26	0512	Aux Accel Amp 5-8 Off	03:48:06	0737(2)	Thrust $\phi$ Pwr Off
29:31	0516	T.D. Strain Gage Pwr Off	48:22	0522	PropStrainGage Pwr Off
29:36	0232	ESP Off	48:23	0512	Aux Accel Amp 5-8 Off
29:41	0506	Mode 5 On	48:23	0516	T.D. StrainGage Pwr Off
33:48	0510	AESP Off	48:24	0205	1100 bits/sec
33:54	0226	Mode 1 On	48:39	0232	ESP Off
33:58	0521	PropStrainGage Pwr On	48:49	0506	Mode 5 On
34:05	3617	Interlock	49:22	0504	137 bits/sec
34:06	M0005	Magnitude (5 counts) (0.25 Sec)	49:28	0204	Coast $\phi$ Clock Rates
34:24	0727	FC Thrust $\phi$ Pwr On	49:34	0220	7.35 kc SCO Off
34:33	3617	Interlock	49:43	0500	960 cps SCO On
34:33	0721	M/C Correction (25)	50:06	0107	Xmtr Hi Volt Off
34:35	0735	Terminate M/C	50:12	0130	Xfr Sw Lo Pwr
34:35	0735	Terminate M/C	50:17	0110	Xmtr Fil Pwr Off
34:42	0737	Thrust $\phi$ Pwr Off	51:34	3617	Interlock
34:48	0522	PropStrainGage Pwr Off	51:34	0311	FC Power Off
34:54	0512	Aux Accel Amp 5-8 Off	04:15:55	0300	FC Power On
34:57	0516	T.D. Strain Gage Pwr Off	16:14	0510	AESP Off
35:02	0232	ESP Off	16:22	0226	Mode 1 On
35:07	0506	Mode 5 On	16:29	0521	PropStrainGage Pwr On
38:21	0510	AESP Off	16:43	3617	Interlock
38:26	0226	Mode 1 On	16:43	M0005	Magnitude (5 counts) (0.25 Sec)
38:30	0521	PropStrainGage Pwr On	17:11	0727	FC Thrust $\phi$ Pwr On
38:38	3617	Interlock	17:31	3617	Interlock
38:38	M0005	Magnitude (5 counts) (0.25 Sec)	17:31	0721	M/C Correction (28)
38:53	0727	FC Thrust $\phi$ Pwr On	17:33	0735(2)	Terminate M/C
39:07	3617	Interlock	17:40	0737(2)	Thrust $\phi$ Pwr Off
39:07	0721	M/C Correction (26)	17:56	0232	ESP Off
39:09	0735(3)	Terminate M/C	18:06	0506	Mode 5 On
39:14	0737(2)	Thrust $\phi$ Pwr Off	22:42	0510	AESP Off
39:19	0522	PropStrainGage Pwr Off	22:49	0226	Mode 1 On
39:23	0512	Aux Accel Amp 5-8 Off	22:55	0521	PropStrainGage Pwr On
39:26	0516	T.D. Strain Gage Pwr Off	23:05	3617	Interlock
39:31	0232	ESP Off	23:06	M0005	Magnitude (5 counts) (0.25 Sec)
39:36	0506	Mode 5 On	23:38	0727	FC Thrust $\phi$ Pwr On
41:34	0105	Xmtr B Fil Pwr On	23:53	3617	Interlock
43:46	0127	Xfr Sw B Hi Pwr	23:53	0721	M/C Correction (29)
43:52	0103	Xmtr Hi Volt On	23:55	0735	Terminate M/C
44:44	0502	960 cps SCO Off	24:00	0737(2)	Thrust $\phi$ Pwr Off
44:57	0216	7.35 kc SCO On	24:12	0232	ESP Off
45:03	0205	1100 bits/sec	24:20	0506	Mode 5 On
45:40	0510	AESP Off	28:26	0510	AESP Off
45:50	0226	Mode 1 On	28:34	0226	Mode 1 On
46:48	0521	PropStrainGage Pwr On	28:58	3617	Interlock
47:03	3617	Interlock	28:58	M0005	Magnitude (5 counts) (0.25 Sec)
47:03	M0110	Magnitude (40 counts) (2.0 Sec)	29:36	0727	FC Thrust $\phi$ Pwr On
47:35	0727	FC Thrust $\phi$ Pwr On	29:51	3617	Interlock
47:56	3617	Interlock	29:51	0721	M/C Correction (30)
47:56	0721	M/C Correction (27)	29:53	0735	Terminate M/C
47:59	0735(2)	Terminate M/C	30:00	0737(2)	Thrust $\phi$ Pwr Off

Table 4.1-9 (continued)

GMT, hr:min:sec	Command	Function	GMT, hr:min:sec	Command	Function
04:30:21	0232	ESP Off	04:58:24	0130	Xfr Sw Lo Pwr
30:28	0506	Mode 5 On	58:30	0110	Xmtr Fil Pwr Off
34:38	0510	AESP Off	59:16	3617	Interlock
34:45	0226	Mode 1 On	59:16	0311	FC Power Off
34:59	3617	Interlock	05:30:18	0300	FC Power On
34:59	M0005	Magnitude (5 counts) (0.25 Sec)	30:52	0105	Xmtr B Fil Pwr On
35:18	0727	FC Thrust $\phi$ Pwr On	32:53	0127	Xfr Sw B Hi Pwr
35:33	3617	Interlock	32:59	0103	Xmtr Hi Volt On
35:34	0721	M/C Correction (31)	33:52	0502	960 cps SCO Off
35:35	0735(2)	Terminate M/C	34:06	0216	7.35 kc SCO On
35:41	0737(2)	Thrust $\phi$ Pwr Off	34:11	0205	1100 bits/sec
35:52	0232	ESP Off	34:49	0507	Mode 6 On
36:00	0506	Mode 5 On	37:08	0720	Reset Group IV
40:22	0510	AESP Off	38:58	3617	Interlock
40:29	0226	Mode 1 On	38:58	0724	Retro Sequence Mode On
40:40	3617	Interlock	39:22	0521	Prop Strain Gage Pwr On
40:41	M0005	Magnitude (5 counts) (0.25 Sec)	39:45	0715	Manual Delay Mode On
41:04	0727	FC Thrust $\phi$ Pwr On	40:27	0732	Emergency Retro Eject
41:19	3617	Interlock	41:34	0727	FC Thrust $\phi$ Pwr On
41:20	0721	M/C Correction (32)	43:19	3617	Interlock
41:21	0735(3)	Terminate M/C	43:19	0721	M/C Correction (34)
41:26	0737(2)	Thrust $\phi$ Pwr Off	43:22	0735(2)	Terminate M/C (after 2.5 Sec)
41:37	0232	ESP Off	43:47	0737(2)	Thrust $\phi$ Pwr Off
41:45	0506	Mode 5 On	44:02	0720	Reset Group IV
45:05	0105	Xmtr B Fil Pwr On	44:20	0701	Rate Mode On
52:36	0127	Xfr Sw B Hi Pwr	44:55	0522	Prop Strain Gage Pwr Off
52:46	0103	Xmtr Hi Volt On	45:00	0512	Aux Accel Amp 5-8 Off
53:28	0502	960 cps SCO Off	45:04	0516	T,D. Strain Gage Pwr Off
53:40	0216	7.35 kc SCO On	45:20	0506	Mode 5 On
53:47	0205	1100 bits/sec	46:08	0504	137 bits/sec
54:26	0510	AESP Off	46:14	0204	Coast $\phi$ Clock Rates
54:38	0226	Mode 1 On	46:25	0220	7.35 kc SCO Off
55:03	3617	Interlock	46:34	0500	960 cps SCO On
55:03	M0110	Magnitude (40 counts) (2.0 Sec)	47:01	0107	Xmtr Hi Volt Off
55:26	0727	FC Thrust $\phi$ Pwr On	47:06	0130	Xfr Sw Lo Pwr
56:11	3617	Interlock	47:10	0110	Xmtr Fil Pwr Off
56:12	0721	M/C Correction (33)	48:51	3617	Interlock
56:15	0735(2)	Terminate M/C	48:51	0311	FC Power Off
56:21	0737(2)	Thrust $\phi$ Pwr Off	Day 265 - DSS 42		
56:30	0522	Prop Strain Gage Pwr Off	06:30:29	0105	Xmtr B Fil Pwr On
56:30	0512	Aux Accel Amp 5-8 Off	32:38	0127	Xfr Sw B Hi Pwr
56:31	0516	T,D. Strain Gage Pwr Off	32:45	0103	Xmtr Hi Volt On
56:31	0205	1100 bits/sec	34:14	0502	960 cps SCO Off
56:49	0232	ESP Off	34:29	0216	7.35 kc SCO On
56:59	0506	Mode 5 On	34:38	0205	1100 bits/sec
57:15	0504	137 bits/sec	35:19	0631(5)	Unlock Solar Panel (Transit)
57:21	0204	Coast $\phi$ Clock Rates	40:27		
57:55	0220	7.35 kc SCO Off	41:39	0401(10)	Step Solar Panel Plus
58:05	0500	960 cps SCO On	41:44		
58:19	0107	Xmtr Hi Volt Off	42:51	0402	Step Solar Panel
			43:47	(110)	Minus

Table 4. 1-9 (continued)

GMT, hr:min:sec	Command	Function	GMT, hr:min:sec	Command	Function
06:45:41 to 45:46	0401(10)	Step Solar Panel Plus	07:46:12	0721	M/C Correction (36)
46:07 to 46:11	0402(10)	Step Solar Panel Minus	46:14	0735(3)	Terminate M/C
46:32 to 46:37	0401(10)	Step Solar Panel Plus	46:45	3617	Interlock
46:55 to 47:00	0402(10)	Step Solar Panel Minus	46:45	M0005	Magnitude (5 counts) (0.25 Sec)
47:17 to 47:23	0401(10)	Step Solar Panel Plus	47:14	3617	Interlock
47:43 to 49:35	0402(34)	Step Solar Panel Minus	47:15	0721	M/C Correction (37)
50:33	0504	137 bits/sec	47:17	0735(2)	Terminate M/C
50:40	0204	Coast $\phi$ Clock Rates	47:48	3617	Interlock
50:54	0220	7.35 kc SCO Off	47:49	M0005	Magnitude (5 counts) (0.25 Sec)
51:11	0500	960 cps SCO On	48:18	3617	Interlock
53:32	0502	960 cps SCO Off	48:18	0721	M/C Correction (38)
53:47	0216	7.35 kc SCO On	48:20	0735(2)	Terminate M/C
53:54	0205	1100 bits/sec	48:50	3617	Interlock
54:33	0635	Unlock Solar Panel (Lunar)	48:50	M0005	Magnitude (5 counts) (0.25 Sec)
55:06 to 55:49	0402(87)	Step Solar Panel Minus	49:25	3617	Interlock
58:02	0504	137 bits/sec	49:25	0721	M/C Correction (39)
58:09	0204	Coast $\phi$ Clock Rates	49:27	0735(2)	Terminate M/C
58:24	0220	7.35 kc SCO Off	49:31	0737(2)	Thrust $\phi$ Pwr Off
58:41	0500	960 cps SCO On	49:54	0232	ESP Off
59:12	0107	Xmtr Hi Volt Off	50:01	0506	Mode 5 On
59:21	0130	Xfer Sw Lo Pwr	50:23	0504	137 bits/sec
59:28	0110	Xmtr Fil Pwr Off	50:29	0204	Coast $\phi$ Clock Rates
07:34:49	0300	FC Power On	50:47	0220	7.35 kc SCO Off
39:54	0105	Xmtr B Fil Pwr On	50:54	0500	960 cps SCO On
41:42	0127	Xfer Sw B Hi Pwr	51:17	0107	Xmtr Hi Volt Off
41:49	0103	Xmtr Hi Volt On	51:24	0130	Xfer Sw B Lo Pwr
42:23	0502	960 cps SCO Off	51:38	0110	Xmtr Fil Pwr Off
42:38	0216	7.35 kc SCO On	59:04	0105	Xmtr B Fil Pwr On
42:50	0205	1100 bits/sec	08:00:46	0127	Xfer Sw B Hi Pwr
43:19	0510	AESP Off	00:52	0103	Xmtr Hi Volt On
43:26	0226	Mode 1 On	01:12	0502	960 cps SCO Off
43:43	0521	PropStrainGage Pwr On	01:26	0216	7.35 kc SCO On
44:05	3617	Interlock	02:11	0205	1100 bits/sec
44:06	M0005	Magnitude (5 counts) (0.25 Sec)	02:28	0507	Mode 6 On
44:36	0727	FC Thrust $\phi$ Pwr On	02:46	0720	Reset Group IV
44:59	3617	Interlock	03:08	3617	Interlock
45:00	0721	M/C Correction (35)	03:09	0724	Retro Sequence Mode On
45:02	0735(2)	Terminate M/C	03:23	0521	PropStrainGage Pwr On
45:51	3617	Interlock	03:38	0715	Manual Delay Mode On
45:52	M0005	Magnitude (5 counts) (0.25 Sec)	03:59	0706	Enable Gas Jets
46:12	3617	Interlock	04:16	0732	Emergency Retro Eject
			04:31	0727	FC Thrust $\phi$ Pwr On
			05:12	3617	Interlock
			05:12.5	0721	M/C Correction (40)
			05:34.0	0735(3)	Terminate M/C (after 21.5 Sec)
			05:45	0737(2)	Thrust $\phi$ Pwr Off
			06:01	0720	Reset Group IV
			06:10	0701	Rate Mode On
			07:56	0506	Mode 5 On
			08:33	0504	137 bits/sec

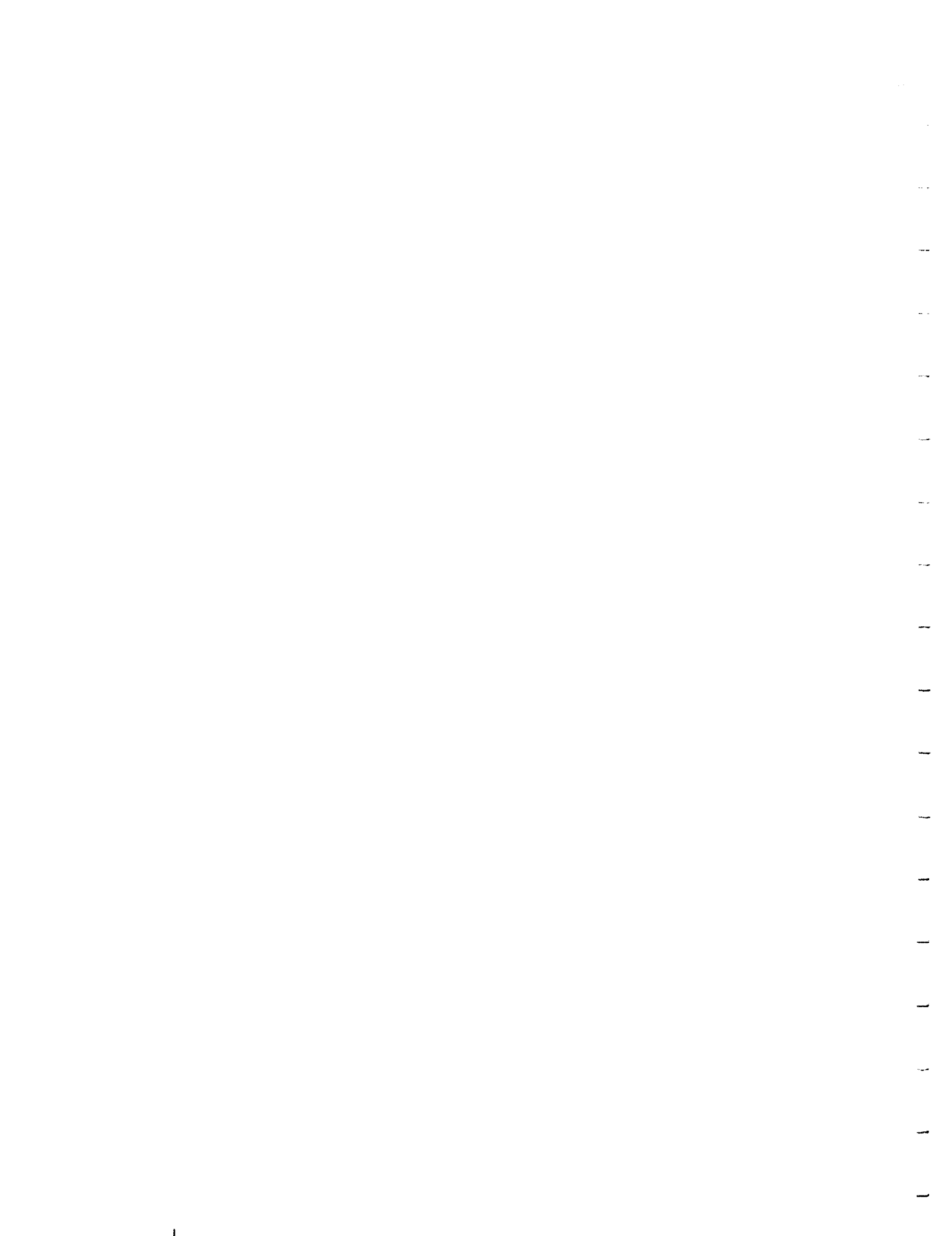
Table 4.1-9 (continued)

GMT, hr:min:sec	Command	Function	GMT, hr:min:sec	Command	Function
08:08:39	0204	Coast $\phi$ Clock Rates	09:23:46	0322	Hi Current Mode On
08:54	0220	7.35 kc SCO Off	24:24	0320	Restore Main Batt Mode
09:02	0500	960 cps SCO On	24:54	0317	Aux Batt Mode On
09:19	0107	Xntr Hi Volt Off	25:29	0323	Hi Current Mode Off
09:28	0130	Xfer Sw B Lo Pwr	27:09	0322	Hi Current Mode On
09:35	0110	Xntr Fil Pwr Off	27:27	0320	Restore Main Batt Mode
10:28	3617	Interlock	27:43	0321	Disable Batt Xfer Logic
10:28	0311	FC Power Off	28:01	0323	Hi Current Mode Off
09:09:41	0105	Xntr B Fil Pwr On	30:09	3617	Interlock
11:44	0127	Xfer Sw B Hi Pwr	30:09	0630	RADVS Power Off
11:50	0103	Xntr Hi Volt On	30:33	0706	Enable Gas Jets
12:14	0502	960 cps SCO Off	30:53	0716	Manual Lock On
12:22	0216	7.35 kc SCO On	31:12	0723	Reset Nom Thrust Bias
12:34	0205	1100 bits/sec	31:51	3617	Interlock
13:00	0300	FC Power On	31:51	M0500	Magnitude (160 counts) (8.0 Sec)
13:16	3617	Interlock	32:11	0510	AESP Off
13:16	0610	Dump Helium	32:19	0227	Mode 2 On
18:42	0302	Disable Battery Pressure Logic	32:55	0720	Reset Group IV
19:06	0727	FC Thrust $\phi$ Pwr On	33:14	3617	Interlock
19:56	3617	Interlock	33:14	0724	Retro Sequence Mode On
19:57	0637	RADVS Power On	34:17	0730	Emergency AMR Signal
22:16	0320	Restore Main Batt Mode	35:00		Loss of Command Link: END OF MISSION



## 4.2 PRELAUNCH COUNTDOWN

The final prelaunch countdown proceeded smoothly with the exception of one reported difficulty. The telemetry indicated approximately 10 to 17 db weaker signal strength into receiver B than into receiver A. During pre-launch, it was felt that this failure was due to a change in the RF link with the gantry moved back (i. e., no RF repeater used under these conditions). The failure was thus attributed to a change in the test setup. Subsequent analysis of flight data showed that the failure was probably due to a shift in the receiver B automatic gain control curve. It was felt that the problem was not serious enough to prevent launch. After encountering difficulty in pressurizing the Atlas propulsion system, the spacecraft was finally launched just before close of the daily launch window at 12:32 GMT at an azimuth of 114.361 degrees.



## 4.3 LAUNCH, INJECTION, AND SEPARATION

### 4.3.1 LAUNCH TRAJECTORY PROFILE

SC-2 was launched from AFETR launch site 36A on Tuesday, 20 September 1966, using a General Dynamics/Convair Atlas/Centaur (AC-7) boost vehicle. The launch was held until near the close of the launch window when difficulties were experienced with the Atlas boil off and LOX topping valve. Liftoff occurred at 12:31:59.824. Two seconds after liftoff the launch vehicle began a 13-second programmed roll that oriented the vehicle from a pad-aligned azimuth of 105 degrees to a launch azimuth of 114.361 degrees. At 15 seconds, a programmed pitch maneuver was initiated. The nominal and actual times for the Atlas/Centaur boost phase events are summarized in Table 4.3-1. All mark times were nominal. The launch phase ascent trajectory profile is illustrated in Figure 4.3-1.

Separation of Surveyor from Centaur occurred at 12:44:32.6 at a geocentric latitude and longitude of 12.9 and 309.8 degrees, respectively. The spacecraft was in sunlight at separation and never entered the earth's shadow during the transit trajectory.

### 4.3.2 SPACECRAFT PERFORMANCE

The boost phase was normal and resulted in SC-2 being injected properly, thereby placing the spacecraft on the desired lunar trajectory to the moon target site. Subsequent to injection and prior to its separation from the spacecraft, Centaur issued the preprogrammed commands for extending the spacecraft landing legs (L + 11M51S), extending the omnidirectional antennas (L + 12M1S), and turning on the transmitter high power (L + 12M23S). Normal response was verified from telemetry data\*. A minor spacecraft anomaly occurred during this period when the flight control subsystem switched from rate to inertial mode. However, this anomaly had no effect on the mission since the flight control subsystem was returned to the rate mode by separation of the spacecraft from the Centaur. Separation was initiated by the Centaur at L + 12M27S by accomplishing electrical disconnect, and was completed satisfactorily at L + 12M33S.

---

\*An apparent anomaly was noted in real time, as the leg 1 position signal (V-5) indicated 17 degrees in the extended position. However, postmission analysis shows that the SFOF computer had an incorrect coefficient for this signal.

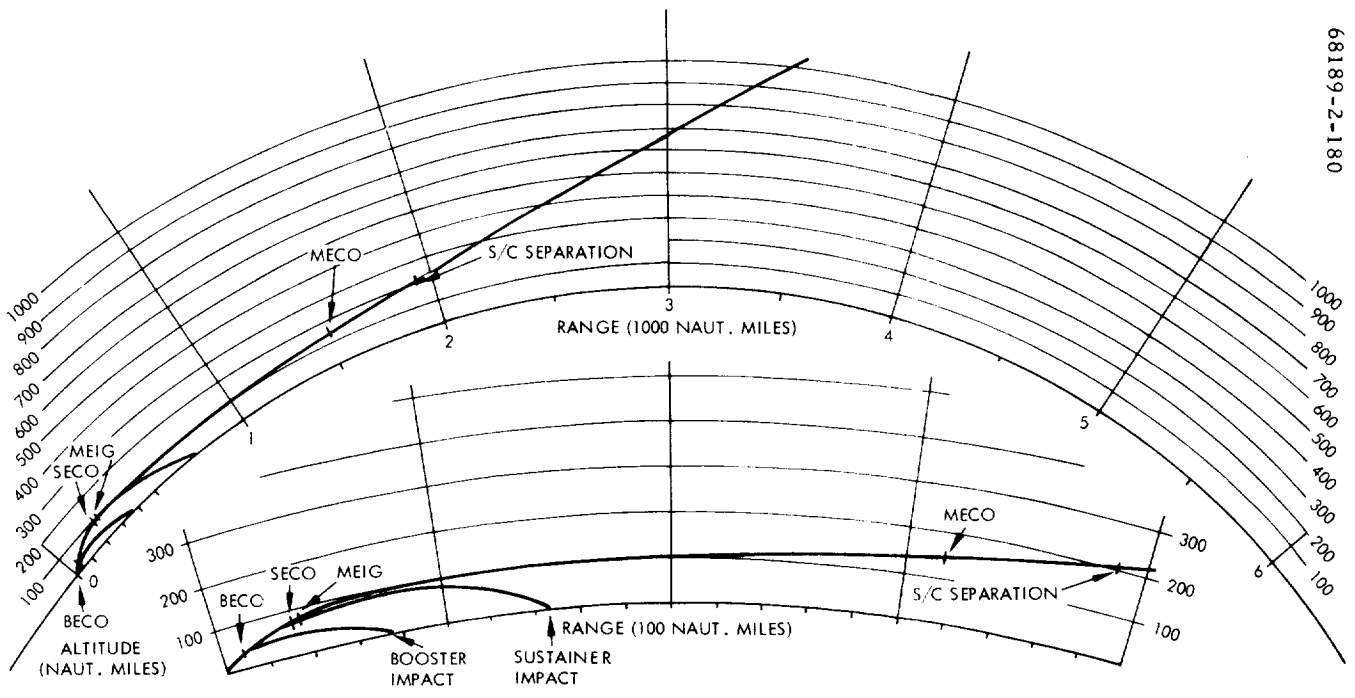


Figure 4.3-1. Launch Phase Trajectory Profile

TABLE 4.3-1. MARK EVENTS

Mark Number	Event	Nominal Time, seconds	Actual Time, seconds
	2-inch motion (liftoff 12:31:59.824 GMT)	0.0	0.0
1	Booster engine cutoff (guidance discrete, staging acceleration 5.7 g)	143.0	142.29
2	Jettison booster package	146.1	145.75
3	Jettison insulation panels	177.0	176.06
4	Jettison nose fairing	204.0	202.90
5	Sustainer engine cutoff (by propellant depletion)	236.0	235.17
6	Atlas/Centaur separation	238.0	237.03
7	Start Centaur main engines (SECO + 11.5 seconds)	247.5	246.58
8	Centaur main engine cutoff (guidance discrete)	684.0	686.3
9	Surveyor landing gear extend command	715.0	710.7
10	Surveyor omnidirectional antenna extend command	725.0	720.7
11	Surveyor high power transmitter on	746.0	741.4
12	Centaur/Surveyor electrical disconnect	752.0	742.08
13	Separate spacecraft	753.7	752.58
14	Admit guidance	758.0	754.7
15	Start H <sub>2</sub> O <sub>2</sub> engines (V), 180-degree turnaround mode	798.0	NA
16	Stop H <sub>2</sub> O <sub>2</sub> engines, 180-degree turnaround mode	818.0	NA
17	Start retrothrust (Centaur tank blowdown)	993.0	992.8
18	Stop retrothrust	1243.0	1242.9
19	Energize power changeover switch	1243.0	1242.9

Following separation, the spacecraft performed the designed automatic sequences. By using the cold gas jets which were enabled at separation, the flight control subsystem nulled out the rotational rates imparted by the separation springs and initiated a roll-yaw sequence to acquire the sun. At L + 16M15S, after a minus roll of approximately 72 degrees and a plus yaw of 16.5 degrees, sun acquisition and lockon were completed. Concurrent with the spacecraft sun acquisition sequence, the A/SPP stepping sequence was initiated for deploying the solar panel axis and roll axis of 85 and 60 degrees, respectively. At approximately L + 23M, stepping was completed, resulting in positioning of the solar panel to the desired transit position. All these operations were confirmed in real time from the spacecraft telemetry.

#### 4. 3. 3 EVALUATION OF VIBRATION DATA FOR AC-7/SC-2 BOOST ENVIRONMENT

##### 4. 3. 3. 1 Instrumentation

Two accelerometer channels (IRIG channels 14 and 17) of vibration data were recorded in real time on a direct write oscillograph during the launch of SC-2/AC-7 and also for the initial 5 minutes of powered flight. Telemetry channel 17 transmitted the continuous signal of accelerometer CY 52 0. Channel 14 produced a commutated signal from CY 53 0, CY 54 0, CY 77 0, and CY 78 0. Accelerometers CY 52 0, CY 53 0, and CY 54 0 were located on the spacecraft at the legs 1, 2, and 3 column bases, respectively, with their axes of maximum sensitivity parallel to the spacecraft Z axes. Accelerometer CY 77 0 was located on the upper flange of the Centaur adapter adjacent to leg 1 and was sensitive to motion in a radial direction. Accelerometer CY 78 0 was mounted in the flight control sensor group and sensed the vertical response of this unit. The SC-2 dynamic instrumentation was identical to the instrumentation aboard SC-1/AC-10.

##### 4. 3. 3. 2 Evaluation of Data and Anomalies

Accelerometer CY 54 0 and CY 78 0 were the only SC-2 accelerometers that operated normally in flight. Accelerometers CY 52 0, CY 53 0, and CY 77 0 produced no intelligible data during the entire recording period. Since the two operating accelerometers were commutated on an equal time basis with two inoperative transducers, the flight environment was monitored only during 36 of the 90 commutator segments or 40 percent of the time. Most of the shock transients experienced on SC-1 during various jettisons and shutdown events were not recorded during the SC-2 flight and, therefore, only very limited data are available for comparison. Table 4. 3-2 presents vibration levels recorded during similar flight events for SC-1 (AC-10), SC-2 (AC-7), and SD-2 (AC-6).

TABLE 4.3-2. VIBRATION LEVELS

Spacecraft	Accelerometer	Launch, g rms*	Atlas BECO g 0 to peak**	Boost Engine Jettison*** g 0 to peak	Nose Fairing Jettison, g 0 to peak****
SC-1	CY 54 0	0.4	†	†	†
SC-2	CY 54 0	0.3	†	†	†
SC-1	CY 78 0	0.4	†	†	0.5
SC-2	CY 78 0	0.2	0.8	7.5	0.6
SC-1 ††	CY 52 0	0.4	1.0	8	0.5
SD-2 ††	CY 52 0	0.7	1.3	5	0.8

\*Nonstationary random signal with a superimposed 6 to 8 cps sine wave.

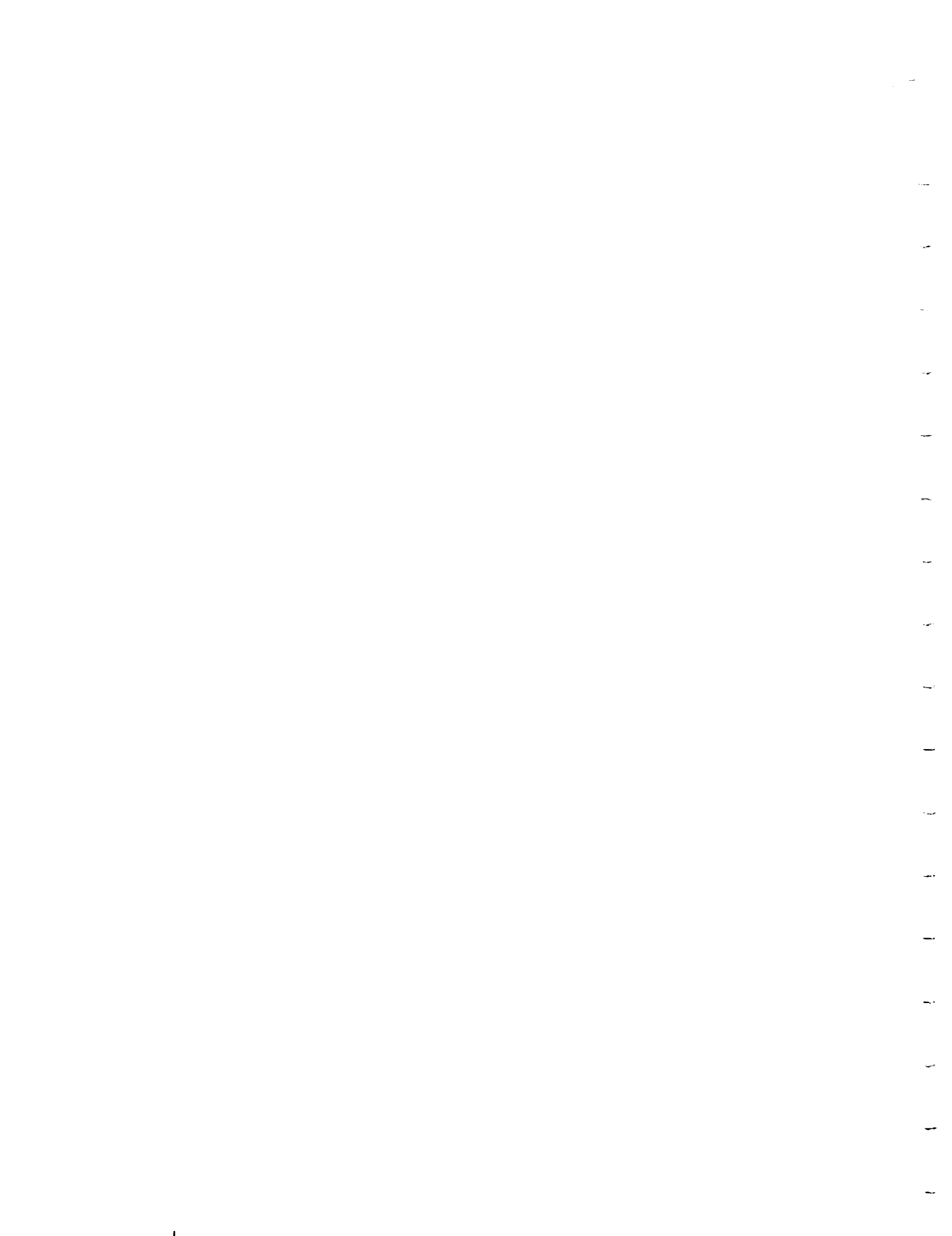
\*\*One-half to full sine wave pulse of 1/2 to 3/4 second duration.

\*\*\*Single high frequency spike.

\*\*\*\*Four to 7 cycles of 30 to 40 cps sine wave.

† Not being transmitted at time of event.

†† Continuous signals presented for comparison.





## 4. 4 DSIF ACQUISITION

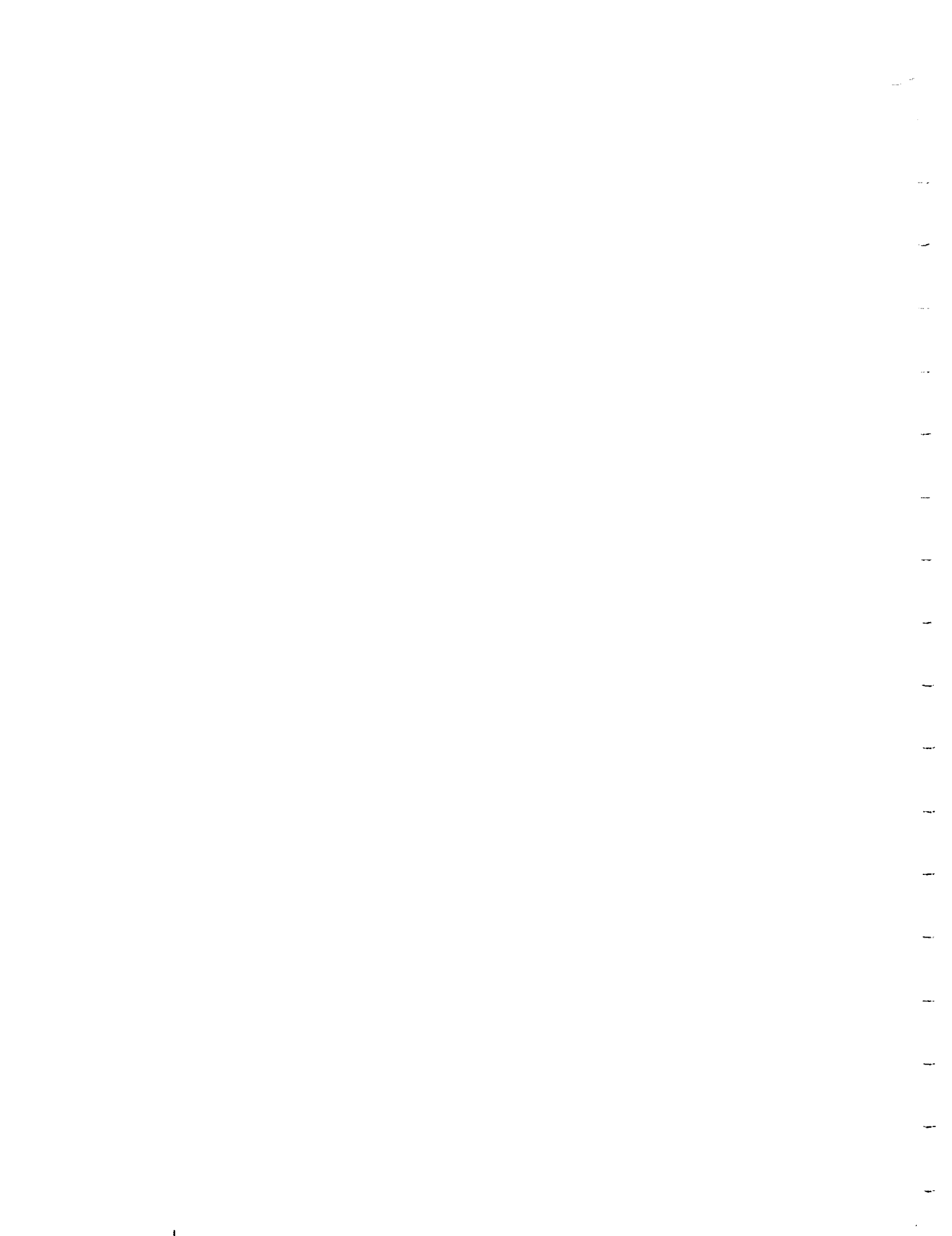
### 4. 4. 1 ACQUISITION PREDICTIONS

Predictions indicated Surveyor II rise at DSS-51 at 12:55:00 on 20 September 1966. DSS-51 reported good one-way data at 12:55:17, auto-track on the SCM (antenna main beam) at 13:00:07, and good two-way data at 13:05:07; thus, DSS-51 required 10 minutes from spacecraft rise to obtain good two-way data. Had the acquisition been optimum, DSS-51 could have had good data, two-way lock at approximately 12:58, or about 3 minutes after spacecraft rise. In comparison, DSS-51 reported good data, two-way lock less than 4 minutes after spacecraft rise in the Surveyor I mission.

This delay of about 6 minutes from an optimum acquisition was due partly to a hardware problem (the SCM monitor-receiver was initially saturated by high signal strength) and partly to a procedural problem at DSS-51 precipitated by the same hardware problem.

### 4. 4. 2 SPACECRAFT PERFORMANCE

At approximately L + 25M, the spacecraft became visible to DSS-51, and the initial DSIF acquisition procedure for establishing the communication and tracking link between the spacecraft and the ground station was initiated. The first ground-controlled sequence (initial spacecraft operations) was initiated at L + 45M, and consisted of commands for turning off equipment required only for the launch-to-DSIF acquisition phase (e. g. , transmitter high-power off, accelerometer amplifiers off, etc. ) for seating the solar panel and roll axis locking pins securely, for increasing the telemetry bit rate to 1100 bits/sec, and for initially interrogating all telemetry commutator modes. All spacecraft responses to commands were normal. As a result of data assessment, it was determined that the star intensity telemetry signal was indicating that an object (thought to be the earth) was in the Canopus sensor field of view. Therefore, it was recommended that the roll axis be held in the inertial mode and that the cruise mode command (which would have caused the spacecraft roll attitude to be slaved to the position of the earth) not be sent to the spacecraft. It was also recommended that transponder A not be turned on, since the receiver A automatic frequency control indicated that this receiver was tracking the ground station signal.



#### 4.5 COAST PHASE I (INCLUDING CANOPUS ACQUISITION)

The spacecraft continued to coast normally, with its pitch-yaw attitude controlled to track the sun and with its roll axis held inertially fixed. Tracking and telemetry data were obtained by use of transponder B and transmitter B operating in low power.

At L + 4H33M, control of the spacecraft was transferred to DSS-72 to provide additional tracking data. This transfer necessitated a decrease in telemetry data rate from 1100 bits/sec to 137.5 bits/sec due to the lower antenna gain available at DSS-72. At L + 5H23M, spacecraft control was returned to DSS-51 and, at L + 5H30M, the telemetry data rate was increased again to 1100 bits/sec.

At L + 6H6M, a spacecraft roll maneuver was initiated to make a star map and locate Canopus. Per real-time recommendations, the maneuver was begun with omnidirectional antenna B and transmitter B in high power (transponder off). Mode 5 data were available at 1100 bits/sec. Two complete revolutions were made to generate the star map, the first with antenna B and the second with A. The earth, moon, and stars Shaula, Rasalhague, Menkalinan, and Theta Ophiuchi were identified. Canopus was located after 237 degrees of roll. As was the case in the SC-1 mission, a Canopus lockon signal was not generated as the star sensor swept past Canopus, since the Canopus intensity signal was above the lockon range upper threshold. As the vehicle continued to roll, the time for sending the proper command to achieve manual lockon to Canopus was computed, with manual lockon being achieved at approximately L + 6H38M. Roll attitude was now precisely determined, a prerequisite for the premidcourse maneuvers.

Following this successful lockon, a gyro drift check was initiated (L + 6H54M). The vehicle continued to coast as before, but with its attitude held inertially so that the sun and star sensors continued to point at the sun and Canopus, respectively. At L + 9H3M, the check was terminated.

With the DSS-51 visibility period ending at L + 9H46M, a potential gap existed in the coverage since DSS-11 would not yet have visibility. Because DSS-72 had visibility of the spacecraft for part of the gap, spacecraft control was transferred to DSS-72, requiring telemetry bit rate reduction to 17.2 bits/sec. Unfortunately, DSS-72 had considerable difficulty in

providing good data; it was estimated that 80 percent of the data was bad. At L + 10H12M, the spacecraft became visible to DSS-11, and two-way lock was achieved by this station at L + 10H35M. The bit rate was increased to 1100 bits/sec at L + 10H40M.

Because analysis of the spacecraft receiver B automatic gain control telemetry data obtained during star verification and acquisition indicated a signal strength which was approximately 18 db below the predicted value, a special test for performing an in-flight calibration of this data channel was recommended. This test was required to establish whether transponder operation two-way tracking could be used during the midcourse correction, since a degradation of 16 db in receiver B sensitivity (i. e. , a receiver malfunction) might cause loss of two-way lock during midcourse. Following satisfactory completion of the scheduled premidcourse low power engineering interrogation, the special calibration test was initiated at L + 13H6M. During this sequence, DSS-11 transmitter power was reduced in 2-db steps until the command threshold level (as indicated by an indexing of the receiver-decoder-select unit) was reached. This occurred after a total reduction of 24 db at a telemetry-indicated signal strength of -133 dbm for receiver B and -121 dbm for receiver A. It was concluded that receiver B calibration had changed, but that the signal strength could be lowered by 24 db without causing a receiver index and by 30 db without causing a loss of carrier signal in receiver B. Therefore, it was recommended that the midcourse correction be done in two-way lock.

Also recommended for midcourse was the roll-yaw maneuver pair (plus roll of 75.3 degrees, followed by a plus yaw of 110.5 degrees), primarily from an analysis of the telecommunication performance expected for each of the four maneuver-pair candidates (i. e. , roll-yaw, roll-pitch, yaw-pitch, and pitch-yaw).

At L + 14H27M, the scheduled premidcourse engineering interrogation was initiated. This sequence was executed using low power transmitter operation, since a data-rate of 1100 bits/sec was still available. As part of this sequence, the gyro speeds were measured and were reading nominal values (i. e. , 50 cps).

## 4.6 MIDCOURSE CORRECTION

### 4.6.1 MIDCOURSE MANEUVER ANALYSIS

A midcourse correction of 9.587 m/sec was computed to soft land Surveyor II at a desired site, +0.55 degree latitude and +359.17 degrees longitude, on the lunar surface. This correction was executed upon ground command at 05:00 GMT on 21 September. Due to hardware failures, the midcourse correction was unsuccessful, and there was no soft landing.

Proximity of the uncorrected and the original aiming point is shown in Figure 4.6-1. The uncorrected, unbraked impact point is located on the western edge of Sinus Medii just northeast of the crater Mosting. The selenographic coordinates of this point are approximately -0.0837 degree latitude and 354.658 degrees longitude. The targeted aiming point was 0.0 degree latitude and 359.33 degrees longitude. The two points are approximately 142 kilometers (88 miles) apart on the moon's surface. Also shown in Figure 4.6-1 is the approximate final impact site of the spacecraft. Figure 4.6-2 shows the prelaunch target site, the in-flight aim point, and the associated dispersions.

The 99-percent dispersions are shown as an ellipse on the surface with a semimajor axis of 53.9 kilometers (1.77 degrees), a semiminor axis of 17.17 kilometers (0.56 degree), and an orientation angle of -57.1 degrees (Figure 4.6-2). In order to maximize the probability of soft landing, the aim point was biased from the original target value of 0.0 degree latitude and 359.33 degrees longitude. The biasing was based on a detailed examination of Lunar Orbiter photographs.

The maximum midcourse correction capability, as a function of the unbraked impact speed, is shown in Figure 4.6-3. The expected  $3\sigma$  Centaur injection guidance dispersions and the effective lunar radius are also shown. The midcourse capability contours are in the conventional R-S-T coordinate system.

The maneuver execution time of 16.2795 hours after injection was chosen. This time allowed 6 hours and 17 minutes of premidcourse and 1 hour and 11 minutes of postmidcourse visibility from the Goldstone tracking facility. Nominally, the midcourse time was 14.5295 hours after injection, but was delayed 1 hour and 45 minutes because of operational difficulties.

68189-2-181

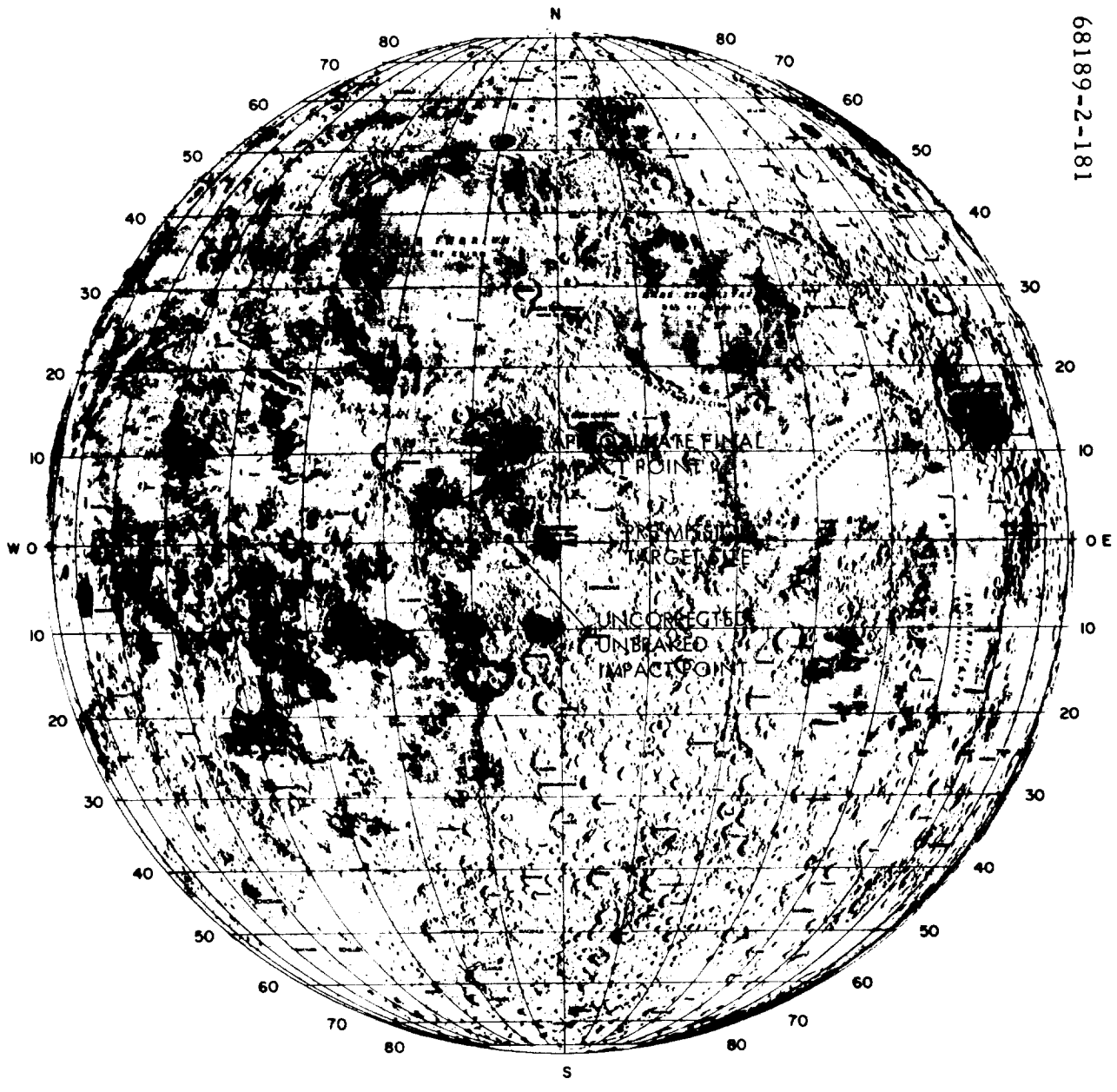


Figure 4.6-1. Surveyor II Target and Uncorrected Impact Points

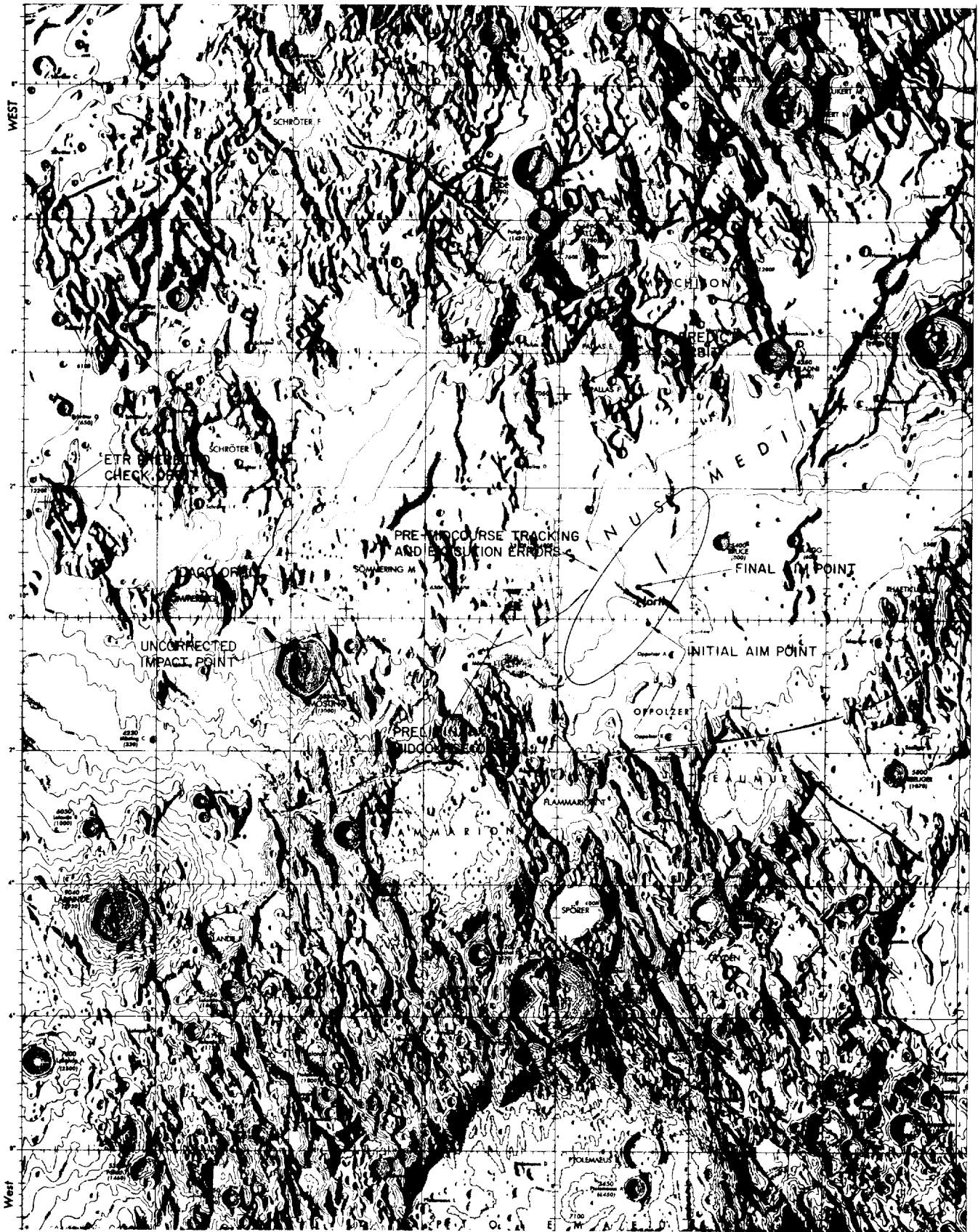


Figure 4.6-2. Surveyor II Impact Locations

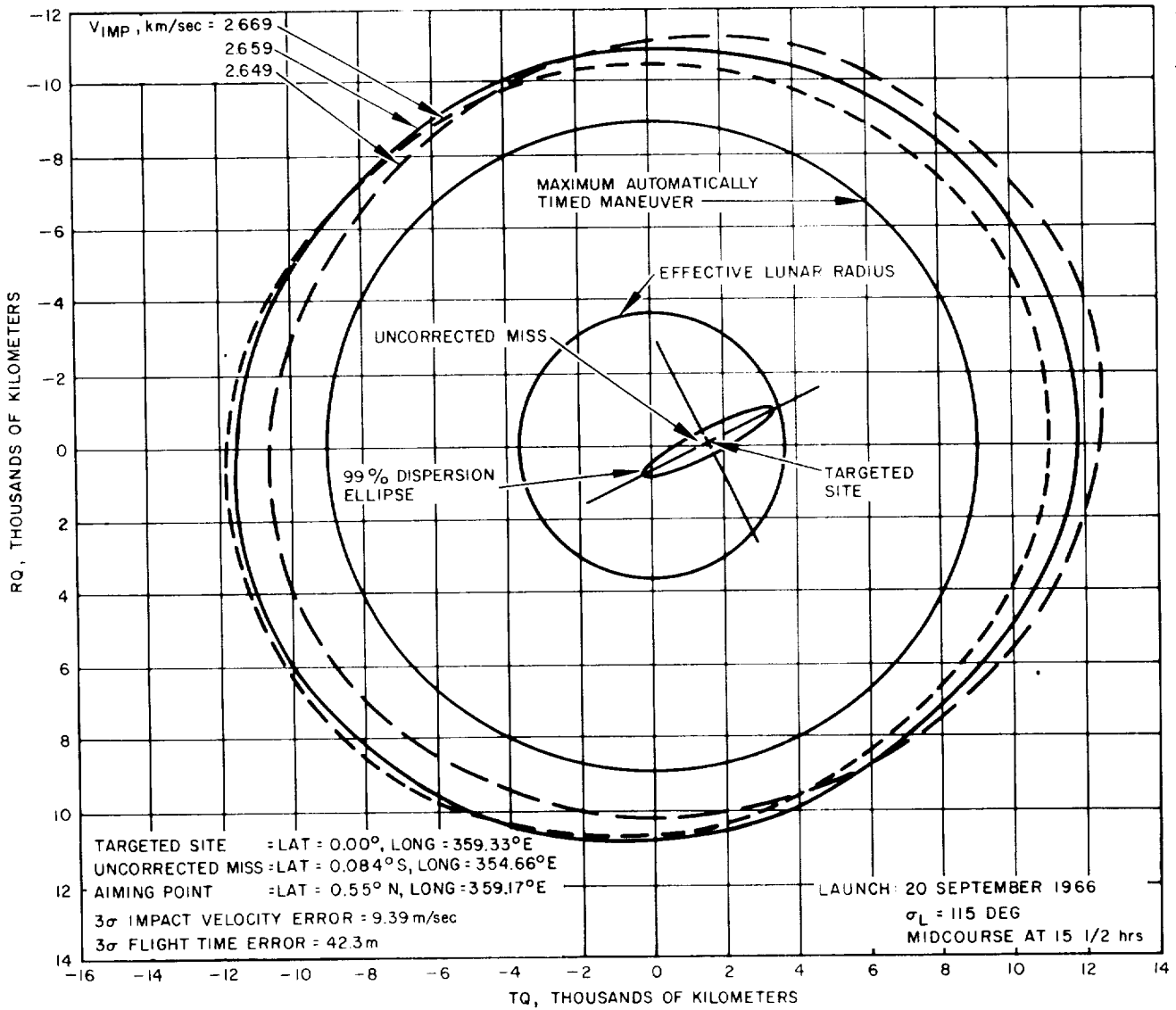


Figure 4.6-3. Midcourse Capability Contours



The predicted results of the selected midcourse correction and other alternatives considered are given in Table 4.6-1. The required velocity component in the critical plane, to correct miss only, was 1.185 m/sec. The noncritical direction component that resulted from a weighted selection of flight time, main retro burnout velocity, and vernier propulsion system fuel margin was 9.5 m/sec. Figure 4.6-4 shows the possible flight times, burnout velocities, and fuel margins for the range of available noncritical component velocity corrections. Since all three were acceptable over a wide range of values, a nominal burnout velocity of 450 fps was chosen. This gave favorable landing site errors and backup midcourse correction capability in the event the first midcourse correction became nonstandard. If the maneuver strategy were to correct miss plus flight time, the required noncritical component would have been 4.325 m/sec, giving a total of approximately 4.48 m/sec.

Since the aim point was changed during the flight, the above required correction does not properly evaluate the performance of the Centaur guidance system. Using the results of the last premidcourse orbit and correcting to the original aim point gives a miss only requirement of 1.015 m/sec. Miss plus flight time was 4.44 m/sec.

#### 4.6.1.1 Alternate Considerations

During the premidcourse phase, the following alternate possibilities were analyzed and eliminated:

- 1) No midcourse correction. This case would have resulted in acceptable burnout velocity, fuel margin, and arrival time values, but since a landing site of +0.55 degree latitude and 359.17 degrees longitude was desired, it was eliminated. The uncorrected site was -0.084 degree latitude and 354.66 degrees longitude (Figure 4.6-2).
- 2) Injection plus 14.5 hour corrections.
  - a) A minimum midcourse velocity correction of 2 m/sec was considered and eliminated because the nominal burnout velocity would have been higher than desired, or 505 fps,
  - b) Two midcourse velocity corrections that would have resulted in a burnout velocity of 400 fps were considered. The first one, at +15 m/sec, was eliminated because mission success could be achieved with the selected maneuver without requiring as large a correction. A smaller correction gives greater backup capability if the first correction presents problems. The second possibility, -33 m/sec, was eliminated because of significantly greater landing site errors and lower fuel margin.

TABLE 4.6-1. MIDCOURSE MANEUVER ALTERNATIVES

Item	Final Midcourse (16.5 Hour)	Alternate Considerations					
		No Midcourse	14.5 Hour	14.5 Hour	14.5 Hour	38.8 Hour	
Critical plane.m/sec	1.8		0.51	0.51	0.51	1.0	2.24
Noncritical direction, m/sec	9.50		2.0	15.0	-33.4	1.7	17.0
Total m/sec	9.59		2.1	15.0	33.4	2.0	17.2
Propellant, pounds	7.96		1.6	12.0	26:4	1.6	14.26
Impact speed, km/sec	2.658	2.663	2.662	2.654	2.681	2.662	2.656
Burnout velocity, fps	450	515	505	400	400	505	408
Fuel margin, pounds	30.5	31	31	31	33.4	31	30.
Arrival time, day 266, GMT	3:42	3:20	3:25	3:57	3:42	3:22	3:38
Visibility							
Prelanding	4H41M	4H19M	4H24M	4H56M	4H41M	4H21M	4H37M
Postlanding	3H25M	3H47M	3H42M	3H10M	3H25M	3H45M	3H29M
Landing errors							
SMAA (3σ), kilometers	53.9	20	20	33.5	63	5.5	16.3
SMIA, kilometers	17.7	5	5	27	55	3.7	15.6
Theta, degrees	-57	-56	-56	-55	-60	-46	-52

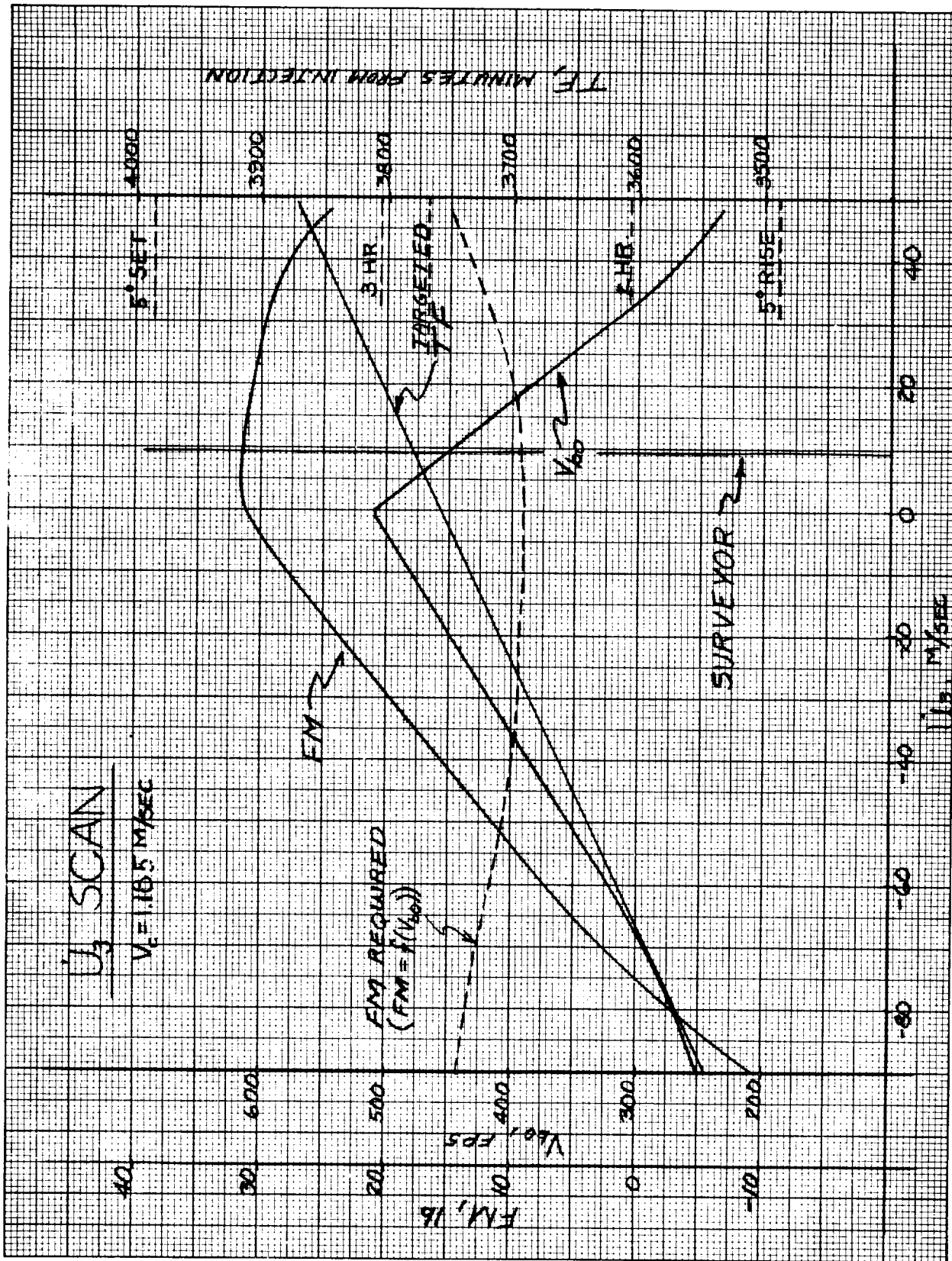


Figure 4.6-4. U<sub>3</sub> Ullage

- 3) Injection plus 38.8 hour corrections: Maneuvers similar to the 14.5 hours cases were considered and eliminated because a 14.5 hour correction was desired.

#### 4.6.1.2 Attitude Maneuver Considerations

Following computation of the magnitude and direction of the mid-course vector ( $\Delta V_{m/c}$ ), four pairs of spacecraft rotations and corresponding DSIF motions were calculated and the results compared with respect to pre-stored omnidirectional antenna patterns in the midcourse command program. Figure 4.6-5 shows the trace of the DSIF vector, in spacecraft coordinates, for each rotation pair. The figure shows that the cruise mode DSIF vector immediately prior to midcourse is located at  $\theta = 99.77$  degrees and  $\phi = -95.11$  degrees in spacecraft coordinates.

A negative roll of 14.67 degrees will increase  $\phi$  to -80.44 degrees, with  $\theta$  remaining constant. A subsequent pitch of -110.50 degrees will change the DSIF position to  $\theta = 148.30$  degrees and  $\phi = +71.85$  degrees. However, a positive roll maneuver of 75.33 degrees will decrease  $\phi$  to -170.44 degrees, and a following yaw will move the DSIF position to  $\theta = 148.30$  degrees and  $\phi = -18.15$  degrees. Two other alternate runs were pitch-yaw and yaw-pitch sequences  $\theta = 148.30$ ,  $\phi = 77.08$  and  $\theta = 148.30$ ,  $\phi = 108.62$  degrees, respectively.

As any one maneuver pair will correctly position the spacecraft prior to midcourse, the pair that maximizes probability of mission success through continuous, high antenna gain and maximum sun lock time is chosen. In as much as omnidirectional antenna B was oriented toward the DSIF in cruise mode, analysis of spacecraft rotations was directed toward constraining the DSIF to high gain regions of omnidirectional antenna B, thus avoiding antenna switching between or during rotations. As shown in Figure 4.6-5, the DSIF trace terminates in a low gain region for three of the four maneuver sequences (roll-pitch, pitch-yaw, and yaw-pitch). The obvious selection of roll-yaw was made because the antenna gain during and following the rotations remains high. Minor considerations contributing to this choice were: 1) sun lock is retained during the initial roll, and 2) the spacecraft had previously performed a yaw maneuver during sun acquisition and a roll maneuver during Canopus acquisition. The selected maneuvers were a roll of 75.33 degrees and a yaw of 110.50 degrees. The required engine burn time was 9.81 seconds.

The maneuver timing plan, as shown in Figure 4.6-6, illustrates the computation of various maneuver and ignition times. The earliest and latest allowable midcourse execution times bound the nominal execution time and are shown to be 10 minutes before and after the nominal time. The 10-minute values represent a tradeoff between operational times and required landing accuracy. Execution of engine burn time outside this 20-minute window would result in a considerable bias in terminal parameters.

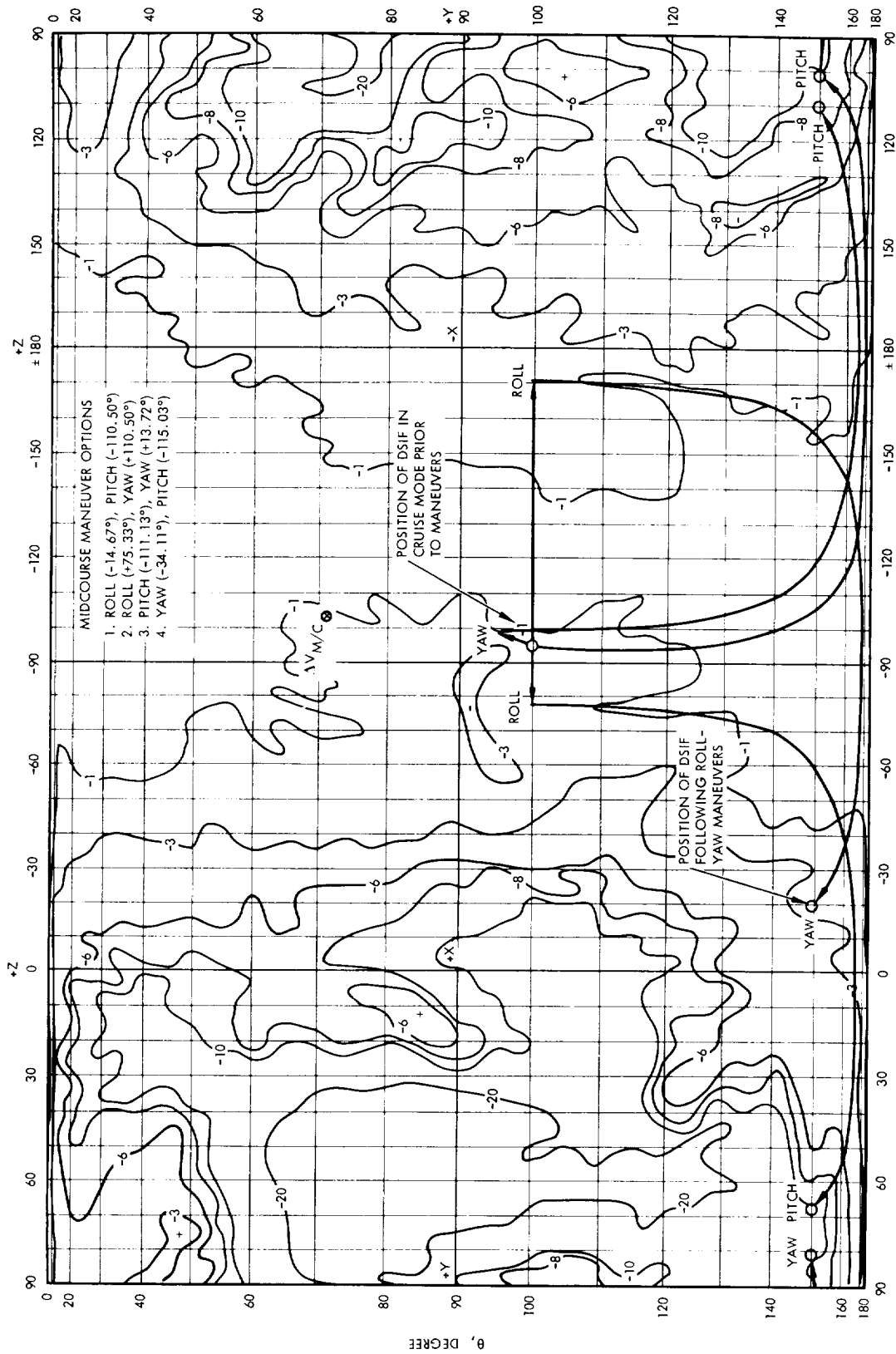
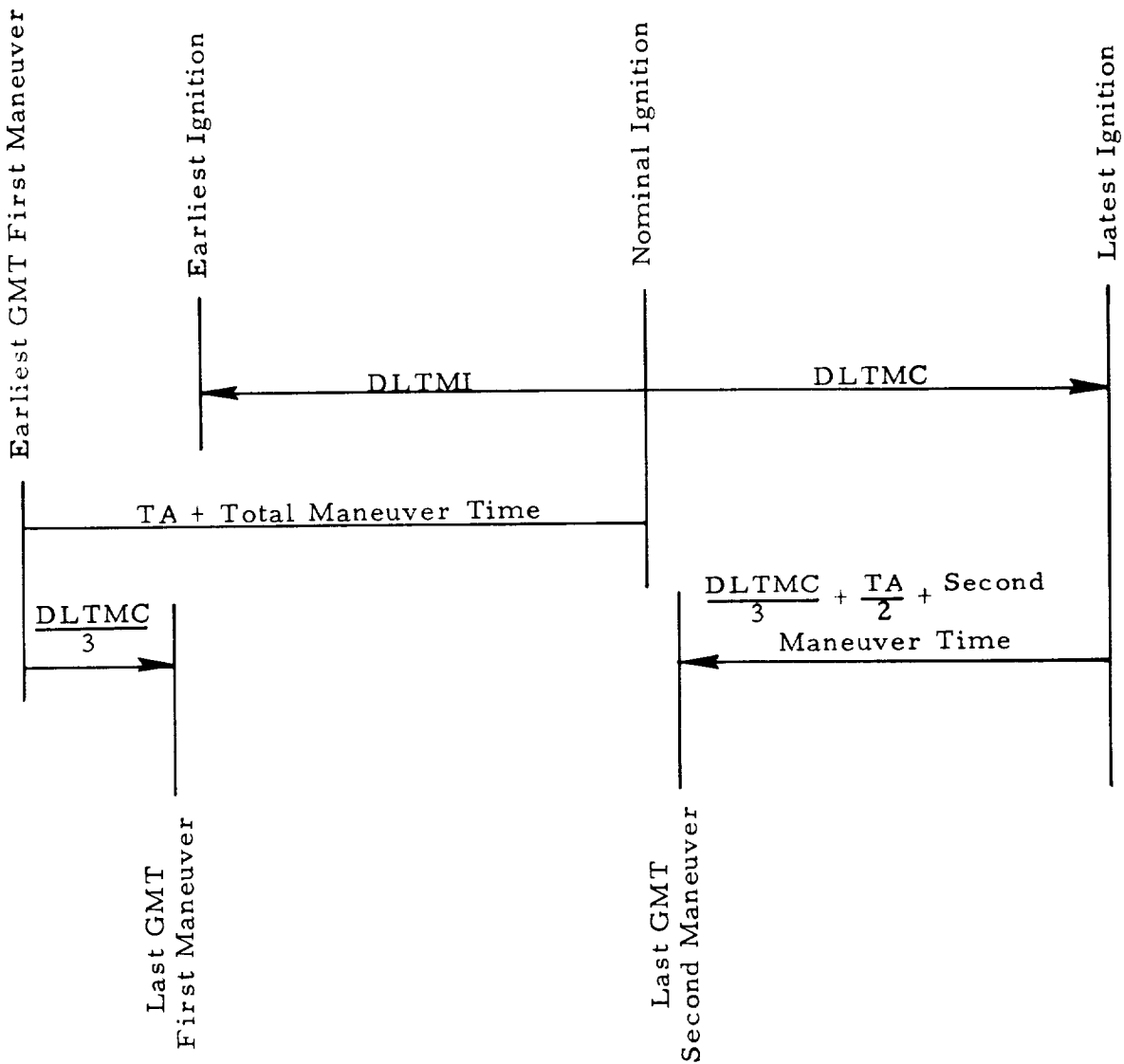


Figure 4.6-5. Omnidirectional Antenna B Downlink



For Surveyor 1:

- TA = 10 minutes
- DLTMI = 10 minutes
- DLTMC = 10 minutes
- First maneuver = 150.7 seconds
- Second maneuver = 221.0 seconds

Figure 4.6-6. Maneuver Timing Plan

It is notable that engine burn was begun within 1 second of the nominal ignition time. The earliest first maneuver (GMT) or earliest allowable break of sun lock is shown to be nominal ignition less total maneuver time, less TA (the operational time necessary to transmit and verify spacecraft commands). By previous agreement, a value of 10 minutes was used. The last times of the first and second maneuvers are computed based upon DLTMI, DLTMC, TA, and the maneuver times. These two times serve as guides to proper execution of spacecraft rotations.

The resulting midcourse message, as shown in Figure 4.6-7, contains the operational data necessary for properly executing the midcourse maneuver.

#### 4.6.2 SPACECRAFT PERFORMANCE

The midcourse correction sequence was initiated at L + 15H42M with the engineering interrogation, which indicated that the spacecraft was ready for midcourse operations. At L + 16H11M53S, the first attitude maneuver (plus roll of 75.3 degrees) was executed and confirmed as being satisfactory. At L + 16H16M5S, the second attitude maneuver (plus yaw of 110.5 degrees) was executed satisfactorily, thereby aligning the spacecraft in the desired direction for applying the midcourse thrust.

Following the pressurization of the vernier propulsion system (L + 16H21M) and the loading of the desired thrust time in the flight-control programmer magnitude register (L + 16H23M), thrusting of the vernier engines was commanded at L + 16H28M. At this time, vernier engine 3 strain gage indicated that this engine was not thrusting properly, and the gyro error signals became saturated (pitch error negative, yaw error positive, and roll error negative). After the previously commanded vernier engine thrust duration of 9.8 seconds, the engines shut off. However, DSIF receiver automatic gain control showed that the vehicle was rotating at a rate of approximately 1.22 rps, with a secondary motion having a period of approximately 12 seconds. In an attempt to stabilize the spacecraft, the flight control subsystem was commanded to the rate mode. Approximately 10 minutes later, when it became evident that the gas jets were not going to stop the spinning (since approximately 60 percent of the gas had been used, and the spin rate was still 0.97 rps), the gas jets were inhibited. The remaining gas supply was thus conserved for use in the event that the malfunction could be cleared and the vehicle stabilized by vernier engine firing.

```

LINK + 13 I/O MONITOR SFLOAD DATE 09 06 66
                                     MIDCOURSE COMMAND FORMAT
NOMINAL GMT OF IGNITION              JULIAN DATE 2439389.70833332 SEPT. 21, 1966 4 59 59.999
FIRST GMT OF IGNITION                JULIAN DATE 2439389.70138887 SEPT. 21, 1966 4 49 59.999
LAST GMT OF IGNITION                 JULIAN DATE 2439389.71527776 SEPT. 21, 1966 5 9 59.999
EARLIEST GMT OF FIRST MANEUVER       JULIAN DATE 2439389.69708718 SEPT. 21, 1966 4 43 48.333
MAGNITUDE OF FIRST MANEUVER          ROLL TURN 75.3309 DEG. ROLL TURN COMMAND TIME 150.6619 SEC.
MAGNITUDE OF SECOND MANEUVER         YAW TURN 110.5023 DEG. YAW TURN COMMAND TIME 221.0046 SEC.
MAGNITUDE OF DELTA-V +.95864819E-02 K/S. ENGINE BURN TIME 9.8065 SEC.
OMNIDIRECTIONAL ANT FIRST MANEUVER  B
OMNIDIRECTIONAL ANTESECOND MANEUVER B
LAST GMT OF FIRST MANEUVER           JULIAN DATE 2439389.69940199 SEPT. 21, 1966 4 47 8.332
LAST GMT OF SECOND MANEUVER         JULIAN DATE 2439389.70693281 SEPT. 21, 1966 4 57 58.994

MCCOM TRANSMISSION TO SPAC SUCCESSFUL
READ MCCOM INTERFACE
WRITE MCCOM INTERFACE

```

Figure 4.6-7. Midcourse Maneuver Message



## 4.7 DYNAMIC ANALYSIS OF SC-2 MIDCOURSE PHASE

### 4.7.1 INTRODUCTION

Because of the failure of vernier engine number 3 to provide proper thrust in response to thrust commands, the spacecraft could not maintain inertial attitude control when the remaining two vernier engines ignited at the start of midcourse (Figure 4.7-1). The thrust commands to the vernier engines were a combination of two effects: the acceleration loop trying to develop the proper acceleration along the spacecraft roll axis and the attitude control loops trying to maintain the vehicle in a stable inertial attitude. An analysis of resultant spacecraft motion was performed in order to assist in determining the cause of failure. One major question to be settled was whether engines 1 and 2 responded normally to their thrust commands.

In order to analyze the spacecraft motion, analog and digital simulations were used to generate outputs that were compared to flight data. For the final analysis, a closed-loop analog computer combined with flight hardware was used to verify that thrust commands from flight control to the vernier engines were proper. A digital simulation was used to determine spacecraft motion resulting from selected vernier engine thrust profiles. The analog system, incorporating flight hardware, properly simulated the saturation characteristics of the control loops which significantly affect thrust command generation under these nonstandard conditions. The digital simulation developed the required accuracy and flexibility of output required for comparison with flight data.

The data used to verify the results of the simulations fall into three categories: gyro initial response and crossover data, sun sensor illumination signals, and DSIF station automatic gain control data reflecting spacecraft omnidirectional antenna gain variations. Each of these will be analyzed separately in one of the following subsections. A great deal of interplay occurred between these various techniques before finally arriving at a description of spacecraft motion which was reasonably consistent for all. In Figure 4.7-2, sun and earth vector positions at the start of midcourse are shown in spacecraft coordinates as an introduction to the dynamic analyses that will follow.

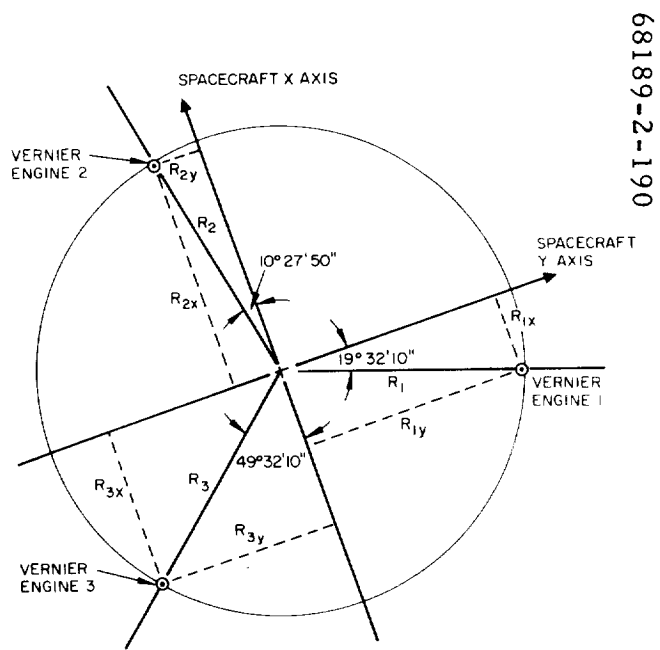


Figure 4.7-1. Orientation of Vernier Engines in Spacecraft Coordinates

68189-2-191

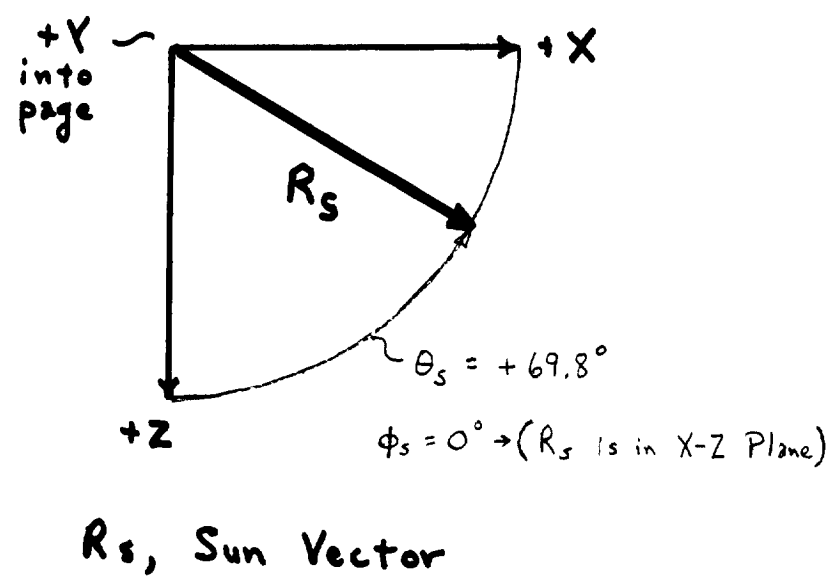
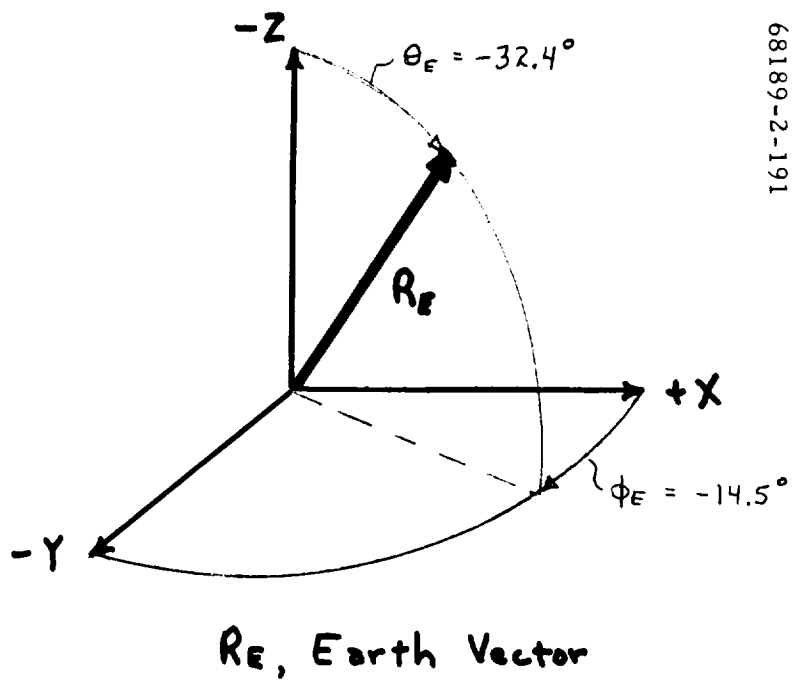


Figure 4.7-2. Sun and Earth Vectors and Midcourse Ignition

#### 4.7.2 CONCLUSION

The closed-loop analog simulation generated thrust commands in the form of pitch and yaw gyro error signals which agree favorably with the initial transients observed on flight telemetry. Conditions for the simulation were normal thrust for engines 1 and 2, and zero thrust for engine 3. Based on these results, it was concluded that the flight control was providing the proper thrust commands to the vernier engines for this period.

The digital computer dynamic simulation was used to evaluate vernier engine performance during the attempted maneuver. When near equal percentages of commanded thrust were used as inputs to the simulation, the outputs provided a good match to the sun sensor and telemetry automatic gain control flight data for selected levels near 100 percent. One of the best fits was obtained with the case of 100 percent thrust for engines 1 and 2 and a constant 2-pound level for engine 3. Since the thrust from engine 3 generates near equal moments about the pitch and yaw axes, while thrust from engines 1 and 2 essentially produce moments only about pitch and yaw, respectively, equivalent results can be obtained by increasing or decreasing thrust levels for engines 1 and 2 in proper proportion to values selected for engine 3 (97 percent levels on engines 1 and 2 with no thrust on engine 3 produces nearly identical results to the case discussed above).

The above cases do not provide a good match to the pitch and yaw gyro telemetry output angles for the first second of the period. In order to approximate the flight data, it was necessary to select percentage thrust levels for engines 1 and 2 in a ratio of near 1.2 or delay the equivalent of engine 2 ignition approximately 40 milliseconds after engine 1 ignition. Since ratios of one or slightly less than one provide a better match for the sun and automatic gain control data and since delays of the above magnitude produce insignificant effects on these results, it is considered more likely that engine 2 ignition occurred later than engine 1, producing a slower angle increase in yaw as compared with pitch.

Using the standard moment of inertia matrix values (see Table 4.7-1) from mass properties calculations, and the cases that tend to match the sun sensor, automatic gain control or initial gyro response data, the pitch gyro crossover (produced by a reversal in pitch angular velocity direction) obtained during the 20-second simulation, does not compare with the two crossovers occurring in the flight data. Also, the simulated crossover of the yaw gyro occurs over one-half second early, and the time between crossovers is more than 2 seconds less than that observed in flight. Simulations in which the initial values of the moment of inertia matrix elements were varied from the standard values yielded improved fit to the gyro flight data; however, a close match was not obtained. Simulation results indicated that by varying thrust levels and the moment of inertia matrix element values it would be possible to obtain a close fit to the gyro crossover, sun sensor, and automatic gain control data; it is not known if such a set of conditions would be unique. However, results of the simulations match flight data closely enough to strongly indicate that engines 1 and 2 were responding to thrust commands in a near normal manner.

TABLE 4. 7-1 STANDARD MOMENT OF INERTIAL MATRIX

$\begin{bmatrix} 208.86 & -7.24 & 7.71 \\ -7.24 & 204.99 & -1.87 \\ 7.71 & -1.87 & 216.17 \end{bmatrix}$					
$I_{xx}$	$I_{yy}$	$I_{zz}$	$I_{xy}$	$I_{yz}$	$I_{xz}$
208.86	204.99	216.17	-7.24	-1.87	7.71

A comparison of the thrust command and strain gage flight data during the first second reveals very close agreement in profile shape between these two curves for engines 1 and 2 (see Figures 4. 7-3 and 4. 7-4). This agreement is probably the strongest evidence that engines 1 and 2 were operating normally. The comparison for later times rapidly becomes invalid because of the sensitivity of the vernier engine mounting brackets to thermal effects and forces resulting from the spacecraft motion.

Vernier engine thrust duration varied in the simulation runs, and the effect on the simulation results was found to be negligible for the burn time limits of 9. 75 to 9. 85 seconds as determined from telemetry data.

#### 4. 7. 3 COMPUTER SIMULATION

In order to simulate spacecraft spin-up during the attempted mid-course maneuver, the existing six-degree-of-freedom simulation (previously used for terminal descent analysis) was modified and a new digital spin simulation was developed. The six-degree program was available first and produced some initial results; however, the spin program was used to generate the data for this report because of its greater accuracy and flexibility.

A block diagram of the digital spin simulation program is given in Figure 4. 7-5. This program calculates spacecraft motion resulting from thrusts applied at the individual vernier engine locations. By use of the direction cosine matrix relating spacecraft and inertial axes, the motion of the sun and earth vectors in spacecraft coordinates is calculated. The earth vector motion is applied to an antenna gain map representation, generating antenna gain as a function of time for comparison with telemetry automatic gain control. From integration of spacecraft angular rates with limiting to simulate gyro stops, the gyro output profile is obtained for comparison with the flight gyro crossover data. This signal is not corrected for delay introduced by the telemetry filter circuit which is negligible at the crossover times of interest. A simulated gyro output during the first second of the midcourse burn was generated by modifying the calculated spacecraft angles with the gyro telemetry transfer function (a simple lag with a 57 millisecond time constant). This time constant produced a significant effect on the simulated gyro output, when compared with the initial gyro response.

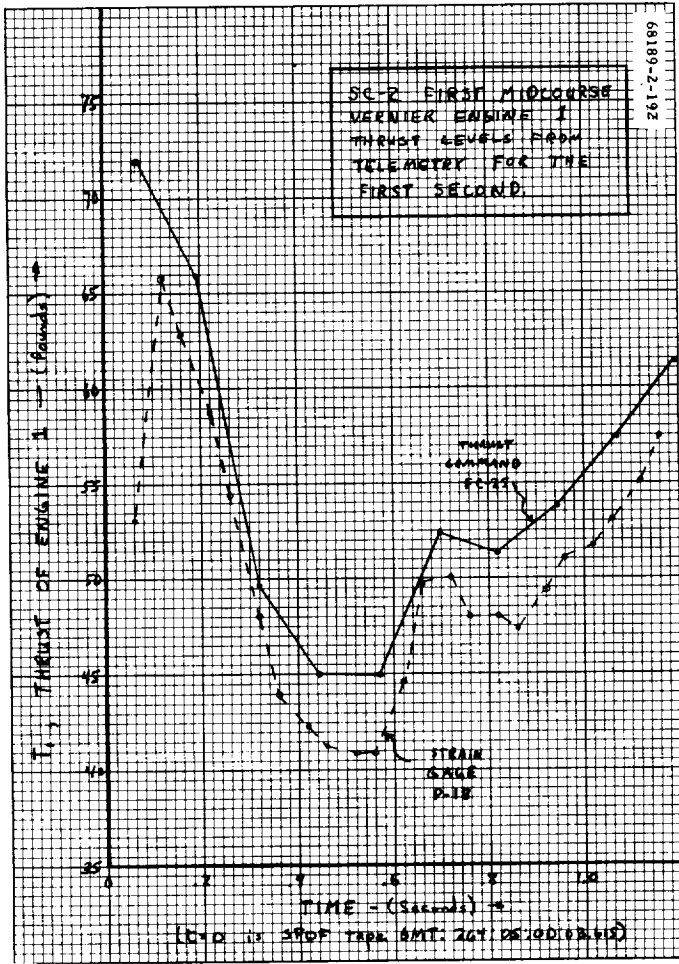


Figure 4.7-3. Vernier Engine 1 Midcourse Thrust Levels for First Second

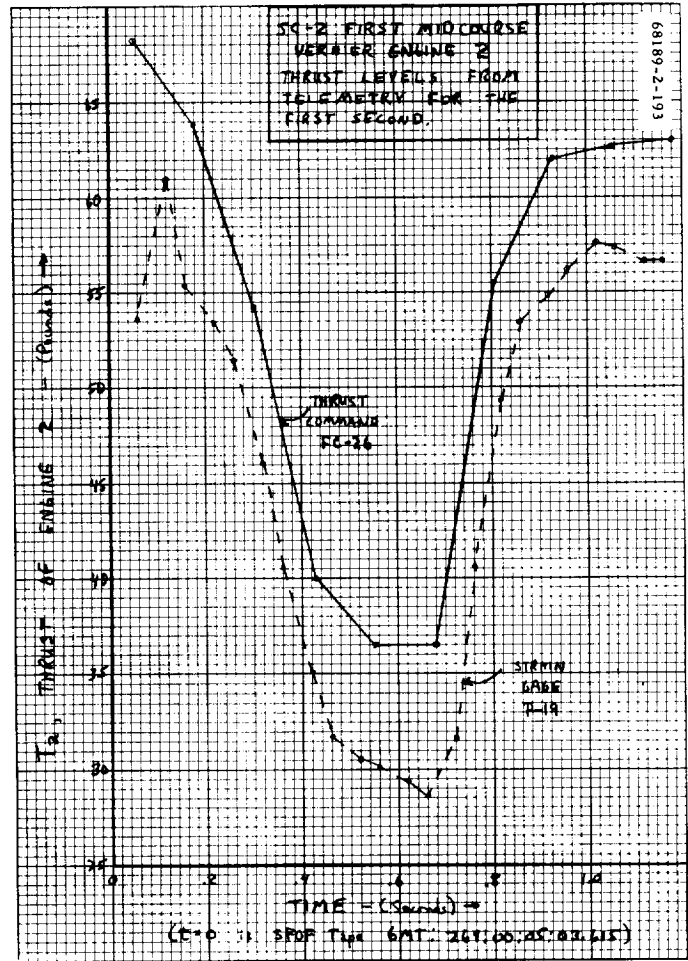


Figure 4.7-4. Vernier Engine 2 Midcourse Thrust Levels for First Second

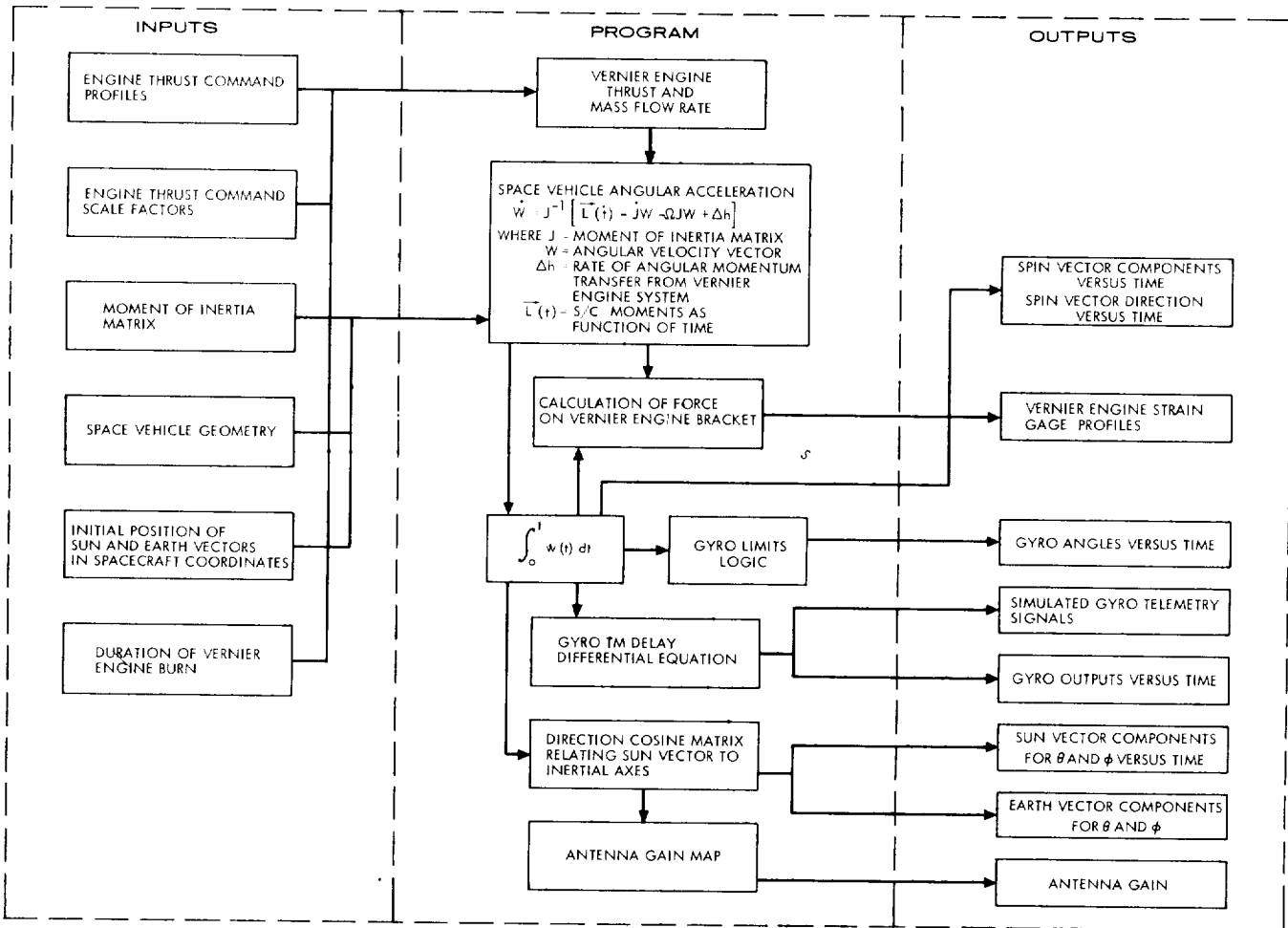


Figure 4.7-5. Digital Simulation

Spacecraft angular motion is calculated with respect to the vehicle center of gravity. The initial values of the spacecraft moment of inertia matrix are input to the program. The thrust level of each engine is divided by the appropriate value of specific impulse, and the calculated change in mass in the propellant tanks is used to update the moment of inertia matrix. For the case of normal thrust on engines 1 and 2, and 2 pounds thrust on engine 3, the percentage change in the moment of inertia matrix elements for the 9.8-second midcourse thrust period are  $I_{xx} = -0.25$  percent,  $I_{yy} = -0.14$  percent,  $I_{zz} = -0.33$  percent,  $I_{xy} = 1.77$  percent,  $I_{xz} = 0.98$  percent, and  $I_{yz} = -2.57$  percent.

An analytical model was developed to calculate the force on the vernier engine brackets as a function of vernier engine thrust, angular rate, angular acceleration, linear acceleration, and engine burn time. This model was developed from tests performed on flight engine brackets. The torsional effects introduced by the engine center of gravity displacement from the bracket centerline were not included in the model as measurements of these reactions have not been made. Because of gross disagreement between the initial computer-developed strain gage outputs and the flight data (probably caused by lack of a torsional effect model), no attempt was made to obtain better comparison by varying engine thrust levels.

#### 4.7.4 COMPUTER SIMULATION INPUT

The thrust level functions for engines 1 and 2 input to the computer simulation were obtained from telemetry and corrected as per the SC-1 procedure (Reference 2). The thrust profiles used are given in Table 4.7-2. FC-26 first indicated an abnormal thrust value at 05:00:03.669 (SFOF data timing), and this has been used as the reference time in Table 4.7-2. The 15-millisecond delay between telemetry samples of FC-25 and FC-26 has been ignored to simplify the simulation. A selected constant value of thrust was used for engine 3 (FC-27).

To determine if the engines were producing the commanded thrust, computer runs were made with the above thrust level functions multiplied by a scale factor. The code adopted to identify the individual cases is  $[a, b]c$  where  $a$  and  $b$  are the thrust factor multipliers on engines 1 and 2, respectively, and  $c$  is the constant value of thrust (in pounds) for engine 3.

Strain gage data were not used to develop thrust input for the simulation, since a review of SC-1 data indicated that these data were not as reliable for this purpose as thrust command telemetry (Figures 4.7-6, 4.7-7, and 4.7-8). In addition, use of strain gage data was also undesirable because of susceptibility to vehicle motion effects.

Moment of inertia values for the standard moment matrix were obtained from Reference 1. Reference 3 supplied the product of inertia values. The signs of the XZ and YZ product of inertia values had to be reversed since they were for a left-handed coordinate system with the positive Z axis in the opposite direction to the engine exhaust, while the simulation uses a



TABLE 4.7-2. THRUST COMMAND TELEMETRY AT MIDCOURSE

Reference time = 05:00:03.669

Time, seconds	T <sub>1</sub> Vernier Engine 1 (FC-25), pounds	T <sub>2</sub> Vernier Engine 2 (FC-26), pounds	Time, seconds	T <sub>1</sub> Vernier Engine 1 (FC-25), pounds	T <sub>2</sub> Vernier Engine 2 (FC-26), pounds
0	72.0	68.2	5.000	75.7	62.7
0.125	65.9	63.8	5.125	75.7	62.7
0.250	49.6	54.2	5.250	76.1	62.7
0.375	45.0	40.0	5.375	76.4	62.7
0.500	44.9	36.5	5.500	76.4	62.3
0.625	52.4	36.5	5.625	76.8	62.3
0.750	51.3	55.5	5.750	76.8	62.0
0.875	53.8	62.0	5.875	77.2	62.0
1.000	57.4	62.7	6.000	77.2	62.0
1.125	61.3	63.0	6.125	77.2	62.0
1.250	63.6	64.0	6.250	77.2	62.0
1.375	64.0	66.1	6.375	77.6	62.0
1.500	64.4	67.8	6.500	77.6	62.0
1.625	64.8	68.5	6.625	77.6	62.0
1.750	65.6	68.9	6.750	77.6	62.0
1.875	66.7	68.9	6.875	77.9	62.0
2.000	68.2	68.9	7.000	77.9	61.6
2.125	69.4	68.2	7.125	77.9	61.6
2.250	69.4	68.2	7.250	77.9	61.6
2.375	69.7	68.2	7.375	77.9	62.0
2.500	69.7	67.4	7.500	77.9	61.6
2.625	70.1	67.4	7.625	78.1	61.6
2.750	70.5	67.1	7.750	78.1	62.0
2.875	70.5	66.9	7.875	78.3	62.0
3.000	71.3	66.4	8.000	78.3	61.6
3.125	71.6	66.1	8.125	78.3	62.0
3.250	72.0	65.7	8.250	78.3	61.6
3.375	72.4	65.4	8.375	78.3	62.0
3.500	72.8	65.0	8.500	78.3	62.0
3.625	73.1	65.0	8.625	78.7	62.0
3.750	73.5	64.7	8.750	78.7	62.0
3.875	73.9	64.3	8.875	78.7	62.0
4.000	73.9	64.3	9.000	78.7	62.0
4.125	74.3	64.0	9.125	78.7	62.0
4.250	74.7	63.6	9.250	78.7	62.0
4.375	75.0	63.3	9.375	78.7	62.0
4.500	75.0	63.3	9.500	78.7	62.0
4.625	75.4	63.3	9.625	78.7	62.0
4.750	75.4	63.3	9.750	77.6	77.9
4.875	75.7	63.0	9.875	0	0

right-handed coordinate system with positive Z in the direction of engine exhaust. Percentage perturbations of the initial moment values were made with the simulation in an attempt to match the gyro crossover data, and these cases are identified in abbreviated form as follows:

$$\left[ \Delta I_{xx}, \Delta I_{yy}, \Delta I_{zz}, \Delta I_{xy}, \Delta I_{xz}, \Delta I_{yz} \right]$$

#### 4.7.5 SIMULATION OF SUN SENSOR DATA

Throughout this subsection, inertial vector directions in spacecraft coordinates will be specified using a clock angle  $\phi$  and a cone angle  $\theta$ , as defined in Figure 4.7-9.

From Figures 4.7-10 through 4.7-13, it is apparent that all acquisition cells of the secondary sun sensor were illuminated seven distinct times during the commanded 9.8-second midcourse burn. An individual cell is considered to have been illuminated if it produced at least 2.0 volts out of an approximate 4.0-volt maximum. If the sun is located in a given cell's quadrant, it is actually possible for that cell to be fully illuminated while the sun is slightly below the plane of the solar panel. Reference 4 specifies the depression angle of the secondary sun sensor for four sun clock angles. In order to obtain approximations of the depression angle at other than the specified clock angles, a third order polynomial was fitted to the four specified data points. The resulting function yielded the depression angle as a function of distance from the secondary sun sensor to the edge of the solar panel. Measuring these distances for other clock angles then permitted construction of an approximate depression function over the entire range of clock angles. The function obtained is plotted in Figure 4.7-14.

The first premidcourse attitude maneuver was a 75.3-degree roll which did not affect the spacecraft/sun vector direction since the motion was around the roll axis. The second maneuver was a 110.5-degree yaw which moved the spacecraft/sun vector to a position in the XZ plane 20.5 degrees from the X axis in the direction of the Z axis. Since the sun vector was in this position at vernier engine ignition, the sun sensors were not illuminated by the sun.

As a result of spacecraft angular motion due to the unbalanced moments produced by the vernier propulsion system, the cells were first illuminated 2.55 seconds after vernier engine ignition, followed by cycles of darkness and illumination as the spacecraft revolved. The illumination periods varied from 1.13 seconds following ignition to 0.25 second at engine cutoff since the spacecraft experienced continuous angular acceleration during the burn interval. At the end of this interval, the attitude of the vehicle was such that illumination did not occur for five revolutions of the spacecraft.

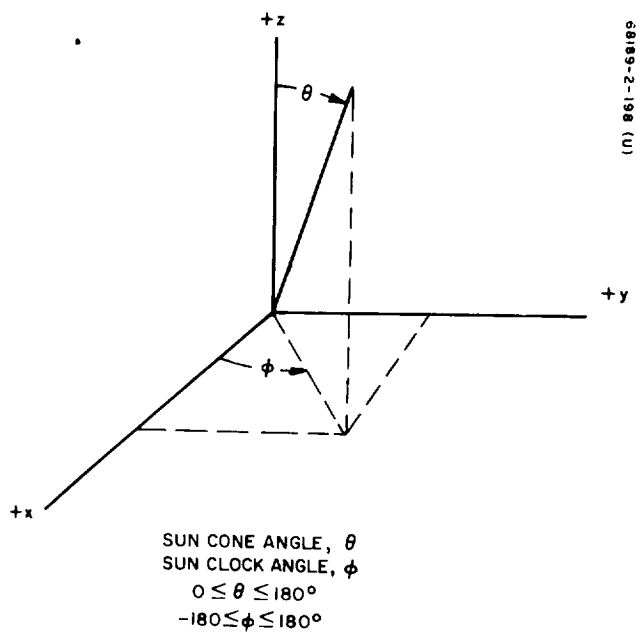


Figure 4.7-9. Definition of Sun Clock and Cone Angles

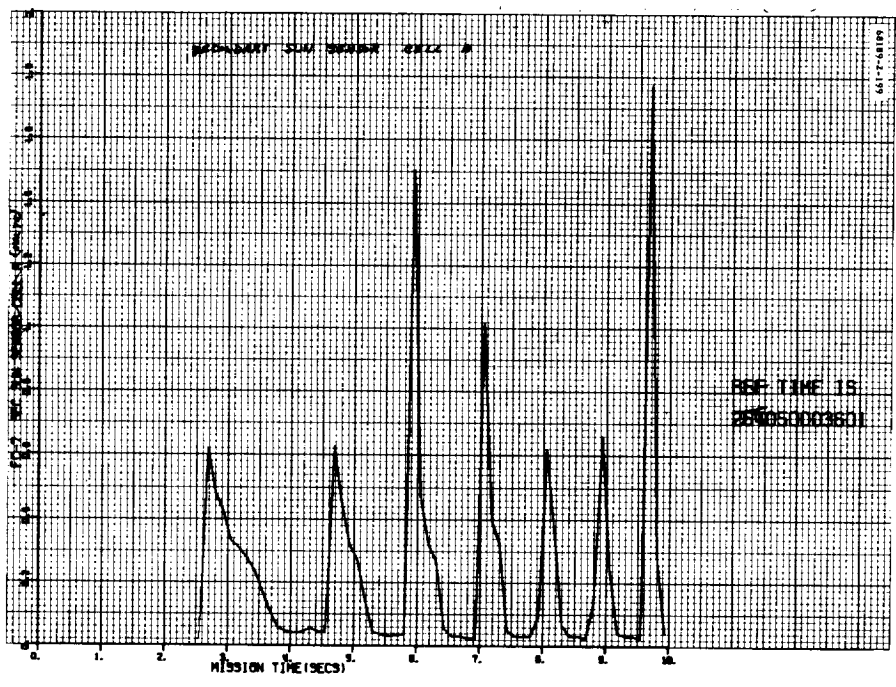


Figure 4.7-10. Secondary Sun Sensor Cell A

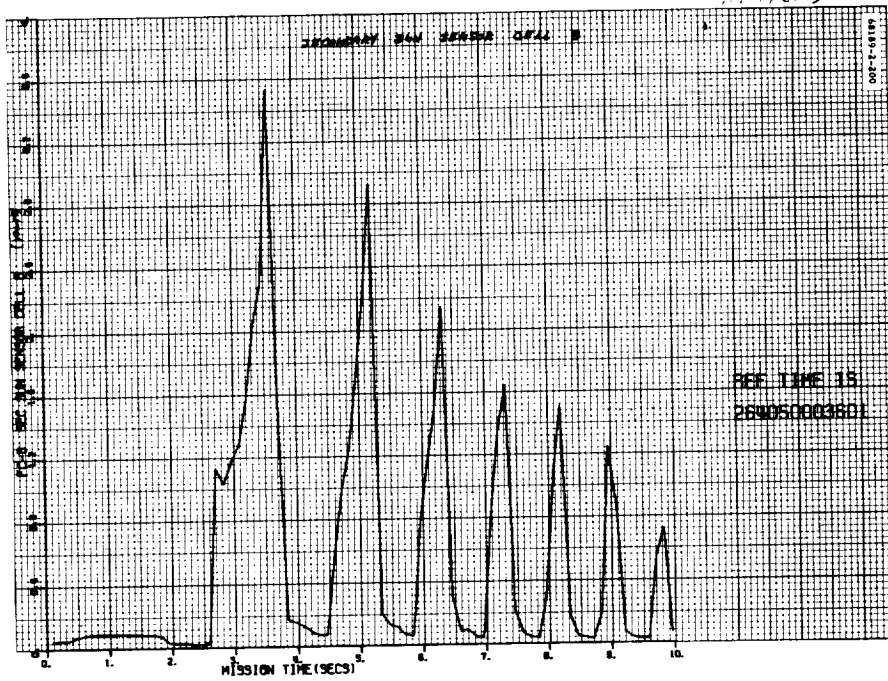


Figure 4.7-11. Secondary Sun Sensor Cell B

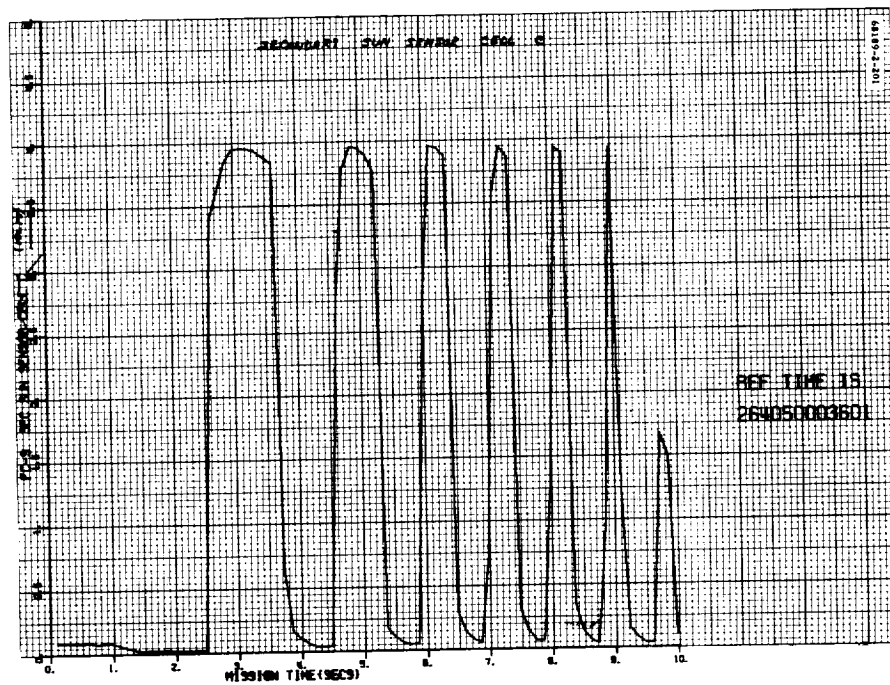


Figure 4.7-12. Secondary Sun Sensor Cell C

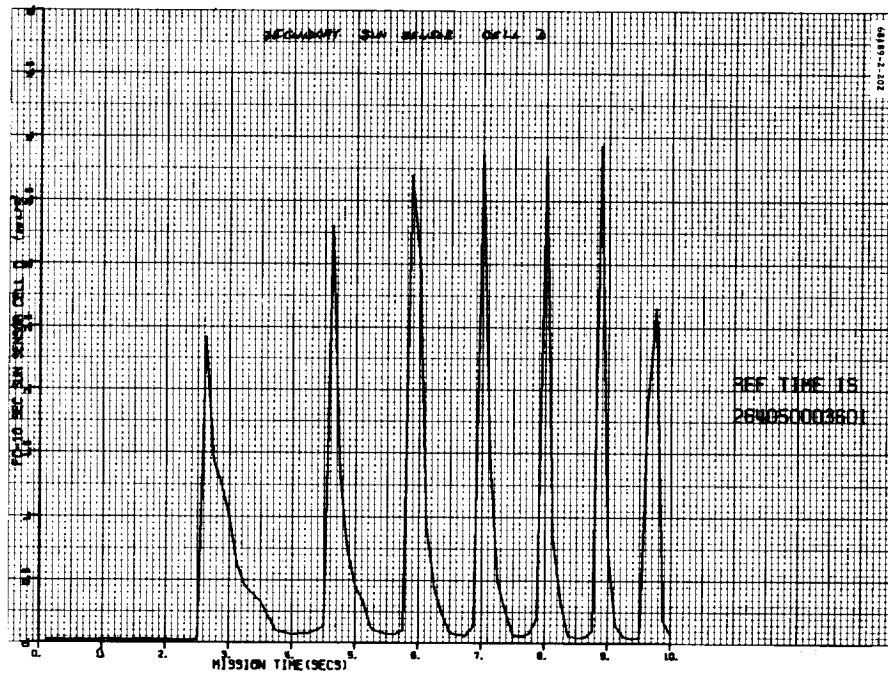


Figure 4.7-13. Secondary Sun Sensor Cell D

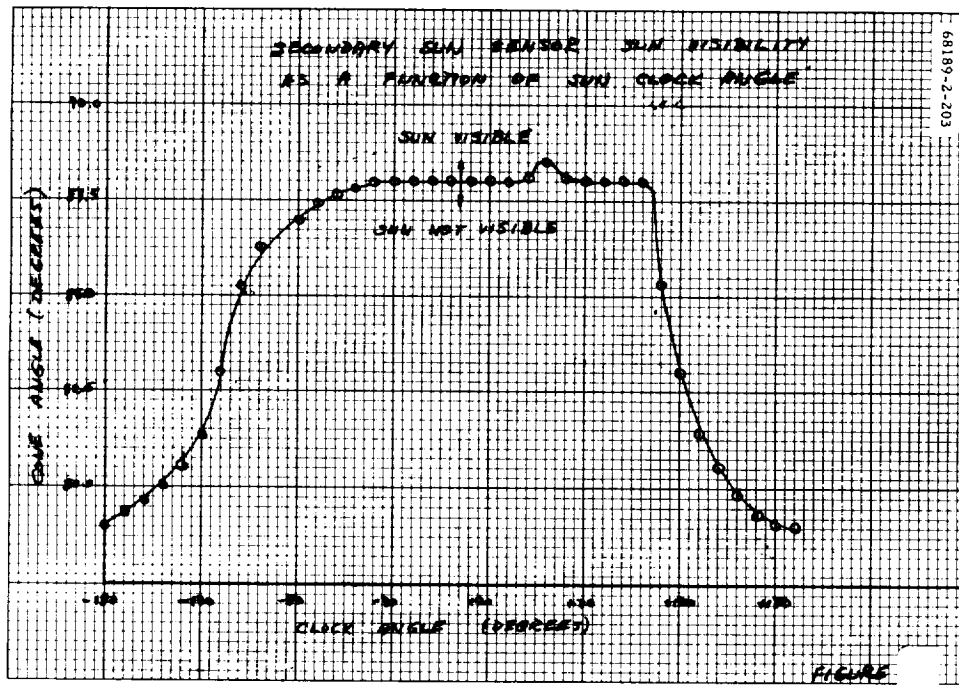


Figure 4.7-14. Secondary Sun Sensor Sun Visibility as Function of Sun Clock Angle

To match computer outputs to secondary sun sensor flight telemetry, emphasis was placed on comparative characteristics at transition times when the sun was passing into or out of sensor view. The primary characteristics examined at these times included spin periods, precession periods, and sun clock angles. These particular times were used since they provided the most accurate determination of sun position at specific instants. At all other times, especially when the sun is within 20 degrees of the spacecraft -Z axis, the position of the sun vector cannot be accurately determined.

From sun sensor telemetry data, the cone and clock angles at the transition times were plotted in Figures 4.7-15 and 4.7-16. In addition, the transition points from the computer simulation of five thrust configurations are also plotted for comparison. These cases were selected for more detailed study from the results of more than 30 runs made with the spin simulation program. A standard initial moment of inertia matrix was input. The effects of changing the initial moment of inertia matrix values to fit the gyro crossover data is indicated in the figures of subsection 4.7.7. Figure 4.7-16 indicates that the best frequency and phase agreements are obtained with the  $[1, 1]_2$  and the  $[1, 0.9]_0$  cases. Of these two cases, only the  $[1, 1]_2$  case provides good agreement with the clock angles at transition for the first revolutions, as indicated in Figure 4.7-15. The computer generated cone and clock angles, as a function of time for this best fit case, are plotted in Figures 4.7-17 and 4.7-18.

To determine whether solar panel deflection would affect the above results, equations relating solar panel deflection and spacecraft motion were developed from spacecraft geometry and data from the flexible response computer program. These equations were added to the spin simulation program, but the maximum deflection obtained was less than 0.1 degree, indicating that deflection of the panel would not materially affect the simulation results.

#### 4.7.6 SIMULATION OF AUTOMATIC GAIN CONTROL DATA

The purpose of this study was to help verify assumed thrust level profiles in the 20 seconds after the start of midcourse by comparing simulated and flight automatic gain control data. The technique employed used downlink signal power received at the Goldstone DSIF station (i.e., receiver automatic gain control data;\* see Figures 4.7-19 and 4.7-20)

---

\*Oscillographs of automatic gain control data were made in nonreal time by JPL from DSIF magnetic tapes.

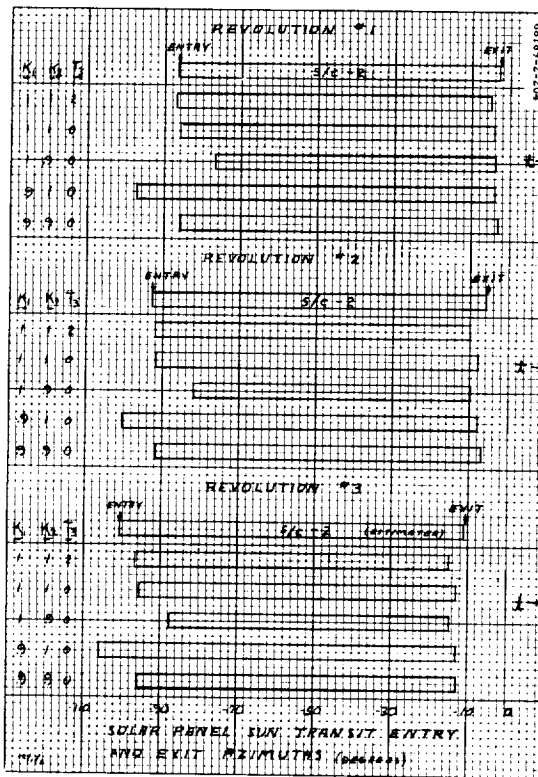


Figure 4.7-15. Solar Panel Sun Transit Entry and Exist Azimuths

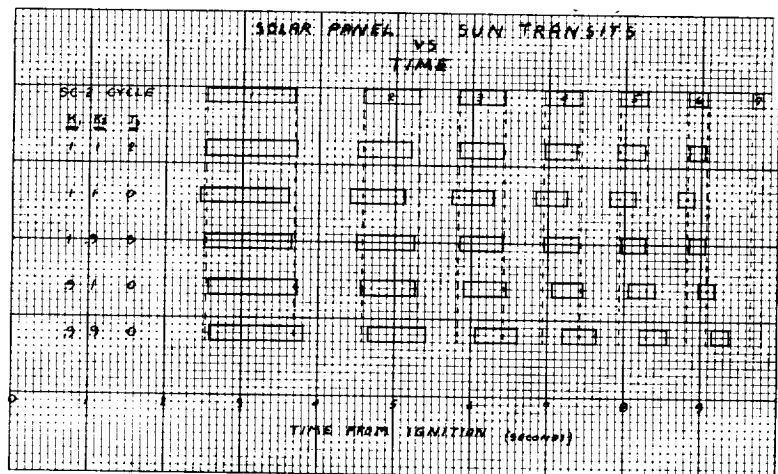


Figure 4.7-16. Solar Panel Sun Transits Versus Time

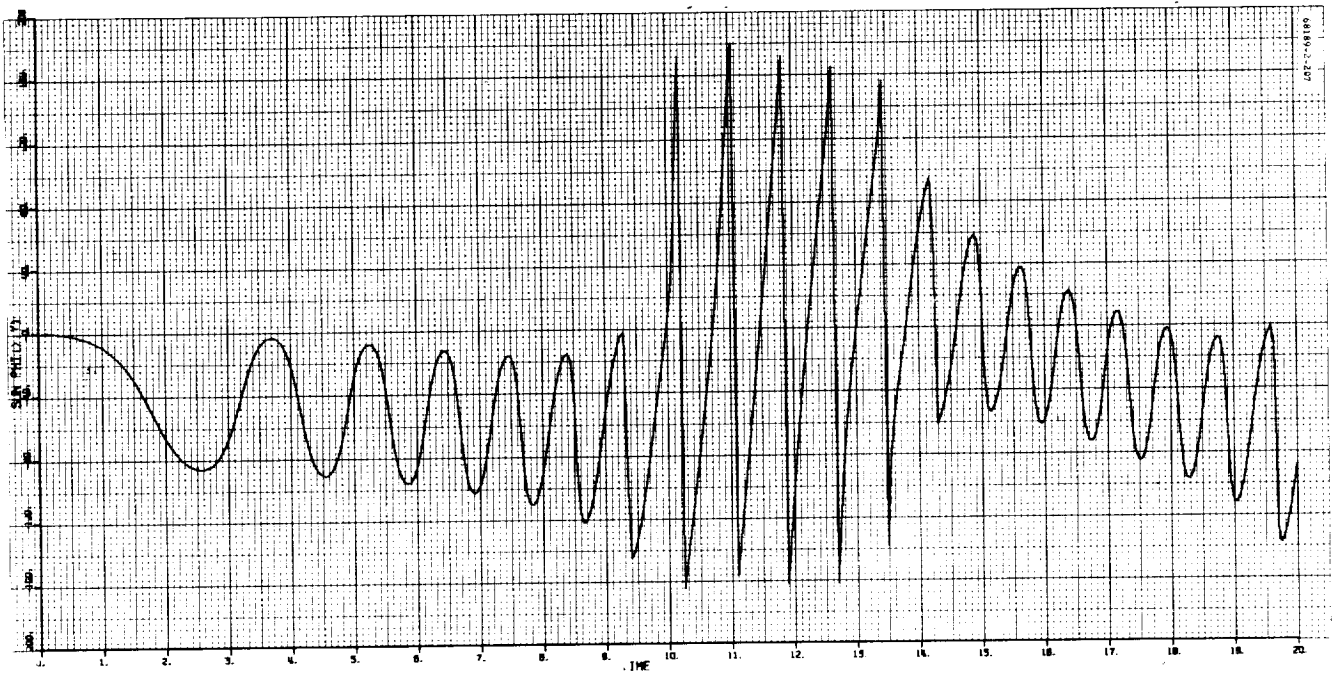


Figure 4.7-17. Sun Clock Angle for (1,1)2 Thrust Condition

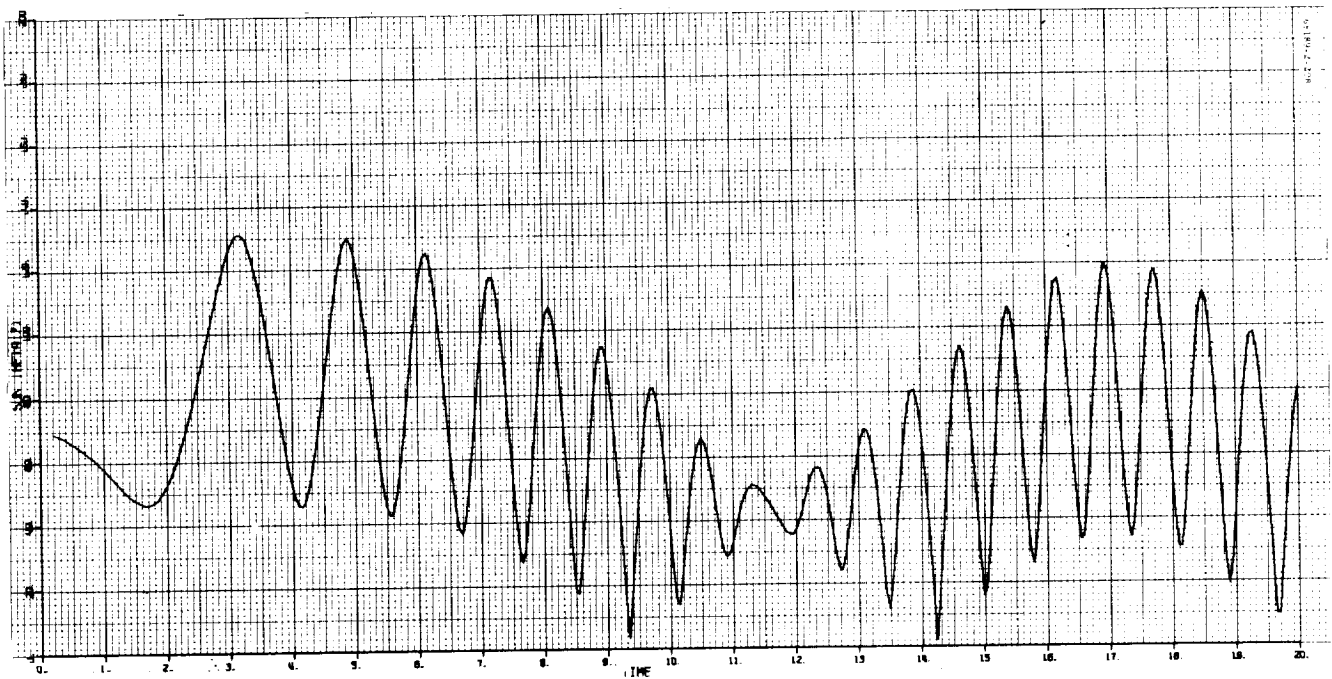


Figure 4.7-18. Sun Clock Angle for (1,1)2 Thrust Condition



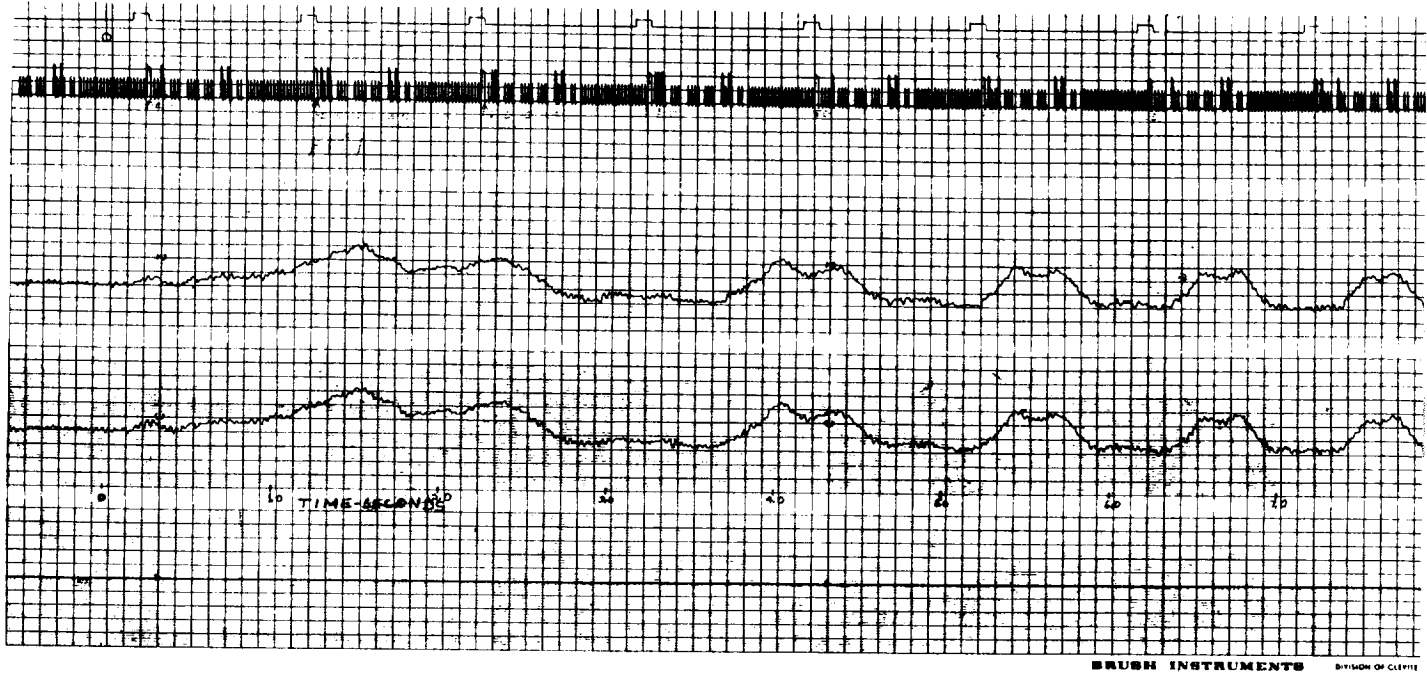


Figure 4.7-19. DSIF Receiver Automatic Gain Control Signal  
(High Magnification)

Reference time: 264:05:00:03.750

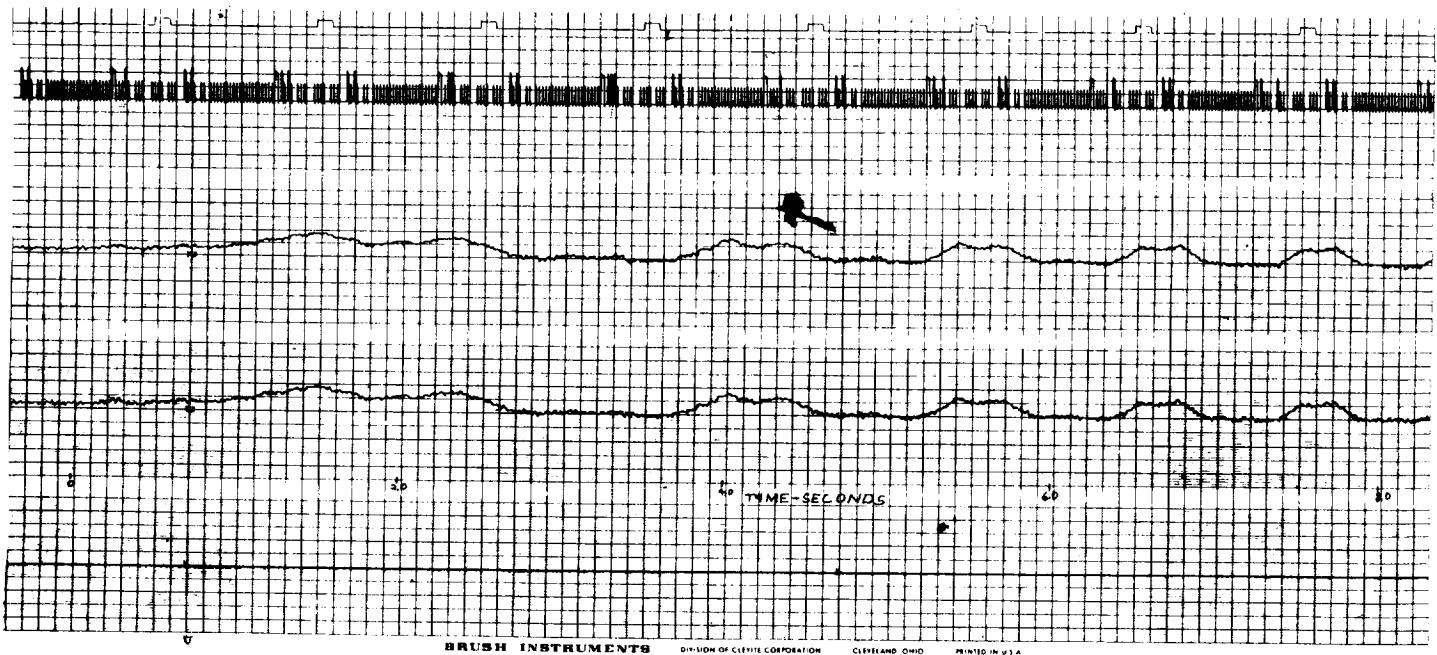


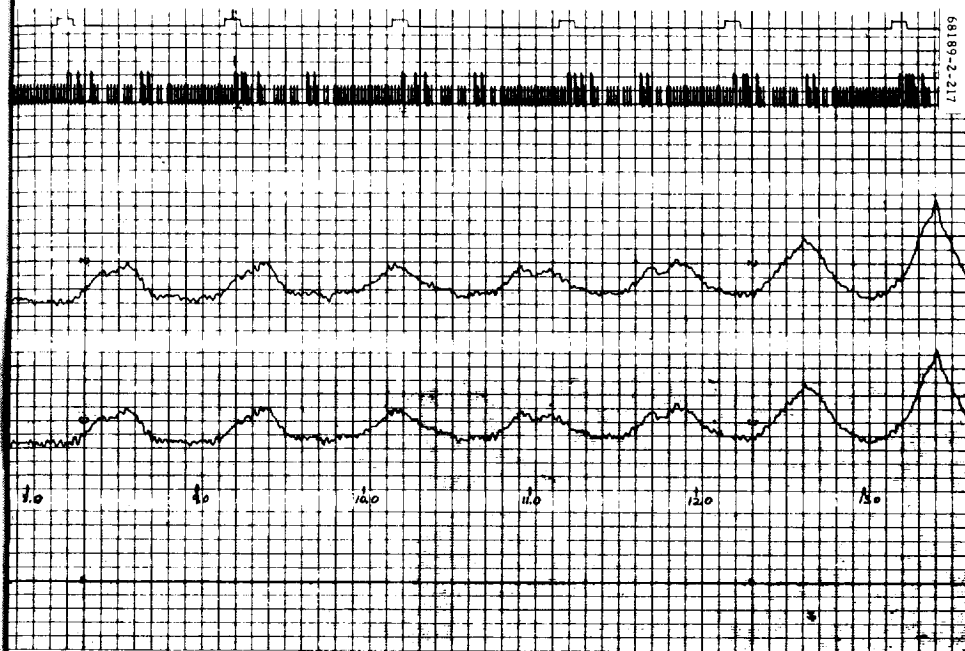
Figure 4.7-20. DSIF Receiver Automatic Gain Control Signal

Reference time: 264:05:00:03.750

4.7-19A

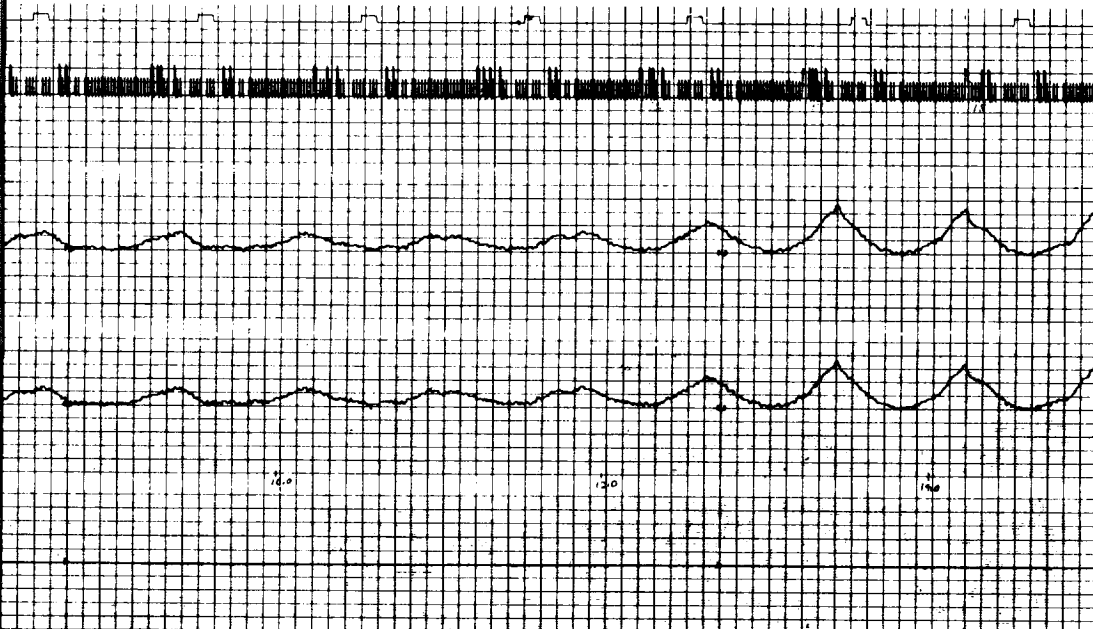
FOLDBOUT FRAME /





68189-2-217

CORPORATION CLEVELAND OHIO PRINTED IN U.S.A.

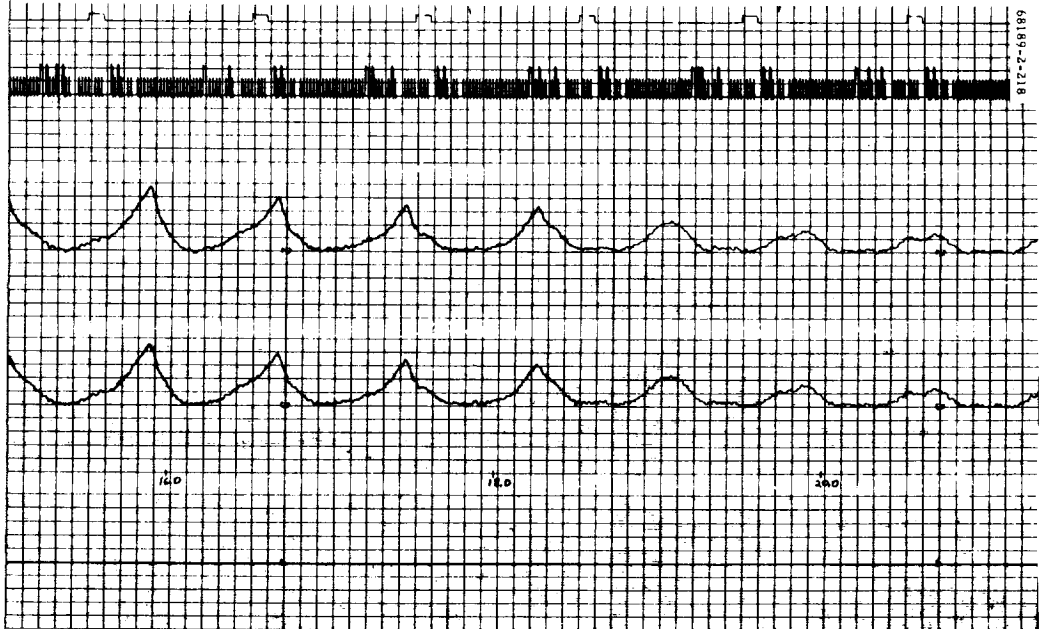


BRUSH INSTR

~~FOURTH~~ FRAME 2  
4.7-19 B



68189-2-218



INSTRUMENTS DIVISION OF CLEVELITE CORPORATION CLEVELAND, OHIO PRINTED IN U.S.A.

FOLDOUT FRAME 3 4.7-19C



PRECEDING PAGE BLANK NOT FILMED.

to verify the calculated spacecraft motion output from the digital simulation as a function of assumed thrusts. During the short interval studied, the only RF link parameter that should have changed appreciably was omnidirectional antenna gain. This gain variation is a direct result of look-angle (from spacecraft to DSIF) changes due to tumbling; a map of the spacecraft transmitting antenna gain contours in spacecraft coordinates is shown in Figure 4.7-21.

The spacecraft dynamic motion from the mathematical model was transformed into a track of the earth vector in spacecraft coordinates suitable for superposition on the omnidirectional antenna gain map (see Figure 4.7-22 for the look-angle trajectory for final selected thrust and moments combination). The intersection of these two functions produces a gain profile in time, which is directly comparable to station automatic gain control variations. The correlation between salient features of the simulated gain profile and the DSIF AGC data was the criterion used to evaluate the various thrust level and moment matrix combinations chosen. Any inaccuracy in the simulation model was not considered in this analysis.

The initial part of this study was mainly concerned with matching the two M-shaped waveforms which occur near times 4 and 5.5 seconds (reference time is 264:05:00:03.750) in Figure 4.7-19. These waveforms can best be reproduced when the earth vector traverses the -6 db contour (located at coordinates  $\theta = 84$  degrees,  $\phi = 10$  degrees) in such a way that  $\phi$  is relatively constant. Many of the thrust level combinations proposed could be immediately discarded since it was obvious that they could not produce the correct waveforms at the proper times.

Based on the preliminary study and analysis of sun sensor and gyro data in this 20-second time period, it was decided to investigate in detail certain cases which were still considered reasonable. These included modified thrust levels for the two engines that did fire, a non-zero (but small) thrust level for the third engine, and a modified moment of inertia matrix. For simplicity, the combinations used are referred to as  $(T_1, T_2, T_3)^M$ ,

where

$T_1$  = ratio of assumed and telemetered thrust levels for engine 1

$T_2$  = ratio of assumed and telemetered thrust levels for engine 2

$T_3$  = assumed engine 3 thrust in pounds

M = modified moments of inertia matrix

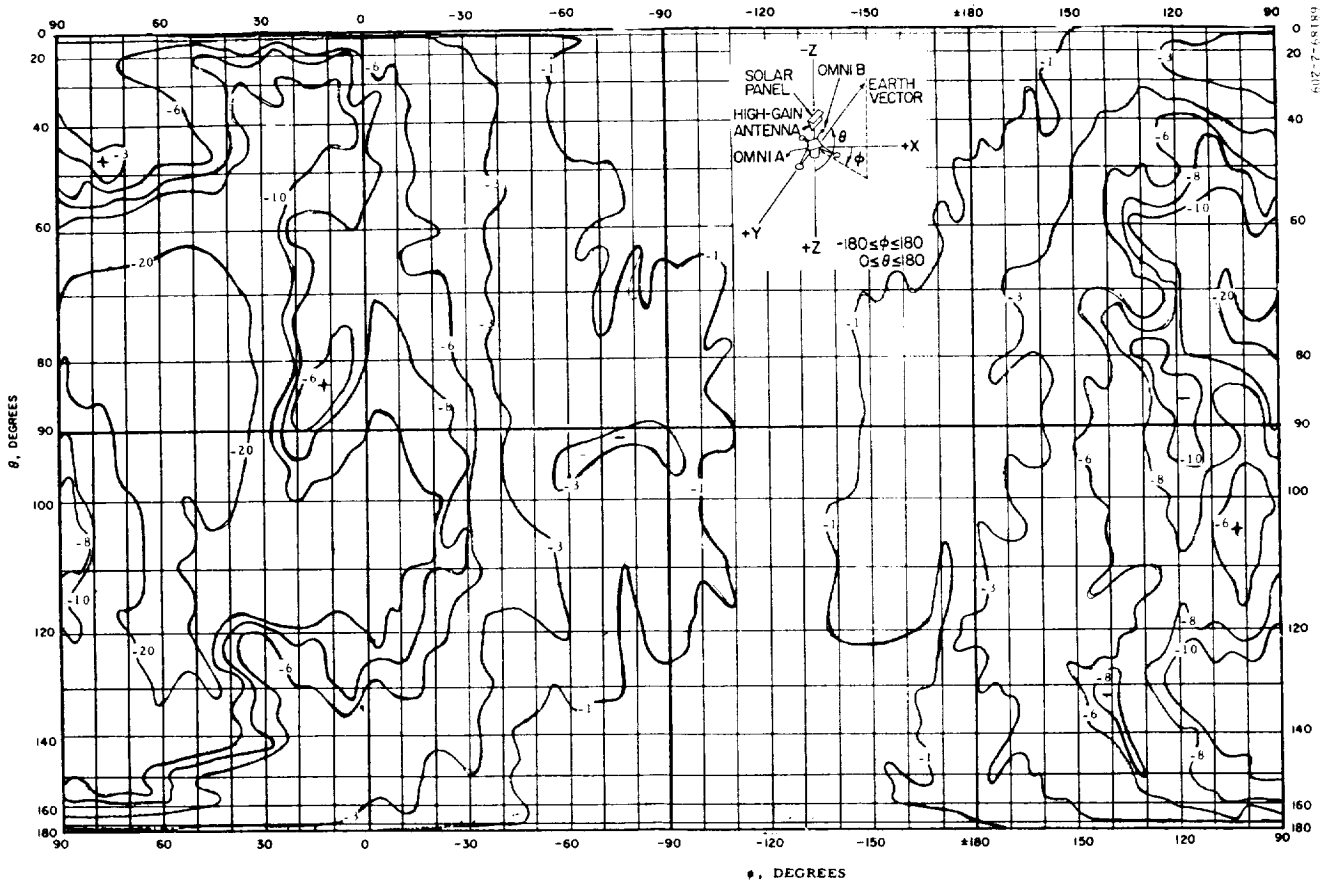
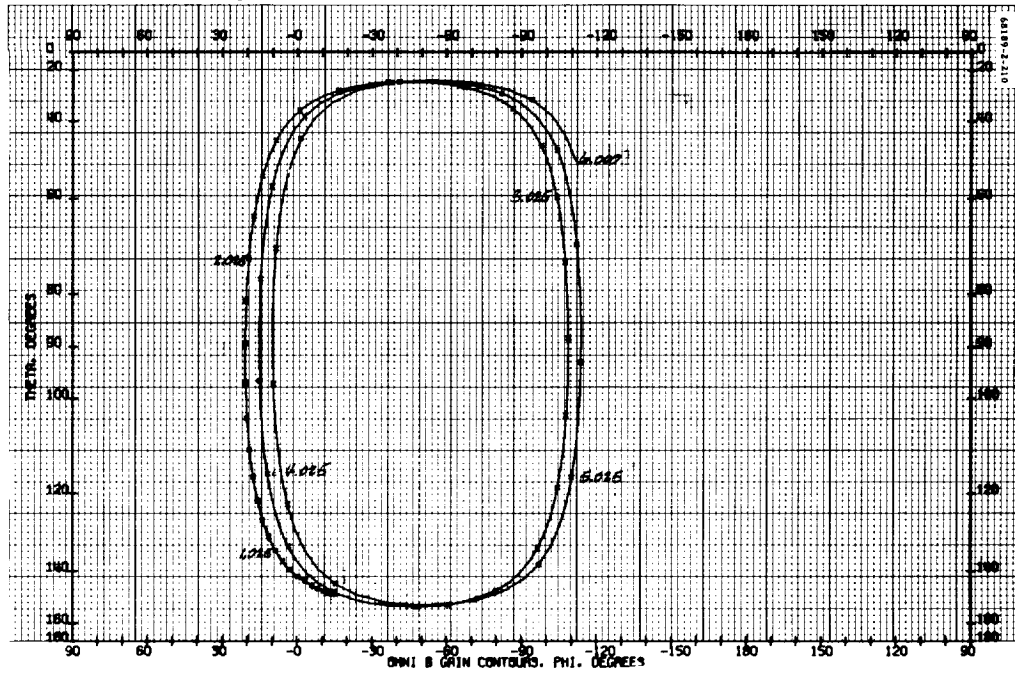
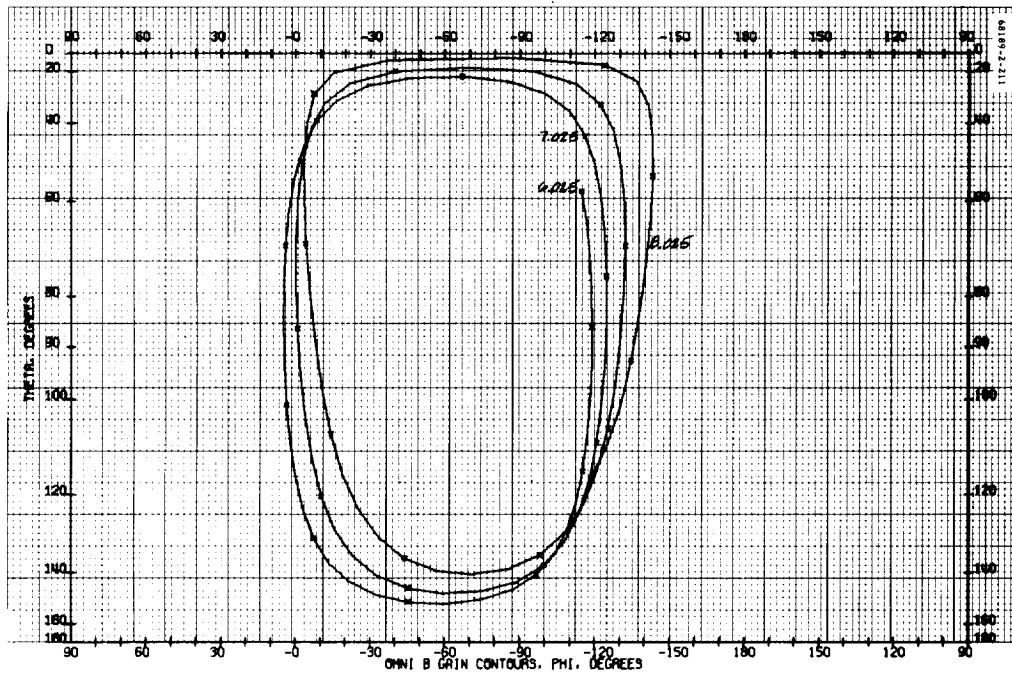


Figure 4.7-21. Omnidirectional Antenna B Gain Contours, 2295 MHz



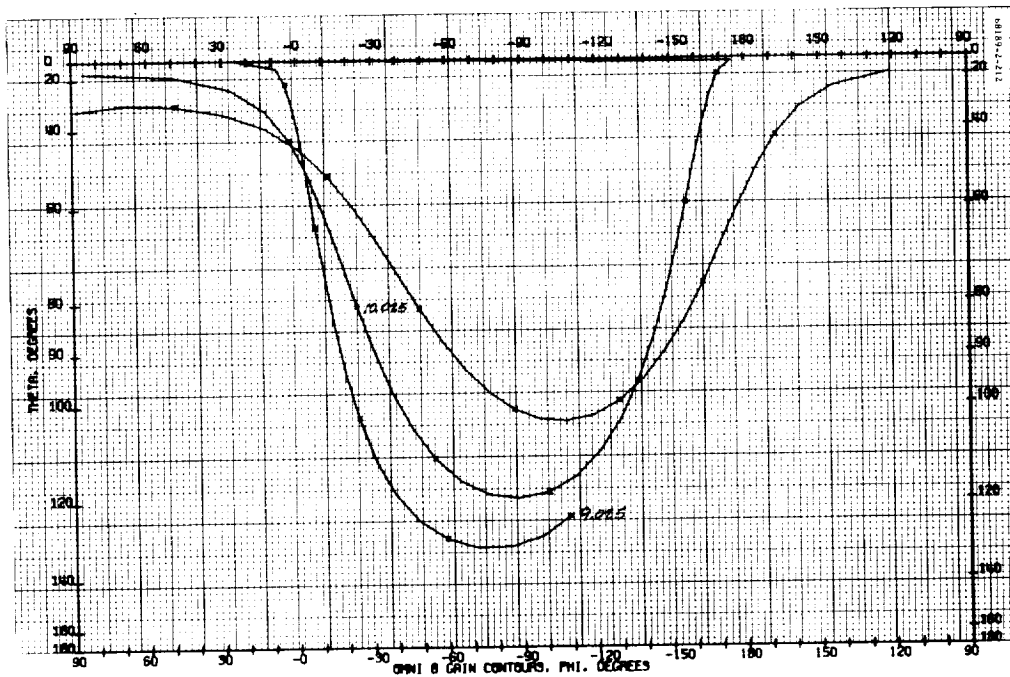


a) From 0 to 6 seconds

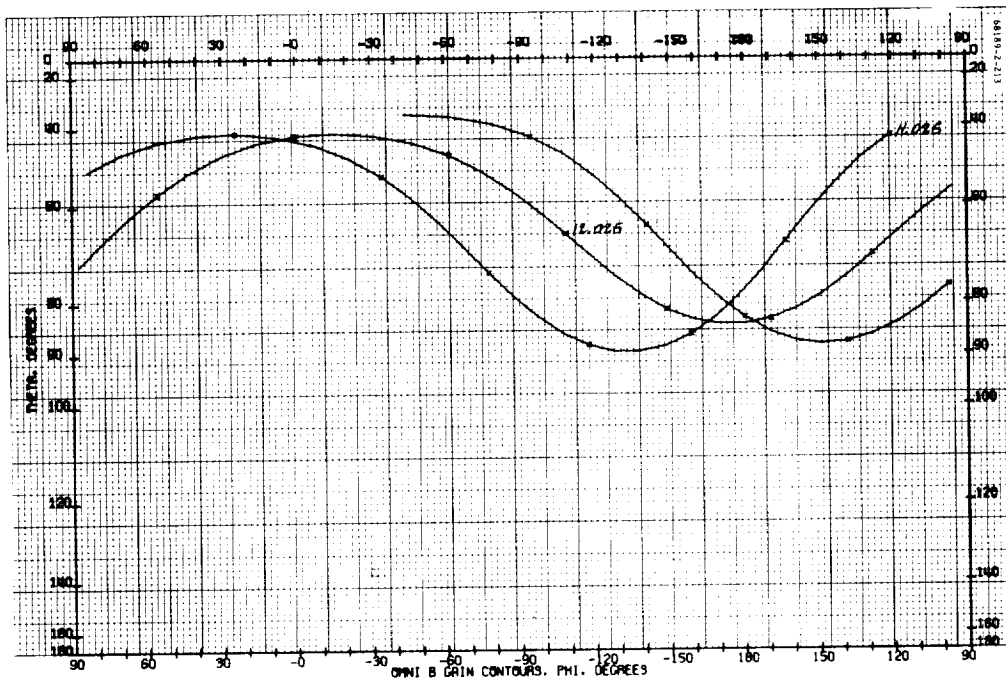


b) From 6 to 9 seconds

Figure 4.7-22. Look Angle Trajectory for  $(1, 1, 2)^m$  Thrust Condition  
Reference time: 264:05:00:3.7



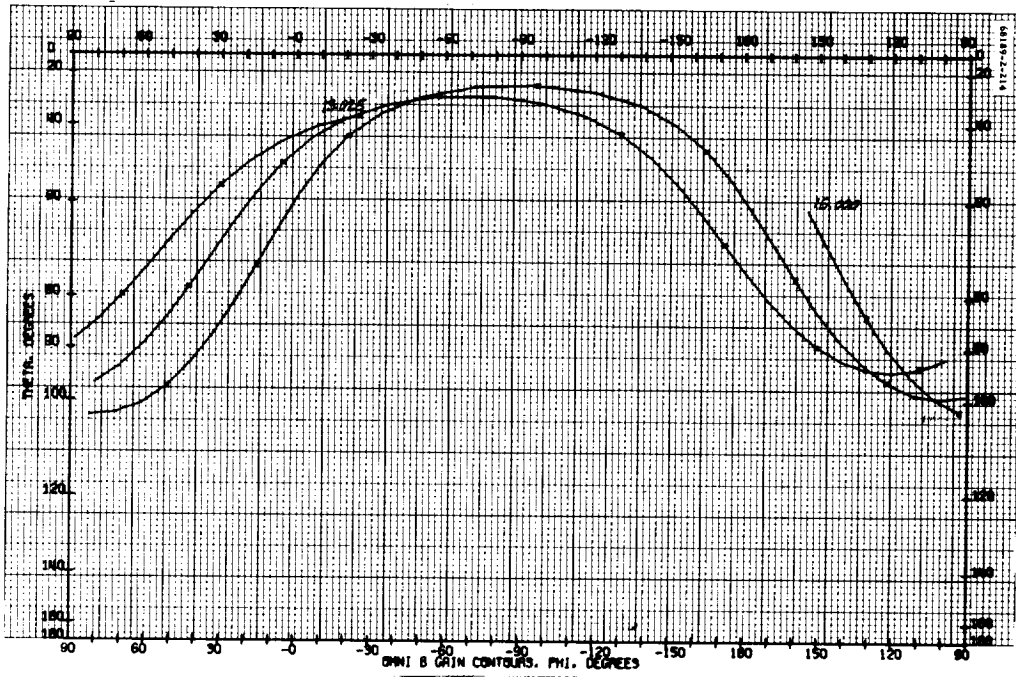
c) From 9 to 11 seconds



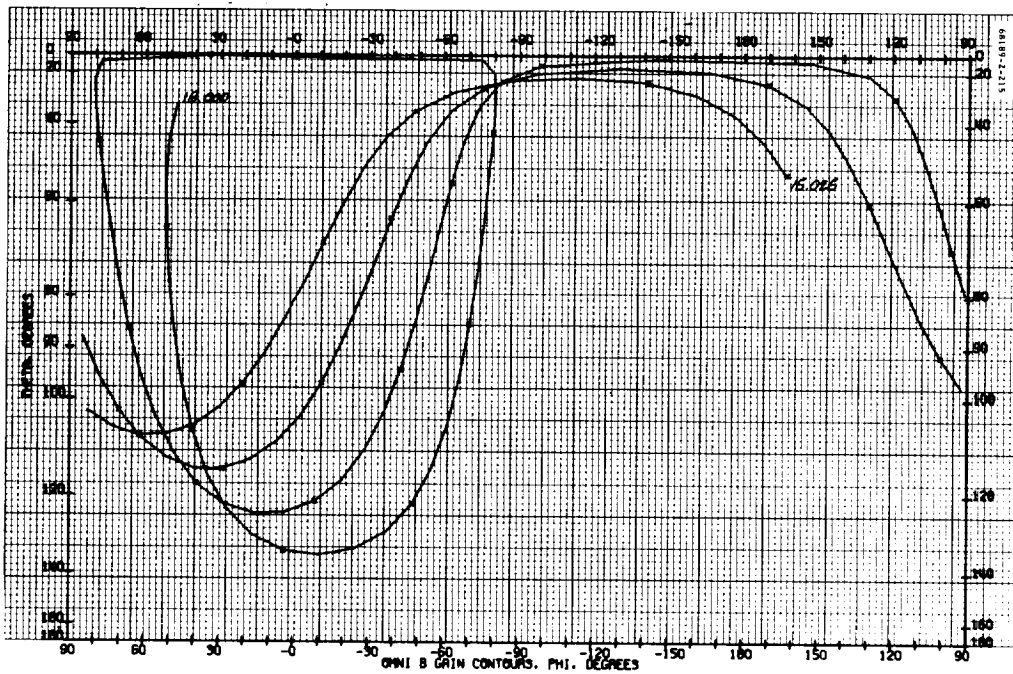
d) From 11 to 13 seconds

Figure 4.7-22(continued). Look Angle Trajectory for  $(1, 1, 2)^m$  Thrust Condition

Reference time: 264:05:00:3.7



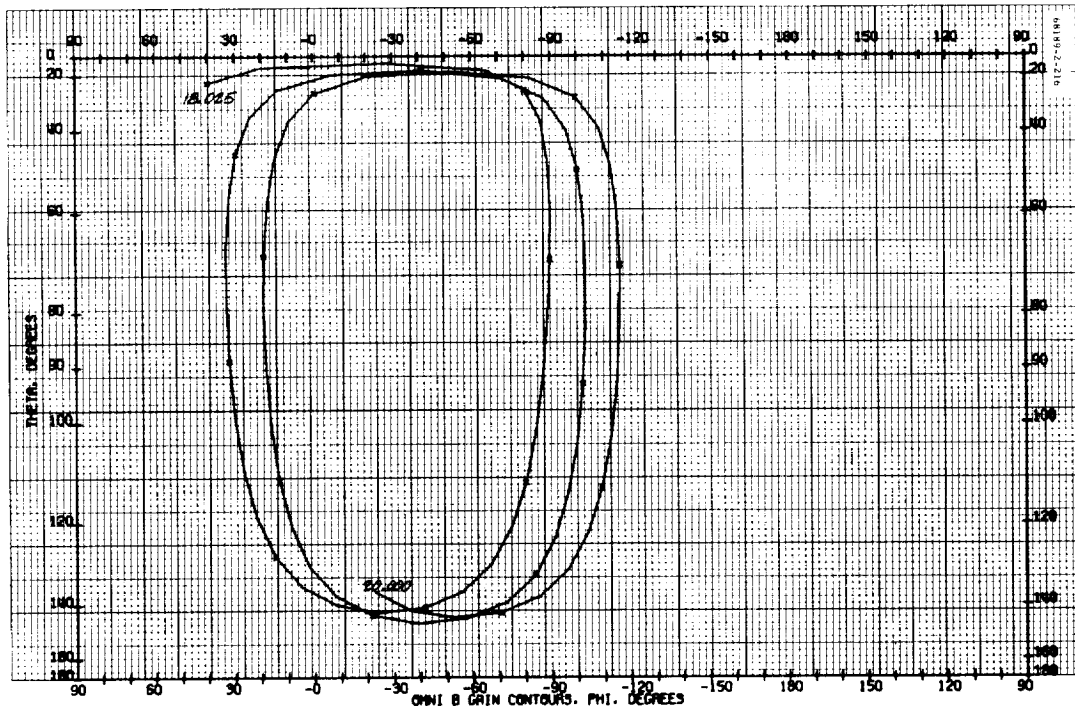
e) From 13 to 15 seconds



f) From 15 to 18 seconds

Figure 4.7-22(continued). Look Angle Trajectory for  $(1, 1, 2)^m$  Thrust Condition

Reference time : 264:05:00:3.7



g) From 18 to 20 seconds

Figure 4.7-22(continued). Look Angle Trajectory for  $(1, 1, 2)^m$  Thrust Condition

Reference time: 264:05:00:3.7

In this way, the six cases investigated in detail can be called (0.9, 1, 0), (0.9, 0.9, 0), (1, 0.9, 0), (1, 1, 0), (1, 1, 2), and (1, 1, 2)<sup>M</sup>.

Comparison of the gain and automatic gain control waveshapes (see Figures 4.7-23 through 4.7-28) for these six cases resulted in the conclusion that (1, 1, 2)<sup>M</sup> produced the best fit with station automatic gain control. Table 4.7-3 summarizes the considerations that led to this choice. Two of the cases were immediately rejected, since the spacecraft motion did not have the correct period, producing a time displacement between the gain and automatic gain control curves that was quite obvious after the fifteenth revolution. A choice among the remaining four cases was much more subjective, involving comparison of subtle features of the waveshapes. It should be stressed that the antenna gain tolerances are large (2 db for high gains and 8 db for low gains), and that small changes in look-angle could appreciably alter the waveshape details.\* Also, the antenna gain waveshapes had to be "mentally smoothed" during the comparison to compensate for the low-pass filtering used in processing the DSIF automatic gain control oscillographs. Therefore, none of the four cases with the proper period should be considered unequivocally eliminated.

#### 4.7.7 SIMULATION OF GYRO CROSSOVER PROFILE

Using the standard moment of inertia matrix discussed previously, the simulated gyro outputs disagree significantly with the flight data for all thrust factors selected which provide a reasonable fit to the sun sensor and automatic gain control flight data. A plot of gyro output telemetry to the same scales used for simulation outputs is given in Figure 4.7-29. A typical example of the simulated gyro output for the standard inertia matrix, [0, 0, 0, 0, 0, 0], is given in Figure 4.7-30 with flight data points plotted for comparison. This [1, 1]<sup>2</sup> thrust case is typical of the set of cases used to fit the sun sensor and automatic gain control data ([0.9, 1]0, [1, 0.9]0, [0.9, 0.9]0) in that the simulated pitch gyro crossover does not occur, the simulated yaw gyro crossover occurs early, and the duration of the negative saturation interval is approximately 2 seconds less than that of the flight data.

In order to improve the correlation between gyro crossover, sun sensor, and automatic gain control flight data, percentage variations were made in the initial moment of inertia matrix elements. Although an exact match to the flight data was not obtained, gyro simulated output is presented in Figures 4.7-31 through 4.7-35 in which best match cases obtained are presented. The sun sensor comparison plots for these cases is given in Figures 4.7-36 and 4.7-37.

---

\*On some curves, 10 db errors occasionally occur on some of the peaks. Estimated values have been drawn in for these instances.

TABLE 4.7-3. SUMMARY OF AUTOMATIC GAIN CONTROL/GAIN COMPARISON FOR THRUST LEVEL COMBINATIONS

<u>Case</u>	<u>Comments</u>
(1, 1, 2) <sup>M</sup>	Period correct. Dips in cycles 9 and 10 correct. Peaks for cycles 11 through 14 correct.
(1, 1, 2)	Period correct. Cycle 11 waveshape too smooth. Peak of cycle 14 late.
(1, 1, 0)	Period correct. Waveshape of cycle 10 too pointed.
(1, 0.9, 0)	Period correct. Waveshape of first cycle has three instead of two peaks, but otherwise correct.
(0.9, 1, 0)	Signal has wrong period.
(0.9, 0.9, 0)	Signal has wrong period.

#### 4.7.8 SIMULATION OF INITIAL GYRO RESPONSE

In an attempt to match the pitch and yaw gyro angle response during the first second of the midcourse period, perturbations were made in the following:

- Ignition time
- Difference in ignition time between engines
- Engine thrust level
- Moments of inertia

The moment of inertia changes which were required to bracket the gyro crossover response produced negligible effect on the simulated gyro outputs (Table 4.7-4).

A plot of gyro outputs (FC-16 and FC-17) and simulated gyro outputs for the (1,1)2 thrust level condition is plotted in Figure 4.7-40. The effect of the uncertainty in ignition time (see subsection 4.7.9) is indicated in the maximum and minimum values plotted. A close fit to the pitch gyro data could be obtained by appropriately selecting the ignition time; however, a fit to the yaw gyro data could not be obtained. It should be noted that due to the saturation characteristics of the gyro telemetry output, the curve shape is not representative of the actual flight motion for gyro angles greater than 4 degrees.

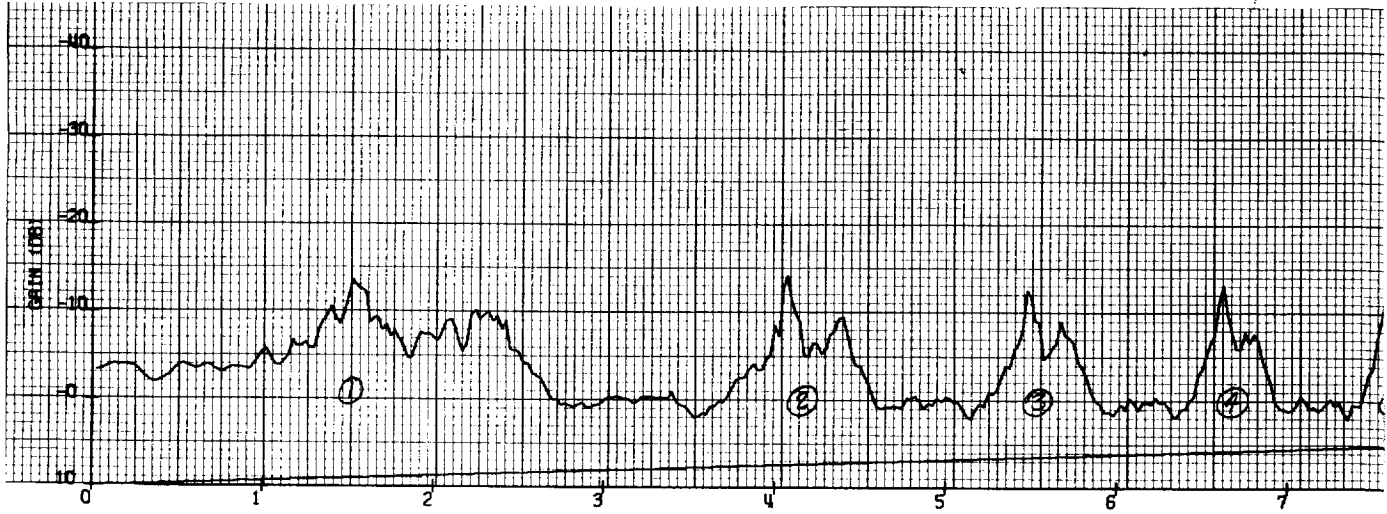


Figure 4.7-23. Antenna Gain Versus Time for  $(1, 1, 2)^m$

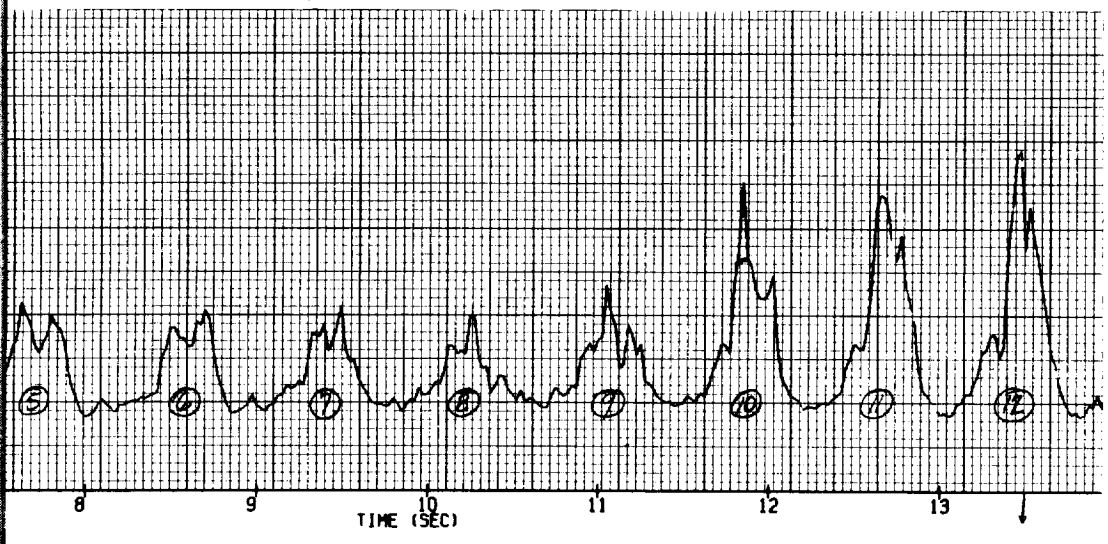
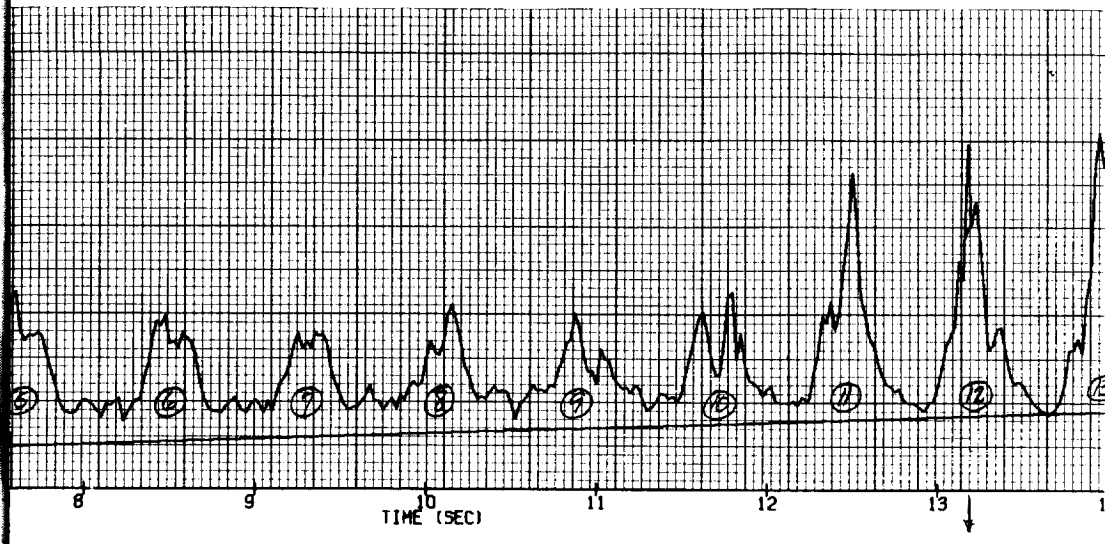


Figure 4.7-24. Antenna Gain Versus Time for  $(1, 1, 2)$

~~VOIDOUT FR. 11~~ /



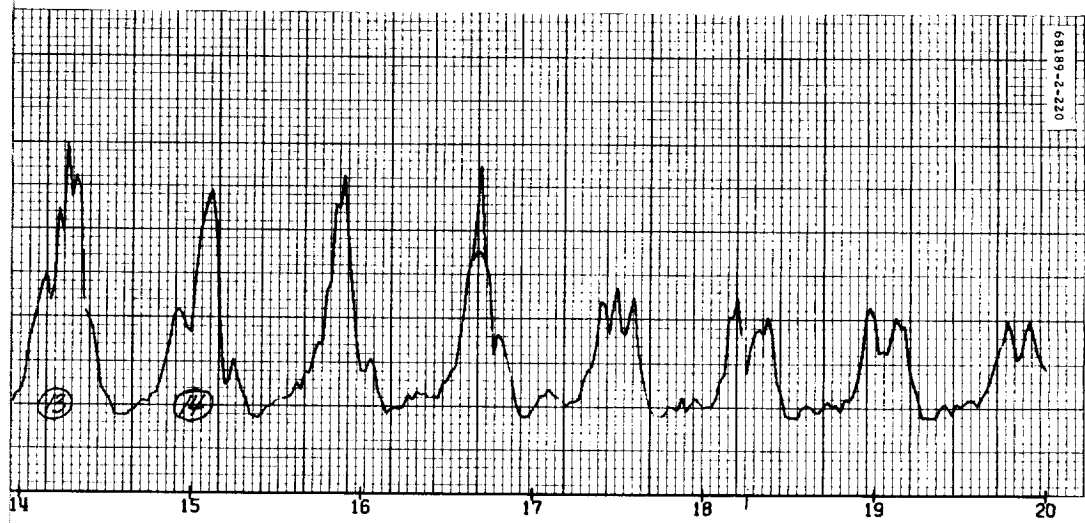
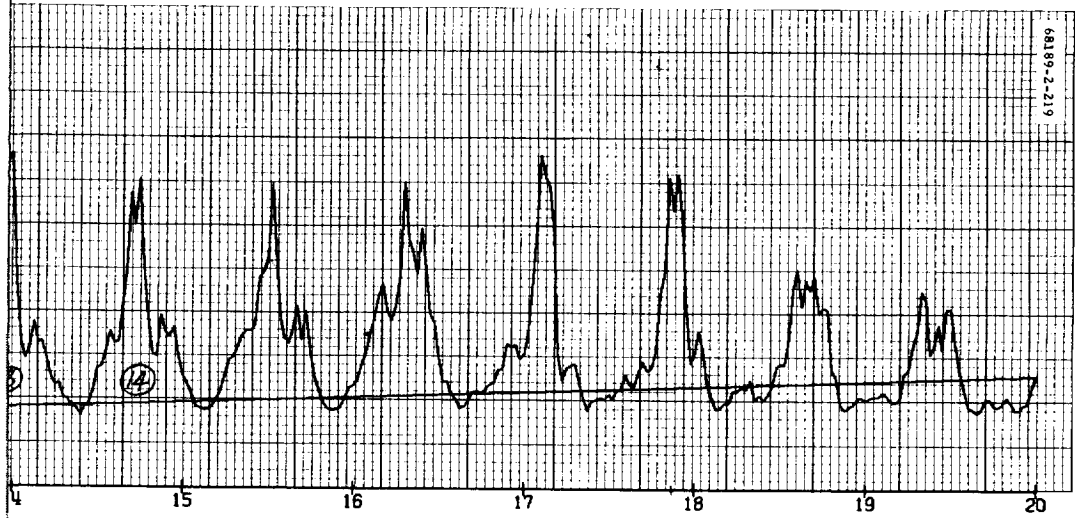




WALDOUT FRAMES 2

4.7-29B





FOLDOUT FRAME 34.7-29C



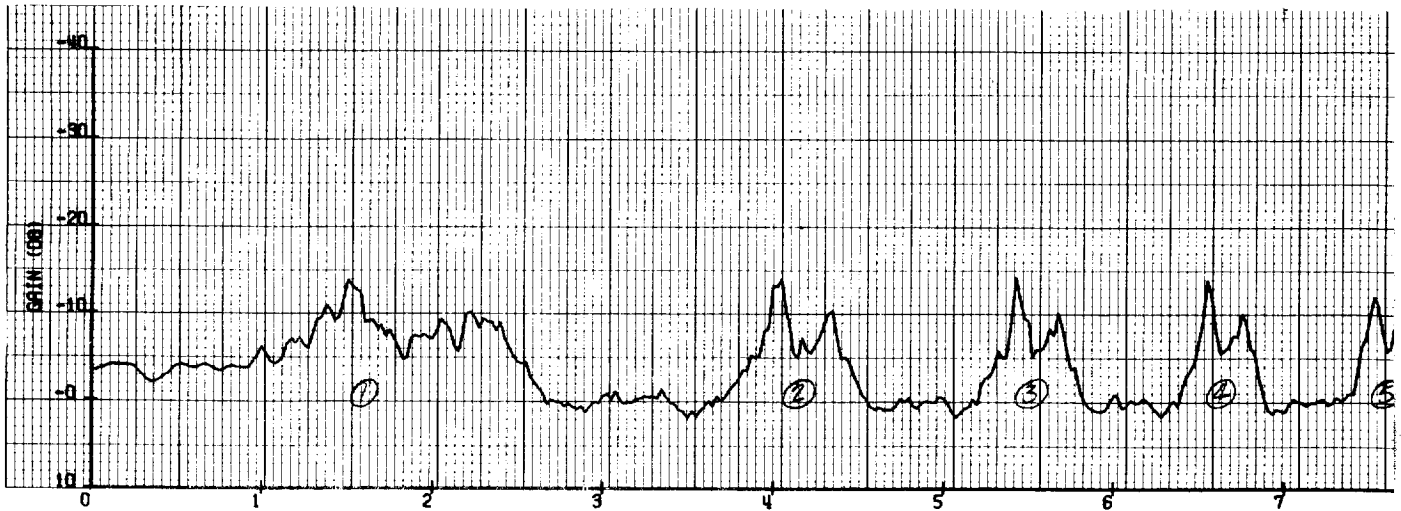


Figure 4.7-25. Antenna Gain Versus Time for (1, 1, 0)

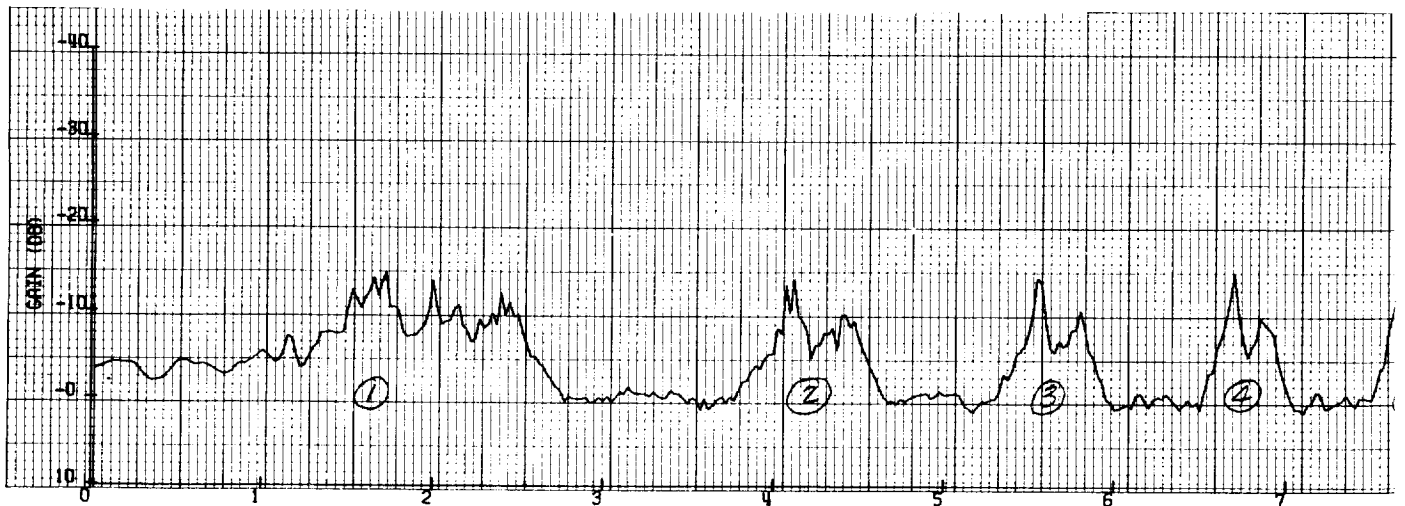
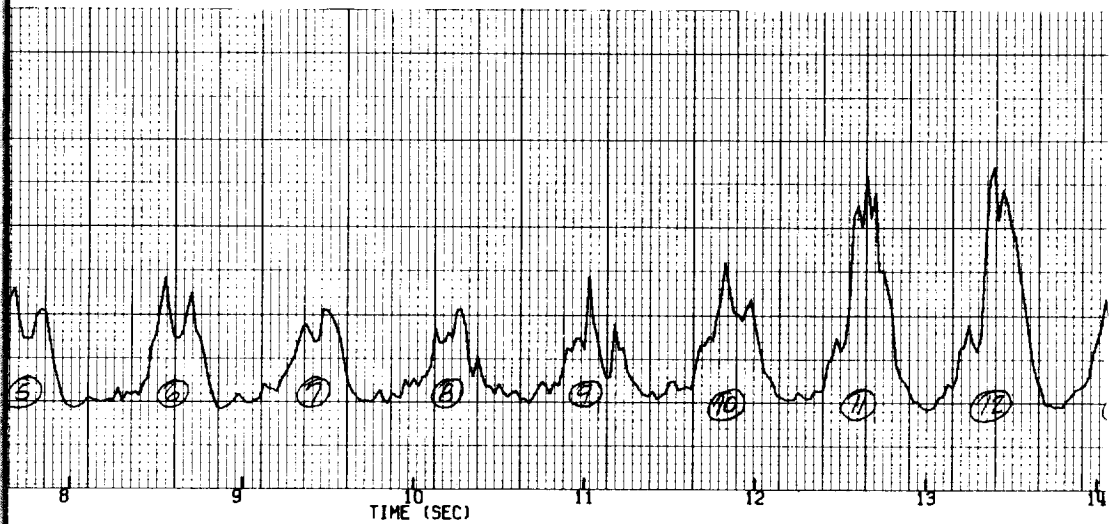
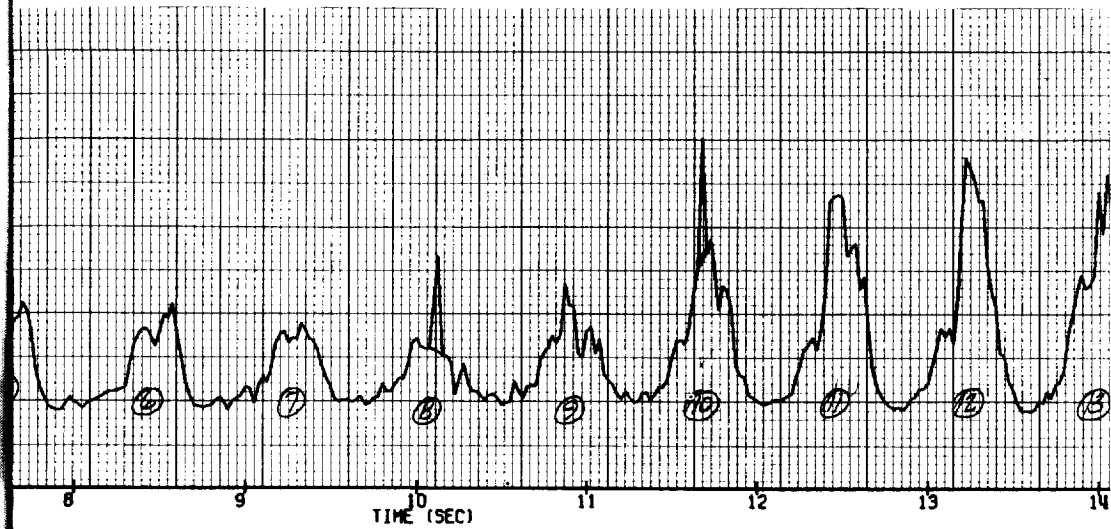


Figure 4.7-26. Antenna Gain Versus Time for (1, 0.9, 0)

FOLDOUT FRAME /



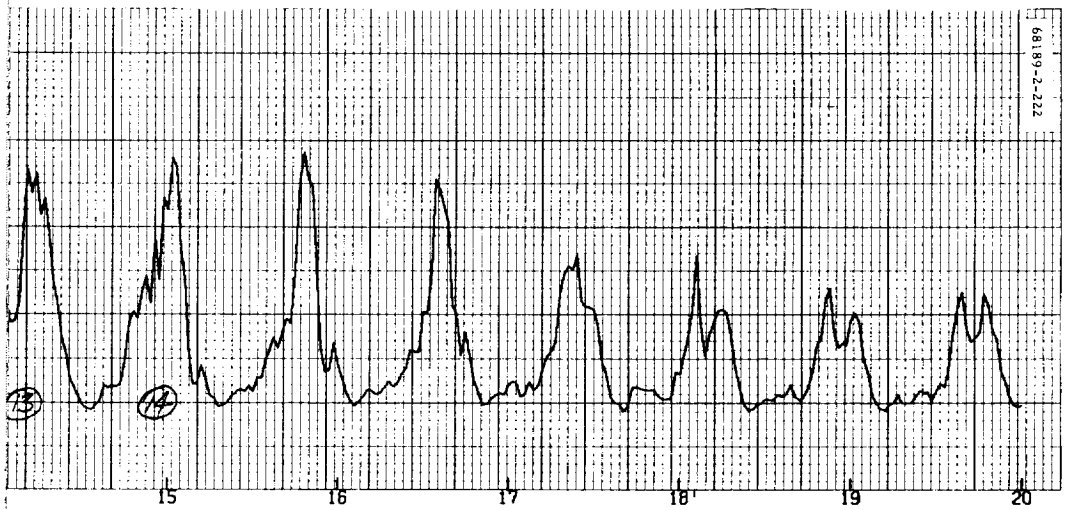
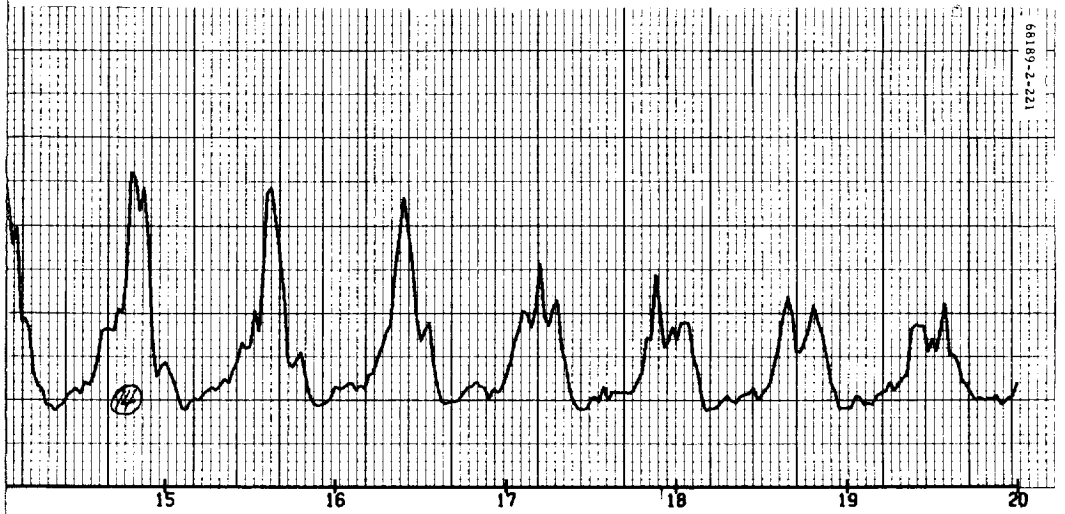


FOLDOUT FRAME 2

4.7-31B







FOLDOUT FRAME 3  
4.7-31C



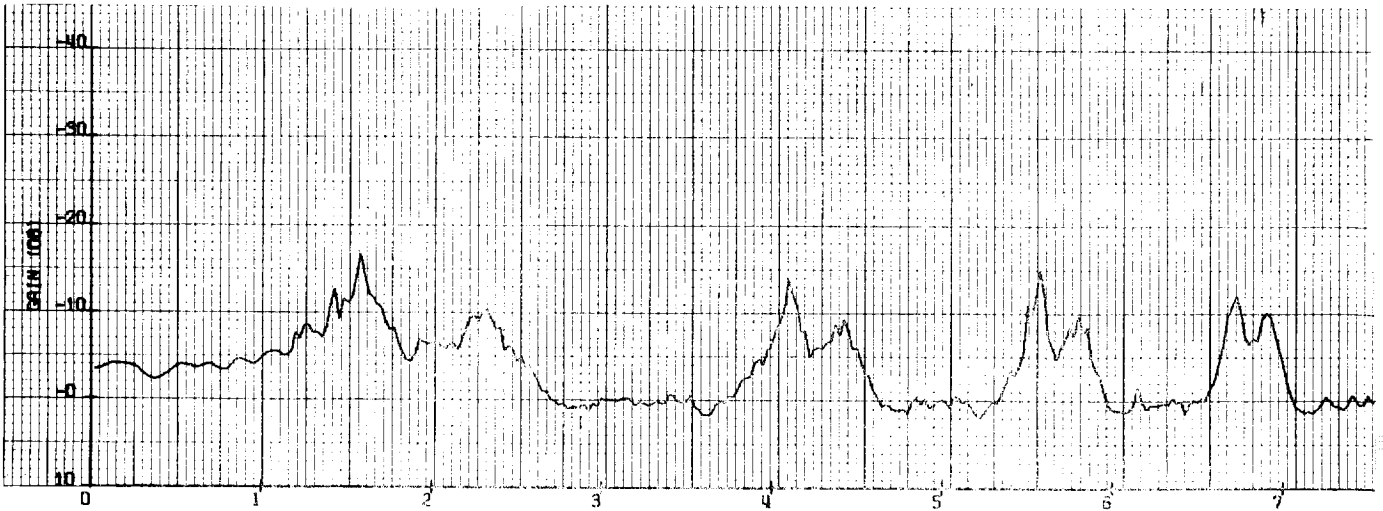


Figure 4.7-27. Antenna Gain Versus Time for (0.9, 1, 0)

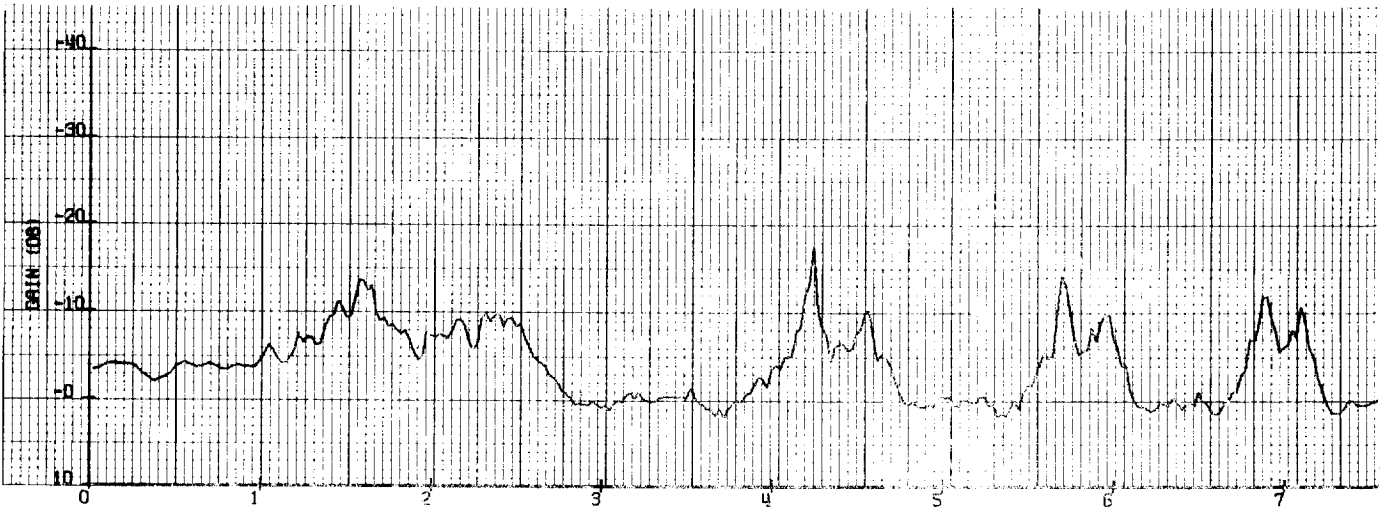
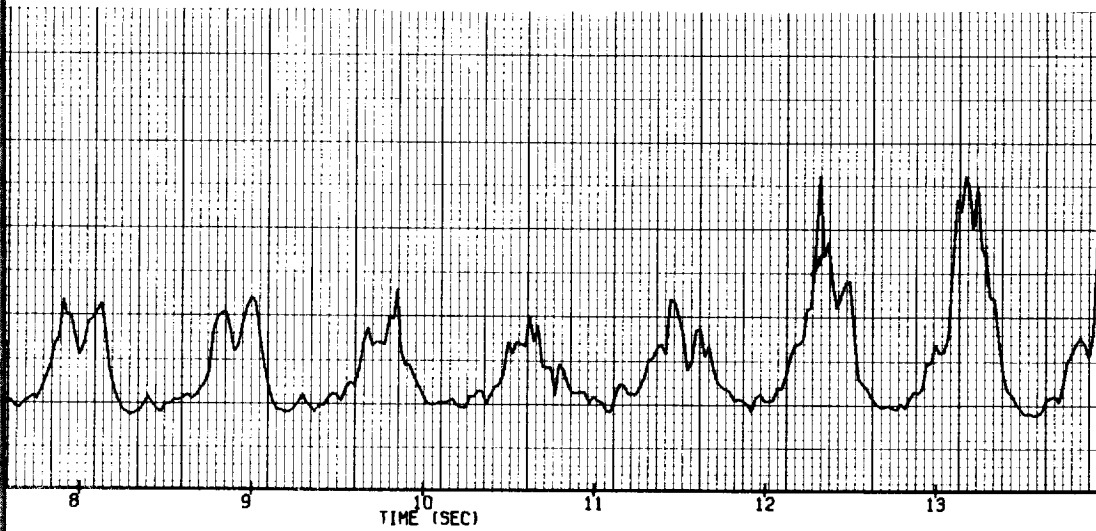
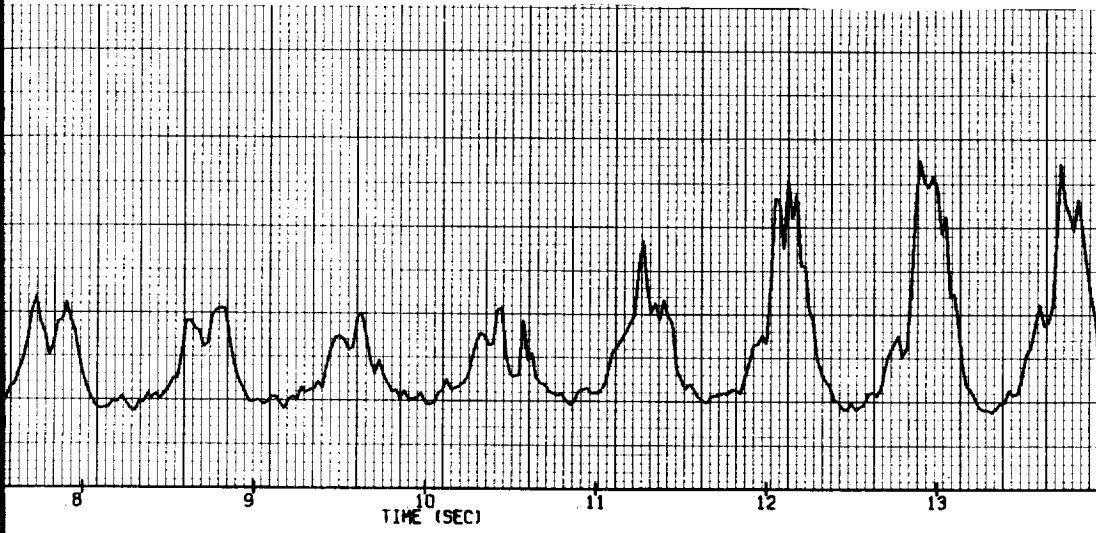


Figure 4.7-28. Antenna Gain Versus Time for (0.9, 0.9, 0)

FOLDOUT FRAME /

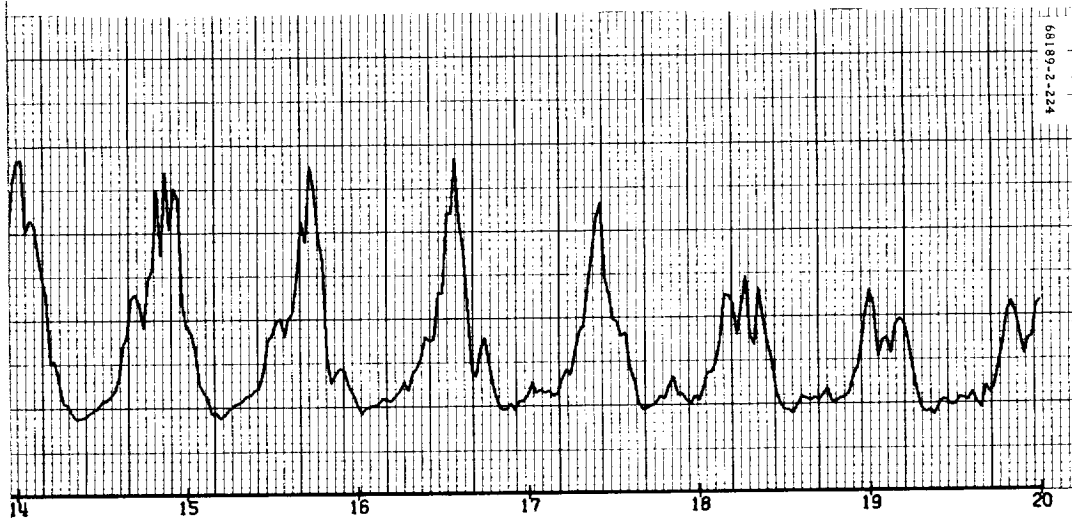
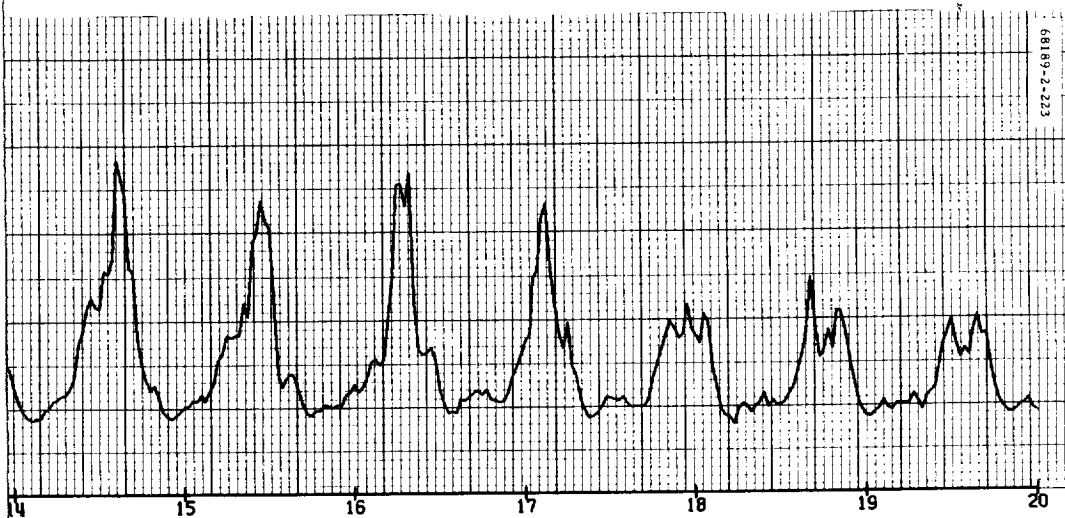




FOLDOUT FRAME 2

4.7-33B





ECG OUT PRINT 3

4.7-5'00





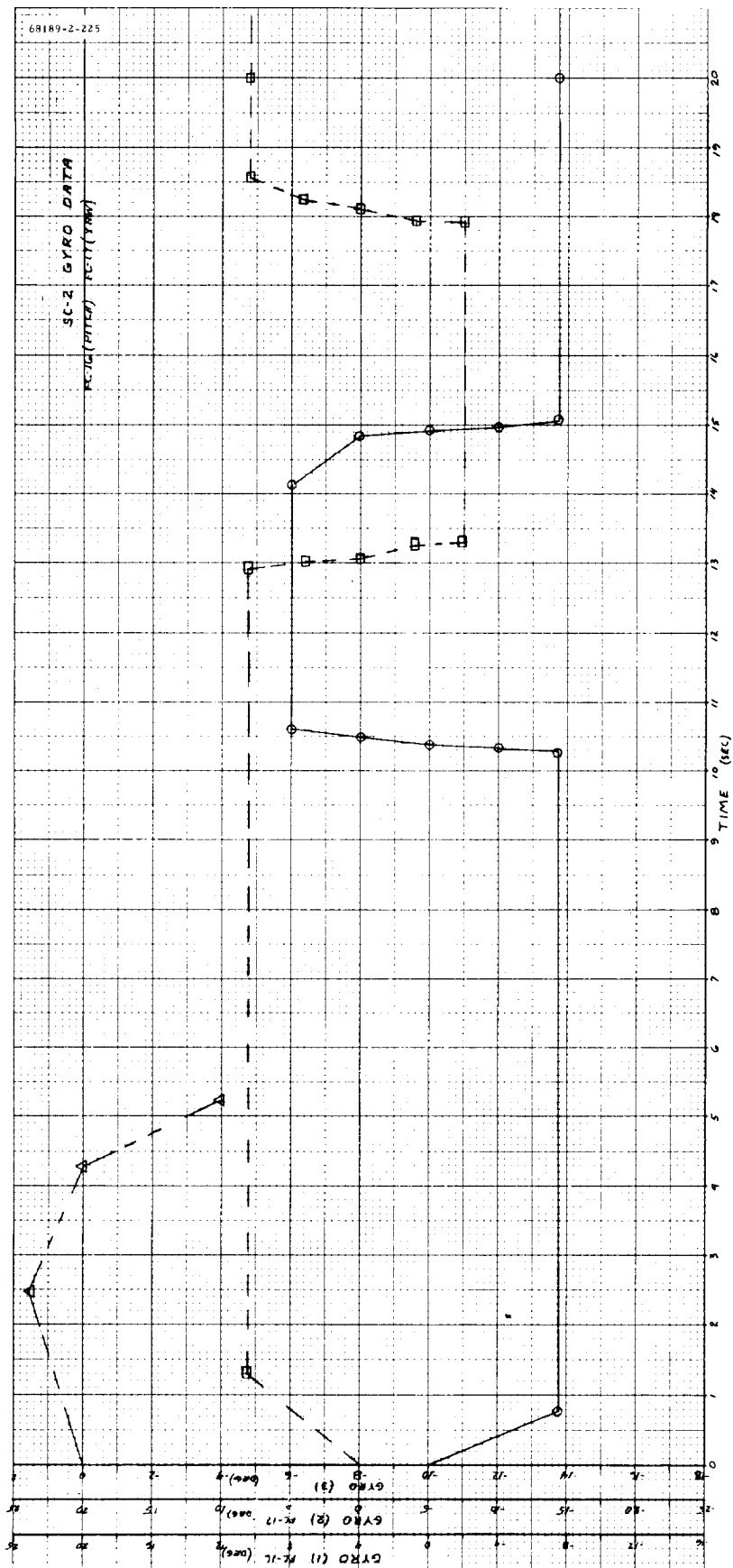


Figure 4.7-29. Gyro DATA - FC-16 (Pitch) and FC-17 (Yaw)

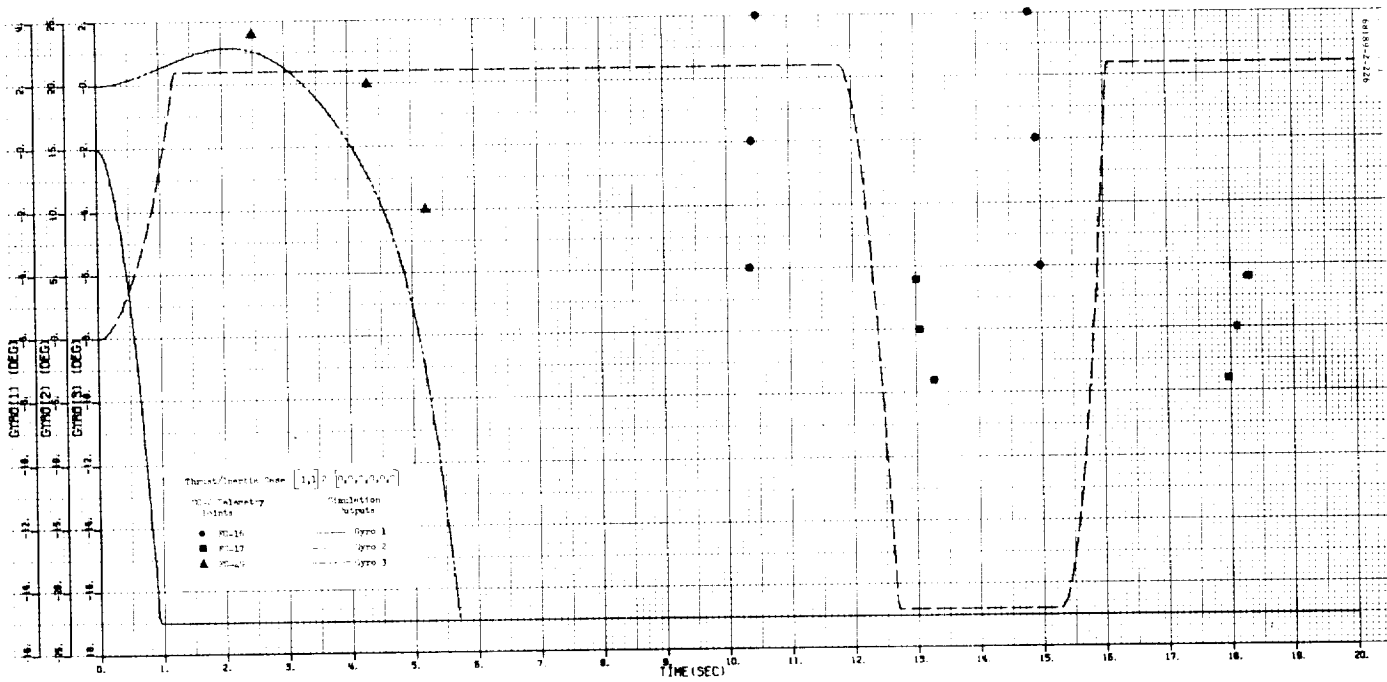


Figure 4.7-30. Simulated Gyro Outputs for Standard Inertia Matrix

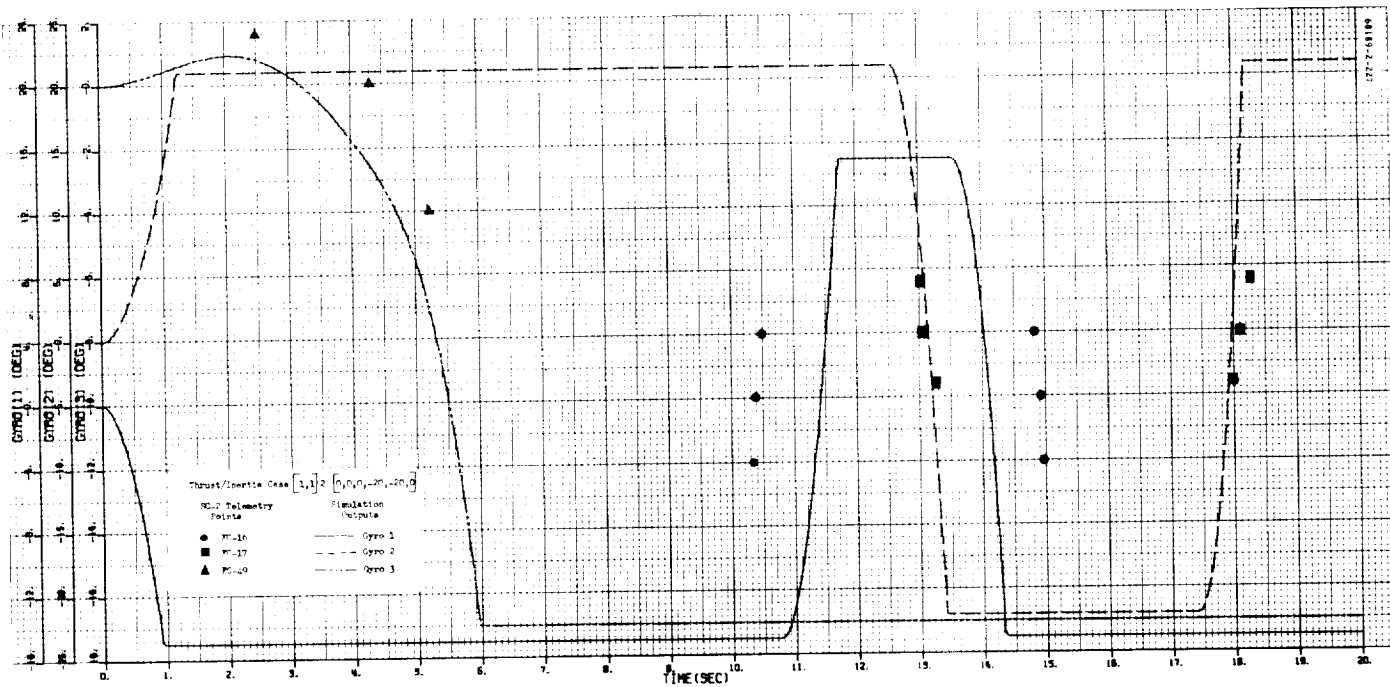


Figure 4.7-31. Simulated Gyro Outputs, Case 1

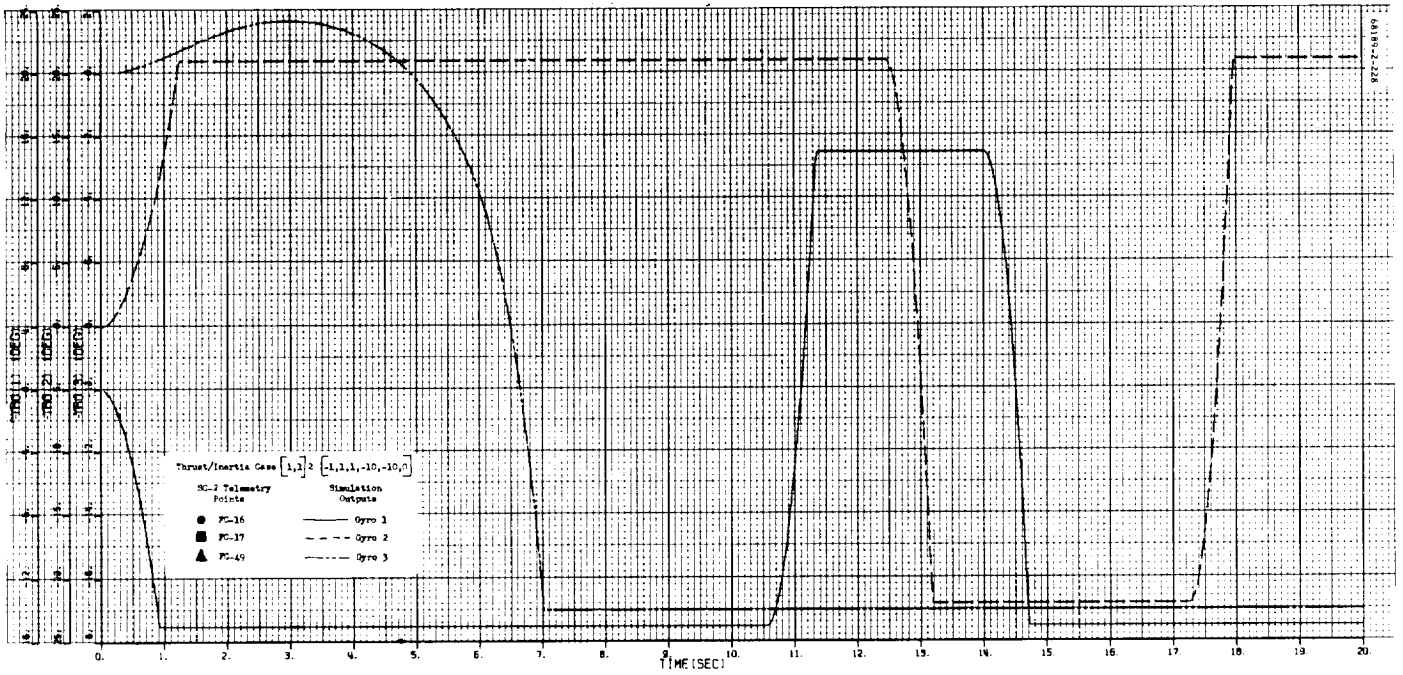


Figure 4.7-32. Simulated Gyro Outputs, Case 2

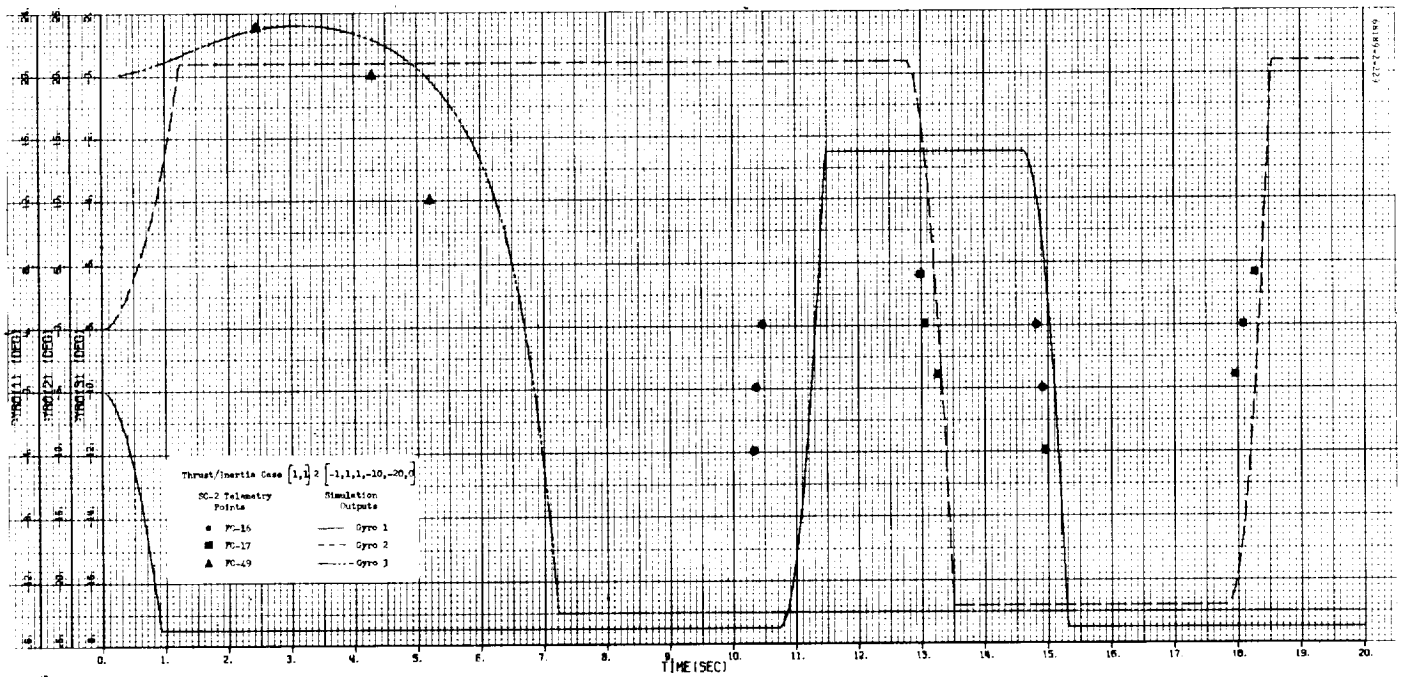


Figure 4.7-33. Simulated Gyro Outputs, Case 3

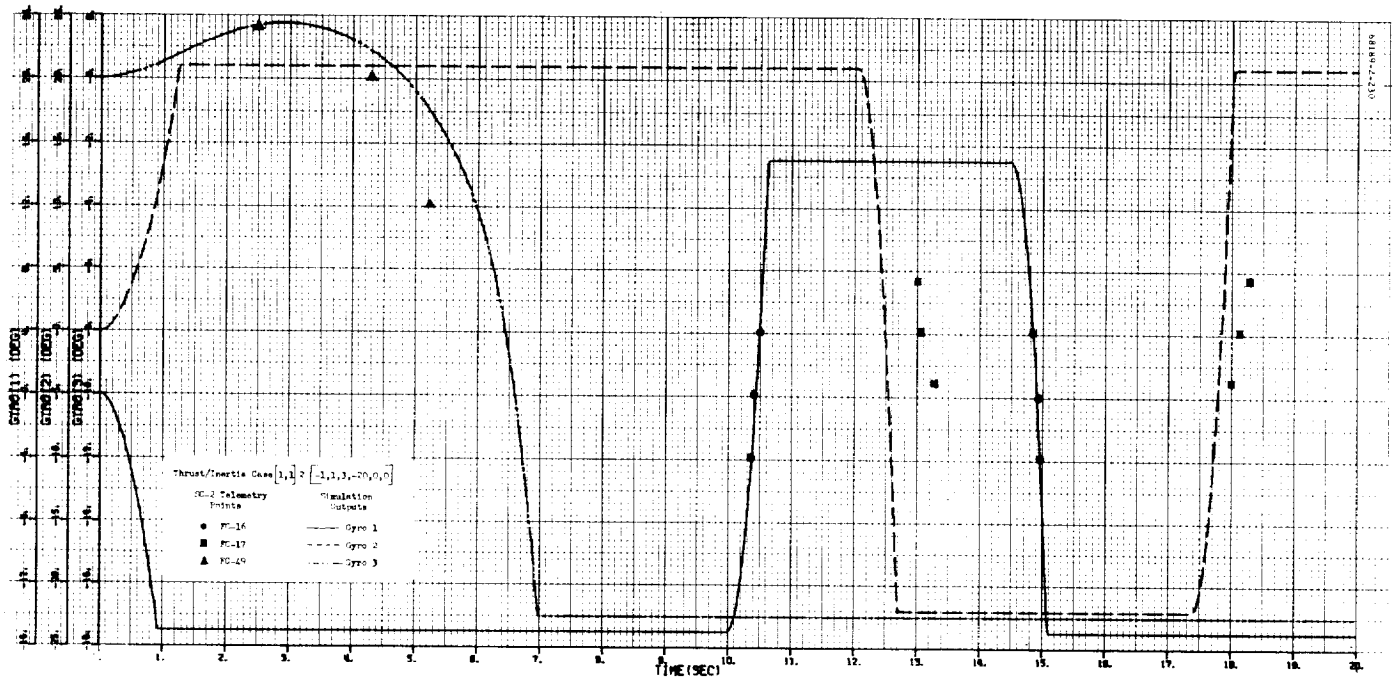


Figure 4.7-34. Simulated Gyro Outputs, Case 4

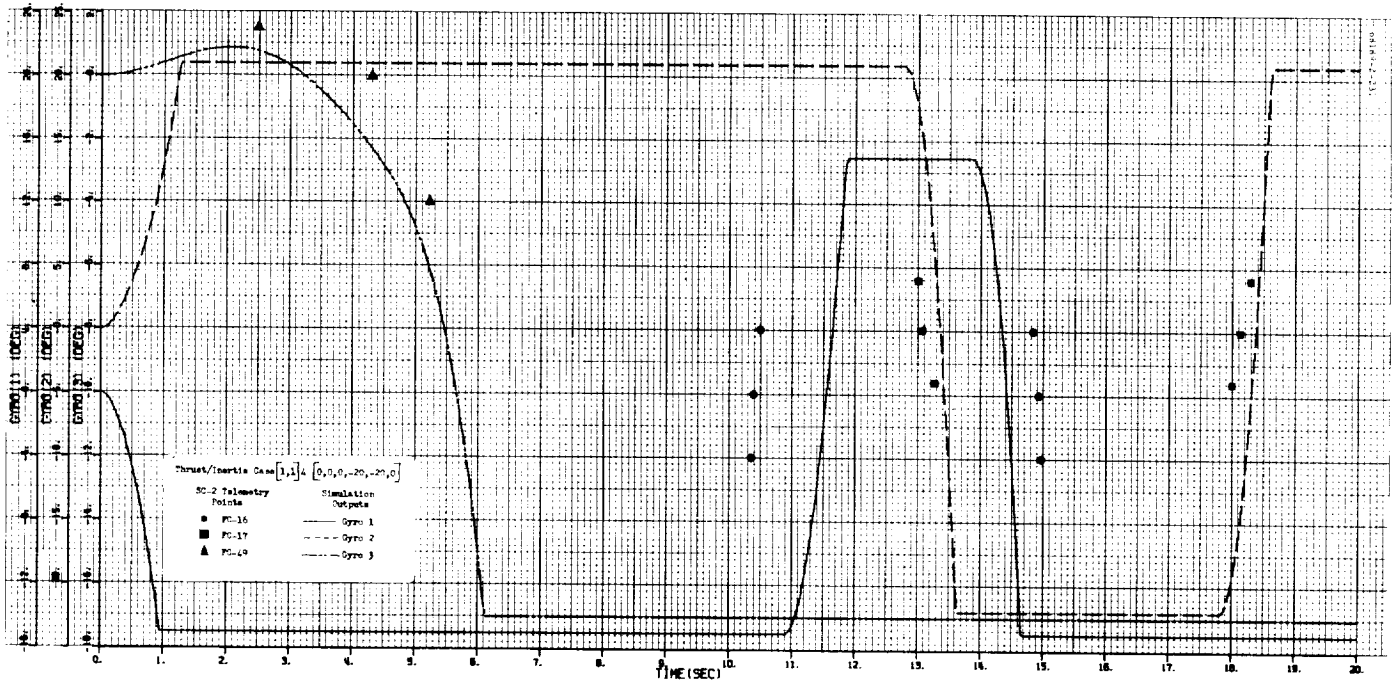


Figure 4.7-35. Simulated Gyro Outputs, Case 5

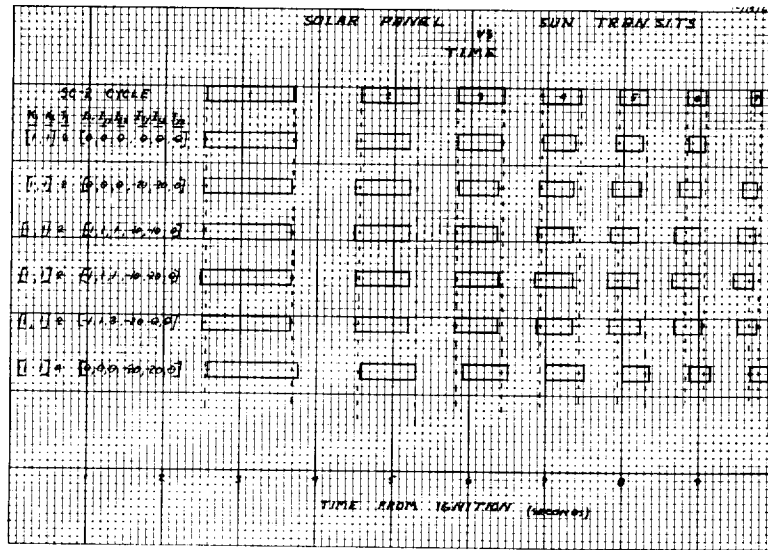


Figure 4.7-36. Solar Panel Sun Transits Versus Time

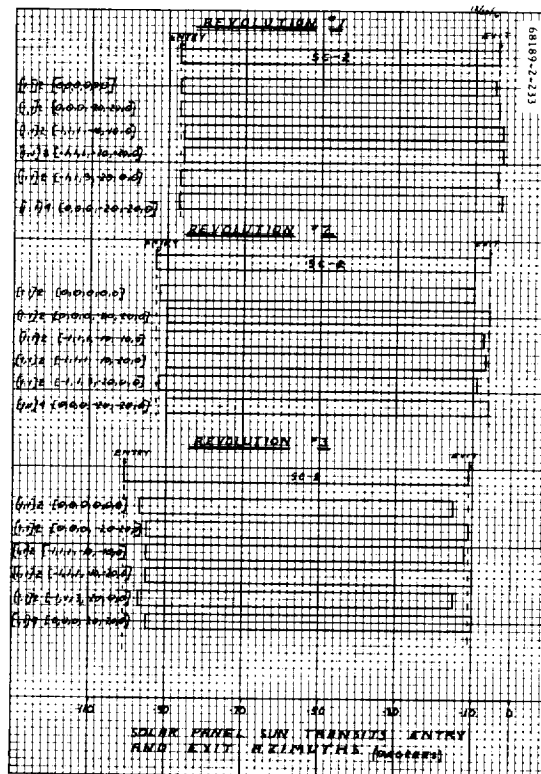


Figure 4.7-37. Solar Panel Sun Transits Entry and Exit Azimuths

TABLE 4.7-4. GYRO COMPARISONS FOR VARIATIONS IN MOMENTS AND PRODUCTS OF INERTIA

Thrust factor (1, 1, 2)

Time, seconds	Moments of Inertia $\rightarrow$		Products of Inertia $\rightarrow$		Products of Inertia $\rightarrow$		Products of Inertia $\rightarrow$	
	$[0, 0, 1]$	$[-1, 0, 1]$	$[-1, 1, 1]$	$[-1, 1, 3]$	$[-1, 1, 3]$	$[-1, 1, 3]$	$[0, 0, 0]$	$[0, 0, -20]$
0.3	-1.84°	-1.84°	-1.84°	-1.86°	-1.87°	-1.86°	-1.86°	-1.86°
	-4.7°	-4.7°	-4.7°	-4.73°	-4.75°	-4.72°	-4.72°	-4.72°
	-6.55°	-6.6°	-6.6°	-6.6°	-6.64°	-6.6°	-6.6°	-6.6°
0.5	1.49°	1.49°	1.49°	1.49°	1.50°	1.49°	1.49°	1.49°
	3.84°	3.84°	3.84°	3.82°	3.86°	3.82°	3.82°	3.82°
	5.33°	5.33°	5.27°	5.25°	5.30°	5.25°	5.25°	5.25°
0.6	1.49°	1.49°	1.49°	1.49°	1.50°	1.49°	1.49°	1.49°
	3.84°	3.84°	3.84°	3.82°	3.86°	3.82°	3.82°	3.82°
	5.33°	5.33°	5.27°	5.25°	5.30°	5.25°	5.25°	5.25°

The effect of an engine 2 ignition delay with respect to engine 1 is indicated in Figure 4.7-41. Engine 1 ignition time was selected to provide a best fit to the pitch gyro output. From this figure, it appears that an ignition delay of engine 2, with respect to engine 1, of 50 milliseconds would be required to match the yaw gyro data.

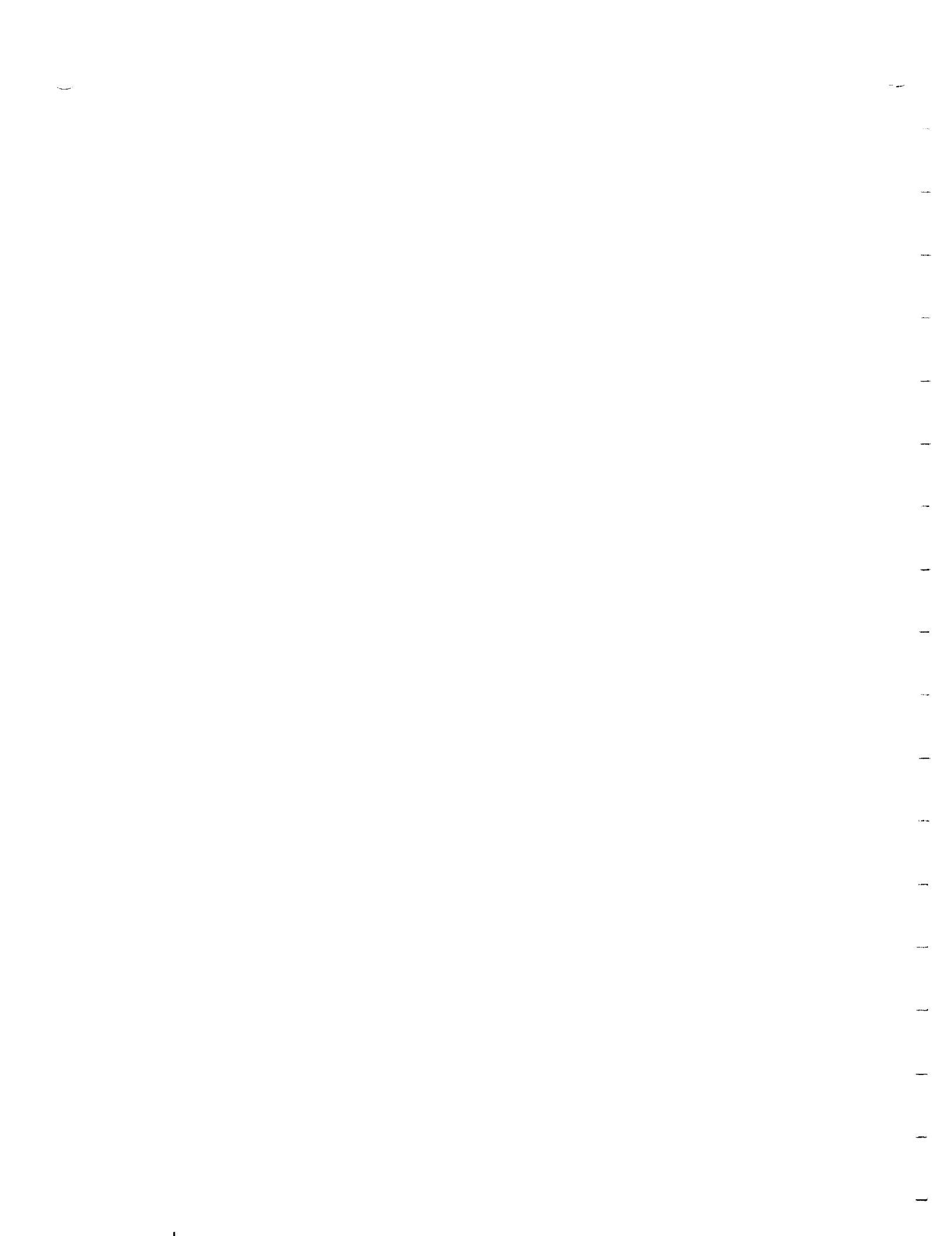
In order to obtain a better fit to the curve shape of the yaw gyro, the thrust factors were varied in addition to the above. The best fit case is indicated in Figure 4.7-42. If ignition delay between engines 2 and 1 is not included, the ratio between engines 1 and 2 thrust factors to obtain a good fit to the yaw gyro data must be increased to nearly 1.2.

#### 4.7.9 MIDCOURSE THRUST DURATION

To establish time intervals within which telemetry data indicate that the events of vernier ignition and shutdown must have occurred, all telemetry signals correlated to these events were examined. Acceleration error signal, pitch and yaw gyro errors, roll precession command, engine thrust commands, and engine strain gages are affected by ignition and shutdown. However, the gyro error signals do not show a sufficiently large change at ignition and are saturated at the expected time of shutdown. Also, midcourse was conducted in a constant acceleration mode, causing an acceleration error signal to appear as soon as the ignition command was received. The acceleration error, in turn, produced thrust commands; yet none of these events specifically required the vernier engines to be actually firing. Therefore, the signals employed to accurately establish the events of ignition and of shutdown were the strain gage channels, P-18, P-19, and P-20. Since vernier engine 3 strain gage gave no evidence of thrust from that engine, only P-18 and P-19 could be used.

The following specific times are defined for the thrust phase:

- 1)  $t_0$ , actual time at which vernier engines ignited
- 2)  $t_1$ , time when end of operational thrust occurred and thrusts began decaying toward zero
- 3)  $t_2$ , time when thrust had decayed to zero





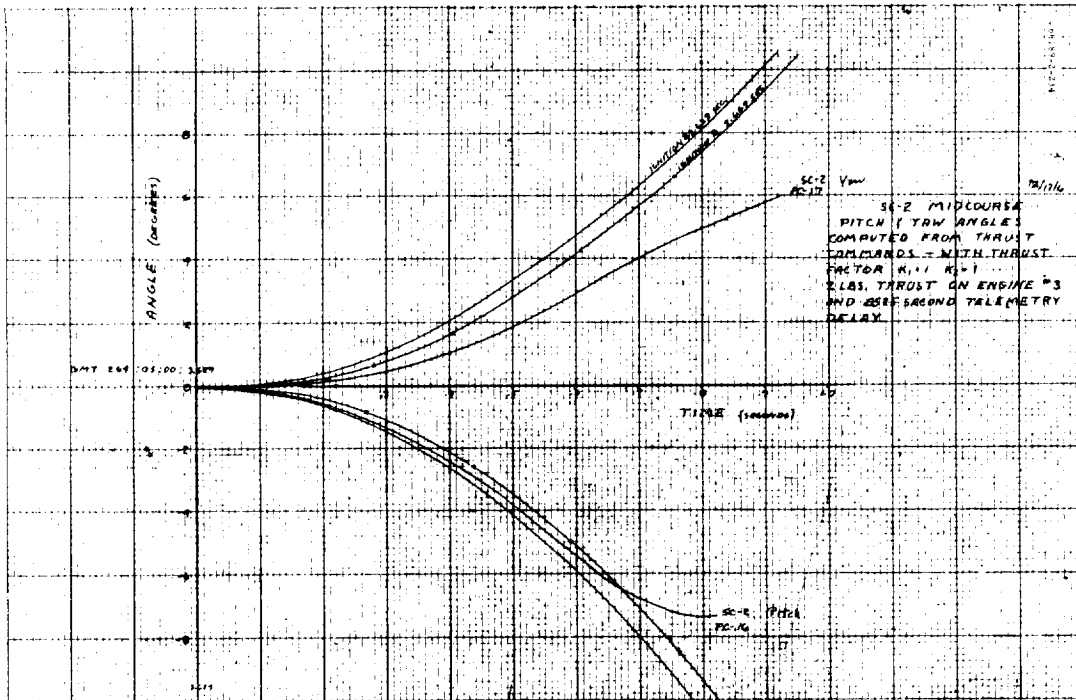


Figure 4.7-40. Pitch and Yaw Gyro Angles in First Second After Midcourse For (1,1)2 With 0.525-second Delay

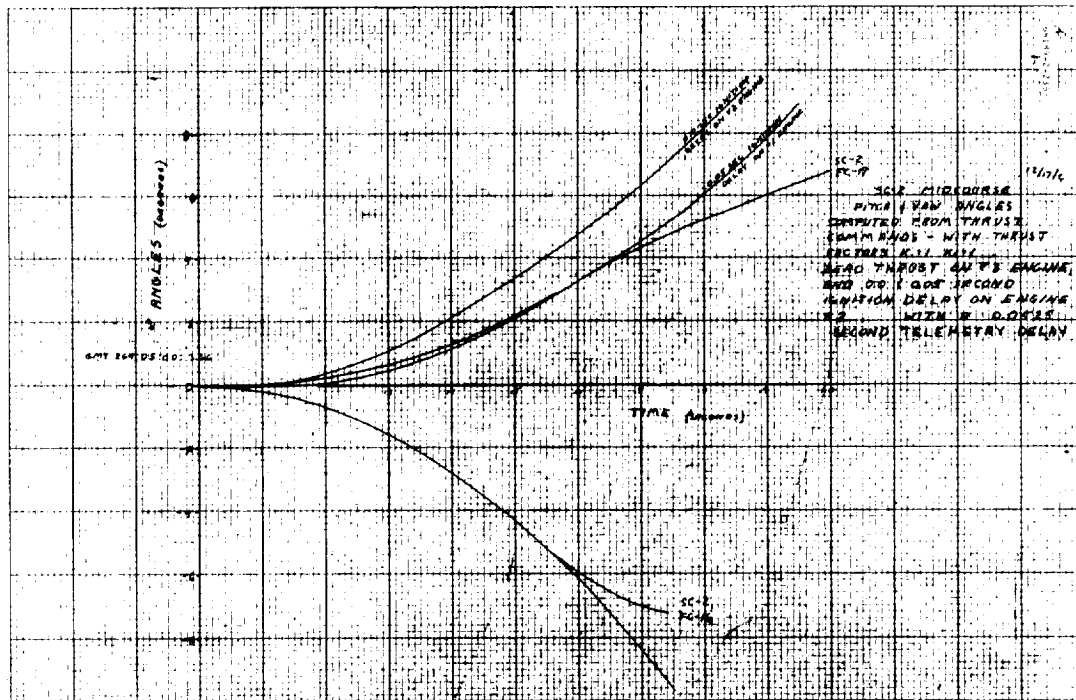


Figure 4.7-41. Pitch and Yaw Gyro Angles in First Second After Midcourse For (1,1)0 for 0.5-second Delay

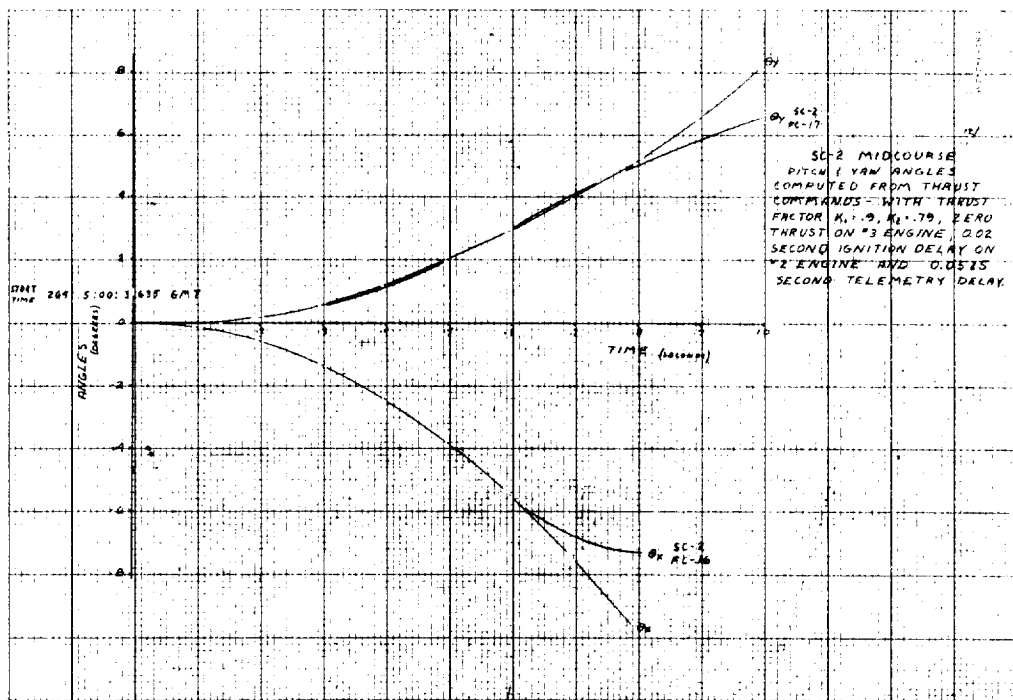


Figure 4.7-42. Pitch and Yaw Gyro Angles in First Second After Midcourse For (0.9, 0.79)0 With 0.525-second Delay

The occurrence of a given event can be restricted by a single telemetry signal to the interval between successive samples. When two telemetry signals are available, this interval can be further restricted, as seen in Figure 4.7-43, by combined estimates. This procedure has been used to determine the maximum and minimum values of the following in Figure 4.7-44:

$\Delta t_{o1}$  = operational vernier engine thrust, from ignition at  $t_o$  to start of thrust decay at  $t_1$

$\Delta t_{o2}$  = engine thrust period, from zero thrust at  $t_o$  to zero thrust at  $t_2$

$\Delta t_{12}$  = engine decay time, from start of decay at  $t_1$  to zero thrust at  $t_2$

#### 4.7.10 MOMENT OF INERTIA UNCERTAINTY

Two independent sources introduce errors in the moment of inertia matrix. The first source includes prelaunch weight and center of gravity uncertainties of each spacecraft component and, in addition, positional uncertainty (mounting error) relative to the spacecraft frame. The second source is the shift of the vernier engine propellant center of gravity away from the spacecraft roll axis ( $\hat{Z}$ ) due to an angular velocity about the  $\hat{Z}$  axis.

##### 4.7.10.1 Prelaunch Uncertainties

Values of the moments of inertia and the products of inertia are calculated by the Mission Mass Properties Profile computer program. The accuracy of the computed values for the moments of inertia was demonstrated on SC-2 when actual measurements (accurate to approximately  $\pm 1$  percent) of these moment of inertia matrix elements were performed. For those tests, the computed values were shown to agree with the measured moments of inertia within  $\pm 2.5$  percent for the dry landed weight configuration. No actual measurements of the spacecraft products of inertia have been made to determine the accuracy of the mass properties calculations.

The program calculates the entries to the moment of inertia matrix — moments of inertia and products of inertia — using weights and locations from specification drawings or actual measurements for all spacecraft units. The inertia matrix is determined with respect to the spacecraft coordinate origin, then axes are relocated by the parallel axis theorem at the center of gravity, which is also computed. When the actual weight and center of gravity location in the X-Y plane are measured at AFETR, the inputs to the program are "corrected" to ensure that the computed and measured values of weight and center of gravity position agree.

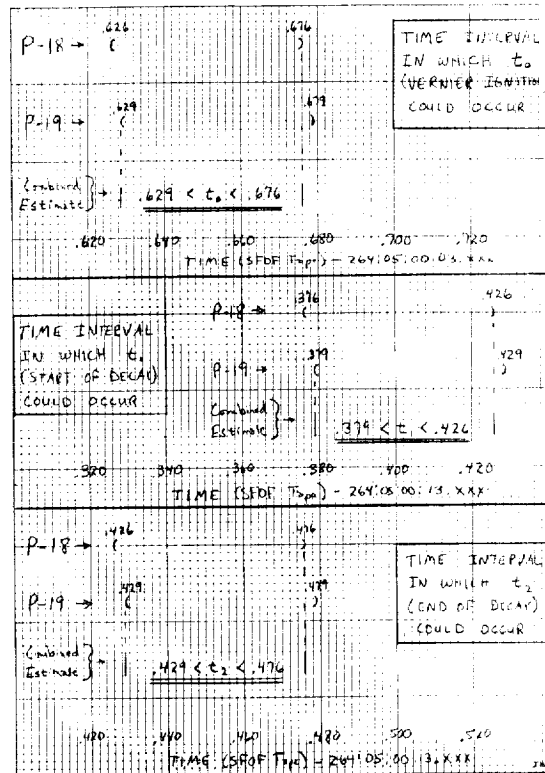


Figure 4.7-43. Time Interval in Which Vernier Ignition Could Occur

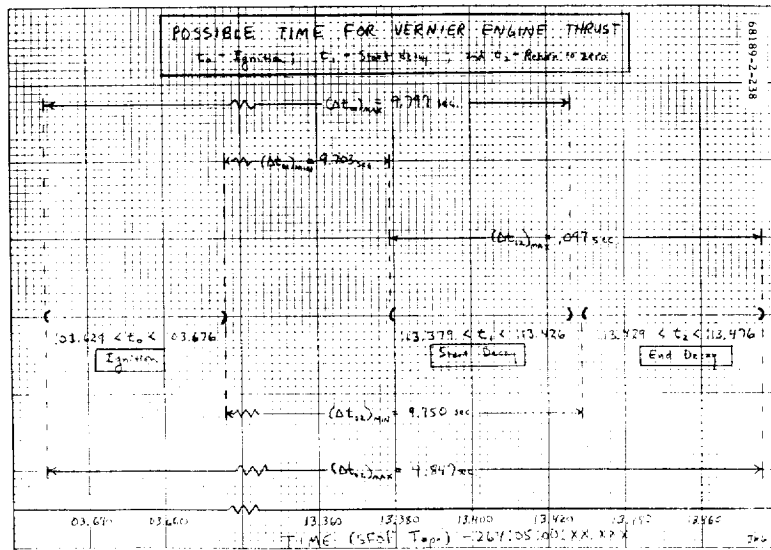


Figure 4.7-44. Possible Time for Vernier Engine Thrust

Analysis of this correction procedure has shown that, for the magnitude of correction in weight and center of gravity location required for SC-2, the products of inertia determined in subsequent computations could be in error by as much as 5 to 6 percent.

The spacecraft center of gravity vertical location is only known to within 0.25 inch and is not measured at AFETR when the spacecraft is in its final configuration. Transformation from the spacecraft coordinate origin to the center of gravity as the reference point for the inertia matrix introduces an error in  $I_{xx}$  and  $I_{yy}$  on the order of 1 percent due to uncertainty in the Z coordinate of the center of gravity.

This discussion is not intended to specify the inaccuracies involved in the moment of inertia matrix entries, but rather to point out that they exist and give a general indication of their magnitude. The accuracy of the products of inertia calculated by the mass properties program can not be specified since there are no measurements for comparison. However, test data indicate that the computed moments of inertia are within 2 to 4 percent of the true spacecraft values.

#### 4.7.10.2 In-flight Uncertainties

As the spacecraft spins about the roll axis ( $\hat{Z}$ ), the resultant centrifugal force causes the vernier engine propellant to shift away from the  $\hat{Z}$  axis (see Figure 4.7-45). This produces a change in the moment of inertia of each of the six propellant tanks about the  $\hat{Z}$  axis, which, in turn, change the spacecraft moment of inertia ( $I_{zz}$ ). To compute the maximum change in  $I_{zz}$ , assume the propellant in each tank moves such that its surface is parallel to the  $\hat{Z}$  axis. Figure 4.7-45 shows how the liquid moves from its prelaunch condition to the position in a zero g field under the influence of a centrifugal force. For ullage of 48.7 in<sup>3</sup> in each tank, the center of gravity shift is 0.28 inch. This shift corresponds to a propellant loading of 182.4 pounds and produces a change in  $I_{zz}$  from all six propellant tanks of 0.6 slug ft<sup>2</sup> or 0.3 percent.

#### 4.7.11 CLOSED-LOOP ANALOG SIMULATION RESULTS

Spacecraft behavior during midcourse thrusting has been investigated with a closed-loop mixed simulation involving flight-type flight control electronics hardware and an analog computer mechanization of vehicle dynamics (Figure 4.7-46). The major advantage of the mixed simulation approach is the accurate representation of all electronic saturation characteristics. Previous simulation studies, involving only analog computer equipment, were not successful at reproducing the thrust command profile during the 1-second period following midcourse ignition. This was due mainly to the difficulty of simulating the saturation characteristics which have a strong influence on actual vernier engine thrust levels.

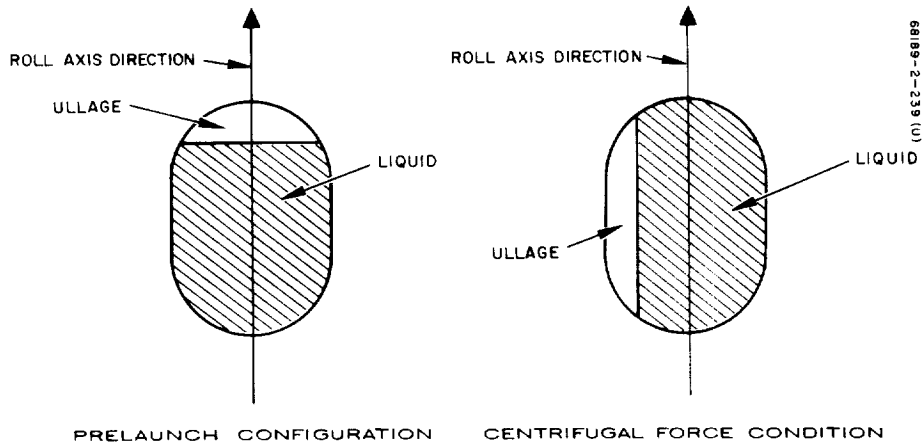


Figure 4.7-45. Effect of Rotation on Liquids in Fuel Tanks

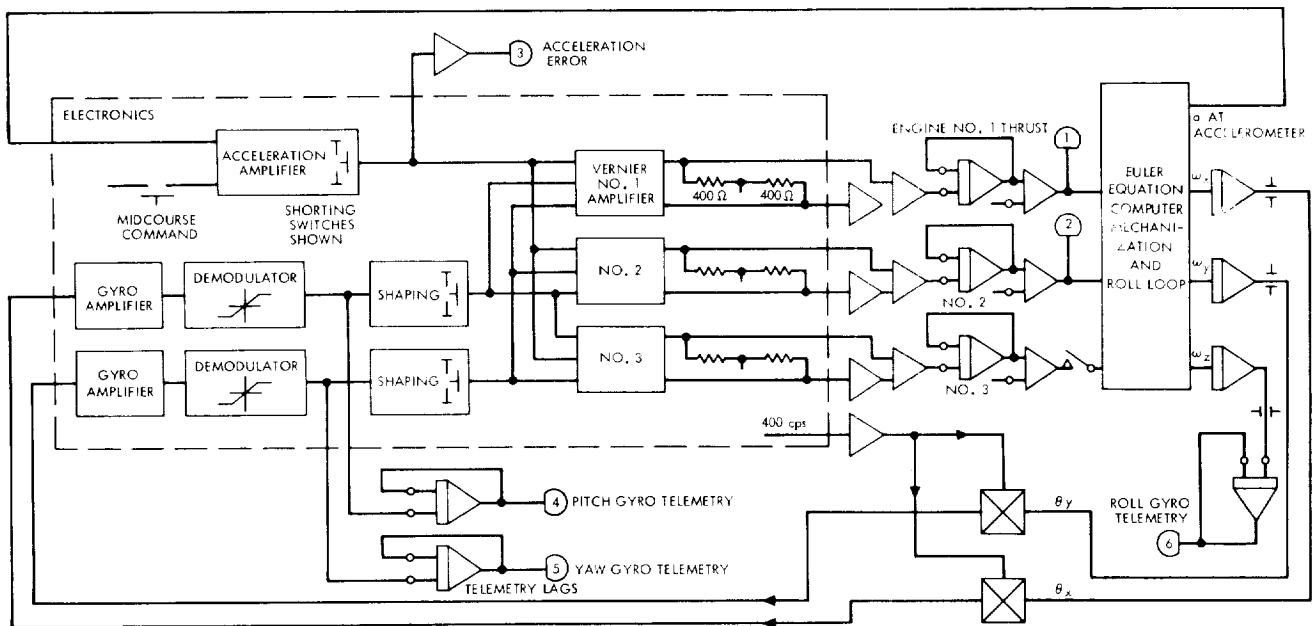


Figure 4.7-46. Analog Computer Mechanization

Also included in the mixed simulation (and not considered previously) were the effects of pitch and yaw gyro errors at midcourse ignition. Initial errors are possible up to  $\pm 0.4$  degree per axis due to limit cycle deadband and electronic offset, and have a strong influence on initial vernier thrust levels.

The assumed conditions for engine thrust response were zero thrust from engine 3 and normal thrust from engines 1 and 2. By selecting realistic initial gyro errors and engine ignition delays, a good reproduction of initial pitch and yaw gyro error telemetry signals was obtained (Figure 4.7-47). Also, simulated vernier engine thrust behavior showed qualitative agreement with strain gage telemetry signal waveforms. These results demonstrate that the initial pitch and yaw motions observed at midcourse ignition are reasonable responses under the conditions listed above.

The mixed simulation mechanization is shown in Figure 4.7-46 with the flight electronics contained in the dashed rectangle. All other equipment used is part of the analog computer. The engine throttle response, gyros, and telemetry lags were mechanized on the analog computer along with the spacecraft rigid body dynamics. The roll loop was mechanized entirely on the computer. Relay switching was set up to start analog computation when midcourse was commanded from the electronics. Vernier engine thrust was delayed from this command to simulate the ignition delays.

The computer simulation was run for the following condition:

Gyro saturation, degrees	Pitch 15.5 Yaw 21.6 Roll 16.8
Engine ignition delays, seconds	Engine 1 0.050 Engine 2 0.100
Initial conditions, volts	
Pitch demodulator output	0.0
Yaw demodulator output	0.26 (0.4 degree)

A recording of the simulation results is given in Figure 4.7-47 with telemetry data points superimposed on the vernier engine thrust traces ( $T_1$  and  $T_2$ ) and the pitch and yaw gyro errors ( $\theta_x$  and  $\theta_y$ ). The computer output matches the flight data reasonably well.

#### 4.7.12 SPACECRAFT MOTION

To describe the spacecraft motion for 20 seconds after the midcourse correction was attempted ( $t = 0$  sec), the digital spin program was used to generate time dependent curves for spacecraft axes motions, angular velocity, angular momentum, and sun vectors in both inertial and body coordinates. All of these quantities have been plotted for the same thrust level/moment of inertia combination of (1, 1) 3; (0, 0, 2, -10, -20, 0).

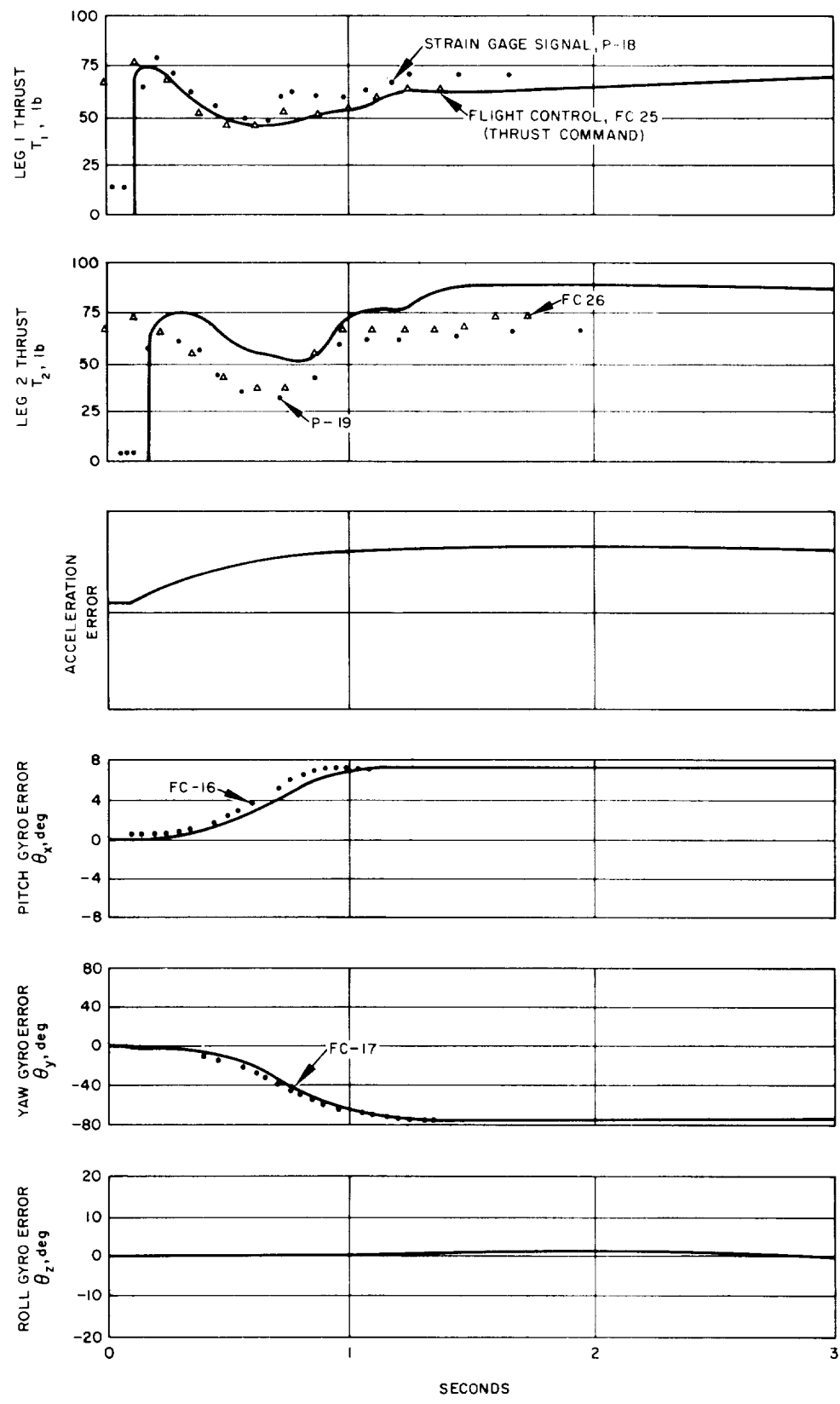


Figure 4.7-47. Mixed Simulation, Midcourse

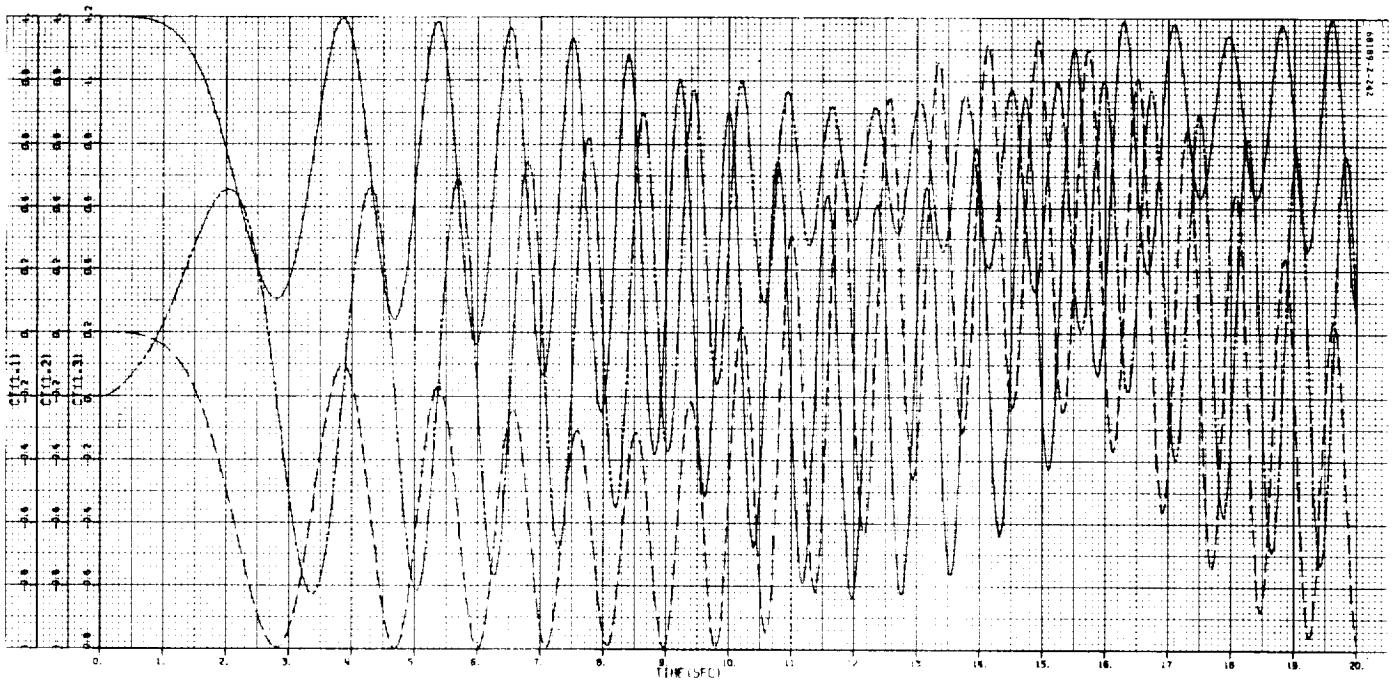


Figure 4.7-48 represents the elements of the direction cosine matrix (CT) which transforms a body fixed vector into inertial coordinates. To obtain the motion of the roll axis ( $\hat{Z}_B$ ) in inertial coordinates, for example, the direction cosines can be plotted at CT(1, 3), CT(2, 3), and CT(3, 3) of the  $\hat{Z}_B$  axis relative to the inertial  $\hat{X}_I$ ,  $\hat{Y}_I$ , and  $\hat{Z}_I$  axes, respectively, on a unit sphere. This presents a visual representation of the  $\hat{Z}_B$  axis for the 20-second period of interest. (The motion of the spacecraft pitch ( $\hat{X}_B$ ) and yaw ( $\hat{Y}_B$ ) axes are obtained similarly.) Figure 4.7-49 shows the time dependent behavior of angular velocity and angular momentum. Both the spin and angular momentum magnitudes increase almost linearly until vernier engine thrust is terminated (9.8 seconds) and are constant from then until the next thrust period.

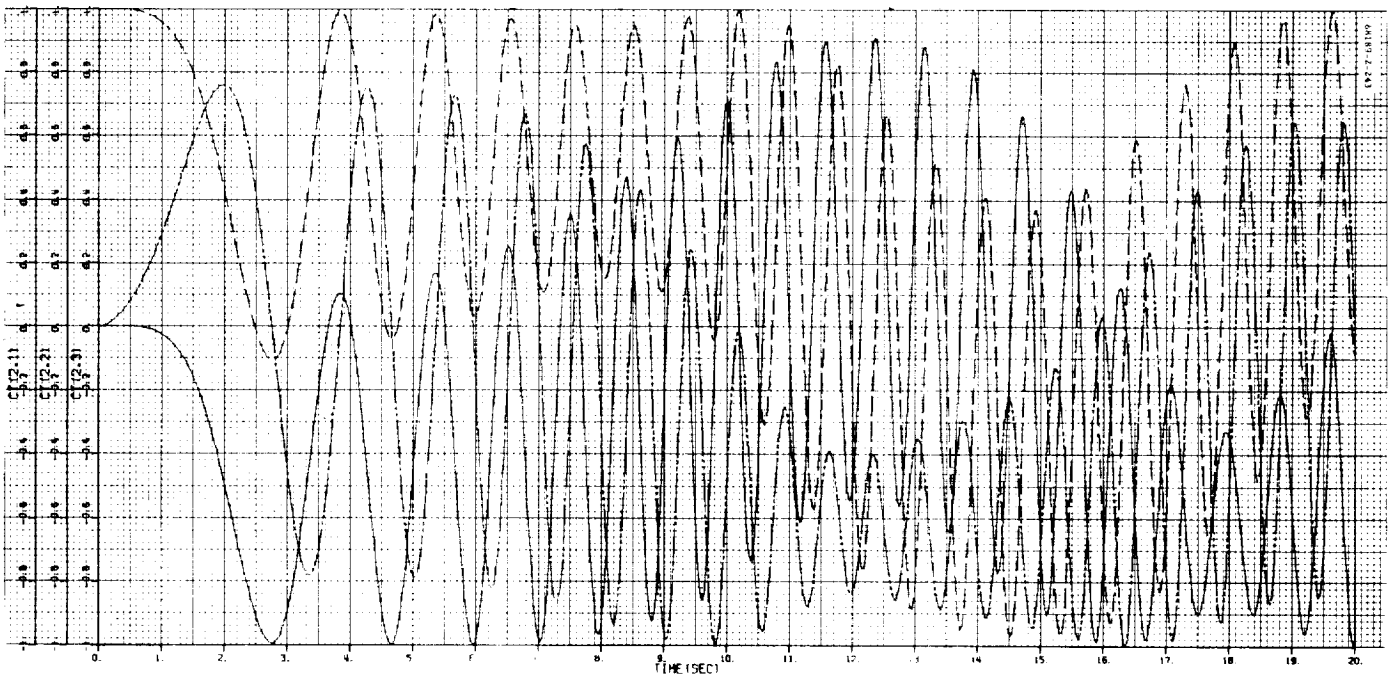
Figures 4.7-50 through 4.7-53 describe the spacecraft angular velocity vector ( $\dot{W}$ ) motion in spacecraft and inertial coordinates. Figure 4.7-50 shows the components of  $\dot{W}$  in inertial coordinates. The X, Y, and Z components increase when the vernier engines are thrusting and then oscillate about values of approximately -350, 300, and -22 deg/sec, respectively. Figure 4.7-52 is a graph of the components of  $\dot{W}$  expressed in body coordinates. After thrust has been terminated, the components are sinusoidal in nature. Figure 4.7-53 gives the clock angle  $\phi$  and the cone angle  $\theta$  for the direction of  $\dot{W}$  in spacecraft coordinates. Figure 4.7-54 shows how the direction of the angular momentum changes over the 20-second period of observation in inertial and body coordinates, respectively. In inertial coordinates, both the cone angle and clock angle are essentially sinusoidal from 4 to 9.8 seconds and, as would be expected, are constant from 9.8 seconds until the next vernier engine firing. In body coordinates, the clock angle completes one revolution, and the cone angle turns 350 degrees in this same 20-second period. Figure 4.7-55 gives the clock angle and cone angle for the sun vector expressed in body coordinates. When the cone angle exceeds 90 degrees (roughly), the sun illuminates the solar panel. Figure 4.7-56 is a time plot of the computed gyro output angles.

#### 4.7.12 REFERENCES

1. C. T. Dorsett, "Mass Properties Monitoring Report, SSD 64226R, Revision C, Surveyor SC-2," IDC 2225.05/464, 15 September 1966.
2. J. H. Green, "Correction of Throttle-Valve Current Telemetry for SC-1 and SC-2," IDC 2292/32, 23 August 1966.
3. "Surveyor Spacecraft Monthly Assessment Report," SSD 68202R, 21 September 1966.
4. J. H. Spotts, "Secondary Sun Sensor Performance Characteristics," Report No. SEAR-16, 26 October 1965.

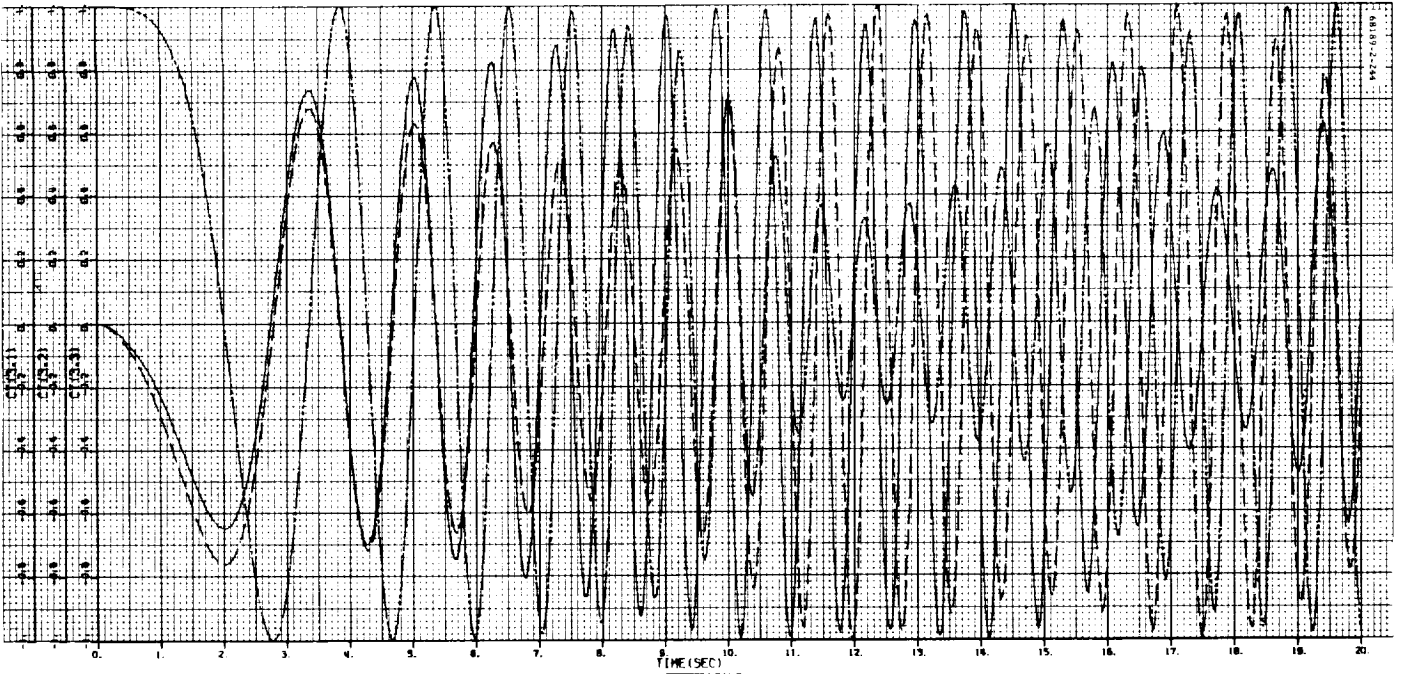


a) CT (1,i)



b) CT (2,i)

Figure 4.7-48. Direction Cosine Matrix (CT) Elements for  $[1, 1]_3$ ,  $[0, 0, 2, -10, -20, 0]$



c) CT (3, i)

Figure 4.7-48(continued). Direction Cosine Matrix (CT) Elements for  $[1, 1] 3, [0, 0, 2, -10, -20]$

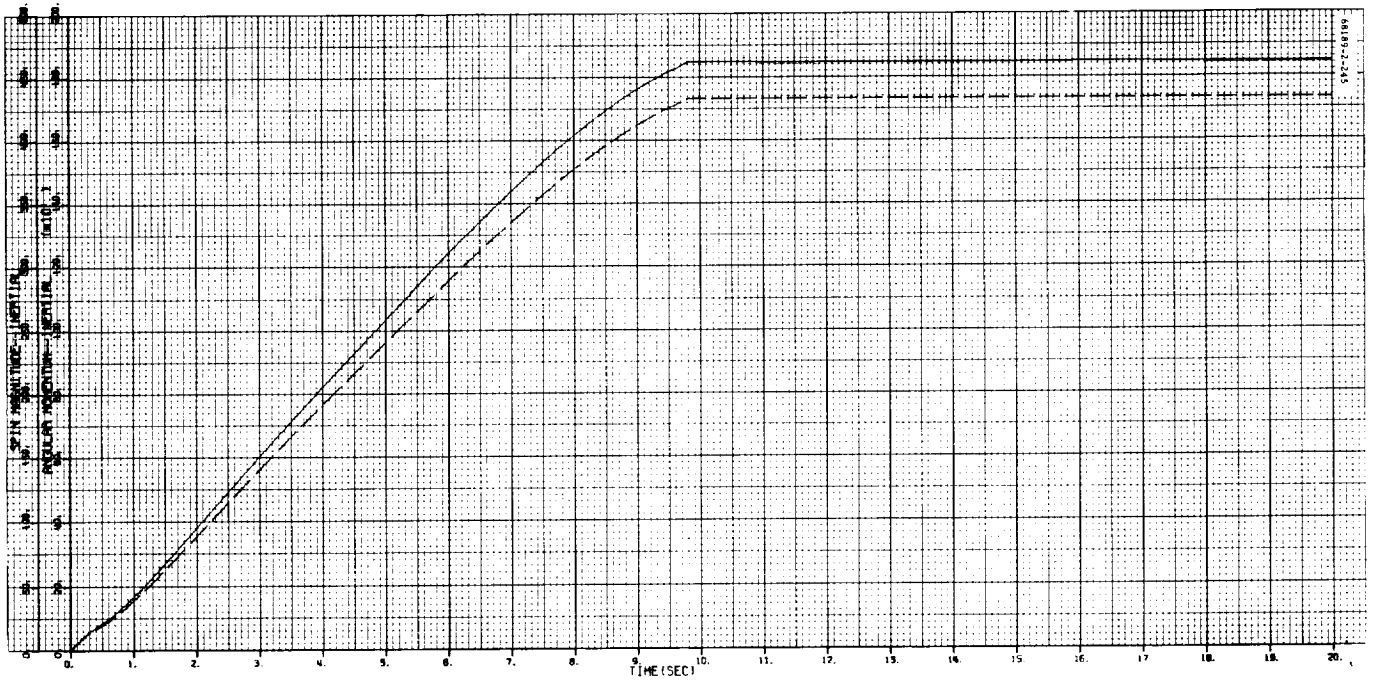


Figure 4.7-49. Inertial Spin Magnitude and Angular Momentum

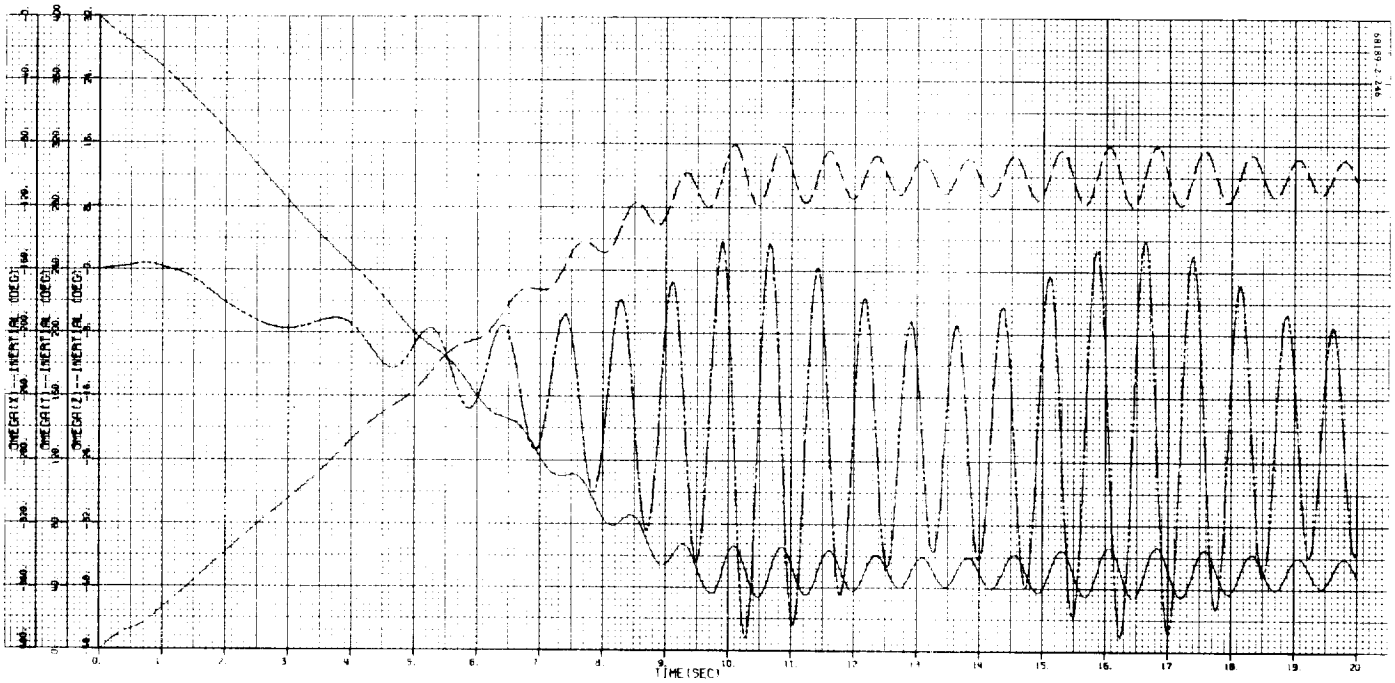


Figure 4.7-50. Angular Velocity Vector Components, Inertial Coordinates

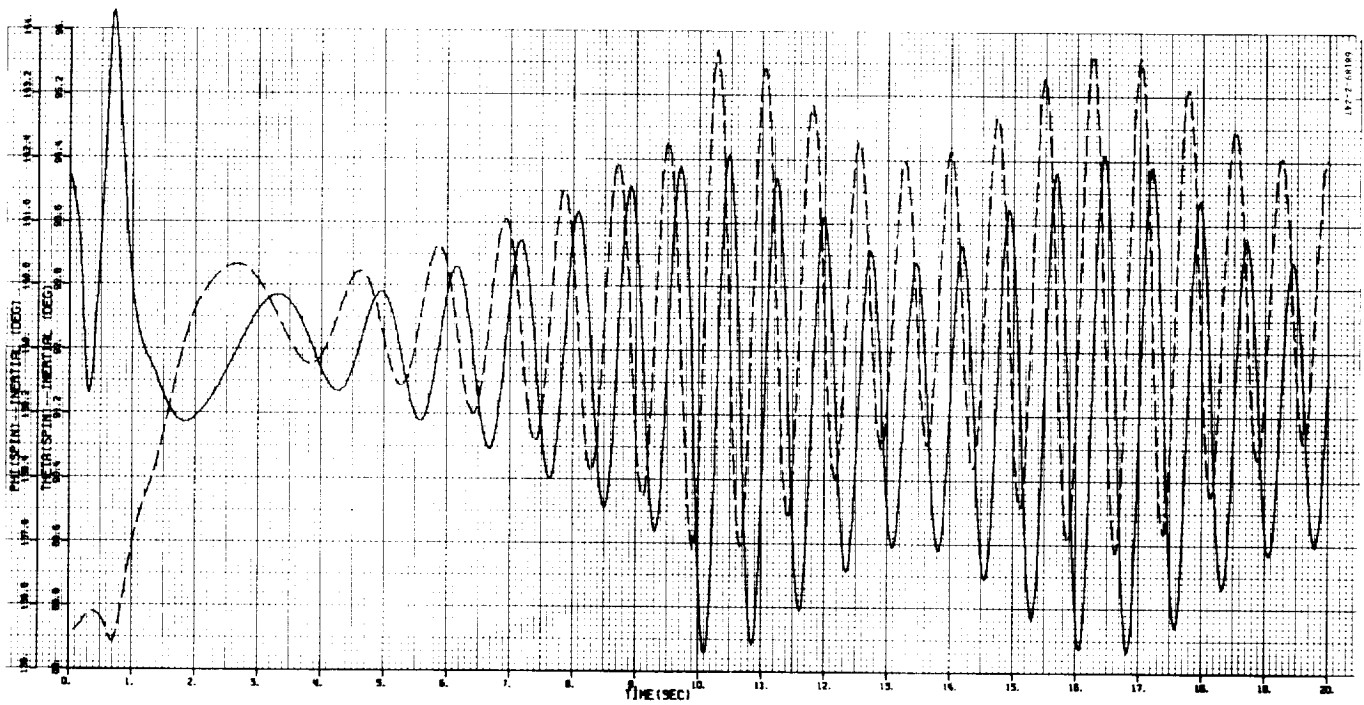


Figure 4.7-51. Q and  $\theta$  Inertial Coordinates

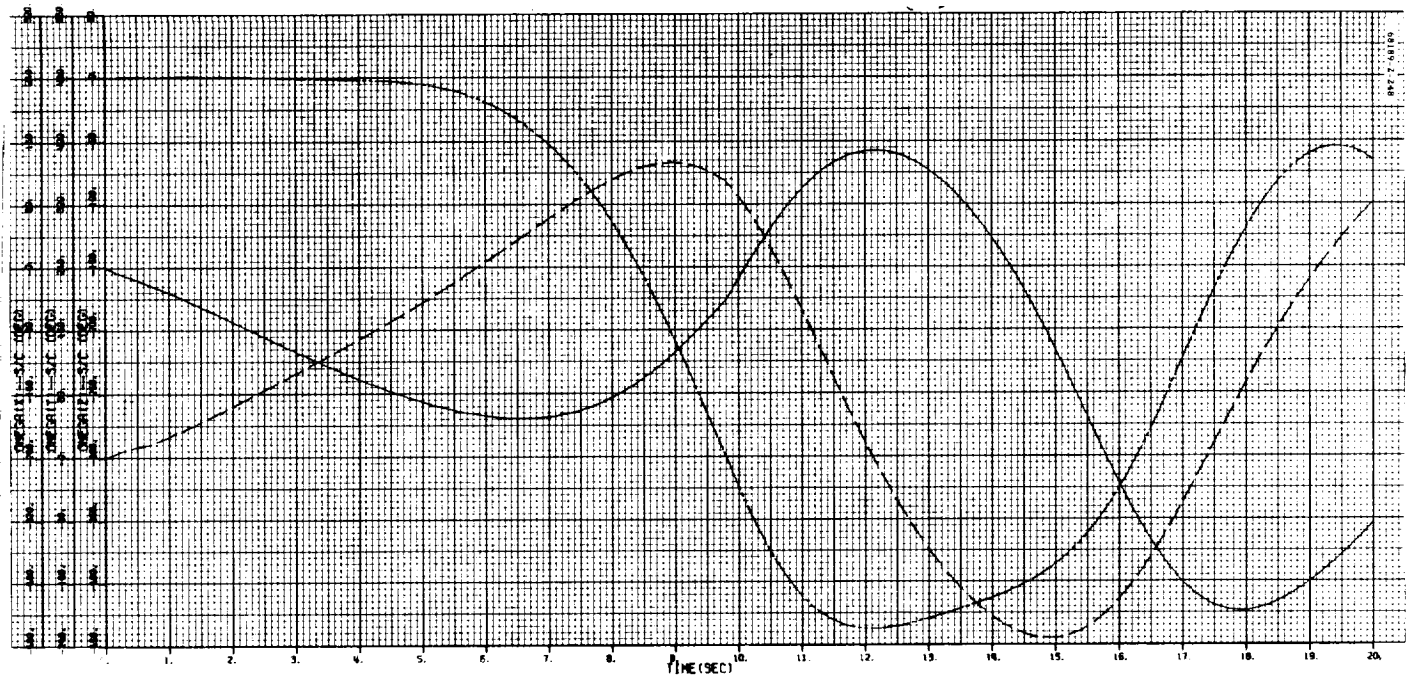


Figure 4.7-52. Angular Velocity Vector Components, Spacecraft Coordinates

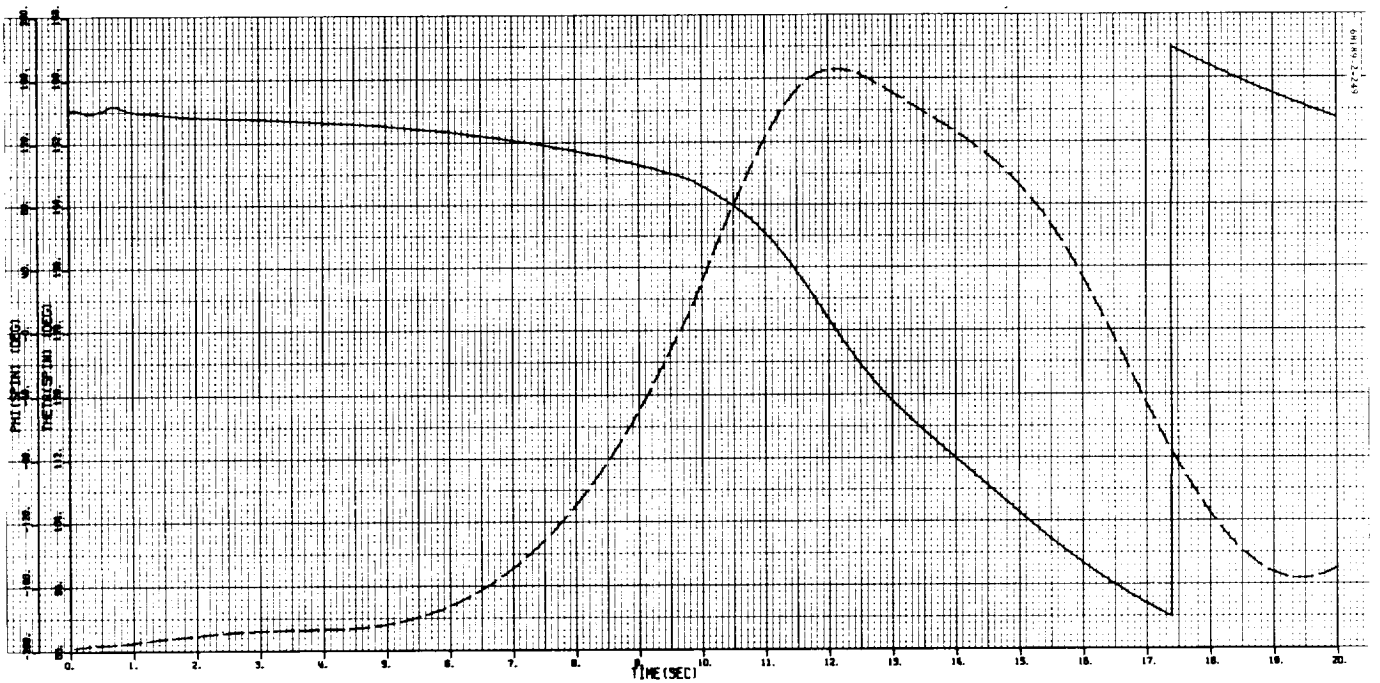
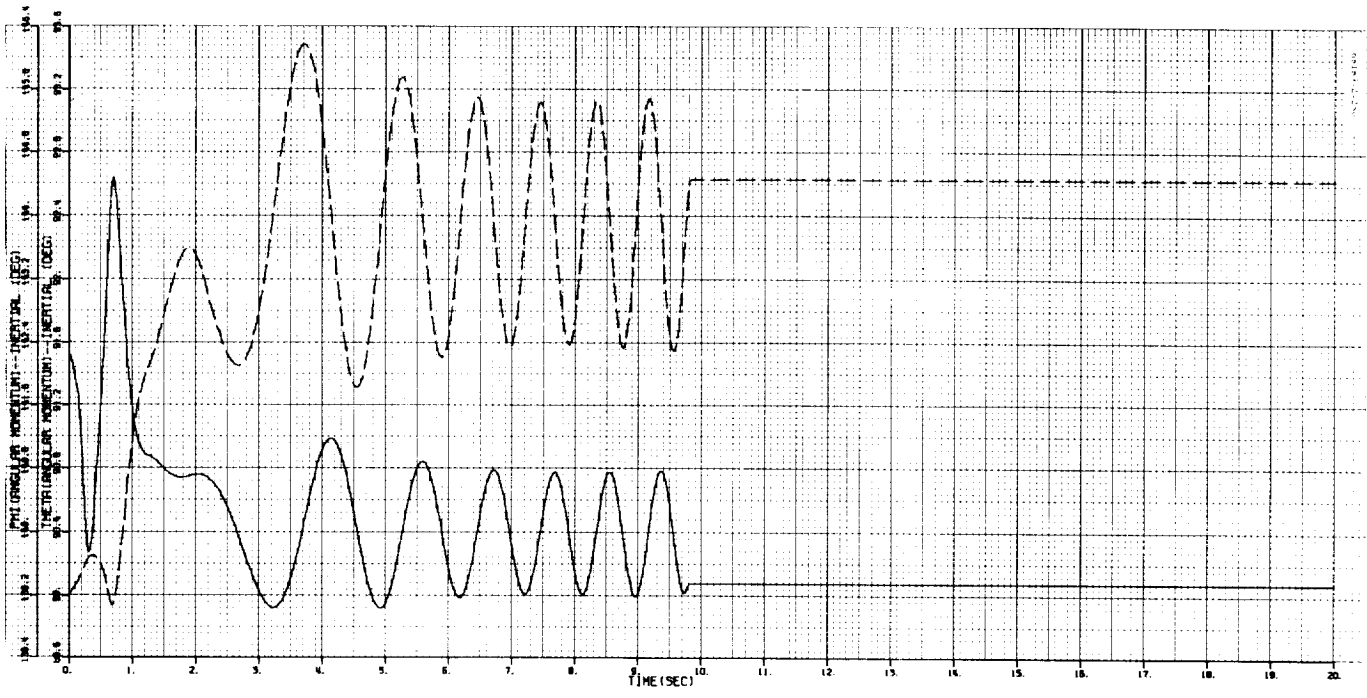
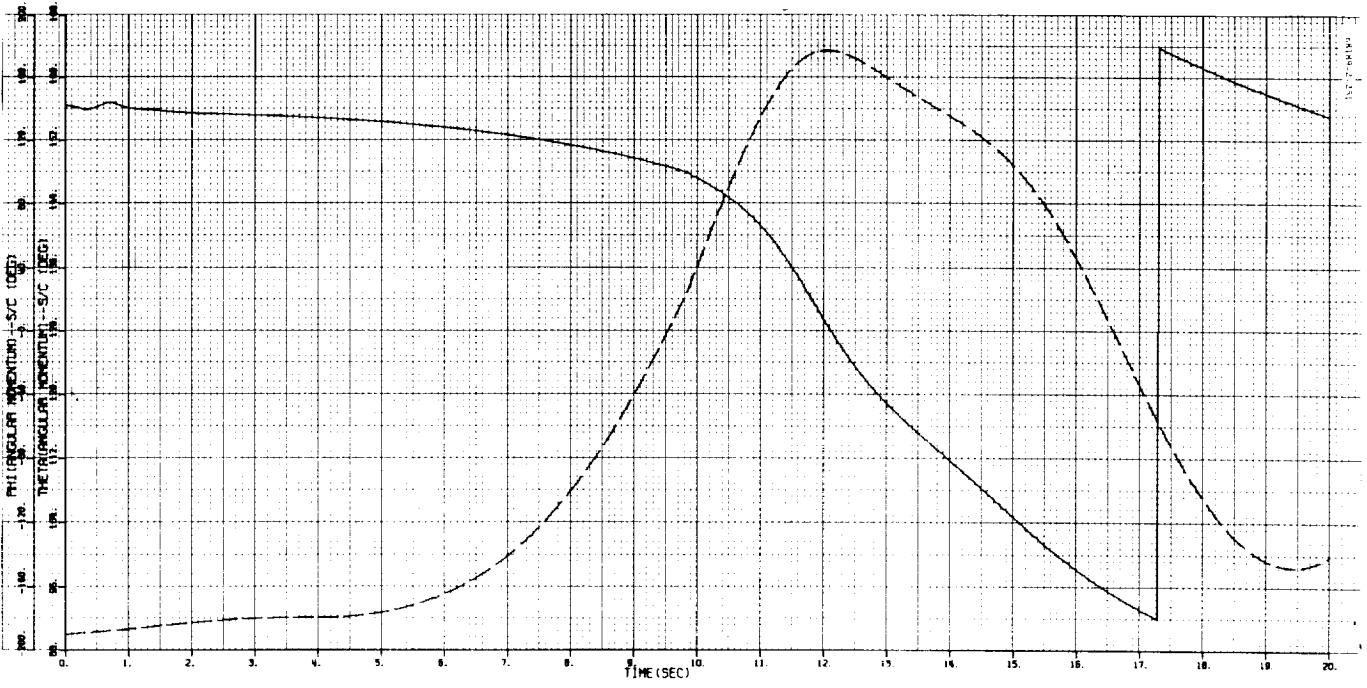


Figure 4.7-53. Q and  $\theta$  Spacecraft Coordinates



a) Inertial Coordinates



b) Spacecraft Coordinates

Figure 4.7-54. Angular Momentum Components

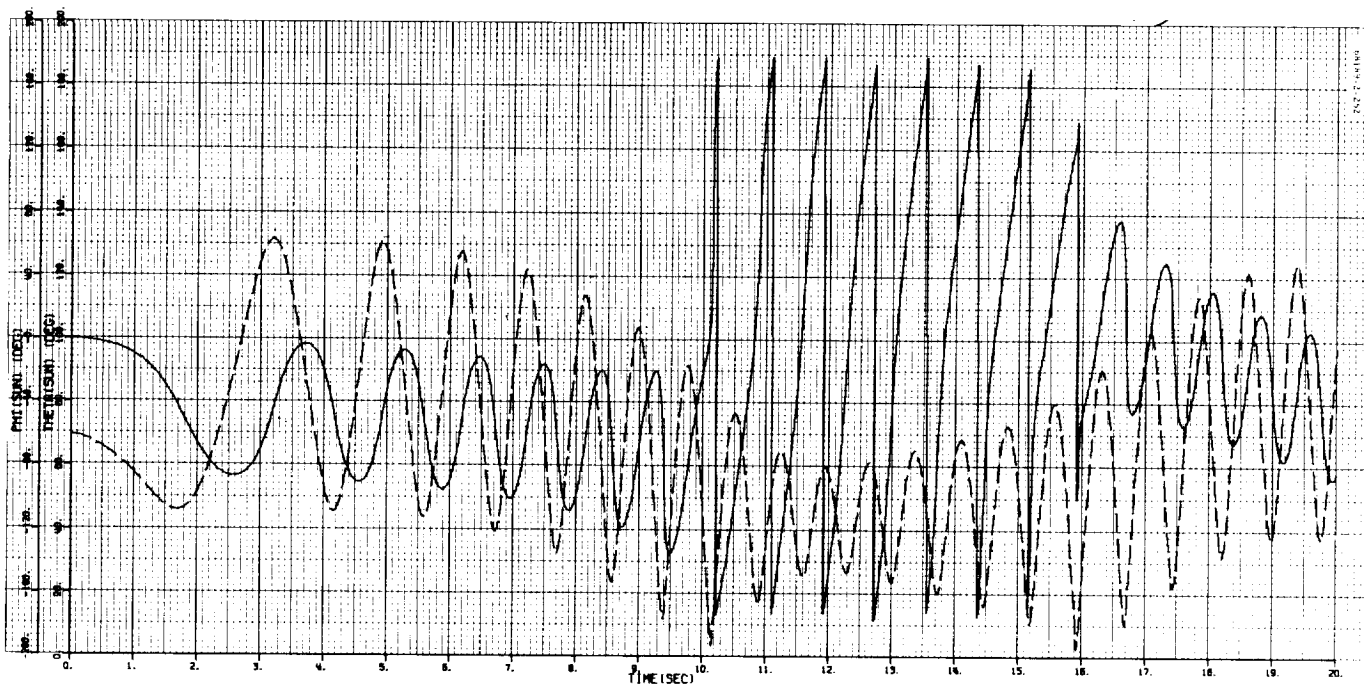
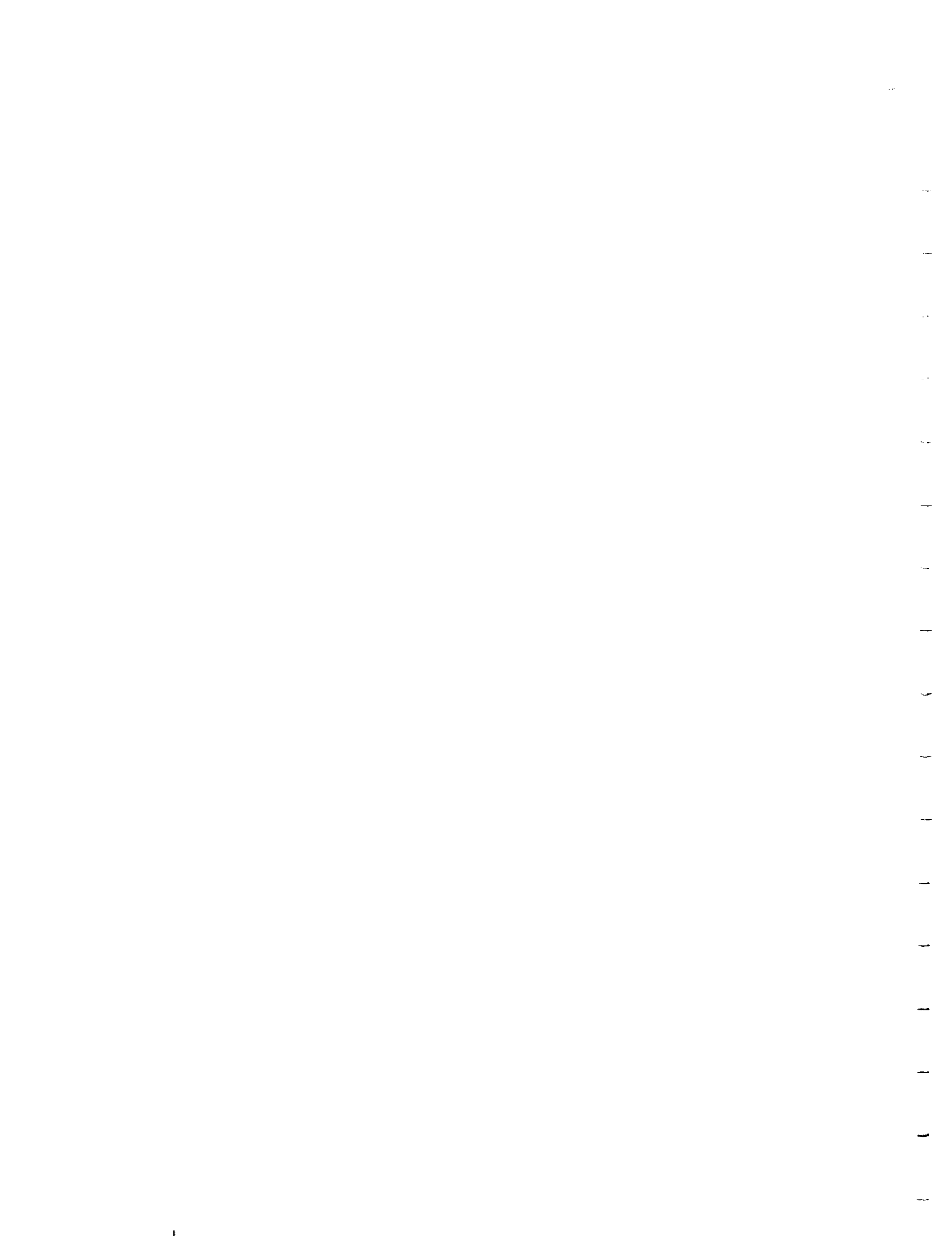


Figure 4.7-55. Clock and Cone Angles for Sun Vector, Spacecraft Coordinates



Figure 4.7-56. Gyro Output Angles





## 4.8 POSTMIDCOURSE SEQUENCES

### 4.8.1 OPERATIONAL DISCUSSION

Additional 2-second firings were recommended to attempt to clear the vernier engine 3 problem, and, if successful, to possibly restabilize the spacecraft. A firing sequence, using the midcourse thrusting level, was attempted at L + 18H56M and again at L + 19H18M without success.

Since the spacecraft was rotating such that solar panel output was zero, the only sources of power for the spacecraft loads were the main and auxiliary batteries. To conserve energy, flight control coast phase power was turned off periodically (i. e., power on for 40 minutes and off for 90 minutes) while maintaining the flight control gyro and electronic temperatures above 70 and 0° F limits, respectively.

An interrogation of modes 2 and 4 at hourly intervals was initiated. Also, auxiliary battery mode was commanded when the auxiliary battery temperature was 35° F to utilize the energy of this battery and to keep it from approaching its lower operational limit.

Since a possible cause of the vernier engine failure was a stuck fuel regulator valve, it was decided to pulse fire the engines five times (with a 0.2-second period per firing and a 5-minute interval between firings) and then fire the engines for a 2-second interval. This sequence was first used at L + 31H12M and completed at L + 35H2M. Engine 3 did not appear to fire.

Four additional attempts to achieve thrusting with the same procedure were made at hourly intervals (i. e., initiated at L + 36H28M, L + 37H29M, L + 38H45M, and L + 39H45M), but all proved ineffective. It was then decided to try a higher thrust level with less rise time by placing the flight control subsystem in the postretro eject condition. This was accomplished by commanding retro sequence mode on and emergency retro eject prior to turning on the flight control thrust phase power, thereby preventing the ejection of the main retro engine while placing the flight control programmer in the desired state. This sequence was completed at L + 41H11M with the commanding of vernier engine ignition for approximately 2 seconds controlled manually (i. e., engine shutoff by ground command). Again, the results were negative. With each attempt to fire the engines, the spacecraft rotation rate increased so that by the time of the postretro eject thrusting completion, the spin rate was approximately 1.54 rps.

Between the second and third vernier engine firings, the planar array was commanded upward from its launch position to lower the solar panel for partial illumination. This was desirable for two reasons: 1) to obtain more energy for the spacecraft, and 2) to illuminate some of the secondary sun sensor cells (mounted on the solar panel face) so that the actual spacecraft orientation could be established. Two attempts, at L + 38H13M and L + 38H19M, to move the planar array were unsuccessful, apparently due to the opposing force created by the spacecraft spinning.

Preparations were then made for the following operations: 1) stepping the solar panel, illuminating its active face and the secondary sun sensor cells, 2) determining whether a zero-shift had occurred in the helium pressure telemetry signal by dumping the helium and recording the pressure decay function, 3) evaluating the capability of the main battery to continue to supply power reliably under the heavy terminal descent load conditions (i. e., flight control thrust phase power on, high power transmitter on, RADVS on, etc.) when the remaining battery energy is low (i. e., on the order of 15 to 30 amp-hr remaining), and 4) firing the main retro engine in the normal terminal descent mode. At L + 42H22M, the unlock solar panel squib was blown by ground command, resulting in a solar panel position telemetry signal change of approximately 23 degrees, indicating that the force on the panel created by the spacecraft spinning caused the panel to move. Further attempts to move the panel by command were mostly unsuccessful.

At L + 43H13M, a new sequence for pulse firing the engines five times (0.2 second for each firing, with 1 minute between firings), followed by a 20-second firing in the postretro eject mode, was executed, ending with the 20-second thrusting at L + 43H33M. Although vernier engine 3 temperature rose approximately 24° F (as compared to approximately 100° F for engines 1 and 2) during the 20-second firing, the engine did not respond properly.

At L + 44H41M, the helium dumping sequence was initiated, confirming that a zero shift in the helium pressure telemetry had occurred and accounted for the relatively large decrease when the system was initially pressurized.

At L + 44H48M, flight control thrust phase power and RADVS were turned on. At this time, the estimated energy remaining in the main battery was 10 amp-hr. The bus voltage dropped from 19.4 to 17.3 volts, with a load of 47 amperes on the battery. RADVS was then turned off before proceeding with retro firing.

At L + 45H2M, the emergency AMR command was sent to initiate the retro engine firing sequence. Ignition of vernier engines 1 and 2, as well as the main retro engine, were verified. Contact with the spacecraft was lost approximately 30 seconds after retro engine ignition.

Although there were no more telemetry or tracking data available, the spacecraft continued on its trajectory toward the moon, striking the surface at approximately 265:03:42:54 (flight time was 63.2 hours). The landing location is believed to be 0.55 degree north latitude, 0.83 degree west longitude. These data were taken from the last trajectory prediction made after midcourse, and are not as accurate as data from a normal flight.

#### 4.8.2 ANALYSIS OF SPACECRAFT ROTATIONAL MOTION

Simulation of spacecraft motion during midcourse firing, as discussed in Section 4.7 depends on the integration of the equations of motion under a set of assumptions concerning engine performance and other pertinent variables. This simulation attempts to find the set of assumptions which allow best approximation of the observed data. It would be desirable to determine from independent sources as many of the parameters of spacecraft motion as possible, so that these could be compared to the values from powered flight simulation, thus providing an additional check on the results of the simulation. Useful parameters for this purpose are the motion of the spin vector in spacecraft coordinates and the location of the angular momentum vector in inertial coordinates. Angular momentum in spacecraft coordinates can be determined from the spin vector and will change as the spin vector moves.

A number of independent types of data provide an indication of spacecraft rotational motion after midcourse. These are as follows:

- 1) Spacecraft temperature distribution
- 2) Gyro crossovers shortly after vernier shutoff
- 3) Variation of DSIF received signal strength
- 4) Behavior of solar panel elevation servo
- 5) Retro accelerometer output during retro firing

##### 4.8.2.1 Spin Vector Orientation From Temperature Distribution

The variation of temperature as a function of location on the spacecraft is the most positive indication of the general direction of the spin axis, although these data provide a less precise determination of the direction of this axis. The thermal analysis indicates that the spacecraft-sun vector was in the quadrant bounded by the +X, -Y, and +Z spacecraft axes (Reference 1). Figure 4.8-1 shows the bounds of the probable sun vector locations. The spin vector would also have to be within this envelope.

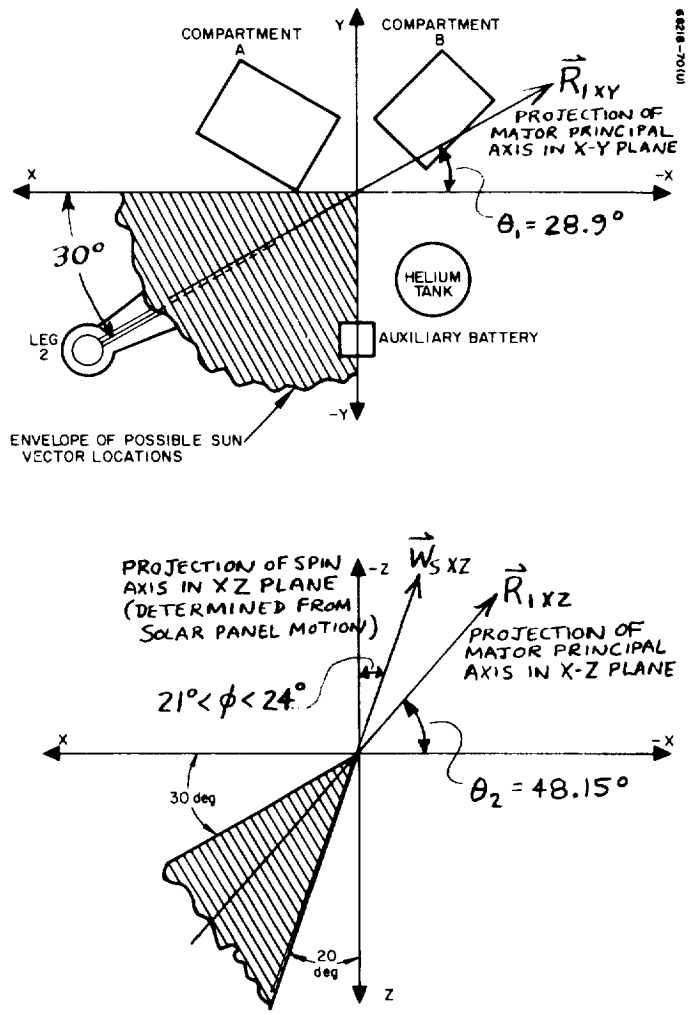


Figure 4.8-1. Probable Location of Sun Vector From Thermal Analysis

#### 4.8.2.2 Gyro Zero Crossings and Postmidcourse Tumbling Dynamics

When the vernier engines were **shut off after midcourse**, the spacecraft was spinning with a period of about 0.8 second, and the spin axis was precessing with a period of 12.5 seconds. About 7 minutes after start of midcourse thrust, the precession was essentially damped out by the non-conservative forces in the spacecraft and the gas jet operation, resulting in a pure spin. The axis of spin was that spacecraft principal axis of inertia with either the largest or the least moment of inertia. In this case, analysis shows that it was the former. This principal axis would also be the axis of precession after midcourse and later firings. By diagonalizing the inertia matrix of the spacecraft, the direction of this principal axis,  $\bar{R}$ , was found to be as follows (Reference 2):

$$\begin{aligned} \theta &= -54^{\circ}15' \\ \phi &= 71^{\circ}13' \quad \text{or} \\ \psi &= -41^{\circ}50' \end{aligned} \quad \begin{aligned} \theta_1 &= 28.9^{\circ} \\ \theta_2 &= 41.8^{\circ} \end{aligned}$$

where  $\theta, \phi, \psi, \theta_1$ , and  $\theta_2$  are defined in Figure 4.8-2. When the precession had been damped out, the pitch and roll gyro error signals were saturated negatively and the yaw gyro error signal was saturated positively (both in rate and inertial mode). This verifies that the spin vector was in the quadrant indicated by thermal analysis.

Since the spin is about a principal axis, this axis must also contain the angular momentum vector. Figure 4.8-1 shows the location of this vector relative to the sun direction. If the angular momentum was about the computed principal axis, it can be seen that the projections in the XZ plane of the sun-spacecraft vector and the inertial angular momentum vector were within about 20 degrees of each other.

An attempt to determine, independently of the powered flight simulation, the angular motion and orientation of the spacecraft at vernier shutoff was made by fitting the pitch and yaw gyro zero crossings after vernier shutoff to Eulers equations for a force-free tumbling body, as follows:

$$\begin{aligned} I_1 \dot{W}_1 &= (I_2 - I_3) W_2 W_3 \\ I_2 \dot{W}_2 &= (I_3 - I_1) W_3 W_1 \\ I_3 \dot{W}_3 &= (I_1 - I_2) W_1 W_2 \end{aligned} \quad (1)$$

where

$W_1, W_2$ , and  $W_3$  = angular rates about the principal axes

$I_1 > I_2 > I_3$  = moments of inertia about these axes

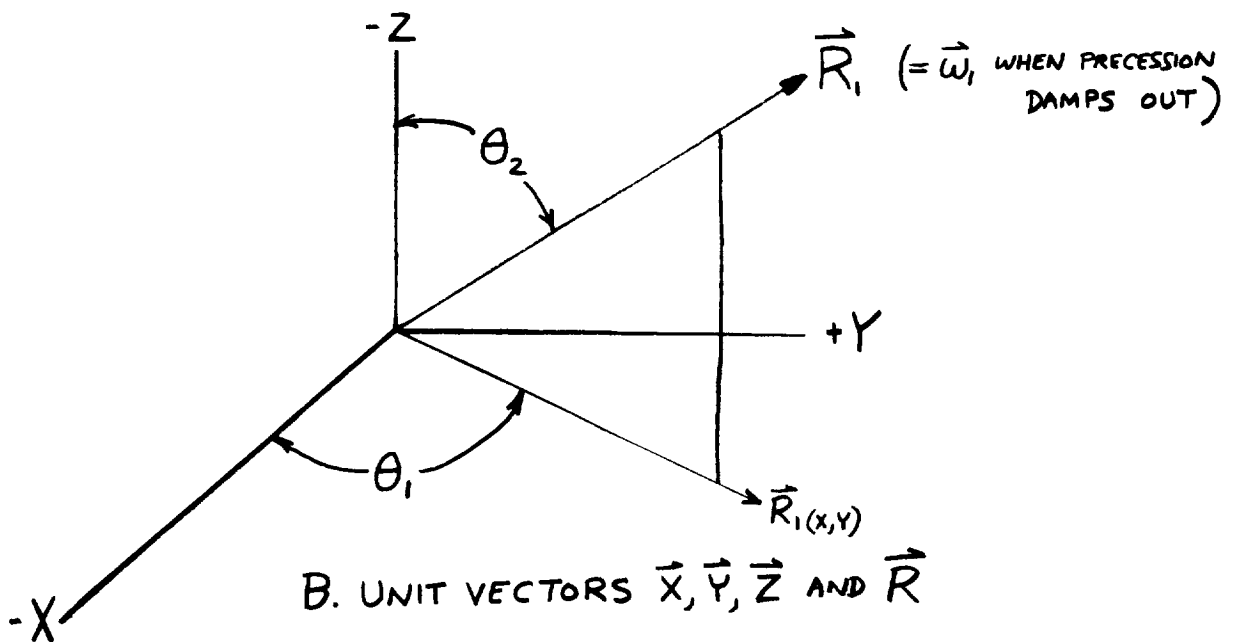
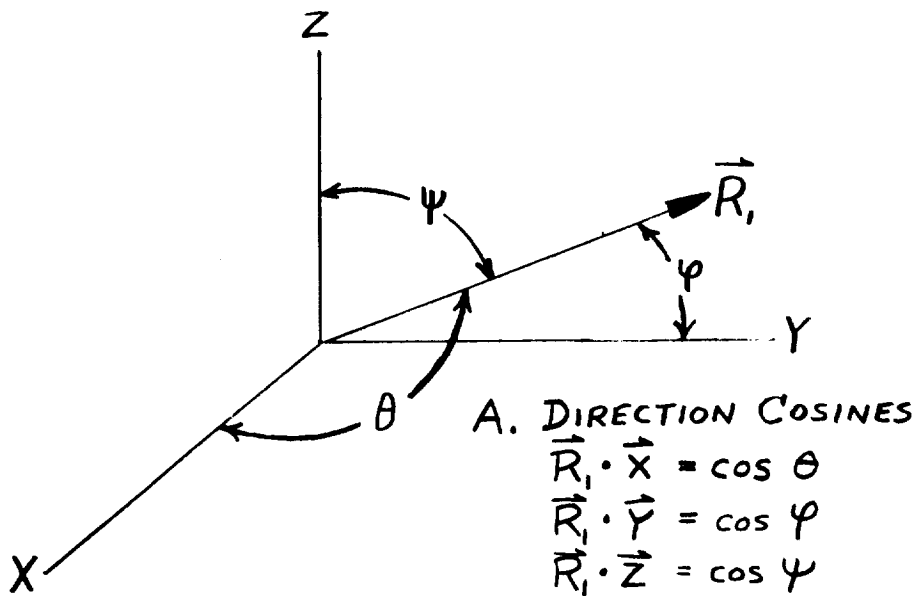


Figure 4.8-2. Definition of Direction Cosines and Unit Vectors

The solution of these equations is the following Jacobian elliptic functions:

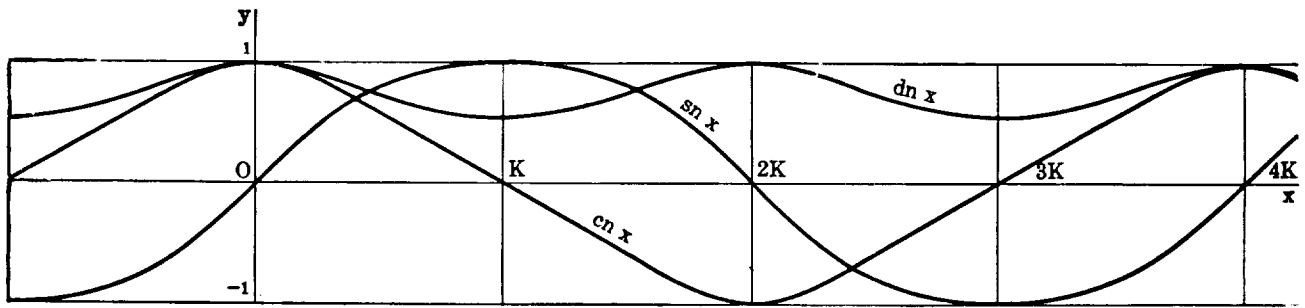
$$\begin{aligned} W_1 &= \alpha \operatorname{dn} [P(t - t_0)] \\ W_2 &= \beta \operatorname{sn} [P(t - t_0)] \\ W_3 &= \gamma \operatorname{cn} [P(t - t_0)] \end{aligned} \quad (2)$$

A typical plot of  $\operatorname{sn}(X)$ ,  $\operatorname{cn}(X) = \sqrt{1 - \operatorname{sn}(X)^2}$ , and  $\operatorname{dn}(X) = \sqrt{1 - k^2 \operatorname{sn}(X)^2}$  is shown in Figure 4.8-3.  $\alpha$ ,  $\beta$ ,  $\gamma$ ,  $P$ , and  $R$  are constants which depend on  $I_1$ ,  $I_2$ , and  $I_3$ , the total angular momentum and total rotational energy. Note that  $W_1 = \alpha \operatorname{dn}[P(t - t_0)]$  never changes sign. This is because the spin vector precesses about principal axis 1 and is never more than 90 degrees away from it.  $W_2$  and  $W_3$  do cross zero due to the precession (Figure 4.8-4). Later, when the precession is damped out,  $W_1 = W$  and  $W_2 = W_3 = 0$ .

The pitch and yaw gyro data following vernier shutoff are shown in Figure 4.8-5. The roll gyro was in negative saturation throughout the period. Although the gyros were in the inertial mode and would have normally measured angular position, in the present case the only quantitative data that can be derived are the times of zero gyro rates. The high angular rates precess the gyro output axis against the stops until the angular rate reverses polarity (due to precession). When the angular rate changes polarity, the gyro is precessed to the other stop. If the gyro dynamic lags are ignored, the gyro will leave the stops at exactly the time the rate reverses sign. The gyro telemetry measurement will unsaturate slightly later because the telemetry range is less than the gyro range (8 degrees versus 15 degrees). Thus, it can be assumed that  $W_P$  or  $W_Y = 0$  shortly before the pitch or yaw gyro telemetry measurement unsaturates.

Figure 4.8-5 shows that  $W_P$  is negative for longer periods than it is positive, and  $W_Y$  is positive for longer periods than it is negative.  $W_Z$  is always negative. This results from the fact that the spacecraft X, Y, and Z axes are not coincident with the principal axes. The equations for pitch yaw and roll rate are as follows:

$$\begin{aligned} W_P &= A_{11} W_1 + A_{12} W_2 + A_{13} W_3 \\ W_Y &= A_{21} W_1 + A_{22} W_2 + A_{23} W_3 \\ W_Z &= A_{31} W_1 + A_{32} W_2 + A_{33} W_3 \end{aligned} \quad (3)$$



Graphs of  $\text{sn } x$ ,  $\text{cn } x$ ,  $\text{dn } x$  ( $k^2 = 0.7$ ).

Figure 4.8-3. Jacobian Elliptic Functions

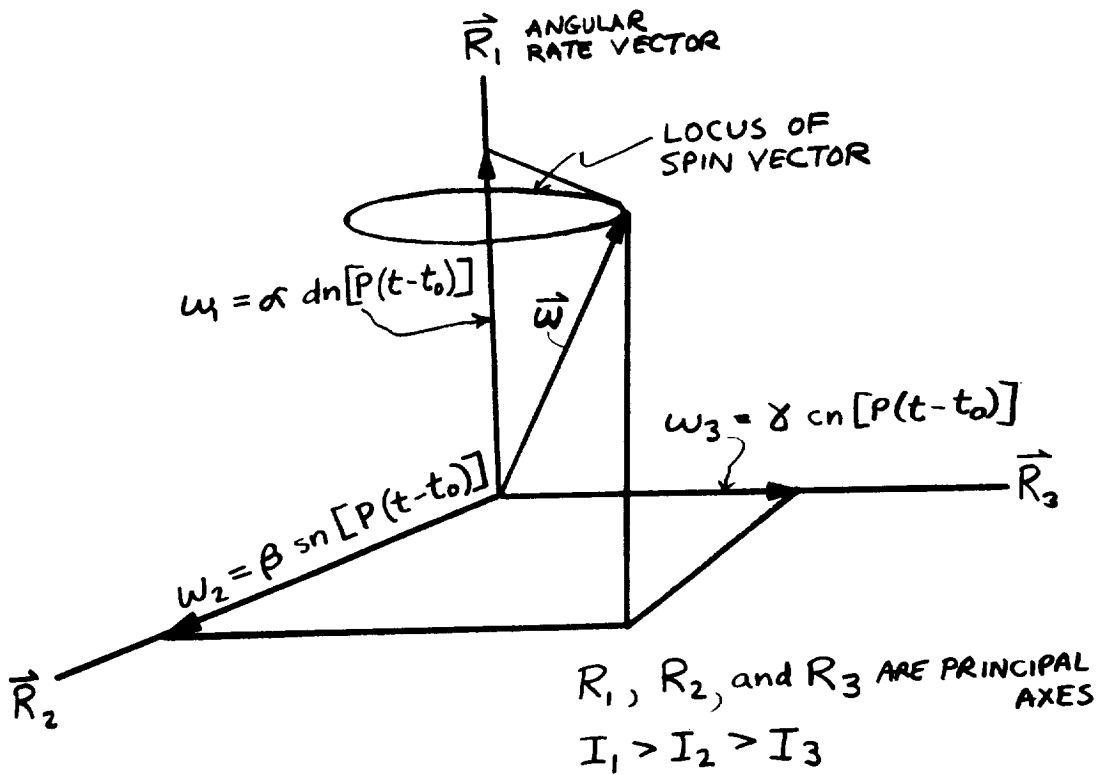


Figure 4.8-4. Precession of Spin Vector About Major Principal Axis



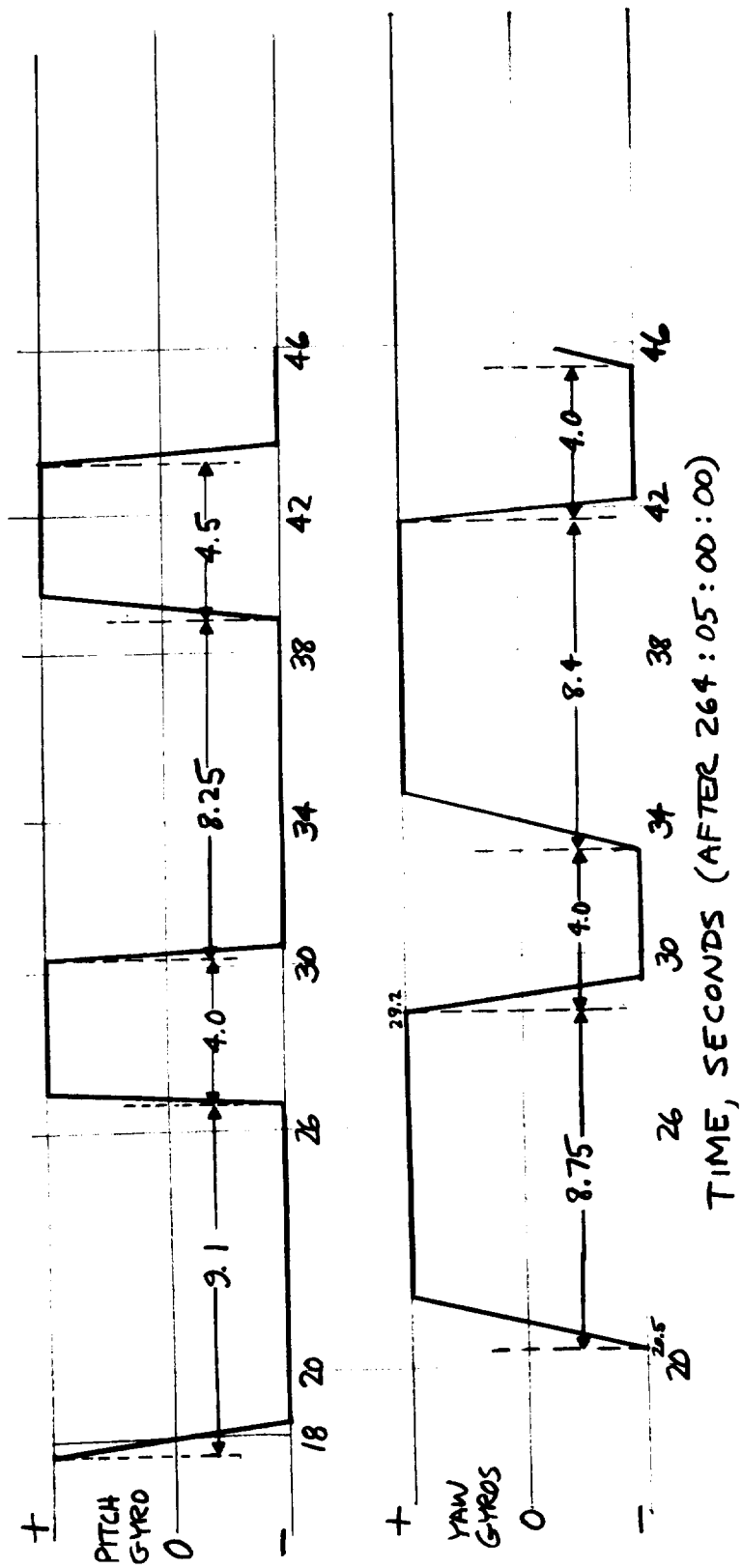


Figure 4.8-5. Pitch and Yaw Gyro Data

where  $A_{ij}$  are the direction cosines between each principal axis and each spacecraft axis. Numerically

$$\begin{aligned}\frac{W_P}{|W|} &= -0.5841 \frac{\alpha}{\gamma} \operatorname{dn} [P(t - t_0)] + 0.4431 \operatorname{sn} [P(t - t_0)] + 0.5357 \operatorname{cn} [P(t - t_0)] \\ \frac{W_Y}{|W|} &= 0.3321 \frac{\alpha}{\gamma} \operatorname{dn} [P(t - t_0)] - 0.6425 \operatorname{sn} [P(t - t_0)] + 0.5478 \operatorname{cn} [P(t - t_0)] \\ \frac{W_Z}{|W|} &= -0.7450 \frac{\alpha}{\gamma} \operatorname{dn} [P(t - t_0)] - 0.6252 \operatorname{sn} [P(t - t_0)] - 0.1832 \operatorname{cn} [P(t - t_0)] \quad (4)\end{aligned}$$

It can be seen that these equations are qualitatively consistent with the gyro data. Since  $\frac{\alpha}{\gamma}$  is a positive constant and  $\operatorname{dn}[P(t - t_0)]$  is always positive, the term  $\frac{\alpha}{\gamma} \operatorname{dn}[P(t - t_0)]$  produces a bias in each gyro measurement. From Equation 4, pitch and roll rate have the same polarity bias; yaw has the opposite bias as observed in the telemetry. Also, the negative bias in roll is larger than in pitch, accounting for the fact that roll rate is always negative. The ratio  $\frac{\alpha}{\gamma}$  and  $P$  depends only on the inertia matrix which is presumed to be known and a constant  $R$ . Since  $\frac{\alpha}{\beta}$  depends only on the inertia matrix, if value of  $R$  can be found which causes  $W_X$ ,  $W_Y$ , and  $W_Z$  to fit the telemetry data, the spacecraft rotational motion can be completely described in spacecraft coordinates for the period following the midcourse maneuver. A computer program that computes  $W_X(t)$ ,  $W_Y(t)$ , and  $W_Z(t)$  for a given value of  $R$  has been written. A fairly good fit to the data can be obtained (Figure 4.8-6). However, it is not believed that the uncertainty in the gyro zero crossing times is sufficient to account for the differences between the data and the simulation. Furthermore, it can be shown that a better fit is not possible with the inertia matrix used. In order to improve the fit, it would be necessary to change the inertia matrix to shift the principal axes.

A similar conclusion arose in the analysis of the spacecraft dynamics during the thrust period (Section 4.7). It has not yet been determined whether or not there is enough independent data to refine the inertia matrix, as well as determine the parameters of the motion.

An attempt was made to fit the solution of Euler's equations to the telemetered strain gage measurements since, with the engines off, the strain gage output is due entirely to spacecraft angular motion. However, it was not possible to fit these data, apparently, because the formula for strain gage output did not include the effect of torsional stress on the gage output. The response of the strain gages to torsional motion is being measured.

It should be noted that the location of the principal axes was such that there was not time (when the orientation of the spacecraft would have made it possible) to cancel out the spin rate by firing the vernier engines. However, this was not true in general. If an engine other than  $W_3$  had failed, it would

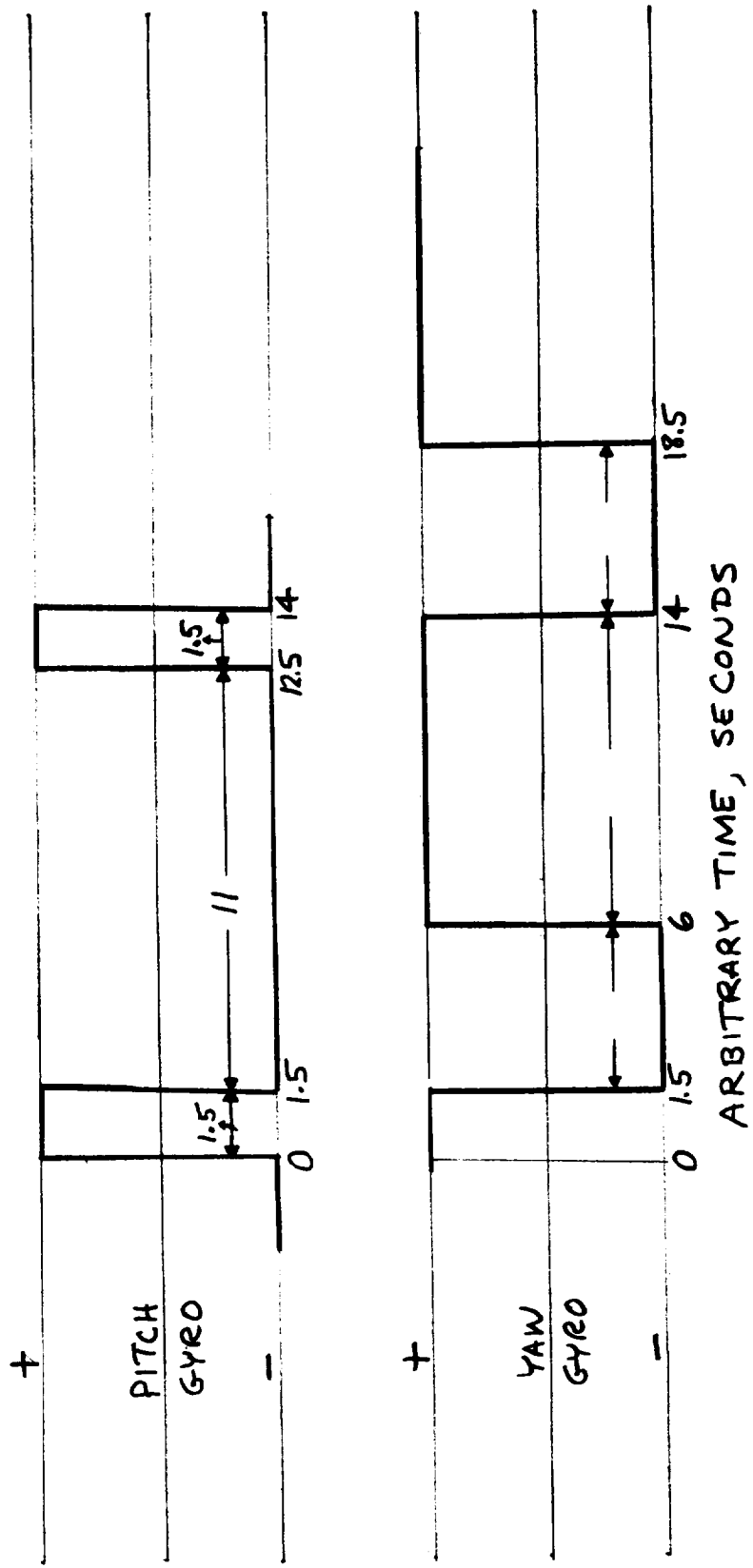


Figure 4.8-6. Pitch and Yaw Gyro Rate Reversals From Simulation

have been theoretically possible to find a time, while the spacecraft was precessing, when the torque vector, due to the thrust imbalance, would have been opposed to the angular momentum vector and thus capable of reducing the spin rate.

#### DSIF Signal Variation Due to Spin

Another source of information concerning spacecraft motion after the midcourse maneuver is the oscillation in signal strength observed at the DSIF. These data have been used in the analysis of the motion during midcourse thrusting (Section 4.7). After midcourse, these data were used to determine the variation of spin rate with time and to observe the effect on spin rate of the 39 vernier engine firings that followed midcourse (Figure 4.8-7).

#### Solar Panel Motion

On 265:06:35, the solar panel was unlocked by radio command. The panel subsequently moved from its transit position at 270 degrees to a position of approximately 249 degrees (Figure 4.8-8). The solar panels were then stepped 87 times in the negative direction, which should have moved them 10.9 degrees to 238.1 degrees, but the panel only moved to 246 degrees. Thus, it appears very likely that the spin axis projection in the XZ plane is perpendicular to the solar panel when the panel is between 246 and 249 degrees. Then the component of the spin vector in the XZ plane is between 21 and 24 degrees from the -Z axis (Figure 4.8-1). This is within the range of values consistent with the results of the thermal analysis, but is in disagreement with the location of the major principal axis (which should also be the spin axis) whose projection on the XZ plane is 41.8 degrees from the -Z axis.

The disagreement between the location of the principal axis and the spin axis indicated by the solar panel motion could be due to errors in the inertia matrix. However, it should be noted (Figure 4.8-1) that the XZ component of the spacecraft-sun vector location estimated from the thermal analysis is between 20 and 60 degrees from the Z axis. The spin vector calculated from the solar panel motion is near the extreme end of this band (21 to 24 degrees from the Z axis). It would be expected that the spin vector would be further inside the band of Figure 4.8-1, and it appears that the results of this figure are more consistent with the spin vector indicated by inertia matrix considerations than with the spin vector from solar panel motion analysis. Unfortunately, the significance ascribed above to the solar panel motion is questionable. Also, no measure of the spin vector Y component can be determined from the solar panel motion.

#### Retro Accelerometer Data

Spacecraft rotation also produces a centrifugal acceleration on the retro accelerometer. An analysis (Reference 3) has been performed to determine the spin vector orientation which, combined with the measured spin rate (92.3 rpm), would produce the retro accelerometer output observed

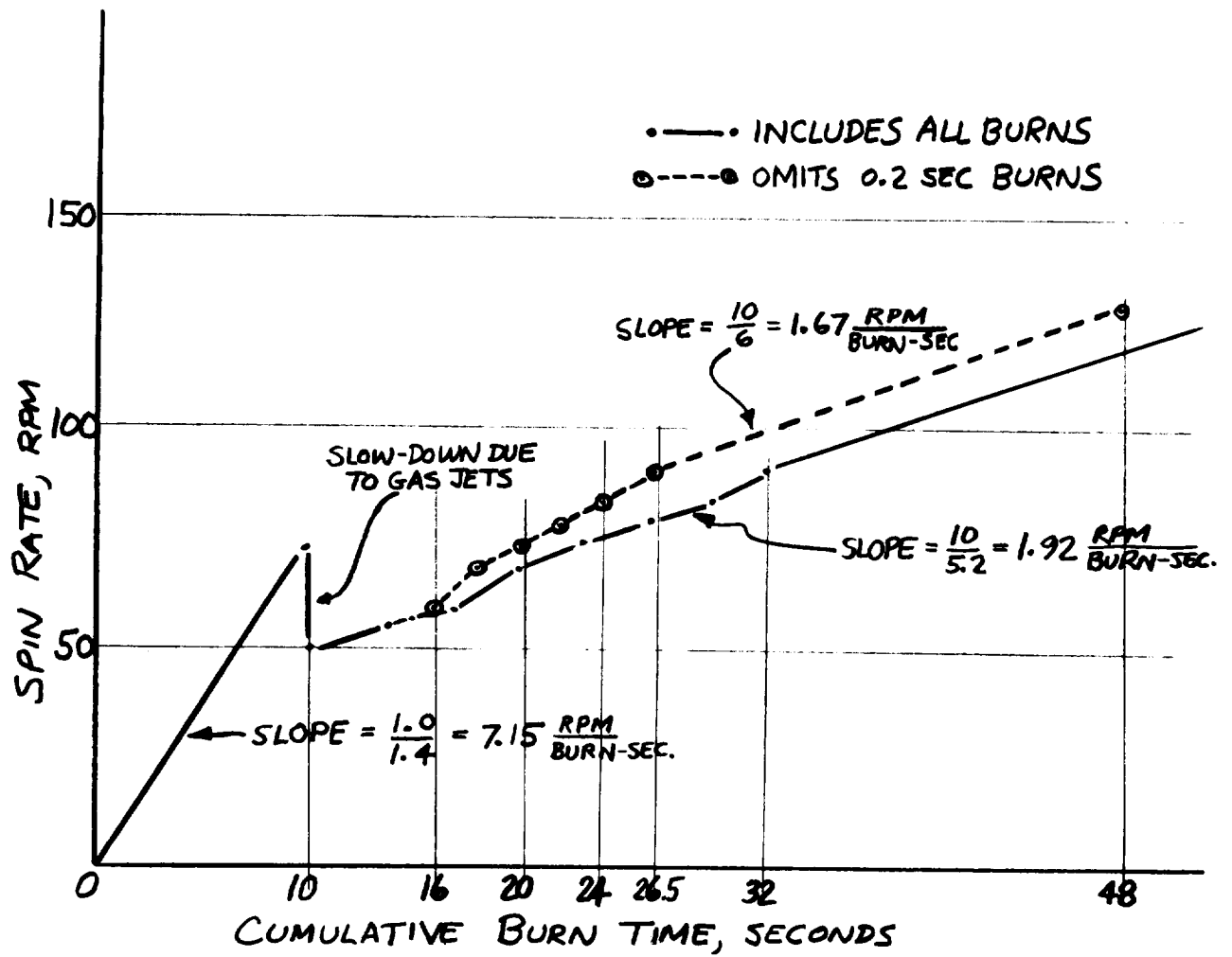


Figure 4.8-7. Spin Rate

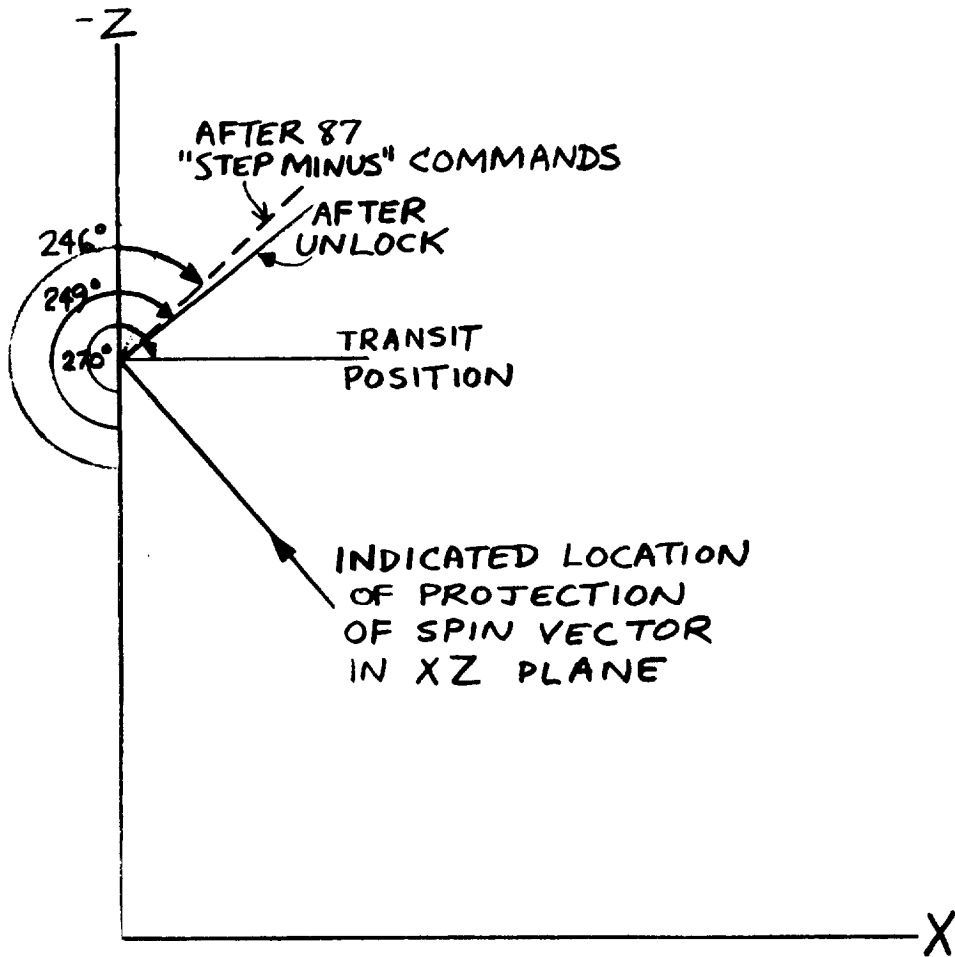


Figure 4.8-8. Spin Axis Location From Solar Panel Motion

during the period just preceeding the 20-second firing. The results are shown in Figure 4.8-9. The spin axis would have to lie on the contour of the ellipse-like curve to cause the observed retro accelerometer output of 3.42 g. Orientation of the major principal axis is also shown in this figure. This principal axis, which should be the steady-state location of the spin axis, falls reasonably close to the curve. The difference is about 5 degrees in  $\theta_1$  and 4 degrees in  $\theta_2$ . The uncertainty in the location of the curve is due to accelerometer errors, errors in spin rate, and errors in the location of the center of gravity relative to the accelerometer are probably considerably greater than the distance between the curve and the point that represents the principal axis. The uncertainty in the calculation of spin axis location from retro accelerometer data will receive more detailed examination. The results presented here are somewhat different than those in Reference 3. The results given in this reference were obtained from data taken just after the 20-second retro firing when the spin axis had been torqued away from its steady-state position and when the spin axis was precessing. The results presented in this report were calculated from retro accelerometer data taken just before the 20-second firing (265:08:02).

#### 4.8.3 SUMMARY

The values of  $\theta_1$  and  $\theta_2$  for the steady-state spin vector (Figure 4.8-2), derived from the various data sources are listed in Table 4.8-1. The angular momentum vector in inertial coordinates appears from the thermal analysis and inertia matrix considerations to be within 20 degrees of the sun-spacecraft vector.

TABLE 4.8-1. SUMMARY OF SPACECRAFT ROTATION AXIS ANALYSES

	$\theta_1$ , degrees	$\theta_2$ , degrees	Notes
Thermal analysis	*	-30 to -70	
Inertia matrix	28.9	-48.5	Probably most accurate determination
DSIF signal strength variation	**	**	
Solar panel motion	*	-66 to -69	Questionable
Retro accelerometer	-8 to +34	-35 to -55	$\theta_1$ and $\theta_2$ are correlated (See Figure 4.8-9)

\*Cannot be determined from this data source.

\*\*Has not been analyzed for this purpose. Data does not appear capable of improving estimates of  $\theta_1$  and  $\theta_2$ .

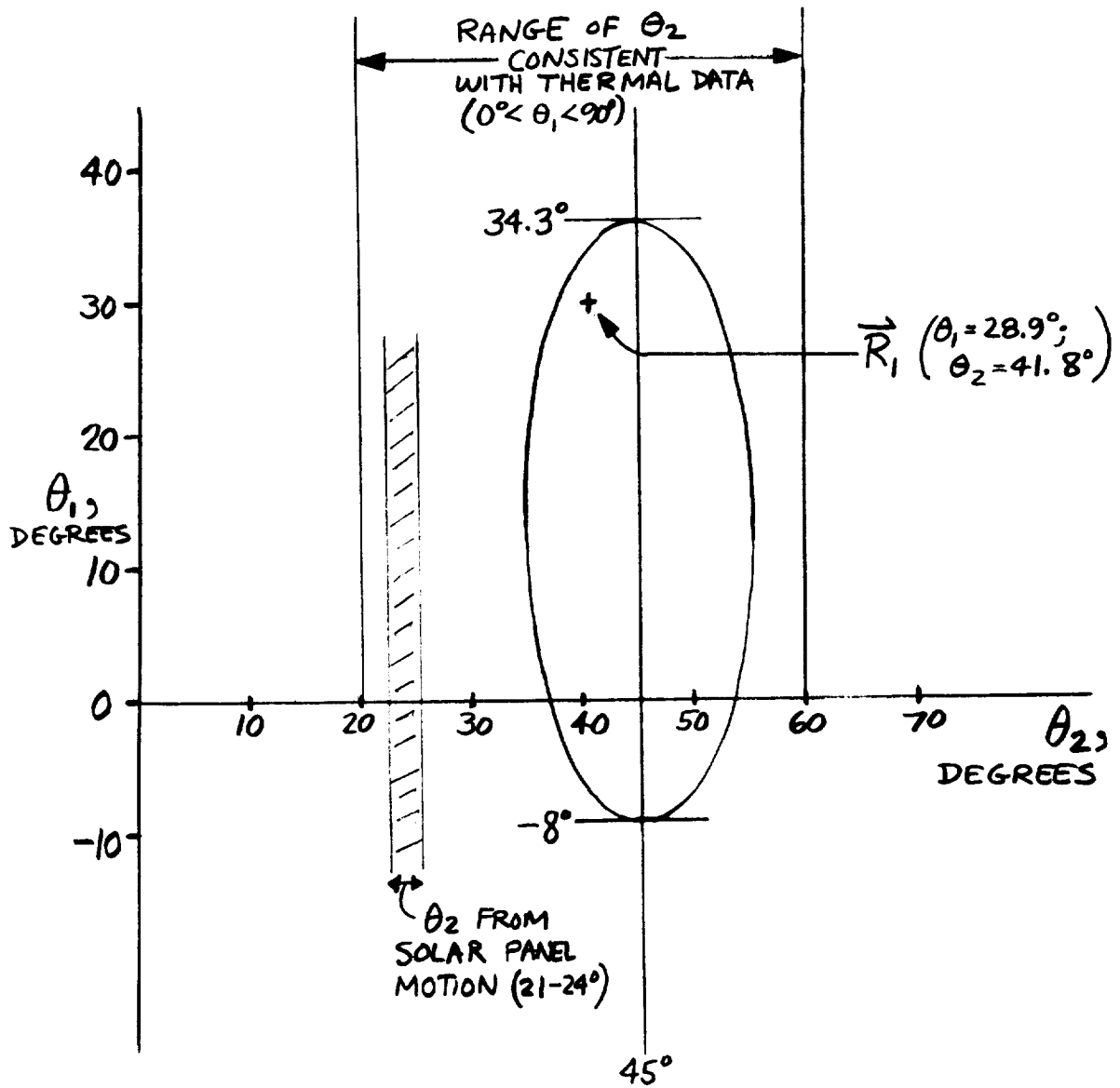
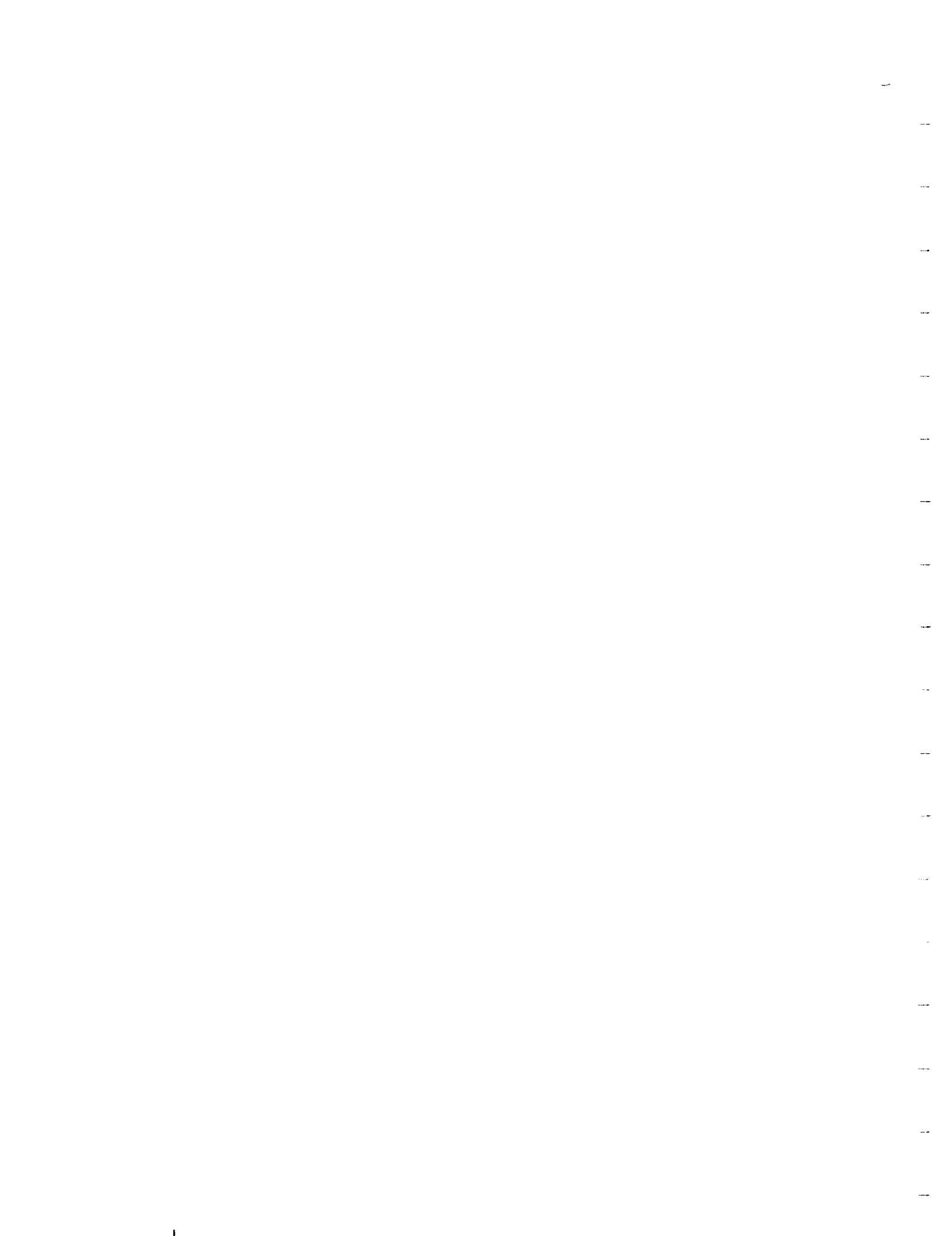


Figure 4.8-9. Loci of Spin Axis Determinations by All Methods



#### 4.8.4 REFERENCES

1. H. E. Knudson, "SC-2 Tumbling Mode Thermal Observations," IDC 2221.19/86, 5 October 1966.
2. L. M. Bronstein, "Principle Axes of SC-2," IDC 2292/114, 8 November 1966.
3. E. W. White, "Study of SC-2 Retro Accelerometer Data," IDC 2293/50, 7 December 1966.



## 4.9 RELIABILITY ANALYSIS

### 4.9.1 PERFORMANCE

Assessment of performance from a reliability standpoint mainly concerns relevant failures and unit operating time. To date, there are four failure modes (TFRs) (Reference 1) pertaining to the mission. They are listed in Table 4.9-1 with descriptions and current status. Unit operating experience is listed in Table 4.9-2 with unit part and serial numbers. The unit operating time and cycle information was developed by translating commands transmitted to the spacecraft.

### 4.9.2 PERFORMANCE VERSUS PREDICTIONS

The predicted reliability for the transit phase was 0.66. The growth pattern of reliability estimates prior to launch is shown in Figure 4.9-1. These predictions excluded consideration of the use of nonstandard procedures. For comparison, the SC-1 growth pattern is included.

Although two mission attempts, successful or not, cannot in themselves completely justify or vitiate prediction methods, data collected during those missions do serve as a basis for investigation of areas of possible improvement in prediction.

#### 4.9.2.1 Reliability Math Model (Nonoperating Equipment)

An assumption used throughout the reliability math model is that electronic equipment in the nonoperating state has a failure rate equal to 1/100 of the failure rate during its operating state

$$\lambda_{\text{off}} = 0.01 \lambda_{\text{on}}$$

Experience gained on both SC-1 and SC-2 indicates that this factor may be too high. Detailed analysis of this parameter has been initiated.

TABLE 4.9-1. MISSION TFR SUMMARY

TFR Number	Description	Status (on 1 December 1966)*
18247	At approximately the time of the legs extend signal (35 seconds prior to Centaur separation) the flight control sensor group reverted to inertial mode from rate mode (should have remained in rate mode until 52 seconds after Centaur separation).	Closed. Relevant. Cause of failure is attributed to noise pulse sensitivity of flight control output latches. ECA 11175 and related drawings 284544 and 284546 provide corrective action and will be incorporated for SC-3 and subsequent spacecraft.
18248	Spacecraft failed to maintain stable attitude during midcourse correction.	Open. Failure Review Board to provide detailed analysis.
18249	Receiver B was reading below specification values from 90 minutes before launch to end of mission.	Open. Under investigation.
18250	Canopus sensor failed to achieve automatic star acquisition.	Open. Affects only spacecraft operational procedures by requiring manually commanded lockon.
18251	No intelligible data were received from commutated signal of flight accelerometer CY 53 0 during launch.	Closed. Relevant. Cause of failure is unknown. Loss of some engineering data on launch vibration only.
18252	No intelligible data were received from the commutated signal of flight accelerometer CY 52 0.	Closed. Relevant. Cause of failure is unknown. Loss of some engineering data on launch vibration only.
18253	Vernier line 2 heater was full on and line temperature still decreased prior to midcourse correction.	Open. ECA 113043 initiates investigation of line heater assembly unit level tests.
18254	Helium tank pressure sensor (P-1) experienced a -528 psi "zero shift" at helium release squib actuation.	Closed. Relevant. Cause of failure was shock seen by the transducer at squib release. For SC-3, the P-1 helium tank pressure signal will be displayed in analog form during squib release to permit immediate positive verification of a "zero shift" prior to midcourse correction.

\* For additional data, see subsection 3.1.

TABLE 4.9-2. MISSION B UNIT OPERATING TIME AND CYCLE DATA\*

Subsystem and Unit	Part Number	Serial Number	Time, hours (or number of flight cycles)
<b>Telecommunications</b>			
Central command decoder	232000-5	3	45.6
Engineering signal processor	233350-7	1	7.6
Auxiliary engineering signal processor	264900-3	3	36.6
Signal processing auxiliary	232540-1	1	1.0
Low data rate auxiliary	264875-2	2	29.0
Omnidirectional antenna A	232400	12	45.6
Omnidirectional antenna B	232400	21	45.6
Omnidirectional mechanism A	287300-1	2	1 cycle
Omnidirectional mechanism B	273880-1	1	1 cycle
Central signal processor	232200-8	2	45.6
Transmitter A	263220-4	15	—
Transmitter B	263220-4	11	45.6
Receiver A	231900-3	15	45.6
Receiver B	231900-3	16	45.6
Low pass filter A	233466	1	45.6
Low pass filter B	233466	2	45.6
Telemetry buffer A	290780	13	45.6
Telemetry buffer B	290780	14	45.6
RF transfer switch	283984	15	—
SPDT RF switch	283983	13	2 cycles
<b>Television</b>			
Survey camera	284312-3	11	—
Approach camera	284302-1	13	—
Television auxiliary	232106-5	11	—
<b>Vehicle mechanisms</b>			
Thermal sensors (total for 23)	988653		1048.8
Thermal control and heater assembly A	232210-1	15	45.6
Thermal control and heater assembly B	232210-2	18	45.6
Thermal switches compartment A	238810		416.4
Thermal switches compartment B	238811		273.6
Thermal shell compartment A	286459	1	45.6
Thermal shell compartment B	286460	1	45.6
Spaceframe	264178-1	1	45.6
Engineering mechanism auxiliary	263500-6	12	45.6
Landing gear 1	261278	4	—
Landing gear 2	261279	3	1 cycle
Landing gear 3	261280	4	1 cycle
Footpad leg 1	263947		—
Footpad leg 2	263947		—
Footpad leg 3	263947		—
Crushable blocks			
Shock absorber leg 1	264300-1	9	1 cycle
Shock absorber leg 2	264300-1	10	1 cycle
Shock absorber leg 3	264300-1	11	1 cycle
Wiring harness compartment A	286207	4	45.6
Wiring harness compartment B	286242	4	45.6
Wiring harness basic bus 1	3025357	1	45.6
Wiring harness basic bus 2	286398	2	45.6
Wiring harness antenna solar panel positioner	286417	1	0.2
Wiring harness auxiliary battery	264100	3	3.0
Wiring harness TV camera	276979	5	—
Wiring harness RF cabling			36.9
Wiring harness retro motor	286390	2	0.1
Wiring harness battery cell voltage	3025155	2	15.6
Antenna solar panel positioner	287580	1	
Roll			700 cycles
Solar			1001 cycles
Polar			
Elevation			
Separation sensing and arming device	293400	1	1 cycle
		9	each
		7	
<b>Propulsion</b>			
Retro rocket system	238612	A21-27	
Vernier engine 1	285063-1	542	
Vernier engine 2	285063-2	546	
Vernier engine 3	285063-3	544	
<b>Electrical power</b>			
Battery charge regulator	274100-4	12	45.6
Boost regulator	274200-12	14	45.6
Auxiliary battery control	273000-2	16	45.6
Main power switch	254112	5	45.6
Main battery	237900	63	45.6
Auxiliary battery	237921-1	64	3.0
Boost regulator unregulated filter	290080	12	45.6
Boost regulator unregulated choke	290390	12	45.6
Solar panel	237760-3	2	45.6
<b>Flight controls</b>			
Flight control sensor group			
Coast phase	235000-9	1	38.5
Thrust phase			3.0
<b>Radar and guidance RADVS</b>			
Signal data converter	232908-2AM7	9	0.2
Klystron power supply	232909-AM3	5	0.2
Altitude velocity sensor antenna	232910-AM4	6	0.2
Velocity sensor antenna	232911-1AM3	5	0.2
Waveguide	232912-AM3	5	0.2
Altitude marking radar	283827-1	13	0.1
Roll actuator	235900-3	7	3.0
Altitude jet leg 1	235700-2	1	984 cycles
Altitude jet leg 2	235700-3	4	984 cycles
Altitude jet leg 3	235700-3	6	904 cycles
Secondary sun sensor	235450-1	2	22.8
Pin pullers			9 cycles
Pin puller cartridges			9 cycles

\*Data source: DSS tapes.

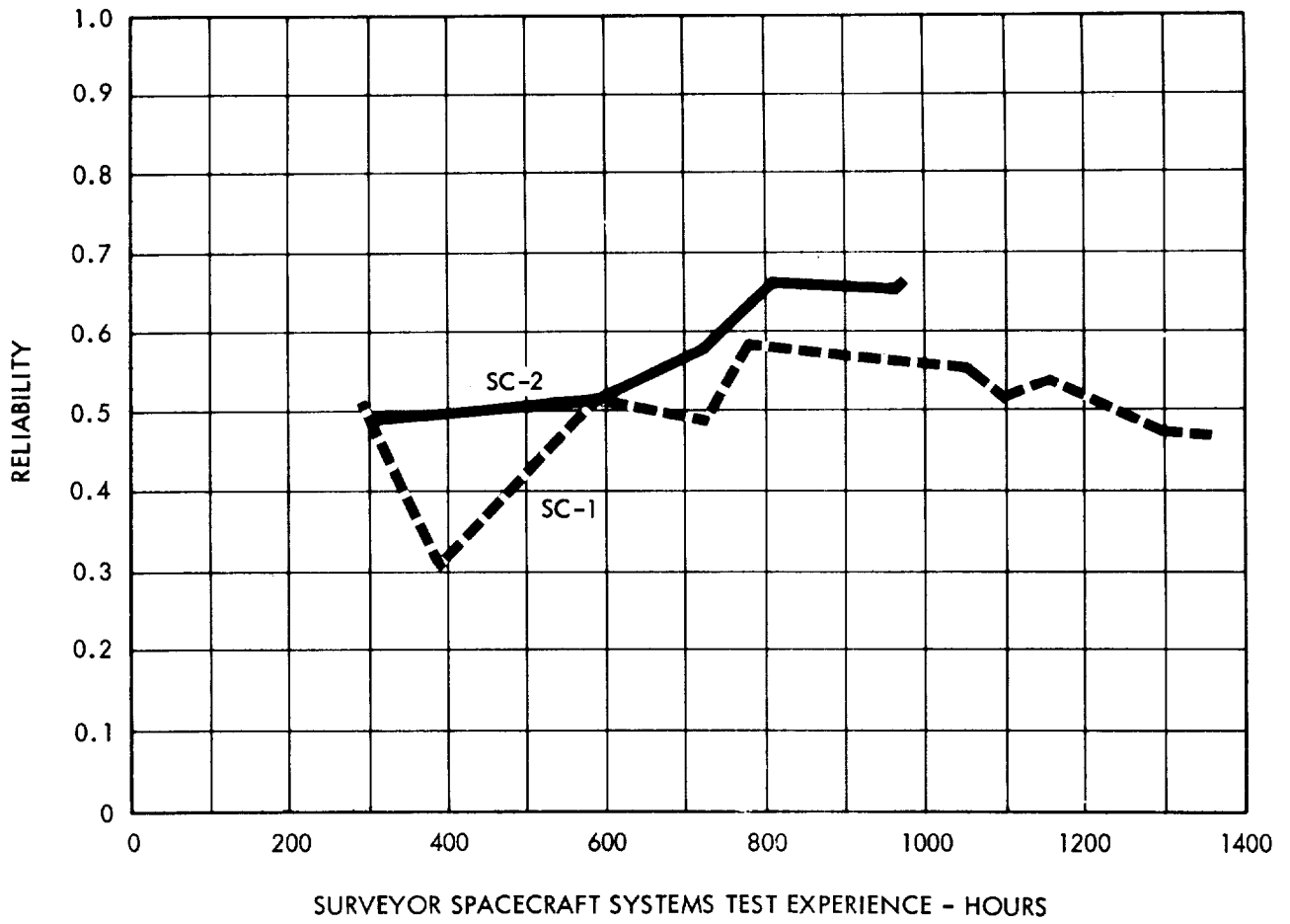


Figure 4.9-1. Reliability Estimate (Flight and Landing)

#### 4.9.2.2 Reliability Math Model (Boost Vibration Effects)

Boost phase (vibration stress) failures in electronic equipment are assumed to occur at a rate equal to 80 times the failure rate during non-boost periods,

$$\lambda_{\text{on boost}} = 80 \lambda_{\text{on}}$$

$$\lambda_{\text{off boost}} = 80 \lambda_{\text{off}}$$

This factor may also be too high and is included in the analysis of off time failure rates.

#### 4.9.2.3 Reliability Math Model (Propulsion Subsystem)

Data-based estimates of the propulsion subsystem reliability assumed a binomial distribution of successes and failures. Experience gained on SC-1 and SC-2 test programs and flights indicates a possible requirement for inclusion of additional parameters. In particular, within the vernier propulsion system, the following are presently under investigation: distribution of the difference between thrust realized and thrust commanded, effect of these dispersions upon moment control, and effect upon probability of propulsion subsystem success.

#### 4.9.3 FUTURE RELIABILITY PREDICTIONS

Reliability predictions for future spacecraft will include SC-2 mission unit experience, as well as SC-1 transit and lunar phase experience, where there are no significant design differences among units.

#### 4.9.4 REFERENCE

1. "Reliability Relevant Failures," IDC 2258.2/328, 24 February 1966.

#### 4.10 ADDITIONAL REFERENCE MATERIAL

The following reference material was used without specific acknowledgement in the preparation of many parts of Sections 2, 3, and 4:

1. "Surveyor I Flight Performance Final Report," Hughes Aircraft Company, SSD 68189R, October 1966.
2. "Spaceflight Operations Plan - Surveyor Mission B," JPL EPD 180, Revision S/MB, September 1966.
3. "SC-2 Consent to Launch," Hughes Aircraft Company, SSD 64229R, September 1966.
4. "Surveyor SC-2, ETR Test Phase Data Evaluation Report," Hughes Aircraft Company, SSD 64208I, September 1966.
5. "Surveyor Mission B, Space Flight Operations Report," Hughes Aircraft Company, SSD 64257R, November 1966.
6. "Surveyor II, Flight Path Analysis and Command Operations Report," Hughes Aircraft Company, SSD 64260R, November 1966.
7. G. A. Young to R. H. Leuschner, "Mission B Command List," IDC 2292/91, 10 October 1966.
8. B. D. Love, "Surveyor II Transit Command Sequence," JPL IOM 292-66-219, 13 October 1966.

#### 4.11 ACKNOWLEDGEMENTS

The material in Sections 1, 2, 3, and 4 was coordinated (and in many cases originated or compiled) by G. A. Young and R. H. Leuschner. In addition to the general references in subsection 4.10 which were frequently used, special mention is due to the following people:

L. M. Bronstein, for the analysis in Section 4.8

W. McIntyre, for final compilation of Section 3

L. K. Cooley, for Section 4.9 on reliability

P. E. Sterba, for direction of the tremendous labor that produced Section 4.7, and to all those who also contributed through analysis, programming, or writing:

F. R. Fagerlund  
D. J. Giem  
J. H. Green  
J. D. Haller  
W. R. Heathcote  
E. R. Kopitzke

J. McFerson  
C. D. Passey  
A. L. Reynolds  
F. K. Rickman  
M. R. Weiner



## 5.0 PERFORMANCE ANALYSIS

### 5.1 THERMAL CONTROL SUBSYSTEM

#### 5.1.1 INTRODUCTION

##### 5.1.1.1 Surveyor Thermal Control Techniques

The Surveyor thermal design uses a variety of temperature control techniques. Both active and passive systems are employed to provide the required temperature control throughout the transit and lunar phases of the mission. Each spacecraft subsystem is individually controlled, and the thermal coupling between subsystems is minimized by using conduction and radiation isolation wherever advantageous. Subsystem analyses are accomplished by evaluating in detail the thermal environment for each subsystem, with consideration being given to all significant interactions between the subsystems whenever a high degree of isolation is not possible.

The following temperature control techniques are used on the Surveyor spacecraft:

- 1) Passive thermal control utilizing combinations of paints and metal processes to provide solar absorptance and infrared emittance characteristics that produce required subsystem temperatures.
- 2) Active thermal control systems utilizing heaters to provide energy in cases where sufficient solar illumination is not available.
- 3) High conduction and radiation isolation utilizing superinsulation for systems having a large heat capacity. Such systems never reach equilibrium conditions and therefore depend on their stored heat capacity.
- 4) Bimetallically activated thermal switches that control the temperature of the electronics compartments during transit and lunar operations.

Combinations of the above techniques are used on many of the subsystems to optimize the temperature control system.

### 5.1.1.2 Analysis Organization

The spacecraft has been divided into a number of subsystems for thermal analysis. The thermal behavior within each of those listed below is discussed in subsection 5.1.4, with comparison to test and SC-1 data.

- 1) Compartments A and B
- 2) Auxiliary battery
- 3) A/SPP
- 4) Spaceframe
- 5) Landing gear and crushable blocks
- 6) Thrust chamber assemblies
- 7) Propellant tanks
- 8) Propellant lines
- 9) Helium tank
- 10) Main retro engine
- 11) Flight control electronics and Canopus sensor
- 12) Roll actuator
- 13) Nitrogen tank
- 14) Attitude gas jets
- 15) RADVS
- 16) Altitude marking radar
- 17) Television system

Included in subsection 5.1.2 is not only a discussion of the vernier line thermal anomaly, but also considerable analysis, as outlined below, done in support of the vernier engine anomaly:

- 1) Analysis of vernier system temperature data
- 2) Vernier burn thermal inconsistency
- 3) Tumbling mode thermal observations

### 5.1.1.3 Major Events and Times

Some of the major events that affected the thermal subsystem are tabulated in Table 5.1-1 as a function of mission time. A complete tabulation of spacecraft high power periods, thrust power on periods, and all vernier burns can be found in subsection 4.1.1 of the system discussion.

### 5.1.2 ANOMALIES AND FAILURE SUPPORT DATA

Only one primary anomaly existed in the thermal control subsystem: vernier line heater cycling (see subsection 5.1.2.1). Also included here are two extensive analyses prepared in support of the vernier engine failure investigation (see subsections 5.1.2.2 and 5.1.2.4). Study of the data from each of the 40 vernier engine firings after midcourse disclosed a second potential anomaly, since engine burns of the same duration sometimes produced different thermal results (see subsection 5.1.2.3). This secondary anomaly may possibly have been caused by spacecraft spinning following the midcourse attempt. One of the anomalous burns (number 27) is probably due to a burn interval that was more than twice as long as commanded. But the remaining burns are discussed here in the absence of other plausible theories.

#### 5.1.2.1 Vernier Line Thermal Anomaly

An examination of sensor P-4 thermal data presented in Figure 5.1-33\* indicates that the heaters on the propellant lines feeding vernier engine 2 began to cycle 90 minutes after launch. Thermal data indicate that the heater operational duty cycle increased with mission time during the first 4 hours of flight. The cycling exhibited by the vernier line 2 heater terminated at approximately L + 3H, and the line heater remained on. Termination of vernier line heater cycling during the course of a mission is considered a thermal anomaly.

Since the spaceframe and other subsystems in the proximity of the lines do not reach their respective steady-state equilibrium temperature during coast phase I, an increase in the line 2 heater operational or "on" time as the mission progresses is considered normal. The thermal response exhibited by subsystems in the vicinity of the engine 2 propellant lines is shown by sensors P-10, P-16, and V-38 (Figures 5.1-38, 5.1-44, and 5.1-67).

As the spaceframe and other subsystems in the propellant line environment continue to cool, the thermal environment of the lines becomes colder, creating a greater demand for more energy from the line heaters so as to increase the line temperature to the upper limit (26° F) of the heater

---

\*SC-2 thermal mission plots are located at the end of the section. The thermal predictions superimposed on these plots were taken from Reference 1.

TABLE 5.1-1. MAJOR THERMAL EVENTS AND TIMES

GMT,		Time from Launch,		Event
day:	hr: min: sec	hr: min: sec		
263 : (9-20-66)	12: 32 : 00	00: 00 : 00	Launch	
	12: 35 : 23	00: 03 : 23	Nose fairing jettison	
	12: 44 : 27	00: 12 : 27	Separation from Centaur	
	12: 49 : 45	00: 17 : 45	Sun acquisition	
	18: 33 : 00	06: 01 : 00	Star acquisition	
	19: 16 : 00	06: 44 : 00	Canopus verification	
	19: 26 : 24	06: 54 : 24	Begin gyro drift check	
	21: 35 : 22	09: 03 : 22	End gyro drift check	
	264 : (9-21-66)	04: 36 : 44	16: 04 : 44	Transmitter high power on for midcourse
		04: 44 : 00	16: 12 : 00	Start roll maneuver
04: 48 : 05		16: 16 : 05	Start yaw maneuver	
04: 54 : 20		16: 22 : 20	Thrust power on for midcourse	
05: 00 : 02		16: 28 : 02	Start midcourse burn (9.85 seconds)	
05: 00 : 41		16: 28 : 41	Thrust power off	
05: 14 : 29		16: 42 : 29	Inhibit gas jet amplifiers	
11: 41 : 09		23: 09 : 09	Auxiliary battery selected	
265 : (9-22-66)		02: 44 : 58	38: 12 : 58	A/SPP stepping attempt
		06: 35 : 19	42: 03 : 19	Solar panel unlock and step attempt
	09: 13 : 16	44: 41 : 16	Dump helium	
	09: 19 : 57	44: 47 : 57	RADVS power on	
	09: 30 : 09	44: 58 : 09	RADVS power off	
	09: 34 : 17	45: 02 : 17	Emergency AMR signal command	
	09: 34 : 27.2	45: 02 : 27.2	Retro ignition (telemetry)	

thermostat range. Since the thermal dissipation ( $P = E^2/R$ ) of the propellant line heaters is relatively constant for a given supply voltage, the lines' increased energy demand is achieved by increasing heater operational or on time.

The vernier engine 2 propellant line heater on time is illustrated in Figure 5.1-1 as a function of mission time for SC-1 and SC-2. Effects of the changing thermal environment and the decay in bus voltage on the line temperature level for SC-1 is readily observed. The curves indicate that the line thermal environment continues to cool throughout the mission. The ordinate of Figure 5.1-1 is simply the heater on time divided by the total time for one cycle, that is, on time plus off time for any cycle taken at a discrete time interval during the mission.

The data presented in Figure 5.1-1 indicate that the SC-2 vernier line 2 heaters reached a saturated state both during solar thermal vacuum testing and flight. Current data indicate that the line heaters were on and functioning properly; however, the line temperature continued to decrease. SC-1 thermal data indicate that the line 2 heater maintained the propellant lines within the cyclic deadband range of the thermostat throughout the mission and that this heater did not saturate or reach a continuous on condition. The thermal dissipation capability of the line heaters was sufficient to maintain line temperatures within the thermostat cyclic range of 19 to 26° F. Thermal behavior of the vernier engine 2 oxidizer line is shown in Figure 5.1-2 for the Mission A transit coast phase. Failure of the SC-2 line 2 heater to maintain line temperatures within the thermostat deadband range suggests that the emittance of the exterior surface of the aluminum foil wrap covering the line heater may have exceeded the specification value. The line heaters are designed to give satisfactory operation with exterior surfaces whose emittance is less than or equal to 0.10.

The propellant lines are thermally controlled by means of active thermal control techniques. Ideally, the thermal design attempts to decouple the lines from other subsystems by using thermal surfaces that are insensitive to infrared radiation interchange. The use of low infrared emittance surfaces also minimizes the net heat loss, by radiation, between the lines and heat sinks in the environment. Increases in the infrared emittance by the wrap covering the line tends to: 1) couple the line with its thermal environment, 2) increase the line radiation into space, and 3) increase the power required to maintain the line temperature within the thermostat deadband range of 19 to 26° F.

Thermal analyses indicate that emittance of the exterior surface of the vernier engine 2 oxidizer line could have been in the range of 0.30 to 0.50. However, because of the many variables affecting the propellant line energy balance, the exact oxidizer line emittance cannot be determined more precisely. Therefore, the range of emittance values presented in this discussion is not to be taken as exact, but serves to demonstrate that the emittance on the exterior surface of the oxidizer 2 line was significantly higher than expected. Ultraviolet (black light) inspections at Cape Kennedy

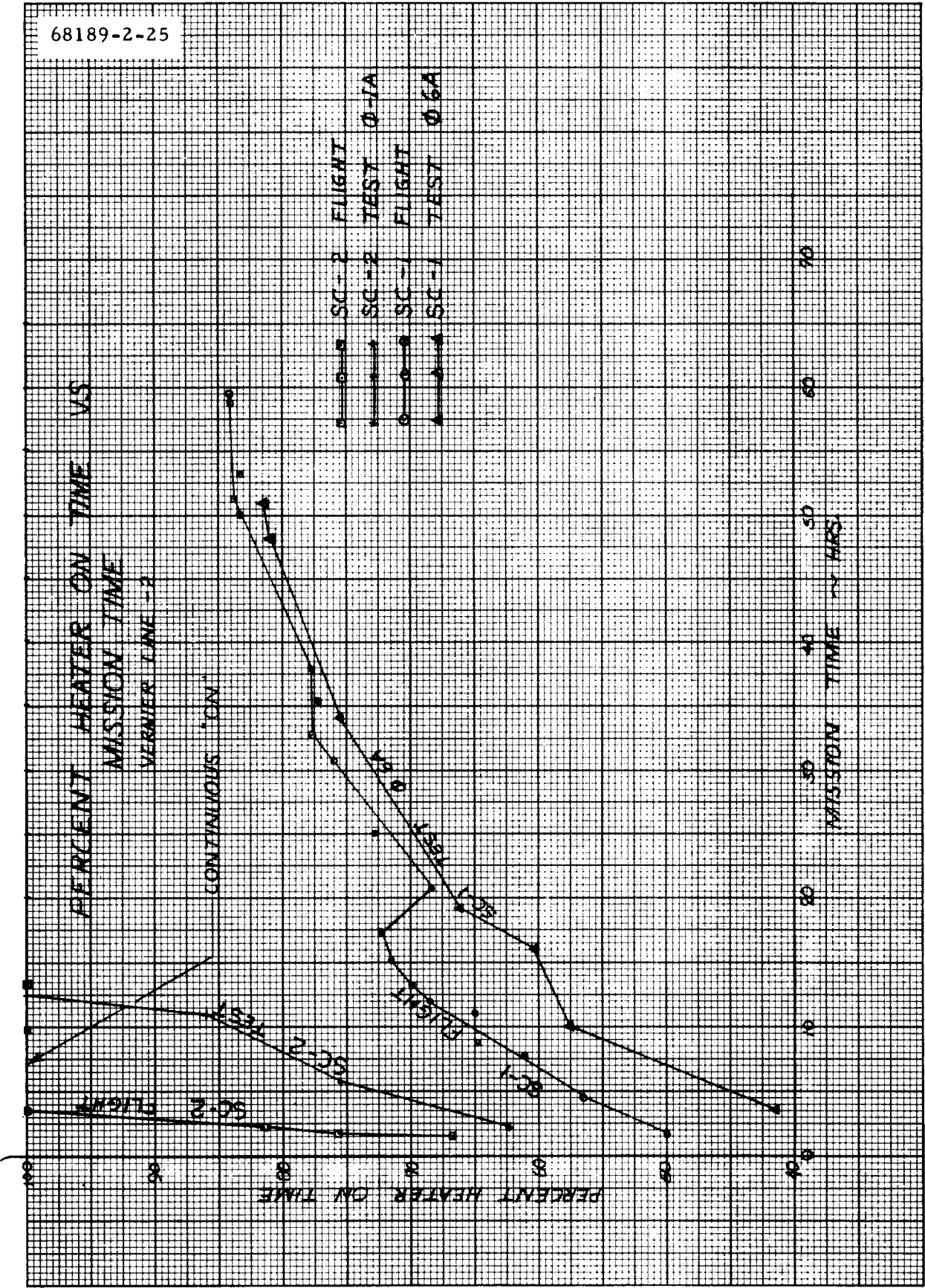


Figure 5.1-1. Vernier Line 2 Percent Heater On-Time During SC-1 and SC-2 STV Tests and Missions

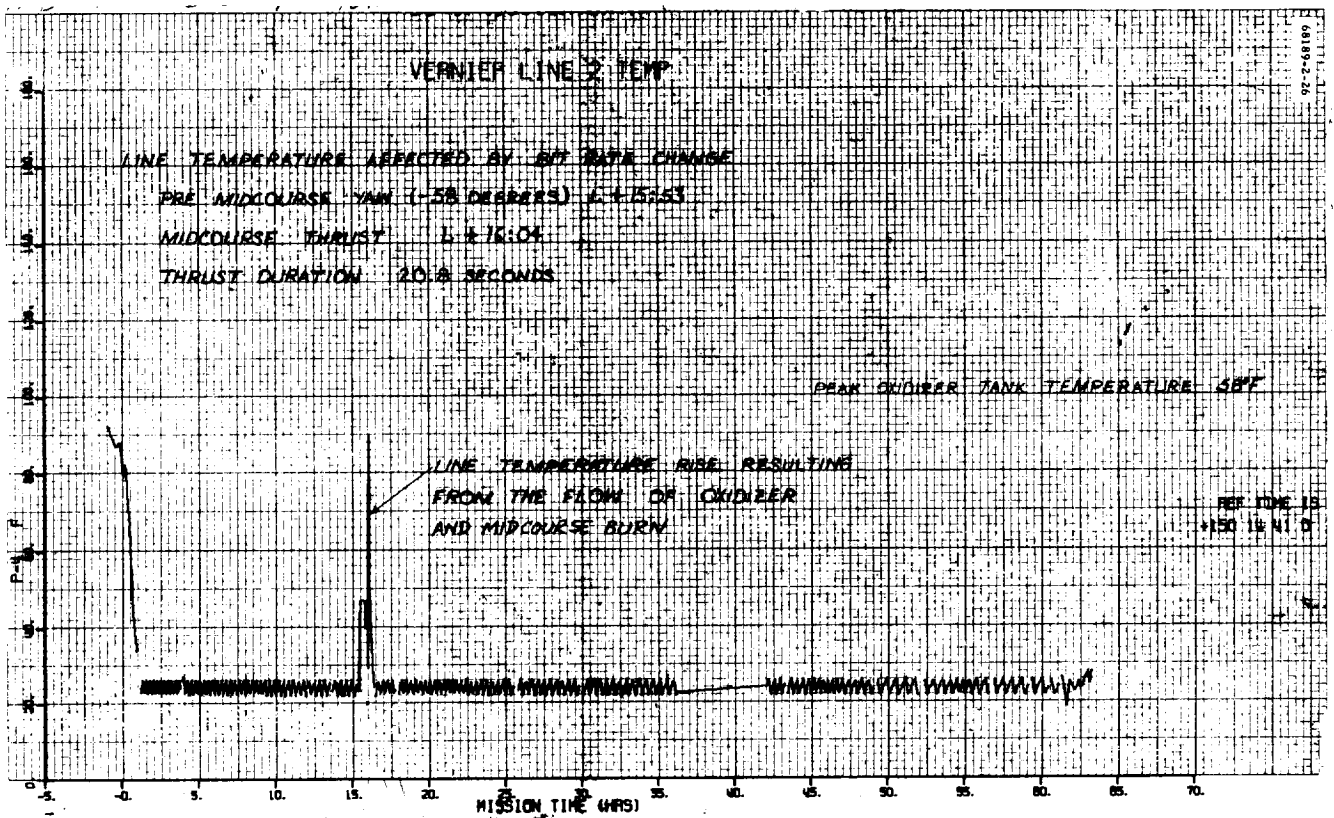


Figure 5.1-2. Vernier Line 2 Temperature Cycling During Mission A

revealed that the exterior surfaces of the vernier engine 2 propellant lines were contaminated with epoxy residue which would not be detected during routine daylight thermal inspections.

In conclusion, it can be said that the high emittance of the vernier oxidizer line exterior surface is the probable cause of the thermal anomaly.

#### 5.1.2.2 Thermal Analysis of Vernier System Temperature Data (Failure Review Support)

Thermal data indicate that vernier engines 1 and 2 ignited as commanded during the midcourse correction maneuver, but vernier engine 3 did not exhibit any positive indications of ignition. The apparent failure of thrust chamber assembly (TCA) 3 to ignite as commanded resulted in spacecraft tumbling. Table 5.1-2 is a summary of propellant flow determinations during long burns. Individual burns are discussed in the following arguments.

##### Oxidizer Flow Arguments

An examination of the vernier line temperature responses, as indicated by the flight sensors installed on the vernier oxidizer lines, shows positive temperature changes on oxidizer lines 1 and 2 at midcourse. The thermal data show only a small negative temperature perturbation on the oxidizer line feeding vernier engine 3. The vernier line temperature profiles are shown in Figure 5.1-3 for the midcourse interval.

Vernier line temperature perturbations may result from line heater cycling, spacecraft attitude other than the nominal transit attitude, or propellant flow which is at a temperature different from the line temperature. Effects of vernier line heater cycling are readily distinguishable in the thermal data because of the constant amplitude cyclic waveform exhibited by the line thermostat on-off duty cycle. Nominal transit line temperatures may change as a result of a misalignment in the vehicle sun attitude whereby the vehicle sustains a yaw or pitch maneuver. Line temperatures may increase or decrease depending upon the relative orientation of the vehicle with respect to the sun vector. In general, decreases in line temperature will be observed by an increase in the line heater duty cycle; increases can be observed by a decrease in the line heater duty cycle and/or a gradual increase in the line temperature level. Temperature perturbations resulting from the flow of propellant through the lines are readily distinguishable by: 1) rapid change in line temperature, and 2) return of the lines to their nominal temperature level subsequent to engine shutdown. These generalizations are best demonstrated by data obtained during Mission A, as shown in Figure 5.1-4. Only lines 2 and 3 are shown, since line 1 is similar to line 2.



68189-2-27

# SC-2 VERNIER LINE TEMPERATURE PROFILES AT MIDCOURSE

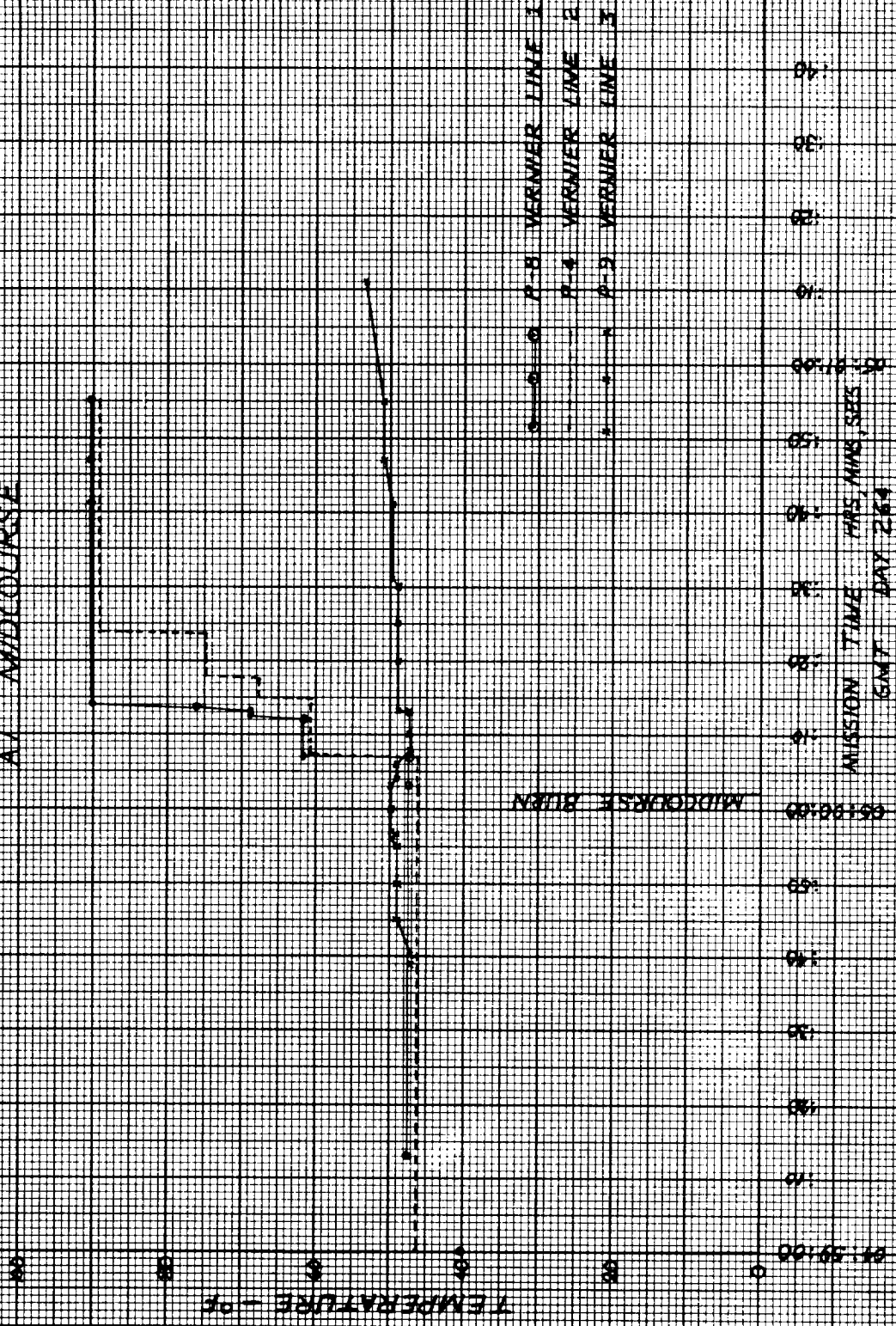
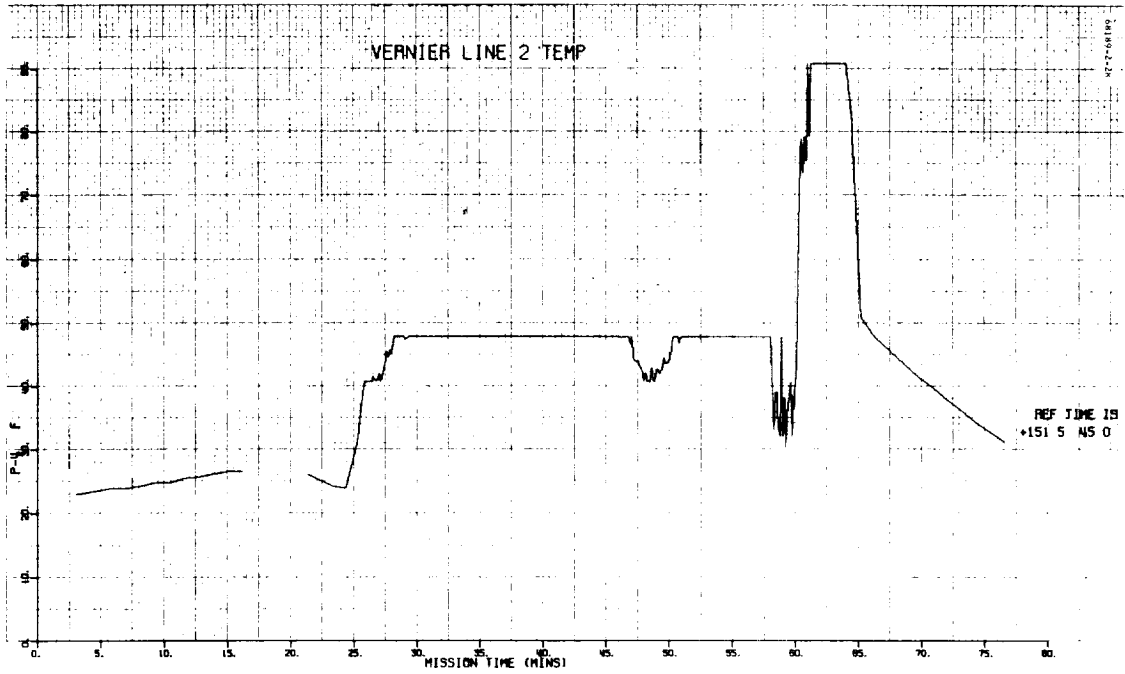
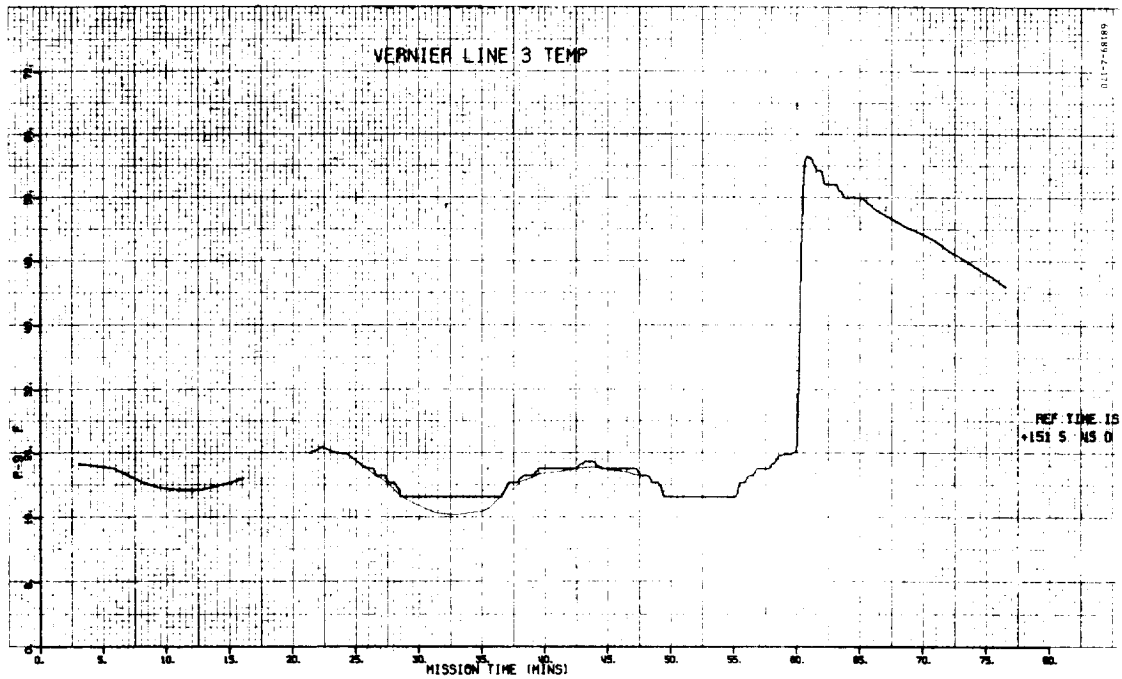


Figure 5.1-3. SC-2 Vernier Line Temperature Profiles at Midcourse



a) Vernier Line 2



b) Vernier Line 3

Figure 5.1-4. Vernier Line Temperatures at Midcourse, Mission A

During Mission B, all vernier lines began to warm at completion of the premidcourse yaw maneuver. The rates of temperature change were 2, 3, and 3.5 deg/min for three lines. At vernier engine ignition (264:05:00:02), the line temperatures were 41, 44, and 51°F respectively (approximate values; see subsection 5.1.4.8). Vernier lines 1 and 2 temperatures increased to 66 and 60°F, respectively, following vernier ignition. In each case, these values were 6°F below the postmidcourse temperature of the corresponding oxidizer tank. Vernier line 3 did not exhibit the rapid temperature change characteristic of normal propellant flow. Instead, the line 3 temperature decreased by 2 degrees at midcourse. The positive temperature increases on lines 1 and 2 to values near the true oxidizer tank temperatures, along with the ignition of engines 1 and 2, indicate normal oxidizer flow to these engines. The failure of vernier line 3 to experience a similar increase strongly suggests that little or no oxidizer flowed into thrust chamber assembly 3 at midcourse. Table 5.1-3 summarizes the above data, with a comparison to corresponding SC-1 values.

#### Fuel Flow Arguments

A second proposed conclusion is that fuel flowed through the engine 3 fuel line at midcourse. The propellant line temperature sensors are mounted on the oxidizer lines, and thus there is no direct thermal measure of fuel flow. Transit temperature profiles (sensors P-7, P-10, and P-11) for the vernier engines are shown in Figures 5.1-35, 5.1-38, and 5.1-39 for TCAs 1, 2, and 3, respectively. Prior to the midcourse burn, the last recorded thermal data for the TCAs were acquired approximately 43 minutes before vernier engine ignition. Subsequent to engine ignition, approximately 34 minutes elapsed before TCA data was reacquired.

TCA 1 and 2 temperatures were decreasing and TCA 3 temperature was increasing when vernier engine thermal data was reacquired. The temperature of engine 3 was 71°F when TCA thermal data was obtained following the midcourse burn. A careful observation of Figure 5.1-5, which shows the first 6 minutes subsequent to the reacquisition of TCA data, indicates that the temperature of vernier engine 3 was increasing at the rate of 0.5°F/min. A straight line interpolation of the data back to midcourse results in an engine temperature of 54°F at the time of vernier ignition. However, a straight line interpolation of the data presented in this figure is optimistic and unrealistic. It is reasonable to postulate that the temperature rate of change of TCA 3 is in excess of 0.5°F/min subsequent to the midcourse vernier engine burn and prior to the acquisition of engine thermal data. The straight line interpolation suggests a temperature change of 17°F for the interval bounded by engine ignition (264:05:00:02 GMT) and the acquisition of engine thermal data (264:05:34 GMT).

The temperature of TCA 3 at initiation of the 110.6-degree yaw turn (264:04:48 GMT) was 64°F. An examination of the SC-2 solar thermal vacuum test data indicates that the maximum temperature drop of TCA 3, as indicated by the flight sensor (P-11), was 10 degrees in 12 minutes. Vernier engine 3 was not completely eclipsed prior to the initiation of engine thrusting; to the contrary, the engine was partially illuminated. Therefore, a maximum

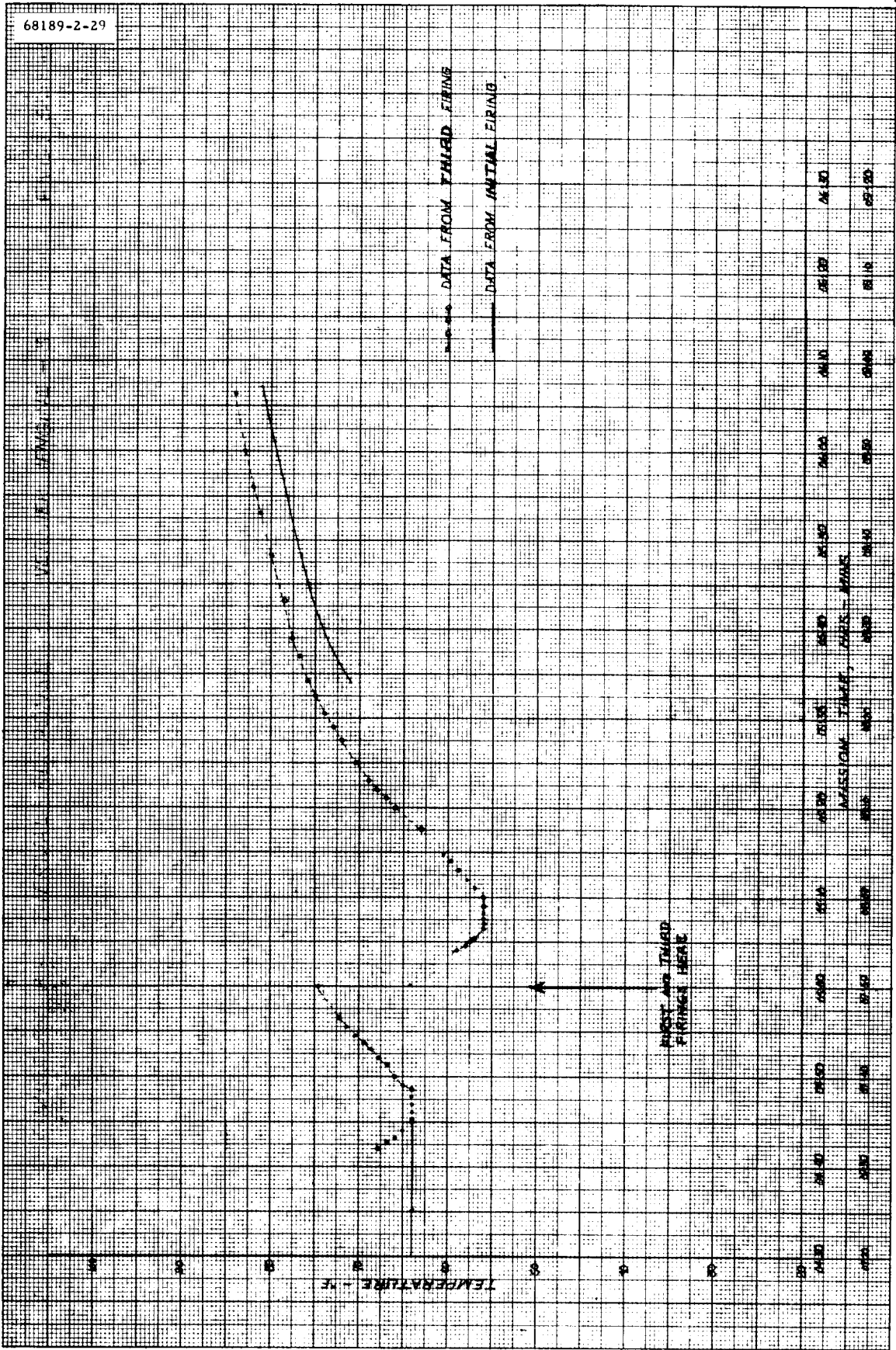


Figure 5.1-5. Vernier Engine 3 Thermal Response

TABLE 5.1-2. SUMMARY OF PROPELLANT FLOW INDICATIONS  
(LONG BURNS)

Burn Number	Fuel Flow	Oxidizer Flow (Less Than Normal)
1	Yes, Inferred	Questionable
2	Inferred	Yes
3	Inferred	Yes
9	Yes	Yes
15	Yes	Yes
21	Yes	Yes
27	Yes	Yes
33	Yes	Yes
34	Yes	No determination
40	Yes	No determination
41	Yes	No determination

TABLE 5.1-3. OXIDIZER TANK AND LINE TEMPERATURES AROUND  
MIDCOURSE (°F)

Temperatures	SC-2 Data			SC-1 Data		
	1	2	3	1	2	3
Vernier lines before maneuvers	23	16	24	24	23-27	20-24
Vernier lines at ignition	37-45	41-47	51	24	36	24
Vernier lines after ignition (uncorrected)	91	90	49	91	91	61
Vernier lines after ignition (corrected for 4400 bits/sec error)	66	60	49	69-71	59-61	61
Oxidizer tank after ignition	73	66	70	67	59	68
Oxidizer tank before ignition	50	35	46	58	44	53

temperature decrease of 10 degrees during the interval bounded by the initiation of the yaw turn and vernier engine ignition is probably reasonable. Maximum temperature decrease conditions are synonymous with total solar eclipse conditions. Working from this argument, it can be hypothesized that the temperature of vernier engine 3 would not decrease below 54° F as a result of cooling due to partial shadowing and off-axis solar illumination.

Certain inferences can be made if the following two propositions are accepted:

- 1) TCA 3 temperature rate of change (increase) was greater than 0.50° F/min during the interval bounded by the midcourse burn and acquisition of engine thermal data at 05:34.
- 2) TCA 3 could experience a temperature decrease no greater than 10° F during the interval bounded by the initiation of the pre-midcourse yaw maneuver and initiation of vernier ignition.

Statement 1 suggests a TCA temperature lower than 54° F at midcourse, while the second statement suggests that a temperature lower than 54° F cannot be achieved as a result of the partial solar eclipse condition. Hence, the temperature of engine 3 will decrease below 54° F only if the engine is cooled by a superficial process.

A cooling process can be considered in which fuel flows into vernier engine 3 and expands in the combustion chamber. During the expansion, energy is extracted from the thrust chamber body, causing a decrease in the thrust chamber temperature level. Absence of engine thermal data during the midcourse burn does not permit verification of the suggested cooling. However, an evaluation of other TCA ignition attempts, where engine thermal data is available, strongly indicates the aforementioned cooling. Burns 2 and 3 infer some superficial cooling for TCA 3; however, it must be kept in mind that the oxidizer line temperature sensor indicates oxidizer flow during burns 2 and 3.

An investigation of other burns, 34 and 40 for example, infers that the observed TCA 3 temperature perturbations (increases) are the result of fuel flowing. Burns 34 and 40 indicate that the engine 3 thrust chamber temperature approaches the fuel temperature and then cools very rapidly. A cross sectional view of a vernier engine (Figure 5.1-6) illustrates that propellant enters the barrel through a fuel inlet manifold located at the bottom of the thrust chamber barrel. The fuel then travels through a spiral groove along the thrust chamber wall and enters the combustion chamber through the injector head.

A comparison of the engine 3 temperature profiles for the midcourse (burn 1) and third burn are presented in Figure 5.1-5. The thrust chamber barrel thermal response curves are similar for the midcourse and third burn attempts in the regions where data are available. A generalization to

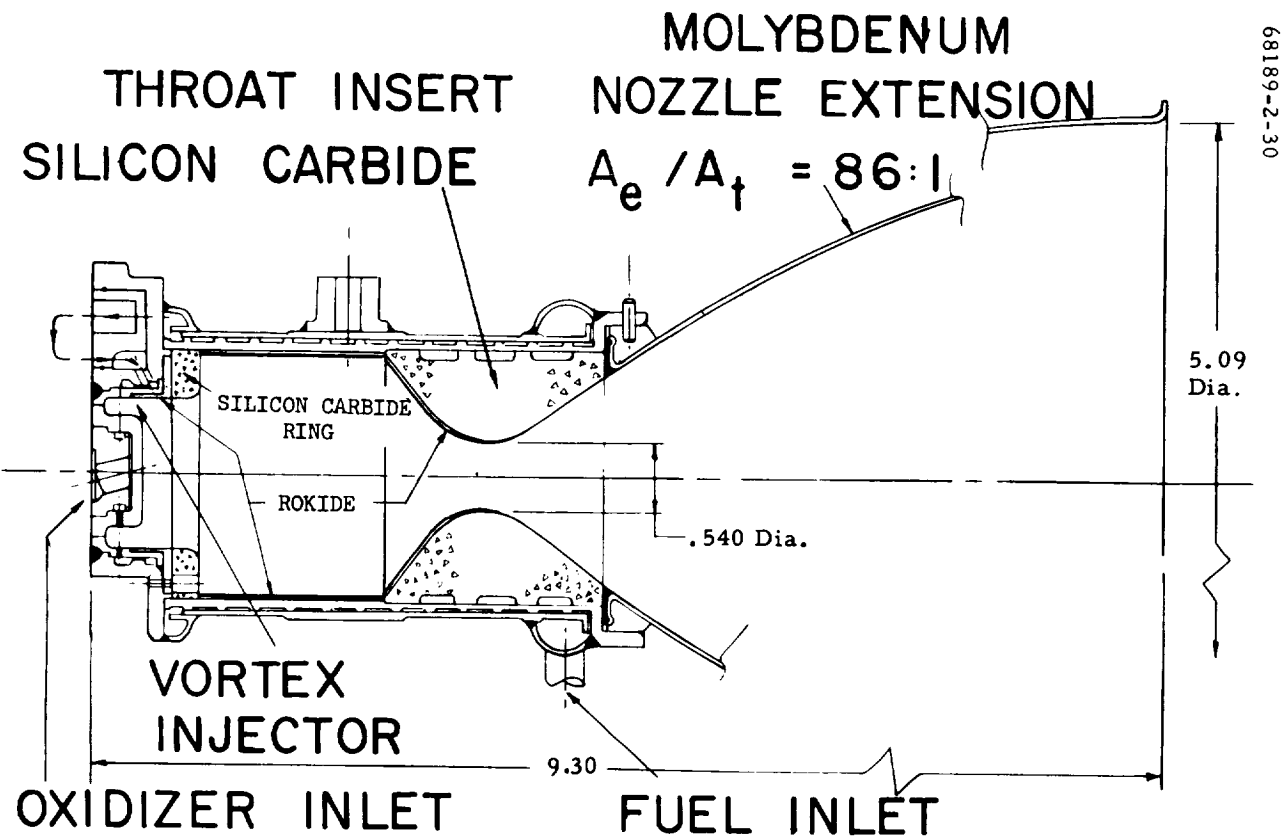


Figure 5.1-6. Thrust Chamber and Injector Assembly

all subsequent burns indicates that the thermal response (warmup following the ignition attempt) of the engine is similar for burns 2 through 40. In fact, overlays of the long duration ignition attempts indicate that engine thermal behavior is repetitive. Because of the similarity and repetitive nature of the data obtained during burns 2 through 40 and the similarity that exists between the warmup transients for burns 1 and 3, it can be inferred that the same phenomena occurred during midcourse and subsequent ignition attempts. One important exception to this is that the thermal data do not positively indicate oxidizer flow during midcourse but suggest limited oxidizer flow in the engine 3 line during subsequent firing attempts.

The second proposition, which states that fuel flowed through the engine 3 fuel line during midcourse burn, is primarily inferred from the similarity in the thermal response exhibited by TCA 3 following burn 1 and the response due to subsequent burns. Again, arguments regarding TCA 3 premidcourse temperature drop and postmidcourse rate of change (identical to those of the preceding discussion) are required. A careful examination of the flight data (Figure 5.1-7) indicates that fuel flowed during all firing attempts subsequent to the midcourse burn. The fuel flow phenomena is verified by the increase or decrease in engine 3 thrust chamber barrel temperature during the engine operational interval and the period immediately following engine operation. A comparison of engine 3 thrust chamber barrel data obtained during the 21.5-second burn (burn 40) and engine data obtained during similar engine operational periods at the Edwards Test Station are shown in Figure 5.1-8. Visual inspection of the data indicates that the thermal behavior of the thrust chamber assembly barrels are similar during fuel flow periods. Curve C of Figure 5.1-8 is an analytical curve based on the engine and fuel thermal parameters for the maximum flow condition.\* The correlation between the analytical and actual data is excellent.

### 5.1.2.3 Vernier Burn Thermal Inconsistency

An investigation of the thermal data obtained for all 41 ignition attempts indicates that the thrust chamber assembly thermal behavior (engines 1, 2, and 3) was inconsistent. The data indicate that the thermal behavior of vernier engines 1 and 2 was different for burn intervals of the same duration. With the exception of the midcourse burn where it is questionable whether oxidizer flowed to the engine, the thermal behavior of engine 3 appears to be consistent for all burns. This is best illustrated by

---

\*Curve C of Figure 5.1-8 is based on semiempirical formulae for heat transfer in pipes and assumes fully developed flow. No attempt was made to correct the formulae for the effects of the gravitational field. Therefore, the analytical curve is subject to valid criticism.



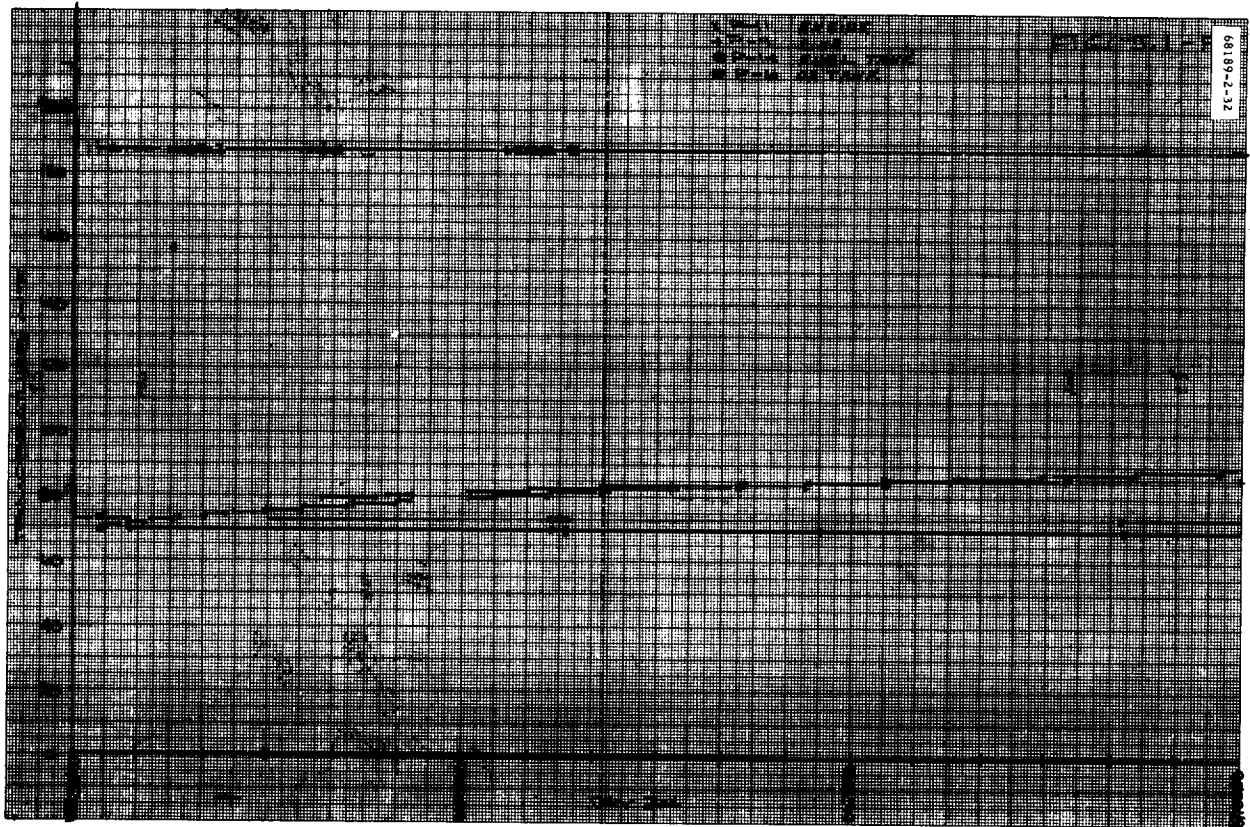
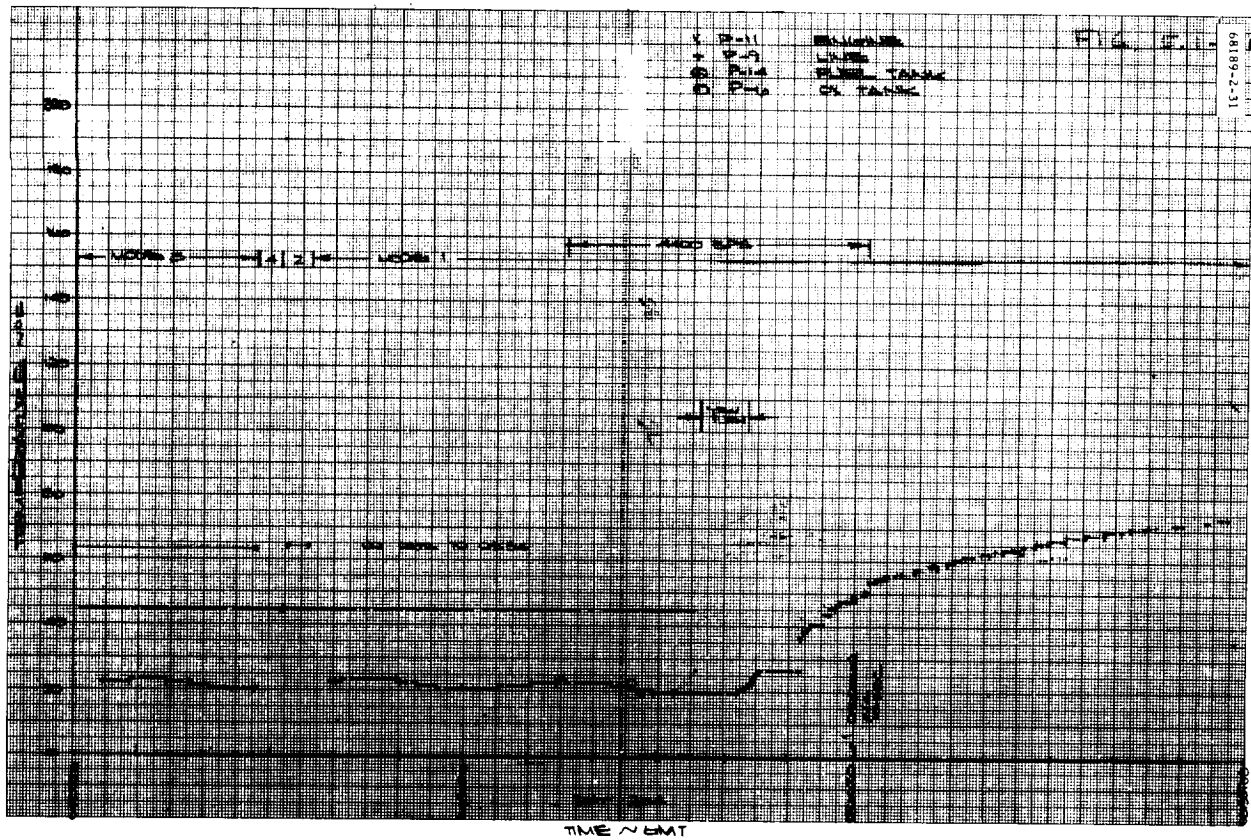


Figure 5.1-7. SC-2 VPS Thermal Response, Leg 3

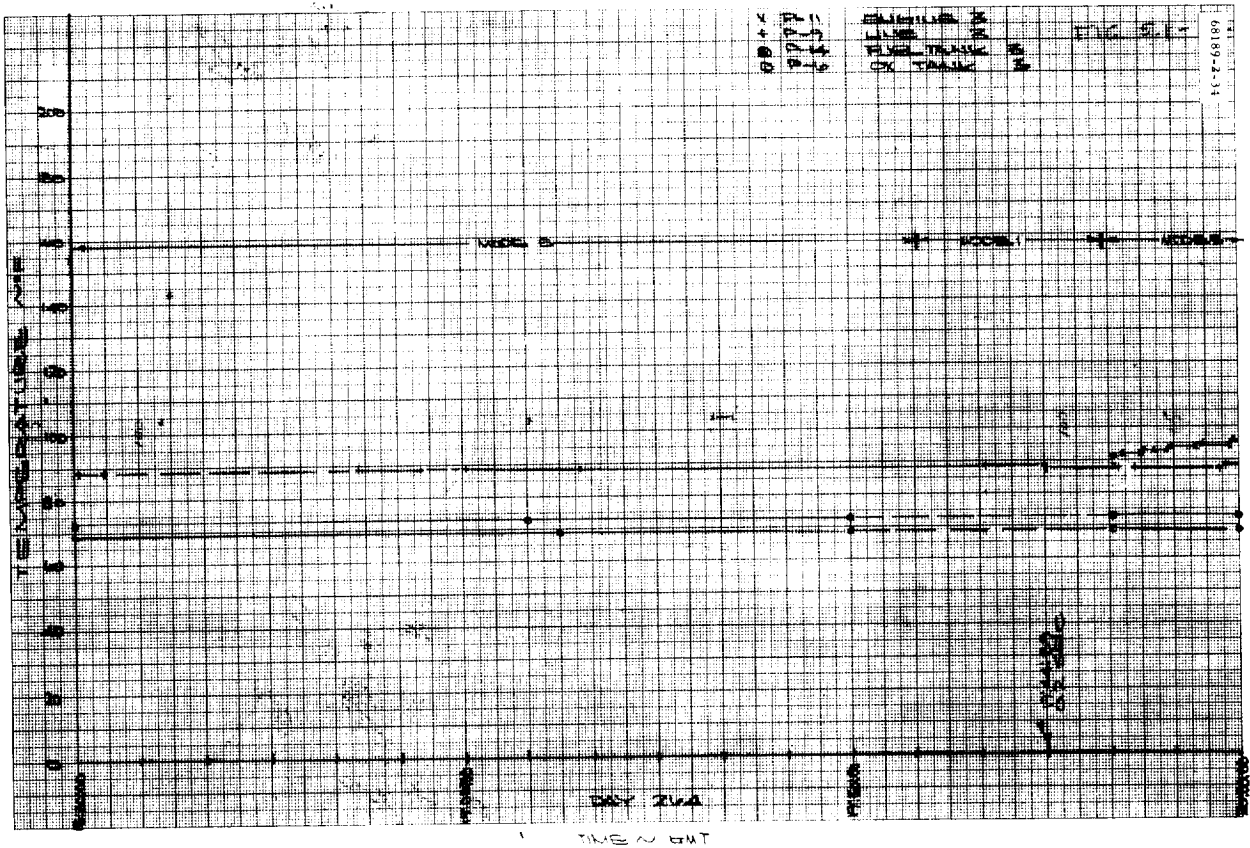
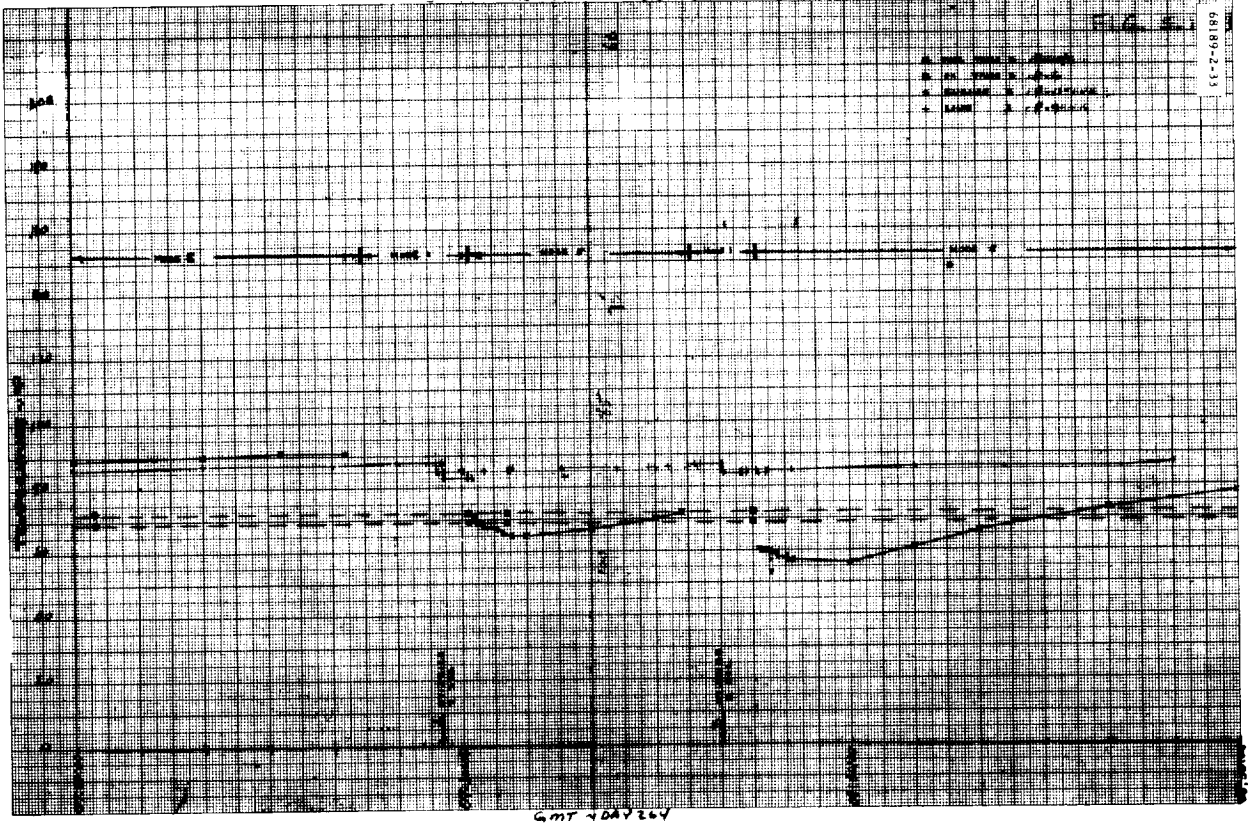


Figure 5.1-7 (continued). SC-2 VPS Thermal Response, Leg 3

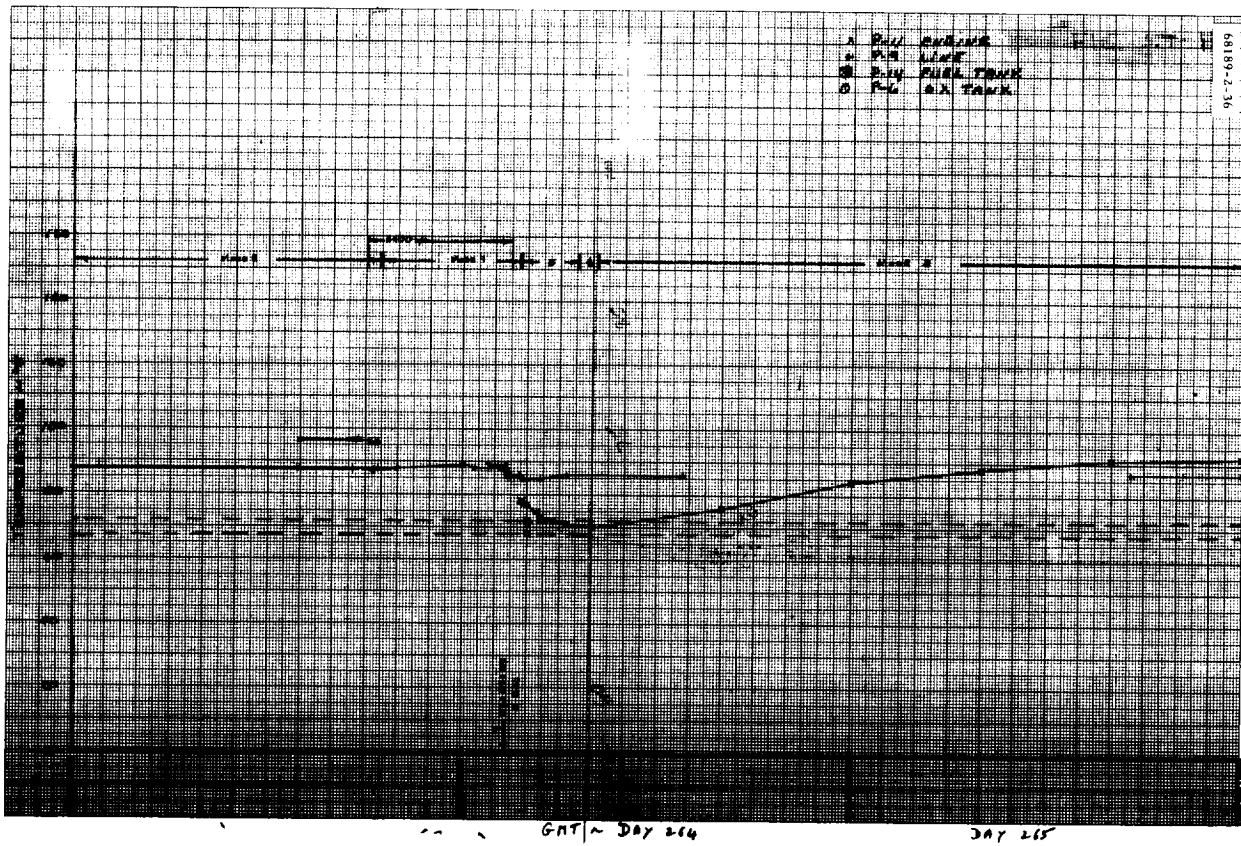
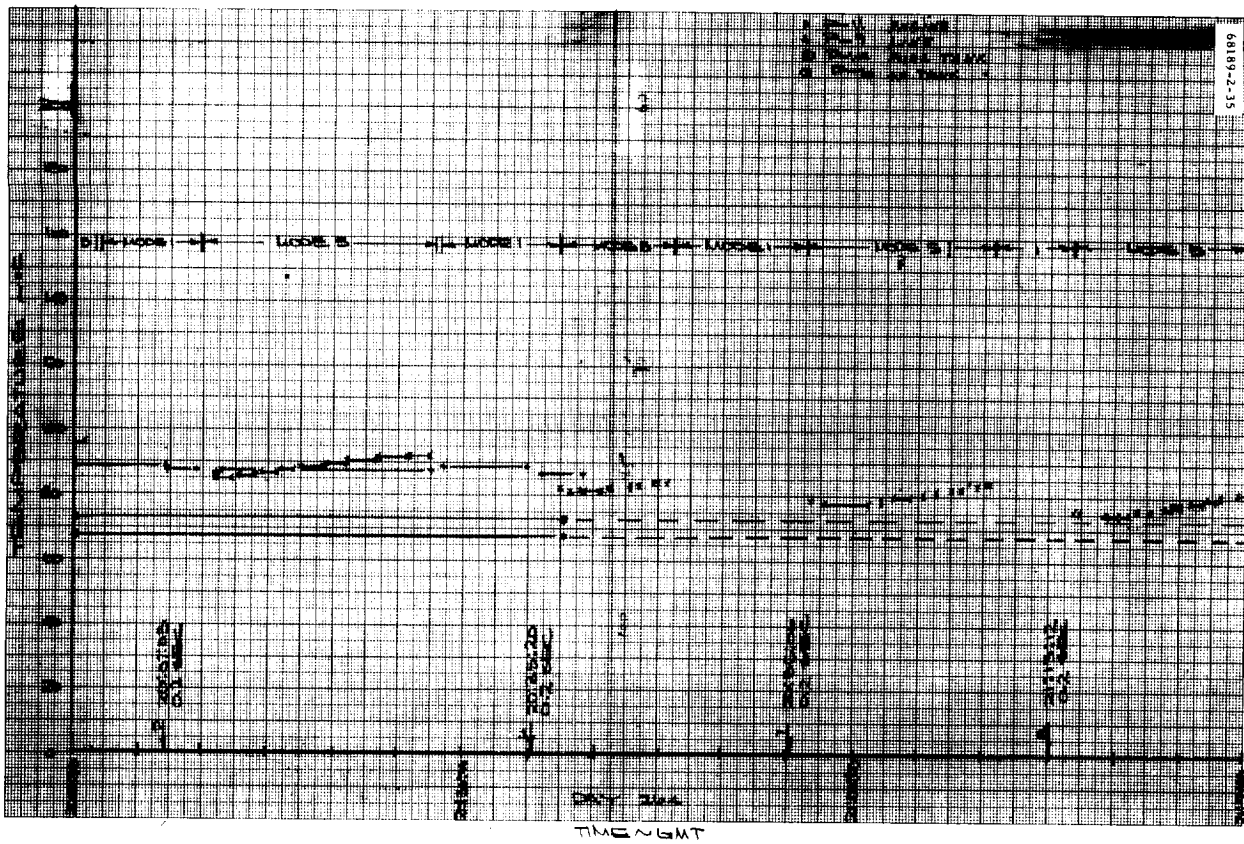


Figure 5.1-7 (continued). SC-2 VPS Thermal Response, Leg 3

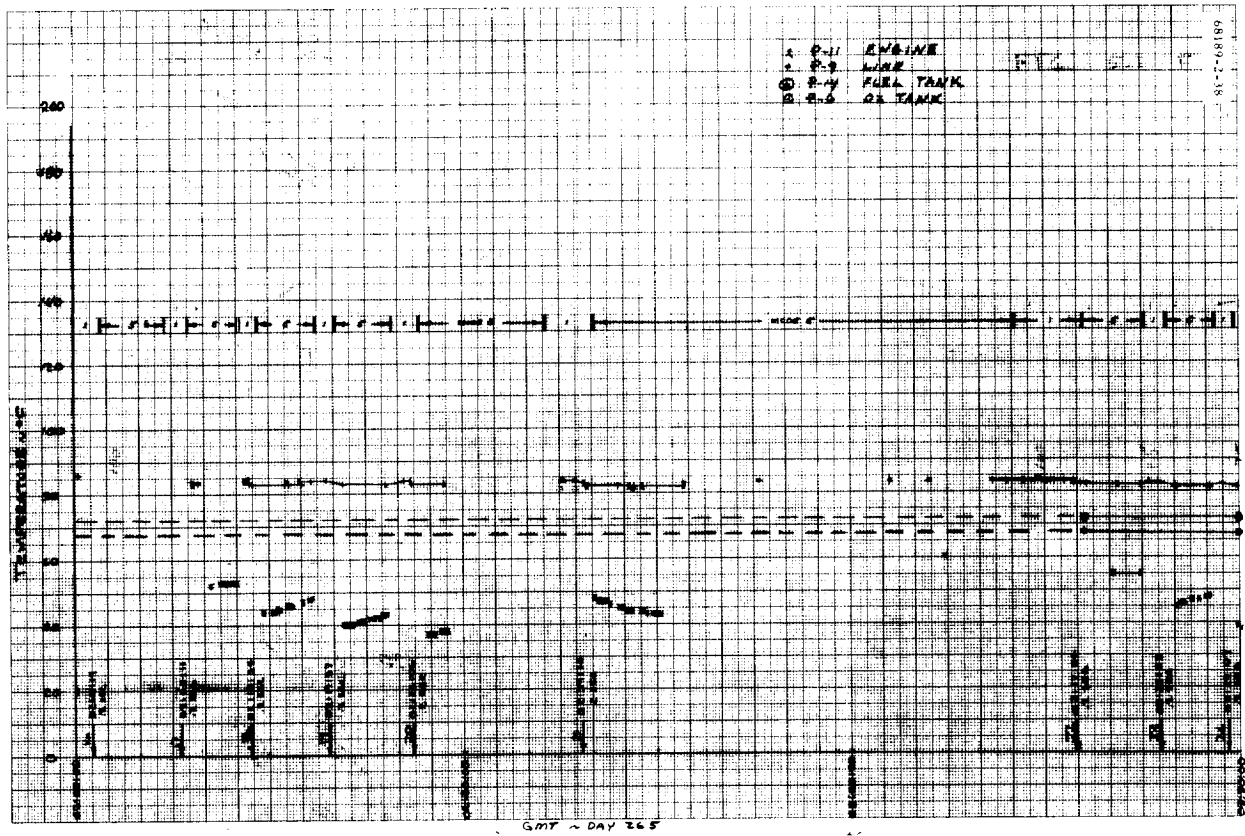
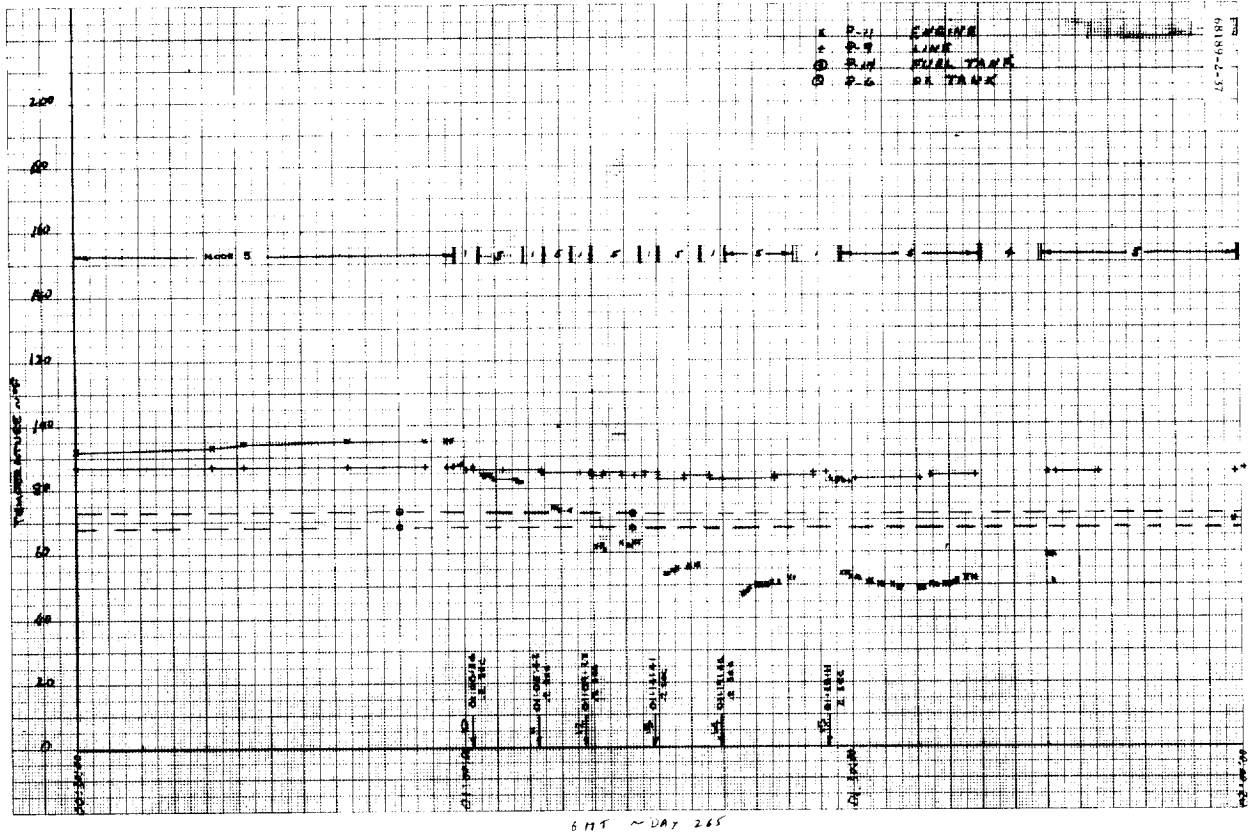
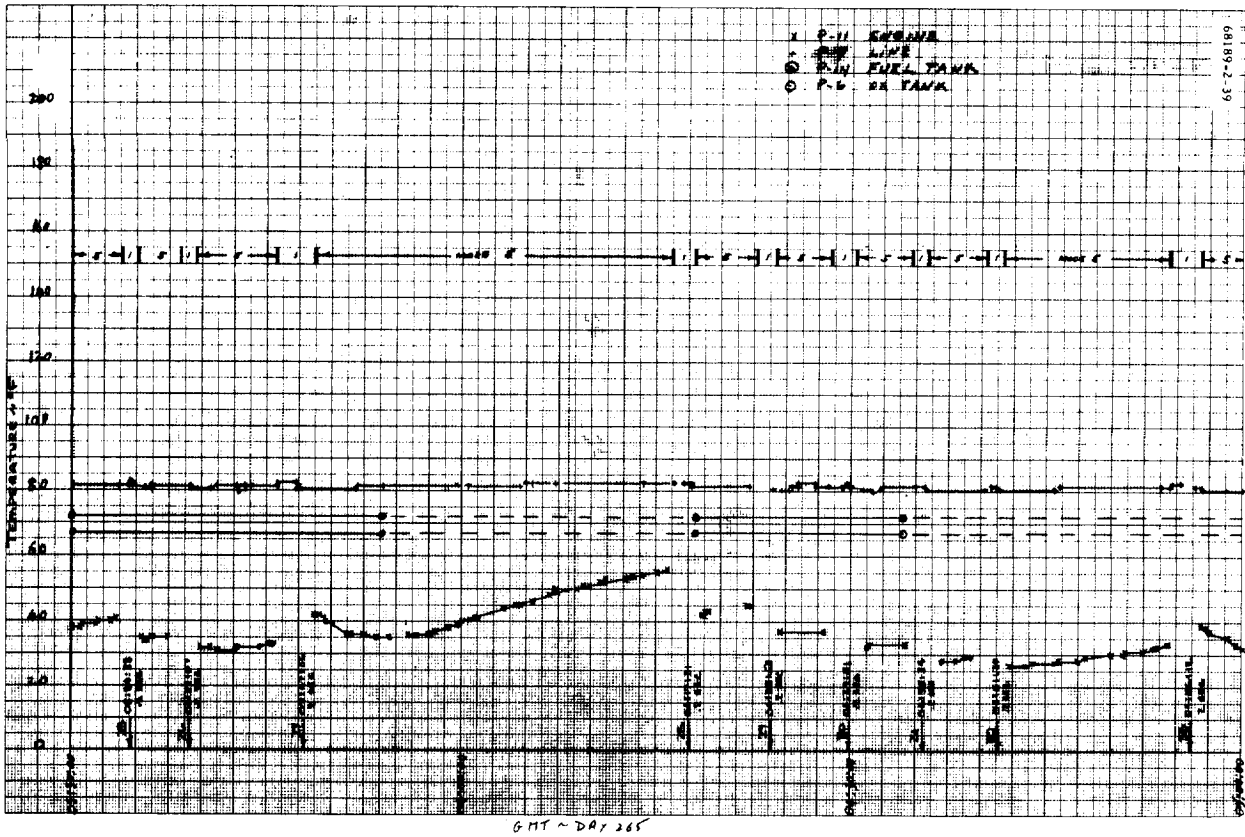
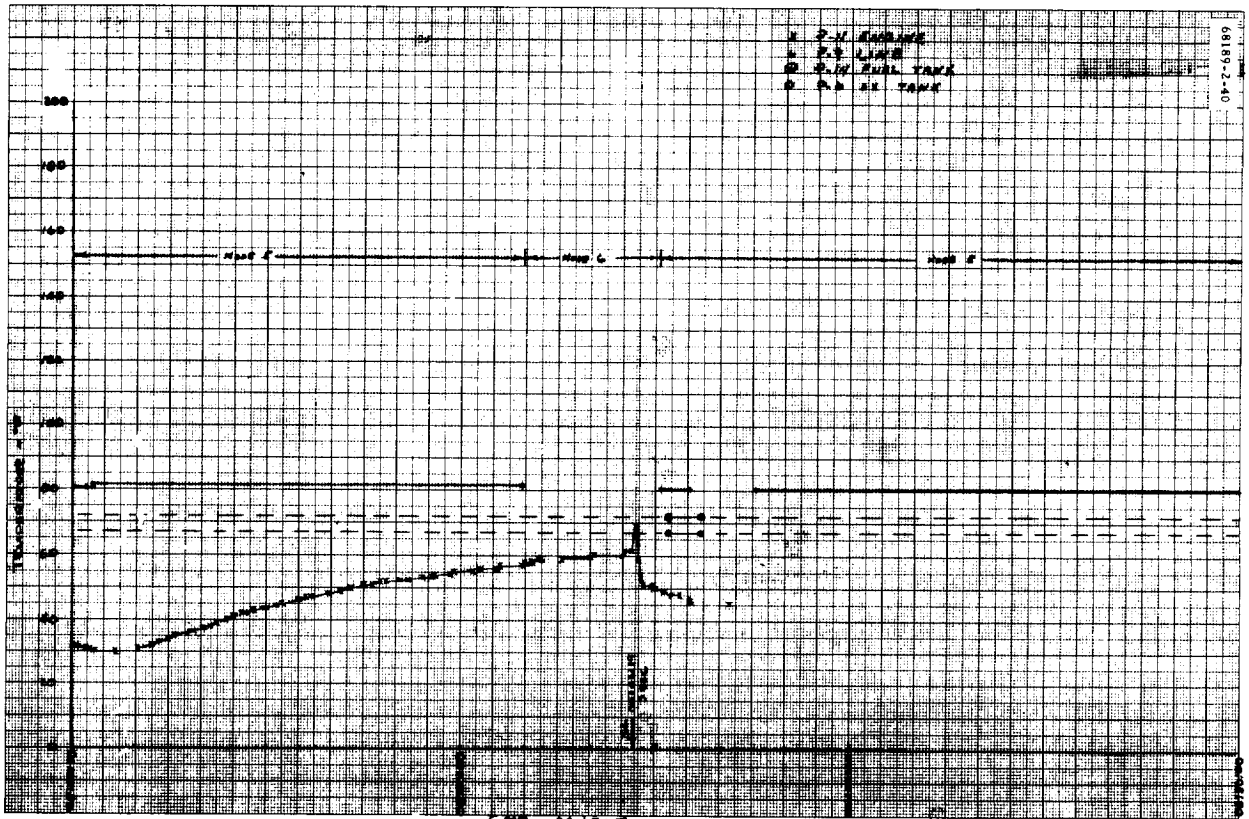


Figure 5.1-7 (continued). SC-2 VPS Thermal Response, Leg 3



GMT ~ DAY 265



GMT ~ DAY 266

Figure 5.1-7 (continued). SC-2 VPS Thermal Response, Leg 3

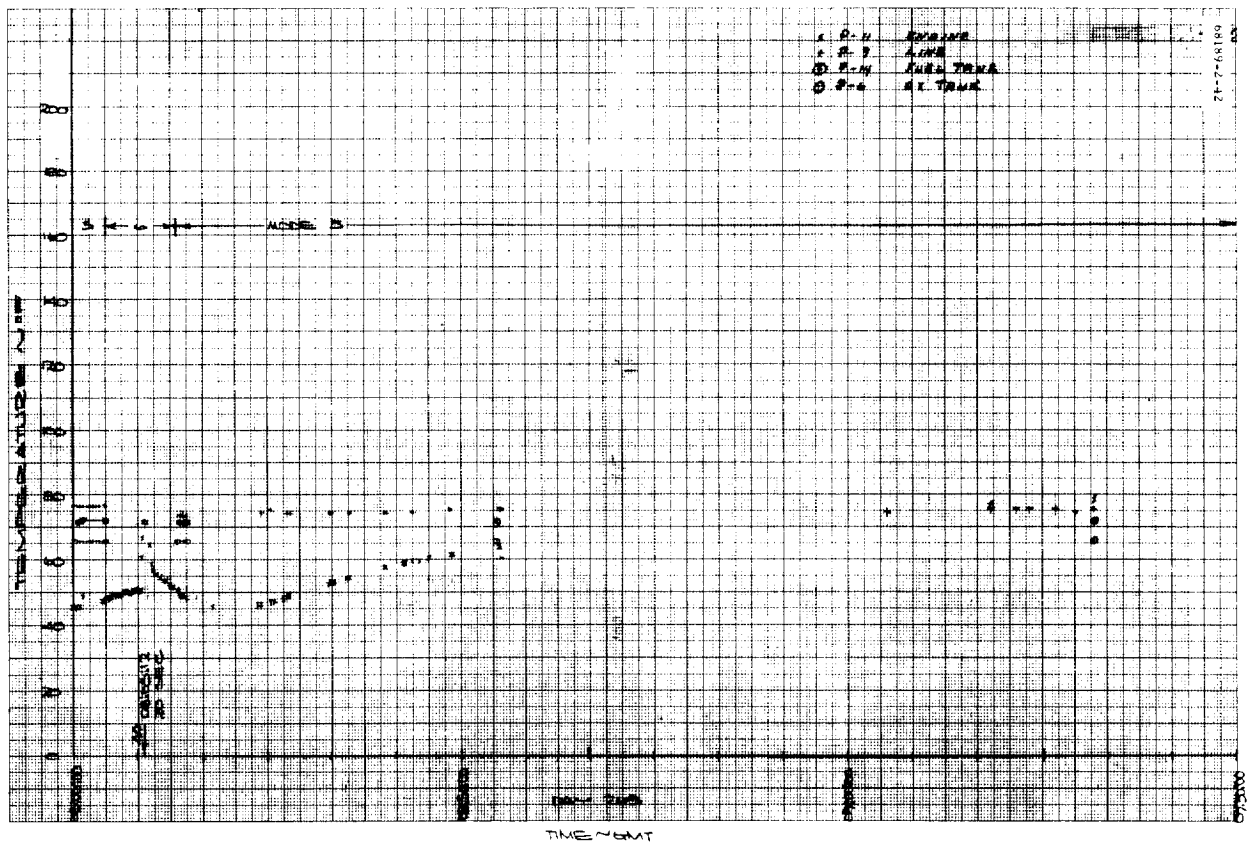
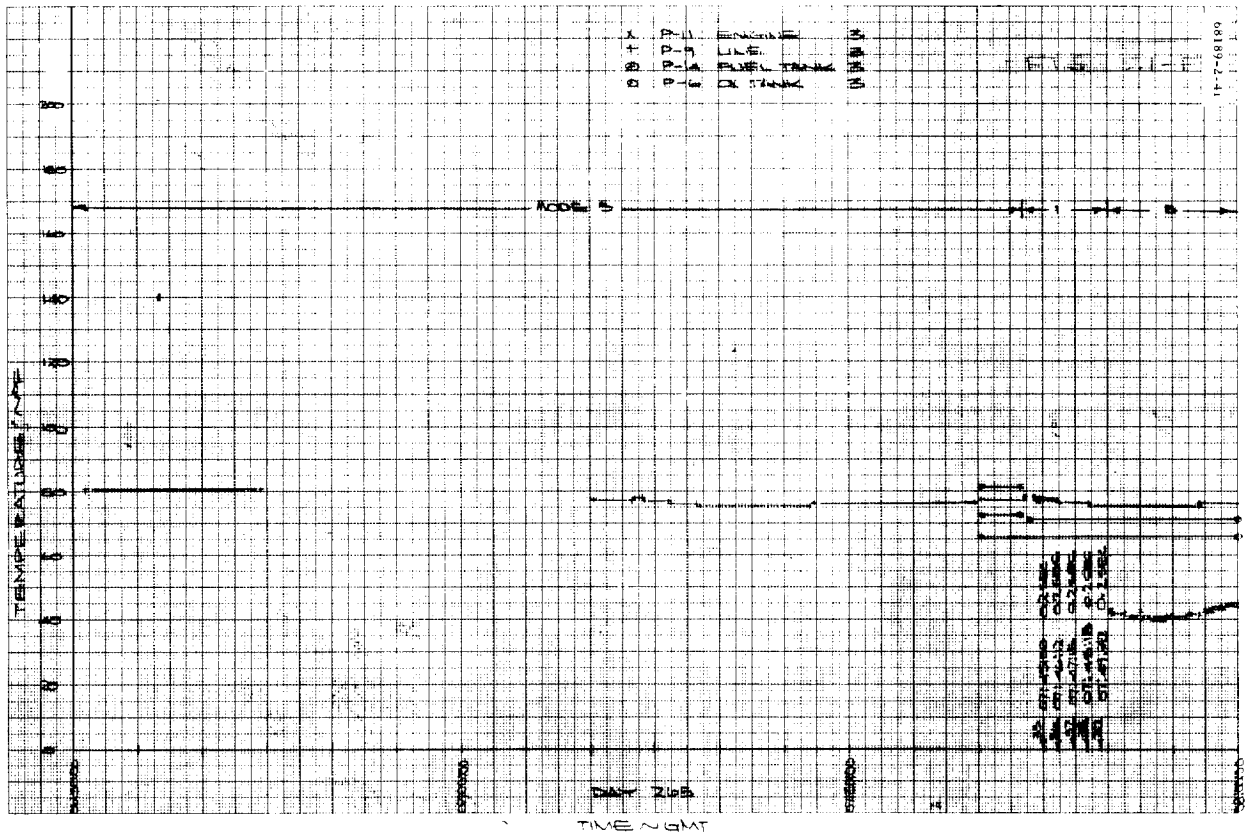


Figure 5.1-7 (continued). SC-2 VPS Thermal Response, Leg 3

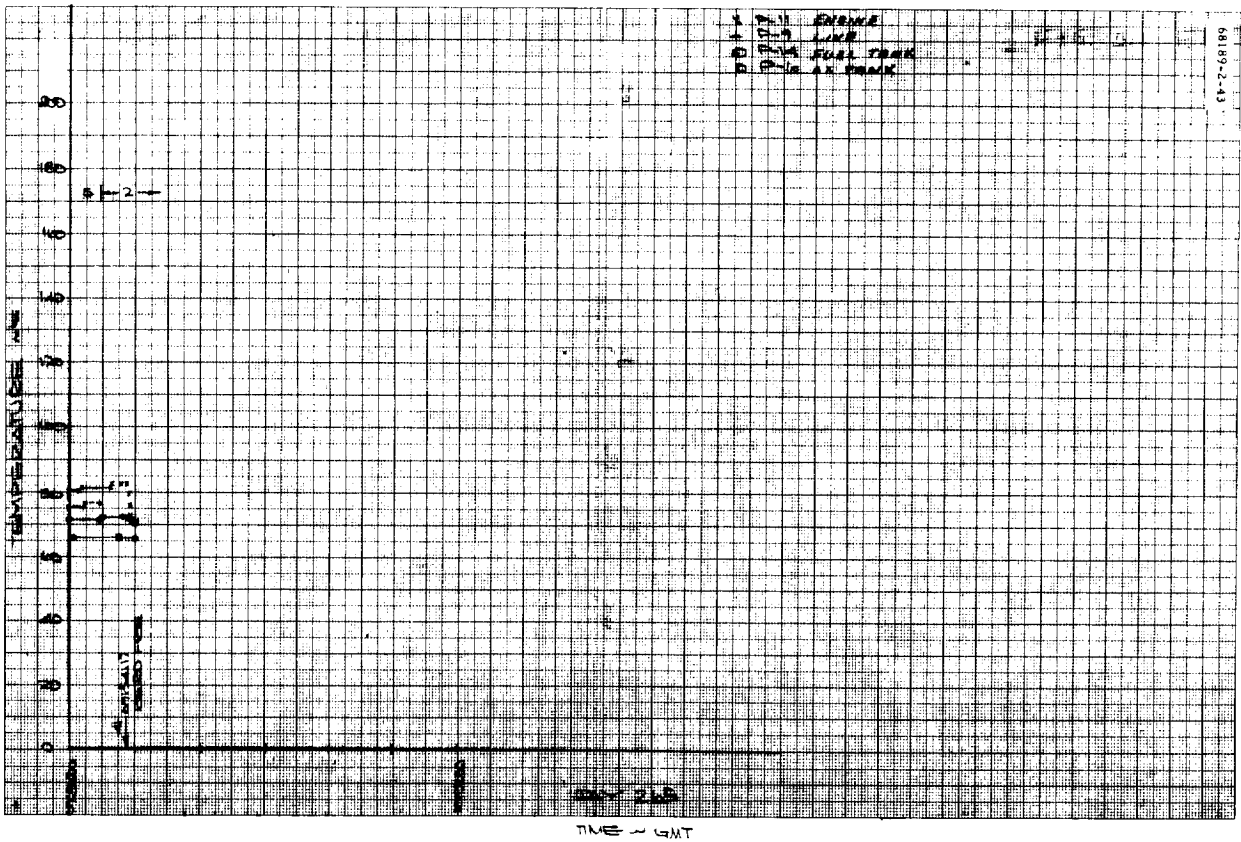


Figure 5.1-7 (continued). SC-2 VPS Thermal Response, Leg 3

THE THERMAL RESPONSE OF VERNIER ENGINE  
FLIGHT SENSOR TO FUEL FLOW

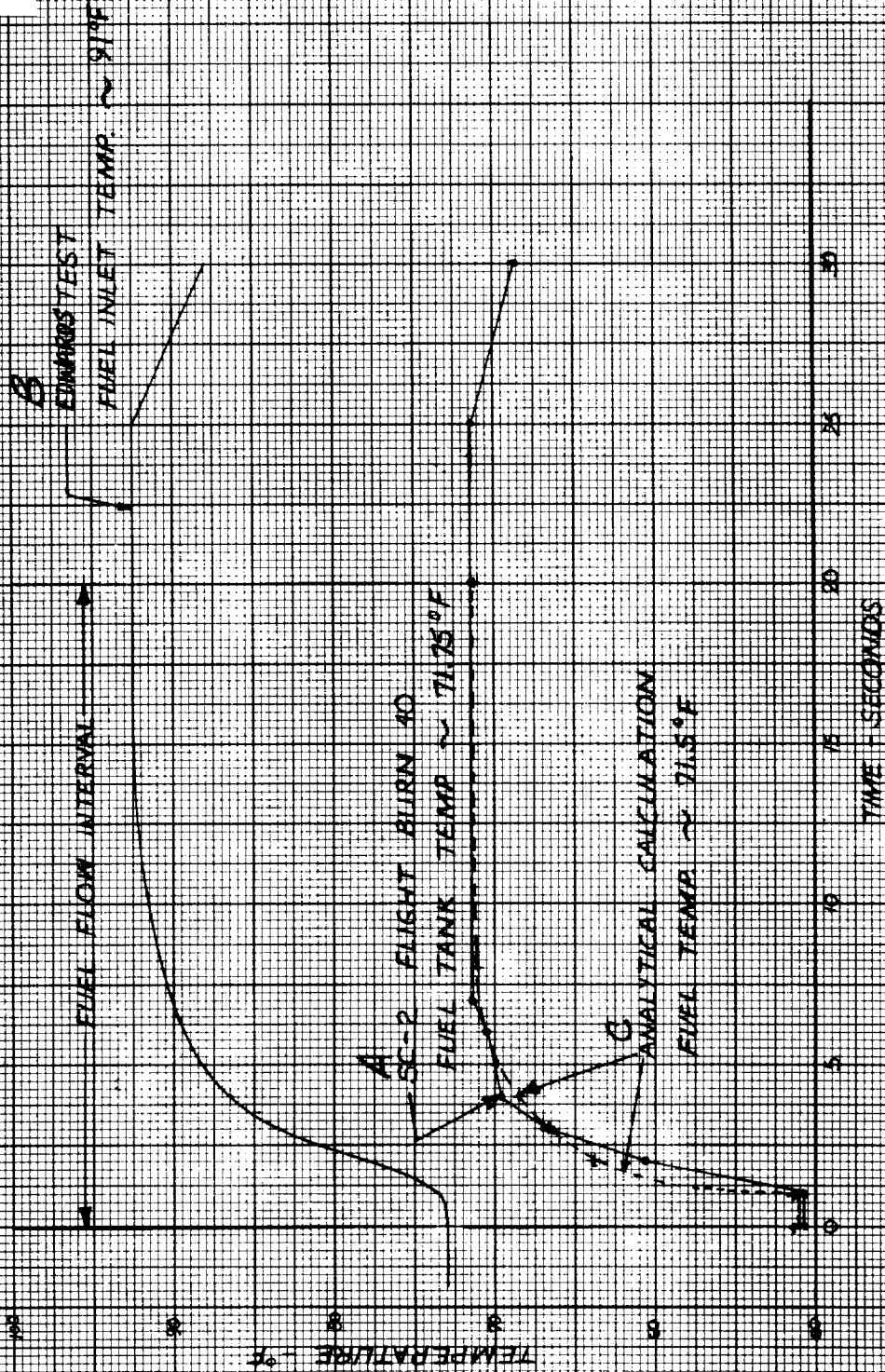


Figure 5.1-8. Thermal Response of Vernier Engine Flight Sensor to Fuel Flow



observing the thermal behavior of TCA 1 during the 0.25-second burn attempts. Burn 11 of the 0.25-second series exhibited thermal characteristics similar to the 2.00-second burn attempts for that engine. Likewise, burn 27 of the 2.0-second burn attempts appears to be longer in duration. A similar comparison of the thermal data for TCA 2 indicates that the temperature rise resulting from burns 2 and 3 was approximately 20°F; the increase resulting from burns 9, 15, 21, 27, and 33 was approximately 60°F. Hence, it is concluded that the thermal behavior of the thrust chamber assemblies is inconsistent within themselves even when viewed on an individual engine basis.

The above anomalous engine behavior is demonstrated in Figure 5.1-9 where the thrust chamber barrel temperature increase resulting from engine ignition is shown as a function of burn number. The data presented in this figure is merely a quantitative measure of the energy released by the engines during the 2.0-second burns. Energy release is synonymous with temperature change. While Figure 5.1-9 does not give any qualitative information regarding TCA thermal behavior, it does indicate, for example, that the thermal behavior of TCA 2 during burns 2 and 3 was substantially different from the thermal behavior of the engine during burns 9, 15, 21, 27, and 33. This is further illustrated by observing the flight data presented in Figure 5.1-10 and extrapolating back to the peak temperatures for all 2.0-second burns.

Similarly, burn 11 of the 0.25-second burns and burn 27 of the 2.0-second burns appear to be anomalous for TCA 1. The engine total temperature rise during burn 11 is very similar in magnitude to the temperature rise exhibited by TCA 1 during the 2.0-second burns. An inspection of Figure 5.1-11 indicates that the thrust chamber barrel (engine 1) temperature change ( $\Delta T$ ) increased by more than a factor of 3 for burn 27 when compared with the barrel temperature change for other 2.0-second burns. An investigation of the command signals indicates that the engine was commanded on and off for a nominal 2.0-second burn. However, a review of the strain gage data (Figure 5.1-12) indicates that the engine operated at the minimum thrust level (-80 milliamperes) as commanded for 2.0 seconds. Strain gage data indicate that the engine probably did not shut off after 2.0 seconds, but continued to burn at midthrust level for an additional 2.50 seconds. TCA 1 thermal behavior during burn 27 is not anomalous, and the larger than expected temperature rise is indeed explainable.

The data presented in Figure 5.1-9 also indicate that the temperature rise of the engine 1 barrel continued to increase with each successive 2.0-second firing. One explanation for this behavior would be an error in the extrapolation process that determines the engine peak temperature. Another and probably more logical inference is that the thermal resistance to the flow of heat through the combustion chamber wall gradually decreased as a result of the successive firing attempts.

It is interesting to note and compare the temperature increases resulting from burns 2 and 3 with those for burns 9, 15, 21, 27, and 33. The data suggest that some type of irreversible change took place within engine 2 between burns 3 and 9. The data further suggest two discreet, but yet consistent, levels of operation for TCA 2 during the 2.00-second burn attempts.

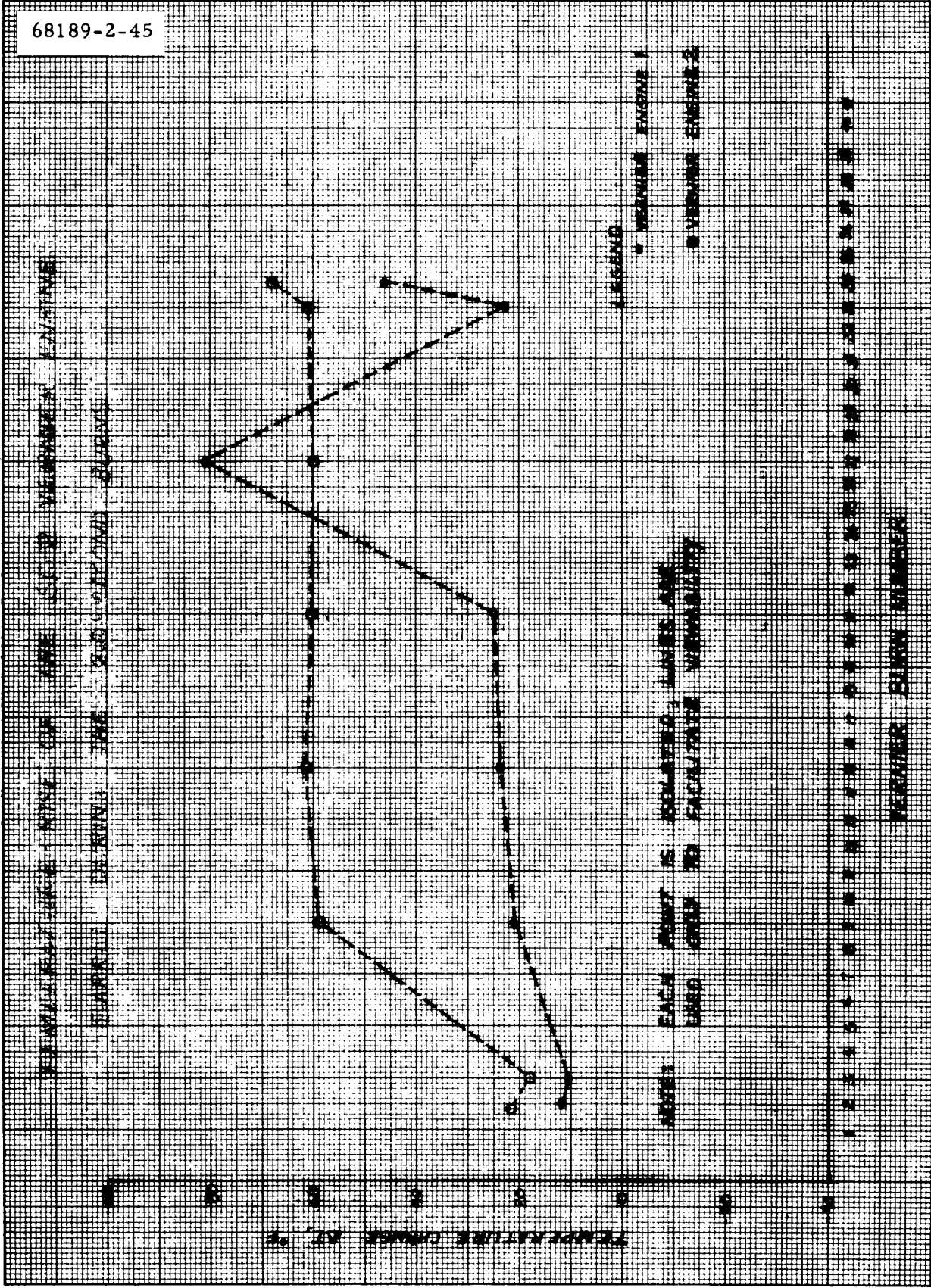


Figure 5.1-9. Vernier Engine Temperature Rise During 2.0-Second Burns

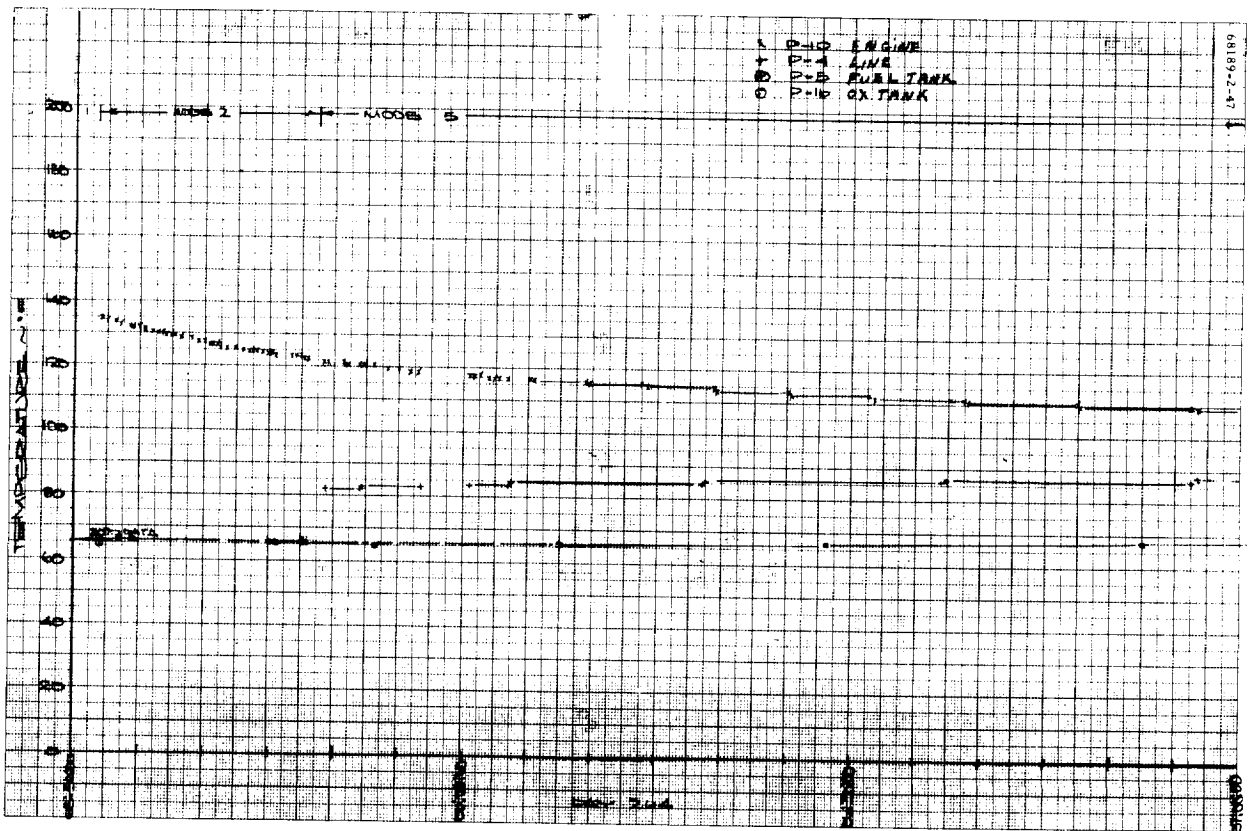
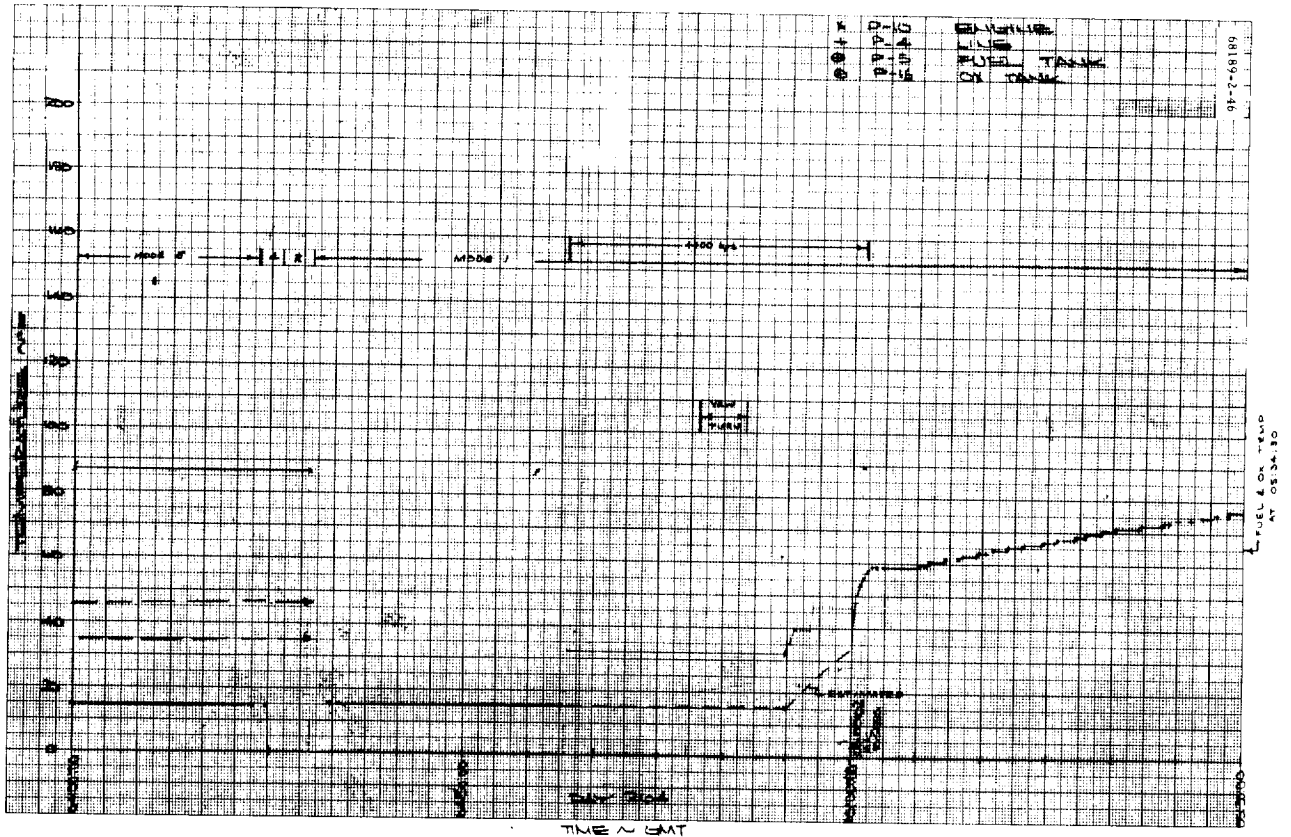


Figure 5.1-10. SC-2 VPS Thermal Response, Leg 2

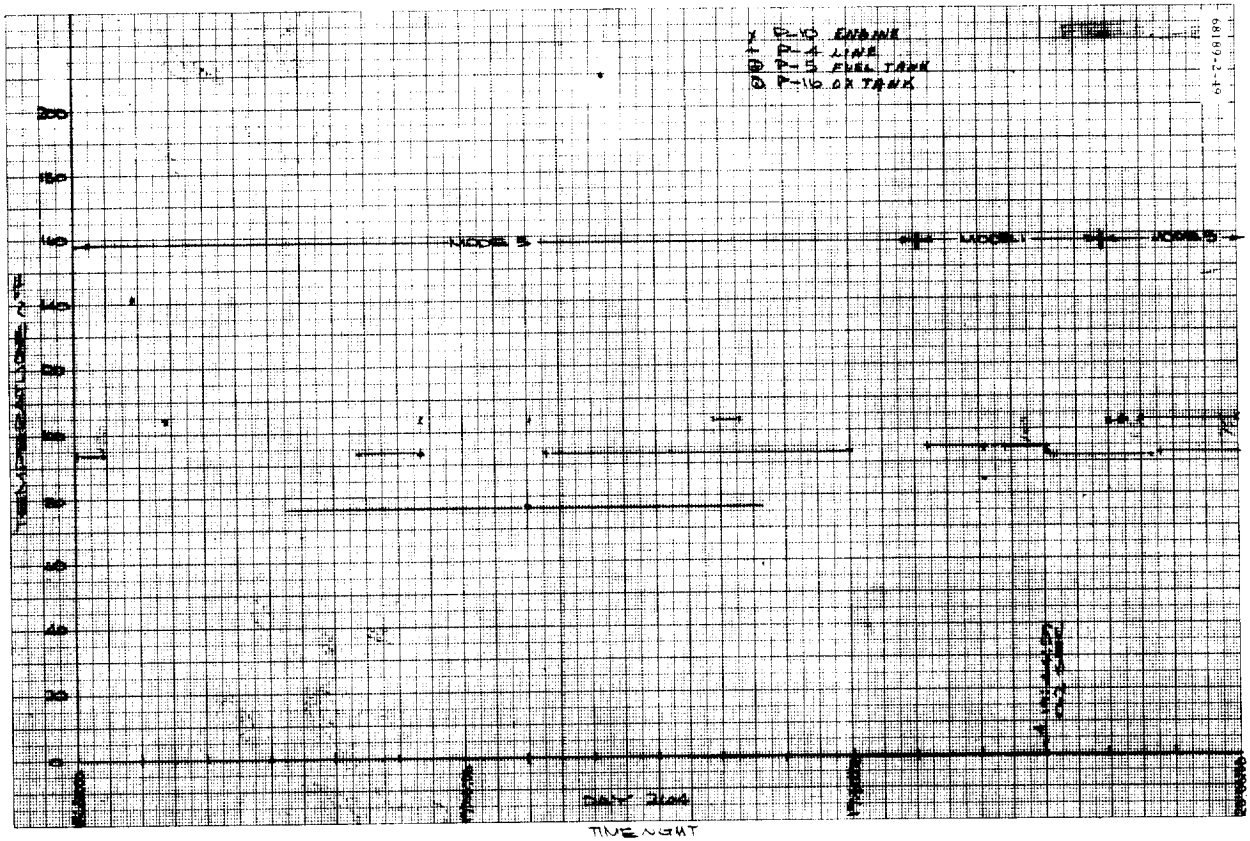
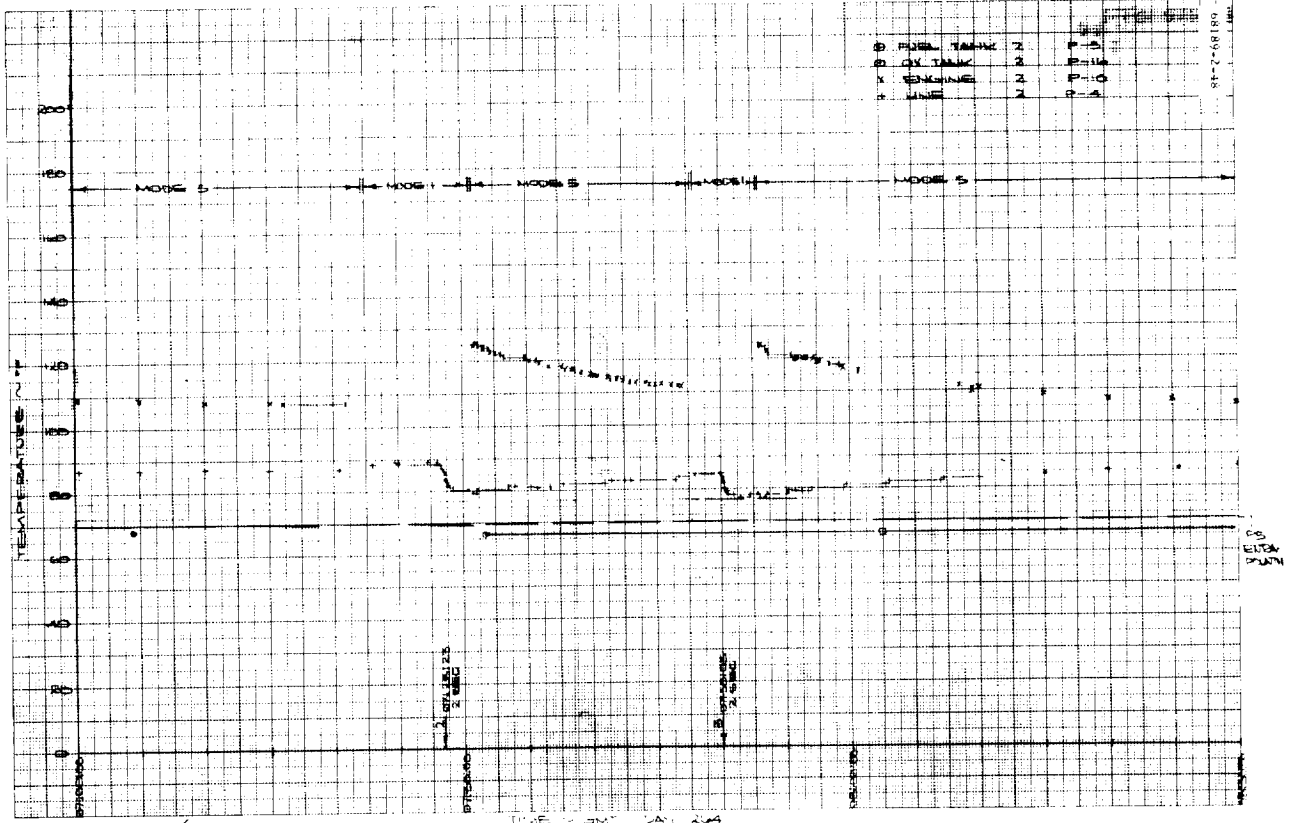


Figure 5.1-10 (continued). SC-2 VPS Thermal Response, Leg 2

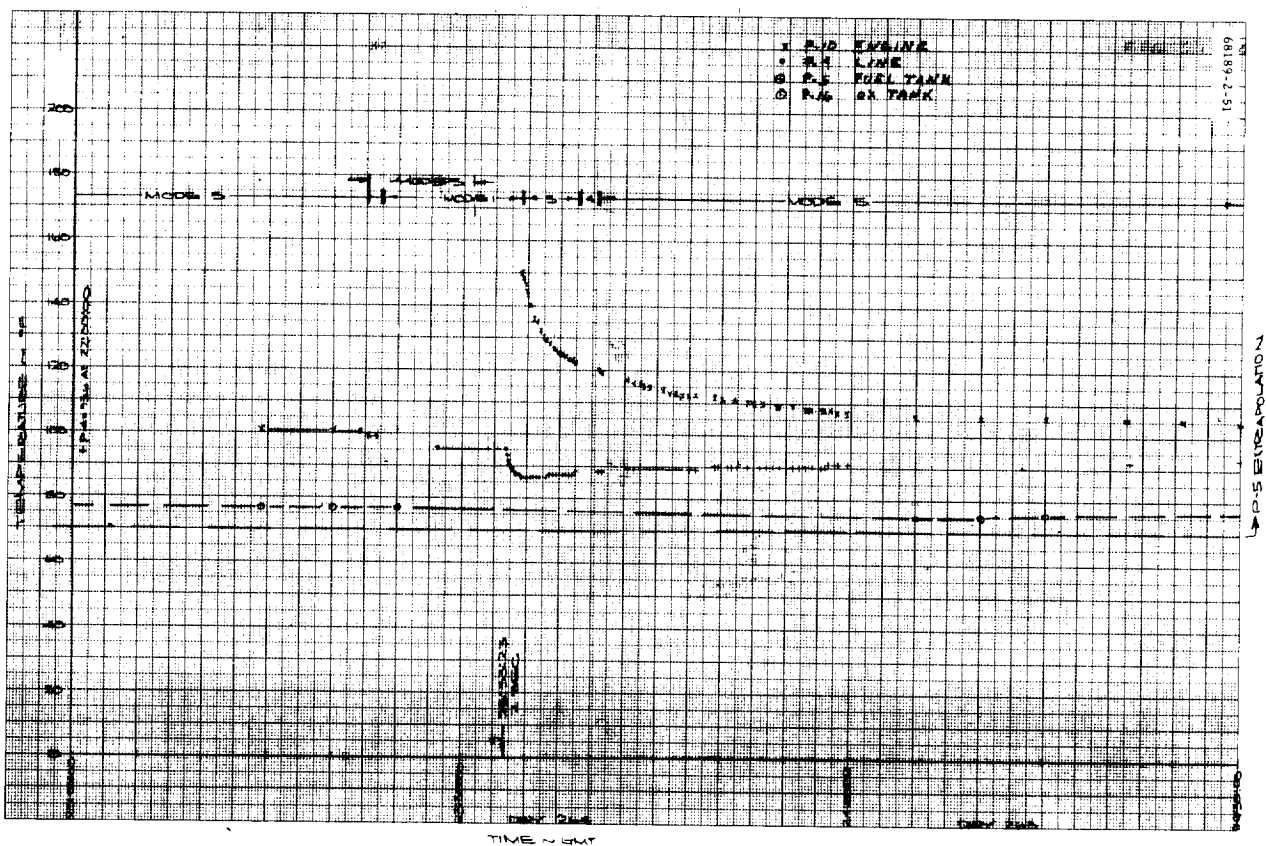
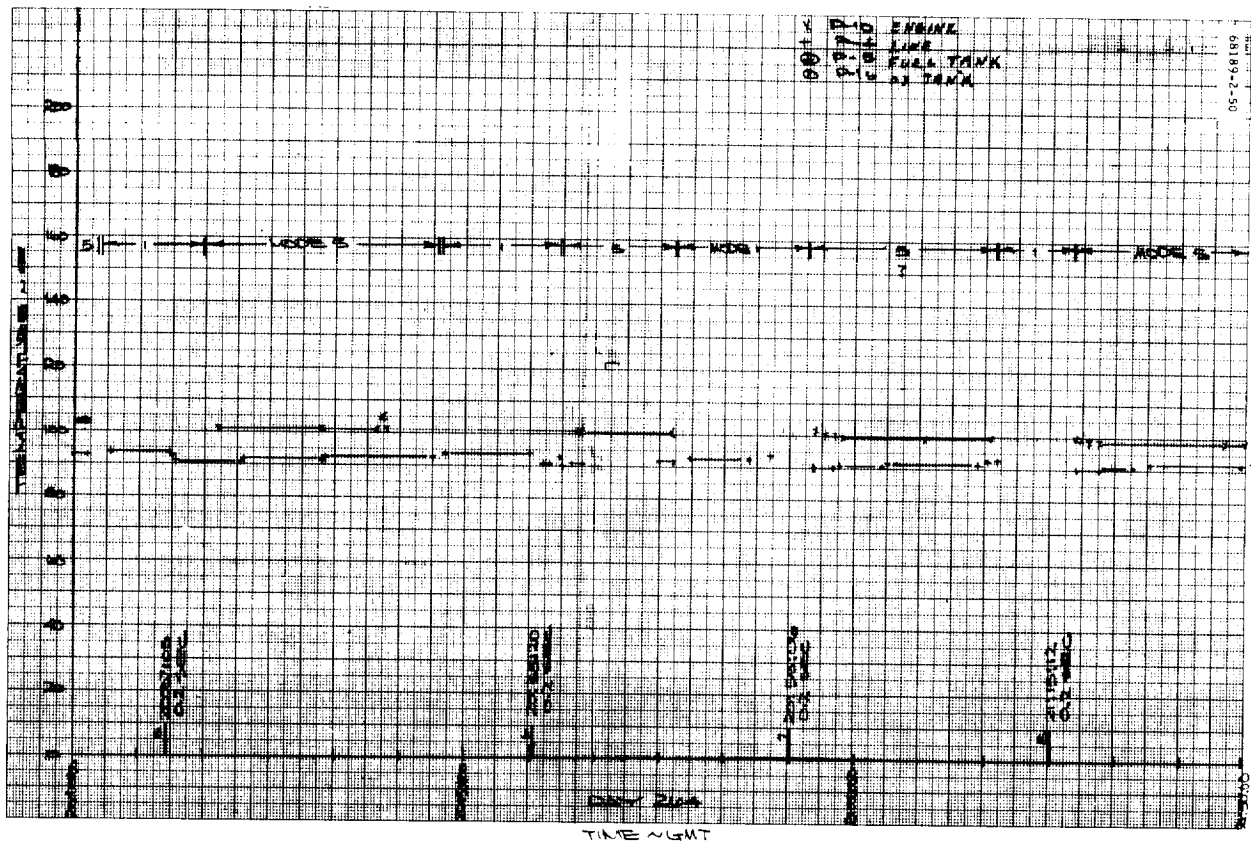


Figure 5.1-10 (continued). SC-2 VPS Thermal Response, Leg 2

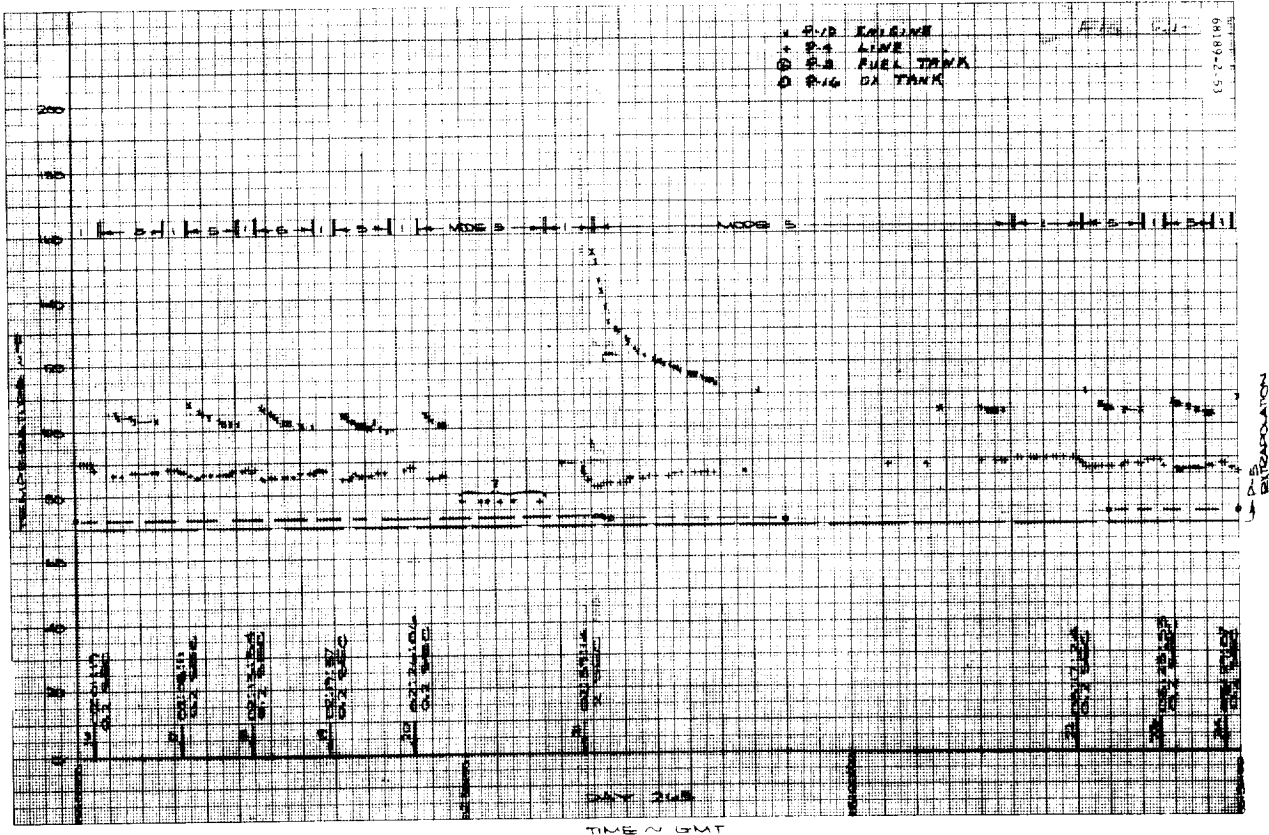
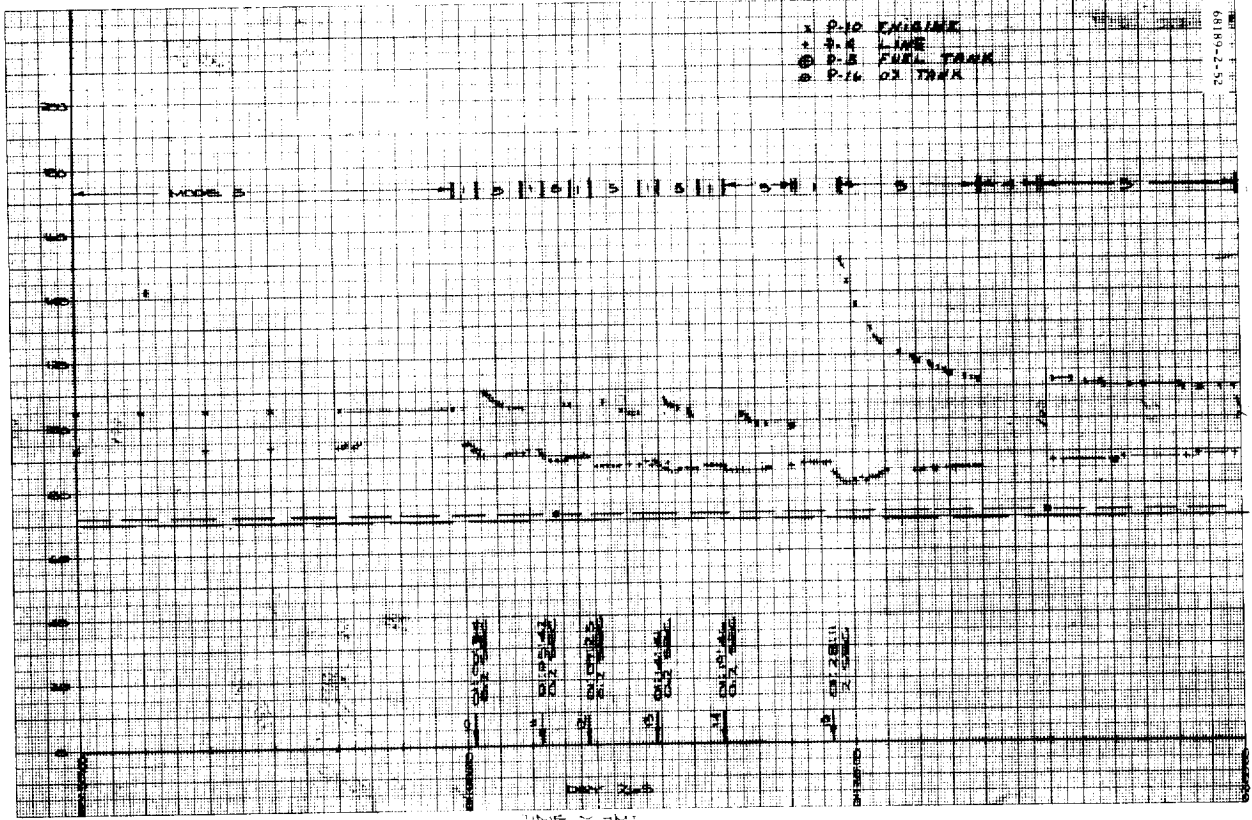
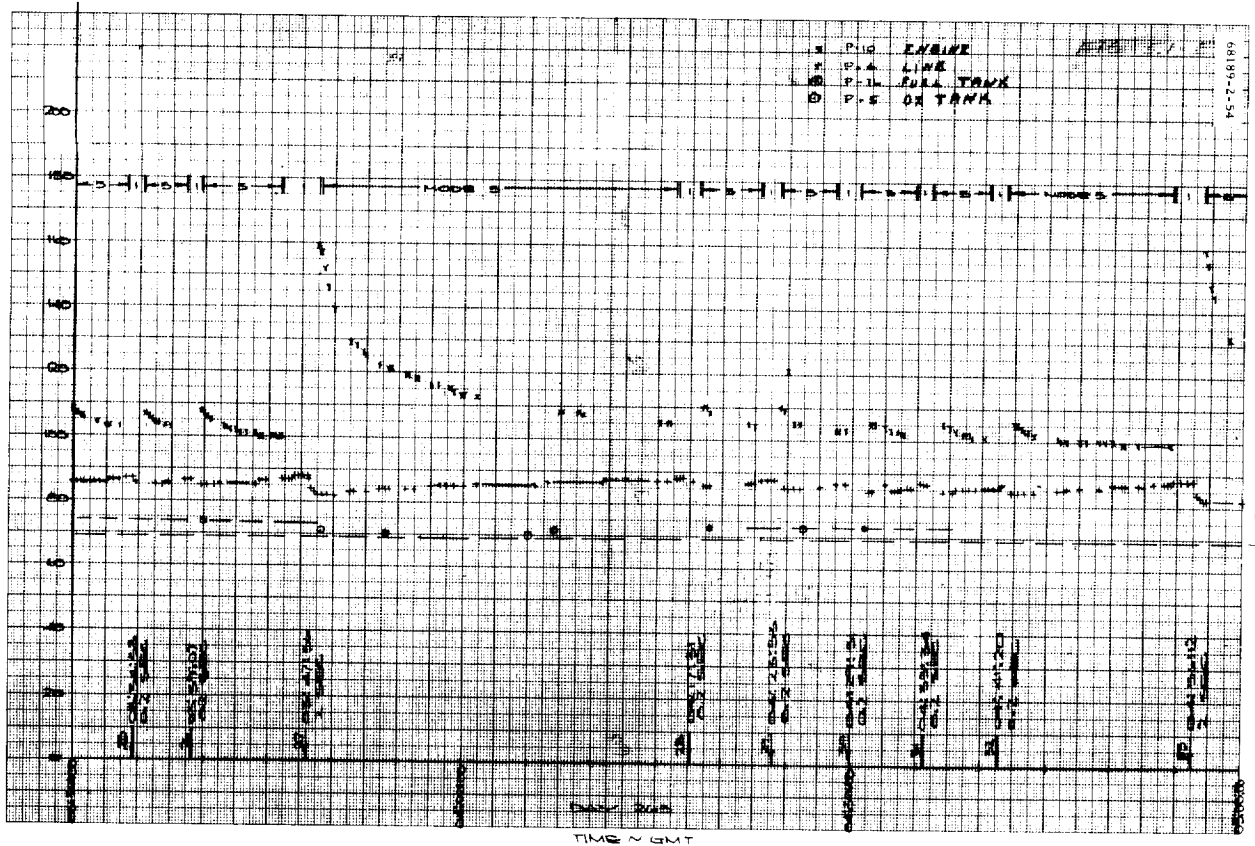


Figure 5.1-10 (continued). SC-2 VPS Thermal Response, Leg 2



LEG 2

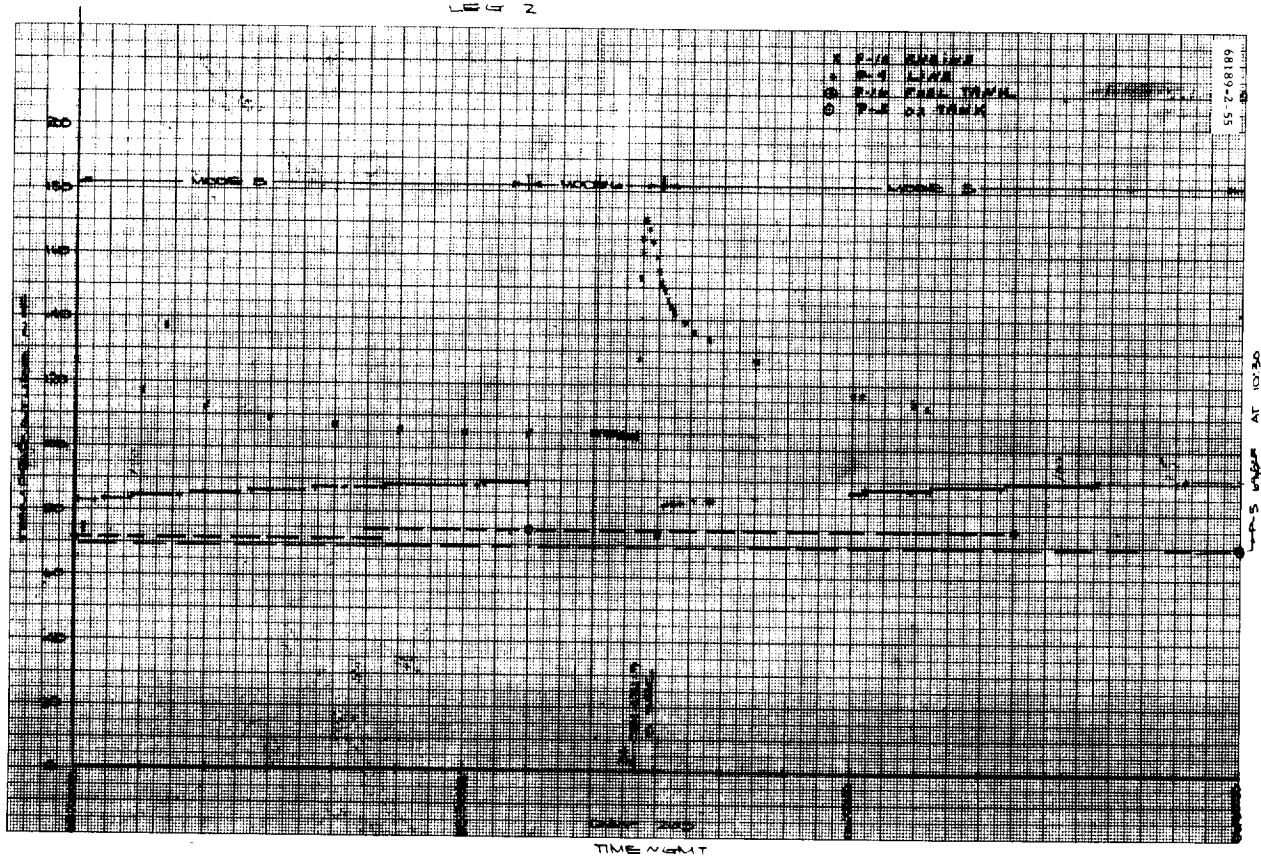


Figure 5.1-10 (continued). SC-2 VPS Thermal Response, Leg 2

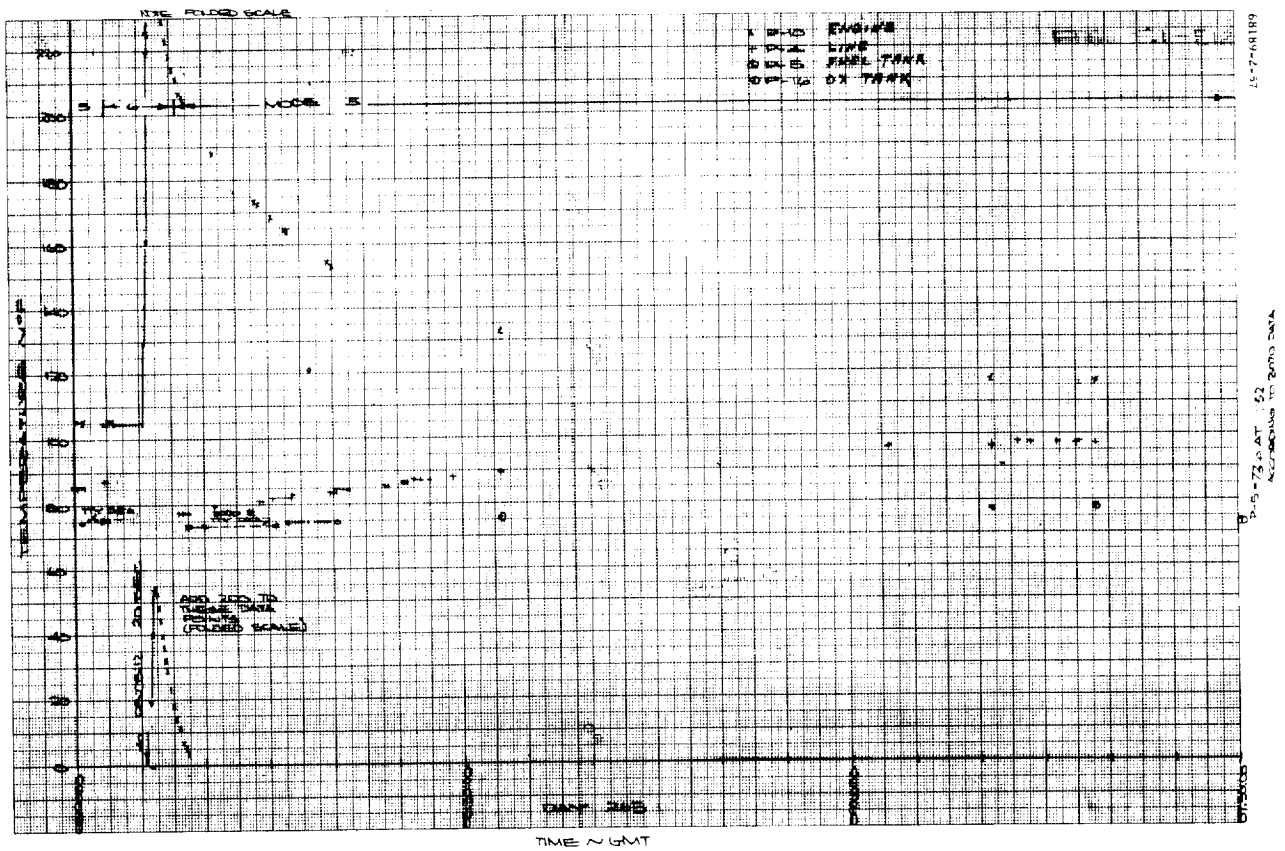
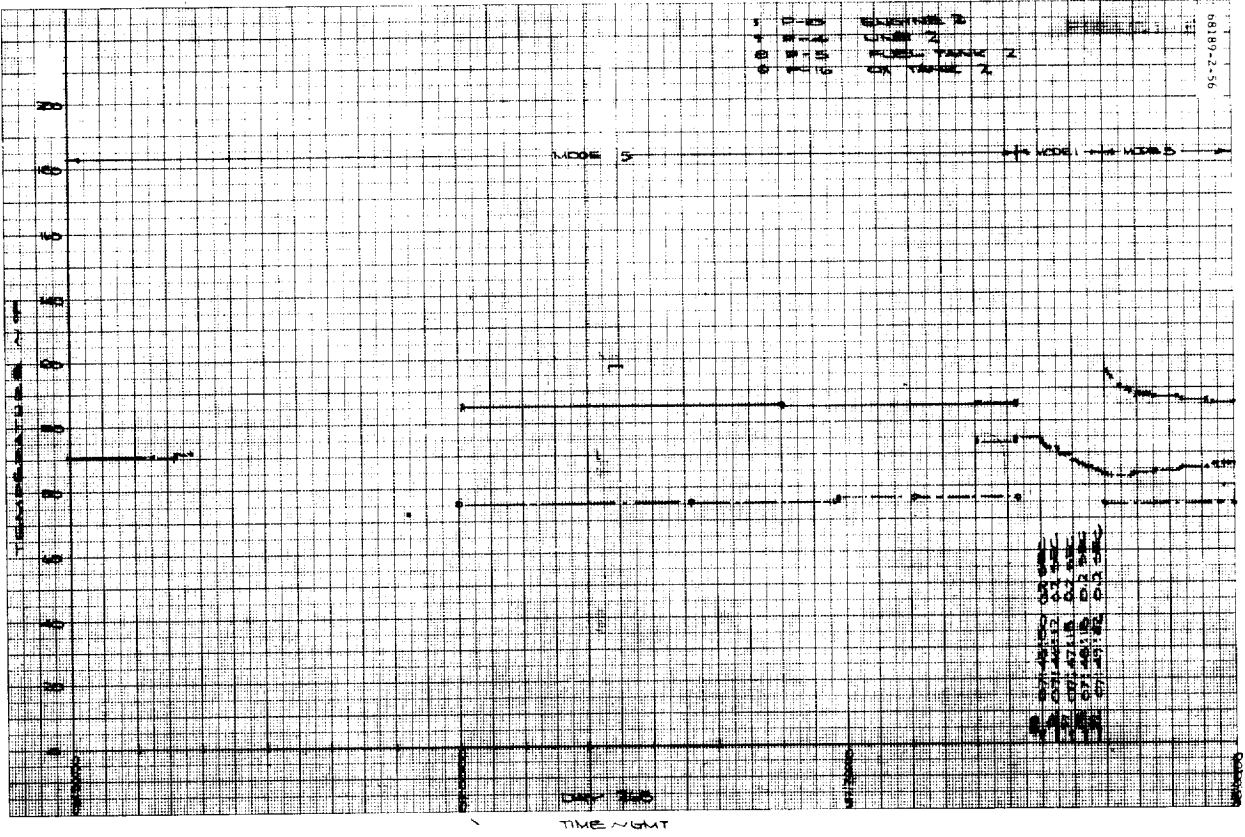


Figure 5.1-10 (continued). SC-2 VPS Thermal Response, Leg 2



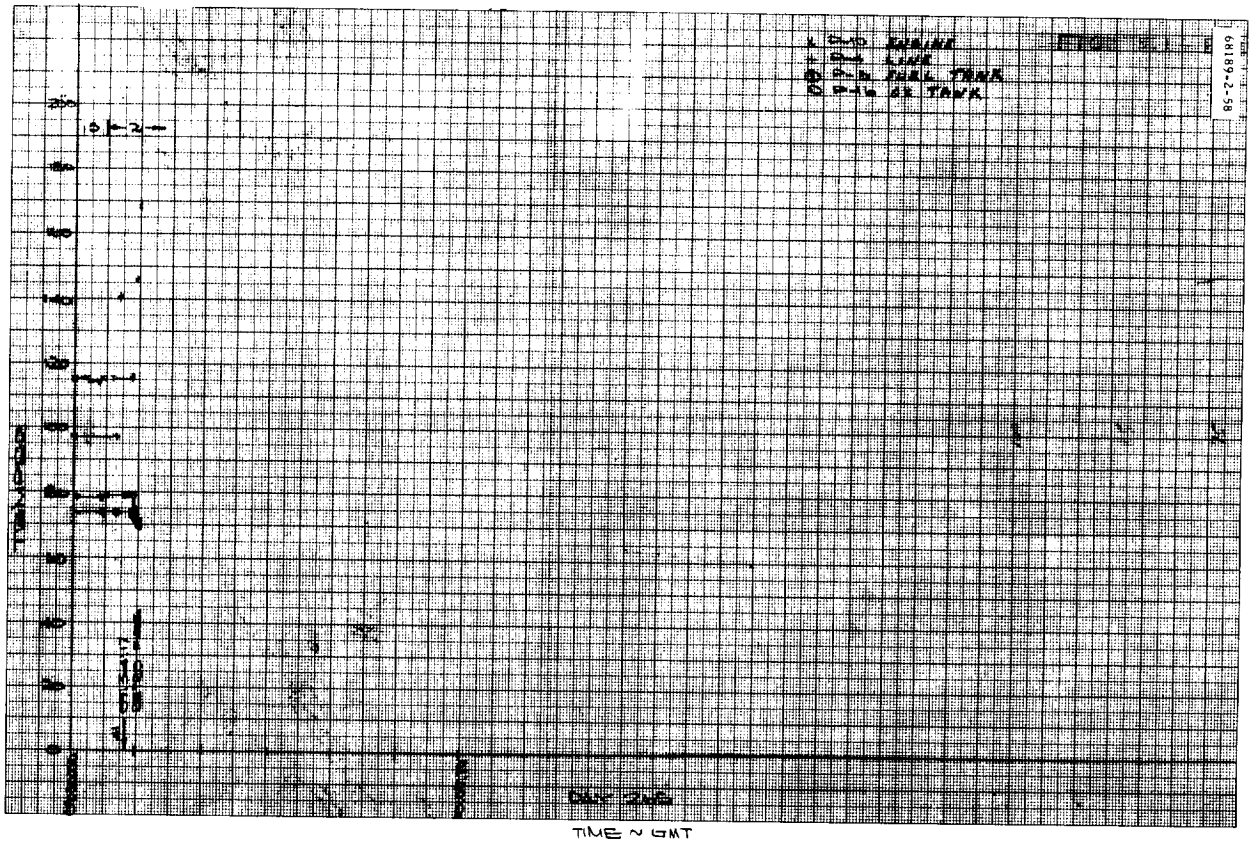


Figure 5.1-10 (continued). SC-2 VPS Thermal Response, Leg 2

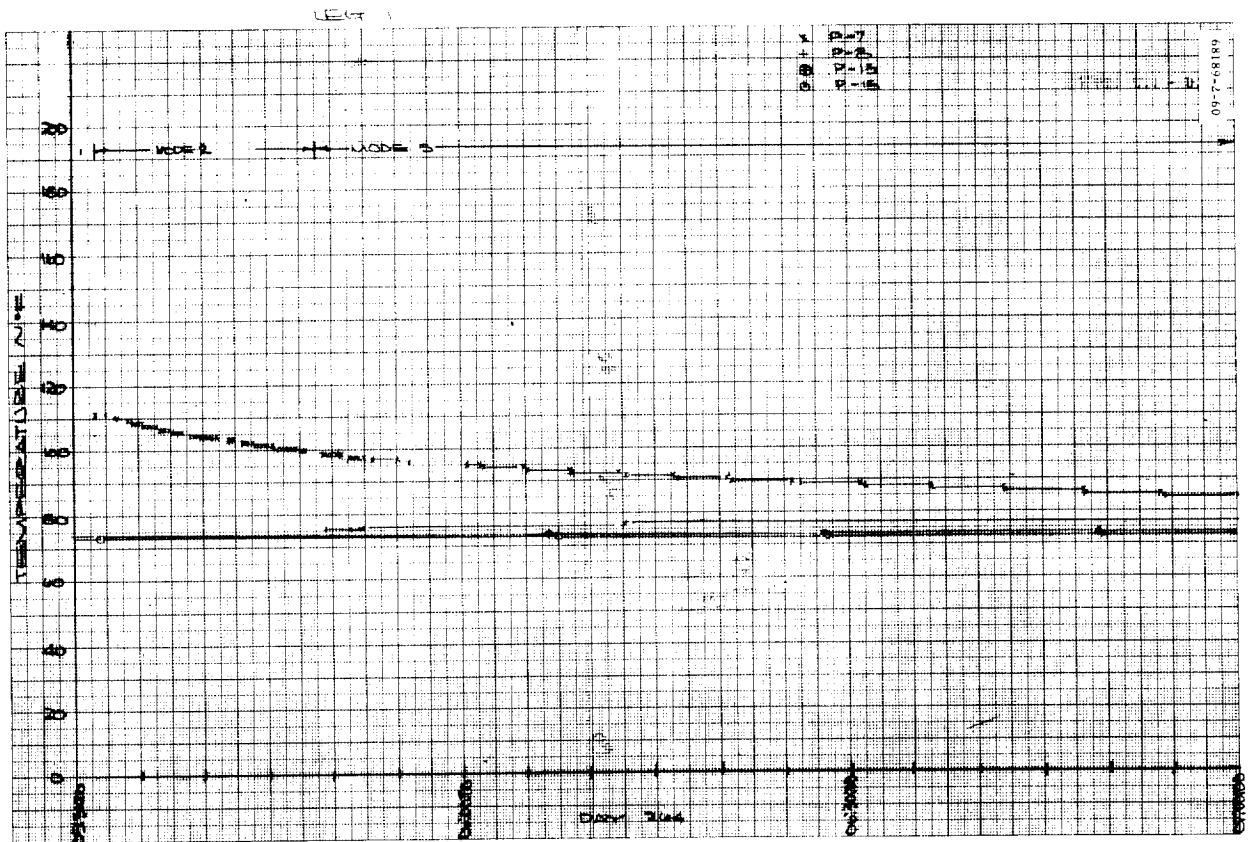
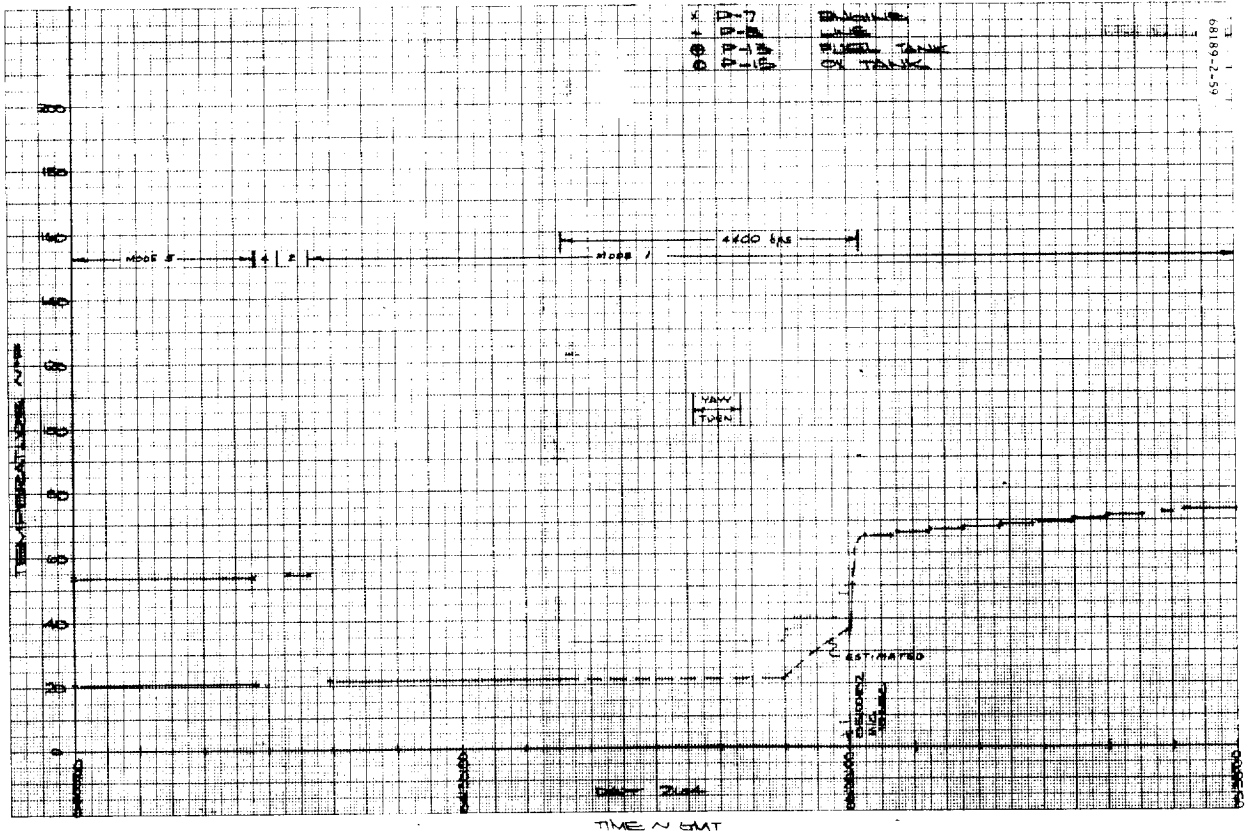


Figure 5.1-11. SC-2 VPS Thermal Response, Leg 1

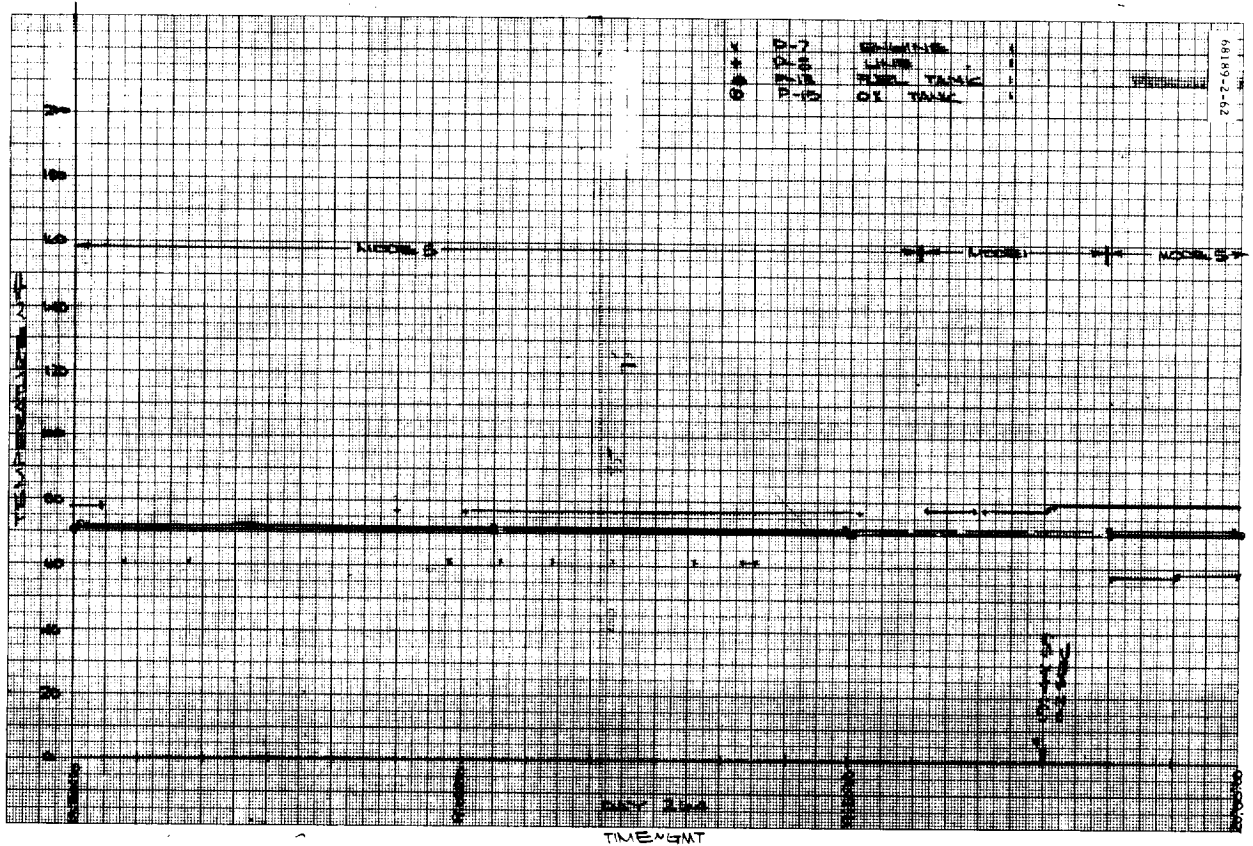
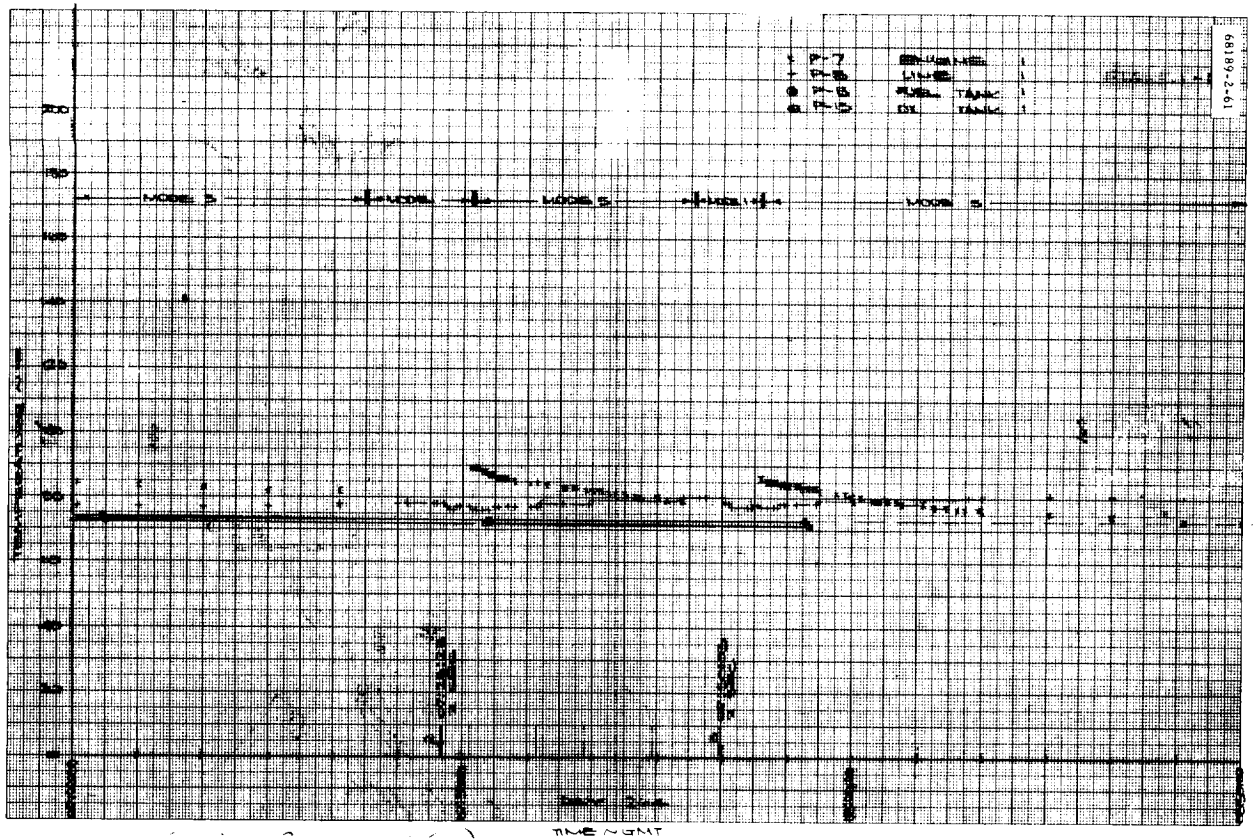


Figure 5.1-11 (continued). SC-2 VPS Thermal Response, Leg 1

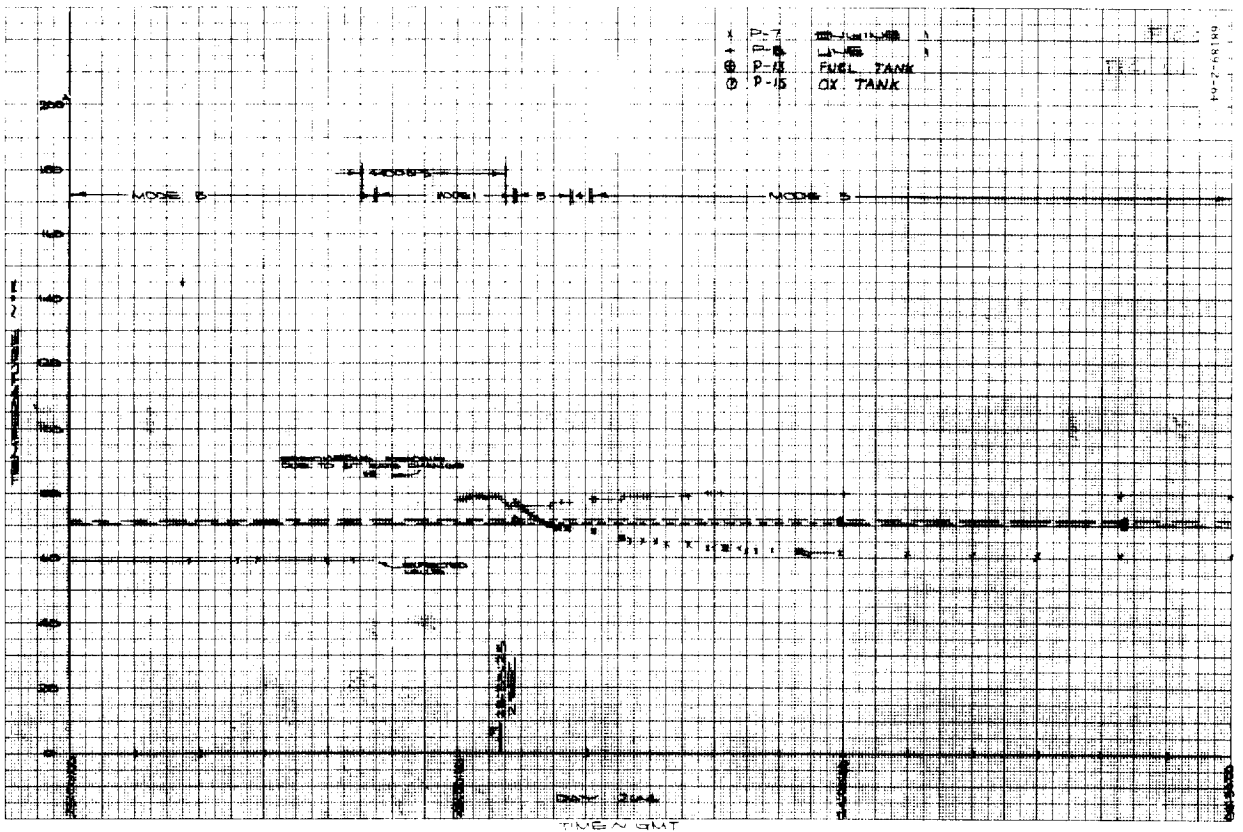
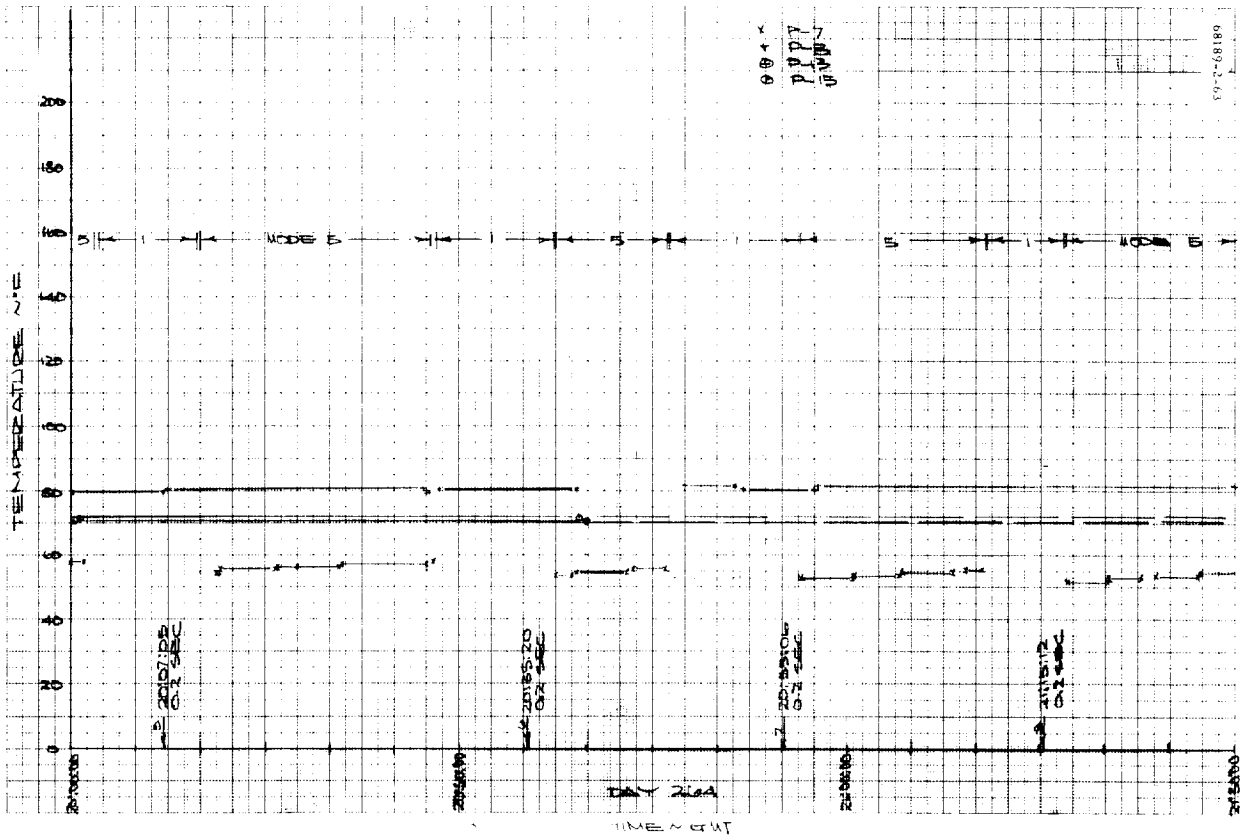


Figure 5.1-11 (continued). SC-2 VPS Thermal Response, Leg 1

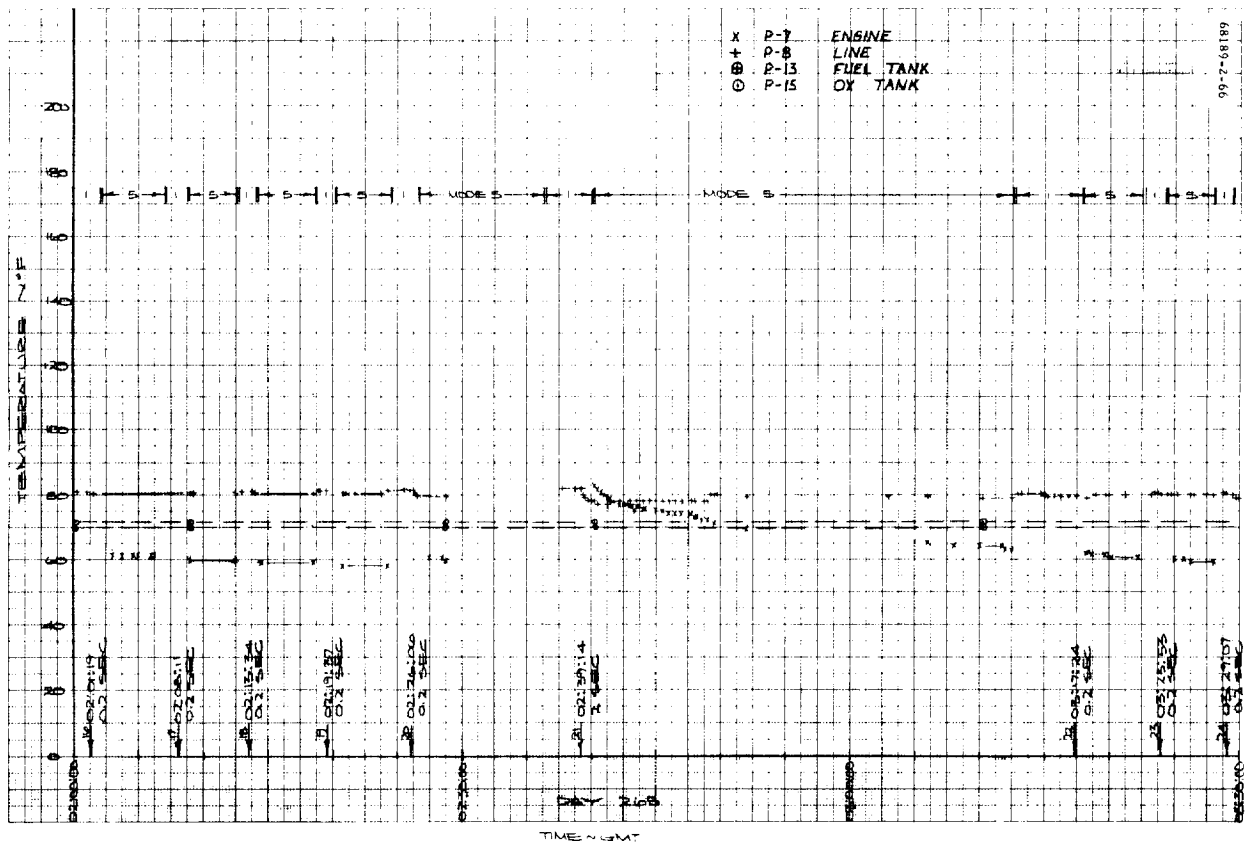
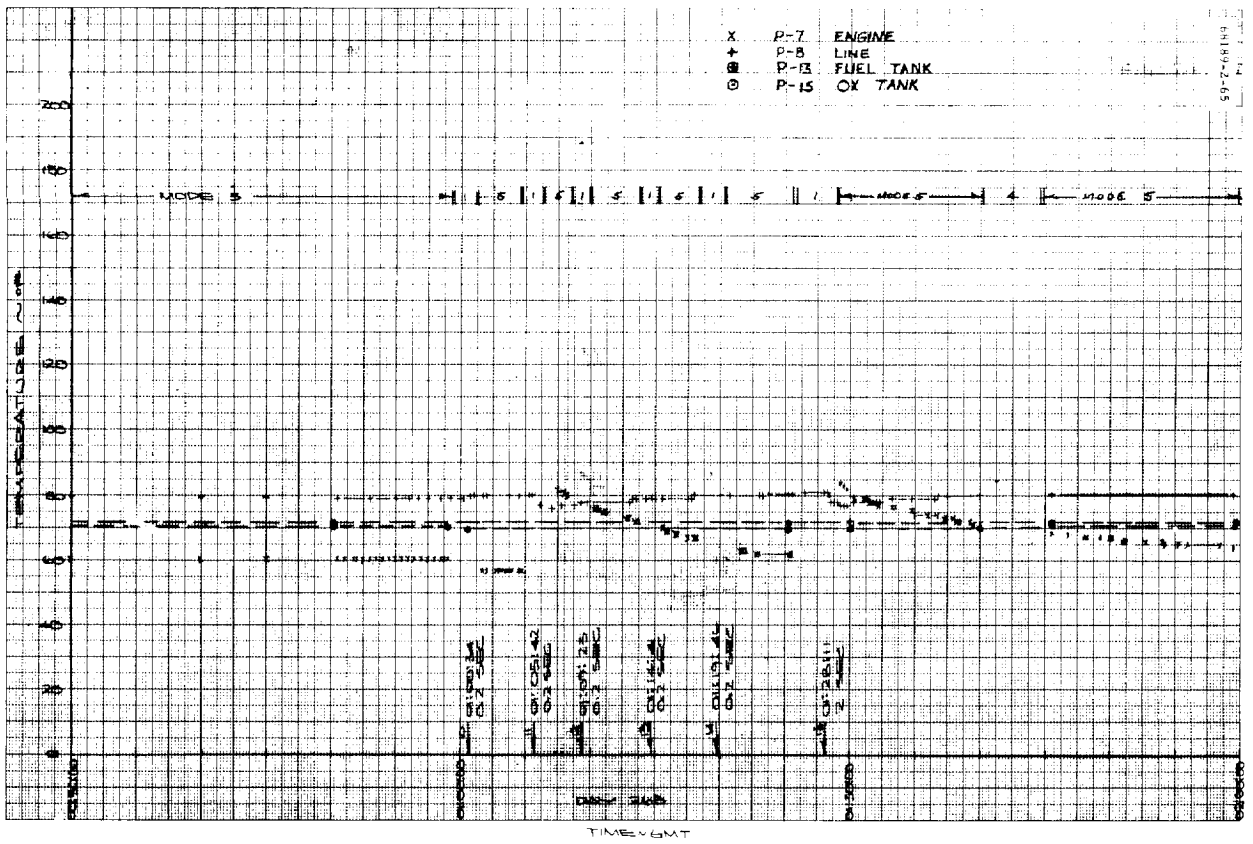


Figure 5.1-11 (continued). SC-2 VPS Thermal Response, Leg 1

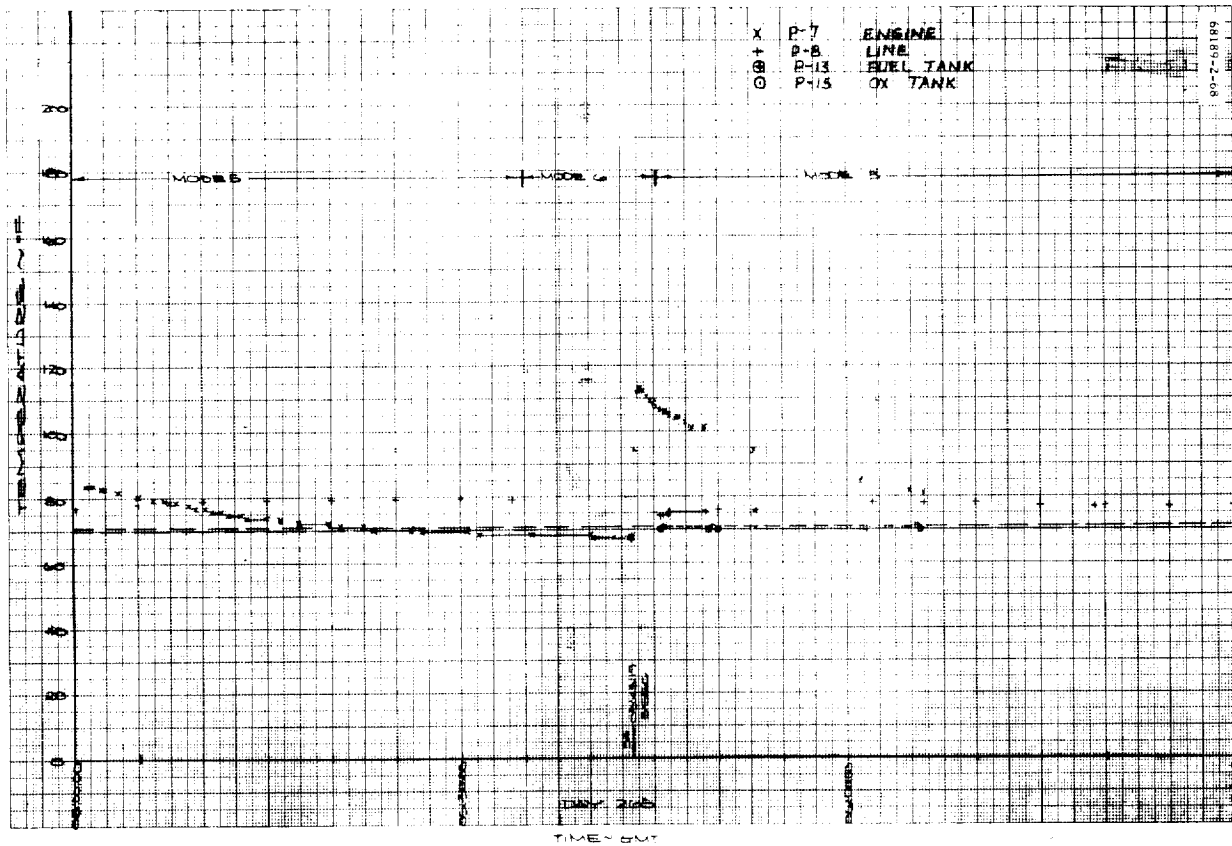
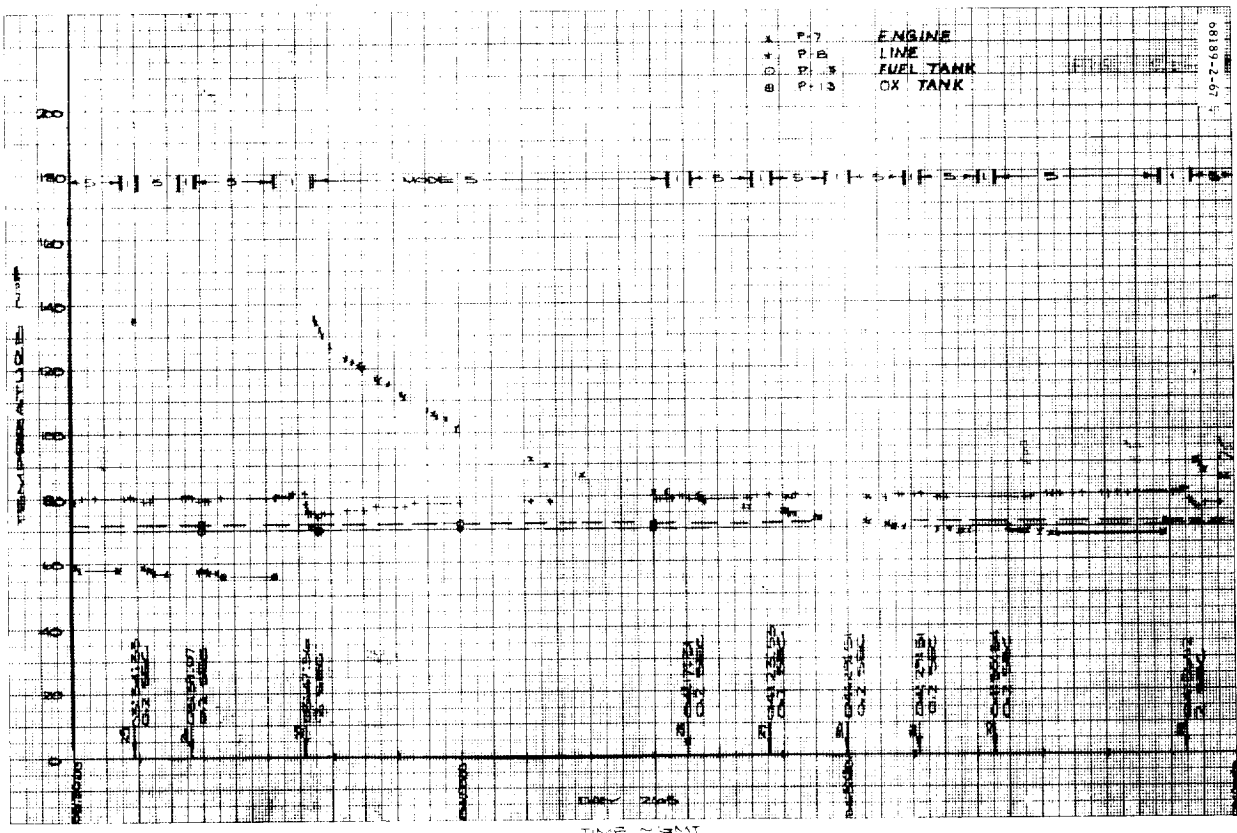


Figure 5.1-11 (continued). SC-2 VPS Thermal Response, Leg 1

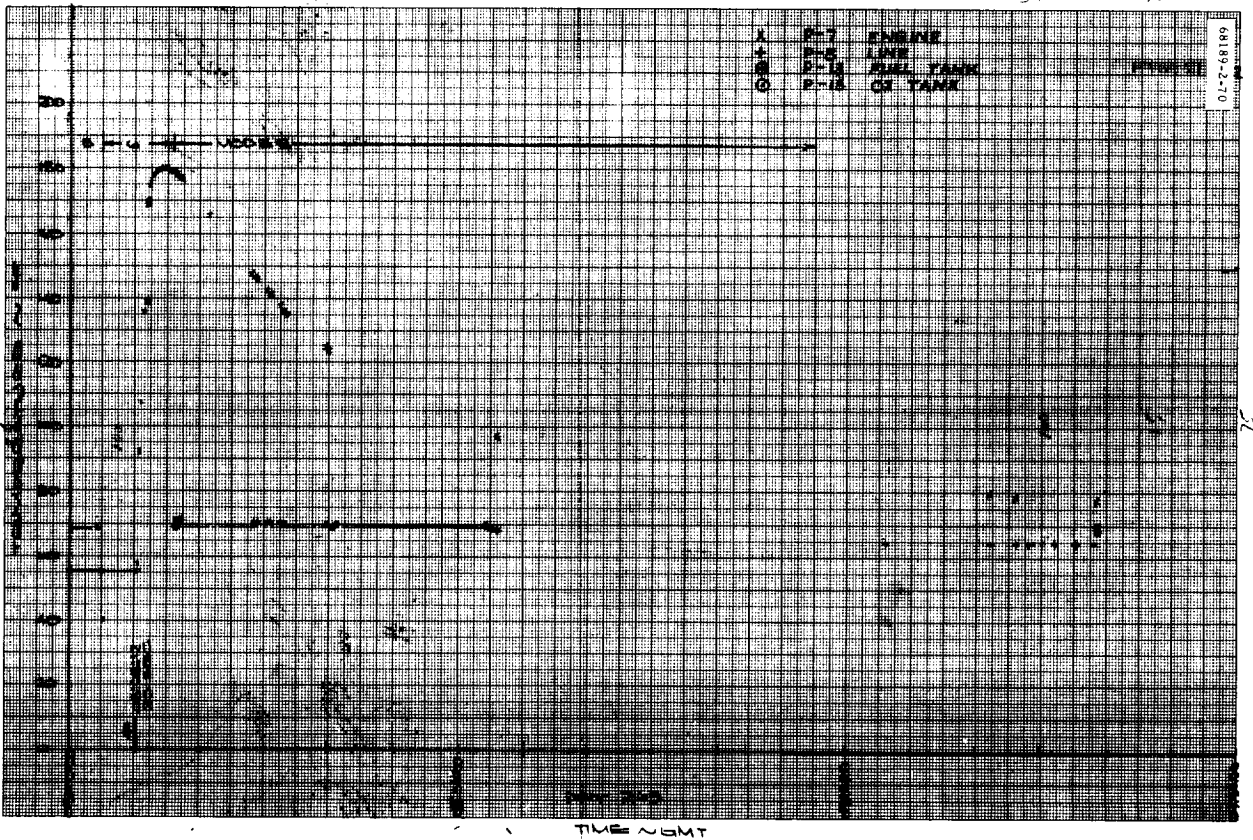
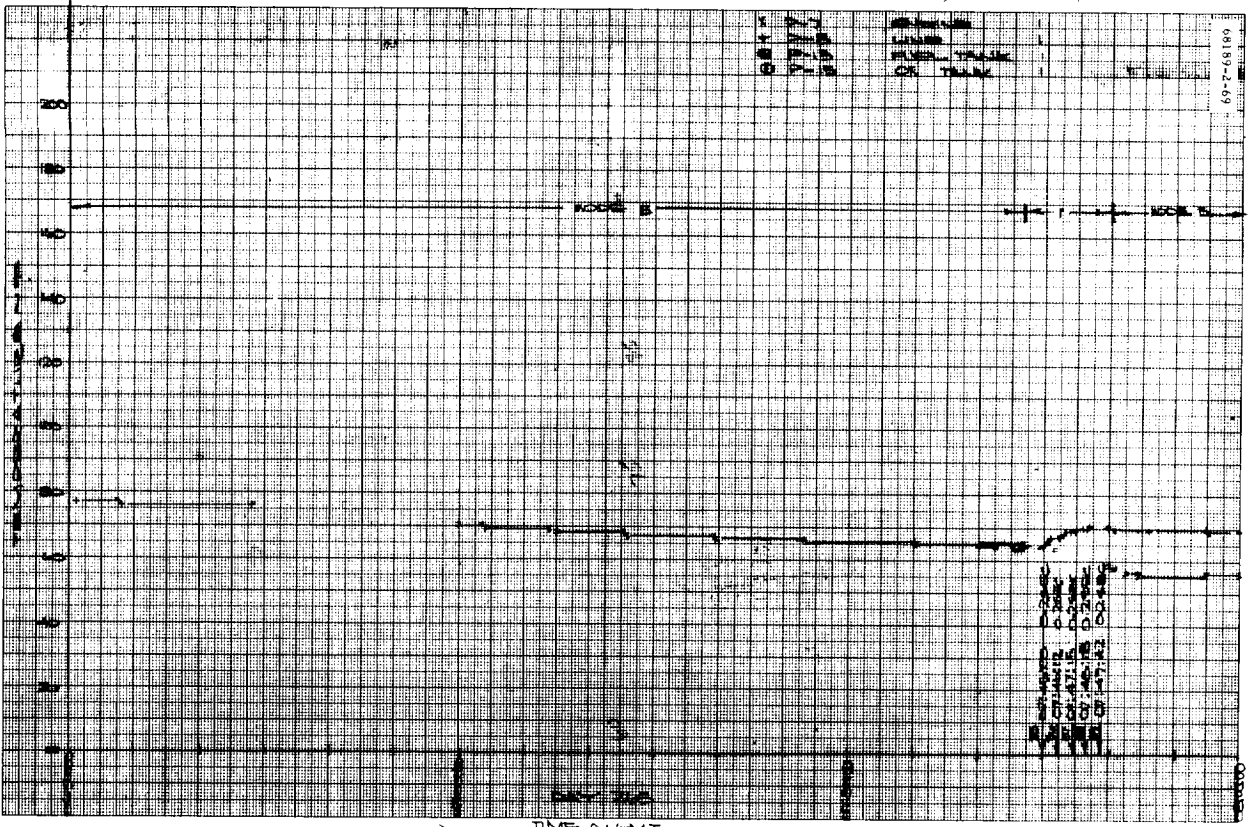


Figure 5.1-11 (continued). SC-2 VPS Thermal Response, Leg 1

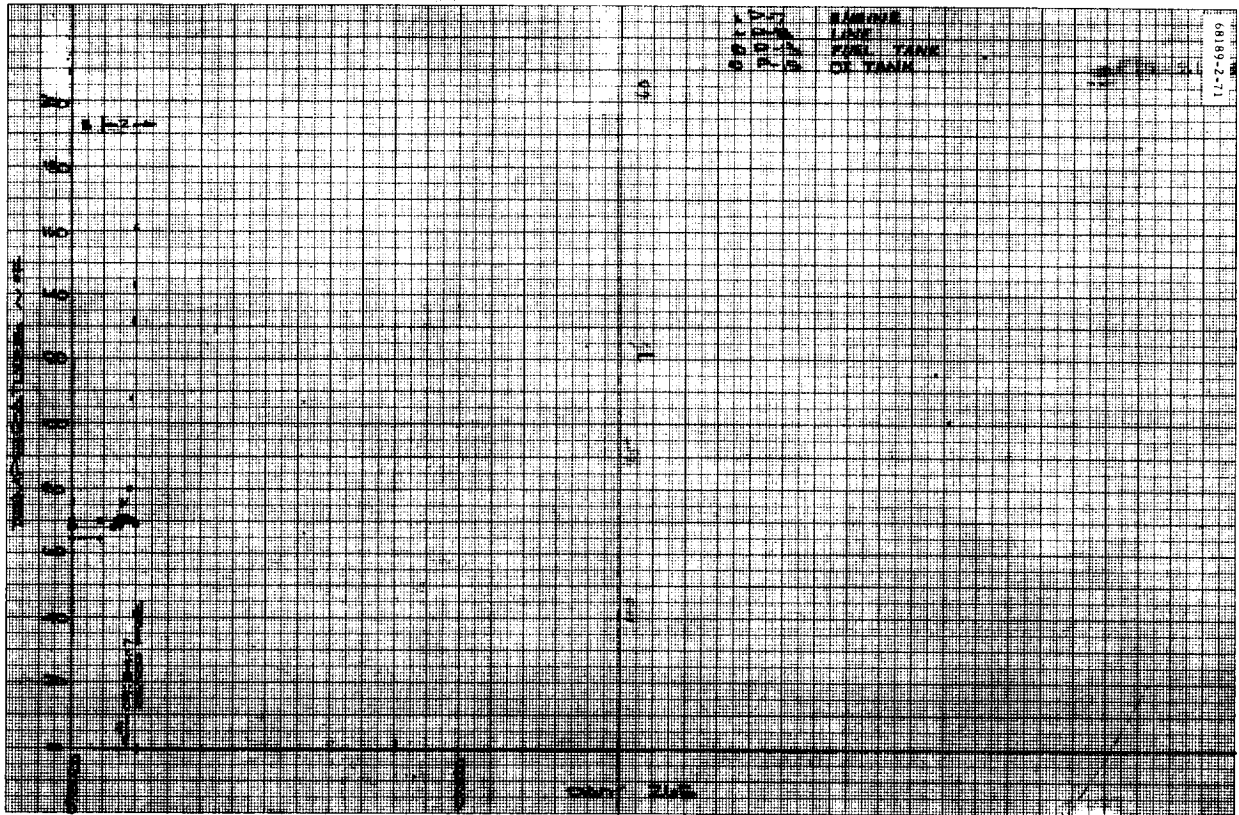


Figure 5.1-11 (continued). SC-2 VPS Thermal Response, Leg 1



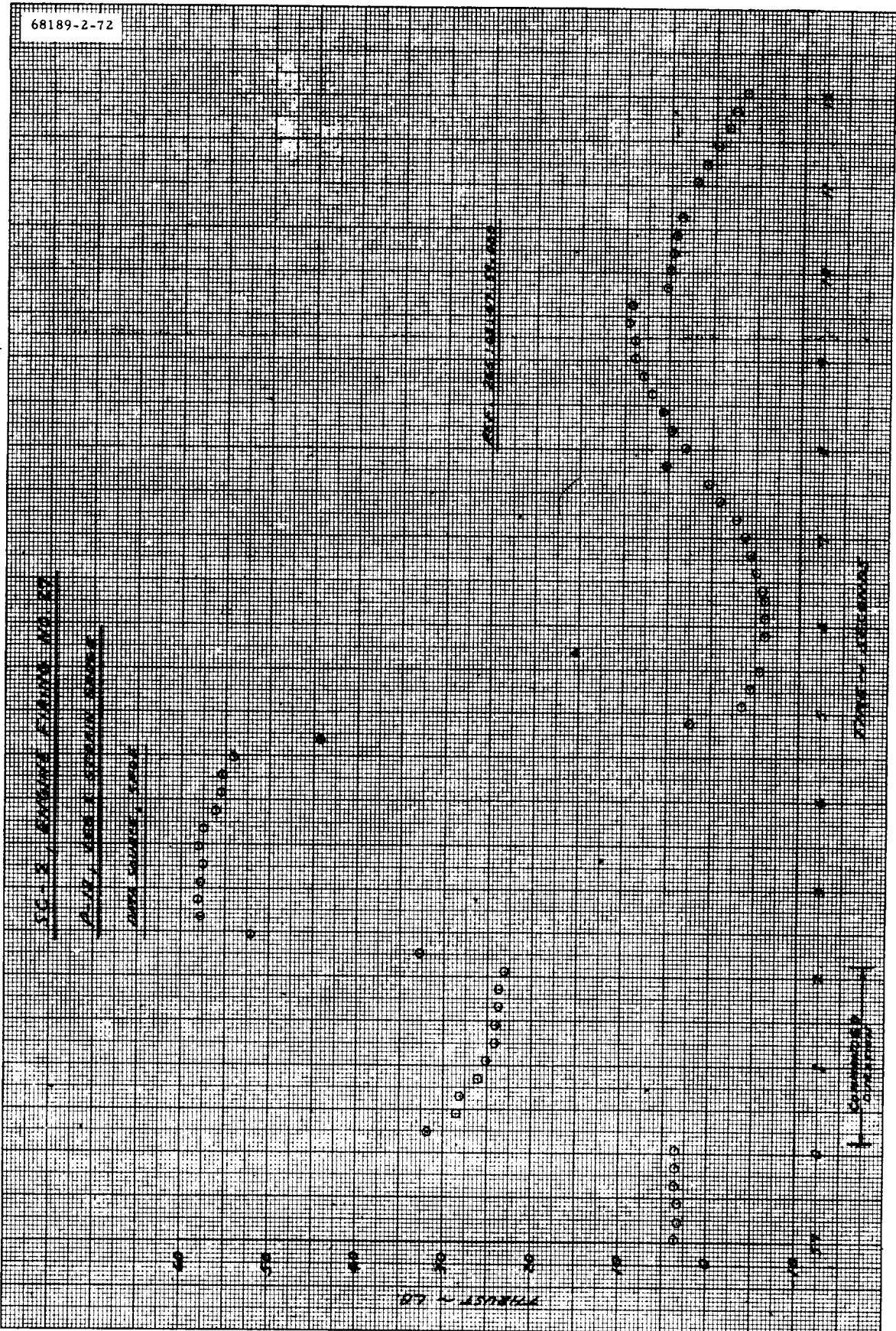


Figure 5.1-12. Engine Firing 27, Leg 1 Strain Gage (P-18)

The type of phenomenon observed on this engine is probably what would be expected if the engine lost some of its physical mass or if the thermal resistance of the engine to the flow of heat from the combustion chamber through the combustion chamber walls was lessened significantly.

Another possible explanation of the burn inconsistencies is suggested from an examination of test data obtained during vernier engine firings at the Edwards Test Station. Simulation tests to reproduce the thermal results observed during the flight indicate that the oxidizer/fuel ratio may vary for firings of the same duration. This phenomenon results in the propellants releasing different amounts of energy for firings of the same duration. Since the engine barrel temperature rise is directly related to the oxidizer/fuel ratio, one would expect variations in the barrel temperature with variations in the oxidizer/fuel ratio.

Figure 5.1-13 presents a quantitative measure of the energy released or absorbed by the propellant lines during the 2.0-second burns. (Energy release is synonymous with temperature change,  $\Delta T$ ). While 5.1-13 does not give any qualitative information regarding vernier line thermal behavior, it does indicate, for example, that the thermal behavior of vernier line 2 was very consistent during the 2.0-second burns. That is, the line temperature change is relatively constant for all 2.0-second burns. This suggests that the quantity of oxidizer flow during all these burns was the same. Figure 5.1-14 shows the oxidizer line temperature sensor thermal response as a function of propellant flow rates. Figure 5.1-14 is based on semi-empirical formulae.

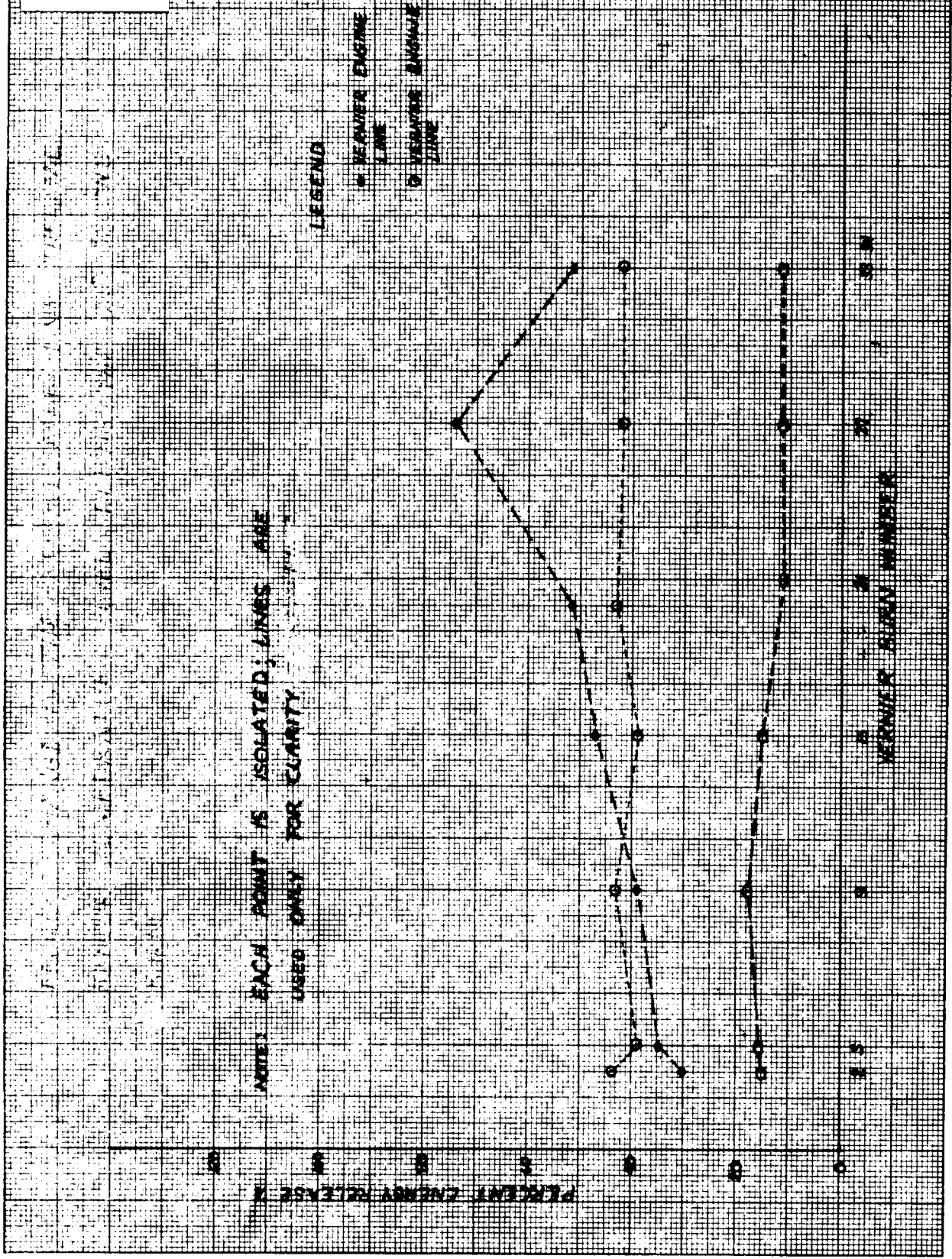
#### 5.1.2.4 Tumbling Mode Thermal Observations (Failure Review Support)

An SC-2 "tumbling mode" thermal analysis was performed in an attempt to determine the location of the sun vector with respect to the vehicle during the postmidcourse tumbling period. The analysis was based on the temperature changes noted on the 75 temperature sensors as the spacecraft orientation changed from that of normal transit to the tumbling mode. Most temperatures attained a new equilibrium condition in the tumbling mode; however, some temperatures continued to change until the spacecraft was lost.

The following list of thermal responses covers the most significant indicators:

- 1) A thermal switch opened on each compartment, and the radiator temperature dropped to a level which could only exist if there were no solar energy incident on the radiators. This indicates that the sun vector never intersected the spacecraft from a direction above the x-y plane and must have been incident from the lower hemisphere.
- 2) The lower spaceframe warmed up considerably, indicating that the sun was incident from below the X-Y plane.

68189-2-73



NOTE: EACH POINT IS ISOLATED; LINES ARE  
USED ONLY FOR CLARITY

LEGEND

□ VERNIER ENGINE 1  
○ VERNIER ENGINE 2

Figure 5.1-13. Percent Change in Propellant Line Thermal Sensor Temperature During 2.0-Second Burns

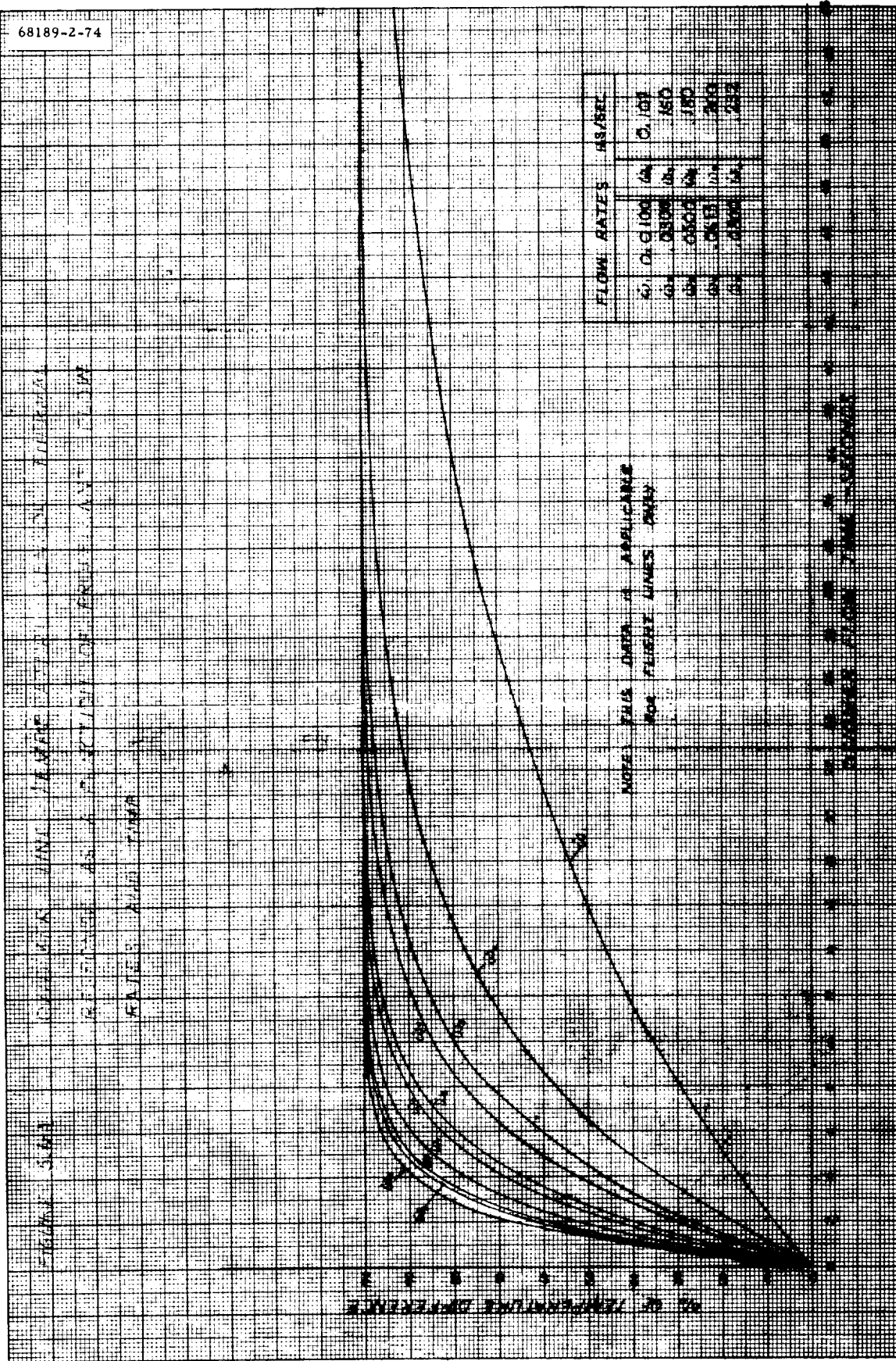


Figure 5.1-14. Oxidizer Line Temperature Sensor Thermal Response As Function of Propellant Flow Rates and Time

- 3) The main retro nozzle, crushable block heat shield, and AMR temperatures increased considerably, indicating that the sun was striking the bottom of the spacecraft.
- 4) All vernier engine propellant lines increased in temperature, indicating that the sun was incident from the bottom of spacecraft.
- 5) The SDC temperature dropped considerably and never reached equilibrium, indicating that it was perhaps completely shaded.
- 6) The solar panel dropped to a temperature which would exist with the sun striking the back side of the panel at an angle of 34 degrees off normal. Intermittent shading could also produce this temperature.
- 7) The planar array temperature increased to a value which would exist with the sun incident at an angle of 78 degrees off normal. Intermittent shading could cause the same temperature result.
- 8) All three shock absorbers dropped to a temperature which indicates only partial solar illumination.
- 9) The KPSM increased in temperature, indicating that it was perhaps being illuminated from the bottom, since the bottom has a higher solar absorptance than the top.
- 10) The auxiliary battery temperature dropped, but the polished aluminium case which is isolated from the battery reached a very high temperature, indicating that the sun was illuminating the compartment from the sides or bottom but not significantly on the top prime radiator plate.
- 11) The upper spaceframe tubes in the vicinity of leg 1 appeared to be shaded continuously.
- 12) The A/SPP solar axis dropped in temperature, indicating that it was being illuminated from a direction not normal to the solar axis or rotation. During normal transit, the sun is normal to the axis of rotation.
- 13) The outboard face of the compartment A canister was receiving the same amount of solar heating during tumbling as it did during the normal transit attitude since the temperature never changed. This indicates that the solar load was equivalent to a 70-degree off normal incidence. The compartment B canister temperature dropped considerably; however, it appears that it was getting a small amount of solar illumination based on the equilibrium temperature.

Tumbling about many of several different axes could produce the temperature changes discussed above, and any reference to the incident angle of

the sun on a given surface is merely intended to give an equivalent heating orientation. The tumbling rate of the vehicle was such that no fluctuations were observed on any of the temperature sensors; therefore, no conclusions were drawn as to whether or not the various components were tumbling in and out of the sun to produce the observed equilibrium temperatures wherever partial illumination was apparent.

Based on the steady-state temperatures after midcourse, a bounding of the most probable locations of the sun vector has been presented in Figure 5.1-15. The figure indicates that the sun is coming from the lower hemisphere and from that quadrant formed by the +X, -Y, and +Z axes.

No definite conclusions can be reached as to how closely the tumbling axis coincides with the sun vector. There was no definite indication of any continual change in tumbling axis throughout the tumbling period; however, some small temperature shifts were noted on some items which could have been caused by the successive engine firings rather than a slow transient in the tumble axis.

Perhaps one of the strongest conclusions that can be drawn from the thermal study is that the sun had to be coming from the lower hemisphere due to the temperatures observed on the compartment radiators after the thermal switches opened.

### 5.1.3 SUMMARY AND CONCLUSIONS

#### 5.1.3.1 Thermal Performance Summary

Thermal performance of the Surveyor II spacecraft was highly satisfactory. Prior to the attempted midcourse maneuver, 40 of the 75 temperature sensors indicated temperatures within  $\pm 5^\circ\text{F}$  of their predicted values. The largest deviation between actual and predicted temperatures was  $19^\circ\text{F}$  on the noncritical spacecraft structure. No temperatures were outside their predicted temperature ranges prior to the postmidcourse tumbling mode.

The thermal performance was very nearly the same as that of SC-1 with the exception of those specific areas where thermal finish changes were incorporated to improve thermal performance. Thermal finish changes were incorporated on the auxiliary battery, Canopus hood, elevation axis motor housing of the A/SPP, and the helium tank. Each of these changes produced temperature changes in accordance with predictions, thereby satisfying their respective objectives.

Mission B predicted and actual thermal data are presented in Table 5.1-4. Most subsystems that normally reach equilibrium conditions during the transit coast mode had reached equilibrium prior to the attempted midcourse maneuver. Data are also present in Table 5.1-2 for that time period immediately following the attempted midcourse and for the equilibrium conditions attained during the tumbling mode.

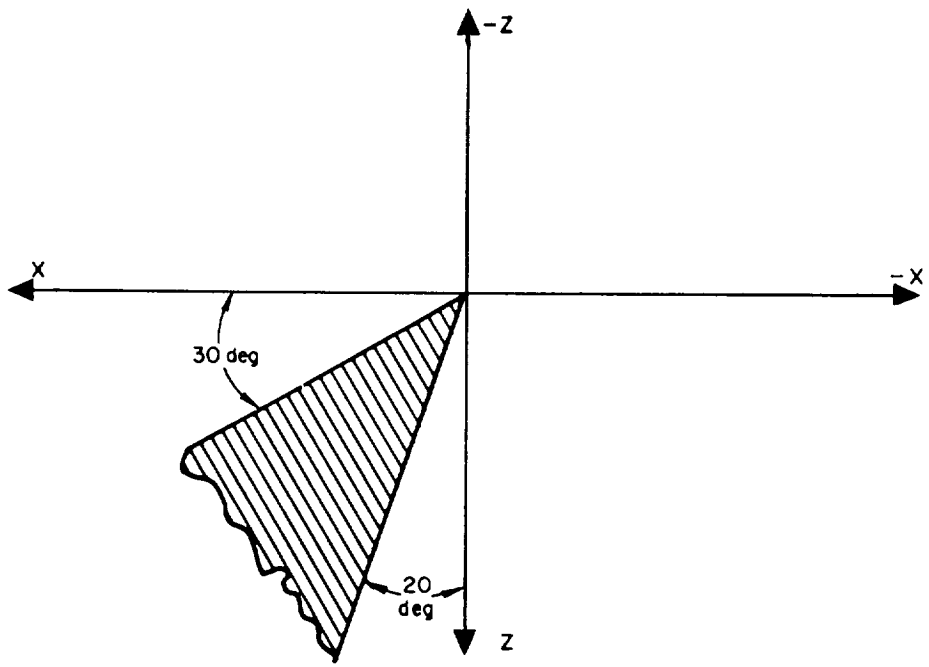
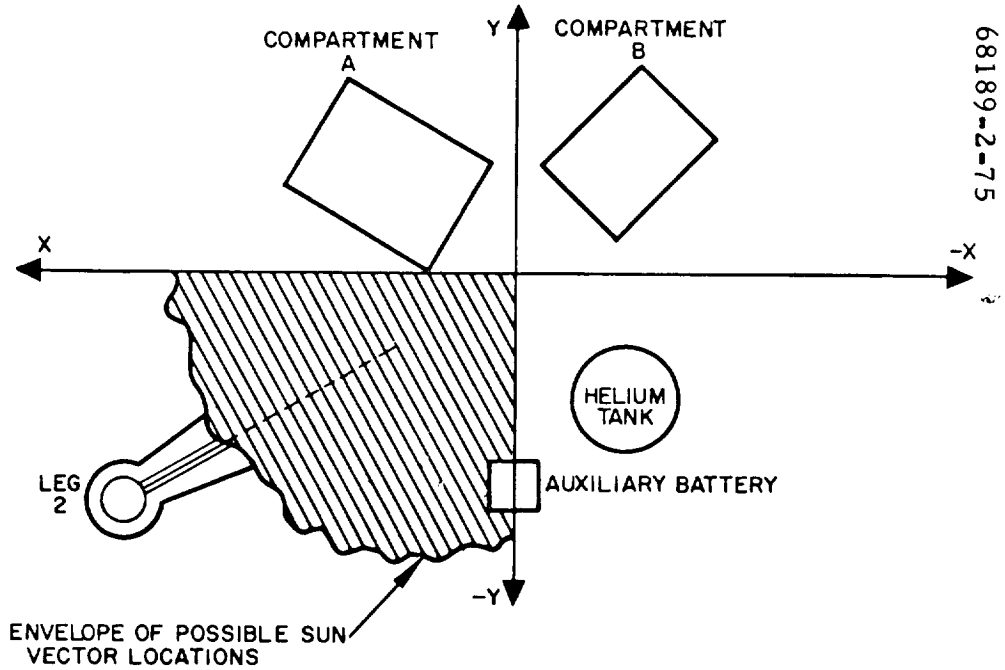


Figure 5.1-15. Probable Location of Sun Vector During Tumbling

TABLE 5.1-4. SUMMARY OF PREDICTED AND ACTUAL MISSION TEMPERATURES

Signal/Nomenclature	Launch	Predicted Premidcourse	Mission Premidcourse	Mission Postmidcourse	Postmidcourse Steady State	Operation Limits	Survival Limits
D-13 transmitter A	85	72	71	70	64	210/0	
D-14 transmitter B	87	73	73	74	64	210/0	
EP-8 main battery	81	99	99	107	89	125/40	145/0
EP-12 solar cell array	84	110	111	-33	-42	165/-200	250/-200
EP-13 boost regulator	126	123	128	115	80	185/0	195/0
EP-26 auxiliary battery	74	66	64*	59	28**	130/20	145/0
EP-34 battery charge regulator	88	120	118	97	80	185/0	200/0
FC-44 flight control electronics unit 1	91	100	90		76	165/0	
FC-45 flight control electronics unit 2	126	138	137	143	137	190/0	
FC-46 roll gyro	172	177	176	171	171	185/175	185/150
FC-47 Canopus sensor	92	89	85	75	35	130/-20	145/-20
FC-48 nitrogen gas tank	84	52	40	7	43	115/-10	
FC-54 pitch gyro	171	174	174	169	169	185/170	185/150
FC-55 yaw gyro	174	177	176	171	165	185/170	185/150
FC-70 attitude gas jet 2	82	77	86	-	6	160/-50	
FC-71 roll actuator	83	88	82	71	42	200/0	
M-8 planar array	83	-50	-50	46	48	280/-280	280/-280
M-10 solar panel stepping motor	84	60	45	32	7	165/-225	300/-320
M-12 elevation axis stepping motor	79	-8	-16	-2	2	165/-225	300/-320
P-3 upper retro case	72	72	73	72	65***	70/40	77/20
P-4 vernier lines 2	84	20 to 27	15	59	87	100/0	
P-5 vernier fuel tank 2	83	44	47	66	68***	100/15	
P-6 vernier oxidizer tank 3	75	50	46	66	66	100/15	
P-7 vernier engine 1	84	65	54	92	61	125/20	
P-8 vernier lines 1	84	18 to 28	22	65	77	100/0	
P-9 vernier lines 3	83	20 to 27	23	40	86	100/0	
P-10 vernier engine 2	83	80	87	115	103	140/20	
P-11 vernier engine 3	83	70	63	82	104	130/20	
P-12 lower retro case	76	60	59	60	69***	70/25	
P-13 vernier fuel tank 1	77	58	57	73	71***	100/0	
P-14 vernier fuel tank 3	75	57	53	73	73***	100/0	
P-15 vernier oxidizer tank 1	76	49	50	73	70***	100/0	
P-16 vernier oxidizer tank 2	75	38	35	66	75***	100/15	
P-17 helium tank	84	75	72	48	24	100/10	
P-22 retro nozzle	82	-120	-118	15	53	DNA	
R-6 AMR antenna 1	79	-12	-14	19	78	135/-50	145/-52
R-7 AMR electronics	83	16	18	26	99	120/-5	110/-40
R-8 altimeter doppler klystron	83	15	11	20	41	100/-22	165/-50
R-9 radar signal data converter	85	63	63	26	-86	140/-18	112/-42
R-10 doppler radar sensor	83	11	14	11	48	112/-42	

\* Not at steady state.  
 \*\* Lowest temperature reached; unit did not equilibrate.  
 \*\*\* At end of mission.



TABLE 5.1-4. (continued)

Signal/Nomenclature	Launch	Predicted Premidcourse	Mission Premidcourse	Mission Postmidcourse	Postmidcourse Steady State	Operation Limits	Survival Limits
R-13 altimeter radar sensor	83	10	20	49	95	110/-40	110/-40
R-27 AMR antenna 2	77	-185	-191	155	155	200/-300	200/-300
T-3 approach camera 4 electronics	83	-116	-106*	-58	68	165/-20	250/-180
TV-16 survey camera 3 electronics	76	-123	-131*	-107	-48	150/-20	200/-250
TV-17 survey camera 3 mirror assembly	83	-113	-120	-86	-59	180/-50	200/-250
V-15 compartment A thermal tray top	87	73	74	75	65	140/0	
V-16 compartment A thermal tray bottom	83	94	94	94	79	125/0	
V-17 compartment A thermal tray shell inside	81	91	92	-	73	125/0	
V-18 compartment A thermal tray shell outside	84	-90	-82	-85	-82	125/0	
V-19 compartment A thermal tray switch inside	80	69	69	-	61	125/0	
V-20 compartment A radiator 5	82	42	31	18	35	150/-300	
V-21 compartment B thermal tray top	98	106	99	83	47	125/0	
V-22 compartment B thermal tray bottom	94	111	103	96	53	125/0	
V-23 compartment B thermal tray shell outside	84	-65	-72	-	-131	125/0	
V-24 compartment B radiator 4	86	77	70	34	-3	150/-300	
V-25 compartment A radiator 8	85	35	28	-12	-135	150/-300	
V-26 compartment B switch 4 inside	88	101	93	-	45	125/0	
V-27 upper spaceframe 1	85	65	53	-41	-68	160/-140	
V-28 lower spaceframe 1	85	50	42	90	103	160/-140	
V-29 wiring harness thermal tray tunnel	85	94	90	91	53	125/0	
V-30 shock absorber 1	84	84	76	-	-29	125/-20	300/-50
V-31 landing gear 2	84	55	74	-26	-29	160/-140	
V-32 shock absorber 2	85	82	73	16	-17	125/-20	300/-50
V-33 shock absorber 3	84	84	82	-	-29	125/-20	300/-50
V-34 A/SPP mast	83	-86	-88	-	-58	160/-140	
V-35 upper spaceframe 2	85	-75	-81	-	-13	160/-140	
V-36 lower spaceframe 2	85	-24	-24	-	123	160/-140	
V-37 retro attach point 1	85	46	44	-	110	160/-140	
V-38 retro attach point 2	84	-24	-32	61	142	160/-140	
V-39 retro attach point 3	83	50	44	-	-99	160/-140	
V-44 crushable pad	82	-51	-48	145	153	160/-140	
V-45 compartment B radiator 1	88	91	84	45	13	150/-300	
V-46 compartment B radiator 5	86	78	70	35	-190	150/-300	
V-47 compartment A radiator 2	85	36	34	34	24	150/-300	
V-48 auxiliary battery compartment	83	28	9*	136	138	130/0	130/-30

\* Not at steady state.

Temperatures observed during the postmidcourse tumbling mode indicate that the sun vector intersected the spacecraft from below the X-Y plane and between the +X and -Y axes. A comparison of equilibrium temperature data between SC-1 and SC-2 is presented in Table 5.1-5.

#### 5.1.3.2 Vernier Burn Thermal Data Summary

Thermal data indicate that TCA 3 did not ignite during the midcourse burn. The results of thermal control investigations to date have not produced any positive conclusions regarding the seemingly anomalous behavior of vernier engines. At most, studies have shown that the thermal behavior exhibited by the vernier engines was inconsistent during the 41 firing attempts. Specific inconsistencies are tabulated below:

- 1) Vernier engine 1
  - a) TCA 1 thermal behavior during burn 11 is different from that for any other 0.20-second burn.
  - b) TCA 1 thermal behavior during burn 27 is different from that for any other 2.00-second burn. However, this was not a thermal problem, since the strain gages indicate that the engine probably burned for 4.5 seconds instead of the commanded 2.0 seconds.
- 2) Vernier engine 2
  - a) TCA 2 thermal behavior during burns 2 and 3 is substantially different from that for burns 9, 15, 21, 27, and 34. Temperature rise of the engine barrel, resulting from the 2.0-second burn, was approximately 20°F for firings 2 and 3 and approximately 60°F for the later firings.
  - b) TCA 2 appeared to burn consistently at two temperature levels.
- 3) Vernier engine 3
  - a) Thermal data do not show any positive indications of ignition during the midcourse maneuver. TCA 3 thermal behavior always seems consistent for all 41 burn attempts.
  - b) Thermal data tend to support arguments that fuel flowed at midcourse but that there was little or no oxidizer flow; however, the data are not conclusive. Thermal data indicate both oxidizer and fuel flow during burns subsequent to midcourse; however, the data do not indicate engine 3 ignition on any of the 41 burn attempts.

TABLE 5.1-5. COMPARISON OF STEADY-STATE TEMPERATURES  
IN MISSION A AND MISSION B, PREMIDCOURSE

Flight Sensor Location by Subsystem		Actual Steady-State Temperature, °F		
		Mission A	Mission B	Operation Allowable Limits
Vehicle and mechanisms				
Compartment A				
Upper tray	V-15	70	74	140/0
Lower tray	V-16	93	94	125/0
Transmitter A	D-13	68	71	210/0
Transmitter B	D-14	68	73	210/0
Main battery	EP-8	97	99	125/40
Battery charge regulator	EP-34	123	118	185/0
Radiators				
No. 5	V-20	42	31	150/-300
No. 8	V-25	44	28	150/-300
No. 2	V-47	35	34	150/-300
Thermal shell inside	V-17	92	92	120/0
Thermal shell outside	V-18	-85	-82	
Thermal switch				
No. 5 inside	V-19	66	69	150/-300
Compartment B				
Upper tray	V-21	93	99	125/0
Lower tray	V-22	98	103	125/0
Boost regulator	EP-13	115	128	185/0
Radiators				
No. 4	V-24	67	70	150/-300
No. 1	V-45	73	84	150/-300
No. 5	V-46	66	70	150/-300
Thermal shell outside	V-23	-70	-72	
Thermal switch				
No. 4 inside	V-26	88	93	125/0
Wiring harness	V-29	88	91	125/0
Auxiliary battery	EP-26	35	64*	130/20
Auxiliary battery compartment	V-48	-2	9	130/30
Landing gear assembly				
Leg 2	V-31	83	74	160/-140
Crushable block	V-44	-62	-48	160/-140
Shock absorber				
No. 1	V-30	84	76	125/-20
No. 2	V-32	72	73	125/-20
No. 3	V-33	82	82	125/-20

TABLE 5.1-5. (continued)

Flight Sensor Location by Subsystem		Actual Steady-State Temperature, °F		
		Mission A	Mission B	Operation Allowable Limits
Antenna/solar panel positioner mechanism				
Solar panel drive	M-10	60	45	165/-225
Elevation axis drive	M-12	1	-17	165/-225
Solar cell array	EP-12	109	111	165/-200
Planar array	M-8	-50	-50	280/-280
A/SPP mast	V-34	-84	-88	160/-140
Spaceframe and substructure				
Upper spaceframe				
Near leg 1	V-27	60	53	160/-140
Near leg 2	V-35	-79	-81	160/-140
Lower spaceframe				
Under compartment B	V-28	48	42	160/-140
Under compartment A	V-36	-27	-24	160/-140
Retro attach points				
Leg 1	V-37	39	44	160/-140
Leg 2	V-38	-36	-32	160/-140
Leg 3	V-39	44	44	160/-140
Propulsion				
Vernier engine thrust chamber assembly				
No. 1	P-7	59	54	125/20
No. 2	P-10	72	84	140/20
No. 3	P-11	59	63	130/20
Propellant tanks				
Oxidizer 1	P-15	75/41 †	76/50 ††	100/0
Fuel 1	P-13	76/52 †	77/57 ††	100/0
Oxidizer 2	P-16	77/24 †	75/35 ††	100/15
Fuel 2	P-5	75/34 †	83/47 ††	100/15
Oxidizer 3	P-6	79/40 †	75/46 ††	100/15
Fuel 3	P-14	76/53 †	75/53 ††	100/0
Propellant lines				
Leg 1	P-8	23 to 29	18 to 28	100/0
Leg 2	P-4	21 to 26	20 to 27	100/0
Leg 3	P-9	21 to 26	20 to 27	100/0
Helium tank	P-17	60	72	100/10

TABLE 5.1-5. (continued)

Flight Sensor Location by Subsystem		Actual Steady-State Temperature, °F		
		Mission A	Mission B	Operation Allowable Limits
Main retro				
Upper case	P-3	73/67 †	72/73 ††	70/40
Lower case	P-12	74/46 †	76/59 ††	70/25
Nozzle	P-22	-124 †	-118	
Flight control				
Flight control electronics				
Chassis board 1	FC-44	90	90	165/0
Chassis board 6	FC-45	124	137	190/0
Canopus sensor	FC-47	78	85	130/-20
Roll gyro	FC-46	170**	175**	185/175
Pitch gyro	FC-54	175**	175**	185/170
Yaw gyro	FC-55	180**	174**	185/170
Roll actuator	FC-71	79	82	200/0
Nitrogen tank	FC-48	45	40	115/-10
Radars	FC-70	88	86	160/-50
RADVS				
KPSM	R-8	12	11	100/-22
SDC	R-9	56	63	140/-18
VS preamplifier	R-10	22	14	112/-42
A/VS preamplifier	R-13	33	20	110/-20
Altitude marking radar				
Electronics	R-7	14 to 16	18	120/-5
Antenna dish	R-6	-12	-14	135/-20
Edge of dish	R-27	-185	-191	200/-300
Television				
TV 3 mirror	TV-17	-120	-120	180/-50
TV 3 ECU	TV-16	-134	-128	150/-20
TV 4	T-3	-124	-103	165/-20

\* Not at steady state.

\*\* Corrected for bit rate error.

† Launch + 63 hours.

†† Launch + 15 hours.

### 5.1.3.3 Recommendations from Line Heater Anomaly

The discussion in subsection 5.1.2.3 indicated that failure of the vernier line heater to cycle was caused by epoxy contamination. The following recommendations are believed to effectively correct the problem with minimum impact on current spacecraft launch schedules:

- 1) Increase thermal dissipation capability of the vernier engine 2 line heater, which will result in a reduction in the line heater duty cycle as defined by this investigation.
- 2) Prohibit attachment of wire harnesses with high emittance surfaces to the lines in solar thermal vacuum tests to avoid invalidation of test results.
- 3) Perform a black light inspection at Hughes after epoxy application (but before curing) on the unit level, and remove any excess epoxy that could contaminate the lines.
- 4) Perform a final black light inspection on the spacecraft before shipping to Cape Kennedy.

### 5.1.4 ANALYSIS DISCUSSION

#### 5.1.4.1 Compartments A and B

Compartment A interior temperatures (sensors D-13, D-14, EP-8, EP-34, V-15, and V-16) are shown in Figures 5.1-16, 5.1-17, 5.1-18, 5.1-22, 5.1-54, and 5.1-55; external temperatures (sensors V-18, V-20, V-25, and V-47) are shown in Figures 5.1-56, 5.1-57, 5.1-61, and 5.1-71. Compartment B interior temperatures (sensors EP-13, V-21, and V-22) are shown in Figures 5.1-20, 5.1-58, and 5.1-59; external temperatures (sensors V-24, V-45, and V-46) are shown in Figures 5.1-60, 5.1-69, and 5.1-70. The thermal tunnel internal temperature (sensor V-29) is shown in Figure 5.1-64.

Compartment system temperatures during the mission were approximately 5°F higher than those of SC-1 for compartments A and B at the same time in the mission. No anomalies were observed during the normal transit period, and all compartment system temperatures correlated well with predictions. The seasonal change in the solar constant between the SC-1 and SC-2 missions was sufficient to cause a maximum temperature increase of 3°F in compartment B. Solar thermal vacuum test data accumulated prior to the flight indicated that a 15°F temperature differential would exist between the SC-1 and SC-2 temperatures in compartment B at the same solar intensity. Flight data did not support this evidence and, consequently, suggests that those temperature differences observed between SC-1 and SC-2 solar thermal vacuum tests were related to test operations or environmental simulation rather than vehicle differences.

During the tumbling mode, the compartments appeared to be in an orientation such that the radiators were not receiving any solar illumination. One thermal switch on each compartment opened after the attempted mid-course correction. Compartment A thermal switch 8 and compartment B thermal switch 5 opened at approximately 12 and 10 hours (28.5 and 26.5H mission time), respectively, after the attempted midcourse correction. The thermal switches appeared to open within specified temperature tolerances.

#### 5.1.4.2 Auxiliary Battery

The auxiliary battery temperature profile (sensor EP-26) (Figure 5.1-51) prior to midcourse maneuver was within 3° F of predictions. The temperature had not reached a steady-state value at this time. After mid-course, the battery temperature dropped at a rate of 4° F/hour as a result of vehicle misorientation. When the auxiliary battery temperature reached 34° F (at approximately L + 23H9M), auxiliary battery mode was commanded on in order to utilize the auxiliary battery power before the battery became too cold to function properly. Auxiliary battery mode remained on for approximately 9 hours and 46 minutes, whereupon main battery mode was restored. The auxiliary battery reached 79° F during the operational period. The auxiliary battery remained off for the next 11 hours and 52 minutes and declined to 28° F. At this time, RADVS was commanded on, and the magnitude of the electrical load caused a switching to the auxiliary battery. Although the auxiliary battery was well below the desired temperature of 95 ± 15° F at the time of RADVS turn on, it functioned nominally until it was commanded off during RADVS operation.

The SC-2 auxiliary battery case thermal design was modified from that of SC-1 in an effort to increase the auxiliary battery transit equilibrium temperature by approximately 30° F. Comparison of Missions A and B auxiliary battery temperature profiles reveals that the Mission B auxiliary battery temperature was 64° F and close to steady-state as opposed to 35° F during nonoperational steady-state for Surveyor I. Overall, auxiliary battery performance was excellent.

#### 5.1.4.3 Antenna and Solar Panel Positioner (A/SPP)

The A/SPP mechanisms, solar panel, and planar array temperatures prior to the midcourse maneuver were at equilibrium temperatures within 10° F or less of preflight predictions as determined by flight sensors EP-12, M-8, and M-10 (Figures 5.1-19, 5.1-31, and 5.1-32). Following the mid-course maneuver, the solar panel, planar array, mast, elevation axis motor, and solar panel stepping motor stabilized at -42, 48, -58, 2, and 9° F, respectively, within approximately 6 hours or less following midcourse maneuver. Comments about the A/SPP temperatures during the tumbling mode are contained in subsection 5.1.2.

#### 5.1.4.4 Spaceframe

Spaceframe temperatures (sensors V-27 and V-28) are presented in Figures 5.1-62 and 5.1-63. Spaceframe steady-state temperatures during coast phase 1 were about the same as during SC-1 flight and were from 0 to 12°F lower than the predicted temperatures.

Tables 5.1-2 and 5.1-3 show the comparison between SC-1 and SC-2 flight data, the predicted temperatures for flight, and postmidcourse flight temperatures.

#### 5.1.4.5 Landing Gear and Crushable Blocks

##### Landing Gear

The leg 2 steady-state temperature of 72°F (sensor V-31) occurred approximately 90 minutes after launch and was 18 degrees warmer than the predicted value of 54°F (Figure 5.1-65). The leg temperature gradually increased during the normal transit phase and, at L + 15H, had risen to 75°F. This increase can be attributed to continued degradation of the organic white paint on the leg.

Although the solar intensity during Mission B was higher than during Mission A, the Mission B leg temperature was lower. This lower temperature is attributed to the initially nondegraded white paint on the legs due to the protective wrapping used on SC-2 during solar thermal vacuum testing. Legs 1 and 3 are not instrumented in flight, but should be warmer than leg 2 due to the absence of any shadowing caused by the solar panel.

##### Shock Absorbers

Shock absorbers 1, 2, and 3 ran 8, 9, and 2°F cooler, respectively, than the predicted steady-state temperatures (sensor V-32) as indicated in Figure 5.1-66. SC-1 and SC-2 shock absorber temperatures were about the same, with the exception of shock absorber 2 which ran approximately 8°F cooler on SC-2 even though the solar intensity during the flight was greater than that of SC-1. This could be caused by either the lower leg plate temperature or merely variations in the thermal finish of the shock absorber. In any event, the deviation is well within the temperature uncertainty tolerance of ±25°F.

##### Crushable Block

The crushable block heat shield steady-state temperature of -48°F (sensor V-44) occurred approximately 6 hours after launch and agreed very well with the predicted temperature of -51°F (Figure 5.1-68).

#### 5.1.4.6 Thrust Chamber Assemblies (TCA)

Vernier engine thermal performance was as expected. Prior to initiation of the premidcourse yaw maneuver, vernier engines 1, 2, and 3



were within the predicted temperature range. Predicted temperatures for TCAs 1, 2, and 3 were 65, 80, and 70°F, respectively. Actual temperatures at the initiation of the premidcourse yaw maneuver were 54, 88, and 63°F for TCAs 1, 2, and 3, respectively. The steady-state equilibrium temperatures for TCAs 1 and 3 were 11 and 7°F lower than the nominal predictions for these engines. An extrapolation of the actual flight data indicates that TCA 2 would have reached a steady-state equilibrium temperature of approximately 85°F, or 5°F higher than the nominal predicted temperature of 80°F.

Thermal effects of the gyro drift check on TCA 2 temperatures (sensor P-10) can be seen in Figure 5.1-38. TCA 2 reached a peak temperature of 93°F during the gyro drift check which was initiated at L + 06H54M24S. A positive temperature perturbation indicated that TCA 2 received increased solar illumination during the gyro drift check. An increase in solar illumination is experienced by TCA 2 during a positive yaw maneuver because the shadow line cast by the solar panel shifts inboard, thereby exposing more of the TCA to the sun.

Peak TCA temperatures are not available for the midcourse burn because vernier engine telemetry data was not sampled during this interval. (Vernier engine data is not sampled during telemetry mode 1.)

TCA transit temperature profiles (sensors P-7, P-10, and P-11) are presented in Figures 5.1-35, 5.1-38, and 5.1-39 for vernier engines 1, 2, and 3, respectively.

#### 5.1.4.7 Propellant Tanks

Fuel tank temperatures (sensors P-13 and P-14) (Figures 5.1-41 and 5.1-42) up to midcourse maneuvers were within 3°F of preflight predictions. During midcourse maneuvers, the fuel tank temperature sensors indicated increases of 17, 21, and 20°F on tanks 1, 2, and 3, respectively. These increases are attributable to: 1) mixing of the fuel within the tank, subsequently breaking up the isothermal stratification within the tanks and increasing the conduction film coefficients between the fluid and tank well, and 2) flowing of fuel through the standpipe assembly to which the sensor is attached. Thus, the fuel which was warmer than the standpipe outlet imparted a temperature increase to the flight sensor. Spacecraft tumbling after the attempted midcourse maneuver produced mount and blanket temperatures higher than those observed during transit. These higher temperatures prevented the tanks from cooling as they normally do during this phase of the mission.

Oxidizer tank temperatures (sensors P-6, P-16, and P-17) (Figures 5.1-34, 5.1-44, and 5.1-45) up to midcourse maneuvers were within at least 6°F of preflight predictions. During midcourse maneuvers, the oxidizer tank temperature sensors indicated increases of 25, 33, and 26°F on tank 1, 2, and 3, respectively. Following midcourse maneuver, the fuel tank temperatures remained at higher levels (66 to 75°F).

The same explanation formulated above for the fuel tank temperature profiles also applies to the oxidizer tanks. It has been suggested that oxidizer tank 3 may have been empty at launch. However, an analytical investigation of the thermal response of oxidizer tank 3 indicates the presence of propellant before and after the attempted midcourse correction.

#### 5.1.4.8 Propellant Lines

The vernier propellant lines for engines 1 and 3 behaved properly during the transit phase. Thermal data from P-4 (Figure 5.1-33) indicates that engine 2 line cycled during the early stages of the transit mission as expected; however, line temperature cycling terminated at approximately L + 3H. The line then gradually decreased in temperature. Prior to the premidcourse yaw maneuver, vernier 2 line temperature was 14° F. (Subsection 5.1.2.1 provides further discussion on the vernier engine 2 oxidizer line.)

Subsequent to the completion of the premidcourse yaw maneuver, the propellant lines exhibited a positive temperature increase. Oxidizer line temperatures were 48\*, 47\*, and 51° F for engines 1, 2, and 3, respectively, at the initiation of the midcourse burn. Vernier oxidizer lines 1 and 2 exhibited large temperature perturbations as a result of the warm propellants ( $65 \pm 5^\circ \text{F}$ ) flowing through the cooler propellant lines (30 to 48° F); however, the thermal sensor on the engine 3 oxidizer line showed only a slight negative perturbation during the midcourse burn. Propellant line temperatures (sensors P-4, P-8, and P-9) are presented in Figures 5.1-33, 5.1-36, and 5.1-37 for vernier oxidizer lines 1, 2, and 3, respectively.

An examination of the data presented in Figure 5.1-33 indicates that the vernier engine 2 propellant line heaters commenced to cycle at L + 90M. Figure 5.1-33 also illustrated an increase in the heater on time with mission time until the heater remained on at L + 3H. As the transit mission progressed, the engine 2 line heater was unable to maintain the oxidizer 2 line within the cyclic dead band of the thermostat (19 to 26° F), and the line temperature level gradually decreased as shown by the data.

Thermal analyses indicate that the exterior surface of the aluminum foil heater blanket surrounding the propellant line and line heaters may have been contaminated by a high emittance substance. The emittance of clean uncontaminated aluminum foil is  $0.04 \pm 0.01$ . Calculations indicate that the emittance of the exterior surface of the blanket was probably an order of magnitude larger than normal.

---

\*Value uncorrected for 4400 bits/sec error. The actual line 1 and 2 temperature regions are estimated to be (37-45) and (41-47)° F.

#### 5. 1. 4. 9 Helium Tank

Helium tank thermal performance was as expected. Prior to initiation of the premidcourse yaw maneuver, the transit steady-state equilibrium temperature was 72°F, or 3°F lower than the nominal prediction of 75°F.

The thermal finish design for the SC-1 and SC-2 helium pressurization tanks differed in the quantity of 3M black velvet paint on the inboard face of the tank. The 38°F black band spans the entire circumference of the SC-2 helium tank. The black band covered approximately three-fourths of the circumference of the SC-1 tank with the inboard face painted white. The SC-1 helium tank stabilized at 59°F during the Mission A coast phase. The transit temperature profile (sensor P-17) of the SC-2 helium tank is shown in Figure 5. 1-45.

#### 5. 1. 4. 10 Main Retro Engine

The main retro temperature profiles (sensors P-12 and P-22) shown in Figures 5. 1-40 and 5. 1-46 were exactly as predicted for the upper and lower motor case and within 2°F of preflight predictions for the nozzle prior to midcourse maneuver. Following midcourse maneuver, the upper retro case continued to cool at a slightly higher rate than during normal transit attitude. The lower retro case temperature slowly increased (25°F/hr) to 72°F, and the nozzle temperature experienced a 177°F rise.

The lower retro case and the retro nozzle temperatures increased due to the solar load impinging on these areas during the postmidcourse period. The retro case temperature reacts very slowly to changes in heat input due to its very high mass, whereas the retro nozzle, which has a much lower mass, reacts quite rapidly to sudden environmental changes.

#### 5. 1. 4. 11 Flight Control Electronics and Canopus Sensor

The flight control electronics chassis boards, gyros, and Canopus sensor internal temperatures are presented in Table 5. 1-6. These temperature results are for the steady-state coast phase. The actual temperatures are within the predicted accuracy of ±20°F (or ±2°F for the gyro temperatures).

TABLE 5. 1-6. FLIGHT CONTROL TEMPERATURE, °F

Items	Sensors	Predicted	Actual
Electronics board 1	FC-44	100	90
Electronics board 6	FC-45	138	138 ± 2
Canopus	FC-47	89	85
Roll gyro	FC-46	177	176
Pitch gyro	FC-54	174	174
Yaw gyro	FC-55	177	176

In the mission plots for FC-46, FC-54, and FC-55 (Figures 5.1-24, 5.1-27, and 5.1-28), the apparent discrepancy between flight data and predictions is actually due to telemetry errors in these "high accuracy" temperature channels. At the 1100 bits/sec data rate which prevailed before midcourse, this error is 8 to 10° F.

Due to the possibility of fogging of the Canopus window, the Canopus hood paint pattern was changed to increase the window temperature. Effect of the change was indicated by the Canopus sensor temperature (V-47) which rose from 78° F in Mission A to 85° F in Mission B. It is expected that the Canopus window temperature increased much more than the temperature sensor since the sensor is located on the electronics inside the unit and is somewhat removed from the Canopus sensor. Therefore, the objective of the change was accomplished.

#### 5.1.4.12 Roll Actuator

Roll actuator thermal performance was as expected. Prior to initiation of the premidcourse yaw maneuver, the roll actuator reached a steady-state equilibrium temperature of 82° F. The SC-1 roll actuator also stabilized at 82° F. The nominal predicted temperature for the roll actuator was 88° F. The transit temperature profile (sensor FC-71) of the roll actuator is shown in Figure 5.1-30.

#### 5.1.4.13 Nitrogen Tank

The nitrogen tank steady-state temperature prior to midcourse was 40° F as compared to 45° F for Mission A, and was 12° F below the predicted value. The tank remained within its operational limits throughout the mission. It was found that the tank temperature (sensor FC-48) dropped rapidly to 10° F during midcourse due to gas expansion in the valve resulting from spacecraft tumbling (Figure 5.1-26).

#### 5.1.4.14 Attitude Gas Jets

The gas jet 2 steady-state temperature of 87° F (sensor FC-70) occurred approximately 3 hours after launch (Figure 5.1-29). This temperature is about 10 degrees warmer than the predicted value of 77° F.

Gas jet 3 probably ran warmer than gas jet 2, although there was no flight sensor on jet 3 to confirm this. Although jets 2 and 3 are attached to their respective legs in a similar manner, the jet on leg 3 is probably warmer because the temperature of that leg is expected to be higher due to lack of solar panel shading. Jet 1 was expected to be the warmest based on a landing gear solar thermal vacuum test.

#### 5.1.4.15 RADVS

As evidenced in Table 5.1-1 and Figures 5.1-48, 5.1-49, 5.1-50, and 5.1-51, all RADVS temperatures (sensors R-8, R-9, R-10, and R-13) were within 10° F of premidcourse predictions and were essentially at equilibrium.

However, after the midcourse correction was initiated and the spacecraft subsequently went into a tumbling mode, RADVS temperatures changed considerably. The KPSM and preamplifier components achieved a steady-state temperature at approximately 25 to 30 hours after launch. The signal data converter temperature was still decreasing at the time of activation, which was 44.8 hours after launch. Although the KPSM and preamplifier temperature differed considerably from nominal values at postmidcourse equilibrium, these units remained within operational limits. Only the signal data converter exceeded operational or survival temperature boundaries, as shown in Table 5.1-2. Postmidcourse equilibrium temperatures of the KPSM, doppler sensor, and altimeter sensor were 41, 48, and 95°F, respectively. The signal data converter temperature went below its lower operation limit of -18°F and lower survival limit of -50°F at approximately L + 21.0H and L + 25.5H, respectively, and was -85°F at the time the RADVS system was energized.

The RADVS system was energized for a 10.2-minute period at L + 44.8H, and all components came on as evidenced by the temperature increase shown in Figures 5.1-48, 5.1-49, 5.1-50, and 5.1-51. The component temperature sensors indicated the following:

- 1) KPSM temperature (R-8) increased from 31 to 129°F at a rate of 9.53°F/min.
- 2) Signal data converter temperature (R-9) increased from -86 to +3°F at a rate of 8.64°F/min.
- 3) Doppler velocity sensor preamplifier temperature (R-10) increased from 38 to 53°F at a rate of 1.4°F/min.
- 4) Altimeter/velocity sensor preamplifier temperature (R-13) increased from 90 to 104°F at a rate of 1.24°F/min.

Although the signal data converter was 35°F below its survival temperature limit, the radar system apparently remained operable. However, possible degradation to the signal data converter was not ascertainable since the radar system was not exercised in a descent maneuver. All that can be said is that the unit responded normally to the RADVS on command as evidenced by its rapid temperature rise.

#### 5.1.4.16 Altitude Marking Radar (AMR)

The AMR unit temperature profile was as predicted and was within 5°F of premidcourse predictions prior to the midcourse maneuver (approximately L + 16H). Mission plots of sensors R-7 and R-27 are shown in Figures 5.1-47 and 5.1-52. Following the midcourse maneuver, the AMR unit reached steady-state temperatures which were much higher than nominal values for a properly stabilized spacecraft. The electronics platform

ECU heat sink and the two antenna sensors equilibrated at approximately 78, 99, and 155°F, respectively, whereas nominal flight temperatures should be -12, -16, and -185°F, respectively. However, the AMR unit remained within transit operational limits throughout the mission despite spacecraft disorientation.

Command 0730 (emergency AMR signal) was sent at 265:09:34:17 GMT. Telemetry indicated that sensor R-7 (AMR ECU heat sink) went from 97°F at 09:34:28 to a full-scale reading at 09:34:29. Thus, it appears that the AMR was expelled from the retro nozzle within this time interval, thereby verifying retro ignition. The SC-2 AMR heater duty cycle was 1.65 hr/cycle, whereas the SC-1 duty cycle was 1.16 hr/cycle. However, the SC-2 duty cycle was determined using only a few cycles due to the shortness of the mission. The longer SC-2 duty cycle can be explained by a warmer retro nozzle than SC-1.

#### 5. 1. 4. 17 Television System

##### Approach TV

The approach TV temperature prior to the midcourse maneuver was -108°F, within 8°F of the preflight prediction. Following midcourse, its temperature increased 176°F to a steady-state value of 68°F, indicating that a considerable amount of solar energy was impinging on the unit during the postmidcourse tumbling mode. The approach TV electronics temperature (T-3) is presented in Figure 5.1-53.

##### Survey TV

The survey TV electronics temperature was as predicted. Prior to midcourse, the electronics temperature was -132°F, 7°F below prediction. Following midcourse, the electronics temperature increased to -48°F, indicating an increased solar energy load on the unit.

The hood and mirror assembly was within 9°F of the predicted steady-state temperature (-113°F) prior to midcourse maneuver, although the rate of cooldown was actually much greater than predicted (see Figure 5.1-73). Following midcourse, the assembly temperature increased to -59°F, thereby indicating an increase in solar illumination.

#### 5. 1. 5 REFERENCE

1. B. N. Taylor, "Temperature Predictions for Surveyor Mission B for September 20 Launch Date," IDC 2221, 19/77, 13 September 1966.

### 5. 1. 6 ACKNOWLEDGEMENTS

This section was coordinated by H. E. Knudson. Other acknowledgements go to the following:

- 1) The entire Hughes Surveyor Thermal Control Section for contributions made in the analysis of the Mission B thermal data.
- 2) Dr. J. M. F. Vickers and D. L. Ayers, JPL, who prepared the vernier system temperature plots discussed in the failure review analysis (subsection 5. 1. 2. 2).
- 3) Jerry Lewis, Hughes thermal control, for his extensive work in analyzing the vernier propulsion system thermal data in connection with the failure review analysis (subsection 5. 1. 2. 2).

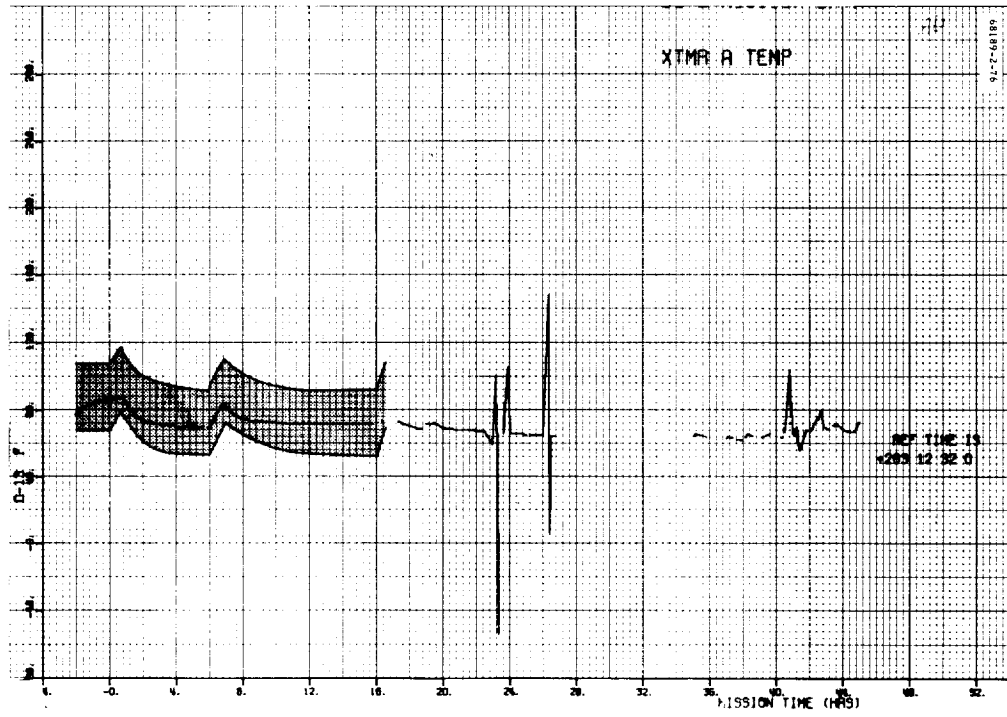


Figure 5.1-16. Transmitter A

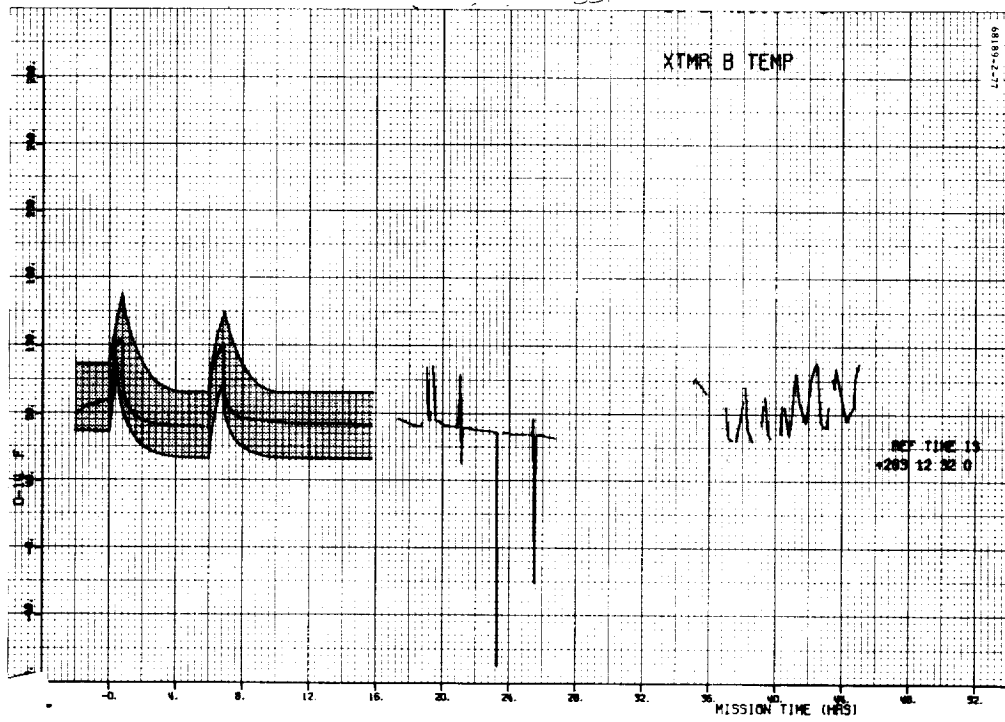


Figure 5.1-17. Transmitter B



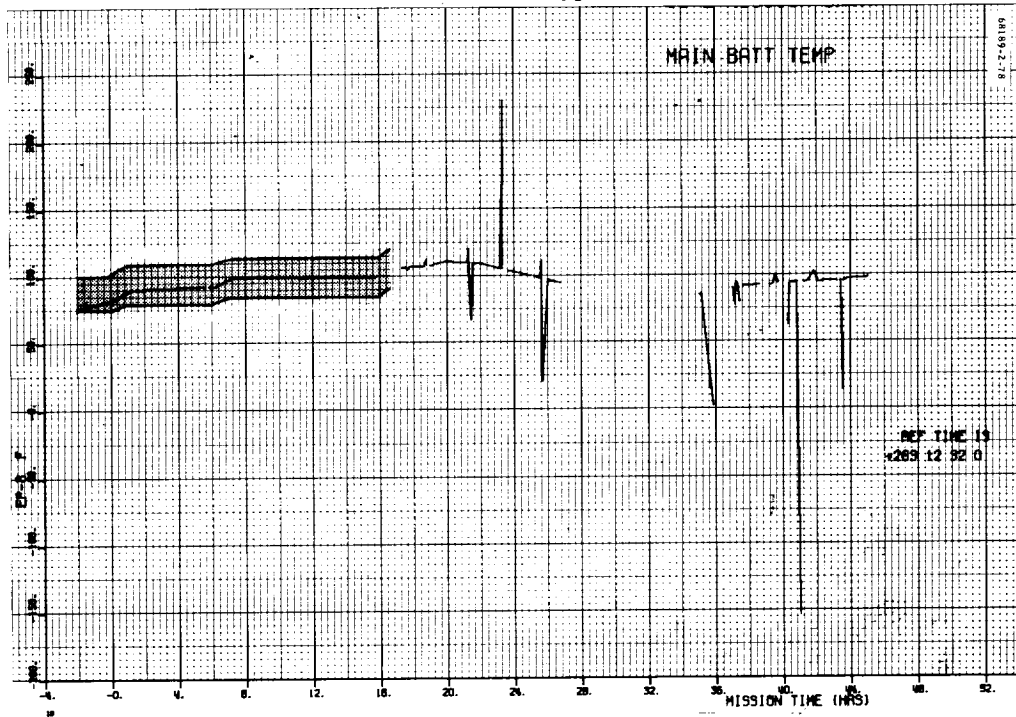


Figure 5.1-18. Main Battery

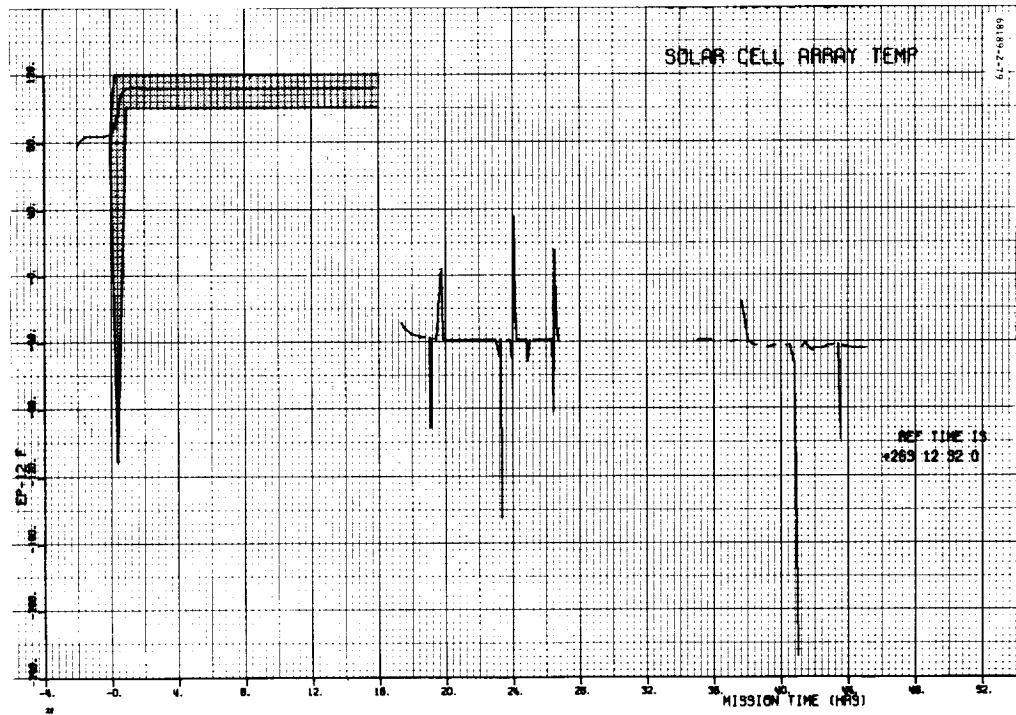


Figure 5.1-19. Solar Cell Array

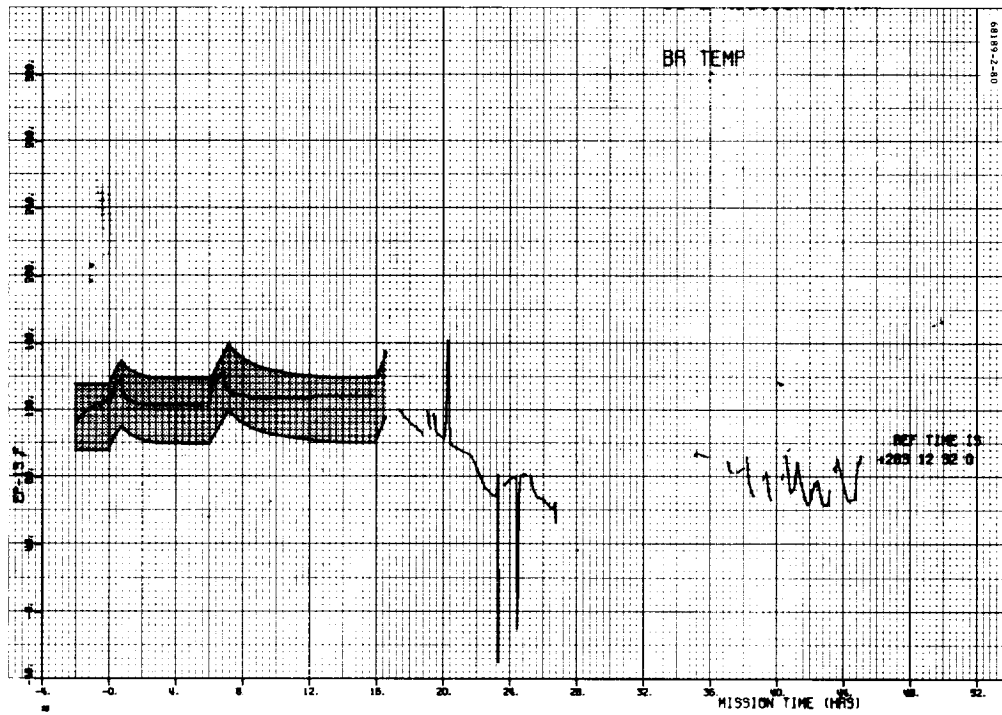


Figure 5.1-20. Boost Regulator



Figure 5.1-21. Auxiliary Battery



Figure 5.1-22. Battery Charge Regulator

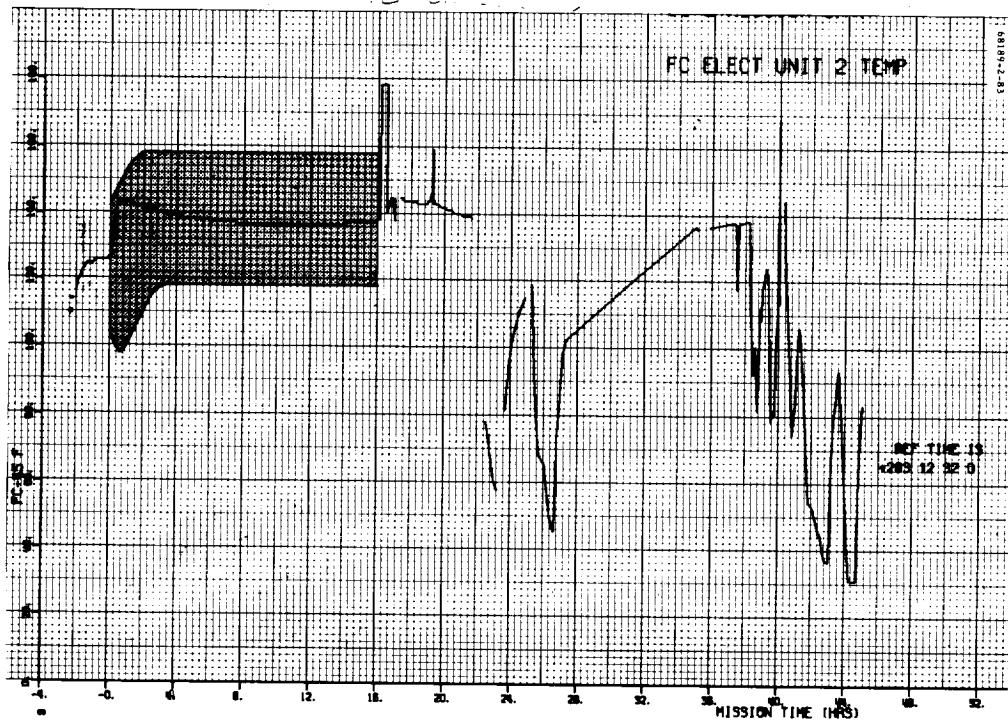


Figure 5.1-23. Flight Control Electronics Unit 2

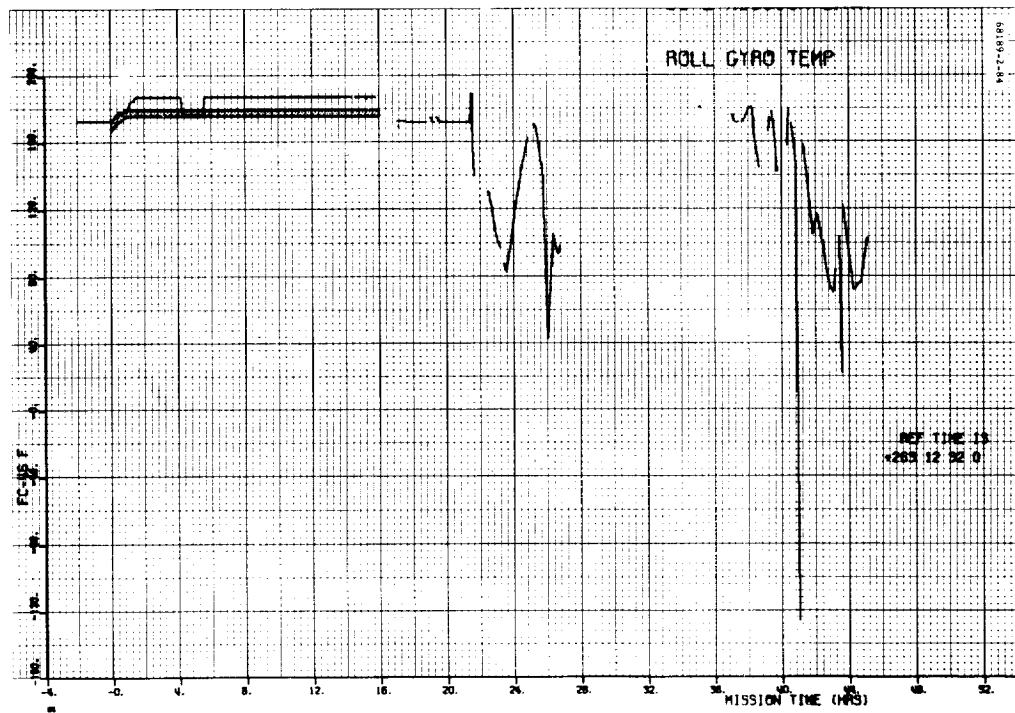


Figure 5.1-24. Roll Gyro

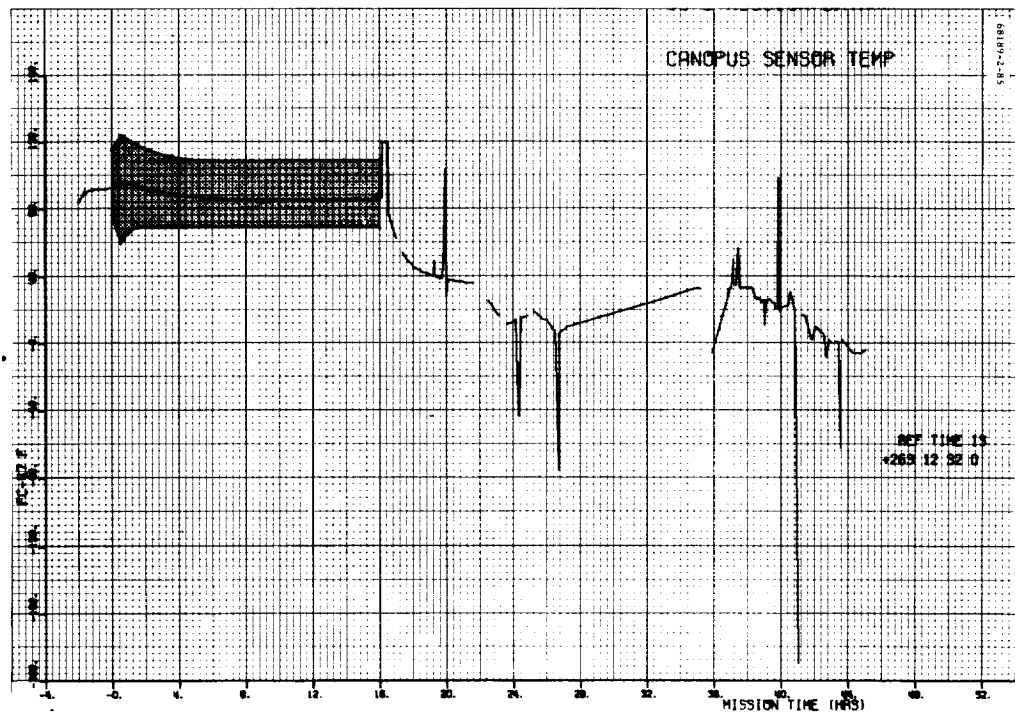


Figure 5.1-25. Canopus Sensor

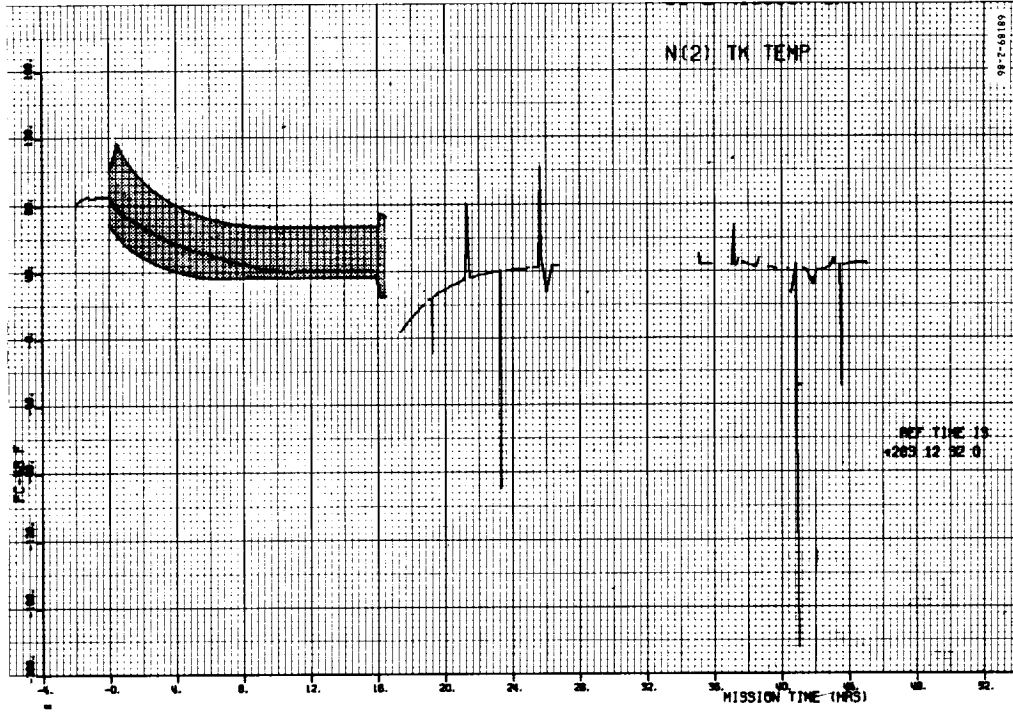


Figure 5.1-26. Nitrogen Gas Tank

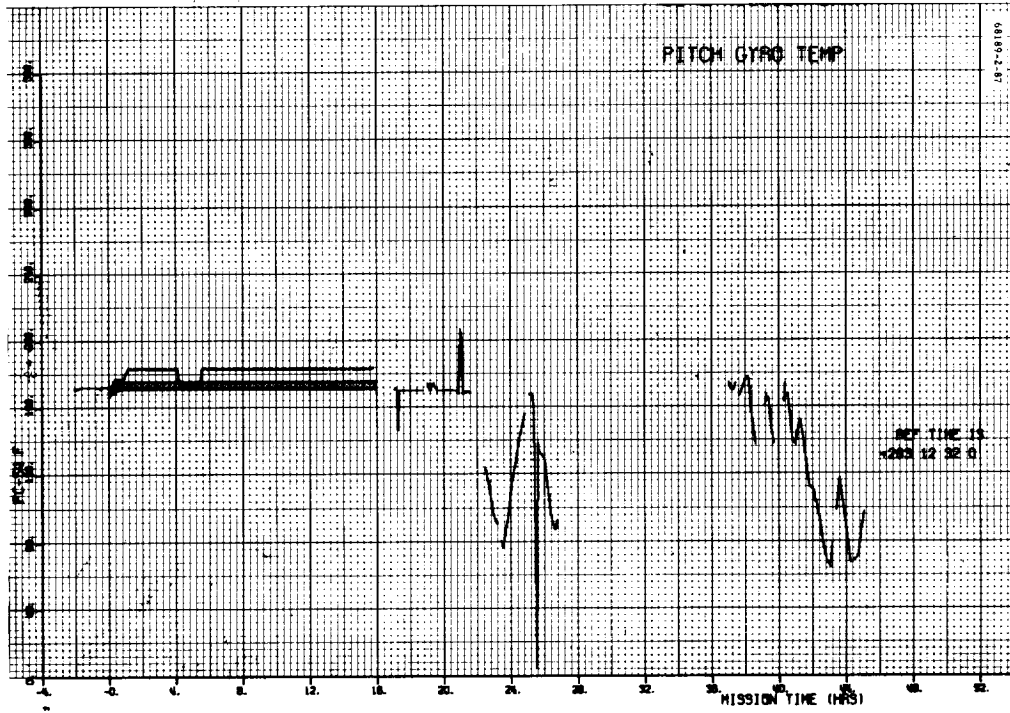


Figure 5.1-27. Pitch Gyro

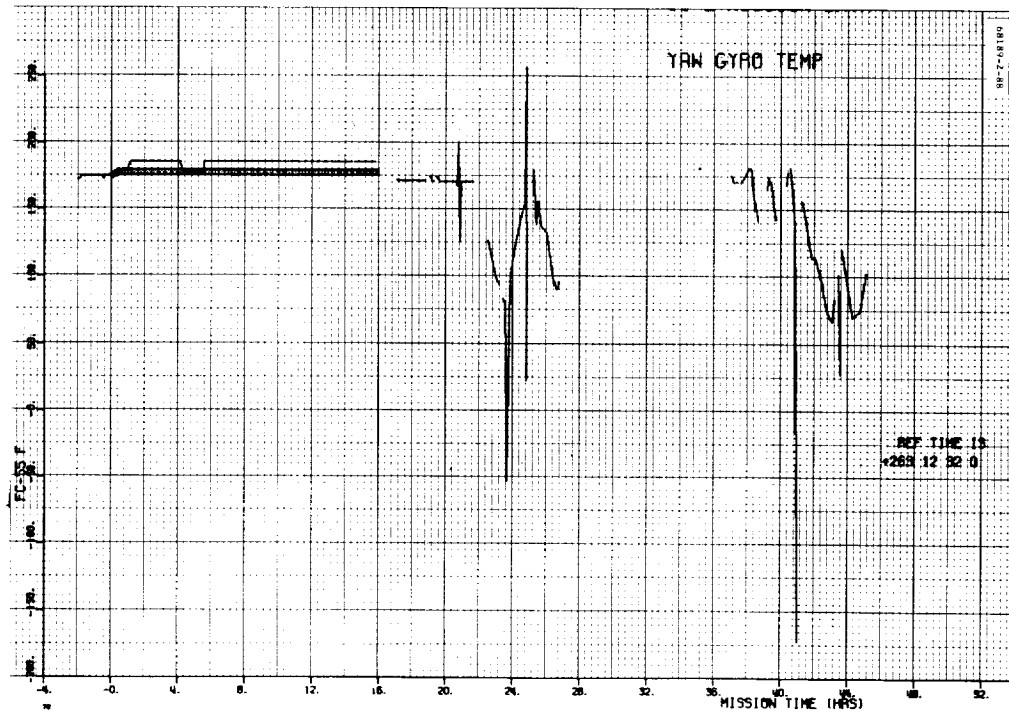


Figure 5.1-28. Yaw Gyro

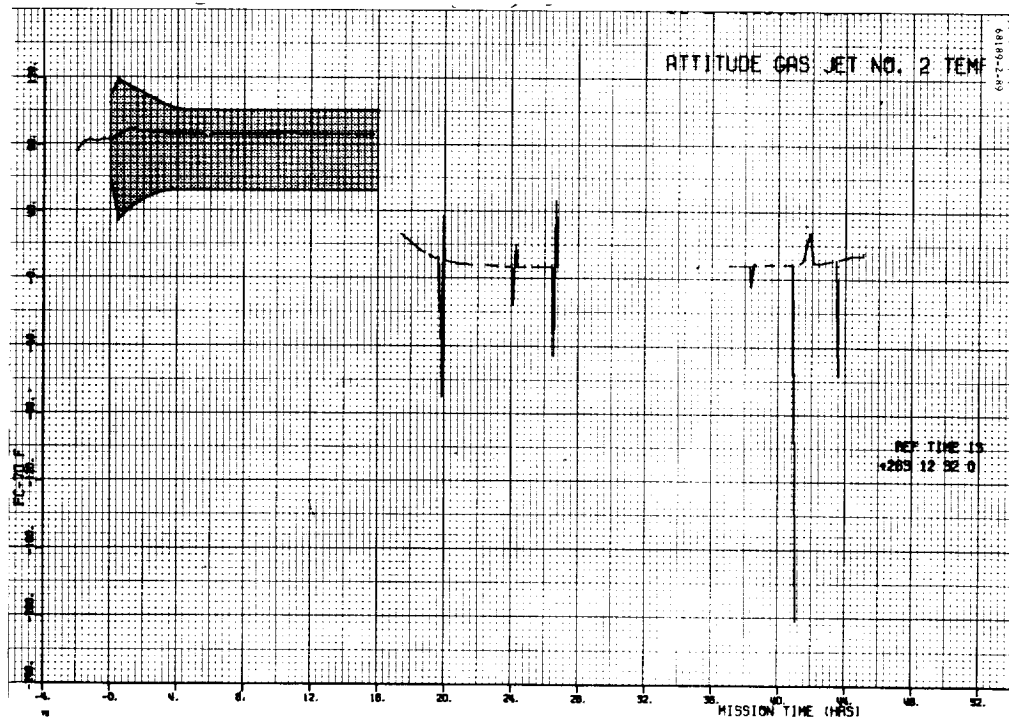


Figure 5.1-29. Attitude Gas Jet 2

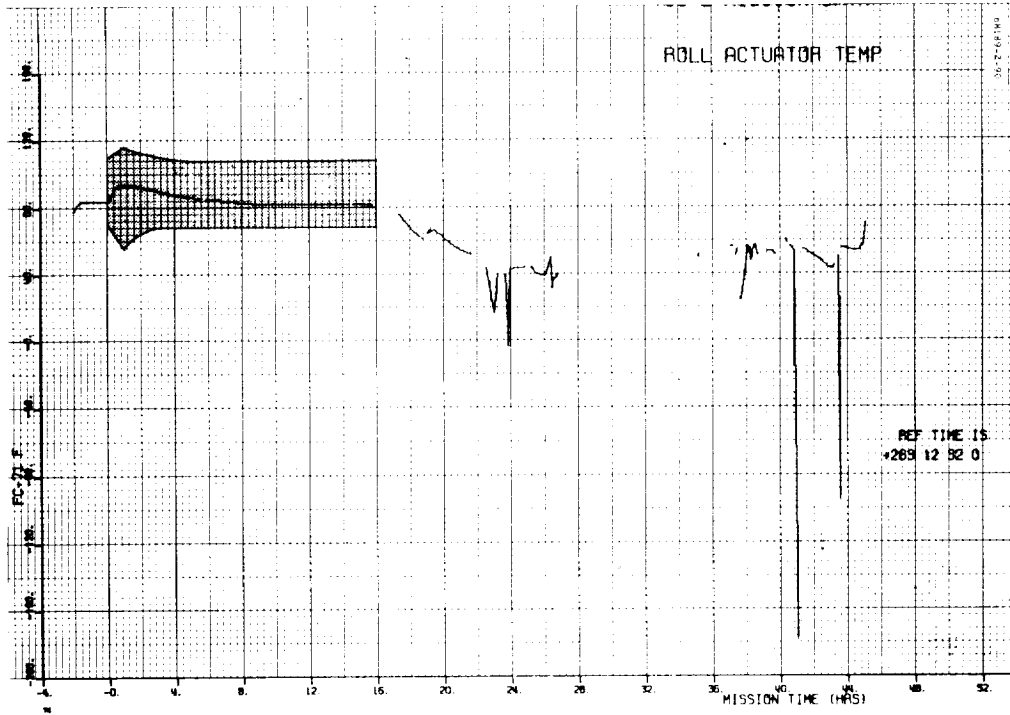


Figure 5.1-30. Roll Actuator

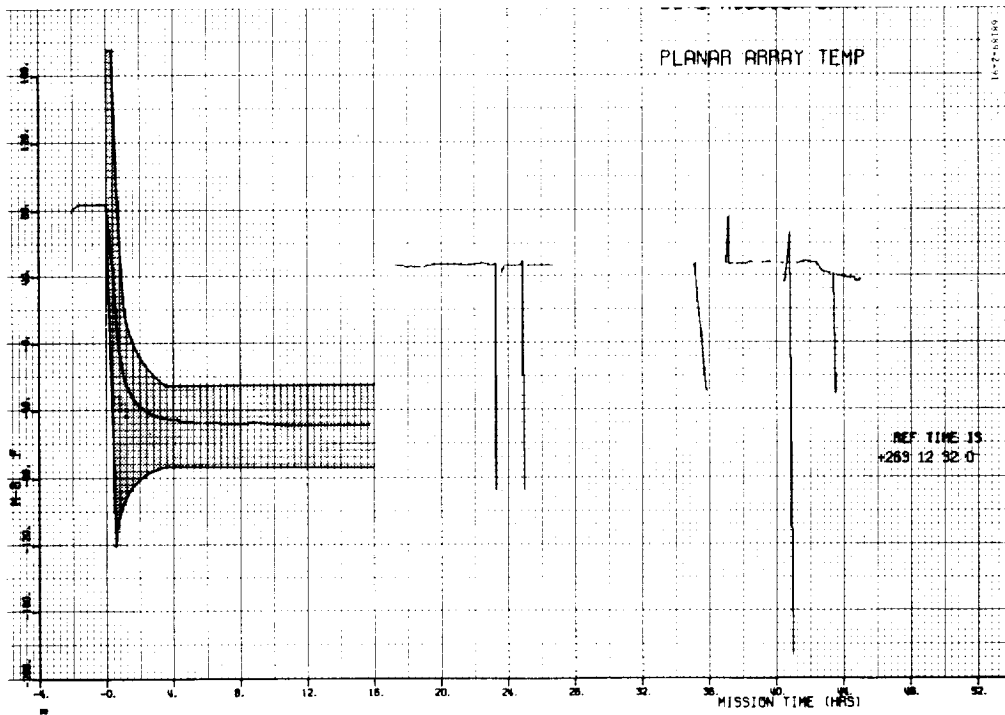


Figure 5.1-31. Planar Array

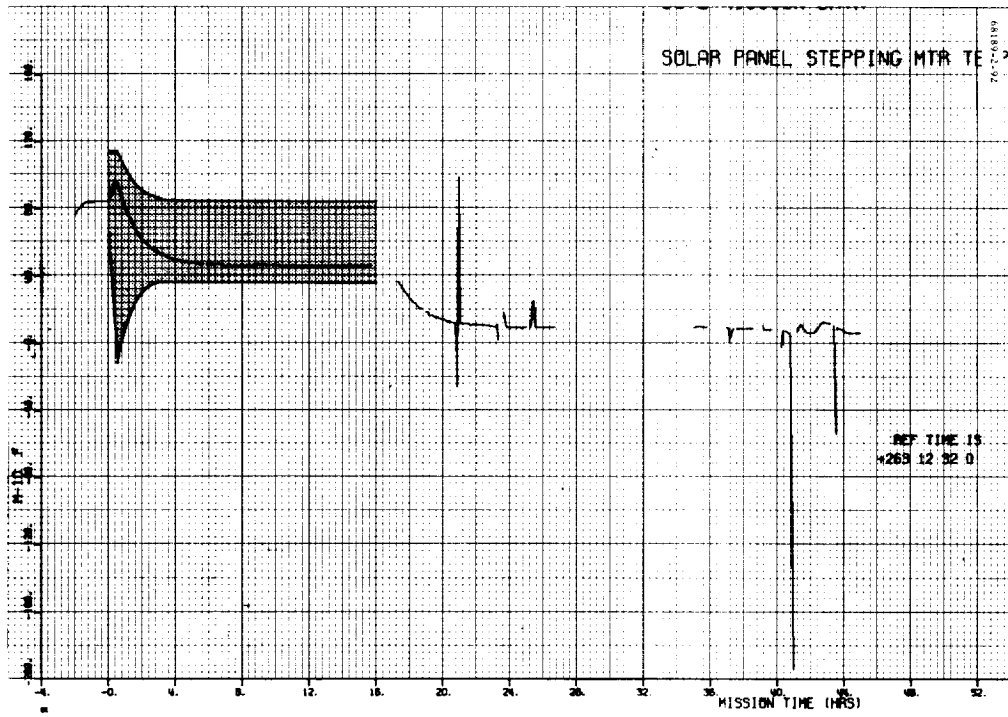


Figure 5.1-32. Solar Panel Stepping Motor

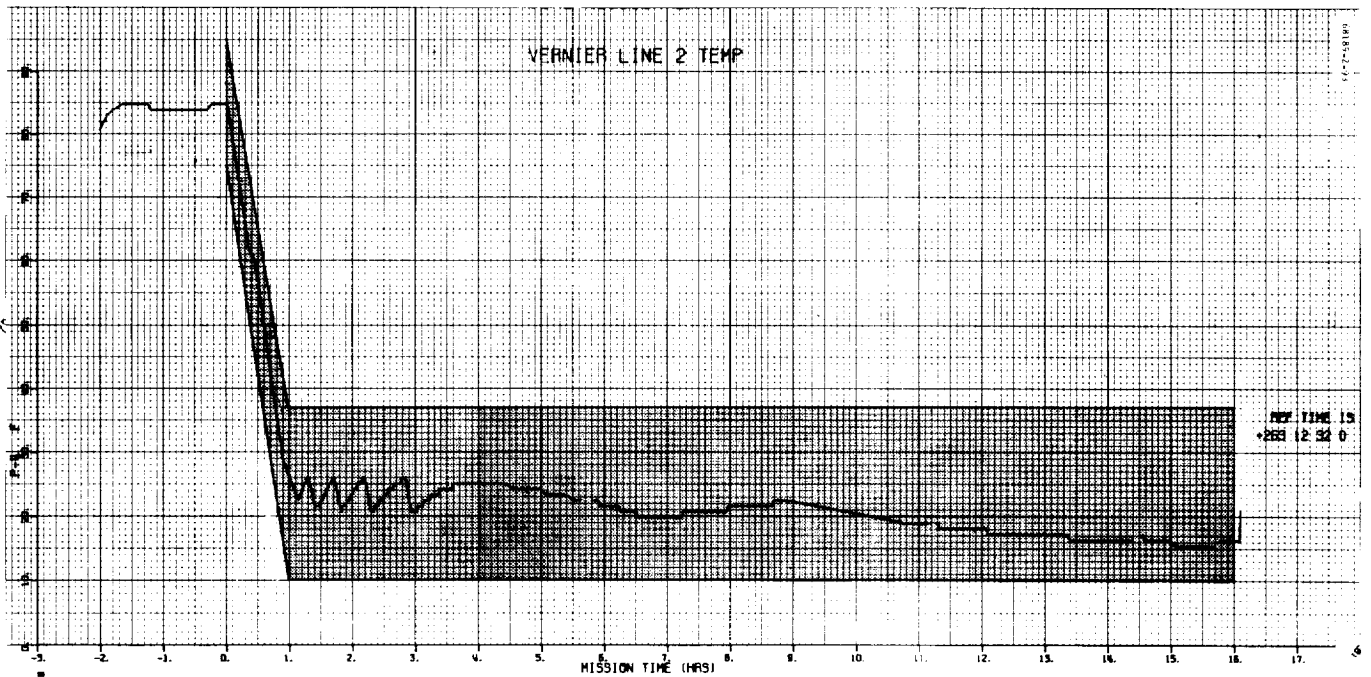


Figure 5.1-33. Vernier Lines 2



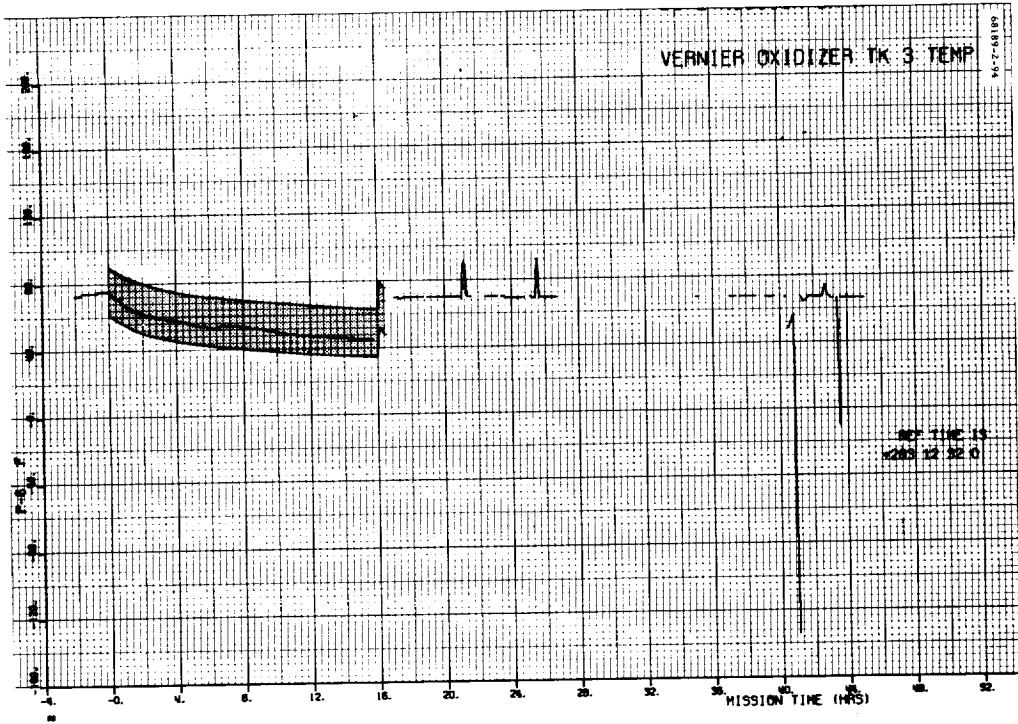


Figure 5.1-34. Vernier Oxidizer Tank 3

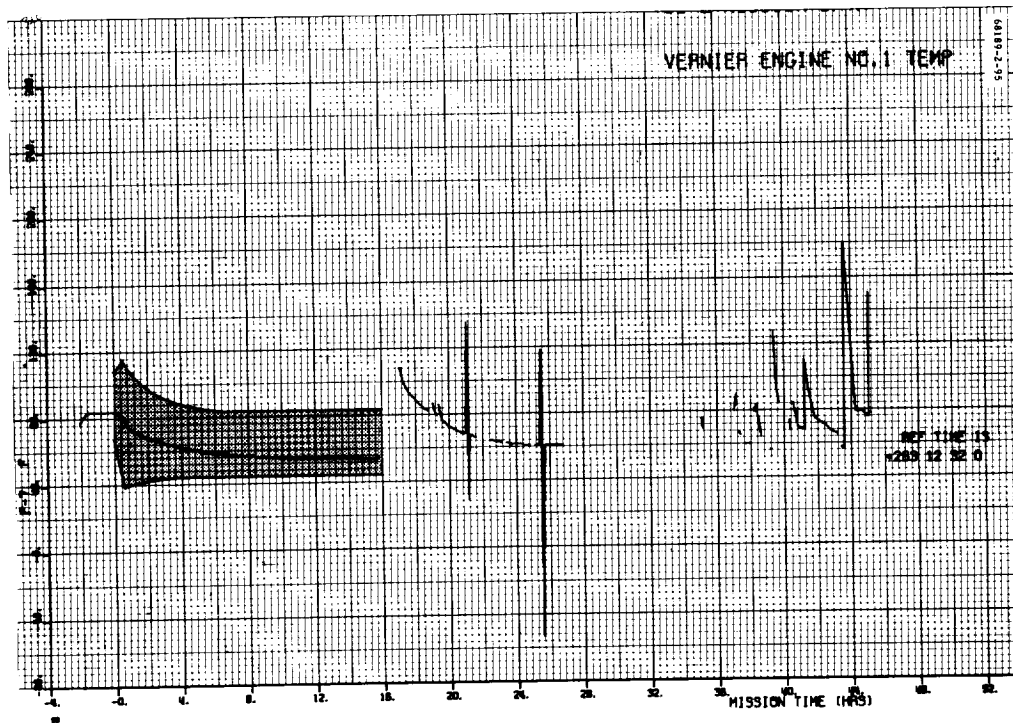


Figure 5.1-35. Vernier Engine 1

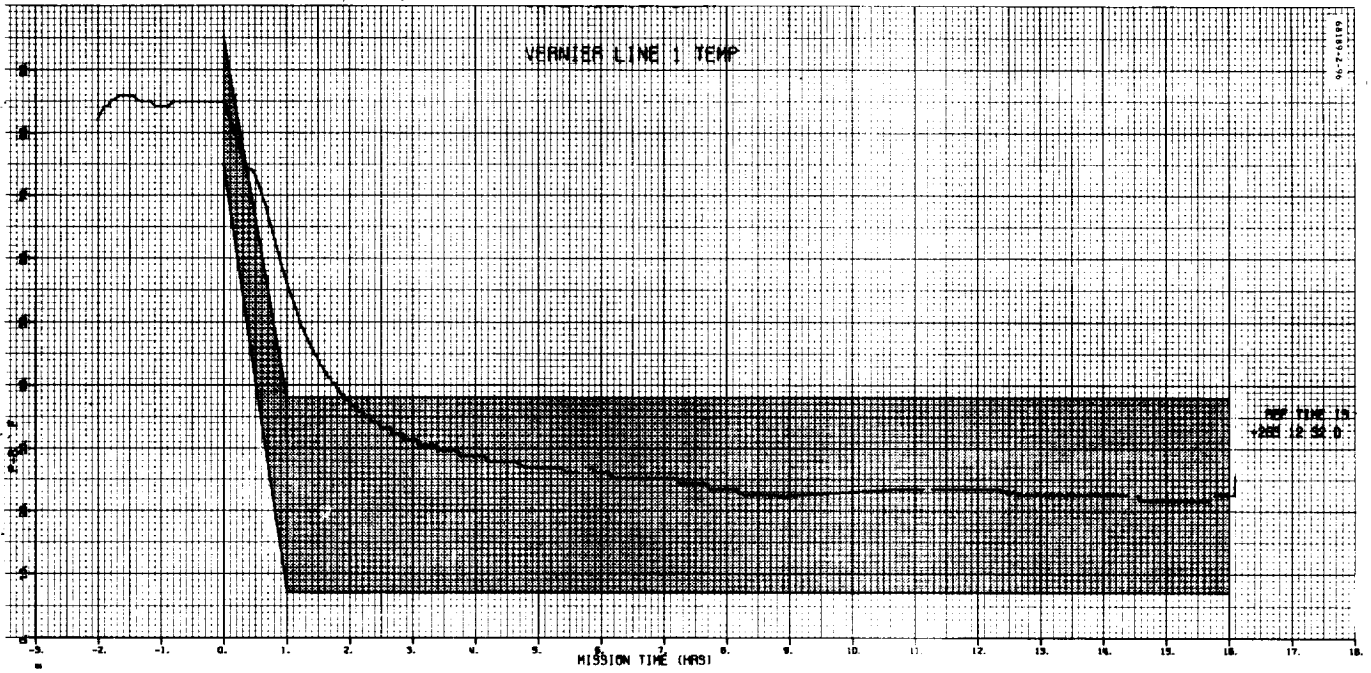


Figure 5.1-36. Vernier Lines 1

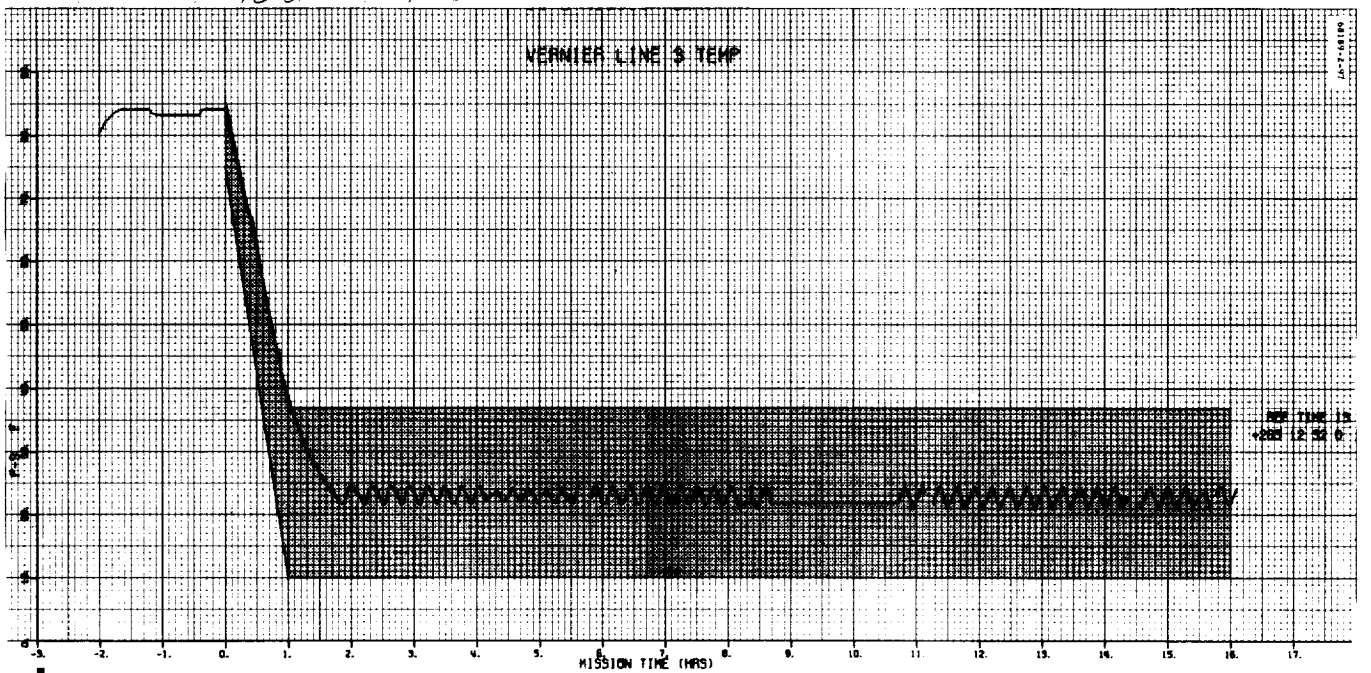


Figure 5.1-37. Vernier Lines 3

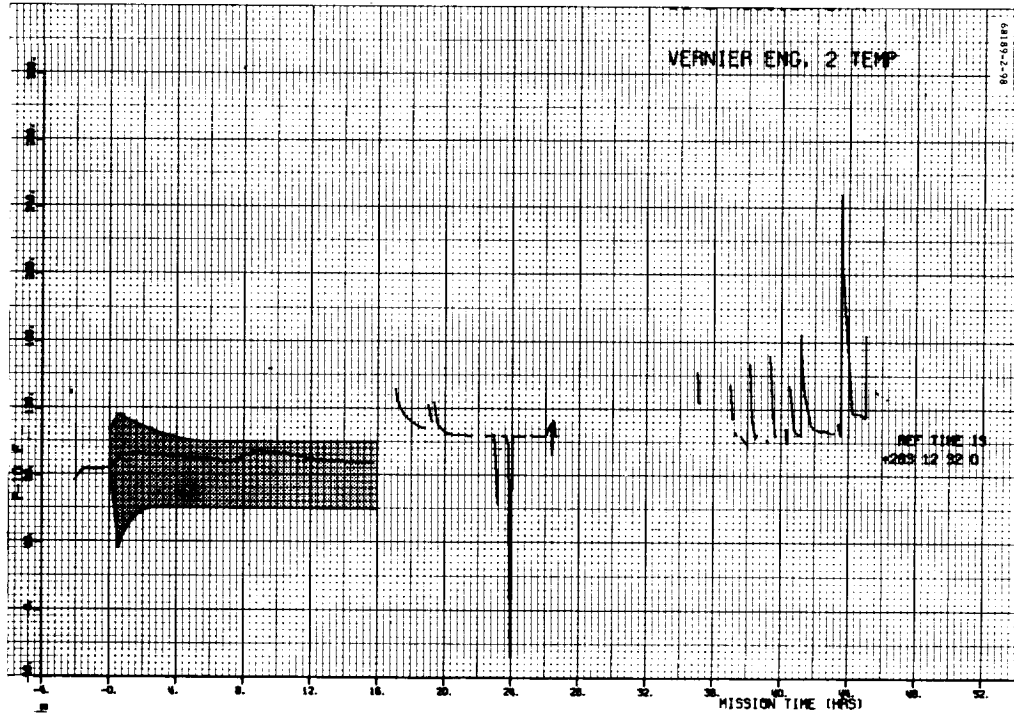


Figure 5.1-38. Vernier Engine 2

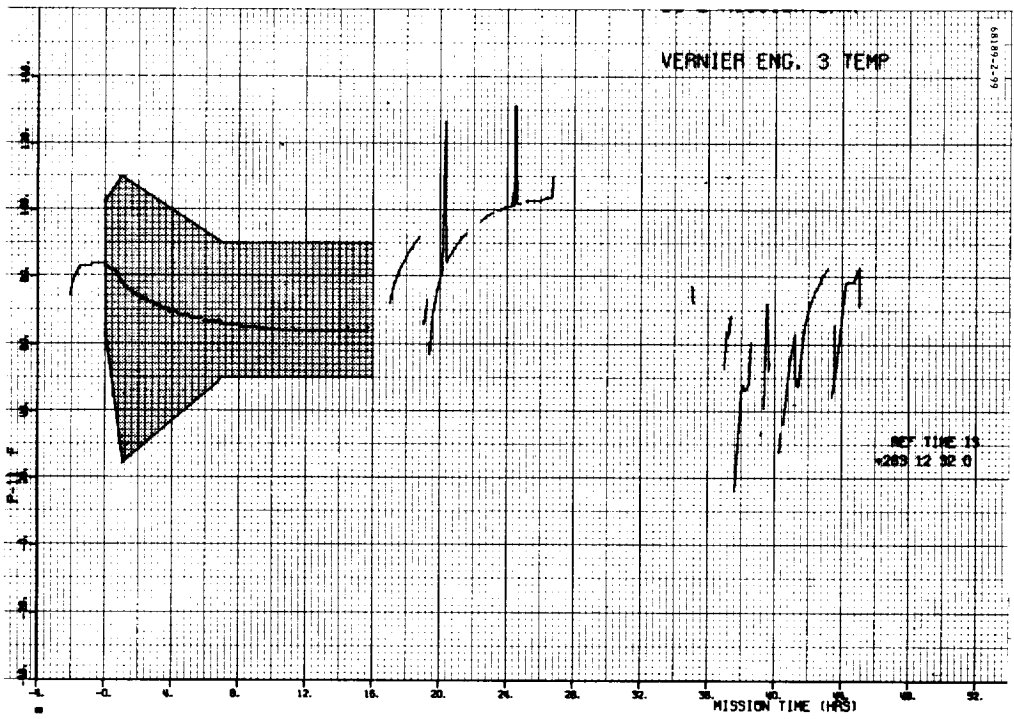


Figure 5.1-39. Vernier Engine 3

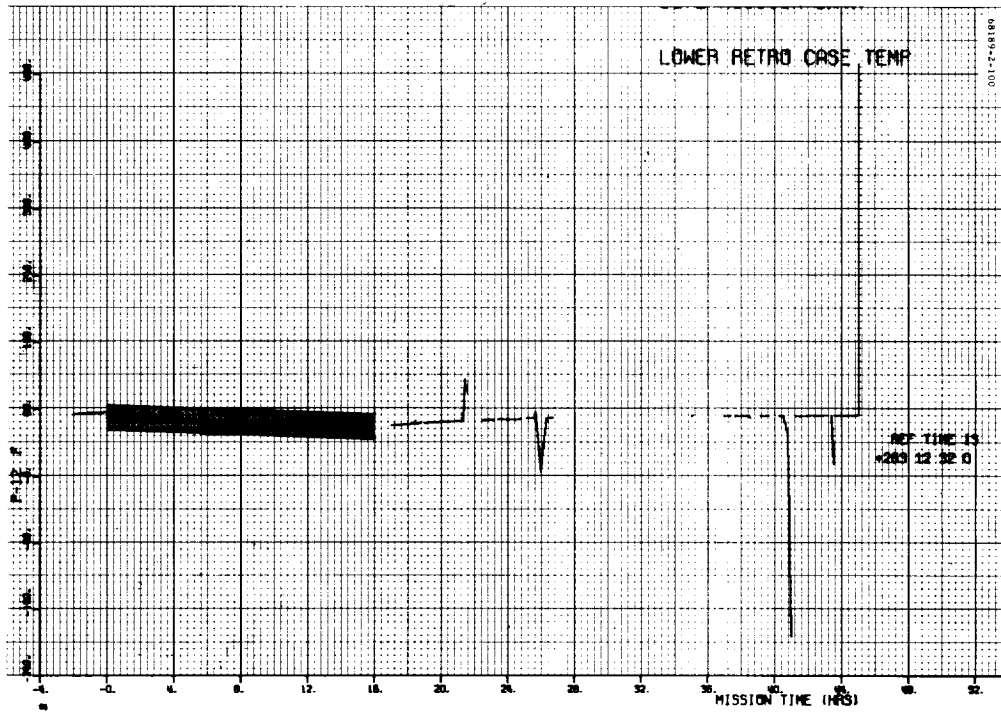


Figure 5.1-40. Lower Retro Case

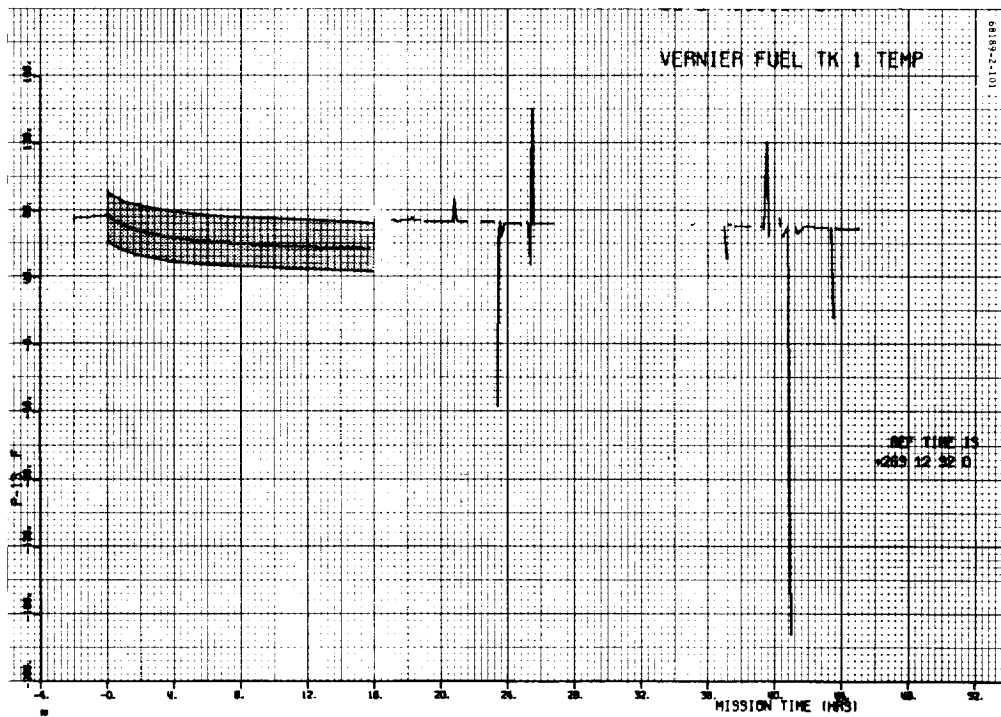


Figure 5.1-41. Vernier Fuel Tank 1

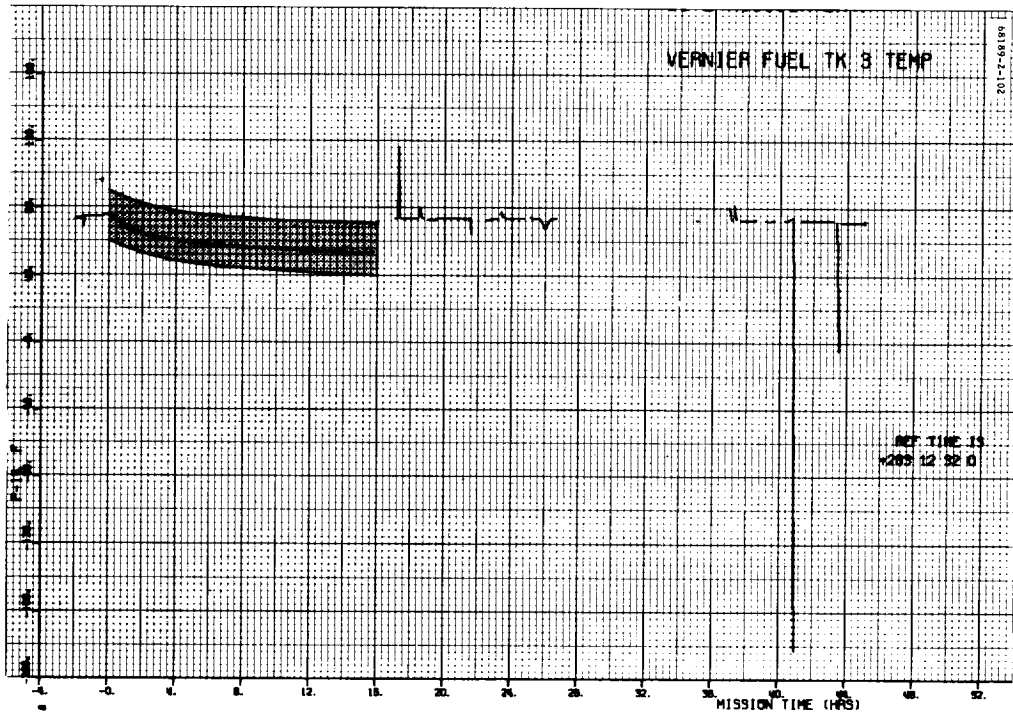


Figure 5.1-42. Vernier Fuel Tank 3

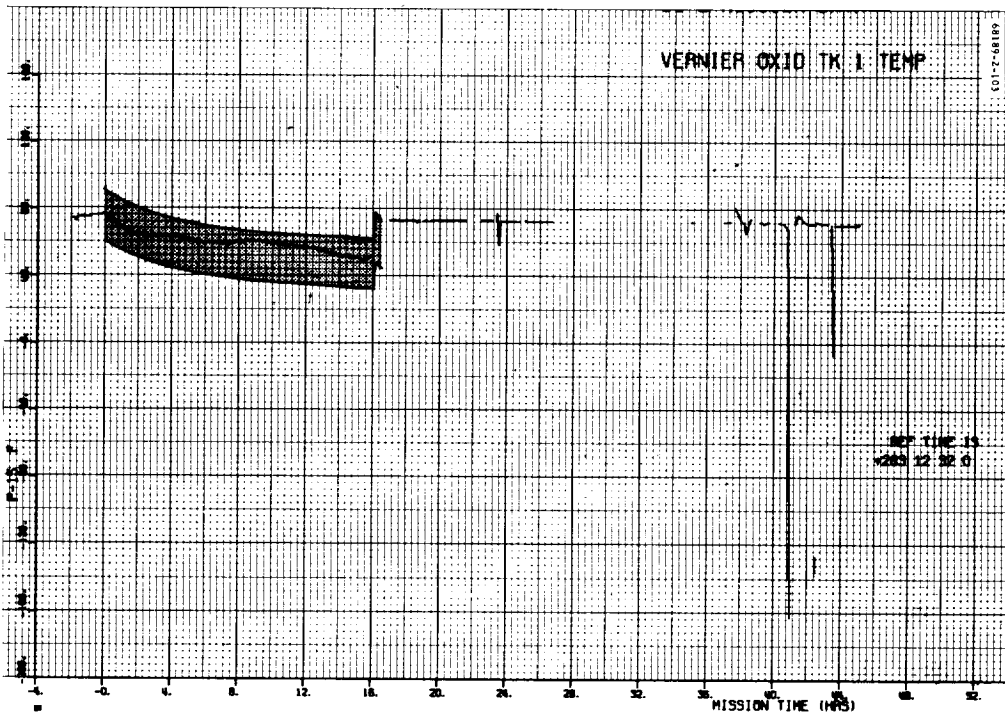


Figure 5.1-43. Vernier Oxidizer Tank 1

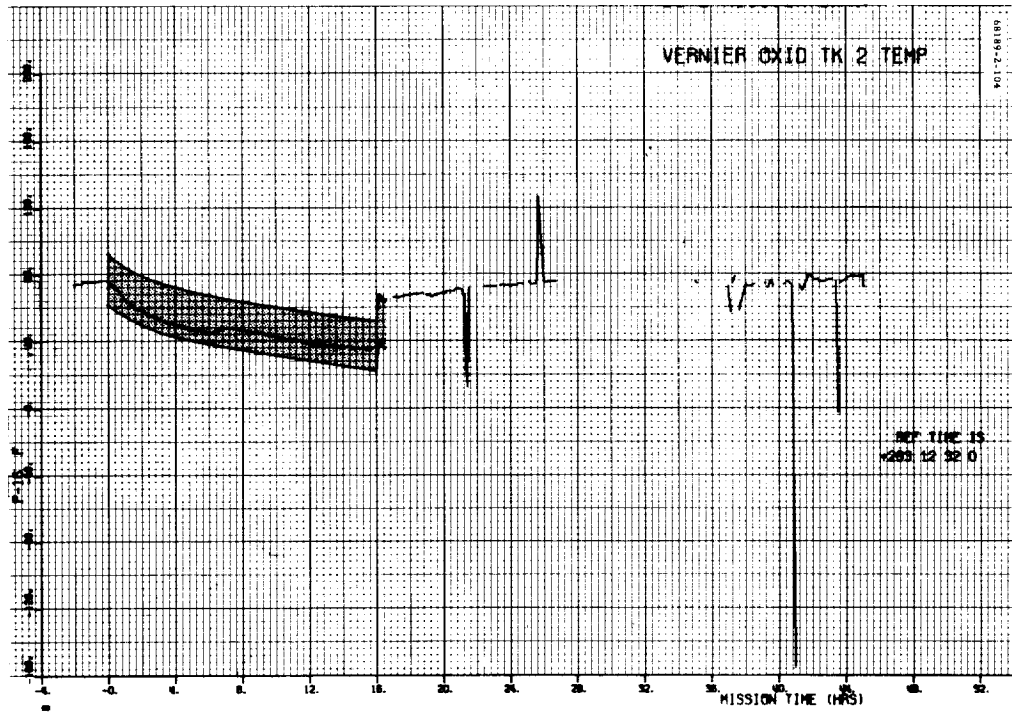


Figure 5.1-44. Vernier Oxidizer Tank 2

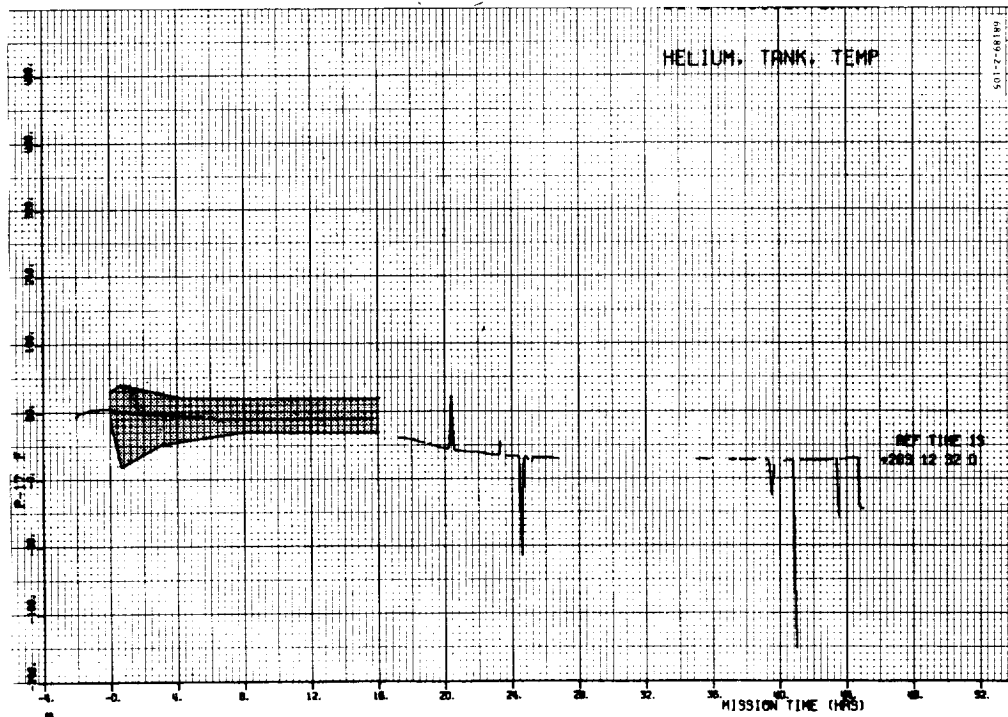


Figure 5.1-45. Helium Tank

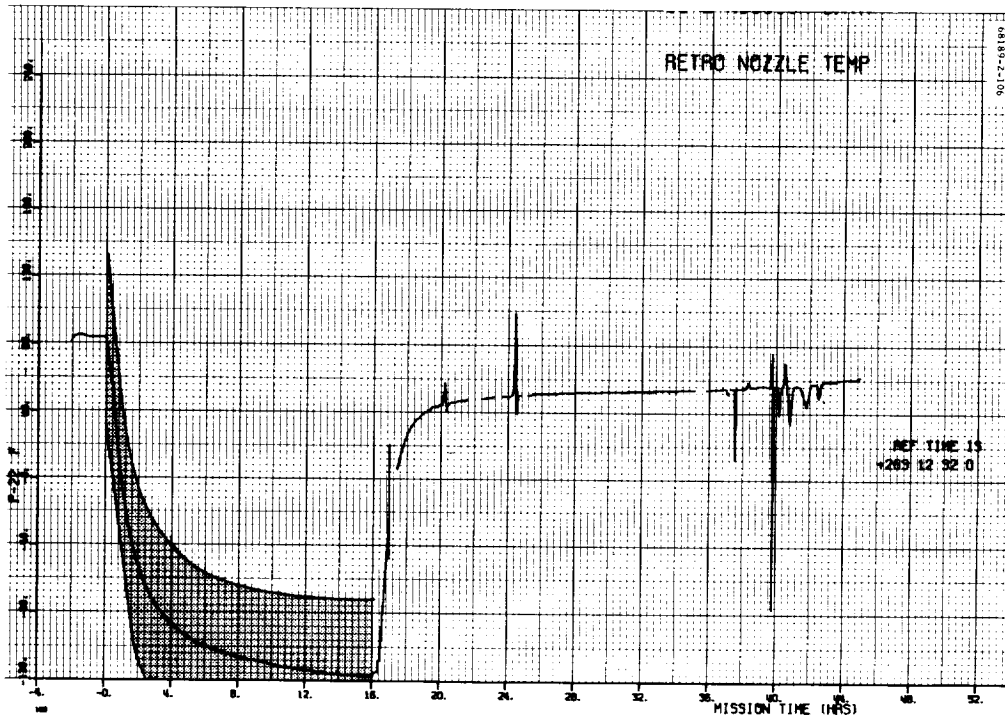


Figure 5.1-46. Retro Nozzle

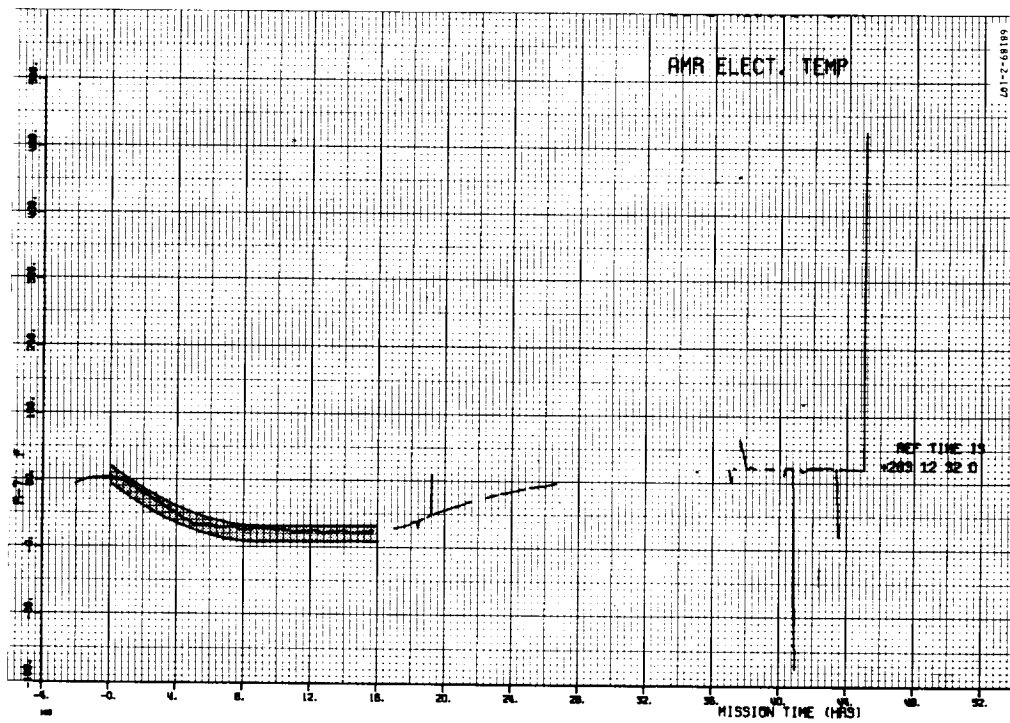


Figure 5.1-47. AMR Electronics

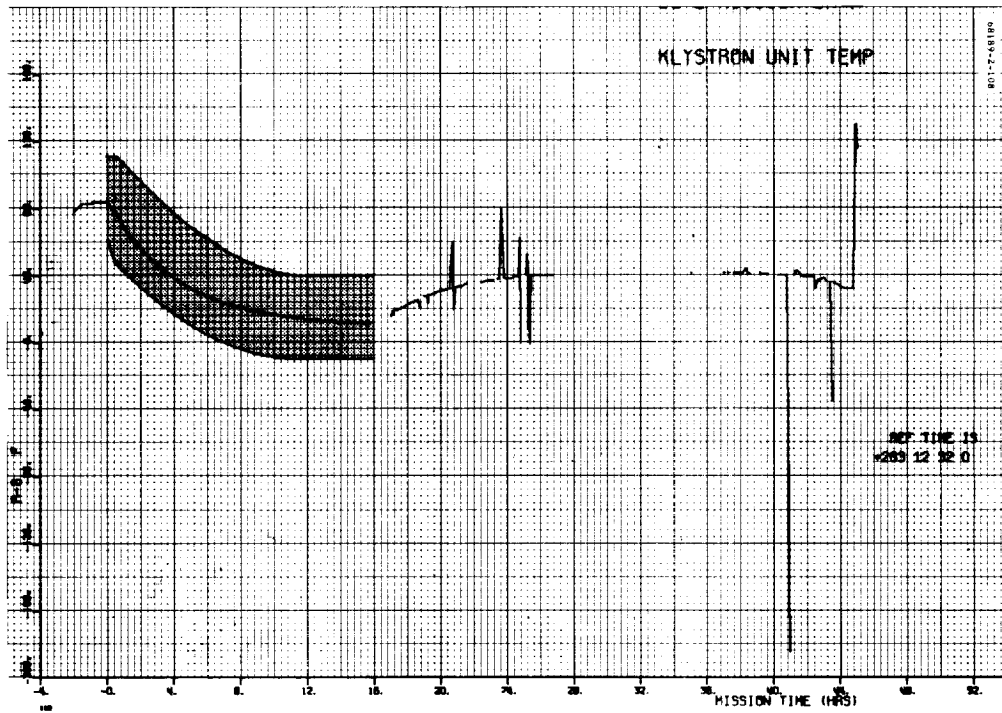


Figure 5.1-48. Altimeter Doppler Klystron

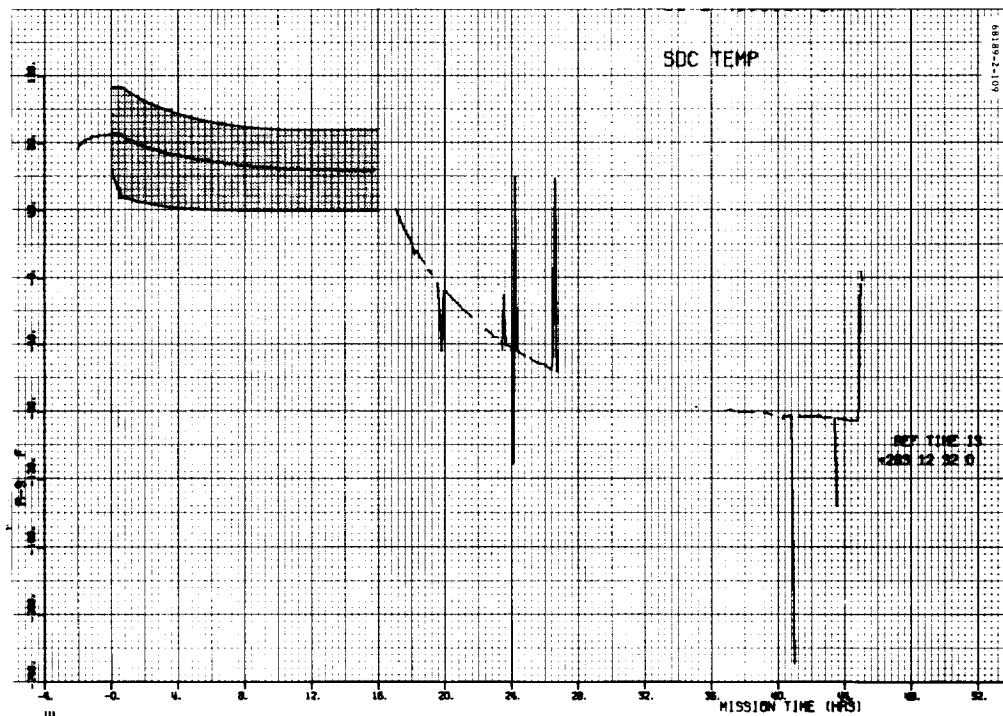


Figure 5.1-49. Radar Signal Data Converter





Figure 5.1-50. Doppler Radar Sensor

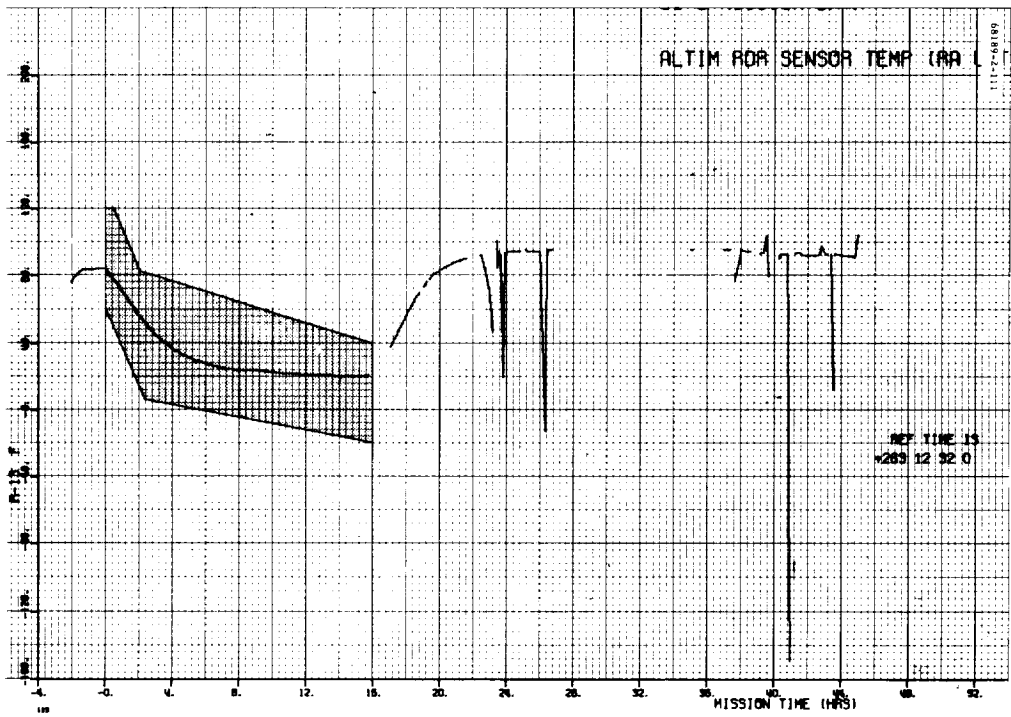


Figure 5.1-51. Altimeter Radar Sensor

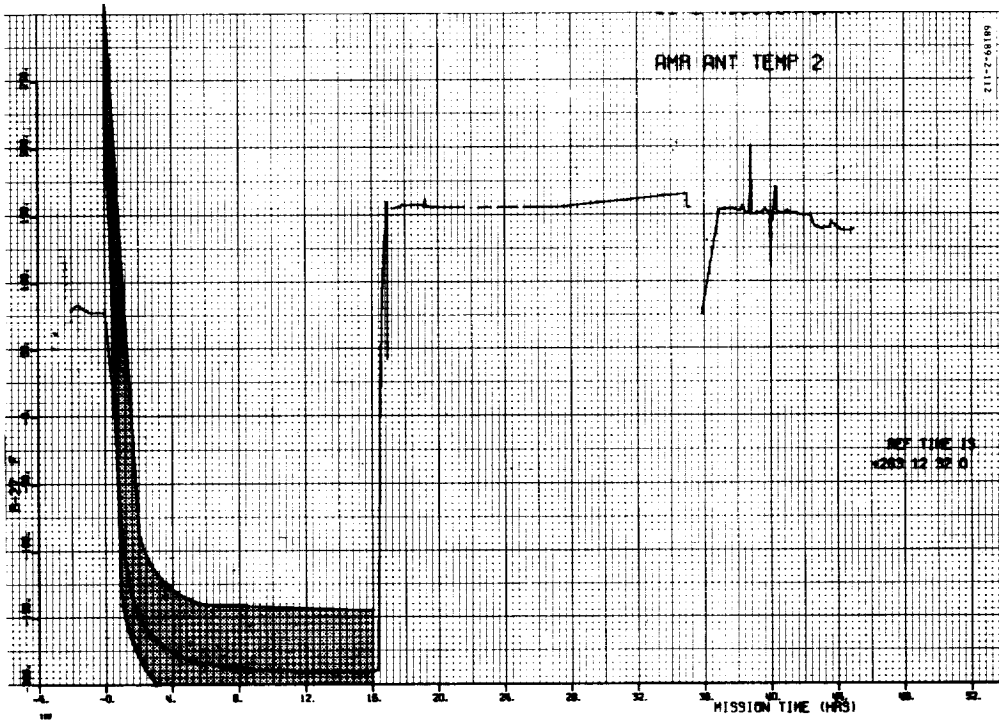


Figure 5.1-52. AMR Antenna 2

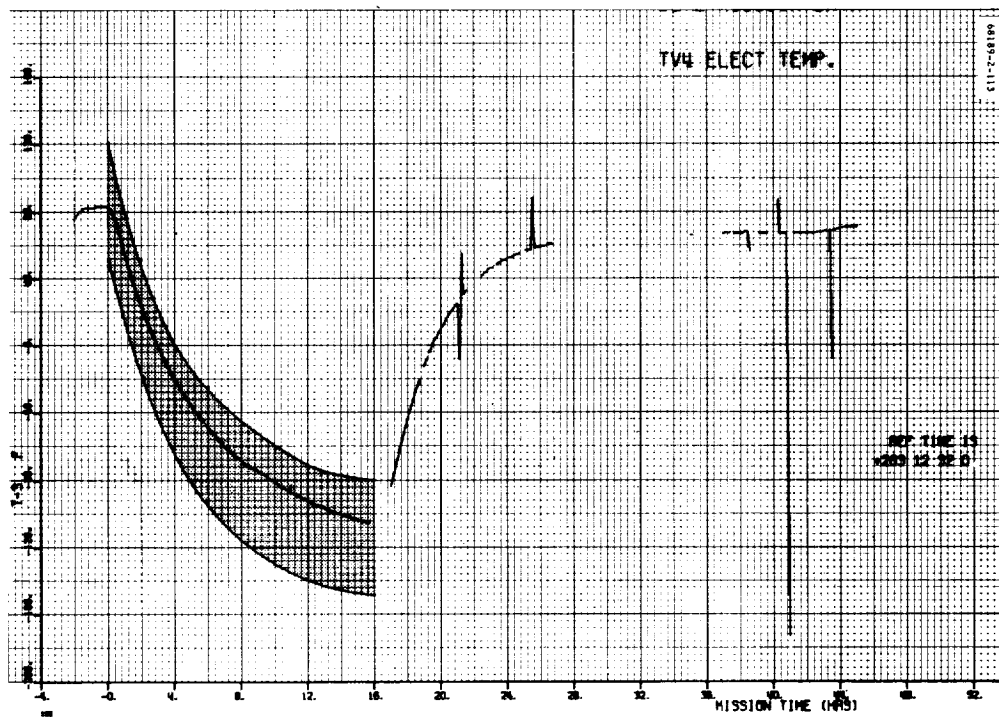


Figure 5.1-53. Approach Camera 4 Electronics

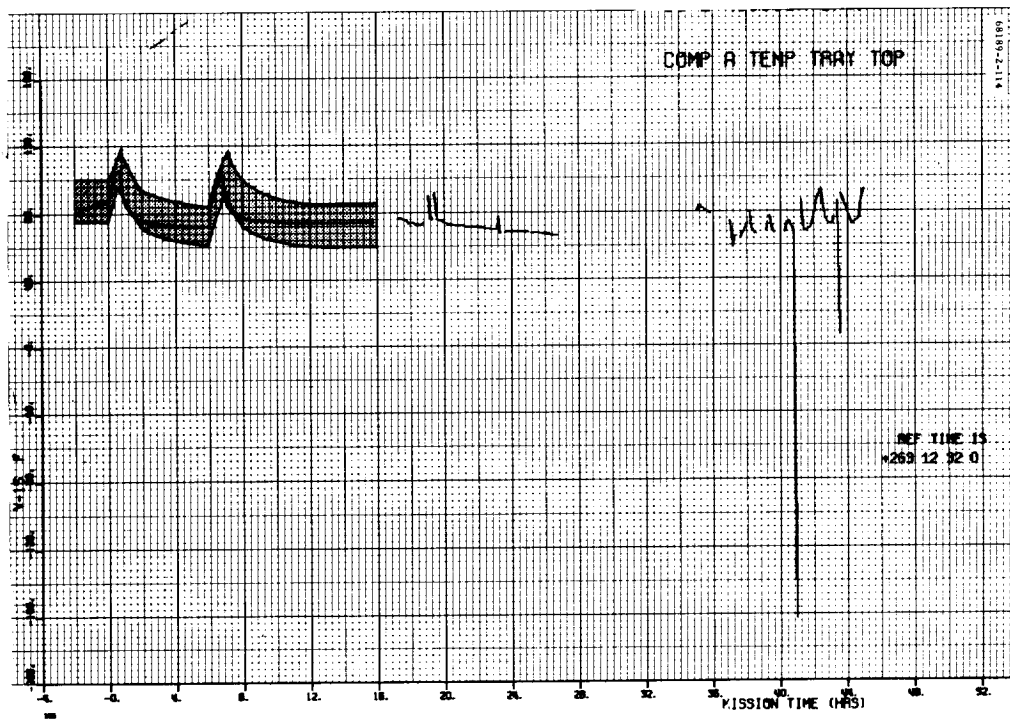


Figure 5.1-54. Compartment A Thermal Tray Top

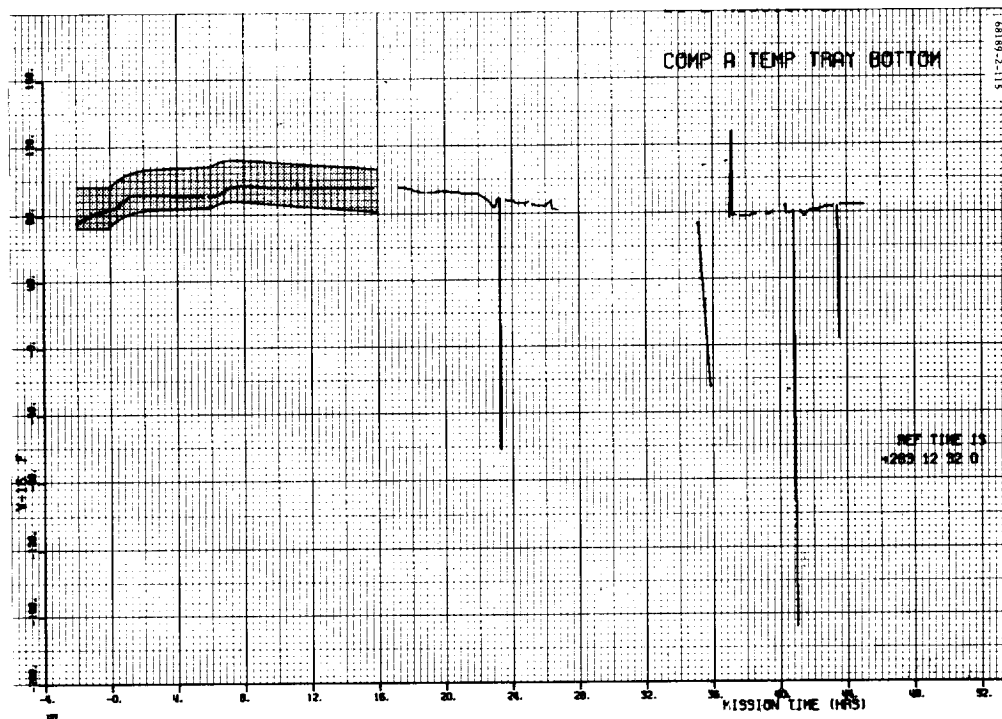


Figure 5.1-55. Compartment A Thermal Tray Bottom

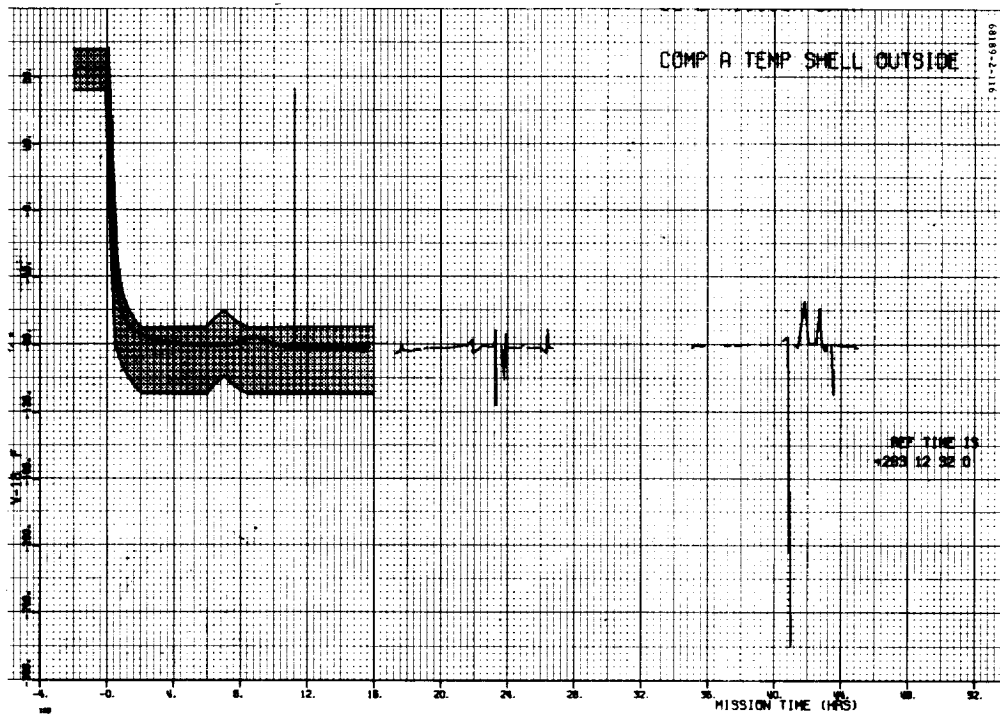


Figure 5.1-56. Compartment A Thermal Tray Shell Outside

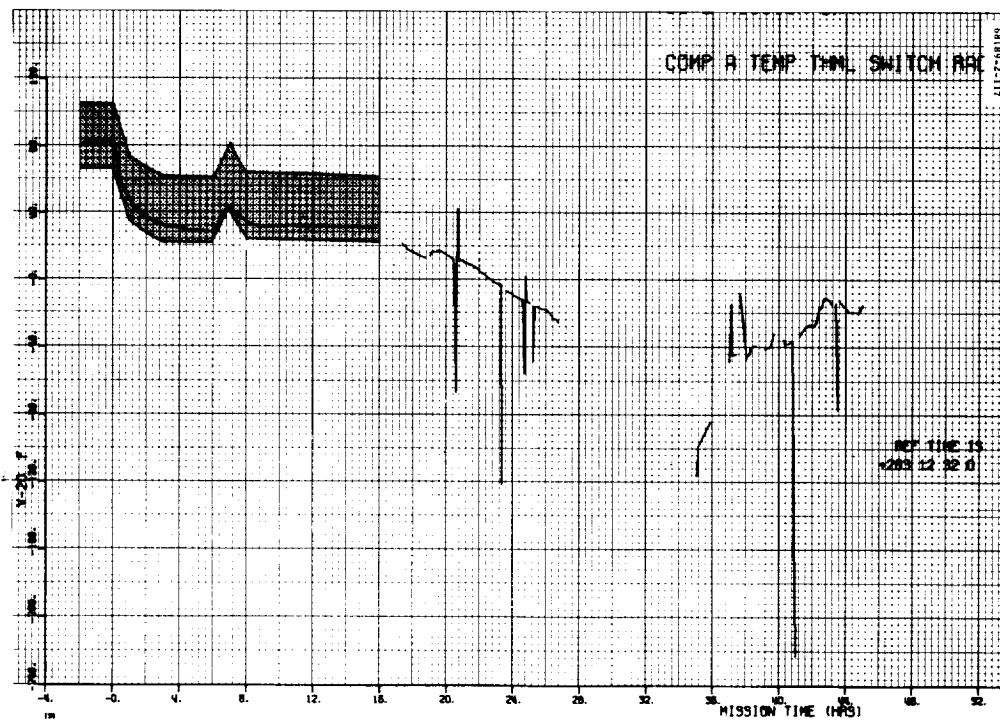


Figure 5.1-57. Compartment A Radiator 5



Figure 5.1-58. . Compartment B Thermal Tray Top

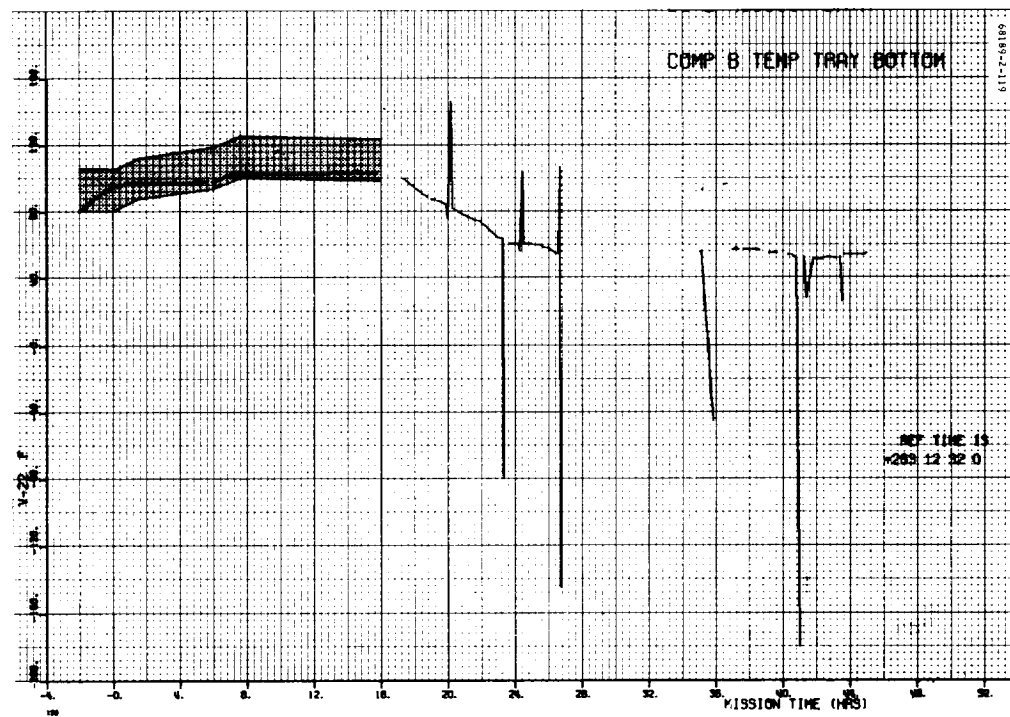


Figure 5.1-59. Compartment B Thermal Tray Bottom

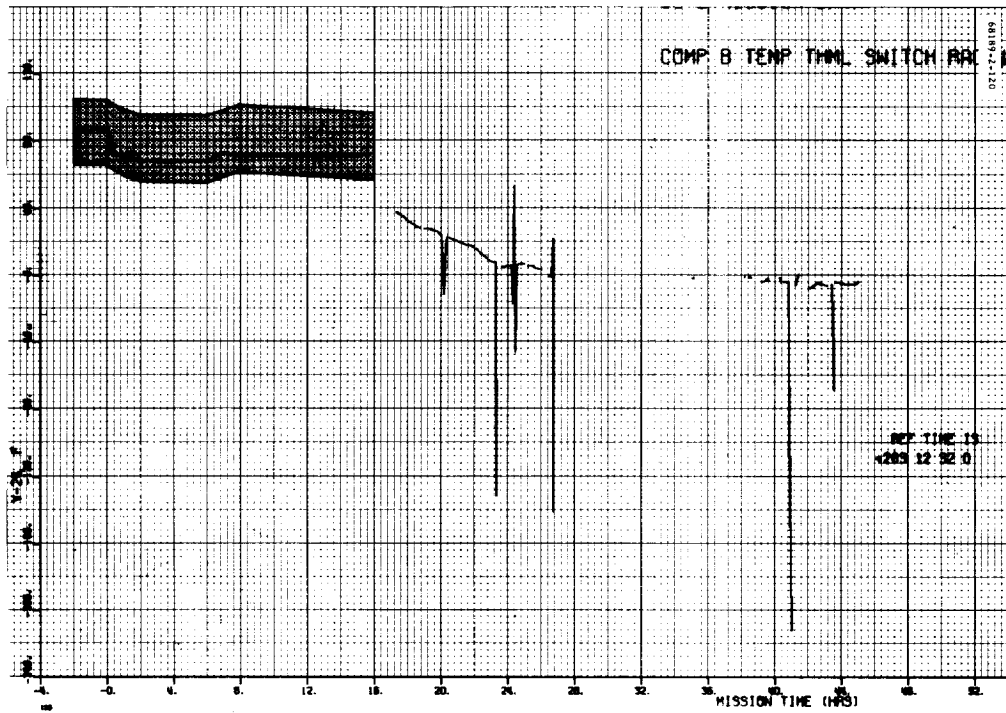


Figure 5.1-60. Compartment B Radiator 4

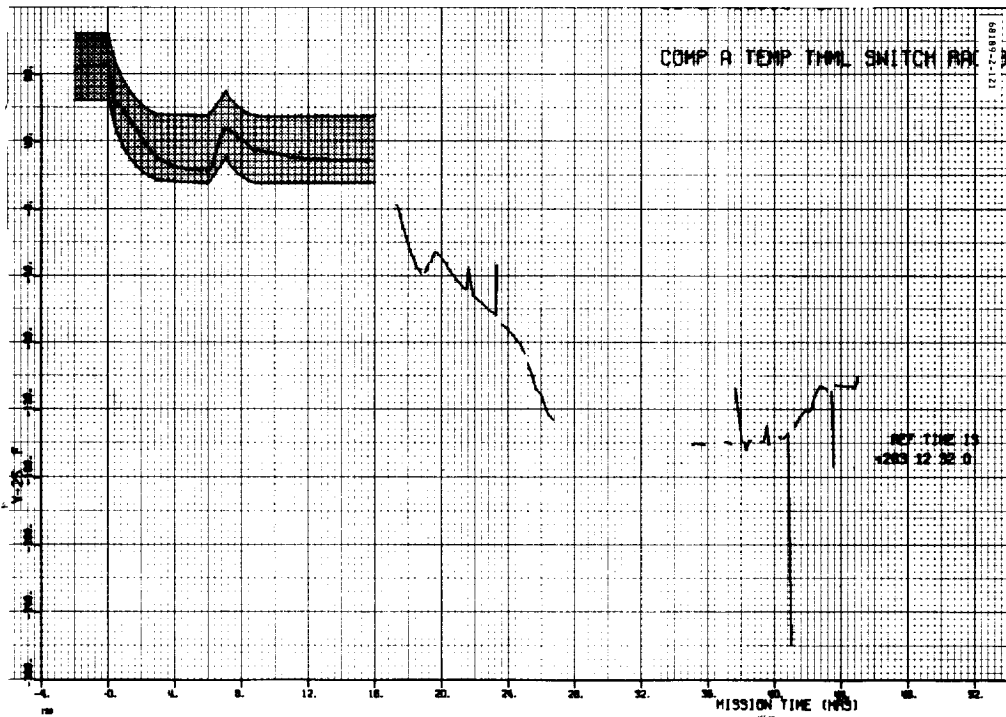


Figure 5.1-61. Compartment A Radiator 8

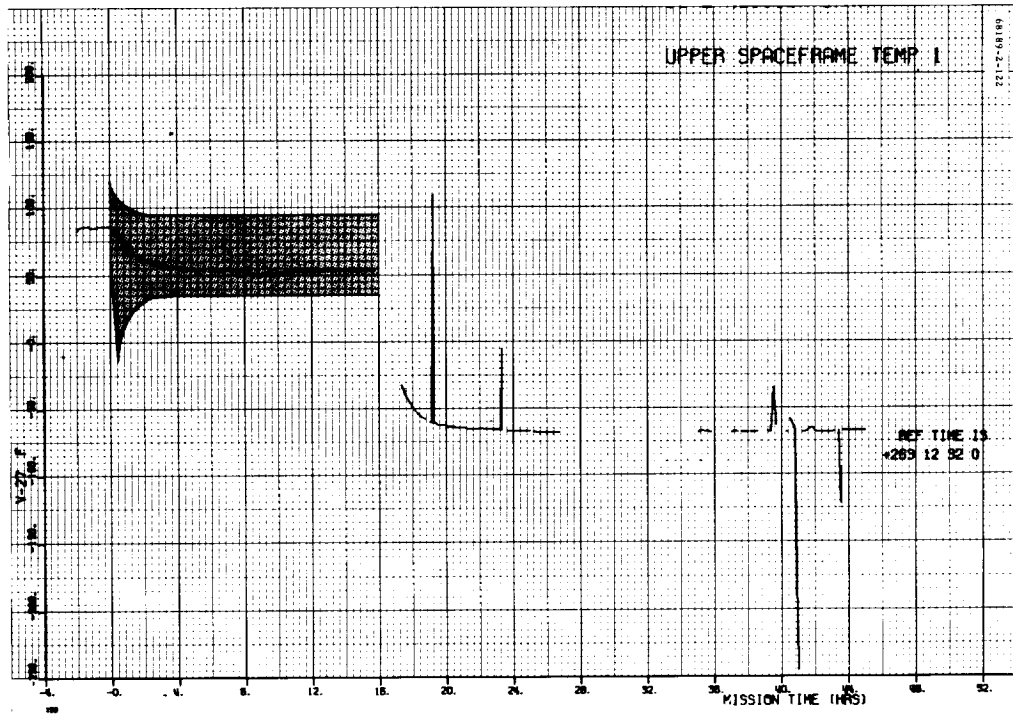


Figure 5.1-62. Upper Spaceframe

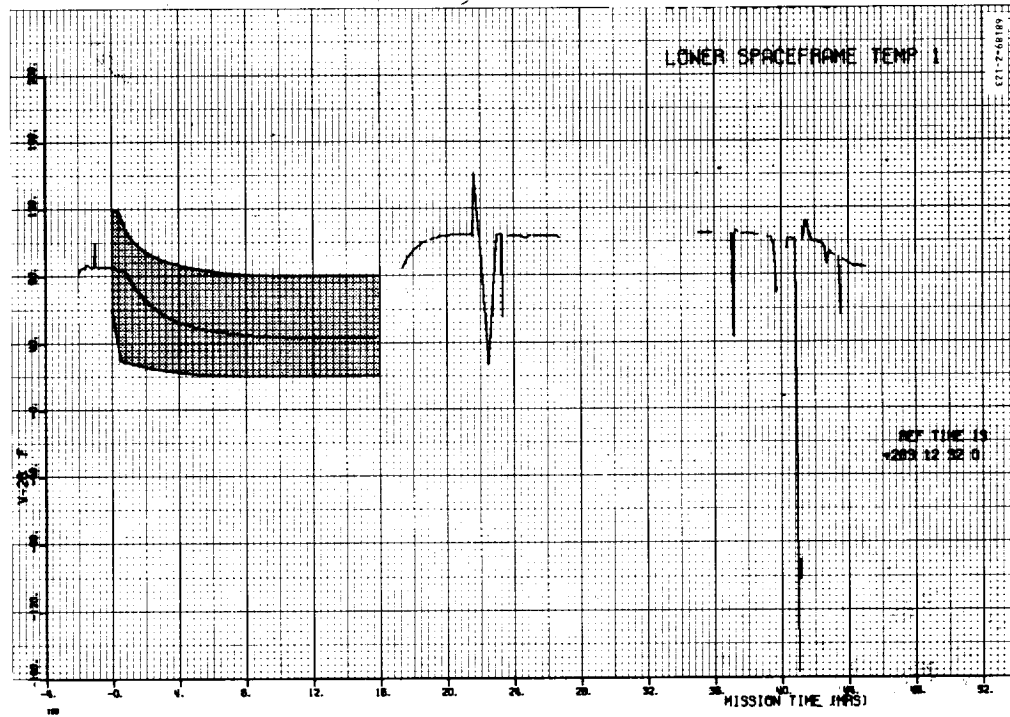


Figure 5.1-63. Lower Spaceframe

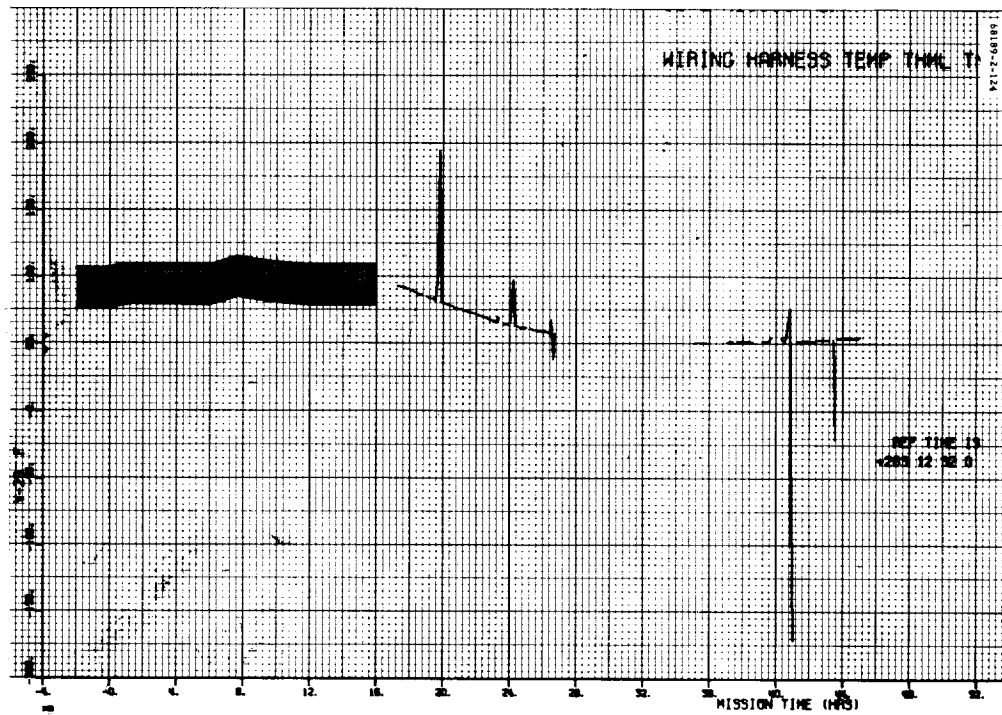


Figure 5.1-64. Wiring Harness Thermal Tunnel

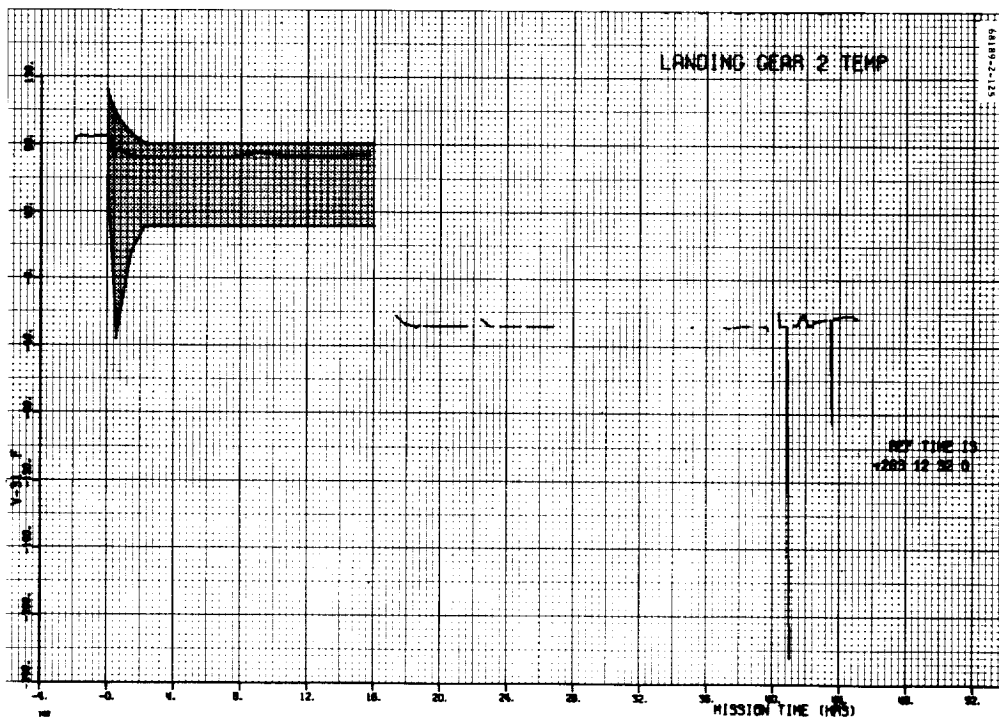


Figure 5.1-65. Landing Gear 2



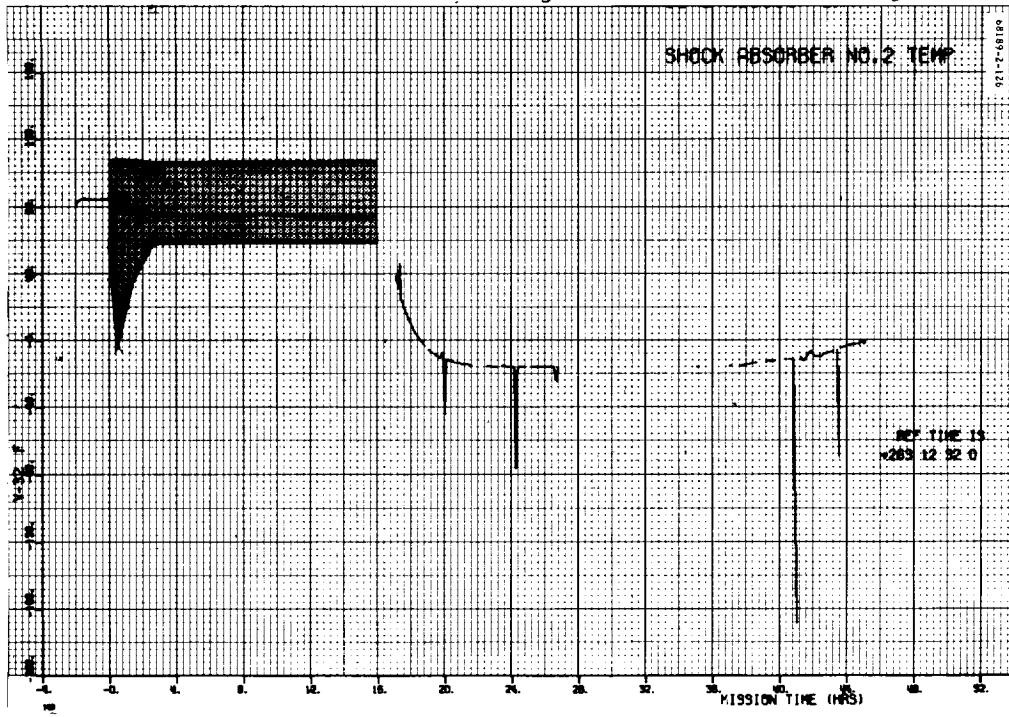


Figure 5.1-66. Shock Absorber 2

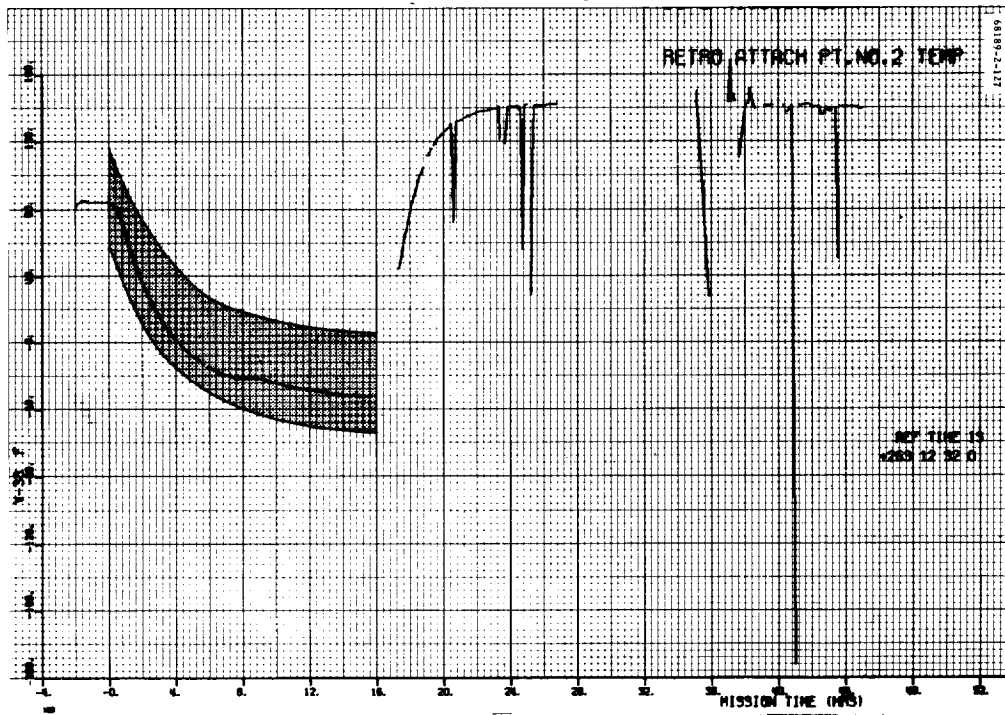


Figure 5.1-67. Retro Attach Point 2

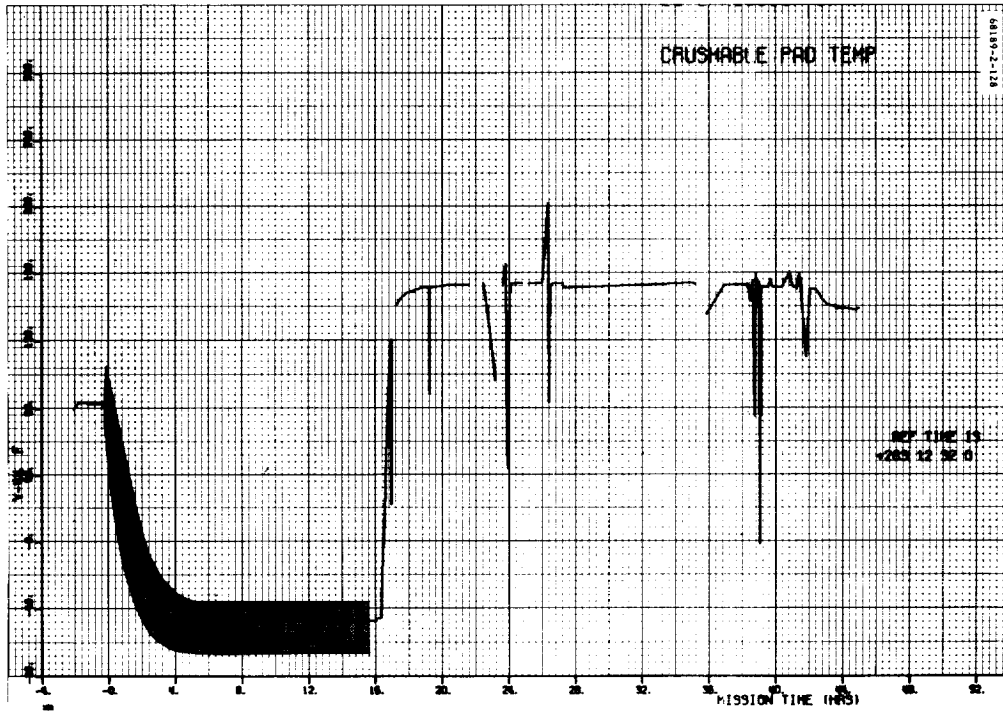


Figure 5.1-68. Crushable Pad

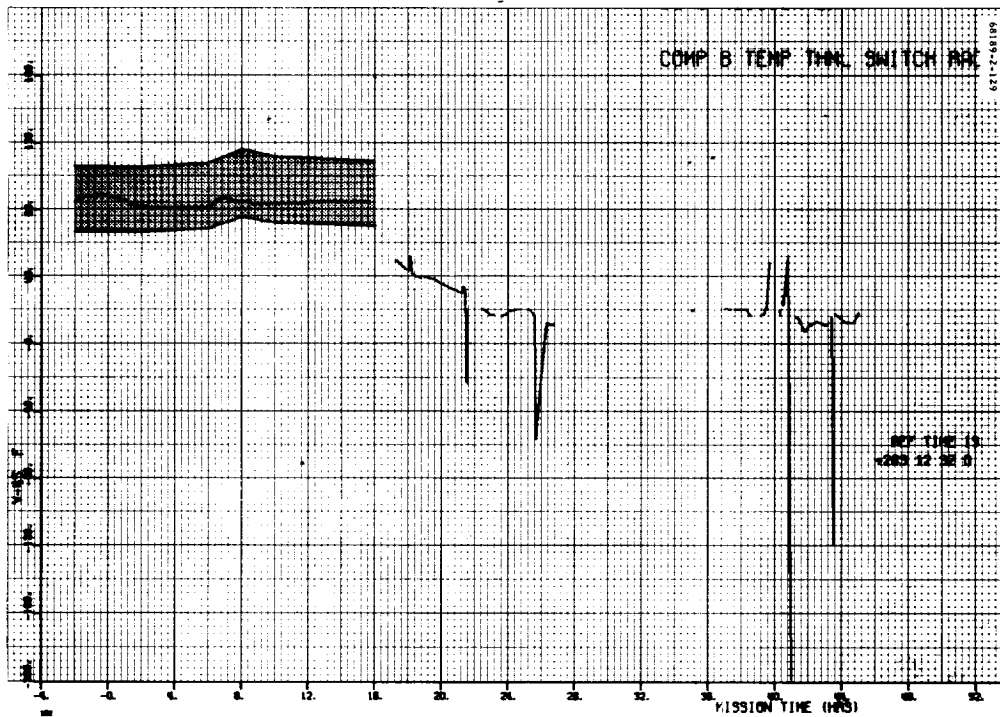


Figure 5.1-69. Compartment B Radiator 1

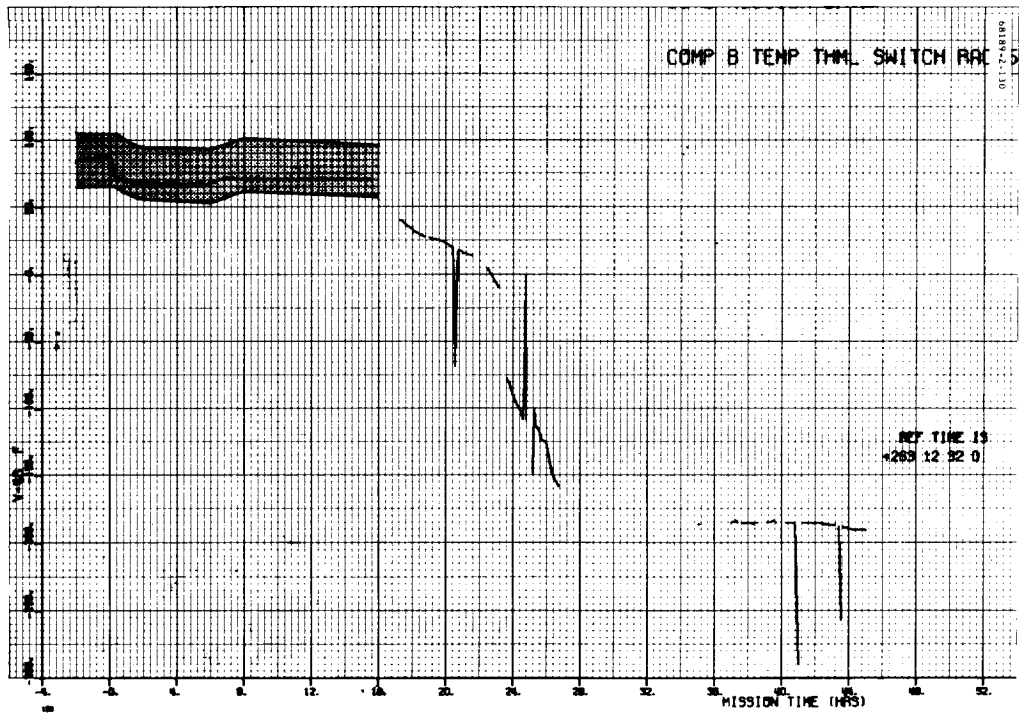


Figure 5.1-70. Compartment B Radiator 5

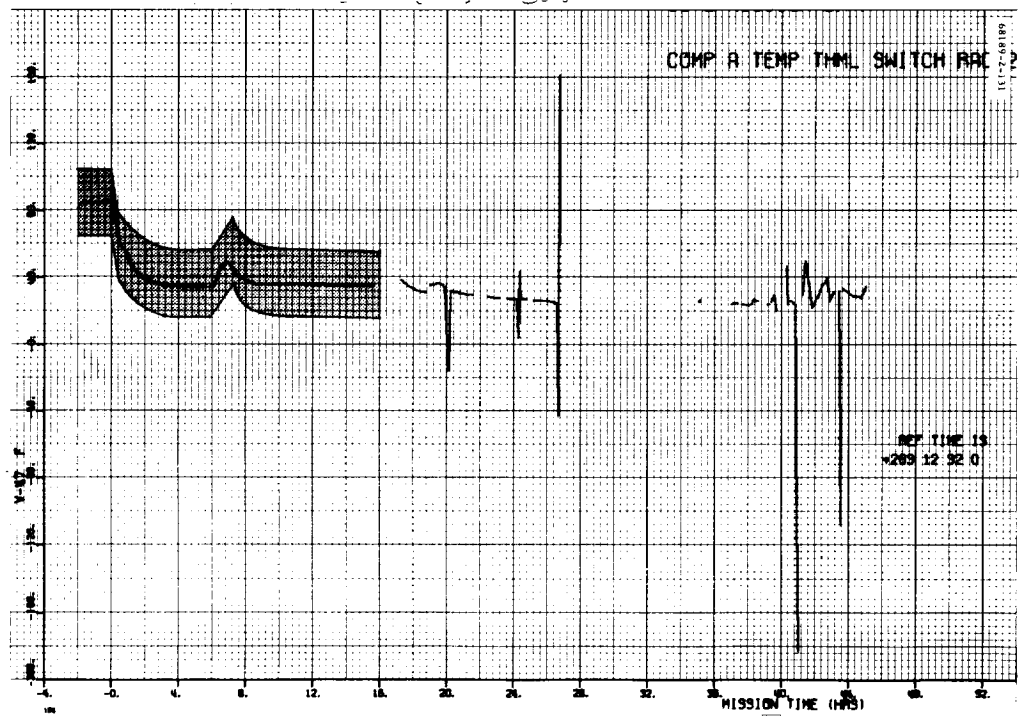


Figure 5.1-71. Compartment A Radiator 2

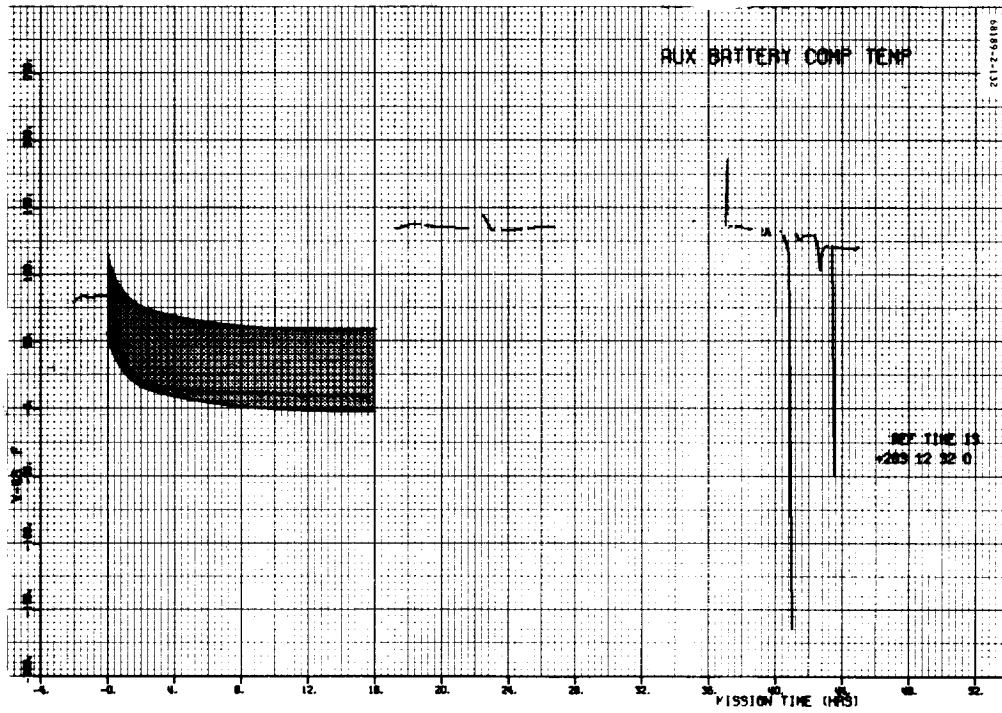


Figure 5.1-72. Auxiliary Battery Compartment

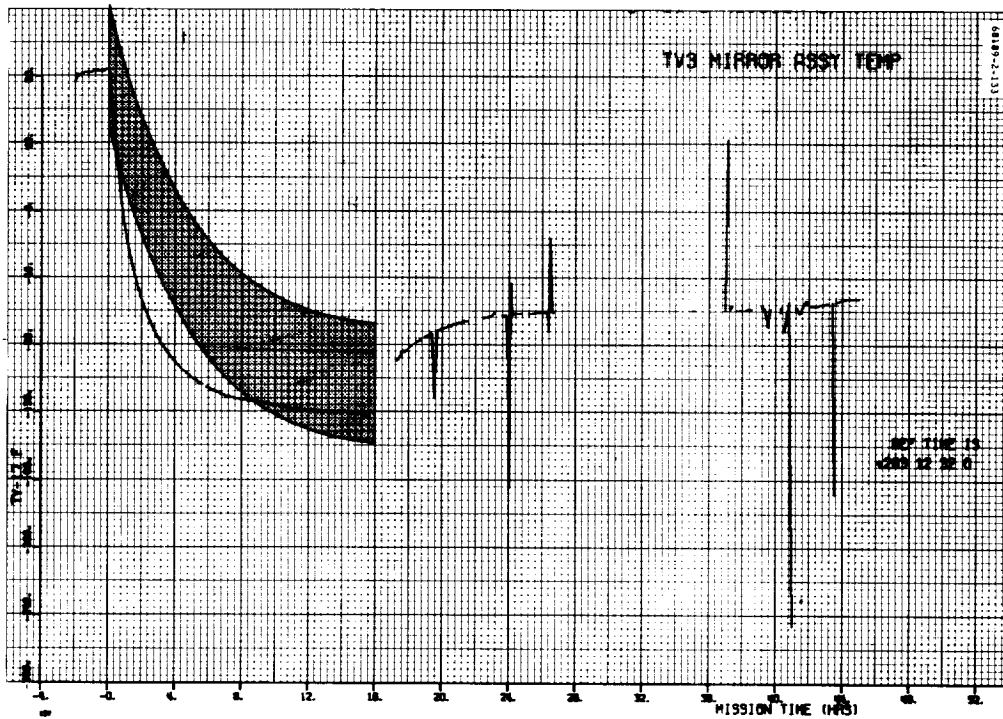


Figure 5.1-73. Survey Camera 3 Mirror

## 5.2 ELECTRICAL POWER SUBSYSTEM

### 5.2.1 INTRODUCTION

The electrical power (EP) subsystem generates, stores, converts, and controls electrical energy for distribution to other spacecraft subsystems. There are two sources for this energy: 1) storage batteries, and 2) radiant energy converted directly to electrical energy used for system loads or battery charging. During transit, the primary source of power is radiant energy via the solar panels. Figure 5.2-1 shows associated equipment groupings.

The performance of the EP subsystem during the SC-2 flight was nominal as compared to test data and simulation analysis predictions. Subsequently, specific comparisons will be made in the body of this subsection.

Regarding the total system, various loads, solar panel input power, and regulator efficiencies are calculated from flight data. Analysis of specific loads, comparison to prediction, and explanation of discrepancies will be considered.

In Table 5.2-1, major events are presented with 1) time from launch for easy reference to mission plots (subsection 5.2.4.2) and 2) time in GMT for reference to various list information, i.e., commands and engineering data reduction system (EDRS) processed data. In general, the divisions of Table 5.2-1 correspond to flight phases of importance to the EP subsystem; consequently, it may not correspond to flight phases in other subsections. Basically, the flight region is divided into times corresponding to significant changes in electrical loads. The time sequence 16.84 to 44.79 hours after launch was not further subdivided due to insufficient data. Load changes corresponding to these flight phases are partially illustrated by the regulated current (EP-14) and more completely by the battery discharge current (EP-9).

### 5.2.2 ANOMALY DESCRIPTION

Even though the SC-2 flight was not a nominal mission, no anomalies were detected in the electrical power system during flight.

Lack of information and seeming misrepresentations in the mission plots after midcourse are due to ground data processing of scanty data. Where possible, plots have been annotated for guidance and clarification.

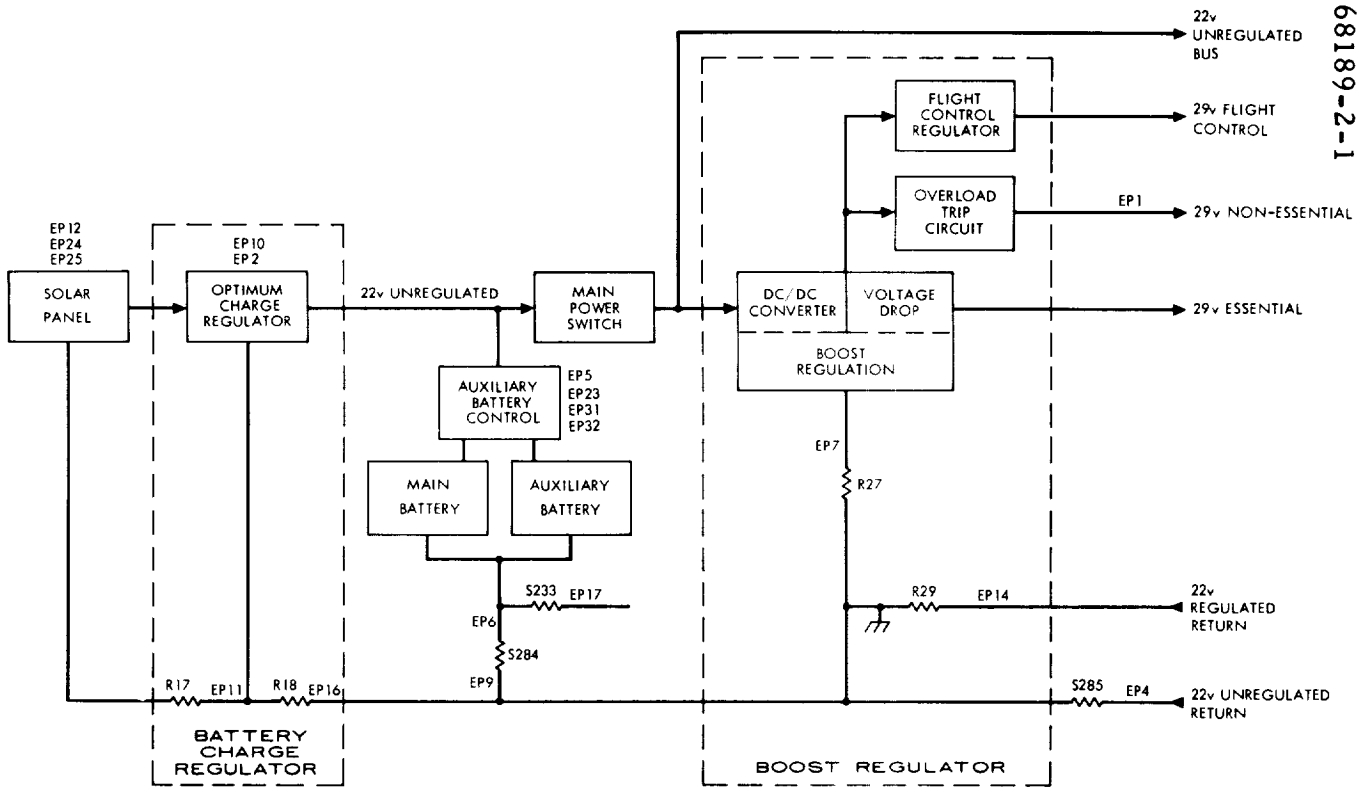


Figure 5.2-1. Electrical Power Schematic

TABLE 5.2-1. EVENTS AND TIMES, ELECTRICAL POWER

Total flight time = 45.035 hours

Time, GMT (day:hr:min:sec)		Time From Launch, hours			Comments
From	To	From	To	Increment	
263:12:32:00	263:12:48:23	0	0.273	0.273	Launch to sun acquisition (transmitter high power on)
263:12:48:23	263:13:16:33	0.273	0.742	0.469	Transmitter high power
263:13:16:33	263:18:30:46	0.742	5.979	5.237	Coast
263:18:30:46	263:19:22:05	5.979	6.834	0.855	Transmitter high power
263:19:22:05	264:04:36:44	6.834	16.078	9.244	Coast
264:04:36:44	264:04:54:20	16.078	16.371	0.293	Transmitter high power
264:04:54:20	264:05:00:41	16.371	16.477	0.106	Midcourse maneuver transmitter high and FC thrust phase power on
264:05:00:41	264:05:23:02	16.477	16.849	0.372	Transmitter high power
264:05:23:02	265:09:19:57	16.849	44.798	27.949	Many engine starts and transmitter high power
265:09:19:57	265:09:30:09	44.798	44.968	0.170	RADVS power on power mode cycling
265:09:30:09	265:09:34:17	44.968	45.035	0.067	Retro sequence End of mission

## 5.2.3 SUMMARY AND CONCLUSIONS

### 5.2.3.1 Summary

Table 5.2-2 presents a summary of the comparison of flight data for SC-2 to test data for the electrical power subsystem.

### 5.2.3.2 Conclusion

Operation of the electrical power subsystem was nominal throughout the spacecraft's flight. Information detailing the unregulated current change during midcourse vernier correction and emergency vernier ignitions are presented in Table 5.2-3. The various values of vernier burn at midcourse are associated with the various techniques of analyzing the flight data. The most probable value of this current change is 1725 milliamperes, where the expected value of the change in current is about 1670 milliamperes. The various techniques used in calculating this change in current varied from averaged data, unmanipulated nonaveraged data, and reduced nonaveraged data analyses of the midcourse velocity correction to averaging of leading and trailing edge current jumps for all long vernier burns. Further considerations as to the uncertainties associated with the determination of the vernier engine solenoid valve current are of continuing concern.

Energy remaining in the auxiliary and main batteries is shown in Figure 5.2-2. At midcourse, nominally predicted and flight data practically coincide. After midcourse, the spacecraft tumbled, and practically no energy was available from the solar panels; hence, the spacecraft was totally dependent on the batteries for energy. Toward the end of the flight when available energy was low, the RADVS power was turned on. During the time of RADVS turnon, the batteries were switched through various modes of operation, as noted in Table 5.2-6 and Figure 5.2-18. The low unregulated bus voltage (Figure 5.2-23) during RADVS power supports the prediction that the batteries, especially the auxiliary battery, were nearly depleted of energy. The main battery was able to supply the current load alone until the end of RADVS power on. When RADVS power was turned off, the main battery provided energy to the end of flight which occurred shortly thereafter.

## 5.2.4 ANALYSIS

The analysis considers six areas: mission telemetry plots, power loads and sources budget, comparison of flight loads and flight acceptance test (FAT) loads, cyclic loads, vernier engine solenoid power, and power mode cycling.

### 5.2.4.1 Mission Telemetry Plots

Figures 5.2-2 through 5.2-9 are selected mission plots which are pertinent to the electrical power subsystem. They represent the averaging of the analog signals over a time period corresponding to 30 telemetry frames. Consequently, due to the scale of these plots and data averaging, they give excellent information for consideration of trends in data flow. Many annotations have been made on these plots related to commands and ground data processing.



TABLE 5.2-2. SUMMARY OF RESULTS, ELECTRICAL POWER

Item	From Flight Data	Predicted, Specification, or FAT
Boost regulator efficiency	77.5 percent	75 percent (minimum)
OCR efficiency	80 percent	75 percent (minimum)
Solar panel output energy	1400 ± 80 w-hr	1440 w-hr
OCR output energy	1120 ± 64 w-hr	1140 w-hr
Battery energy used	4578 ± 200 w-hr	4770 ± 192 w-hr
Total energy used	5698 ± 225 w-hr	5910 ± 192 w-hr
Selected loads		
Transmitter B high voltage (average value)	58.0 ± 3.4 watts	63.8 watts
Transmitter A high voltage (average value)	55.2 ± 10.3 watts	63.2 watts
FC power on/off, regulated (average value)	47.6 ± 3.6 watts	49.87 watts
FC thrust phase power on		
Regulated	31.6 ± 8.7 watts	33.65 watts
Unregulated	9.2 ± 0.9 watts	10.34 watts
RADVS power on, unregulated	534.5 ± 12.3 watts	550 watts
Vernier burns		
Midcourse-averaged data	39.2 ± 10 watts	36.7 watts
Midcourse-unaveraged data	36.2 watts	36.7 watts
Midcourse-unaveraged data	28.4 to 33.6 watts	36.7 watts
Average of many burns	42.0 watts	36.7 watts
Vernier line 3 heater	1.9 watts	2.2 watts (100 milliamperes)
AMR heater	4.5 watts	5.1 watts (230 milliamperes)
Gyro heater	10.5 watts	11.0 watts

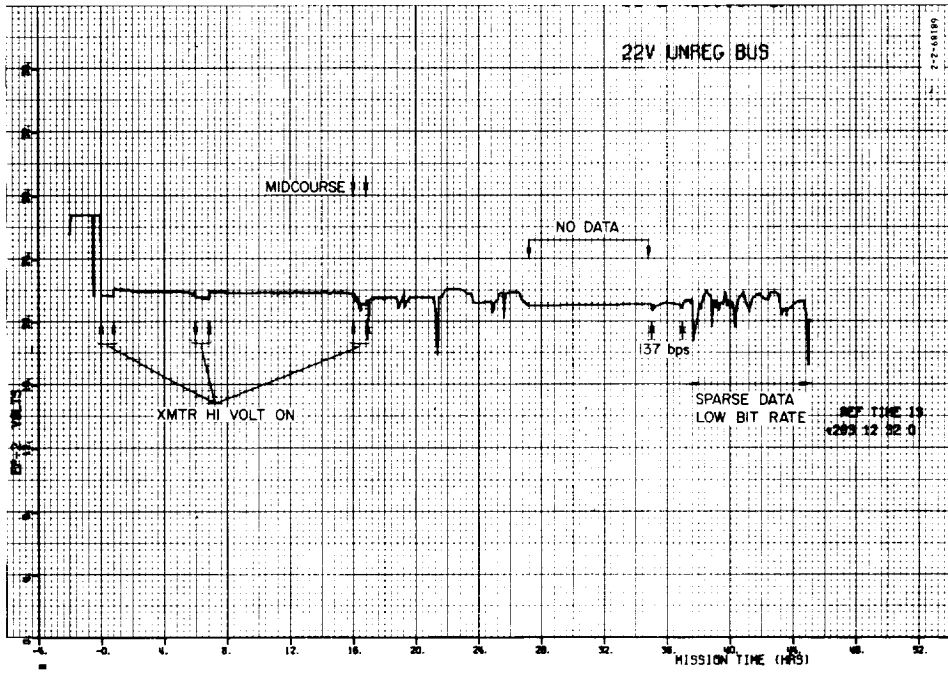


Figure 5.2-2. 22-Volt Unregulated Bus

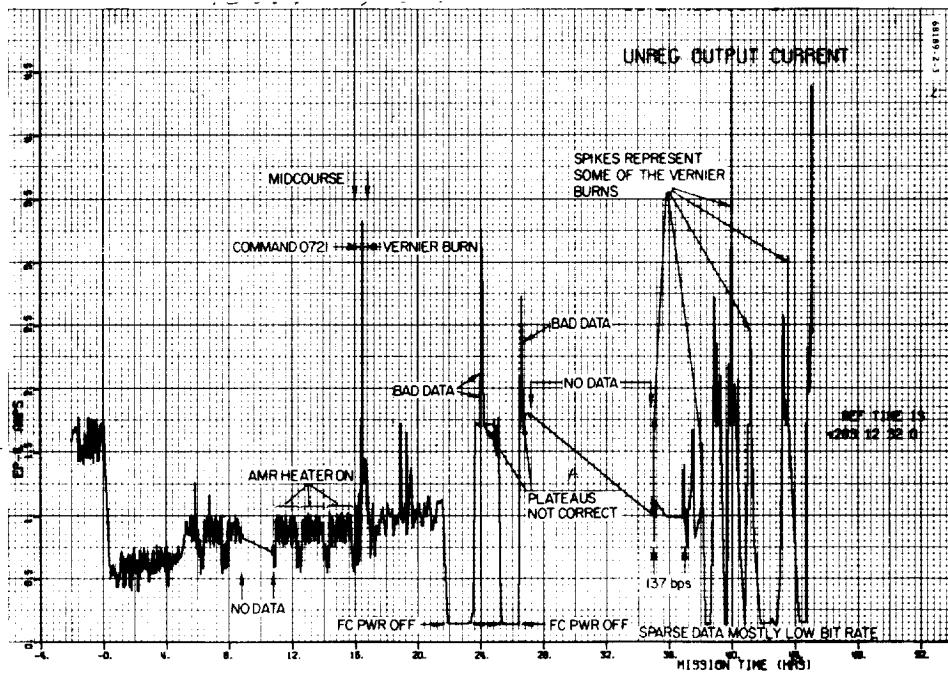


Figure 5.2-3. Unregulated Output Current

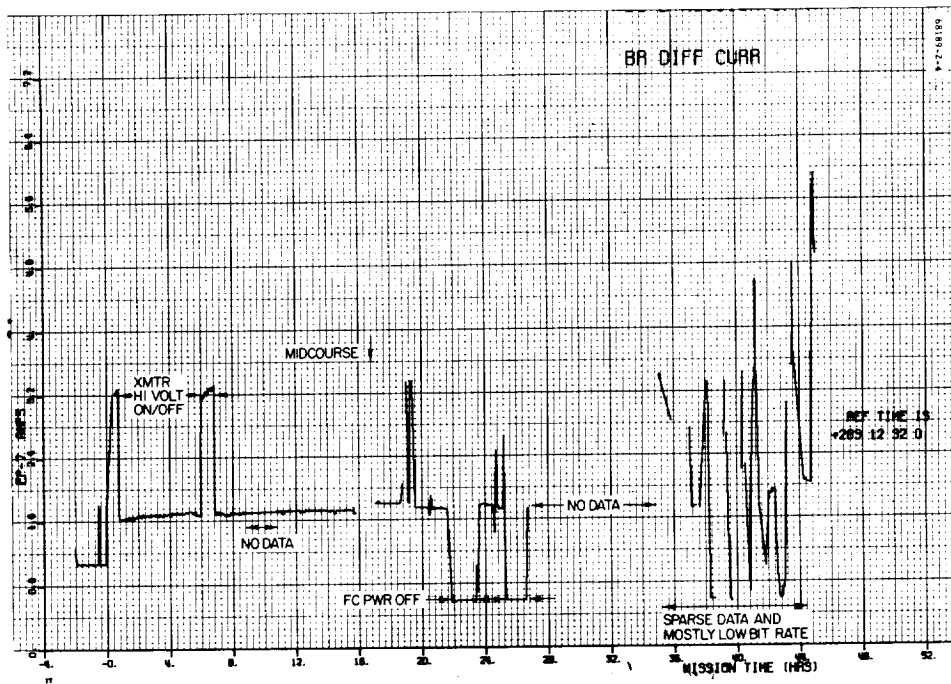


Figure 5.2-4. Boost Regulator Differential Current

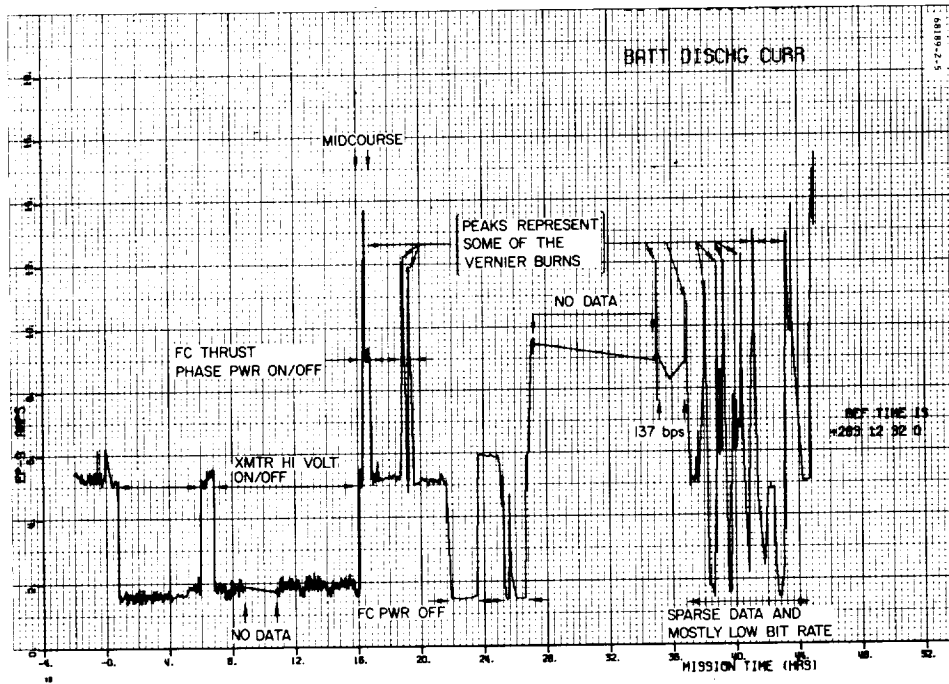


Figure 5.2-5. Battery Discharge Current

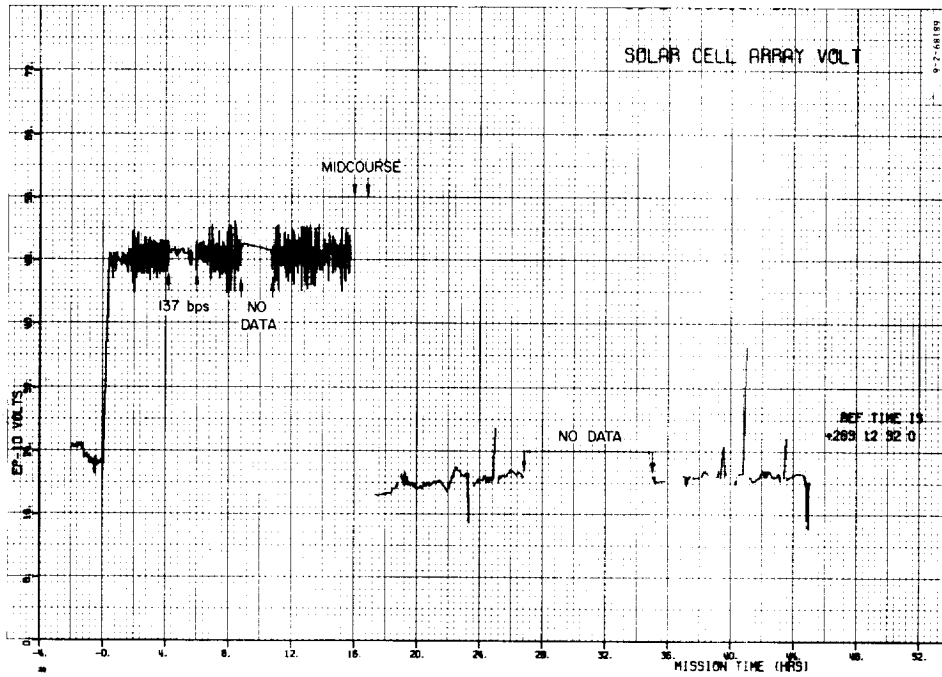


Figure 5.2-6. Solar Cell Array Voltage

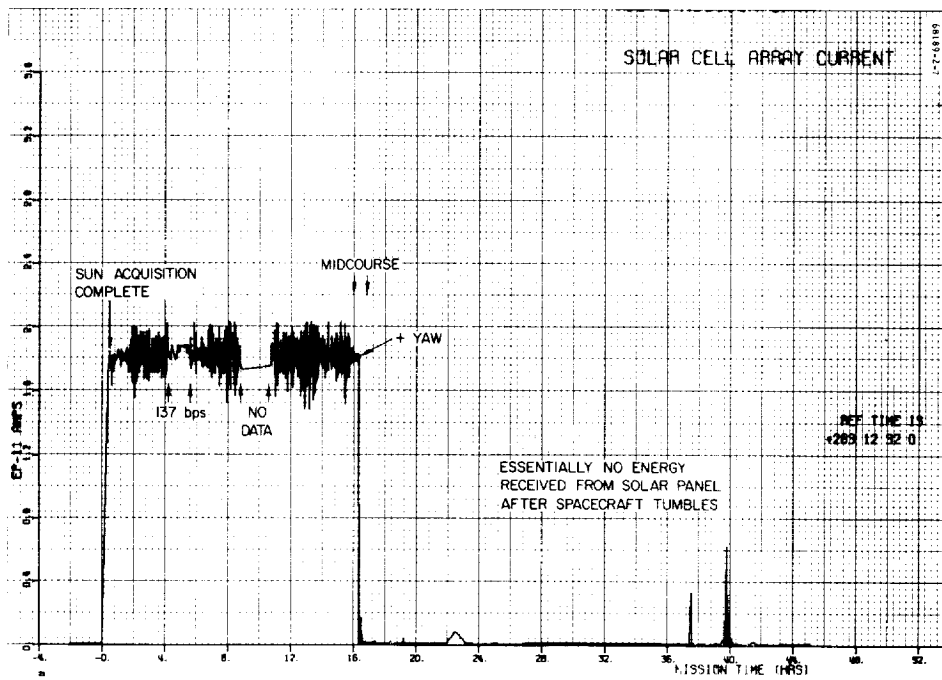


Figure 5.2-7. Solar Cell Array Current

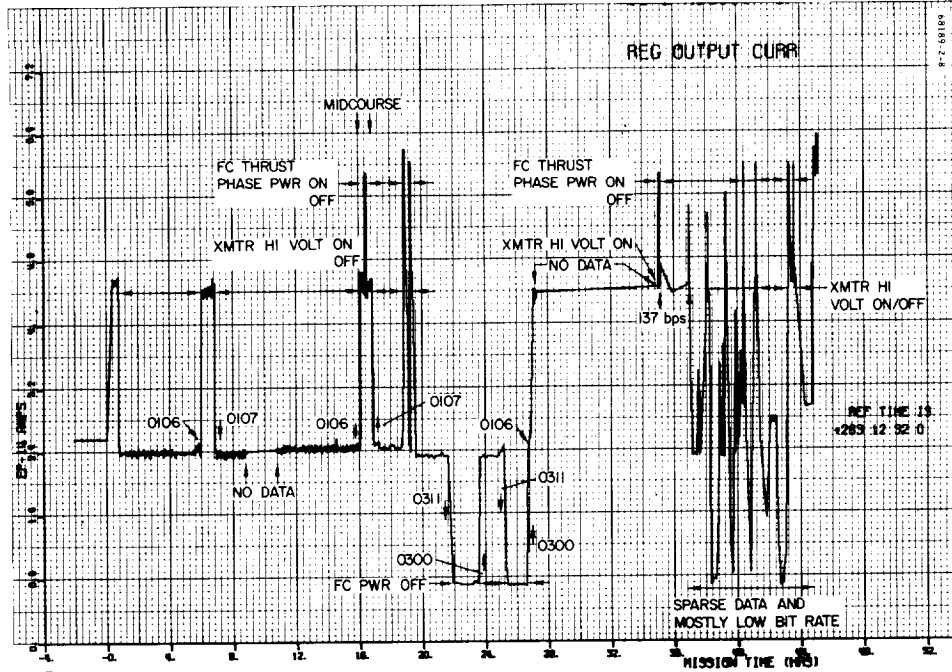


Figure 5.2-8. Regulated Output Current

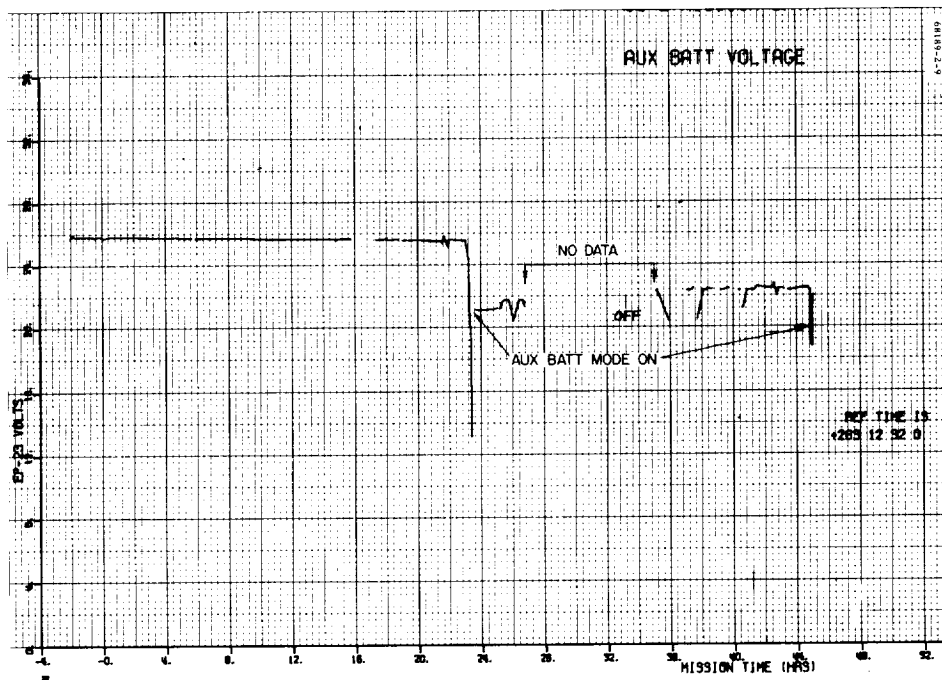


Figure 5.2-9. Auxiliary Battery Voltage

## 5.2.4.2 Power Loads and Sources Budget

### Energy Used

Figure 5.2-10 presents the battery energy remaining as a function of time. Table 5.2-3 gives the battery energy used during flight in approximately each mode of battery usage. Predicted battery energy remaining results from an updating of a portion of the SC-2 nominal mission energy prediction (Reference 1). The energies used from flight data and predicted loads are almost identical until after midcourse. The flight data lacks the bumps representing transmitter high voltage on and midcourse maneuver which are correctly represented in the predict plots since the plot points are at large intervals (Table 5.2-3). Reference 1 predicts that, at end of midcourse, total energy used is 1940 w-hr, and that energy out of the optimum charge regulator (OCR) is 1140 w-hr. This compares very favorably to a solar panel energy input of 1120 w-hr and a total energy usage of 1930 w-hr at end of midcourse.

### Power Data

Figures 5.2-11 through 5.2-17 present various power parameters as calculated from EDRS flight data. The parameters are calculated directly from the following telemetry channels (averaged data):

- 1) OCR efficiency =  $((EP-2 * EP-16)/(EP-10 * EP-11)) * 100$
- 2) Solar panel power =  $EP-10 * EP-11$
- 3) Boost regulator efficiency =  $((EP-1 * EP-14)/((EP-7 + EP-14) * EP-2)) * 100$
- 4) Shunt unbalance current =  $(EP-9 + EP-16 + EP-17) - (EP-4 + EP-14 + EP-7)$
- 5) Total loads =  $(EP-9 + EP-16 + EP-17) * EP-2$
- 6) Regulated power =  $EP-1 * EP-14$
- 7) Unregulated power =  $EP-2 * EP-4$

TABLE 5.2-3. BATTERY ENERGY USED

Time From Launch, hours	Battery Mode	Solar Panel Energy, w-hr	Battery Energy Used, w-hr	Main Battery Energy Used, w-hr	Auxiliary Battery Energy Used, w-hr
0 to 16.3	Main battery	1120	810	810	-
16.3 to 23.1	Main battery	-	828	828	-
23.1 to 32.9	Auxiliary battery (0317)	-	1220	488	732
32.9 to 45.0	Main battery*	-	1720	1480	240
		Total	4578	3606	972

\*Power mode cycling while RADVS power is on.

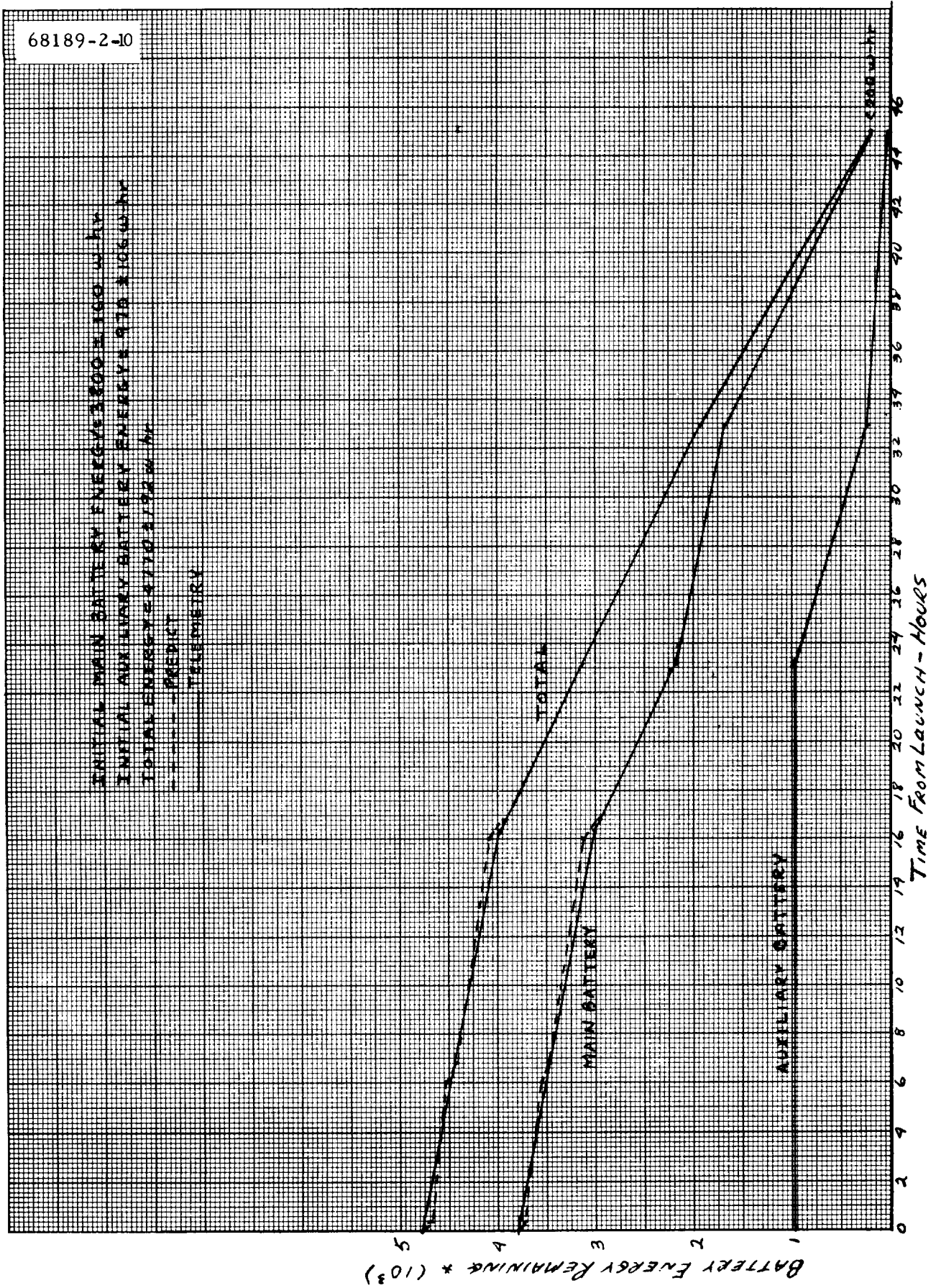


Figure 5.2-10. Battery Energy Remaining

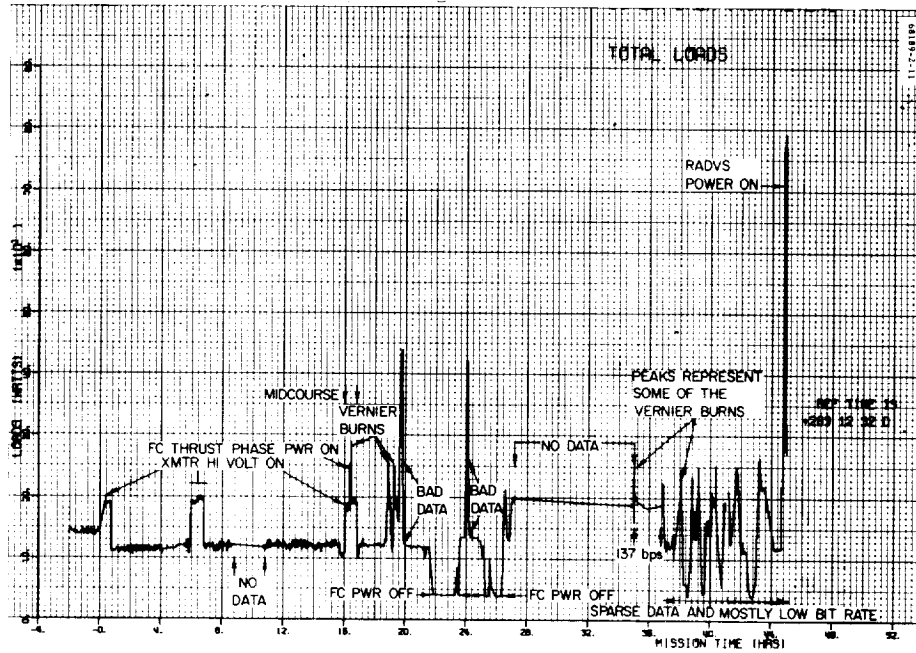


Figure 5.2-11. Total Loads

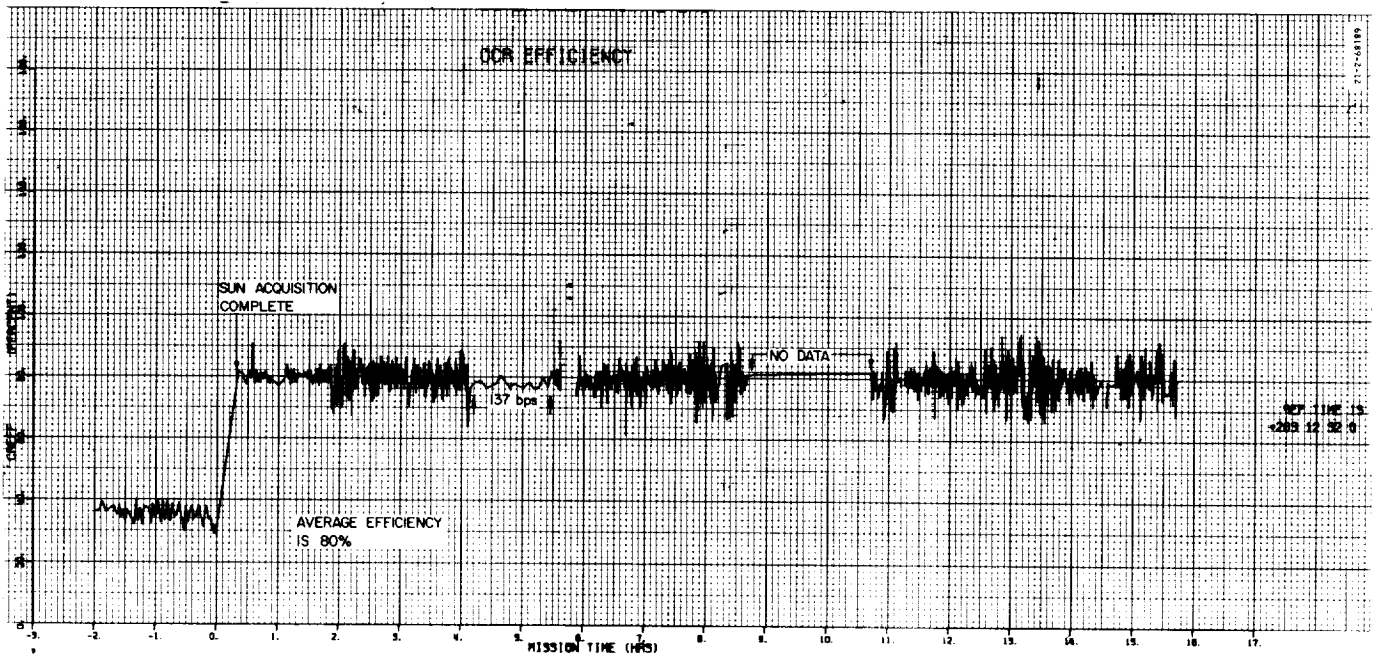


Figure 5.2-12. Optimum Charge Regulator Efficiency



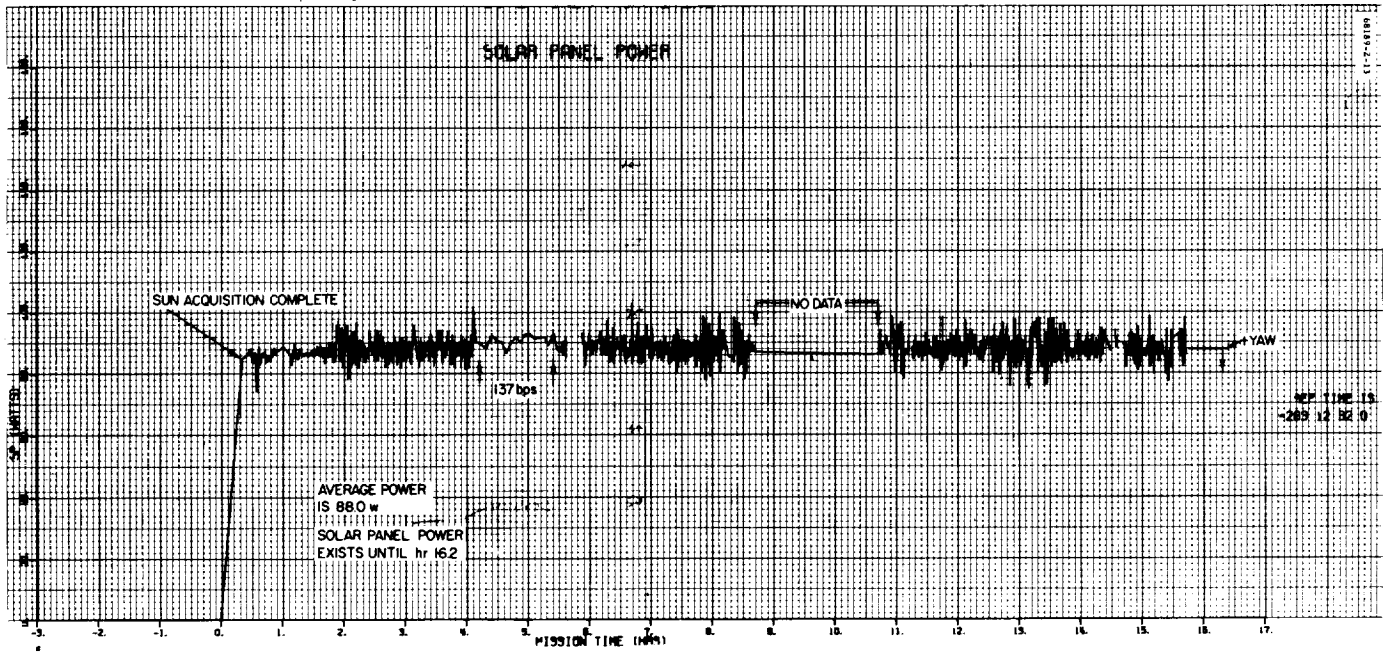


Figure 5.2-13. Solar Panel Power

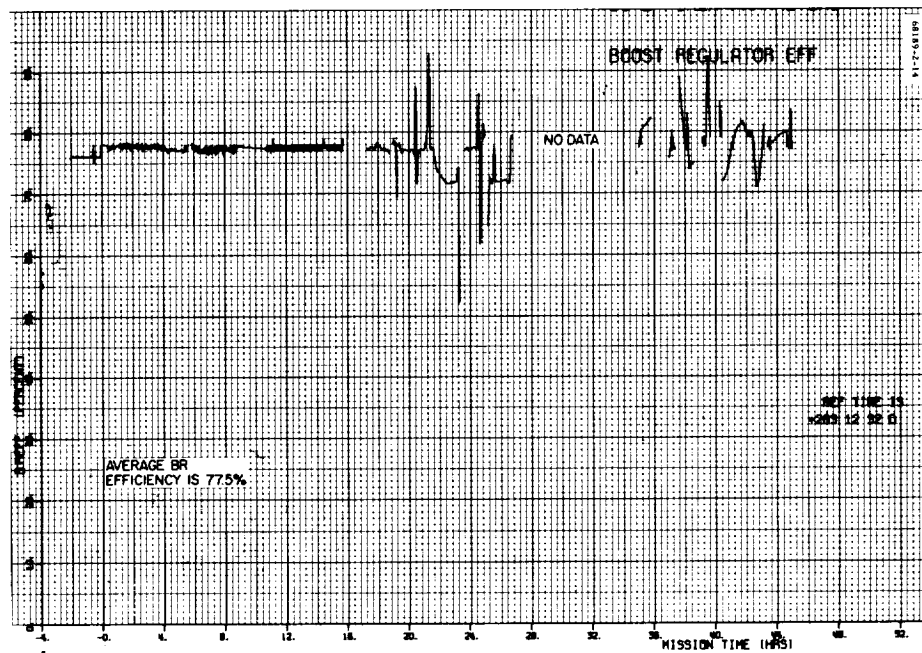


Figure 5.2-14. Boost Regulator Efficiency

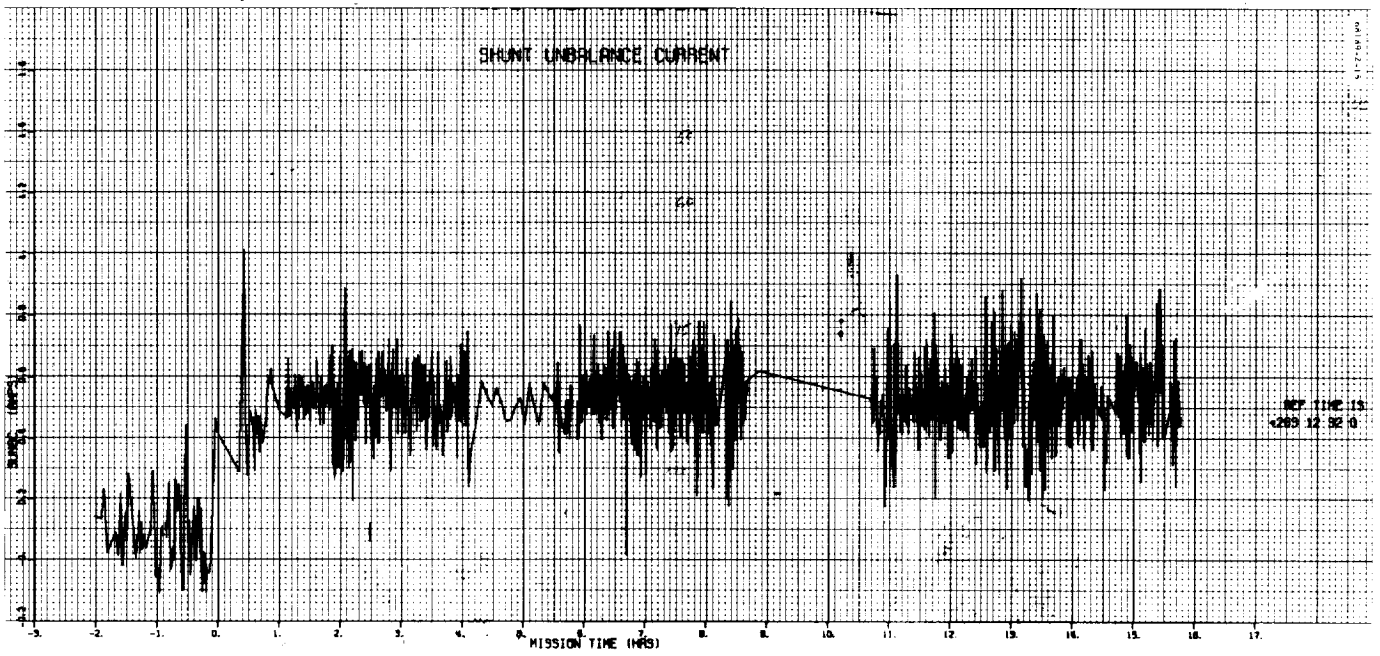


Figure 5.2-15. Shunt Unbalance Current

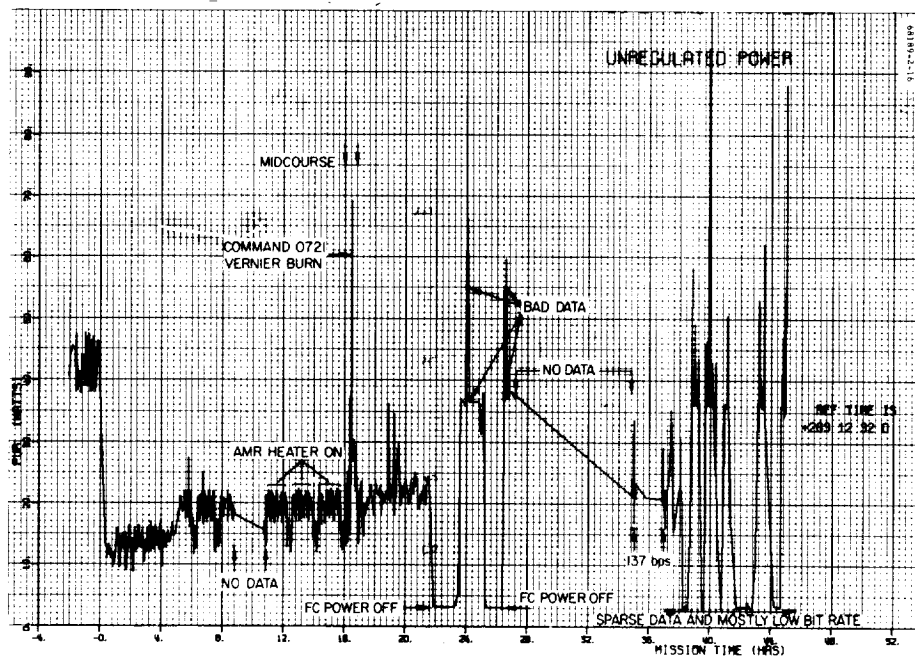


Figure 5.2-16. Unregulated Power

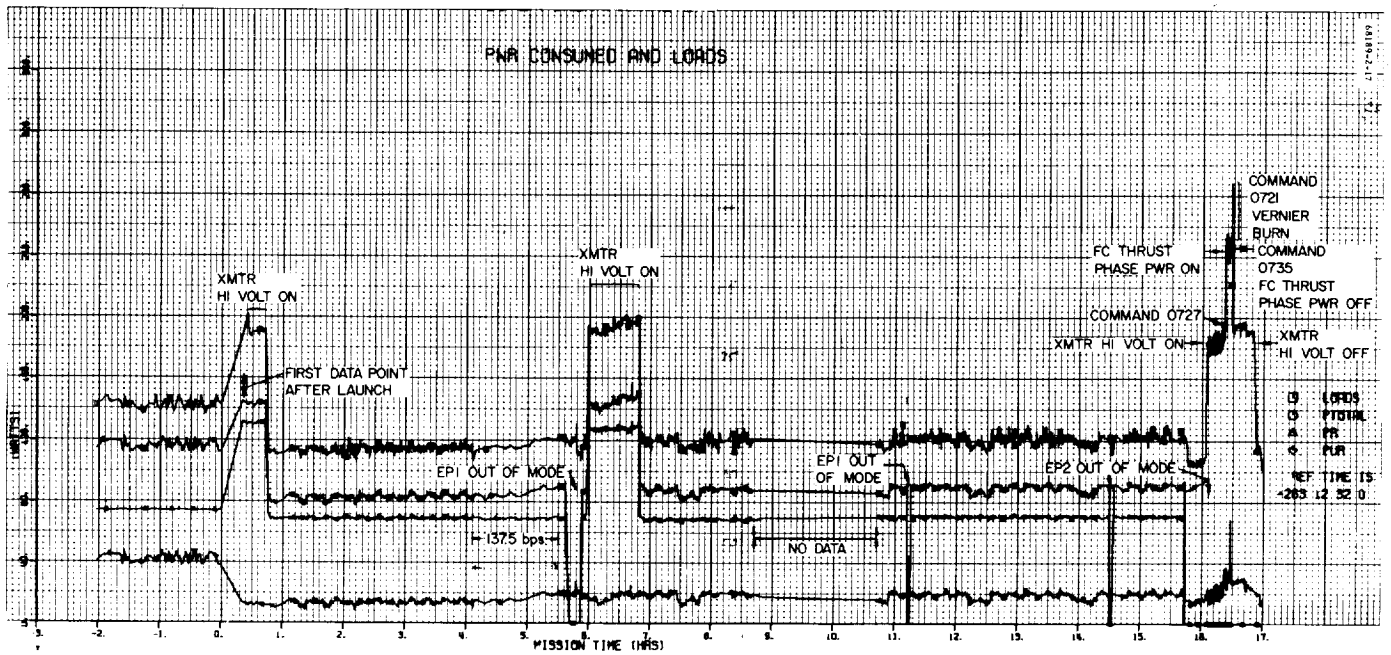


Figure 5.2-17. Power Consumed and Loads

Figure 5.2-11 shows the total loads for the electrical power subsystem for the entire SC-2 flight. Total energy used during the flight can be estimated from this plot, and this estimate is recorded in Table 5.2-3. Figure 5.2-12 is a plot of the OCR efficiency. The average efficiency appears to be 80 percent.

Figure 5.2-13 is a plot of solar panel power. This power is received for 15.9 hours of the SC-2 flight (16.2 - 0.3). This represents an energy input of approximately 1120 w-hr (average solar panel power of 88.0 watts \* OCR efficiency of 80 percent \* 15.9 hours). After midcourse, the spacecraft tumbled, and no significant energy was received from the solar panel.

Figure 5.2-14 is a mission plot of boost regulator efficiency which is relatively constant at 77.5 percent. After midcourse, the telemetry data is sparse. Out of mode and no data, as well as bad data conditions, exist. Yet, after midcourse, the low data rate telemetry provides data for computation of the boost regulator efficiency which agrees with the 77.5 percent efficiency before midcourse.

Figure 5.2-15 shows the shunt unbalance current through midcourse. The current is generally biased at about +0.52 ampere. This includes the EP-17 input. Figure 5.2-16 is a mission plot of the unregulated power. Transfer to spacecraft internal power is shown vividly at hour zero.

Figure 5.2-17 shows total power consumed, as well as the sum of the regulated and unregulated loads through the midcourse maneuver. Transmitter high voltage on conditions, vernier ignition at midcourse, and thrust phase power can be observed. Prelaunch power is also plotted.

#### Comments on Load Sharing

During high current mode on condition, load sharing was assumed to be 1:1 without the diode. During auxiliary battery mode on, where the diode was between the main battery and unregulated bus, load sharing was assumed to be 3:2 (auxiliary to main). This is the same as for SC-1 (Reference 2).

These assumptions are reflected in the construction of the plot of battery energy remaining in Figure 5.2-10 and the calculation of the values in Table 5.2-3. It is estimated from the unregulated bus voltage (EP-2) at the end of RADVS power on that there was less than 100 w-hr of energy remaining in the main battery 5 minutes before the end of the flight. This is reasonably close to the indicated remaining energy in Figure 5.2-10 for the main battery. Tolerance on the remaining battery energy is of the same order of magnitude as the estimate of the remaining energy.

### 5.2.4.3 Comparison of Flight Loads and FAT Loads

Comparison of telemetry-measured and FAT-measured loads (Reference 3) will be made for selected units, various heaters, and large current drains. Specification values (Reference 4) and special test results (Reference 5) will also be used in comparison.

#### Selected Equipment Loads

Results of comparing flight and test specification selected equipment loads are presented in Table 5.2-4. The loads and equipments considered are as follows:

- 1) Transmitter High Voltage On/Off. Data are presented in Table 5.2-4. FAT data for the transmitters is taken from Reference 3. Flight values are somewhat lower than the FAT values; however, the tolerances associated with the regulated flight power data bracket the FAT values.
- 2) Flight Control Power On and Off. The load changes due to commands 0300 and 0311 are well within specification (Reference 4) limits.
- 3) Flight Control Thrust Phase Power On. The first of the many 0727 commands is within specification.
- 4) RADVS Power On. Command 0637 applies power to the RADVS. The power consumed is close to that expected. Figure 5.2-18 (EP-17, radar and squib current) shows the current profile. The average value of EP-17 was about 28 amperes. It should be noted that RADVS power on occurs near the end of the SC-2 flight where energy remaining in the batteries was almost completely exhausted.

### 5.2.4.4 Cyclic Loads

#### Gyro Heater

The periodic loading that occurs in EP-4 contains gyro heater effects. The gyro heaters have a short on-off cycle when compared to the altitude marking radar (AMR) and vernier line heaters. A graph of frame-by-frame nonaveraged telemetry was examined. Figure 5.2-19 (EP-4) contains such data prior to the midcourse ignition. The average gyro heater load is approximately 0.5 ampere, which compares favorably to the FAT data.

#### AMR and Vernier Line Heaters

Figure 5.2-20 is an EDRS plot of EP-4 at 20 min/in. Gyro heater effects are averaged out in this plot. The cyclic load effects of the AMR and vernier line 3 heaters are apparent. A trace of vernier line 3 temperature (P-9) has been placed above EP-4 in order to show how the middle frequency

TABLE 5.2-4. SELECTED EQUIPMENT LOADS

Command(s)*	Command Time, GMT (day:hr:min:sec)	Current, milliamperes		Power, watts	
		Flight	Specification/Test	Flight	Specification/Test
Transmitter high voltage on/off			(Reference 3)		(Reference 3)
R 0105 (filament only on)	263:18:28:59	170 ± 10	2200	4.9 ± 0.3	63.8
R 0106 HV on	263:18:30:46	1860 ± 40		53.9 ± 1.2	
R 0110 off	263:19:22:13	2140 ± 40	2200	61.7 ± 1.2	63.8
R 0106 on	264:04:36:44	1860 ± 180		53.9 ± 5.2	
R 0107 off	264:05:23:02	2000 ± 330	2200	56.9 ± 9.5	63.8
R 0103 on	264:07:19:16	1830 ± 300		52.8 ± 8.6	
R 0107 off	265:02:42:21	1990 ± 200	2180	57.7 ± 5.8	63.2
Flight control power on			(Reference 4)		(Reference 4)
R 0300	264:12:05:57	1590 ± 100	1720	46.2 ± 2.9	49.87
Flight control power off			(Reference 4)		(Reference 4)
R 0311	264:13:47:16	1640 ± 20	1720	49.1 ± 1.0	49.87
Flight control thrust phase power on			(Reference 4)		(Reference 4)
R 0727	264:04:54:20	1090 ± 30	1160	31.6 ± 8.7	33.65
U 0727		440 ± 40	470	9.2 ± 0.9	10.34
RADVS power on			(Reference 4)		(Reference 3)
U 0637	265:09:19:57	28130 ± 500 (average)	29000	534.5 ± 12.3	0.550
Vernier burns**			(Reference 5)		(Reference 5)
U 0721 (EDRS)	264:05:00:02	1865 ± 509	1670	39.2 ± 10	36.7
U 0721 (SSP)	264:05:00:02	1725	1670	36.2	36.7
U 0721	264:05:00:02	1350 to 1600	1670	28.4 to 33.6	36.7
U 0721 (average)	Table 5.2-5, Figure 5.2-19	1998 (average)	1670	42.0	36.7

\*R = regulated; U = unregulated.

\*\*Different values result from different techniques.

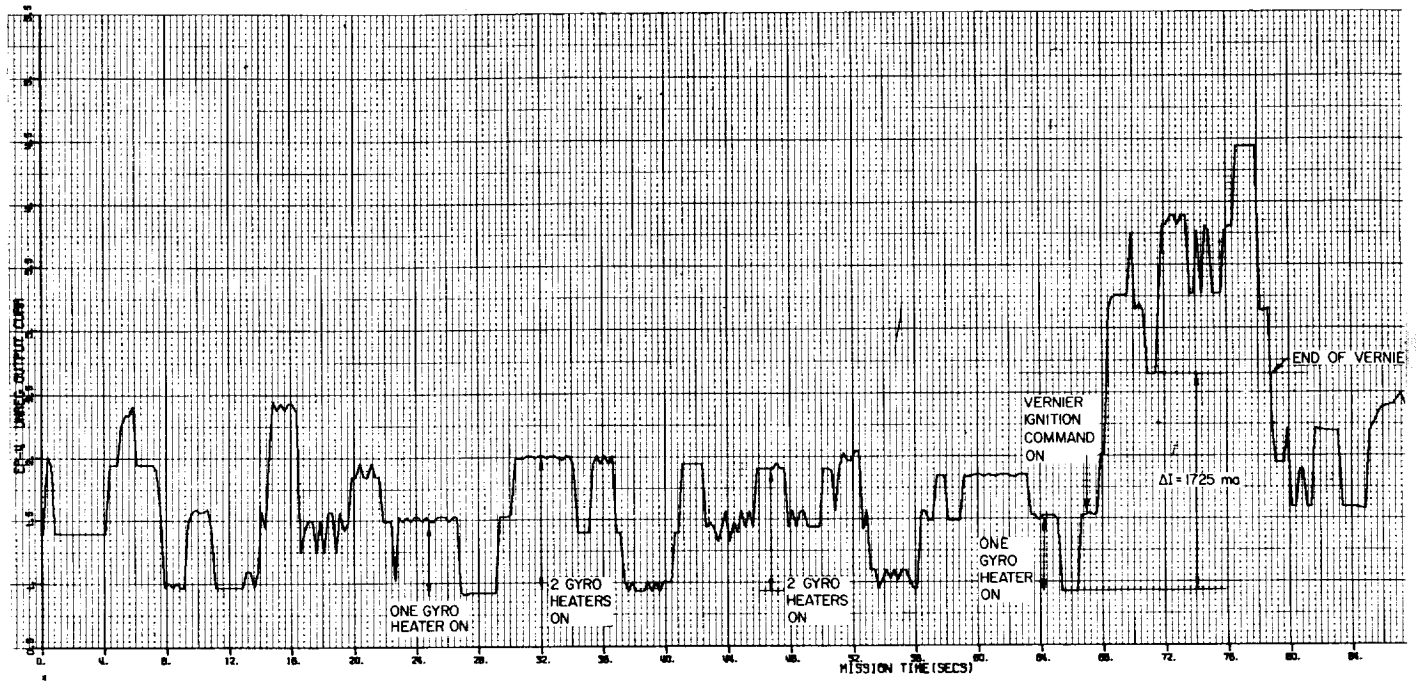


Figure 5.2-18. Unregulated Output Current, Midc

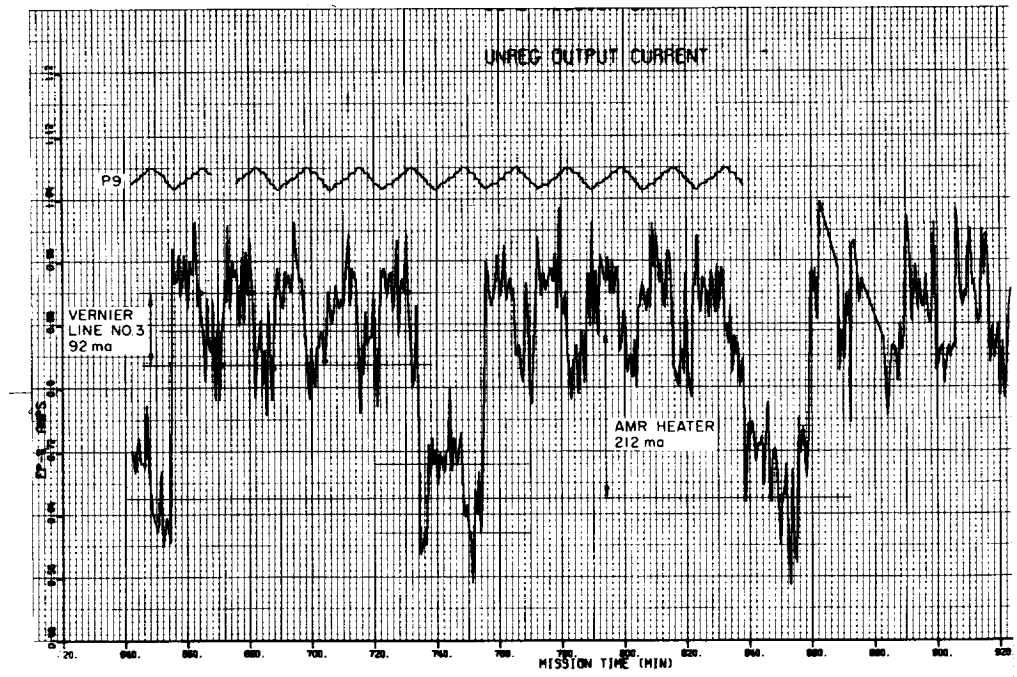


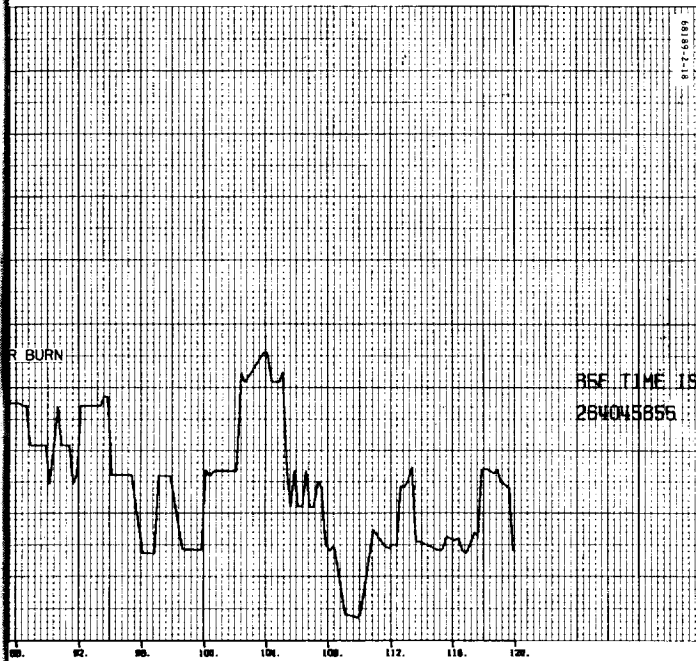
Figure 5.2-19. Unregulated Output Current, Coa

5.2-19A

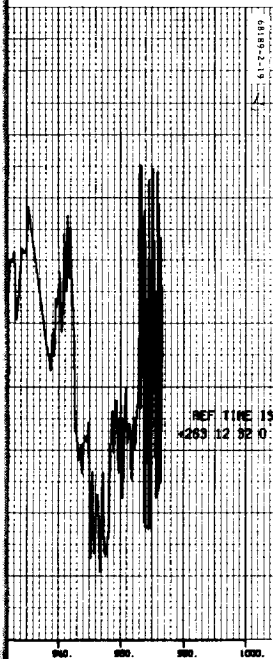
WIDOUT FRAME /







course



st I

5.2-1913

WILDOUT FRAME 2



oscillation in EP-4 is associated with the vernier line heater. Only the AMR and vernier line 3 heaters are cyclic at this time. The vernier line 3 heater uses approximately 92 milliamperes, and the AMR heater draws about 212 milliamperes. This agrees very favorably with test data, indicating that vernier line heater 3 should draw about 100 milliamperes and that the AMR heater should draw about 230 milliamperes. Figure 5.2-21 shows an approximate flight history of which heaters are on, off, or cycling.

#### 5.2.4.5 Vernier Engine Solenoid Valve Current

As part of the vernier engine failure study, a careful attempt was made to determine, by observing the change in the unregulated current telemetry (EP-4) and the battery discharge current telemetry (EP-9), the actual current drain required when the engines were turned on. This determination is clouded and made somewhat uncertain by the presence of the following interfering data on these same telemetry channels:

- 1) Other cyclic heater loads changing during this time (gyro, AMR, and vernier line heaters)
- 2) Noise-like effects of the roll actuator saturated signal waveform on the analog-to-digital converter
- 3) Other undefined noise on these channels.

These data can be examined in several different ways, each of which gives a different result that varies between a low of 1.36 amperes to a high of 2.38 amperes. These values, summarized in Table 5.2-4, were obtained as described below.

- 1) Change in averaged EP-4 current level at midcourse —  
1.87 ± 0.51 amperes

The average value (averaged over 30 samples or 7.5 seconds) before engine ignition was subtracted from the similar averaged value during engine ignition. This value has a large uncertainty due to the presence of the various cyclic heater loads, as well as the roll actuator effect.

- 2) Change in unaveraged EP-4 current level at midcourse —  
1.73 amperes

Obtained by comparing the unaveraged value of EP-4 before and after engine ignition when the gyro heaters are in the same condition, i.e., all off or one on. This value is only subject to the uncertainty of the roll actuator effect (see Figure 5.2-18).

- 3) Change in unaveraged EP-4 current level at midcourse —  
1.35 to 1.6 amperes

Obtained by deleting gyro heater loads from the unaveraged value of EP-4. The higher value of current change is associated with the leading edge difference, whereas the smaller value of current



68189-2-21

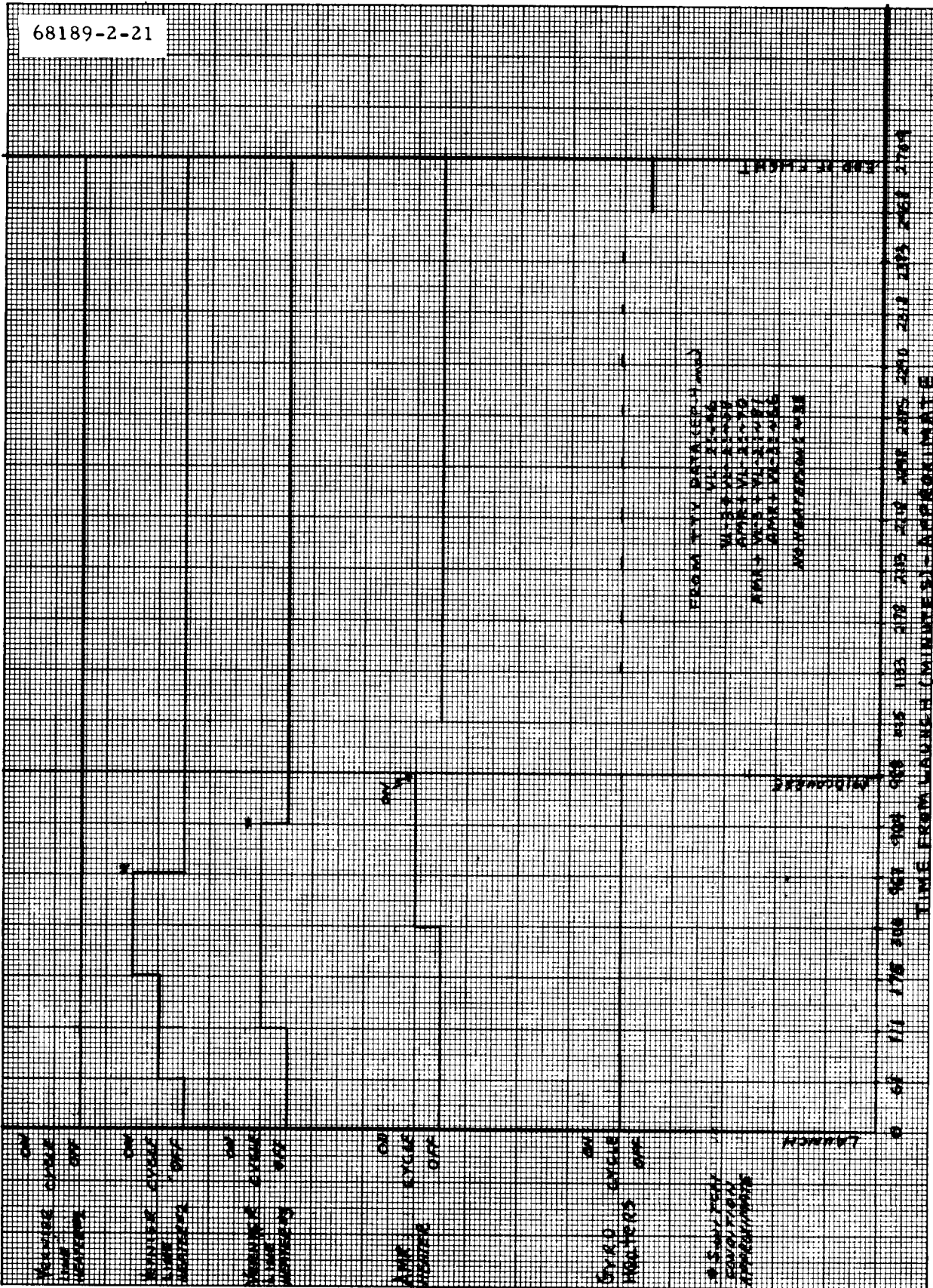


Figure 5.2-21. Heater Loads On/Off

change is at termination of midcourse burn. The difference in initial and final values indicates that these are not the best values, e.g., perhaps another load turned on at the end of midcourse. The various possibilities associated with the difference in initial and final changes in current values constitute a continuing investigation.

- 4) Average change of unaveraged EP-4 and EP-9 leading and trailing edge current changes - 2.0 amperes

Table 5.2-5, is a summary of all vernier firings with data for the long burns (9.85, 2.0, and 20 seconds). Figure 5.2-22 is a frequency distribution of the current change ( $\Delta I$ ) values. The data in this figure indicate that the most probable value of  $\Delta I$  is 2.00 amperes. Figure 5.2-23 shows a plot of  $\Delta I$  versus burn number. This scatter plot places most of the  $\Delta I$ s between 1.7 and 2.1 amperes, with no particular trend in the data. The range in the values is partially due to the effects of the roll actuator, as well as other load effects.

#### 5.2.4.6 Power Mode Cycling

##### RADVS Power On

Near the end of the SC-2 flight, RADVS power was turned on (265:09:19:57 to 265:09:30:09). During this time interval, the auxiliary battery control (ABC) was cycled through various modes of operation. Table 5.2-6 is a summary of this power mode cycling. Figure 5.2-18 (EP-17) and Figure 5.2-24 (EP-2) supplement this table.

Interestingly, at the end of RADVS power on (265:09:30:09), only the main battery was carrying the electrical load. As previously indicated under the discussion of load sharing, the main battery is almost discharged - perhaps as little as 100 w-hr of energy are available.

In general, Figure 5.2-24 (EP-2) expresses the expected changes due to the various power modes. Especially noted are the initial automatic battery transfer at 265:09:22:16 when RADVS power was coming on and the attempt to switch to main battery mode (265:09:22:16) without disabling the battery transfer logic.

Removal of the isolation diodes (265:09:24:24) and (265:09:27:27) caused an increase of about 0.5 volt in EP-2.

TABLE 5.2-5. VERNIER BURNS

Number	Time, GMT (day:hr:min:sec)	Burn Time, seconds	Bits/sec	$\Delta I$ (EP-4), milliamperes		$\Delta I$ (EP-9), milliamperes	
				Leading Edge (L)	Trailing Edge (T)	Leading Edge (L)	Trailing Edge (T)
1	264:05:00:02	9.85	4400	1610	1310	1560	1610
2	264:07:28:25	2.0	1100	2480	2266	2369	2710
3	264:07:50:03	2.0	1100	2099	2080	1538	1709
4	264:19:44:59	0.25	137.5	2373	2373	1758	2099
5	264:20:07:05	0.25	137.5				
6	264:20:35:20	0.25	137.5				
7	264:20:55:06	0.25	137.5				
8	264:21:15:12	0.25	137.5				
9	264:23:33:23	2.0	1100	2051	2325	1929	2051
10	265:01:00:34	0.25	137.5				
11	265:01:05:42	0.25	137.5				
12	265:01:09:23	0.25	137.5				
13	265:01:14:41	0.25	137.5				
14	265:01:19:46	0.25	137.5				
15	265:01:28:11	2.0	1100	2373	2373	1758	2099
16	265:02:01:19	0.25	137.5				
17	265:02:08:11	0.25	137.5				
18	265:02:13:34	0.25	137.5				
19	265:02:19:37	0.25	137.5				
20	265:02:26:06	0.25	137.5				
21	265:02:39:14	2.0	1100	2109	1797	1929	1758
22	265:03:17:24	0.25	137.5				
23	265:03:23:53	0.25	137.5				
24	265:03:29:07	0.25	137.5				
25	265:03:34:33	0.25	137.5				
26	265:03:39:07	0.25	137.5				
27	265:03:47:56	2.0	1100	2051	2071	(7495)	2002
28	265:04:17:31	0.25	137.5				
29	265:04:23:53	0.25	137.5				
30	265:04:29:51	0.25	137.5				
31	265:04:35:34	0.25	137.5				
32	265:04:41:20	0.25	137.5				
33	265:04:56:12	2.0	1100	1836	1758	1855	2344
34	265:05:43:19	2.0	1100	2109	2109	1660	(-6812)
35	265:07:45:00	0.25	1100				
36	265:07:46:12	0.25	1100				
37	265:07:47:15	0.25	1100				
38	265:07:48:18	0.25	1100				
39	265:07:49:25	0.25	1100				
40	265:08:05:12	20.0	1100	2168	1718	1636	2099

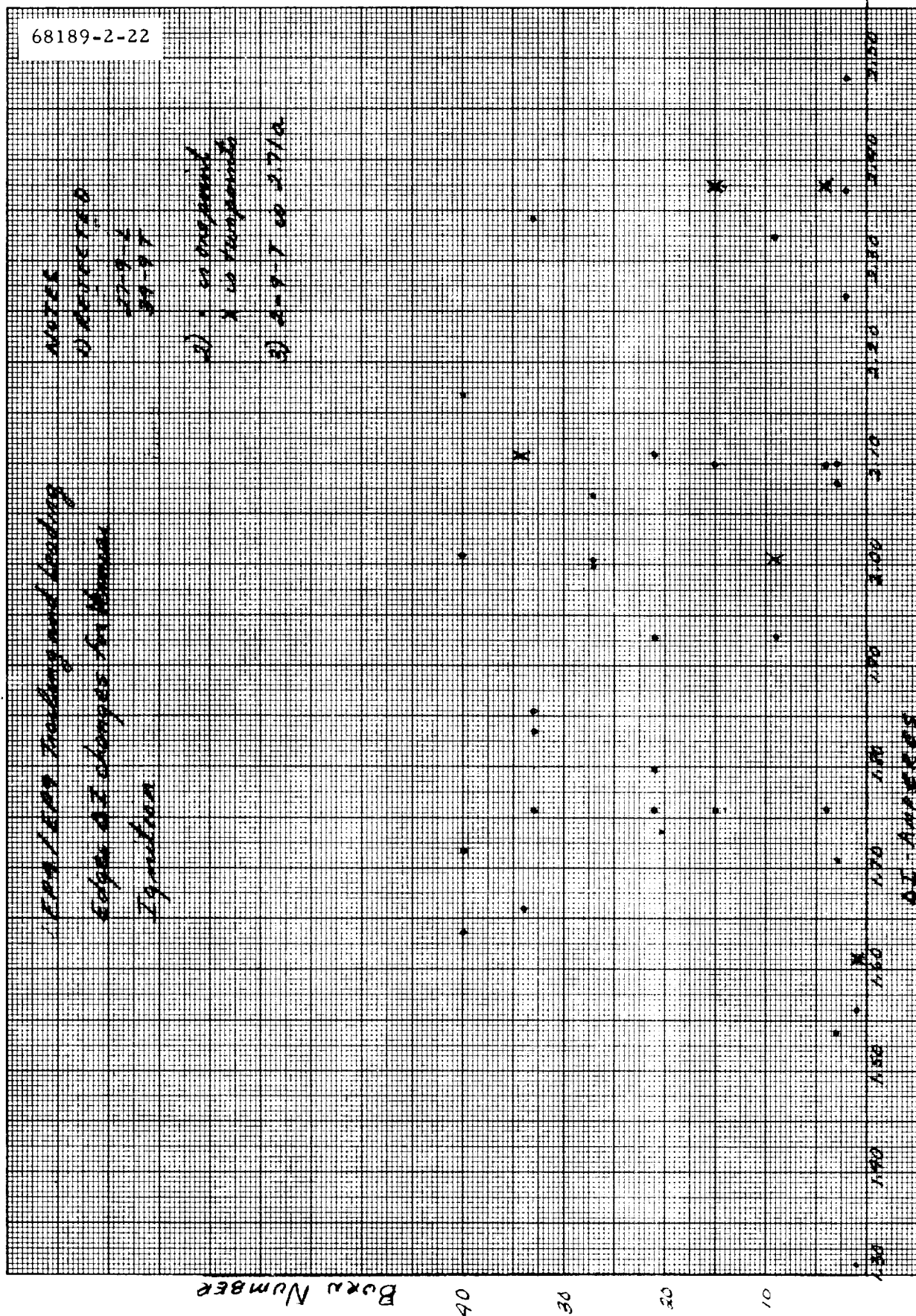


Figure 5.2-22. Current Change Versus Burn Number



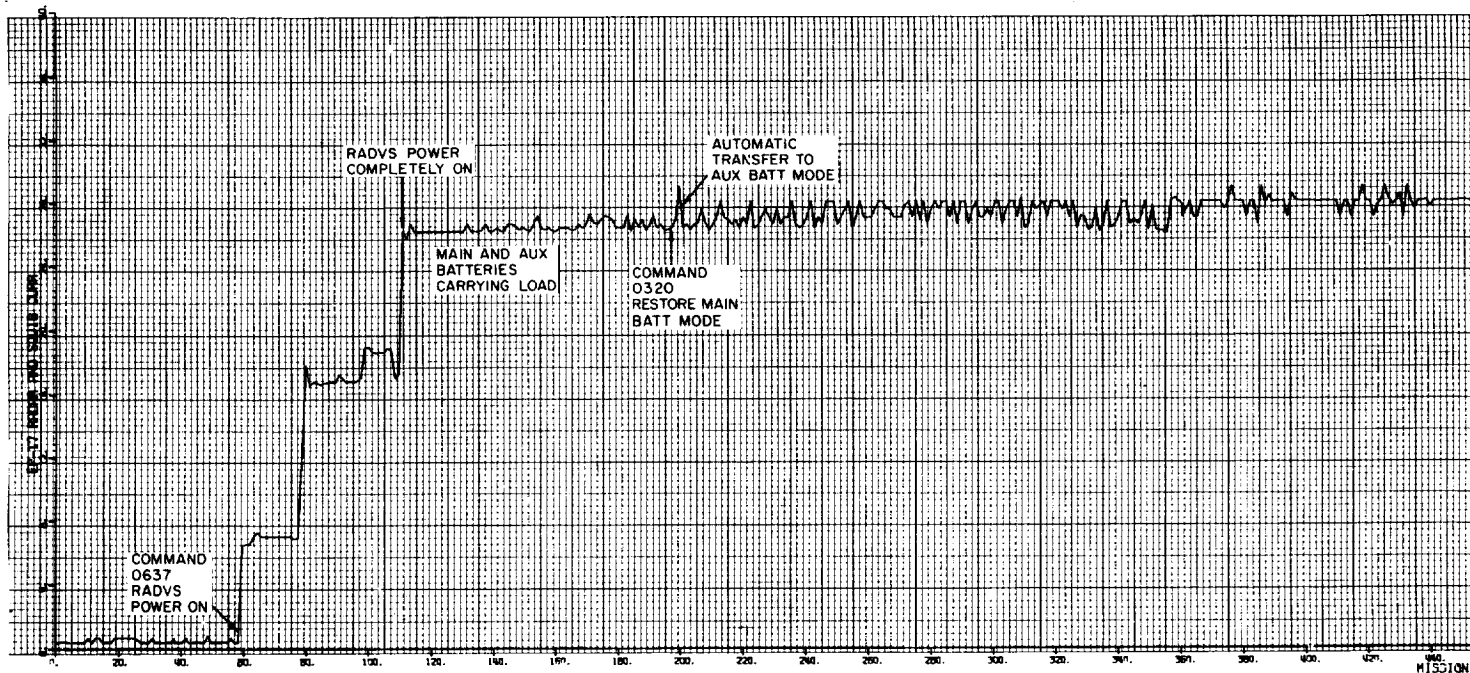


Figure 5.2-23. Radar and Squib Current (RADVS Power On)

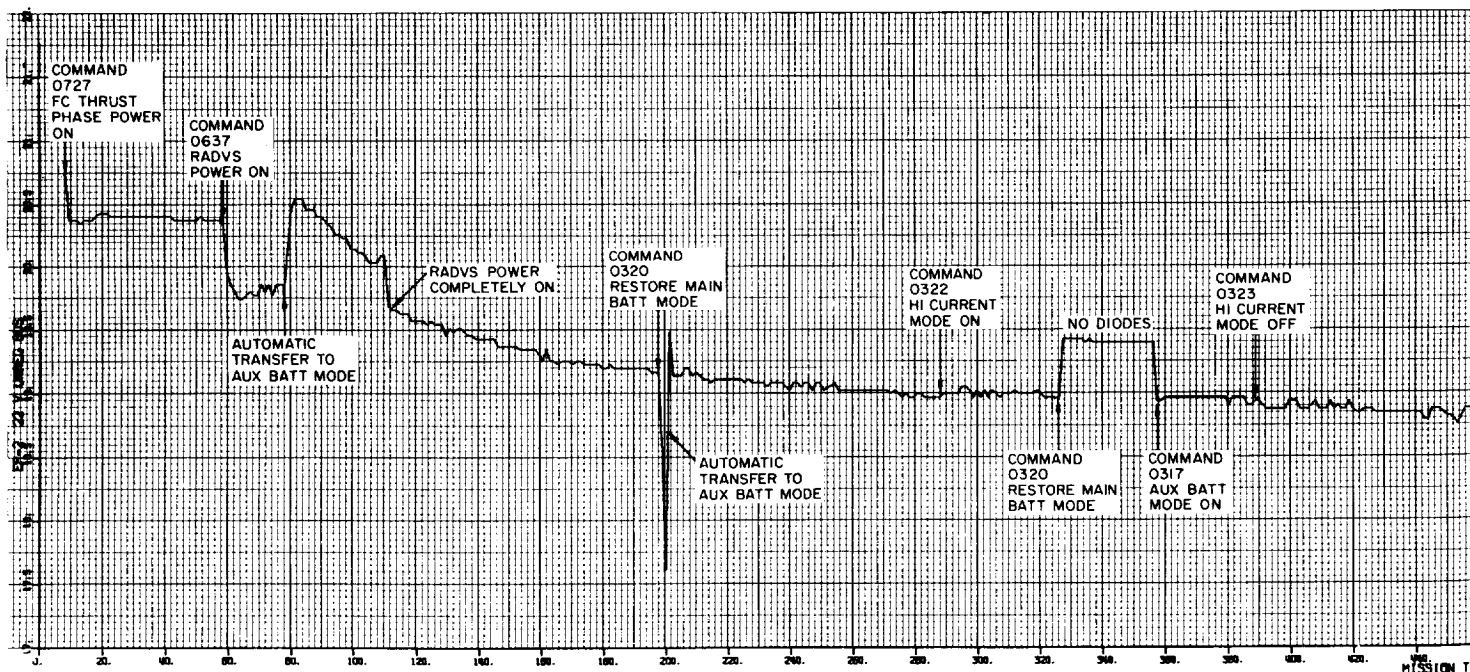
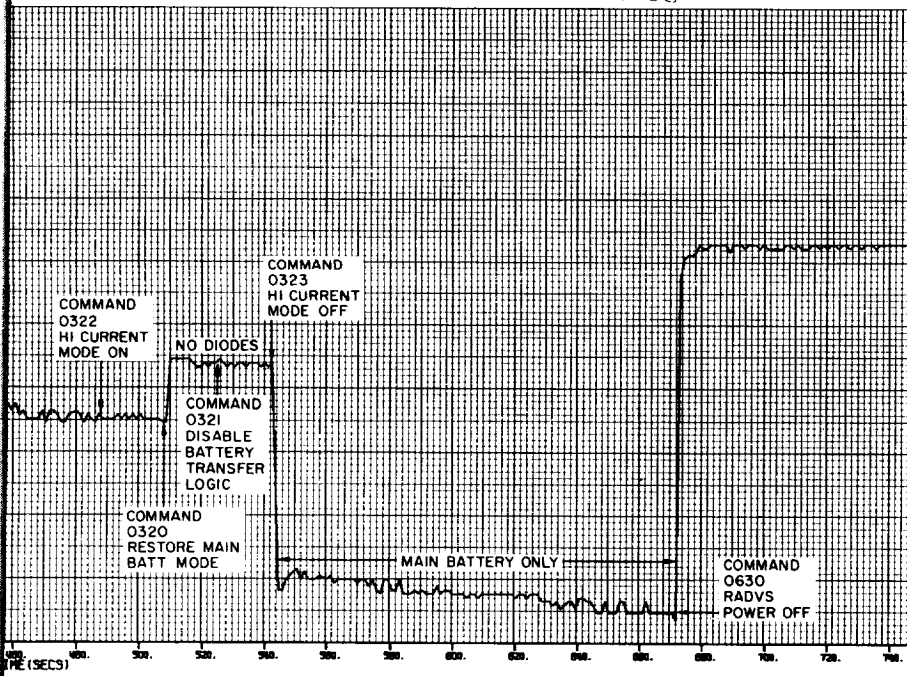
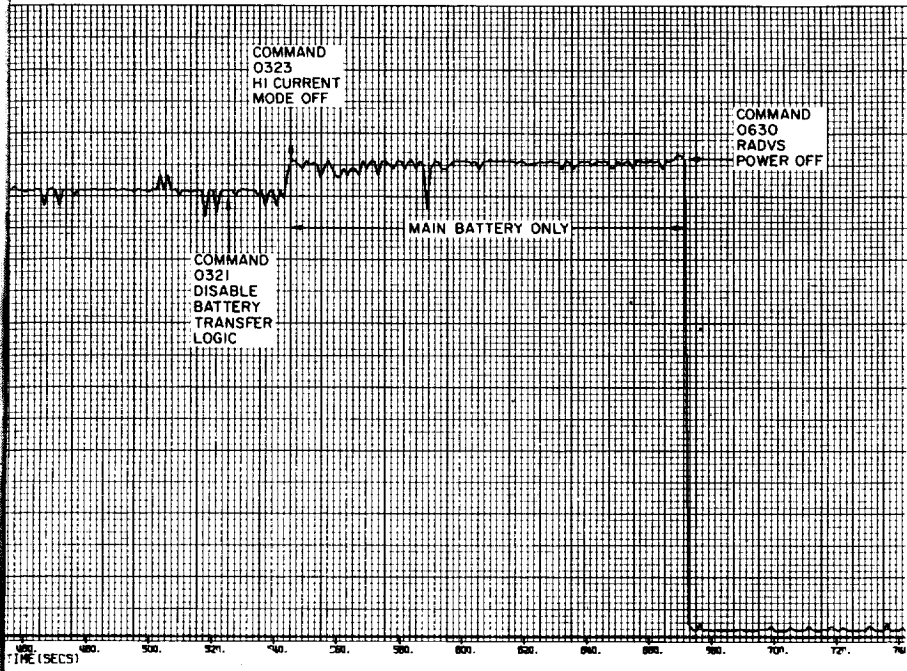


Figure 5.2-24. 22-Volt Unregulated Bus (RADVS Power On)

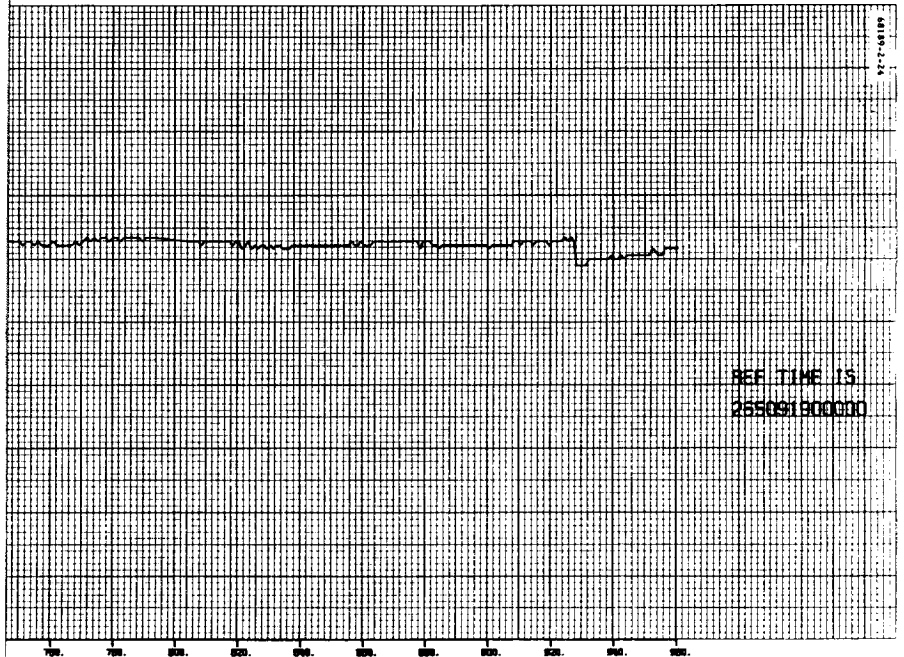
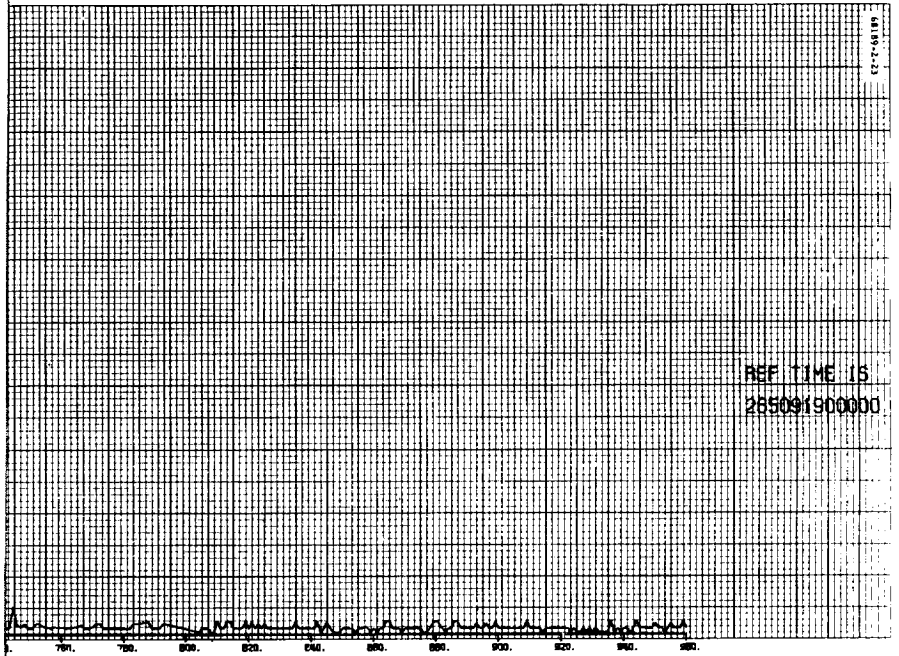




2-27B

2-27B





ECG OUT FRAME 3

5.2-27C



TABLE 5.2-6. POWER MODE CYCLING

Command and Time, GMT (day:hr:min:sec)	Command Title	Comments (Apply to Figure 5.2-18 Unless Otherwise Indicated)	Reference Figures 5.2-18 and 5.2-23, seconds
0727 265:09:19:06	FC thrust phase power on.	Voltage drop: 20.7 to 20.4 volts dc in main battery mode	8
0637 265:09:19:57	RADVS power on.	Voltage drop: 20.37 to 19.8 volts dc initially in main battery only. Figure 5.2-23 shows initial RADVS current drain in steps.	59
265:09:20:13		Automatic transfer to auxiliary battery mode.	78
0320 265:09:22:16	Restore main battery mode, enable battery transfer logic.	Attempt to have RADVS load carried by main battery. Auxiliary battery mode restored immediately by automatic transfer due to low voltage.	188
0322 265:09:23:46	High current mode on.	Little change in unregulated voltage. Already in aux- iliary battery mode.	288
0320 265:09:24:24	Restore main battery mode, enable battery transfer logic.	Voltage rise: 18.96 to 19.4 volts dc in main battery without isolation diodes in parallel with auxiliary battery.	326
0317 265:09:24:54	Auxiliary battery mode on.	Voltage drop: 19.4 to 18.96 volts dc in main battery with isolation diodes in parallel with auxiliary battery.	357
0323 265:09:25:29	High current mode off.	Voltage dropping due to load (18.88 volts dc). Still in auxiliary battery mode.	389
0322 265:09:27:09	High current mode on.	Voltage dropping due to load (18.76 volts dc). No par- ticular change due to 0322.	489
0320 265:09:27:27	Restore main battery mode, enable battery transfer logic.	Voltage rise: 18.73 to 19.22 volts dc in main battery without isolation diodes in parallel with auxiliary battery.	509
0321 265:09:27:43	Disable battery transfer logic.	Switch, no apparent affect on unregulated current.	525
0323 265:09:28:01	High current mode off.	Voltage drop: 19.19 to 17.5 volts dc in main battery without isolation diodes; has entire load. Auxiliary battery not allowed to switch in via automatic transfer to auxiliary battery mode.	542
0630 265:09:30:09	RADVS power off.	Voltage rise: 17.18 to 20.0 volts dc in main battery mode.	672

### 5.2.5 REFERENCES

1. J.R. Oelschlaeger, "SC-2 Nominal Mission Energy Prediction," Hughes Aircraft Company, IDC 2292/71, 19 September 1966.
2. "Surveyor I Flight Performance Final Report," Volume II, Section 5.3, Hughes Aircraft Company, SSD 68222R, October 1966.
3. "Surveyor A-21 SC-2 Flight Acceptance Test, Solar Thermal Vacuum Final Test Phase Report," Volume II, Section 4.0, Hughes Aircraft Company, SSD 69190R, July 1966.
4. J. Mundy, "System Specification Power and Thermal Dissipations by Functional Event for Engineering Payload," Hughes Aircraft Company, No. 239523, Revision C, 1 July 1965.
5. J.E. Mundy, "Results of Special Tests Performed on SC-4 to Investigate Vernier Engine Solenoid Value Current," Hughes Aircraft Company, IDC 2294.2/50, 5 December 1966.

### 5.2.6 ACKNOWLEDGEMENTS

W. McIntyre	Technical coordinator and writer
J. Berger	Signal processing
L.M. Bronstein	Midcourse data
T.H. Mansfield	Vernier burn data
S.F. McCormick	Loads analysis
J.E. Mundy	Midcourse data
S.A. Volansky	Signal processing



## 5.3 RF DATA LINK SUBSYSTEM

### 5.3.1 INTRODUCTION

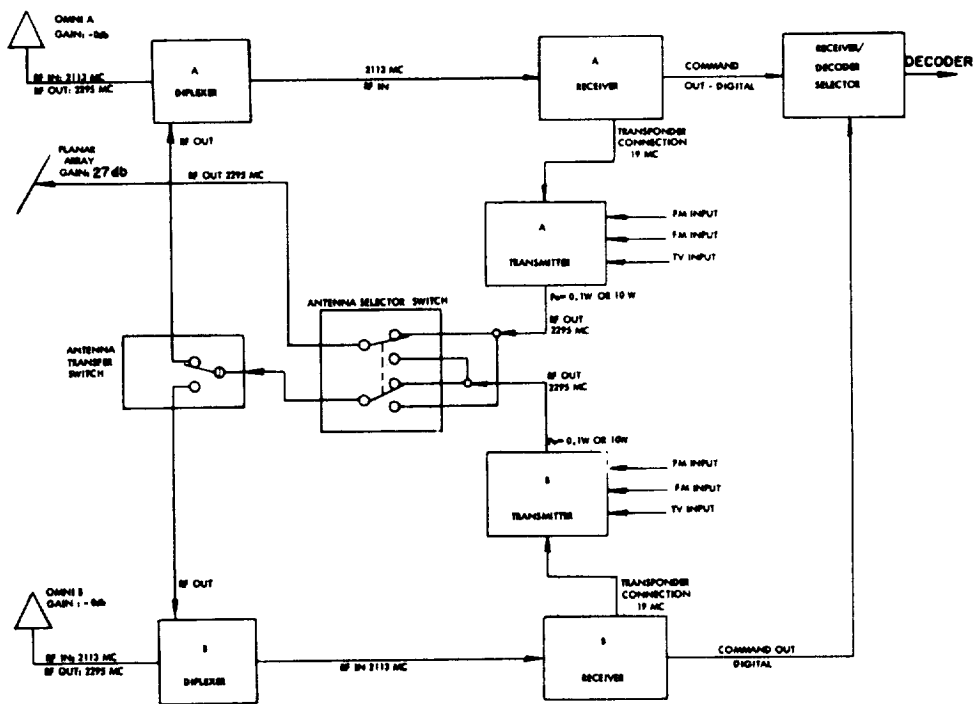
This section contains a summary and analysis of the performance of the data link subsystem during Surveyor Mission B.

The data link subsystem consists of the transmitters, transponders, receivers, command decoders, and antennas. It is the function of this subsystem to: 1) provide engineering data transmission from the spacecraft at bit rates compatible with specific mission phases, 2) provide analog data, such as that from television and strain gages, at signal levels high enough for proper discrimination, 3) provide phase coherent two-way doppler for tracking and orbit determination, and 4) provide command reception capability throughout the mission to allow for complete control of the spacecraft from the ground. A simplified block diagram of the communications subsystem is shown in Figure 5.3-1.

The pertinent subsystem units on the spacecraft during the mission are as follows:

<u>Unit</u>	<u>Part Number</u>	<u>Serial Number</u>
Receiver A	231900-3	15
Receiver B	231900-3	16
Transmitter A	263220-4	15
Transmitter B	263220-4	11
Command decoder unit	232000-5	3

Unlike most subsystems, individual data link subsystem parameters such as losses, threshold sensitivity, modulation index, etc., are not measured or individually determined from mission data. The composite effect of these parameters on the performance is measured as received signal power at the spacecraft and the tracking station (DSIF) and as telemetry and command error rates. Consequently, it is impossible to compare individual link parameters to specified performance criteria. The best that can be done is to compare measured signal levels to predicted levels, and telemetry quality and command capability to predicted capabilities. To further cloud the analysis, omnidirectional antenna gain is a major contributor to the



68189-2-134

Figure 5.3-1. Communications Subsystem Block Diagram

uncertainty in received signal levels. Accurate omni-gain measurements are difficult to achieve and, in most cases, deviations from predictions can most likely be attributed to antenna gain uncertainty. Because of the problems outlined above, analysis of the data link subsystem performance will, in general, be a qualitative analysis of the performance of the entire subsystem rather than a quantitative assessment of the performance of the individual subsystem parameters. Equally as important as subsystem performance evaluation in this analysis is the qualitative assessment of the premission and real-time prediction techniques used during the mission, since future missions must rely on these techniques as guidelines during the real-time operation.

In general, the RF data link subsystem performed as expected. The single exception was the performance of receiver B, which was degraded. Consequently, the actual and predicted performances were not in agreement. All other subsystem units performed very close to the nominal predictions.

The data contained in this report consist of spacecraft telemetered, DSIF, and mission event time data. Where meaningful, the data is correlated to and compared with equipment specifications, previous test data, preflight predictions, and in-flight analysis predictions. Specifically, this section contains the following discussions which are shown with the appropriate subsection notation:

Anomaly Discussion (subsection 5.3.2) – This subsection contains a discussion of the degraded receiver B, as well as the RF effects caused by the tumbling spacecraft.

Summary and Conclusions (subsection 5.3.3) – This subsection contains a summary of subsystem performance with conclusions and recommendations relative to performance and postflight analysis.

Subsystem Performance Analysis (subsection 5.3.4) – This subsection contains the following items:

- 1) General discussion of data, equations used, and path of the earth vector relative to omni-gain contours.
- 2) Discussion of subsystem performance during specific mission phases.
- 3) Discussion of pertinent subsystem telemetry signals plotted as a function of time from launch.

The major mission event times relative to the RF data link subsystem are tabulated in Tables 5.3-1 and 5.3-2. Table 5.3-1 contains telemetry mode and bit rate, primary tracking station number, and station automatic gain control (AGC) values as a function of time for the pretumbling and post-tumbling phases. Table 5.3-2 contains a tabulation of the subsystem configuration as a function of time for the pretumbling and post-tumbling phases. In some cases, the times in these tables are accurate only to the nearest minute.

TABLE 5.3-1. TELEMETRY MODE SUMMARY

GMT, day:hr:min:sec	Mode	Bit Rate	DSIF Station	DSIF AGC, dbm	Comments
Pretumbling Phase					
263:12:31:59.824	5	550		Liftoff	Low modulation index
12:55:07	5	550	51	-118.0	Initial acquisition (SAA)
13:04:59	5	550	51	- 90.0	Two-way lock (SCM)
13:15:00	5	550	51	- 90.0	High power   Preparation for
13:17:08	5	550	51	-111.6	Low power   transit I phase
13:26:29	1	550	51		
13:29:26	1	1100	51		Normal bit rate selection
13:32:51	4	1100	51		
13:34:50	2	1100	51		
13:37:37	3	1100	51		
13:39:24	5	1100	51		
16:38:38	5	137.5	51	-137.1	Bit rate reduction for DSS-72 track
16:51:35	5	137.5	72	-146.2	DSS-72 in two-way lock
17:45:02	5	137.5	51		DSS-51 in two-way lock
17:52:02	5	137.5	51	-138.5	
18:01:26	5	1100	51	-135.6	Bit rate increase for DSS-51 track
18:09:41	4	1100	51		
18:13:25	2	1100	51		
18:20:15	1	1100	51		
18:24:35	5	1100	51		
18:30:46	5	1100	51	-114.8	High power - pre-Canopus
19:21:00	5	1100	51	-112.0	High power   star lock
19:22:05	5	1100	51	-132.9	Low power
21:50:06	5	17.2	51		Bit rate reduction for DSS-72 track
22:02:00	5	17.2	72	-139.8	DSS-72 in two-way lock
22:18:00					DSS-51 set
22:50:50	5	17.2	11	-148.0	DSS-11 rise
23:12:10	5	1100	11	-138.2	Bit rate increase for DSS-11 track
23:21:40	5	1100	11		Transmitter off   DSS-11 having
23:24:18	5	1100	11		Transmitter on   transmitter
23:29:32	5	1100	11		Two-way lock   trouble
23:40:31	4	1100	11		
23:44:45	2	1100	11		
23:47:46	5	1100	11		
264:01:23:40	5	1100	11		Start receiver B test
01:40:07	5	1100	11	-138.1	Start reduction of power
02:14:00	5	1100	11	-138.4	End receiver B test
02:54:44	5	1100	11		DSS-11 having transmitter trouble
02:59:37	4	1100	11		
03:02:28	2	1100	11		

Table 5. 3-1 (Continued)

GMT, day:hr:min:sec	Mode	Bit Rate	DSIF Station	DSIF AGC, dbm	Comments
03:04:08	1	1100	11		
03:05:41	5	1100	11		
03:07:42	Gyro	1100	11		Gyro speed check
03:13:18	5	1100	11		
04:14:00	4	1100	11		
04:15:51	2	1100	11		
04:18:10	1	1100	11		
04:36:43	1	1100	11		High power - premidcourse
04:37:53	1	4400	11	-123.3	Bit rate increase for midcourse
04:51:50	1	4400	11	-123.3	End premidcourse
05:00:02	1	4400	11		Midcourse thrust execution
Post-tumbling Phase					
264:05:00:00	1	4400	11	-123.3	Start nonstandard phase
05:20:50	1	550	11	≈-130.0	
05:23:16	1	550	11	-135 to -140	Low power
05:29:20	1	137.5	11	-143 to -144	
05:31:45	2	137.5	11		
05:34:39	2	137.5	11	-142 to -153	
05:48:51	5	137.5	11		Prior to station transfer to 42
05:58:33	5	137.5	42	-142 to -152	$4.5 \times 10^{-3}$ bit error rate
07:05:43	5	137.5	42	-142 to -151	Spin period, 1.2 seconds
07:19:16	5	137.5	42	≈-120.0	High power
07:21:08	5	1100	42		
07:22:20	1	1100	42		2-second thrusting
07:29:53	1	550	42		
07:30:37	5	550	42	-117 to -126.5	
07:34:04	5	137.5	42		
07:35:06	5	137.5	42	-142 to -151	Low power
07:46:36	5	137.5	42	≈-120	High power
07:47:31	5	1100	42		
07:47:58	1	1100	42		2-second thrusting
07:51:37	1	550	42		
07:53:02	5	550	42		
07:57:54	5	137.5	42		
07:58:04	5	137.5	42		Low power
10:21:05	4	137.5	42		
10:25:00	4	137.5	42	-142 to -152	Spin period, 1.06 seconds
10:29:58	2	137.5	42		
10:38:23	5	137.5	42	-147 mean	
11:41:34	4	137.5	42		

Table 5.3-1 (Continued)

GMT, day:hr:min:sec	Mode	Bit Rate	DSIF Station	DSIF AGC, dbm	Comments
11:52:14	2	137.5	42		
12:04:28	5	137.5	42		
12:15:30	5	137.5	42	-145 to -160	Transmitting on omnidirectional antenna A
12:15:30	5	137.5	42	-145 to -155	Transmitting on omnidirectional antenna B
13:22:14	4	137.5	42		
13:37:08	2	137.5	42		
13:41:25	5	137.5	42		
15:30:56	1	137.5	51	=-126	High power
15:36:02	1	1100	51		
15:47:32	1	137.5	51		
15:49:00	1	137.5	51		Low power
15:50:22	5	137.5	51		
16:00:00	5	137.5	51	-144 to -148	
18:00:00	5	137.5	51	-144.5 to -147.5	
19:35:18	1	137.5	51		0.2-second thrusting
19:50:06	5	137.5	51		
20:02:12	1	137.5	51		0.2-second thrusting
20:09:50	5	137.5	51		
20:28:32	1	137.5	51		0.2-second thrusting
20:37:28	5	137.5	51		
20:46:24	1	137.5	51		0.2-second thrusting
20:56:27	5	137.5	51		
21:10:51	1	137.5	51		0.2-second thrusting
21:16:53	5	137.5	51		
22:06:30	5	137.5	61		Two-way lock
22:30:00	5	137.5	61	-147.0	
22:55:50	5	137.5	51		61 transmitter off; 51 two-way lock
23:19:58	5	137.5	11		High power
23:22:17	5	4400	11		
23:23:25	1	4400	11		
23:28:08	1	1100	11		2-second thrusting
23:34:24	5	1100	11		
23:38:46	4	1100	11		
23:40:17	5	1100	11		
23:40:42	5	137.5	11		
23:43:31	5	137.5	11		Low power
265:00:59:21	1	137.5	11		0.2-second thrusting
01:01:12	5	137.5	11		
01:04:38	1	137.5	11		0.2-second thrusting
01:06:16	5	137.5	11		

Table 5.3-1 (Continued)

GMT, day:hr:min:sec	Mode	Bit Rate	DSIF Station	DSIF AGC, dbm	Comments
01:08:23	1	137.5	11		0.2-second thrusting
01:09:54	5	137.5	11		
01:13:44	1	137.5	11		0.2-second thrusting
01:15:11	5	137.5	11		
01:18:21	1	137.5	11		0.2-second thrusting
01:20:20	5	137.5	11		
01:21:36	5	137.5	11		High power
01:24:22	5	1100	11		
01:25:37	1	1100	11		2-second thrusting
01:29:09	5	1100	11		
01:29:38	5	137.5	11		
01:30:24	5	137.5	11		Low power
01:39:53	4	137.5	11		
01:44:36	5	137.5	11		
01:59:51	1	137.5	11		0.2-second thrusting
02:01:58	5	137.5	11		
02:06:53	1	137.5	11		0.2-second thrusting
02:08:40	5	137.5	11		
02:12:38	1	137.5	11		0.2-second thrusting
02:14:01	5	137.5	11		
02:18:34	1	137.5	11	-143 to -152	0.2-second thrusting
02:20:07	5	137.5	11		
02:24:27	1	137.5	11		0.2-second thrusting
02:26:35	5	137.5	11		
02:34:00	5	137.5	11		High power
02:35:36	5	1100	11		
02:36:22	1	1100	11		2.0-second thrusting
02:40:08	5	1100	11		
02:41:16	5	137.5	11		
02:42:21	5	137.5	11		Low power
03:12:40	1	137.5	11		0.2-second thrusting
03:17:56	5	137.5	11		
03:22:39	1	137.5	11		0.2-second thrusting
03:24:23	5	137.5	11		
03:28:06	1	137.5	11		0.2-second thrusting
03:29:36	5	137.5	11		
03:33:48	1	137.5	11		0.2-second thrusting
03:35:02	5	137.5	11		
03:38:21	1	137.5	11		0.2-second thrusting
03:39:31	5	137.5	11		
03:43:46	5	137.5	11		High power

Table 5.3-1 (Continued)

GMT, day:hr:min:sec	Mode	Bit Rate	DSIF Station	DSIF AGC, dbm	Comments
03:44:44	5	1100	11		
03:45:51	1	1100	11		2.0-second thrusting
03:48:50	5	1100	11		
03:50:19	5	137.5	11		Low power
04:16:14	1	137.5	11		0.2-second thrusting
04:17:56	5	137.5	11		
04:22:42	1	137.5	11		0.2-second thrusting
04:24:12	5	137.5	11		
04:28:26	1	137.5	11		0.2-second thrusting
04:30:21	5	137.5	11		
04:34:38	1	137.5	11		0.2-second thrusting
04:35:52	5	137.5	11		
04:40:22	1	137.5	11		0.2-second thrusting
04:41:37	5	137.5	11		
04:52:36	5	137.5	11		High power
04:53:28	5	1100	11		
04:54:26	1	1100	11		2.0-second thrusting
04:56:49	5	1100	11		
04:57:55	5	137.5	11		
04:58:19	5	137.5	11		Low power
05:32:53	5	137.5	11		High power
05:35:52	6	1100	11		2.0-second thrusting
05:45:20	5	1100	11		
05:46:34	5	137.5	11		
05:47:10	5	137.5	11		Low power
06:32:45	5	137.5	42		High power
06:34:38	5	1100	42		
06:50:40	5	137.5	42		
06:53:54	5	1100	42		
06:58:41	5	137.5	42		
06:59:12	5	137.5	42		Low power
07:31:00	5	137.5	42	-150.0	
07:41:49	5	137.5	42		High power
07:42:50	5	1100	42		
07:43:26	1	1100	42		Five 0.2-second thrusts
07:50:02	5	1100	42		
07:50:54	5	137.5	42		
07:51:17	5	137.5	42		Low power
07:54:21	5	137.5	42	-147 to -152	
08:00:52	5	137.5	42		High power
08:02:11	5	1100	42		



Table 5.3-1 (Continued)

GMT, day:hr:min:sec	Mode	Bit Rate	DSIF Station	DSIF AGC, dbm	Comments
08:02:28	6	1100	42		21.5-second thrusting
08:07:56	5	1100	42		
08:09:02	5	137.5	42		
08:09:19	5	137.5	42		Low power
09:11:50	5	137.5	42		High power
09:12:34	5	1100	42		
09:32:19	2	1100	42		
09:34:17	2	1100	42		Emergency AMR command
09:35:00	2	1100	42	-123 to -128	Abrupt loss of signal

TABLE 5.3-2. SPACECRAFT CONFIGURATION SHEET

GMT, day:hr:min:sec	Major Sequence Title	Transmitter		Omnidirectional Antennas A/B	A/D Converter 1/2	Receiver A		Receiver B		Command Decoders A/B	Comments
		A/B	Power H/L			ØL/AFC	Transponder A	ØL/AFC	Transponder B		
Pretumbling Phase											
263:11:39:00	Prelaunch	B	L	B	1	AFC	Off	Ø/L	On	B	No transmission to spacecraft
12:44:21	Launch		H								
13:04:59	DSS-51 acquisition					AFC		Ø/L		A	
13:16:33			L								
14:12:--											
18:30:46	Star verification		H					AFC	Off		
18:33:01											
18:54:45				A							
Time not known										B	
19:06:37				B							
19:14:21	Coast								On		
19:15:39								Ø/L			
19:22:05			L								
23:21:40								AFC			DSS-11 transmitter off
23:29:32								Ø/L		A	
264:01:23:50	Special test Receiver B									B	Modulation interrupts
01:24:31										A	Receiver B
02:02:54										B	Approximate time
Approximately 02:05:00								AFC			DSS-11 transmitter off
Approximately 02:07:00								Ø/L		A	
02:07:35										B	Approximate time
02:54:50								AFC			DSS-11 transmitter off
02:56:00								Ø/L		A	
04:36:43	Premidcourse maneuvers		H								

Table 5.3-2 (Continued)

GMT, day:hr:min:sec	Major Sequence Title	Transmitter		Omnidirectional Antennas A/B	A/D Converter 1/2	Receiver A		Receiver B		Command Decoders A/B	Comments
		A/B	Power H/L			ØL/AFC	Transponder A	ØL/AFC	Transponder B		
05:00:00			Mission became nonstandard								
05:23:02			L								
07:18:28			H								
07:23:57										B	Approximate time
07:34:47			L								
07:46:36			H								
07:58:16			L								
12:12:12				A							
12:15:00				B							
15:19:00										A	Approximate time
15:30:56			H								
15:48:51			L								
23:19:58			H								
23:43:31			L								
265:01:21:36			H								
01:30:24			L								
02:34:00			H								
02:42:21			L								
03:43:46			H								
03:50:19			L								
04:52:36			H								
04:58:19			L								
05:32:53			H								
05:47:01			L								
06:32:45			H								
06:59:12			L								
07:41:49			H								

Table 5.3-2 (Continued)

GMT, day:hr:min:sec	Major Sequence Title	Transmitter		Omnidirectional Antennas A/B	A/D Converter 1/2	Receiver A		Receiver B		Command Decoders A/B	Comments
		A/B	Power H/L			ØL/AFC	Transponder A	ØL/AFC	Transponder B		
07:51:17			L								
08:00:52			H								
08:09:19			L								
09:11:50			H								
09:35:00											Abrupt loss of signal

## 5. 3. 2 ANOMALY DESCRIPTION

### 5. 3. 2. 1 Degraded Receiver B Performance

The only subsystem anomaly observed during the mission was the threshold degradation of receiver B which was most apparent during the first 16 hours of flight. A comprehensive review of test data by systems engineering taken at AFETR (Reference 1) revealed that receiver B had similar problems prior to the prelaunch countdown, apparently masked by RF air link variations. Postflight analysis of the flight data and postflight tests on other spacecraft receivers led to the final conclusion that receiver B had become degraded, probably prior to the countdown. For completeness, a brief history of events relating to this anomaly will be given prior to an analysis of the pertinent flight data.

After the gantry was removed during the countdown, receiver B AGC indicated that the signal level was about 25 db below the level at receiver A. Since no change of this nature had been noted during Mission A countdown, a possible anomaly was suspected. Discussion among analysts at AFETR, spacecraft/performance/analysis/command, and spacecraft consulting analysis team led to the conclusion that a multipath effect had caused the change, since it was first reported when the gantry was removed.

After launch and initial spacecraft acquisition at Johannesburg, the signal level at receiver B was still 18 db below the level at receiver A. Since the spacecraft roll attitude was unknown prior to Canopus acquisition, the difference in signal level was not immediately considered a problem. However, during this pre-Canopus acquisition period, a comparison of spacecraft receiver signal levels, DSIF signal levels, and corresponding omnidirectional gains indicated that no earth vector position could be found which satisfied the observed conditions.

Six hours after launch, Canopus acquisition was initiated. Receiver B AGC data taken during the 360-degree roll was compared to that from antenna gain patterns. They agreed relatively well with the expected variations. However, the absolute values were about 16 db below the expected values. This data indicated that the antenna patterns were correct, and that either the receiver AGC characteristics had changed or a loss of 16 db existed between the diplexer and receiver B.

In order to investigate the anomaly and to determine the two-way (transponder mode) capability for the midcourse maneuver, a special threshold test was run at 01:24 GMT. The DSIF transmitter power was lowered in 2-db steps, and AGC telemetry from receivers A and B was recorded. The point of observed receiver/decoder indexing was also noted. This test indicated that: 1) expected gain variations for the proposed midcourse maneuver were less than 24 db and, hence, the maneuver could be made in the transponder mode, 2) receiver A AGC calibration data was nearly correct (signal level changes closely agreed with known changes in DSIF transmitter power),

and 3) receiver B AGC calibration was not correct, showing excessive changes in receiver signal levels. (A change of 2 db at the transmitter caused a 3- or 4-db change at receiver B.)

The fact that the observed receiver/decoder index could have been caused by either receiver did not allow a direct assessment of whether receiver B was degraded or had merely shifted AGC calibration. A planned postmidcourse test to determine if receiver B was degraded was eliminated after the mission became nonstandard.

Data from the special threshold test run 13 hours after launch is tabulated in Table 5.3-3. Figure 5.3-2 shows the receiver A in-flight calibration data (separate curves for index caused by receiver A or B) compared with preflight calibration data for temperatures of 75 and 125° F. The flight temperature was close to 90° F, indicating that the proper calibration curve should lie between the latter two curves. As mentioned before, the receiver that caused the index during this test was not known, but by assuming each receiver in turn and then comparing the AGC curve generated with the preflight curves, a reasonable conclusion can be reached. First, assume receiver A caused the index. From prelaunch test data, that index point was -122 dbm. This can be used to tie down the relative test data from Table 5.3-3 to the absolute dbm scale of Figure 5.3-2. The curve thus generated lies outside either of the preflight curves and would require a further assumption that receiver A had a 3- to 4-db error in its AGC calibration. Next, assume receiver B caused the index. In this case, the telemetered signal level for receiver A at the start of the threshold test can be used as an absolute value. Thus, the second curve of Figure 5.3-2 was constructed. This curve lies between the two preflight curves and, in fact, indicates crossovers very near those shown in the preflight data. A deviation from the preflight curves does exist at levels below -114 dbm, but the overall close agreement with preflight data leads to the conclusion that receiver B did cause the index, and was therefore degraded.

Based on that assumption, a revised calibration curve was generated. This data is shown in Figure 5.3-3, compared with the preflight calibration data for 75 and 125° F.

Special tests were subsequently run by systems engineering on a spacecraft receiver to determine if a failure mode could be found which would shift the receiver AGC characteristics and degrade the threshold performance as had been observed. The tests indicated that such a failure could be duplicated by simulating a loss in gain in either the A6 or A8 modules. Figure 5.3-4 shows the special test data taken when simulating losses of 3- and 6-db in the A6 or A8 modules. These modules have caused problems in the past and, in fact, receiver degradation due to them was noted on SC-1 during solar thermal vacuum tests and on SC-3 during vibration tests. In addition, these special tests revealed that there was no obvious failure that would just shift the AGC without also causing degraded performance (Reference 1).

TABLE 5.3-3. SUMMARY OF RECEIVER THRESHOLD TEST DATA

GMT, day 264 (hr:min:sec)	DSS-11 Transmitter Attenuation, db	Receiver A, BCD	Receiver B, BCD
Start test	0	207	215
01:37:03	-2	224	234
01:39:48	-4	242	255
01:42:04	-6	259	279
01:44:21	-8	278	301
01:47:15	-10	299	321
01:49:23	-12	318	338
01:51:28	-14	336	353
01:53:30	-16	355	363
01:56:12	-18	375	371
01:57:22	-20	388	376
02:00:27	-22	401	379
02:04:33	-24*	410	381

\*Decoder index indicated from spacecraft telemetry.

Based on the evaluation of flight data and the special receiver test, it is concluded that receiver B was degraded and probably had become degraded before launch. On the strength of these conclusions, all telemetered AGC flight data in this report are analyzed using the calibration curves contained in Figures 5.3-2 (assuming B-caused index) and 5.3-3.

If the mission had proceeded successfully beyond midcourse, this anomaly would not have been catastrophic. Extrapolation of flight data, assuming 16-db degradation in receiver B threshold, would still have resulted in a positive command margin of 1 to 2 db at lunar distances.

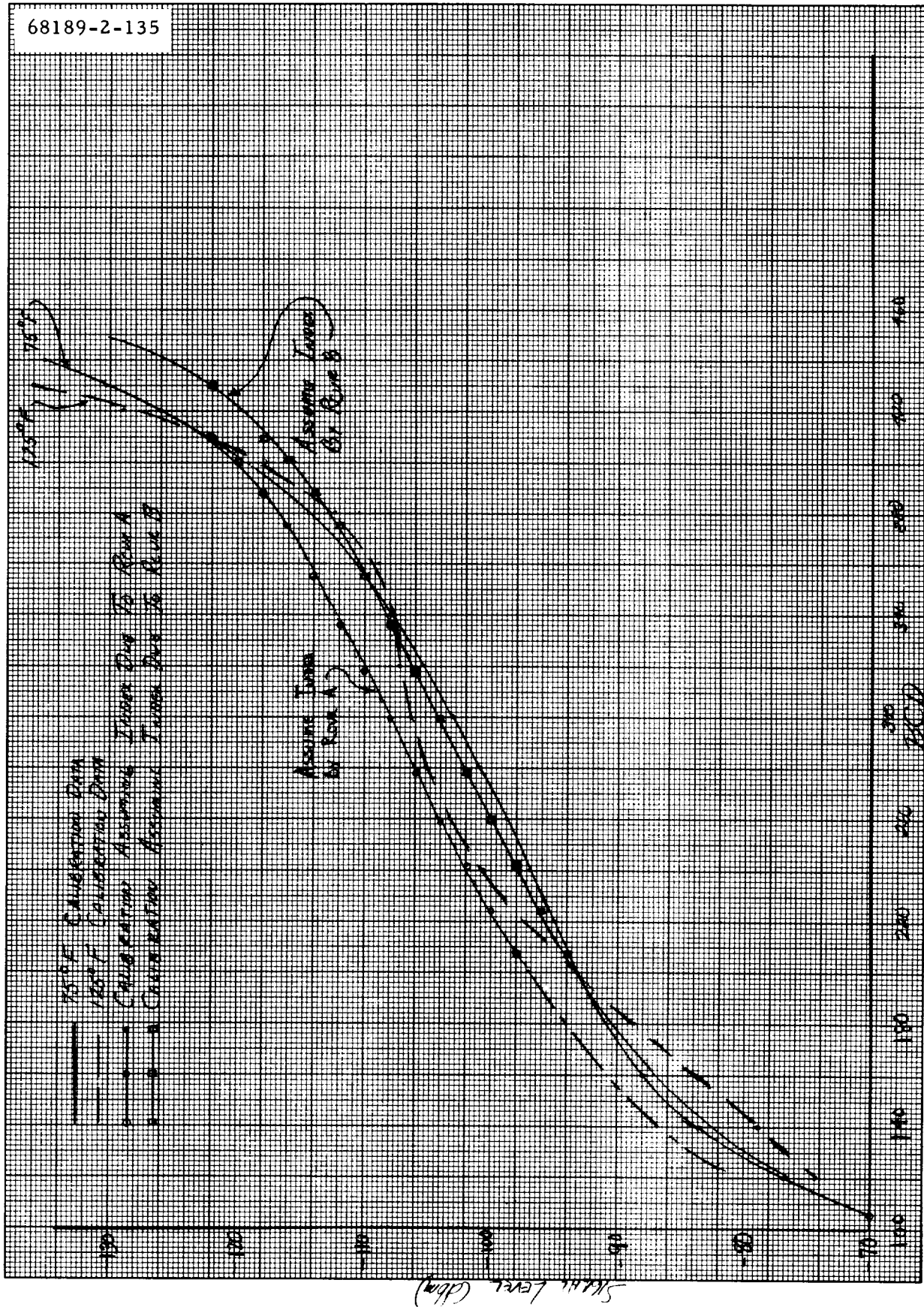


Figure 5.3-2. Receiver A Automatic Gain Control Calibration



68189-2-136

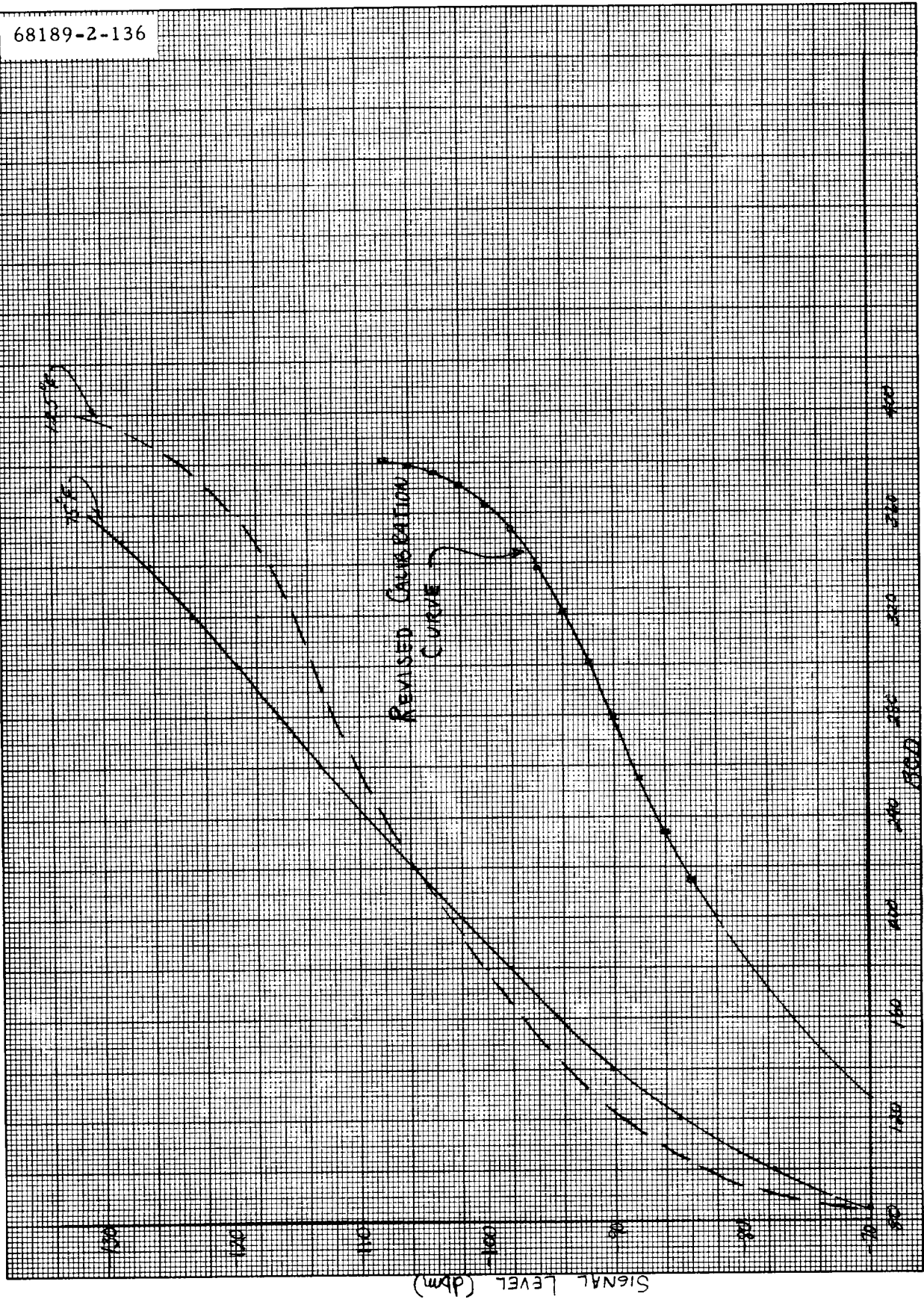


Figure 5.3-3. Receiver B Automatic Gain Control Calibration

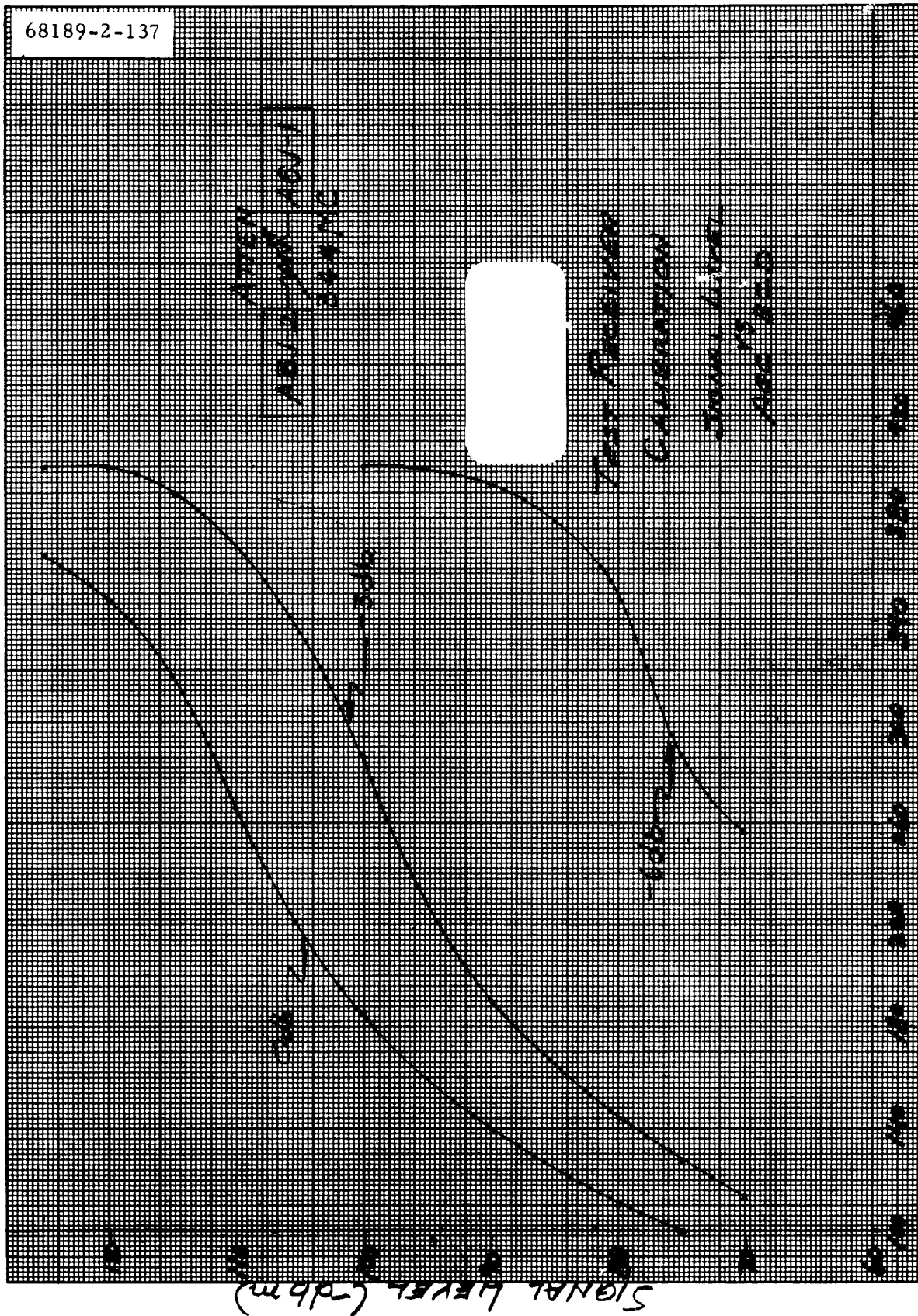


Figure 5.3-4. Test Receiver Calibration Signal Level Versus Automatic Gain Control BCD

### 5. 3. 2. 2 RF and Data Link Problems Associated With the Tumbling Spacecraft

The anomaly that caused the spacecraft to tumble during midcourse thrust and eventually resulted in mission failure was not in any way due to the RF subsystem. However, once the failure occurred, the performance of the data link was substandard. Under the circumstances, the RF subsystem performed as expected, though the resulting link was substandard relative to a normal mission.

The link degradation due to tumbling resulted in lower allowable telemetry bit rates and an increased bit error rate. A maximum bit rate of 137.5 bits/sec was available for low power and 1100 bits/sec for high power transmitter operation.

The telemetry quality was apparently degraded by two separate effects. First, telemetry signal to noise ratio (SNR) was changing as the spacecraft tumbled, resulting in below threshold SNRs during some periods after midcourse. Reported DSIF signal levels during high power operation were cycling between -117 to -127 dbm right after midcourse and between -127 to -132 dbm near the end of the mission. The nominal threshold signal level for 1100 bits/sec was -138 dbm, indicating that the levels were well above threshold. For low power operation, however, the reported DSIF signal levels were cycling between -135 to -140 dbm after midcourse and between -145 to -155 dbm later on in the mission. The nominal threshold for 137.5 bits/sec was -152 dbm, indicating, in this case, that bad telemetry was in part a result of below threshold SNRs.

The second degradation effect was less obvious, causing bad data during periods of high power operation or during periods of low power operation when the reported signal levels were above threshold. During these periods, word errors occurred in a periodic manner at the spacecraft tumble rate. (A more detailed discussion of data quality can be found in Section 5.4, signal processing.) Correct telemetry discrimination and decommutation require that the DSIF receiver be phase coherent, or phase locked, to the spacecraft transmitted carrier. Momentary loss of phase lock will, in general, result in transients in the data stream or short periods of bad data. Phase lock is maintained as long as errors in the tracking loop remain within  $\pm 90$  degrees. The tumbling spacecraft resulted in excessive tracking loop errors which could have caused periodic bad data.

The primary loop errors are phase jitter due to noise and error caused by the sinusoidal carrier modulation resulting from the spinning omnidirectional antenna. Figure 5.3-5 shows the primary loop errors as a function of a single omnidirectional rotation. At the top of the figure, the omnidirectional antenna is shown in four positions relative to the DSIF station. The typical omnidirectional antenna gain pattern is shown at each position with the relative gain in the direction of the DSIF station as  $G_1$ ,  $G_2$ ,  $G_3$ , and  $G_4$ .

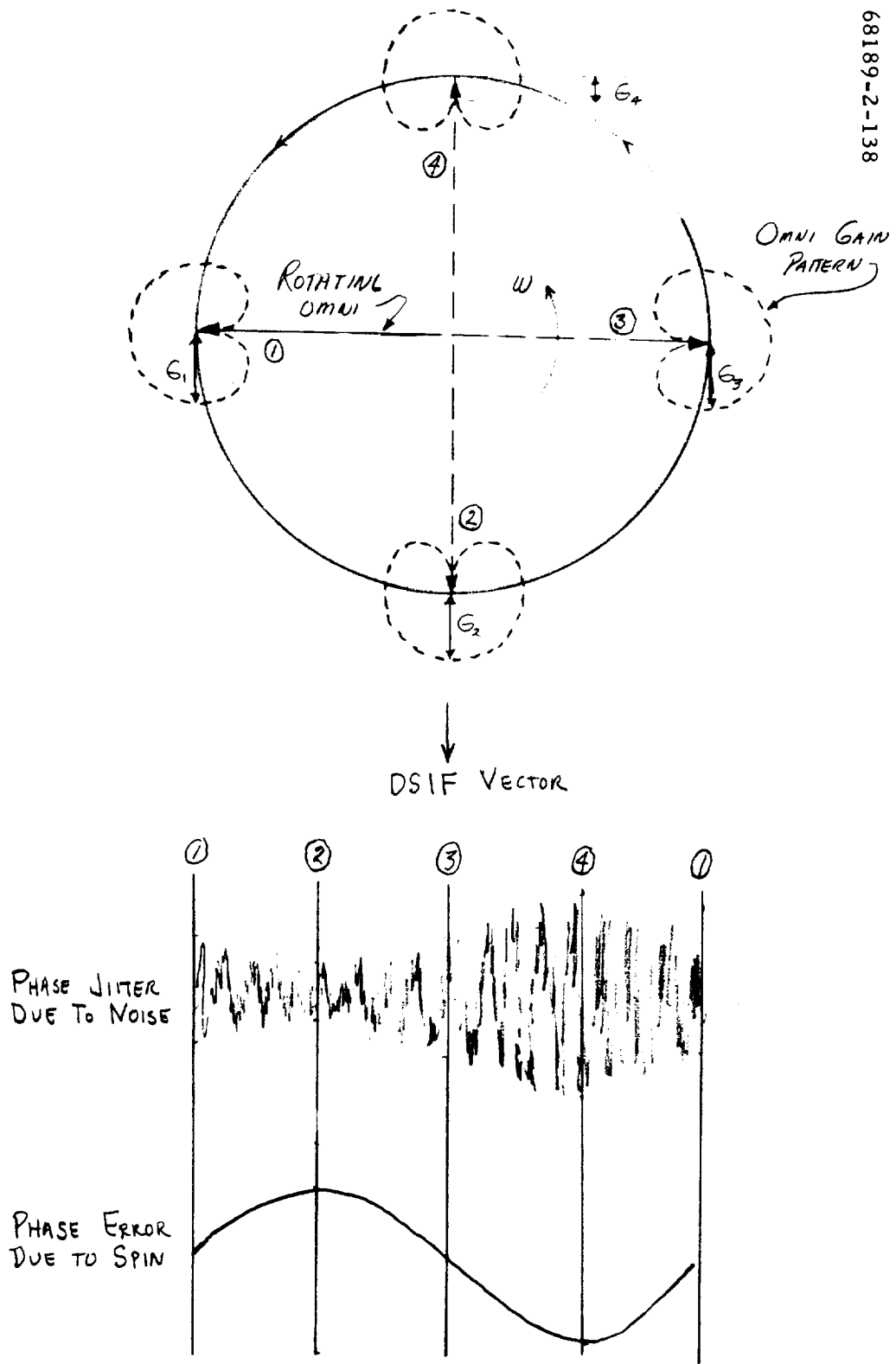


Figure 5.3-5. Carrier Tracking Loop Error

The gain goes through a maximum and minimum value on every rotation. The phase jitter due to receiver noise is shown as a function of omnidirectional position. The expression for the RMS jitter due to noise is given by

$$e_{\text{jitter}} \text{ (RMS)} = \sqrt{\frac{N}{S}} \quad (1)$$

where

N = receiver noise power  
S = received carrier power

Since received carrier power is directly related to transmitter antenna gain, Equation 1 can be expressed as

$$e_{\text{jitter}} \text{ (t)} = \sqrt{\frac{N}{KG(t)}} \quad (2)$$

where

G(t) = omnidirectional antenna gain  
K = lumped constant link parameters

The phase error due to spacecraft spin is also shown as a function of omnidirectional antenna position. The spinning motion of the omnidirectional antenna causes a doppler shift of the transmitted carrier given by

$$\Delta W_D = \frac{W_c W_s A}{c} \sin W_s t$$

where

$W_c$  = carrier frequency (rad/sec)  
 $W_s$  = spin frequency (rad/sec)  
A = maximum displacement of the omnidirectional head in the direction of the station  
c = velocity of light

The carrier tracking loop error resulting from the existence of this modulation being tracked by the phase lock loop is given by

$$e_{\text{steady state}} = \frac{\Delta W W_s}{B_o^2} \left[ \frac{S/N (W_s t)}{\sqrt{\frac{1}{\mu^2} + \frac{2W_s^2}{\mu^2 B_o^2} (1 - \mu) + \left(\frac{W_s}{B_o}\right)^4}} \right]$$

where

- $\Delta W$  = maximum frequency shift due to spin
- $B_0$  = loop natural frequency at threshold
- $\mu$  = ratio of limiter voltage suppression factors for threshold and actual signal level

Since the RMS jitter due to noise will ride on top of the sine error, it is clear that at position 4 (Figure 5.3-5) the peak loop error is maximum and, at this point, the loop could momentarily lose lock.

Figure 5.3-6 has plots of DSIF receiver AGC and dynamic phase error starting at 7 seconds after midcourse (05:00:19 GMT). As can be noted, the time of the decrease in receiver AGC corresponds to the time when large noise spikes occurred in the dynamic phase error. Also, the noise spikes occurred on the negative peak of the sine wave, as predicted.

Figure 5.3-7 shows the dynamic phase error at DSIF-42 during retro ignition. The loop error shows the effect described above and, in fact, right after ignition loss of lock can be seen on almost every negative peak of the sine wave. (Loss of lock occurs when the peak goes to the outer limit of the grid.) The loop bandwidth ( $B_0$ ) at DSIF-42 had been modified prior to this time to accommodate the tumbling spacecraft and was approximately two times wider than the other DSIF station bandwidths. These data clearly show that the proposed problem did exist, even with a wider loop bandwidth. It is thus concluded that this mechanism also caused periodic bad data throughout the tumbling phase of the mission.

### 5.3.3 Summary and Conclusions

Table 5.3-4 contains a summary of the measurable performance parameters compared with applicable requirements and premission predictions. Most subsystem parameters are not directly measurable, and those that are measurable are difficult to summarize due to time variability.

Received signal level, for example, is a function of time and spacecraft attitude. The summary for these parameters reflects wide tolerances, with corresponding wide variations in actual performance, in cases when the earth vector was in the omnidirectional antenna null. Performance and predictions outside the null are much more closely bounded. More detailed information is found in the subsections dealing with each mission phase.

The following conclusions can be drawn as a result of the foregoing analysis:

- 1) RF subsystem performed as expected with the exception of receiver B. In most cases, close to nominal performance was experienced in both the up- and downlinks.

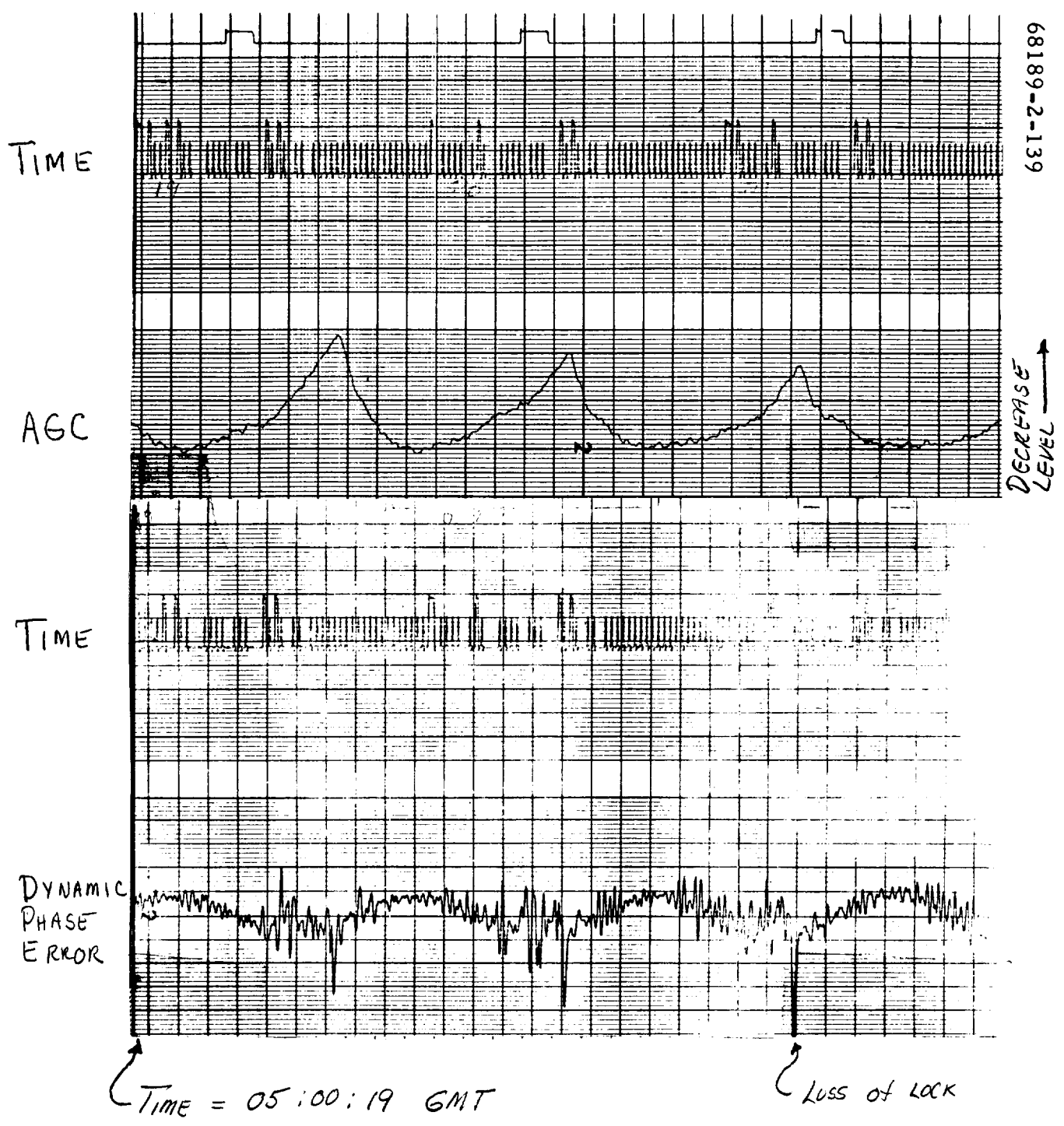
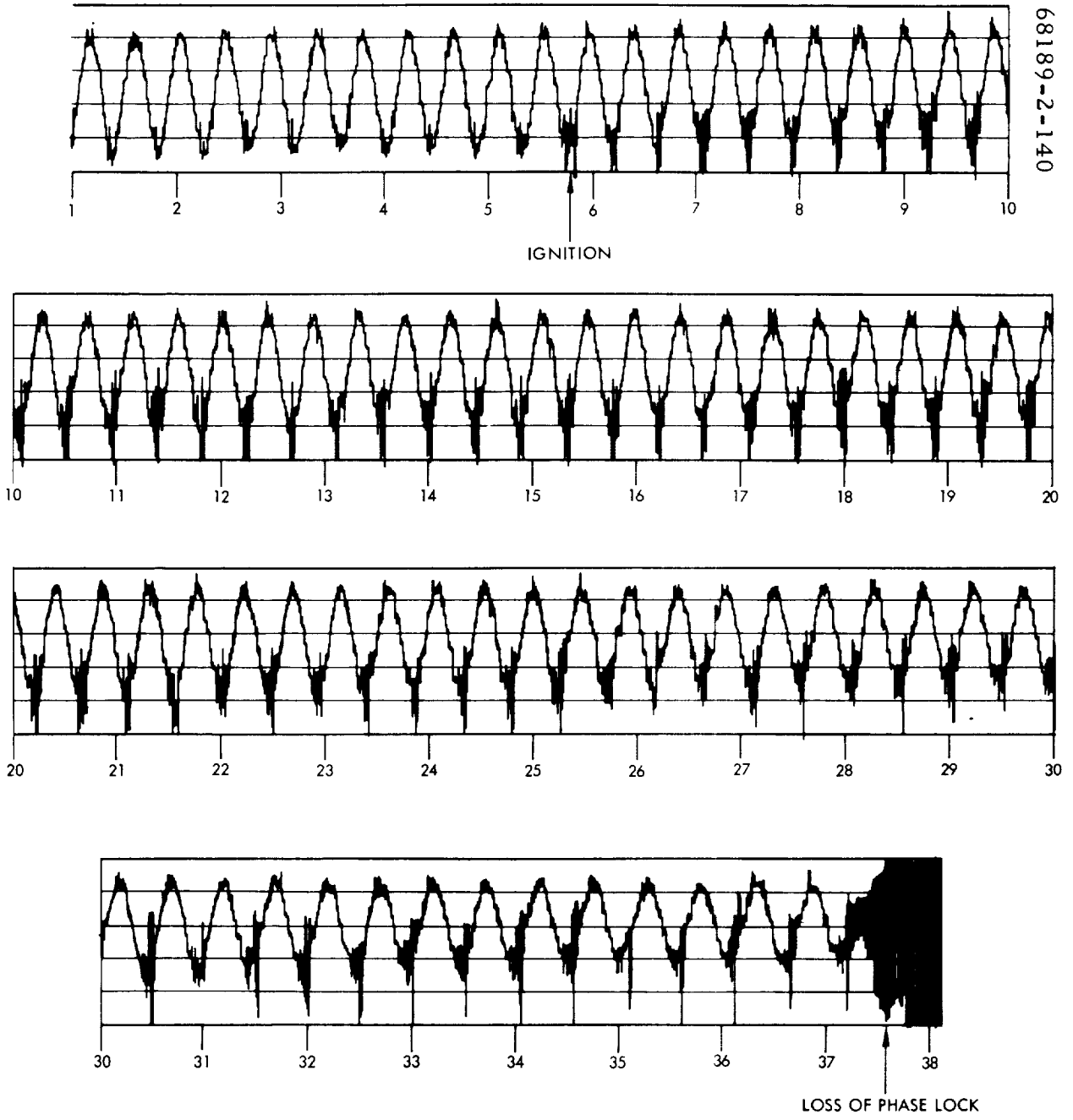


Figure 5.3-6. DSIF Automatic Gain Control and Dynamic Phase Error at Midcourse



NOTE:  
VERTICAL LINES ARE TIMING TICKS  
LOCATED ONE SECOND APART.  
NUMBERS ARE INCLUDED ONLY TO  
INDICATE SEQUENCE AND HAVE NO  
TIME MEANING.

Figure 5.3-7. DSIF-42 Dynamic Phase Error Variations During Retro Ignition



TABLE 5.3-4. PERFORMANCE PARAMETER SUMMARY

Parameter	Predicted Value	Requirement	Actual Performance
Transmitter frequency at acquisition	2295.001694 mc	2295 mc $\pm$ 23 kc	2294.999779 mc (5 seconds after one-way acquisition)
Receiver B frequency at acquisition	2113.309168 mc	2113.31 mc $\pm$ 21 kc	2113.318944 mc (at two-way acquisition)
Receiver A signal levels during coast phases	Time variable predictions. Predicts are some nominal value $\pm$ 12 db.	> -114 dbm*	Level between 2 and 4 db above nominal and $\geq$ -95 dbm
Receiver A signal** levels during star maneuver	Time variable predictions. Predicts are some nominal value $\pm$ 10 db.	> -114 dbm*	Level between +17.0 and -13.0 db about nominal and > -116 dbm
Receiver B signal levels during coast phases	Time variable predictions. Predicts are some nominal value $\pm$ 7 db.	> -114 dbm*	Level between +1.0 and +3.6 db above nominal and $\geq$ -107 dbm
Receiver B signal** levels during star maneuver	Time variable predictions. Predicts are some nominal value $\pm$ 10 db.	> -114 dbm*	Level between 6 and -7 db about nominal and > -112 dbm
DSIF signal levels during coast phases	Time variable predictions. Predicts are some nominal value $\pm$ 8 db.	> -136.7 dbm (carrier power) (17.2 bits/sec threshold)	Level between +0.5 and -2.5 db of nominal and > -139 dbm at 1100 bits/sec
DSIF signal levels** during star maneuver	Time variable predictions. Predicts are some nominal value $\pm$ 10 db.	None	Level between +4 and -13 db of nominal and > -150 dbm
DSIF signal levels during midcourse maneuver	Time variable predictions. Predicts are some nominal value $\pm$ 3 db.	> -135.4 dbm (carrier power) (at 4400 bits/sec - high power)	Level between +1 and -3.0 db of nominal and > -124 dbm
Transmitter A high power output	40.6 <sup>+0.3</sup> <sub>-0.05</sub> dbm	> 39.6 dbm	No data
Transmitter A low power output	21.09 <sup>+0.21</sup> <sub>-1.19</sub> dbm	> 19.1 dbm	No data
Transmitter B high power output	40.6 <sup>+0.1</sup> <sub>-0.1</sub> dbm	> 39.6 dbm	Output between 40.6 and 40.0 dbm
Transmitter B low power output	21.1 <sup>+1.2</sup> <sub>-0.2</sub> dbm	> 19.1 dbm	Output between 19.8 and 19.2 dbm
Phase jitter 12 cps bandwidth	< 36 degrees	< 36 degrees (3 $\sigma$ )	No data
Phase jitter 152 cps bandwidth (thrust phase)	< 22 degrees	< 22 degrees (3 $\sigma$ )	Jitter < 4.0 degrees (3 $\sigma$ ) prior to midcourse thrust
Command reject rate	< 1/2000	$\leq$ 1/2000 at signal level > 114 dbm	No rejected commands in 125 sent at signal levels > -95 dbm
Telemetry bit error rate	< 3/1000	$\leq$ 3/1000 at input SNR $\geq$ 11 db	Minimum BER $\approx$ 2.8 $\times$ 10 <sup>-3</sup> at input SNR = 10 $\pm$ 0.7 db

\*Threshold value applies to command threshold and, as such, only requires one of the two receivers to be above -114 dbm at any one time.

\*\*The star maneuver caused the earth vector to pass through deep antenna nulls where the greatest uncertainty in gain exists.

- 2) Performance of receiver B was not as predicted. The telemetered AGC was grossly in error, requiring a complete in-flight recalibration. Postmission analysis of pertinent data and special tests indicate that the receiver was degraded by approximately 16 db. Although operational problems would have resulted, this degradation would not have aborted the mission had it continued to the terminal descent phase.
- 3) New omnidirectional antenna pattern measurement data, taken on the JPL range, was quite accurate in the regions viewed during the mission. Very good agreement was noted where gain levels were above -10 db, with lesser but still surprisingly good agreement at -15 to -20 db. Omnidirectional antenna A uplink patterns (2113 mc) were noted to be less in agreement with measured data. This was expected since the patterns were measured with a dipole angle which was different than that of SC-2. It is concluded that these data demonstrate the sensitivity of the patterns to positional tolerances of the omnidirectional antennas.
- 4) RF subsystem premission predictions and real-time analysis techniques used during Mission B were relatively accurate and, in most cases, were conservative.
- 5) RF link performance was good during the tumbling phase of the mission for both telemetry and command links. Data quality was substandard relative to a normal mission, but still adequate. The fact that a two-way (transponder) link was maintained with a degraded receiver (receiver B) and with 1-second doppler oscillation on the signal level is a measure of how well the system performed.

The following recommendations are made:

- 1) Both Missions A and B had problems with receiver AGC telemetry. Considering this, it is strongly recommended that a system calibration be made during STV tests and that all applicable prelaunch tests run at AFETR clearly check for AGC changes. This information is not only required for postmission analysis, but also may help flag any impending receiver failures or partial failures leading to degraded performance.
- 2) Temperature transducers should be placed on the transmitter and receiver modules that contain the respective VCXOs. It is very difficult, if not impossible, to correlate unit temperature data to any single presently telemetered temperature. The ability to check prelaunch frequency reports and to update DSIF tracking predictions is severely lessened because of this lack of correlation between frequencies and telemetered temperature data.

- 3) Recovery of DSIF station data for use in postmission analysis is not being done correctly. Although much data was received for SC-2, there was an almost complete lack of all the calibration data needed to translate oscillograph deflections back to physical parameters (i. e., dbm) at the DSIF station. Many pieces of calibration information were provided, but never enough to determine the final curve in absolute engineering units.

#### 5.3.4 SUBSYSTEM PERFORMANCE ANALYSIS

##### 5.3.4.1 General Discussion

Before specific phases are discussed, a general treatment of the mission will be undertaken. Information applicable to all mission phases is included in this subsection.

##### Subsystem Parameters

Most quantitative estimates of performance are based on received signal levels which, in turn, are determined from individual link parameters. Those parameters used in the performance predictions and the subsystem analyses are tabulated in Table 5.3-5. Equations using these data are derived here; parameters discussed in later portions can be evaluated from these data. Tables 5.3-5 and 5.3-6 consist of measured data taken from flight acceptance (FAT), solar thermal vacuum (STV), and command and data handling console (CDC) tests or specification values where measurements were not available.

##### Computations Used

In this subsection, reference is made to received signal levels and quantities computed from these levels. The equations used are listed below and will not be derived again:

- 1) Spacecraft transmitter high power output is

$$P_{xmtr}(\text{dbm}) = 10 \log (P_{tm} \times 10^3) + L$$

where

$$P_{xmtr} = \text{transmitter power (dbm)} = P_{high}$$

$$P_{tm} = \text{telemetered power output (watts)}$$

$$L = \text{loss from transmitter to power monitor} \approx 1.5 \text{ db (value determined from pre-STV hardline calibration data)}$$

TABLE 5.3-5. UPLINK PARAMETERS FROM FAT, STV, AND CDC TESTS

<u>Description</u>	<u>Value</u>
Transmitting system (DSIF)	
RF power	70.0 <sup>+0.5</sup> <sub>-0.0</sub> dbm
Antenna gain	
SAA	20.0 ± 2.0 db
SCM	51.0 (+1.0, -0.5) db
Circuit loss	
SAA	-0.5 ± 0.0 db
SCM	-0.4 ± 0.1 db
Receiving system (SC-2)	
Circuit loss	
Receiver A	-3.2 ± 0.3 db
Receiver B	-3.7 ± 0.3 db
Uplink carrier tracking loop	
Equivalent noise	
Bandwidth	240 ± 24 Hz
Threshold SNR	12 db
Uplink channel	
Threshold SNR	9 db
System noise	
Temperature	2700°K
Equivalent noise	
Bandwidth (predetection)	13430 Hz
Data/subcarrier modulation index	7.2
Subcarrier/carrier modulation index	1.6 ± 0.16

TABLE 5.3-6. DOWNLINK PARAMETERS FROM FAT,  
STV, AND CDC TESTS

<u>Description</u>	<u>Value</u>
Transmitting system (SC-2)	
RF power	
Transmitter A (low power)	21.09 (+0.21, -1.19) dbm
Transmitter B (low power)	21.1 (+1.2, -0.2) dbm
Transmitter A (high power)	40.6 (+0.3, -0.05) dbm
Transmitter B (high power)	40.6 (+0.1, -0.1) dbm
Planar array gain	27.0 ± 0.5 db
Circuit loss	
Transmitter A Omnidirectional antenna A	-2.0 (+0.2, -1.0) db
Transmitter B Omnidirectional antenna A	-1.8 (+0.2, -1.0) db
Transmitter A Omnidirectional antenna B	-2.8 (+0.2, -1.0) db
Transmitter B Omnidirectional antenna B	-2.7 (+0.2, -1.0) db
Planar array	-2.2 (+0.0, -0.3) db
Carrier frequency	2295 MHz
Receiving system (DSIF)	
Antenna gain	
SAA (acquisition aid antenna)	21.0 ± 1.0 db
SCM (85-foot antenna)	53.0 (+1.0, -0.5) db

Table 5.3-6 (continued)

<u>Description</u>	<u>Value</u>
Circuit loss	
SAA	-0.5 ± 0.0 db
SCM	-0.18 ± 0.05 db
Effective noise temperature	
Maser	55 ± 10°K
Parametric	
Amplifier (Johannesburg SAA antenna)	320 ± 50°K
Lunar temperature	110 ± 25°K
Carrier channel	
Equivalent noise bandwidth for maneuvers (at threshold)	152 Hz
Equivalent noise bandwidth for coast mode (at threshold)	12 Hz
Threshold SNR	
Acquisition	9.0 db
Maneuvers	14.0 ± 1.0 db
Coast mode	11.4 db
SCO descriptions	
Equivalent predetection noise bandwidth, Hz ± 10 percent	
4400 bits/sec	4770
1100 bits/sec	1190
550 bits/sec	644
137.5 bits/sec	158.5
17.2 bits/sec	25.1
Strain gage 1	281
Strain gage 2	524
Strain gage 3	464
Reject/enable	377
Gyro speed	874

Table 5.3-6 (continued)

<u>Description</u>	<u>Value</u>
SCO center frequencies, KHz	
4400 bits/sec	33.0
1100 bits/sec	7.35
550 bits/sec	3.90
137.5 bits/sec	0.96
17.2 bits/sec	0.56
Strain gage 1	1.70
Strain gage 2	3.00
Strain gage 3	5.40
Reject/enable	2.3
Gyro speed	5.4
Threshold signal-to-noise ratio for telemetry data, $\pm 1.0$ db	
4400 bits/sec	10.0
1100 bits/sec	10.0
550 bits/sec	10.0
137.5 bits/sec	10.0
17.2 bits/sec	10.0
Strain gage 1	7.0
Strain gage 2	7.0
Strain gage 3	7.0
Reject/enable	10.0
Gyro speed	10.0
SCO modulation indices, $\pm 10$ percent	
4400 bits/sec	1.6
1100 bits/sec	0.935
550 bits/sec (acquisition)	0.3
550 bits/sec	1.15
137.5 bits/sec	1.45
17.2 bits/sec	1.45
Strain gage 1	0.615
Strain gage 2	0.615
Strain gage 3	0.61
Reject/enable	0.655
Gyro speed	1.600

2) Spacecraft transmitter low power output is

$$P_{\text{low}} = P_{\text{high}} - P_{\text{DSIF}_H} + P_{\text{DSIF}_L} \text{ (dbm)}$$

where

$P_{\text{low}}$  = transmitter low power output

$P_{\text{high}}$  = telemetered transmitter high power output

$P_{\text{DSIF}_H}$  = DSIF received signal level at high power

$P_{\text{DSIF}_L}$  = DSIF received signal level at low power

3) Spacecraft omnidirectional antenna gain (uplink) is

$$G_R = \frac{P_R}{P_T G_T \left(\frac{\lambda}{4\pi R}\right)^2 L}$$

where

$G_R$  = received omnidirectional antenna gain (uplink gain)

$P_R$  = received signal level (determined from spacecraft AGC)

$P_T$  = DSIF nominal transmitter power

$G_T$  = DSIF nominal antenna gain

$\lambda$  = wavelength of uplink signal

$R$  = slant range at time of computation

$L$  = nominal spacecraft and DSIF losses

(Note: For downlink gain, appropriate downlink parameters are inserted in a similar equation.)



4) Signal-to-noise ratio (SNR) for any subcarrier is

$$\text{SNR} = \frac{P_S}{P_N} = \frac{M P_R}{K T_{\text{eff}} \text{BW}_{\text{sc}}}$$

where

$P_S$  = signal power in predetection noise bandwidth

$P_N$  = total noise power in predetection noise bandwidth

$M$  = carrier to subcarrier modulation loss adjustment constant based on subcarrier oscillation modulation index on the carrier

$P_R$  = received carrier power reported by the DSIF

$K$  = Boltzmann's constant

$T_{\text{eff}}$  = DSIF system temperature reported by the DSIF

$\text{BW}_{\text{sc}}$  = subcarrier equivalent predetection noise bandwidth

When using these equations, attention must be given to the desired accuracy of the answer. Since several parameters not measurable in flight, spacecraft telemetry, and DSIF station reports are used, computed parameters have potentially large errors. Their validity is thus weighed against similar test data and/or is judged quite subjectively based on past experience. These equations are not used so much for their numerical results as for the total picture of subsystem performance generated. Any gross subsystem problems or computation errors will tend to be uncovered in this analysis, but subtle errors will not.

#### Bit Error Rate Calculations

One subsystem parameter of interest is telemetry bit error rate (BER). This parameter serves as an example of the problems encountered when attempting to evaluate postmission data. BER is required to be less than  $3 \times 10^{-3}$  at input SNR ratios of  $10 \pm 1$  db. (A change effective with SC-3 will allow only  $9 \pm 1$  db for a BER of  $3 \times 10^{-3}$ .) BER cannot be measured in flight, but the word error rate can. Therefore, real-time printer data were used, assuming a bad parity word represented a single bit error. With the additional assumption that the data used were representative, the worst observed BER was computed (see Table 5.3-7).

TABLE 5.3-7. BIT ERROR RATE DATA SUMMARY FOR DAY 265

Time, hr:min:sec	Number of Bits	Parity Errors	BER
03:29:59 to } 03:35:42 }	3256	2	$0.6 \times 10^{-3}$
03:35:55 to } 03:47:28 }	5192	4	$0.8 \times 10^{-3}$
03:48:06 to } 03:56:34 }	4224	3	$0.7 \times 10^{-3}$
03:57:10 to } 04:04:47 }	4224	14	$\frac{25}{8888} = 2.8 \times 10^{-3}$
04:05:24 to } 04:15:51 }	4664	11	

The SNR at this time of the observed high BER was computed as shown below from Equation 3:

DSIF AGC/1100 bits/sec at 04:07:45 = -138.7 dbm

System noise temperature = 44.7°K = 16.5 db  
(DSIF-11 pretrack)

Boltzmann's constant = -198.6 dbm/deg/cps

Bandwidth = 1190 Hz ± 10 percent = 30.75 (+0.41, -0.46) db

Noise power = -151.35 (+0.41, -0.46) dbm

Modulation loss

Carrier -2.01 (+0.40, -0.46) db

Subcarrier -4.56 (+0.62, -0.73) db

Δ modulation loss = -2.55 (+0.22, -0.27) db

Subcarrier power = -141.25 (+0.22, -0.27) dbm

SNR = subcarrier power - noise power = 10.10 ± 0.68 db

The tolerance on this computation is only approximate and is probably greater. Based on the SNR requirement of  $10 \pm 1$  db, the measured parameter (BER) meets the specification. However, it is not clear that the new requirement of a SNR of  $9 \pm 1.0$  would have also been met.

### Omnidirectional Antenna Gain Maps

In order to better visualize and interpret the significance of the signal level data, traces of the earth vector on the omnidirectional antenna gain contour maps are presented. Figures 5.3-8 and 5.3-9 show the antenna up- and downlinks. Since signal level variations are, for the most part, the result of increasing range (i.e., more space loss) and changing omnidirectional gain, these plots allow visualization of the expected signal level changes for comparison with plots of uplink and downlink signal levels versus time.

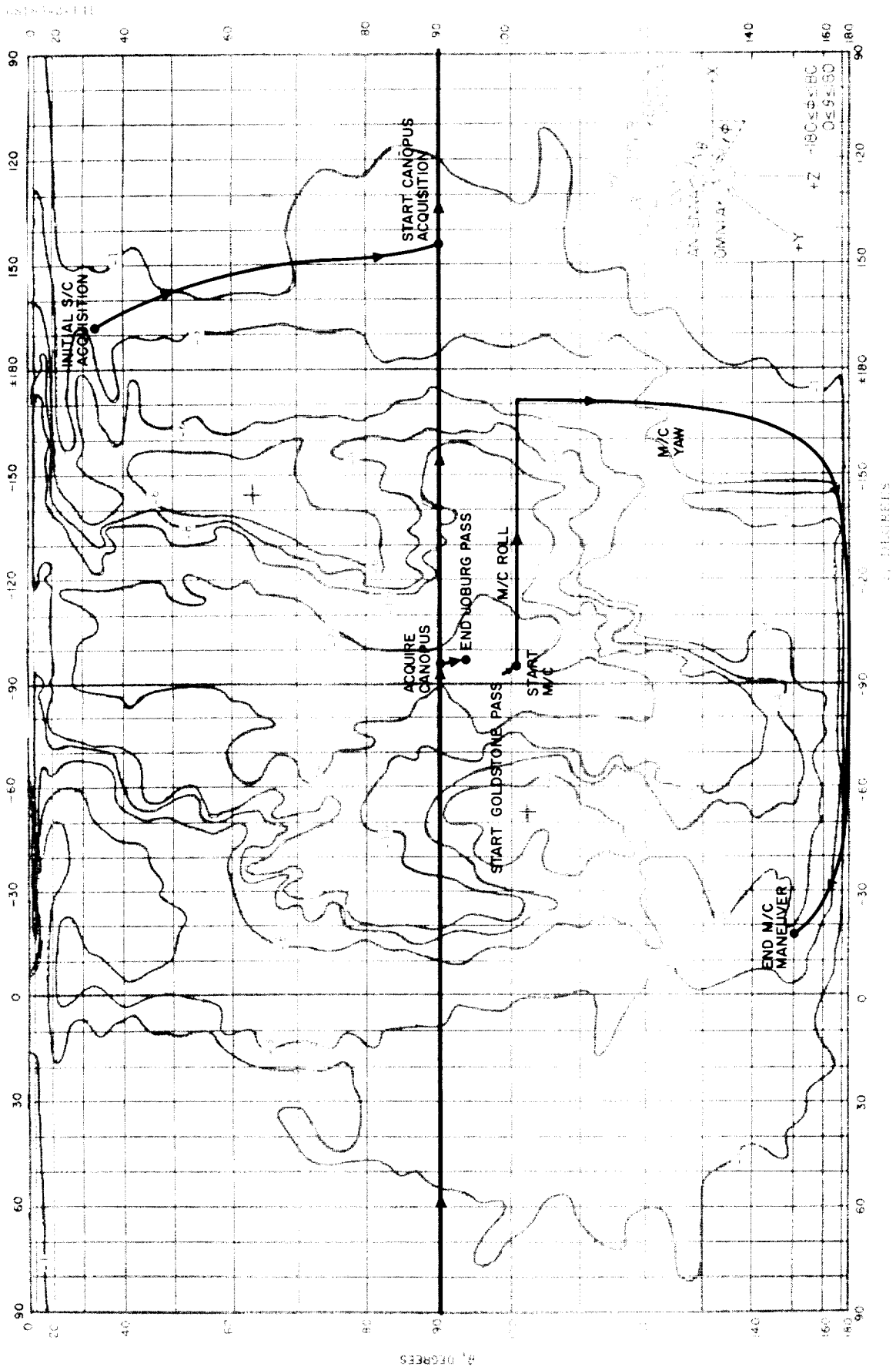
#### 5.3.4.2 Mission Phase 1: Prelaunch to Spacecraft Acquisition

During the prelaunch phase, subsystem performance is assessed during the launch pad systems readiness test (SRT) and prelaunch countdown test. Next to assuring normal system performance prior to launch, the most important subsystem data taken during this phase are transmitter and receiver frequency data. Frequency data are used to predict the frequencies at initial acquisition and are transmitted from the Cape prior to launch. The DSIF, in turn, uses these data to tune the DSIF receiver for one-way lock and the DSIF transmitter for eventual two-way lock.

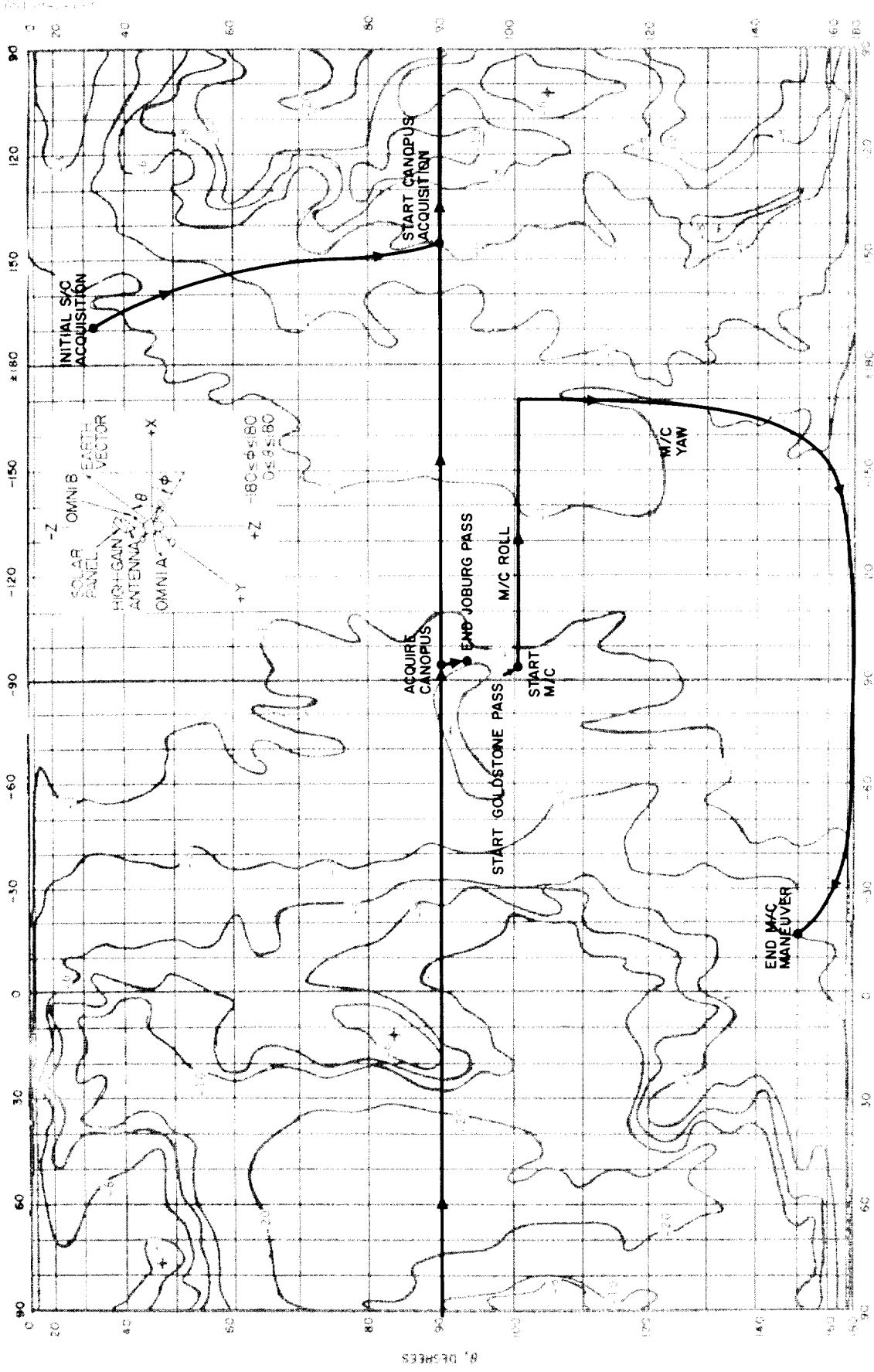
The prelaunch frequency data for the transmitter and receiver are plotted in Figure 5.3-10. Also, the measured frequencies, as well as the predicted frequencies at acquisition, are noted. These frequencies tended to decrease with time, with the notable exception of the receiver best-lock frequency in the L-10 report. Since a temperature increase always causes a frequency decrease, and since the temperature in the compartment was increasing, the data were considered reasonable with the exception of the receiver frequency at L-10. The temperature directly affecting the frequency is not actually measured, since the telemetered sensor is in the thermal tray and not at the voltage controlled crystal oscillator. Relative temperature versus frequency information is thus considered to be most reliable. (See recommendation 2 in subsection 5.3.3.) Based on this judgment, the receiver prediction frequency was taken from the L-20 report and the transmitter prediction frequency from the L-10 report.

The predicted frequencies were thus:

Transmitter (one-way) = 2295.001694 MHz  
Receiver (two-way) = 2113.309168 MHz

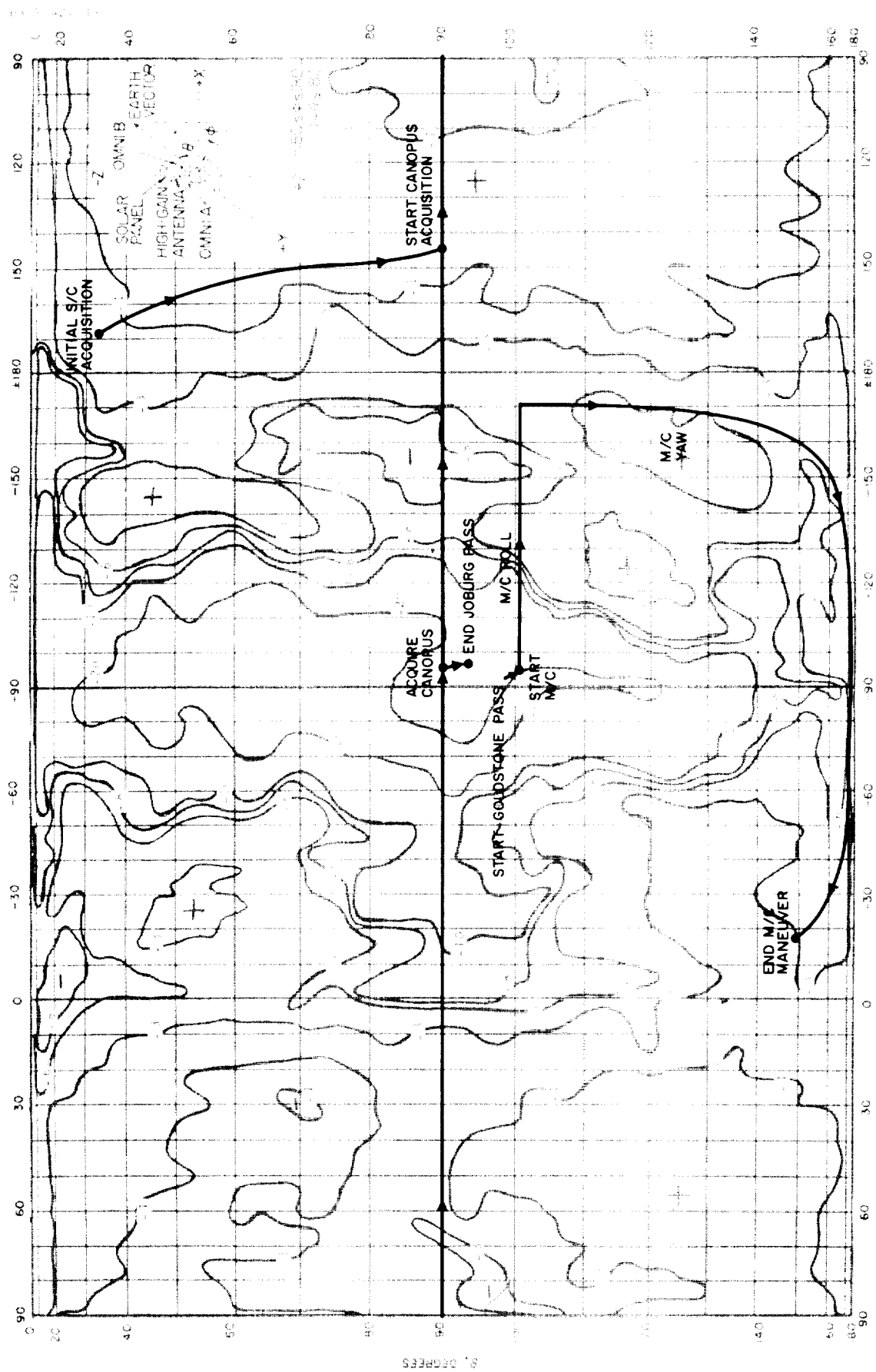


a) Omnidirectional Antenna A  
 Figure 5.3-8. Uplink (2295 MHz) Omnidirectional Antenna Gain Map



5. DEGREES

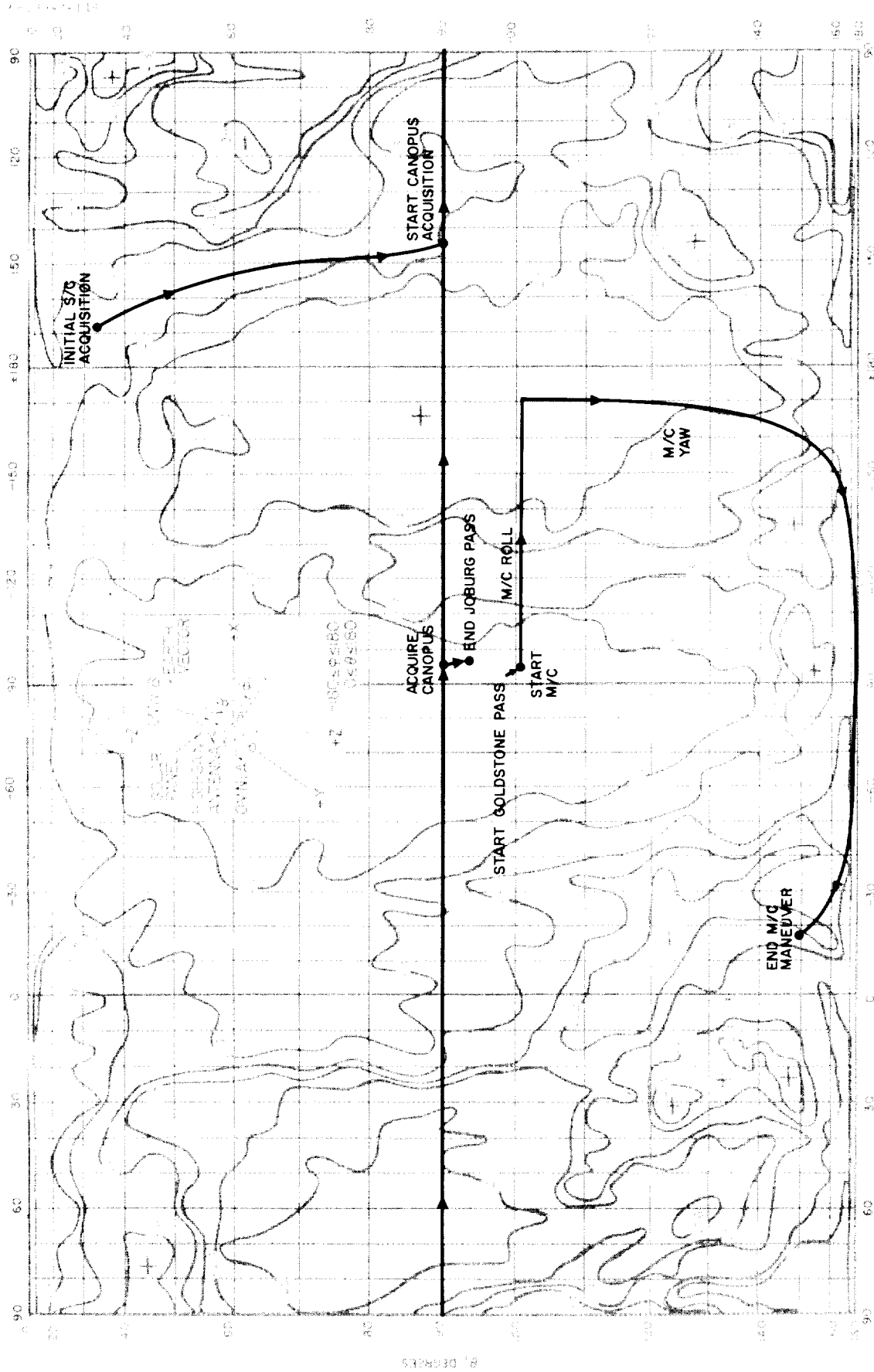
b) Omnidirectional Antenna B  
 Figure 5.3-8(continued). Uplink (2295 MHz) Omnidirectional Antenna Gain Map



SECRET

a) Omnidirectional Antenna A

Figure 5.3-9. Downlink (2113 MHz) Omnidirectional Antenna Gain Map



b) Omnidirectional Antenna B

Figure 5.3-9(continued). Downlink (2113 MHz) Omnidirectional Antenna Gain Map

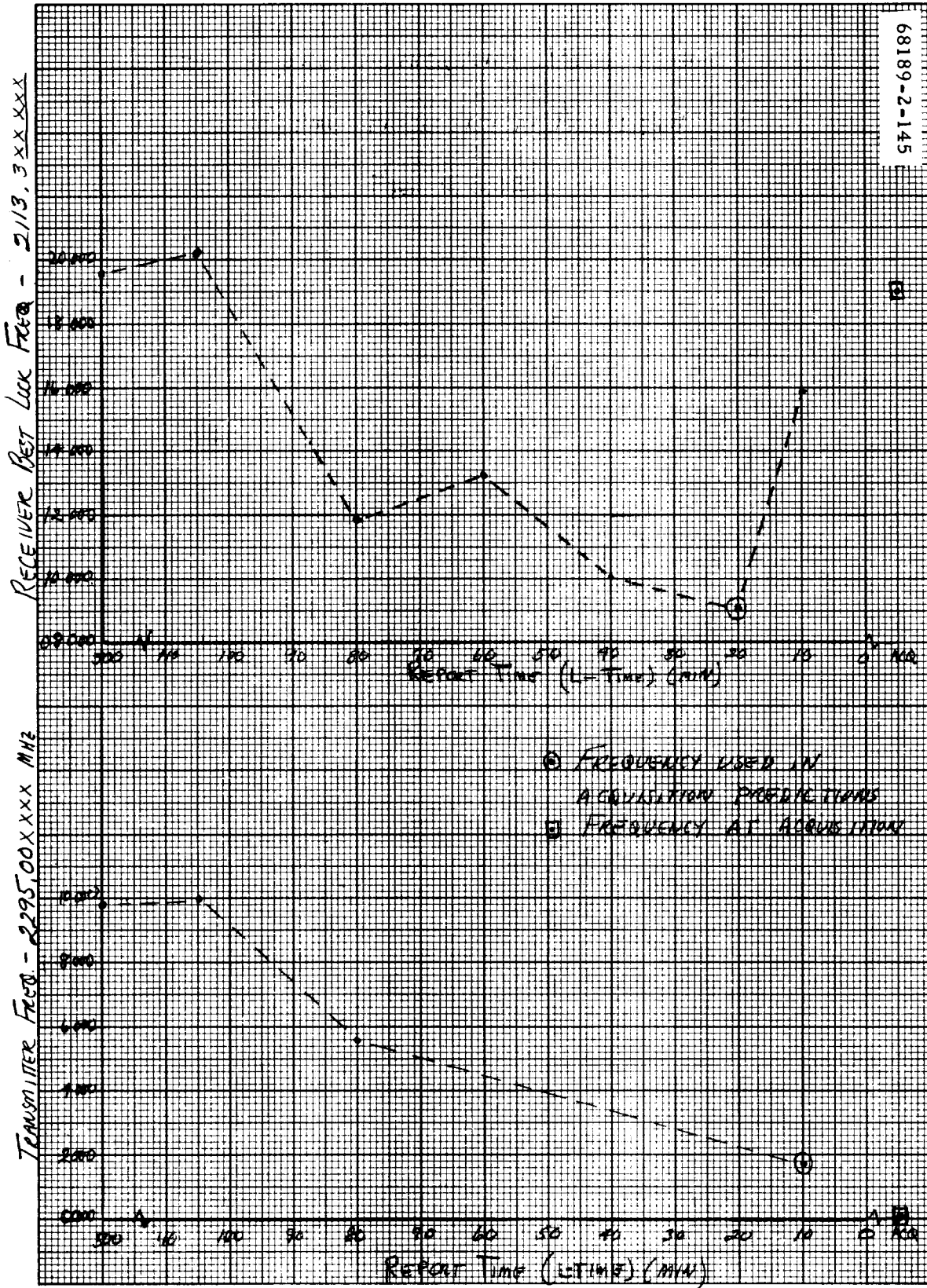


Figure 5.3-10. Prelaunch Frequency Data and Actual Frequency at Acquisition



The actual frequencies at initial acquisition (as shown on Figure 5.3-10) were:

Transmitter (one-way) = 2294.999779 MHz  
Receiver (two-way) = 2113.318944 MHz

The difference between predicted and actual was:

Transmitter = 1915 Hz  
Receiver = 9776 Hz

It should be noted that the actual receiver acquisition frequency was closer to the L-10 report frequency, which was discarded. Had this frequency been used, the error in prediction would have been reduced to 3.0 KHz.

Table 5.3-8 is a summary of the significant events during the initial RF acquisition at Johannesburg. The signal levels at receivers A and B during acquisition are shown in Figures 5.3-11 and 5.3-12. One-way acquisition was accomplished in about 12 seconds from first RF contact, and two-way lock was accomplished in 10 minutes. Problems with the antenna drive, coupled with a low receiver best-lock prediction frequency, caused a 5- to 6-minute delay in the two-way acquisition as compared with an optimum acquisition. Figure 5.3-11 shows that receiver A was captured in the AFC mode right after DSIF transmitter turned on. Antenna drive problems are also clearly shown as signal level variations in the receiver passband. Figure 5.3-12 indicates that the signal was in the passband of receiver B at turnon (the receiver has a 13 KHz passband), but because the turnon frequency was low, the doppler shift caused the signal to go out of the passband without locking up. DSIF transmitter tuning resulted in the signal slewing back into the receiver passband. Receiver phase lock is shown occurring about 3 minutes and 12 seconds after initial transmitter turnon.

The spacecraft high power transmitter was turned off 32 minutes and 12 seconds after being commanded to high power by the Centaur. The maximum allowable time to accomplish turnoff is 1 hour.

TABLE 5.3-8. ACQUISITION EVENTS

Event	GMT (Day 263), hr:min:sec	Comments
Transmitter B high power on	12:44:21	Spacecraft commanded to high power by Centaur.
Spacecraft signal first heard by DSIF	12:54:55	Initial contact 5 seconds prior to predicted first visibility.
DSIF acquires spacecraft in one-way mode	12:55:07	One-way acquisition in 23 minutes and 7 seconds from launch.
DSIF switch from acquisition antenna (SAA) to 85-foot dish (SCM)	12:57:10	DSIF unable to maintain contact with spacecraft on SCM.
DSIF switch from SCM to SAA	12:57:50	
DSIF switch from SAA to SCM	12:58:15	DSIF unable to maintain contact with spacecraft on SCM.
DSIF switch from SCM to SAA	12:58:20	
DSIF switch from SAA to SCM	13:00:00	DSIF now able to track spacecraft on SCM. Signal level at ground receiver increased 26 db due to increased gain.
DSIF transmitter turned on	13:01:36	
Signal in passband of both spacecraft receivers	13:01:46	(From telemetry) Receiver A in AFC capture mode. Receiver B not phase locked.
Phase lock receiver B	13:04:53	DSIF receiver dropped phase lock, indicating phase lock on receiver B.
DSIF acquires spacecraft in two-way mode	13:04:58	DSIF reacquired downlink, indicating complete two-way acquisition in 32 minutes and 58 seconds from launch.
DSIF confirms good two-way phase lock	13:04:59	
DSIF switch from SCM to SAA	13:05:10	DSIF unable to maintain contact with spacecraft on SCM.
DSIF switch from SAA to SCM	13:06:20	DSIF now able to track spacecraft on SCM. Signal level at ground receiver increased 27.8 db.
Transmitter B high power off	13:16:33	Spacecraft was in high power for 32 minutes and 12 seconds for initial acquisition phase (a maximum time of 1 hour is allowed).

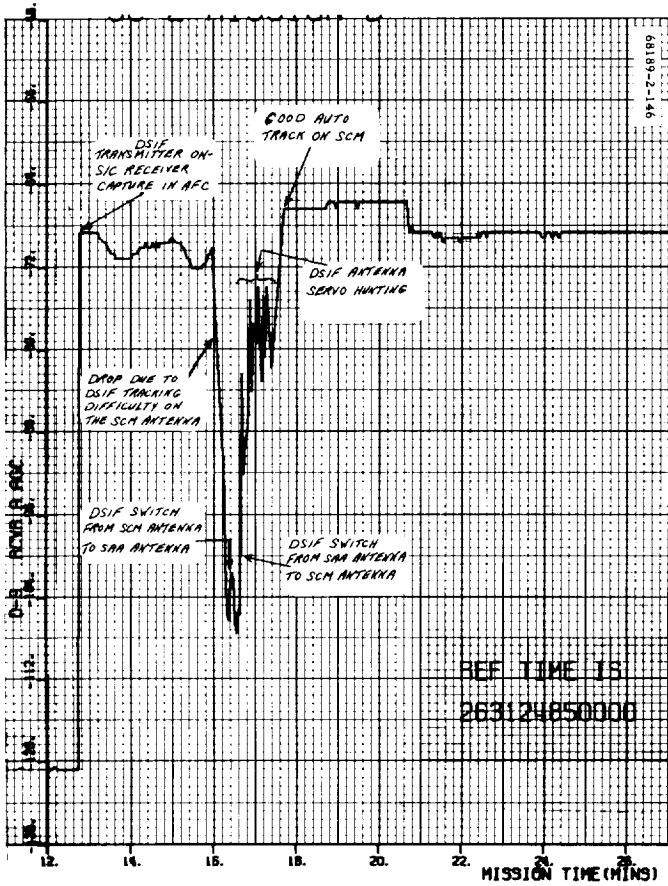


Figure 5.3-11. Signal Level at Receiver A During Acquisition

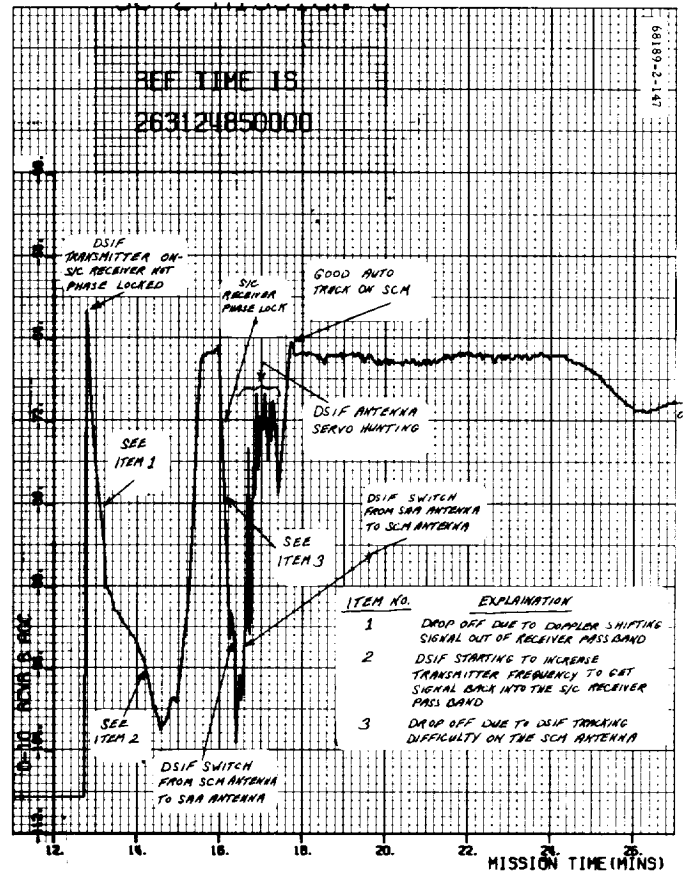


Figure 5.3-12. Signal Level at Receiver B During Acquisition

#### 5.3.4.2 Mission Phase Two: Coast

The coast phases consist of the following:

- 1) Pre-Canopus acquisition - Period from initial spacecraft acquisition until Canopus acquisition, during which time the spacecraft attitude is random in roll and the spacecraft -Z axis is pointed toward the sun.
- 2) Premidcourse - Period from Canopus acquisition until the midcourse maneuvers.

A normal mission would contain a third coast or postmidcourse phase. However, since the mission became nonstandard, the postmidcourse or tumbling phase will be treated separately.

Figures 5.3-13, 5.3-14, and 5.3-15 are plots of DSIF, Receiver A, and Receiver B signal levels from launch to the midcourse maneuver. The premission predicted signal level after Canopus acquisition is shown on each of these figures. Since the spacecraft attitude is random in roll prior to Canopus acquisition, no premission predictions are made for this period. After Canopus was acquired, the signal levels came into close agreement with the following predictions:

- 1) DSIF levels agreed to within +0.5 to -2.5 db of predicts.
- 2) Receiver A levels were +2 to +4 db above predictions.
- 3) Receiver B levels were +1 to +3 db above predictions.

Referring to Figures 5.3-8b and 5.3-9, which show traces of the earth vector relative to omnidirectional antenna B downlink and omnidirectional antennas A and B uplink gain contours, it can be noted that changes in signal levels during the pre-Canopus acquisition phase and right at Canopus acquisition are in complete agreement with the antenna gain contour maps. The antenna gains during the pre-Canopus phase were as follows approximately:

- 1) Omnidirectional antenna B downlink => -1 to -4 db going to -1 db at Canopus acquisition
- 2) Omnidirectional antenna A uplink => -2 to -1 db going to -10 db at Canopus acquisition
- 3) Omnidirectional antenna B uplink => -5 to -3 db going to -1 db at Canopus acquisition

Figures 5.3-14 and 5.3-15 show signal level variations caused by specific events during the coast phases. The special receiver threshold test (see subsection 5.3.2.1) and the station transfer from Johannesburg to Goldstone are of particular interest.

68189-2-148

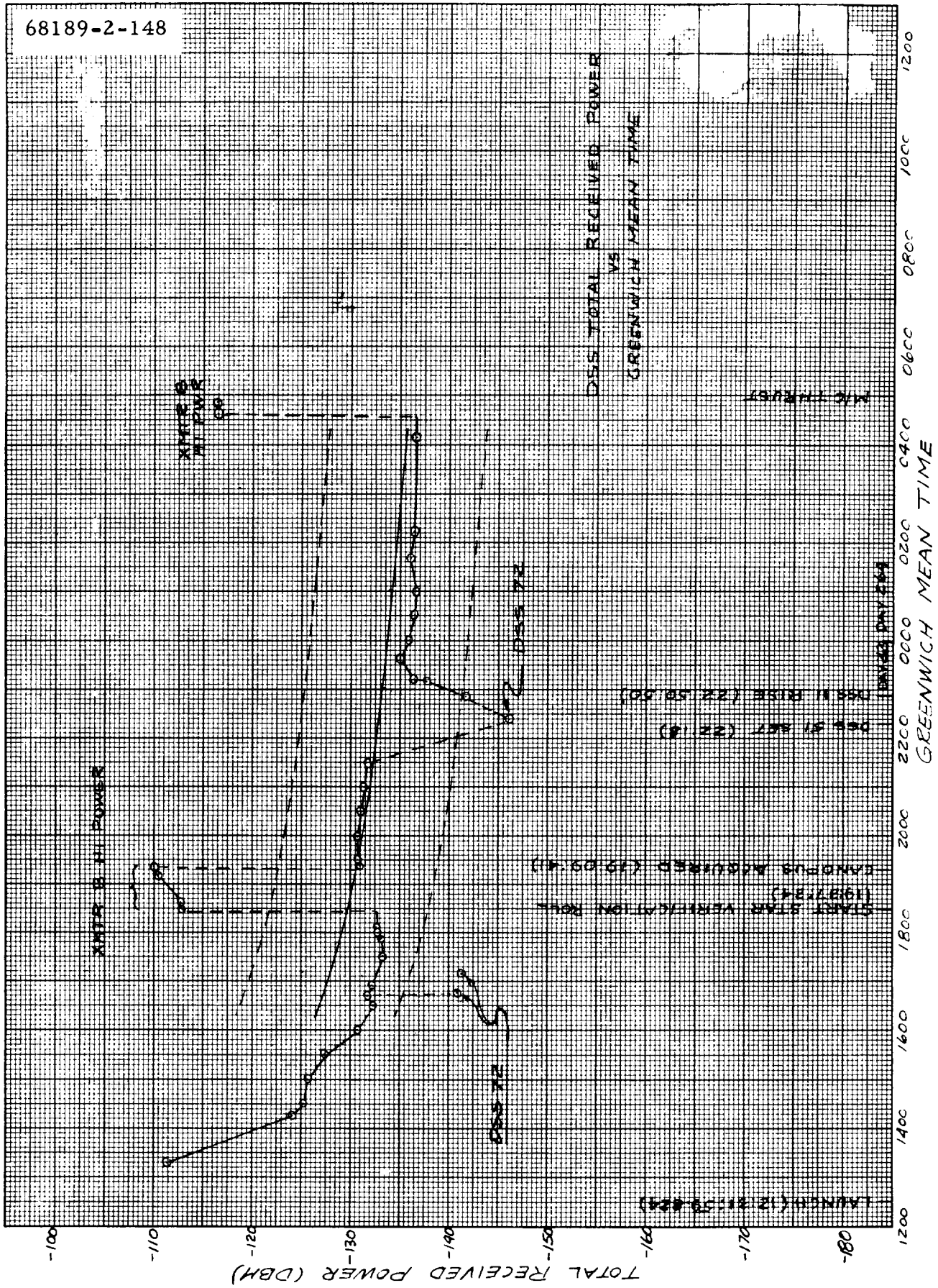


Figure 5.3-13. DSIF Total Received Power

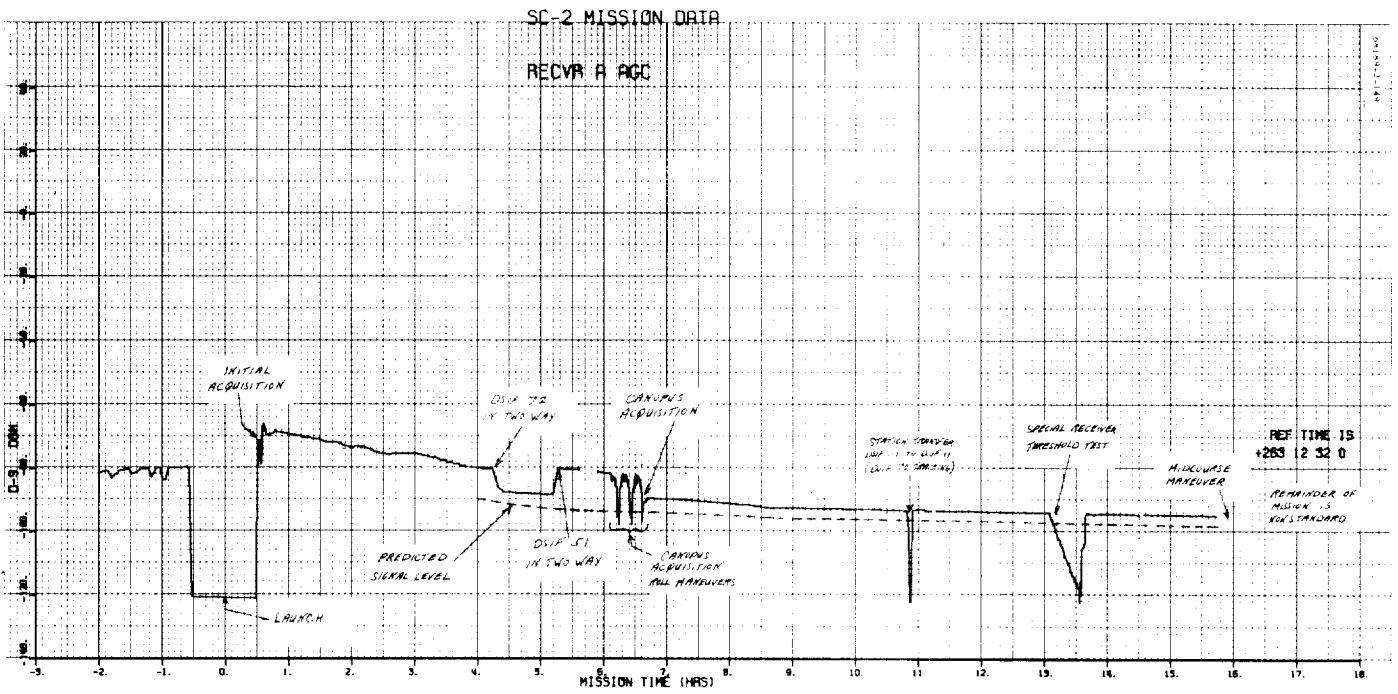


Figure 5.3-14. Receiver A Automatic Gain Control

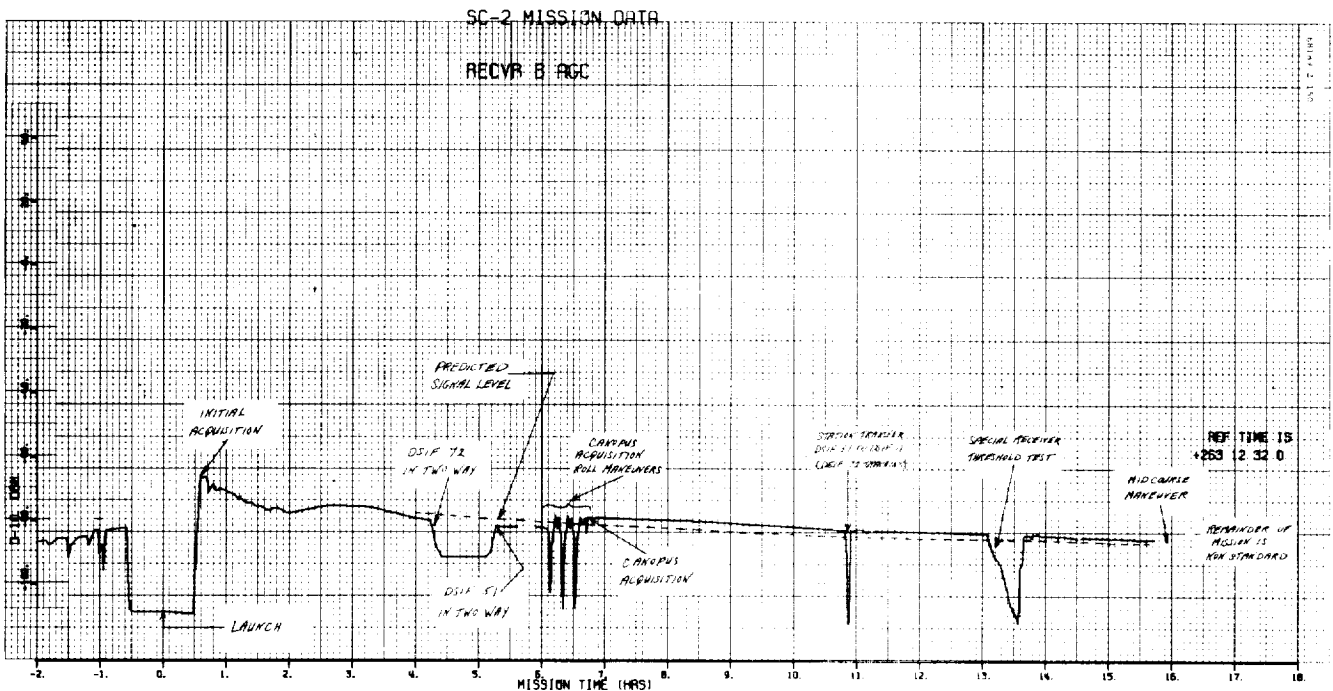


Figure 5.3-15. Receiver B Automatic Gain Control

#### 5.3.4.3 Mission Phase Three: Canopus Acquisition Maneuver

At approximately  $L + 7$  hours, the star acquisition maneuver was initiated. Two complete rolls about the Z axis were required in order to make a star map adequate to identify Canopus. An additional 240 degrees of roll were required to finally acquire the star.

Real-time analysis indicated that the roll maneuver would take the earth vector through deep antenna nulls, thus requiring that the data link be in one-way (nontransponding) mode. Also, analysis indicated that the downlink telemetry threshold could be exceeded during a portion of the roll maneuver if only omnidirectional antenna B was used for transmission. Omnidirectional antenna gains of  $-30.0 \pm 10$  db were predicted during this maneuver.

At 18:30:46 GMT, transmitter B was commanded to high power. Transponder B was turned off at 18:33:01 GMT, and DSS-51 reacquired the spacecraft in the NBVCXO mode. Star mapping was initiated at 18:37:34 GMT with the spacecraft transmission data in mode 5. The initial roll on omnidirectional antenna B produced downlink signal variations of approximately 40 db which agreed with the premaneuver predictions. Spacecraft data were sustained throughout the maneuver but were sufficiently noisy that another roll on omnidirectional antenna A was initiated at 18:54:45 GMT. A complete star map was obtained from the two rolls. Spacecraft-received signal levels during the roll maneuver indicated deviations of approximately 34 db on receiver A and 30 db on receiver B. This again agreed with premaneuver predictions. However, it was at this point that the 20-db bias in the receiver B absolute signal level was detected. This anomaly was discussed earlier in subsection 5.3.2.1. Omnidirectional antenna B was again selected at 19:06:37 GMT and the spacecraft allowed to roll until Canopus was acquired. It was necessary to manually lock on to Canopus, and this step was initiated at 19:11:57 GMT.

At 19:14:21 GMT, transponder B was turned on, and DSS-51 acquired the spacecraft in two-way lock at 19:15:39 GMT. Transmitter B high power was commanded off at 19:22:05 GMT, which resulted in 51 minutes and 19 seconds of high power operation for star acquisition. The DSS-51-received signal level for low power operation was  $-132.9$  dbm, a 20.9-db decrease from high to low power operation. A nominal 1100 bits/sec telemetry margin of +5.0 db existed at this point.

Figure 5.3-16 is a plot of the DSIF signal level during the period of the star maneuver, with significant event times noted. Figures 5.3-17 and 5.3-18 are expanded plots of the same data taken from station reports. The equivalent omnidirectional antenna gain is also shown. Since the resolution of the expanded data is relatively poor, comparative antenna gains are shown only at selected points. Signal level variations agree well with the antenna gain values, giving a high degree of confidence in the antenna patterns.

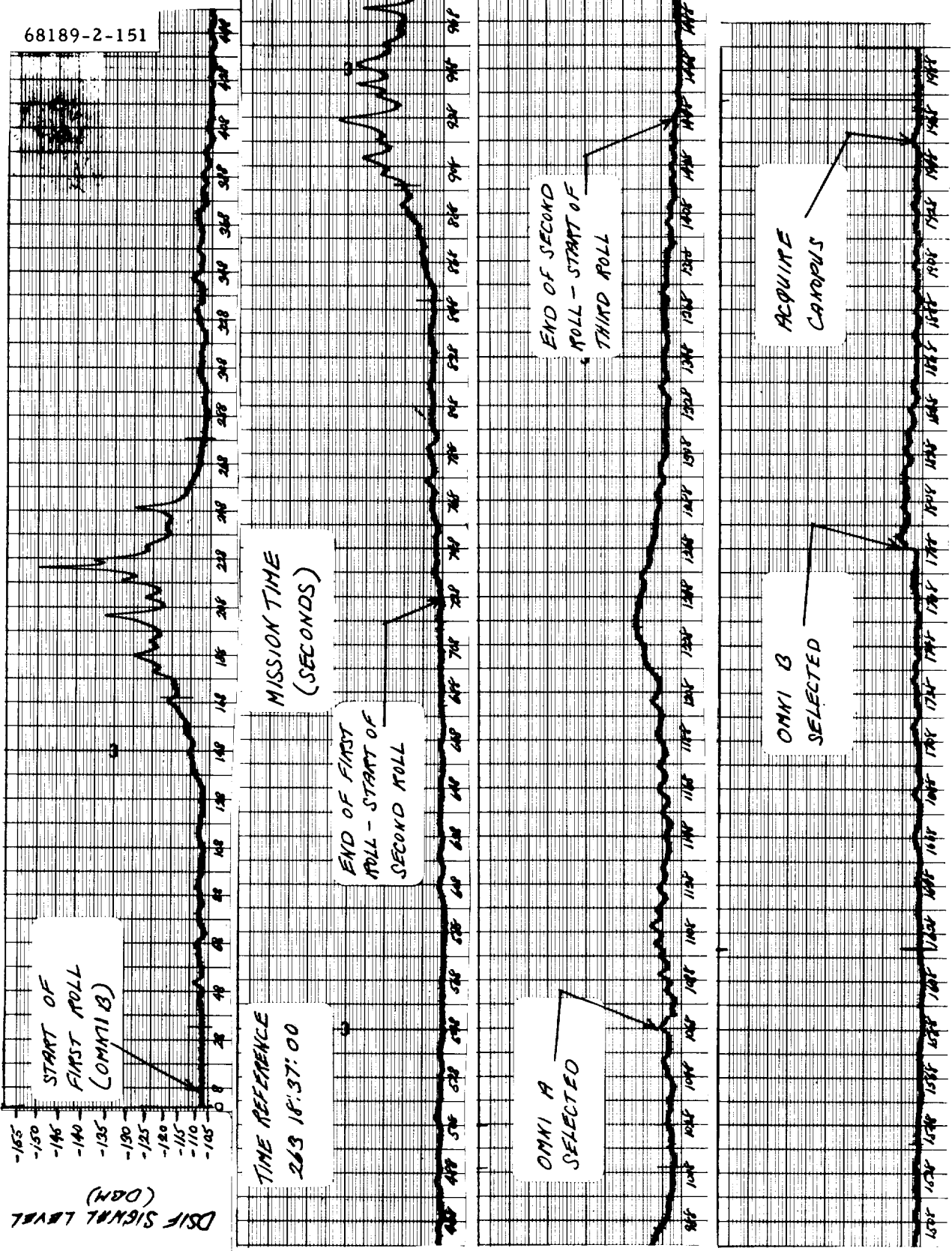


Figure 5.3-16. DSIF Signal Level During Star Maneuver



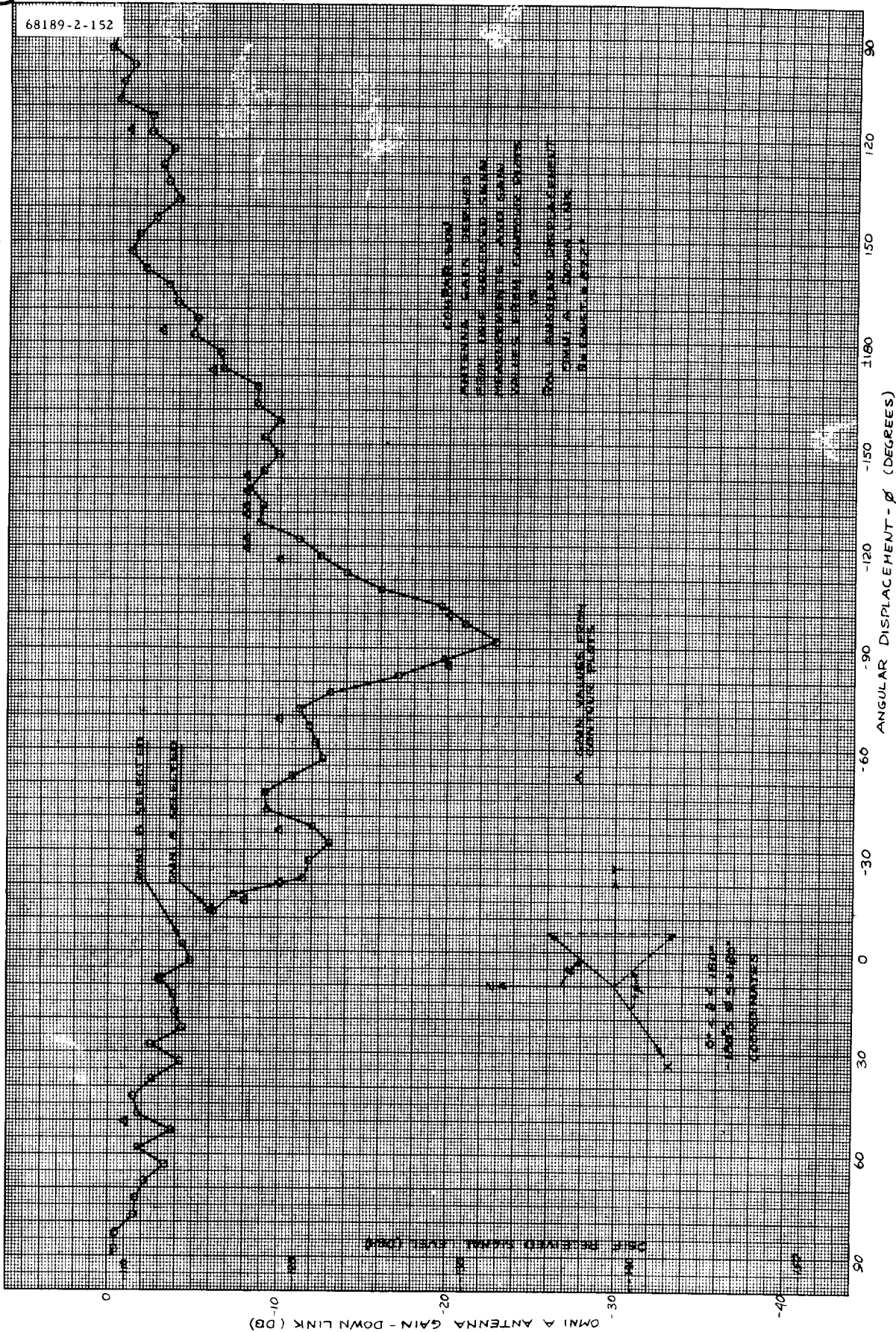


Figure 5.3-17. Comparison of Antenna Gain Derived From DSIF Received Signal Measurements and Gain Values From Contour Plots Versus Roll Angular Displacement of Omnidirectional Antenna Downlink

$\theta = \text{constant} = 87.2 \text{ degrees}$

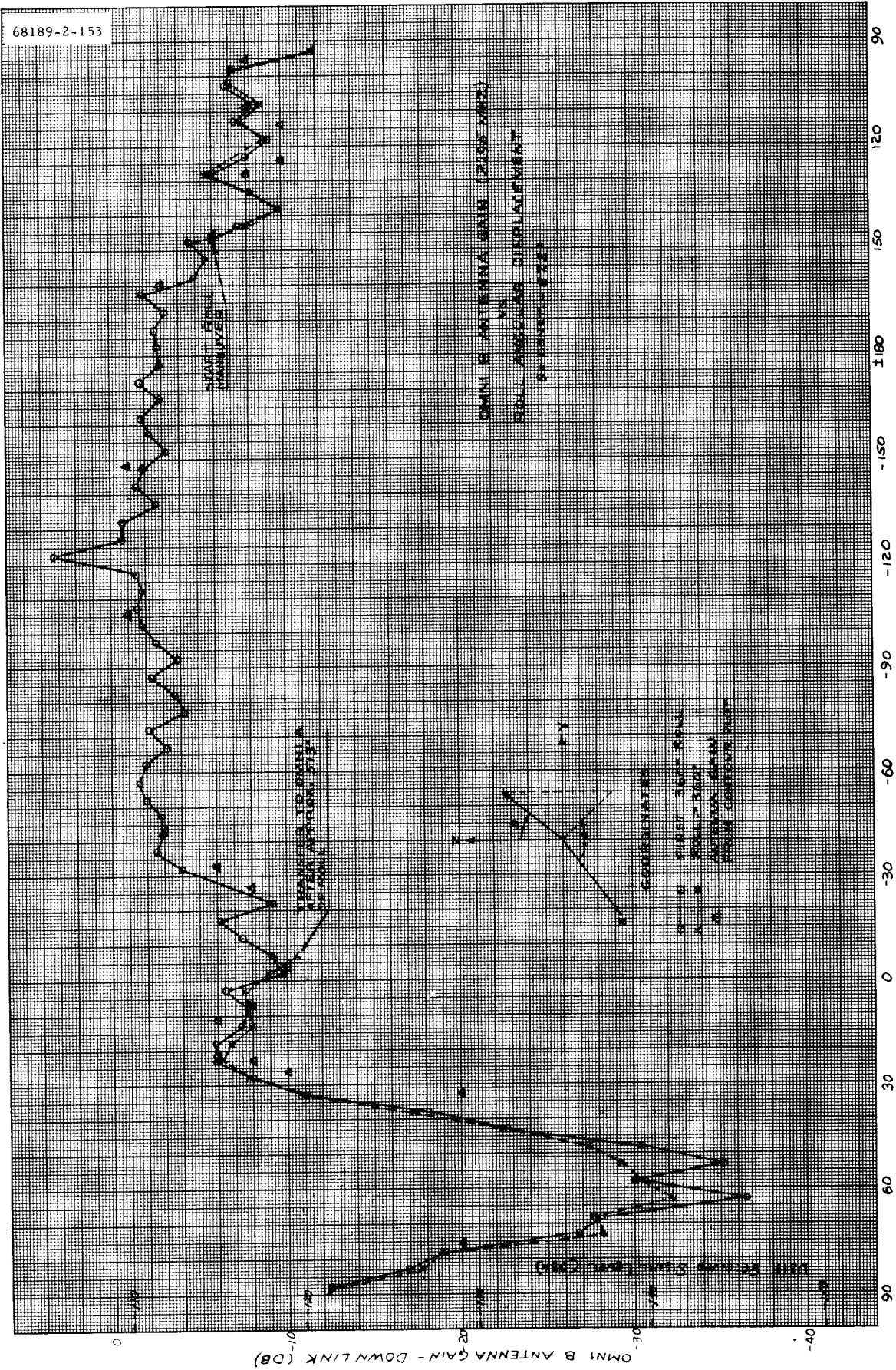


Figure 5.3-18. Omnidirectional Antenna B Gain (2295 MHz) Versus Roll Angular Displacement

$\theta = \text{constant} = 87.2 \text{ degrees}$

Figure 5.3-19 shows the signal level at receiver A during the entire star maneuver. These data, taken from spacecraft telemetry, have much better resolution than the DSIF data. Telemetry points are plotted for every degree of spacecraft motion, showing equivalent omnidirectional antenna gain for a complete spacecraft revolution. Relatively good agreement existed between the omnidirectional gain values and the signal level except in the primary antenna null. This disagreement is hypothesized to be caused by the omnidirectional antenna dipole angle difference between the SC-2 omnidirectional antenna and the omnidirectional antenna pattern data. Although expected, this null shift demonstrates the sensitivity of the antenna patterns to omnidirectional antenna positional tolerances. In future missions, external spacecraft configuration changes will result in omnidirectional antenna pattern changes, especially at the nulls; therefore, operation in or near these nulls may cause poor correlation between actual and predicted signal levels.

Figure 5.3-20 shows the signal level at receiver B during a portion of the roll maneuver. As in the case of receiver A automatic gain control data, this figure contains predicted omnidirectional antenna gain values over a complete roll period. There is good agreement between the omnidirectional antenna pattern and automatic gain control data in the gain region above -8 db and to a lesser extent down in the null. As expected, the pattern in the null agrees much better than did that for omnidirectional antenna A.

#### 5.3.4.4 Mission Phase Four: Midcourse Maneuvers

Roll-yaw was selected from four possibilities as the midcourse maneuver and was optimum for the communications link. Real-time analysis predicted the following variations in nominal omnidirectional antenna gain during the maneuver:

- 1) Omnidirectional antenna B downlink:  $-2 < G < 1.6$  db
- 2) Omnidirectional antenna A uplink:  $-6 > G > -20$  db
- 3) Omnidirectional antenna B uplink:  $-1 > G > -15$  db

Predicted minimum margins were 16.0 db for 4400 bits/sec telemetry, 8.0 db on receiver A, and 13.0 db on receiver B command links. Two-way (transponder) mode was recommended as a result of the special threshold test run at 01:36 GMT.

At 04:36:43 GMT, the spacecraft was commanded to high power, and at 04:37:54 GMT the 4400 bits/sec data rate was selected. DSS-11 signal level was -123.3 dbm prior to maneuver. At 04:44:00 GMT, the roll maneuver was initiated, and at 04:48:06 GMT the yaw maneuver was initiated. The pre-midcourse maneuver ended at 04:51:57 GMT with the DSS-11 signal level reading -123.3 dbm and having indicated approximately a 2-db variation during the maneuver, as predicted. The maneuver performed is mapped on the

specific gain patterns as shown in Figures 5.3-8 and 5.3-9. Since the maneuvers were performed in telemetry mode 1, no receiver AGC data are available to check against the premission prediction. However, the command link was maintained with no receiver indexing, indicating above-threshold operation.

Figure 5.3-21 shows the DSIF receiver signal level variations during the maneuvers. The large amount of noise in the data (a data processing problem?) allows only limited analysis. Data points taken from this plot are compared to predicted omnidirectional gain levels in Figure 5.3-22, with relatively good correlation.

#### 5.3.4.5 Mission Phase Five: Nonstandard Spacecraft Tumbling (Postmid-course)

At 05:00:02 GMT, the vernier engines were fired for the midcourse correction. Because vernier engine 3 apparently did not fire, the spacecraft became unstable and began to tumble. Figure 5.3-23 shows a plot of the DSIF-receiver signal levels for the period just prior to engine burn through 70 seconds after ignition. Large signal level variations began here and continued throughout the rest of the mission.

Ground link AGC was used in the postmission tumbling dynamics analysis (see Section 4.7) to determine spacecraft motion during the first 20 seconds after ignition. Assumed earth vector paths on the omnidirectional antenna B downlink contour map generated plots of signal level versus time for comparison to actual DSIF signal levels.

Table 5.3-8 contains a summary of the primary spacecraft tumbling periods throughout the remainder of the mission. Except in cases where good data were not available, the period was determined from station AGC and dynamic phase error.

During spacecraft tumbling, the telemetry bit rate was 1100 bits/sec for high power and 137.5 bits/sec for low power transmitter operation. Two-way transponder lock was also maintained throughout the remainder of the mission. The downlink signal level was -117 to -135 dbm (high power) or -135 to -155 dbm (low power).

#### 5.3.4.6 Mission Data Plots

Subsystem telemetry signals are shown in Figures 5.3-24 through 5.3-28. (See also Figures 5.3-14 and 5.3-15 in the coast phase discussion for AGC signals.) The plots were terminated at midcourse because spacecraft tumbling thereafter caused many bad data points (from double bit errors). Postmidcourse plots generally were mis-scaled and unreadable, but some of the more usable are found in Figures 5.3-29 and 5.3-30. Comments are omitted since most of the sudden variations are due to telemetry processing problems.

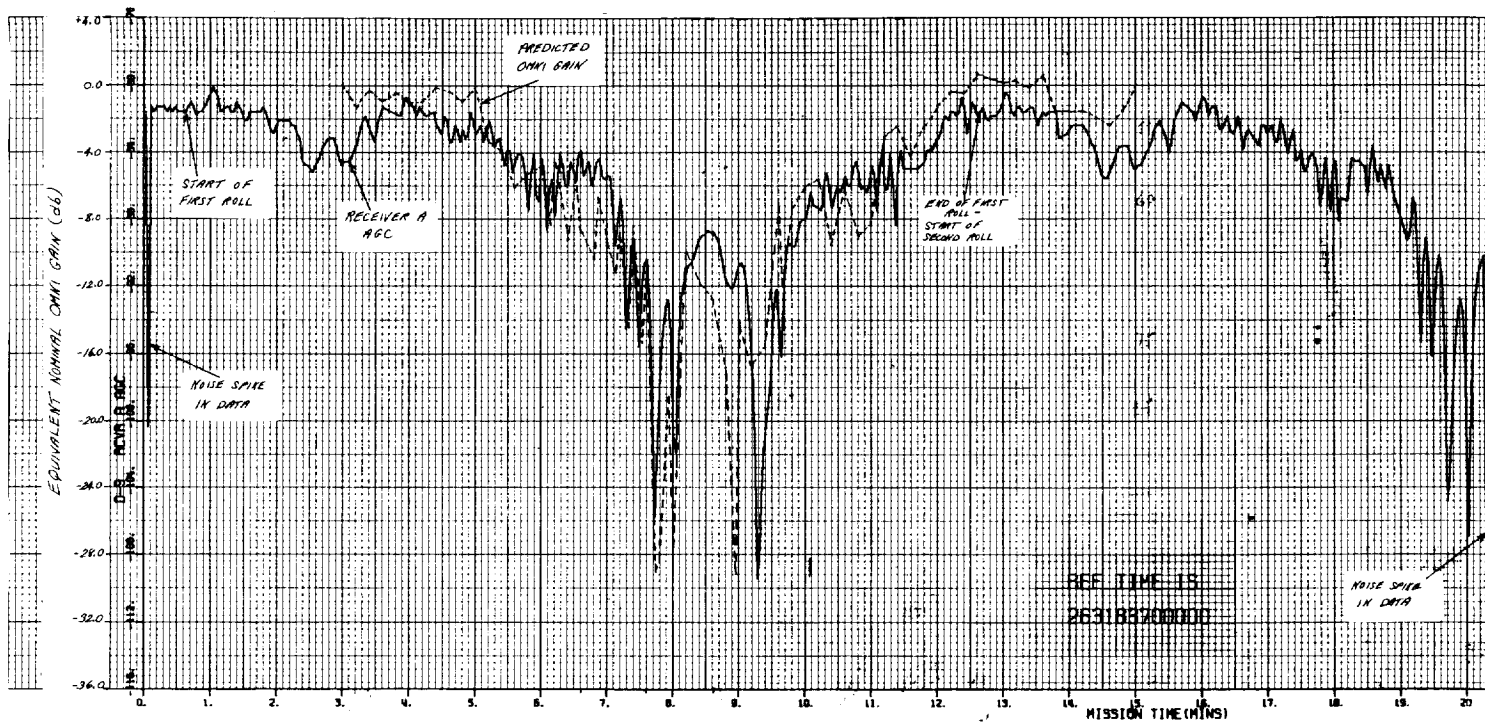


Figure 5.3-19. Receiver A Automatic Gain Control (Teler

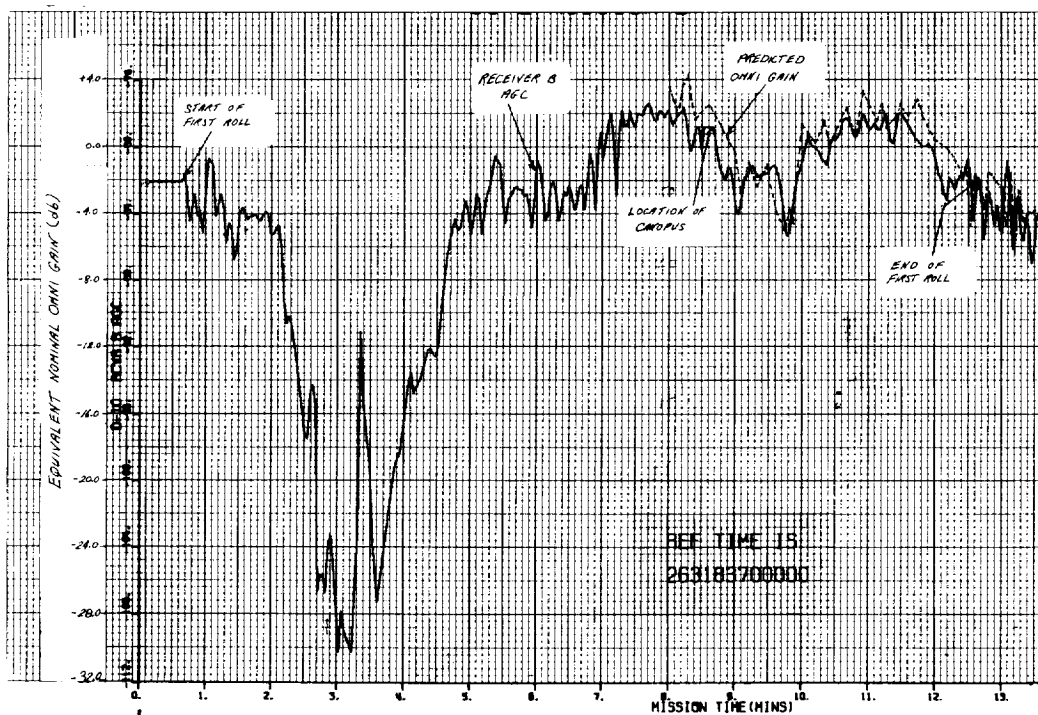


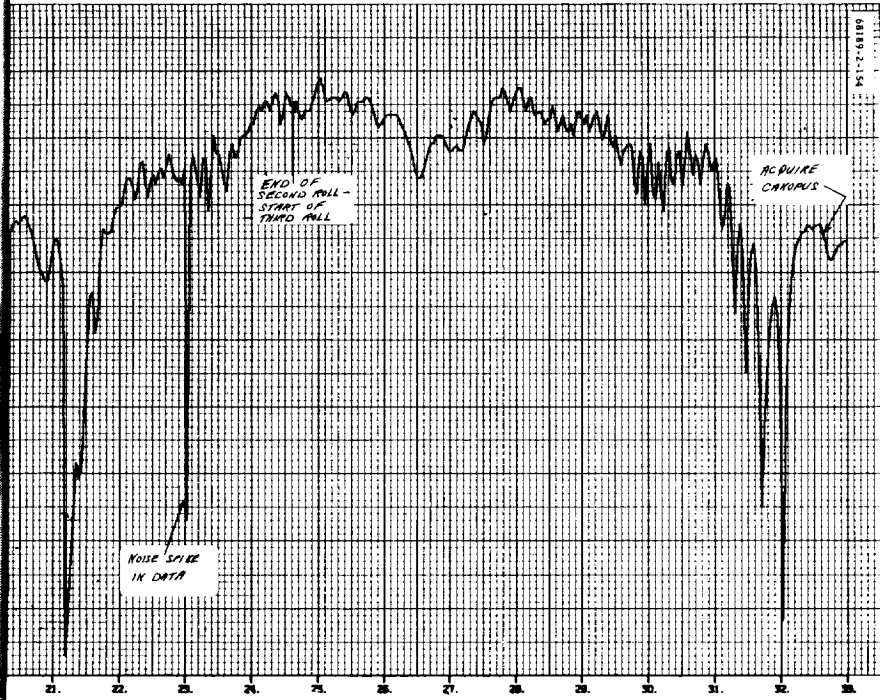
Figure 5.3-20. Receiver B Automatic Gain Control (Teler

EOLDOUT FRAME /

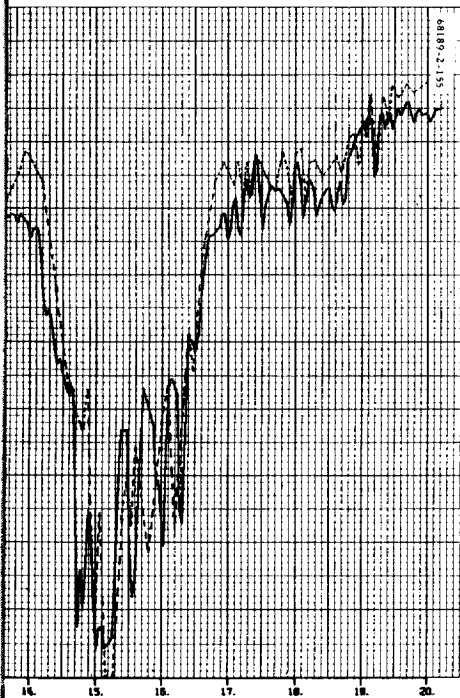
2024.01.15

1

2



metry) During Star Map



metry) During Star Map

FOLDOUT FRAME 2

5.3-53B





68189-2-156

TIME REFERENCE  
264 04:38:00

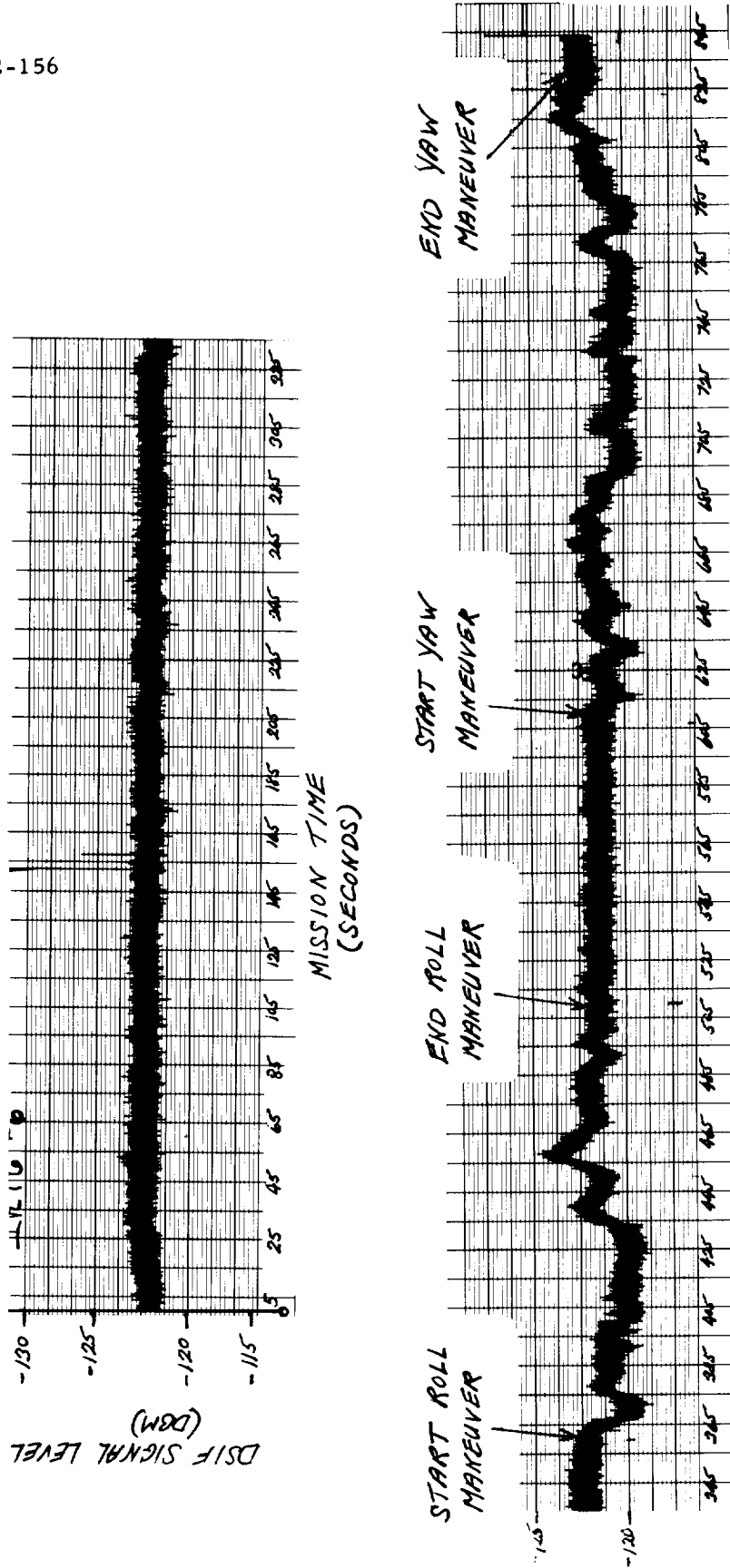


Figure 5.3-21. DSIF Receiver Signal Level Variations During Midcourse Maneuvers

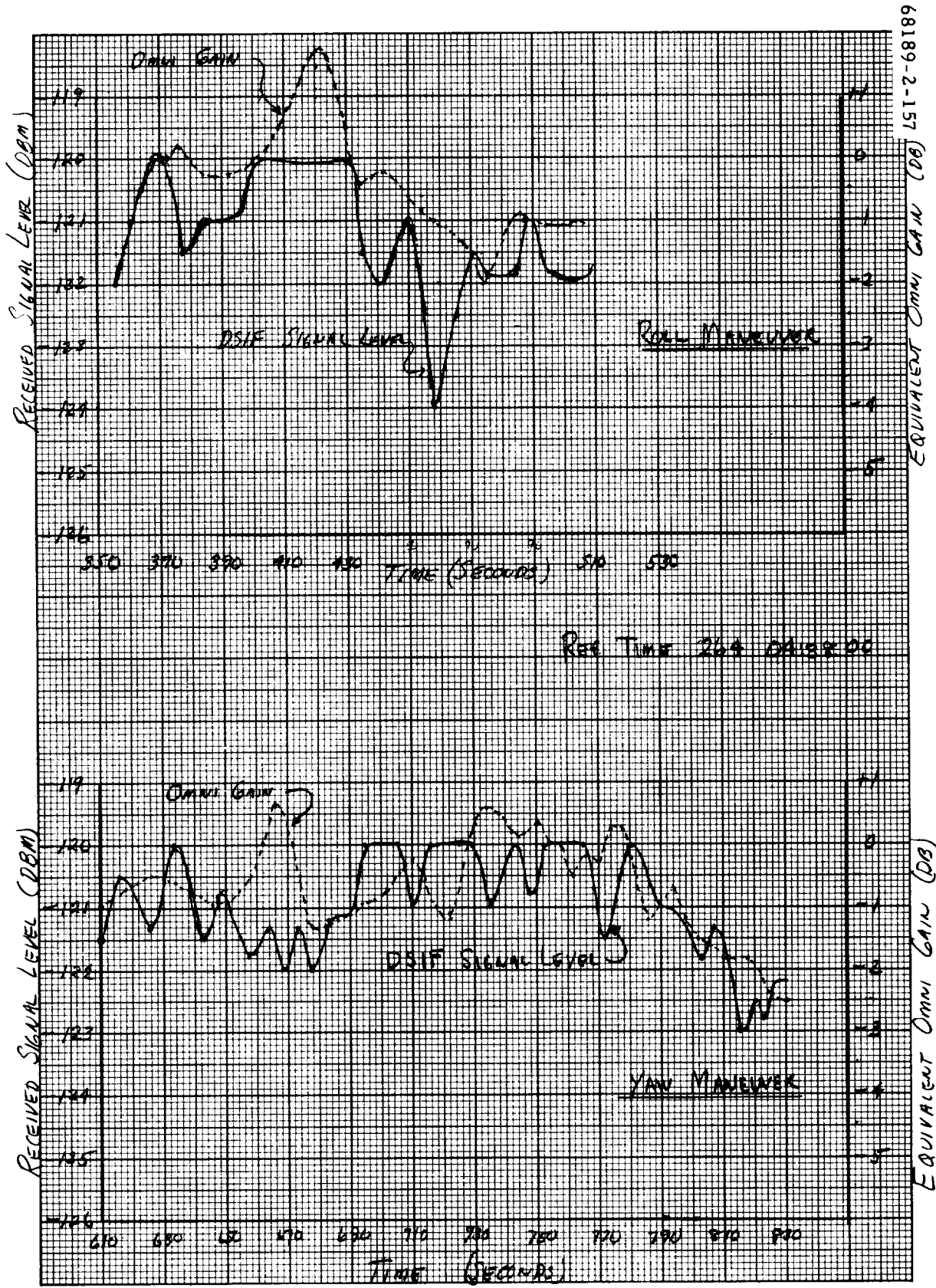


Figure 5.3-22. Predicted DSIF Signal Levels During Midcourse Roll and Yaw Maneuvers

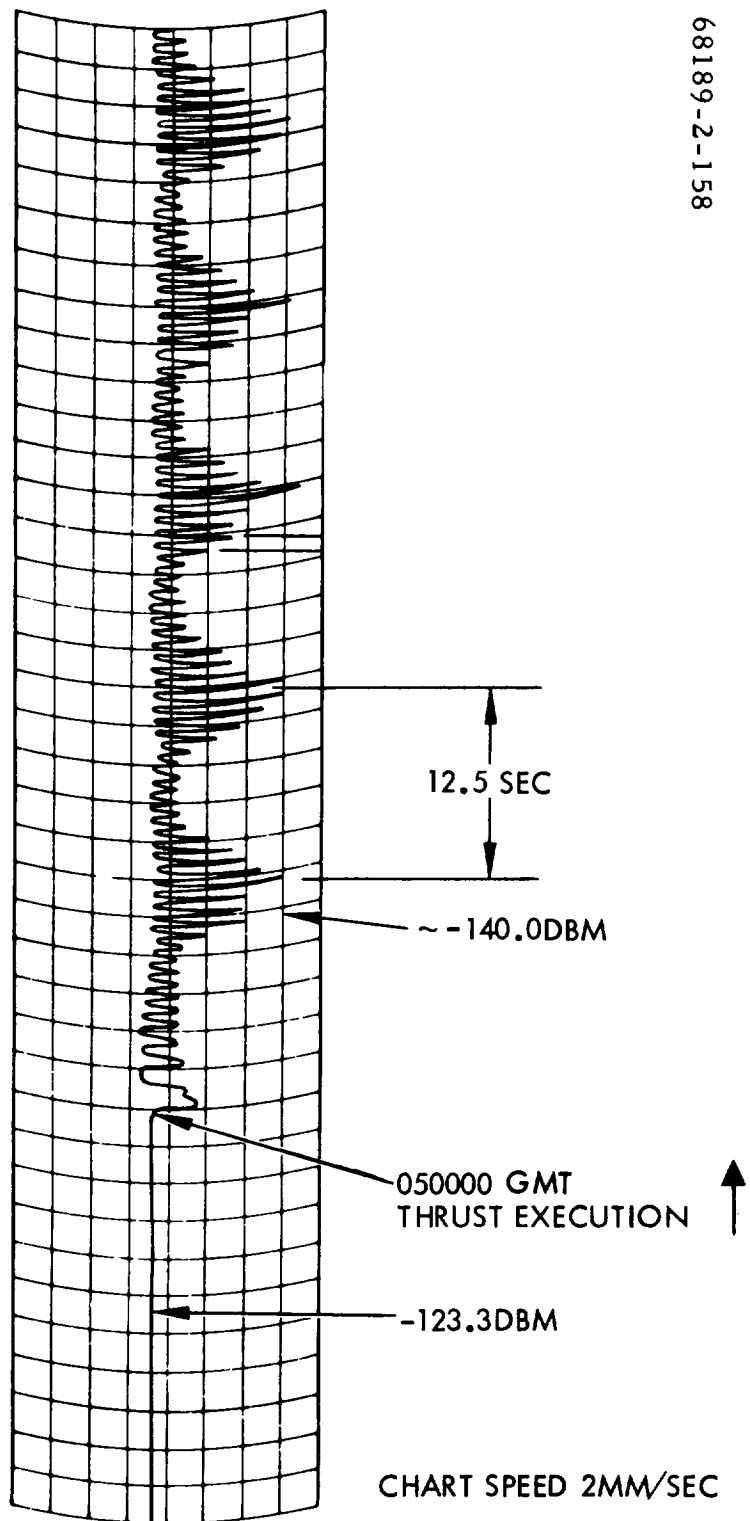


Figure 5.3-23. DSIF-11 Automatic Gain Control Variations for Initial Spacecraft Tumbling

TABLE 5.3-8. SPACECRAFT ROTATION PERIODS

Operation	Time of Commands, day: hr: min: sec	Time Interval Used, hr: min: sec	Period, seconds
Midcourse terminate (first firing)	264: 05:00:13	05:00:30-38	0.81
Thrust power off	05:00:41	05:03:44-45	0.883
Rate mode on	05:03:48	05:04:48-51 05:11:45-48	0.89 1.08
Inhibit gas jet amplifier (end rate mode)	05:14:29	05:14:46-48	1.18
2nd engine firing (2 seconds)	07:28:25		No data
3rd engine firing (2 seconds)	07:50:03		No data
4th through 8th engine firing	19:44:59	19:44:58-59 20:07:04-05	1.2 (resolution poor)
9th engine firing (2 seconds)	23:33:23	23:59:59-00:00:01	0.99 (waveshapes vary)
10th through 15th engine firing*	265: 01:28:11	02:01:15-18	0.91
16th through 21st engine firing*	02:39:14	03:17:21-23	0.86
22nd through 26th engine firing**	03:39:07	03:47:53-55	0.82
27th engine firing (2 seconds)	03:47:56	04:17:28-29	0.74
28th through 32nd engine firing**	04:41:20	04:56:09-12	0.73
33rd engine firing (2 seconds)	04:56:12	05:43:16-18	0.705
34th engine firing (2 seconds)	05:43:19	05:59:58-59	0.68
35th through 39th engine firing**	07:49:25		No data
40th engine firing (20 seconds)	08:05:12	09:34:09-28	0.44
Retro firing, delayed	09:34:28	09:34:54-59	0.52

\*Group consists of five 0.2-second burns followed by one 2.0-second burn.

\*\*Group consists of five 0.2-second burns.

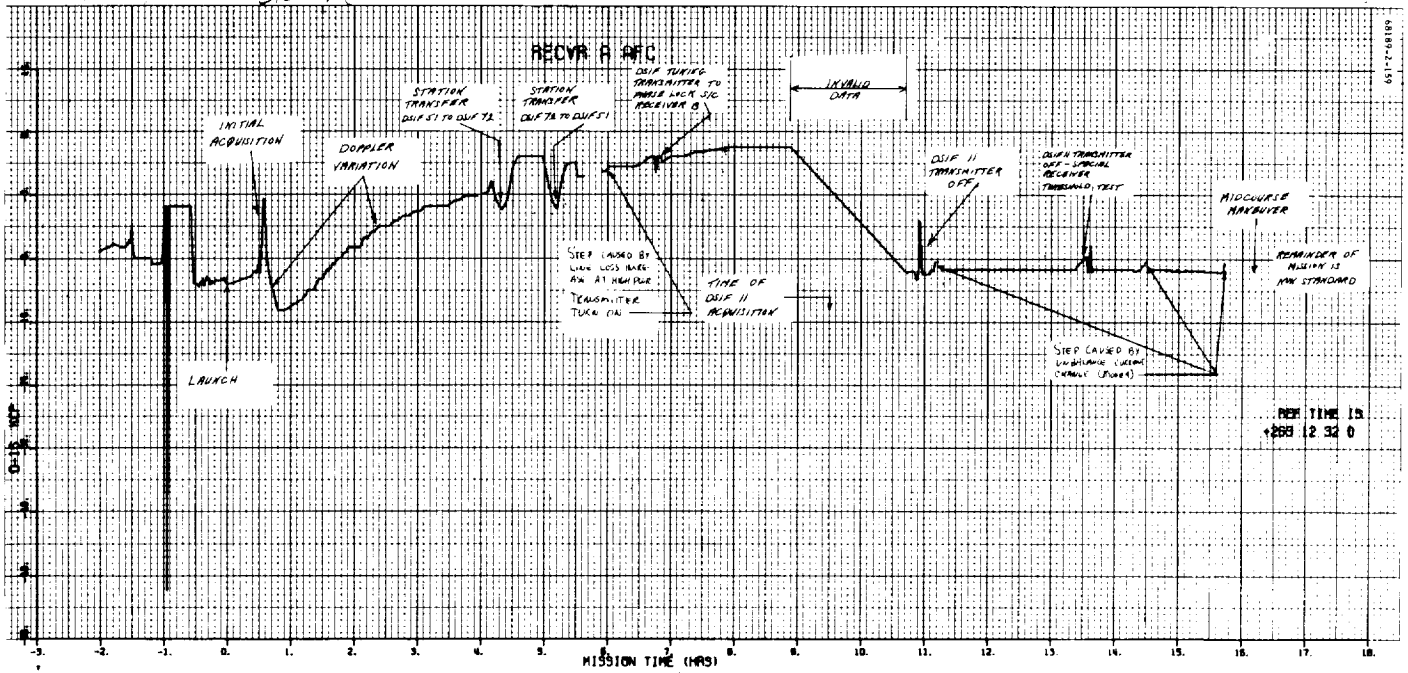


Figure 5.3-24. Receiver A Automatic Frequency Control

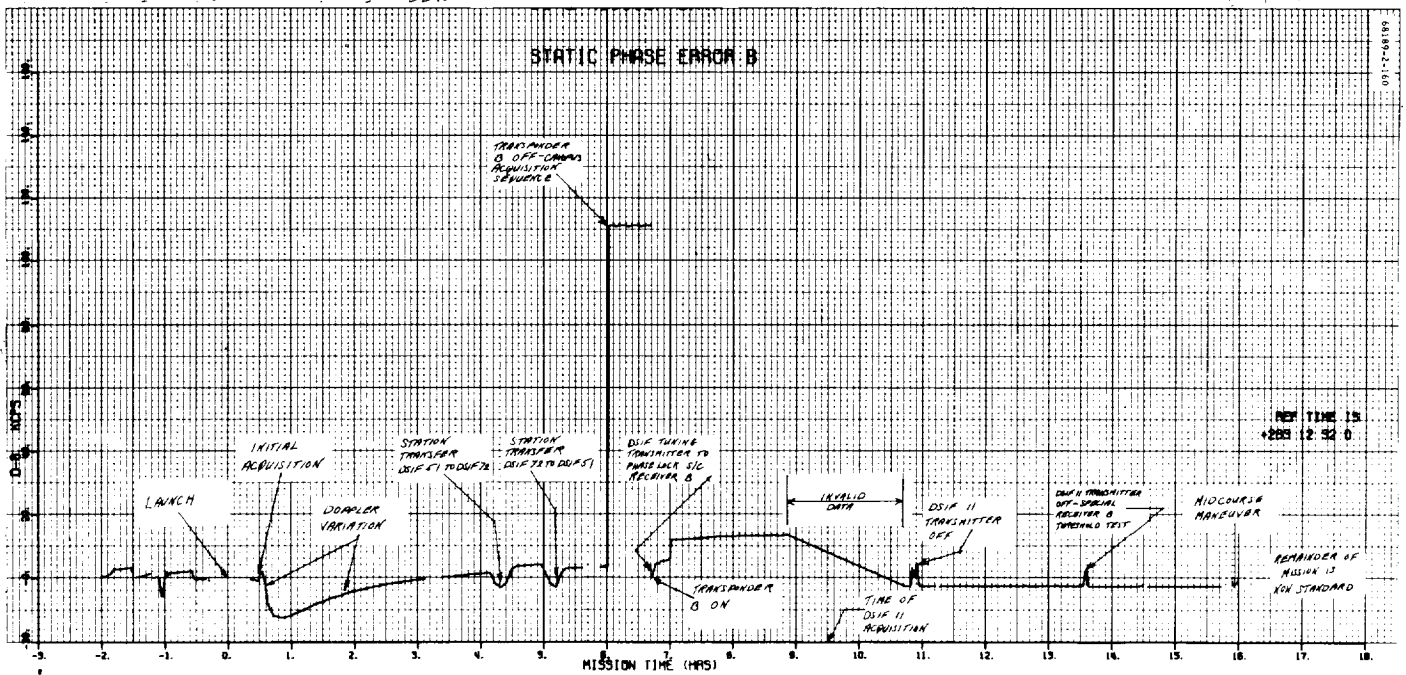


Figure 5.3-25. Receiver B Static Phase Error B

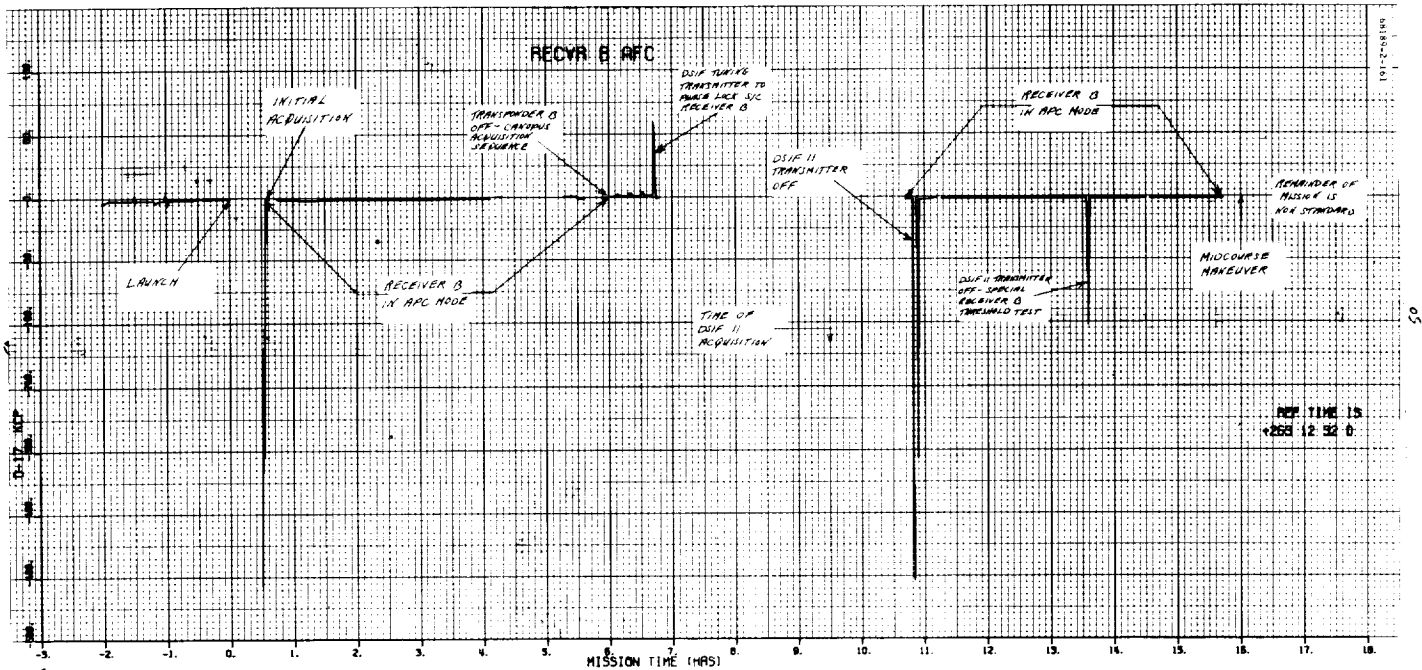


Figure 5.3-26. Receiver B Automatic Frequency Control

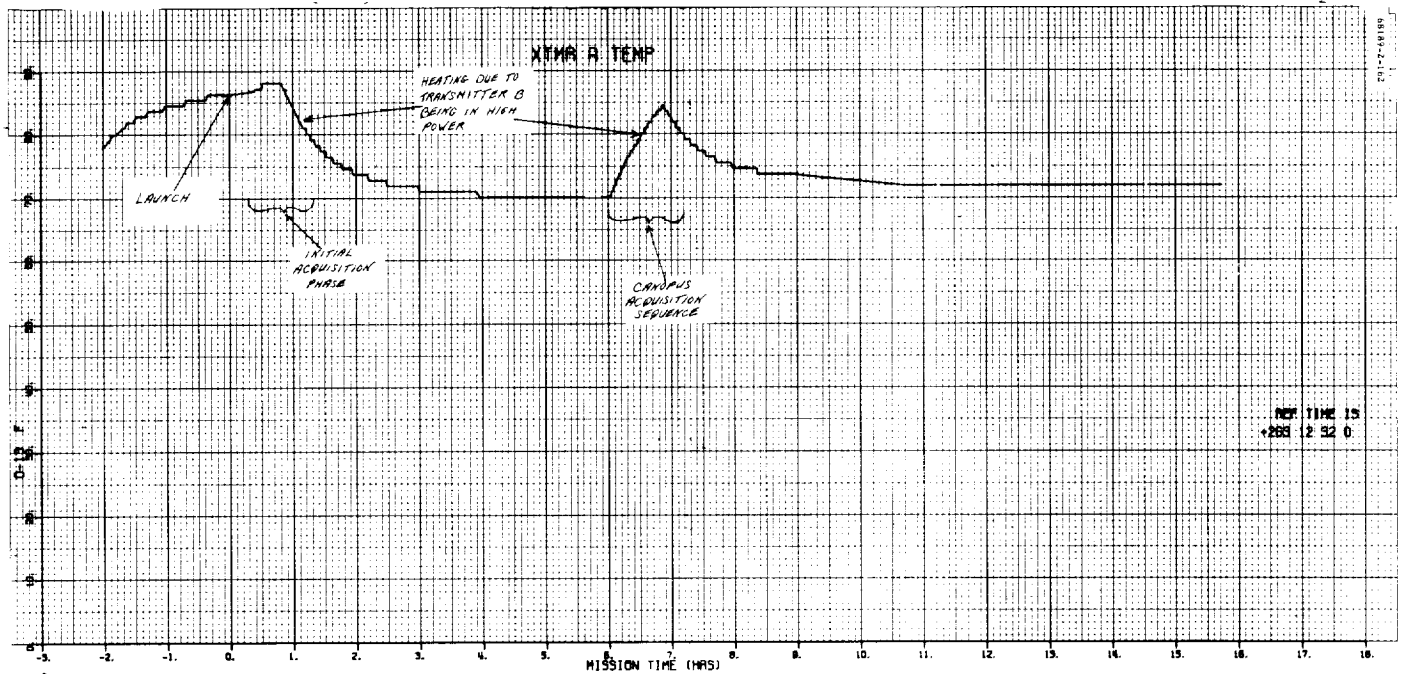


Figure 5.3-27. Transmitter A Temperature, Premidcourse

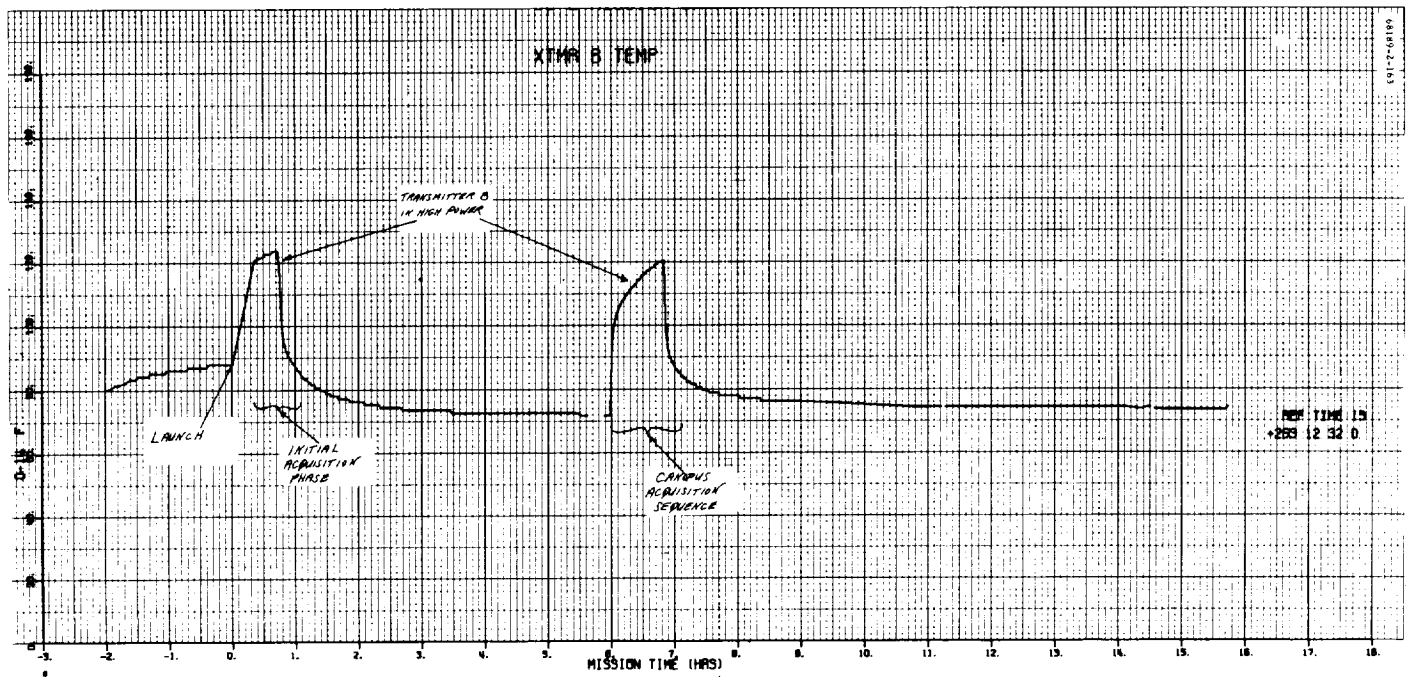


Figure 5.3-28. Transmitter B Temperature, Premidcourse

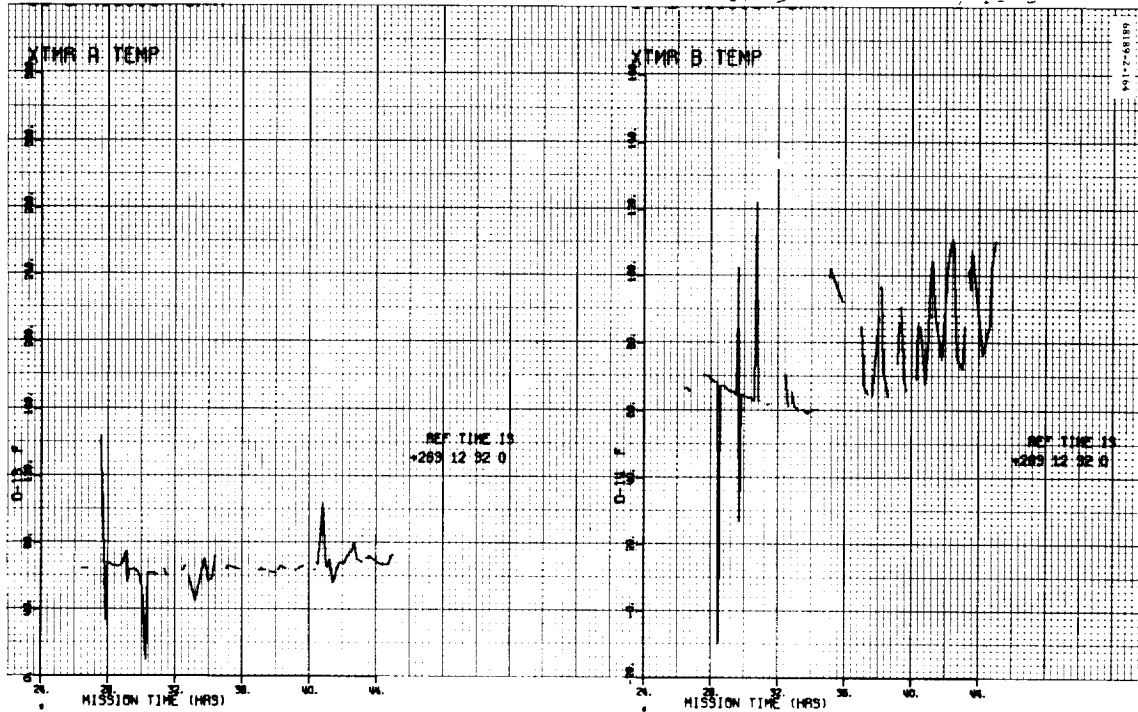


Figure 5.3-29. Transmitter A and B Temperatures, Postmidcourse

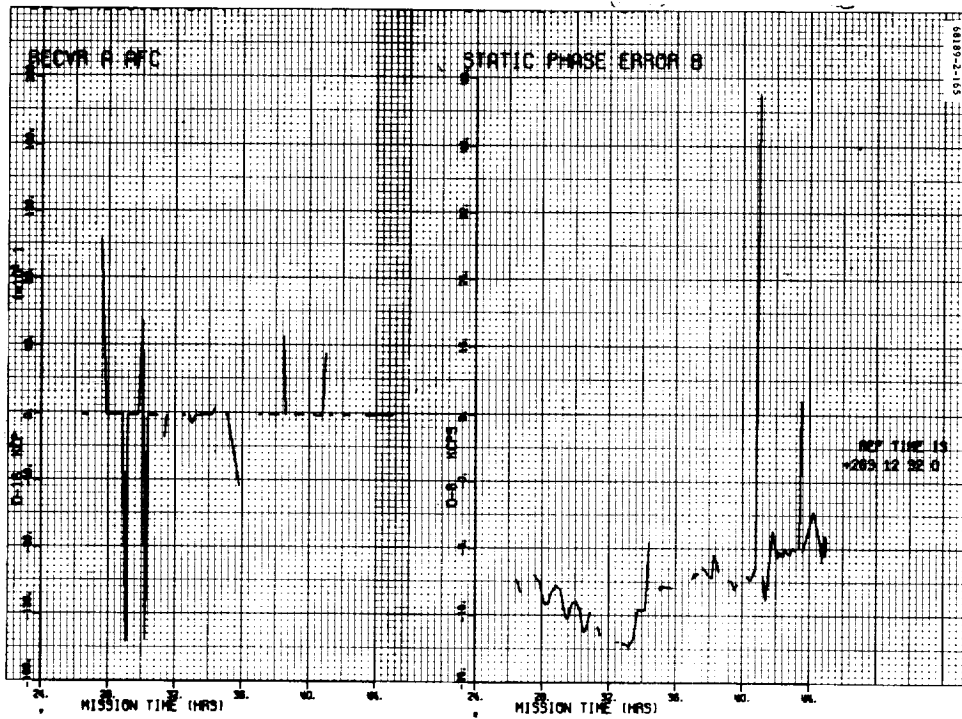


Figure 5.3-30. Receiver A Automatic Frequency Control and Receiver B Static Phase Error



For the premidcourse plots, all data indicated normal subsystem performance, and no unexplainable variations were noted. A brief summary of each figure and the more significant events follows:

Receiver A Automatic Frequency Control (Figure 5.3-24) – Receiver A was in the automatic frequency control mode throughout transit. These data represent the DSIF transmitter frequency offset from the automatic frequency control center frequency during the transit phase. A large error due to doppler shift rate is noted at acquisition. Steps in the data occurred at station transfer because the stations retuned their transmitters. Due to the high impedance of this signal, several predicted signal processing effects are apparent. Steps occurred in the data at high power turnon due to return line drop caused by the additional current in the ground return lines during high power operation. Spikes occurred during engineering interrogations of mode 4 due to step change in commutator unbalance current.

Receiver B Static Phase Error (Figure 5.3-25) – Receiver B was used for transponding through most of the mission. These data thus represent the DSIF transmitter frequency offset from the receiver phase lock center frequency. Since these data are analogous to the automatic frequency control data discussed above, the comments apply equally well to these data. It should be noted, however, that this signal is not as sensitive to signal processing effects.

Receiver B Automatic Frequency Control (Figure 5.3-28) – Since the receiver was phase locked during the majority of the transit phase, this telemetry signal was not a valid signal. Unlike the static phase error signal, which has a 0-volt output when not being selected, the automatic frequency control telemetry does vary with frequency changes even when the receiver is not in the automatic frequency control mode. However, the telemetry is not valid and is essentially meaningless.

Transmitter Traveling-Wave Tube Temperatures (Figures 5.3-27 and 5.3-28 for premidcourse period and Figure 5.3-29 for postmidcourse data) – These data represent the traveling-wave tube temperatures used for high power transmitter operation. Figure 5.3-29 contains telemetry glitches caused by the spacecraft tumbling, as discussed earlier, and shows temperature variations during the short high power transmitter operation times.

Receiver A Automatic Frequency Control and Receiver B Static Phase Error (Figure 5.3-30) – This plot is similar to figures 5.3-25 and 5.3-26 except for the period after midcourse when telemetry processing glitches occur. This information is included, however, to show the effects of tumbling-induced doppler shifts.

### 5.3.5 REFERENCES

1. W.C. Collier, "The Change In Receiver B AGC Characteristics Prior to and During Flight of SC-2," Hughes Aircraft Company, IDC 2294.2/44.
2. "Surveyor Mission B Space Flight Operations Report," Volume 1, Hughes Aircraft Company, SSD 64257R, November 1966.
3. "Surveyor I Flight Performance Final Report," Volume 2, Hughes Aircraft Company, SSD 68189R, October 1966.
4. "Surveyor Mission B - Telecommunications Subsystem Prediction and Performance Summary," Hughes Aircraft Company, SSD 64241R.

### 5.3.6 ACKNOWLEDGEMENTS

Frank K. Rickman, coordinator and coauthor

Joe Votaw, coauthor

Notes and records made in real time by the spacecraft/performance/analysis/command telecommunications team (Vic Amstader, Bill Mitchel, John Steineck, Vern Story, Joe Votaw, Mike Weiner, and Mike Williams) were of great use in postmission analysis.

## 5.4 SIGNAL PROCESSING

### 5.4.1 INTRODUCTION

The signal processing subsystem is composed of the following units:

- 1) Engineering signal processor (ESP)
- 2) Auxiliary engineering signal processor (AESP)
- 3) Central signal processor (CSP)
- 4) Signal processing auxiliary (SPA)
- 5) Low data rate auxiliary (LDRA)

These units contain 2 electronic commutators with a total of 6 operational modes, 2 analog-to-digital converters that have available 5 digital bit rates, 17 subcarrier oscillators for transmission of pulse coded modulation data and continuous real-time data, 9 summing amplifiers, and signal conditioning circuits for the measurement of electrical currents and temperatures. The subsystem performed normally throughout the mission.

A summary of test and flight values for signal processing telemetry can be found in Table 5.4-1. Values for the SC-1 flight have been included for comparison. A complete mode, bit rate, and configuration log can be found in Section 5.2 (RF data link) and will not be repeated here. All signal processing corrections made to telemetry signals on the full-mission plots throughout this report are given in Table 5.4-2. The details of each correction will be discussed in Subsection 5.4.4.

### 5.4.2 ANOMALIES

No anomalies were attributed to signal processing in the SC-2 flight.

TABLE 5.4-1. COMPARISON OF SIGNAL PROCESSING VALUES FROM TEST AND FLIGHT

Telemetry Signal	SC-2 Test Values			SC-2 Flight Values, Day 263	SC-1 Flight Values for Comparison
	STV-2B, Day 132	STV-3B, Day 152	STV-1C, Day 163		
S-1 reference voltage, volts	4.86-4.91	4.86-4.90	4.87-4.91	4.90	4.88
S-2 reference voltage return, volts	0-0.005	0-0.005	0.005	0.003	0.0024-0.0072
S-5 ESP commutator unbalance current, microamperes	-1.2*	-1.2*	-1.2 to -1.5*	-1.4*	-3.1*
	-2.6**	-2.55 to -2.75**	-2.6 to -2.8	-2.64 to -2.68**	-4.4**
S-7 AESP commutator unbalance current, microamperes	-	-1.7 to -1.9	-1.9 to -2.1	-1.7 (after launch) -2.1 (tumbling, day 265)	-2.8

\*Mode 4 value.

\*\*Mode 2 value.

TABLE 5.4-2. IN-FLIGHT CALIBRATION CORRECTIONS  
MADE ON SC-2 MISSION PLOTS

<u>Correction</u>	<u>Telemetry Signals</u>
Reference voltage	M-3, M-4, M-6, M-7, P-1, P-2
Unbalance current	D-7, D-8, EP-1, EP-2, EP-3, EP-5, EP-10, EP-23, EP-30, FC-4, FC-32, FC-53, P-1, R-29
Current calibration	EP-4, EP-6, EP-7, EP-9, EP-11, EP-14, EP-16, EP-17, EP-21, EP-22, EP-24, EP-25

### 5.4.3 SUMMARY AND RECOMMENDATIONS

#### 5.4.3.1 Signal Processing Performance Summary

The signal processing subsystem performed properly throughout the mission. All telemetry channels gave proper indications in all modes used. On-board calibration signals (reference voltage, unbalance current, and current calibration) were used for telemetry accuracy improvement. A possible method to correct certain temperatures for 4400-bits/sec errors has been developed.

#### 5.4.3.2 Recommendations

The following recommendations are made:

- 1) Initial processing of the DSIF magnetic tapes should be modified to record (on digital tapes) all telemetry bit stream data. At present, data are discarded whenever decommutator is not in lock.
- 2) A previous recommendation to replace current calibration signal corrections with values constant for the entire flight should be reconsidered. Loss of accuracy may result.
- 3) An investigation should be initiated on the use of the unbalance current correction. Means must be provided to handle capacitive outputs and individual switch factors if these are shown to be significant.

## 5.4.4 SIGNAL PROCESSING ANALYSIS

### 5.4.4.1 Unbalance Current Corrections

In each telemetry commutator, transistor switches connect each analog output voltage (representing a spacecraft voltage, current, or temperature) with a common commutator line connected to the input of one of two analog-to-digital converters. A bootstrap unloader circuit is connected to this common line to reduce the stray capacitance, equalize the load impedance, and provide bias currents for the commutator and master switches. Since these bias currents are not exactly equal, a difference or unbalance current exists. The telemetry circuit being sampled must supply this current, causing an error in the measured voltage proportional to the output impedance of the circuit.

The unbalance current for a specific telemetry channel in each commutator (S-5 for ESP and S-7 for AESP) is measured in telemetry modes 2, 4, and 5. Figure 5.4-1 shows S-7 up to midcourse. A warmup effect can be noted in that each time the AESP commutator is turned on, the initial value of unbalance current is up to 0.2 microampere lower than the value assumed after a few minutes of operation. Although no plot of S-5 has been included, typical values have already been given in Table 5.4-1. The change in unbalance current from mode 2 to mode 4, due to internal ESP load changes, is readily apparent. This effect also occurred on SC-1, and is part of the spacecraft signature list.

The final report for SC-1 made a number of recommendations for unbalance current corrections in automatic processing. Many of these have been accepted (for instance, delete corrections for temperature and capacitor-output channels), but as yet no means has been provided for individual selection switch corrections. A limit ( $\pm 10$  microamperes) has been put in the correction processing to prevent wildly inaccurate "corrections", based on bad data values of unbalance current, from being made.

### 5.4.4.2 Potentiometer Reference Voltage Corrections

The nominally 4.85 reference voltage is supplied by either the ESP or AESP units to the landing gear and solar panel position potentiometers, to the propulsion pressure transducers, and to the secondary sun sensors. This reference voltage, derived from the 29-volt nonessential bus, varies due to load and input supply voltage changes. The ESP voltage is telemetered in modes 2 and 4, and can be used to correct the affected signals whose calibrations are based on a reference voltage of exactly 4.85 volts. Since the AESP voltage is never telemetered, it must necessarily be obtained through computation.

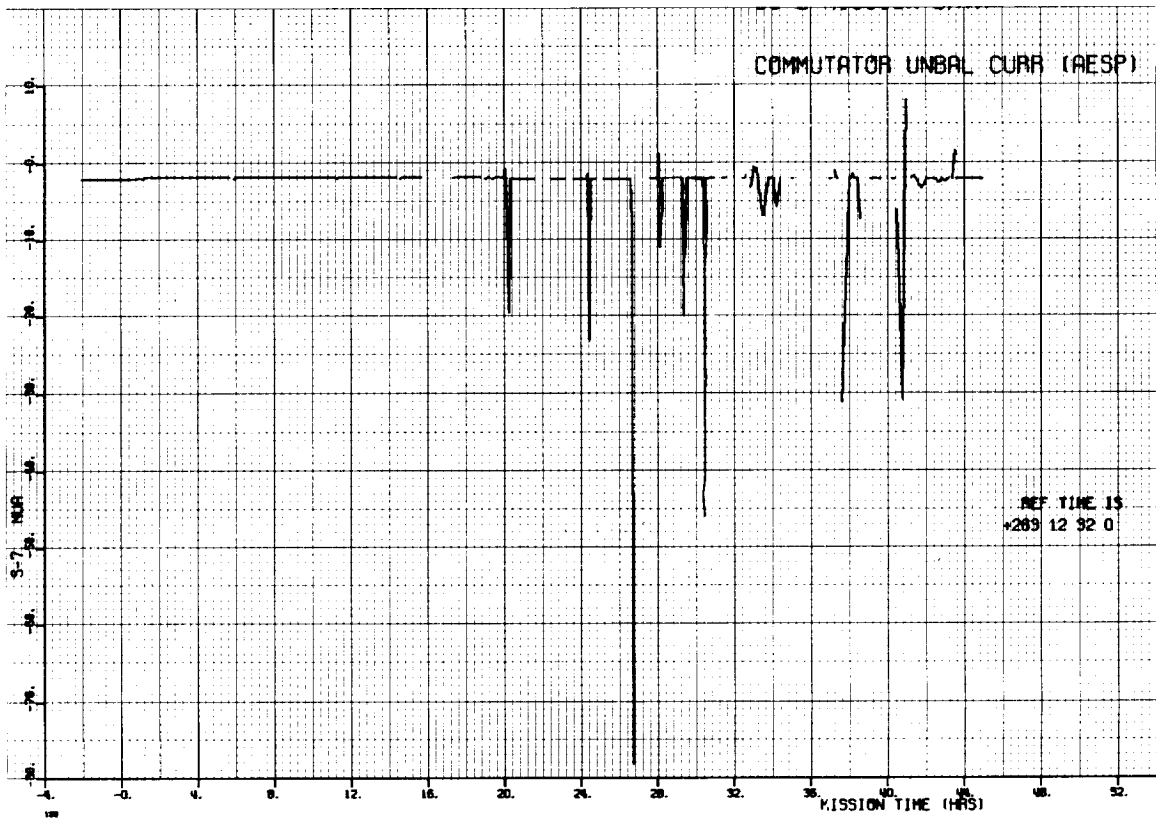


Figure 5.4-1. AESP Commutator Unbalance Current

The mechanism position signals do not normally change in flight after initial deployment, since they are mechanically held. Therefore, any apparent difference in a given signal reading from the ESP commutator to the AESP can be due only to a corresponding change in commutator-supplied reference voltage. Based on this assumption, Table 5.4-3 was prepared to show both prelaunch and coast phase I calculations of the AESP reference voltage. Due to the granularity of the signal values used in the calculations, it seems reasonable to use a median, rather than a mean, value. Thus, the calculated AESP reference voltage was 1006 bcd (4.92 volts) at prelaunch and 1010 bcd (4.94 volts) at L + 15H.\*

#### 5.4.4.3 Current Calibration Signals

Current measurements are accomplished by measuring the voltage drop across a low resistance shunt which is in series with the power line being monitored. This measurement is in the range of 0 to 100 millivolts. Since this voltage is not referenced to ground and is not scaled to the 0- to 5-volt telemetry input level range, it is necessary to amplify it with a differential amplifier. The nominal gain of this amplifier is 50, but its actual gain linearity and stability are not specified to a tight tolerance. To determine the current amplifier parameters and thereby increase the accuracy of current measurements, three calibration signals (with 0.2 percent stability) are amplified and telemetered in each commutator. These signals can thus be used by postmission processing for a continual in-flight calibration of the current amplifier.

Telemetry plots of these calibration signals show that the gain of the ESP and AESP current amplifiers was reasonably constant over the mission. For SC-2, a new system of "calibrating" these signals in percent, not telemetry volts, was used. The zero point on the scale is set at the unit flight acceptance test (FAT) measured value. The change in voltage of a given signal is divided by 5 volts (full scale) to convert to percent. Thus, it can be said that the current calibration signals, in general, have increased by 0.6 percent since unit FAT (see Table 5.4-4). This percentage change is not passed on to the current signal measurements, however, since the in-flight calibration process removes this effect completely. Only if the every-frame correction were replaced by a constant correction (as has been recommended) would this variation be passed on directly as an error to the current measurements. The range of variation is 0.2 percent for AESP and 0.3 percent for ESP. For the latter, this would mean a 100-milliampere error on a 35 ampere current shunt.

---

\*It must be noted that this value was not calculated in time to be used in processing the mission plots. Thus, the pressure plots of P-1 and P-2 in Section 5.6 are generally too high, being based on an assumed 4.85-volt reference. Correct values occur at commutator assessments, when the ESP commutator (which has a telemetered reference voltage) was used.



TABLE 5.4-3. CALCULATION OF AESP REFERENCE VOLTAGE

GMT, day:hr:min	Mode	Signal	Telemetry Value, BCD	Calculation of $X = V_{ref}$ (AESP)	AESP Reference Voltage, BCD
263:11:05	5	M-3 M-4 M-7	910 380 338		
263:11:09	4	M-3 M-4 M-7 S-1 reference voltage	904 378 336 1000	$\frac{X}{1000} = \frac{910}{904}$ $\frac{X}{1000} = \frac{380}{378}$ $\frac{X}{1000} = \frac{338}{336}$	1006.6 1005.3 1006.0
263:11:15	2	M-4 S-1	377 996	$\frac{X}{996} = \frac{380}{377}$	1003.6
264:02:40	5	M-3 M-4 M-7	675 384 508		
264:03:02	4	M-3 M-4 M-7 S-1	668 381 504 1002	$\frac{X}{1002} = \frac{675}{668}$ $\frac{X}{1002} = \frac{384}{381}$ $\frac{X}{1002} = \frac{508}{504}$	1012.5 1009.9 1009.9

TABLE 5.4-4. SUMMARY OF CURRENT CALIBRATION  
SIGNAL DATA

Signal	Function	Flight Data, percent	Remarks
EP-18	ESP, 90%	0.62	Mode 4
		0.52 - 0.54	Mode 2
		0.36 - 0.43	Mode 1
		0.12	Mode 1 at 4400 bits/sec
EP-19	ESP, 50%	0.6	Constant
EP-20	ESP, 10%	0.64	Mode 4
		0.60	Modes 2 and 1
		0.32	Mode 1 at 4400 bits/sec
EP-27	AESP, 90%	0.8	
EP-28	AESP, 50%	0.6	Prelaunch
		0.8	Near midcourse
EP-29	AESP, 10%	0.6	Prelaunch and after midcourse
		0.7	Launch to midcourse

The ESP current calibration flight data are presented in Figure 5.4-2. EP-19 was not shown since it was relatively constant. It can be seen that the signals vary not only from mode to mode (this was known previously and is part of the spacecraft signature) but also are changed considerably at 4400 bits/sec, an effect not previously reported. In Figure 5.4-3, signal variation over a 7-minute period surrounding midcourse is shown. The data involved here have been averaged such that one point represents a 7.5-second (30 frame) interval, but an examination of unprocessed data in that same interval shows only slightly more variation than the 3 to 4 bcd shown in Figure 5.4-3.

Investigations thus far have not shown any direct correlation between frame-to-frame variations in current calibration signals and changes in other current calibrations. But mode- and bit rate-dependence and long term changes in amplifier gain do exist, and thus an on-going calibration should be retained to avoid the errors associated with using constant factors for the entire flight.

#### 5.4.4.4 Temperature Measurement Errors at 4400 Bits/Sec Data Rate

The errors in temperature measurements at 4400 bits/sec result from insufficient settling time for the constant current source used to convert resistance (which is proportional to temperature) into telemetry voltage. The output capacitor on the constant current source, when unloaded, charges to about 6.8 volts. At the highest data rate, this capacitor does not have time to restabilize at the lower voltage (typically 2.5 to 3.0 volts) before the particular data channel is sampled. At 1100 bits/sec, there is four times as much time for settling, and no inaccuracy apparently exists.

In the SC-1 Final Performance Report, a detailed discussion determined which temperature measurements would be most in error. A table was also presented which listed the range of true values for a given telemetered value. It is the intention of this analysis to carry the investigation one step further: to present a means of reclaiming the true temperature values from 4400 bits/sec data. Application of this technique is of particular importance to SC-2 analysis, since the midcourse failure occurred when the bit rate was 4400, and since temperatures are an important factor. Thus, the two vernier line sensors (P-4 and P-8) will be used as an example for the reconstruction.

The first and only prerequisite to proper interpretation of a temperature signal is that it be changing unidirectionally with time, the faster the better. The vernier line signals satisfy this requirement (see Figure 5.4-4), since after the yaw maneuver they were warming due to solar radiation. It is necessary to revise the temperature correction table to stress the fact that the only values transmitted are those listed in the table: the intermediate values never occur (see Table 5.4-5). The transmitted value uniquely limits the true value within the stated range (plus the uncertainties associated with this uncontrolled design process). These results can be qualitatively explained by studying the digitization process.

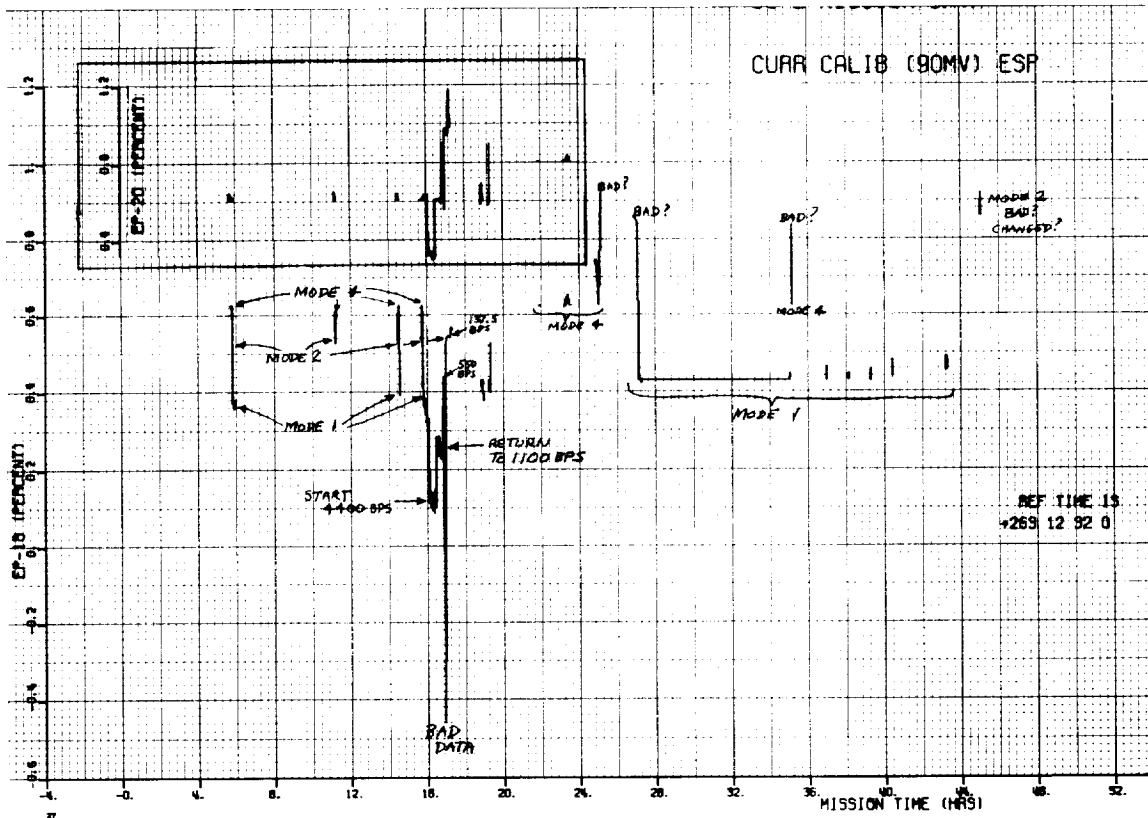
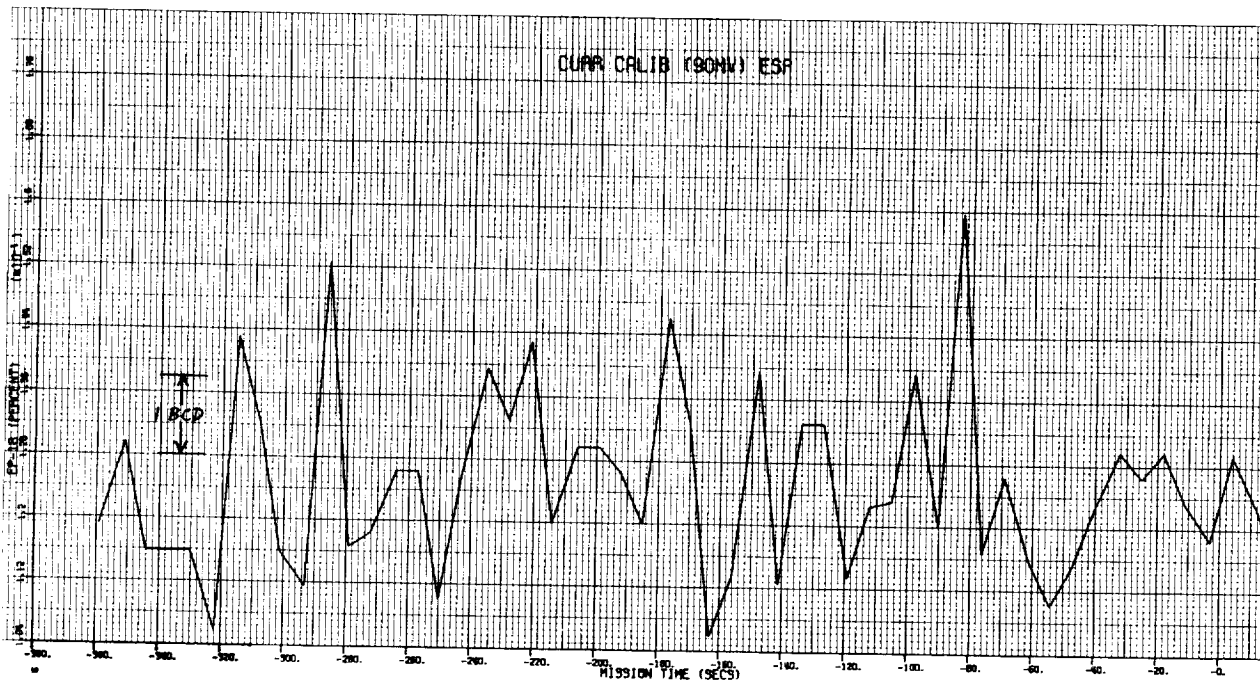
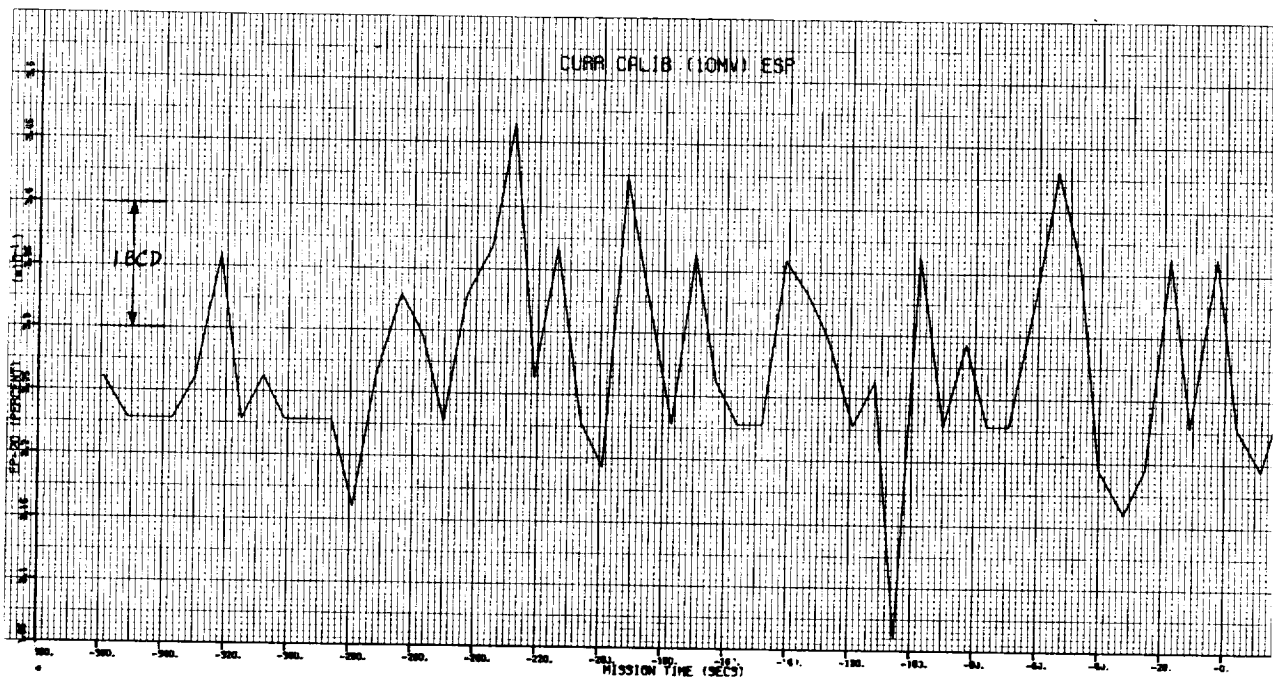


Figure 5.4-2. Mode and Bit Rate Dependence of Current Calibration Signals (EP-18 and EP-20)



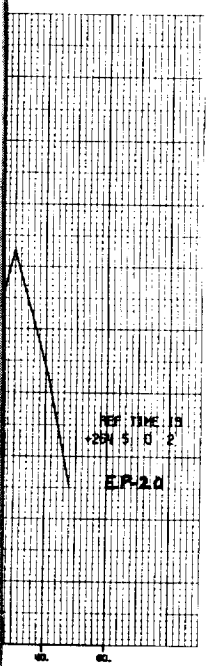
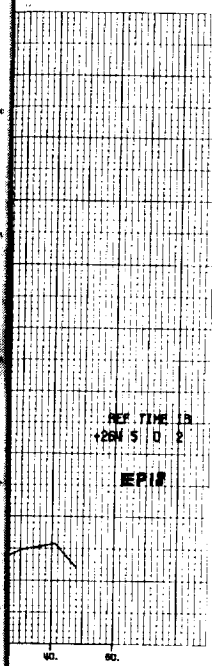
a) 90 Millivolts (EP-18)



b) 10 Millivolts (EP-20)

Figure 5.4-3. Current Calibration Signal Variation Over 7 Minutes at Mi

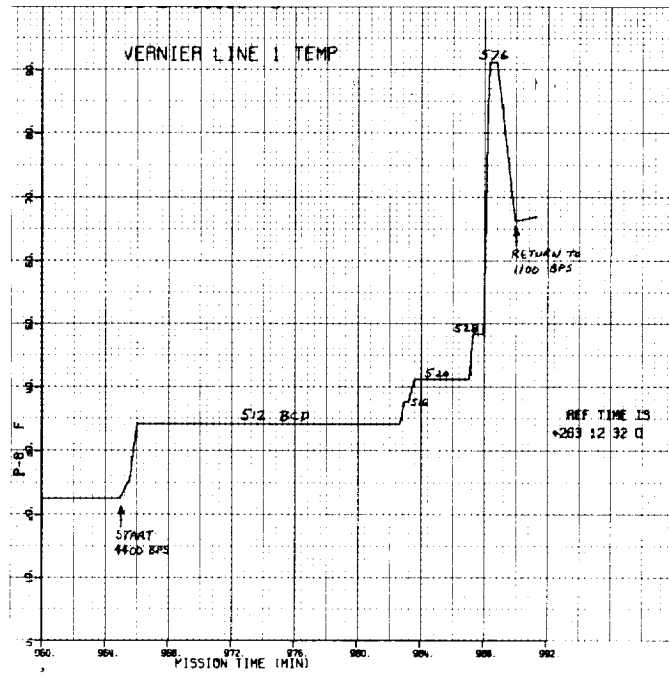




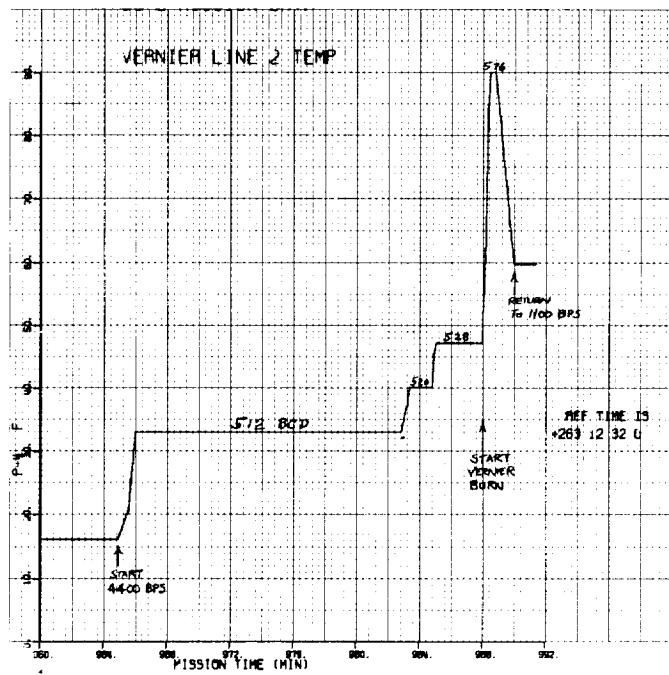
course







a) Line 1



b) Line 2

Figure 5.4-4. Vernier Line Temperatures at Midcourse

TABLE 5.4-5. RELATION OF TRANSMITTED AND TRUE VALUES OF TEMPERATURE MEASUREMENTS AT 4400 BITS/SEC

Transmitted Value, BCD	Range of Corresponding True Values, BCD	Transmitted Value, BCD	Range of Corresponding True Values, BCD
1023	997-1023	680	657-659
1022	992- 996	672	640-659
1020	986- 991	656	631-639
1016	977- 985	648	628-630
1008	964- 976	640	598-627
1000	961- 963	608	589-597
992	941- 960	592	573-588
976	932- 940	584	569-572
968	929- 931	580	568
960	902- 928	576	549-567
944	900- 901	560	544-548
936	898- 899	552	540-543
928	878- 897	548	538-539
912	869- 877	544	525-537
904	867- 868	532	523-524
896	830- 866	528	515-522
864	817- 829	520	510-514
848	808- 816	516	508-509
840	806- 807	512	474-507
832	779- 805	480	468-473
816	778- 779	472	465-467
808	776- 777	468	463-464
800	757- 775	466	462
784	748- 756	464	456-461
776	746- 747	460	455
768	702- 745	457	454
736	698- 701	456	450-453
720	689- 697	452	448-449
712	687- 688	450	447
704	662- 686	448	436-446
688	660- 661	440	435

Here, a series of yes/no decisions are made, starting with the question of whether the measured voltage is greater than 2.5 volts (half-scale). Each succeeding decision involves an incremental voltage half that of the preceding, until the final tenth step refers to only 5 millivolts. If the measured voltage is higher than its final settled value at some decision point in time, the wrong decision may be made, and then there is no way that the following decisions can correct for this, since

$$1 > \left[ (1) (0.5) + (0.5) (0.5) \dots \right]$$

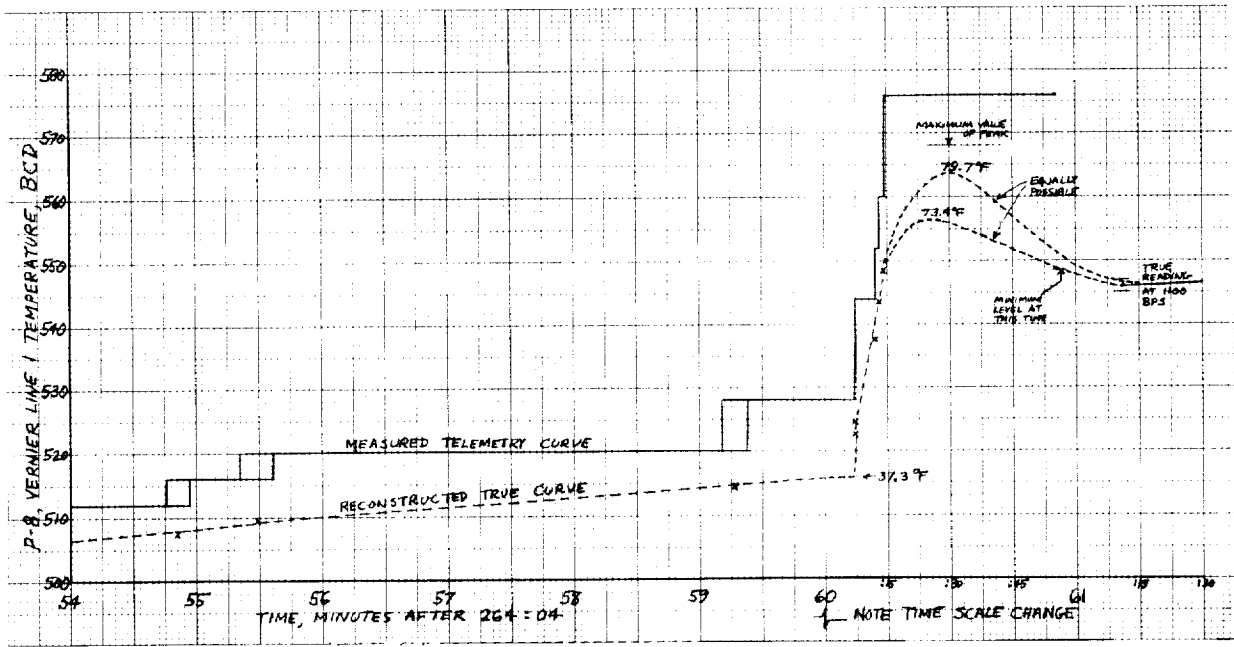
$$1 > \sum_{i=1}^N (0.5)^i \quad \text{for any finite } N$$

The preceding discussion and Table 5.4-5 apply only to temperature measurements for which the current source output is initially charged to its positive maximum, which is the case for P-4 and P-8 in mode 1.

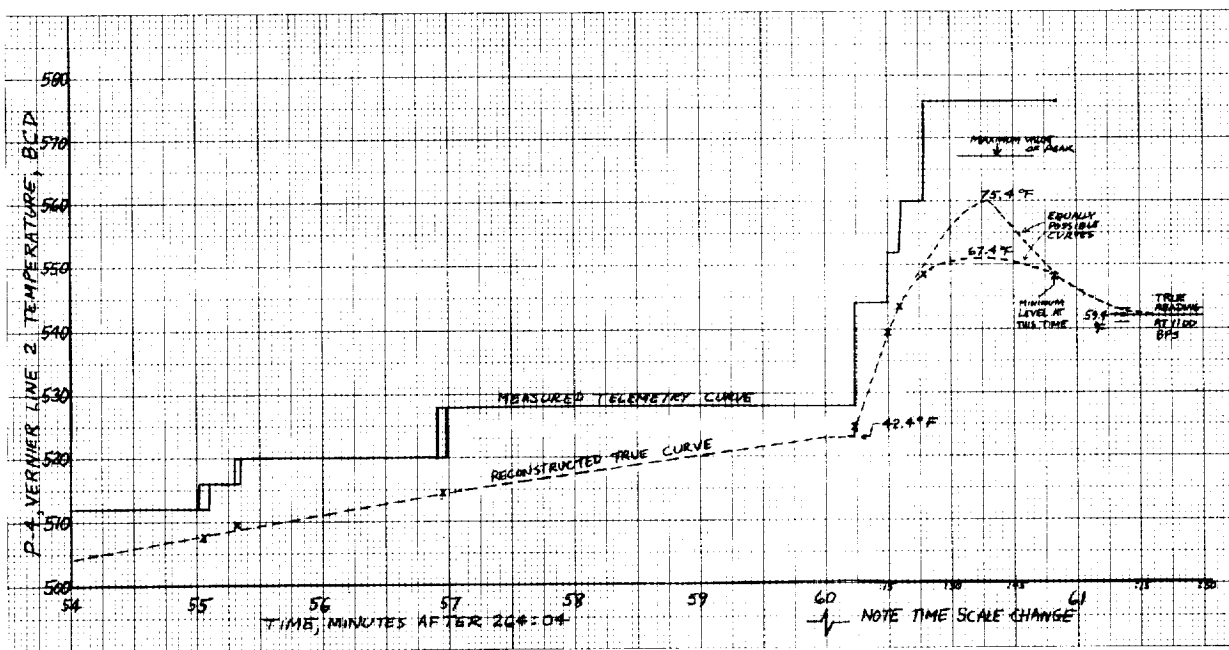
The correction process itself is extremely simple, granted that the above is valid. For example, assume that the telemetered value of a signal has been 512, and then changes to 516. At the time of change, the true value of the signal must be 507-8 bcd, since that is the borderline between the two transmitted value states. In the example of the vernier line signals (Figure 5.4-5), the corrected curves were constructed from a series of points at the measured state transition times. After the midcourse burn, the line temperatures start to cool, thus violating the requirement of unidirectional change. From this point on, the curve reconstruction becomes highly speculative, and no great faith should be put in the curve shapes or peak values. At 05:01:11, data are available at 1100 bits/sec, which requires no correction. The most difficulty was experienced in fitting a reasonable curve to the vernier line 2 data. This signal remained at 576 bcd through 05:00:55, requiring that the true value should have been above 548 bcd at least up to that time. But this situation requires a sudden drop of over 6 bcd (5.4°F) in the following 16 seconds, which is hard to explain in physical terms. In conclusion, the reconstruction method presented is believed to give accurate values up to the 548 bcd level, but the remainder of the curve is subject to the analyst's judgment.

#### 5.4.4.5 Telemetry Bit Stream Characteristics

Data quality before the midcourse correction was excellent, with a very low word error rate even though the data rate was generally maintained at 1100 bits/sec. After midcourse, the situation changed drastically. On almost every mission plot in this report, many extremely spurious values can be seen on that part of the curve after midcourse. It is therefore of great interest to present a possible explanation for the rapid deterioration of telemetry data quality that began when the spacecraft started to tumble (see Reference 1).



a) Line 1



b) Line 2

Figure 5.4-5. Comparison of Corrected and Uncorrected Vernier Line Temperatures

Investigation of an unexplainable value of EP-9 (battery discharge current) during burn 27 led to discovery of a general mechanism that could explain most, if not all, errors that occurred in telemetered data throughout the period when the spacecraft was tumbling. A definite pattern was established which indicated that the telemetry quality, i.e., bit error rate, was not constant in time but varying as the spacecraft tumbled. For most of the tumble period, the data were good, but once a cycle, the data became very bad. Consequently, the average word error rate was low (at 1100 bits/sec) which would normally lead to the conclusion that errors of more than 1 bit per word were unlikely. This, however, is an erroneous conclusion since the data quality was varying with time.

Analysis of a frame-by-frame dump of the telemetered data during a 16-second period surrounding the time of engine ignition (265:03:47:59) revealed that very few parity errors were occurring per frame of data. Some frames had no parity error, and others had, at most, four parity errors per frame. Initially, this low word error rate led to the tentative conclusion that the data point of interest (EP-9) was valid and not a result of 2 bit errors. However, it was noted that, in the case where multiple parity errors occurred in a single frame, the errors were grouped together rather than distributed throughout the frame. This observation led to a more detailed study which clearly showed that the errors were occurring in a cyclic manner. Table 5.4-6 contains a tabulation of the position, in 16 frames of data surrounding the time of ignition, of the noted word errors. (Ignition took place in frame 0.) The asterisk in the table denotes suspected double bit errors, and hence no parity errors. The number of words between the observed word errors is also tabulated. As can be noted, the errors were occurring approximately every 83 words before engine firing, and the period began to change right after firing. In the last two frames of data, the errors appeared to be occurring approximately every 74 words. A change in rate corresponding to the time of engine firing is clearly indicated.

The words containing double bit errors were located by extrapolating the bad parity flagged data assuming periodicity. A double bit error was detected by noting the values of the same words in surrounding frames and comparing them to the suspected value. The binary representations of the words were compared and, if two bits were different, it was concluded that a double bit error occurred.

EP-9 (word 72) had the following binary values in the three frames of interest:

Frame	-1	1	0	0	0	0	1	1	0	0	0		
		0	1	1	0	1	0	0	1	0	1	1	(suspect data)
	+1	1	0	0	1	0	1	1	0	1	1		
			↑				↑						
			BIT 2				BIT 6						

TABLE 5.4-6. WORD ERROR POSITION SUMMARY AROUND BURN 27

Relative Frame Number	Word Position of Error	Number of Words Between Errors
-8*	46	
-7	28	82
-6	11	83
	94	83
-5*	77	83
-4*	59	82
-3	42	83
-2	24	82
-1	7/8	83-84
	90	83-82
0*	72	82
1*	52	80
2	32	80
3*	12	80
	88	76
4	61/63	73-74
5	31/32	70-71
6*	7/8/11	76-78
	81/82	73-74
7	56	74-75
8*	30	74

\*Frame containing suspected words with 2 bit word errors.

Since the current is expected to change at the time of engine firing, the word in the preceding frame (-1) was not used for comparison. The word in the frame following engine firing (+1) is thus considered a most likely value. As can be noted, the suspect data in frame 0 shows probable bit errors in bits 2 and 6 relative to the word value in frame +1.

For further evidence that double bit errors were indeed occurring, several temperature channels were investigated to find a telemetered temperature change during a single frame of data. Since the actual temperature could not change significantly in 1 second, it was felt that any large change would definitely be a telemetry problem. Temperature channel P-9 (word 82) was found to have changed 22 degrees in frame +6. The BCD value in the surrounding frames of data was 574 counts, with a change to 550 counts occurring in frame 6. The binary representation of the two BCD values is as follows:

BCD 574	1	0	0	0	1	1	1	1	0
BCD 550	1	0	0	0	1	0	0	1	0
						↑	↑		
						BIT 6	BIT 7		

A difference of two bits was found, leading to the conclusion that a double bit error indeed occurred in the word. Also, the word position of P-9 agreed precisely with the predicted position based on the data contained in Table 5.4-6.

Examination of the spacecraft tumbling rate, which was determined from DSIF automatic gain control data, indicated that the tumble period was 0.82 second at 03:47:54 and 0.74 second at 04:17:28. These times bound the time of engine firing (03:47:59). The telemetry mode during this period was mode 1 at 1100 bits/sec. This mode contains 100 words per frame, resulting in one word being transmitted every 0.01 second.

The data in Table 5.4-6 show about 83 words between word errors, or 0.83 second, prior to engine firing and 0.74 second after engine firing. These data correlate almost exactly with the spacecraft tumble period at the time of interest. It is therefore concluded that the observed word errors were caused by the tumbling spacecraft.

In retrospect, this result is not too surprising since the RF link was experiencing considerable variations due to the tumbling spacecraft. Signal levels at the ground receiver were varying due to spacecraft omnidirectional antenna gain variations, and the DSIF carrier tracking loop was experiencing large errors due to the frequency variations resulting from the transmitting omnidirectional antenna spinning in space. It is not clear at this time if the bad data were caused by low signal-to-noise ratios, by a momentary loss of carrier phase lock, or by a combination of both effects. There is no doubt, however, that the periodic bad data were caused by the effects of the tumbling spacecraft on the RF link.

#### 5.4.5 REFERENCES

1. F. K. Rickman, "Discussion of Behavior of EP-9 during Burn Number 27," IDC 2292/140, 1 December 1966.

#### 5.4.6 ACKNOWLEDGMENTS

This section was coordinated by R. H. Leuschner. Recognition is due to F. K. Rickman for the analysis of the correlation between word errors and spacecraft tumbling rate.



## 5.5 FLIGHT CONTROL

### 5.5.1 INTRODUCTION

The principal requirements of the Surveyor flight control system are attitude control, accurate angular maneuvers, precision velocity corrections, and soft lunar landing. In order to accomplish these functions, the control system utilizes such hardware as gyros, gas jets, solid fuel engine, liquid fuel engines, optical sensors, timing devices, radars, and acceleration sensing mechanisms.

#### 5.5.1.1 Attitude Control

Attitude control is accomplished by two basic types of active control systems. During coast phase, a bang-bang type of attitude gas jet system is employed which utilizes a novel technique of artificial rate feedback for loop stabilization and, during periods of large moment disturbances such as the main retro phase, the throttle-controlled vernier engine system is used. The error signals required for controlling the propulsion systems are derived from optical sensors or rate integrating gyros which are mounted on the spacecraft in such a way as to provide a three-axis coordinate system. During coast phase, where the gas jet system is used, two modes of operation are available. One choice is celestial referencing, using the sun and Canopus, and the second is self-contained inertial referencing (gyros). The first mode is used to establish accurate attitude, and the second mode is generally used when momentary inertial reference is desired; such an instance occurs during an attitude maneuver.

#### 5.5.1.2 Angular Maneuvers

The rate integrating gyros are also used for accurate angular maneuvers which are accomplished by precessing the gyros at precise rates for given time intervals and slaving the spacecraft to the gyros through the gas jet system.

#### 5.5.1.3 Velocity Correction

Midcourse velocity correction capability of exact magnitudes is provided by a system consisting of three vernier engines, a precision timer,

and an accurate acceleration sensing device. The difference between the commanded acceleration level and the output from the accelerometer provides the error signal that commands the vernier engines to the required thrust levels. The constant acceleration and variable time concept used by the Surveyor flight control system provides the flexibility of choosing velocity corrections from 0 to 50 m/sec.

#### 5.5.1.4 Soft Landing

Surveyor's soft landing capability is provided by a sophisticated technique utilizing radars for computing velocities and range. The range information is then used by an on-board computer to provide velocity commands to the vernier engine system according to an approximate, constant acceleration,  $V^2/R$  function. The velocity information is used by the vernier engine-attitude control loop to produce a near-gravity turn descent by caging the spacecraft thrust axis to the true velocity vector. The velocity information is also used, along with velocity commands, to generate error signals for the velocity control loop.

In order to provide low velocity for the soft landing phase, approach velocity is decreased by a solid fuel rocket engine during the initial portion of terminal descent. The spacecraft attitude during this phase is inertially stabilized by the gyro-vernier engine control system.

#### 5.5.1.5 Mission Performance

Surveyor II successfully performed all commanded maneuvers from launch to midcourse vernier engine firing, including Centaur separation, sun acquisition, star acquisition, coast mode, and premidcourse maneuver (Table 5.5-1). Failure of the leg 3 vernier engine to fire at the midcourse command caused immediate loss of attitude control and spacecraft tumble. Attitude control was not regained during any of 40 postmidcourse vernier engine firing attempts.

#### 5.5.1.6 Analysis

In order to properly evaluate the spacecraft performance, a list of analysis items was prepared (see subsection 5.5.1.7). The items are categorized under major mission phases (such as launch through separation, coast phase, and midcourse correction) for easier identification and performance evaluation. A time and events log is presented in Table 5.5-1, and a summary of results is given in subsection 5.5.3. In subsection 5.5.2, a table of anomalies is presented along with a brief description of each anomaly. Subsection 5.5.3 also contains the conclusions and recommendations of the investigation, and subsection 5.5.4 contains the analysis effort.

TABLE 5.5-1. TIME AND EVENTS LOG

Item	Command	DSIF GMT, day:hr:min:sec	Mission Time, hr:min:sec
Launch (2-inch motion)		263:12:31:59.8	
Separation (indicated by M-9)		12:44:27.4	00:12:27.6
Start of sun acquisition minus roll		12:45:18.3	00:13:18.5
Acquisition sun sensor illuminated (plus yaw)		12:47:41.3	00:15:41.5
Primary sun sensor lockon		12:48:13.0	00:16:13.2
Start of star mapping sun and roll (positive)	0714	18:37:34	06:05:34
Termination of roll (cruise mode on)	0704	19:09:38	06:37:38
Canopus acquisition (manual lockon)	0716	19:11:57	06:39:57
Gyro drift check (start) inertial mode on	0700	19:26:24	06:54:24
Gyro drift check (stop) cruise mode on	0704	21:35:22	09:03:22
Canopus lockon (manual lockon)	0716	21:39:23	09:07:23
Gyro speed check on	0221	264:03:07:43	14:35:43
Next gyro	0222	03:09:05	14:37:05
Next gyro	0222	03:10:06	14:38:06
Next gyro	0222	03:10:31	14:38:31
Gyro speed check off	0223	03:13:07	14:41:07
Start premidcourse sun and roll (plus 75.3 degrees)	0714	04:44:00	16:12:00
Start premidcourse plus yaw (110.5 degrees)	0713	04:48:05	16:16:05
Unlock roll actuator and pressurize helium	0605	04:53:38	16:21:38
Thrust $\phi$ power on	0727	04:54:20	16:22:20
Midcourse velocity correction	3617	05:00:01	16:28:01
	0721	05:00:02	16:28:02
Rate mode on	0701	05:03:48	16:31:48
Inhibit gas jets	0707	05:14:29	16:42:29
2.0-second burn 1 (midcourse thrust levels)	0721	07:28:25	18:56:25
2 (midcourse thrust levels)	0721	07:50:03	19:18:03
3 (midcourse thrust levels)	0721	23:33:23	35:01:23
4 (midcourse thrust levels)	0721	265:01:28:11	36:56:11
5 (midcourse thrust levels)	0721	02:39:14	38:07:14
6 (midcourse thrust levels)	0721	03:47:56	39:15:96
7 (midcourse thrust levels)	0721	04:56:12	40:24:12
Approximate 2.0-second burn (high thrust)	0721	05:43:19	41:11:19
Approximate 20-second burn (high thrust)	0721	08:05:12	43:33:12
Emergency AMR signal command	0730	09:34:17	45:02:17

### 5.5.1.7 Analysis Items – Flight Control System

The following list constitutes the postflight performance analysis effort for the flight control system. The degree to which the individual items were investigated depended on the impact of that parameter on the overall flight control performance assessment.

- 1) Prelaunch
  - a) Temperatures
  - b) Nitrogen weight (nitrogen pressure telemetry calibration)
- 2) Launch through Centaur separation
  - a) Centaur separation
    - Rate stabilization verification
    - Separation rate magnitudes
    - Time to stabilize
    - Total angular excursion
    - Nitrogen gas utilization
  - b) Rate mode latch reset anomaly
  - c) Response of Canopus sensor
- 3) Sun acquisition
  - a) Automatic sun acquisition verification
  - b) Maneuvers
  - c) Roll
  - d) Yaw
  - e) Acquisition time
  - f) Response of Canopus sensor
  - g) Nitrogen gas utilization

- 4) Canopus (star) acquisition
  - a) Acquisition verification
  - b) Star maps
    - Star intensities (predicted/observed)
    - Effect of pitch/yaw limit cycle on map
    - Mean roll rate
    - Dynamic telemetry calibration
    - Other stars identified
  - c) Sensor performance
    - Field of view setting
    - Sensor effective gain
    - Lockon characteristics
  - d) Acquisition maneuver
    - Roll control system performance
    - Manual lockon required
    - Average roll rate
    - Nitrogen gas utilization
- 5) Coast phase attitude control
  - a) Limit cycle
    - Inertial mode
      - Frequency
      - Amplitude
    - Optical mode
      - Frequency
      - Amplitude
  - b) Attitude control errors
    - Noise
    - Tracking
  - c) Gyro drift
  - d) Gas jets
    - Nitrogen gas utilization
    - Thrust level

- 6) Premidcourse attitude maneuver
  - a) Timing accuracy
  - b) Maneuver rates
  - c) Attitude maneuver error
  - d) Nitrogen gas utilization
- 7) Midcourse velocity correction
  - a) Detailed description of spacecraft motion (in terms of flight control variables)
  - b) Roll actuator performance
  - c) Gas jets
    - Reduction in tumble rate
    - Nitrogen gas utilization
  - d) Vernier engine transients predicted from spacecraft attitude transients
- 8) Postmidcourse vernier engine firings
- 9) Retro firing
- 10) Postmission tests and analyses
  - a) Gyro error and thrust command telemetry characteristics
  - b) 22-volt thrust phase bus current during midcourse
  - c) Dynamic versus static calibration of Canopus sensor mapping telemetry signal
  - d) Computer simulations
- 11) Total nitrogen gas utilization

## 5.5.2 ANOMALY DESCRIPTION

The flight control anomalies that occurred during the mission are described briefly below (anomaly details are presented under the appropriate heading).

### 5.5.2.1 Rate Mode Latch Reset During Launch

At a time corresponding approximately to the generation of the legs extend signals, the flight control programmer logic was reset from the normal rate mode to inertial mode. This condition remained until electrical separation from Centaur, at which time data were lost for approximately 30 seconds. When data were restored, the programmer logic circuit had returned to the rate mode, and no other anomalies were observed for the remainder of the mission. A detailed discussion of this anomaly is presented in subsection 5.5.4.2.

### 5.5.2.2 Canopus Lockon Signal Failure

As in the SC-1 mission, it was necessary to operate the Canopus lockon circuits manually because the sensor did not generate a lockon signal. The failure was not completely unexpected because the sensor gain was increased intentionally by approximately 20 percent, based on calibration data, to compensate for possible sensor window fogging. The anomaly is discussed further in subsection 5.5.4.5.

### 5.5.2.3 Midcourse Velocity Correction Failure

The midcourse velocity correction attempt was characterized by vernier engine 3 failure to ignite and subsequent tumbling of the spacecraft which resulted in saturation of the telemetered gyro error signals in a minus pitch, plus yaw, and minus roll direction. The approximate tumble rate at vernier engine shutoff was 448 deg/sec. Ignition failure was confirmed by telemetered strain gage and engine temperature data. Subsection 5.5.4.8 contains a description of this anomaly.

### 5.5.2.4 Late Shutoff of Leg 1 Vernier Engine During Postmidcourse Burn

Review of flight control data, in conjunction with strain gage data, for the postmidcourse vernier engine firings shows that on burn 27 the leg 1 engine continued burning after the commanded termination. This phenomenon is of interest due to the possibility of losing control of the spacecraft, particularly should such burning occur during terminal descent. This anomaly is discussed in subsection 5.5.4.8.

## 5.5.3 SUMMARY AND CONCLUSIONS

### 5.5.3.1 Performance Summary

An SC-2 flight control performance summary is presented in Table 5.5-2.

TABLE 5.5-2. FLIGHT CONTROL RESULTS

	Controlling Specification	Specification Value	Results	Comments
Prelaunch				
Proper gyro temperature control			Roll 172.3°F Pitch 170.2°F Yaw 172.0°F	Time was 12:32
Verification of N <sub>2</sub> loading		4.5 pounds	4.5 pounds	
Centaur separation				
Time required to null rates to less than 0.1 deg/sec	224510E (3.3.3.3)	<0.1 deg/sec within 50 seconds	<20 seconds	
Magnitude of angular rate at separation	224510E (3.3.2.1)	≤3.0 deg/sec	0.113 deg/sec (pitch)	
Sun acquisition	224510E (3.4.1)	Minus roll maneuver until activation of acquisition sun sensor and then a plus yaw maneuver until primary sun sensor illumination		
Proper sun acquisition				
Roll			-71.5 degrees of roll	
Yaw			15.0 degrees of yaw	
Total time			174.8 seconds	
N <sub>2</sub> gas used	Design	0.054 pound (average)	<0.05 pound	Tank temperature may not have been at steady state.
Star acquisition	224510E (3.4.2)	Positive roll maneuver sufficient to produce an adequate star map for Canopus verification. Provide a lockon signal when Canopus appears in the sensor field of view		
Proper acquisition and verification of Canopus			Manual lock	High gain setting of Canopus sensor to compensate for possible window fogging removed the capability of automatic star lockon.
Roll angle from beginning of maneuver to Canopus			240.0 degrees	
Stars identified			Zeta Draconis, Beta Draconis, Ras Alhague, Shaula, Theta Scorpii, Alpha Arae, Gamma Arae, Alpha Tr. Australis, Zeta C. Majoris, and Canopus	
Mean roll rate during star map phase	224510E (3.4.2.1.1)	0.5 deg/sec	+0.4998 deg/sec	
Effective gain (relative to nominal Canopus) of Canopus sensor			+1.5 x Canopus	Normally the gain setting is 1 x Canopus
Magnitude of window fogging over 63-hour mission			None	
N <sub>2</sub> gas used	Design	0.048 pound (average)	0.01 pound	
Coast mode				
Sun and star tracking errors - tracking noise	224510E (4.3.1.1)	Roll axis shall be held to within 0.20 degree of sun-spacecraft line, plus a ±0.30 degree limit cycle		Sun and star error signal noise level were low enough to have no effect on the limit cycle performance.
Average error from sun line			-0.07 (pitch) -0.1 (yaw)	
Average error from Canopus line of sight		Same magnitudes as above for Canopus-spacecraft line	-0.08 (roll)	
Limit cycle (gas jet system)				
Optical mode/inertial mode	224510E (4.3.1.1 and 4.3.1.2)	±0.30 degree		Values are that of the total deadband. Predicted values were:
Average amplitude - roll			0.441/0.47 (roll)	0.44/0.44
Average amplitude - pitch			0.45/0.42 (pitch)	0.44/0.44
Average amplitude - yaw			0.37/0.43 (yaw)	0.44/0.44
Average period			64 (optical) and 61 sec/pulse (inertial)	80 (optical) and 117 sec/pulse (inertial)
Average N <sub>2</sub> usage	Design	0.0012 lb/hr (average)	0.0012 lb/hr	
Gyro drift	224510E (4.3.1.5)	<1 deg/hr		
Roll			Roll -0.78	
Pitch			Pitch +0.24	
Yaw			Yaw +1.09	
Gas jet thrust level	224510E (4.3.3.2)	>0.052 pound	0.056 pound (roll)	Design value is 0.057 pound
Premidcourse maneuvers				
Maneuver angles	224510E (4.3.2.1)	Rates shall be controlled to be 0.5 ± 0.0011 deg/sec		Assuming a precession level of 0.5000 deg/sec
Roll			-75.372 degrees	
Yaw			-110.591 degrees	
Precession command times	224510E (3.6.4.8)	0.2 second plus 0.02 percent of command interval magnitude		These times were obtained from the gyro error signal response profile
Roll			150.744 seconds	
Yaw			221.182 seconds	
Attitude maneuver accuracy (includes drift, initial attitude errors, and limit cycle)			0.39 degree (pitch) 0.04 degree (yaw)	Calculated using actual data of drift, attitude errors, and execution errors

\*These are mean times between gas jet pulses.



### 5.5.3.2 Conclusions

#### Anomalies

Four flight control anomalies exist. Of these, the rate mode latch reset during launch and the Canopus lockon signal failure cannot be classed as primary failures since they did not and would not result in a significant reduction in mission scope. Further, modifications have been performed on the respective subsystems to prevent future occurrences of these anomalies. The midcourse correction failure and the burn 27 anomalies, while not necessarily related, both involve failures of the vernier engine system. Seriousness of the midcourse failure is a matter of record. The effect of a burn 27-type failure on a terminal descent could well be serious.

#### Launch Through Centaur Separation

Proper nulling of the separation rates was achieved well within the 51-second period allowed. The Centaur and Surveyor telemetry separation rate values agree within the accuracy limits of the respective telemetry circuits.

#### Automatic Sun Acquisition

Automatic sun acquisition was completed 51.365 seconds after first indication of the programmer clock countdown at separation. The Canopus sensor was looking at an illuminated earth at the conclusion of sun acquisition.

#### Canopus Acquisition

It was again demonstrated that successful Canopus acquisition can be achieved using the manual lockon. Based on the good correlation between measured and predicted star map angles, it was possible to positively identify ten stars plus the moon and earth.

None of the expected visible stars would have been missed due to either pure yaw or combined pitch and yaw limit cycling. Also, no sufficiently bright stars were near the desired field of view to have been seen due to the limit cycling.

Effective gain of the Mission B Canopus sensor was over 1.5 times Canopus; a 1.17 gain was expected due to the sun filter change. It is concluded that no sensor window fogging occurred, and that the three star sensor outputs were normal for the actual Mission B conditions. Thus, the star sensor performed in a normal and satisfactory manner.

#### Coast Mode

Limit cycle behavior was quite similar to that of Mission A. Some double pulsing was again experienced, but with a very small nitrogen penalty (~0.002 pound) and no measurable effect on limit cycle amplitude.

The gyros operated in a normal manner during coast phase operations. The gas jet attitude control system operation was normal as indicated by satisfactory limit cycle performance, automatic sun acquisition, Canopus verification and acquisition, and nitrogen gas usage.

#### Premidcourse Maneuvers

The net attitude error components were 0.39 degree along the negative yaw axis and 0.04 degree along the negative pitch axis. The resultant pointing error has a 99 percent circular probable uncertainty of 0.20 degree.

#### Midcourse Velocity Correction

At the midcourse correction signal, vernier engines 1 and 2 began producing thrust in a near-normal manner, while engine 3 did not produce appreciable thrust, causing loss of control and spacecraft tumbling. Flight control system performance during the midcourse burn appeared to be normal under the prevailing circumstances. The flight control system outputs (vernier engine throttling signals and roll actuator position) behaved in a predictable manner during the vernier ignition transient and throughout the burn period.

Roll actuator response during the midcourse phase appeared normal. Zero BCD change in the roll gyro error over the first 250-millisecond interval is consistent with analog computer study results.

The nitrogen gas jets were active for 869 seconds following midcourse ignition, during which period 2.6 jets operated continuously at 64 seconds of specific impulse and a tumble rate reduction efficiency of 1.0 deg/sec per lb-sec of total jet impulse.

#### Postmidcourse Vernier Engine Firings

Thirty-nine vernier engine firing periods were commanded between the midcourse and retro firings. Analysis of these firings is continuing, but results to date provide strong indications that at burn 27 (2.0-second commanded duration) the leg 1 vernier engine did not shut off when commanded and, in fact, burned for over 2 seconds after the shutoff command.

#### Postmission Tests and Analyses

Gyro error telemetry signals were not appreciably affected by a degradation in gyro transfer function. The accuracy of these signals is better than that associated with the thrust command telemetry signals. The gyro transfer functions at midcourse were not significantly different from those that established the telemetry calibrations.

The nominal saturation curve for use in correction of SC-2 gyro telemetry data has been validated for angles above 6 degrees.

The present analog computer model of spacecraft and flight control dynamics provides a close match with observed SC-2 behavior under the assumption that engine 3 produced no thrust.

### 5.5.3.3 Recommendations

The following recommendations are made:

1) Data acquisition

- a) Mechanize onboard calibration for flight control variables.
- b) Mechanize onboard clock (to standardize mission time base).
- c) Provide a number of continuous analog data channels (e. g. , FM/FM. )
- d) SFOF operations

Add NASA time code (36 bit) to all SFOF data (plotters, brush recorders, etc. ). Both slow and fast codes should be provided for selection keyed to paper speed.

Record telemetry signal voltages WBFM on magnetic tape with time code. (Compensation track will be required.)

Provide dub copies of all necessary magnetic tapes (digital or analog, e. g. , PCM or WBFM analog) plus copies of all SPAC brush recordings to Hughes.

Add sufficient brush recorders to SPAC so that 90 to 100 percent of quick-look analysis requiring continuously recorded data can be performed independent of digital data processing operations.

Provide an interlocked (electrical) event marker on all brush recorders. (It may be of value to insert same signal into digital tapes as well.)

Provide 1-second marking pens on all brush recorders (paper edge). Note that the event marker can be mechanized to use the same pen by means of an override.

Standardize brush paper speeds (one mm/sec and 5 mm/sec are recommended).

- e) Expedite acquisition of DSIF data (in the form of PCM/FM tapes), and assume DSIF to be the primary source. SFOF data can be used to fill in whenever DSIF data contains gaps.
- f) Sync magnitude register start of countdown with telemetry word time.

## 2) Data processing

- a) Graphic presentation of data is recommended as primary mode of data presentation, with tabs as backup for use in interpreting details and checking digital word structure of questionable points.
- b) Point plots (every available point) are preferred for detailed analysis. However, continuous line plots would be adequate for majority of flight control postmission analysis.
- c) Time base: Must be exactly determinable. Should be standardized as much as possible (particularly during vernier engine firing periods).
- d) Ordinate

Use of data variation to determine ordinate scale is not adequate.

Scale and limits must be individually selectable, depending on nature of data (both with respect to sample rate and curve slope).

Except where otherwise specified, raw BCD should be plotted.

However, both BCD and engineering units are required on tabs (the commutator word number and frame number associated with each data point would be desirable, i. e. , coordinates of each data point).

- e) Fortran data tape outputs from RFM tape processors are recommended so that Fortran data tapes may be produced either in parallel with other processor outputs or independently, as may be required.
- f) Develop methods for producing wideband FM tapes of flight control variables (0 to 5 volts, analog, staircase) from both PCM data and RFM data. Full exploitation of Hughes capabilities in this regard could save money and time in failure review or normal postmission analysis.

## 3) Subsystem measurements (additions and changes)

- a) Thrust chamber pressure (all legs) should be added.
- b) Propellant shutoff valve inlet pressure (all legs) for both oxidizer and fuel should be added.

- c) Thrust commands should be measured by coil currents rather than coil voltage drops (this change is now planned for all remaining spacecraft).
- d) If vernier engine strain gages remain primary measure of engine response, then all three legs should be sampled at as high a rate as possible in all applicable modes. Ten samples per second should be the minimum.

4) SPAC operations

In order to increase effectiveness of terminating midcourse velocity correction early, if required, the following SPAC operational changes are proposed:

- a) Assign responsibility for decision to terminate to one person in flight control area. This person would communicate his decision directly to SPAC bus chief.
- b) Prearrange to have DSIF operator immediately send necessary termination commands upon verbal request of bus chief or his designee.

5) Canopus sensor

Install higher transmissibility filter in the Canopus sensor sun channel to set effective gain nearer to nominal.

6) Limit cycle double pulsing

Investigate double pulsing phenomenon observed by means of both SC-1 and SC-2 telemetry data, even though to date no known failures have been caused by this problem.

#### 5.5.4 PERFORMANCE ANALYSIS

##### 5.5.4.1 Prelaunch

A comparison of prelaunch flight control temperatures with those temperatures obtained during the 16 August 1966 joint flight acceptance composite, system readiness, and countdown tests at AFETR is presented in Table 5.5-3. The prelaunch data, which were recorded immediately after turnon of flight control coast phase power at 09:45 GMT, reflects the expected lower temperature. Data received at launch compares favorably with the joint flight acceptance, system readiness, and countdown test data which were taken 40 minutes after application of flight control coast phase power. All data were obtained at 550 bits/sec.

TABLE 5.5-3. FLIGHT CONTROL TEMPERATURES, °F

Telemetry Channel	Prelaunch	Launch	Joint Flight Acceptance Composite Test, System Readiness Test, and Countdown, 16 August 1966
Electronics unit (chassis 1), FC-44	74.4	NA	100.4
Electronics unit (chassis 6), FC-45	94.3	125.8	126.3
Roll gyro temperature, FC-46	172.3	172.3	172.4
Pitch gyro temperature, FC-54	166.6	170.2	170.3
Yaw gyro temperature, FC-55	170.2	172.0	170.3
Canopus sensor temperature, FC-47	73.9	91.9	90.1
Nitrogen tank, FC-48	71.2	84.5	76.2
Attitude gas jet 2, FC-70	69.1	82.3	88.0
Roll actuator, FC-71	70.1	-	84.4

Nitrogen on-board prelaunch weight (10:35 GMT) was 4.5 pounds based on a corrected pressure reading of 4586 psi and a corrected nitrogen tank temperature of 79.74°F measured at 550 bits/sec. The telemetry calibration curve for nitrogen pressure is shown in Figure 5.5-1. Table 5.5-4 presents the nitrogen tank temperature sensor calibration data obtained during the SC-2 gas depressurization and calibration test of 17 August 1966.

#### 5.5.4.2 Launch Through Centaur Separation

Events observed during the period from launch until separation of the spacecraft from Centaur are described in Table 5.5-5. Portions of this table were included in the flight control spacecraft/performance/analysis/command report (Reference 1).

After extending its landing legs, Surveyor is separated from the Centaur booster. When the three legs down and separation signals have been generated, the programmer removes the logic signal that inhibits operation of the gas jet amplifiers. At this same instant, the magnitude register begins to count down to zero for a total of 1024 counts, or a 51-second interval; register counting inhibits the start of sun acquisition for these 51 seconds to give the cold gas attitude control system opportunity to rate stabilize the spacecraft. Table 5.5-5 presents these events in time sequence.

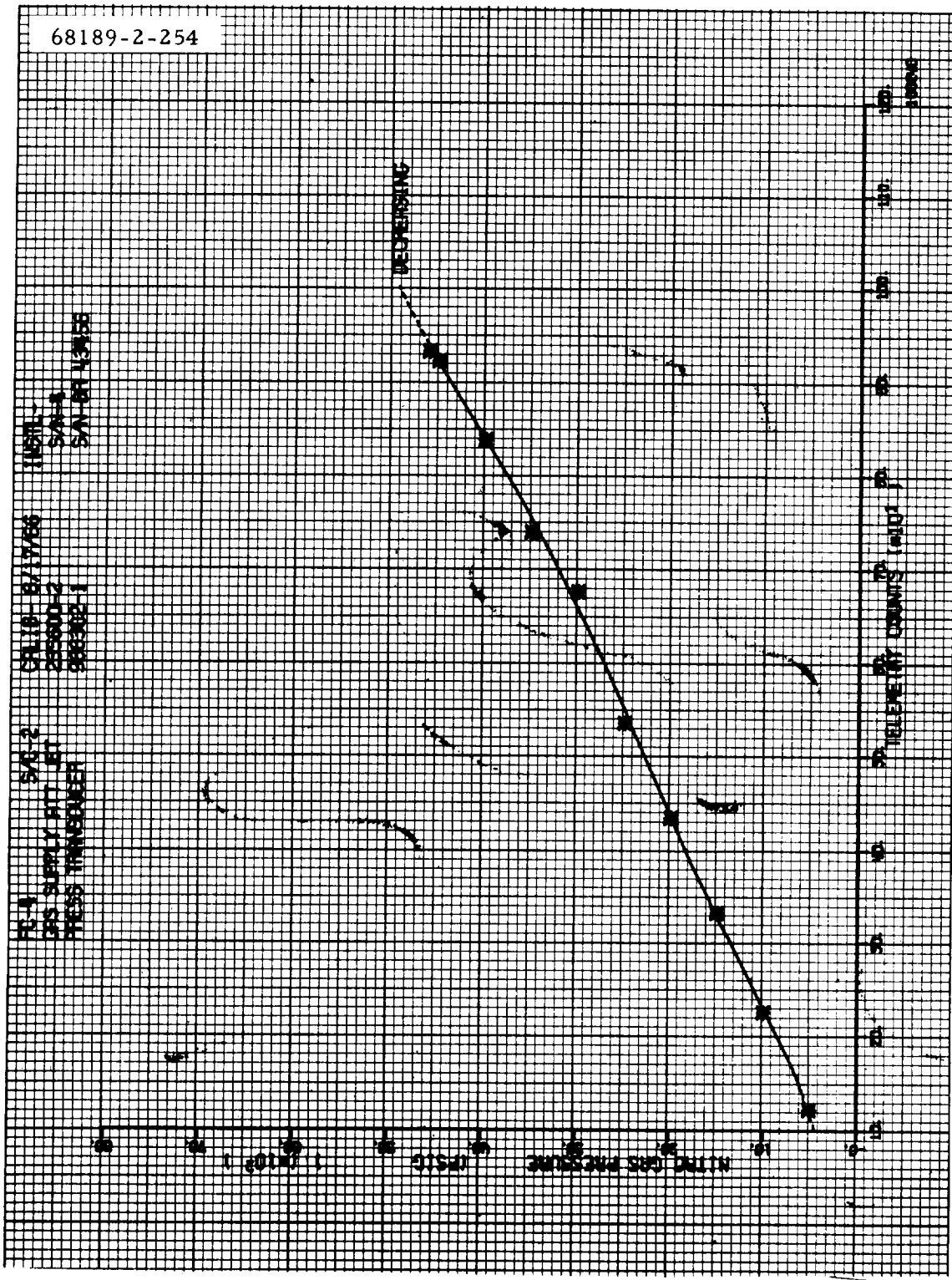


Figure 5.5-1. Nitrogen Pressure Telemetry Calibration Curve

TABLE 5.5-4. NITROGEN PRESSURE CALIBRATION DATA

GMT, 17 August 1966, hr:min:sec	FC-4 Telemetry, BCD	Gage Pressure, psig	Telemetry Mode	Nitrogen Tank Temperature Telemetry		FC Line Drop, FC-77, BCD	Commutator Unbalance Current S-05, BCD
				BCD	°F		
16:39:45	0931	4600	2			0008	0131
16:42:03	0932	4600	C	0566	79.74		
16:50:03	0922	4500	C	0566	79.74		
16:51:53	0921	4497	2			0008	0132
17:17:12	0838	4000	C	0560	73.54		
17:18:37	0838	4000	2			0007	0132
17:34:52	0739	3500	2			0007	0132
17:36:41	0739	3500	C	0555	70.00		
17:47:01	0641	3000	C	0553	68.23		
17:48:26	0641	3000	2			0008	0131
18:00:15	0535	2500	C	0560	74.42		
18:01:11	0535	2500	2			0007	0131
18:07:57	0435	2000	2			0008	0131
18:09:08	0434	2000	C	0567	80.63		
18:18:13	0332	1500	C	0555	70.00		
18:19:43	0332	1500	2			0007	0131
18:28:37	0225	1000	2			0008	0131
18:29:52	0225	1000	C	0559	73.54		
18:44:42	0122	510	C	0561	74.42		
18:45:55	0122	510	2			0008	0131



TABLE 5.5-5. LAUNCH THROUGH SEPARATION EVENTS

Hr:Min:Sec	GMT			Event	Observation
	From Launch				
	Min:Sec	Seconds	Expected, seconds		
12:32:00				Liftoff	No noticeable effect on telemetry.
12:32:03	00:03	3	3	Atlas roll started	FC-49 roll precession command indicated start of roll.
12:32:16	00:16	16	16	Atlas pitch started	FC-16 (pitch gyro error) and FC-50 (pitch precession command) indicated start of pitch. Pitchover continued for 130 seconds at an average rate of about -0.4 deg/sec and a peak pitch rate of -0.79 deg/sec.
12:32:33	00:33	33	-		20-second loss of data. This was the first postliftoff loss of data. All data outages are annotated on the mission generated brush recordings.
12:33:48	01:48	108	-	Inertia switch opens	Acceleration reaches about 3.6 g.
12:34:22	02:22	142	-	Inertia switch closes	Acceleration decays to about 3.35 g.
12:34:28	02:28	148	145.6	Mark 2 booster engine jettison	Gyros indicated separation rates caused by booster engine separation. Pitch at separation rose to -1.386 deg/sec; yaw rate rose to 0.534 deg/sec.
12:34:53	02:53	173			Atlas/Centaur attitude was restabilized.
12:35:24	03:24	204	203.5	Mark 4 jettison nose fairing	As with SC-1, secondary sun sensors FC-7, -8, -9, and -10 rose to values between 2.5 and 3 volts. Also, primary sun sensor saw nose fairings and indicated pitch and yaw sun sensor errors. Canopus intensity, FC-14, also rose as with SC-1 to 3 volts. For a detailed description of star intensity and star error from Mark 4 through sun acquisition, see subsection 5.5.4.3.
12:35:58	03:58	238	241.7	Marks 5 and 6; ATLAS SECO and VECO	Indicated by pitch and yaw gyro errors.
12:36:08	04:08	248	243.6	Mark 7 Atlas/Centaur separation	Atlas/Centaur separation rates were indicated by the flight control sensor group gyros.
12:36:16	04:16	256	251.9	Mark 8 start Centaur main engine	Nulling of Atlas/Centaur separation rates as indicated by the flight control sensor group gyros.
12:43:24	11:24	684	681	Mark 9 injection	Indicated by gyro errors.
12:43:50	11:50	712	-	Flight control to inertial mode	Corresponding to approximate time of legs-extend signal, flight control reverted to inertial mode from rate mode. This occurred 35 seconds prior to spacecraft/Centaur separation. Pitch and yaw gyro error signals began registering. Maximum pitch error, FC-16, was 3.4 degrees; maximum yaw error, FC-17, was -4.9 degrees.
12:44:25	12:25	805	-	Mark 13 Surveyor/Centaur separation	Instantaneous loss of data for 30 seconds. At resumption of data, rate mode was on and magnitude register was counting down to zero before starting automatic sun acquisition. Change from inertial mode to rate mode at separation resulted from programmer logic. (Subsequent review of data for this period indicated completion of rate stabilization in approximately 20 seconds following separation.)

Rate stabilization is accomplished by using the three-axis gas jet attitude control system to torque the spacecraft and drive the caged integrating rate gyros to within the deadband of each gas jet amplifier. Thus, at the end of a nominal rate stabilization maneuver, the spacecraft achieves a low angular velocity with a random orientation in inertial space. This system response is dependent upon the magnitude and direction of the initial velocity vector and the gas jet thrust levels.

Flight control system performance just after booster separation was evaluated in terms of verification of proper nulling of separation rates, time required to null rates to less than 0.1 deg/sec, total angular excursion, and magnitude of angle rates at separation.

Spacecraft telemetry data showing the tipoff transient are presented in Figures 5.5-2 and 5.5-3. Other pertinent data are found in Reference 2 as follows:

- 1) Time of separation command (commutated data) T + 752.58 ± 0.02 second (or ≈ 263:12:44:32.6 GMT)
- 2) Time of spring extension

<u>Measurement Number</u>	<u>Spring Number</u>	<u>Time of First Motion, seconds</u>	<u>End of Motion, seconds</u>	<u>Spring Extension Time, seconds</u>
CY2D	1	752.584	752.713	0.129
CY4D	2	752.584	752.713	0.129
CY5D	3	752.584	752.713	0.129

- 3) Combined Centaur plus SC-2 pre-separation rates (deg/sec):
  - Pitch 0.12
  - Yaw 0.15
  - Roll 0.03

Table 5.5-6 presents a comparison of SC-2 data analysis results with the referenced GDA Report results.

Centaur and Surveyor telemetry separation rate values agree within the accuracy limits of the respective telemetry circuits. The differences in sign are due to the different coordinate references used by General Dynamics/Astronautics and Hughes.

The change in angular rates at mechanical separation could not be determined accurately because of the transition from inertial mode to rate mode at the time of electrical separation (causing the gyros to be caged). The caging transients tended to mask the effect of any change in angular rates. An analog computer run was made to separate the effect of the caging transients from the separation induced transients, if any. The computer run was started with the simulated initial conditions that existed at the time of electrical separation, with gas jets inhibited. Five seconds after electrical separation (the time of mechanical separation) the gas jets were enabled. A comparison of the simulated separation transients (with no change in angular rates at mechanical separation) and the actual separation transients

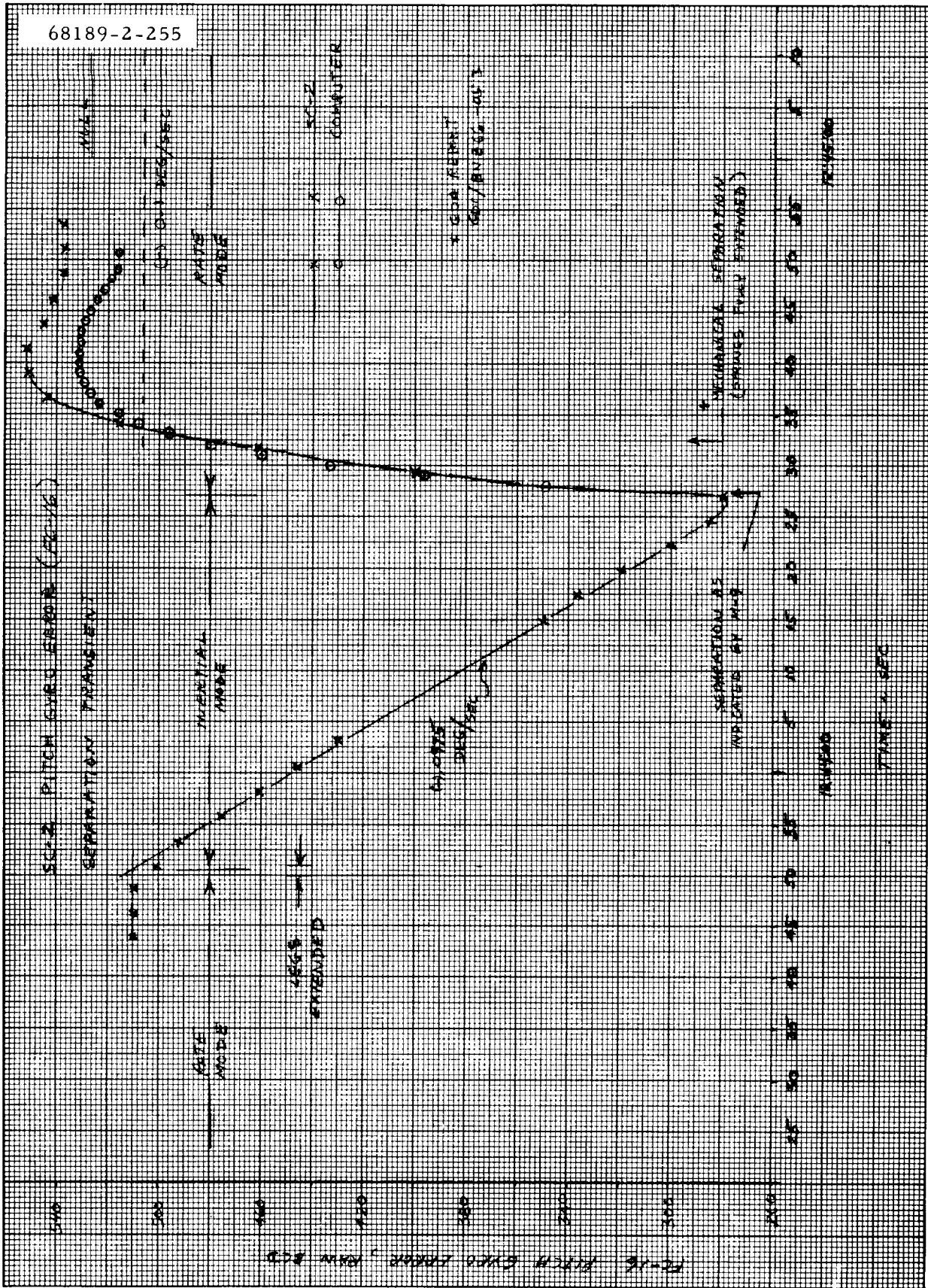


Figure 5.5-2. Pitch Gyro Error (FC-16) Separation Transient

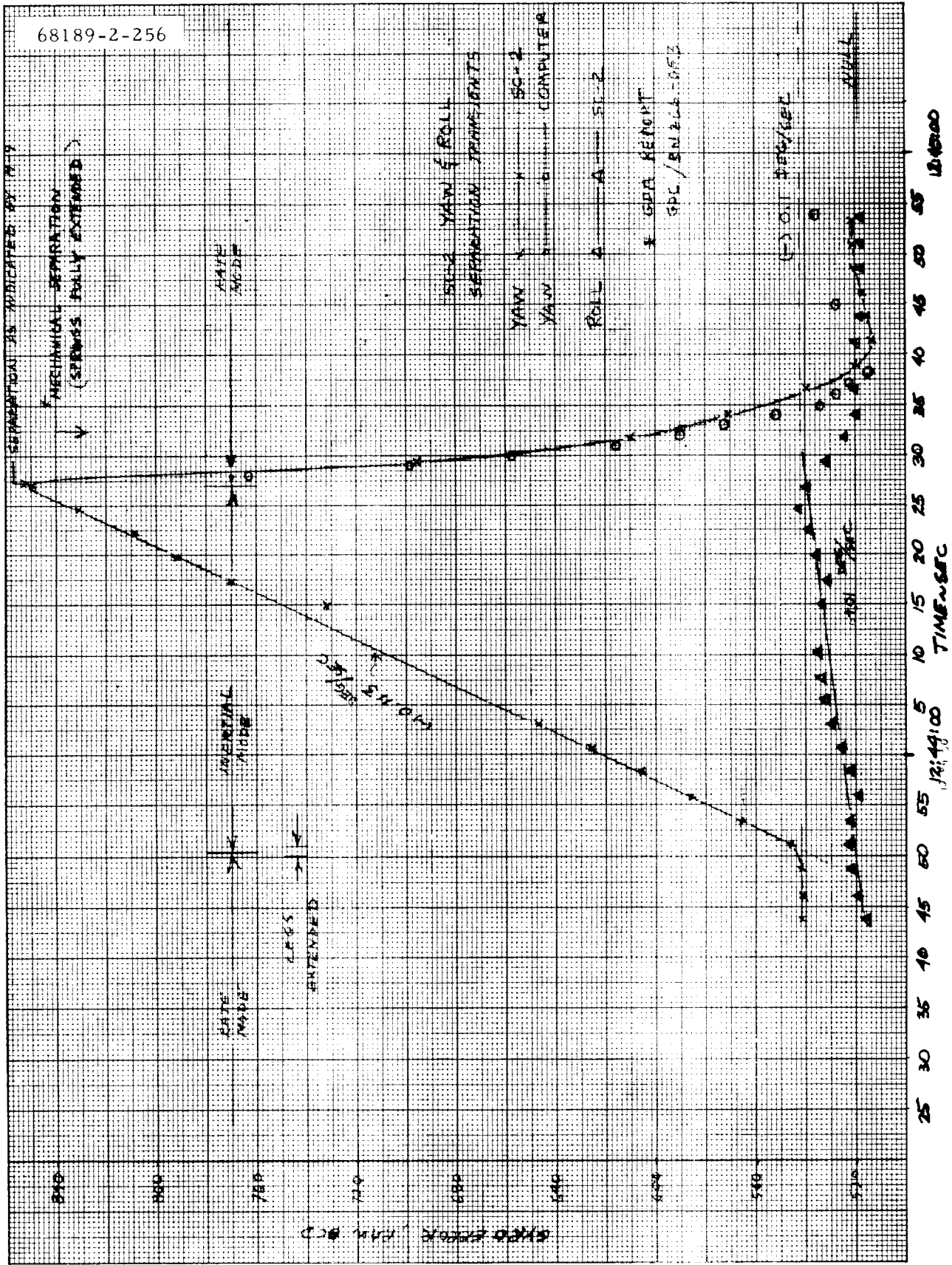


Figure 5.5-3. Yaw and Roll Separation Transients

is shown in Figures 5.5-2 and 5.5-3. Based on this comparison, it can be concluded that the change in spacecraft angular rates at mechanical separation was essentially zero and the time required to dissipate the existing rates to 0.1 deg/sec was less than 4 seconds, well within the allowable 51-second period.

TABLE 5.5-6. CENTAUR SEPARATION RATES

Parameter	Telemetry Signal	Preseparation Rates		Time to Reduce Separation Rates to <0.1 deg/sec, seconds
		Spacecraft, deg/sec	Centaur, deg/sec*	
Pitch gyro error	FC-16	0.0915	0.12	< 4
Yaw gyro error	FC-17	-0.113	0.15	< 4
Roll precession command	FC-49	0.01	0.03	0

\*General Dynamics/Astronautics Report No. GDC/BNZ66-053.

Note: See Reference 3 for calibration coefficients used in this analysis.

Rate Mode Latch Reset Anomaly

At approximately 12:43:52:588 (+0, -2.4 seconds), the flight control programmer rate mode latch was reset to zero with no command being sent. This placed the flight control system in the inertial mode with the gyros uncaged. The latch was apparently reset by transients generated by the legs extend signals at approximately 12:43:53.788 (+0, -2.4 seconds). This anomaly did not affect flight control system performance because the rate mode latch was automatically set high at separation of the spacecraft from Centaur and remained that way as required until the programmer 20-cps clock counted down to zero. This portion of the flight control system operation was normal in all respects, with the significant events occurring as shown below.

<u>Event</u>	<u>GMT</u>
Magnitude register starts to count down	12:44:26.935
Spacecraft separation (as indicated by M-9)	12:44:27.385 (+0, -2.4 seconds)
Rate mode on	12:44:28.585 (+0, -2.4 seconds)
Sun mode on } Rate mode off }	12:45:18.982 (+0, -2.4 seconds)

The actual period during which the magnitude register counted was extrapolated from magnitudes at 12:44:27.985 and 12:45:15.982 and calculated to be 51.147 seconds.

Operation of the programmer at anomaly occurrence can be described as follows: 1) a transient voltage for less than 2 milliseconds was received by the legs-down/separation "and" gate at the time of leg extension even

though the separation switch had not yet opened. This resulted in generation of MV04 signal which initiated the initial condition signal AR03, which reset the rate mode latch (Figure 5.5-4). 2) Although AMV5 and MV05 signals were possibly generated, these signals do not reach their normal duration of 20 milliseconds unless the input to the legs-down/separation "and" gate exceeds 20 milliseconds; if the input is less than 20 milliseconds, then AMV5 and MV05 are of the same duration as this input. Therefore, with an input of less than 20 milliseconds, the duration of AMV5 and MV05 did not exceed that of AR03. Thus, they did not reset the gas jet inhibit latch, set the rate mode latch, or start automatic sun acquisition. (For this to happen, the duration of AMV5 and MV05 must be greater than MV04). 3) At receipt of spacecraft separation signal, the signals were normal and a normal sun acquisition was initiated.

That transients produced on the legs down and/or separation lines could cause incorrect conditioning of the programmer latches on the SC-1 and SC-2 configuration programmer was known from SC-1 tests (see TFR 45321). However, the system was deemed flight acceptable since the possible occurrence of such a malfunction would not jeopardize the mission. To prevent this condition occurring on future missions, the programmer latches were redesigned to reduce transient susceptibility on the SC-3 and subsequent programmers (for further details, see ECA 112307).

#### Response of Canopus Sensor From Launch Through Centaur Separation

Although the star window shutter is closed and the outputs of the Canopus sensor are not utilized by the flight control system during this phase of flight, the Canopus sensor outputs are examined along with other telemetered signals in order to completely understand the behavior of the sensor and ascertain whether or not it is operating satisfactorily.

At launch (263:12:32:00), the telemetered values for FC-12 (star angle) and FC-14 (star intensity) were 0 degree and 0.55 volt, which are nominal values for an encapsulated spacecraft. When the nose fairing was jettisoned at Mark 4 (263:12:35:24), permitting light to reach the spacecraft, the star intensity signal increased to 3.2 volts, and the Canopus lockon signal came on. Although the star window shutter is closed, it is not light tight; thus any light flooding the light shield registers as star intensity. Approximately 40 seconds later, after shutdown of Atlas sustainer and vernier engines at Marks 5 and 6 (263:12:35:58), the star intensity signal decreased to its nominal sun channel not illuminated value of 0.55 volt, indicating that the source of light seen by the sensor was either sun or earthshine reflecting from a jettisoned nose fairing.

As the Centaur continued to thrust and pitch, the star intensity signal increased from 0.55 to over 3.0 volts, and the Canopus lockon signal came on. When injection occurred (263:12:43:53), the intensity signal decreased to 0.55 volt, and the Canopus lockon signal went off. This response sequence was probably caused by sun or earthshine reflecting from stowed leg 3 and other parts of the spacecraft in the Canopus light shield. As the Centaur/Surveyor continued to pitch, the reflections terminated when the injection maneuver changed the sun and earth lines.

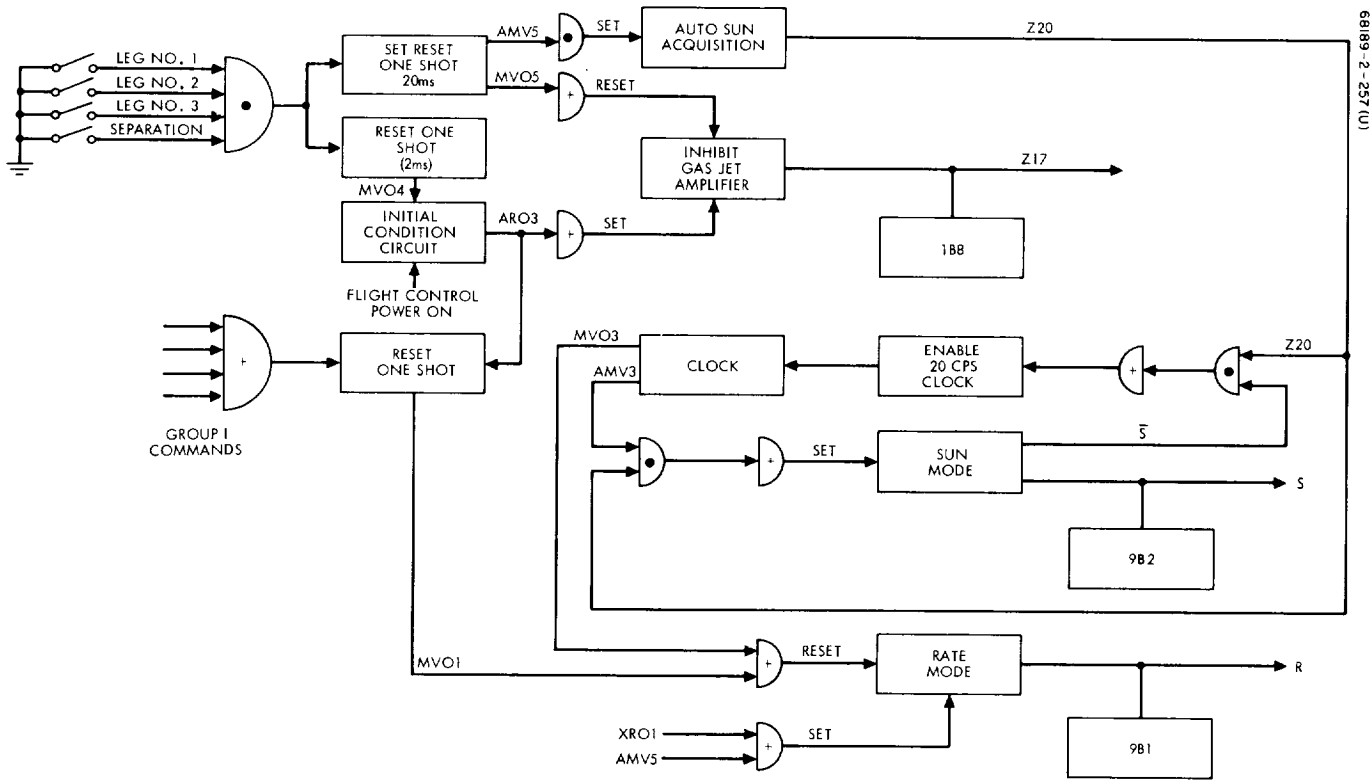


Figure 5.5-4. Rate Mode Latch Reset Anomaly

#### 5.5.4.3 Automatic Sun Acquisition

Sun acquisition is initiated automatically by a negative roll maneuver command from the flight control programmer approximately 51 seconds after separation. The spacecraft rolls at 0.5 deg/sec until the sun enters the acquisition sun sensor field of view which is approximately 3 degrees wide and includes the negative pitch half of the pitch-roll plane. When this occurs, the negative roll command is removed and a positive yaw command is initiated. The spacecraft yaws at 0.5 deg/sec until the sunline enters the primary sun sensor field of view, causing a lockon signal to be generated which switches pitch and yaw control of the spacecraft from the gyros to the primary sun sensor.

The automatic sun acquisition mode was initiated at 263:12:45:18.3 as indicated by the start of the negative roll maneuver (Figure 5.5-5). This maneuver occurred 51.365 seconds after first indication of the programmer clock countdown at separation. Completion of the roll maneuver (acquisition sun sensor illuminated) and start of the positive yaw maneuver occurred at 12:47:41.3 and 12:48:13, respectively (Figure 5.5-6). Elapsed times for the roll and yaw maneuvers were 143.0 and 31.7 seconds, respectively. Based on a fixed precession rate of 0.5 deg/sec, the total yaw maneuver was 15.9 degrees to the point where the primary sun sensor lockon signal was generated. From that point, a combined pitch and yaw maneuver was performed to null the primary sun sensor error signals. As shown in Figure 5.5-7, the final pitch and yaw optical maneuver magnitudes were 2.5 and 12.5 degrees, respectively. A polar plot of the complete automatic sun acquisition sequence is shown in Figure 5.5-8.

#### Response of Canopus Sensor From Centaur Separation Through Sun Acquisition

Separation disturbance torques caused spacecraft movements that resulted in the star intensity signal increasing to over 3.0 volts, indicating that light was being reflected into the sensor from either extended leg 3, other parts of the spacecraft, or Centaur. When the roll maneuver portion of the automatic sun acquisition sequence got under way, the star intensity signal decreased to less than 1.0 volt, again indicating that the direction of reflected light was changing.

At the conclusion of automatic sun acquisition, sun lockon occurred (263:12:48:13), thereby opening the star window shutter and resulting in a full-scale, 5-volt, star intensity signal. There were three possible sources of light at that time: Centaur, moon, and earth. Of these, Centaur and the moon could not have been in the field of view regardless of roll angle, but the earth could have. The star intensity signal gradually decreased in the subsequent 5.6 hours when the pitch and yaw spacecraft axes were locked to the sun and the roll axis was in inertial mode (i. e., subject to any gyro drift). Therefore, it is concluded that the Canopus sensor was looking at an illuminated earth at the conclusion of automatic sun acquisition.

#### Nitrogen Utilization

Following sun acquisition, the remaining nitrogen was estimated to be 4.45 pounds, indicating that approximately 0.05 pound was consumed by the



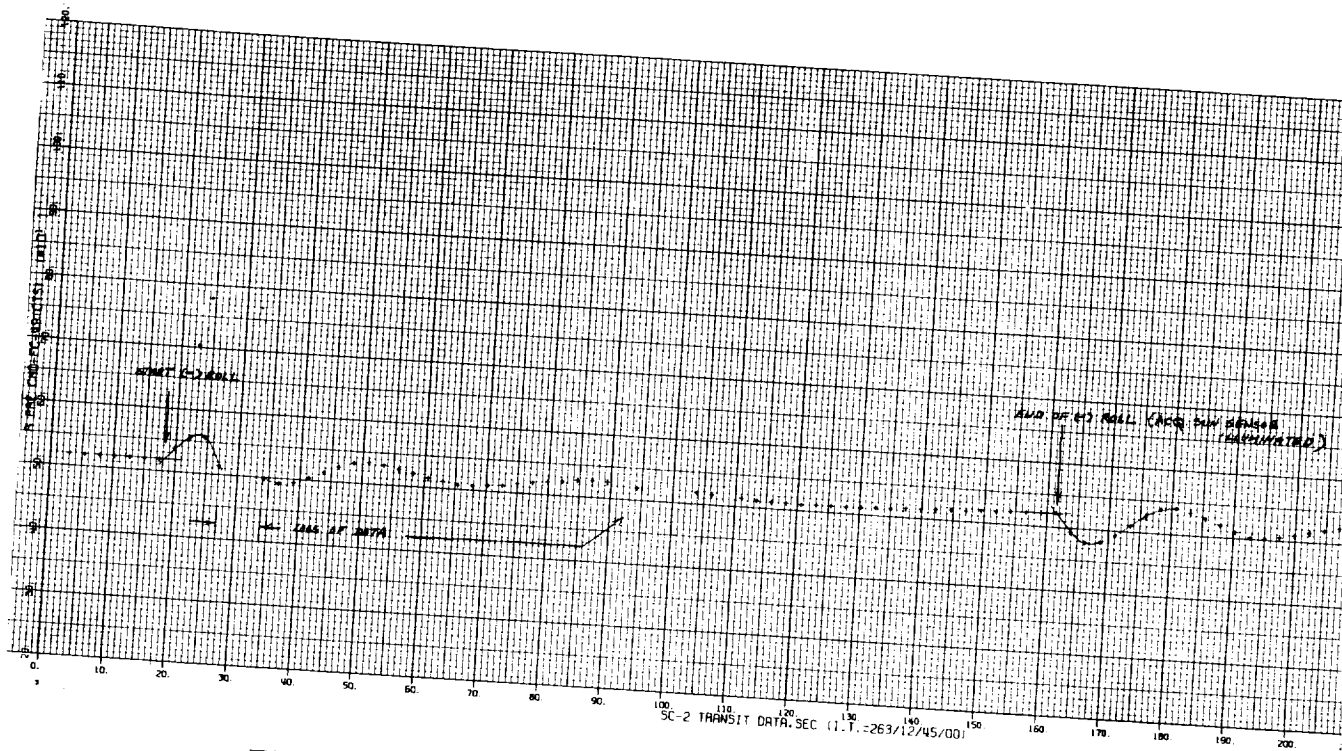


Figure 5.5-5. Sun Acquisition Roll Maneuver

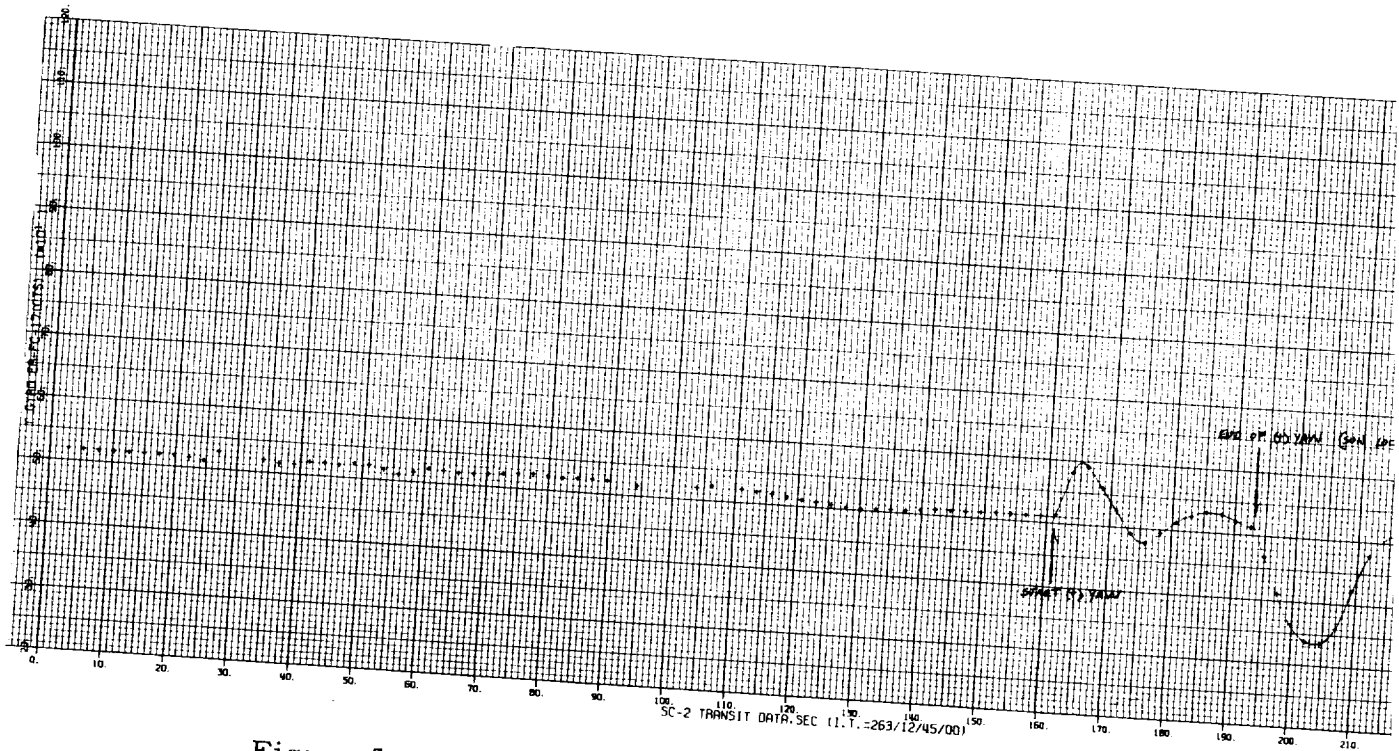


Figure 5.5-6. Sun Acquisition Yaw Maneuver







PRECEDING PAGE BLANK NOT FILMED.

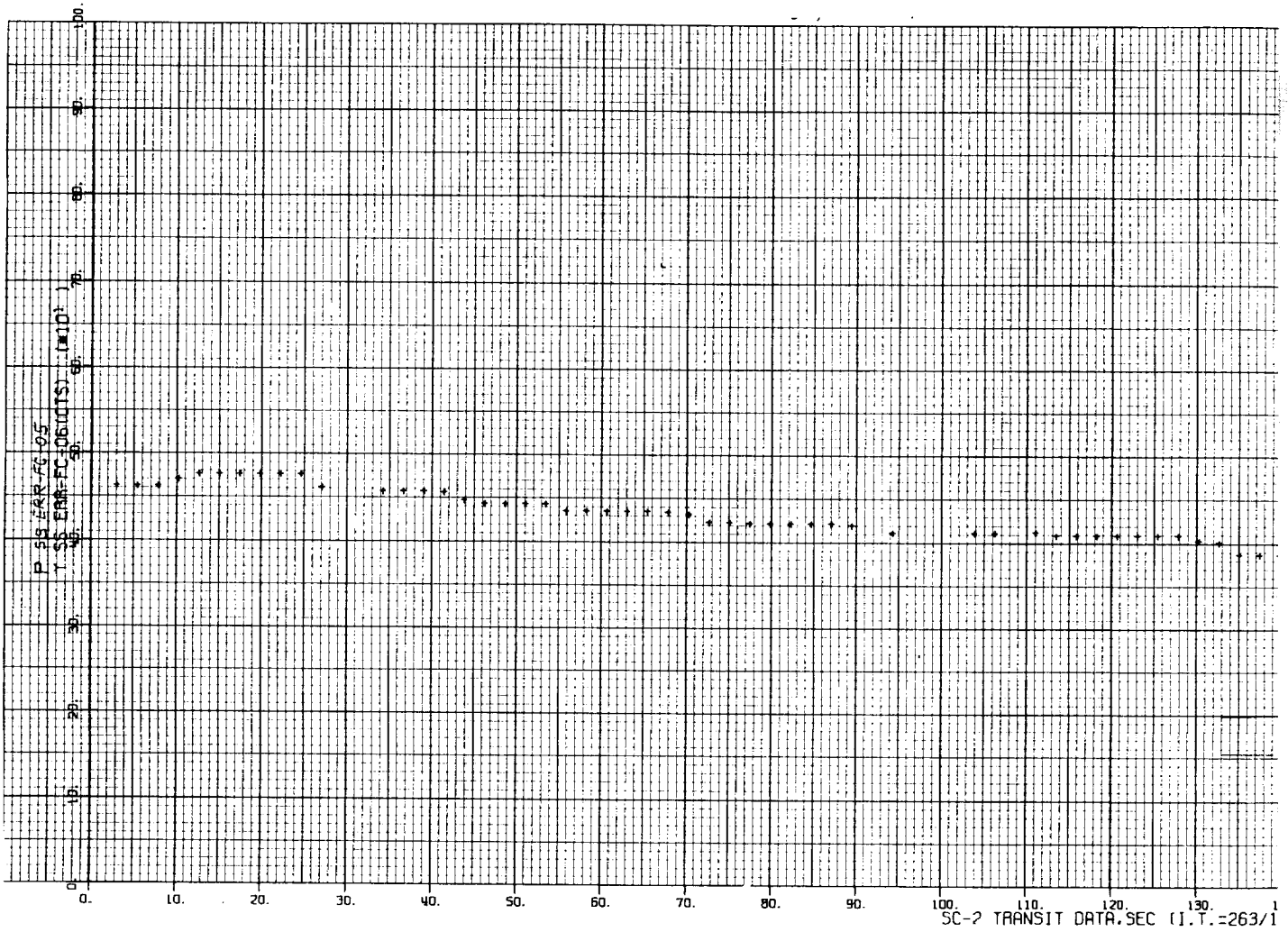
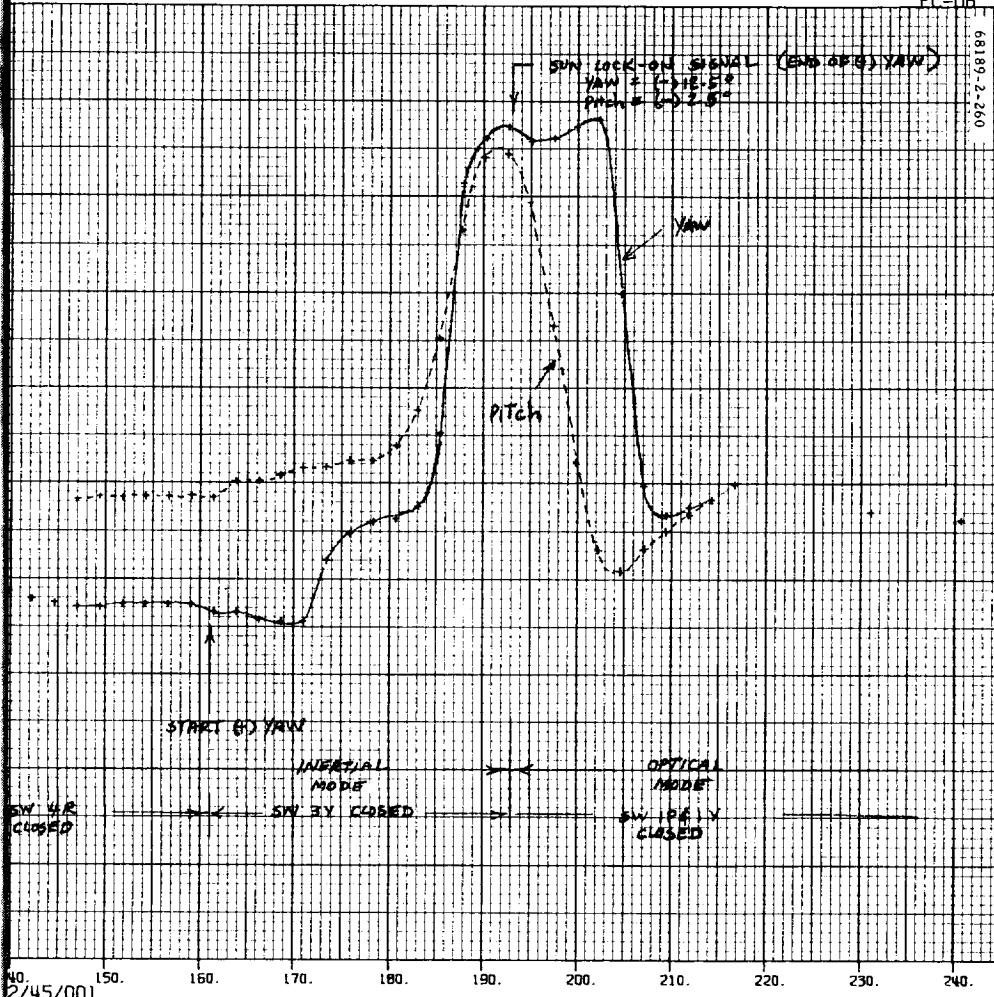


Figure 5.5-7. Sun Lockon Signal  
End of (+) yaw



FC-06

68189-2-260



5.5-27A

FOLDOUT FRAME 2





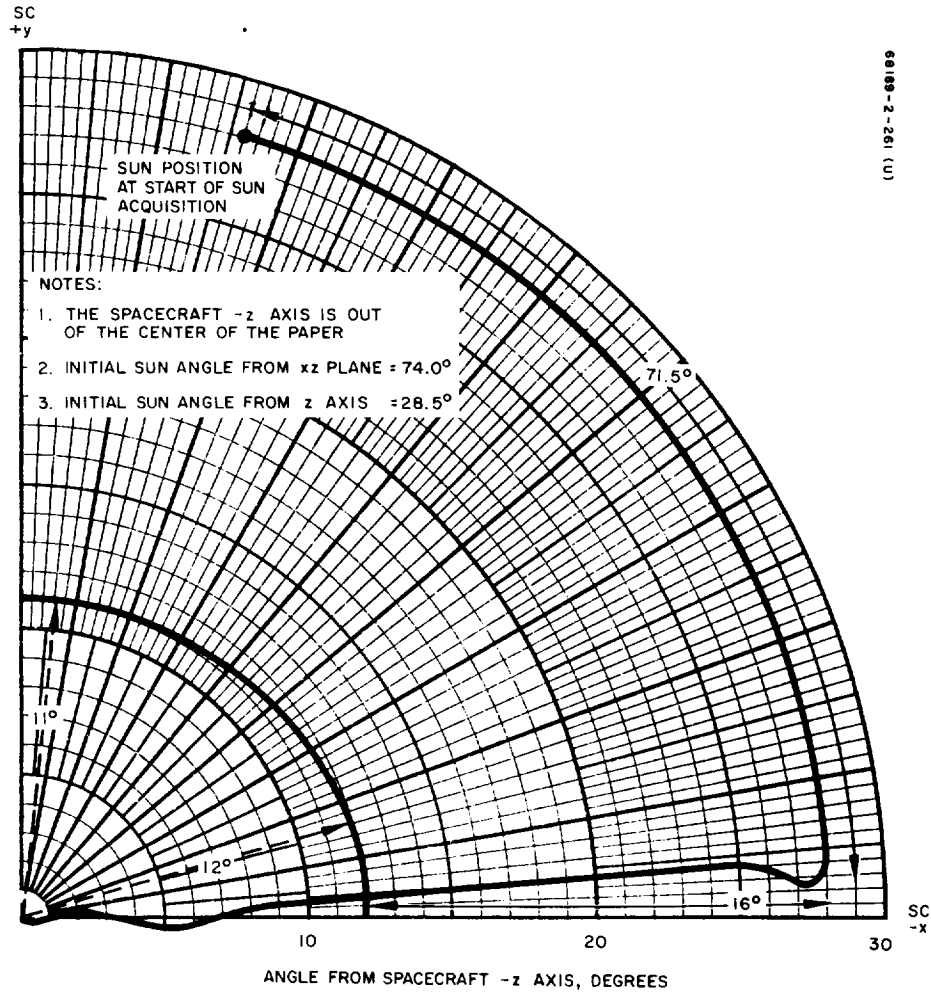


Figure 5.5-8. Sun Acquisition

rate dissipation and sun acquisition maneuvers. This is less than the expected gas consumption of 0.054 pound for sun acquisition alone. As indicated in Reference 4, this is not unusual because the expected value is based on conservative calculations.

#### 5.5.4.4 Canopus (Star) Acquisition

As defined in Reference 5, paragraph 3.4.2:

"... the spacecraft is commanded to roll up to 720° in one continuous roll. During this roll, the unthresholded star intensity signal, as well as the normal thresholded signal, is monitored. From these signals, a star map is made and Canopus identified. The capability for performing at least 4 of these verifications shall be provided. This verification shall be performed before the normal star acquisition mode is initiated. The star acquisition command starts a vehicle positive roll of 0.5 deg/sec until a star of the correct brightness falls into the sensor field-of-view. When this occurs, a lock-on signal is generated which stops the 0.5 deg/sec roll rate and switches the vehicle roll control to the star sensor error signal."

During Mission B, a sun and roll command was sent at 263:18:37:34 to roll the spacecraft at a rate of +0.5 deg/sec. During the roll, a star map was generated by recording the analog signals star intensity (i.e., unthresholded star intensity) and star angle or roll error (i.e., normal threshold) on a strip chart recorder. From this map, Canopus was positively identified (based on identifying four other objects) while the spacecraft was still rolling and prior to the completion of 720 degrees of roll. While the spacecraft was still rolling, it was decided to continue the roll and acquire Canopus when the star entered the field of view during the third revolution, i.e., beyond 720 degrees. It had been observed during the first two roll revolutions that the Canopus lockon signal did not come on when Canopus was in the field of view, indicating that the effective gain of the star sensor was high enough to put the star signal outside the upper lockon gate. Therefore, it was necessary to employ the optional command sequences and send two commands to effect the acquisition of Canopus, rather than employ the single command used, (sun and star) if Canopus lockon were present. The first command, cruise mode on, was sent at 263:19:09:38, when Canopus was in the field of view, to stop the 0.5 deg/sec roll rate. The second command, manual lockon, was sent at 263:19:11:57, which switched vehicle roll control to the star angle or roll error signal from the roll gyro inertial signal.

#### Star Map

Star mapping began with command 0714 (sun and roll) at 263:18:37:35 and continued for two complete revolutions in roll, the first revolution on omnidirectional antenna B and the second on omnidirectional antenna A. The roll maneuver was continued into a partial third revolution, which is considered the Canopus acquisition portion of the maneuver, on omnidirectional antenna B.

The technique used in identifying stars is that of visually determining, from plots of FC-12 (star angle) and FC-14 (star intensity) versus time (i. e., roll angle since roll rate is a constant 0.5 deg/sec) which responses are actually stars and which are not (light from moon, Milky Way, earth, etc.). Preflight estimates indicated that as many as 12 stars, including Canopus, might be observed, but many of these would be extremely weak and possibly indiscernible from signal noise.

Both FC-12 and FC-14 signals were sampled by telemetry once every 1.2 seconds, equivalent to 0.6 degree of roll, thus providing 13 or 14 data points during the  $\pm 4$ -degree Canopus sensor field of view.

Figure 5.5-9 depicts FC-12 and FC-14 during the 37 minute and 25 second period (from 263:18:37:35 to 263:19:15:00), which covers both the star mapping and star acquisition portions of the total roll maneuver. Figure 5.5-10 depicts FC-12 with the two full and one partial roll revolutions superimposed by roll angle, and Figure 5.5-11 depicts FC-14 on the same basis.

Figures 5.5-10 and 5.5-11 are plotted on expanded scales to assist in the identification of weak stars. By superpositioning the three roll revolutions, it is possible to determine which responses are repeatable and therefore considered to be objects in the field of view. It is also possible to determine which responses are nonrepeatable and therefore considered to be noise.

Table 5.5-7 indicates the times (and therefore roll angle) that each object, as identified from Figures 5.5-9, 5.5-10, and 5.5-11, crossed the center of the Canopus sensor field of view.

In general, the correlation between measured angles and predicted angles is within a one-sample resolution, i. e., 0.6 degree, although some of the weaker stars show poorer correlation on one or two revolutions. The poor correlation shown for the moon is attributed to the analyst's inability to accurately determine the exact center of a low amplitude, broad, slowly varying signal. The poor correlation shown for Shaula is attributed to the fact that another star, Upsilon Scorpii, approximately one-quarter Shaula's brightness, is simultaneously in the field of view, but displaced sufficiently to affect the center measurement of Shaula.

The good correlation between measured and predicted angles leads to the conclusion that ten stars, plus the moon and earth, were positively identified from the DSIF-51 data. During the star mapping portion of the mission in real time, it was possible to positively identify only Ras Alhague, the moon, Shaula, Canopus, and earth. The Space Flight Operations Facility received data at only half the spacecraft rate; thus the sample granularity was equivalent to 1.2 degrees of roll. The Canopus roll orientation was positively determined at the completion of the second roll revolution, at which time it was decided to acquire Canopus when the spacecraft rolled to its orientation during the third revolution.

TABLE 5.5-7. ROLL ANGLES OF OBJECTS SEEN DURING STAR MAPPING MANEUVER

GMT, hr:min:sec	Elapsed Time, seconds	Roll Angle, degrees	Object	Measured Angle From Canopus, degrees	Predicted Angle From Canopus, degrees	Angular Difference (Predicted-Measured), degrees
18:37:34.9	0	0	(Start of roll)	-240.0	-240 or -300	0 or -60
18:39:09.1	94.2	47.1	Zeta Draconis	-192.9	-193.1	-0.2
18:39:36.1	121.2	60.6	Beta Draconis	-179.4	-179.4	0
18:40:55.9	201.0	100.5	Ras Alhague	-139.5	-139.5	0
18:42:07.9	273.0	136.5	Moon	-103.5	-102.7	0.8
18:42:36.7	301.8	150.9	Shaula	-89.1	-89.7	0.6
18:42:46.3	311.4	155.7	Theta Scorpii	-84.3	-83.9	0.4
18:43:00.7	325.8	162.9	Alpha Arae	-77.1	-77.0	0.1
18:43:12.7	337.8	168.9	Gamma Arae	-71.1	-70.4	0.7
18:43:40.3	365.4	182.7	Alpha Tr. Australis	-57.3	-57.2	0.1
18:45:35.5	480.6	240.3	Canopus	-	-	-
18:46:21.1	526.2	263.1	Zeta C Majoris	23.1	22.7	-0.1
18:48:25.3	650.4	325.2	Earth	85.2	85.0	-0.2
Start of Second Revolution						
18:51:10.2	815.3	407.6	Zeta Draconis	-192.4	-193.1	-0.7
18:51:34.2	839.3	419.6	Beta Draconis	-180.4	-179.4	-1.0
18:52:55.8	920.9	460.4	Ras Alhague	-139.6	-139.5	0.1
18:54:07.8	992.9	496.4	Moon	-103.6	-102.7	0.9
18:54:39.0	1024.1	512.0	Shaula	-88.0	-89.7	-1.7
18:54:47.4	1032.5	516.2	Theta Scorpii	-83.8	-83.9	-0.1
18:55:01.8	1046.9	523.4	Alpha Arae	-76.6	-77.0	-0.4
18:55:13.8	1058.9	529.4	Gamma Arae	-70.6	-70.4	0.2
18:55:40.2	1085.3	542.6	Alpha Tr. Australis	-57.4	-57.2	0.2
18:57:35.4	1200.5	600.2	Canopus	-	-	-
18:58:21.0	1246.1	623.0	Zeta C Majoris	23.0	22.7	-0.3
19:00:23.1	1369.2	684.6	Earth	84.6	85.0	0.4
Start of Third Revolution						
19:03:09.0	1534.1	767.0	Zeta Draconis	-193.0	-193.1	-0.1
19:03:35.4	1560.5	780.2	Beta Draconis	-179.8	-179.4	-0.4
19:04:55.8	1640.9	820.4	Ras Alhague	-139.6	-139.5	0.1
19:06:11.4	1716.5	858.2	Moon	-101.8	-102.7	-0.9
19:06:39.0	1744.1	872.1	Shaula	-87.9	-89.7	-1.8
19:06:46.2	1751.3	875.6	Theta Scorpii	-84.4	-83.9	0.5
19:07:01.8	1766.9	883.4	Alpha Arae	-76.6	-77.0	-0.4
19:07:15.0	1780.1	890.0	Gamma Arae	-70.0	-70.4	-0.4
19:07:40.2	1805.3	902.6	Alpha Tr. Australis	-57.4	-57.2	0.2
19:09:35.2	1920.3	960.2	Canopus	-	-	-

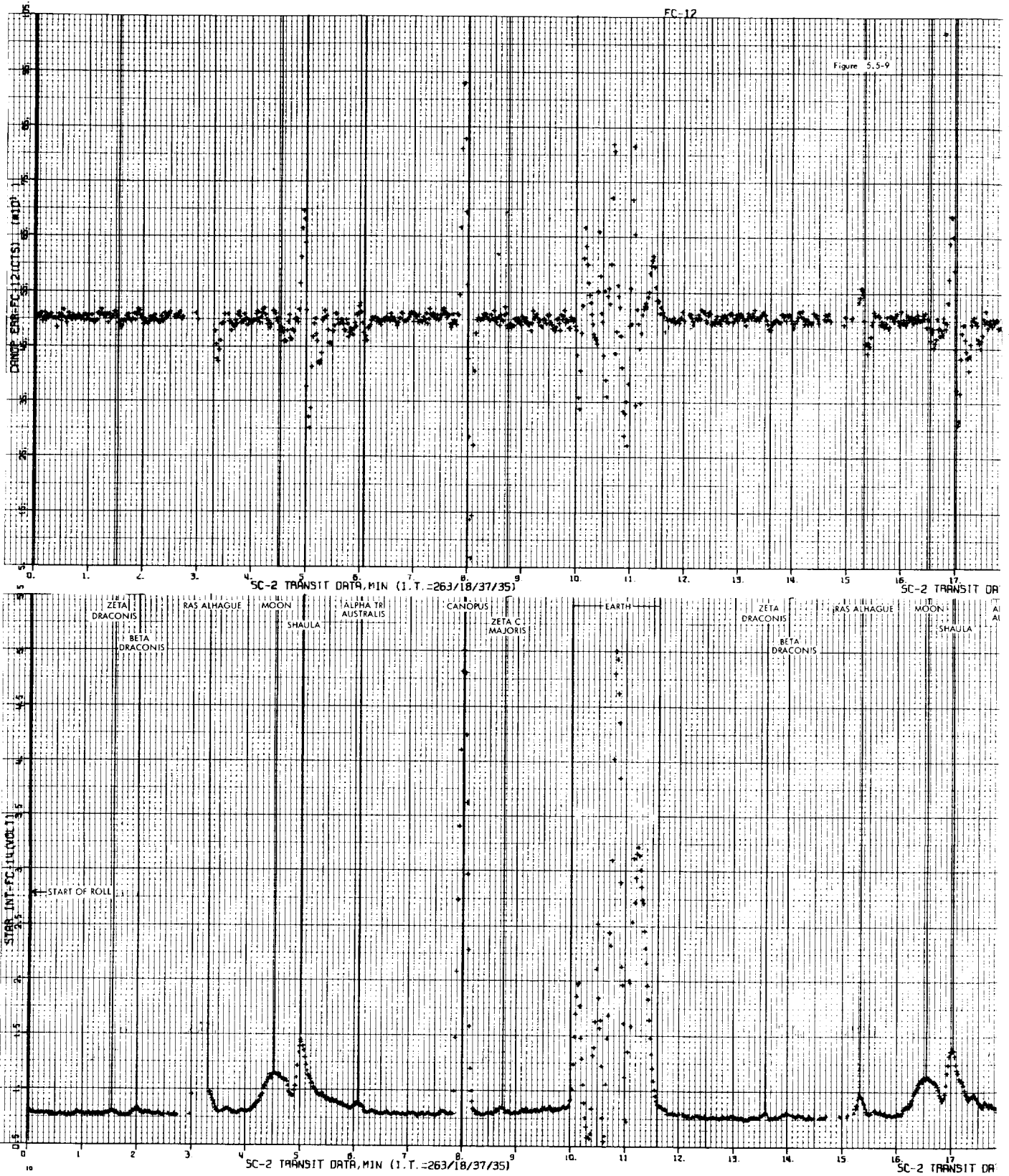
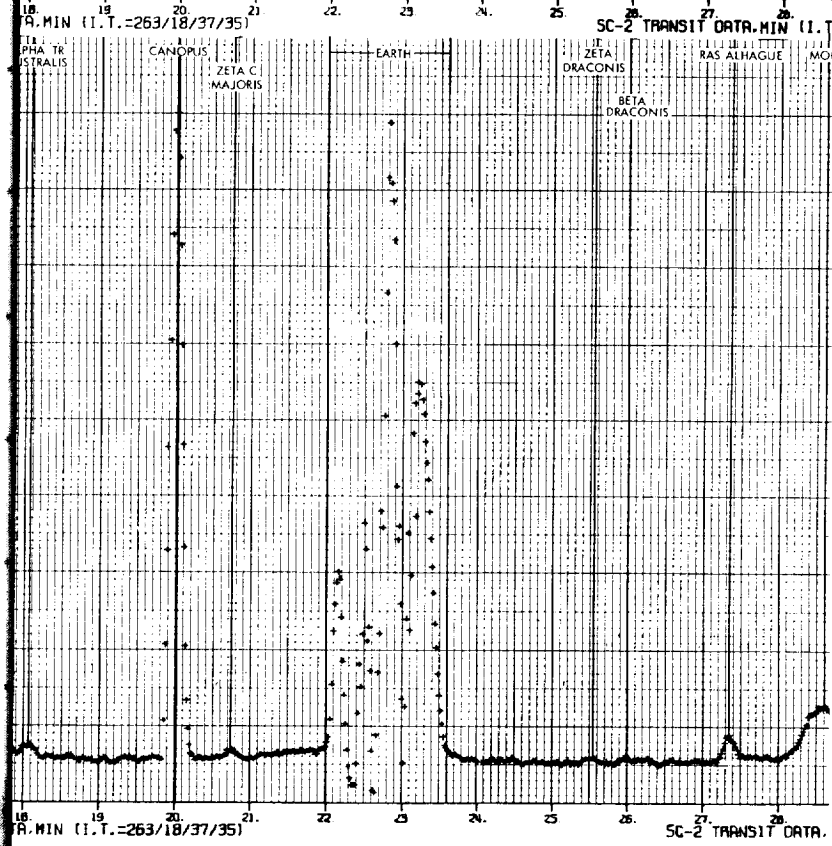
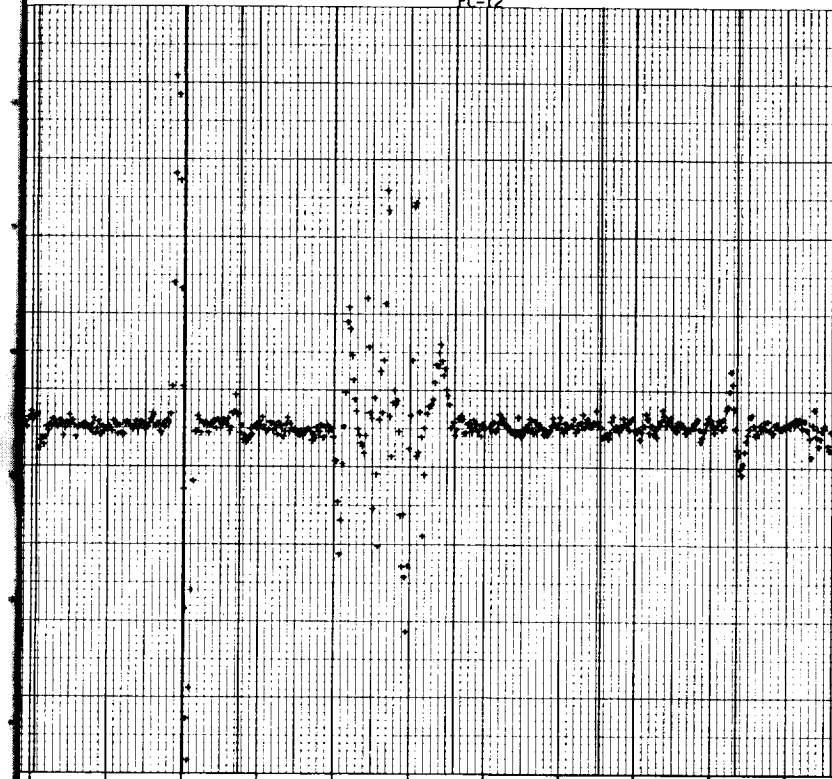


Figure 5.5-9. Star Map and Canopus Acquisition





18. MIN (I.T.-263/18/37/35) SC-2 TRANSIT DATA. MIN (I.T.

PHI TR CANOPUS EARTH ZETA RAS ALHAGUE MOJ  
STRALIS MAJORIS DRACONIS BETA DRACONIS

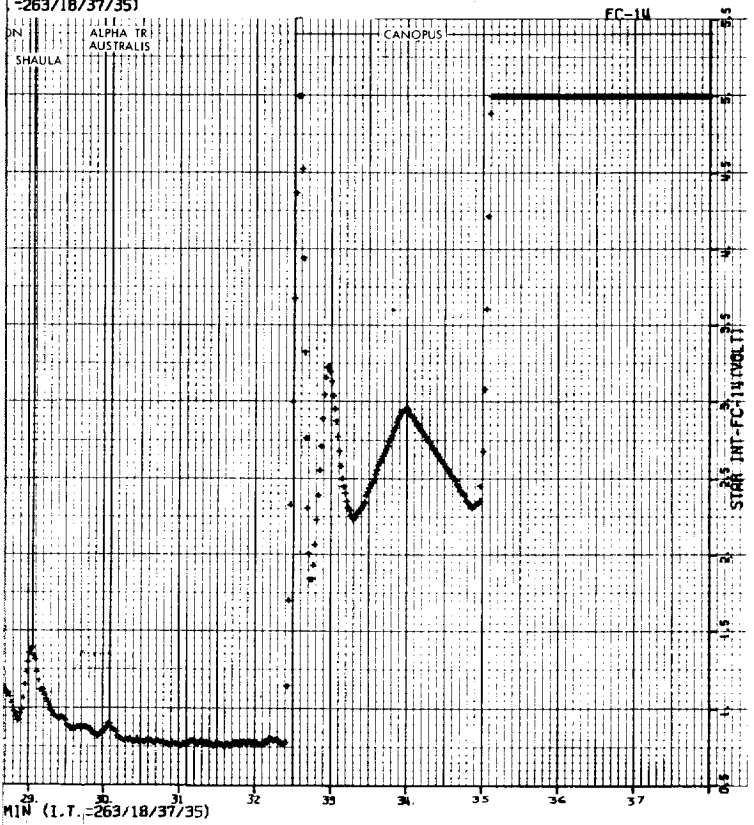
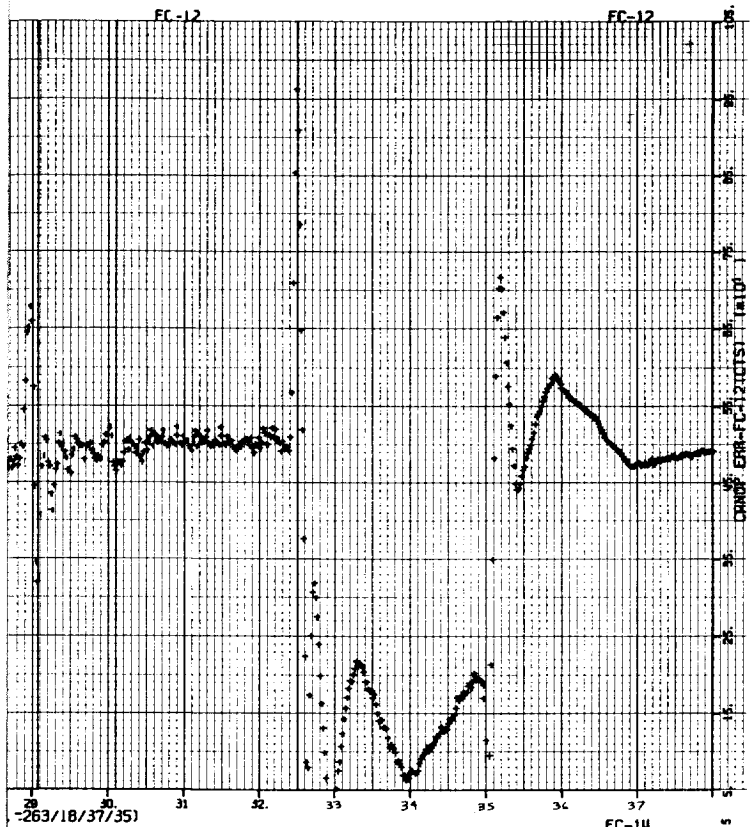
18. MIN (I.T.-263/18/37/35) SC-2 TRANSIT DATA.

FOLDOUT FRAME 2

5.5







MIN (I.T. -263/18/37/35)

23A FOLDOUT FRAME 3



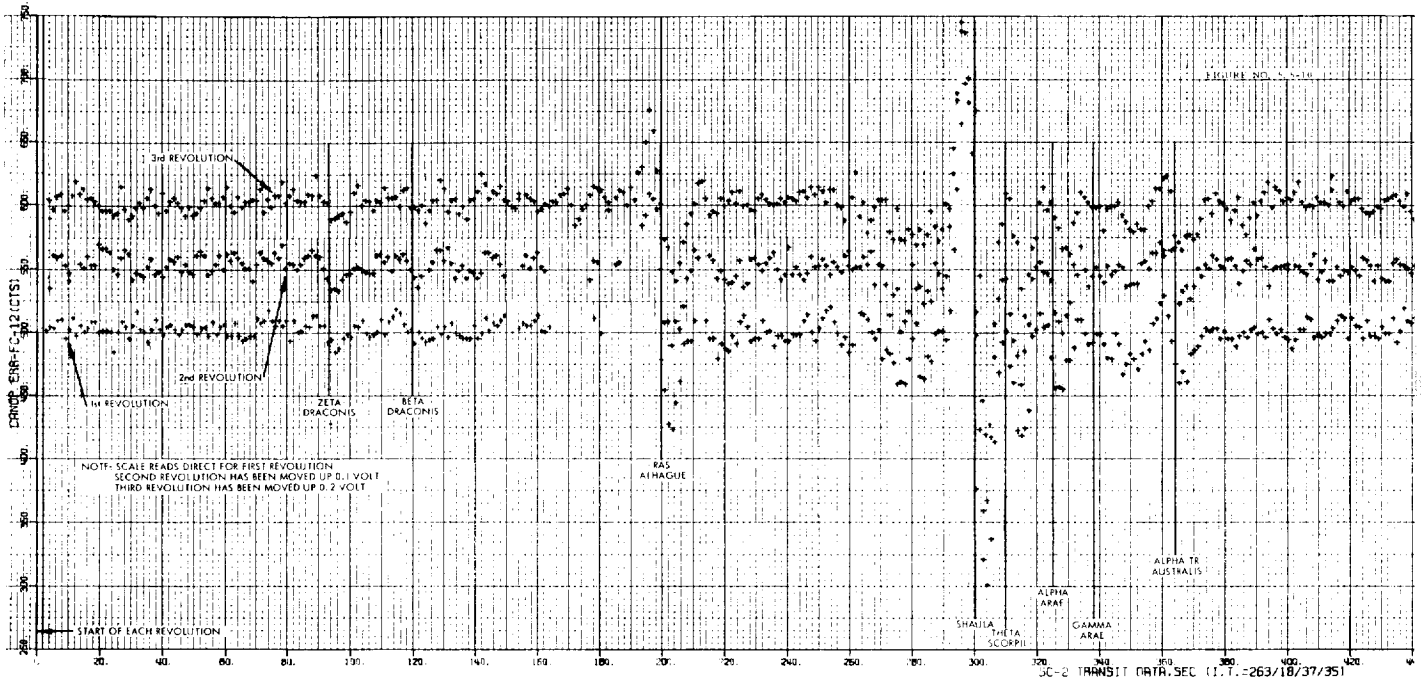


Figure 5.5-10. Canopus Error During Star Map

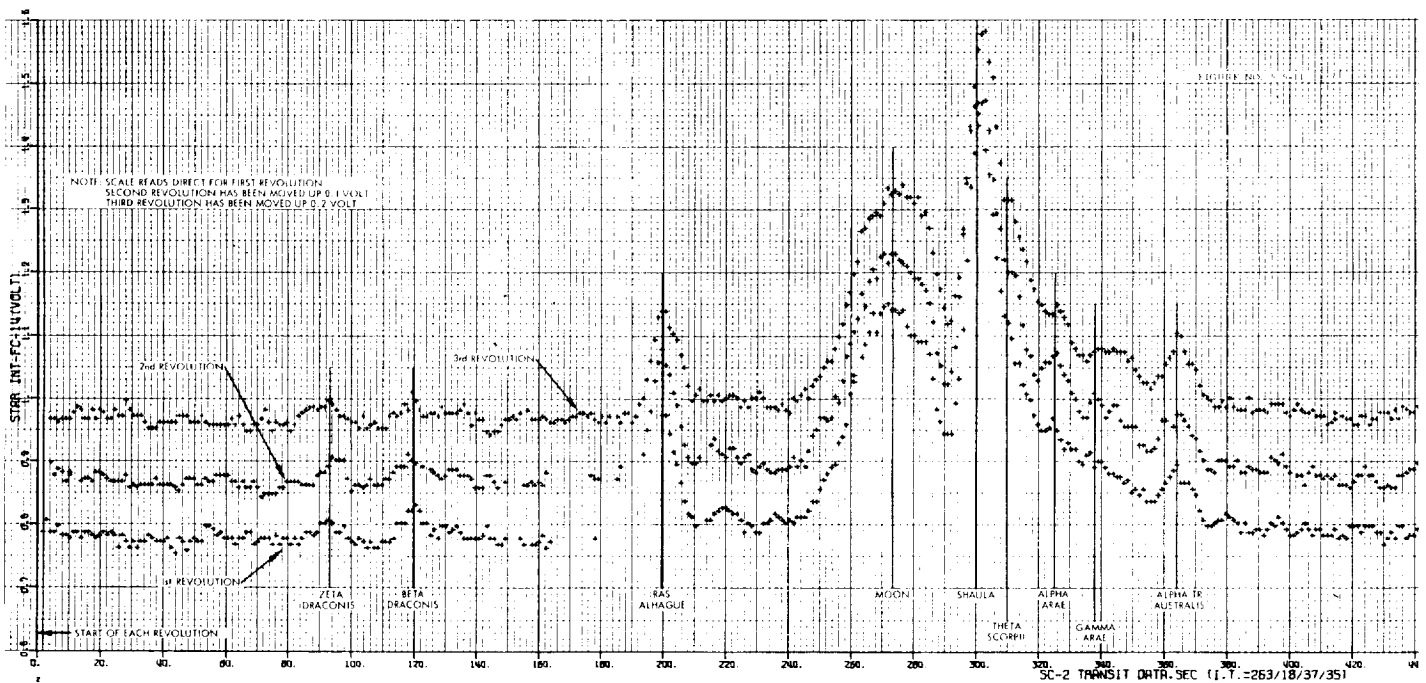
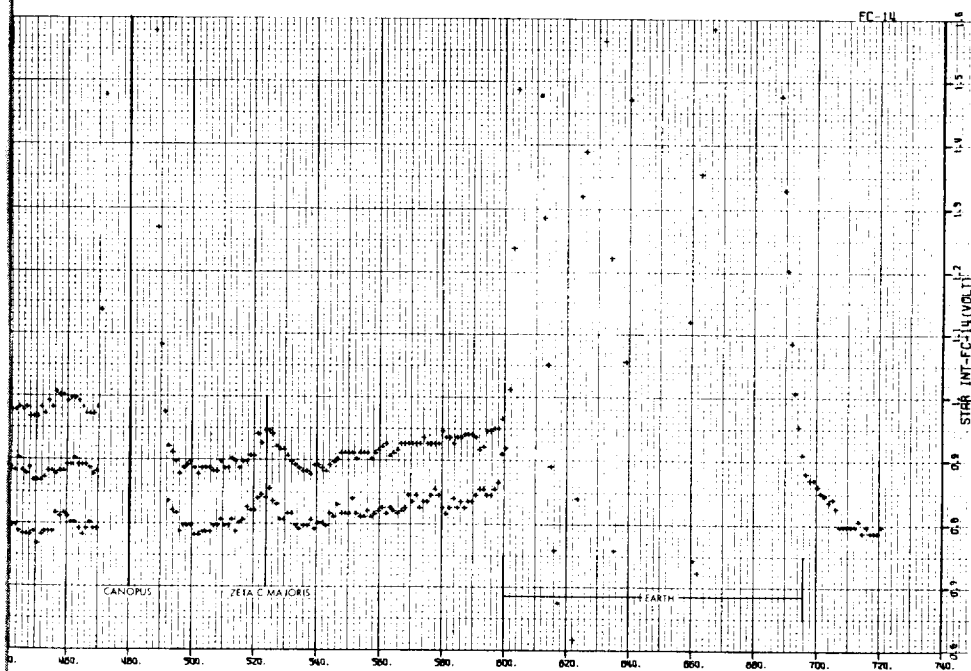
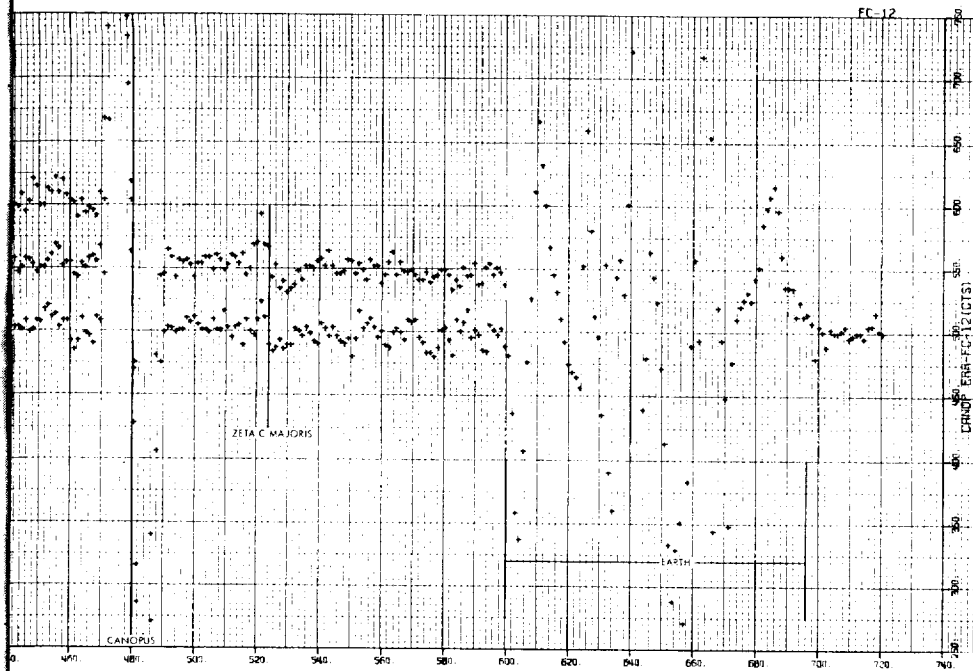


Figure 5.5-11. Star Intensity During Star Map





5.5-35A

FOLDOUT FRAME 2



PRECEDING PAGE BLANK NOT FILMED.

PRECEDING PAGE BLANK NOT FILMED.

### Effect of Pitch and Yaw Limit Cycles on Star Map

The Canopus sensor is mounted on the spacecraft such that its line of sight is in the X-Z plane and pointing in the general direction of the -X axis. The line of sight is adjustable in this plane and can be pointed along the -X axis, above the -X axis towards the -Z axis, or below the -X axis towards the +Z axis. This adjustment is in the yaw direction; therefore, any plus yaw motion is equivalent to moving the line of sight down towards the +Z axis, and any minus yaw motion is equivalent to moving the line of sight up towards the -Z axis.

The Canopus sensor field of view is  $\pm 4$  degrees in the roll direction (i. e. , in the X-Y plane), and  $\pm 2.5$  degrees in the yaw direction (i. e. , in the X-Z plane). Therefore, both yaw and roll motions will change the field of view and cause objects to be "seen." Roll motion is commanded in order to generate a star map which, in effect, "looks" at a 5-degree wide section of sky. Any yaw motion due to yaw loop limit cycling will cause this 5-degree wide field of view to move normal to the star mapping plane. It is therefore possible to see objects that would normally be outside the nominal field of view, or conversely to not see objects that would normally be within the nominal field of view. Any pitch motion due to pitch loop limit cycling will cause the field of view to twist, and it is possible for objects close to the corners of the 5 by 8-degree field of view to be either seen or missed.

The angular orientations, with respect to the field of view, of the 12 stars that are bright enough for possible detection are all (except for Theta Ophiuchi) a minimum of 0.48 degree away from a side of the field of view. Theta Ophiuchi is 0.15 degree away from the minus yaw side, which means that a yaw angle greater than 0.15 degree would cause the star to not be seen. Since Theta Ophiuchi is masked by the moon, it could not be identified, and therefore it was not possible to view any yaw motion effects.

The maximum yaw limit cycle observed during the star mapping roll maneuver was  $\pm 0.18$  degree, and the maximum pitch limit cycle was  $\pm 0.13$  degree. Therefore, none of the expected visible stars would have been missed due to either pure yaw or combined ( $\pm 0.24$  degree) pitch and yaw limit cycling. Further star table investigations indicated there were no sufficiently bright stars in the 0.24-degree band on either side of the field of view that could have been seen due to combined pitch and yaw limit cycling.

### Mean Roll Rate During Star Mapping Maneuver

The mean roll rate during the star mapping maneuver was determined by averaging the time intervals of each revolution for the ten stars seen during the maneuver. Eight stars were seen three times and two stars were seen two times during the two full and one partial roll revolutions. Thus, eight stars each yield time intervals for two complete revolutions, and two stars yield time intervals for one complete revolution for a total of 18 time intervals.

The average of these 18 time intervals is 720.2 seconds, which is equivalent to a mean roll rate of 360 deg/720.2 sec, or 0.4998 deg/sec. Accuracy of the time intervals is one data sample period, i. e., 1.2 seconds, which means the equivalent rate accuracy is 0.0008 deg/sec.

### Star Sensor Performance

The star sensor is designed to provide three outputs, all of which are telemetered and two of which are utilized by the flight control subsystem during the star mode of operation. The three outputs are star intensity (FC-14), star angle or roll error (FC-12), and Canopus lockon (FC-13).

Star intensity is an analog signal used primarily during star mapping to identify the angular spacing in the X-Y plane of all objects in the swept field of view. The nominal values (from unit flight acceptance test data) of star intensity voltages versus simulated star intensities for the Mission B Canopus sensor (S/N 11) are as follows:

<u>Star Intensity (Ratio to Canopus)</u>	<u>Star Intensity, volts</u>
0	0.55
0.076	0.70
0.67	3.18
1.00	4.72
1.50	5.62

Note: These voltage measurements were made with the sun channel illuminated by a nominal 1.0 sun and the simulated star stationary in the center of the field of view. Voltage values decrease linearly with roll angle and are symmetrical about the center; they are unaffected by the yaw orientation of the simulated star.



Star angle is an analog signal that varies proportionally with roll angle (but is insensitive to yaw angle) and whose polarity depends on whether the star is at a plus or minus roll orientation with respect to the sensor's line of sight. The signal is used: 1) as a star angle signal during star mapping to aid in identifying that an object sensed is a point source and therefore a star, 2) as a star angle signal during roll maneuvers when a star is in the field of view to aid in determining the direction of roll, and 3) as a roll error signal during the star mode of roll control to provide a roll error signal to the roll control loop to keep the spacecraft's X-Z plane pointing towards Canopus. The nominal values (from unit flight acceptance test data) of star angle telemetry voltages and roll error voltages versus roll angles at 1.0X and 1.5X Canopus intensities for the Canopus sensor are given in Table 5.5-8.

Canopus lockon is a digital signal that comes on when a star, whose intensity is within certain limits, appears in an inner portion of the field of view. This signal is used by the flight control subsystem to switch the roll control loop to the roll error signal and to cage the roll gyro. The nominal values (from unit flight acceptance test data) of simulated star intensities versus lockon signal level for the Canopus sensor are given in Table 5.5-9.

The star sensor is internally mechanized such that all three outputs, star intensity, star angle or roll error, and Canopus lockon, are derived from an internal signal known as the star signal. The magnitude of this signal is dependent upon: 1) intensity of the object in the field of view, 2) roll angle orientation (from -4 to +4 degrees) within the field of view, and 3) effective gain. Star sensor gain is a function of the photomultiplier tube scale factor which is controlled by the intensity of the sunlight actually reaching the tube through a sun filter in the sun channel optics. During star sensor development, a sun filter value was selected such that unit sun intensity and unit Canopus intensity would produce a star intensity close to 5.0 volts dc. The sun filter value thus selected is referred to as a unit (1.0X) Canopus filter and, during star sensor fabrication, internal electronic gains are adjusted such that testing with a simulated 1.0X sun and 1.0X Canopus yield specified responses.

Mission A was flown with a 1.50X Canopus sun filter which yielded Canopus star intensity signals greater than 1.50X Canopus and no Canopus lockon signal. Based on Mission A performance, it was decided to fly Mission B with a 1.17X Canopus sun filter. Canopus star intensity values were expected to be approximately 17 percent greater than the 1.0X Canopus values obtained during unit testing, and Canopus lockon was expected to come on.

TABLE 5.5-8. STAR ANGLE AND ROLL ERROR  
VERSUS ROLL ANGLE

At 1.0X Canopus			At 1.5X Canopus		
Roll Angle, degrees	Star Angle Telemetry, volts	Roll Error, volts	Roll Angle, degrees	Star Angle Telemetry, volts	Roll Error, volts
4.0	2.81	0.50	4.0	2.88	0.60
3.0	4.11	2.55	3.0	4.12	2.60
2.13	5.12	4.20	2.15	5.12	4.20
2.0	4.98	3.95	2.0	4.95	3.90
1.0	3.75	2.00	1.0	3.70	1.90
0.5	3.13	1.00	0.5	3.08	0.90
0	2.55	0.085	0	2.54	0.070
-0.5	1.90	-0.95	-0.5	1.96	-0.85
-1.0	1.25	-2.00	-1.0	1.30	-1.90
-2.0	0.01	-3.98	-2.0	0.05	-3.90
-2.15	-0.12	-4.20	-2.20	-0.10	-4.15
-3.0	0.87	-2.60	-3.0	0.80	-2.70
-4.0	2.05	-0.70	-4.0	2.00	-0.80
Peak to peak angle = 4.28 degrees			Peak to peak angle = 4.35 degrees		

Note: A plus roll angle denotes a star that is at a plus roll orientation with respect to the sensor's line of sight. During closed-loop control, a minus roll motion would cause Canopus to appear at a plus roll angle with respect to the sensor line of sight, thus producing a plus roll error voltage which is phased to command a plus roll, thereby offsetting the initial minus roll motion.

TABLE 5.5-9. STAR INTENSITY FOR CANOPUS LOCKON

Star Intensity (Ratio to Canopus)	Canopus Lockon Level	On Range, degrees roll
0.60	Off	
0.67	Intermittent	
0.74	On	-2.7 to +3.3
1.00	On	-3.6 to +4.2
1.35	On	-3.6 to +4.2
1.50	Intermittent	
1.65	Off	

Star Intensity

During the two full and one partial roll revolutions of the star mapping and Canopus acquisition maneuver, Canopus was in the moving field of view three times. From Figure 5.5-9, it is noted that the Canopus star intensity telemetry signal is saturated in the center of the field of view, thereby preventing a direct reading of Canopus intensity. It is also noted that the no-star intensity values on either side of Canopus are equal at 0.79 volt.

Also, during the gyro drift check period from 263:19:26:22 to 263:21:35:20, Canopus was in the field of view which was moving very slowly due to gyro drift and oscillating very slowly about this drift rate due to normal limit cycling of the roll control loop.

Several analysis techniques were used to compare earth-obtained star intensity values with mission-obtained values in order to determine the effective gain of the sensor. The first technique was to extrapolate the mission-obtained intensity values to the center of the field of view by using earth-obtained intensity versus roll angle plots without telemetry limiting. The peak values, in volts, thus obtained for Canopus readings are as follows:

First revolution	5.61
Second revolution	5.67
Third revolution	5.60
Average peak	5.63
Gyro drift check	5.88

The earth-obtained star intensity values (from unit flight acceptance test data) previously listed were static values, i. e., zero roll rate, and can only be related to intensity values obtained during the gyro drift check when roll motion was essentially static from a star sensor standpoint. Recent earth-obtained star intensity measurements (Reference 6) at 0.5 deg/sec roll rate indicate that maximum values reached are only 93 percent of corresponding static values. Applying this correction factor to the average dynamic peak value of 5.63 volts yields  $5.63/0.93 = 6.05$  volts. By comparing the gyro drift check extrapolated maximum value of 5.88 volts and the star mapping extrapolated and corrected maximum value of 6.05 volts with the unit flight acceptance test data values, both flight values exceed the unit static value of 5.62 volts for 1.50X Canopus. Therefore, it is concluded that the star sensor effective gain was over 1.50X Canopus by an indeterminate amount.

The second technique was to calculate the ratio of the earth-obtained no-star intensity value to the mission-obtained no-star intensity value. This ratio of 0.79 to 0.55 volts (= 1.44) is a measure of the increased gain from a nominal 1.0X to 1.44X Canopus. However, since it is not known if effective gain varies with intensity, particularly at low intensities, less importance is given to this calculated gain than to the gain from Canopus intensity values.

The third technique was to compare mission-obtained star intensity values versus premission calculated intensity values for all other stars identified. The static unit flight acceptance test data relating star intensities at a nominal gain of 1.0X Canopus to star intensity telemetry volts was plotted in order to obtain telemetry voltages at intensities other than the discrete data points, i. e., 0.14 and  $1.2 \times 10^{-12}$  watts/cm<sup>2</sup>.

The average ratio of 1.30 (see Table 5.5-10) is a measure of the increased gain from a nominal 1.0X to 1.30X Canopus. However, the accuracy of the low intensity telemetry voltage values is on the order of 15 to 20 percent, and the accuracy of the calculated star intensities, as converted to the same spectral response as the star sensor, is also on the order of 15 to 20 percent. Therefore, it is concluded that this third technique does not yield useful quantitative data but does grossly indicate that the effective gain was indeed higher than the 1.17 expected due to the sun filter change.

Summarizing the results of these three analysis techniques, it is concluded that the effective gain was in excess of 1.50X Canopus, or over 28 percent greater than expected. This larger effective gain was helpful in the identification of the weaker stars but caused the internal star signal to exceed the Canopus lockon upper gate limit when the star was in view, thereby not providing a Canopus lockon signal.

TABLE 5.5-10. STAR INTENSITY

Star	Calculated Intensity, $\times 10^{-12}$ watts/cm <sup>2</sup>	Predicted Static Telemetry, volts	Predicted Dynamic Telemetry, volts	Mission Telemetry, volts	Ratio
Zeta Draconis	0.059	0.620	0.668	0.802	1.20
Beta Draconis	0.034	0.595	0.640	0.816	1.28
Ras Alhague	0.140	0.703	0.758	0.963	1.28
Shaula	0.330	1.12	1.205	1.403	1.16
Theta Scorpil	0.140	0.703	0.758	1.110	1.46
Alpha Arae	0.077	0.640	0.689	0.963	1.40
Gamma Arae	0.062	0.625	0.671	0.899	1.34
Alpha Tr. Australis	0.051	0.615	0.661	0.890	1.34
Zeta C. Majoris	0.085	0.650	0.699	0.850	1.22
				Average ratio	1.30

An analysis of possible window fogging in Mission B was made, since this was the reason for using non-unity Canopus gain. The extrapolated peak Canopus intensity values obtained during the star mapping maneuver and during the premidcourse roll maneuver are considered equal (due to the limitations of the extrapolation method). Thus, it is concluded that no window fogging occurred over this 10-hour period.

#### Canopus Lockon

During the two full and one partial roll revolutions of the star mapping and Canopus acquisition maneuver, Canopus was in the field of view three times. Each time the Canopus lockon signal did not indicate on during the 8-degrees-of-roll angle but did come on for one or two data sample periods as Canopus moved out of the field of view.

Since the effective gain was something over 1.50X Canopus, this would cause the internal star signal to exceed the Canopus lockon upper gate limit when the star was in full view. As Canopus moved out of view, the star signal magnitude would decrease through the upper gate and, during the short transition to the lower gate, the lockon signal would be on. The lockon gate circuitry timing characteristics are such that increasing the star signal, i. e., when Canopus comes in to view, at the same rate as the decreasing star signal will not result in a Canopus lockon on signal.

#### Star Angle or Roll Error

During the two full and one partial roll revolutions (for star mapping and Canopus acquisition), the star angle signal responded in a normal manner (Figures 5.5-9 and 5.5-10) to the ten stars crossing the field of view. Erratic responses were noted when the moon and earth were in view. These responses are considered normal when viewing objects that are not point sources.

As seen in Figure 5.5-9, the star angle values, when Canopus is in view, are rounded at the inflection points instead of peaking as previously noted in the listing of unit flight acceptance test data. By extrapolating the linear portions of the three Canopus star angle plots, average peak values of 4.98 volts maximum and 0.05 volt minimum are obtained, and the average angle between peaks is 4.4 degrees. Comparable 1.5X Canopus earth-obtained values were 5.12 volts maximum, -0.10 volt minimum, and 4.35 degrees between peaks.

The difference between mission-obtained and earth-obtained values is 2.8 percent for the maximum peak, 3.0 percent for the minimum peak, and 1.2 percent for the angle between peaks. The good correlation leads to the conclusion that the star angle signal functioned as designed.

## Conclusions

Based on the above analyses, it is concluded that the three star sensor outputs were normal for the actual operating conditions of Mission B, thus indicating that the star sensor performed in a normal and satisfactory manner.

## Canopus Acquisition Sequence

As previously discussed, the first two revolutions of the plus 0.5 deg/sec roll maneuver comprise the star mapping sequence and the remainder of the maneuver (a partial third revolution) is considered the Canopus acquisition sequence.

Canopus had been positively identified by the end of the second revolution, and the decision was made to continue rolling and acquire Canopus when it appeared in the field of view during the third revolution. Since Canopus lockon did not come on when Canopus was in the field of view, it was necessary to use the optional sequence of a cruise mode command to stop the roll, followed by a manual lockon command to switch the roll control loop from gyro output to star sensor roll error output.

Cruise mode on was commanded at 263:19:09:38 and, as seen in Figure 5.5-9, the star intensity signal went through a maximum, then to about one-quarter amplitude, and then to a damped oscillation about one-half amplitude. The star angle signal went through a maximum, then to about one-eighth amplitude, and then to a damped oscillation about one-eighth amplitude. These signals indicate that the cruise mode command was received after Canopus had crossed the center of the field of view and was in the negative half of the field. Both signals indicate that the spacecraft rolled past -2 degrees to about -3 degrees and then damped out very slowly about -2.5 degrees. Two minutes and 19 seconds later at 263:19:11:57, the manual lockon command was sent. As seen in Figure 5.5-9, the star intensity signal went to a maximum, while the star angle or roll error signal went through a damped oscillation about its null.

Roll motion had not damped out completely when the manual lockon command was sent 2 minutes and 19 seconds later, but the roll response had completely damped out within 3 minutes. These responses are normal for the gyro controlled roll loop with an initial 0.5 deg/sec roll rate and for the Canopus roll error controlled roll loop with an initial roll error of 2.5 degrees.

## Summary

Canopus acquisition results are summarized in Table 5.5-11. The conclusions and recommendation are as follows.

Conclusions. The Canopus sensor performed without malfunction. The star intensity signal, when looking at Canopus, was too high due to an intentional high gain setting to produce a Canopus lockon signal. It was again demonstrated, as in Mission A, that Canopus manual lockon can be successfully accomplished in the absence of a Canopus lockon signal.

Recommendation. Install a lower transmissibility filter in the Canopus sensor sun channel to set the effective gain in the vicinity of 1.10.



TABLE 5.5-11. CANOPUS ACQUISITION RESULTS

Star Acquisition Proper identification and acquisition of Canopus	Specification*	Specification Value	Results	Comments
Roll angle from start of roll to Canopus	Paragraph 3.4.2	Positive roll maneuver sufficient to produce an adequate star map for Canopus identifica- tion. Provide a lockon signal when Canopus appears in field of view.	Manual lockon  240.0 degrees	Intentional high gain setting of Canopus sensor, to compensate for possible window fogging, removed capability of automatic star lockon.
Stars identified			Ras Alhague, Shaula, and Canopus, plus moon and earth	Several addi- tional weak stars were identified from postmission analysis of raw DSIF-51 data.
Mean roll rate during star mapping maneuver	Paragraph 3.4.2.1.1	No specification requirement. Nominal value is 0.5 deg/sec.	0.4998 deg/ sec (note: data resolution is 0.0008 deg/ sec).	Mean calculation is based on 18 average revolu- tion times of ten stars.
Effective gain of Canopus sensor			1.5(+) X Canopus	Nominal value is 1.00X Canopus. Mission B Canopus sensor was set to 1.17X Canopus.
Nitrogen gas used			0.01 pound	Expected usage was 0.06 pound.

\*"Surveyor System Functional Requirements," Revision E, 7 January 1966.

#### 5. 5. 4. 5 Coast Mode

The three-axis cold gas attitude control system is designed to maintain an optical or inertial reference during the nonthrusting portions of the Surveyor flight. The spacecraft pitch and yaw optical references are provided by a narrow field of view sun sensor; the roll optical reference is provided by a Canopus sensor whose field of view is 5 degrees latitude and 8 degrees longitude. The spacecraft inertial references are provided by three body-fixed rate integrating gyros.

The actuators used in the coast mode are the cold gas jets. The on-off operation of these jets, plus the deadbands built into the system at the gas jet amplifiers, cause the spacecraft to function in a three-axis limit cycle. In the steady state, the Surveyor attitude coasts along a straight line within the three-dimensional deadband of  $\theta$ ,  $\varphi$ ,  $\psi$  space. Upon intercepting a bounding plane, a gas jet pulse is emitted, driving the system back within the deadband along a new straight line. These motions are entirely analogous to the motions of a ball bouncing internally within a closed three-dimensional, planar-sided, six-sided polygon, wherein the law of reflection determines that the velocity components of the ball change by discrete amounts (as caused by a jet pulse), these amounts being constant for any one plane. The motions are aperiodic and are a strong function of initial velocity conditions.

The non-g sensitive drift rates of the integrating rate gyros were measured during Mission B by slaving the spacecraft to the drifting inertial references and observing the drift rates by means of the telemetered optical references.

The principal items of analysis for the flight control system coast phase were as follows:

- 1) Limit cycle frequency and amplitude
- 2) Sun and star tracking errors and tracking noise
- 3) Nitrogen gas used
- 4) Results of gyro drift measurement

The major events for the coast phase, together with their corresponding times, are presented for reference in Table 5. 5-12. Table 5. 5-13 is a summary of the analysis results for the coast phase.

TABLE 5. 5-12. MAJOR EVENTS AND TIMES

Event	GMT, day; hr: min: sec	Command
Sun lockon	263:12:48:13	Automatic sequence
Star map (begin)	263:18:37:34	0714
Canopus acquire (manual lockon)	263:19:11:57	0716
Begin gyro drift check 1	263:19:26:24	0700
End gyro drift check 1	263:21:35:22	0704
Begin premidcourse maneuvers	264:04:44:00	0714

Conclusions and Recommendations

- 1) Limit cycle behavior was as predicted except that the roll limit cycle occasionally exhibited the tendency to double-pulse at each side of the deadspace (ideally, it should always single-pulse). About 20 percent of the fuel consumed during the sampled limit cycle period was a result of double pulsing. However, since the fuel penalty was very low (about 0.002 pound) and the limit cycle amplitude was unchanged, this additional pulsing was readily tolerated.
- 2) Sensor noise did not affect the coast mode control system performance.
- 3) Extrapolated fuel consumption was about what was predicted (after allowing for the additional double-pulsing of the jets).

Analysis Details

Limit Cycle Frequency. The three-axis limit cycle is characterized by a crosscoupling of the torques resulting from a gas jet pulse. This coupling is shown by the following:

- 1) A pulse from the No. 1 gas jet pair causes a change in rotational velocity about the roll and yaw axes.
- 2) A pulse from the No. 2 or 3 gas jet pair causes a change in rotational velocity about the pitch and yaw axes.

TABLE 5.5-13. SUMMARY OF RESULTS

Limit Cycle Frequency			
<u>Mission B</u>		<u>Predicted</u>	
Inertial:	61 sec/pulse	117 sec/pulse	(Reference 7, page 3)
Optical:	64 sec/pulse	80 sec/pulse	(For 1σ Canopus sensor noise: Reference 7, Figure 1).
Limit Cycle Amplitude (Single Axis)			
<u>Mission B</u>		<u>Predicted</u>	
Inertial, degrees:			
Roll	0.47	} From DSIF data, gyro drift test	0.44
Pitch	0.42		0.44
Yaw	0.43		0.44
Optical, degrees:			
Roll	0.441	} From DSIF data, 264:00:03:01 to 264:01:00:00	0.44
Pitch	0.45		0.44
Yaw	0.37		0.44
Sun and Star Tracking Errors, degrees			
<u>Mission B</u>		<u>Specification</u>	
Roll null:	-0.08	±0.10	
Pitch null:	-0.07	±0.10	
Yaw null:	-0.10	±0.10	
Nulls obtained from DSIF data: 264:00:03:01 to 264:01:00:00			
Sun and Star Tracking Noise			
The sun and star error signal noise levels were low enough to have no effect upon limit cycle performance.			
Fuel Consumption			
<u>Mission B</u>		(For 16 hours of limit cycle operation)	
0.020 pound			
<u>Predicted</u>		(nominal) - See Reference 8, "Fuel Budget" - corrected for a 16-hour limit cycle period	
0.018 pound			
Gyro Drift Measurements			
Drift rates (deg/hr) measured in flight* are as follows:			
<u>Check</u>	<u>Roll</u>	<u>Pitch</u>	<u>Yaw</u>
1	-0.78	0.24	1.09

\*Taken from 263:19:26:00 to 263:21:35:25.

Consequently, limit cycle frequency determination is simply a matter of simultaneously examining the pitch, yaw, and roll error signals and counting slope changes, making sure that a pulse is not counted twice because of the system crosscoupling.

A 148-minute sample of the optical limit cycle (Figure 5.5-12) had a mean time between gas jet pulses of 64 seconds. The data were taken from DSIF tapes of 264:00:30:00 to 264:02:58:00. A 77-minute sample of the inertial limit cycle (Figure 5.5-13) had a mean time between gas jet pulses of 61 seconds. The data were taken from DSIF tapes of 263:19:26:00 to 263:20:43:00.

Limit Cycle Amplitude. The roll optical and inertial deadspaces were determined from the roll error sensors during limit cycle operation. Both the roll optical and inertial deadspaces were consistent throughout the sampling period.

In pitch and yaw, there is an additional measurement consideration. A No. 2 or 3 gas jet will fire whenever the sum or difference of the pitch and yaw error signals exceeds either's single-axis deadspace voltage. Hence, a pure pitch or yaw deadspace measurement can only be made when one or the other is at null. This point will result in the maximum possible swing of the error signal which is met at null. The values recorded in Table 5.5-13 were the maximum total deadspaces observed during the indicated sample period.

Tracking Noise. Because the single-axis deadspaces are approximately equal for both inertial and optical modes and because the mean time between gas jet pulses was about the same for both the optical sample and the inertial sample, it is certain that optical sensor noise had no harmful effect upon limit cycle operation.

Tracking Errors. The tracking errors, recorded in Table 5.5-13, were taken to be the optical nulls during limit cycle operation.

Fuel Consumption. Both samples had double-pulsing at a deadband boundary which accounts for about 22 percent of the gas jet pulses. (Double-pulsing is detected from the telemetry signals by noting the magnitude of the error slope change at a boundary.)

The predicted nominal limit cycle fuel consumption (corrected for a 16-hour coast mode) is  $(0.075 \text{ pound}) (16/66) = 0.018 \text{ pound}$  (see Reference 8, "Fuel Budget"). The overage is thus  $(0.020 - 0.018 \text{ pound}) = 0.002 \text{ pound}$ . This 11 percent overage is accounted for by the double-pulsing noted above.

### Gyro Drift

A gyro drift check was made from 19:26:24 until 21:35:22 on 20 September. The drift rate values obtained from plots of the primary sun error signals (FC-5 and FC-6) and Canopus sensor error signal were as follows:

Roll gyro (S/N 72) = -0.78 deg/hr

Pitch gyro (S/N 70) = 0.24 deg/hr

Yaw gyro (S/N 51) = 1.09 deg/hr

The non-g sensitive drift history of the three gyros is shown in Table 5.5-14. The data do not appear to predict a trend.

The in-flight, i. e., zero-g, Mission B gyro drift rate values cover a range of values that compares very favorably with the limits of  $\pm 1$  deg/hr placed on earth-based measurements of non-g sensitive drift rate. Since in-flight conditions are zero-g along all axes, as compared to earth-based conditions of zero-g along only two of the three axes, there is no valid method of directly comparing in-flight zero-g and ground-based non-g sensitive drift rates.

Based upon these in-flight drift rate values obtained along with the gyro responses observed during all portions of Mission B, it is concluded that the gyros were operating in a normal manner.

### Gas Jet Thrust Level

Although the "Surveyor Functional Requirements Specification," 224510E (Reference 5) does not directly dictate the minimum allowable thrust level, it does infer these levels by specifying the minimum allowable gas jet torque values, as presented in Table 5.5-15.

It is apparent from these data that the minimum allowable gas jet thrust is 0.052 pound. The gas jet system was designed for a nominal thrust value of 0.057 pound.

In References 9 and 10 a method is proposed whereby the gas jet thrust level can be determined from the time response of the gyro error signal received during a roll maneuver. This method also mentions that a weighting factor may be required for the basic equation derived in the references. The equation is

$$T = \frac{I_z \dot{\phi}_c}{R t_p}$$

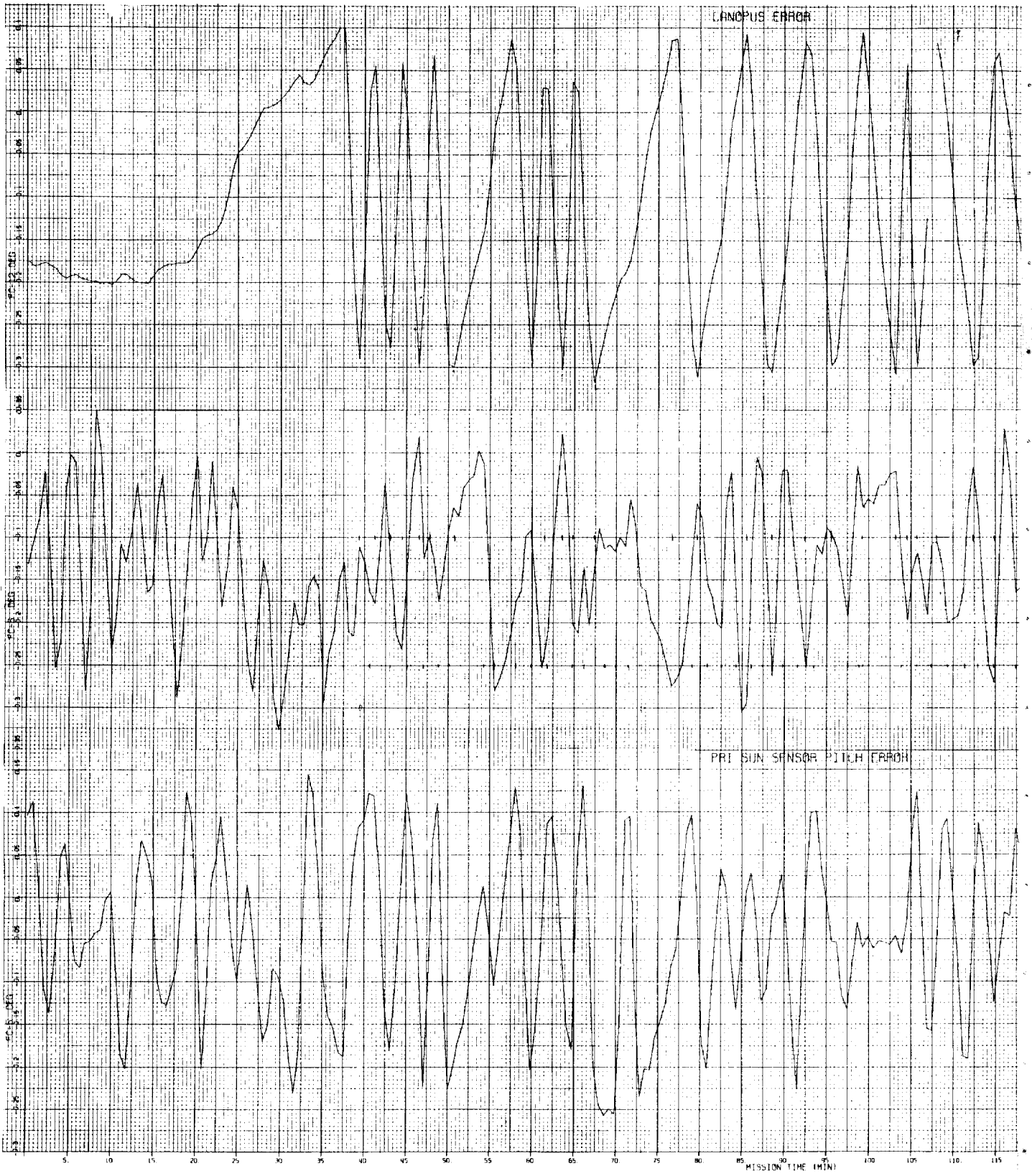
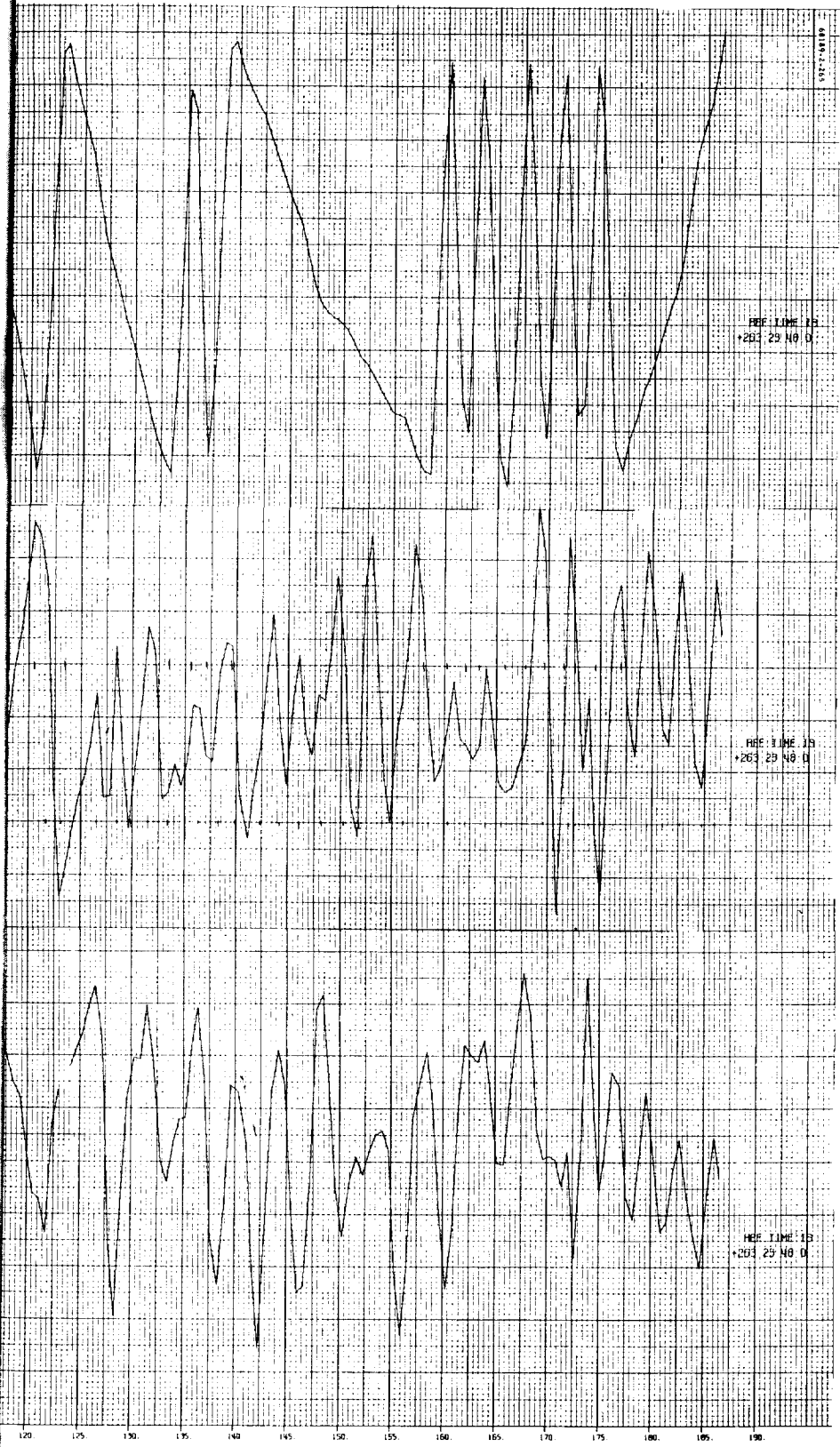


Figure 5.5-12. Optical Limit Cycle







5.5.53A  
FOLDOUT FRAME 2



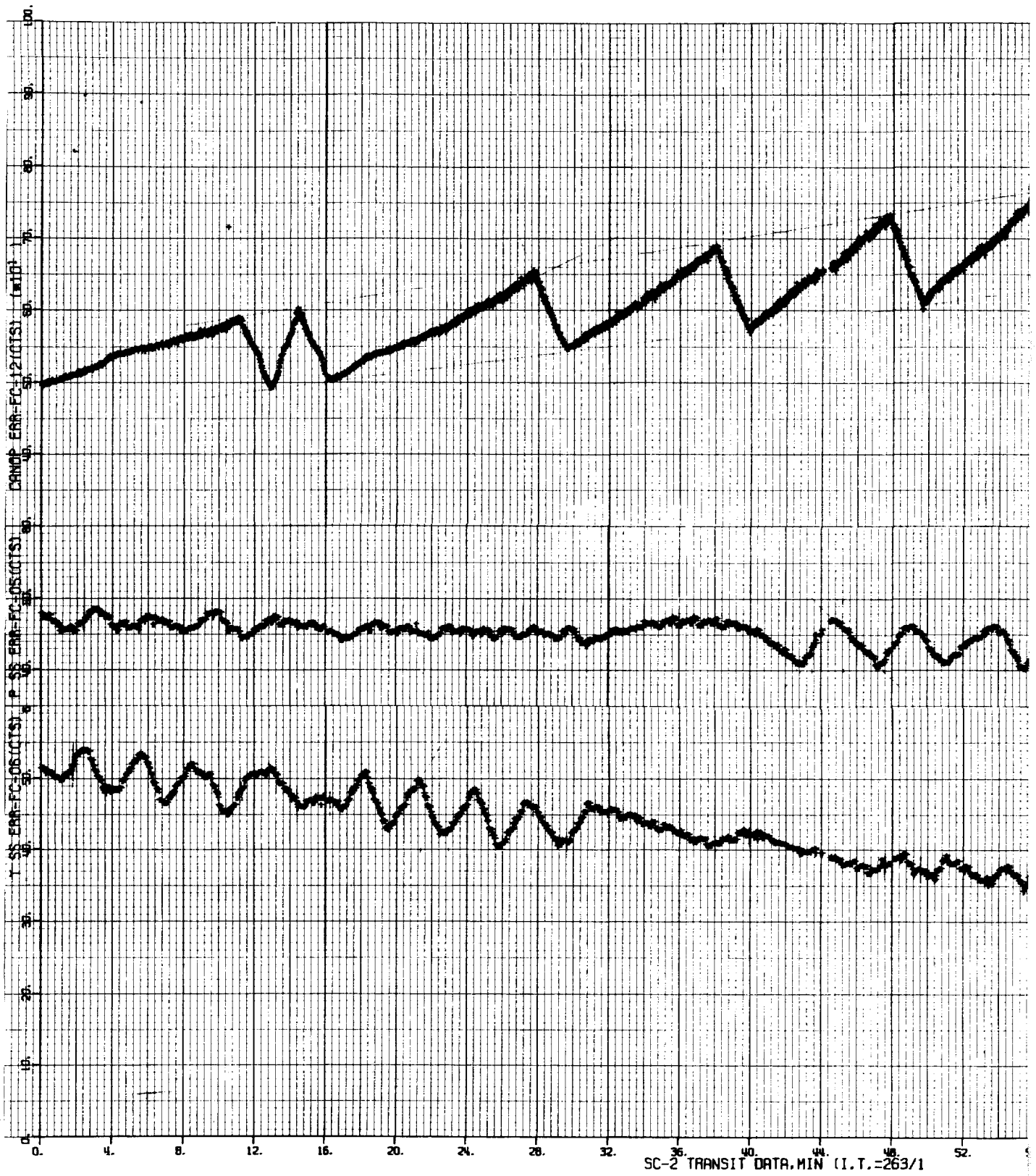
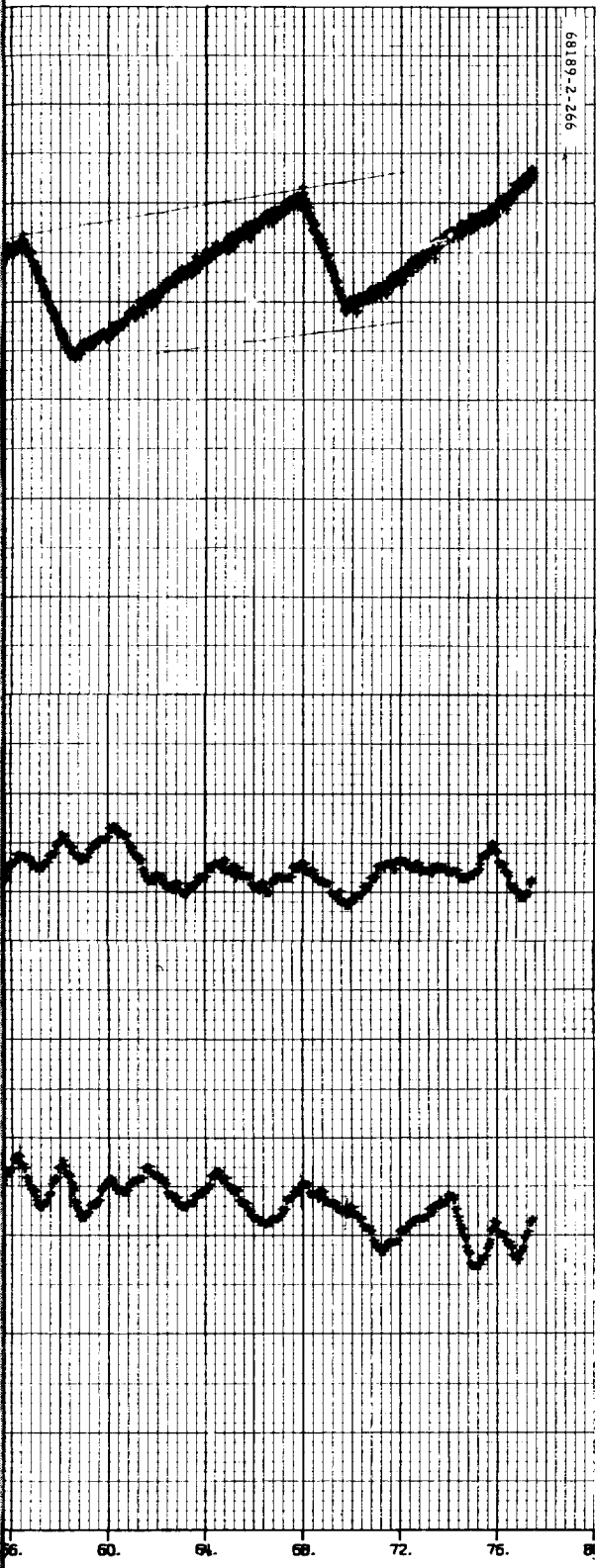


Figure 5.5-13. Inertial Limit Cycle



68189-2-266



5.5-55A

FOLDOUT FRAME 2



TABLE 5. 5-14. SUMMARY OF GYRO NON-G SENSITIVE  
DRIFT RATE MEASUREMENTS

Pitch Gyro (S/N 70)		Roll Gyro (S/N 72)		Yaw Gyro (S/N 51)	
On-Time, hours	Drift Rate, deg/hr	On-Time, hours	Drift Rate, deg/hr	On-Time, hours	Drift Rate, deg/hr
100	-0.3	78	-	66	-0.02
115	0.1	118	-0.1	116	-0.487
139	-0.09	128	0	126	-0.13
235	-0.19	152	-0.33	149	-0.73
260	0	248	-0.95	162	-0.30
296	0.38	322	-0.055	207	-1.24
309	-0.065	334	-0.055	211	E-W -0.57 N-S -0.58
321	-0.065	357	-0.2	237	-0.38
344	-0.05	370	-0.48	279	-0.571
357	0.17	415	-0.19		
402	0.43	487	-0.762		
406	0.095				
432	0.19				
474	0				
SC-2 flight	0.24	SC-2 flight	-0.78	SC-2 flight	1.09

Note: Flight control sensor group, P/N 23500-9, S/N 1; inertial reference unit, P/N 235100-1, S/N 9.

TABLE 5. 5-15. MINIMUM ALLOWABLE GAS JET TORQUE VALUES

Spacecraft Axis	Minimum Torque Requirement, in-lb	Moment Arm, inch	Number of Gas Jets	Minimum Thrust Value, pounds
Roll	4. 00	77	1	0. 052
Pitch	4. 25	45	2	0. 047
Yaw	7. 00	68	2	0. 052

From an analog computer simulation program of the gas jet system, the average weighting value was determined to be 0. 85. The values for the various parameters in the previous equation are as follows:

$$I_z = 189 \text{ slug-ft}^2$$

$$R = 6. 4 \text{ feet}$$

$$\dot{\phi}_c = 0. 500 \text{ deg/sec}$$

$$t_p = 5. 5 \text{ seconds}$$

$t_p$  represents the time from maneuver command initiation to the period when gyro output reached its first maximum. This time was approximated, as shown in Figure 5. 5-14. Multiplying the value of  $t_p$  with the weighting factor of 0. 85, the corrected time is 4. 72 seconds. Thus, the gas jet thrust level for roll was  $T = 0. 056$  pound.

#### 5. 5. 4. 6 Premidcourse Maneuvers

In order to accomplish the required velocity correction, it was necessary to perform a positive roll maneuver of 75. 3 degrees and a positive yaw maneuver of 110. 5 degrees. An attempt was made to reconstruct the total premidcourse maneuver phase from the beginning of the first roll maneuver to vernier ignition and to compute the roll axis pointing error exclusive of any tracking data.

Several variables affect the accuracy of an angular maneuver, including precession rate accuracy, precession command time, gyro drift, and initial attitude errors due to biases and limit cycle. When several maneuvers are performed with large time intervals between them, attitude errors due to gyro drift must be included. A list of all parameters affecting midcourse maneuver accuracy is presented in Table 5. 5-16 along with the allowable  $3\sigma$  values and actual performance values whenever possible.



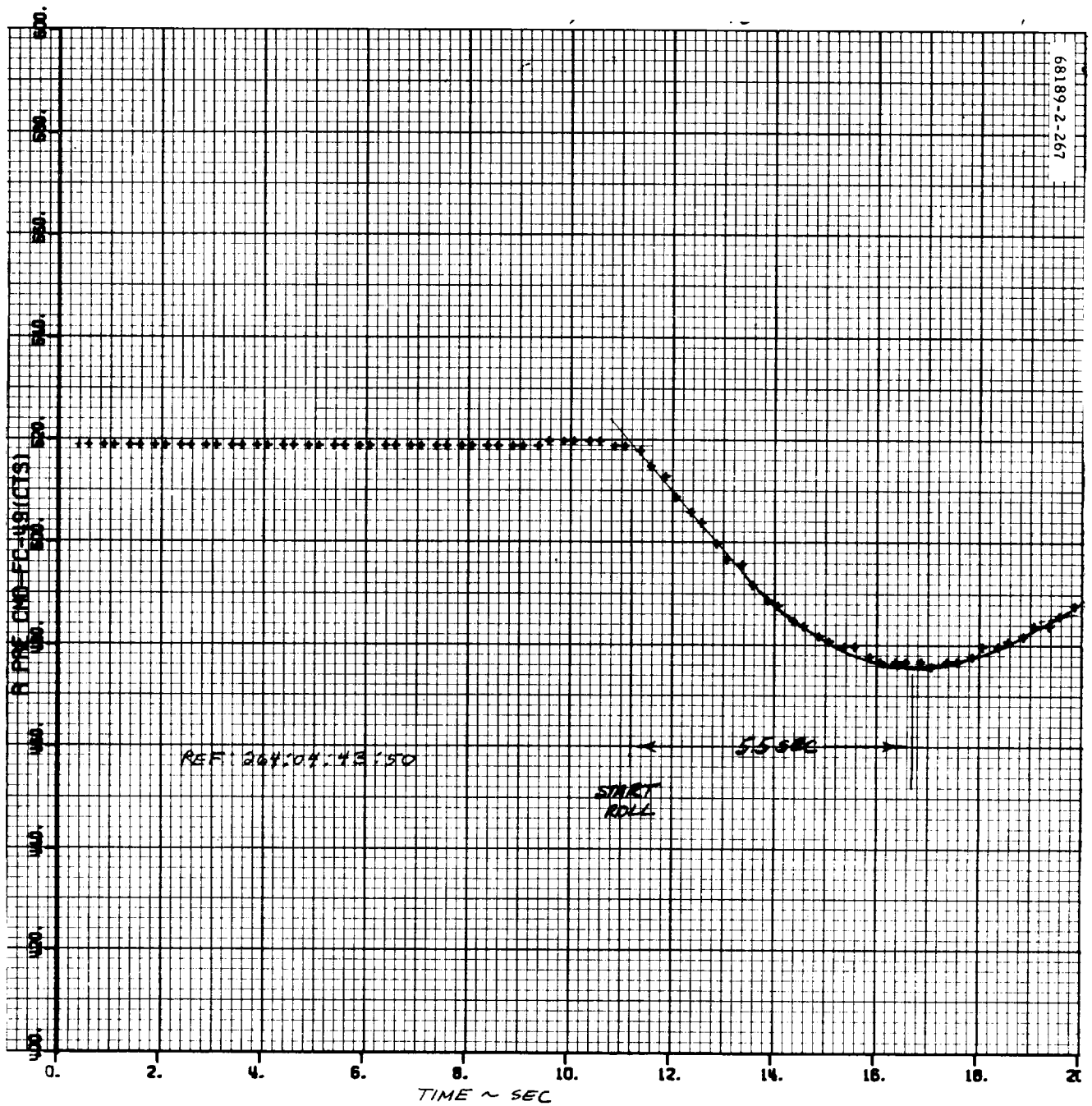


Figure 5.5-14. Roll Gyro Response Time During Premidcourse Roll

TABLE 5. 5-16. PREMIDCOURSE ATTITUDE ERROR SUMMARY

Parameter	3 $\sigma$ Requirement	References	Measured Value	Comments
Primary sun sensor null with respect to FCSG roll axis	0. 2 degree	5 , paragraph 4. 3. 1. 1	Pitch = +0. 087 degree Yaw = -0. 04 degree	
Canopus sensor null with respect to FCSG roll/pitch plane	0. 2 degree	5 , paragraph 4. 3. 1. 2	+0. 055 degree	
Pitch/yaw limit cycle	0. 3 degree	5 , paragraph 4. 3. 1. 1	+0. 05 degree/ +0. 066 degree	Based on sun sensor error signals at start of yaw
Roll limit cycle	0. 3 degree	5 , paragraph 4. 3. 1. 2	+0. 073 degree	Based on Canopus error signal at start of roll
Gyro torquer scale factor	0. 15 percent	11, paragraph 3. 2. 5. 1. 3	0. 2 percent	Spacecraft precession rate determined from star map was 0. 4498 $\pm$ 0. 0008 deg/sec
Precession current source accuracy	0. 13 percent			
Precession current source drift	0. 1 percent			
Timing source accuracy	0. 2 second $\pm$ 0. 02 percent		Roll = +0. 028 degree Yaw = +0. 01 degree	Based on timing errors determined in subsection 5. 5. 4. 6
Gyro alignment to FCSG roll axis	0. 14 degree	11, paragraph 3. 2. 5. 1. 4	Pitch = +0. 037 degree Yaw = +0. 100 degree	
FCSG/spacecraft roll axis alignment	0. 1 degree	5 , paragraph 4. 1. 3. 7. 1	+0. 023 degree (Yaw = +81 seconds) (Pitch = -3 seconds)	
Gyro non-g sensitive drift	1. 0 deg/hr	5 , paragraph 4. 3. 1. 5	Roll = -0. 2 degree Yaw = +0. 2 degree Pitch = +0. 05 degree	Based on measured -0. 78 deg/hr in roll for 16 minutes and 1 second; +1. 0 deg/hr in yaw for 11 minutes and 56 seconds; +0. 25 deg/hr in pitch
Total attitude error prior to ignition			+0. 39 degree along negative yaw axis with 0. 2 degree uncertainty	

### Determination of Precession Times

The register was loaded with 377 bits for roll and 553 bits for yaw. With a clock rate of 2.5 cps, the respective times are 150.8 and 221.2 seconds with a maximum error of 0.20 second.

The gyro error signal telemetry data were used to determine the actual precession time. The sampling rate during the maneuvers was 20 times/sec, giving a resolution of 0.05 second. The results are as follows (Figures 5.5-15 and 5.5-16):

$$T = 150.744 \text{ seconds (roll)}$$

$$T = 221.182 \text{ seconds (yaw)}$$

### Attitude Maneuver Error

Reference 12 develops two orthogonal equations that specify the spacecraft thrust axis pointing error during midcourse thrusting. The equations were derived for a roll-pitch rotation sequence.

Rewriting these equations for a roll-yaw rotation sequence and neglecting error sources that are present only after engine ignition results in the following equations:

$$\begin{aligned} \text{Error along pitch axis} = & \sin \psi (\phi_{A_E} + \phi_{R_E}) + \theta_{A_E} \cos \psi \cos \phi \\ & - \psi_{A_E} \cos \psi \sin \phi \end{aligned}$$

$$\text{Error along yaw axis} = -\psi_{R_E} - \cos \phi \psi_{A_E} - \sin \phi \theta_{A_E}$$

where  $(\phi, \theta, \psi)_{A_E}$  are spacecraft inertial reference alignment errors and  $(\psi, \phi)_{R_E}$  are rotation errors.

Use of  $\phi = 75.3$  degrees,  $\psi = 110.5$  degrees, and the errors listed in the summary chart results in an attitude error of 0.39 degree along the negative yaw axis and an error of 0.04 degree along the negative pitch axis. The resultant pointing error has a 99 percent circular probable uncertainty of 0.20 degree.

68189-2-268

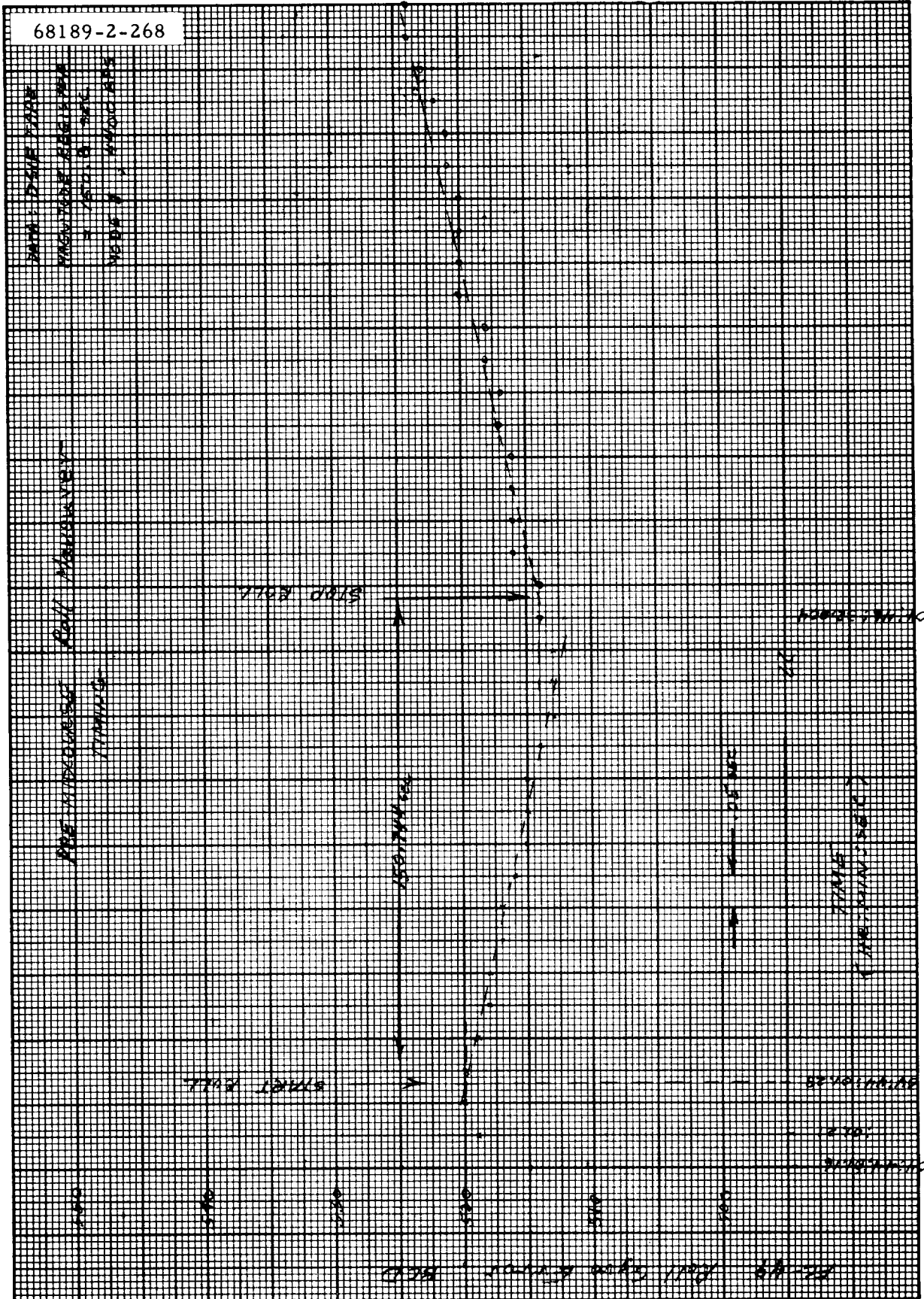


Figure 5.5-15. Premidcourse Roll Maneuver Timing

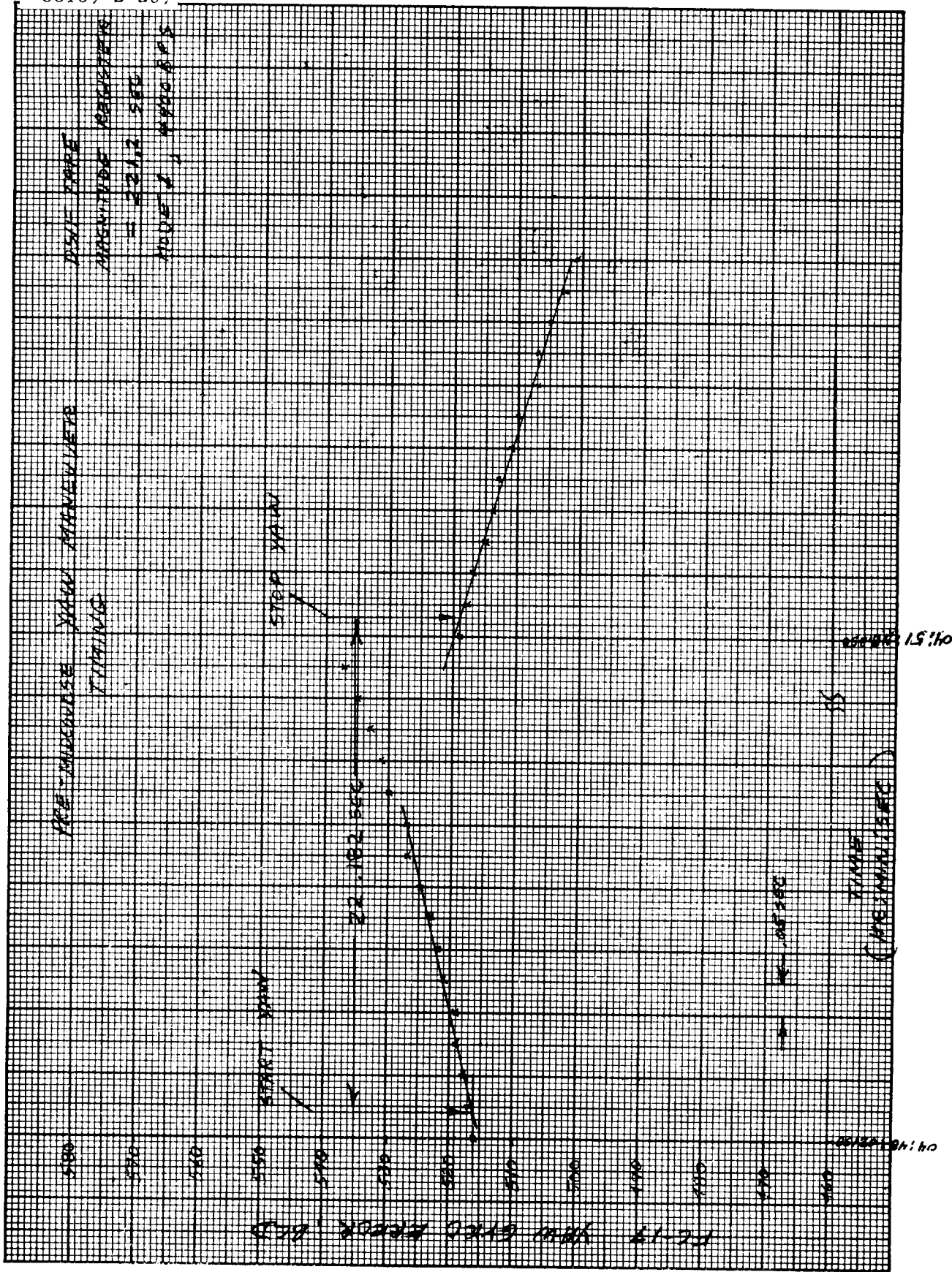


Figure 5.5-16. Premidcourse Yaw Maneuver Timing

### Precession Rates

Accuracy of the precession rates imposed by the "Surveyor System Functional Requirements Specification" (Reference 5) is  $0.5000 \pm 0.0011$  deg/sec. The precession rate obtained during the star mapping phase indicates that the positive precession rate is 0.4998 deg/sec with a data granularity of 0.0008 deg/sec.

#### 5.5.4.7 Nitrogen Gas Consumed

Since the nitrogen tank temperature is not available in commutator mode 1, an accurate estimate of the nitrogen gas consumed during the premidcourse attitude maneuvers could not be made. If it is assumed that the nitrogen tank temperature did not change appreciably during the maneuvers, the estimated gas usage was 0.06 pound. This compares favorably with an expected value of 0.055 pound (Reference 4).

#### 5. 5. 4. 8 Midcourse Velocity Correction

The desired midcourse burn duration of 9. 850 seconds was entered into the spacecraft magnitude register 5 minutes before the planned ignition time of 05:00:00. Bulk printer data indicated ignition (magnitude register started to count down) at 05:00:02. 5.

Within a few seconds after ignition, flight control telemetry signals indicated hard-over pitch, yaw, and roll gyro errors, roll actuator position, and acceleration error. Vernier engine strain gage telemetry signals indicated thrust on legs 1 and 2, but zero on leg 3. The leg 3 throttling signal telemetry went hard-over to the maximum thrust command position and remained there throughout the burn.

Loss of thrust on leg 3 caused the spacecraft to spin-up initially about a lateral axis. Effects due to the roll actuator and nonsymmetrical inertia properties of the spacecraft caused the ensuing motion to become a tumbling about all axes. During the 9. 85-second burn time, the tumble rate built up to 1. 25 rps, as indicated by fluctuation of the receiver automatic gain control or secondary sun sensor telemetry signals.

Following vernier engine cutoff, the tumble rate was decreased 32 percent by action of the gas jet attitude control system. The gas jets were inhibited by ground command 14 minutes and 20 seconds after cutoff after 50 percent of the premidcourse fuel load had been expended. The tumble rate by then had been reduced to 0. 85 rps.

Flight control system performance during the midcourse burn appeared to be normal under the prevailing circumstances. The flight control system outputs (vernier engine throttling signals and roll actuator position) behaved in a predictable manner during the vernier ignition transient and throughout the burn period. Engines 1 and 2 had an ignition delay time of less than 120 milliseconds (see subsection 5. 5. 4. 8) and responded well to their respective throttling signals.

The calculation of vernier engine startup and shutdown impulse dispersions, as done in the case of SC-1 from pitch and yaw gyro telemetry data, was not possible for SC-2. The relatively small effects produced were masked by the engine 3 failure.

#### Description of Flight Control System Behavior

Behavior of the flight control system during the 9. 85-second burn period is depicted by the real-time SPAC brush recordings shown in Figure 5. 5-17. The inertial sensor signals – pitch, yaw, and roll gyro errors, and acceleration error (the processed accelerometer signal) – are given by telemetry analog channels FC-16, FC-17, FC-49, and FC-15, respectively. The flight control system outputs – vernier throttle-valve signals, and roll actuator position – are given by telemetry analog channels

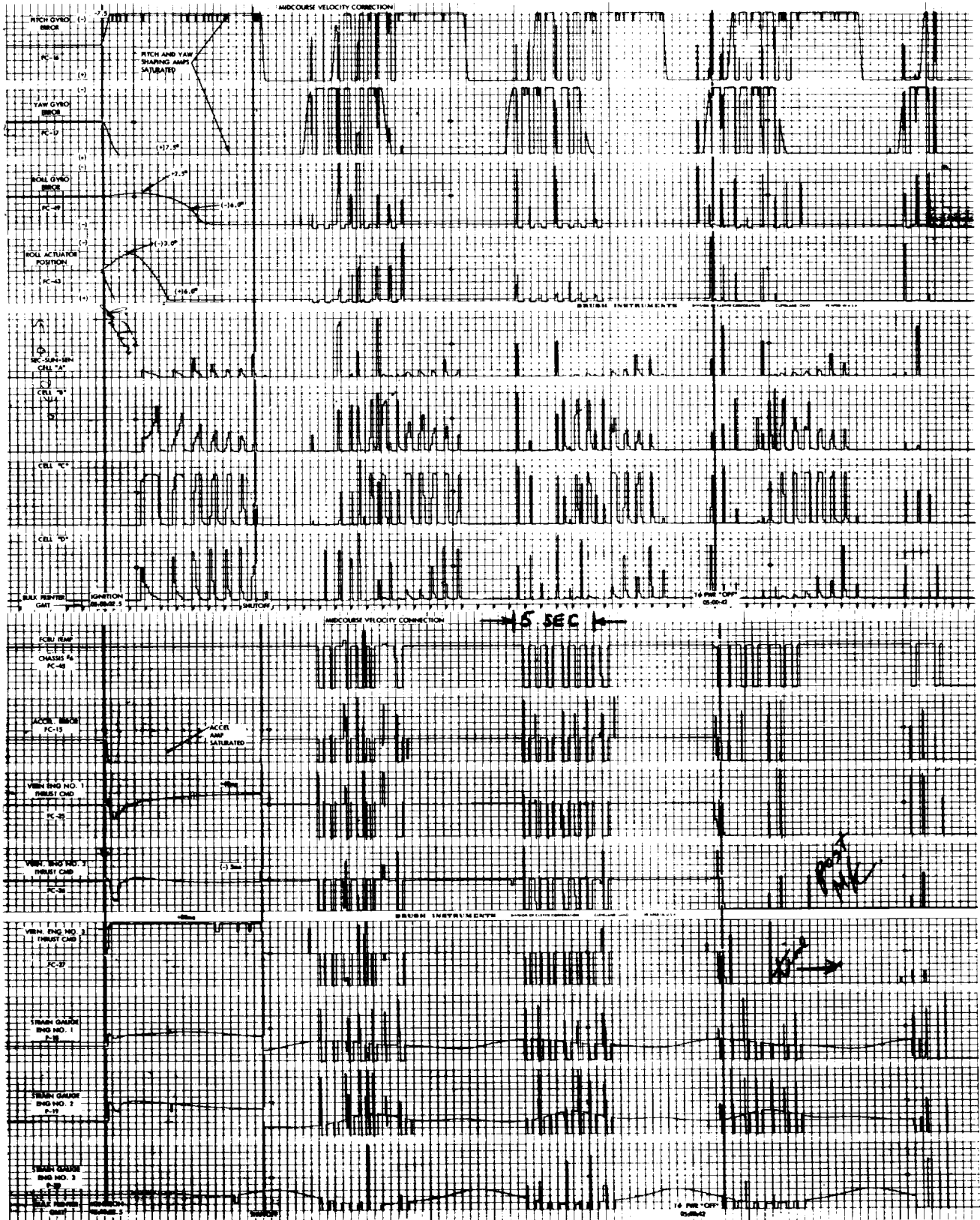


Figure 5.5-17. Midcourse Thrust



FC-25, FC-26, FC-27, and FC-43, respectively. Also shown in Figure 5.5-17 are the three vernier strain gage signals and the indications from the four secondary sun sensor cells. The time period shown extends from 30 seconds before ignition until 1 minute and 30 seconds past cutoff.

Pitch/Yaw Behavior. With the loss of engine 3 thrust, spacecraft pitch and yaw motion diverged beyond the gyro telemetry range ( $\pm 7.5$  degrees) within 2 seconds after ignition. Although no direct indication of angular rate is available, the rate buildup during the burn period is apparent from the increasing fluctuation rate of the secondary sun sensor signals. Final rotation rate at the end of burn was 448 deg/sec (1.24 rps) as indicated by receiver automatic gain control fluctuations. Following engine cutoff, pitch and yaw gyro errors moved from stop to stop, indicating polarity changes in pitch and yaw body rates due to the tumbling motion. This general behavior exhibited in flight has been duplicated by analog computer simulation (see subsection 5.5.4.10).

In the transient motion which occurred at ignition, negative pitch and positive yaw motions were obtained. This follows from the locations of engines 1 and 2 relative to pitch and yaw body axes as shown in Figure 5.5-18. Also, yaw divergence was slower than pitch divergence. This is attributed to the fact that engine 2 was commanded to a lower thrust level than engine 3, which is evident from a comparison of FC-25 and FC-26 in Figure 5.5-17. The engine geometry also contributes to this, since equal thrust on engines 1 and 2 would cause pitch motion to diverge somewhat faster (17 percent) than in yaw. This initial motion has been duplicated in a mixed flight control electronics analog computer simulation (see subsection 5.5.4.10), where it was found that the small residual attitude errors (less than  $\pm 0.4$  deg/axis) due to gas jet deadband and electronic nulls have a strong influence on the initial thrust transients.

The tumbling motion that continued after cutoff is difficult to describe since it involved fluctuating angular rates about all three body axes. It is further complicated by the fact that the spacecraft is nearly an inertial sphere, i. e., the principal moments of inertia are nearly equal, so that an analytical description is extremely complex. The motion has been closely duplicated by analog computer simulation (subsection 5.5.4.10), however, so only a few remarks on the general nature of the motion will be made here.

From the pitch, yaw, and roll gyro error traces shown in Figure 5.5-17, it is apparent that pitch and yaw angular rates reversed polarity periodically (period = 13 seconds) and that roll rate was of constant polarity. This is consistent with the general form of the theoretical solution for the unforced tumbling motion (Reference 13). In the general case (for zero cross-products of inertia), the angular rates about the axes of least inertia will fluctuate periodically about zero, whereas the rate about the axis of maximum inertia will fluctuate at twice the frequency about some bias level.

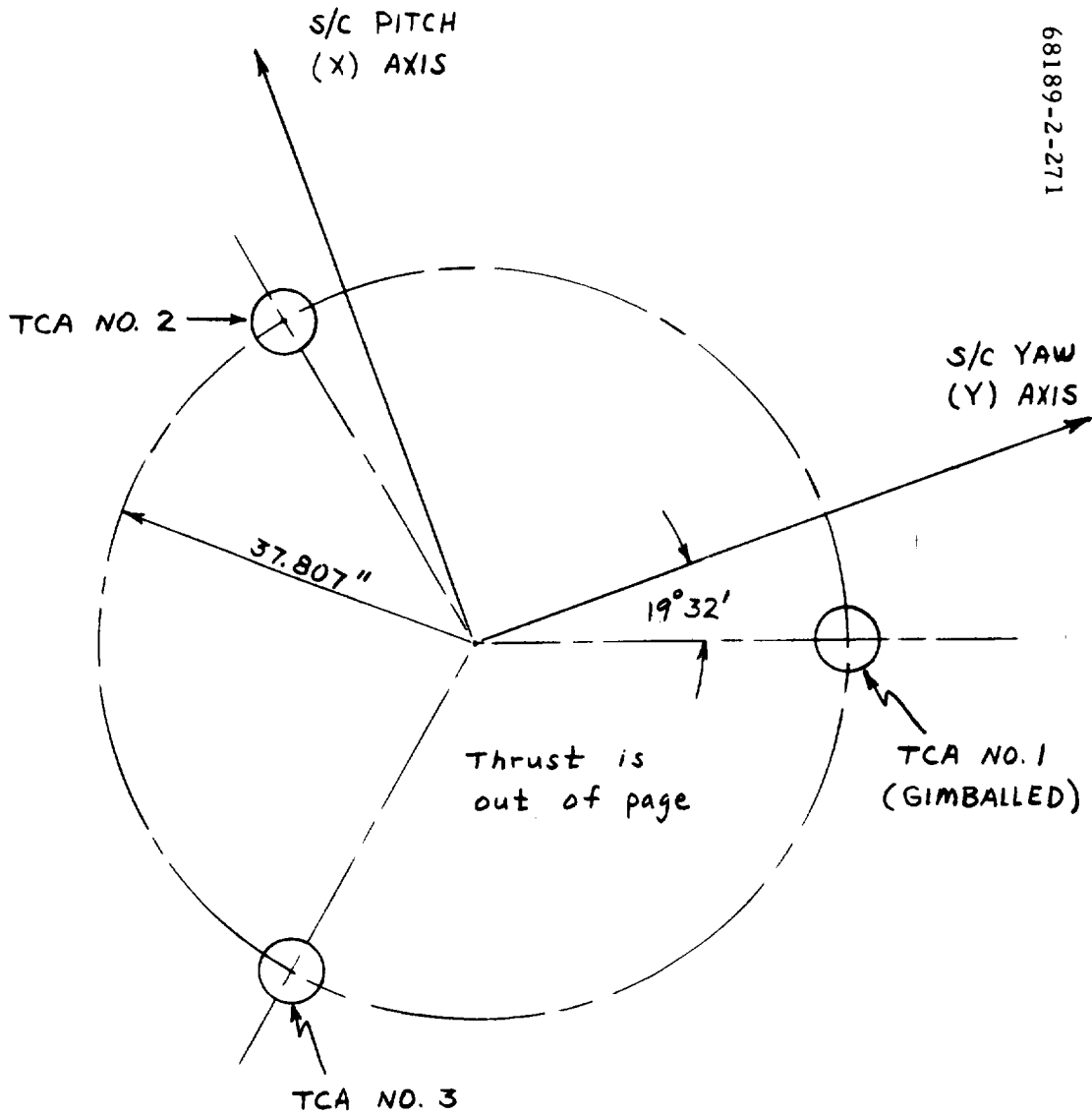


Figure 5.5-18. Vernier Thrust Chamber Locations

The SC-2 inertia properties were as follows (Reference 14):

Pitch	$I_{xx} = 208.3 \text{ (slug-ft}^2\text{)}$
Yaw	$I_{yy} = 204.7$
Roll	$I_{zz} = 215.4$
Cross products	$I_{xy} = -7.3$
	$I_{xz} = 7.8$
	$I_{yz} = -1.8$

Thus, since the roll axis was aligned roughly with the axis of maximum inertia, roll angular rate did not change sign, whereas pitch and yaw rates reversed sign periodically.

#### Vernier Throttling Signals

Behavior of the vernier engine throttling signals (FC-25, FC-26, and FC-27) is shown in the brush recordings (Figure 5.5-17). Each signal is a linear combination of command signals generated by the pitch and yaw attitude control loops and the acceleration control loop according to the following relationships (Reference 11):

$$\begin{pmatrix} \hat{\Delta T}_1 \\ \hat{\Delta T}_2 \\ \hat{\Delta T}_3 \end{pmatrix} = \begin{pmatrix} -0.212 & -0.074 & 0.333 \\ 0.041 & 0.222 & 0.333 \\ 0.171 & -0.147 & 0.333 \end{pmatrix} \begin{pmatrix} \hat{L}_x \\ \hat{L}_y \\ \hat{\Delta T}_z \end{pmatrix}$$

where  $\hat{L}_x$  and  $\hat{L}_y$  are pitch and yaw moment commands, and  $\hat{\Delta T}_z$  is the net thrust increment command.

Thus, as seen in Figure 5.5-17,  $\hat{\Delta T}_3$  (FC-27) became saturated in the positive direction immediately after ignition, since all three control channels were commanding more thrust from engine 3. On the other hand,  $\hat{\Delta T}_1$  and  $\hat{\Delta T}_2$  (FC-25 and FC-26) were each commanded up by the acceleration loop and down by the attitude loops, and approached compromise levels inside the saturation limits. Assuming that all control channels are saturated in the polarities indicated by the SC-2 telemetry, the resulting throttle-valve signals can be calculated as shown in Table 5.5-17 where the predicted values agree well with those observed in flight.

TABLE 5.5-17. COMPARISON OF CALCULATED AND OBSERVED THROTTLE-VALVE SIGNALS

Command Source	Throttle Valve Signals, milliamperes		
	Leg 1	Leg 2	Leg 3
Acceleration loop	150	150	150
Pitch loop	-175	36	148
Yaw loop	64	-192	127
Net, calculated	39	-6	>80*
Net, observed	40	-5	80**

\*Maximum capability of vernier valve amplifiers.  
 \*\*Telemetry saturation level.

As noted from Figure 5.5-17, the acceleration error signal (FC-15) became saturated shortly after ignition and remained saturated thereafter. This follows from the fact that the commanded midcourse acceleration level (0.1 earth g), requiring 220 pounds of thrust from the vernier propulsion system, was not achieved. A review of vernier engine data shows that engines 1 and 2 were capable of 106 and 108 pounds, respectively, or a maximum total of 214 pounds. Thus, the 0.1  $g_e$  level was unattainable even with both engines operating at their maximum levels.

## Roll Actuator Response

The roll actuator responded normally, under the circumstances, throughout the midcourse burn period. At ignition, a positive roll error signal caused the actuator to deflect a maximum of 2.7 degrees in the negative direction. Then, due to coupling of the uncontrolled tumbling motion into roll, the roll gyro error reversed, causing the actuator to move to its positive 6-degree travel limit where it remained thereafter. Calculations that follow show that the actual actuator response agrees well with predictions based on the roll control system transfer function and the observed roll gyro error.

Initial Transient. During the failure analysis, a question concerning an apparent inconsistency in the initial actuator response was raised at Hughes and JPL. The following discussion and analysis are included here to cover this point.

A review of telemetry data at midcourse ignition yields the following observations:

- 1) Roll gyro error (FC-49, generally referred to as roll precession command) shows no apparent change over a 250-millisecond interval beginning at ignition.
- 2) Roll actuator deflection (FC-43) shows an immediate response at ignition.

Since the roll actuator is driven by a signal derived from the roll gyro error signal, the above observations would lead one to believe that the actuator was responding improperly to an error signal null.

The following analysis shows that the roll actuator response was in fact normal, and that this apparent inconsistency was caused by a combination of the following factors:

- 1) Granularity of roll gyro telemetry signal (0.033 deg/BCD)
- 2) Filter time-constant of roll gyro telemetry circuit (0.28 second)

A plot of the raw telemetry data for  $\delta$  (FC-43) and  $\theta_z$  (FC-49) is shown in Figure 5.5-19. The plot extends for several seconds beyond ignition to indicate general signal behavior. Also shown is the result of a calculation to check actuator response relative to that predicted from the nominal roll channel transfer function. For the calculation checkpoint chosen, the telemetry value of  $\delta$  is -1.88 degrees. To approximately account for the 0.25 second difference in FC-43 and FC-49 telemetry circuit time constants, the prediction of  $\delta$  is based on the values of  $\theta_z$  and  $\dot{\theta}_z$  occurring 0.25 second beyond the checkpoint. As indicated in Figure 5.5-19, the prediction yields  $\delta = -1.79$  degrees, nearly equal to the observed value. It is thus concluded that the observed actuator response was normal.

Figure 5.5-20 shows a plot of  $\delta$  and  $\theta_z$  obtained from a closed-loop analog computer simulation (including actual flight control electronics hardware) of the midcourse startup. The scales in Figure 5.5-20 are identical to Figure 5.5-19. The  $\theta_z$  trace (which includes the effect of a 0.28-second telemetry filter time-constant) is observed to change very little over the initial 250-millisecond interval. In fact, approximately 200 milliseconds are required to develop an amplitude equivalent to 1.0 BCD and, with the spacecraft telemetry system, no change would have been registered over this interval.

Thus, the analog computer result, which yielded a 1.7-degree peak of  $\theta_z$ , indicates no  $\theta_z$  BCD change over a 200-millisecond interval. Since the peak  $\theta_z$  in the SC-2 case was 1.35 degrees, no BCD change would be expected for an interval of

$$\frac{1.7}{1.35} \times 200 \text{ milliseconds} = 250 \text{ milliseconds}$$

which agrees with the observed result in SC-2.

Conclusions. The following conclusions have been reached:

- 1) Roll actuator response during midcourse phase appeared normal.
- 2) Zero BCD change in roll gyro error over the first 250-millisecond interval is consistent with analog computer study results.

#### Gas Jet System Operation

The cold gas attitude control system remained active until 14 minutes and 29 seconds after midcourse ignition, when the gas jet amplifiers were inhibited by ground command. As a result, 2.19 pounds of nitrogen (50.5 percent of premidcourse load) was expended in reducing the spacecraft tumble rate from 448 deg/sec to 306 deg/sec (31.7 percent reduction).

During this time, two gas jets were on continuously, and one jet was on about 60 percent of the time. The net specific impulse of the system was about 64 seconds over this time period, yielding a rate reduction efficiency of approximately 1.0 deg/sec per lb-sec of total jet impulse.

Gas Jet Duty Cycle. The following calculations show that the gas jet system was operating with an average of 2.6 jets thrusting. Reference 15 shows that a large pure pitch or pure roll angular rate would hold the applicable gas jets on continuously. Because of phase detector voltage saturation, a large yaw error signal would hold the No. 2 and 3 gas jets on for 80 percent of the time.







In Section 6.4.2 of Reference 16, a relationship between gas jet duty cycle and steady-state gas jet amplifier input is derived. The same relationship for current system parameter values can be expressed as

$$\begin{aligned} \text{Duty cycle} &= \frac{\text{ratio of on-time}}{\text{to total period}} = \frac{t_{\text{on}}}{\tau} \\ &= \frac{\frac{3.2h}{(9-v)}}{\frac{25.6h}{(9-v)(v-1)}} = \frac{(v-1)}{8.0} \end{aligned}$$

where

$$v = \frac{\text{input voltage}}{\text{deadspace voltage}}$$

Thus,  $v = 7.4$  for an 80 percent duty cycle and, using the measured SC-2 yaw deadspace of 0.22 degree, the yaw phase detector output voltage would be equivalent to  $(7.4)(0.22) = 1.63$ -degree error. Assuming that all phase detectors saturate at the same voltage level, roll and pitch levels of saturation are 2.7 and 2.4 degrees, respectively.

The observed polarities of the saturated gyro signals following mid-course thrusting were as follows:

- 1) Roll: negative
- 2) Pitch: negative
- 3) Yaw: positive

Saturated signals from these gyros would have the following effect upon the three pairs of gas jet amplifiers (after going through the summing matrix):

- 1) No. 1 CCW jet would be commanded on by a roll signal equivalent to 2.7 degrees. This jet would be on continuously.
- 2) No. 3 CCW jet would be commanded on by the pitch and yaw signals and off by the roll signal. Net command to this amplifier would be equivalent to 3.5 degrees. This jet would also be on continuously.

- 3) No. 2 CCW jet would be commanded on by pitch and roll signals and commanded off by yaw signal. Net command to amplifier would be equivalent to 1.29 degrees, which is 5.84 times nominal deadspace. Duty cycle for this jet would then be

$$\frac{t_{\text{on}}}{\tau} = \frac{(5.84-1)}{8.0} = 0.60$$

or, this jet would be on about 60 percent of the time. Thus, on the average, the gas jet system was operating with 2.6 jets thrusting.

Fuel Consumption. Spacecraft consulting analysis team data were used in the fuel consumption calculations as follows:

Nitrogen weight before midcourse = 4.34 pounds  
 Nitrogen weight after midcourse = 2.15 pounds  
 Nitrogen used in rate reduction = 2.19 pounds

I<sub>sp</sub> Determination. Reference 17 notes that the gas jets were enabled for 869 seconds following midcourse ignition.

I<sub>sp</sub> is calculated from the following equation:

$$\begin{aligned} I_{\text{sp}} &= \frac{(\text{time})(\text{total thrust})}{\text{weight of nitrogen used}} \\ &= \frac{(869 \text{ seconds})(2.6 \times 0.0622) \text{ pound}}{2.19 \text{ pounds}} \\ &= 64.3 \text{ seconds} \end{aligned}$$

where the thrust per jet is taken to be the thrust value under full flow conditions as recorded in the SC-2 Surveyor Flight Control Data Package summary data.

The value for I<sub>sp</sub> is between the lower bound (60 seconds) used for fuel budget calculations and 73 seconds, as measured in Reference 18. An I<sub>sp</sub> less than 73 seconds was expected because I<sub>sp</sub> decreases with decreasing temperature, and it is thought that the gas jets were materially cooled by convection as the nitrogen flowed for this long thrusting period.

Rate Reduction Efficiency. A plot of spacecraft tumble rate (determined from SPAC automatic gain control data) is shown in Figure 5.5-21. The initial tumbling rate was 448 deg/sec and, after 14.5 minutes, it has been reduced to 306 deg/sec. In the following,  $\frac{1}{x}$  is an efficiency figure that reflects how many deg/sec of body rate is eliminated for each lb-sec of impulse expended from the cold gas jet control system.

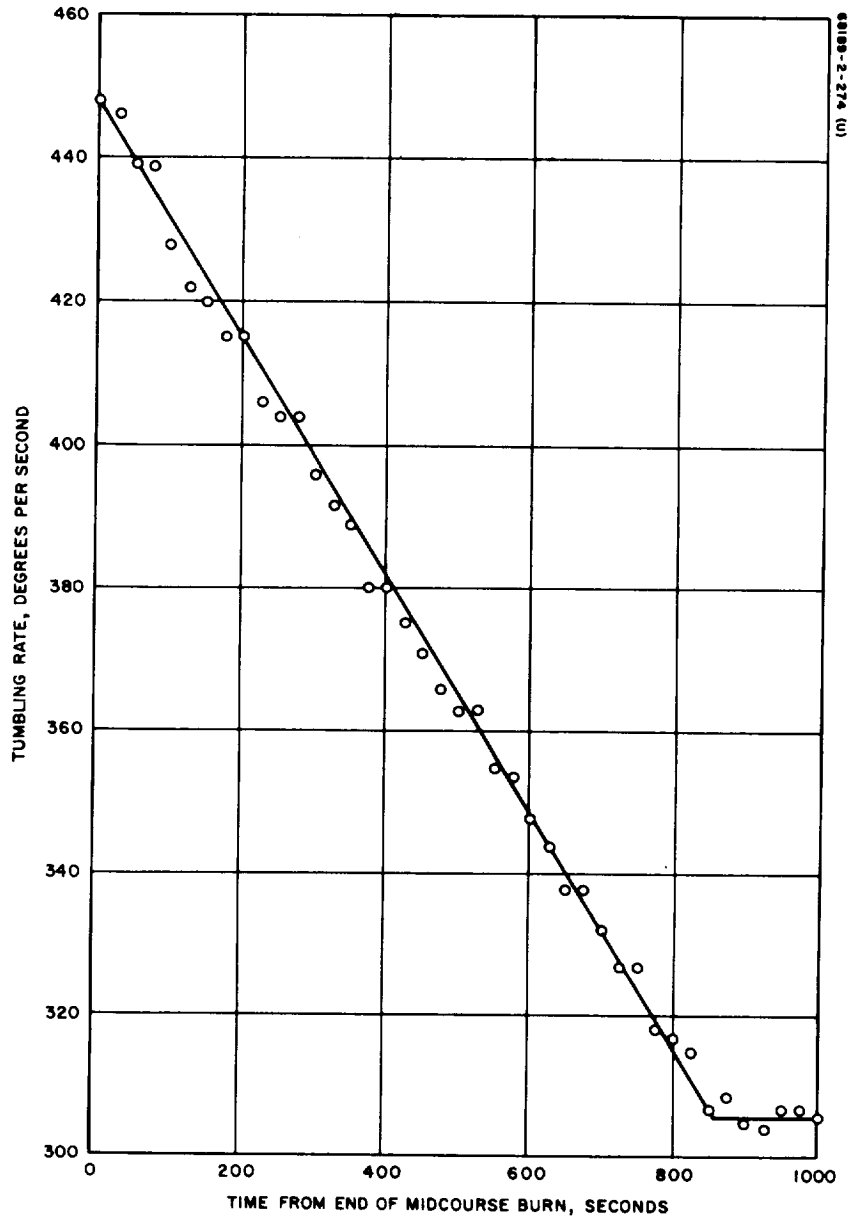


Figure 5.5-21. Spacecraft Tumble Rate After Midcourse

$$\Delta W = \frac{(X)(\Delta \omega)}{I_{sp}} \text{ or } \frac{1}{x} = \frac{(\Delta \omega)}{(\Delta W)(I_{sp})}$$

$$\Delta \omega = 142 \text{ deg/sec}$$

$$I_{sp} = 64.3 \text{ seconds}$$

$$\Delta W = 2.19 \text{ pounds}$$

$$\frac{1}{x} = \frac{(142)}{(2.19)(64.3)} = 1.01 \frac{\text{deg/sec}}{\text{lb-sec}}$$

This rate reduction efficiency figure is consistent with values obtained in previous analog computer studies. Reference 1 records the following efficiency figures (Table 5.5-18) for a 5 deg/sec initial body rate distributed in different ways among the pitch, yaw, and roll axes.

TABLE 5.5-18. RATE REDUCTION EFFICIENCY

Initial Rate Magnitude, deg/sec			Impulse Expended, lb-sec	Efficiency Figure, $\frac{\text{deg/sec}}{\text{lb-sec}}$
Roll	Yaw	Pitch		
5	0	0	3.75	1.33
0	5	0	3.35	1.49
0	0	5	5.20	0.96
3.535	3.535	0	3.58	1.40
0	3.535	3.535	3.70	1.35
3.535	0	3.535	5.50	0.91
2.882	2.882	2.882	4.68	1.07

#### 5. 5. 4. 9 Postmidcourse Vernier Engine Firings

In order to bring about leg 3 vernier engine ignition, 39 additional vernier engine firings were programmed and executed between the time of the midcourse firing command (0721 at 264:05:00:02) and the retro firing command (0730 at 265:09:34:17) (see Section 4. 1). Thirty of these firings were for commanded durations of ~0. 2 second, seven for ~2. 0 seconds, one for ~2. 5 seconds and one for ~21. 5 seconds. (The midcourse commanded duration was 9. 85 seconds.)

A summary of the longer firings (burns) ( $\geq 2. 0$  seconds) in terms of thrust commands, strain gage response, and acceleration error derived from SPAC brush recordings is presented in Figure 5. 5-22. The strain gage and thrust command data are plotted with greater resolution in Figures 5. 5-23 through 5. 5-32.

Postmidcourse burn analysis concentrated on the longer burns in preference to the 0. 2-second burns due to the disparity between sample rate and vernier on time. \* Analysis of the latter burns is to be performed subsequent to submission of this report.

The general aspect of the 2. 0-second firings was as follows:

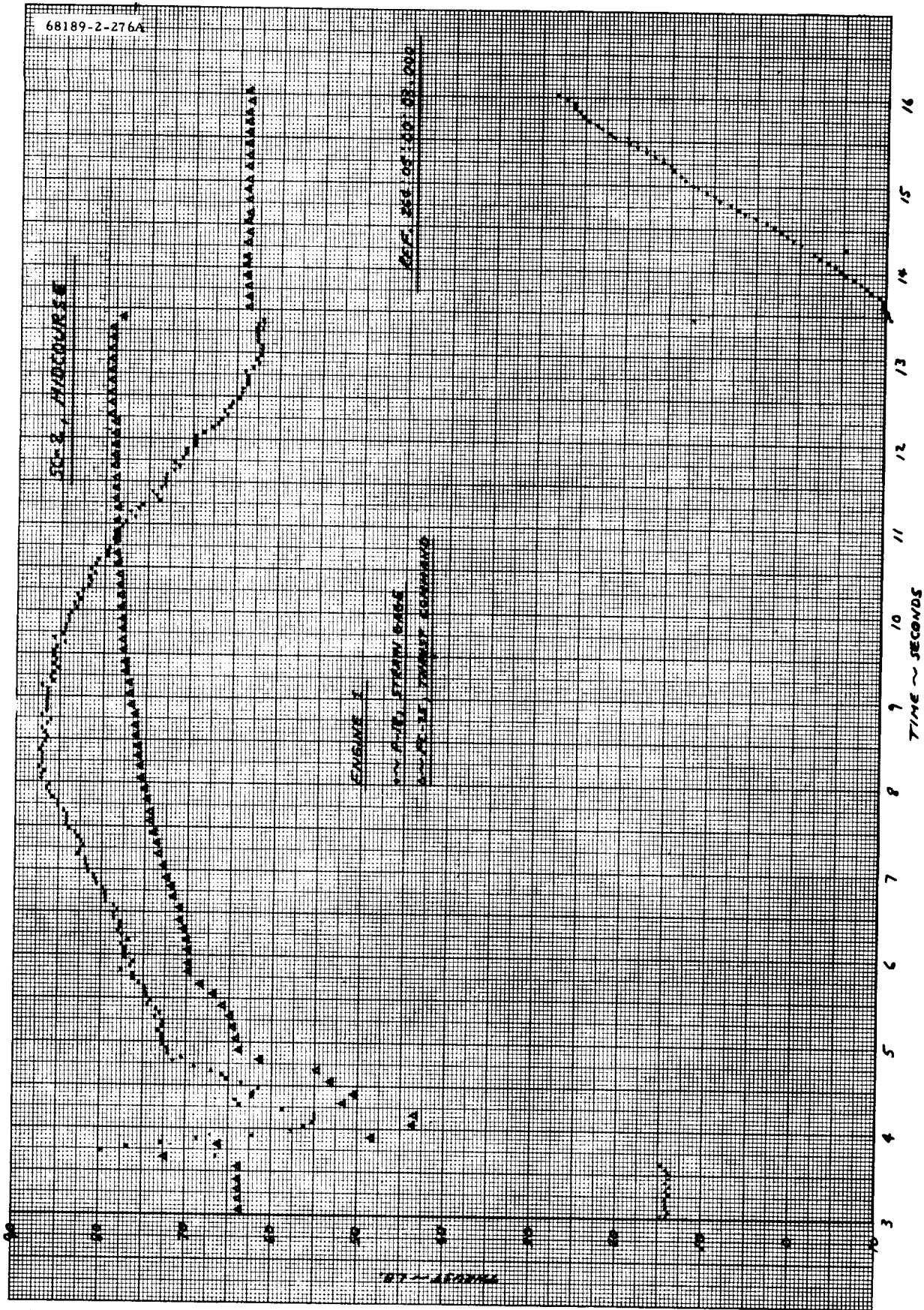
- 1) At the fire command, legs 1 and 2 thrust commands immediately dropped from midthrust to minimum thrust, and the leg 3 thrust command immediately increased from midthrust to maximum thrust. The strain gage readings for legs 1 and 2 increased from zero to the commanded thrust (approximately, making allowance for transducer drift due to spacecraft accelerations and temperature variations). The leg 3 strain gage did not respond according to the thrust command, but did show the effects of acceleration and temperature.
- 2) Acceleration error (FC-15) signal was saturated (+) during each firing period.
- 3) Roll actuator (FC-43) remained hard over at +6 degrees.
- 4) Gas jets were inhibited.
- 5) Pitch (F-16), yaw (FC-17), and roll (FC-49) error signals remained saturated (minus, plus, and minus, respectively).
- 6) Telemetry condition: Mode 1, 1100 bits/sec

---

\*One sample every 1. 6 seconds for the strain gages on all burns except 35 through 39, for which 5 samples/sec were read. (These sample rates correspond to mode 1, 137 bits/sec and mode 1, 1100 bits/sec.)

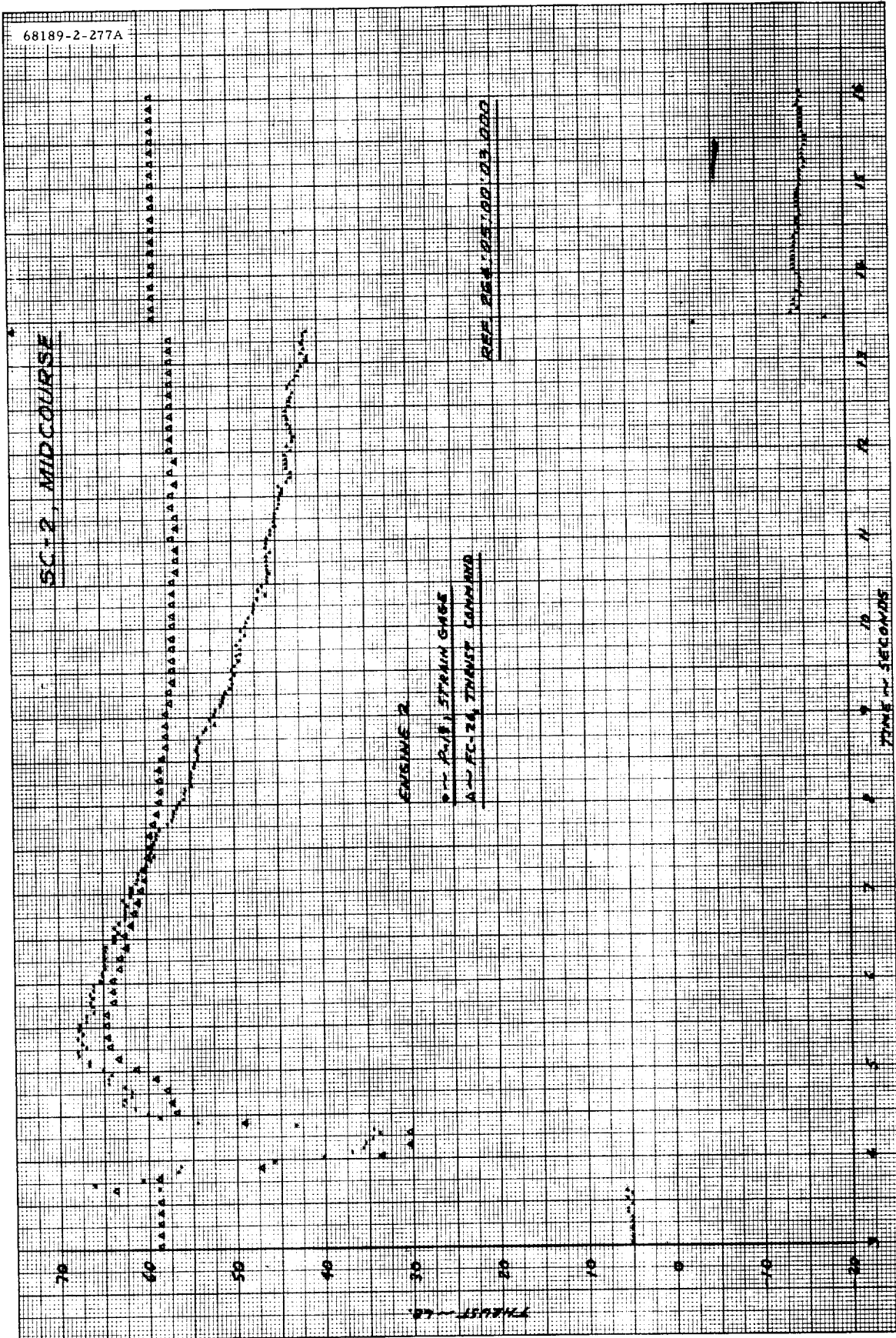
Buyn Number	1	2	3	9	15	21	27	33	34	40
CMD DURATION (SEC)	9.86	2.0	2.0	2.0	2.0	2.0	2.0	2.0	2.5	2.15
DS/F STATION	GOLDSTONE (11)	CAMBERA (42)	CAMBERA (42)	GOLDSTONE (11)	GOLDSTONE (11)	GOLDSTONE (11)	GOLDSTONE (11)	GOLDSTONE (11)	GOLDSTONE (11)	CAMBERA (42)
MODE/BIT RATE	1/4400	1/1100	1/1100	1/1100	1/1100	1/1100	1/1100	1/1100	6/1100	6/1100
RETRO ACCELEROMETER FC-52										
ACCEL. ERROR FC-15										
LEG 1 THRUST CMD FC-25										
LEG 2 THRUST CMD FC-26										
LEG 3 THRUST CMD FC-27										
LEG 1 STRAIN GAGE P-18										
LEG 2 STRAIN GAGE P-19										
LEG 3 STRAIN GAGE P-20										
ROLL ACTUATOR POSITION FC-43										
GAS JETS ON/INHIBIT	ON	INHIBIT	INHIBIT	INHIBIT	INHIBIT	INHIBIT	INHIBIT	INHIBIT	INHIBIT	INHIBIT

Figure 5.5-22. Summary of Firing Attempts



a) Engine 1

Figure 5.5-23. Comparison of Thrust Command and Strain Gage Data, Midcourse



b) Engine 2

Figure 5.5-23 (continued). Comparison of Thrust Command and Strain Gage Data, Midcourse

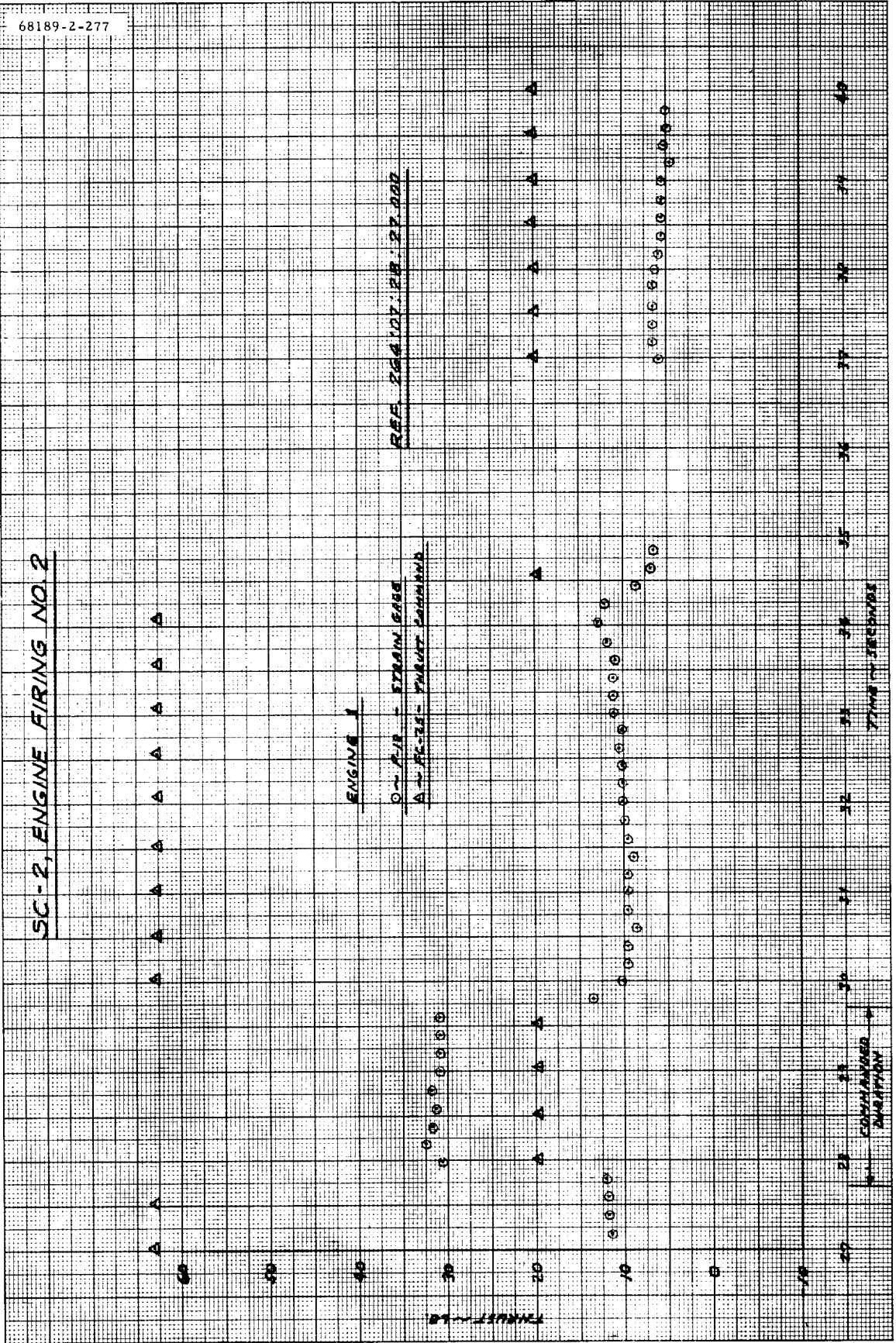




c) Engine 3

Figure 5. 5-23 (continued). Comparison of Thrust Command and Strain Gage Data, Midcourse

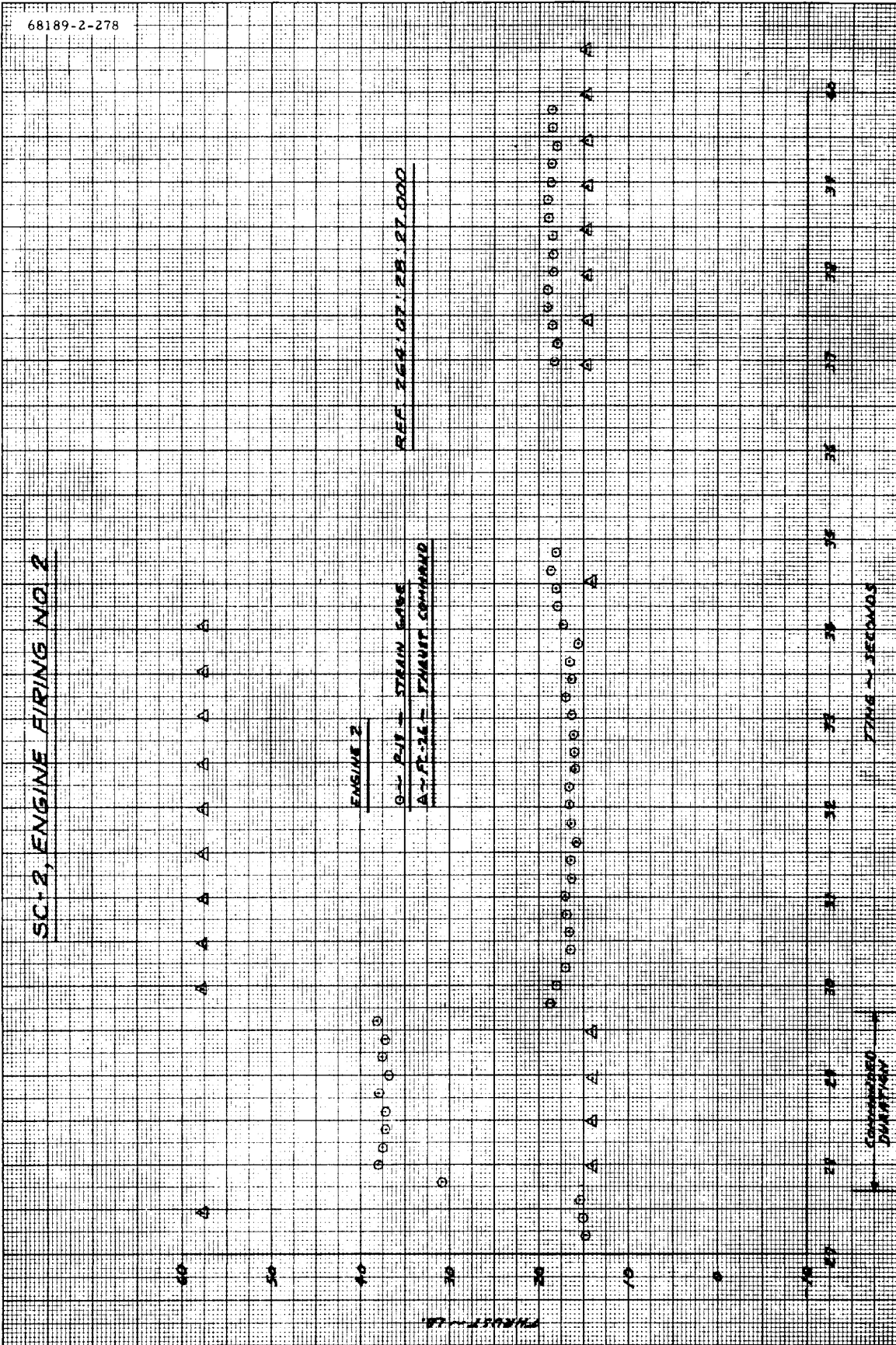
SC-2, ENGINE FIRING NO. 2



a) Engine 1

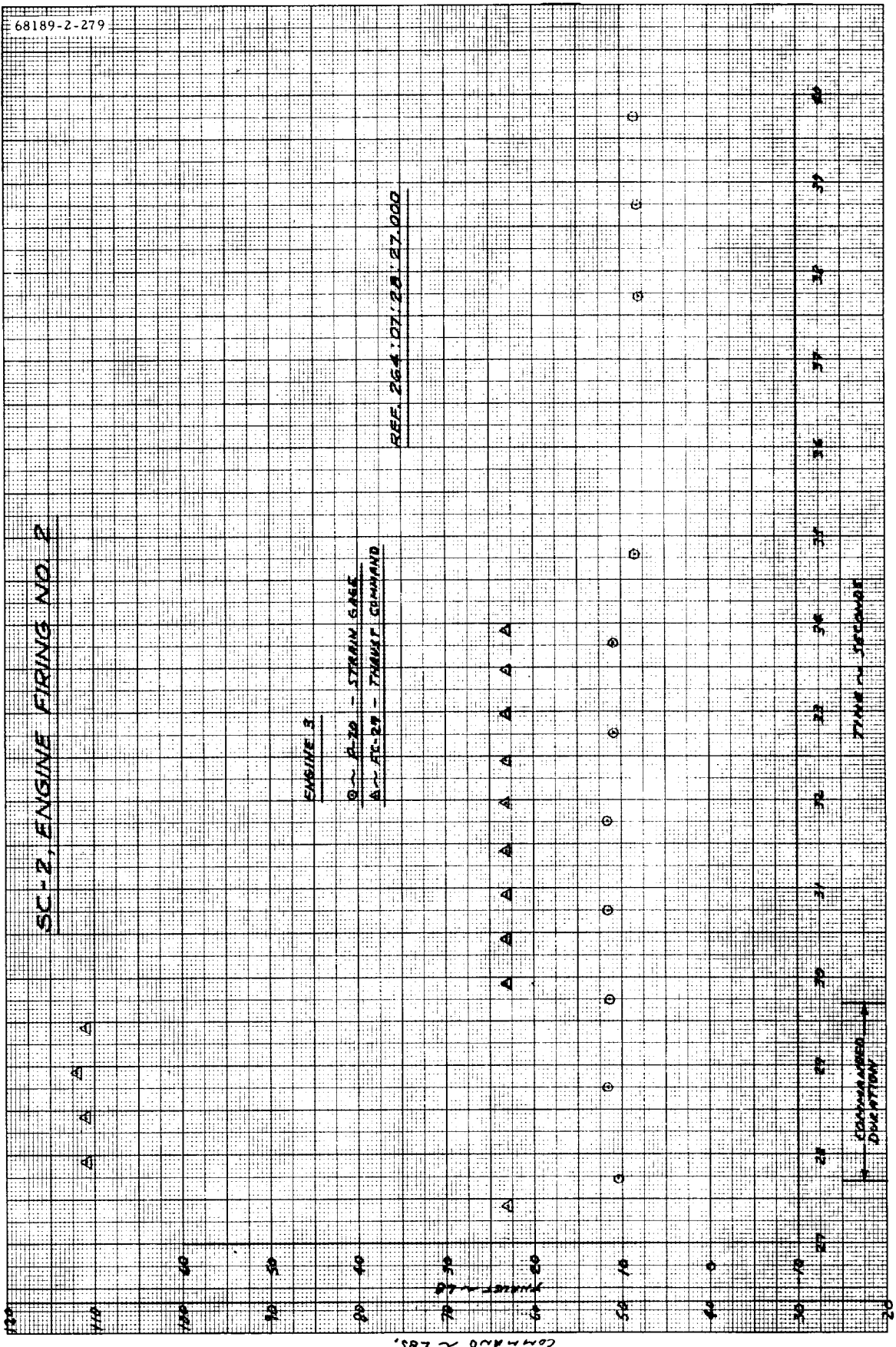
Figure 5.5-24. Comparison of Thrust Command and Strain Gage Data, Burn 2

SC-2, ENGINE FIRING NO. 2



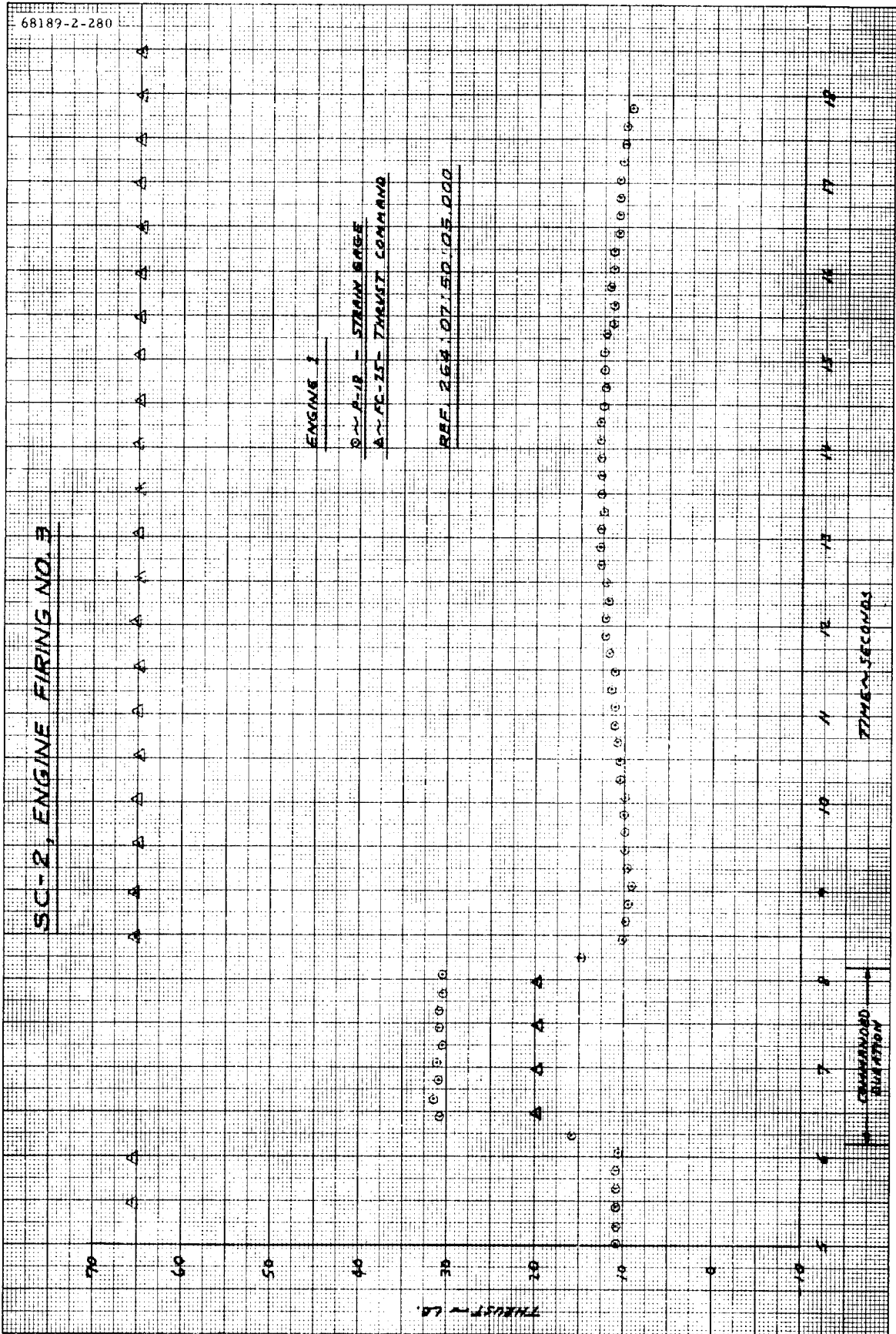
b) Engine 2

Figure 5.5-24 (continued). Comparison of Thrust Command and Strain Gage Data, Burn 2



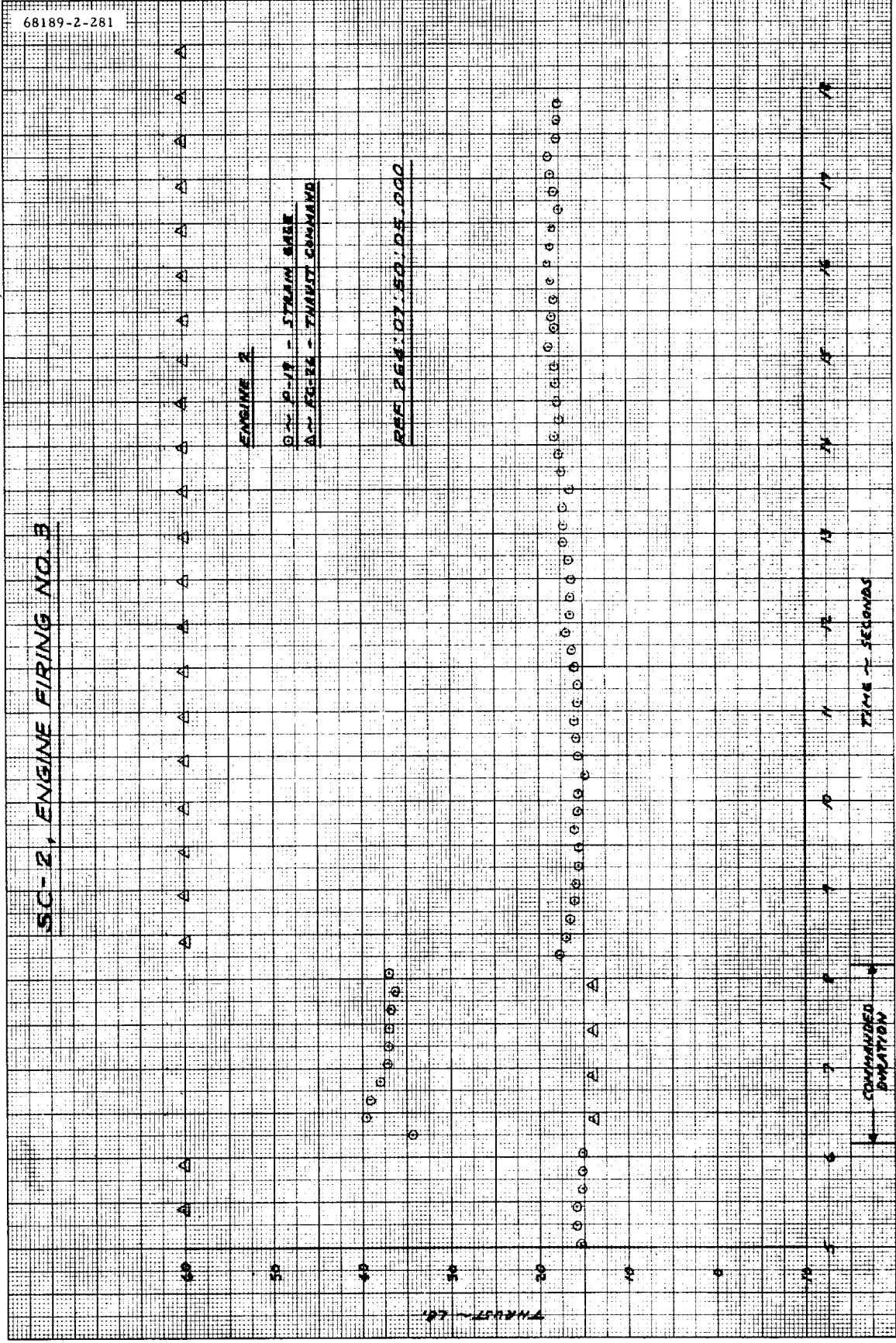
c) Engine 3

Figure 5.5-24 (continued). Comparison of Thrust Command and Strain Gage Data, Burn 2



a) Engine 1

Figure 5.5-25. Comparison of Thrust Command and Strain Gage Data, Burn 3



b) Engine 2

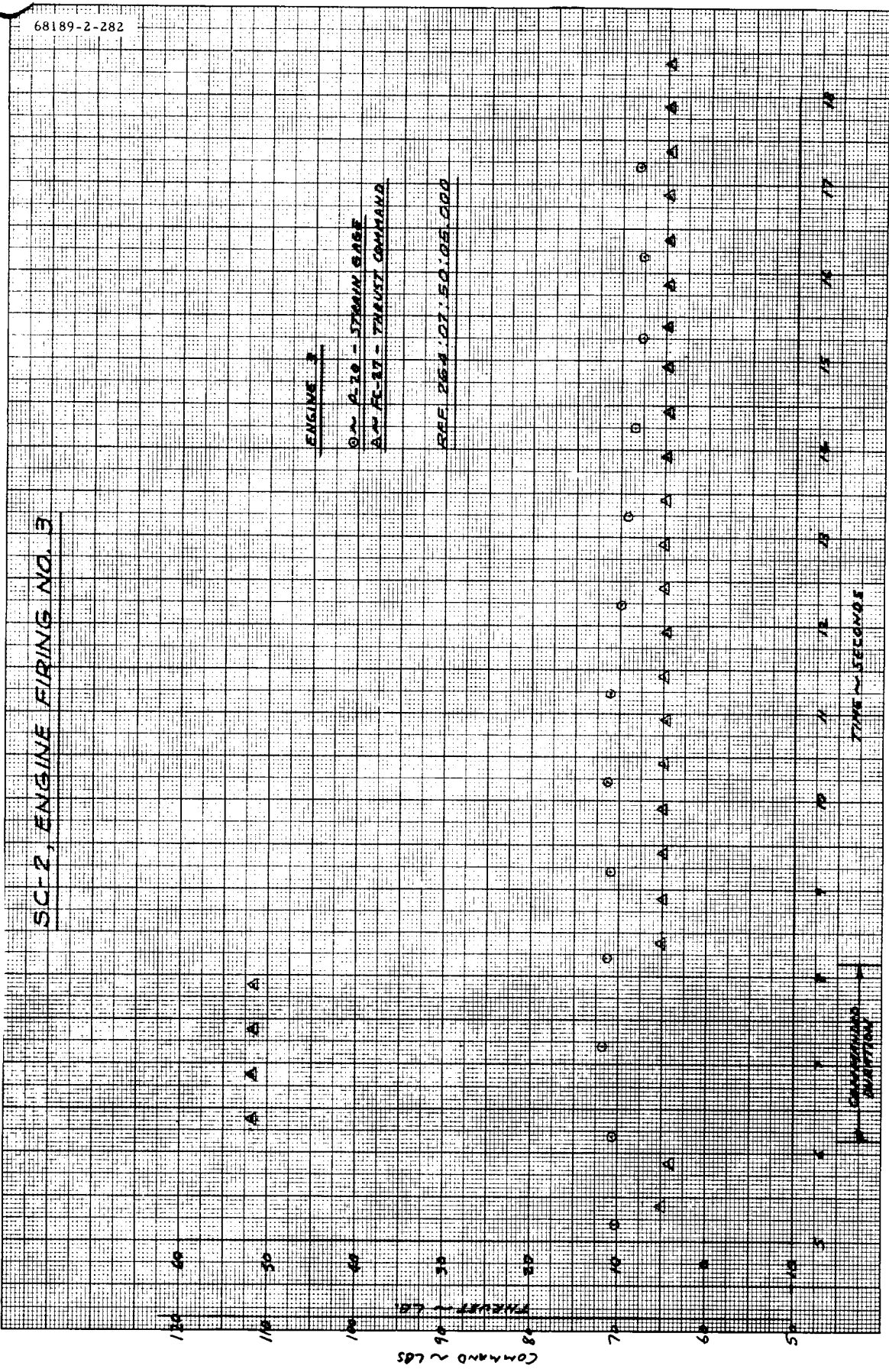
Figure 5.5-25 (continued). Comparison of Thrust Command and Strain Gage Data, Burn 3

SC-2, ENGINE FIRING NO. 3

ENGINE 3

0.~ 0.20 - STRAIN GAGE  
0.~ 0.27 - THRUST COMMAND

REF 264.07.50.06.000



c) Engine 3

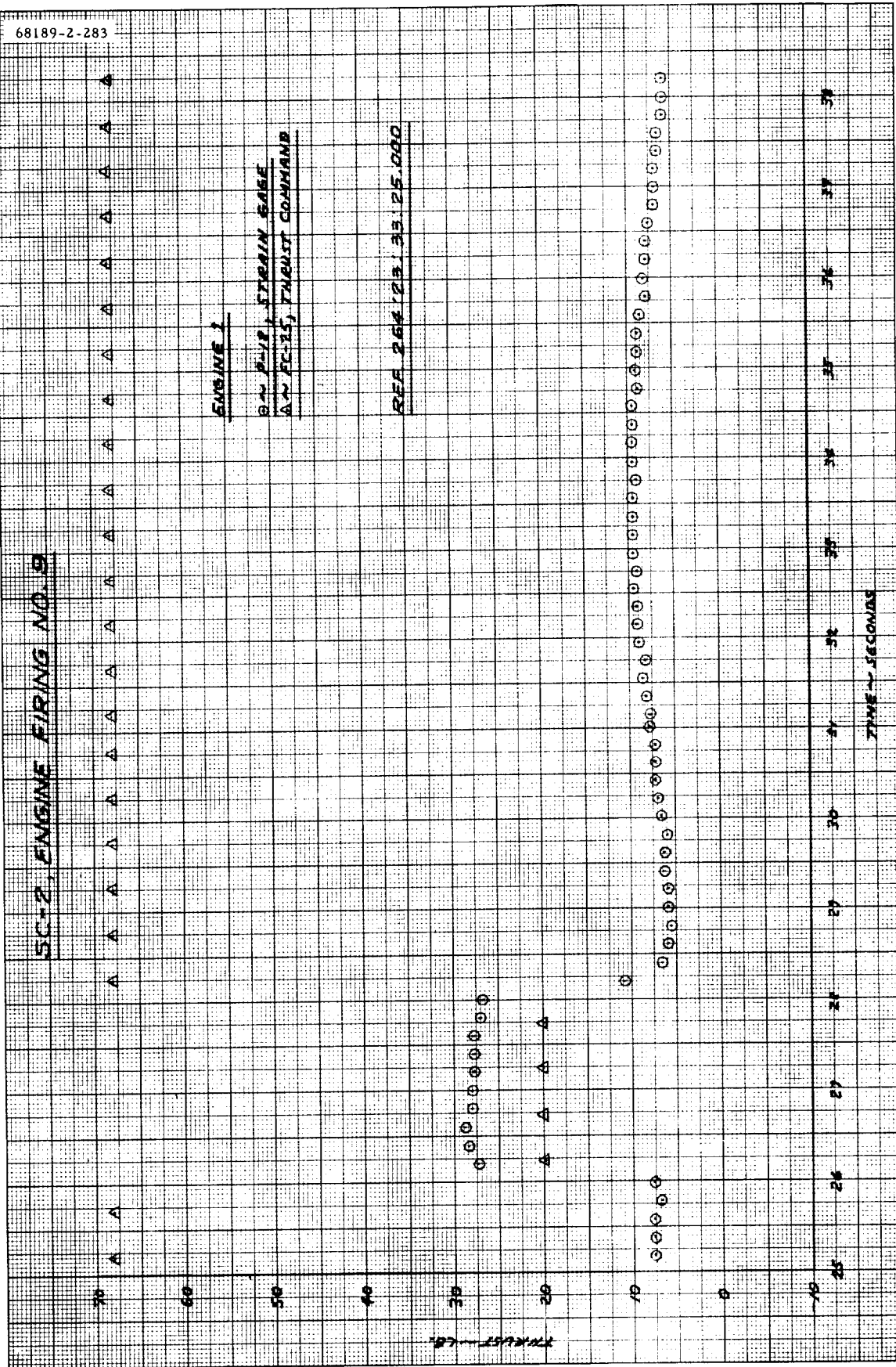
Figure 5.5-25 (continued). Comparison of Thrust Command and Strain Gage Data, Burn 3

5C-2, ENGINE FIRING NO. 9

ENGINE 1

○ ~ FIVE, STRAIN GAGE  
△ ~ FC-25, THRUST COMMAND

REF 264 231 33 25.000

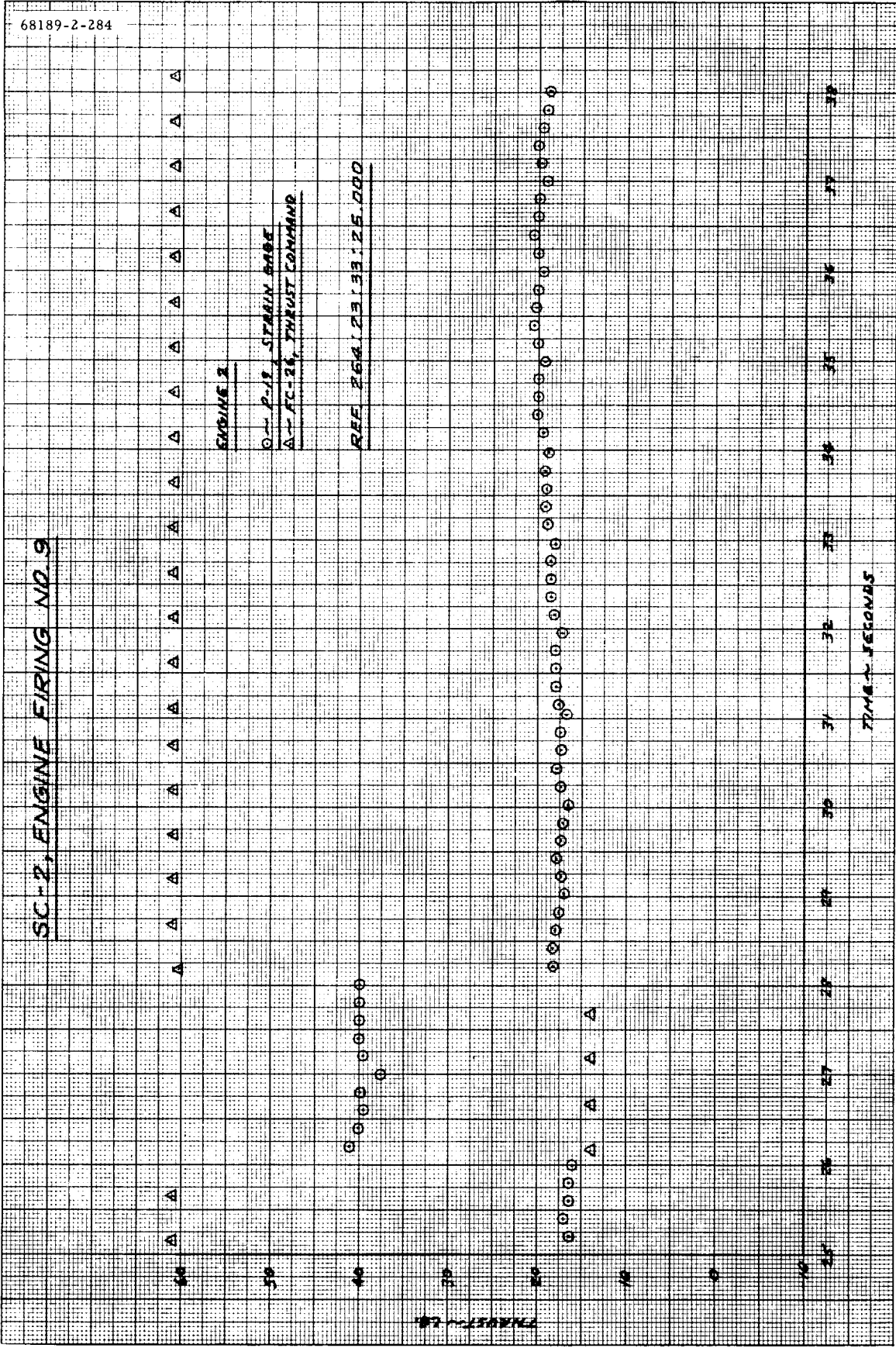


a) Engine 1

Figure 5.5-26. Comparison of Thrust Command and Strain Gage Data, Burn 9



SC-2, ENGINE FIRING NO. 9



b) Engine 2

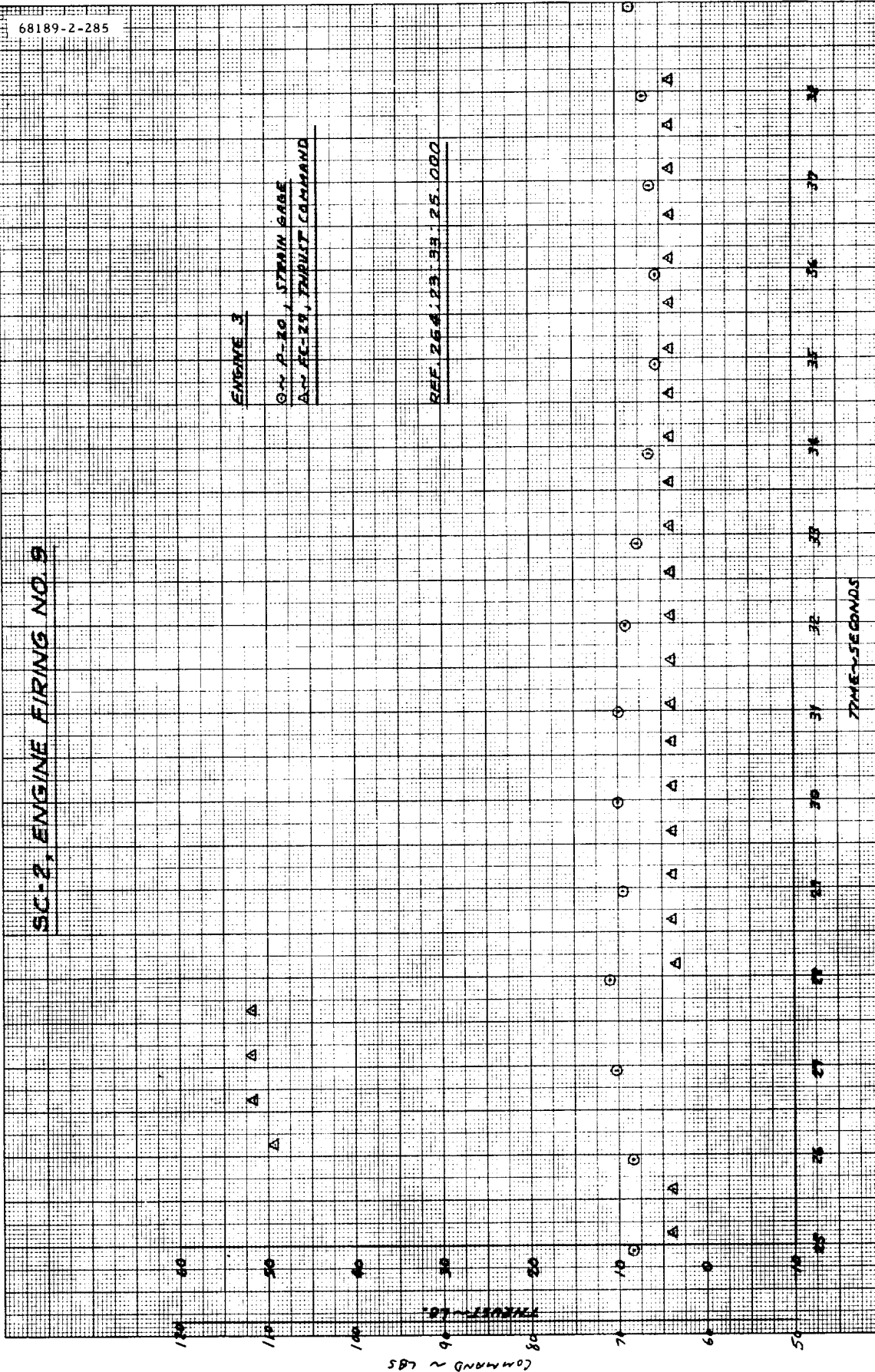
Figure 5.5-26 (continued). Comparison of Thrust Command and Strain Gage Data, Burn 9

SC-2, ENGINE FIRING NO. 9

ENGINE 3

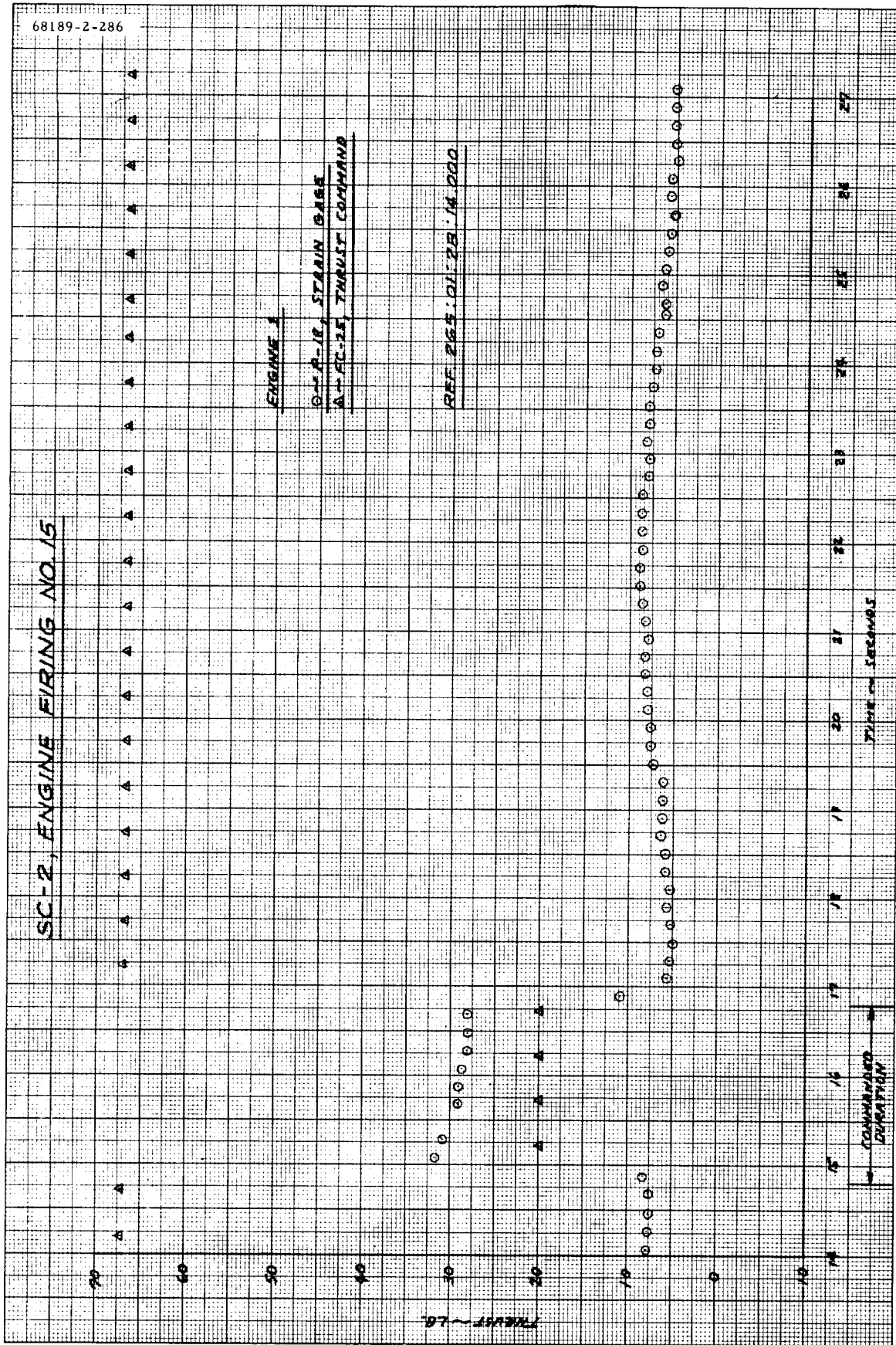
0-4 P-20, STRAIN GAGE  
AS FC-29, THRUST COMMAND

REF. 254, 23, 33, 25, 000



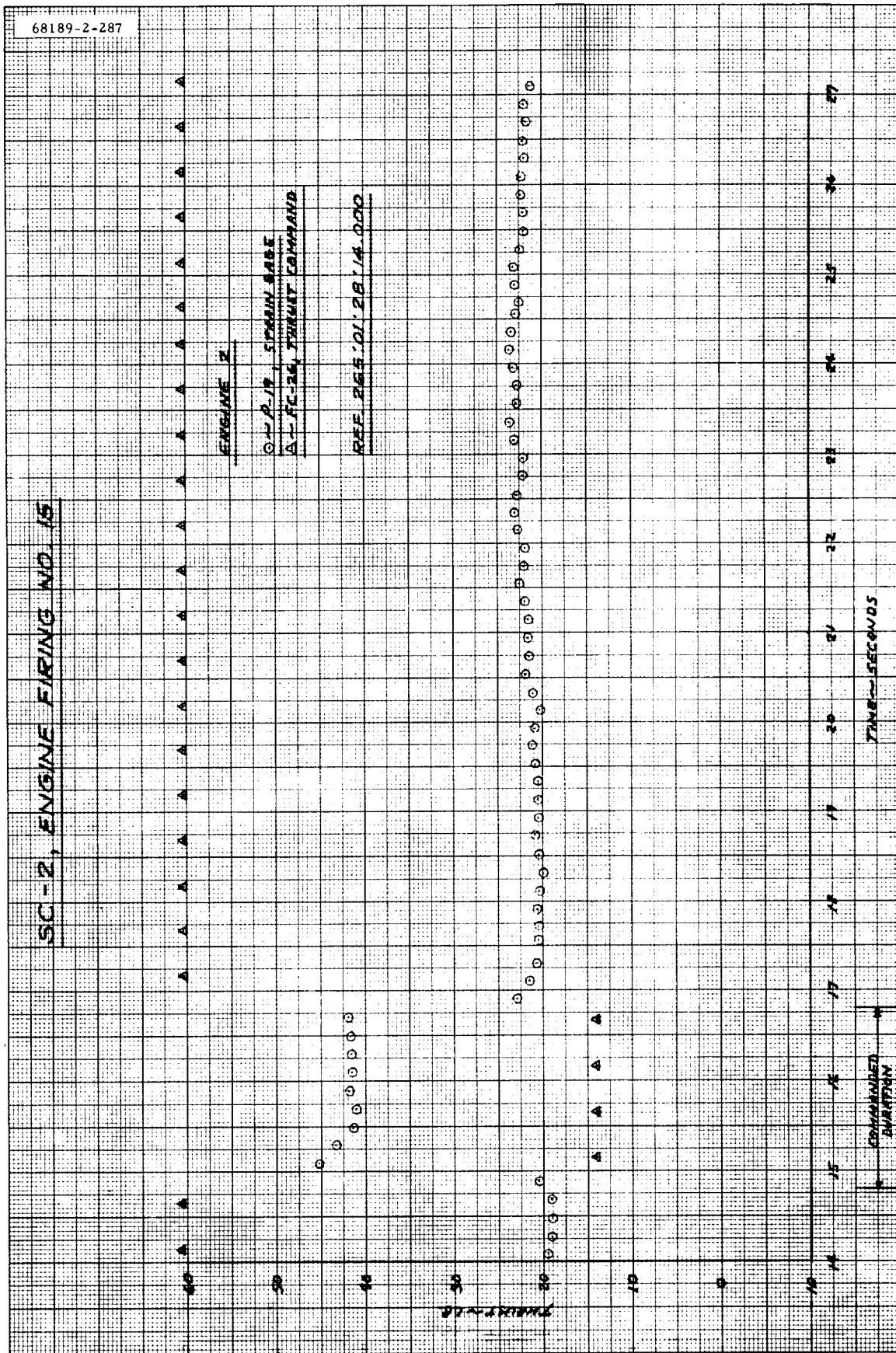
c) Engine 3

Figure 5.5-26 (continued). Comparison of Thrust Command and Strain Gage Data, Burn 9



a) Engine 1

Figure 5.5-27. Comparison of Thrust Command and Strain Gage Data, Burn 15



b) Engine 2

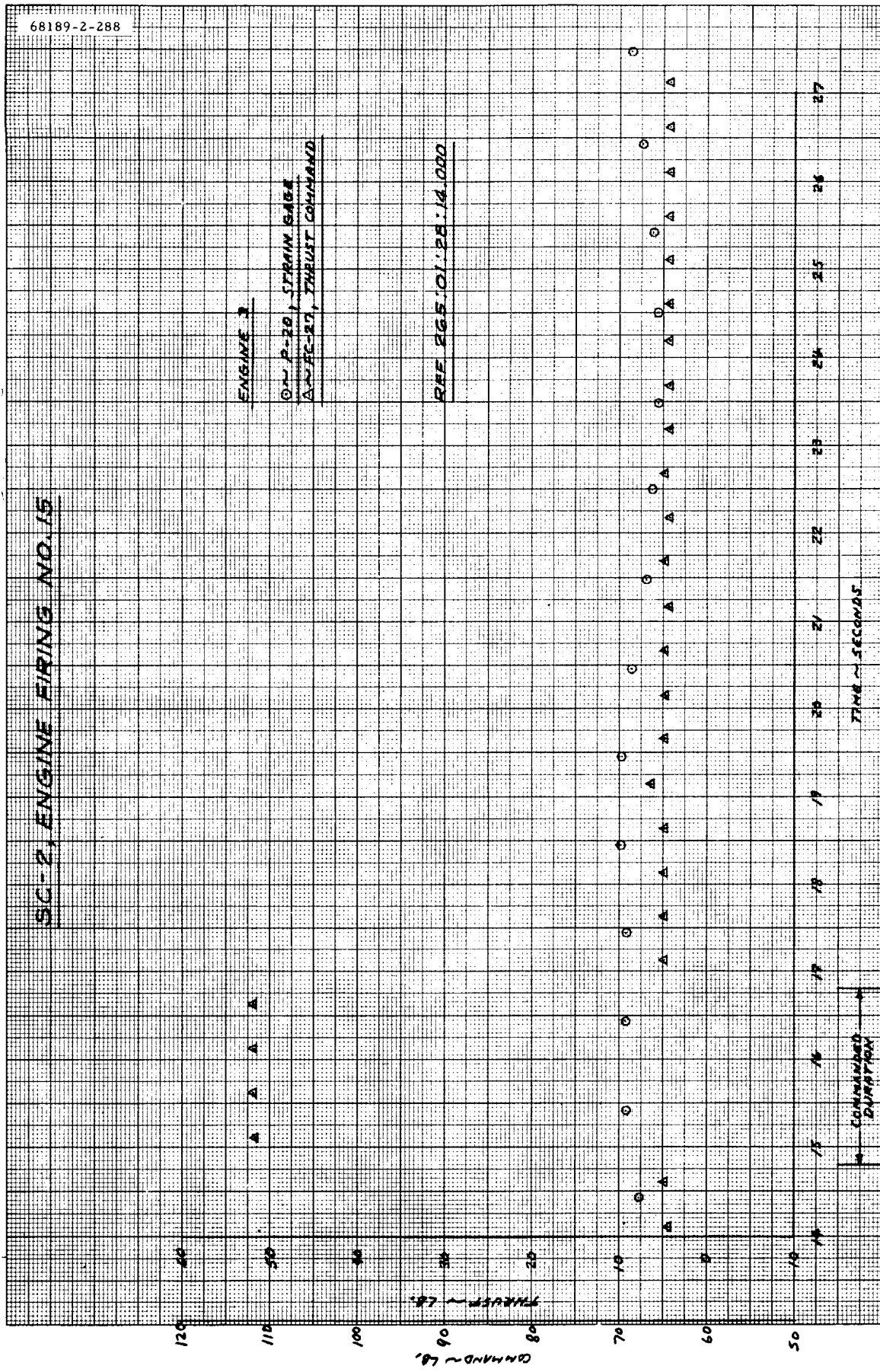
Figure 5.5-27 (continued). Comparison of Thrust Command and Strain Gage Data, Burn 15

SC-2, ENGINE FIRING NO. 15

ENGINE 3

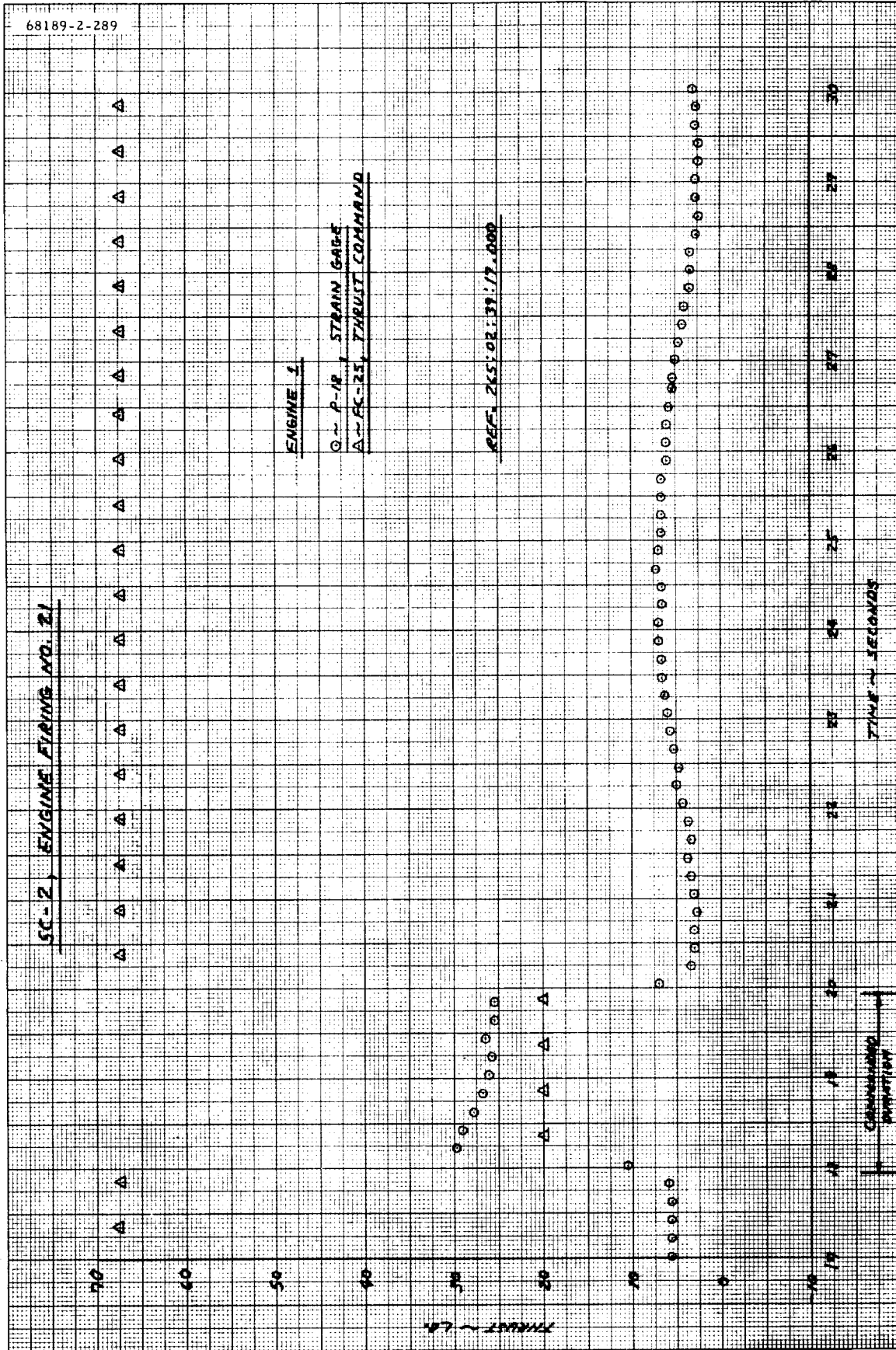
○ ~ P-20, STRAIN GAGE  
△ ~ FC-27, THRUST COMMAND

REF EG 5.01:28:14.000



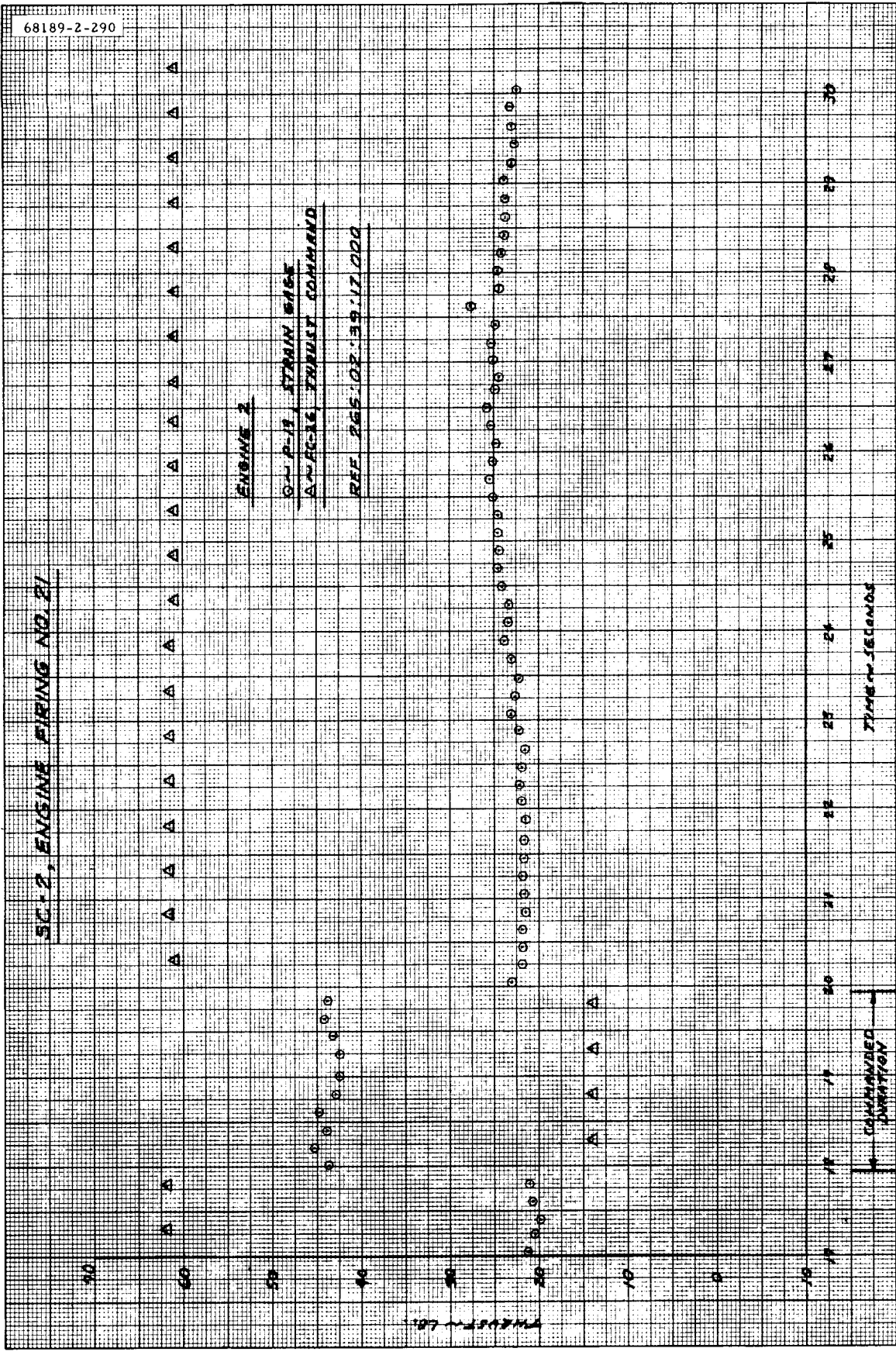
c) Engine 3

Figure 5. 5-27 (continued). Comparison of Thrust Command and Strain Gage Data, Burn 15



a) Engine 1

Figure 5. 5-28. Comparison of Thrust Command and Strain Gage Data, Burn 21



b) Engine 2

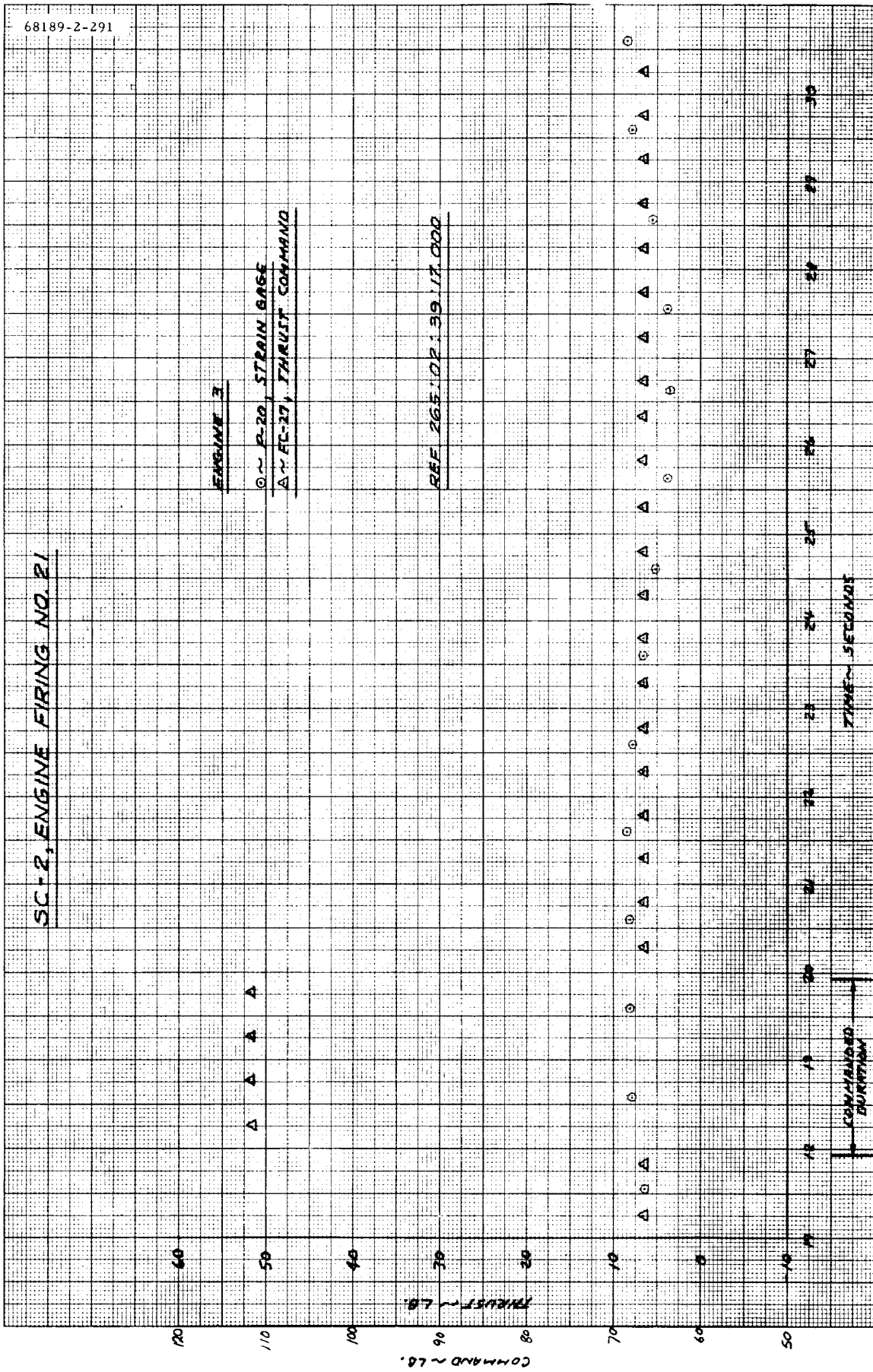
Figure 5.5-28 (continued). Comparison of Thrust Command and Strain Gage Data, Burn 21

SC-2, ENGINE FIRING NO. 21

ENGINE 3

○ ~ P-20, STRAIN GAGE  
△ ~ FE-27, THRUST COMMAND

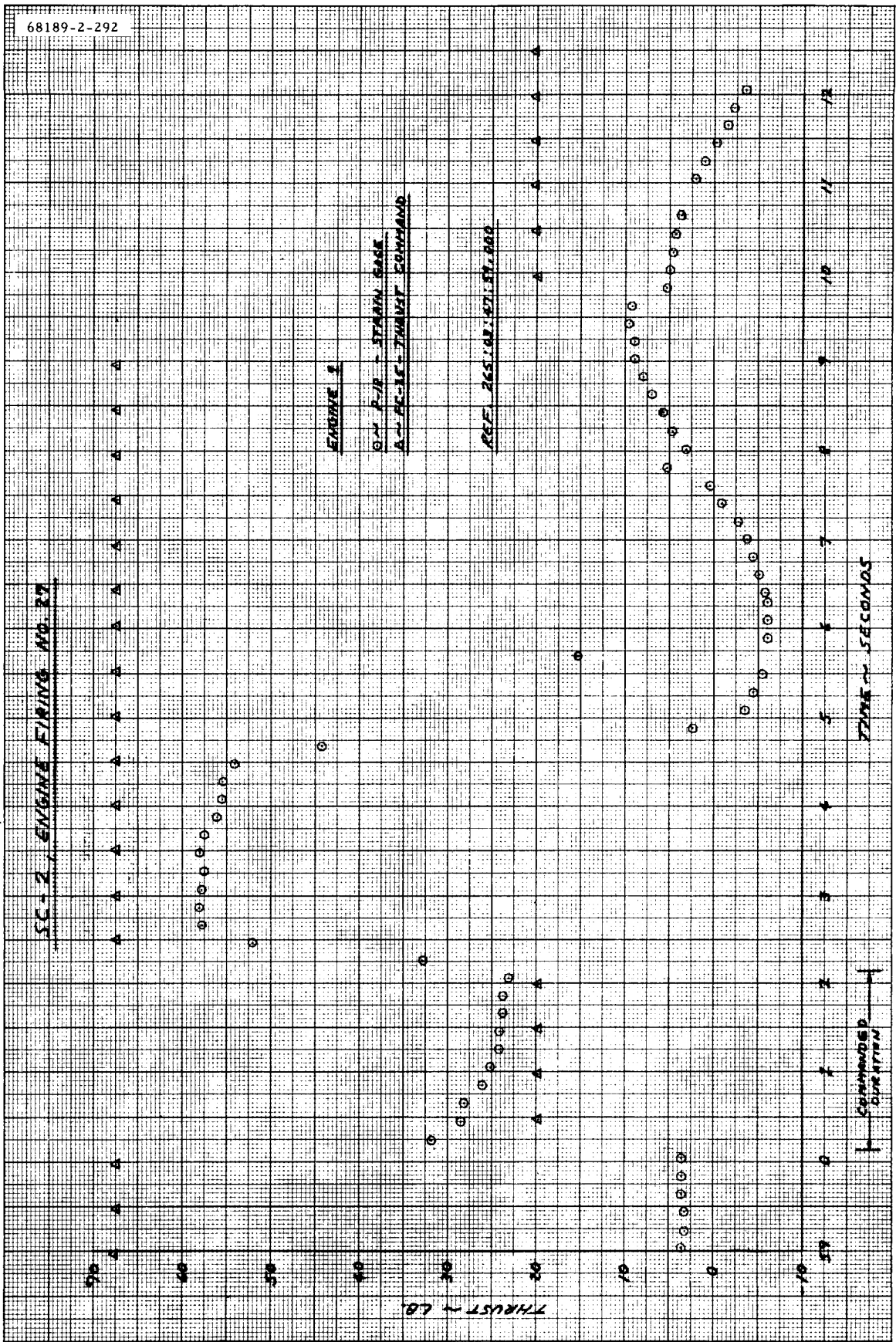
REF 265.000 ± 39.17.000



c) Engine 3

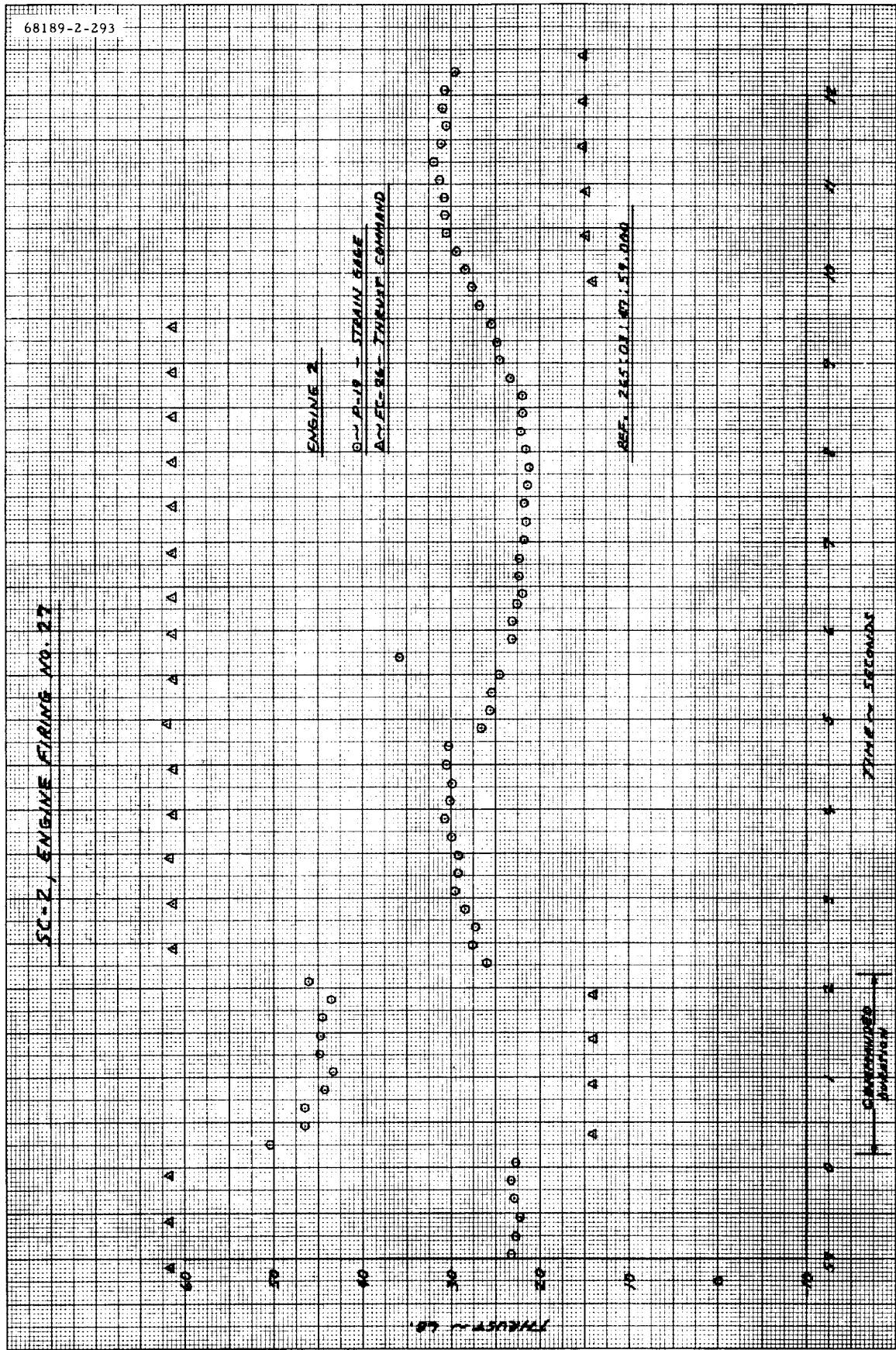
Figure 5. 5-28 (continued). Comparison of Thrust Command and Strain Gage Data, Burn 21





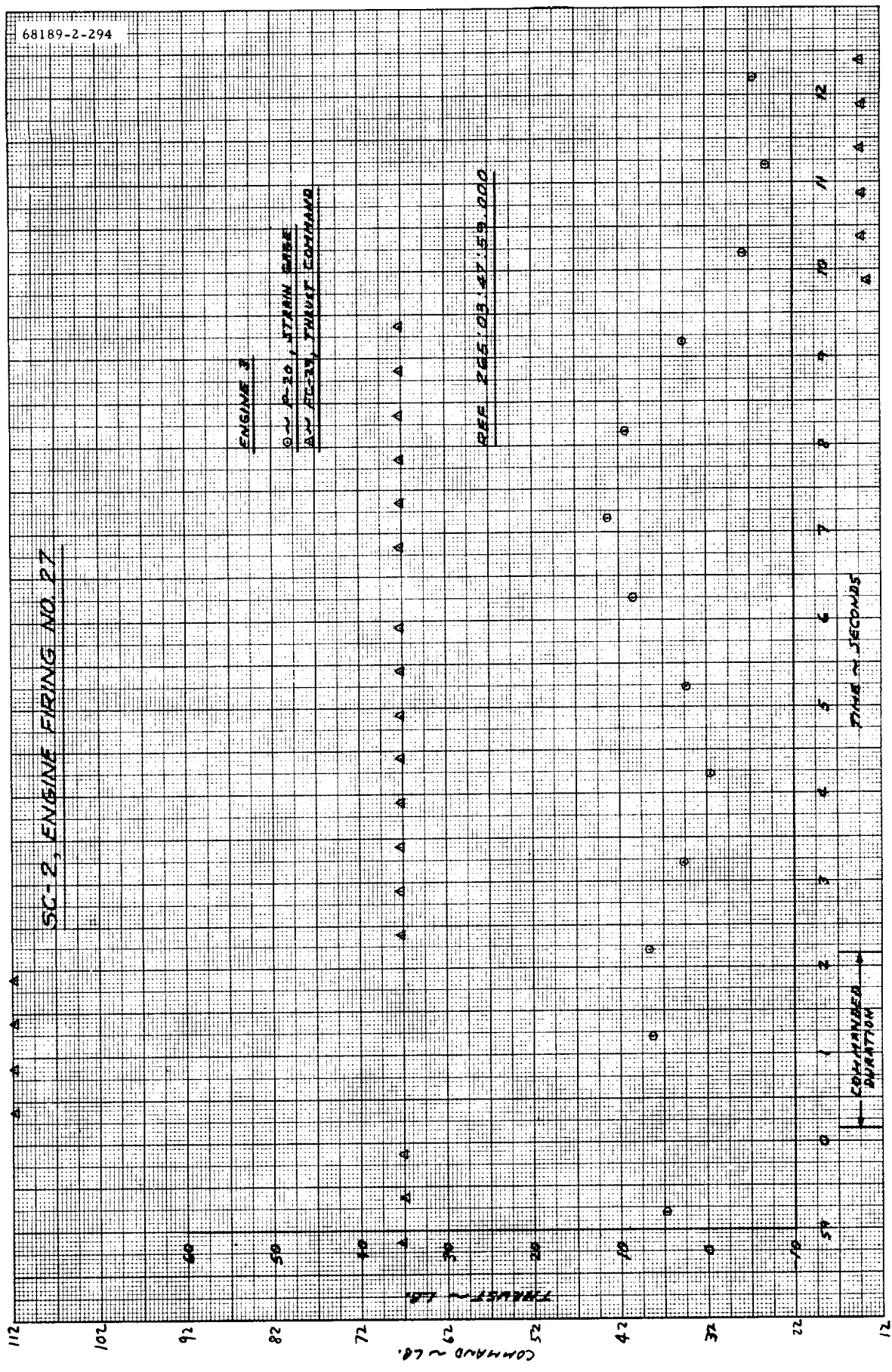
a) Engine 1

Figure 5.5-29 . Comparison of Thrust Command and Strain Gage Data, Burn 27



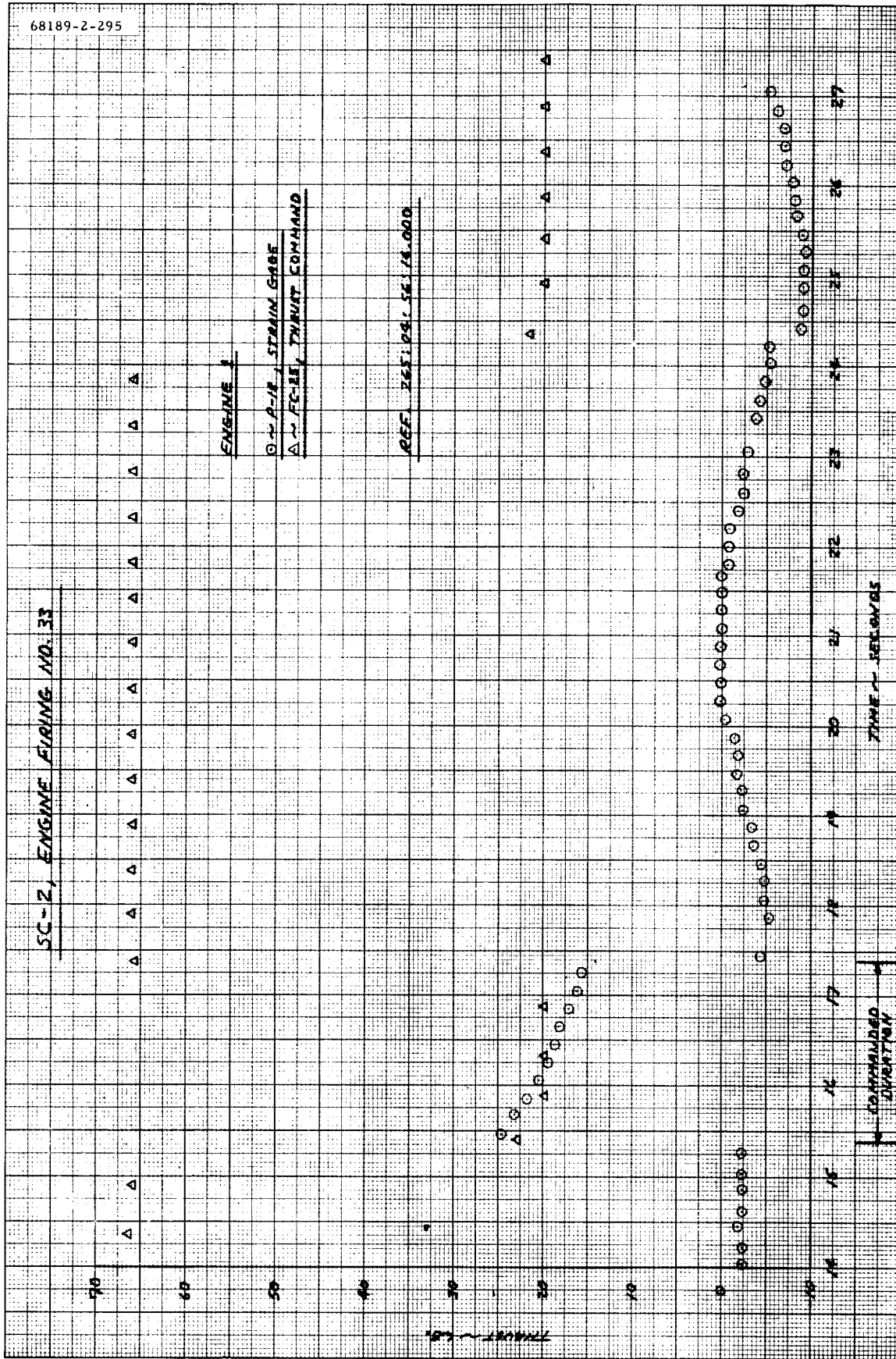
b) Engine 2

Figure 5.5-29 (continued). Comparison of Thrust Command and Strain Gage Data, Burn 27



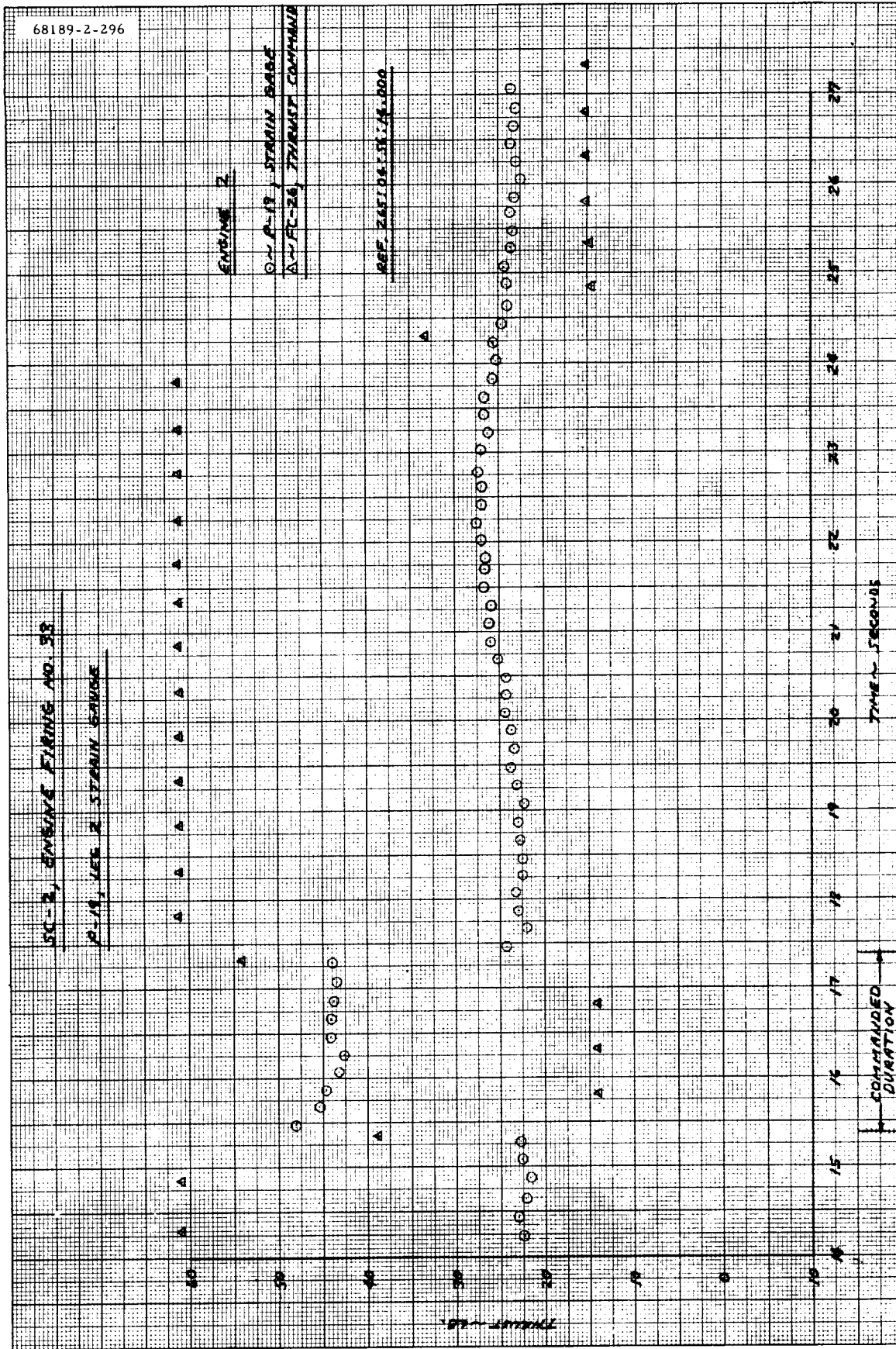
c) Engine 3

Figure 5.5-29 (continued). Comparison of Thrust Command and Strain Gage Data, Burn 27



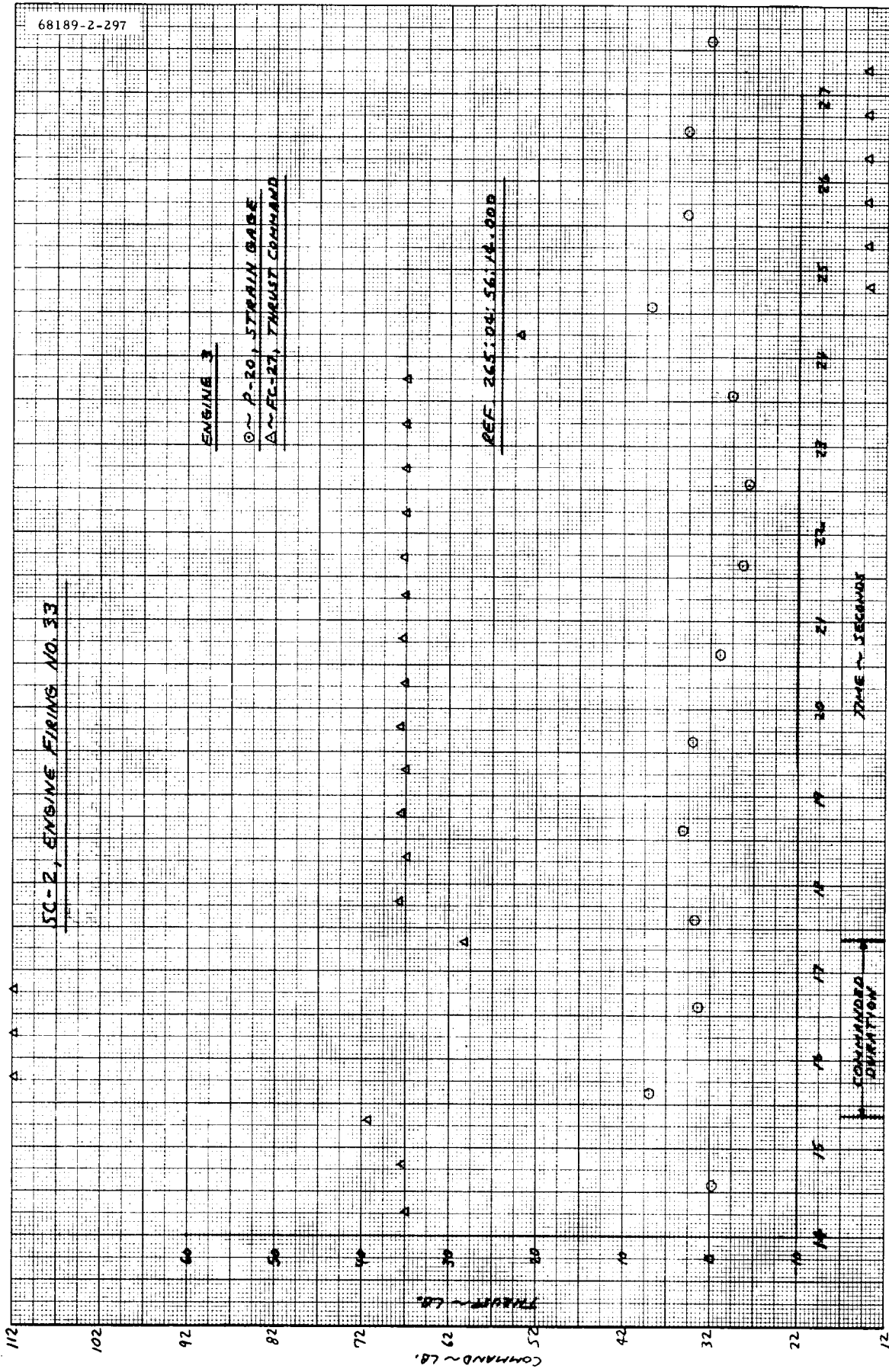
a) Engine 1

Figure 5.5-30. Comparison of Thrust Command and Strain Gage Data, Burn 33



b) Engine 2

Figure 5.5-30 (continued). Comparison of Thrust Command and Strain Gage Data, Burn 33



c) Engine 3

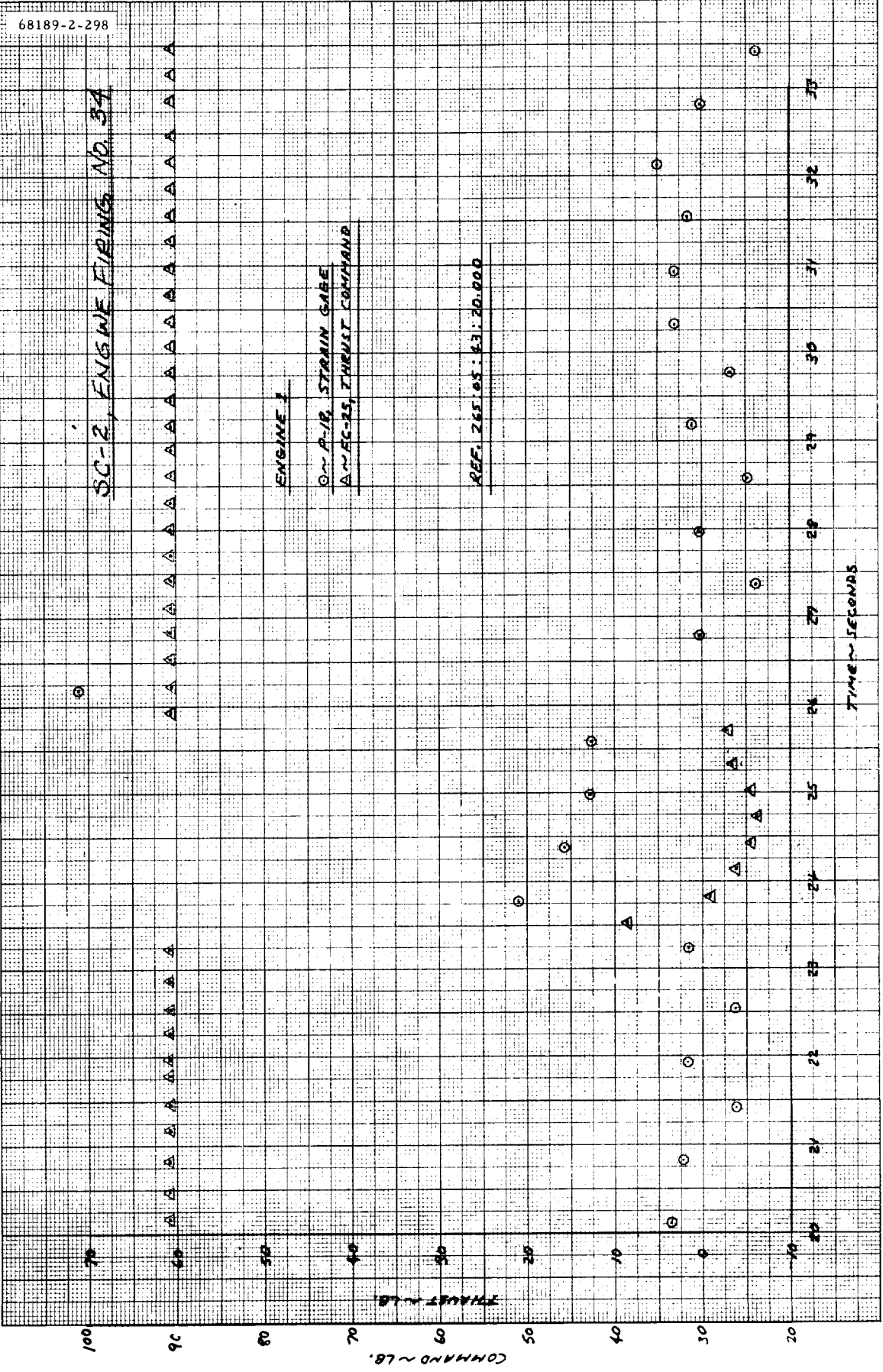
Figure 5.5-30 (continued). Comparison of Thrust Command and Strain Gage Data, Burn 33

SC-2, ENGINE FIRING NO. 34

ENGINE 1

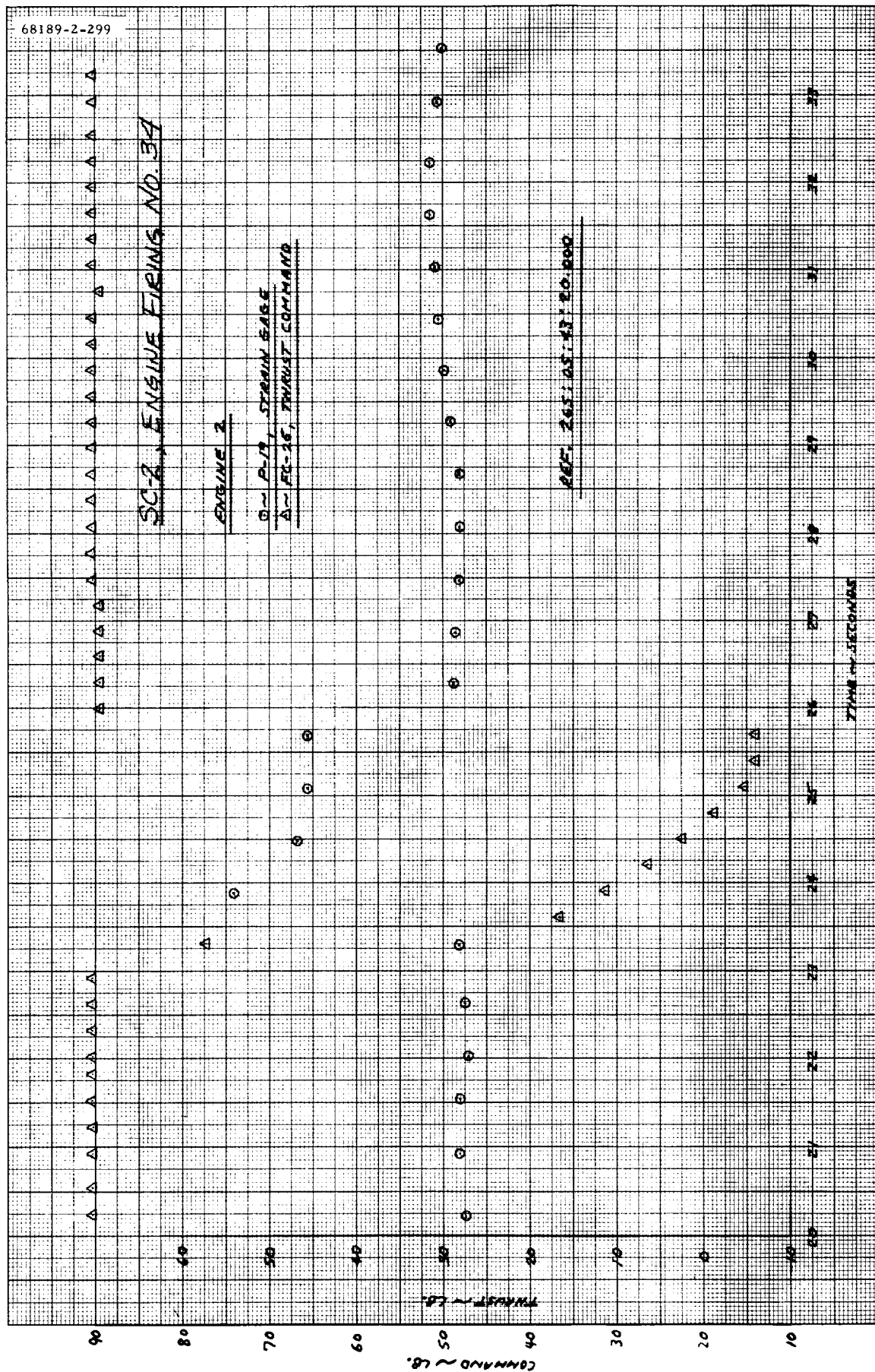
O ~ P-18, STRAIN GAGE  
A ~ EC-85, THRUST FORWARD

REF. ZEE 05: 43: 20.000



a) Engine 1

Figure 5.5-31. Comparison of Thrust Command and Strain Gage Data, Burn 34



b) Engine 2

Figure 5.5-31 (continued). Comparison of Thrust Command and Strain Gage Data, Burn 34

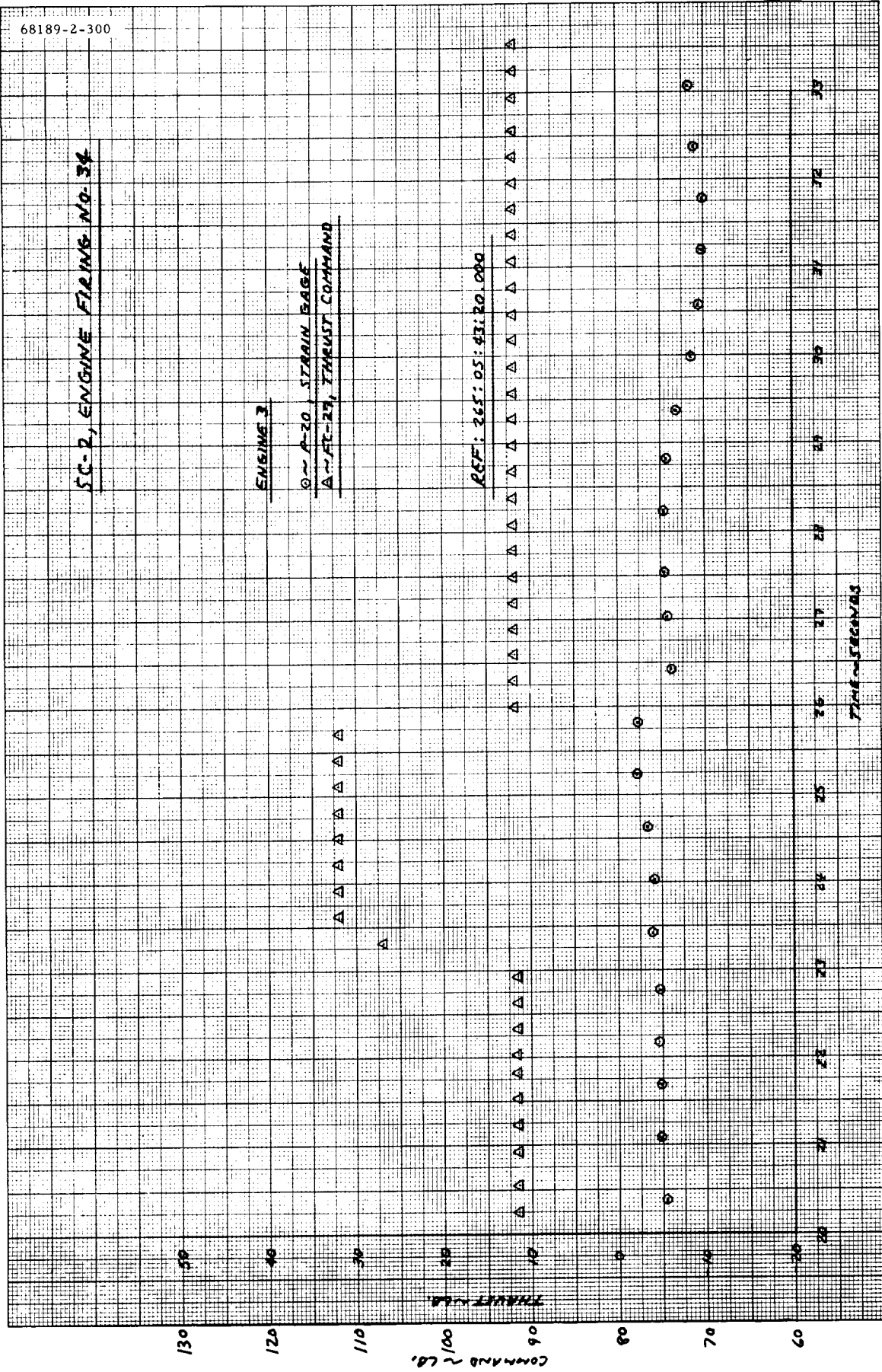


SC-2, ENGINE FIRING NO. 34

ENGINE 3

0-20, STRAIN GAGE  
A-21, THRUST COMMAND

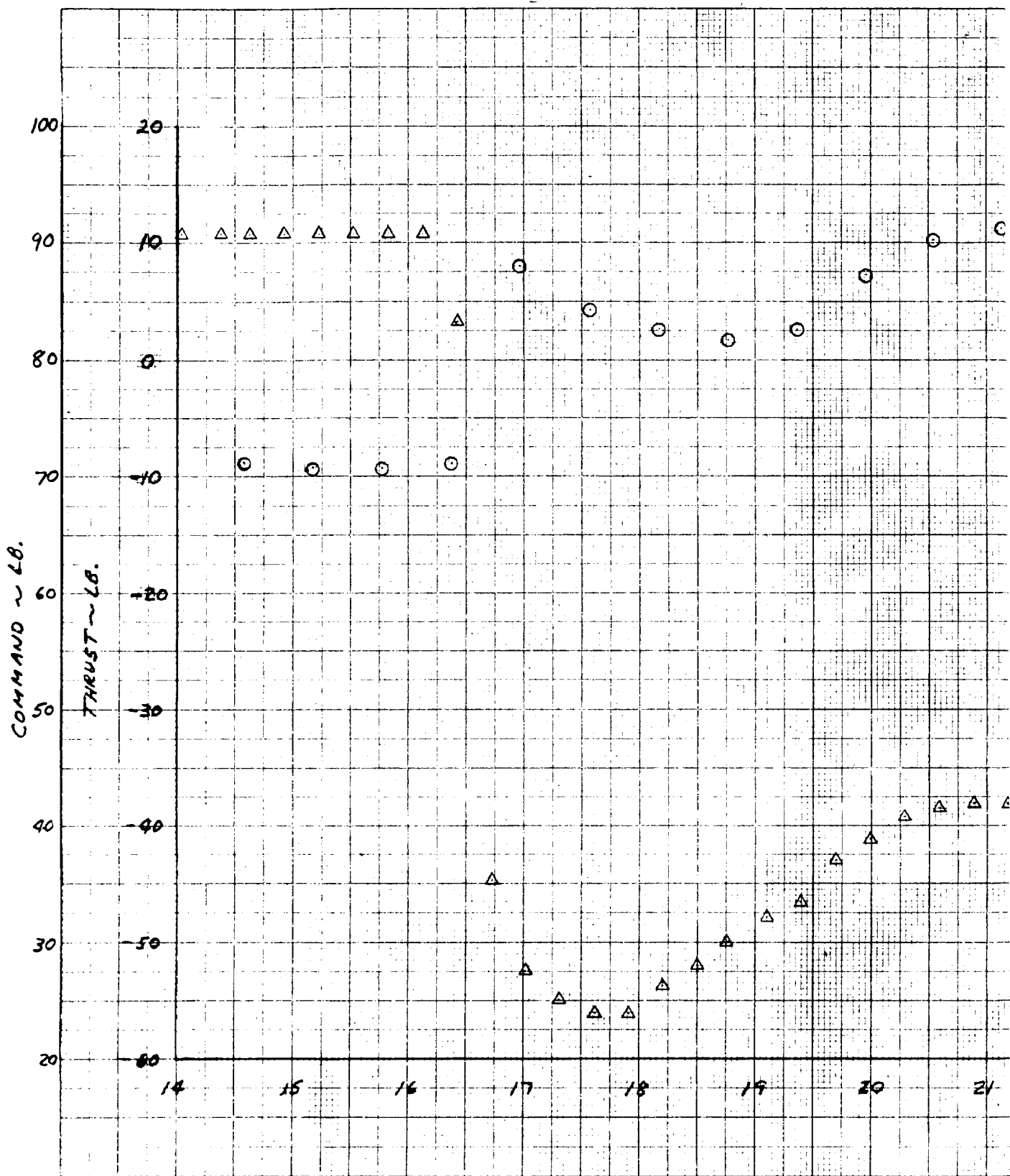
REF: 265: 05: 43: 20.000



c) Engine 3

Figure 5.5-31 (continued). Comparison of Thrust Command and Strain Gage Data, Burn 34





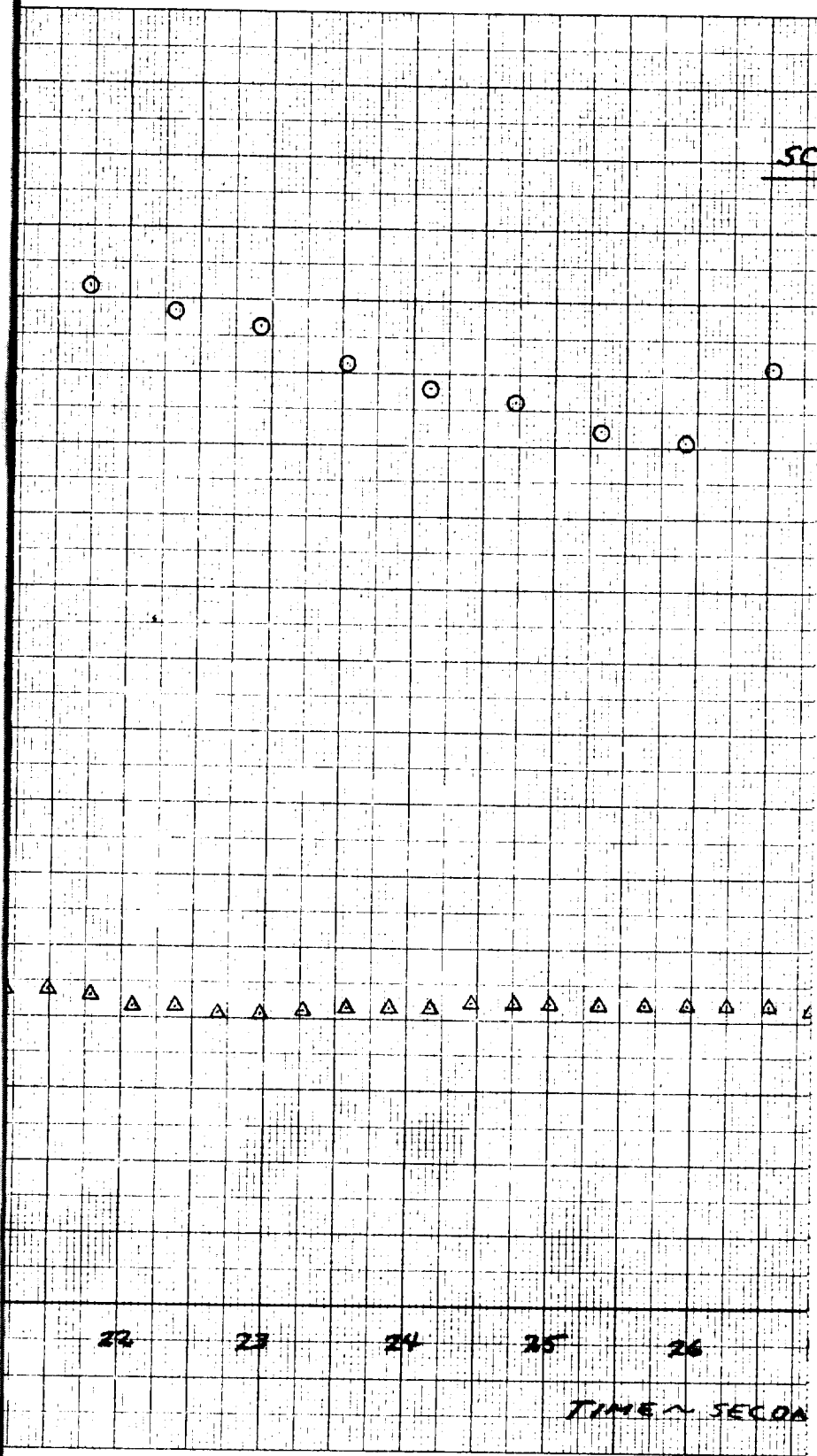
a) Engine 1

Figure 5.5-32. Comparison of Thrust Command and Strain Gage Data, Burn 40

5.5-109A

FOLDOUT FRAME /

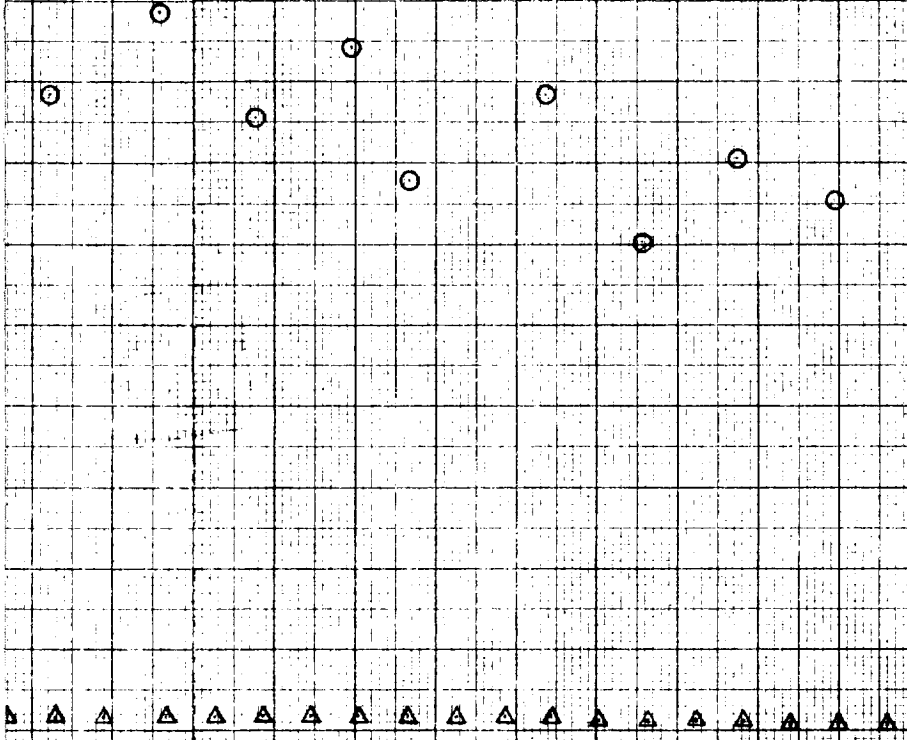




FOLDOUT FRAME 2



-2, ENGINE FIRING NO. 40



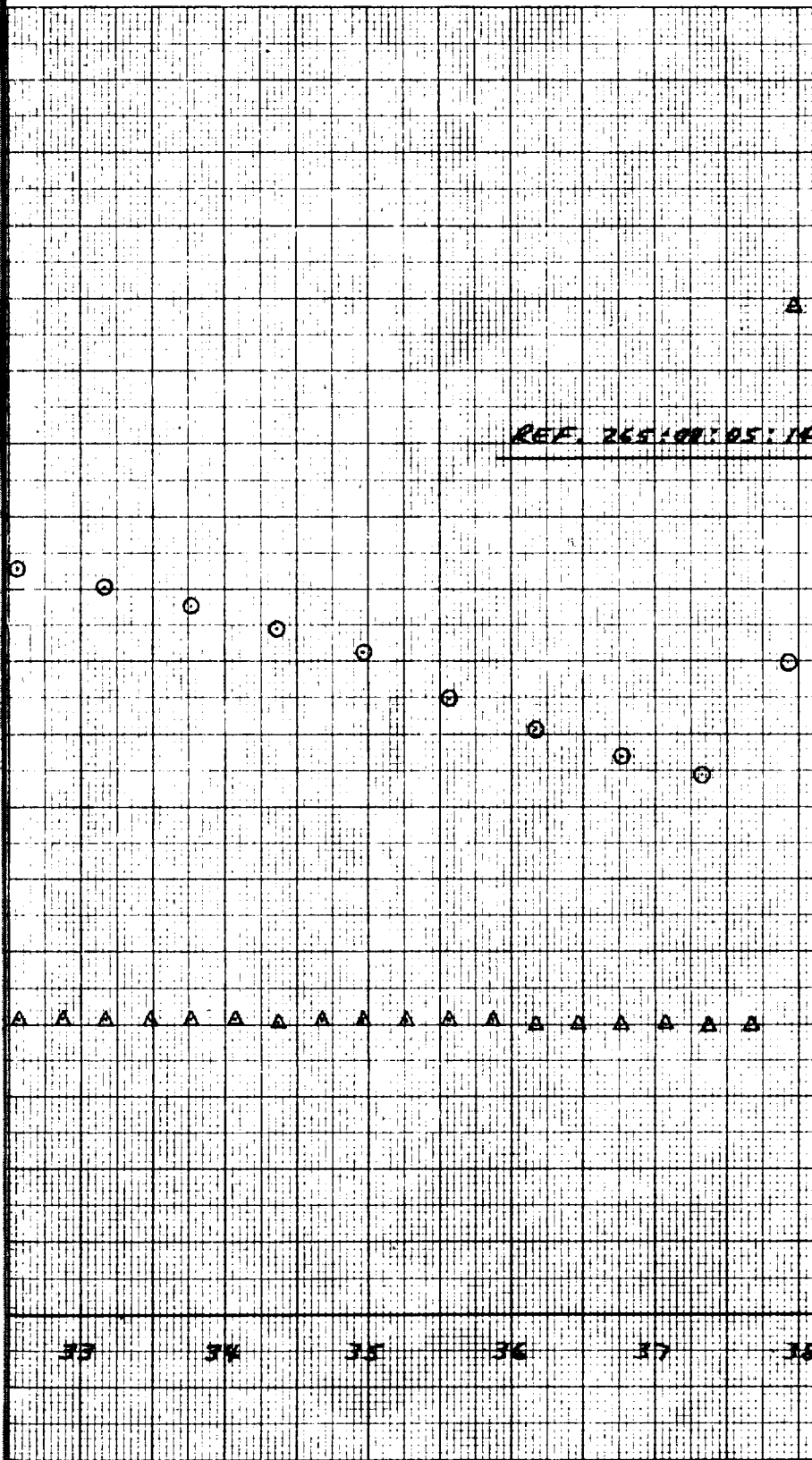
27 28 29 30 31 32  
105

FOLDOUT FRAME 3

.5-109 B







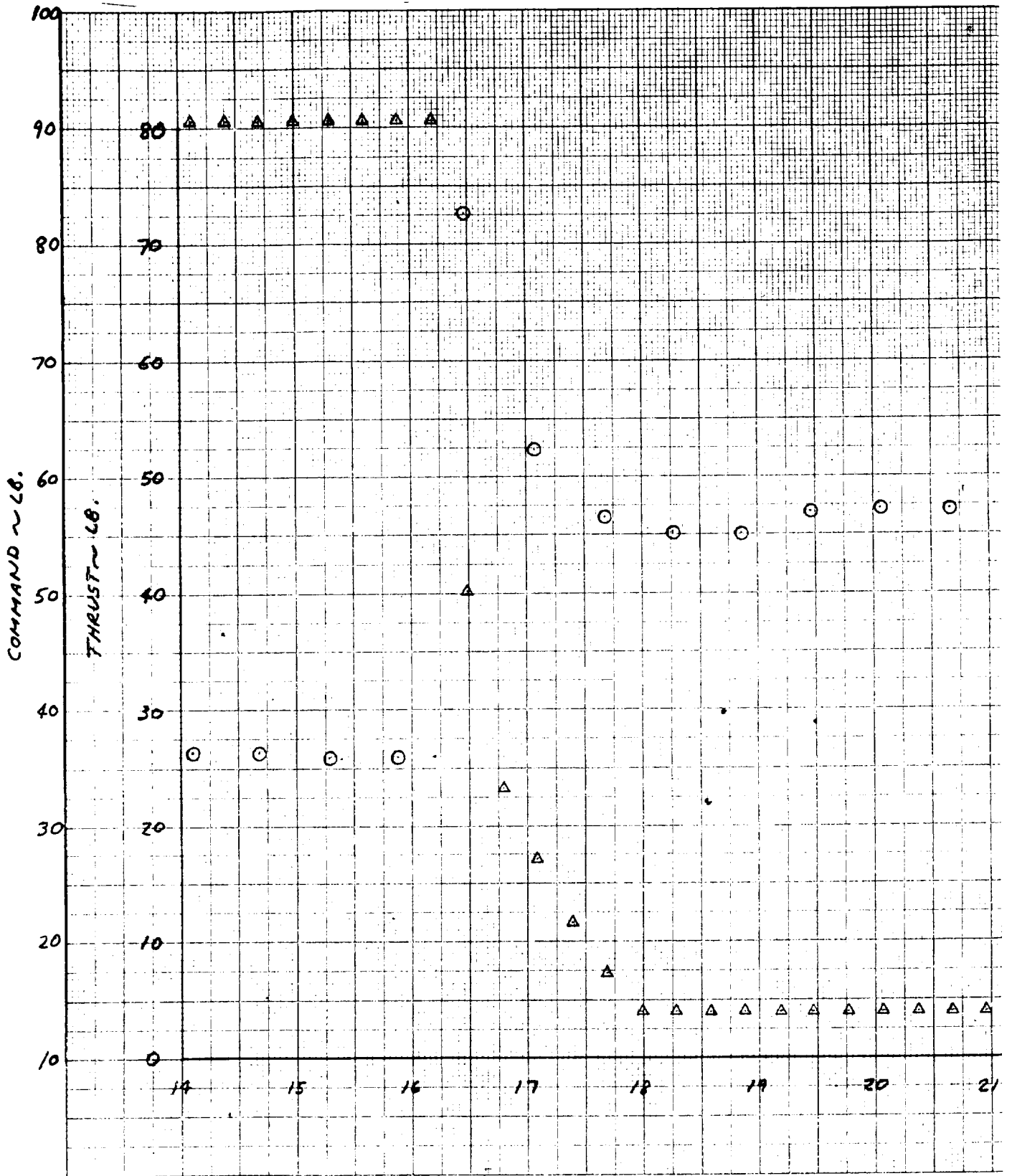
FOLDOUT FRAME 4

5.5-109C









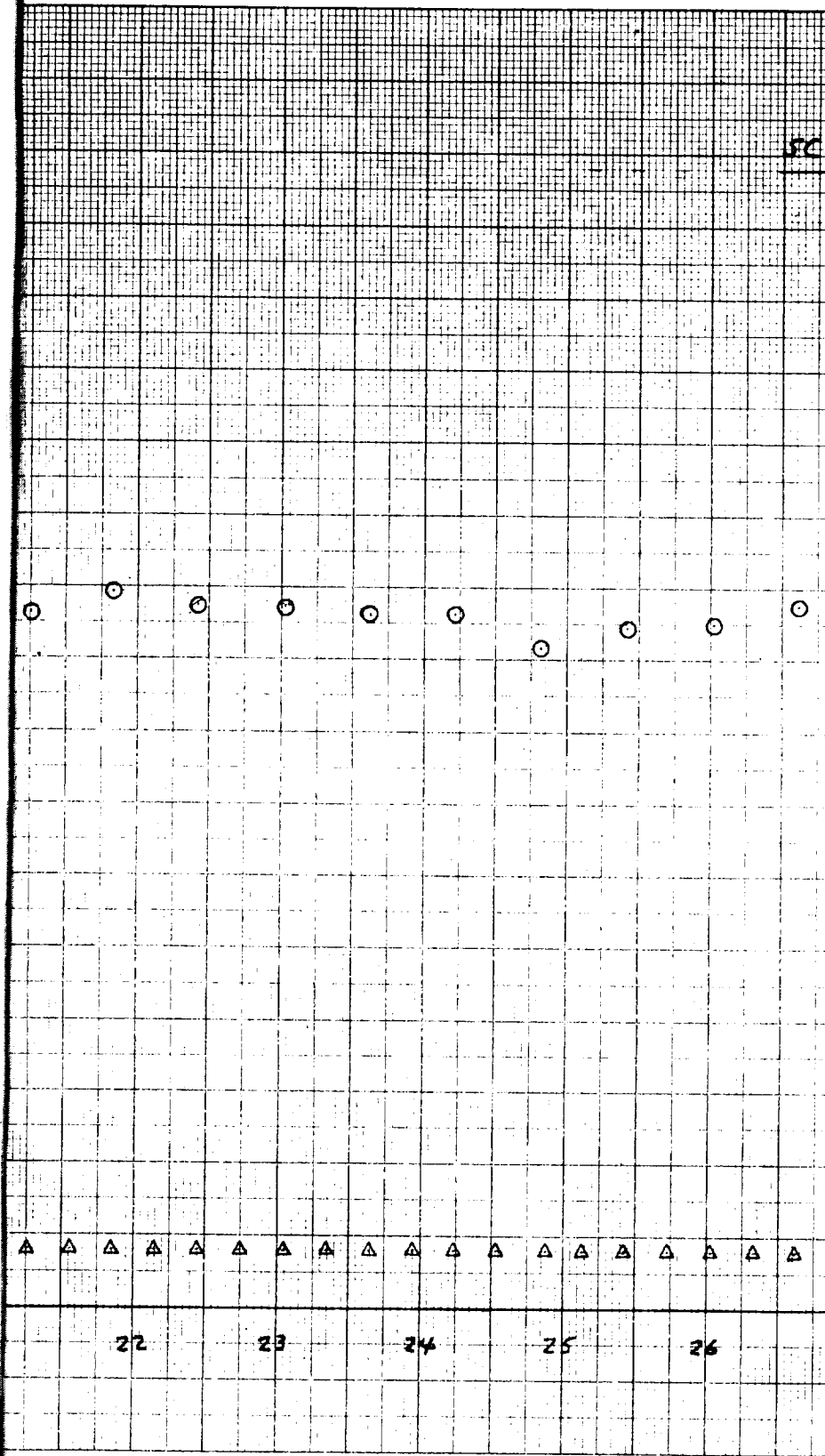
B) Engine 2

Figure 5.5-32 (continued). Comparison of Thrust Command and Strain Gage Data, Burn 40

5.5-111A

FOLDOUT FRAME /





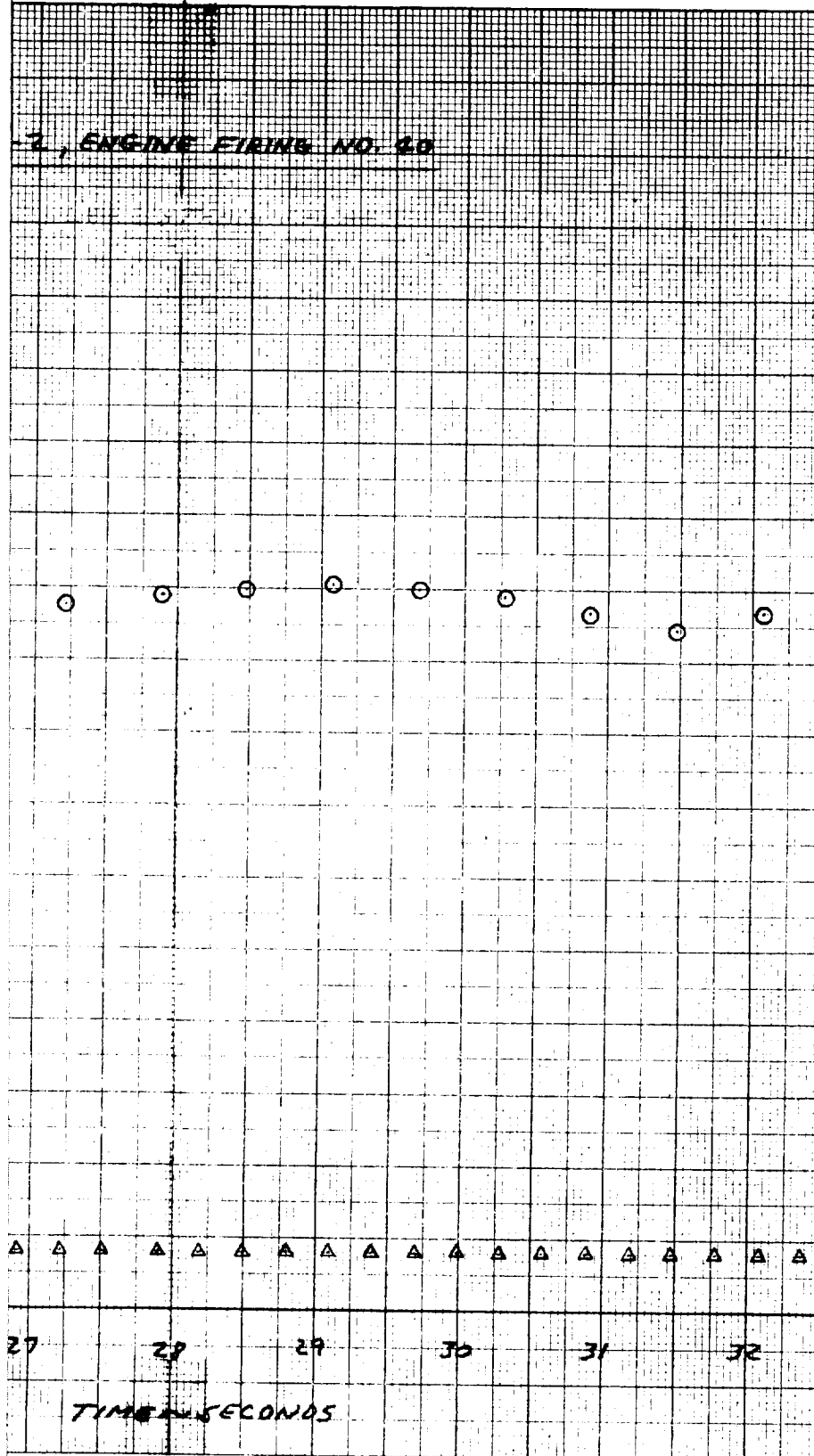
FOLDOUT FRAME 2

5.5-111B





3, ENGINE FIRING NO. 28



- FOLDOUT FRAME 3



REF. 265:08:05:19



△ △ △ △ △ △ △ △ △ △ △ △ △ △ △ △ △ △ △ △

33 34 35 36 37 38

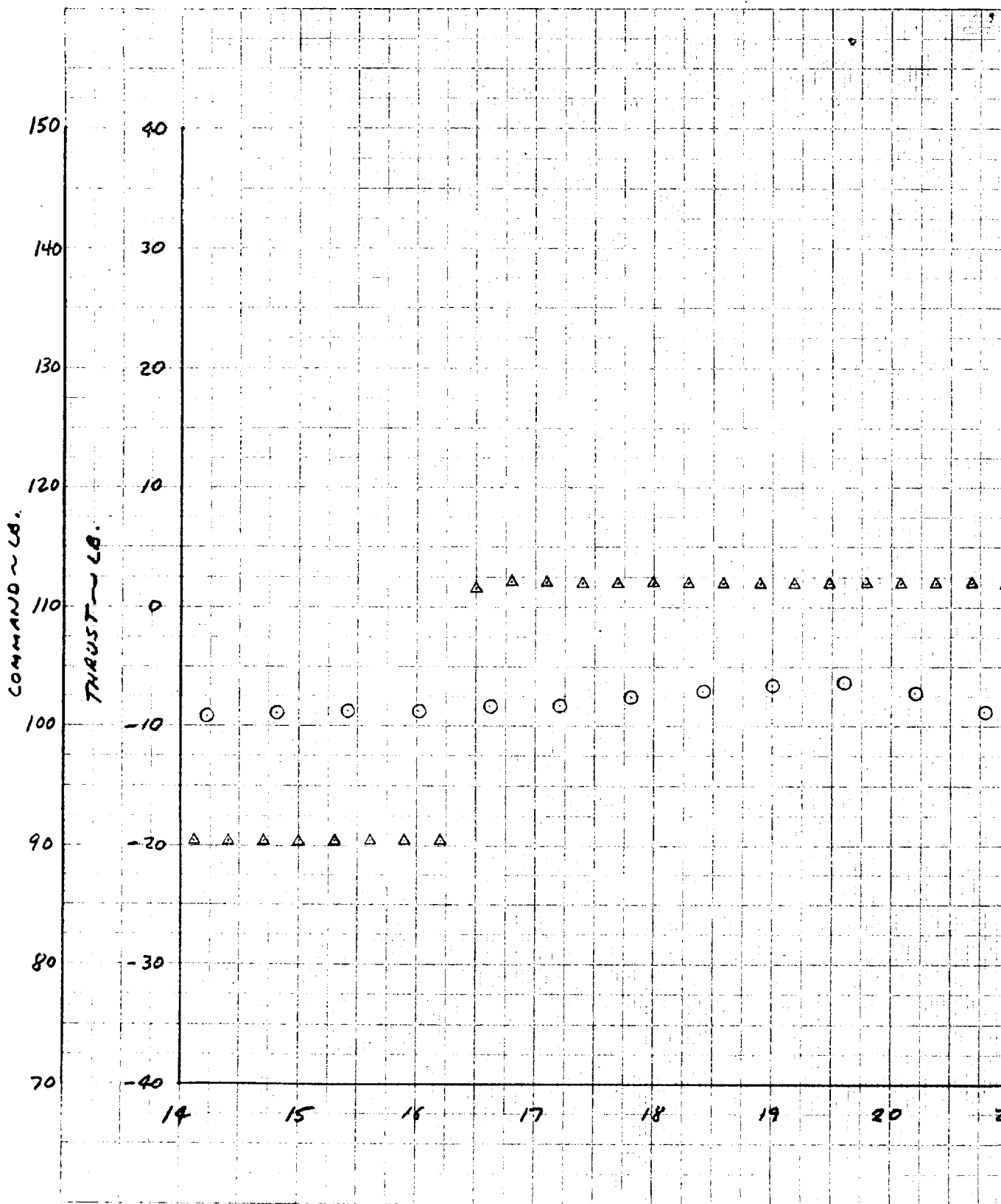
FOLDOUT FRAME 4

5.5-111c









c) Engine 3

Figure 5.5-32 (continued). Comparison of Thrust Command and Strain Gage Data, Burn 40

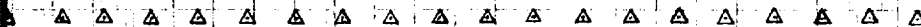
5.5-113 A

FOLDOUT FRAME /





SC-2



22

23

24

25

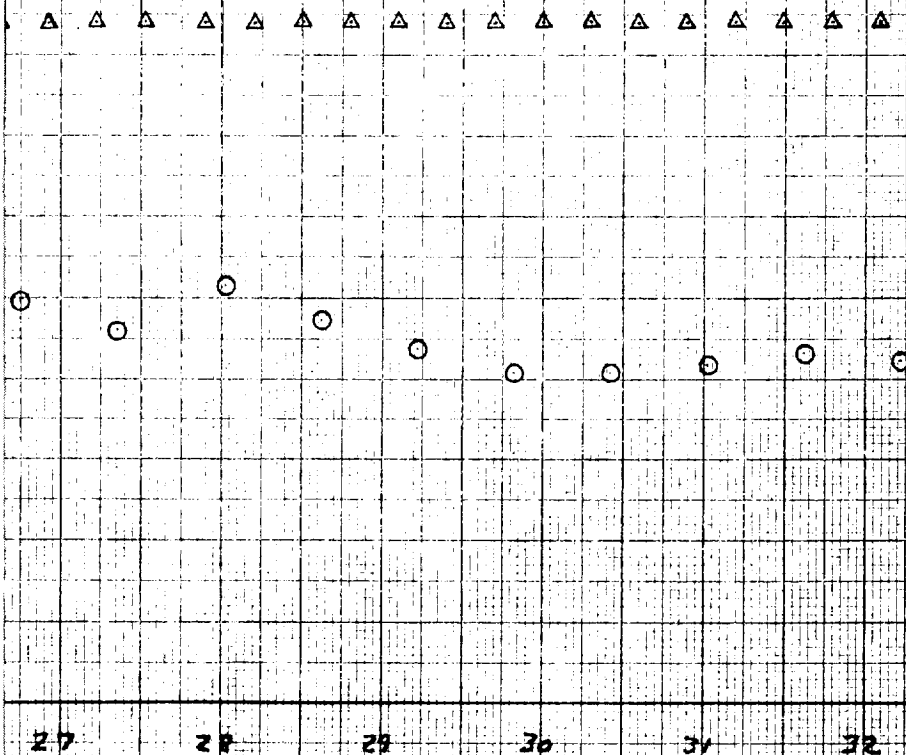
26

FOLDOUT FRAME 2

5.5-113B



ENGINE FIRING NO. 40



27 28 29 30 31 32

TIME - SECONDS

FOLDOUT FRAME 3





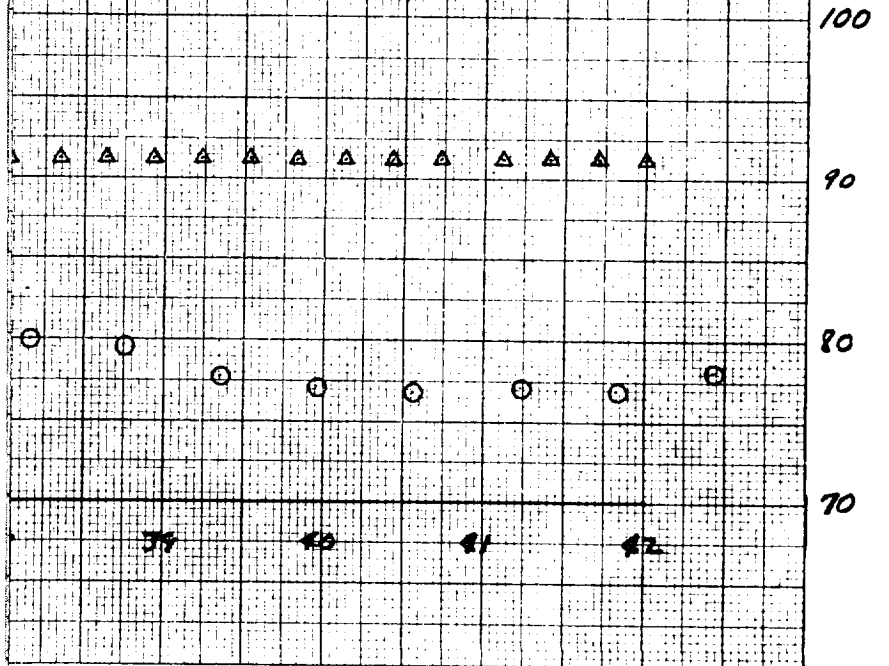


14.000

ENGINE 3

○ ~ P-20, STRAIN GAGE

△ ~ FC-27, THRUST COMMAND



FOLDOUT FRAME 5

5.5-113 D





For the 2.5-second and 21.5-second firings, the vernier engines were ignited at about 90-pound thrust command level (retro mode). Legs 1 and 2 immediately throttled down an increment close to that experienced for the 2.0-second firings, after which throttling control was exercised. The leg 3 command stepped to maximum at ignition and remained there until engine cutoff. Engine throttling during the first 2.5 seconds of the 21.5-second firing was quite similar to that during the 2.5-second firing. The remainder of the flight control signals were the same as for the 2.0-second firings.

#### Burn Duration

An accurate indication of commanded burn duration was obtained from the magnitude register (FC-18) (Table 5.5-19). The register countdown was assumed to be linear with time, allowing extension of the straight line established from two or more data points during the countdown, and thus the determination of the times of zero and full count. The accuracy of burn duration measurements made in this manner is limited by the on-board clock and data processing technique. Of course, the absolute time is in question by  $\pm 50$  milliseconds (i. e. ,  $\pm$  one word time) due to the granularity of the telemetry system.

#### Ignition Time

The data needed to bracket vernier engine ignition times is listed in Table 5.5-20, based on the apparent telemetry response of EP-4 (22-volt bus current), FC-25, FC-26, FC-27 (thrust commands: legs 1, 2, and 3), FC-18 (magnitude register), and P-18, P-19 (strain gages: legs 1 and 2). The interval between "before" and "after" times is due not only to engine ignition delay uncertainty, but also telemetry granularity. The size of the interval depends on telemetry mode, bit rate, and location of the ignition event relative to the data words in the frame (Table 5.5-19). The signals listed above were used to determine the last known time prior to ignition. The ignition response was determined from strain gages alone. Figure 5.5-33 graphically shows the method for burn 27.

Observations relative to the ignition times are as follows:

- 1) Flight acceptance test ignition times for the leg 1 and 2 TCAs were 0.088 and 0.081 second, respectively.
- 2) Ignition times listed in Table 5.5-19 are maximums.
- 3) Effect of data mode and bit rate on measured ignition times can be seen from the time increment between strain gage samples in Table 5.5-19.

TABLE 5.5-19. POSTMIDCOURSE BURN DATA

Burn Number	Burn Duration (From FC-18), seconds	Ignition Time, seconds*		Time Between Strain Gage Samples, seconds	Telemetry Mode and Bit Rate	Post Burn Nutation					
		Leg 1				Leg 2		Leg 1		Leg 2	
		Leg 1	Leg 2			Peak-to-Peak, pounds	Period, seconds	Peak-to-Peak, pounds	Period, seconds	Peak-to-Peak, pounds	Period, seconds
Midcourse	9.850	0.117	0.120	0.050	1/4400	44.8	12.3	41	12.3	44.8	12.3
2	2.015	0.146	0.156	0.200	1/11100	3.5	12	2.5	12	3.5	12
3	2.016	0.147	0.157	0.200	1/11100	4.0	11.5	3.0	11.5	4.0	11.5
9	2.018	0.258	0.268	0.200	1/100	4.0	11	3.0	11	4.0	11
15	2.020	0.103	0.113	0.200	1/11100	4.0	10	2.6	10	4.0	10
21	2.012	0.153	0.163	0.200	1/11100	5.0	9	3.0	9	5.0	9
27	2.019	0.200	0.210	0.200	1/11100	16.0	8	9.5	8	16.0	8
33	2.015	0.287	0.297	0.200	1/11100	6.0	7.5	6.0	7.5	6.0	7.5
34	**	0.570	0.660	0.600	6/11100	4.0	7	3.0	7	4.0	7
40	***	0.280	0.771	0.600	6/11100	***	5	5.0	5	3	5

\*Definition: Time from ignition command to thrust rise (times listed are maximums).  
 Corresponding figures from thrust chamber assembly flight acceptance test data are: Leg 1 = 0.088 second and leg 2 = 0.081 second.  
 \*\*Manual control was used for burns 34 and 40.  
 \*\*\*Strain gage signal apparently saturated.

TABLE 5.5-20. TABULATION OF BURN INITIATION TIMES  
FOR ENGINE FIRINGS

Burn Number	Initiation Interval*	Reference Time, day:hr:min	EP-4, seconds	FC-25, seconds	FC-26, seconds	FC-27, seconds	P-18, seconds	P-19, seconds	FC-18, seconds**	Data Source
Midcourse	After	264:05:00	03.675	03.665	03.650	03.640	03.657	03.660	3.493	DSIF
	Before	264:05:00	03.425	03.540	03.525	03.515	03.507	03.510		
2	After	264:07:28	28.062	28.022	27.962	27.922	27.783	27.793	27.687	SFOF
	Before	264:07:28	27.053	27.513	27.453	27.413	27.583	27.593		
3	After	264:07:50	06.517	06.477	06.417	06.377	06.238	06.248	6.141	SFOF
	Before	264:07:50	05.508	05.968	05.908	05.868	06.038	06.048		
9	After	264:23:33	26.267	26.227	26.167	26.127	26.197	26.207	25.989	SFOF
	Before	264:23:33	25.259	25.719	25.659	25.619	25.989	25.999		
15	After	265:01:28	15.759	15.211	15.151	15.111	14.881	14.891	14.828	SFOF
	Before	265:01:28	14.751	14.711	14.651	14.611	14.681	14.691		
21	After	265:02:39	18.906	18.358	18.298	18.258	18.028	18.038	17.925	SFOF
	Before	265:02:39	17.898	17.858	17.798	17.758	17.828	17.838		
27	After	265:03:48	00.520	00.480	00.420	00.380	00.242	00.252	00.092	SFOF
	Before	265:03:47	59.512	59.972	59.912	59.872	00.042	00.052		
33	After	265:04:56	15.915	15.406	15.346	15.306	15.476	15.486	15.239	SFOF
	Before	265:04:56	14.946	14.906	14.846	14.806	15.276	15.286		
34	After	265:05:43	24.437	23.535	23.305	23.315	23.795	23.895	23.295	SFOF
	Before	265:05:43	23.245	23.235	22.922	22.932	23.195	23.295		
40	After	265:08:05	17.021	16.420	16.490	16.500	16.971	16.480	16.380	SFOF and DSIF
	Before	265:08:05	15.830	16.120	16.190	16.200	16.380	15.880		

\*"Before" and "after" refer to estimate of ignition per given variable.

\*\*Beginning of countdown  $\pm$ 50 milliseconds (the magnitude register was not used during burns 34 and 40).

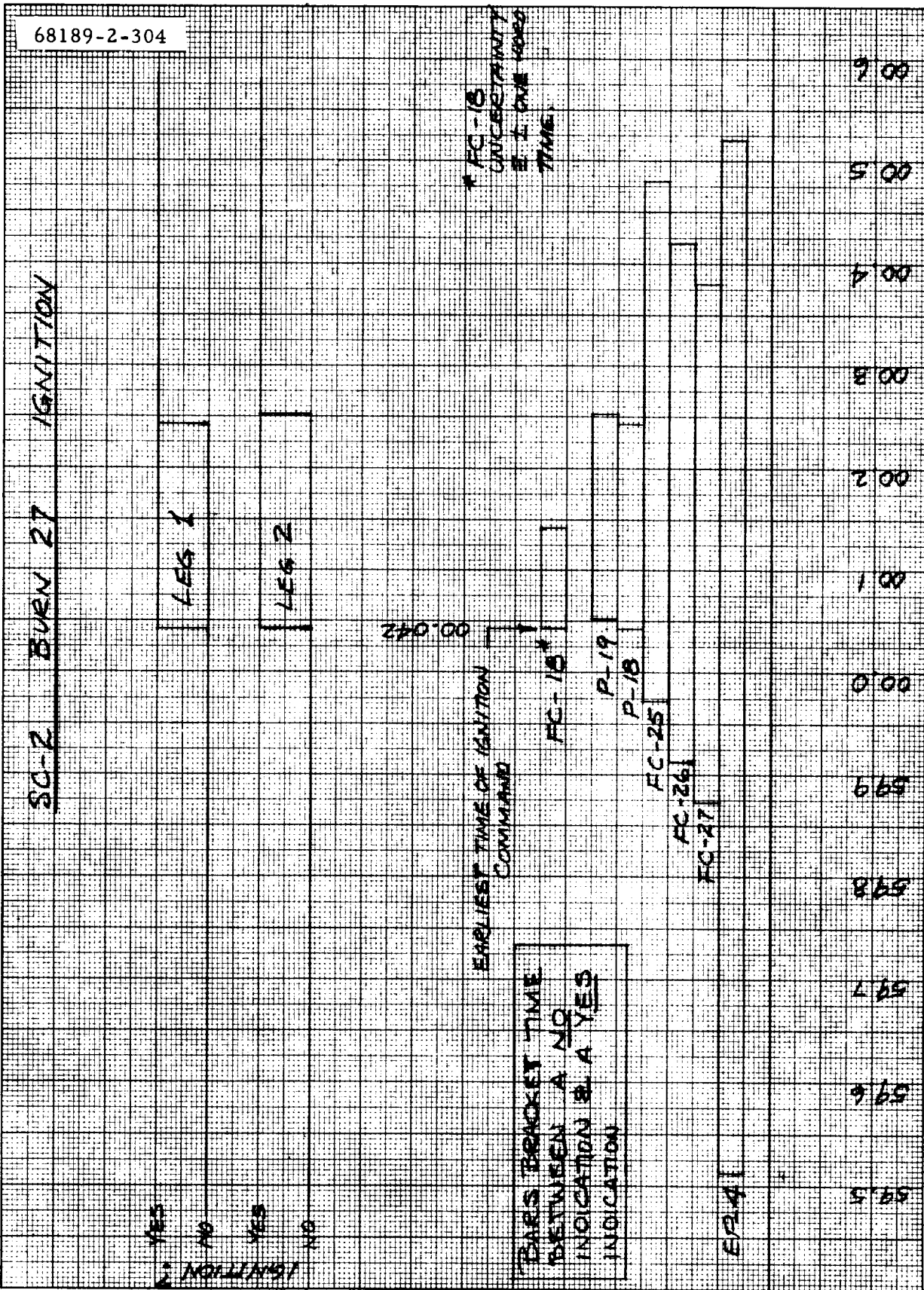


Figure 5.5-33. Determination of Ignition Time Interval, Burn 27

- 4) For the midcourse burn:
  - a) With 50 milliseconds between strain gage samples, ignition time is definitely between 0.067 and 0.117 seconds for leg 1 and 0.070 and 0.120 seconds for leg 2.
  - b) Overlap of the FC-18 uncertainty band and occurrence of "before change" FC-25 reading is ~3 milliseconds.

It may be concluded for the preceding that:

- 1) For the midcourse burn:
  - a) Ignition command is within 3 milliseconds after the "before change" FC-25 reading.
  - b) Ignition on legs 1 and 2 was probably normal (i. e. , <0.100-second ignition time).
- 2) Burn 15 may well have had a normal ignition.
- 3) Ignition times for burns 1 (midcourse), 2, 3, 15, and 21 probably did not experience exceptionally long ignition times.
- 4) Based on data analyzed, it cannot be stated with certainty that anomalous vernier engine ignition performance did or did not occur on any of the vernier engine burns.

#### Spacecraft Nutation

Apart from other detectable characteristics (e. g. , thermal drift), the strain gage data (Figures 5.5-23 through 5.5-32) show the effect of cyclic acceleration following each vernier engine burn. Amplitude and period of oscillation can be used as an indicator of the consistency of the applied torque impulse for the 2-second burns. Amplitude and period data are presented in Table 5.5-19.

Examination of data just prior to and after each burn shows the damped nature of the oscillation.

#### Postmidcourse Firing Anomaly (Burn 27)

It is possible to establish the anomalous performance of the leg 3 vernier engine during all vernier engine burns and the leg 1 vernier engine on burn 27 from the data discussed above. The leg 3 anomaly is considered

a continuation of that occurring at the midcourse correction and causing loss of spacecraft control. However, the anomalous performance of leg 1 during burn 27 does not appear to be (directly) connected with the midcourse failure.

The burn 27 extra-performance, consisting of vernier engine shutoff after the commanded firing termination, is of particular interest from an attitude control standpoint during the terminal descent phase, since loss of spacecraft could result. Burn 27 anomaly supporting data is as follows:

- 1) Strain gage data show (Figures 5.5-22 through 5.5-32):
  - a) Continuation of leg 1 thrust after termination of commanded interval.
  - b) Leg 2 cutoff per command (strain gage data).
  - c) Leg 1 response to throttling commands after termination of commanded interval. (Also, absence of throttling command response for leg 2 in the same interval.)
  - d) A definite change in character of the postburn nutation experienced by the spacecraft for burn 27, compared to the other 2-second burns (Table 5.5-19).
- 2) Thrust commands show the following:
  - a) Programmed duration (i. e. , ~2 seconds).
  - b) Command level changes that correspond to strain gage response.
- 3) Magnitude register (FC-18) shows proper commanded duration.
- 4) Combined telemetry data show engine cutoff on leg 2 compatible with strain gage-indicated time of ignition and commanded duration measured. (Thus, cutoff command was received at the proper time.)

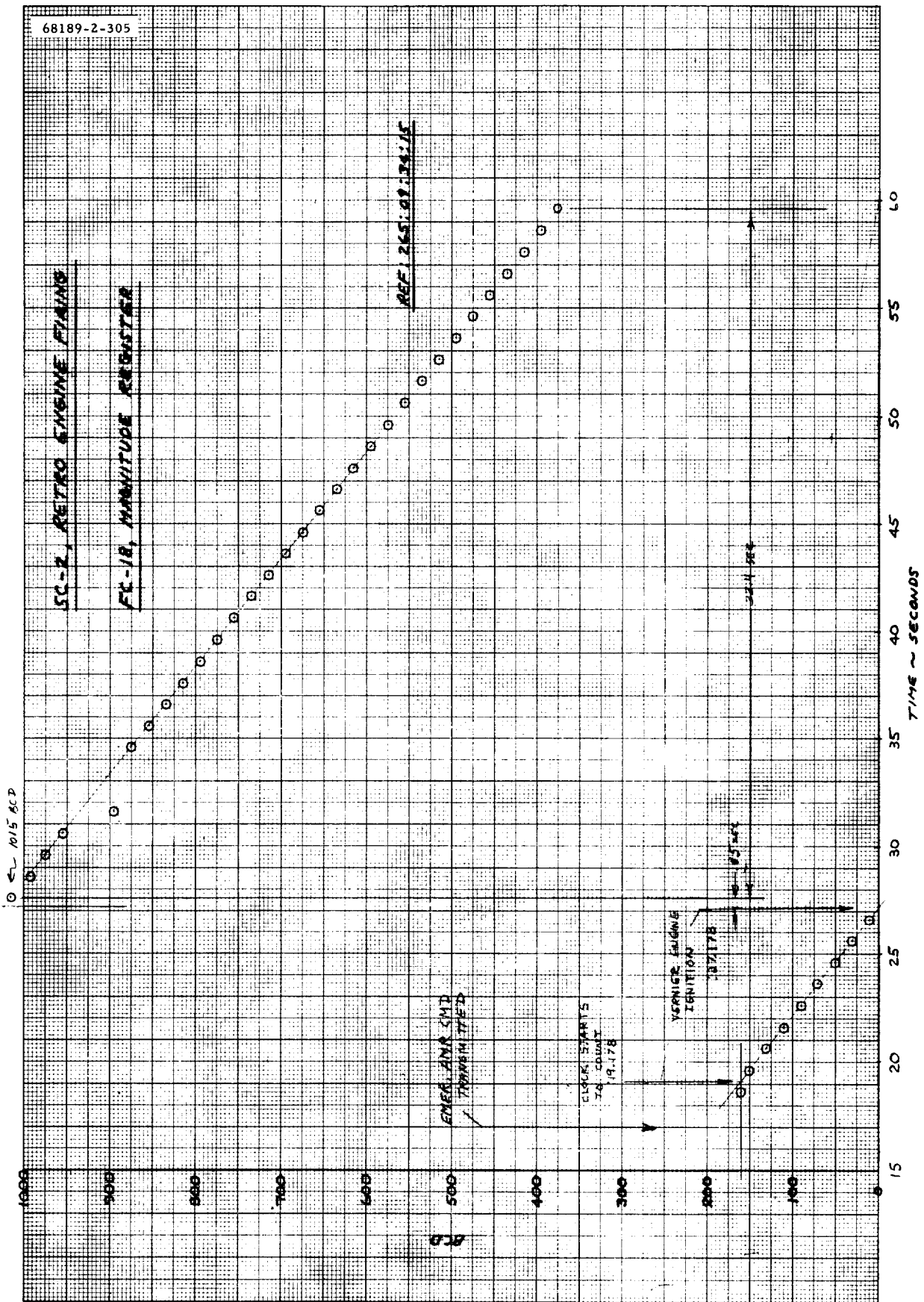
#### 5.5.4.10 Retro Firing

The following commands were transmitted on 22 September as part of the retro firing sequence which ended the SC-2 mission:

<u>Command</u>	<u>GMT, hr:min:sec</u>
Thrust phase power on	09:19:06
Enable gas jets	09:30:33
Manual lockon	09:30:53
Reset nominal thrust bias	09:31:12
Load magnitude register with 8.0-second delay	09:31:51
Mode 2	09:32:19
Reset Group IV	09:32:55
Retro sequence mode on	09:33:14
Emergency AMR mark	09:34:17

The emergency AMR mark command was apparently received at 09:34:19.178 as indicated by start of the magnitude register countdown (Figure 5.5-34a). The clock counted down smoothly for the desired 8 seconds, at which time ignition of vernier engines 1 and 2 occurred as indicated by the telemetered strain gage signals (Figure 5.5-34b and c). The earliest indication of retro ignition by means of the retro ignition latch going high, was at 09:34:28.578. At about the time of retro ignition, vernier engines 1 and 2 were shut off, as indicated by the strain gages, and remained off until all data were lost at 09:35:00. The vernier ignition latch (FC-28), vernier engine command signals (FC-25, FC-26, and FC-27) (Figures 5.5-34e through 5.5-34g), and the magnitude register signals (FC-18) remained normal during this time. At retro ignition, acceleration along the Z axis increased from approximately 7.1 to 10.3 g and remained at this level for around 18 seconds, after which time it gradually increased to 11.5 g when data were lost (Figure 5.5-34h).

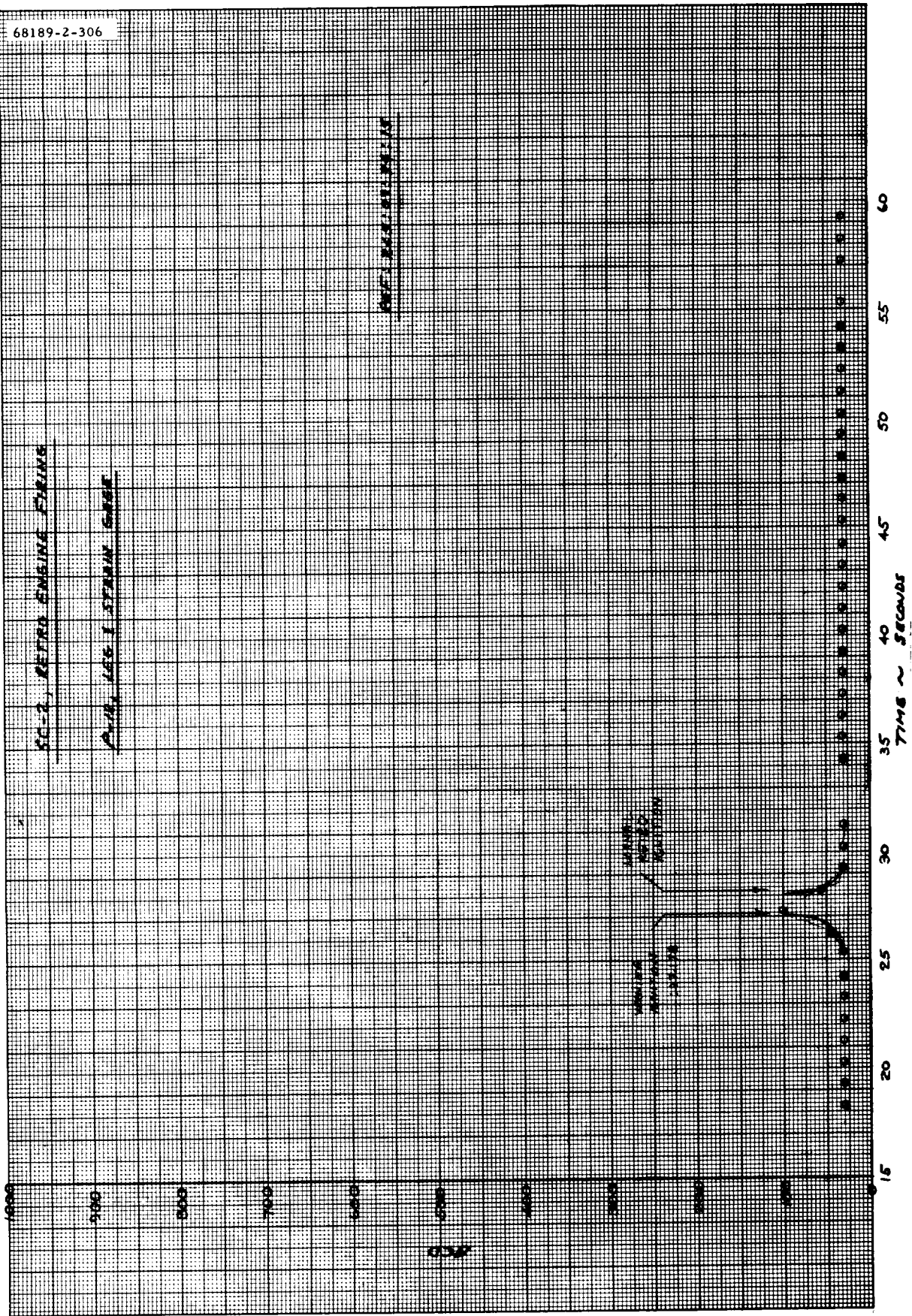
Estimated nitrogen gas remaining when data were lost was 1.62 pounds based on a pressure of 1340 psi at 43°F.



a) FC-18, Magnitude Register

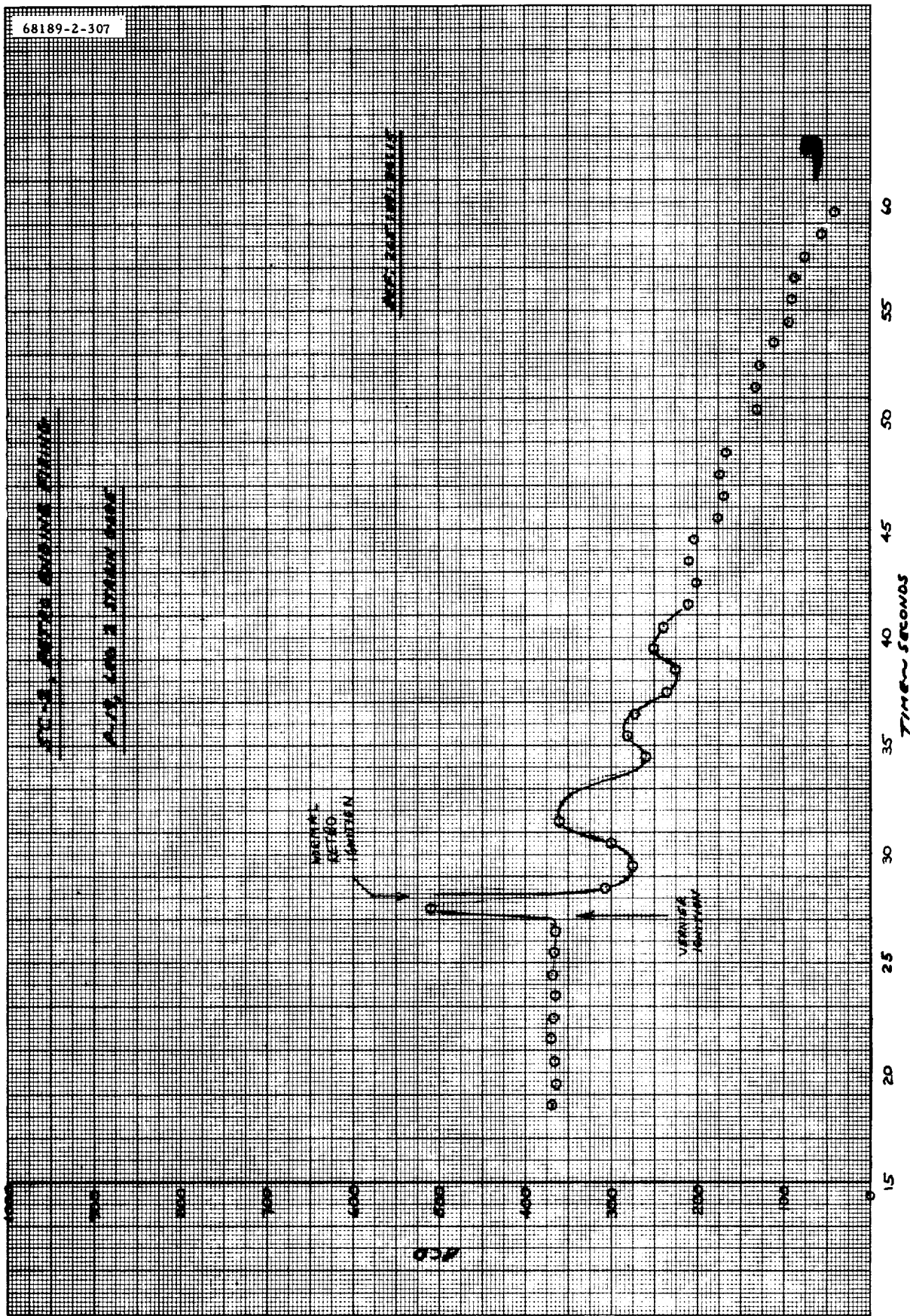
Figure 5.5-34. Retro Engine Firing



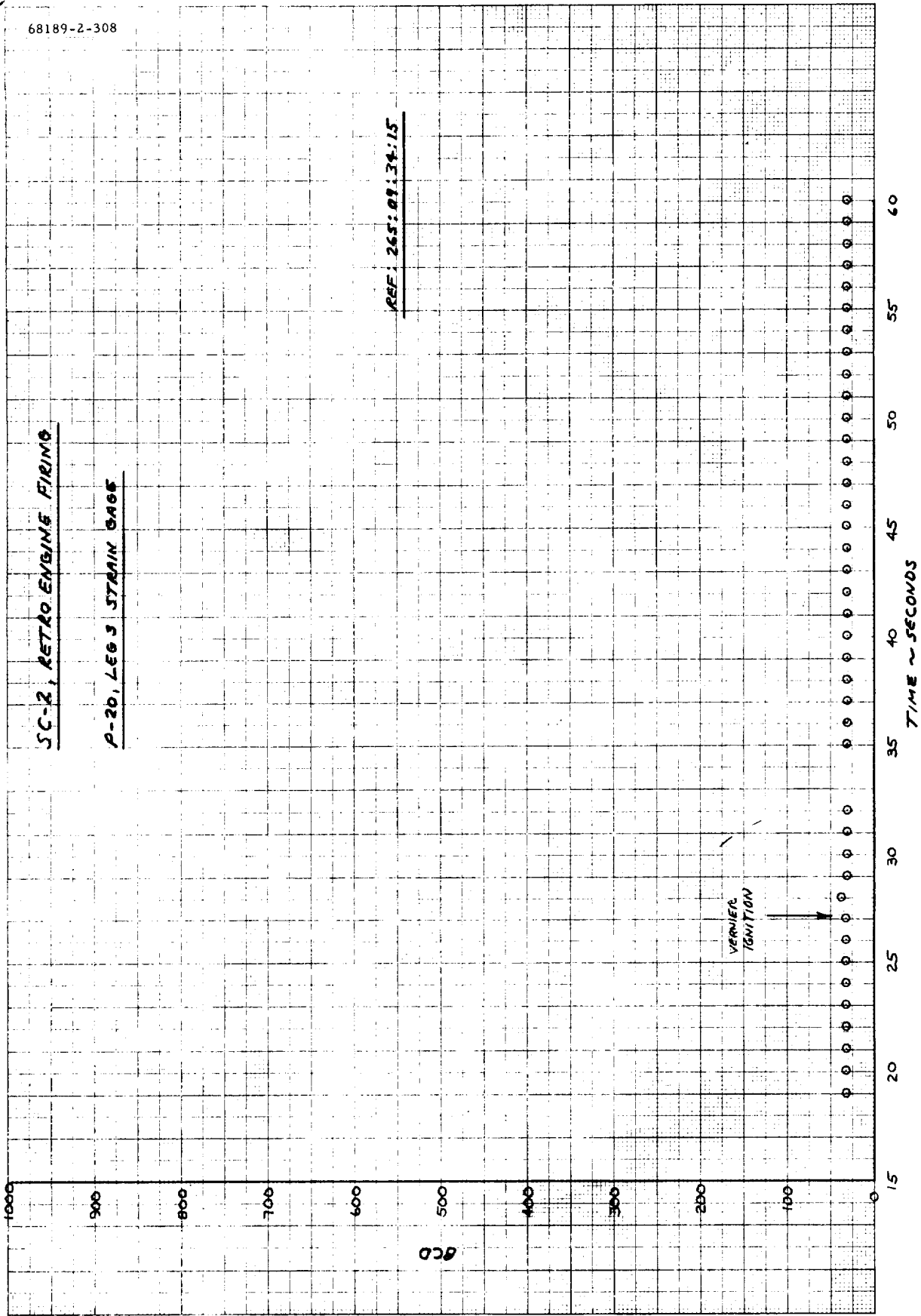


b) P-18, Leg 1 Strain Gage

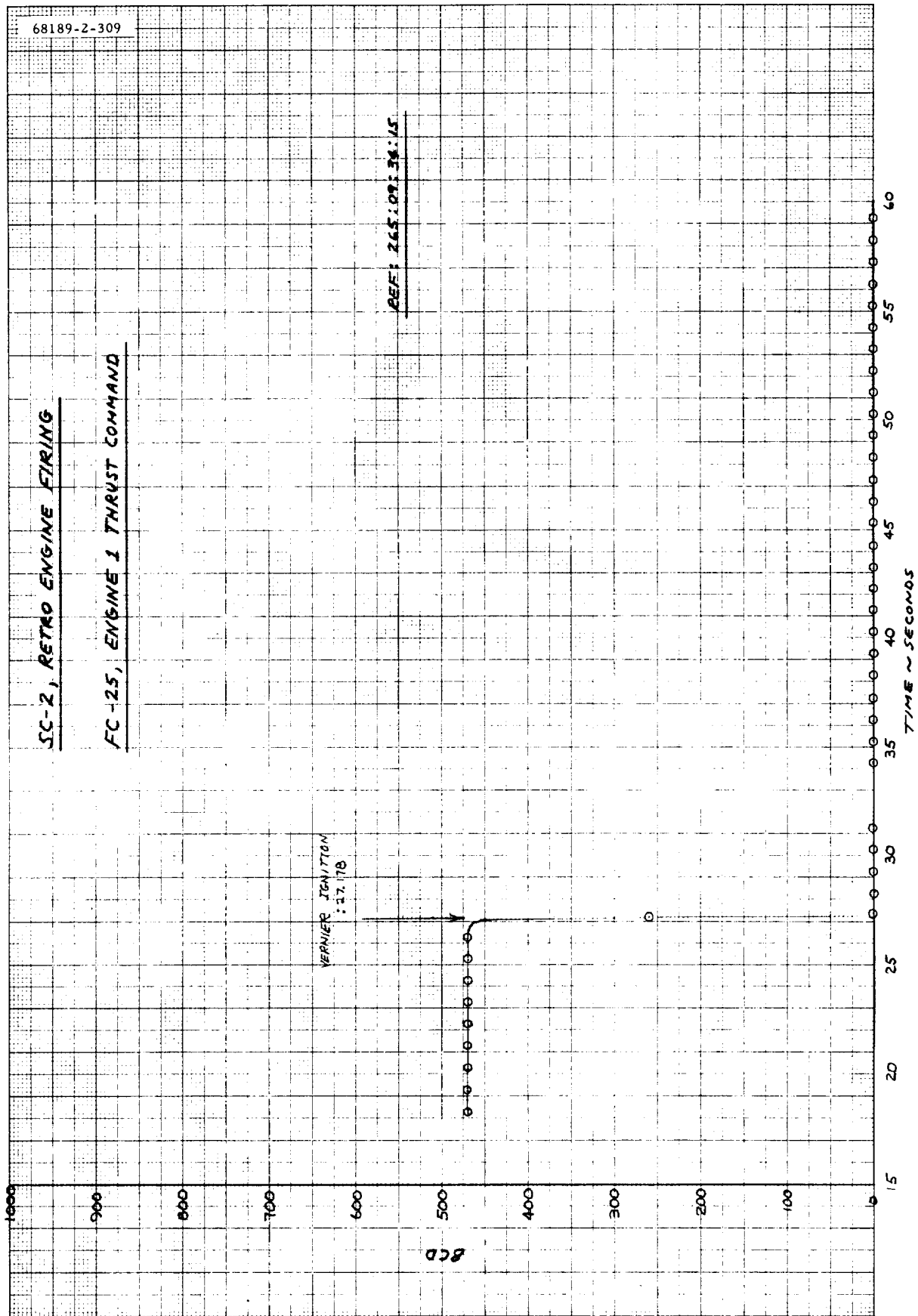
Figure 5.5-34 (continued). Retro Engine Firing



c) P-19, Leg 2 Strain Gage  
Figure 5.5-34 (continued). Retro Engine Firing

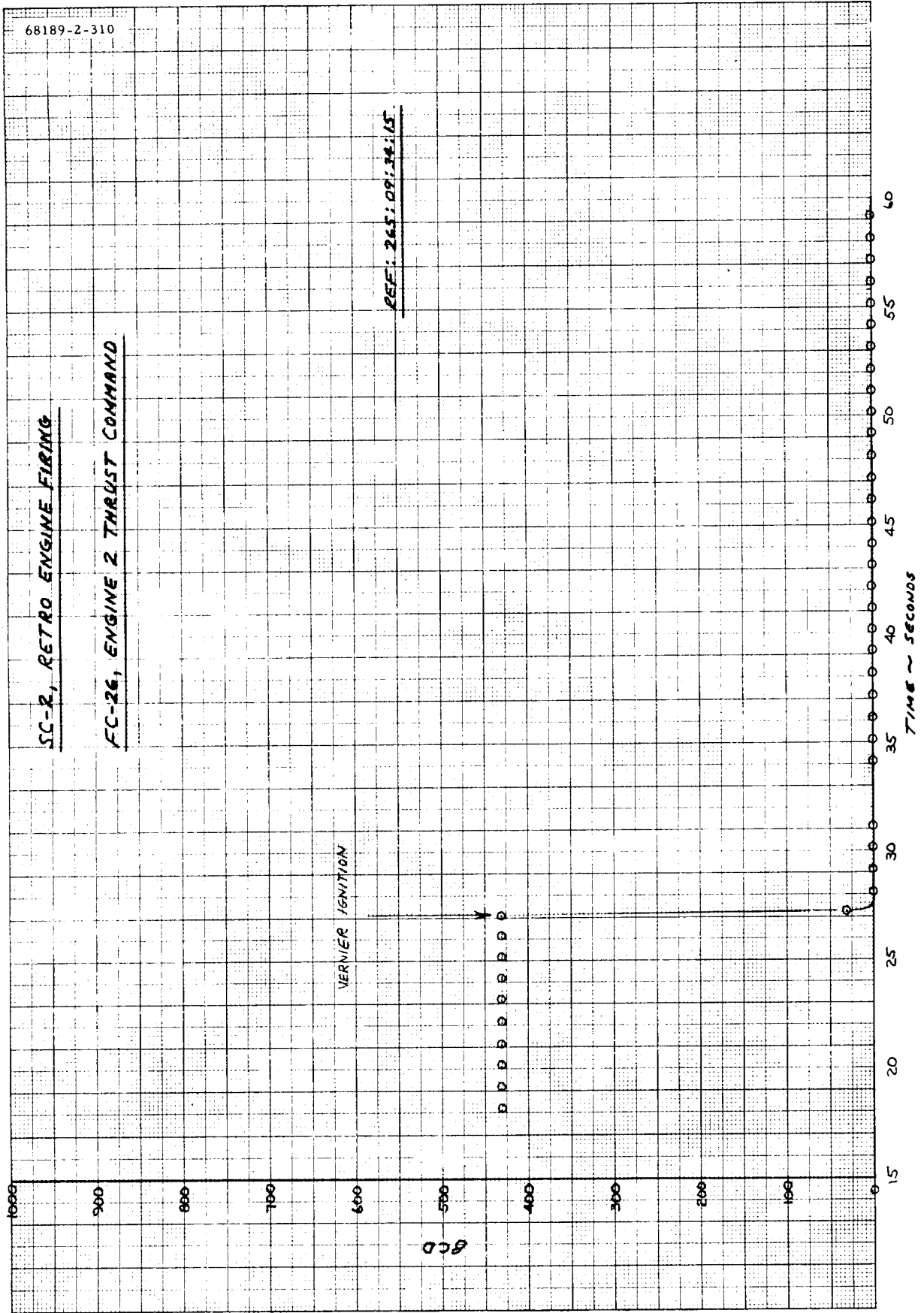


d) P-20, Leg 3 Strain Gage  
Figure 5.5-34 (continued). Retro Engine Firing



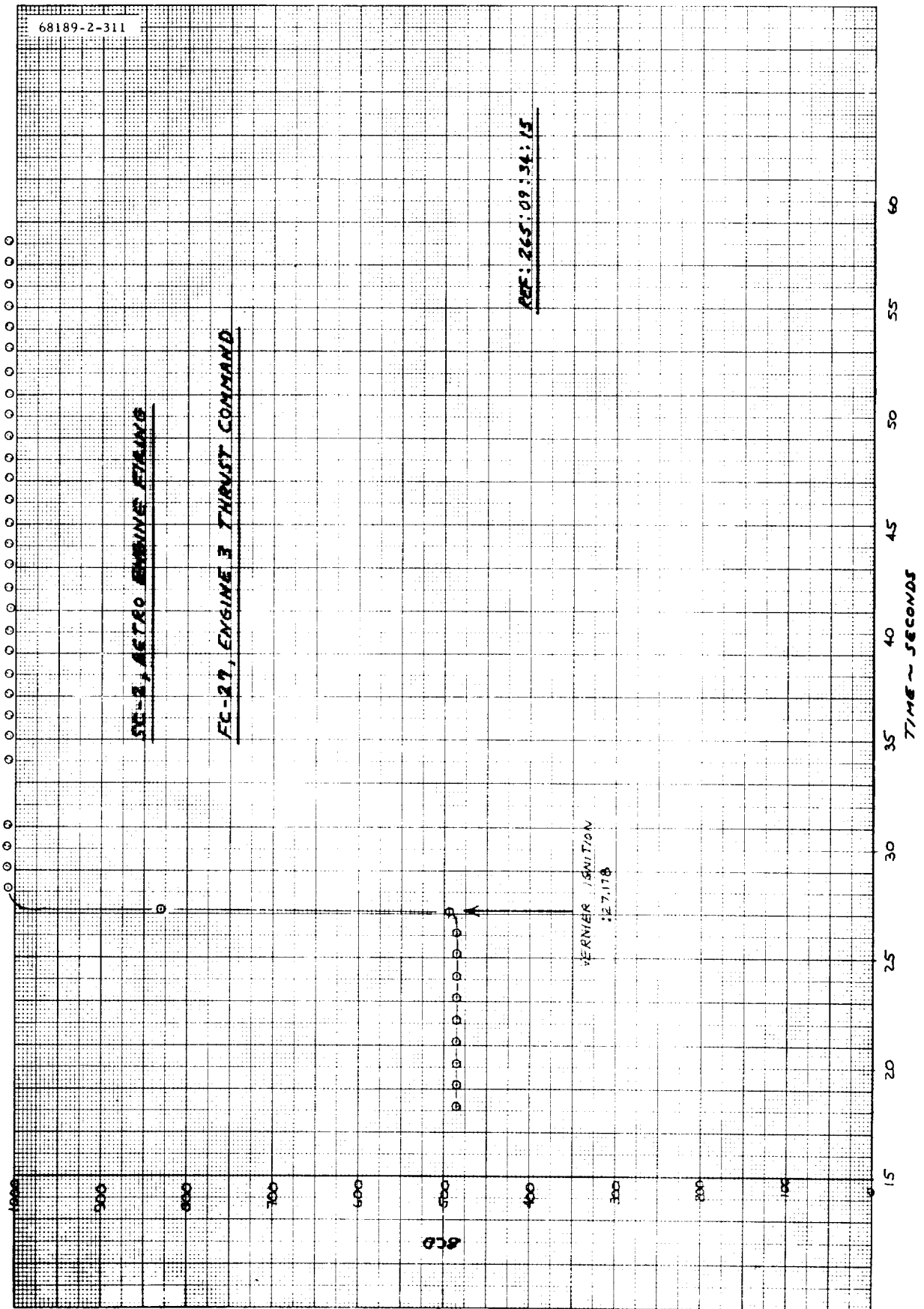
e) FC-25, Engine 1 Thrust Command

Figure 5.5-34 (continued). Retro Engine Firing



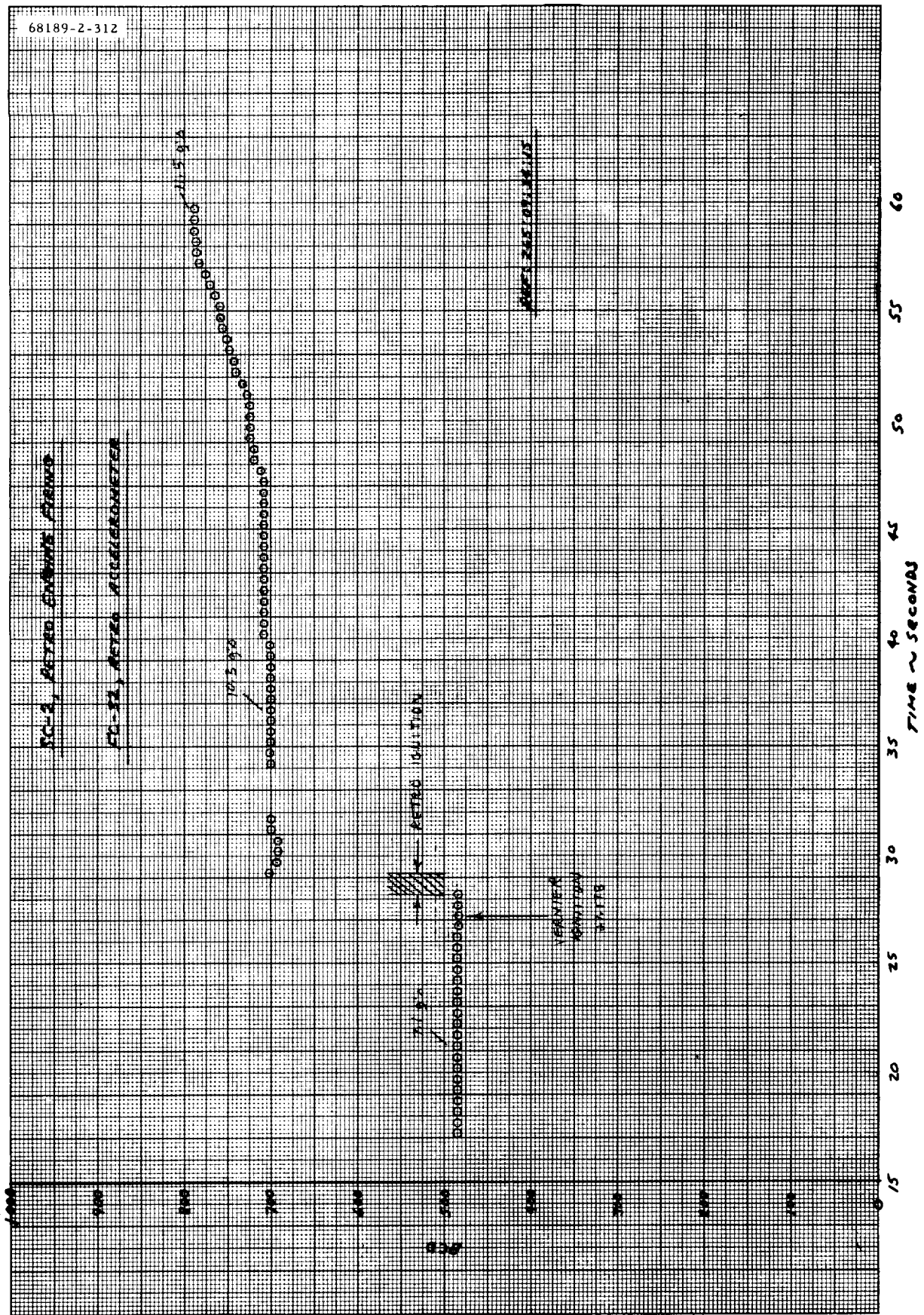
f) FC-26, Engine 2 Thrust Command

Figure 5.5-34 (continued). Retro Engine Firing



g) FC-27, Engine 3 Thrust Command

Figure 5.5-34 (continued). Retro Engine Firing



h) FC-32, Retro Accelerometer

Figure 5.5-34 (continued). Retro Engine Firing

#### 5.5.4.11 Postmission Tests and Analyses

Several special tests were performed in the Hughes Flight Control Laboratory to assist in postmission analyses. These tests and other pertinent analyses are discussed below. (References 20 through 37 comprise control IDCs documenting the postmission activity.)

##### SC-2 Gyro Error and Thrust Command Telemetry Accuracy

It was determined that the gyro error telemetry signals were not appreciably affected by a degradation in gyro transfer function and that their accuracy is better than that associated with the thrust command telemetry signals. A comparison of tolerance allotments for the gyro error and thrust commands telemetry circuit components is shown in Table 5.5-21. Although Reference 12 discusses these tolerances in detail, the following clarification of the values listed should be noted:

- 1) Specification allowance on coil resistance is 400 ohms, +33 percent, -20 percent.
- 2) The 20 percent value listed was taken as a convenient "symmetrical" number approximating the maximum. It is a useful crude limit if baseline coil resistance and temperature are not available.
- 3) The 2 percent value listed is probably the best attainable if a reliable baseline resistance measurement is available and corrections are made for coil temperature. Acceptance test data (taken at Reaction Motors Division of Thiokol prior to delivery) on resistance of the solenoid valve coils are presented in Table 5.5-22. All values were within 3 percent of nominal. Note that coil temperature changes following application of thrust-phase power caused an appreciable resistance change on leg 1 in the 4.5 minutes prior to the 21.5-second burn. A 9 percent drop in the telemetered "null" output was observed.
- 4) Data presented in Table 5.5-21 do not include tolerance on engine performance itself (accuracy of thrust developed at a given level of coil differential current); this is not insignificant.

Since a variation in gyro transfer function (nominally 44 mv/deg) directly affects the gyro error telemetry signal scale factor, the transfer function histories of the three gyros were investigated for their possible effect on postmission analysis. These data are presented as Figures 5.5-35, 5.5-36 and 5.5-37. The results are summarized as follows:

Yaw Gyro: A gradual increase of transfer function with time is noted with some evidence of leveling off in the last 100 hours of inertial lab tests. On this basis, it is believed that the best estimate of 43.2 mv/deg for yaw gyro transfer function, as operating in the spacecraft at midcourse, is the same as that measured at AFETR.





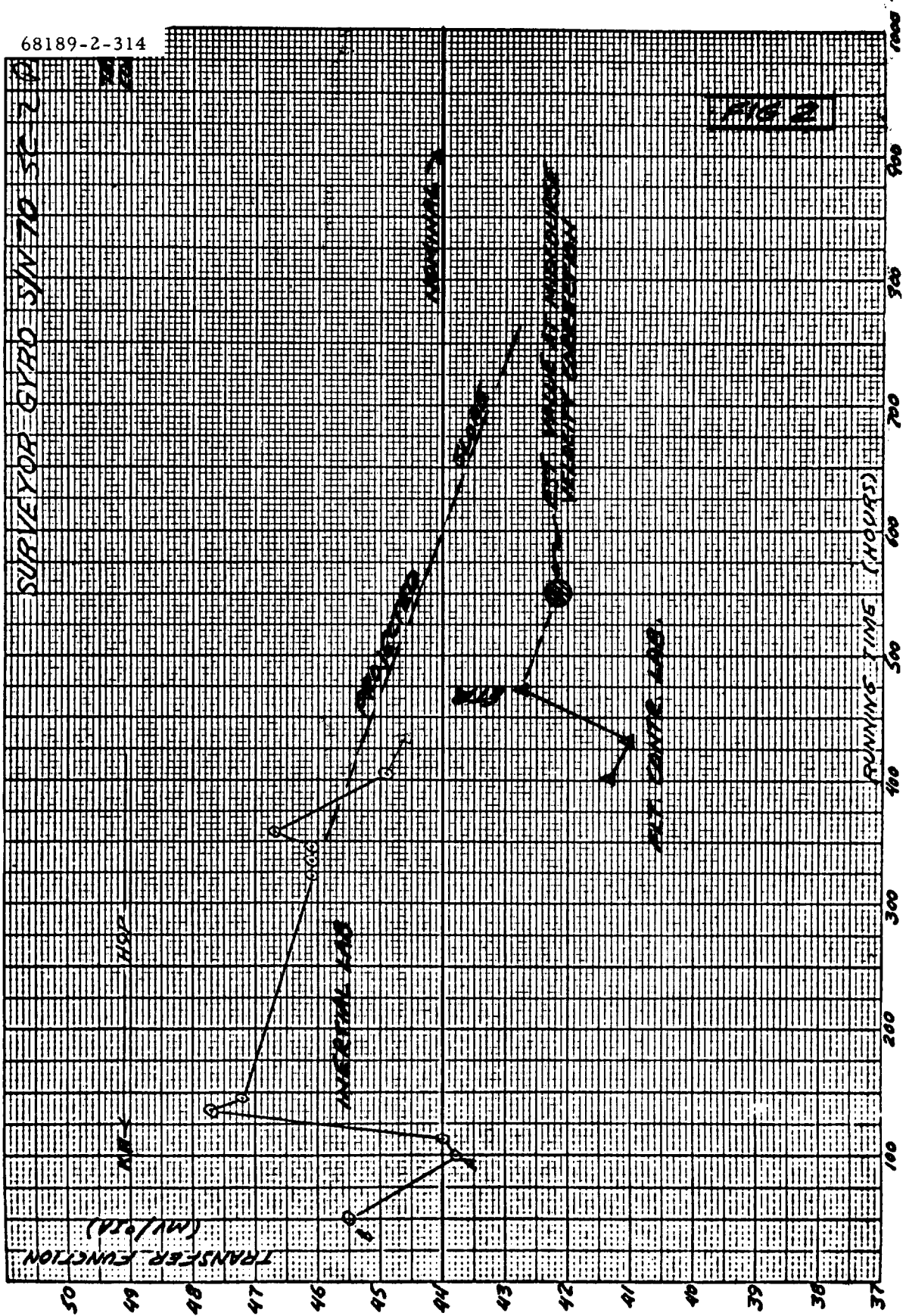


Figure 5.5-36. Gyro 70, Pitch

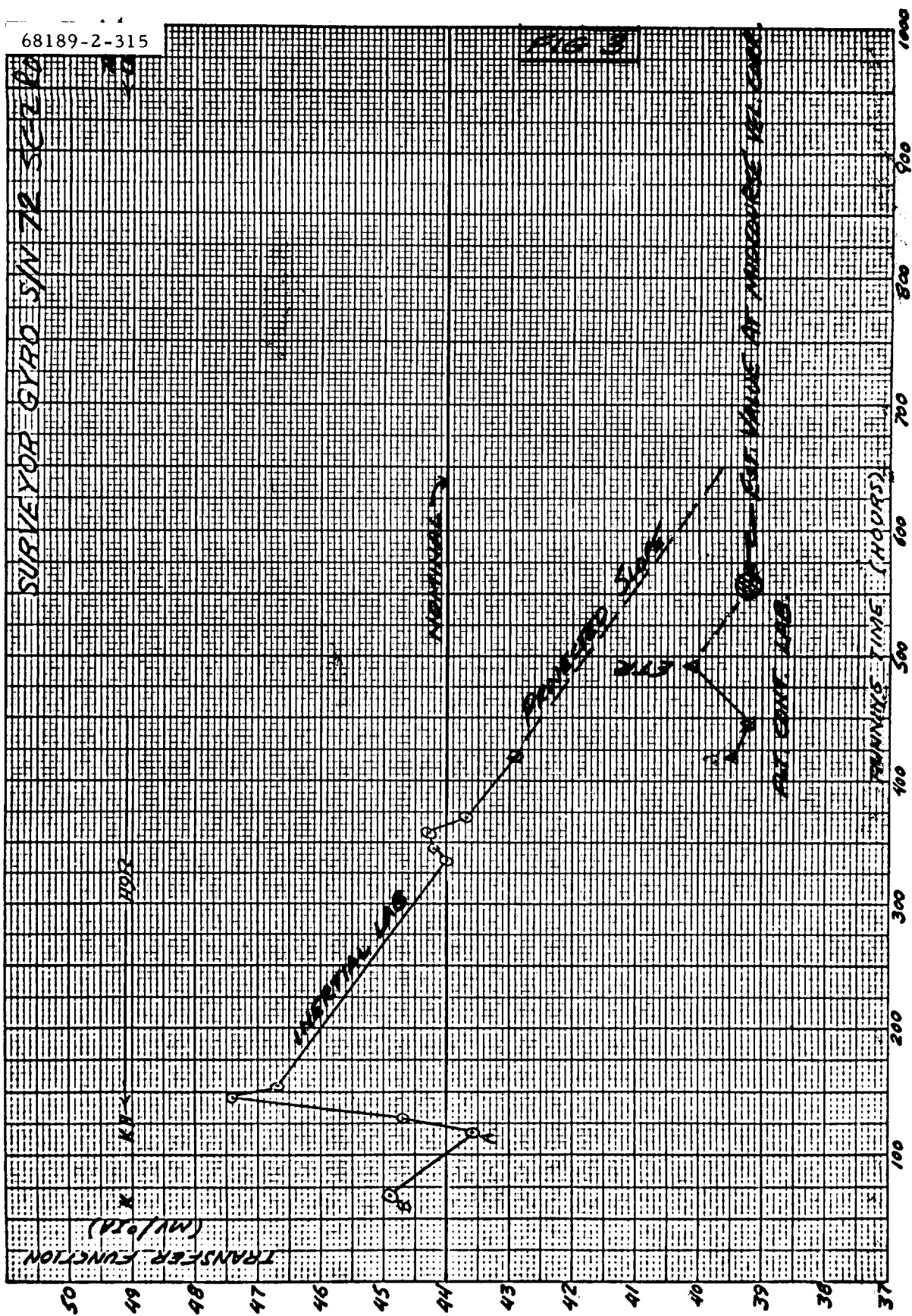


Figure 5.5-37. Gyro 72, Roll

TABLE 5.5-21. RELATIVE ACCURACY OF THRUST  
COMMAND AND GYRO ERROR TELEMETRY, PERCENT

	Telemetry Circuit Error	Errors of Electronics Components in Series	Valve Coil Error	Total Error, RSS
Pitch and yaw gyros	< 2	3 and 5	-	6.2
Roll gyro	1	3 and 5	-	6.1
Thrust command	2	3, 5, and 5	20 2	22. 8.2

TABLE 5.5-22. TORQUE MOTOR COIL RESISTANCE  
OF THROTTLE VALVES

	Leg 1	Leg 2	Leg 3
Valve serial number	5356	5376	5380
Resistance, ohms			
Pin A to pin B*	396.3	391	395.5
Pin C to pin D	398.0	388	406.1

\*High current in this coil closes valve.

Pitch Gyro: A slowly decreasing trend is apparent; the value at midcourse is estimated at 42.2 mv/deg, about 1 percent below the AFETR measurement.

Roll Gyro: A moderately decreasing trend is apparent; value at midcourse is estimated at 39.2 mv/deg, about 2 percent below the AFETR measurement.

Inasmuch as the telemetry calibrations were based on the AFETR data, and no data exist to indicate that the gyros were operating other than normally during the flight, it is concluded that the transfer functions at midcourse were not significantly different from those that established the telemetry calibrations.

While they are a very insensitive indicator, the dynamics of the pre-midcourse yaw maneuver were examined for any evidence of low control-loop gain that might have been attributable to low gyro transfer function. No such evidence was apparent.

Gyro Telemetry Saturation. Limiting characteristics of a demodulator prior to the telemetry pickoff point, and the telemetry output limits of 0 and 5 volts, result in a gyro telemetry saturation characteristic typified by the solid line in Figure 5.5-38. AFETR data for the pitch and yaw gyros, overplotted on this figure, fit the nominal reference very well, with just a hint of the typical break in slope at 6 degrees. To obtain a better idea of the saturating behavior of actual hardware, data were obtained in the Flight Control Laboratory on a prototype inertial reference unit (Figure 5.5-39). The yaw gyro in that unit exhibited characteristics closely comparable to those of the SC-2 pitch and yaw gyros and validated the nominal saturation curve for use in correction SC-2 gyro data telemetry indications at angles above 6 degrees.

#### 22-Volt Thrust Phase Bus Current During Midcourse

An attempt was made to duplicate the current waveforms that existed during the midcourse velocity correction. Measurement of the 22-volt thrust phase bus power and power control waveforms was performed using the SC-1 "ZAP" flight control electronics unit (FCEU) (P/N 273100-6, S/N 13) on the FCSG flight acceptance test console with its associated roll actuator simulator (T284828). Three vernier engine prop valve solenoids (S/N 230, 247, and 236) were obtained for this test. The voltage and current waveforms that appear on the 22-volt power and the FCEU power control circuitry under various operating conditions of the roll actuator are shown in Figures 5.5-40, 5.5-41, and 5.5-42. Figure 5.5-43 depicts the applicable control circuitry in the FCEU. In addition, an attempt was made to obtain the current waveforms by simulating the transient roll conditions that existed during midcourse. The spacecraft roll rates and roll acceleration were simulated with the inertial reference unit mounted on a Genisco rate table. Figure 5.5-44 shows the 22-volt thrust phase current waveforms

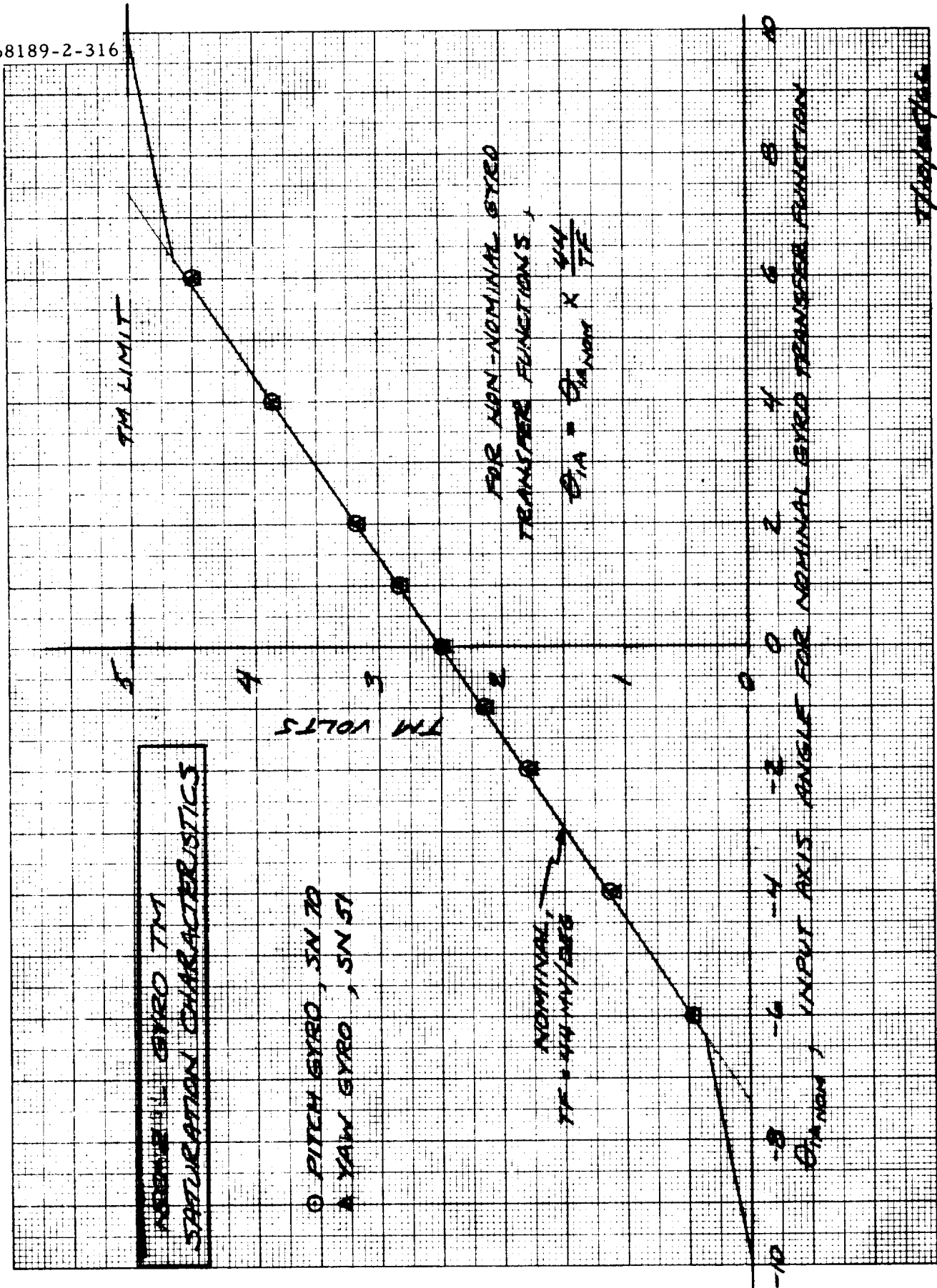
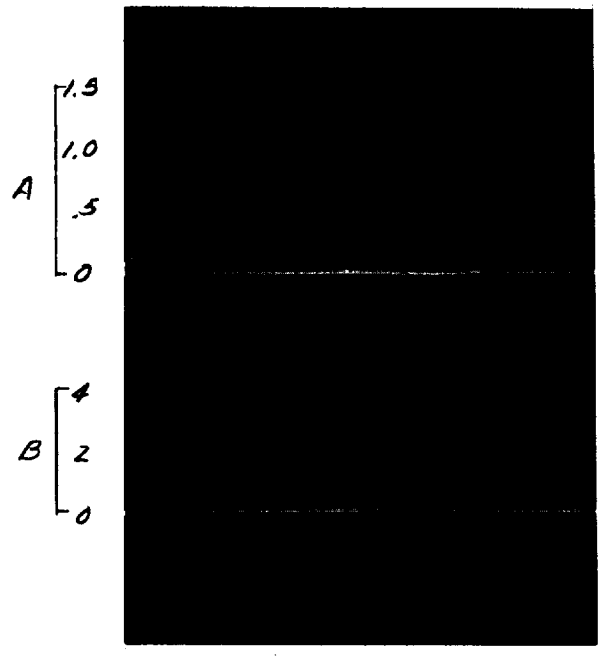
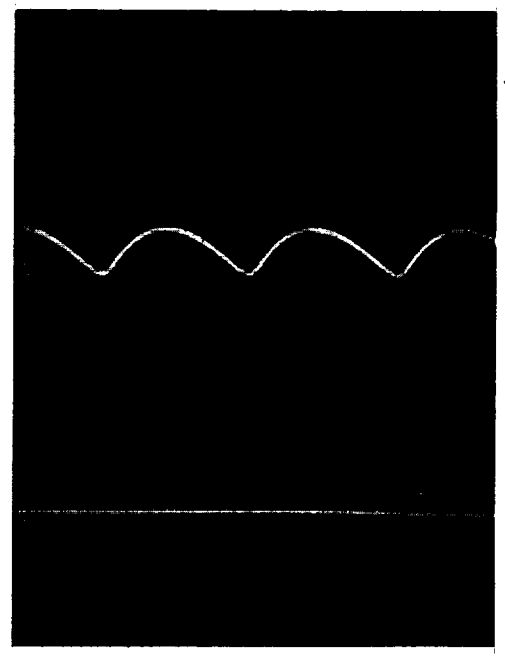


Figure 5.5-38. Gyro Telemetry Saturation Characteristics

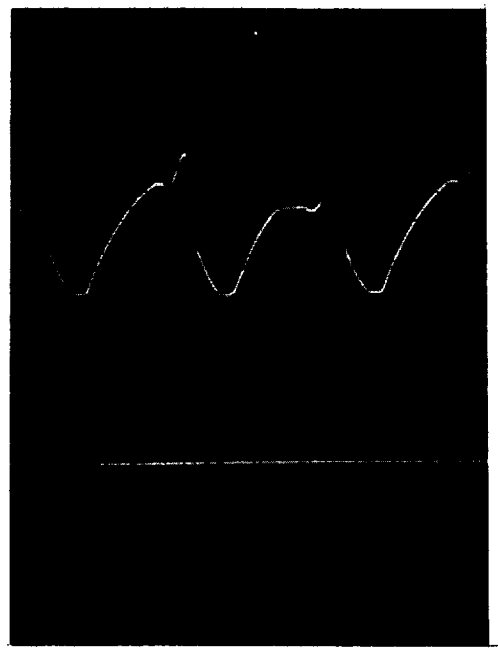




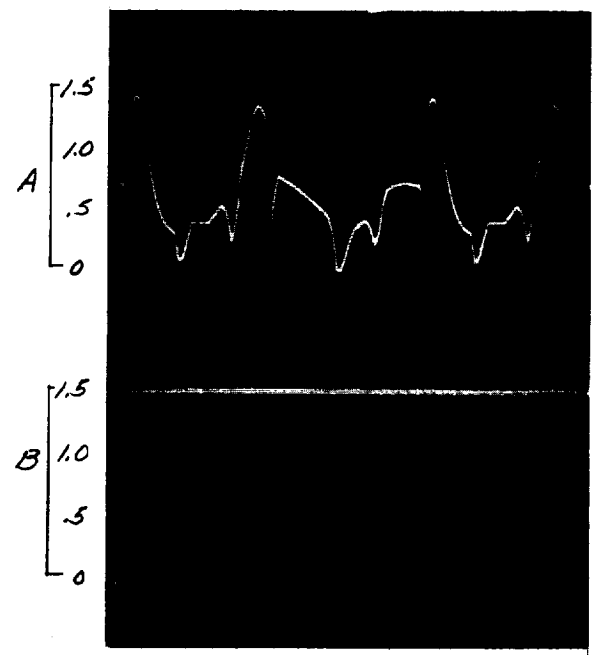
1 msec  
1. COAST PHASE POWER ONLY.



1. THRUST PHASE POWER ON,  
2. ROLL ACTUATOR IN NEUTRAL POSN  
3. VERN ENG PROP VALVES OFF.



1. THRUST PHASE POWER ON.  
2. STEP INPUT AT ROLL GYRO ERROR.  
3. VERN PROP VALVES ON.

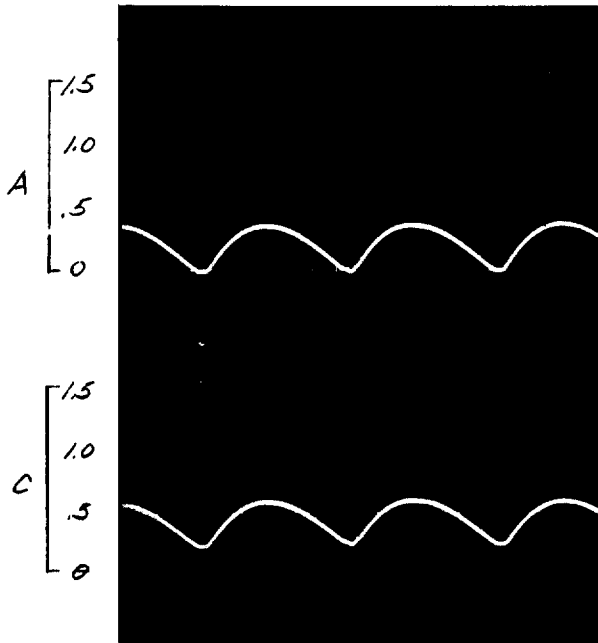


1. THRUST PHASE POWER ON.  
2. ROLL ACTUATOR HARD OVER.  
3. VERN PROP VALVES ON.

TRACE A +27V THRUST PHASE CURRENT TO ROLL ACTUATOR AMP } AMPERES  
TRACE B VERNIER ENGINE PROP VALVE (3) CURRENT. }

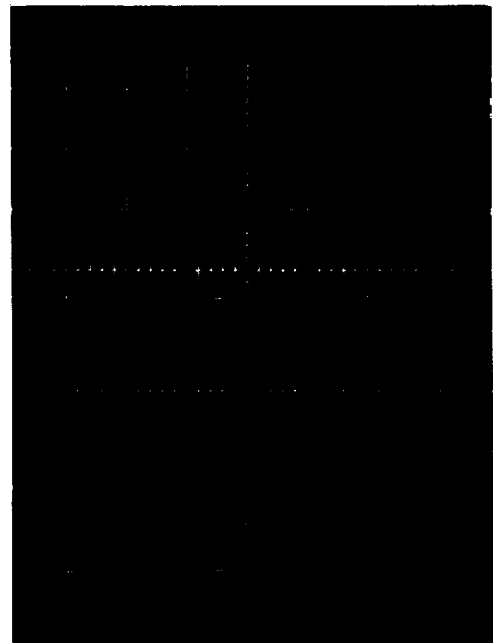
Figure 5.5-40. Current Waveforms





1. THRUST PHASE POWER ON.  
2. ROLL ACTUATOR IN NEUTRAL POSN.

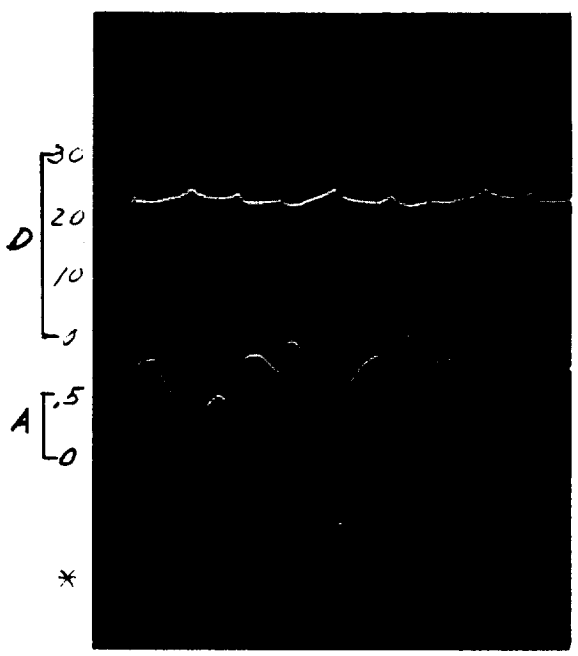
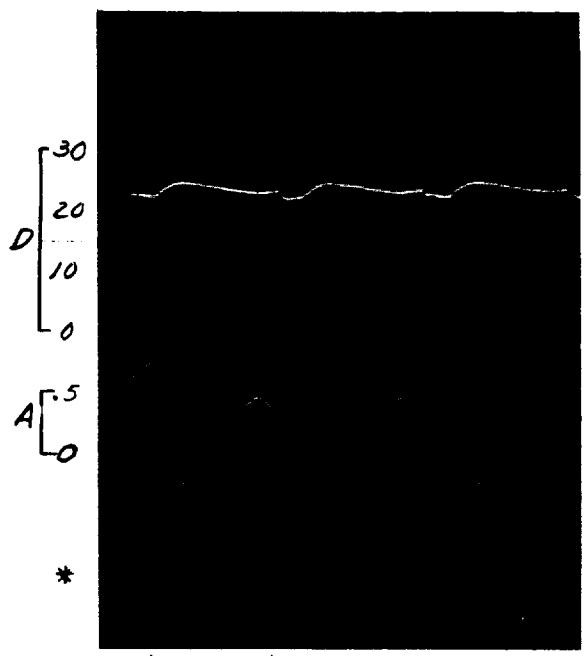
TRACE A +27V THRUST PHASE CURRENT TO ROLL ACTUATOR AMPL-AMPS  
TRACE C +22V BUS CURRENT - AMPS



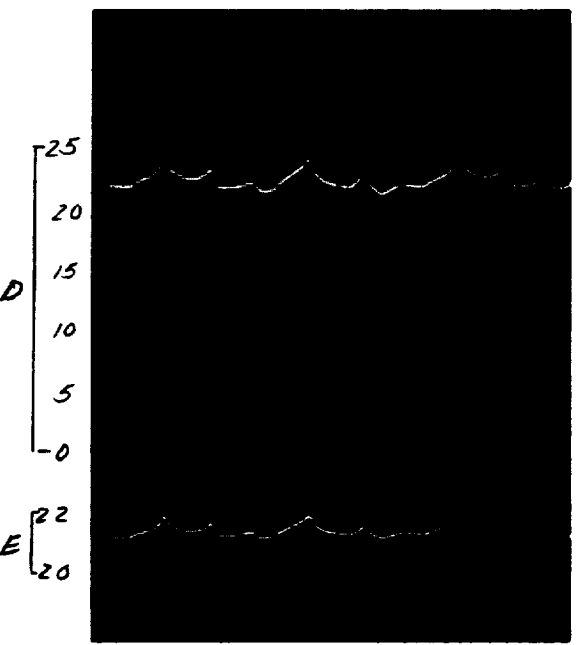
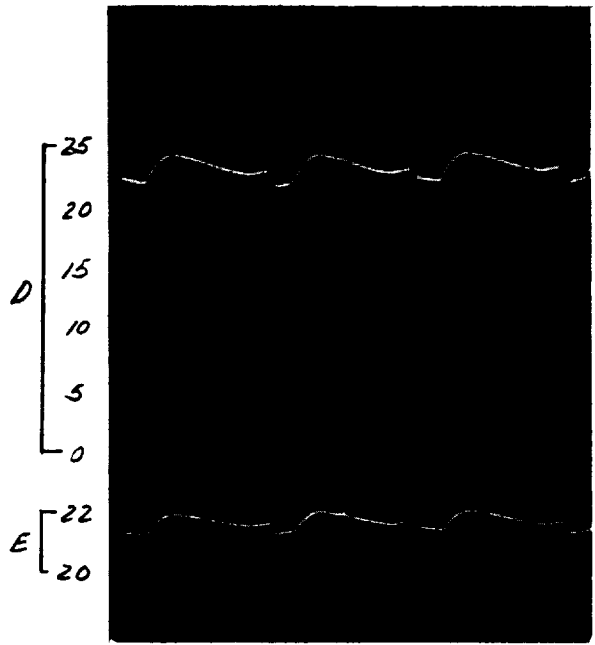
1. THRUST PHASE POWER ON  
2. STEP INPUT AT ROLL GYRO ERR.

68189-2-319

Figure 5.5-40 (continued). Current Waveforms



1 msec  
 1. THRUST PHASE POWER ON,  
 2. STEP INPUT AT ROLL GYRO ERROR.  
 NOTE \* ERRONEOUS CURRENT ZERO REFERENCE (INSTRUMENTATION)  
 TRACE D +27V THRUST PHASE VOLTAGE TO ROLL ACT AMPL-VOLTS  
 TRACE A +27V THRUST PHASE CURRENT TO ROLL ACT AMPL-AMPS



1. THRUST PHASE POWER ON,  
 2. STEP INPUT AT ROLL GYRO ERROR.  
 1. THRUST PHASE POWER ON,  
 2. ROLL ACTUATOR HARD OVER  
 TRACE D +27V THRUST PHASE VOLTAGE TO ROLL ACT AMPL } VOLTS  
 TRACE E +22V BUS VOLTAGE.

Figure 5.5-41. Voltage and Current Waveforms

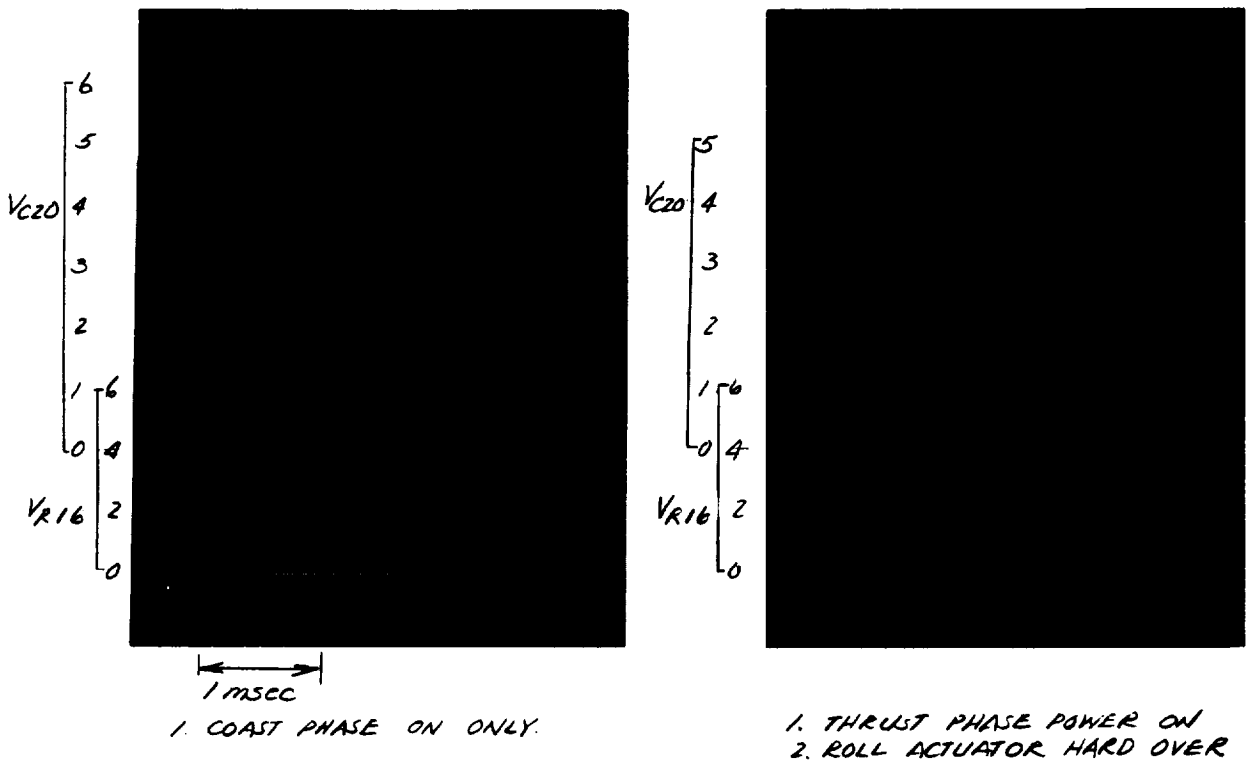


Figure 5.5-42. Voltage Waveforms -  $V_{CZO}$  and  $V_{R16}$

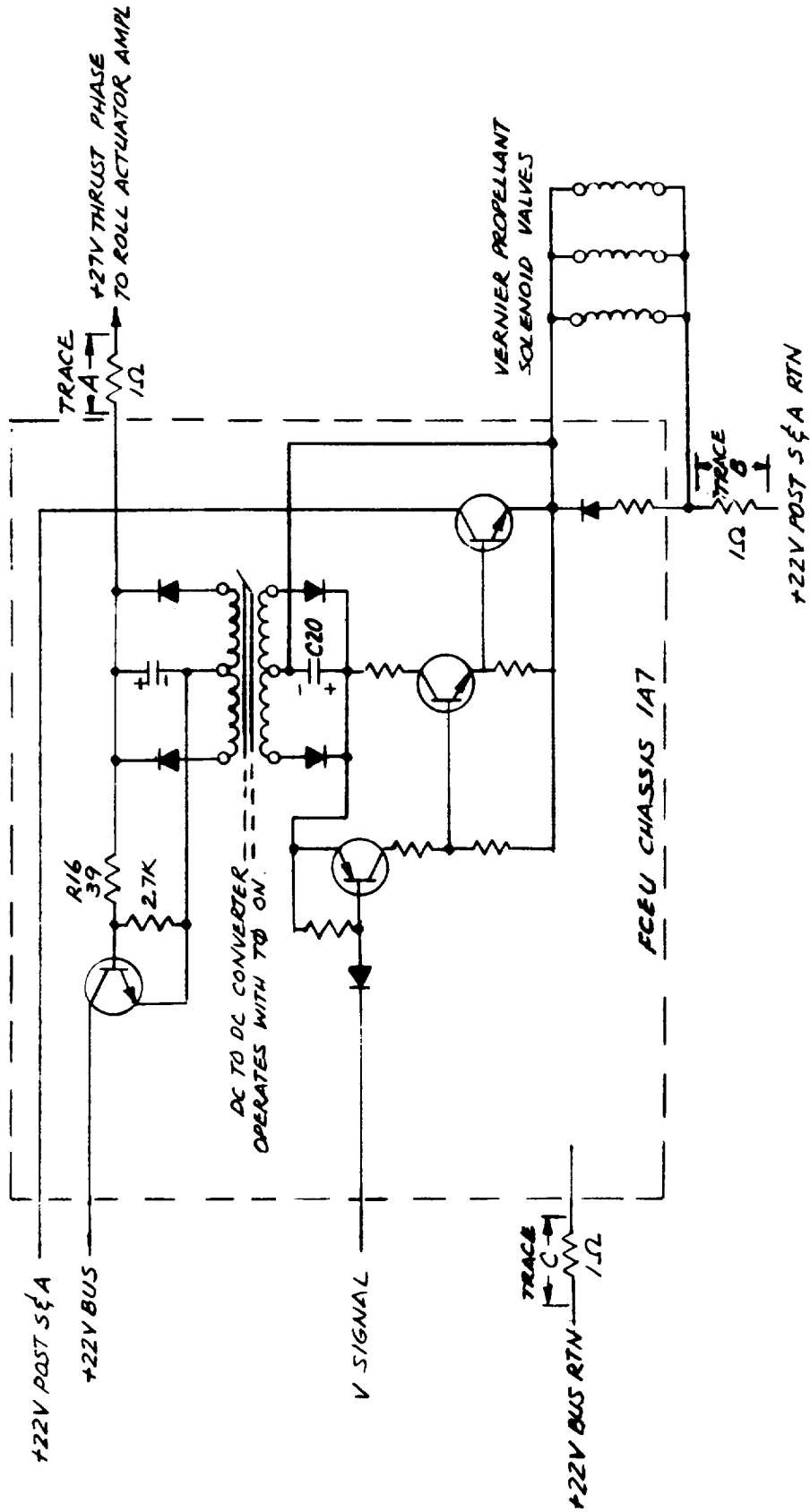


Figure 5.5-43. Vernier Engine Control Circuitry

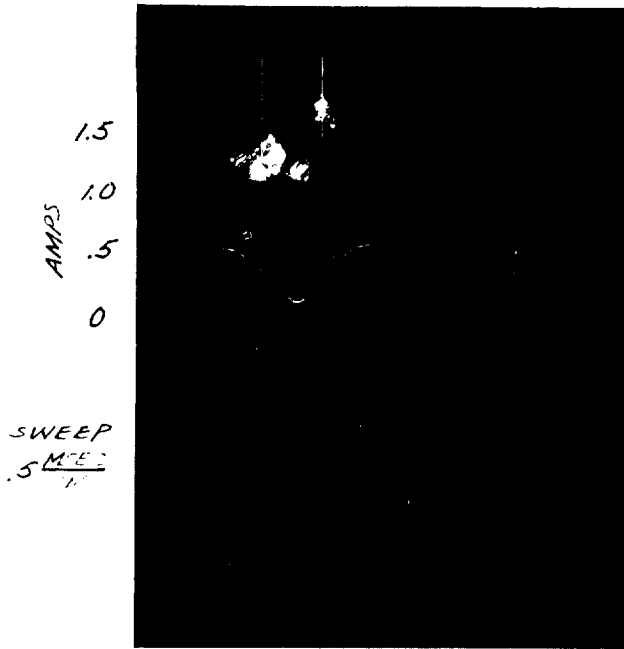


Fig. 1a. Roll Rate = 0  
Roll Actuator at Null.

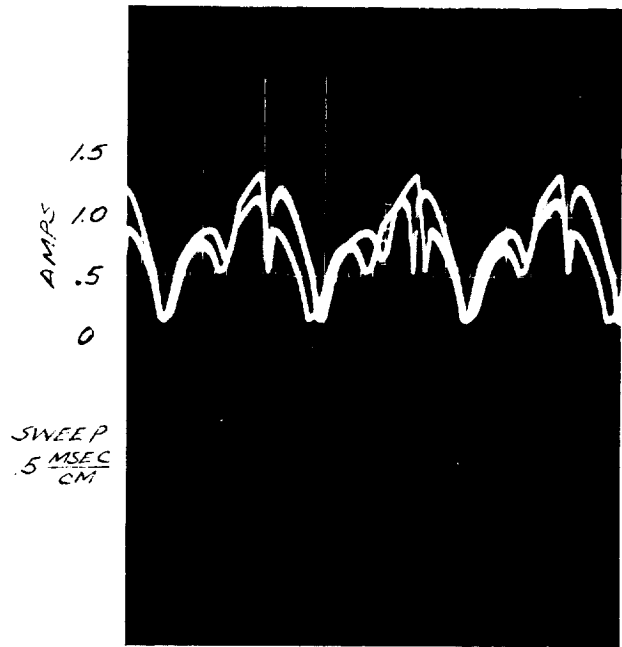


Fig. 1b Roll Rate  $\approx 0.66^\circ/\text{sec}$   
Roll Act. Resp.  $\approx 1.3^\circ/\text{sec}$



Fig. 1c Roll Rate  $\approx 1.16^\circ/\text{sec}$   
Roll Act. Resp.  $\approx 3.38^\circ/\text{sec}$

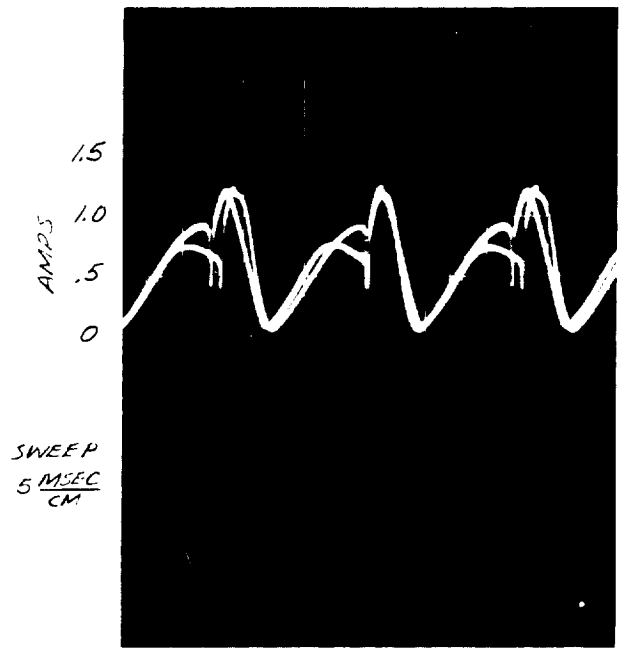


Fig. 1d Roll Accn  $\approx 1.59^\circ/\text{sec}^2$

Figure 5.5-44. 22 volt Thrust Phase Current Waveforms

that were obtained by monitoring on an oscilloscope the voltage across a 1-ohm resistor inserted in the 22-volt thrust phase return line at 1A7-H. Figure 5.5-45 is the brush recording of the roll precession command telemetry (roll gyro error) and the roll actuator position feedback telemetry signals. Numbers for the roll rates and roll acceleration were reduced from the brush recording. These data were used to isolate the unregulated 22-volt bus current due to the roll actuator from that of the vernier engine propellant valves, gas jets, and gyro heaters.

#### Dynamic Versus Static Calibration of Canopus Sensor Mapping Telemetry Signal

In order to determine more effectively the calibration of the Canopus sensor star mapping channel in space, the sensor mapping signal was measured for both static and dynamic conditions. Comparisons of the mapping circuit telemetry output under both conditions for 0.67X Canopus (lower lockon threshold), 1.0X Canopus, and 1.5X Canopus (upper lockon threshold) are shown in Figure 5.5-46. The static calibration corresponds to what is observed in a mission during the gyro drift check while the dynamic calibration, which was done at an equivalent spacecraft roll rate of 0.5 deg/sec, corresponds to what is observed during the normal star mapping phase of the mission. These data were used in conjunction with SC-1 and SC-2 star mapping data to more precisely establish the calibration of the sensor in space, as discussed in subsection 5.5.4.4.

#### Computer Simulations

Analog and digital computer programs have been used to simulate the midcourse firing.\* Some of the simulation was done with the SC-1 ZAP electronics FCEU as part of the closed loop. The spacecraft electronics contain many large signal nonlinear effects that become important for operation when the gyros and accelerometer are hard over.

The best match with SC-2 telemetry data over the first 2 seconds was obtained using a mixed simulation of SC-1 ZAP electronics and analog computer. The best data match over a 25-second period was obtained with the all-analog computer simulation. The better long-term data match was obtained using all analog by compensating for the differences in the test electronics and that of SC-2. These data assumed small engine startup delays and initial gyro angles, as well as no thrust from engine 3.

The first simulation attempts were closed loop (analog simulation of electronics and equations of motion). When the result showed discrepancies with the telemetry data, representation of the nonlinearities in the electronics was suspect. While these were being measured, the simulation continued open loop with programmed thrusts acting into the equations of motion.

---

\*See Reference 19.

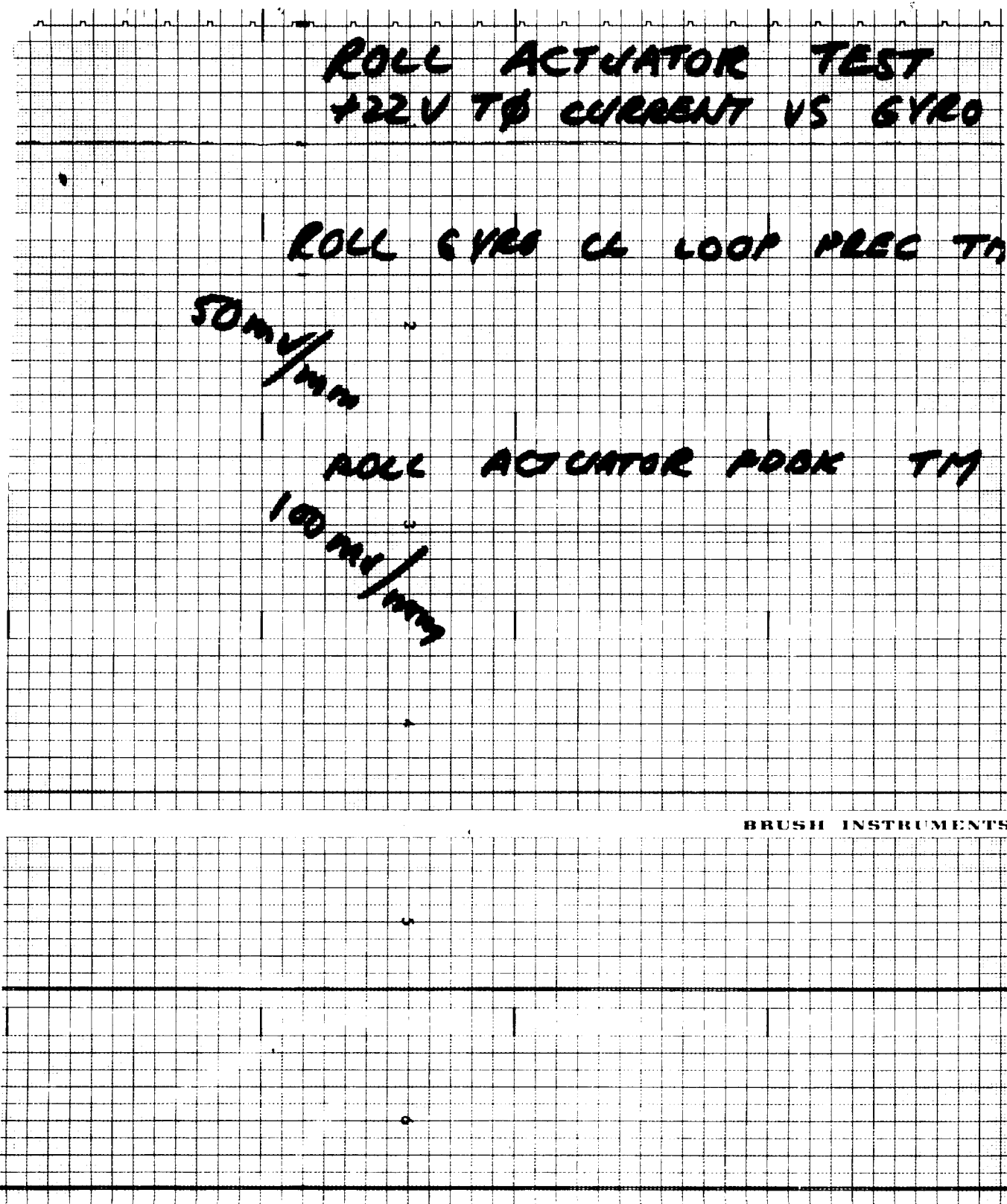
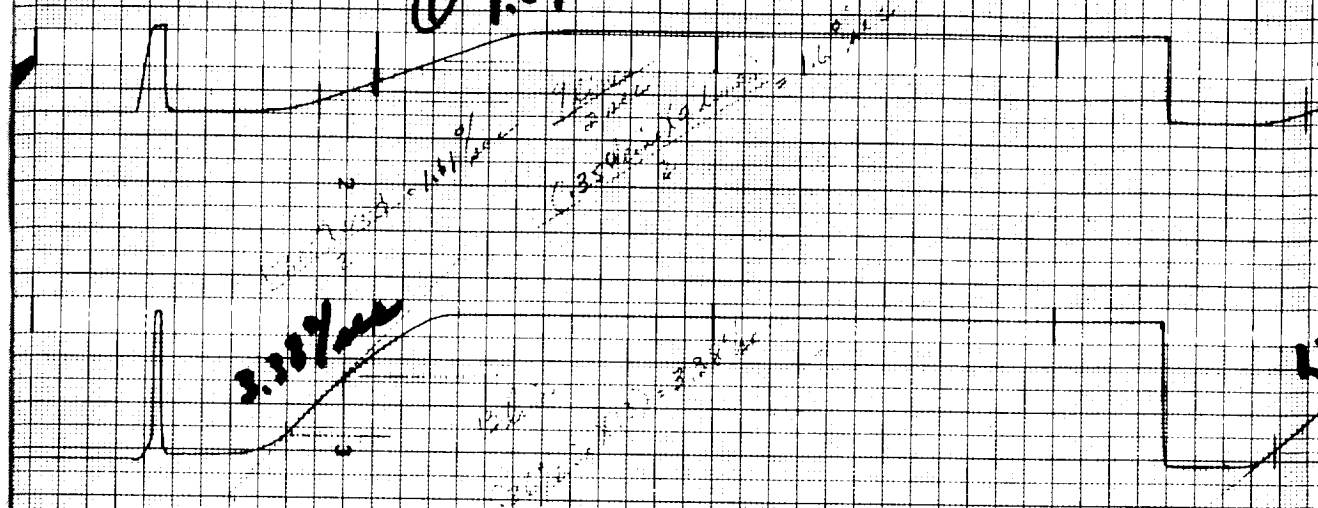


Figure 5.5-45. Roll Actuator Test Results





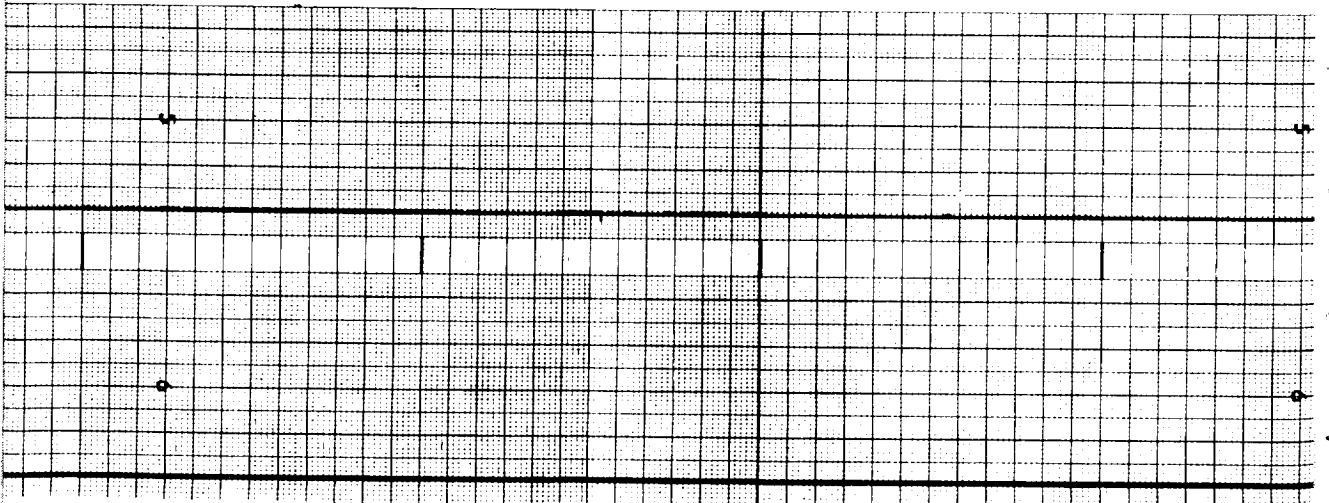
RATES SC-1 RAP 11-11-66  
P-2 IRU  
① 1.5%  
② 1.5%



DIVISION OF CLEVITE CORPORATION CLEVELAND OHIO PRINTED IN U.S.A.

5.5-145B  
FOLDOUT FRAME 2

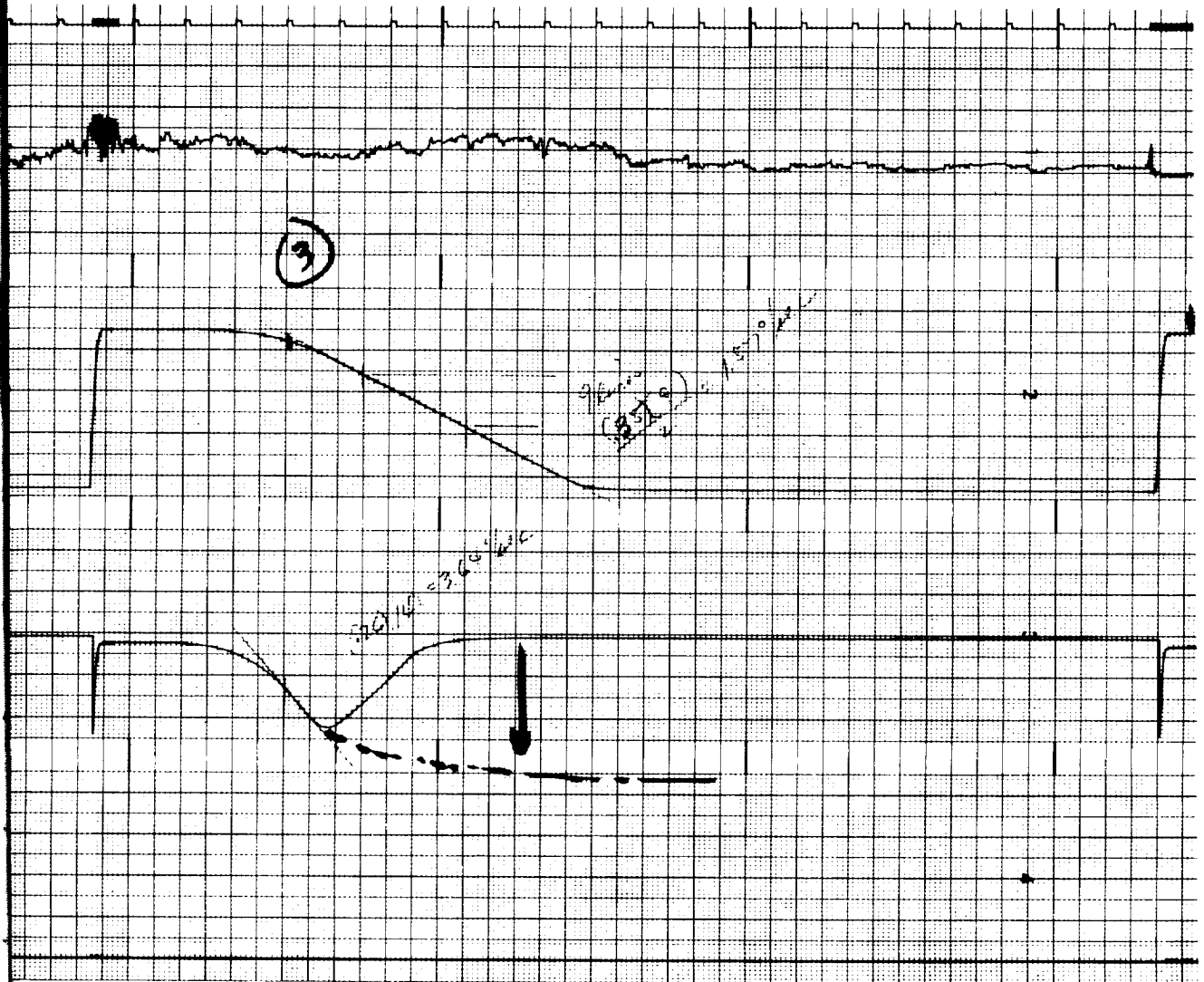




FOLDOUT FRAME 3

5.5-145 c





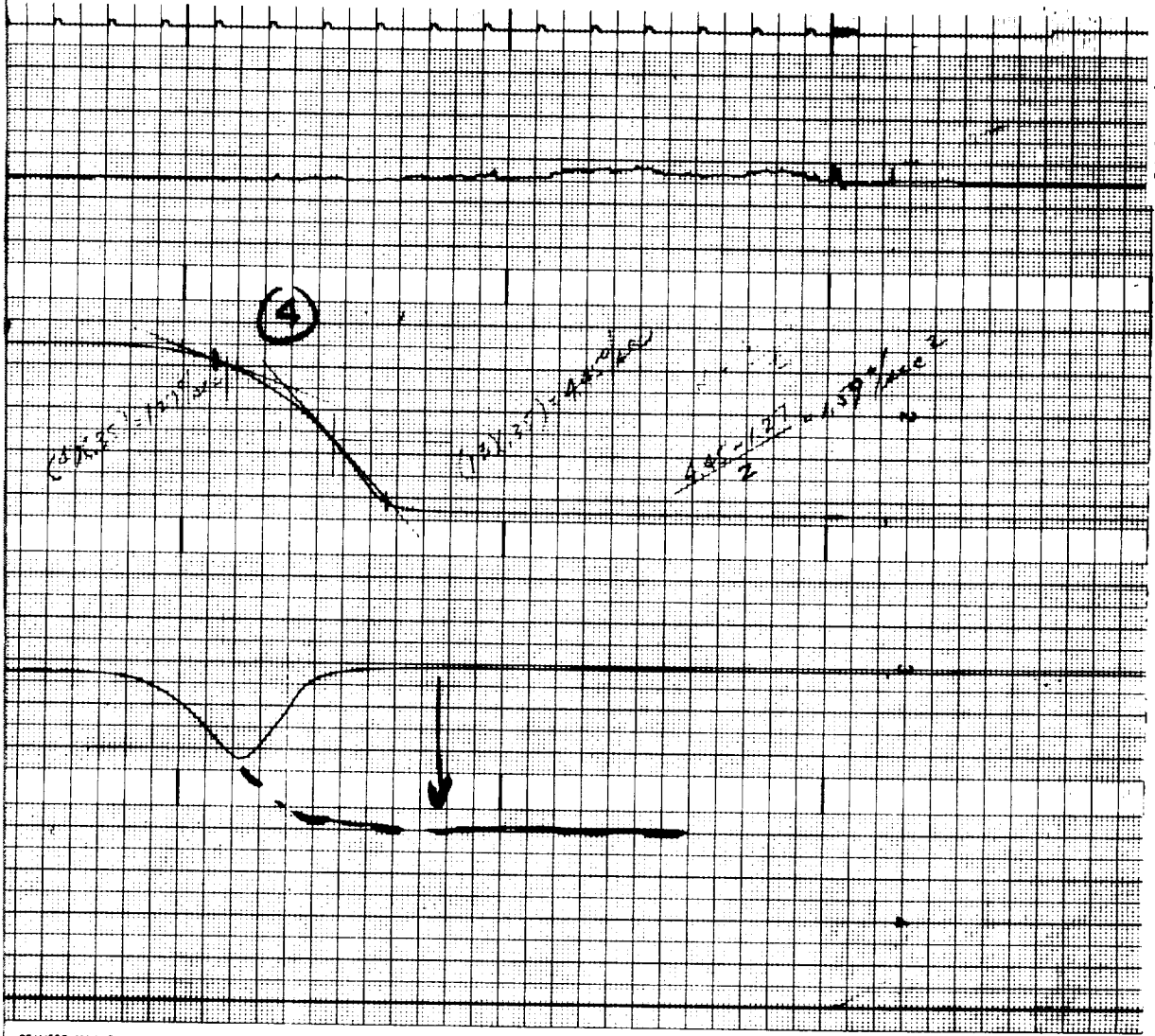
BRUSH INSTRUMENTS

DIVISION OF CLEVELAND CORPORATION

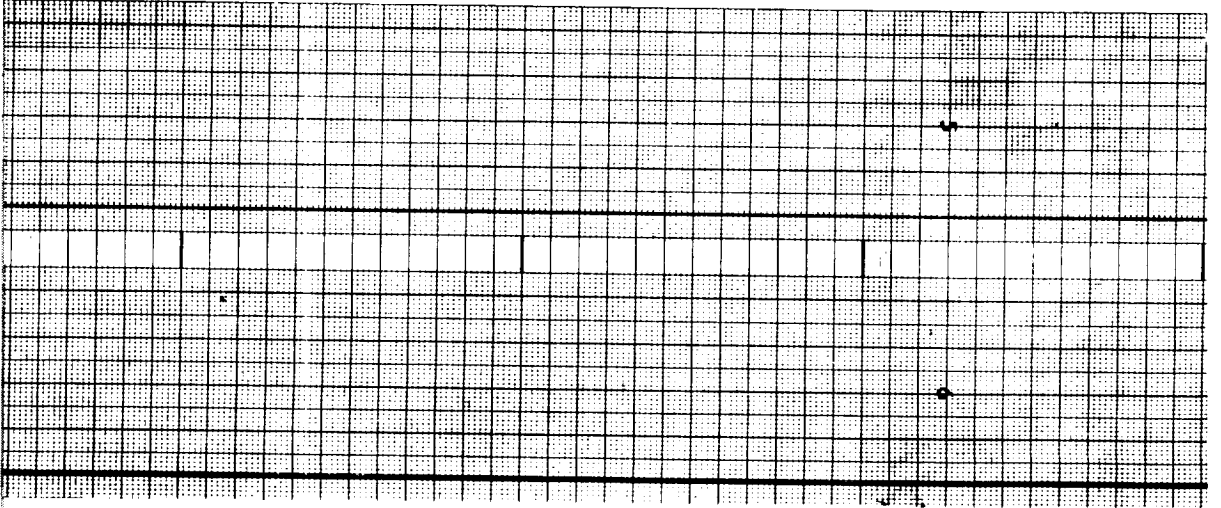
CLEVELAND, OHIO

FOLDOUT FRAME 4 S.S-145 D





PRINTED IN U.S.A.

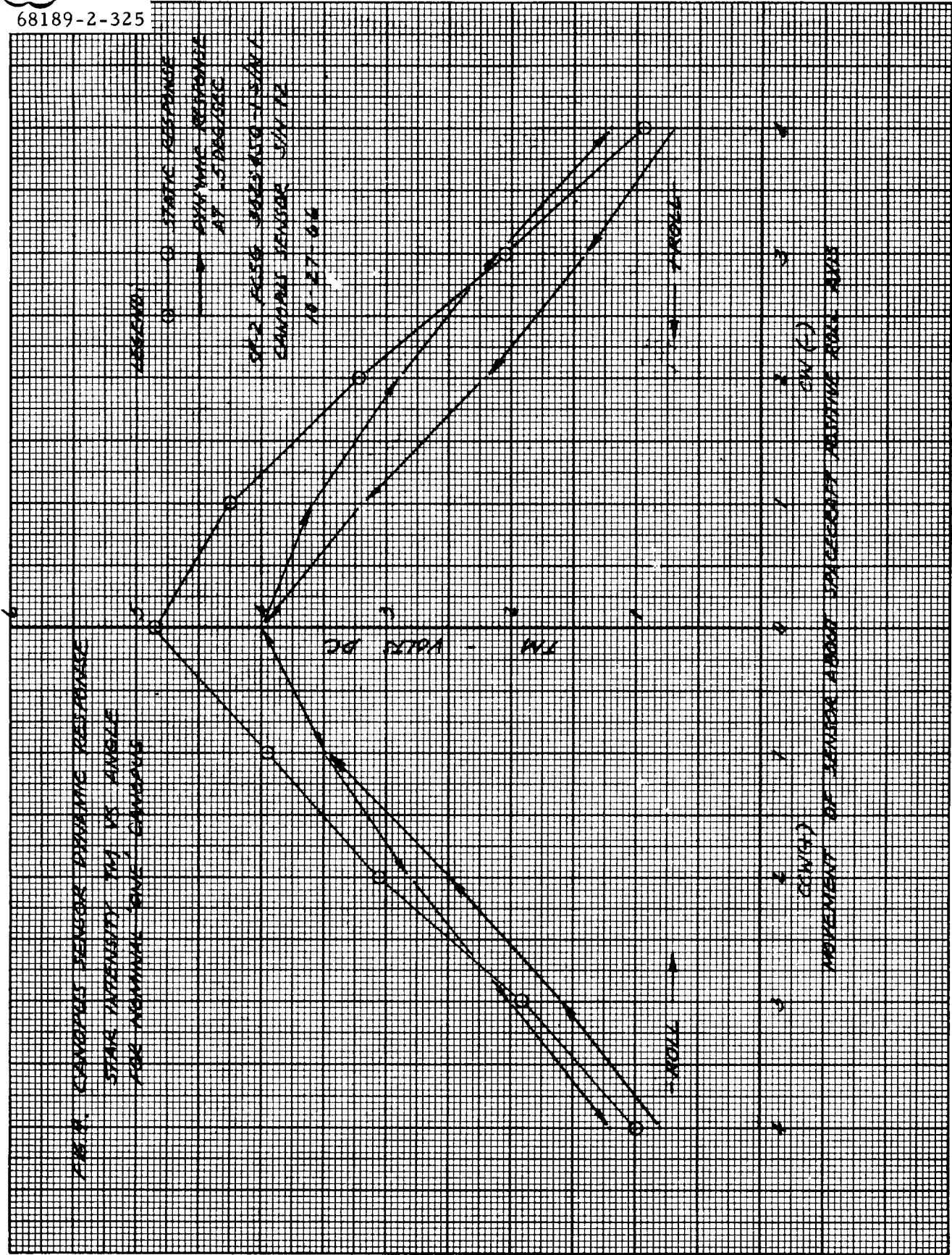


FOLDOUT FRAME 5  
5.5-145 E



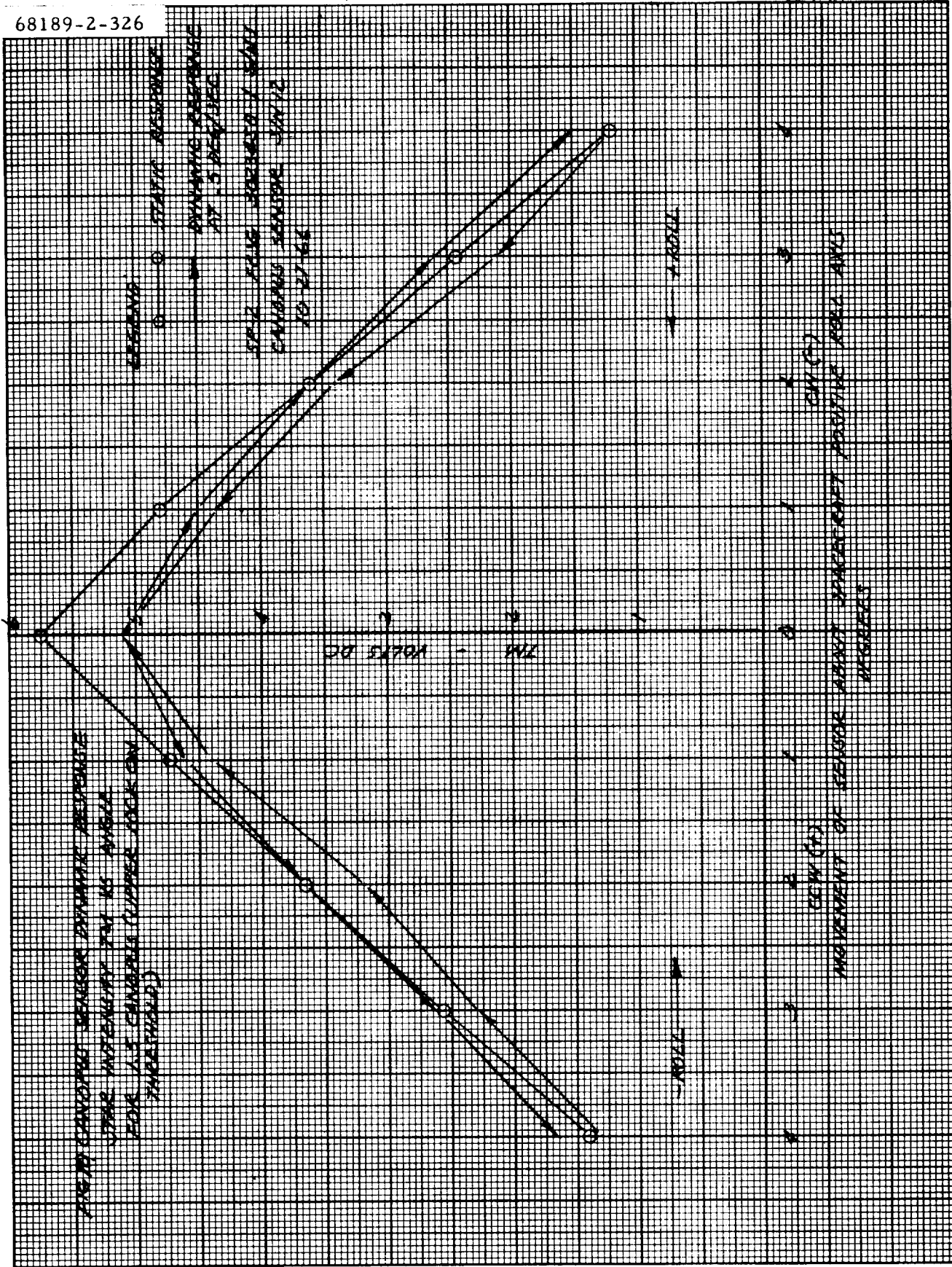


68189-2-325



a) Nominal I Canopus

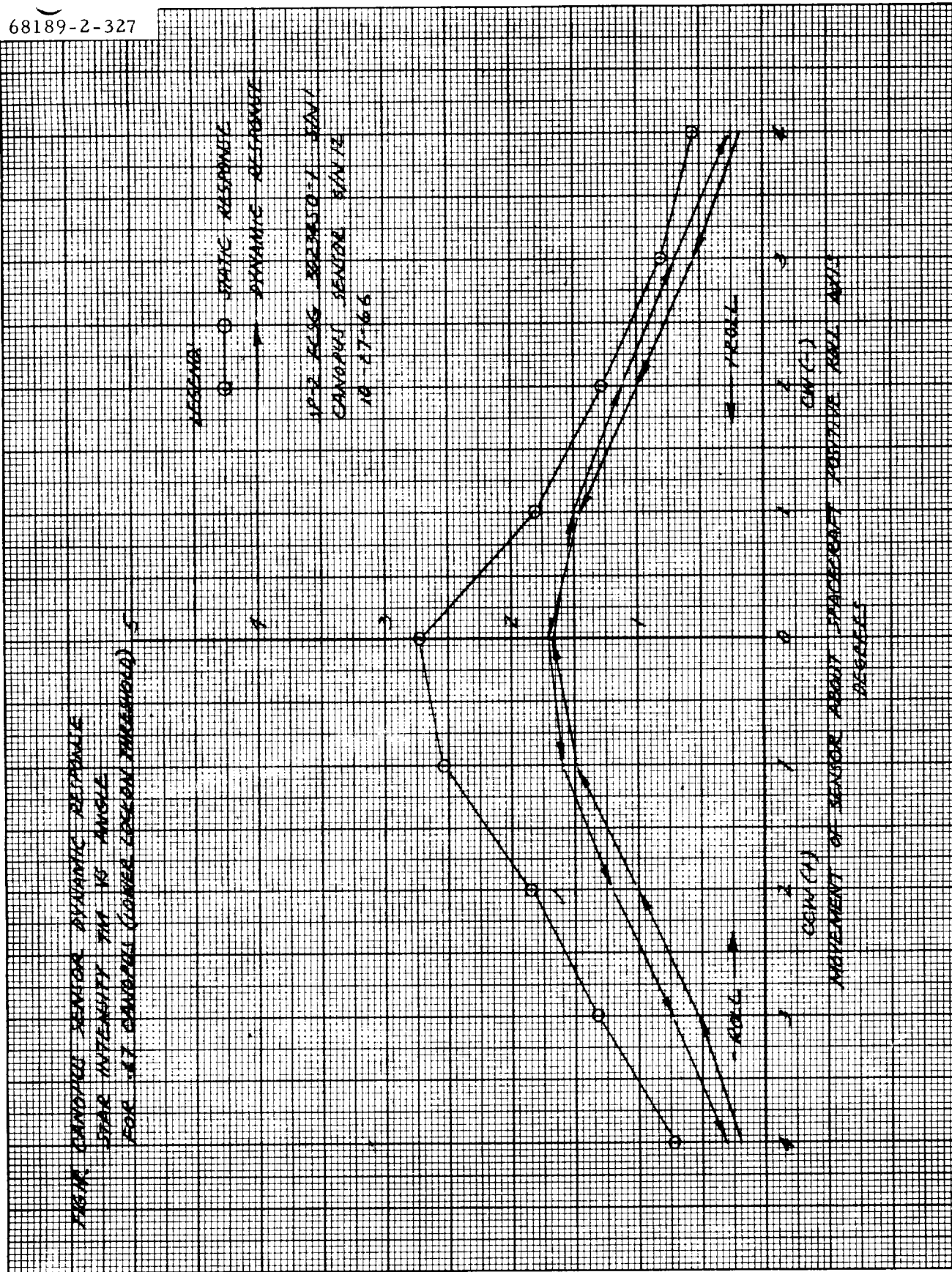
Figure 5.5-46. Canopus Sensor Dynamic Response Star Intensity Telemetry Versus Angle for Canopus



b) 1.5 Canopus

Lower lockon threshold

Figure 5.5-46 (continued). Canopus Sensor Dynamic Response Star Intensity Telemetry Versus Angle for Canopus



c) 0.67 Canopus

Lower lockon threshold

Figure 5.5-46 (continued). Canopus Sensor Dynamic Response Star Intensity Telemetry Versus Angle for Canopus

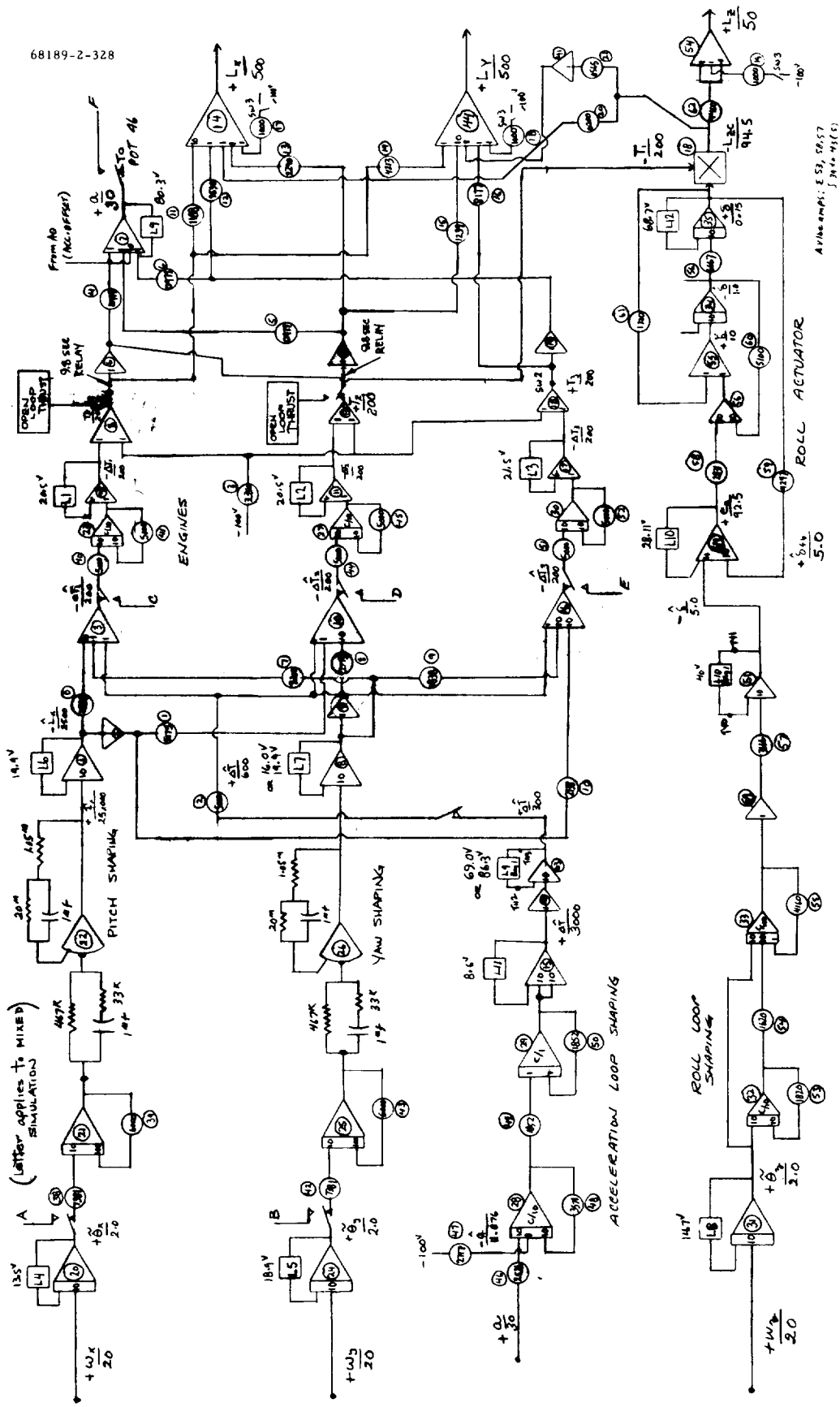
Figures 5.5-47 and 5.5-48 show the details of this, and Figure 5.5-49 is representative of the results. Spacecraft motion is duplicated well, yielding a nutation period of 14.4 seconds and a total angular rate of 417 deg/sec, which is very close to the observed spacecraft data of 13.0 seconds and 448 deg/sec. However, the initial pitch and yaw gyro transients produced were faster than observed in flight. The roll gyro trace provides a good match, peaking at 1.5 degrees and crossing over at 3.5 seconds. This simulation did not incorporate any special large-signal electronics features. The gyro electronics amplifier and demodulation have saturations and gain changes well below the level of the gyro stops which attenuated actual telemetry signals.

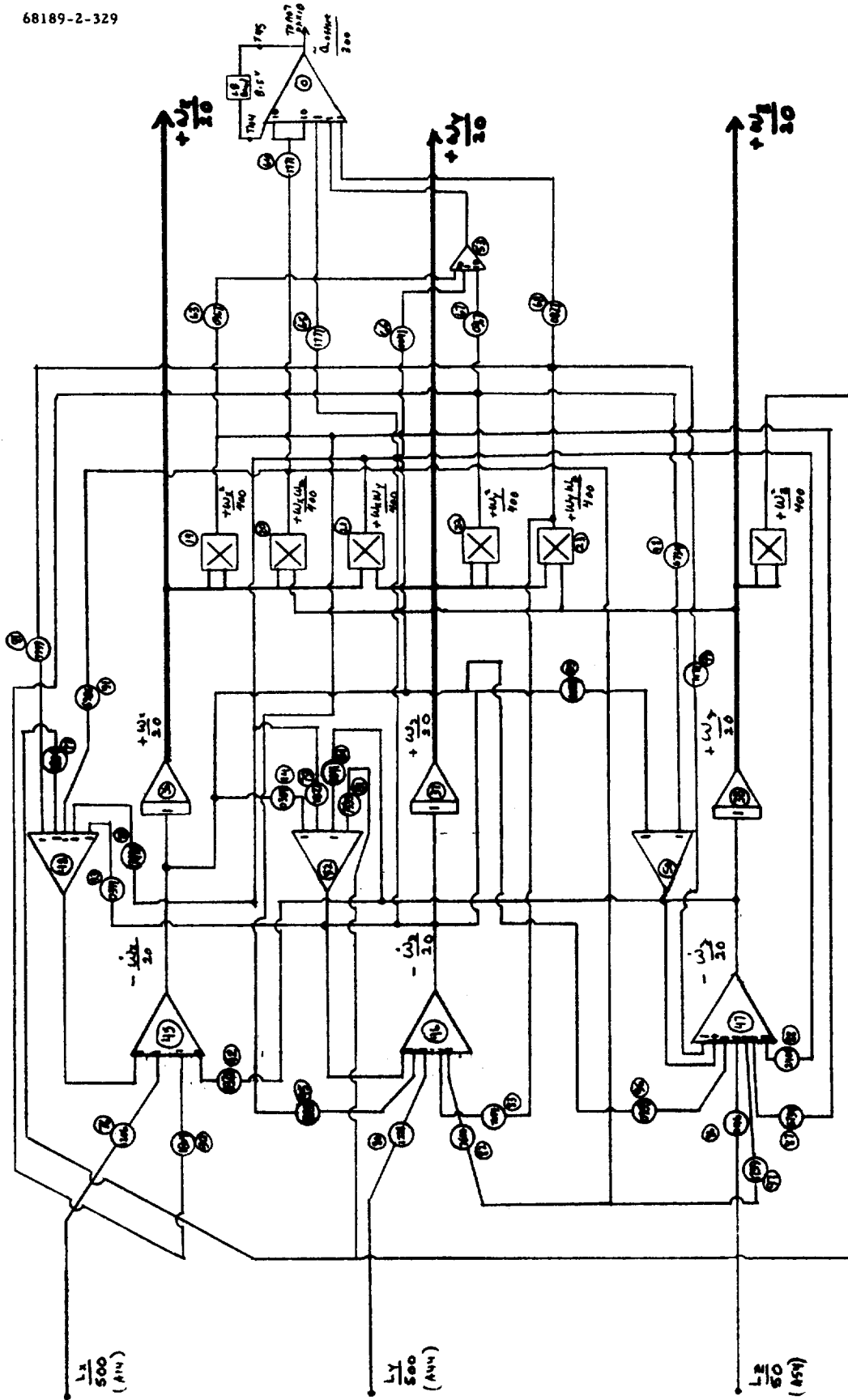
Mixed Simulation. Tests to determine the characteristics of the electronics showed complicated saturation nonlinearities and transient characteristics which would require a vast amount of equipment to duplicate on an all-analog simulation. A mixed simulation incorporating all suspect parts of the electronics, as shown in Figure 5.5-50, was set up. The exact duplication of SC-2 electronics was not possible since dynamic ranges are required only to be greater than some minimum level, and thus are not controlled. The use of actual hardware command switching was also made possible with this setup. By assuming small engine delays and gyro initial conditions, Figure 5.5-51 was obtained. It is the best combination of engine delays and initial gyro angles within known tolerances and knowledge of SC-2 electronics. Figure 5.5-52 also is derived from the mixed simulation, but has slightly different engine delay and somewhat different initial conditions.

The best match was obtained with initial gyro angles in a direction to reduce startup thrust, with engine 2 ignition lagging engine 1. The thrust traces show the same form as that of the SC-2 data, but engine 2 is higher than indicated by the telemetry. The gyro traces match well with flight data. At 6 seconds, the yaw acceleration changes sign, and there is a thrust dip due to the acceleration loop. This did not occur in the flight data, and is the result in the thrust profile differences at the beginning. However, the period of final oscillation and total angular rate is the same as SC-2, indicating the integral of thrust is correct. The roll gyro and roll actuator angles match well with the flight data.

Analog Only. With the knowledge gained by using the mixed simulation, a second all-analog computer simulation was attempted. However, the spacecraft gyro amplifier and demodulator were used in the recording of the gyro traces, as shown in Figure 5.5-48. A passive network was used for the attitude loop shaping. The best long-term results were obtained from this setup. The period of nutation was 13 seconds, and the angular rate was 432 deg/sec. The roll gyro and actuator are very close to an exact match. Figure 5.5-53 shows the initial transient, and Figure 5.5-54 shows the long-term results. Figure 5.5-55 includes vehicle angular rates to detail the motion.

Thus, the present computer model of spacecraft and flight control dynamics provides a close match with observed SC-2 behavior under the assumption that engine 3 produced no thrust.





110ms, 6 divs

Figure 5.5-48. Moment Equation Simulation

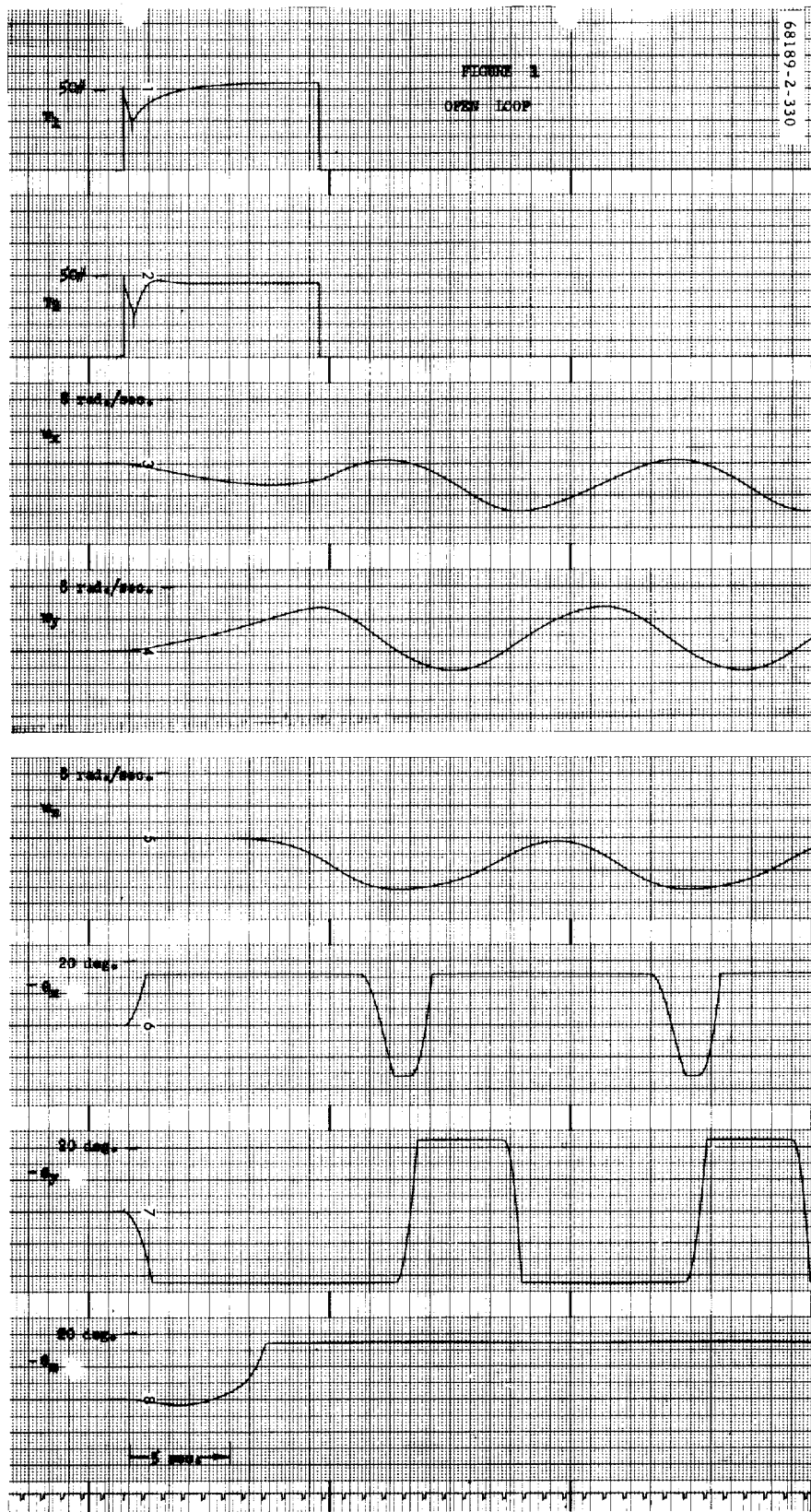
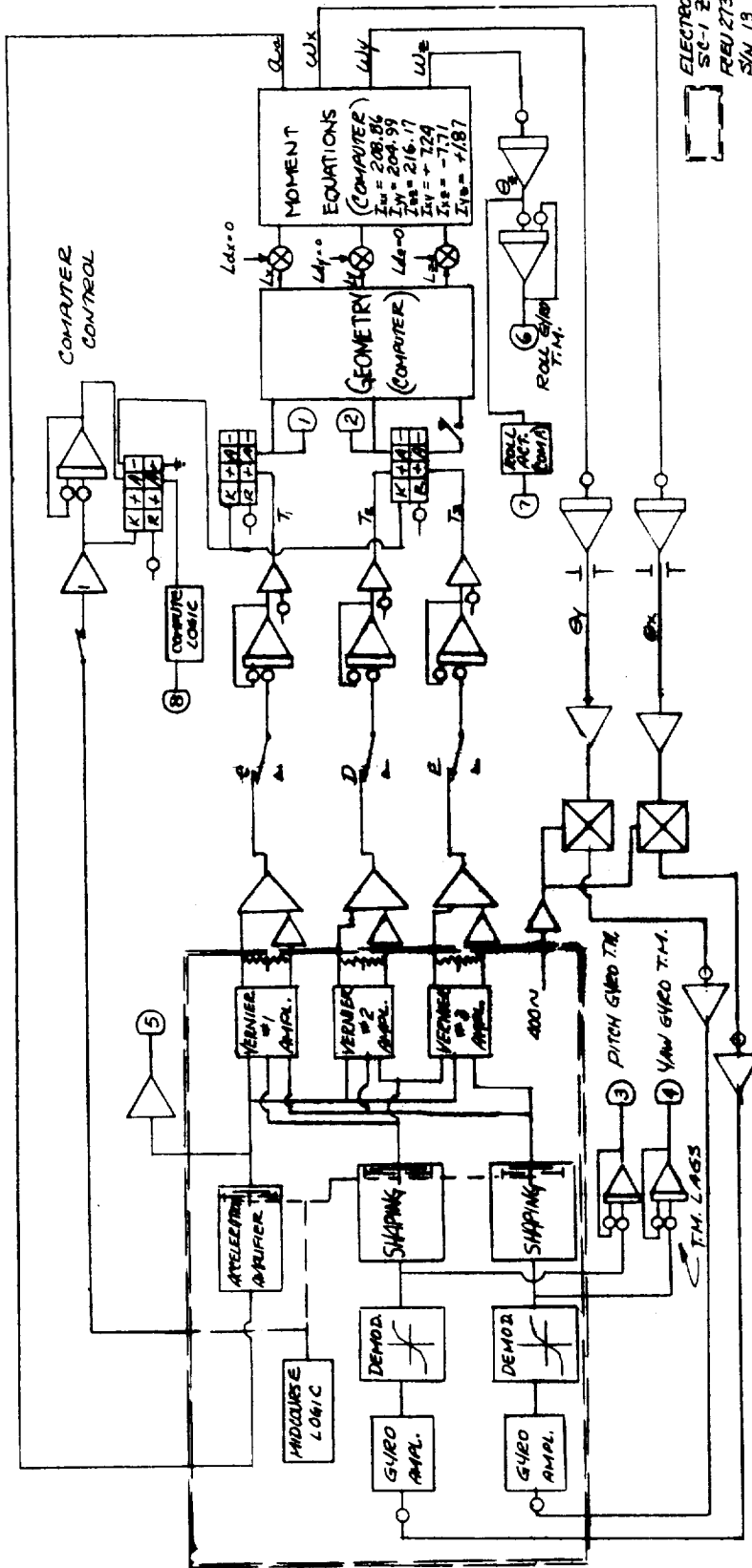


Figure 5.5-49. Open Loop Simulation Results



ELECTRONICS  
SC-1 ZAP  
REV. 2731006  
5/19

Figure 5.5-50. Mixed Simulation Functional Diagram





Digital Results. The analog computer simulation was verified with an independent check by the Surveyor vernier-phase mimic digital simulation. The results of this check are shown in Figures 5.5-56 through 5.5-61 which compare with Figure 5.5-53. These results provide an exact match with the analog computer results and the flight data.

#### 5.5.4.12 Total Nitrogen Gas Consumption

The expected nominal value of nitrogen gas consumption prior to premidcourse attitude maneuvers (Reference 4), was 0.182 pound. The estimated amount consumed during the mission was 0.08 pound. The difference is within the accuracy of the chart (Figure 5.5-62) used to measure gas weight. Table 5.5-23 presents nitrogen usage versus significant mission events.

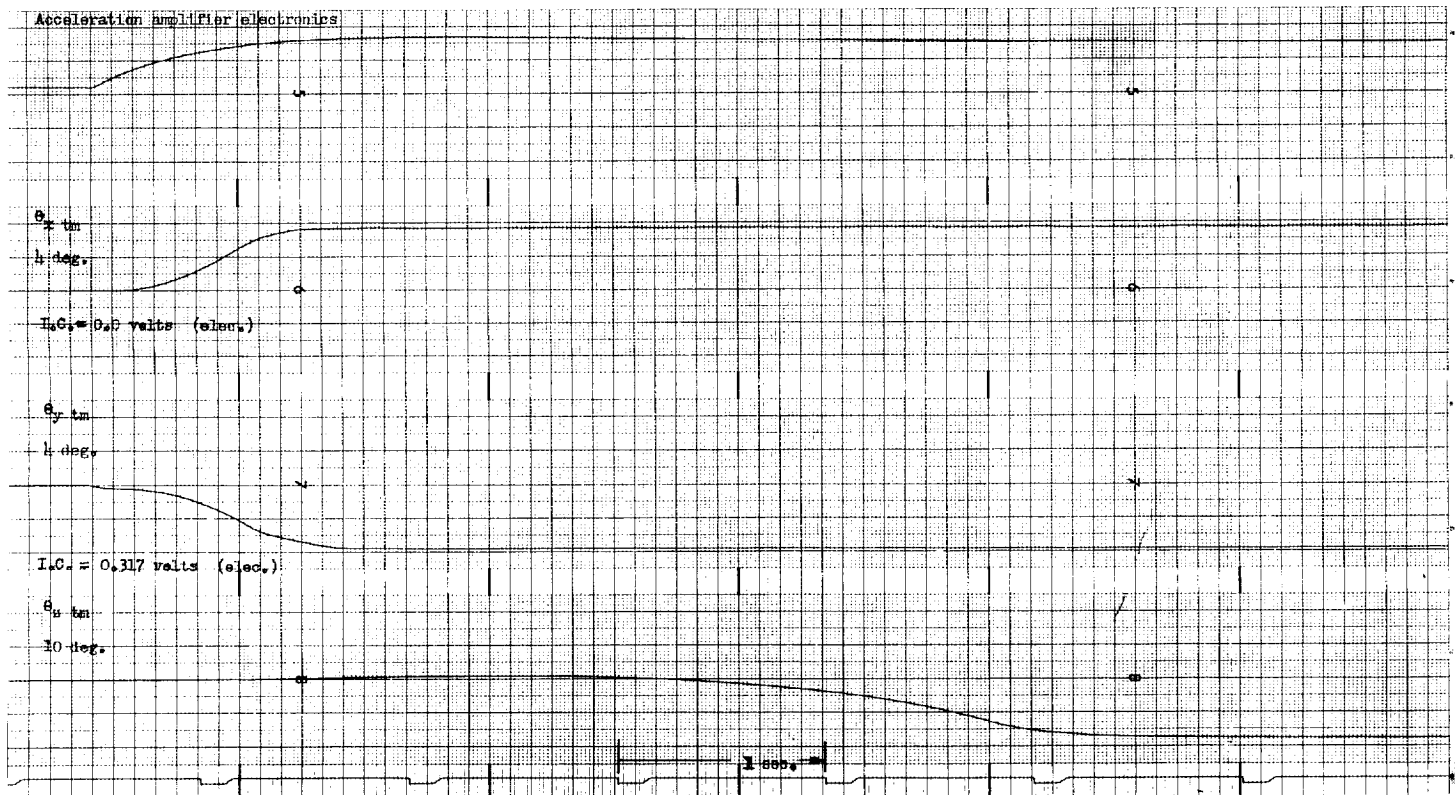
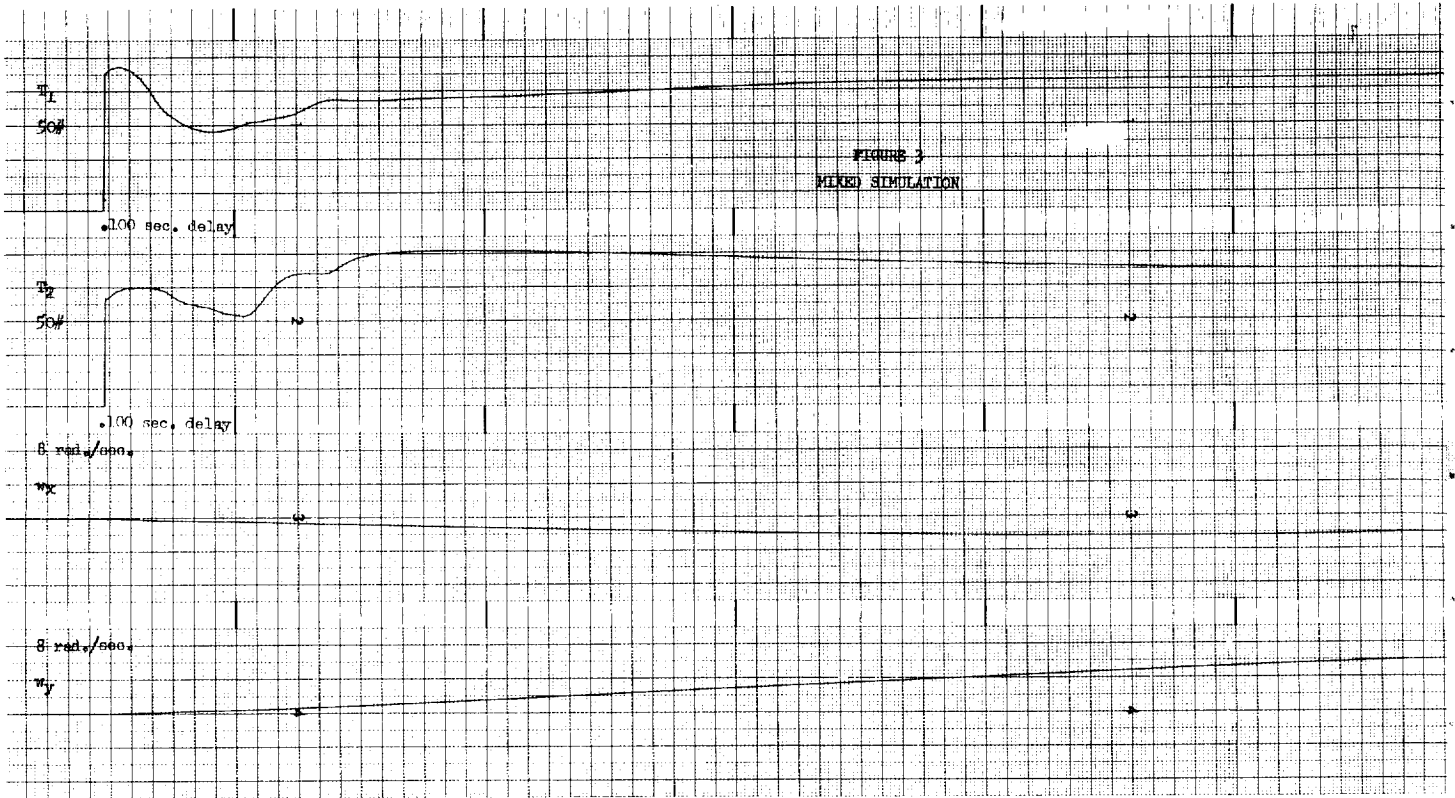
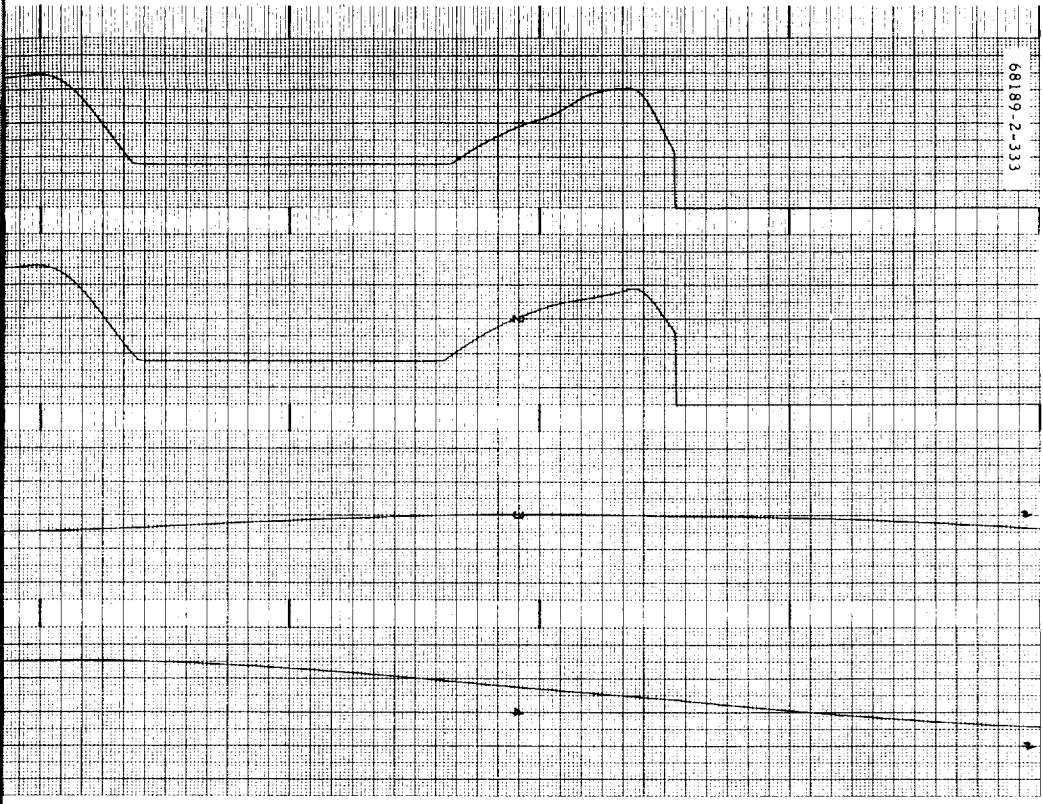


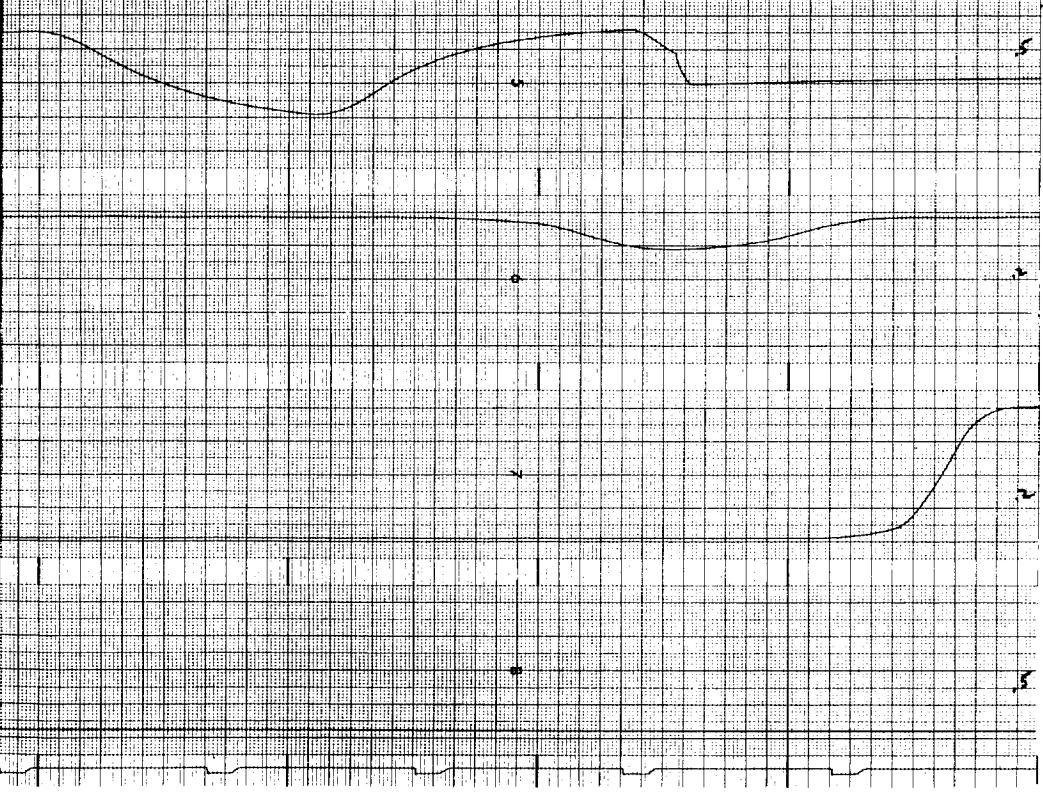
Figure 5.5-52. Mixed Simulation Results: 0.1 second Delay on T1



68189-2-333



BRUSH INSTRUMENTS DIVISION OF CLEVELAND CORPORATION CLEVELAND, OHIO PRINTED IN U.S.A.



FOLDOUT FRAME 2

5.5-157A





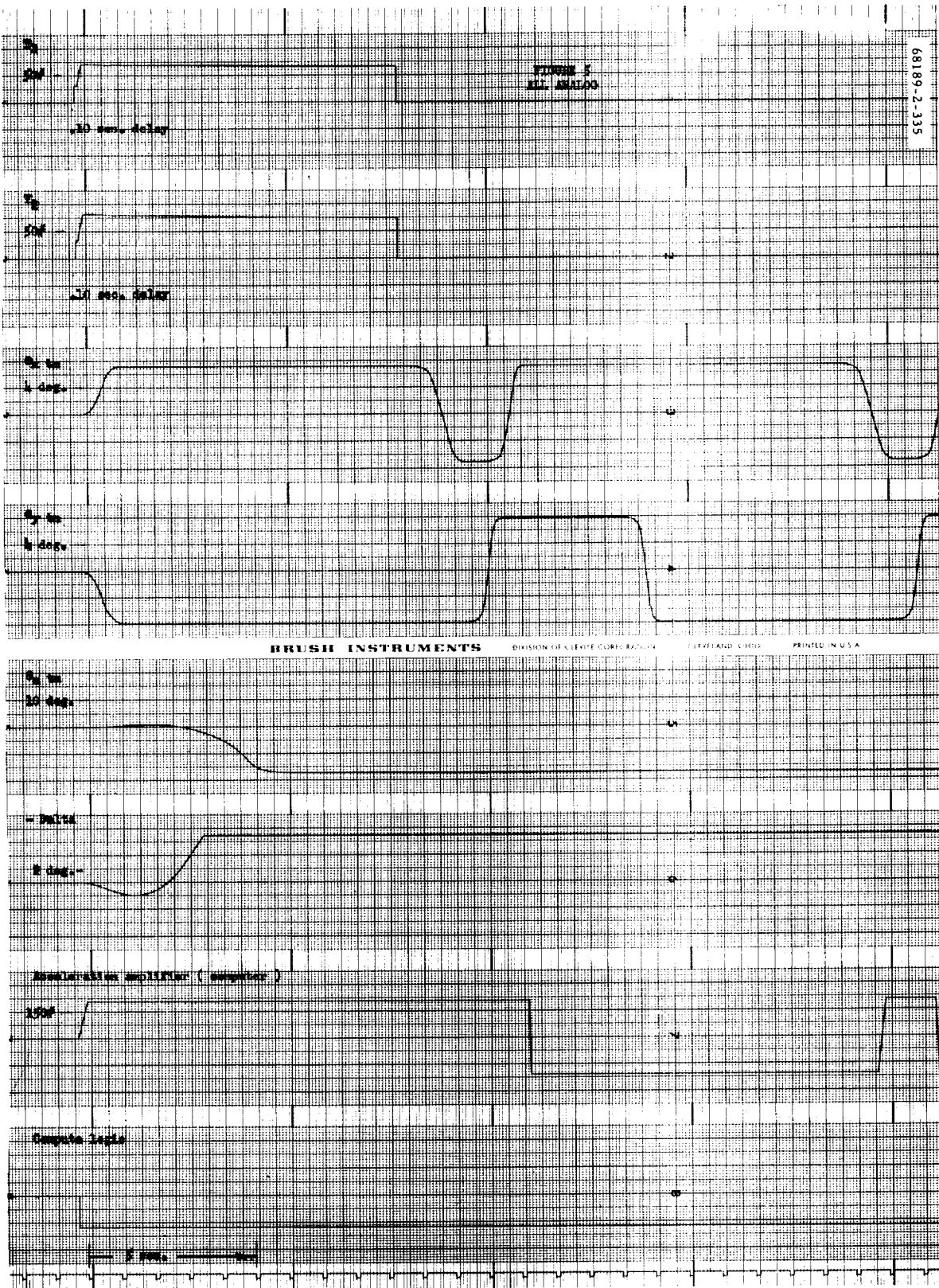


Figure 5.5-54. Final All-Analog Simulation: Long-Term Results



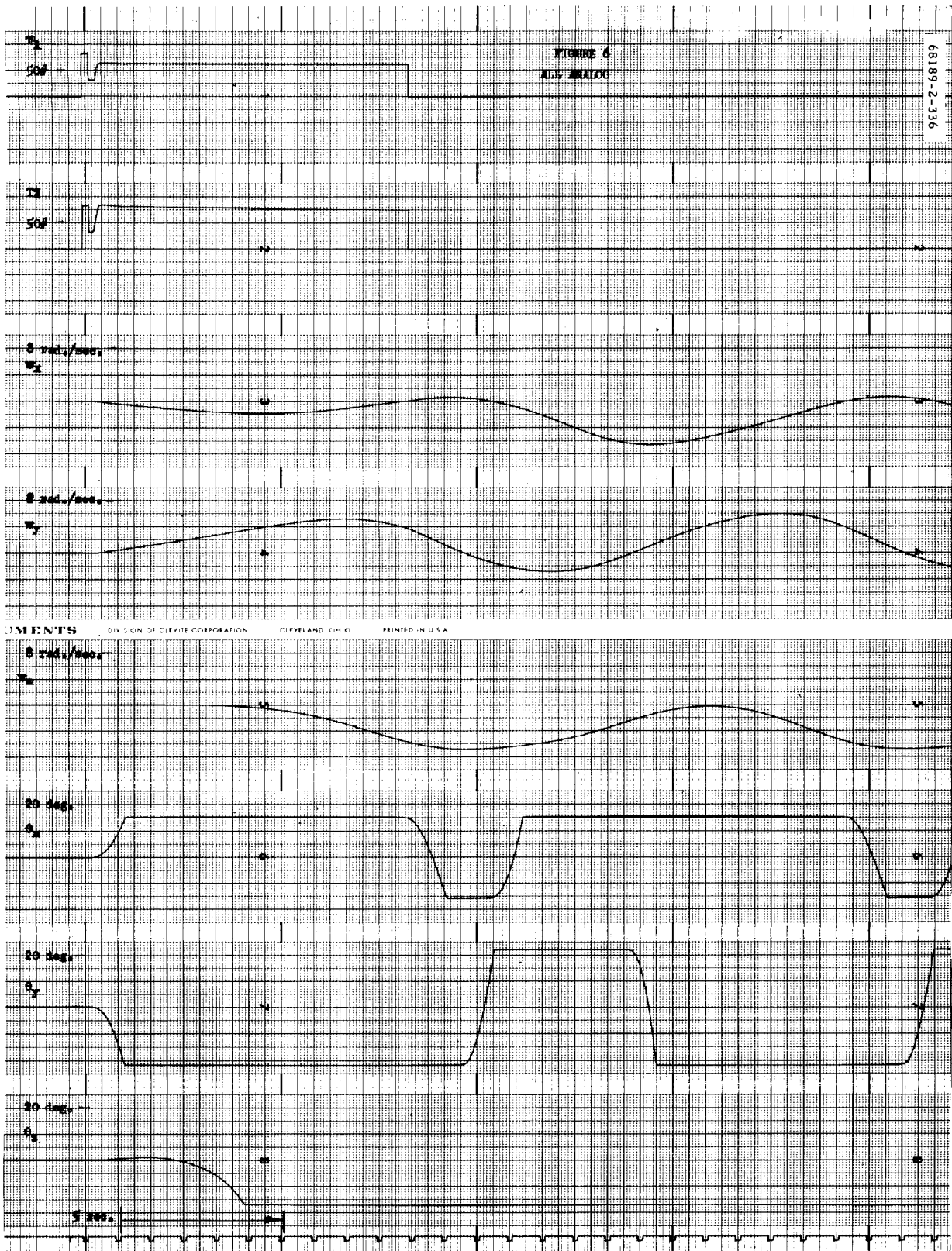


Figure 5.5-55. Final All-Analog Simulation Results: Vehicle Angular Rates

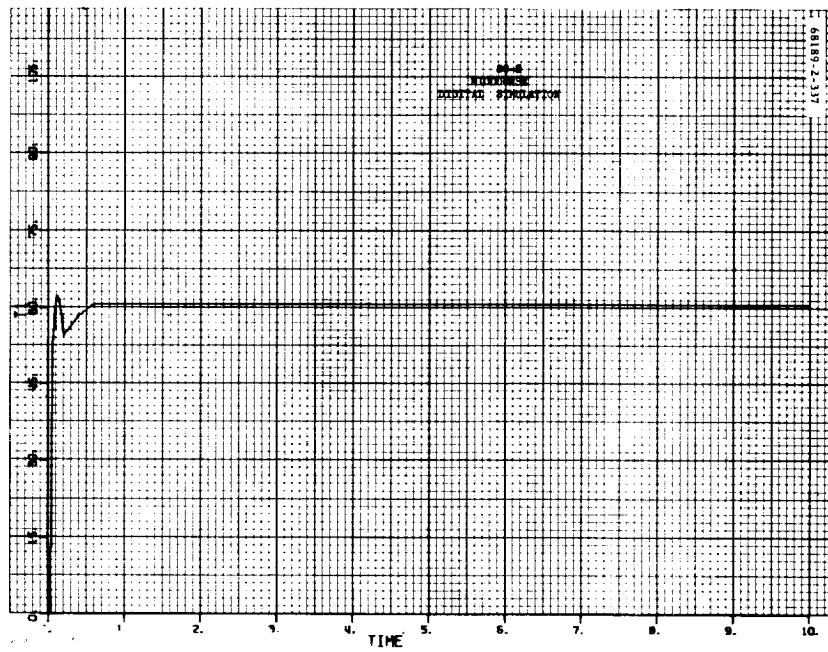


Figure 5.5-56. Digital Simulation: Thrust Command T1

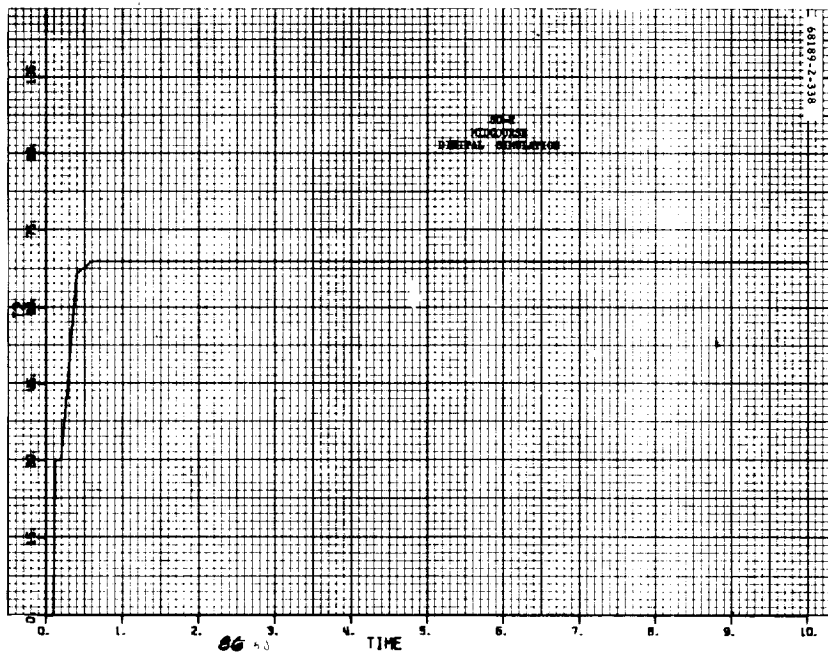


Figure 5.5-57. Digital Simulation: Thrust Command T2

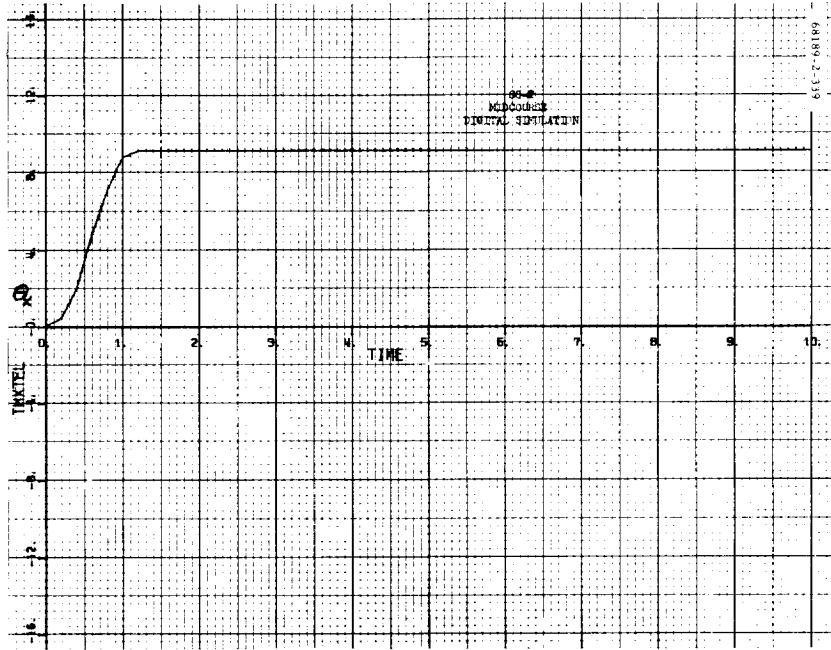


Figure 5.5-58. Digital Simulation:  $\theta_x$

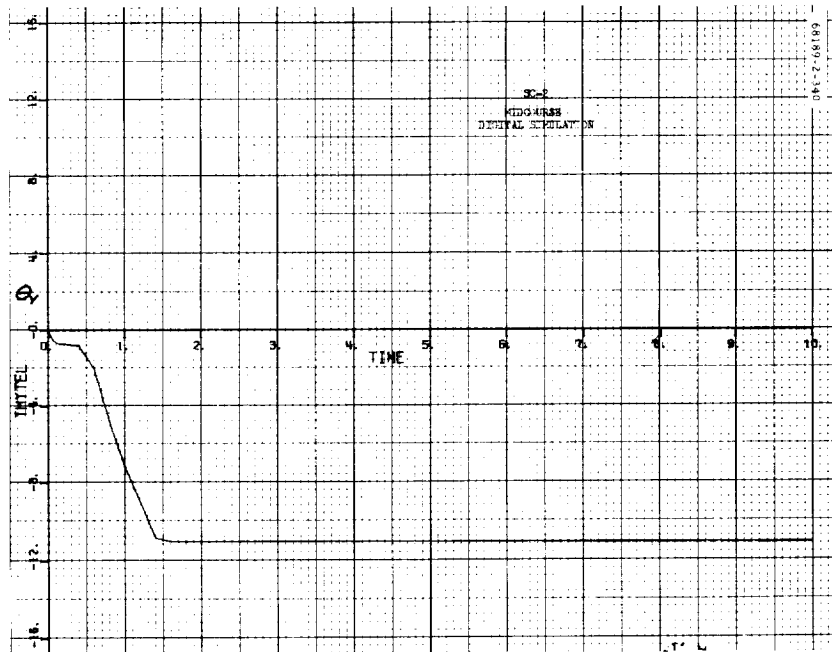


Figure 5.5-59. Digital Simulation:  $\theta_y$

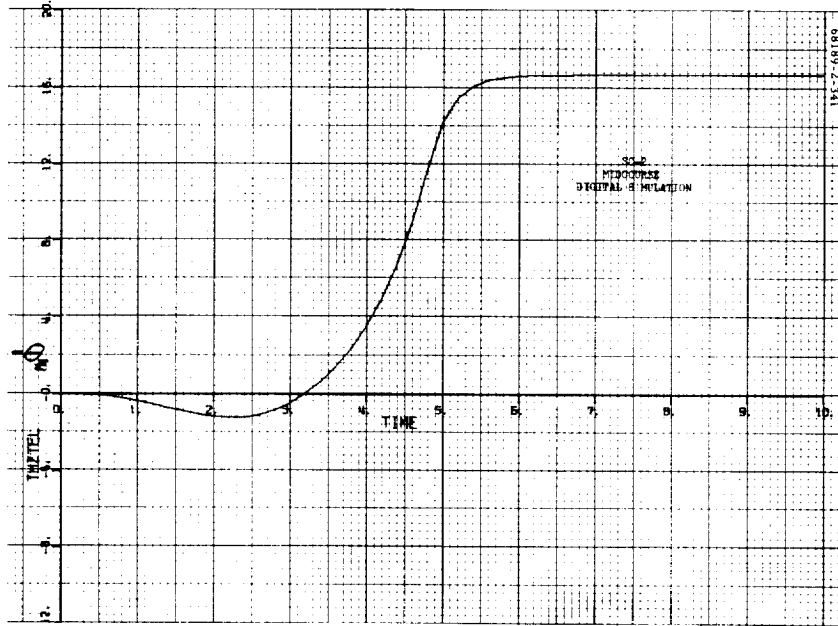


Figure 5.5-60. Digital Simulation:  $-\theta_z$

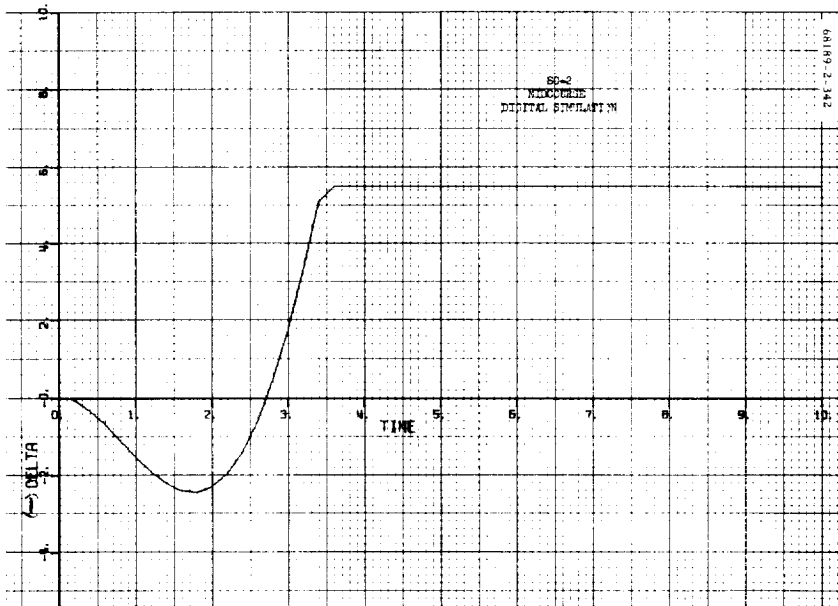


Figure 5.5-61. Digital Simulation:  $-\Delta$

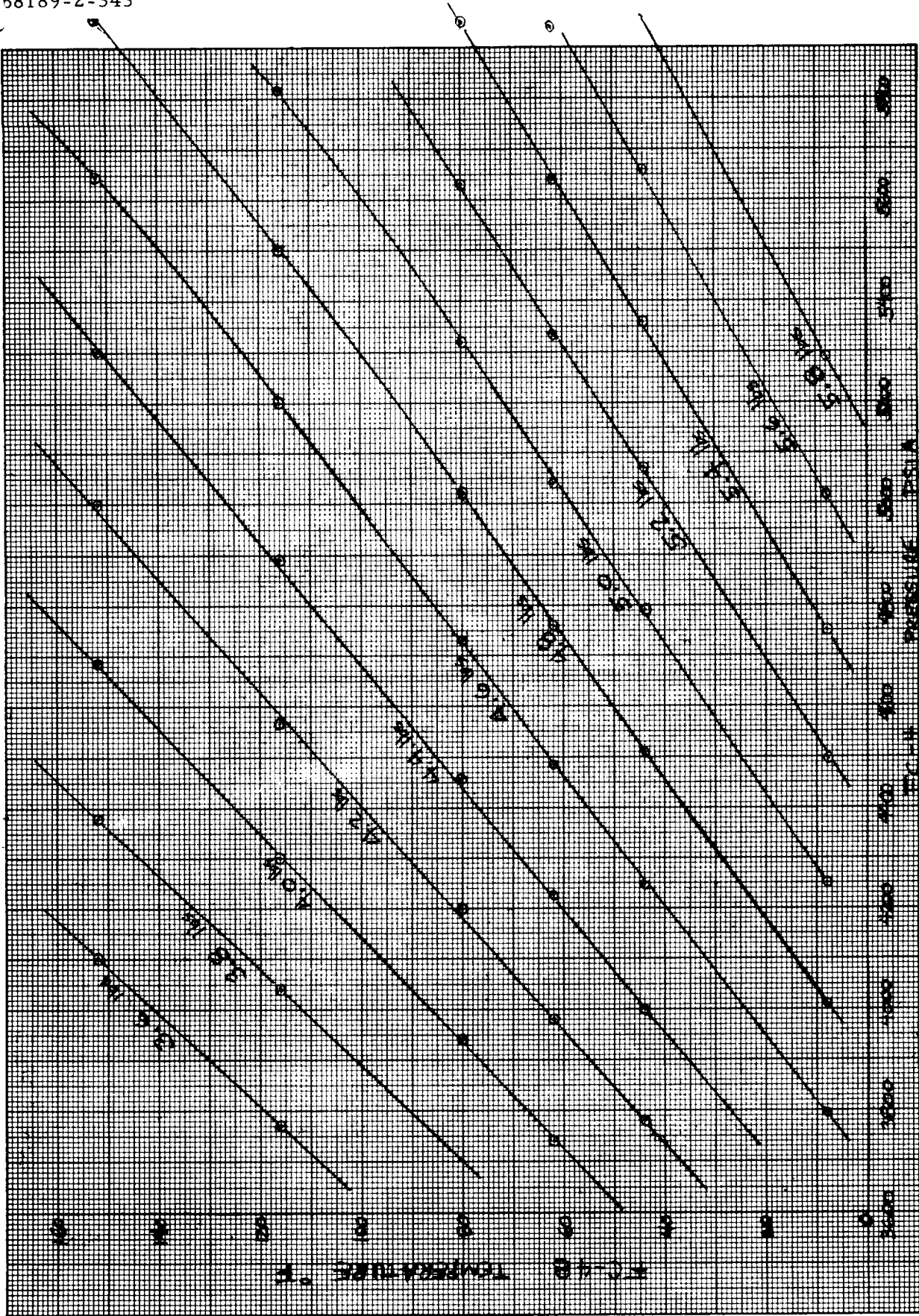


Figure 5.5-62. Attitude Control Nitrogen Supply Weight

TABLE 5.5-23. NITROGEN GAS CONSUMPTION

GMT, day:hr:min:sec	N <sub>2</sub> Pressure, psia		N <sub>2</sub> Temperature, °F		Bit Rate	N <sub>2</sub> Remaining, pounds	Total N <sub>2</sub> Used	N <sub>2</sub> Used		Expected Usage
	FC-4	Corrected	FC-48	Corrected				Event	Amount	
263:10:35	4737	4586*	80.0	79.74*	550	4.50	0	Prelaunch	0	0
13:02:58	4631	4480**	77.4		1100	4.45	0.05	Rate stabilization and sun acquisition	0.05	0.100
19:24:58	4130	4100	47.3			4.44	0.06	Canopus acquisition	0.01	0.159
264:04:00:00	3958	3970	40.2			4.42	0.08	Cruise	0.02	0.182
05:14:29								Gas jets inhibited		
06:09:47	1613	1630	6.8		137.5	2.16	2.34	Attitude maneuver and midcourse thrusting	2.26	0.288
10:13:37	1757	1760	36.7		137.5	2.16	2.34	Post nonstandard midcourse	0	

\* AFETR reading.  
 \*\*Corrected pressure readings  
 based on FC-4 Calibration Handbook,  
 10 August 1966.

### 5. 5. 5 REFERENCES

1. "SPAC Report, SC-2 Flight Control Performance," IDC 2255. 1/1803, 11 October 1966.
2. W. S. Hicks, "Preliminary Analysis of AC-7 Flight Data," General Dynamics/Aeronautics Report No. GDC-BNZ 66-053, 28 September 1966.
3. "SC-2 Telemetry Calibration Handbook," Hughes Aircraft Company, Specification 291032, 12 October 1966.
4. R. H. Bernard, "Revised Gas Jet Consumption for 66 Hour Surveyor Flight," IDC 2223/843, 19 February 1965.
5. "Surveyor System Functional Requirements," Hughes Aircraft Company, Specification 224510 Revision E, 7 January 1966.
6. L. S. Crowell, "Analysis of SC-2 Star Acquisition," IDC 2223/2570, 23 November 1966.
7. R. H. Bernard, "Limit Cycle Behavior of the Surveyor Gas Jet Attitude Control System with Simulated Canopus Sensor Noise Included in the Analog Mechanization," IDC 2223/772, 15 February 1965.
8. O. N. Hertzmann, "SC-1 Mission Performance - Flight Control Report," IDC 2223/2341, 23 June 1966.
9. K. Kobayashi, "A Method of Determining Gas Jet Thrust Level - Post Mission Analysis," IDC 2253. 4/25, 1 March 1966.
10. "Surveyor Spacecraft Post Mission Analysis Handbook - Flight Control," Hughes Aircraft Company, SSD 68117R, 5 May 1966.
11. "Spacecraft Flight Control, Model A-21," Hughes Aircraft Company, Detail Specification 234600 Revision E, 10 June 1965.
12. E. I. Axelband, "Analysis of Inertial Pointing Accuracy of Surveyor Midcourse Thrust Vector," IDC 2242/2206, 17 June 1963.
13. W. T. Thomson, Introduction to Space Dynamics, John Wiley, New York, 1961.
14. L. M. Bronstein, "Principal Axes of SC-2," IDC 2292/114, 8 November 1966.
15. S. Kubo, "FCSG 235000-9 S/N 1 Retest Data," IDC 2223/2298, 14 June 1966.

16. E. I. Axelband, "Surveyor Coast Phase Attitude Control System," IDC 2242/2780, 1 November 1963.
17. E. T. Pfund, "SPAC SC-2 Quick Quick-Look Report No. 2," IDC 2255.1/1786, 21 September 1966.
18. H. T. Lew, "Flow Versus Altitude Thrust, Surveyor Gas Jet Valves - P/N 235700," IDC 2242/2423, 12 July 1963.
19. R. H. Bernard, "Restoration and Updating of Surveyor Coast Phase Analog Computer Mechanization," IDC 2223/77, 29 July 1964.
20. R. O. Crook, "Effect of Absence of Pull-Down Resistor in Vernier Engine Logic Circuit," IDC 2223/2415, 8 September 1966.
21. B. N. Smith, "SC-2 Failure Review Board Flight Control/Prop Valve Modulation Test," IDC 2223/2476, 14 and 15 October, 1966.
22. R. O. Crook, "Reply to SC-2 Failure Review Board Action Item 10-19-11," IDC 2223/2477, 27 October 1966.
23. R. O. Crook, "Reply to SC-2 Failure Review Board Action Item 10-19-9," IDC 2223/2478, 27 October 1966.
24. R. O. Crook, "Reply to SC-2 Failure Review Board Action Item 10-19-8," IDC 2223/2540, 27 October 1966.
25. R. O. Crook, "Reply to SC-2 Failure Review Board Action Item 10-27-2," IDC 2223/2542, 31 October 1966.
26. S. Kubo, "Special Tests for Surveyor SC-2 Post Mission Analysis," IDC 2223/2544, 1 November 1966.
27. B. N. Smith and R. O. Crook, "SC-2 FRB Action Item 11-3-X Effect of Supply Voltage on Solenoid Valve Operation," IDC 2223/2552, 10 November 1966.
28. R. O. Crook, "Reply to SC-2 Failure Review Board Action Item 10-27-4," IDC 2223/2553, 10 November 1966.
29. S. Kubo, "22V Current Due to Roll Actuator," IDC 2223/2554, 11 November 1966.
30. W. N. Turner, "SC-2 Gyro and Thrust Command Telemetry Accuracies," IDC 2223/2555, 14 November 1966.
31. S. Kubo, "Special Test for Surveyor SC-2 Post Mission Analysis II," IDC 2223/2558, 14 November 1966.
32. S. Kubo, "Operation of the Roll Actuator at Reduced Bus Voltage," IDC 2223/2447, 16 November 1966.



33. H. D. Marbach, "Roll Gyro and Actuator Response at SC-2 Midcourse Startup," IDC 2223/2534, 21 November 1966.
34. L. S. Crowell, "Analysis of S/C 2 Star Acquisition," IDC 2223/2570, 23 November 1966.
35. B. N. Smith and M. R. Buehner, "SC-2 TM Strain Gage Data (Midcourse, The Two Second Burns, and The 20 Second Burn)," IDC 2223/2533, 28 November 1966.
36. P. L. Welton, "Results of Mixed, FCE/Analog Computer Simulation of SC-2 Midcourse Thrusting," IDC 2223/2562, 30 November 1966.
37. B. N. Smith and M. R. Buehner, "SC-2 Vernier Engine Ignition Times (Midcourse, The Two Second Burns and The 20 Second Burn)," IDC 2223/2563, 2 December 1966.

#### 5.5.6 ACKNOWLEDGEMENTS

This section was coordinated by B. N. Smith. Those directly responsible for the contents are:

J. R. Angerman  
L. R. Stumpf  
H. D. Marbach  
M. R. Buehner  
P. L. Welton  
R. H. Bernard



## 5.6 VERNIER PROPULSION SUBSYSTEM

### 5.6.1 INTRODUCTION

#### 5.6.1.1 System Description

The Surveyor vernier propulsion system (VPS) is a bipropellant, variable thrust, liquid rocket system utilizing an oxidizer composed of 90 percent nitrogen tetroxide and 10 percent nitric oxide (Mon 10) and a fuel composed of 72 percent monomethyl hydrazine and 28 percent water (Figure 5.6-1). The VPS consists of three regeneratively cooled thrust chamber assemblies (TCAs) with radiation cooled expansion cones. Each TCA has a variable range of 30 to 104 pounds vacuum thrust.

Propellant is supplied to the TCAs from six tanks employing positive expulsion bladders. One fuel tank and one oxidizer tank supply each TCA and are located adjacent to the TCA near each of the three spacecraft landing legs.

Propellant expulsion is accomplished by pressurizing the propellant tanks on the gas side of the bladders with helium gas. The helium is stored under high pressure in a spherical pressure vessel. The helium tank, together with the pressure regulator, dual check and relief valves, and servicing connections, is mounted outboard of the spaceframe between landing legs 2 and 3.

Thermal control of the VPS is both active and passive. Electric heaters are installed on two oxidizer tanks, one fuel tank, and on all propellant feedlines to the TCAs. Passive thermal control consists of the application of black and white paint and vapor-deposited aluminum to selected portions of the VPS, together with super insulation applied to the propellant tanks. The feedlines are wrapped with aluminum foil to deter heat loss.

#### 5.6.1.2 System Purpose

The VPS has three main functions during a Surveyor mission:

- 1) Midcourse velocity correction and attitude control
- 2) Attitude control during retro phase

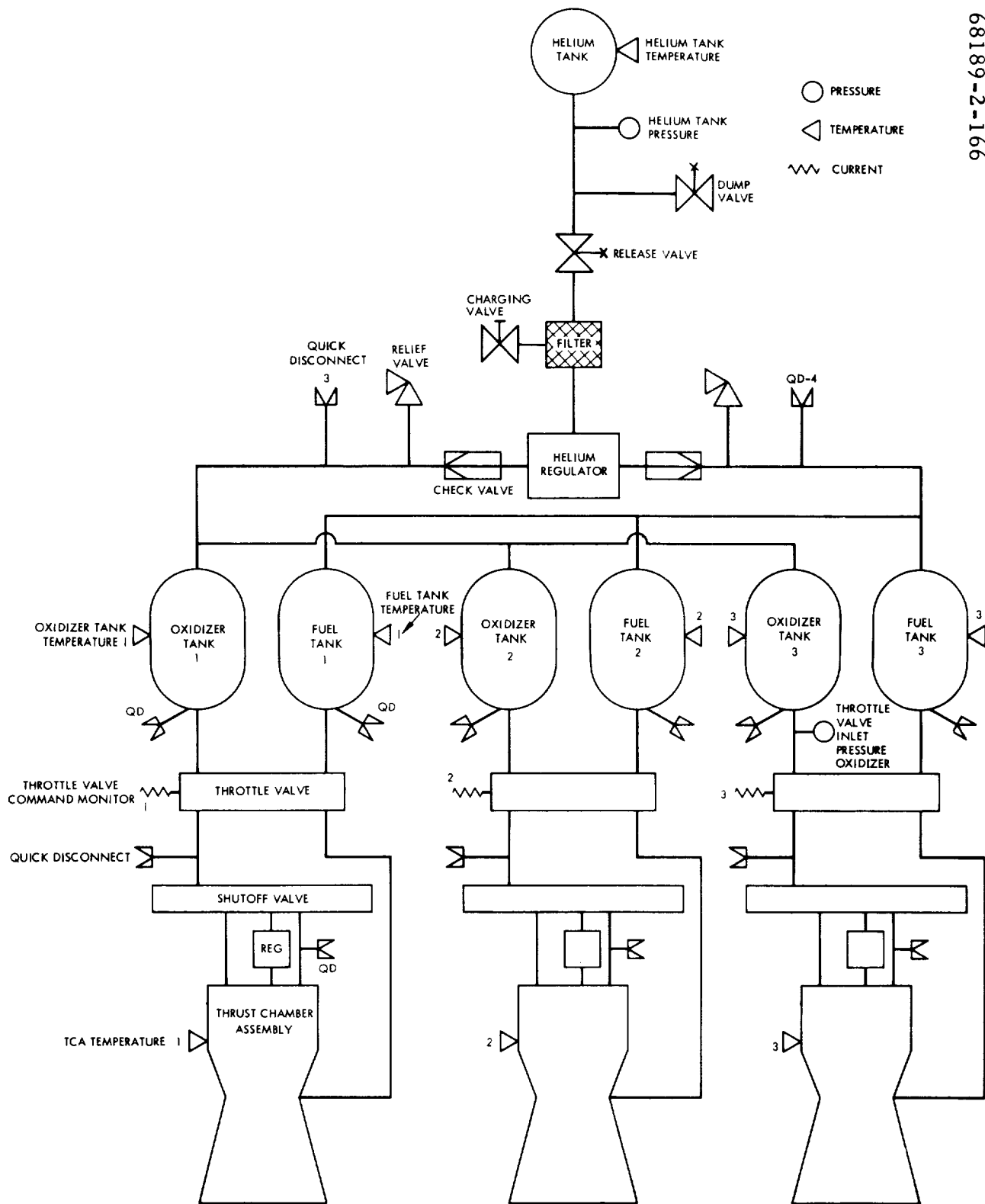


Figure 5.6-1. Vernier Propulsion System Schematic

### 3) Attitude control and velocity correction during the final descent maneuver

A midcourse velocity correction may be required to correct initial launching and injection errors. The Surveyor VPS has the capability of providing velocity corrections up to 50 m/sec with sufficient propellant remaining to successfully land the spacecraft on the moon. The required correction is transmitted to the spacecraft in the form of a desired burn time at constant acceleration of 0.1 g, which results in a thrust level of approximately 70 pounds for each of the three VPS TCAs. In addition to providing the required velocity change, the VPS also provides spacecraft attitude control during the maneuver.

Attitude control during firing of the spacecraft retro motor is provided by the VPS. The VPS is ignited approximately 1.1 seconds prior to retro ignition. Attitude control by the VPS is biased around a total vernier thrust level of either 150 or 195 pounds, depending on predictions of spacecraft attitude and velocity at retro burnout. The desired vernier thrust level is transmitted to the spacecraft several minutes prior to initiation of the retro maneuver sequence. After retro burnout, the vernier thrust level is increased to 267 pounds total thrust to further slow the spacecraft to allow the ejected retro motor case to fall clear.

Following retro motor ejection, the VPS is throttled to approximately 110 pounds total thrust under radar control. When the spacecraft intersects the first "descent segment," the VPS, operating in the closed-loop mode with the radar system, "acquires" the predetermined altitude-velocity profile and keeps the spacecraft on the profile. Each succeeding segment of the profile is acquired in a similar manner. At an altitude of 13 feet, the VPS is shut down and the spacecraft free falls to the lunar surface.

#### 5.6.1.3 General Performance Summary

##### Prelaunch

Final propulsion preparations for the SC-2 launch were begun on 1 September 1966 when propellant loading of the vernier subsystem was initiated. A total of 182.4 pounds was loaded, of which 72.2 pounds of fuel and 108.1 pounds of oxidizer were usable (Reference 1). Preloading calculations of the SC-2 propellant capacity (see subsection 5.6.4.1) indicated a total load of 182.50 pounds, of which 108.2 pounds of oxidizer and 72.1 pounds of fuel were usable. The slight differences noted are well within the specified loading tolerance of Reference 1.

The helium tank was charged on 11 September 1966 to a pressure of 5160 psia at 68°R. Telemetry readings of the tank temperature and pressure were taken on 16 September. Based on this telemetry check and prelaunch telemetry data, an "on pad" leak rate was calculated (see subsection 5.6.4.2).

The calculated leak rate was negative, indicating that any leakage during this period was less than the telemetry sensing accuracy. During the joint flight acceptance composite test, high pressure helium leakage was measured at 0.7 psi/day, which is in agreement with leakage below the telemetry sensing capability.

Thermal conditioning of the spacecraft prior to launch was maintained at 75°F. Two hours prior to launch, the shroud temperature was increased to 85°F.

Table 5.6-1 compares the predicted propulsion temperatures with the actual stabilized values just prior to increasing the shroud temperature to 85°F. All temperatures were within the shroud temperature tolerance, and all propulsion parameters appeared normal at liftoff.

TABLE 5.6-1. ACTUAL VERSUS PREDICTED TEMPERATURES

Temperature Sensor	Prelaunch		Premidcourse	
	Actual, degrees	Predicted, degrees	Actual, degrees	Predicted, degrees
P-4 leg 2 line	71.3	75	15	20-27
P-5 leg 2 fuel tank	70.1	75	46	42
P-6 leg 3 oxidizer tank	70.2	75	43	49
P-7 leg 1 TCA	71.2	75	53	65
P-8 leg 1 line	71.5	75	20	19-29
P-9 leg 3 line	71.0	75	20	20-23
P-10 leg 2 TCA	70.2	75	88	80
P-11 leg 3 TCA	70.4	75	64	70
P-13 leg 1 fuel tank	70.7	75	56	57
P-14 leg 3 fuel tank	70.3	75	53	56
P-15 leg 1 oxidizer tank	70.8	75	48	49
P-16 leg 2 oxidizer tank	71.0	75	34	37
P-17 helium tank	71.2	75	71	75

### Coast Phase I (L + 30M to L + 15H 45M)

The initial postinjection spacecraft interrogation indicated that all propulsion parameters were normal. Indication of heater operation on the leg 2 and 3 feedline heaters was noted at 13:42 and 14:26 GMT, respectively. The temperature drop rate on the leg 1 line was considerably slower, and the heater did not start cycling until 21:40 GMT.

Helium pressure increased from 5168 psia at 71.2°F at L - 2.5H to 5174 psia at 73°F at L + 15H45M (see Figure 5.6-2). Leakage calculations (see subsection 5.6.4.3) indicate a leakage rate of 776 standard cc/hr. The short interval (18.4 hours) used in this computation, coupled with the telemetry sensitivity, place a low confidence in this value. In future reports, similar leakage calculations will not be made over intervals of less than 80 hours.

The oxidizer system pressure, as indicated by the leg 3 oxidizer transducer, dropped from 215 psia at L - 2.5H to 203 psia at L + 15.5H, just prior to premidcourse maneuvers (see Figure 5.6-3). Concurrent with the 12-psi pressure drop, the average oxidizer tank temperature dropped from 70 to 45°F, causing both a decrease in tank ullage temperature and an increase in tank ullage volume resulting from propellant density increase. The pressure profile is similar to that of SC-1 (Reference 2).

Deviations from the nominal spacecraft attitude, with respect to the sun during gyro drift measurements, resulted in temporary temperature changes of the leg 2 TCA and line. The attitude deviations altered the shadow patterns on the TCA and line, causing the temperature changes.

At L + 3.5H (16:00 GMT) after cycling at a progressively slower rate, the heater on the leg 2 line remained on while the line continued to cool. The line temperature briefly rose during a gyro drift check and then continued cooling. Just prior to the initiation of 4400 bits/sec data, the line temperature was 15°F (see subsection 5.6.2.2).

At 17:00 GMT, the leg 2 oxidizer tank was decreasing in temperature slightly faster than had been predicted. At that time, the leg 2 oxidizer tank was indicating 47°F as compared with the 54°F predicted. The actual indication was well within the predictability range, and the only possible effect of the increased temperature drop would be the possibility of enabling the propellant tank heater earlier than scheduled. The most probable cause of the increased temperature drop rate is that the insulation on the tank was more tightly wrapped than on SC-1.

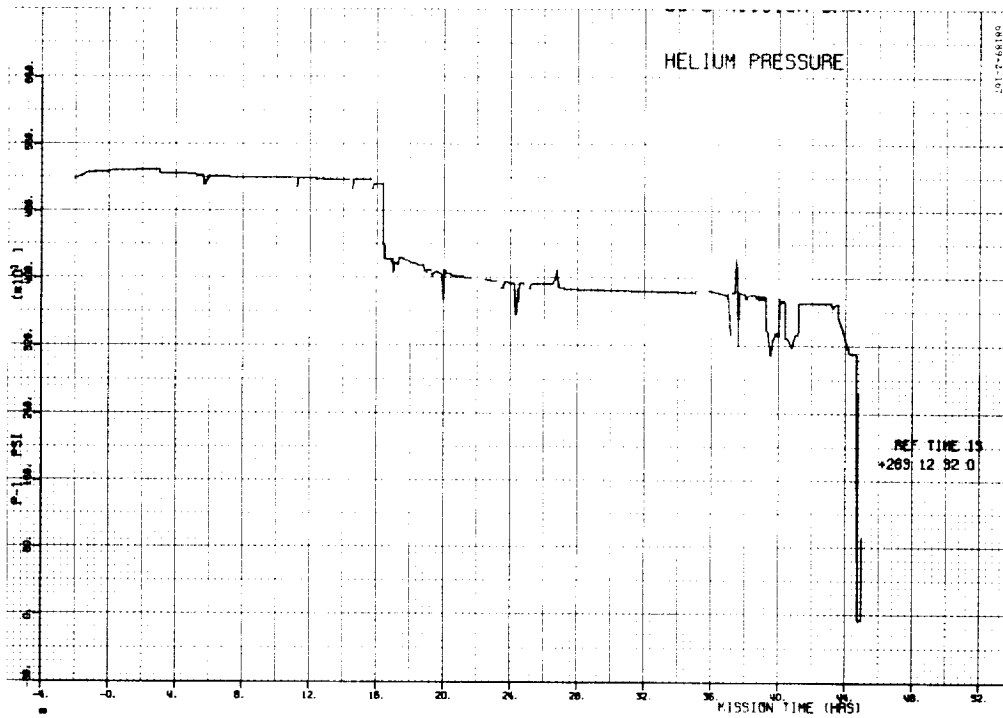


Figure 5.6-2. Mission Plot of Helium Pressure Without Voltage Correction

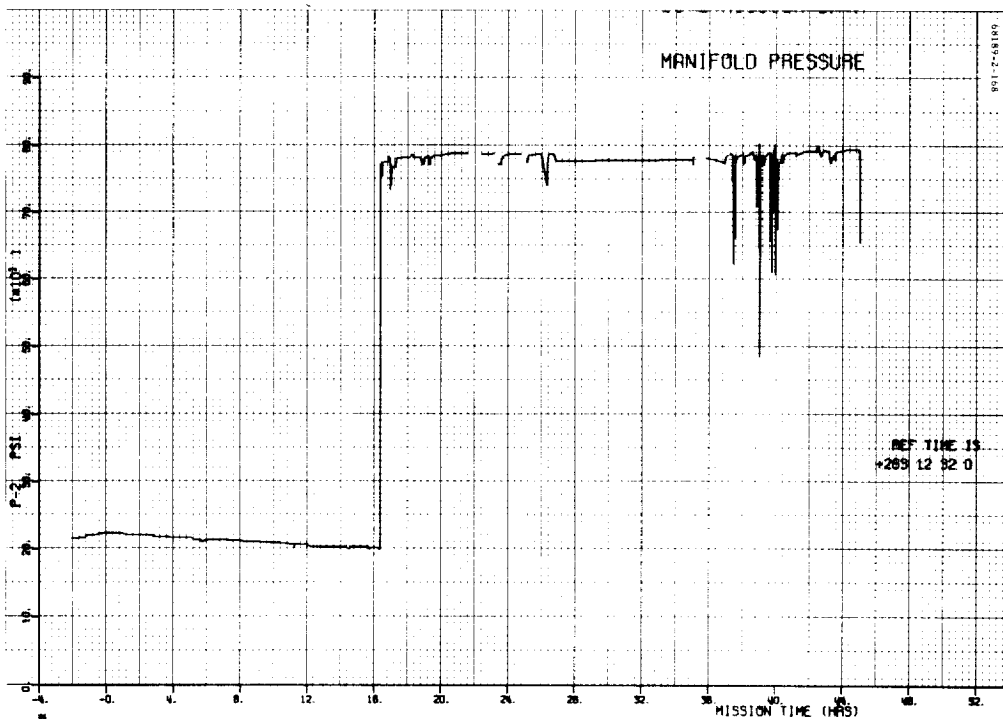


Figure 5.6-3. Mission Plot of Manifold Pressure Without Reference Voltage Correction



## Midcourse Operations

Propulsion system condition just prior to midcourse was normal, and all parameters were within their allowable range. The leg 2 oxidizer tank indicated 34° F, and the leg 2 line indicated 15° F.

The helium release squib was actuated at L + 16H21M39S, and the propellant tank pressure increased from 198 to 769 psia immediately and locked up at 777 psia prior to the midcourse correction. Corrections to this figure indicate a lockup pressure of 772 psia (see subsection 5.6.4.5). This compares favorably with the 765 to 775 psia recorded during regulator flight acceptance test.

At helium release squib actuation, the helium tank pressure dropped 739 psi from 5126 to 4387. The predicted drop was 206 psi. This difference was caused by a helium transducer zero shift experienced at squib actuation (see subsection 5.6.2.1).

At 265:05:00:02 GMT, vernier ignition was commanded on for a planned 9.81-second firing. The leg 3 TCA appeared not to ignite, and the resulting unbalanced moment from the other two TCAs caused the spacecraft to tumble. At the end of the firing, the spacecraft was tumbling at approximately one revolution per second. Since the tumbling rate exceeded the cold gas system correction capability, the gas jets were turned off shortly after firing was terminated. The standard mission ended at this point.

### 5.6.1.4 Major Vernier System Events

Table 5.6-2 lists the time of occurrence of the major events concerning or influencing the vernier propulsion system. Table 5.6-3 summarizes all anomalies affecting the propulsion subsystem.

## 5.6.2 ANOMALY DESCRIPTION

### 5.6.2.1 Pressure Transducer Zero Shift

At helium release squib actuation, an abnormally large pressure drop was noted on the helium tank pressure transducer. Based on computed ullage volumes (see subsection 5.6.4.4), the predicted pressure drop was calculated at 206 psi; the measured drop was 739 psi. A frame-by-frame examination of the data showed a 533-psi drop in helium tank pressure between two consecutive samplings of the helium tank pressure, indicating a flow rate far in excess of system ability. The helium tank pressure decay and the propellant tank pressure rise agree well with experience and with SC-1 behavior. Therefore, the instantaneous drop exhibited by these two consecutive telemetry readings indicates a zero shift in the transducer. The helium tank pressure decay and propellant tank pressure rise transients for both SC-1 and SC-2 are plotted in Figure 5.6-4. The corrected pressure

TABLE 5.6-2. MAJOR VERNIER SYSTEM EVENT COMMAND TIMES

Event	GMT, day:hr:min:sec	Mission Time, hr:min:sec
Launch	263:12:32:00	00:00:00
Pressure VPS	264:04:53:38	16:21:38
Midcourse ignition	264:05:00:02	16:28:02
End of standard mission		
Dump helium	265:09:13:16	44:41:16
Emergency AMR command	265:09:34:17	45:02:17
Vernier ignition (FC-28 telemetry)	265:09:34:27.2	45:02:27.2

Note: A complete listing of all vernier engine firings after mid-course is given in system subsection 4.1.

TABLE 5.6-3. ANOMALY SUMMARY TABLE

<u>Anomaly Number</u>	<u>Anomaly</u>
1	Helium tank pressure transducer experienced a 533-psi zero shift at helium release squib actuation.
2	Leg 2 line was cooling prior to mid-course with the heater operating.
3	Leg 3 TCA appeared not to ignite at midcourse, causing the spacecraft to tumble.

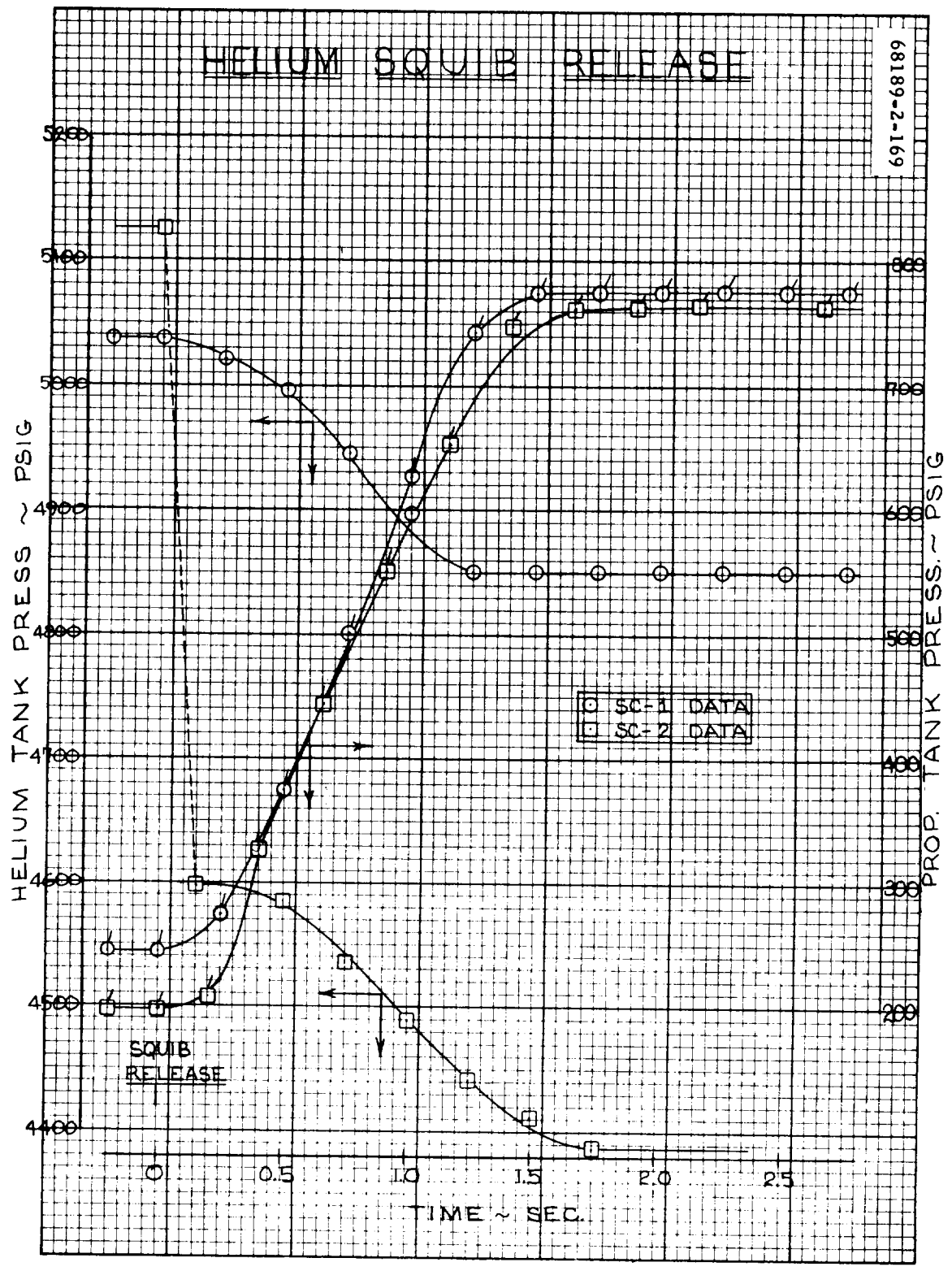


Figure 5.6-4. Helium Squib Release

drop taken from this figure is 211 psi, which compares favorably with the computed value of 206 psi. A comparison of pressure decay and rise rates between SC-1 and SC-2 shows that flow through the regulator was about equal for both spacecraft. This agreement is evidenced by the helium tank pressure decay curve slopes which are nearly the same; the SC-1 value is -150 psi/sec, and the SC-2 value is -141 psi/sec. A comparison of the two propellant tank pressure rise curves indicates that the propellant tank ullages also were nearly the same; the SC-1 rise rate was 354 psi/sec, and the SC-2 rise rate was 344 psi/sec. From this, it is concluded that a zero shift did take place and the VPS pressurization sequence was normal.

A zero shift of this type was noted in two cases during the vernier system development program (Reference 3). Both shifts were less than 200 psi, and a note inserted in the spacecraft signature list indicated a shift of up to  $\pm 150$  psi could be expected (Reference 2). The zero shift is caused by shock loading the transducer during squib actuation, and is a somewhat random function. For future spacecraft, the helium tank pressure will be displayed on an analog recorder so that any zero shift will be readily discernable.

#### 5.6.2.2 Leg 2 Line Heater Cycling Termination

The leg 2 feed line assembly indicated 85° F at launch. The line temperature dropped to 20° F at L + 1H and began to cycle between 20 and 25° F as the heater thermostat began to operate. The thermostat cycled four times between L + 1 and L + 3H. Each "power on" cycle was longer than the last. At L + 3H34M, the line temperature appeared to stabilize at 24° F, which was below the thermostat opening temperature of 25° F. The line then began to cool; just before the premidcourse maneuvers, it had reached a temperature of 15° F. A gyro drift check from L + 7 to L + 9H caused the line temperature to rise slightly, but cooling resumed at the termination of gyro drift check.

Thermal analysis concluded (see Section 5.1) that the line heater was on during the cooling period and that the heat input from the heater was less than the heat loss from the line to space. To prohibit recurrence of this problem on future spacecraft, minimum duty cycle criteria are being established for heater operation during STV testing to prevent a line with marginal thermal characteristics from being accepted.

#### 5.6.2.3 Midcourse Anomaly

At L + 16H28M02S (264:05:00:02 GMT) a 9.85-second midcourse maneuver was initiated. Detailed system-by-system data review indicated that the VPS leg 3 engine failed to ignite, while at least during the midcourse firing, leg 1 and leg 2 engines behaved properly (Reference 5). The flight control system immediately throttled leg 1 and 2 engines to minimum thrust and the leg 3 engine to maximum thrust; however, the vehicle began to tumble and, at the end of midcourse, was tumbling at approximately 1 cps.

Preliminary SPAC/SCAT analysis of oxidizer line, engine temperature, strain gage, and helium and leg 3 oxidizer temperature data (during telemetry mode 2, 32 minutes after midcourse) indicated normal behavior of legs 1 and 2, but no ignition on leg 3 TCA, probably due to failure of fuel to flow to the leg 3 TCA. Following midcourse, a series of 0.2-second and 2.0-second pulse firings were performed, with a final 21-second firing (see Table 5.6-3). While detailed analysis has not resulted in a conclusive diagnosis of the failure to ignite, some conclusions are pertinent regarding the leg 3 vernier engine:

- 1) There was evidence of oxidizer flow at less than commanded rate during all firings after midcourse, and less conclusive indication of some oxidizer flow at midcourse.
- 2) Through direct evidence or by inference, fuel flow can be demonstrated for all firings.
- 3) There was no ignition indicated on any firing attempt.

Subsequent firings possibly showed minor random anomalies as detected by quantitative thermal analysis, which is discussed at length in Section 5.1.

### 5.6.3 SUMMARY AND CONCLUSIONS

#### 5.6.3.1 Summary of Analysis Effort

A summary of the VPS performance parameters, as determined from postflight analysis, is given in Table 5.6-4 along with the predicted values.

#### 5.6.3.2 Conclusions

The following conclusions are given:

- 1) Excessive helium tank pressure drop noted at release squib actuation was due to a transducer zero shift.
- 2) Cooling of the leg 2 line with the heater operating resulted from the line having marginal thermal characteristics.
- 3) Propulsion data availability was insufficient during thrusting periods.
- 4) Positive indication of fuel subsystem pressure would have been valuable during investigation of the SC-2 failure.
- 5) Leakage calculation over time intervals of less than 80 hours are not valid and should not be repeated in future reports.

TABLE 5.6-4. ANALYSIS SUMMARY

Item	Predicted	Actual
Fuel loading	73.00 pounds	73.06 pounds
Oxidizer loading	109.50 pounds	109.34 pounds
Helium consumption at squib release	206 psi	211 psi*
Regulator lockup	765 to 775 psia	772 psia

\*Corrected for zero shift.

#### 5.6.3.3 Recommendations

The following recommendations are made:

- 1) Line and TCA temperatures should be available during thrusting.
- 2) Line heater performance during STV should be subject to more stringent acceptance criteria to detect marginal lines.
- 3) A fuel subsystem pressure measurement should be added to the vernier system telemetry to provide additional propulsion data for both transit and lunar operations.

#### 5.6.4 SUBSYSTEM PERFORMANCE ANALYSIS

##### 5.6.4.1 Predicted SC-2 Propellant Loads

###### Oxidizer System

SC-2 oxidizer system total volume

$$V_{\text{tot}} = 2228.7 \text{ in}^3 \text{ (References 6 and 7)}$$

Unusable volume trapped in lines and TCAs

$$V_{\text{tr}} = 12.6 \text{ in}^3 \text{ (Reference 8)}$$

Unusable volume due to 0.5 percent bladder expulsion inefficiency

$$V_e = 11.1 \text{ in}^3 \text{ (Reference 8)}$$

Loading tolerance = 0.75 pound

$$V_{\text{usable}} = V_{\text{tot}} - V_{\text{tr}} - V_e - \text{loading tolerance}$$

For worst-case conditions, the weight of unusable oxidizer is calculated at 0°F, the minimum expected temperature. Loading is based on zero ullage at 105°F, the maximum expected temperature. A -3σ loading tolerance is also included.

$$\begin{aligned} W_{\text{ox usable}} &= V_{\text{tot}} (\rho_{\text{ox}} 105^\circ\text{F}) - V_{\text{tr}} (\rho_{\text{ox}} 0^\circ\text{F}) - V_e (\rho_{\text{ox}} 0^\circ\text{F}) - 0.75 \\ &= (2228.7) (0.04947) - (12.6) (0.05437) - (11.1) (0.05437) \\ &\quad - 0.75 \\ &= 108.21 \text{ pounds} \end{aligned}$$

### Fuel System

SC-2 fuel system total volume

$$V_{\text{tot}} = 2229.0 \text{ in}^3 \text{ (References 6 and 7)}$$

Unusable volume trapped in lines and TCAs

$$V_{\text{tr}} = 12.9 \text{ in}^3 \text{ (Reference 8)}$$

Unusable volume due to 0.5 percent bladder expulsion inefficiency

$$V_e = 11.0 \text{ in}^3 \text{ (Reference 8)}$$

Loading tolerance = 0.75 pound

$$V_{\text{tot}_{\text{NET}}} = V_{\text{usable}} + V_{\text{tr}} + V_e$$

Fuel loading is based on a nominal oxidizer-to-fuel mixture ratio of 1.5.

$$W_{\text{f usable}} = \frac{W_{\text{ox usable}}}{1.5} = \frac{108.21}{1.5} = 72.14 \text{ pounds}$$

The total net fuel load is

$$W_{\text{f}_{\text{NET}}} = 72.14 + (12.9) (0.03586) + (11.0) (0.03586) = 73.00 \text{ pounds}$$

For a tabulation of predicted SC-2 loads at 105° F, see Table 5.6-5.

To determine the amount of propellant to be offloaded to compensate for the lower than maximum loading temperature, the total loaded propellant must be determined at the loading temperature of 70° F.

#### Oxidizer System

$$W_{\text{loaded}} = V_{\text{tot}} (\rho_{\text{ox}} 70^{\circ}\text{F}), \rho_{\text{ox}} = \text{oxidizer density}$$

$$= (2228.7) (0.05109) = 113.86 \text{ pounds}$$

$$W_{\text{offload}} = W_{70^{\circ}\text{F}} - W_{105^{\circ}\text{F}} = 113.86 - 110.25 = 3.61 \text{ pounds}$$

#### Fuel System

$$W_{\text{loaded}} = V_{\text{tot}} (\rho_f 70^{\circ}\text{F}), \rho_f = \text{fuel density}$$

$$= (2229.0) (0.03450) = 76.90 \text{ pounds}$$

$$W_{\text{offload}} = W_{70^{\circ}\text{F}} - W_{105^{\circ}\text{F}} + W_{\text{offload } 105^{\circ}\text{F}} = 76.90 - 75.14 \\ + 1.66 = 3.15 \text{ pounds}$$

For a comparison of predicted versus actual SC-2 loading, see Table 5.6-5.



TABLE 5.6-5. ACTUAL VERSUS PREDICTED  
SC-2 PROPELLANT LOADING

	SC-2 Predicted at 105°F		SC-2 Predicted at 70°F		SC-2 Actual at 70°F	
	Oxidizer	Fuel	Oxidizer	Fuel	Oxidizer	Fuel
Total loaded gross, pounds	110.25	75.41	113.86	76.90	116.42	76.15
3σ loading tolerance, pounds	0.75	0.75	0.75	0.75	0.75	0.75
Offload, pounds	0	1.66	3.61	3.15	6.33	2.34
Total loaded net, pounds at 1.5 mixture ratio	109.50	73.00	109.50	73.00	109.34	73.06
Unusable at 0°F, pounds	1.29	0.86	1.29	0.86	1.27	0.85
Total usable, pounds at 1.5 mixture ratio	108.21	72.14	108.21	72.14	108.07	72.21

5.6.4.2 Prelaunch Helium Leakage

$$PV = WZRT$$

where

P = helium tank pressure, psia

V = helium tank volume, in<sup>3</sup>

T = helium tank temperature, °R

Z = helium compressibility factor

R = helium gas constant

W = helium tank gas weight, pounds

$$\ln(P) + \ln(V) = \ln(W) + \ln(Z) + \ln(R) + \ln(T)$$

Differentiating and using  $dV$ ,  $dZ$ , and  $dR = 0$

$$\frac{dW}{W} = \frac{dP}{P} - \frac{dT}{T}$$

Dividing by  $dt$ , time

$$\frac{dW}{dt} = \frac{W}{P} \frac{dP}{dt} - \frac{W}{T} \frac{dT}{dt}$$

From Mode 2 telemetry

$$259: 18:22 \text{ GMT} \quad P_1 = 5168 \text{ psia} \quad (4 \text{ days before launch})$$

$$T_1 = 531.7^\circ \text{R}$$

$$263: 09:51 \text{ GMT} \quad P_2 = 5168 \text{ psia} \quad (3 \text{ hours before launch})$$

$$T_2 = 531.2^\circ \text{R}$$

$$P_{AV} = 5168 \text{ psia}$$

$$T_{AV} = 531.5^\circ \text{R}$$

$$Z = 1.17 \text{ (Reference 10)}$$

$$V_{HB} = 1300 \text{ in}^3 \text{ based on expansion data of burst tanks}$$

$$W_{AV} = \frac{PV}{ZRT} = \frac{(5168)(1300)}{(1.17)(386)(12)(531)} = 2.335 \text{ pounds}$$

$$\frac{dP}{dt} = \frac{5168 - 5168}{84.3} = 0 \text{ psi/hr}$$

$$\frac{dT}{dt} = \frac{531.2 - 531.7}{84.3} = -0.00593^\circ \text{R/hr}$$

$$\frac{dW}{dt} = 0 - \frac{2.335}{531} (-0.00593)$$

$$= +0.00002608 \text{ lb/hr}$$

Any leakage is below the telemetry sensing capability.

### 5. 6. 4. 3 Coast I Helium Leakage

From Mode 2 telemetry

$$263:09:51 \text{ GMT} \quad P_1 = 5168 \text{ psia} \quad (3 \text{ hours before launch})$$

$$T_1 = 531.2^\circ \text{R}$$

$$264:04:15 \text{ GMT} \quad P_2 = 5174 \text{ psia} \quad (16 \text{ hours after launch})$$

$$T_2 = 533.0^\circ \text{R}$$

$$P_{AV} = 5171 \text{ psia} \quad T_{AV} = 532.1^\circ \text{R}$$

$$Z = 1.154 \text{ (Reference 10)} \quad V_{HB} = 1300 \text{ in}^3 \text{ based on expansion data of burst tanks}$$

$$W_{AV} = \frac{PV}{ZRT} = \frac{(5171)(1300)}{(1.154)(386.2)(532.1)(12)} = 2.362 \text{ pounds}$$

$$\frac{dP}{dt} = \frac{5174-5168}{18.40} = 0.3268 \text{ psi/hr}$$

$$\frac{dT}{dt} = \frac{533.0-531.2}{18.40} = 0.0978^\circ \text{R/hr}$$

$$\frac{dW}{dt} = \frac{2.362}{5171} (0.3268) - \frac{2.362}{532.1} (0.0978) = 0.0001492 - 0.0004341$$

$$= 0.0002849 \text{ lb/hr leakage}$$

$$= \frac{0.0002849}{0.01054} \frac{\text{std ft}^3}{\text{hr}} = 0.02705 \frac{\text{std ft}^3}{\text{hr}}$$

$$= (0.02705)(1728)(16.4) \frac{\text{std cc}}{\text{hr}} = 766 \frac{\text{std cc}}{\text{hr}}$$

### 5. 6. 4. 4 Helium Consumption - Squib Release

Following the method outlined in Reference 11, initial gas weight is

$$W_{HT_1} = \frac{(5126)(1300)}{(1.16)(386)(12)(532.1)} = 2.331 \text{ pounds}$$

$$(\text{at } 460 + 72.1 = 532.1^\circ \text{R})$$

The gas volume in the propellant tanks (downstream from the squib) is

$$V_{PT} = 2228.7 + 2229.0 - \frac{109.34}{0.05244} - \frac{73.06}{0.03494}$$

$$= 4457.7 - 2085.0 - 2091.0 = 281.7 \text{ in}^3$$

The initial propellant tank gas weight is then

$$\bar{T}_g = \frac{\bar{T}_{ox} + \bar{T}_{f_o}}{2} = \frac{42.8 + 51.6}{2} = 47.2 + 460 = 507.2^\circ \text{R}$$

$$W_{PT_1} = W_{OT_1} + W_{FT_1} = \frac{(198)(281.7)}{(1)(386)(12)(507.2)} = 0.0237 \text{ pound}$$

The final propellant tank gas weight after helium release is

$$W_{PT_2} = \frac{(771)(281.7)}{(1.028)(386)(12)(532.1)} = 0.0857 \text{ pound}$$

The amount of helium transferred is then

$$W = 0.0857 - 0.0237 = 0.0620 \text{ pound}$$

The corresponding postrelease helium tank stabilized pressure at 72.1°F is

$$P_{HT_2} = 5126 \left( \frac{2.331 - 0.062}{2.331} \right) = 5126 \left( \frac{2.269}{2.331} \right) = 4990 \text{ psia}$$

The prestabilization pressure is found from

$$P_1 \left( \frac{V}{W} \right)_1^n = P_2 \left( \frac{V}{W} \right)_2^n$$

where n is the polytropic exponent from Reference 11.

$$\text{Since } V_1 = V_2$$

$$P_2 = P_1 \left( \frac{W_2}{W_1} \right)^n = 5126 \left( \frac{2.269}{2.331} \right)^{1.65}$$

$$= 5126 (0.975)^{1.65} = 5126 (0.959)$$

$$= 4920 \text{ psia (versus 4387 psia recorded)}$$

The discrepancy of -533 psia between predicted and recorded helium tank pressure must be due mainly to a zero shift in the pressure transducer (see subsection 5.6.2.1).

#### 5.6.4.5 Regulator Lockup Determination

264:10:30 GMT

$P_2 = 776.9 \text{ psia} = 775 \text{ BCD (from mode 2 telemetry)}$

Reference voltage, S1 = 998 BCD

Reference return, S2 = 0 BCD

Unbalance current, S5 = 131 BCD

The equation for correcting telemetry signals is

$$TM_{CORR} = TM_{IND} + \delta_{LD} + \delta_{A/D} + \delta_I + \delta_E$$

where

$TM_{IND}$  = actual telemetry reading

$\delta_{LD}$  = line drop correction

$\delta_{A/D}$  = analog-to-digital converter correction

$\delta_I$  = unbalance current correction

$\delta_E$  = reference voltage correction

$$\delta_I = \frac{I_{\text{unbalance}} (R_1 + R_2) (TM_{\text{REF}} - TM_{\text{IND}}) (TM_{\text{IND}})}{(TM_{\text{REF}})^2}$$

$$I_{\text{unbalance}} = 131 \text{ BCD} = -2.12 \mu\text{A}$$

$$\delta_I = \frac{(-2.62 \times 10^{-6})(2 \times 10^3)(998-775)775}{(998)(998)}$$

$$= \frac{(-5.24 \times 10^{-3})(223)(775)}{(998)(998)} = -0.9092 \times 10^3 \text{ volts}$$

$$= (-0.9092 \text{ MV}) / (4.88 \frac{\text{MV}}{\text{BCD}}) = -0.186 \text{ BCD}$$

$$\delta_E = \frac{TM_{\text{IND}}}{TM_{\text{REF}}} (993 - TM_{\text{REF}}) = \frac{775}{998} (993 - 998)$$

$$= \frac{775}{998} (-5) = -3.89 \text{ BCD}$$

$$\delta_{A/D} = +0.5 \text{ BCD}, \quad \delta_{LD} = -1.33 \text{ BCD (Reference 12)}$$

$$TM_{\text{CORR}} = 775 - 0.19 - 3.89 + 0.5 - 1.33 = 770 \text{ BCD}$$

$$P_{2 \text{ CORR}} = 771.9 \text{ psia}$$

FAT data indicates lockup at 4950 psig inlet = 775 psia

at 4000 psig inlet = 765 psia

#### 5.6.4.6 Midcourse Helium Consumption Calculations

Using the methods outlined in Reference 11

$$\Delta P = \frac{n z P_{op} V_p}{V_{HB}}$$

where

- $\Delta P$  = pressure drop,  $P_{initial} - P_{final}$ , psi  
 $n$  = polytropic exponent  
 $z$  = helium compressability factor  
 $V_{P_{op}}$  = propellant tank operating pressure, psia  
 $V_p$  = propellant volume expended, cubic inches  
 $V_{HB}$  = helium bottle volume, cubic inches

$$V_p = V_{ox} + V_f = \frac{W_{ox}}{\rho_{ox}} + \frac{W_f}{\rho_f} = \left( \frac{\dot{W}_{ox}}{\rho_{ox}} + \frac{\dot{W}_f}{\rho_f} \right) \Delta_b^t$$

where

- $V_{ox}$  = oxidizer volume expended, cubic inches  
 $V_f$  = fuel volume expended, cubic inches  
 $W_{ox}$  = oxidizer weight expended, pounds  
 $W_f$  = fuel weight expended, pounds  
 $\dot{W}$  = time rate of change of weight quantity, lb/sec  
 $\rho_{ox}$  = oxidizer density, lb/in<sup>3</sup>  
 $\rho_f$  = fuel density, lb/in<sup>3</sup>  
 $\Delta_b^t$  = burn time, seconds

$$\dot{W}_{ox} = \dot{W}_{ox1} + \dot{W}_{ox2} + \dot{W}_{ox3}$$

$$\dot{W}_f = \dot{W}_{f1} + \dot{W}_{f2} + \dot{W}_{f3}$$

Numerical subscripts refer to TCAs 1, 2, and 3.

$$\Delta P = \frac{nz P_{op} \Delta^t_b}{V_{HB}} \left( \frac{\dot{W}_{ox}}{\rho_{ox}} + \frac{\dot{W}_f}{\rho_f} \right)$$

$$= \frac{nz P_{op} \Delta^t_b}{V_{HB}} \left( \frac{\dot{W}_{ox1} + \dot{W}_{ox2} + \dot{W}_{ox3}}{\rho_{ox}} + \frac{\dot{W}_{f1} + \dot{W}_{f2} + \dot{W}_{f3}}{\rho_f} \right)$$

Assuming

$$\rho_{ox1} = \rho_{ox2} = \rho_{ox3}$$

$$\rho_{f1} = \rho_{f2} = \rho_{f3}$$

$$\dot{W}_{ox1} + \dot{W}_{f1} = \dot{W}_{1TOT} = \frac{F_1}{Isp_1}$$

where

$F_1$  is TCA thrust, pounds

$Isp_1$  is TCA specific impulse, seconds

$$MR_1 = \frac{\dot{W}_{ox1}}{\dot{W}_{f1}}$$

where

$MR_1$  = TCA propellant mixture ratio

$$\dot{W}_{ox1} = \frac{F_1}{Isp_1} - \frac{\dot{W}_{ox1}}{MR_1} = \left( \frac{MR_1}{1+MR_1} \right) \frac{F_1}{Isp_1}$$

Similarly

$$\dot{W}_{f1} = \left( \frac{1}{1+MR_1} \right) \frac{F_1}{Isp_1}$$



Substituting into the original equation

$$\Delta P = \frac{nz P_{op} \Delta^t_b}{V_{HB}} \left[ \frac{\left(\frac{MR_1}{1+MR_1}\right) \frac{F_1}{Isp_1} + \left(\frac{MR_2}{1+MR_2}\right) \frac{F_2}{Isp_2} + \left(\frac{MR_3}{1+MR_3}\right) \frac{F_3}{Isp_3}}{\rho_{ox}} + \frac{\left(\frac{1}{1+MR_1}\right) \frac{F_1}{Isp_1} + \left(\frac{1}{1+MR_2}\right) \frac{F_2}{Isp_2} + \left(\frac{1}{1+MR_3}\right) \frac{F_3}{Isp_3}}{\rho_f} \right]$$

For normal operation

$$\Delta P = \frac{nz P_{op} \Delta^t_b}{V_{HB}} \left[ \sum_{n=1}^{n=3} \frac{\left(\frac{MR_n}{1+MR_n}\right) \frac{F_n}{Ispn}}{\rho_{oxn}} + \sum_{m=1}^{m=3} \frac{\left(\frac{1}{1+MR_m}\right) \frac{F_m}{Ispm}}{\rho_{fm}} \right]$$

For no flow from 1 TCA 3:

$$\Delta P = \frac{nz P_{op} \Delta^t_b}{V_{HB}} \left[ \sum_{n=1}^{n=2} \frac{\left(\frac{MR_n}{1+MR_n}\right) \frac{F_n}{Ispn}}{\rho_{oxn}} + \sum_{m=1}^{m=2} \frac{\left(\frac{1}{1+MR_m}\right) \frac{F_m}{Ispm}}{\rho_{fm}} \right]$$

From SC-2 flight data and SC-2 TCA log books

$F_1$  commanded = 73.6 pounds

$F_2$  commanded = 52.6 pounds

$F_3$  commanded = 104 pounds

$Isp_1$  = 265 seconds

$Isp_2$  = 266 seconds

$Isp_3$  = 275 seconds

$$MR1 = 1.49$$

$$MR2 = 1.54$$

$$MR3 = 1.55$$

$$P_{op} = 754 \text{ psia}$$

$$n = 1.59$$

$$z = 1.17$$

$$\Delta t_b = 9.8 \text{ seconds}$$

$$V_{HB} = 1300 \text{ cubic inches}$$

$$T_{ox1} = 56^\circ F \quad T_{f1} = 57^\circ F \quad \rho_{ox1} = 0.05205 \text{ lb/in}^3 \quad \rho_{f1} = 0.03485 \text{ lb/in}^3$$

$$T_{ox2} = 38^\circ F \quad T_{f2} = 46^\circ F \quad \rho_{ox2} = 0.05288 \text{ lb/in}^3 \quad \rho_{f2} = 0.03506 \text{ lb/in}^3$$

$$T_{ox3} = 46^\circ F \quad T_{f3} = 54^\circ F \quad \rho_{ox3} = 0.05250 \text{ lb/in}^3 \quad \rho_{f3} = 0.03491 \text{ lb/in}^3$$

For normal commanded flow on all three TCAs:

$$\begin{aligned} \Delta P &= \frac{(1.59)(1.17)(754)(9.8)}{1300} [3.191 + 2.266 + 4.379 + 3.202 + 2.222 + 4.248] \\ &= 10.57 [19.508] = 206 \text{ psi} \end{aligned}$$

For assumption of no leg 3 oxidizer flow

$$\Delta P = 10.57 (15.13) = 160 \text{ psi}$$

For assumption of no leg 3 fuel flow

$$\Delta P = 10.57 (15.26) = 161 \text{ psi}$$

For assumption of no leg 3 oxidizer or fuel flow

$$\Delta P = 10.57 (10.88) = 115 \text{ psi}$$

The results of these calculations have been summarized in Table 5.6-6. From the measured pressure drop of 168 psi, it can be concluded that the propellant flow on the leg 3 TCA was nearly equivalent to normal oxidizer or fuel flow above, but not both.

TABLE 5.6-6. CALCULATED HELIUM CONSUMPTION FOR VARIOUS MIDCOURSE FLOW ASSUMPTIONS

TCA Propellant Flow Assumptions			Calculated Pressure Drop, $\Delta P$ , psi	Measured Pressure Drop, psi (for comparison)
Leg 1	Leg 2	Leg 3		
Normal	Normal	Normal	206	168
Normal	Normal	Fuel only	160	168
Normal	Normal	Oxidizer only	161	168
Normal	Normal	None	115	168

### 5.6.5 REFERENCES

1. "Mass Properties Monitoring Report - SC-2," Rev. C, Hughes Aircraft Company, SSD 64226R.
2. "Surveyor I Flight Performance Final Report," Volume III, Hughes Aircraft Company, SSD 68189R.
3. E. Goller to Distribution, "Failure Analysis Transducer S/N 7-5705 HT8VA TAT," IDC 2227.1/1173, 3 December 1965.
4. T. B. Shoebottom to E. T. Pfund, "Zero Shift of UPS Helium Pressure Transducer (P1)," IDC 2227.1/1330, 17 February 1966.
5. P. L. Welton to S. C. Shallon, "Results of Mixed FCE/Analog Computer Simulation of SC-2 Midcourse Thrusting," IDC 2223/2562, 30 November 1966.
6. R. A. Laird to Distribution, "VPS Propellant Tank Capacities of SC-6, SC-1, and SC-2," IDC 2227.1/1543, 13 April 1966.
7. R. A. Laird to Distribution, "Unmanifolded Surveyor Vernier Propulsion System Propellant Inventory," IDC 2227.1/761, 2 June 1965.
8. R. A. Laird to Distribution, "A21 and A21A/114 Vernier Propulsion System Propellant Inventory," IDC 2227.1/1110, 29 September 1965.
9. "Technical Manual, Operating and Maintenance Instructions - Qualification Thrust Chamber Assembly, Model TD-339," Publication No. 8984-H2A, Thiokol Chemical Corporation, Reaction Motors Division, Denville, New Jersey, 15 December 1965.
10. "Hydrogen Handbook," AFFTC, TR-60-19.
11. G. F. Pasley to Distribution, "Surveyor Vernier System Helium Utilization as determined by the S-6 TAT Program," IDC 2227.1/1125, 6 October 1965.
12. "TM Correction Factors - Special Test No. 62B," Hughes Aircraft Company Specification 227152.

### 5.6.6 ACKNOWLEDGMENTS

The following people contributed to the propulsion subsystem section:

J. Amelsberg

J. W. Putt

T. B. Shoebottom

## 5.7 MECHANISMS SUBSYSTEM

### 5.7.1 INTRODUCTION

This section of the report is concerned with the mechanical performance of the spacecraft landing legs, omnidirectional antennas, and antenna/solar panel positioner (A/SPP). For purposes of this report, these mechanisms are collectively defined as the mechanisms subsystem.

Items constituting the main headings for this analysis effort include:

- 1) Landing gear deployment
- 2) Omnidirectional antenna deployment
- 3) A/SPP automatic solar panel deployment
- 4) Mechanisms subsystem performance during nonstandard flight operations

Performance of the above equipment and functions during the mission was satisfactory. The landing gear, omnidirectional antennas, and automatic solar panel deployments were completed within the allotted time span. Telemetry signals for the landing gear and omnidirectional antenna mechanisms continued to indicate normal conditions throughout spacecraft spinning which resulted from the abnormal midcourse maneuver. However, stepping of the A/SPP was not normal while the spacecraft was spinning. This performance is covered in the section on nonstandard flight operations.

Table 5.7-1 lists the major mission events and times pertinent to the analysis of the mechanisms subsystem performance. All Centaur command and event data were taken from Reference 1.

### 5.7.2 ANOMALY DESCRIPTION

There were no anomalies in the mechanisms subsystem performance. Degraded A/SPP performance, discussed in the section on nonstandard operations, is fully attributable to abnormal loading from spacecraft spinning and is not considered anomalous.

TABLE 5.7-1. MISSION MAJOR EVENTS AND TIMES

Event	Mission Time, min:sec	GMT, hr:min:sec
Launch	0.00	12:31:59.824
Centaur extend landing gear command	11:50.22 to 51.20	12:43:50.044 to 51.024
Legs extended (V-1, V-2, and V-3 on)	11:51.26 to 53.96	12:43:51.386 to 53.784
Centaur extend omnidirectional antenna command	12:00.19 to 01.17	12:44:00.014 to 00.994
Omnidirectional antennas extended (M-1, M-2 on)	12:00.56 to 02.96	12:44:00.386 to 02.786
A/SPP solar panel unlocked (M-14 on)	12:31.76 to 34.16	12:44:31.585 to 33.985
A/SPP solar panel relocked (M-11 on)	18:31.89 to 34.29	12:50:31.717 to 34.117
A/SPP roll axis relocked (M-13 on)	22:43.88 to 46.28	12:54:43.708 to 46.108

### 5.7.3 SUMMARY AND CONCLUSIONS

#### 5.7.3.1 Performance Parameters

Table 5.7-2 compares expected and actual values for the mechanisms subsystem performance parameters.

#### 5.7.3.2 Conclusions

Mechanisms subsystem performance during landing gear deployment, omnidirectional antenna deployment, and automatic solar panel deployment was excellent in all respects. No problem was indicated.

Landing leg deployment time compares favorably with the type approval test deployment time (two deployments: 2.31 and 2.34 seconds, respectively).

TABLE 5.7-2. PERFORMANCE PARAMETERS

Parameter	Expected Value, Nominal	Measured Value
Time from Centaur extend landing gear command to legs extended indications (V1, V2, and V3 on)	2.3 seconds	1.34 to 3.74 seconds
Time from Centaur extend omnidirectional antenna command to omnidirectional antennas extended (M-1 and M-2 on)	2.4 seconds	0.37 to 2.77 seconds
Solar axis deployment time (A/SPP solar panel auto deployment)	365 seconds	360 seconds
Roll axis deployment time (A/SPP solar panel auto deployment)	255 seconds	252 seconds
Total A/SPP solar panel auto deployment time	620 seconds	612 seconds
Solar axis launch position	355 degrees	355.0 degrees
Polar axis launch position	0 degree	-1.1 degrees
Elevation axis launch position	0 degree	0.0 degree
Roll axis launch position	-59.9 degrees	-59.8 degrees
Solar axis transit position	270 degrees	271.4 degrees
Roll axis transit position	0 degree	-0.4 degree

The omnidirectional antenna deployment time agrees with the flight acceptance test data at -20° F; omnidirectional antenna A was 2.4 seconds, and omnidirectional antenna B was 1.9 seconds.

Automatic solar panel deployment time corresponds closely to the times recorded during SC-2 solar thermal vacuum retest, as shown in Table 5.7-2. Positions of the various A/SPP axes, using corrected telemetry values, were near the expected values at launch and after automatic solar panel deployment, again as shown in Table 5.7-2.

## 5.7.4 DETAILED ANALYSIS

### 5.7.4.1 Landing Gear Deployment

Table 5.7-3 shows the expected and actual times for the Centaur programmer extend landing gear command and indicates deployment completion. The uncertainty in actual times is due to the telemetry data sampling rates. The expected times are based on Centaur actual times and nominal landing gear type approval test deployment times. No anomalies of any type were noted concerning landing gear deployment.

### 5.7.4.2 Omnidirectional Antenna Deployment

Table 5.7-4 gives the expected and actual times for the Centaur programmer extend omnidirectional antennas command and time of deployment completion. The uncertainty in actual times is due to the telemetry data sampling rates. The expected times are based on Centaur actual times and nominal SC-2 omnidirectional antenna flight acceptance test deployment times. No anomalies occurred in connection with omnidirectional antenna deployment.

### 5.7.4.3 A/SPP Automatic Solar Panel Deployment

Automatic solar panel deployment of the A/SPP was completed in the prescribed manner. Telemetry signal M-9, vehicle separation, occurred at 263:12:44:25 - 27 GMT. M-4, solar panel unlock, followed at 12:44:32 - 34. Solar axis stepping commenced immediately and continued until solar panel relock, which initiated roll axis stepping. The solar panel relocked at 12:50:32 - 34, and the roll axis relocked at 12:54:44 - 46.

It is not possible to determine precisely the response of the solar and roll axes motors to the applied stepping pulses since there is no means of counting the number of pulses applied to the stepping motors during automatic deployment. However, several indicators provide substantial evidence that the response of each axis was essentially 100 percent.

Figure 5.7-1 is a plot of the roll and solar angles versus time during automatic solar panel deployment. Assuming the multivibrator pulse rate to be essentially constant, a significant number of missed steps would be indicated by a nonlinearity in the plot. A study of the plots shows no such nonlinearities.

A comparison of the SC-2 automatic solar panel deployment data with the corresponding data from SC-2 STV 2B and STV retest (Table 5.7-5) shows close correlation in deployment times.

During SC-2 STV 2B, the automatic deployment was completed in 10 minutes and 24 seconds. The number of stepping pulses required was recorded (oscillograph of EP-17), and responses of the solar and roll axes were calculated to be 97.8 and 99.3 percent, respectively. Panel deployment took 10 minutes and 20 seconds during SC-2 STV retest, but no response calculations were available since EP-17 was not recorded. From the above comparisons, it can be assumed that the solar and roll axes responses were essentially 100 percent during automatic deployment.





TABLE 5.7-3. LANDING GEAR DEPLOYMENT TIME

Event	Expected, hr:min:sec	Actual, hr:min:sec
Centaur programmer extend landing gear command	12:43:51.274	12:43:50.044 to 51.024
Legs extended indications (V1, V2, and V3 on)	12:43:53.574	12:43:51.386 to 53.784

TABLE 5.7-4. OMNIDIRECTIONAL ANTENNAS DEPLOYMENT TIME

Event	Expected, hr:min:sec	Actual, hr:min:sec
Centaur programmer extend omnidirectional antennas command	12:44:01.774	12:44:00.014 to 00.994
Omnidirectional antennas extended (M-1 and M-2 on)	12:44:04.174	12:44:00.386 to 02.786

Table 5.7-6 shows A/SPP position and related data for prelaunch and postautomatic deployment. Included also are the known launch and transit locked axes positions and the corresponding calculated positions based on corrected telemetry data and calibration coefficients from the SC-2 Spacecraft Telemetry Handbook.

The maximum difference between predictions and measured values was 1.4 degrees. This result is reasonable considering the following known SC-2 uncertainties:

<u>Potentiometer Calibration Curve Errors, rms</u>	<u>Degrees</u>
Solar axis	0.94
Polar axis	0.32
Elevation axis	0.45
Roll axis	0.16
Other signal processing errors (all axes), rms	0.98

TABLE 5.7-5. SC-2 MISSION, STV 2B, AND STV RETEST SWITCH CLOSURE TIMES

Item	SC-2 Mission	SC-2 STV 2B	STV Retest
M-14 on (solar panel unlock)	12:44:33.985	21:14:01	17:44:13
M-11 on (solar panel relock)	12:50.34.117	21:20:05	17:50:18
M-13 on (roll axis relock)	12:54:46.108	21:24:25	17:54:32
Solar axis stepping time (M-11 on - M-14 on)	360 seconds	364 seconds	365 seconds
Roll axis stepping time (M-13 on - M-11 on)	252 seconds	260 seconds	255 seconds
Total deployment time (M-13 on - M-14 on)	612 seconds	624 seconds	620 seconds

5.7.4.4 Mechanisms Subsystem Performance During Nonstandard Flight Operations

This subsection is concerned with mechanisms subsystem performance after midcourse (when the spacecraft was spinning) until contact was lost after firing of the retro rocket. Mechanism telemetry signals were normal throughout this period.

At 265:02:44:58, the polar axis was commanded in a positive direction for 240 steps. Since this axis is not pinned, there should have been a response, but telemetry indicates that no motion occurred. It is concluded that the stepping motor was unable to overcome the forces induced by spacecraft spinning.

At 265:06:35.19, command 0631, unlock solar panel (transit), was sent. This command was an error, since these pin pullers had been fired at the start of automatic solar panel deployment. The command should have been 0635, unlock solar panel (lunar). Two hundred and four stepping commands were sent to the solar axis with no response, since the solar axis was still locked in transit.

At 265:06:54:33, the correct command, 0635, was transmitted. The immediate effect of this command was a jump in axis position from 271.4 to 249.8 degrees, corrected for reference voltage (see Figure 5.7-2). It is likely that in the latter position, the solar panel had aligned itself normal to the axis of spacecraft rotation at that time. Thirty seconds after unlock, a series of 87 negative solar axis stepping commands was given. At eight

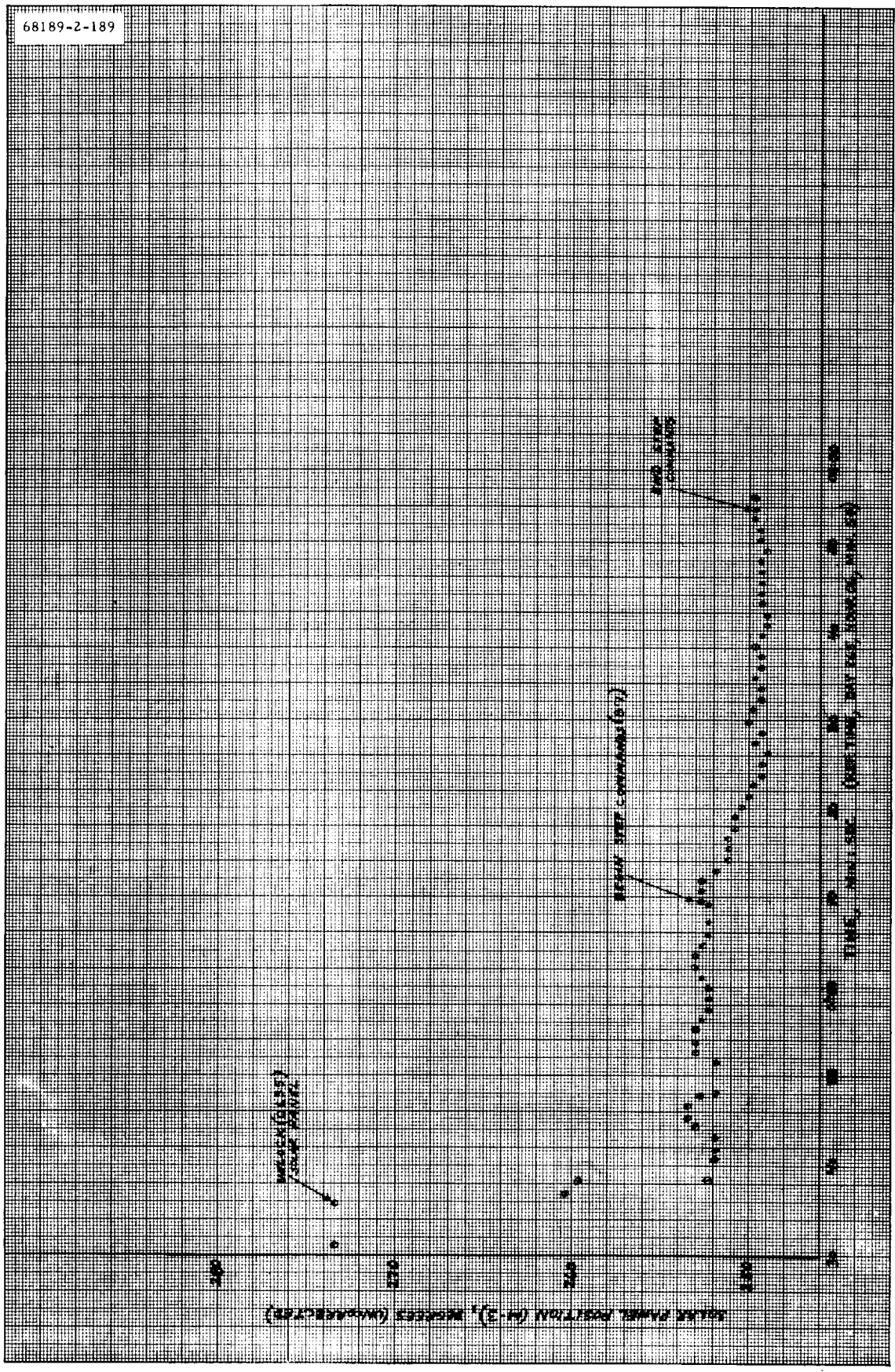


Figure 5.7-2. Solar Panel Position During Unlock and Stepping (Spacecraft Rotating)

TABLE 5.7-6. A/SPP PRELAUNCH/ POSTDEPLOY POSITION DATA (TELEMETRY MODE 4)

Signal	Raw Data		Corrected Data*	
	Prelaunch,** bcd	Post Deploy,*** bcd	Prelaunch, bcd	Post Deploy, bcd
M-3 solar axis	903	668	897	663
M-4 polar axis	378	379	375	376
M-6 elevation axis	520	521	516	517
M-7 roll axis	336	502	334	498
S-1 reference voltage	999	1001	—	—
S-2 reference return	0	0	—	—
S-5 commutator unbalance current	120	119	—	—
Position Indications Based on Calibration Coefficients and Corrected BCD Data				
Signal	Prelaunch		Postdeploy	
	Predicted Angle, degrees	Indicated Angle, degrees	Predicted Angle, degrees	Indicated Angle, degrees
M-3 solar axis	355	355.0	270	271.4
M-4 polar axis	0†	-1.1	0†	-1.1
M-6 elevation axis	0	0.0	0	0.0
M-7 roll axis	-59.9	-59.8	0	-0.4

\*Corrected per Test Requirement MS 112 through MS 117 in System Test Specification 3023926 A. (Corrections for line drop and analog-to-digital conversion were not applied as these corrections are already included in the calibration coefficients.)

\*\* From prelaunch countdown data, 20 September 1966, 10:28:57.492 GMT.

\*\*\* From 263:13:32:51 (telemetry mode 4).

† Polar axis not pinned; based on 8 September 1966 alignment data.

TABLE 5.7-7. A/SPP STEPPING COMMAND LOG

Start Time, day:hr:min:sec	Stop Time, day:hr:min:sec	Command	Quantity
263:13:20:16	263:13:20:21	0402	10
13:20:21	13:20:23	0401	5
13:21:44	13:21:49	0405	10
13:21:49	13:21:51	0406	5
265:02:44:58	265:02:52:12	0403	240
06:35:19	06:40:27	0631	5
06:41:39	06:41:44	0401	10
06:42:51	06:43:47	0402	110
06:45:41	06:45:46	0401	10
06:46:07	06:46:11	0402	10
06:46:32	06:46:37	0401	10
06:46:55	06:47:00	0402	10
06:47:17	06:47:23	0401	10
06:47:43	06:49:35	0402	34
06:54:33	Unlock solar panel (lunar)	0635	1
06:55:06	06:55:49	0402	87

steps per degree, the axis should have rotated upwards approximately 11 degrees. However, the result was only a 3-degree maximum motion, which then settled back to a net change of 2.2 degrees while stepping commands were still being sent. As in the case of the polar axis, the solar motor was not able to counteract the effect of spinning. Table 5.7-7 summarizes all stepping commands transmitted during the SC-2 mission.

#### 5.7.5 REFERENCE

"AC-7 Preliminary Test Results," General Dynamics/Convair Report GD/C-BNZ66-053, 28 September 1966.

#### 5.7.6 ACKNOWLEDGEMENT

R. J. Hausauer coordinated the mechanisms subsystem section.

